

UWMAK-III, A High Performance, Noncircular Tokamak Power Reactor Design

B. Badger, R.W. Conn, G.L. Kulcinski, C.W. Maynard, R. Aronstein, H.I. Avci, D. Blackfield, R.W. Boom, A. Bowles, E. Cameron, E.T. Cheng, R. Clemmer, S. Dalhed, J. Davis, G.A. Emmert, N.M. Ghoniem, S. Ghose, Y. Gohar, J. Kesner, S. Kuo, E. Larsen, E. Ramer, J. Scharer, D. Schluderberg, R.E. Schmunk, T.Y. Sung, I.N. Sviatoslavsky, D.K. Sze, W.F. Vogelsang, T.F. Yang, and W. Young

December 1975

UWFDM-150

FUSION TECHNOLOGY INSTITUTE

UNIVERSITY OF WISCONSIN

MADISON WISCONSIN

UWMAK-III, A High Performance, Noncircular Tokamak Power Reactor Design

B. Badger, R.W. Conn, G.L. Kulcinski, C.W. Maynard, R. Aronstein, H.I. Avci, D. Blackfield, R.W. Boom, A. Bowles, E. Cameron, E.T. Cheng, R. Clemmer, S. Dalhed, J. Davis, G.A. Emmert, N.M. Ghoniem, S. Ghose, Y. Gohar, J. Kesner, S. Kuo, E. Larsen, E. Ramer, J. Scharer, D. Schluderberg, R.E. Schmunk, T.Y. Sung, I.N. Sviatoslavsky, D.K. Sze, W.F. Vogelsang, T.F. Yang, and W. Young

Fusion Technology Institute
University of Wisconsin
1500 Engineering Drive
Madison, WI 53706

http://fti.neep.wisc.edu

December 1975

UWFDM-150

UWMAK-III, A NONCIRCULAR TOKAMAK POWER REACTOR DESIGN

July, 1976

Fusion Feasibility Study Group
Fusion Technology Program - Nuclear Engineering Dept.
University of Wisconsin
Madison, Wisconsin 53706

B. Badger
R. W. Conn
G. L. Kulcinski
C. W. Maynard
R. Aronstein[1]
H. I. Avci
D. Blackfield
R. W. Boom
A. Bowles[1]
E. Cameron
E. T. Cheng
R. Clemmer
S. Dalhed
J. Davis[2]
G. A. Emmert
N. M. Ghoniem
S. Ghose[1]
Y. Gohar
J. Kesner
S. Kuo[3]
E. Larsen
E. Ramer
J. Scharer
D. Schluderberg[4]
R. E. Schmunk[5]
T. Y. Sung
I. Sviatoslavsky
D. K. Sze
W. F. Vogelsang
T. F. Yang
W. D. Young

UWFDM-150

(1) Bechtel Corporation
(2) McDonnell-Douglas Astronautics Co.-East
(3) United Technologies Research Center
(4) Babcock and Wilcox
(5) Idaho National Engineering Laboratory

"LEGAL NOTICE"

"This work was prepared by the University of Wisconsin as an account of work sponsored by the Electric Power Research Institute, Inc. ("EPRI"). Neither EPRI, members of EPRI, the University of Wisconsin, nor any person acting on behalf of either:

"a. Makes any warranty or representation, express or implied, with respect to the accuracy, completeness, or usefulness of the information contained in this report, or that the use of any information, apparatus, method, or process disclosed in this report may not infringe privately owned rights; or

"b. Assumes any liabilities with respect to the use of, or for damages resulting from the use of, any information, apparatus, method or process disclosed in this report."

Preface and Acknowledgment

Conceptual designs of fusion reactors are a method for exploring the technological problems of fusion reactors and developing engineering solutions. They also provide the context for a detailed analysis in many specific areas, and the general results of such studies allow us to make judgments about technical directions to pursue further. We can also make judgments about less promising details. However, it is not possible to cover every potential design approach nor is it possible to exclude categorically solutions to some of the more difficult problems. Thus, this study has been carried out within a set of well-defined ground rules and the results apply within that context. We trust that, together with our earlier work and the work of many others over the past five or six years, this report contributes to the development of the basic understanding required for the new field of fusion reactor technology.

It is a pleasure to acknowledge the financial support of the Electric Power Research Institute under a contract monitored by Mr. William Gough. We also appreciate the encouragement of our University who contributed to this work both financially and by providing an environment supportive of research. This is, of course, consistent with the long standing tradition of teaching and research at Madison but it is important to note that these values have not been eroded.

In any undertaking of this magnitude, there are contributions made by many people. We therefore express our thanks to our support and secretarial staff--Ms. Connie Linehan, Ms. Suzan Steindorf, Ms. Sandy Ingham, and Mr. Richard Vacca--for their extensive efforts.

Robert W. Conn
Professor and Director
Fusion Technology Program

Gerald L. Kulcinski
Professor and Associate Director
Fusion Technology Program

TABLE OF CONTENTS

	Page
Preface and Acknowledgment	1
Table of Contents	TC-1
I. Overview of UWMAK-III	I-1-1
1. Introduction	I-1-1
2. Analysis of the Plasma	I-2-1
3. Impurity Control and Vacuum Pumping	I-3-1
4. Magnet Systems for UWMAK-III	I-4-1
a. Toroidal Field Coils	I-4-1
b. VF and OH Windings	I-4-4
5. Neutron and Photon Transport Analysis of the Blanket and Shield	I-5-1
6. Thermal Hydraulics and Mechanical Design Aspects of the Blanket Design	I-6-1
7. The Tritium Systems on UWMAK-III	I-7-1
8. Radioactivity and Afterheat in UWMAK-III	I-8-1
9. Materials	I-9-1
10. Power Conversion System	I-10-1
11. Plant Design for UWMAK-III	I-11-1
12. Survey of Materials Resource Implications of UWMAK-III	I-12-1
13. Economic Analysis	I-13-1
a. Role of the Study	I-13-1
b. Cost Estimates	I-13-2
c. A Perspective on Costs	I-13-5
d. Analysis of UWMAK-III Costs	I-13-10
14. Remarks	I-14-1
II. Plasma Analysis for UWMAK-III	II-1
A. Plasma Design for UWMAK-III	II-A-1
1. MHD Equilibrium and Stability Theory	II-A-1
2. Calculations for UWMAK-III	II-A-6
B. Startup	II-B-1
C. The RF Supplementary Heating System in UWMAK-III	II-C-1
1. Introduction to Magnetosonic Wave Heating in Tokamaks	II-C-1
2. Reactor Startup Utilizing Supplementary Fast Magnetosonic Wave Heating	II-C-3
3. Conceptual Magnetosonic Wave Launching System	II-C-7
4. Discussion	II-C-10
D. Plasma Burn Analysis	II-D-1
1. Global Balance Model for Plasma	II-D-2
2. Fluid Model of Tokamak Plasma	II-D-5
3. Plasma Burn Conditions	II-D-6

	Page
III. Divertor and Vacuum Pumping	III-A-1
A. Divertor Magnetic Field Design	III-A-1
B. Primary Vacuum Pumping Systems	III-B-1
1. General Description	III-B-1
2. Primary Vacuum Pump Layout	III-B-1
3. Primary Vacuum System Capacity and Base Pressure	III-B-2
4. Cryogenic Requirements	III-B-5
5. Chamber Evacuation and Cleanup	III-B-6
6. Cryo-Pump Regeneration	III-B-7
7. Additional Vacuum Systems	III-B-7
C. The Particle Collector Plates	III-C-1
1. Mechanical Design	III-C-1
2. Tritium Diffusion Considerations	III-C-3
3. MHD and Heat Transfer Calculations	III-C-8
IV. Magnet System	IV-A-1
A. Toroidal Field Magnets	IV-A-1
1. Specifications	IV-A-4
2. Materials	IV-A-4
3. Construction Techniques	IV-A-8
4. General Restraints and Design Factors	IV-A-12
a. Vertical and Radial Support Structure	IV-A-12
b. Radiation Damage to the Toroidal Field Magnets	IV-A-16
c. Dewars	IV-A-18
5. Lateral Support and Structural Safety	IV-A-18
6. Magnet Safety and Protection	IV-A-19
B. Vertical Field and Ohmic Heating Coils	IV-B-1
1. Specifications	IV-B-1
a. Description and Specifications	IV-V-1
b. Comparison with UWMAK-I and UWMAK-II	IV-B-4
2. Design Factors	IV-B-4
a. Design for External Stability	IV-B-4
b. Stress Analysis and Reinforcement	IV-B-6
c. Design for Internal Stability	IV-B-11
d. Coil Winding	IV-B-11
e. Dewars and Supports for the Divertor Coils	IV-B-12
3. AC Losses in Divertor and Transformer Coils	IV-B-12
a. Eddy Current Loss	IV-B-12
b. Coupling Loss	IV-C-1
c. Hysteresis Loss	IV-C-1
C. Refrigeration	IV-C-1
1. Heat Losses	IV-C-1
2. Refrigerators	IV-D-1
D. Power Supplies	IV-D-1
1. Toroidal Field Magnets	IV-D-1
2. Vertical Field and Ohmic Heating Coils	IV-D-1
3. Design of Energy Storage Inductor	IV-E-1
E. Cost Estimate	IV-E-1
1. Toroidal Field Magnets	IV-E-1
2. Vertical Field Coils	IV-E-1
3. Ohmic Heating Coils	IV-E-2
4. Refrigeration System	IV-E-2
5. Power Supplies and Energy Storage Magnet	IV-E-2
6. Entire Magnet System	IV-E-2

	Page
V. Blanket Design and Neutronics Analysis	V-A-1
A. Design Philosophy and Requirements	V-A-1
B. Blanket and Shield Calculations	V-B-1
1. Neutron Source Distribution	V-B-1
2. Nuclear Data	V-B-1
3. One Dimensional Calculations	V-B-3
4. Two Dimensional Calculations	V-B-4
C. Nonuniform Neutron Wall Loading	V-C-1
D. Biological Shielding	V-C-1
VI. Thermal Hydraulics	VI-A-1
A. The Partial ISSEC	VI-A-1
B. Outer Blanket	VI-B-1
1. Description	VI-B-1
2. MHD Calculations	VI-B-6
3. Heat Transfer Calculations	VI-B-7
C. Inner Blanket	VI-C-1
D. Thermal Storage and Heat Exchanger Systems	VI-D-1
E. Mechanical Design of Blanket and Shield	VI-E-1
1. General Description of Blanket	VI-E-1
2. Blanket Stresses	VI-E-6
3. Shield Design	VI-E-11
4. Blanket and Shield Supports	VI-E-12
5. Blanket Replacement	VI-E-14
VII. The Tritium System	VII-A-1
A. Introduction	VII-A-1
B. Basis for Design and Calculations	VII-A-1
1. Design Considerations	VII-A-1
2. Permeation Behavior	VII-A-1
C. Recovery and Reprocessing of Tritium from the Fueling Cycle	VII-C-1
1. Injection, Divertor and Cryopump	VII-C-1
2. Purification and Storage	VII-C-1
D. Recovery of Tritium from Heat Transfer Fluids	VII-D-1
1. Metals	VII-D-1
a. Outer Blanket	VII-D-1
2. Divertor Cycle	VII-E-1
E. Tritium Recovery and Control in Other Systems	VII-E-1
1. Leaks in Piping	VII-E-1
2. Shields	VII-G-1
3. Helium Turbine Seals	VII-G-1
4. Tritium Cleanup from the Reactor Building	VII-G-1
F. Tritium Inventory	VII-G-1
G. Summary and Conclusions	VII-G-1
H. Appendix	VII-H-1

	Page
VIII. Radioactivity and Afterheat	VIII-1
A. Method of Calculation	VIII-1
B. Outer Blanket and First Walls	VIII-1
1. Activity Build Up during Operation	VIII-1
2. Spatial Distribution of Activity	VIII-6
3. Activity after Shutdown	VIII-6
4. Afterheat	VIII-11
C. Hot Shield	VIII-11
D. Outer Shield and Cold Inner Shield	VIII-16
E. Nature of Activity	VIII-24
IX. Radiation Damage and Materials	IX-A-1
A. Introduction	IX-A-1
B. Reasons for the Choice of TZM for UWMAK-III	IX-A-1
1. Physical Properties	IX-B-1
2. Mechanical Properties	IX-B-6
3. Thermal Properties	IX-B-15
4. Fabrication	IX-B-26
5. Neutronics	IX-B-34
6. Chemical Compatibility	IX-B-52
7. Radiation Damage	IX-B-66
8. Availability	IX-B-66
9. Costs	IX-B-68
10. Summary	IX-B-68
C. General Radiation Effects	IX-C-1
1. Molybdenum or Its Alloys	IX-C-1
a. Neutronic Behavior	IX-C-1
b. Prior Irradiation Studies	IX-C-1
c. Bulk Effects	IX-C-4
i. Dimensional Stability	IX-C-4
ii. Mechanical Property Effects	IX-C-19
d. Surface Effects	IX-C-32
i. Sputtering	IX-C-32
ii. Blistering	IX-C-34
2. Carbon	IX-C-40
a. Vacuum Properties	IX-C-40
b. Neutron Induced Damage in Carbon	IX-C-49
i. Damage Cross Sections	IX-C-49
ii. Dimensional Instabilities	IX-C-49
iii. Effect on the Thermal Conductivities	IX-C-49
c. Sputtering of Carbon	IX-C-54
d. Effect of High Helium Content in Carbon	IX-C-60
3. Radiation Effects in Boron Carbide	IX-C-64
4. Lead	IX-C-67
5. Magnet Components	IX-C-67
a. Mylar Insulation	IX-C-67
b. Epoxy Electrical Insulator	IX-C-67
c. Aluminum Stabilizer	IX-C-71
d. TiNb Superconductor	IX-C-71
e. Support Material	IX-C-71

	Page
IX. Radiation Damage (continued)	
D. Specific Radiation Damage Effects in UWMAK-III	IX-D-1
1. Neutron Flux and Energy Spectra	IX-D-1
a. Poloidal Variation	IX-D-1
b. Variation Through Blanket and Shield	IX-D-6
2. Displacement Rates in UWMAK-III	IX-D-6
a. Poloidal Variations	IX-D-6
b. Variation of dpa Rate Through Blanket and Shield of UWMAK-III	IX-D-18
3. Helium Production Rates	IX-D-25
a. Poloidal Variations	IX-D-25
b. Spatial Variation of Helium Production	IX-D-29
4. Charged Particle Fluxes to UWMAK-III Carbon Shields	IX-D-29
5. Temperature Environment for UWMAK-III Materials	IX-D-34
6. Summary of Damage Conditions in UWMAK-III	IX-D-34
a. TZM Environment	IX-D-34
b. Carbon Environment	IX-D-39
7. Anticipated Irradiation Effects in Carbon	IX-D-39
a. Surface Effects	IX-D-39
b. Dimensional Changes in Carbon Materials	IX-D-42
i. Carbon Curtain	IX-D-42
ii. ISSEC	IX-D-42
iii. Reflector	IX-D-42
c. Changes in Thermal Conductivity of Carbon	IX-D-42
8. Anticipated Irradiation Effects in TZM	IX-D-43
a. Dimensional Changes	IX-D-43
b. Embrittlement	IX-D-45
9. Radiation Damage to Stainless Steel	IX-D-46
10. Radiation Damage to B_4C	IX-D-46
11. Radiation Damage to Lead	IX-D-46
12. Damage to Copper in the Vertical Field Coils	IX-D-46
13. Radiation Damage to Al Stabilizer	IX-D-46
14. Radiation Damage to NbTi Super Conductor	IX-D-47
15. Radiation Damage to Organic Insulation	IX-D-47
16. Summary of Major Radiation Effects in UWMAK-III	IX-D-47
X. Power Conversion System for UWMAK-III	X-1
A. Introduction	X-A-1
B. Power Conversion System Requirements and Restraints	X-B-1
C. Parametric Performance Analysis	X-C-1
1. Parametric Variation	X-C-8
2. Configuration Variation	X-C-12
D. Interface and Trade-Off Studies	X-D-1
E. Conceptual Design of System Components	X-E-1
1. Turbomachinery	X-E-3
2. Regenerator	X-E-9
3. Precooler and Intercooler	X-E-12
4. Piping Systems	X-E-12
F. Concluding Remarks	X-F-1
G. Divertor Power Cycle	X-F-4
1. Steam Generator	X-F-4
2. Reheater	X-F-4
3. Turbine-Generator	X-F-4
H. Summary of Power Cycle for UWMAK-III	X-F-9

	Page
XI. Plant Design	XI-A-1
A. Introduction	XI-A-1
B. Plant Heat Rejection System	XI-B-1
1. Energy Conversion Cycle Heat Rejection	XI-B-2
2. Shield Cooling System Heat Rejection	XI-B-2
3. Dry Cooling Towers	XI-B-3
C. Solid Radwaste Handling System	XI-C-1
1. Hot Cell Arrangement	XI-C-3
2. Container and Shipping	XI-C-3
D. Plant Electrical System	XI-D-1
E. Plant Arrangement	XI-E-1
1. General	XI-E-1
2. Containment Building	XI-E-2
a. Function	XI-E-2
b. Equipment Arrangement	XI-E-2
c. Equipment Handling	XI-E-4
d. Penetrations	XI-E-4
3. Hot Cell	XI-E-5
4. Reactor Auxiliary Building	XI-E-5
5. Heat Exchanger Building	XI-E-6
6. Turbine Building	XI-E-7
7. Control Building	XI-E-8
8. Maintenance Building	XI-E-8
9. Other Buildings and Facilities	XI-E-8
a. Radwaste Building	XI-E-9
b. Cooling Towers	XI-E-9
c. Inductive Energy Storage Building	XI-E-9
d. Helium Storage Building	XI-E-9
e. Administration Building	XI-E-10
f. Warehouse and Shop Building	XI-E-10
g. Diesel-Generator Building	XI-E-10
F. Building Design	XI-F-1
1. Plant Structure	XI-F-3
a. Containment Building	XI-F-3
b. The Heat Exchanger Building	XI-F-5
c. Turbine Building	XI-F-6
G. General Comments	XI-G-1
XII. Availability of Metals for UWMAK-III	XII-1
A. General Statement	XII-1
B. Specific Considerations for Individual Elements	XII-1
1. Aluminum	XII-1
2. Boron	XII-1
3. Chromium	XII-1
4. Niobium	XII-1
5. Iron	XII-2
6. Lead	XII-2
7. Lithium	XII-2
8. Copper	XII-2
9. Manganese	XII-2
10. Molybdenum	XII-2
11. Nickel	XII-3
12. Other Metals	XII-3

XIII. Economic Analysis	Page
A. Introduction	XIII-A-1
B. Basis of Estimate	XIII-A-1
1. Reactor Plant	XIII-B-1
2. Balance of Plant	XIII-B-1
a. Civil/Structural	XIII-B-2
b. Piping	XIII-B-3
c. Electrical Bulk Materials	XIII-B-3
d. Instrumentation	XIII-B-3
C. Estimate of Capital Cost	XIII-B-3
1. Direct Field Costs	XIII-C-1
a. Equipment	XIII-C-1
b. Labor	XIII-C-1
c. Subcontracts	XIII-C-3
2. Indirect Costs	XIII-C-3
3. Engineering Services	XIII-C-3
4. Contingency	XIII-C-4
5. Other Owner Costs	XIII-C-4
6. Interest During Construction	XIII-C-4
7. Escalation	XIII-C-5
8. Capital Cost Account Detail	XIII-C-5
D. Engineering and Construction Schedule	XIII-C-5
1. Licensing	XIII-D-1
2. Containment	XIII-D-1
3. Reactor Plant	XIII-D-1
4. Turbo-Generators	XIII-D-3
5. Other Equipment	XIII-D-3
6. Testing and Start-up	XIII-D-3
E. Cost of Electric Power	XIII-D-3
1. Operation and Maintenance Cost	XIII-E-1
a. Salaries	XIII-E-1
b. Miscellaneous Supplies and Equipment	XIII-E-1
c. Outside Support Services	XIII-E-1
d. Miscellaneous and Administrative Costs	XIII-E-1
e. Blanket Rebuilding Costs	XIII-E-1
f. Coolant Makeup	XIII-E-3
2. Fuel Costs	XIII-E-3
3. Annual Return on Capital	XIII-E-3
F. Perspective	XIII-F-1
1. Cost of Electricity Comparison	XIII-F-1
2. Comparison With Updated Previous Studies	XIII-F-1
3. Comments and Sources	XIII-F-3
G. Discussion	XIII-G-1
1. Discussion of the Perspective	XIII-G-1
2. Analysis of UWMAK-III Costs	XIII-G-2

	Page
XIV. General Conclusions	XIV-1
1. Plasma Considerations	XIV-1
a. MHD Analysis of Noncircular Plasmas	XIV-1
b. Heating of Reactor Grade Tokamak Plasmas	XIV-1
c. Spatial Plasma Profile Effects on Fractional Burnup and Tritium Inventory	XIV-2
d. Impurity Control and Divertors	XIV-2
2. Toroidal Field Magnet Design	XIV-2
3. Vacuum Systems for Tokamaks	XIV-3
4. Blanket and Shield Design	XIV-4
5. Tritium and Induced Radioactivity	XIV-5
a. Tritium	XIV-5
b. Radioactivity and Afterheat	XIV-6
6. Materials and Radiation Damage	XIV-7
a. Structural Material	XIV-7
b. Neutron Reflector and ISSEC Spectrum Shaper	XIV-7
c. Shield and Magnets	XIV-8
7. Power Cycle Analysis	XIV-9
8. Balance of Plant Analysis	XIV-11
9. Materials Resources	XIV-13
10. Economics	XIV-14
XV. Appendix A	A-1

I. Overview of UWMAK-III

1. Introduction

The UWMAK-III conceptual tokamak reactor design study has had as its principal goal the detailed, self-consistent examination of a tokamak reactor where design choices are made which represent reasonable extrapolations of present technology in the context of the general timeframe envisioned for the widespread practical application of controlled fusion. The prime examples are the choice of the molybdenum based alloy, TZM (99.4%Mo, 0.5%Ti, 0.08%Zr, 0.01%C) as the structural material and the use of aluminum as the stabilizer and structure in the toroidal field magnets. On the other hand, many of the design features are generic and therefore applicable to near term tokamaks as well. Examples here include the unique blanket design, the MHD analysis and the plasma shape, the method of particle collection in the divertor, the use of RF heating to bring the plasma to ignition conditions, the tritium extraction and recycling processes, and the general design approach to module removal.

An overall view of the UWMAK-III reactor is shown in fig.1-1 and a detailed cross section view of the nuclear island is given on fig.1-2. A summary of the major parameters and characteristics of the design is given in Table 1-1. The reactor is designed to generate 5000 MW_t during the deuterium-tritium plasma burn and 4735 MW_t continuously. The net electrical output is 1985 MW_e. The design has a number of unique features, one of which is the noncircular plasma shape produced by discrete coils outside the blanket and shield zones. The height to width ratio of the plasma is approximately 2 and the shape factor, the ratio of the circumference to the inscribed circle, is 1.6. The plasma is bounded by a separatrix with two null points symmetrically located above and below the horizontal midplane that provides for a poloidal divertor.

The reasons for choosing a noncircular cross section are to take advantage of the potential for higher total beta and therefore to increase the power density in the plasma without substantially increasing the toroidal magnetic field. The plasma current is 15.8 MA and q near the separatrix is above 3. This appears reasonable for future machines and detailed MHD calculations of plasma equilibrium and stability have been carried out to determine the final plasma shape.

A second major characteristic of UWMAK-III is its substantially reduced size compared with our earlier studies, UWMAK-I[1] and UWMAK-II[2], which have the same thermal power output during the plasma burn. The previous designs had circular plasmas with a major radius of 13m compared with 8.1m in the present study. [A comparison of the plasma shape and the toroidal field magnet size for UWMAK-II and UWMAK-III is shown in fig.1-3.] The size reduction is made possible by the design decision to increase the 14 MeV neutron wall loading from ~1 MW/m^2 previously to approximately 2 MW/m^2 in UWMAK-III and by the higher value of power density in the noncircular plasma. The higher value of neutron wall loading was in turn made possible by the unique blanket design based on the concept of using graphite as a neutron spectrum shaper to protect the first structural wall from radiation damage.[3],[4] This will be discussed shortly.

CROSS SECTION VIEW OF UWMAK III TOKAMAK POWER PLANT

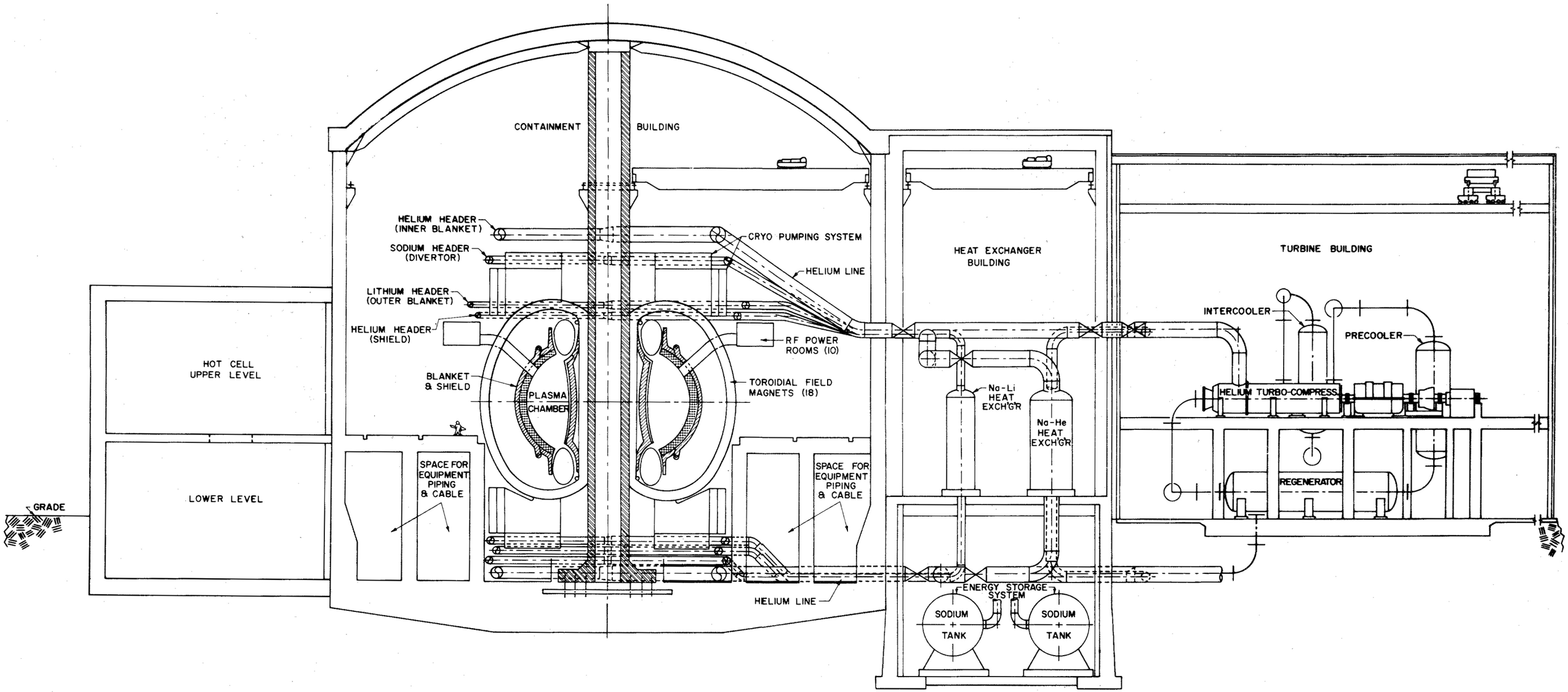

NOTES

1. FOR PURPOSE OF PRESENTATION ALL CONNECTING PIPING IS SHOWN IN THE PLANE OF THIS DRAWING.
2. EQUIPMENT & PIPING CONFIGURATIONS ARE PICTORIAL ONLY.

0 5 10 15 20

METERS

GRAPHIC SCALE

FIGURE 1-2

CROSS SECTION VIEW OF UWMAK III

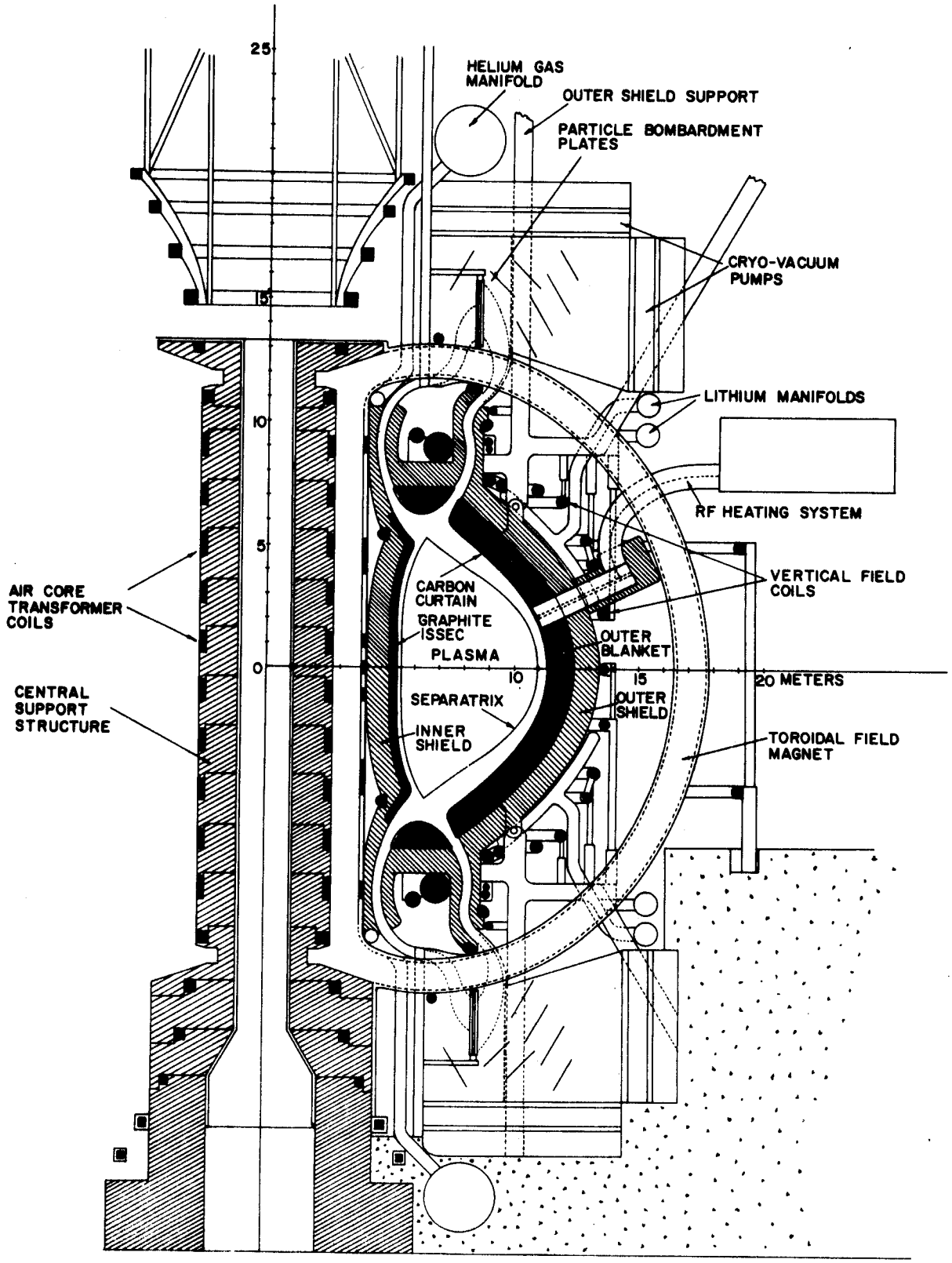

Table 1-1

MAJOR CHARACTERISTICS AND PARAMETERS OF UWMAK-III

Structural Material	Mo Alloy, TZM
Coolant	
Inner Blanket	He
Outer Blanket	Lithium
Fuel Cycle	(D-T), Li
Number of Toroidal Field Magnets	18
Magnet Superconductor	NbTi
Magnet Structural Material	Al Alloy, 2219
Maximum Magnetic Field	8.75T
On Axis Magnetic Field	4.05T
Plasma Dimensions	
Major Radius	8.1m
Half Width	2.7m
Height-to-Width Ratio	2
Plasma Shape	"Triangular D"
Plasma Current	15.8 MA
Impurity Control Method	Divertor + Low Z Liner
Plasma Heating Method	RF (Fast Wave - 60 MHz)
Burn Time	1800 sec
Duty Factor	0.947
Breeding Ratio	1.25
Average Neutron Wall Loading	2.50 MW/m^2
Power Cycle	
Blanket	Closed Cycle He
Divertor	Na-Steam
Power Output During Burn	5000 MW(th)
Average Electrical Output	1985 MW_e
Net Plant Efficiency	41.9%

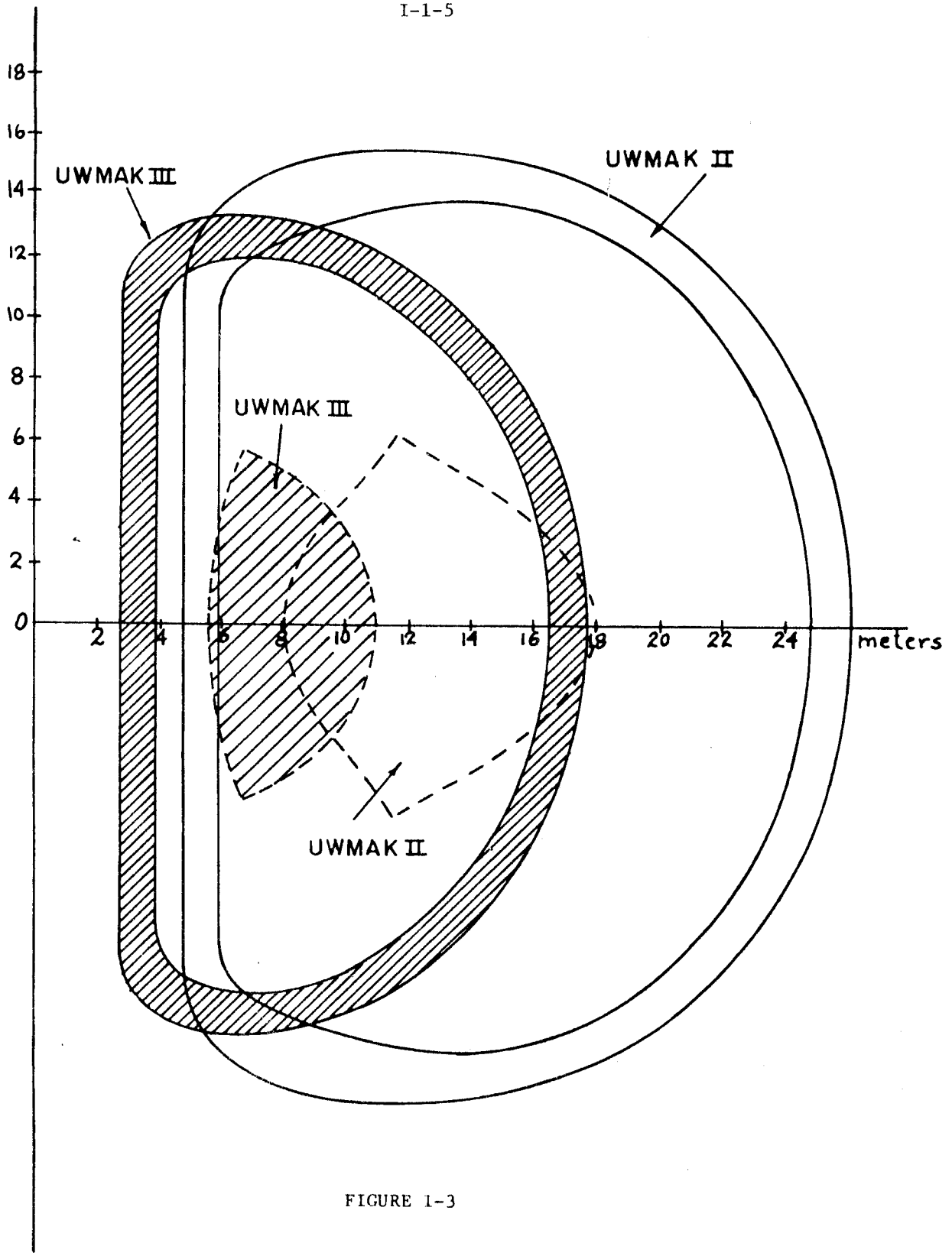
18
16
14
12
10
8
6
4
2
0
UWMAK III
UWMAK II
UWMAK III
UWMAK II
2
4
6
8
10
12
14
16
18
20
22
24
meters

FIGURE 1-3

A unique feature of the UWMAK-III is the use of RF heating to raise the plasma to ignition conditions. The purpose is to assess the potential of RF heating in reactor systems since previous studies of Tokamak reactor systems have employed neutral beam injection heating. A study has been made of several supplementary RF heating wave modes including fast magnetosonic waves at ω_{CD}, $2\omega_{CD}$ (ω_{CD} is the deuteron ion cyclotron frequency) and the two-ion hybrid resonance, lower hybrid waves, and low frequency Alfven waves. Because of the potential for generating large amounts of rf power, accessibility of the wave and energy deposition in the plasma core, and direct heating of the ions, we have concentrated our studies on the fast magnetosonic wave.

Another unusual feature in this work is the magnet design, which uses NbTi superconductor with Al as the stabilizer and a high strength Al alloy as the structural material. The use of high purity Al as the stabilizer allows one to reduce the amount of stabilizer compared to using Cu by a factor between 2 and 5. Alternatively, because the resistance of Al is lower than that for Cu, the heat generated due to I^2R losses is less when the same amount of material is used. All this makes for a better stabilizer. In addition, experiments at Wisconsin[5] have shown that when reinforced, as it is in a magnet, high purity Al does not develop a high resistivity when stressed beyond its yield point. The use of an Al alloy provides a structure of almost equal strength to the use of 316 stainless steel at about one third the weight. It also means there will be a compatible contraction of both the conductor and the structure on cool down.

The blanket and shield design is a unique feature that can be most readily understood by examining the schematic illustrated in fig.1-4. The inner blanket and shield closest to the torus centerline is <u>not</u> designed to breed tritium but only to extract heat and protect the superconducting toroidal field magnet. As such, it really constitutes a shield which is divided into hot and cold zones. Greater than 99% of the energy incident on the inner shield is deposited in the hot zone composed of structure (TZM), boron carbide (B_4C), and helium coolant. The cold inner shield uses 316 stainless steel as the structure. In front of the first wall of the inner shield is a 25 cm graphite zone which is passive (not actively cooled) and which serves to soften the neutron spectrum incident on the first structural wall. This in turn reduces the radiation damage to the structure and the inner hot shield is designed for plant life.

The outer blanket is cooled with liquid lithium which also acts as the breeding material. The overall breeding ratio is 1.25 based on toroidal geometry neutron transport calculations. The structural material in the outer blanket is not protected neutronically and therefore will have to be replaced periodically. The wall life is estimated to be about 2 years. However, the outer portion of a torus is where space is plentiful so that the difficulties involved in blanket module replacement are at least minimized.

The use of a refractory metal alloy as the structural material was primarily motivated by the desire to increase the operating temperature of the coolant to increase the overall efficiency of the power cycle. The choice of the molybdenum based alloy, TZM, over alloys of vanadium or niobium was based on the good high temperature creep strength and fatigue life of TZM, its compatibility with both helium and liquid lithium, its low permeation to tritium,

SCHEMATIC OF THE BLANKET AND SHIELD DESIGN FOR UWMAK-III

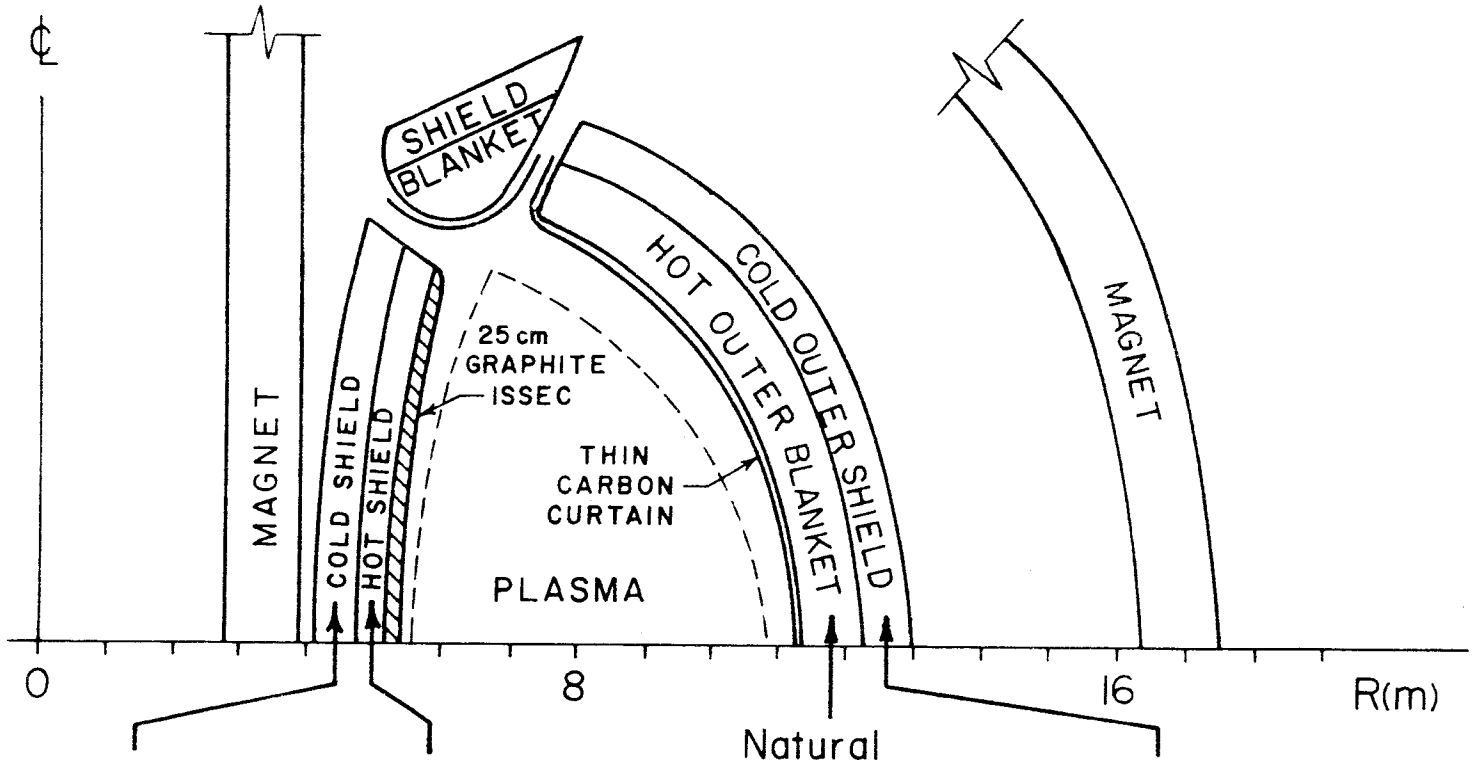

He Cooled	He Cooled	Natural Lithium Cooled	He Cooled
41.4% S.S.	56% TZM	97% Li	36% S.S.
25.9% B_4C	26% B_4C	+	36% B_4C
6.5% Al_2O_3- 2 SiO_2	18% Al_2O_3- 2 SiO_2	3% TZM + GRAPHITE REFLECTOR	18% Pb
16.2% Pb			

FIGURE I-4

its good neutronics properties, its relatively low cost and the good resource position of the United States with respect to Mo. The problem associated with joining TZM is recognized and examined in detail later on.

A final feature of the UWMAK-III design is the use of a closed cycle helium gas turbine power cycle. The coolant from the inner blanket goes directly to a helium turbine while the lithium from the outer blanket goes to an intermediate, Li-Na heat exchanger, and the sodium subsequently goes to a Na-He heat exchanger from which the He is used to drive the turbines. Sodium from the intermediate loop plays the dual role of isolating the tritium containing lithium from the power cycle and providing a working fluid for thermal energy storage which can be used during the down part of a tokamak plasma cycle to keep a continuous hot helium flow to the turbines.

In the followint sections of this overview, we present the main technical details regarding the many different aspects of the UWMAK-III conceptual design.

2. Analysis of the Plasma

Noncircular plasma cross sections offer the potential for achieving higher values of total β (the ratio of plasma to magnetic field pressure) compared with circular plasmas of equal poloidal beta, β_θ, and safety factor, q. The scaling is

$$\beta = \beta_\theta \left(\frac{S}{qA}\right)^2$$

where A is the aspect ratio and S is the plasma shape factor. For UWMAK-III, A equals 3 and S equals 1.6. Of course, the potential benefits of noncircular tokamaks will only be realized if an equilibrium plasma can be made that is stable at values of q and β_θ similar to those in circular machines. If, for example, q must be increased to maintain stability in noncircular systems, the desired increase in β will not come about.

Therefore, for UWMAK-III, a detailed MHD equilibrium and stability study has been carried out to determine the proper plasma shape and a detailed flux plot is shown in Fig. 2-1. A list of the characteristic parameters that go along with this plasma design is given in Table 2-1. The main parameters are the plasma current, 15.8 MA; the axial magnetic field, 4.05 T; the major radius, 8.1 m; plasma shape factor, 1.6; plasma height to width ratio, 2; average poloidal beta, 2.2; aspect ratio, 3; and safety factor on axis, ~1. The plasma has been satisfactorily tested for stability against rigid displacements, general kink modes, and localized interchange modes. The large triangularity of the plasma shape is the result of forcing the vacuum vertical field to have good curvature in the region to the right of the magnetic axis at R_m = 9.0 m.

The design of the transformer to drive the plasma current during startup and burn is based on an air core transformer with superconducting windings. The plasma current is assumed to rise linearly in 15 seconds to the design value of 15.8 MA. The vertical field coils, or divertor coils, provide approximately 96% of the necessary startup flux with the transformer coils providing the remaining amount. A list of all transformer and divertor coils is given in Table 2-2 together with their current carrying capabilities. The total flux swing during the current rise is 254 V-s.

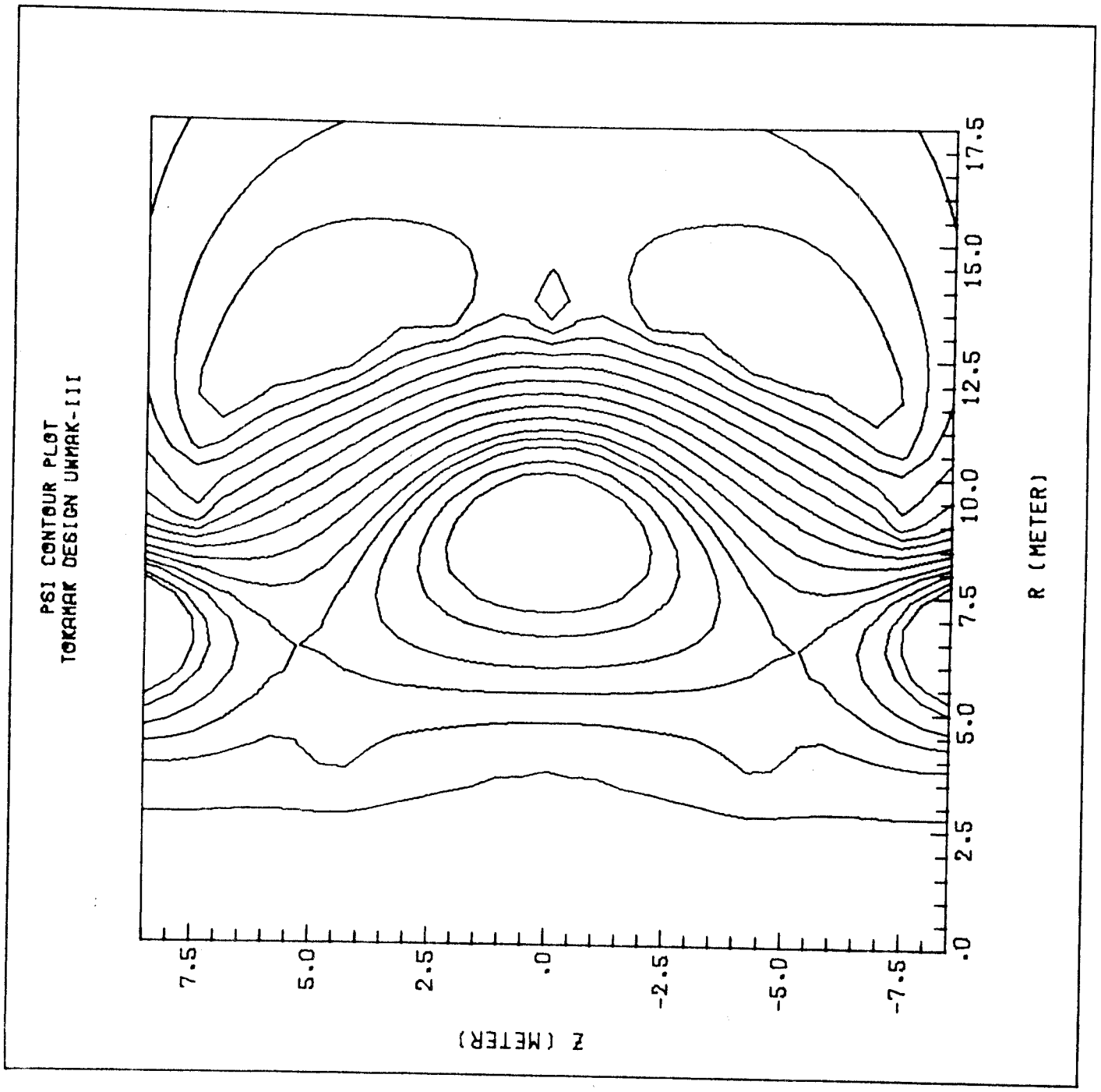
PSI CONTOUR PLOT
TOKAMAK DESIGN UWMAK-III
Z (METER)
7.5
5.0
2.5
.0
-2.5
-5.0
-7.5
.0
2.5
5.0
7.5
10.0
12.5
15.0
17.5
R (METER)

Table 2-1

Plasma Parameters of UWMAK-III

R_o = 8.1 m	I_p = 15.8 mA
B_o = 4.05 T	$\overline{\beta_0}$ = 2.2
R_{in} = 3.75 m	$q_* \cong$ 3.5
B_{max} = 8.75 T	$q_o \cong$ 1.0
R_m = 9.0 m	a = 2.7 m
R_j = 10.0 m	b $\cong$ 5.4 m
Δ_m = 0.8 m	S $\cong$ 1.6
Δ_j = 1.2 m	b/a = 2.0

Table I-2

TRANSFORMER PROGRAMMING

(All Currents in MA)

Coil Number	R(m)	±Z(m)*	Initial Current	Current -End of Startup	Current -End of Plasma Burn
T1	2.502	1.0	4.0528	3.5463	-5.1528
T2	2.508	3.0	4.0376	3.5330	-5.1336
T3	2.522	5.0	3.9900	3.4901	-5.0956
T4	2.546	7.0	3.9168	3.4273	-4.9798
T5	2.591	9.0	3.8034	3.3281	-4.8356
T6	2.675	10.997	3.5917	3.1428	-4.5665
T7	2.854	12.989	3.2211	2.8185	-4.0953
T8	3.227	14.950	2.5632	2.2429	-3.2590
T9	3.857	16.844	1.7693	1.5482	-2.2497
T10	4.725	18.643	1.1418	0.9991	-1.4516
T11	5.489	19.932	0.4159	0.3639	-0.5287
T12	19.0	5.0	0.1588	0.1390	-0.2019
T13	9.0	10.5	0.1512	0.1323	-0.1923

Divertor

Coil Number	R	±Z(m)*	I(MA)
D0	6.8	9.0	15.50
D1	3.9	0.0	.40
D2	3.9	1.0	.40
D3	4.0	4.5	2.00
D4	4.6	5.5	-0.60
D5	3.9	9.0	-1.20
D6	5.9	9.5	-2.20
D7	6.8	13.0	-1.30
D8	8.3	11.7	-4.30
D9	8.5	9.9	-3.00
D10	8.8	10.0	-1.53
D11	8.8	9.3	-1.65
D12	8.8	9.9	-1.10
D13	8.9	7.7	-1.60
D14	9.3	7.5	-1.62
D15	10.8	7.3	-1.55
D16	11.8	6.8	-1.60
D17	12.8	5.3	-1.65
D18	13.0	4.3	-1.65
D19	13.5	2.3	-1.52
D20	13.5	0.0	-1.52

*For each coil at location (R,Z), there is a similar coil at (R,-Z) except for Z = 0.

The flux swing required for the burn phase was determined using a space dependent transport model of plasma behavior. The complete reactor burn cycle is listed in Table 2-3. Using a general expression for the plasma conductivity including trapping and impurity effects, 107 V-s is necessary to drive the plasma current for 1800 s.

The power requirements during the 15 s current rise time are met by a combination of power from the grid and from an energy storage system. With UWMAK-III we propose to take 500 MW off the grid for 15 s. The remaining 413 MW that are required is provided from an inductive energy storage unit similar in design to that used in UWMAK-II.[2] The only other large power demand is for the RF heating system and that follows the current rise phase. As such, this requirement is not added to the 913 MW peak load.

The plasma reaches a temperature of only 1.8 keV during the ohmic heating phase. Thus, auxiliary heating is required to ignite the plasma and bring it to its steady state operating condition during the burn period. We have examined RF heating for this purpose and for reasons described in the introduction have chosen to concentrate on the fast magnetosonic wave at $\omega = 2\omega_{CD}$. Analysis shows that the ion cyclotron harmonic absorption term occurs in a vertical band of finite width, Δ, centered at the plasma major radius. The finite width is less than the plasma radius and is due to thermal effects and the 1/R variation of the toroidal field. R is the major radius. The energy deposited in this slab is then uniformly distributed over the flux surfaces due to the rotational transform. The expression for the ion heating profile is directly proportional to R/r, where r is the local plasma radius, and is therefore strongly peaked at the plasma center.

The existence of toroidal eigenmodes[6] also has a strong effect. In smaller devices, these eigenmodes are well separated. However, we have found that in large reactor systems like UWMAK-III, the density of toroidal eigenmodes in frequency domain becomes a near continuum. This means the eigenmodes will always be available to heat the plasma but the cumulative effect of all excited modes on the loading of the launching structure and heating efficiency is a subject requiring further research.

The theoretical expression for plasma ion heating by the fast magnetosonic wave is used together with a global model of plasma behavior[2,7] to analyze the heatup rate. At the end of the 15 s ohmic heating phase, 40 MW of RF wave heating at 60 MHz is turned on and Fig. 2-2 shows the ion and electron temperatures during this period. After 8 s the plasma reaches ignition and if the RF power is left on for 12 s, the plasma reaches the equilibrium temperature of $T_i \simeq 19$ keV, $T_e \simeq 23$ keV after 15 s.

An alternative case was considered in which 200 MW is used. In this case, ignition occurs after 1.32 s and the wave heating is turned off 0.02 s later. The ions in this case are driven to about 450 eV higher temperature than the electrons. When the supplementary heating is extinguished, the alpha heating is large enough that the plasma continues to heat and reaches equilibrium in 15 s. In this fast heatup case, it is important that the ions are heated sufficiently more than the electrons so that when the auxiliary heating is turned off, the initial small drop in ion temperature does not cause the plasma to become unignited. This scenario is shown in Fig. 2-3.

Table 2-3

UWMAK - III REACTOR CYCLE

Time(Sec).	Phase
0-15	Startup: Plasma and divertor currents rise to full value; transformer currents begin to drop.
15-30	RF Heating: Plasma and divertor currents at full value; transformer currents continue to drop.
30-1830	Burn: Transformer currents drop to maximum negative value.
1830-1850	Shutdown: Plasma and divertor currents drop to zero; transformer currents rise to provide negative startup flux.
1850-1890	Pumpout and recharge: First 20 seconds, hydrogen gas pumped into cool plasma, residual gas pumped out. Final 20 seconds; transformer currents reset to initial values.
1890-1900	Final pumpout and refill: Chamber purged and refilled with fresh fuel.

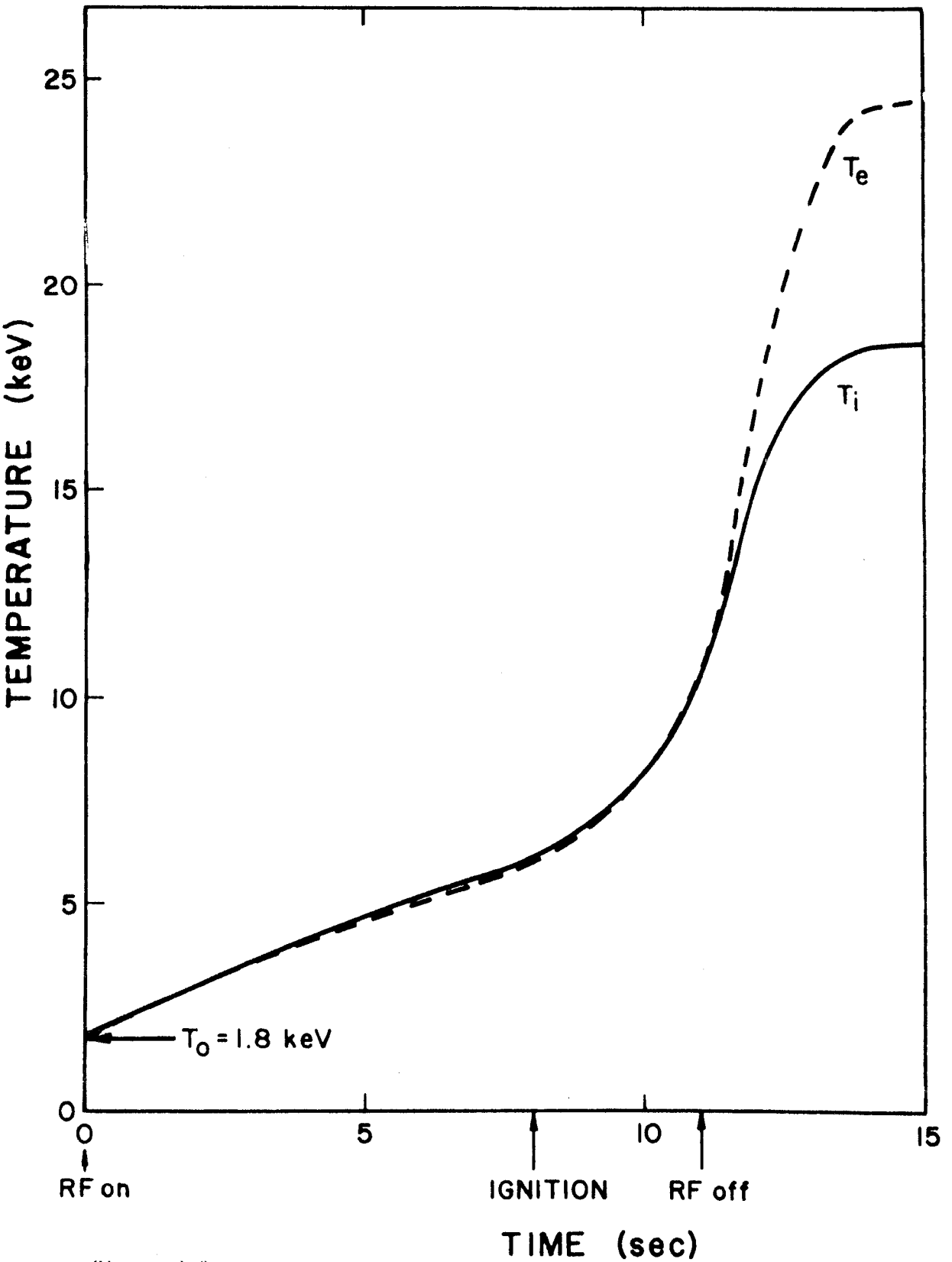

Figure 2-2 - Magnetosonic Wave Heating to Reactor Operating Conditions
P_{RF} = 40 MW

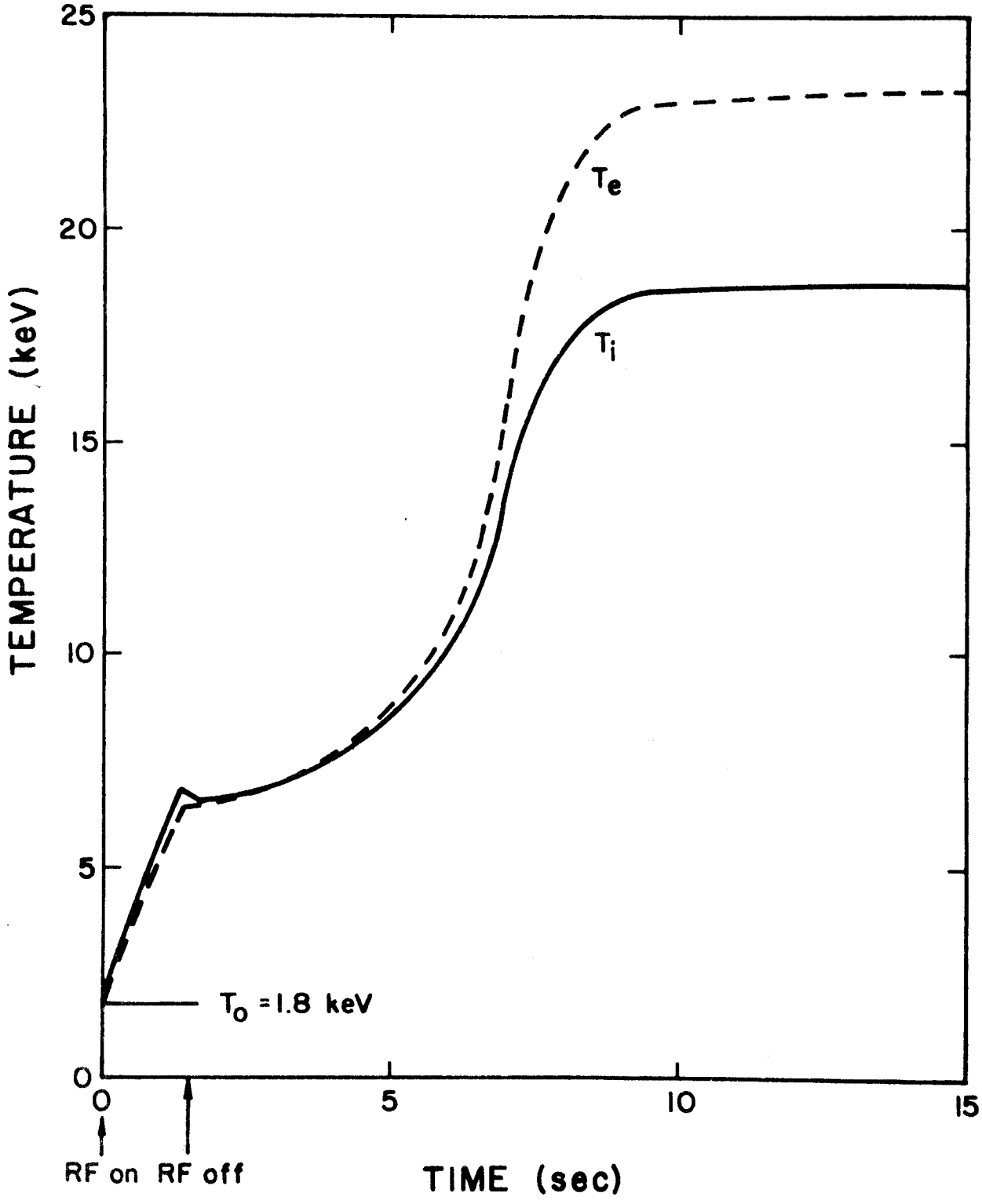

Figure 2-3 - Magnetosonic Wave Heating to Reactor Operating Conditions
P_{RF} = 200 MW

An important problem with RF heating in addition to adequate coupling of the waves to the plasma is the design of a suitable launching structure located on the torus wall. It must be capable of handling 200 MW of power at 60 MHz for a startup period of up to 15 seconds. It must have the property that the RF fields excited have a toroidal magnetic field with an orthogonal electric field as shown in Fig. 2-4-a. It must also excite desirable modes which lead to energy deposition near the plasma core. An ideal system would have a spectrum which excites lower order poloidal m values since higher order m values cause the finite ion gyroradius heating to peak further towards the plasma edge, leading to edge heating rather than core heating. In order to excite only low m numbers, the source distribution would have to cover most of the poloidal circumference. A further problem is caused by the fact that for large tokamaks such as UWMAK-III, the minor circumference is large compared to a free space wave length $2\pi a > \lambda_o$. This introduces phase shifts of a wave traveling in the poloidal direction which contribute to a higher order poloidal spectrum and reduced efficiency. A possibility for overcoming this is to introduce external circuit phase shifts which correct for the natural phase shift of the wave as it travels in the poloidal sense.

A standard rectangular waveguide launcher flush mounted in the wall as shown in Fig. 2-4-b introduces new spectral excitation problems since its toroidal dimension must be larger than half a free space wavelength for propagation of the dominant TE_{10} mode. As noted in the later sections, this can be overcome by using smaller waveguides, possibly filled with high dielectric ceramic which reduces the dimension of the guide and excites larger $k_{//}$ values. If a small excursion of conducting material into the torus can be tolerated, a strip line located over ceramic dielectric inside a rectangular guide could be envisioned which does not have a cut-off limitation due to small aperture size. The conducting strip would have to be coupled to the torus by making a small loop which is electrically connected to the bottom of the guide.

The constraints on the design of the RF power system are as follows: It is assumed that up to 200 MW are provided by as many as twelve separate feed systems placed in pairs located toroidally around the device, with a minimum cross sectional area of the feed so that the field strengths remain below the breakdown level. While the magnitude of electric field strengths for 60 MHz breakdown in a tokamak environment are not precisely known, several estimates are indicated in the literature. In UWMAK-III, we adopt the criteria that the RF field be held to a maximum of 3 kV/cm in the RF feeds during startup. It would be preferable if the startup neutral pressure outside the plasma confinement region was below 10^{-5} Torr, but 10^{-4} Torr is all that can be accommodated given the large device size, pumping capacity, and limited pumping area.

The design of the waveguide feed is obtained subject to the following conditions: (1) each element of the launching structure must be capable of supplying 17 MW of power with a maximum electric field strength of 3 kV/cm. (2) The ratio of wave frequency to cutoff frequency of the feed must be greater than 1.2 in order that the attenuation in the guide due to skin effect is not too large. If we require that the feed be a vacuum region then one can consider

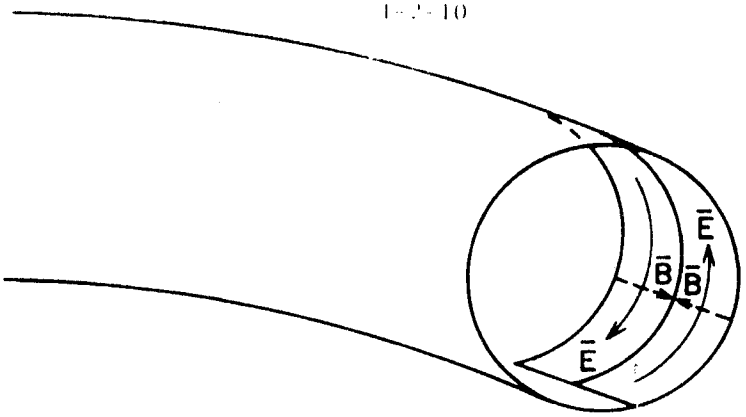

a) IDEALIZED MAGNETOSONIC WAVE FIELD SOURCE DISTRIBUTION :
$k_{||}$ = 6-10 m^{-1} AND DOMINANT m = 0, ±1, ±2 EXCITATION

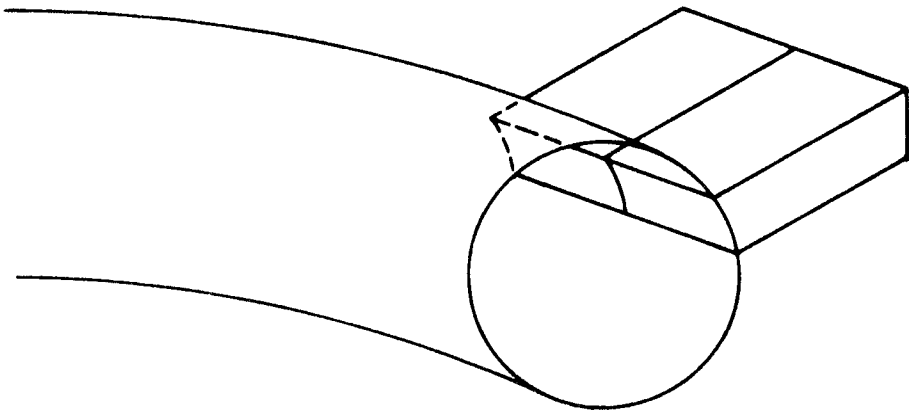

b) EXCITATION BY MEANS OF STANDARD WAVEGUIDES

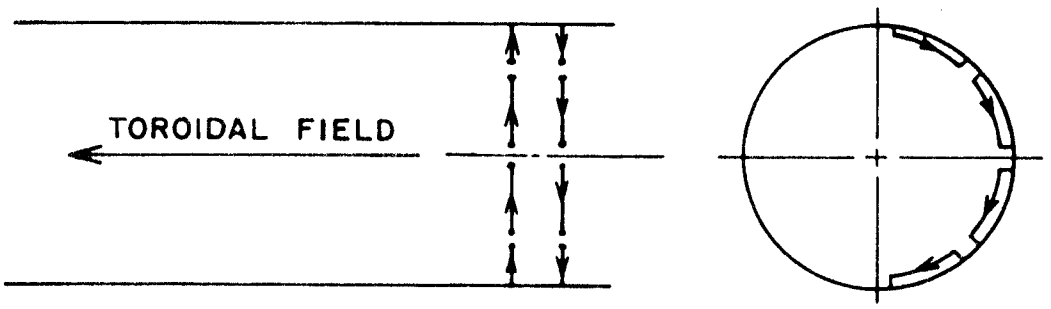

c) HOOP EXCITATION

Figure 2-4 - Considerations for Magnetosonic Wave Heating Launching Structure

two types. In all cases,due to a lower cost of fabrication, it is advisable to consider a copper coaxial line running most of the distance from the RF source to the torus with a 1 m diameter. A coaxial to waveguide transition could be made near the torus wall.

If the neutron and plasma flux to the launching aperture during startup dictate a vacuum filled waveguide, the following designs can be considered. A rectangular guide with a ratio of wave frequency to cutoff frequency of $f/f_c = 1.2$ for the TE_{10} mode. This would require a toroidal inner dimension of 3 m and a poloidal dimension of 1.5 m as shown in Fig. 2-5. A waveguide of this size with the imposed maximum field intensity of 3 kV/cm would have a theoretical power injection energy capability of 500 MW and a wave impedance of 190 ohms.

For the design used in UWMAK-III, a ridged waveguide has been considered in order to reduce the toroidal extent of the guide for improved wave penetration and heating. This reduces the mode conversion potential and provides a means of determining the fraction of wave power initially deposited in the ions vs the electrons. The H-shaped guide would have the inner dimensions of 1 m high by 1 m wide with a gap width of 8.7 cm which is 50 cm in extent as shown in Fig. 2-5. The wave impedance of the dominant TE_{10} mode is 70 ohms and the theoretical power carrying capability is 30 MW.

If neutron and plasma heating of the guide aperture during startup are not too severe, a guide which is partially or fully filled with a dielectric medium can be considered. Alumina ceramic (Al_2O_3) has a relative dielectric constant of $\epsilon_r = 8$, a loss tangent of 10^{-4}, and a maximum temperature of operation of 1500-1900°C. A ridged waveguide which is filled with ceramic 50 cm wide by 50 cm high with a 10 cm gap can be designed as shown in Fig.2-5. The wave impedance is 40 ohms and a theoretical power transfer of 60 MW can be obtained.

It is evident from this discussion that several alternatives for the design of magnetosonic wave launching structures exist. Much further analytical work in relating a given wave source distribution on the torus wall to the heating deposition profiles in the plasma is required. However, with the analysis that has been done to date we put forth a recommendation.

From purely a plasma point of view, we would propose a wave source distribution that goes half way around the minor cross section on the outside edge. A second source located very close to the first but shifted in phase by 180° is proposed in order to set up short wavelengths, $\lambda = 1$ m, in the toroidal sense.

While the above is optimum for plasma physics consideration, it presents obvious problems from the viewpoint of overall vertical field coil placements and access. The added complexity led us in the first place to the design approach shown in Fig. 2-4-b. This was used as the basis in locating the equilibrium vertical field coils used in the MHD analysis described earlier. Again, while we have used this as the base case and shown this layout in Fig. I-2 of the overview, we note again that the wavelaunching system spread out poloidally as shown in Fig. 2-6 would be more optimum from the point of view of wave heating of the plasma.

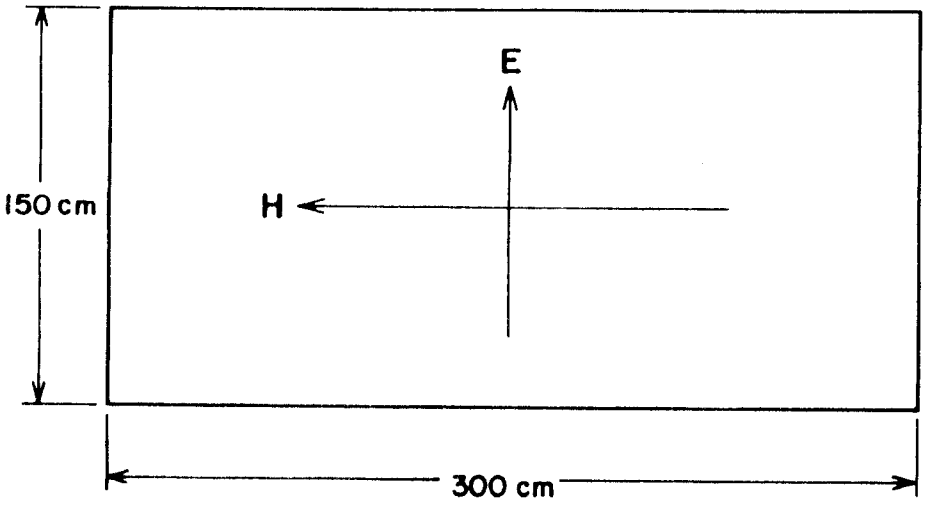

a) STANDARD RECTANGULAR WAVEGUIDE

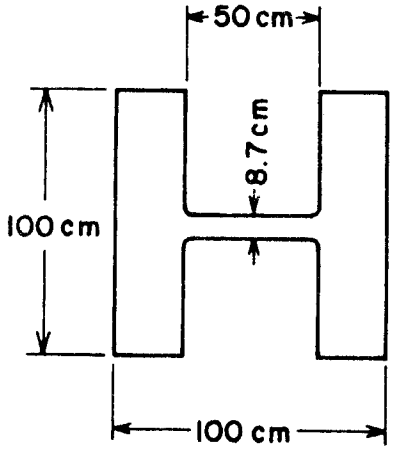

b) RIDGED WAVEGUIDE

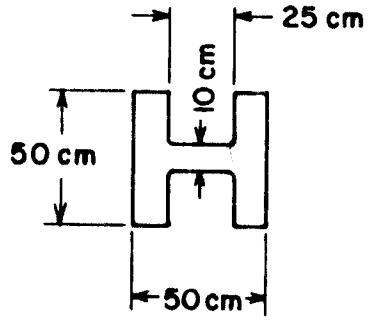

c) RIDGED WAVEGUIDE WITH CERAMIC ($\epsilon_r = 8$) FILLED DIELECTRIC

Figure 2-5 Size Comparison of Te_{10} Waveguide Feeds for 60 MH_Z RF

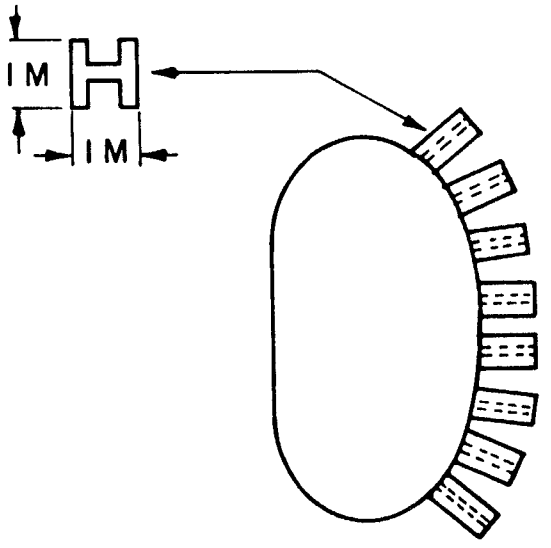

CROSS SECTION VIEW

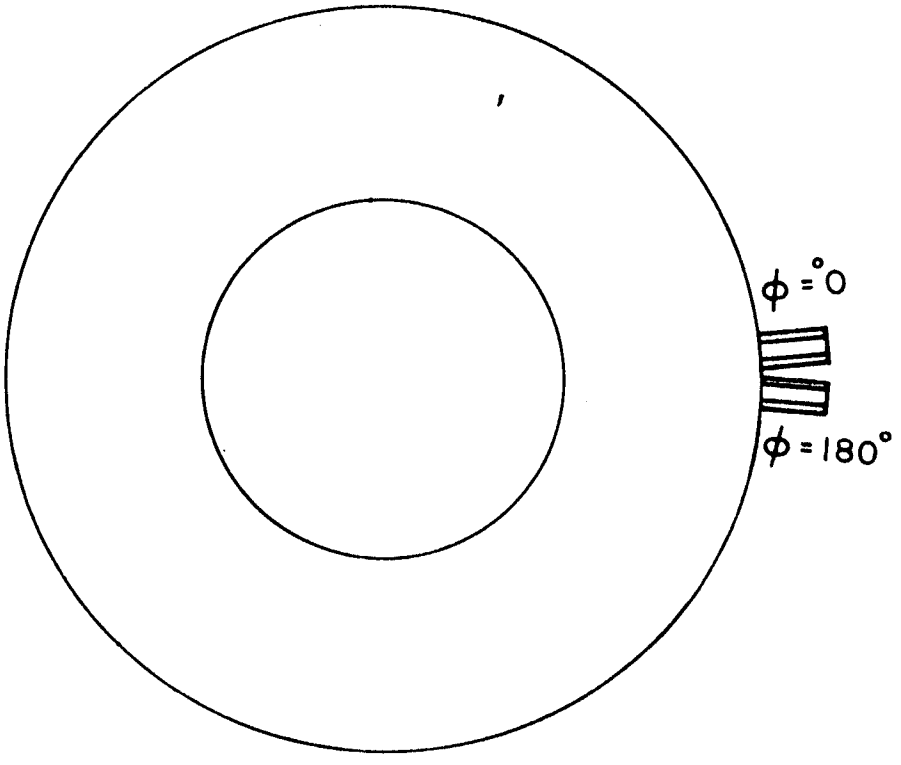

TOP VIEW
CROSS SECTION

Schematic of a Conceptual Magnetosonic Wave Launching System

Figure 2-6

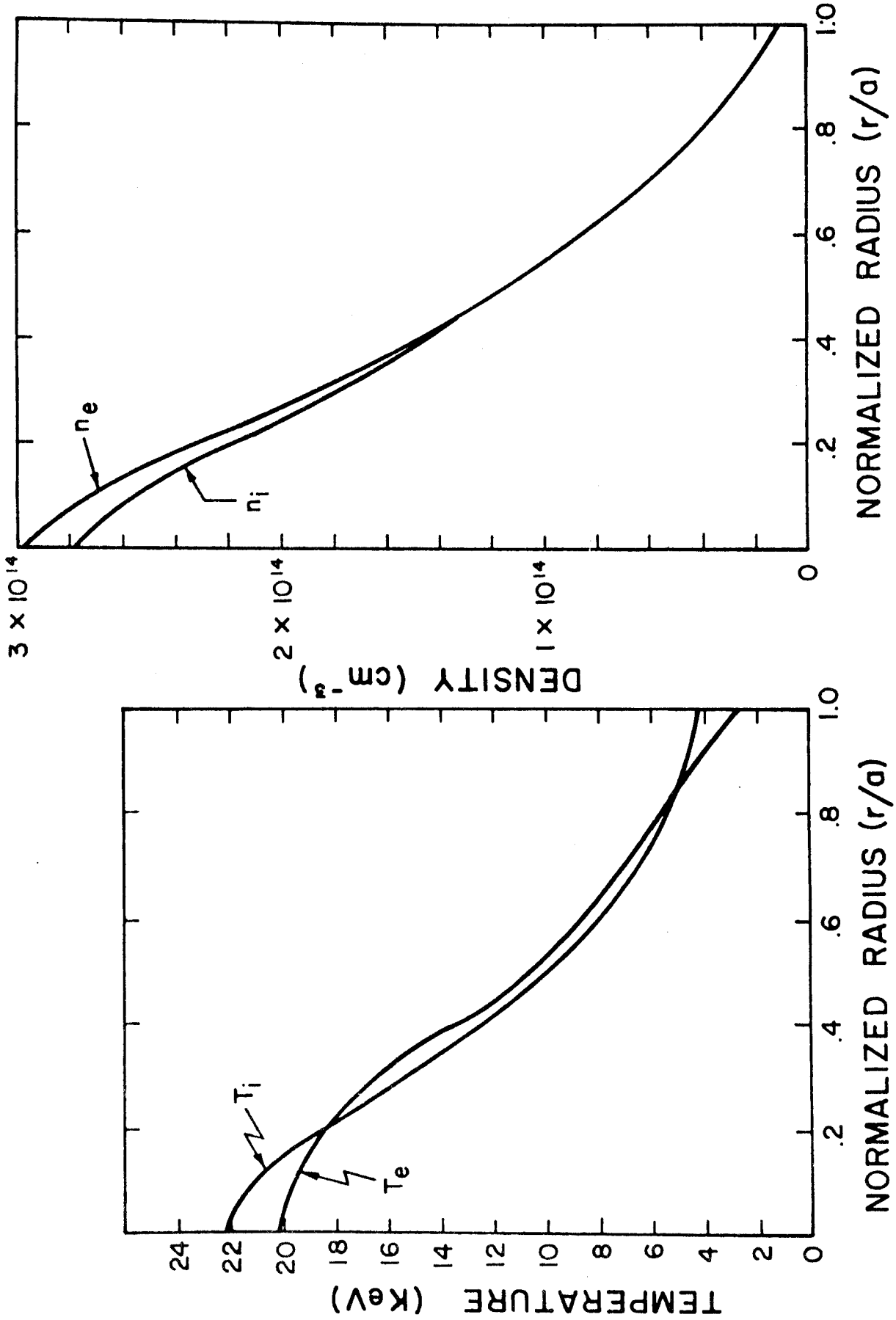
TEMPERATURE (keV)
24
22
20
18
16
14
12
10
8
6
4
2
0
T_i
T_e
.2
.4
.6
.8
1.0
NORMALIZED RADIUS (r/a)
DENSITY (cm^{-3})
3×10^{14}
2×10^{14}
1×10^{14}
0
n_e
n_i
.2
.4
.6
.8
1.0
NORMALIZED RADIUS (r/a)

FIGURE 2-7

The equilibrium plasma conditions during the plasma burn for UWMAK-III have been studied by using both a global plasma energy balance model and a more sophisticated spacetime tokamak code. In both cases, thermal equilibria are found which produce 5000 MW_{th} of power. In the latter case, however, the average ion and electron temperatures, the plasma β_θ, and the particle confinement time are found to be significantly lower than those predicted by the global model because the temperature and density profiles are sharply peaked at the axis of the torus.

The plasma and magnetic field parameters are listed in Tables 2-4 and 2-5. The energy confinement time is 1.6 sec while the particle confinement time is 0.55 sec. The fractional burnup is a very low, 0.83%, and the fueling rate for D and T atoms is 1.43×10^{21}/sec. This low fractional burnup and correspondingly high fueling rate results because the diffusion of particles from the plasma is governed by the diffusion coefficient at the plasma edge. The edge condition associated with the use of a divertor implies a very low density and therefore a quite collisionless plasma. In turn this leads to a large diffusion coefficient assuming microinstability scaling. The low value of τ_p in the space dependent model means the amount of tritium in the refueling cycle will be much larger than heretofore expected on the basis of global model calculations alone. In this case, the fueling rate for tritium is 74.7 kg/day. A plot of the density and temperature profiles during the plasma burn are shown in Fig. 2-7.

3. Impurity Control and Vacuum Pumping

Two forms of impurity control are included in the UWMAK-III design, a magnetic divertor and a low Z liner. The magnetic divertor is of the axisymmetric, poloidal double null type such as we have used previously[1,2] and Fig. 1-2 and 3-1 shows the location of the various coils together with the location of the plate onto which the plasma particles deposit their energy. The vacuum pumps and the baffle system is also shown.

The low Z liner consists of a thick graphite zone (25cm) on the inner portion of the chamber nearest the centerline and a thin carbon curtain, as described in UWMAK-II[2] mounted on the outer blanket first wall. The operation of the carbon curtain is similar to that described previously[2,8] and the temperature during the plasma burn is 1300°C. As such, physical sputtering is expected to dominate and this is the order of 0.01.[9] The thick graphite zone on the inner side of the chamber will operate with a much higher surface temperature in the neighborhood of 1800°C. Again, physical sputtering should be dominant as estimates indicate the formation of acetyline only at somewhat higher temperatures ($\gtrsim$ 2000°C).[10]

TABLE 2-4

Plasma Parameters for UWMAK-III

	Space-Time	Point Model
Mean Ion Temperature (keV)	11.4	18.4
Mean Electron Temperature (keV)	11.9	22.9
Mean Ion Density (cm^{-3})	7.9×10^{13}	6.46×10^{13}
Mean Electron Density (cm^{-3})	8.1×10^{13}	6.86×10^{13}
Mean Alpha Density (cm^{-3})	8.8×10^{11}	1.9×10^{12}
Plasma Current (MA)	15.6	15.7
Stability Factor at Plasma Edge, q(a)	2.7	2.69
Plasma Width (m)	2.7	2.7
Plasma Height (m)	5.4	5.4
Radius of Equivalent Volume Circular Plasma (m)	3.83	---
Major Radius (m)	8.1	8.1
Axial Toroidal Magnetic Field (kG)	40	40
Plasma Volume (m^3)	2370	2360
Electron Poloidal Beta, β_θ^e	0.69	1.05
Total Poloidal Beta, β_θ	1.65	2.3
Total Toroidal Beta, β_ϕ	.058	.083
Energy Content of Plasma (GJ)	1.32	1.63
Wall Surface Area (m^2)	1600	1600
Particle Confinement Time (sec)	0.547	3.33
Energy Confinement Time (sec)	1.64	1.66
$\bar{n}_e \tau_E$	1.33×10^{14}	1.14×10^{14}
Fractional burnup, f_b	0.83%	5.9%
Voltage Around Torus (volts)	0.059	

TABLE 2-5

Power Parameters	
Energy per Fusion (MeV)	21.7
Thermal Power During Burn (MW)	5000
Average Power Density in Plasma (MW/m^3)	1.72
14 MeV Neutron Production Rate (sec^{-1})	1.44×10^{21}
Power to Wall (MW)	71.3
Radiation (MW)	63.2
Particles (MW)	8.1
Power Wall Loading (MW/m^2)	0.44
Power to Divertor (MW)	725
Fueling Parameters	
Tritium (deuterium) Comsumption Rate	1.94×10^{21}/sec
Tritium Burnup Rate	.62 kg/day
Deuterium Burnup Rate	.413 kg/day
Particle Leakage Rate ($D+T+\alpha$)	3.44×10^{23}/sec
Fueling Rate	
Deuterium	49.8 kg/day
Tritium	74.7 kg/day

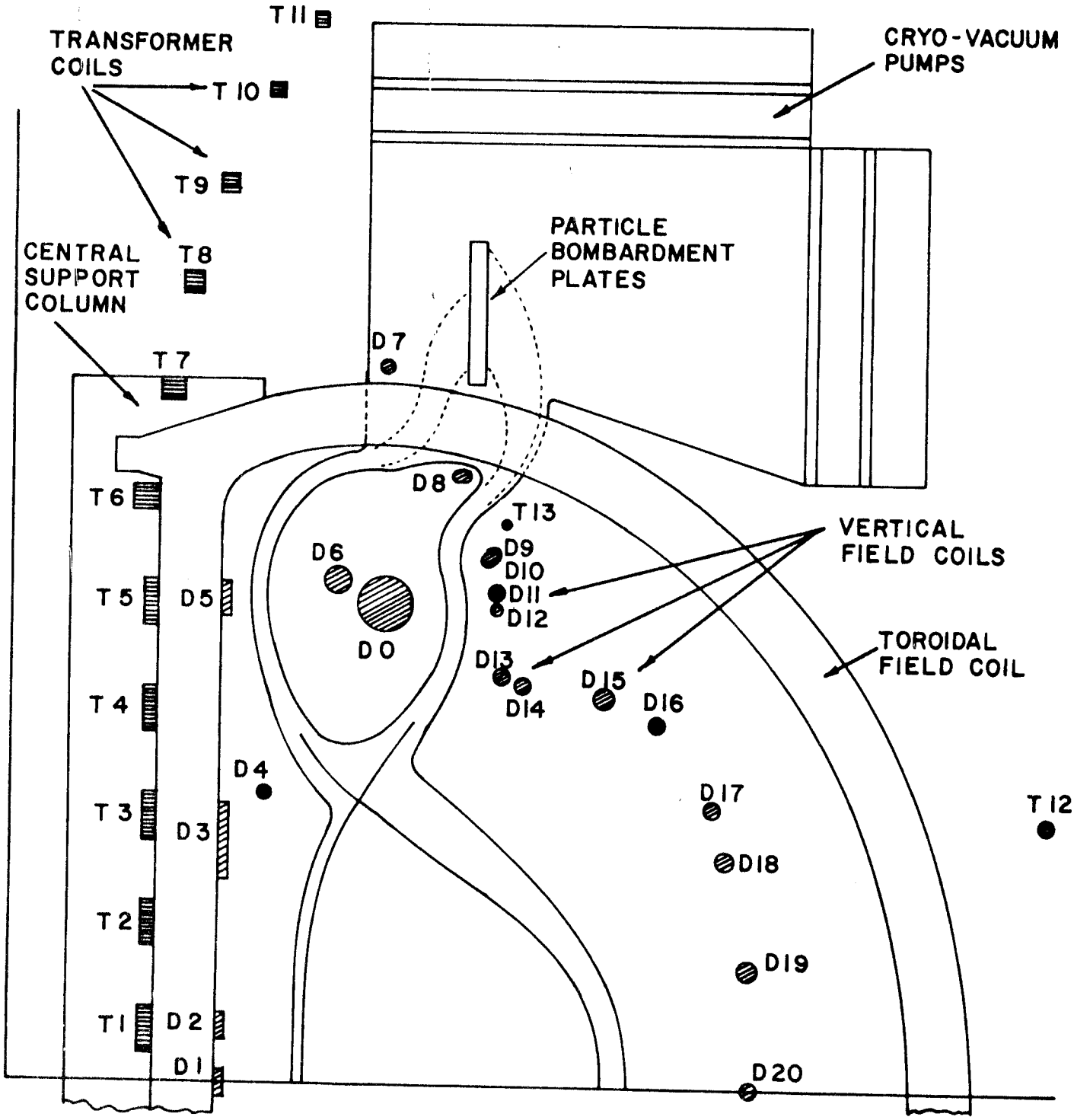
T11
TRANSFORMER COILS
T10
T9
T8
CENTRAL SUPPORT COLUMN
T7
T6
T5
T4
T3
T2
T1
D5
D4
D3
D2
D1
D0
D6
D7
D8
T13
D9
D10
D11
D12
D13
D14
D15
D16
D17
D18
D19
D20
T12
CRYO-VACUUM PUMPS
PARTICLE BOMBARDMENT PLATES
VERTICAL FIELD COILS
TOROIDAL FIELD COIL

FIGURE 3-1

The effectiveness of the divertor in reducing the charged particle flux to the wall has been estimated using the model described previously.[2] The plasma density profile in the scrape-off region is determined by cross field diffusion and by plasma flow along the diverted field lines to the particle bombardment plates. In the outer divertor, the plasma must pass through a region of higher B on its way to the collector so that magnetic mirroring can be important. However, the plasma would have a loss cone distribution and be subject to all the usual microinstabilities associated with mirror machines. This has been reviewed in Ref. 11. As such, we have taken the divertor efficiency to be $\gtrsim$ 99% for collecting particles diffusion from the plasma.

Further, in both in-space dependent and space independent calculations, the plasma is assumed to be essentially free of impurities. This follows simply from the assumption that in the presence of turbulence, high Z impurities will be transported out of the plasma with the same diffusion coefficient as the plasma itself. With this assumption, one can set the flux of high Z impurities leaving the plasma equal to the impurity reflux:

$$-D\frac{\partial n_z}{\partial r} = -S(1-\eta)D\frac{\partial n_{DT}}{\partial r} + \frac{aS_n}{2} n_{DT}^2 \langle\sigma v\rangle + S n_{DT}(a) n_n \langle\sigma v\rangle_{cx} \lambda_{cx} \qquad (1)$$

where D is the diffusion coefficient, n_z is the density of high Z impurities, n_{DT} is the density of plasma ions, n_n is the density of neutrals at the plasma edge, S is the D-T sputtering yield (of order .01), η is the divertor unload efficiency (of order .99), $\langle\sigma v\rangle_{cx}$ is the charge exchange cross section at the plasma edge, λ_{cx} is the charge exchange mean free path at the plasma edge, and S_n is the sputtering coefficient for neutrons ($\sim 10^{-5}$). The first term on the right represents sputtering by plasma ions diffusing out of the plasma core and it is the dominant term. The second and third terms represent neutron and charge exchange neutral sputtering respectively. By setting $\frac{\partial n}{\partial r} \propto \frac{n}{a}$, one finds

$$\frac{\bar{n}_z}{\bar{n}_{DT}} \approx S(1-\eta) \approx 10^{-3} \text{ to } 10^{-4} \quad .$$

Therefore, we have assumed that the plasma is essentially free of impurities.

The design of the divertor in UWMAK-III is unique in several ways. Firstly, the particles bombard a thin, solid plate of TZM located outside the toroidal field magnets and the pumping and heat transfer problems are not coupled. Placing the bombardment plates outside the TF coils allows the field lines to be fanned out, thus reducing the power density of particles on the plates. Combining this with the relatively small flow conductance back through the slots to the plasma, we expect that there will be little backsteaming of neutrals and impurities.

The particles get from the plasma to the collectors by following magnetic field lines into the fringing region of the toroidal field coils. These field lines get "caught" in the poloidal component of the fringing toroidal field and pass through the gaps between the coils.

The surfaces of the magnets will experience direct charged particle bombardment if the separatrix around the coils intercepts the surface or if the particles can cross-field drift (due to curvature and VB drifts) to field lines that intercept the surface. The latter effect is not considered to be important since the particles can only drift a distance of the order of the gyroradius while traversing a distance along the field lines equal to the radius of curvature of the field. The fields are strong (toroidal field = 4T, poloidal field ~1T) and the gyroradius is small ($\lesssim$ 1 cm) so this effect can be ignored. Calculation of the location of separatrix requires extensive 3D field line computer calculations. This has not yet been done for UWMAK-III, but we are preparing to do this work. We have done similar calculations for UWMAK-I[1] and II;[2] in those cases, the coils were protected except near the inner leg of the "D". This leads us to believe the method described will work for UWMAK-III. If the coils suffer some charged particle bombardment, one can place particle collectors on the surface of the magnets, or at other strategic locations, to protect the magnets from erosion and heat input.

The location of the particle collector plates is also shown in Fig. 3-1. This is based on the assumption that the coils are protected by the magnetic field against bombardment. This arrangement requires two collectors back-to-back to receive the flux from the inner and outer scrape-off zones. The particles from the inner scrape-off zone pass by the supports for the portion of the blanket and shield directly above and below the plasma. These supports are guarded against charged particle bombardment by two parallel currents. The line currents create a separatrix and thereby divert the field around the supports. The required current to guard the supports is 1.9 MA per support. Because of the location behind the blanket and shield, this can be a superconducting current.

The particle collection plates in UWMAK-I[1] and II[2] consisted of a flowing lithium film to absorb both the D,T particles and the associated thermal energy. This design is not suitable for UWMAK-III due to the very large thermal load carried on the plates. The average thermal load in UWMAK-I was 1.0 MW/m^2. This load increased to 3 MW/m^2 in UWMAK-II, with the peak load estimated to be around 30 MW/m^2. The lithium temperature can only vary from 186°C (its M.P.) to 350°C (the B.P. at the plasma chamber pressure 10^{-5} torr). With this very small coolant temperature rise available, and with the intense thermal load, the heat transfer problem becomes almost insurmountable.

The design philosophy for the particle collector plates in UWMAK-III has been completely changed. The pumping and heat transfer problems have been decoupled. The vacuum pumping capacity has been increased by more than one order of magnitude to compensate for the loss of pumping by the lithium film. The sole purpose of the collector plates is now to slow down the particles and convert their kinetic energy to thermal energy. A coolant is now required to transfer the thermal energy to a power conversion system,and sodium is used.

The main structure of the collector plate will consist of a bank of tubes which form the coolant passages. To avoid excessive sputtering due to incident high energy particles, a thin sheet of TZM is used to cover the main plate. Good thermal contact between the sheet and the plate is maintained by means of a liquid lithium film which fills the void between them. The main sheet of TZM acts as a sacrificial wall provided against particle sputtering and will be designed to allow frequent replacement. One of the most important questions is then, how often does the sacrificial wall have to be replaced. Two schematic drawings of the particle collector plate are shown in Fig. 3-2 and 3-3.

The location of the collector plate is outside the toroidal magnet as shown in Fig. 3-1, at a major radius of 7 m. There are 36 collector plates, each 1.14 m wide and 3 m high, giving a total surface area of 123 m^2. The sacrificial wall is 0.1 mm thick, weighing a total of 125 Kg per replacement.

For the interaction of TZM with D,T particles, the sputtering yield is about .005. The particle flux is 5.2×10^{23}. The erosion rate from the sacrificial wall is .041 cm^3/sec, at 1490 g/hr. Assuming that 20% of the sacrificial wall material can be eroded, the material required for the sacrificial wall is 180kg/day.

Since the sacrificial wall has to be replaced frequently, a periodic automatic replacement process is envisaged which is shown schematically on Fig. 3-2. The thin TZM sheet is fed from a supply roller and taken up on a spent roller. A frozen lithium seal is provided on the periphery of the plate to prevent lithium from leaking out. After a TZM sheet has been in service for 17 hours, the peripheral seal is melted and the sheet advanced until new material covers the plate. The seal is then allowed to solidify again. This process can be carried out during a burn cycle with no downtime for the reactor.

The TZM plate is cooled with sodium and a calculation of the MHD effects on pressure drop from both Hartmann and end-of-loop effects has been made. The total pressure drop is 100 psi and the sodium exit temperature is 600°C. This sodium is then used to feed a steam generator system so that the 687 MW_t (average) associated with the divertor cycle can contribute to the electrical output. This is discussed in the section on the power cycle.

The particles coming off the TZM plate must be collected by the primary vacuum system. Thus, the main function of the primary vacuum system is to remove the unburned fuel during the burn cycle while maintaining the plasma chamber surrounding the plasma confinement zone at a pressure of 1×10^{-4} torr or better.

FIGURE 3-2

SCHEMATIC DRAWING OF THE COLLECTOR PLATE DESIGN FOR UWMAK III

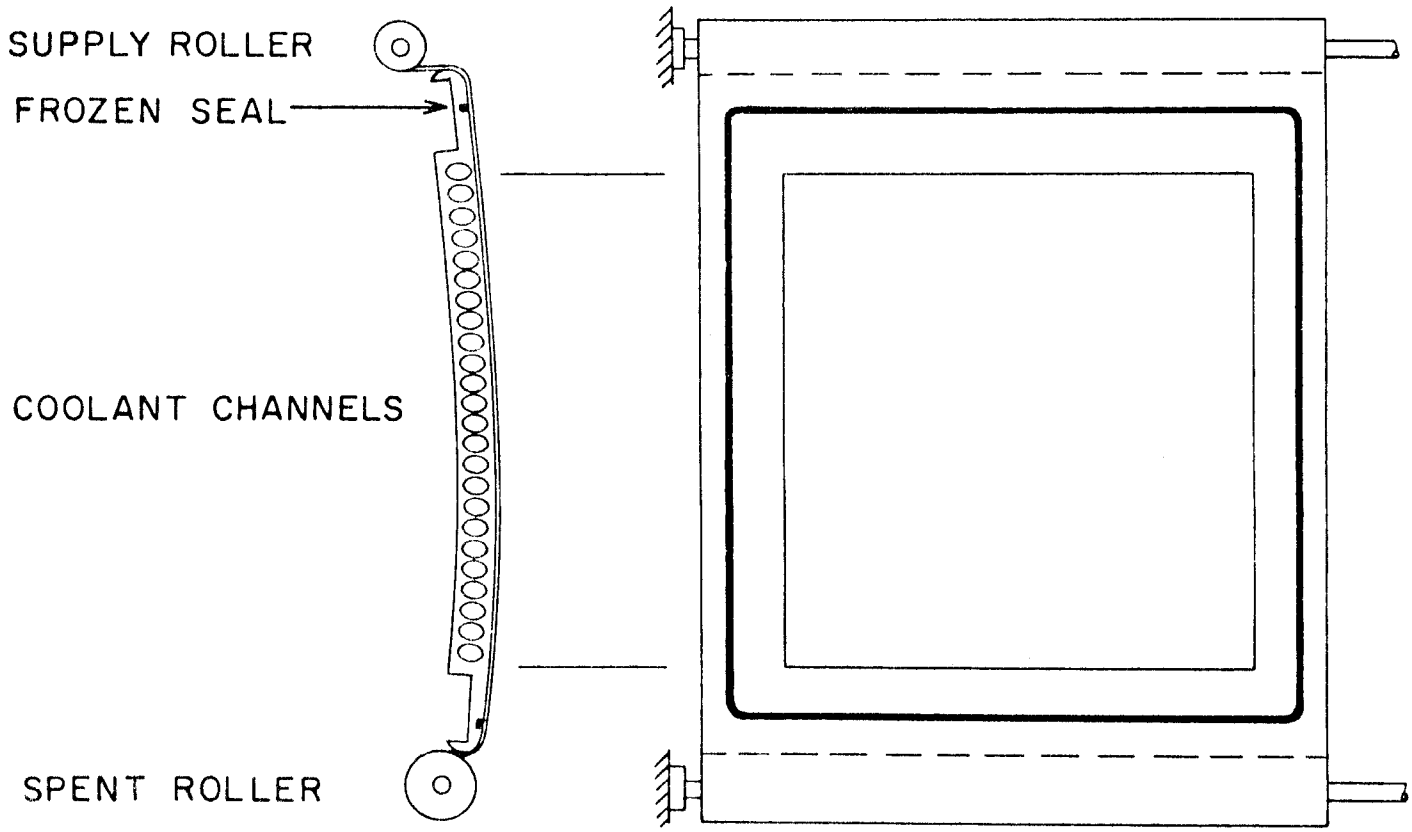

FIGURE 3-3

CROSS SECTION OF COLLECTOR PLATE

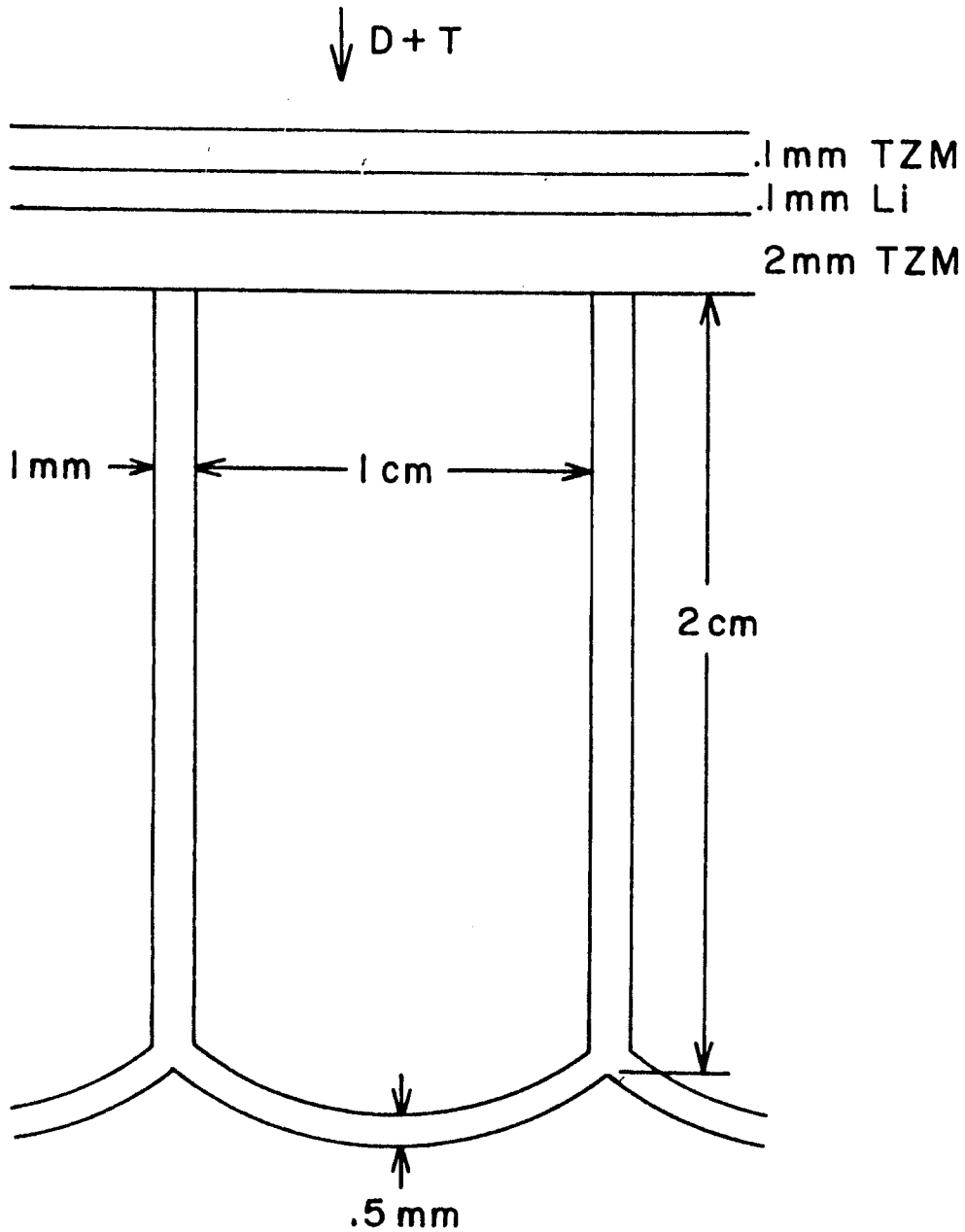

A secondary function, but equally as important, is to pump the chamber down to a relatively high vacuum between burn cycles in order to clean and condition the chamber surfaces.

A pumping scheme for a fusion reactor is complicated by the fact that twice as many pumps as needed in normal operation have to be provided, to allow one half of them to be recycled while the other half is on line. This implies low conductance gate valves, heaters, back up pumps and a maze of ducts and vacuum lines. Nevertheless, a system such as UWMAK-III lends itself rather nicely to a simple design. We envisage that the cryo-pumps will be rectangular in shape and will cover about 65% of the available space. The total pumping area will be 1600m^2, with only one half of it in use at one time.

The pumps will be arranged in even numbers, covering the horizontal and vertical space available in the vacuum plenum. Sliding plates will act as gate valves and will be sealed with conventional elastomer seals. The seals will be shielded from neutrons but will suffer damage from scattered gammas and will have to be replaced periodically. Each sliding plate will serve a pair of pumps, one on-line and the other being regenerated. During change-over, the plate is moved to seal the saturated pump while exposing a freshly regenerated one to the chamber plenum. The back end of the pumps will have a similar gate plate arrangement operating in reverse of the front gate plate. The rear plate isolates the pump on line from the common pump-out plenum while opening the pump being regenerated to it. This scheme will provide essentially no pumping impedance, will save on space and requires no extrapolation of present day vacuum technology. The refrigeration system requires 65,000 1/day of liquid helium and 550,000 1/day of liquid nitrogen. The power required is, however, relatively small, 7.3 kW at 4.2°K and 1 MW at 77°K. The combined power need at 300°K is 6.2 MW.

4. Magnet Systems for UWMAK-III

a. Toroidal Field Coils

The toroidal field coils have a modified constant tension "D" shape, corrected for the field variation due to the finite number (18) of coils. The embedded conductor in a solid "D" shaped alloy aluminum former is used to minimize the material requirements while providing maximum strength and stiffness. This construction was described in detail in the UWMAK-I report[1] and the cold central structure and secondary vacuum wall used in the UWMAK-II[2] design are retained. The superconductor is TiNb superconducting filaments processed in an OFHC copper matrix for convenience but stabilized with high-purity aluminum in the case of the toroidal field magnets. The coils are fully cryogenically stabilized and produce a maximum field of 8.75 T and an axial field at R = 8.1 m of 4.05 T.

The vertically elongated plasma and a new blanket removal scheme coupled with only 18 toroidal field magnets instead of the 24 used in UWMAK-II[2] permits the use of much smaller TF magnets. The inside surface of the outer leg is at 16.5 m as shown in Fig. 4-1. The shape of the constant tension "D" naturally accomodates a vertically elongated plasma. In this case, the plasma, blanket, shield and divertors fit within a "D" shape based on a 1/R field variation

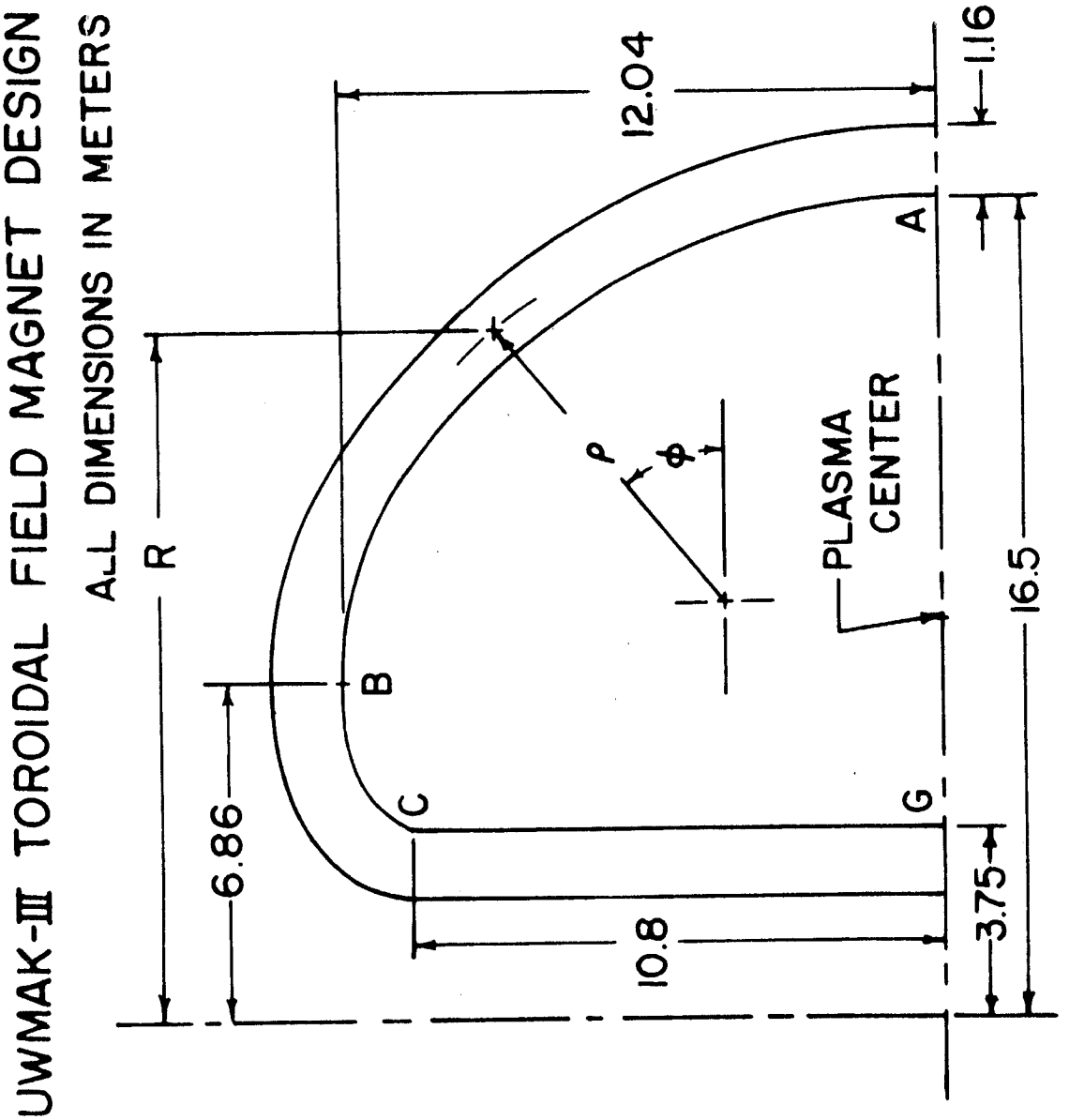

FIGURE I-4-1

"D" Shaped Toroidal Field Magnet Design

without modifications. However, since the local fields near the 18 individual windings are higher due to field perturbations caused by the discreteness of the coils, the specific "D" shape which results becomes vertical at a position on the inside leg that is not high enough to clear the interior structure. Fig. 4-1 shows the shape of the modified "D" chosen for additional height. From point A to point C the maghet has a constant tension shape. For a uniformly wound toroid, the shape A to C could be described by a radius of curvature ρ proportional to the radial distance from the axis of the toroid, as

$$\rho = KR.$$

For discrete toroidal coils, such as those used in UWMAK-III, one should correct for the local perturbations of the magnetic field due to the flux leakage between the finite number of finite coils. An analytic expression for the radius of curvature ρ from work by Moses and Young[12] is

$$\rho = KR \left[\frac{1}{1 + \frac{1}{N}\left(\cos\phi + \frac{R}{\rho} \ell n \frac{1.284R}{CN}\right)}\right]$$

where:

- K = a constant directly proportional to local toroidal field intensity
- R = distance from major toroid
- N = number of discrete magnets in the toroidal field system
- ϕ = angle from midplane to a normal vector
- C = radius of TF coil cross section if the "D" magnet has a round cross section or it is approximately $W/\sqrt{\pi}$ if the cross section is a square of width W.

Solving for a square cross section gives:

$$\rho = \frac{R\left[K - \frac{1}{N} \ell n \frac{2.276R}{WN}\right]}{1 + \frac{\cos\phi}{N}} .$$

This expression, although approximate, gives results that agree within a few percent to values found by much more difficult to use iterative procedures and we have used this result in the toroidal field coil design.

A unique feature of the UWMAK-III TF coils is the use of an Al conductor and an Al alloy structure. The use of 316 stainless steel for the structural material in the toroidal field magnets in the UWMAK-I[1] and UWMAK-II[2] designs was predicted on a limiting maximum strain of 0.002 in the copper stabilizer and a desired high stress level to minimize structural volume. Recent work on alloy aluminum reinforced high purity aluminum stabilizers at the University of Wisconsin-Madison by H. Segal[5] leads to the possibility of cycling the high purity aluminum stabilizer to a strain level of 0.0038 with little degradation of its resistivity ratio. Serious questions regarding the future availability of

nickel and chromium[1,2] have also cast some doubt on the advisability of committing so much stainless steel to the constructruction of a fusion power plant. With these two factors as principal motivation, although recognizing the problems created by the extra volume (lower stress level) required for the alloy aluminum toroidal field magnet structure, the decision was also made to use aluminum alloy 2219 in the UWMAK-III design. This alloy was selected for its strength, ability to be welded and heat treated, and its ability to be formed at a reasonable cost. A complete list of specifications for the toroidal field magnets is given in Table 4-1.

The radiation level on the magnet components is about four orders of magnitude less than for UWMAK-I.[1] In that case at 3×10^{-4} dpa/year we allowed for extra copper end for extra cooling surface and planned for room temperature anneals every ten years. For UWMAK-III, in contrast, the dpa rate on the front surface of the magnet is 1.6×10^{-8} dpa. Therefore we expect up to 40 years of operation without any anneals. The damage to insulators, which was not considered a problem for UWMAK-I, is negligibly small for UWMAK-III.

b. VF and OH windings

The vertical field coils are constructed inside the toroidal field magnets as they were in UWMAK-II.[2] The maximum stored energy in these coils is less than in UWMAK-II primarily due to the increased magnetic field utilization for non-circular plasmas. A 4-element conductor introduced by Cornish[13] has been modified to accomodate the requirements of both the vertical field magnets and the ohmic heating magnets. The improved cooling afforded by this design has allowed an increase in the current density and this fact coupled with smaller diameter coils has resulted in a less expensive set of magnets. The vertical field and ohmic-heating magnets are cold worked OFHC copper for both stabilizer and structure with some stainless steel also used in the more highly stressed vertical field magnets. As with the toroidal field coils, all magnets are cryogenically stabilized.

To reduce the ac losses, the superconducting filaments are extruded with cupronickel in an OFHC copper matrix, drawn to size, twisted, and finally formed into a square cross section. All conductor sections containing the superconductors will have the same size in all the coils but the number of TiNb filaments will depend upon the current being carried and the maximum ambient field at the given coil location. The general specifications of the vertical field and ohmic heating coils are given in Table 4-2.

TABLE 4-1

Specifications of Toroidal Field Magnets for UWMAK-III

a. Field Specifications	
On-axis field, B_o	4.05 @ 8.1m
Field at inside turn of far edge (point A)	1.99T @ 16.5m
Maximum field at the conductor, B_m (point C)	8.75T @ 3.75m
Field Ripple along the far edge of the plasma	≈1%
Total electromagnetic energy stored in TF coils	30 MWh
b. Design Stress	
Maximum design stress in 316 stainless steel at 4.2K for UWMAK-I and II or in 2219-T8T aluminum at 4.2K for UWMAK-III	$3.11 \times 10^8 N/m^2$ (45,000 psi)
Design strain	$\leq$ 0.0038
c. Magnet Components	
Number of magnets	18
Number of discs per magnet	16
Number of conductor turns per disc. In UWMAK-III the two end discs have no turns on outer surface	64 (32 each side)
Conductor current	9,545A @ 16 discs 10,909A @ 14 discs
Disc cross section (see Figure III-A-2)	5 x 116 cm
Superconductor composite: TiNb in copper matrix, filament diameter = 0.038 cm, twisted every 30 cm	182 filaments max.
Stabilizer cross section, copper in UWMAK-I and II, aluminum in UWMAK-III	1.5 x 1.5 cm
Average stabilizer to superconductor ratio (volumetric)	19:1

TABLE 4-1 (continued)

Insulation between conductor and stainless steel disc	0.05 cm reinforced epoxy
Spacer between discs	0.64 cm thick micarta covering 50% of the area
Aluminum alloy bolts to fasten the discs together against slipping, 2.54 cm diameter	1250
Lateral support between the magnet and dewar: reinforced epoxy struts on each side of cross section	3500 cm^2
Each magnet weight	174 Mt
d. Total materials required in magnet system	
TiNb alloy superconductor	76 Mt
Stabilizer material	717 Mt Al
Structural disc material	2290 Mt
Dewars	730 Mt (aluminum) 119 Mt (SS)
Reinforced epoxy in discs	43 Mt
Micarta spacers between discs	108 Mt
Reinforced epoxy struts in dewars	10 Mt
Aluminum alloy bolts to assemble discs	34 Mt
Cryogenic insulation	503,000 m^2
Liquid helium inside dewars	144,000 Liters

TABLE 4-2

General Specifications for the Vertical Field and the Ohmic Heating Coils

(1) Conductor TiNb + CuNi sleeve + Copper stabilizer, fully cryogenically stabilized

(2) Conductor current in Type 1 = 14,160 to 14,520 A
Conductor current in Type 2 = 10,390 to 11,110 A
Conductor current in Type 3 = 4,340 to 6,750 A

(3) Conductor current density in Type 1 = 4880 to 5320 A/cm^2
Conductor current density in Type 2 = 3120 to 3850 A/cm^2
Conductor current density in Type 3 = 1410 to 3580 A/cm^2
(based on gross coil area)

(4) Conductor size range in Type 1 = 1.6 cm x 1.6 cm
Conductor size range in Type 2 = 1.6 cm x 1.6 cm
Conductor size range in Type 3 = 1.6cm x 0.951cm to 1.6cm x 2.09 cm
(this includes the bonded stainless steel reinforcement in Types 2 and 3.)

(5) TiNb - CuNi- Cu composite section: 0.80 cm x 0.80 cm with 34 to 182, 0.038 cm diameter filaments, twisted every 30 cm.

(6) Copper to superconductor ratio = 6.03 to 33.2

(7) Design stress at 4.2K: 1.24 x $10^8 N/m^2$ (18,000 psi) in 10% cold reduced OFHC copper, 2.11 x $10^8 N/m^2$ (30,600 psi) in 316 stainless steel in conductor types 1 and 2.
2.07 x $10^8 N/m^2$ (30,000 psi) in 10% cold reduced OFHC, 3.51 x $10^8 N/m^2$ (50,900 psi) in 316 stainless steel in conductor Type 3.

(8) Spiral wrapped with 0.1 cm thick fiberglass reinforced epoxy over 50% of the surface. Alternate conductors wrapped to produce a spacing of 0.1cm in both vertical and radial directions as the coils are layer wound.

(9) Design limits temperatures to 5.2 K in a 4.2K bath for all normal situations.

(10) Total TiNb superconductor required = 64.5 Mt

(11) Total copper required = 1331 Mt

(12) Total 316 SS reinforcement required = 436 Mt

(13) Total insulation for wrapping conductors = 26 Mt

5. Neutron and Photon Transport Analysis of the Blanket and Shield

The philosophy behind the blanket design was described in part 1 of this section and a schematic illustration of the overall design is given in Fig. I-4. The neutronics behavior of this design has been analyzed thoroughly using one and two-dimensional multigroup S_n neutron and photon transport codes. The data used has been discussed previously. For these calculations, there were 46 neutron groups and 21 gamma groups.

The first set of calculations is two-dimensional and based on using x-y geometry to approximately represent a vertical cut through the system as shown in Fig. 5-1. Toroidal effects are not included here. The inside of a torus in the poloidal direction is the most difficult part of a tokamak to replace because there is little access space. Thus a thick graphite wall region 12 in Fig. 5-1 is introduced in front of the vacuum wall (region 13 in Fig. 5-1 which acts to soften, reflect, and attenuate the neutrons incident from the plasma in the manner described in reference 3. This ISSEC zone (Internal Spectral Shifter and Energy Converter) reduces both the displacement and helium production rates in the first structural wall (region 13 in Fig. 5-1) and thus increases the wall life for this zone. The ISSEC zone is not actively cooled but radiates heat to the first structural wall behind it and also to the first wall on the outer portion of the plasma chamber. The inner blanket is further simplified by use of helium cooling. The absence of flowing liquid lithium eliminates the problem of the high pressure drop that results from using a liquid metal coolant in the high magnetic field region. The absence of lithium also alleviates tritium removal problems by eliminating the need for this function in the inner blanket. Finally, the inner blanket and shield is consciously designed to be as thin as feasible to allow for a lower aspect ratio and to allow higher magnetic fields in the plasma for the same magnetic field at the coil.

The ISSEC cannot be extended around the chamber since it would result in problems in achieving adequate tritium production. For this reason and because one has relatively easy access to the outer blanket and shield (zones 1, 2, 3, 4, 7, 8, 9, 10 of Fig. 5-1), the outer blanket system is designed for convenient replacement. Experience with the UWMAK-1 and UWMAK-II designs indicates that resource limitations make use of Be as a neutron multiplier undesirable. This leads to the choice of a liquid lithium cooled system for the outer blanket to achieve adequate breeding without a contribution from the inner blanket. The choice of zone thickness is made on the basis of results from a series of one-dimensional calculations. The final structural details are chosen on the basis of heat transfer and mechanical design.

Both the plasma and the chamber are noncircular and the magnetic axis which serves as the plasma axis is not at the geometrical center of the plasma. The neutron source distribution is proportional to the square of the ion density and has been approximately represented as a function of x and y in a vertical plane through the torus as

$$S(x,y) = S(0,0)\ [1 - (\frac{x - 50}{200})^2]^3\ [1 - (\frac{y}{580})^2]^3,\ -150 \leq x \leq 250;$$

BLANKET MODEL USED FOR TWO-DIMENSIONAL NEUTRONICS ANALYSIS OF UWMAK-III

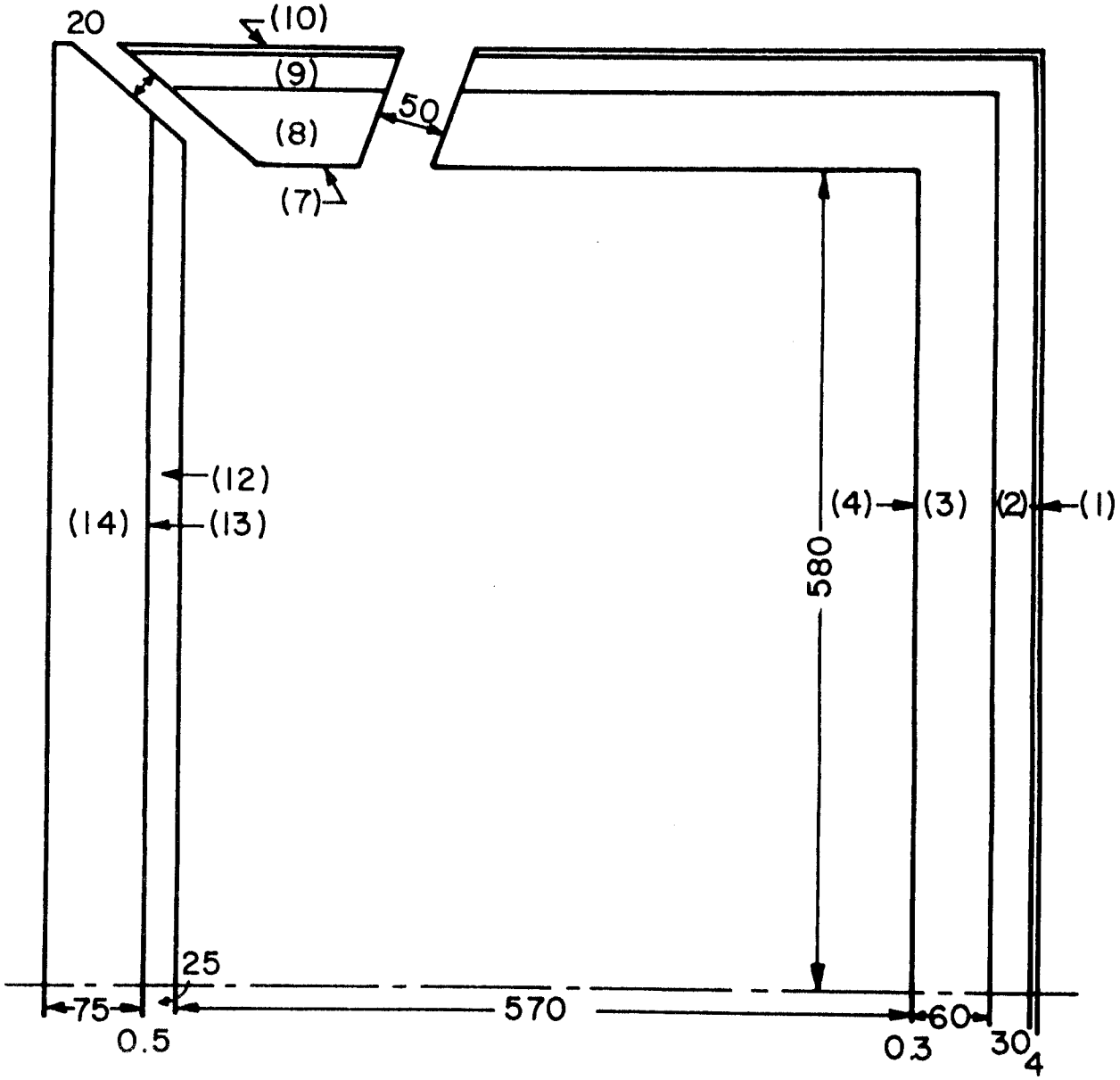

ZONE	COMPOSITION	ZONE	COMPOSITION
1, 3,..8, 10	97% Li + 3% Mo	4, 7, 13 -	Mo
2, 9	99% C + 1% Mo	12	C
14	40% B_4C+6% Mo (DENSITY FACTOR .95)		

FIGURE 5-1

and $S(x,y) = S(150,y)\ [0.01\ x + 2.50]$, $-250 \leq x \leq -150$.

The source has a center at R = 9.0m, shifted out from the geometric center of the plasma by finite β effects as predicted by the MHD calculations.

The major results of the calculation are given on Table 5-1. The breeding ratio exceeds 1 and the total energy per fusion is 21.7 MeV. Also, the ISSEC performs its function well since the neutron radiation damage indicators, such as dpa (displacements per atom) and helium production rate, are substantially reduced in the first wall behind the ISSEC compared with the unprotected outer blanket first wall.

At low aspect ratio, toroidal geometry effects can be very important. This is especially true in systems that are not poloidally symmetric with respect to functions like tritium breeding. Thus, the geometry for one dimensional studies is based on a horizontal cut through the torus midplane as illustrated in Fig. 5-2. This is quite reasonable for vertically elongated systems like UWMAK-III and the model is illustrated in detail in Fig. 5-3. We now find a breeding ratio of 1.27 and a ratio of dpa rates for the outer blanket first wall to the inner blanket first structural wall of 9 to 1.

Finally, a calculation using R-Z geometry to represent the toroidal configuration was undertaken. There are also some other minor geometry and composition changes included for the inner blanket and outer shield. The calculation has been done using the DOT program using S_6 (30 directions) with a P_3 approximation of the scattering cross section.

The neutron source distribution has been represented as a function of R and Z as

$$S(R,Z) = S(R,0)\ [1 - (Z/Zi)^2]^3.$$

$$S(R,0) = S(0,0)[1 - ((R - 900)/180^2]^3, 1080 > R > 900.$$

$$S(R,0) = S(0,0\ [1 - ((900-R)/360)^2]^3, 540 < R < 900.$$

This source represents a distribution peaked at R = 9m (i.e. shifted 90 cm toward the outside blanket from the plasma center at R = 810 cm) but symmetrical about the midplane. Zi is the vertical boundary of the source distribution. This shift of 90 cm rather than 50 cm, as in the x-y calculations, is based on more recent MHD calculations. The geometry model used in this calculation is shown in Fig. 5-4, where the source distribution, divertor slots, and the different coil positions are determined from the plasma physics analysis.

Table 5-2 presents the primary results of the analysis. The total breeding ratio is 1.25, which is about 16% higher than predicted by the x-y calculation. In fact this increase in the breeding ratio is not completely due to the correction from the toroidal effect. Careful comparison with the tritium production rates on a per zone basis shows the toroidal effect increases the breeding by about 9%. The other 7% increase is due to the change in the comparison of the shielding and to a change in the thickness of the last zone of the outer blanket. Also, the first zone of the outer shield has been changed from B_4C and stainless steel to carbon. This change has the effect of reflecting more low energy neutrons to increase the $^6Li\ (n,\alpha)$ reaction rate.

Table 5-1

Nuclear Performance of UWMAK-III Blanket Design (x-y geometry)

Breeding Ratio	1.074	
Energy per Fusion	21.7 MeV	
Energy Attenuation		
of Inner Blanket and Shield	7.1×10^{-8}	MeV/MeV*
of Outer Blanket and Shield	4.3×10^{-8}	MeV/MeV*
DPA Rate Per Year		
Inner Blanket First Wall	2.9*	
Outer Blanket First Wall	18.8*	
Helium Production Rate (appm/Yr)		
Inner Blanket First Wall	10.8*	
Outer Blanket First Wall	157.0*	
Average 14 MeV Neutron Wall Loading (MW/m^2)	1.91	

* at midplane

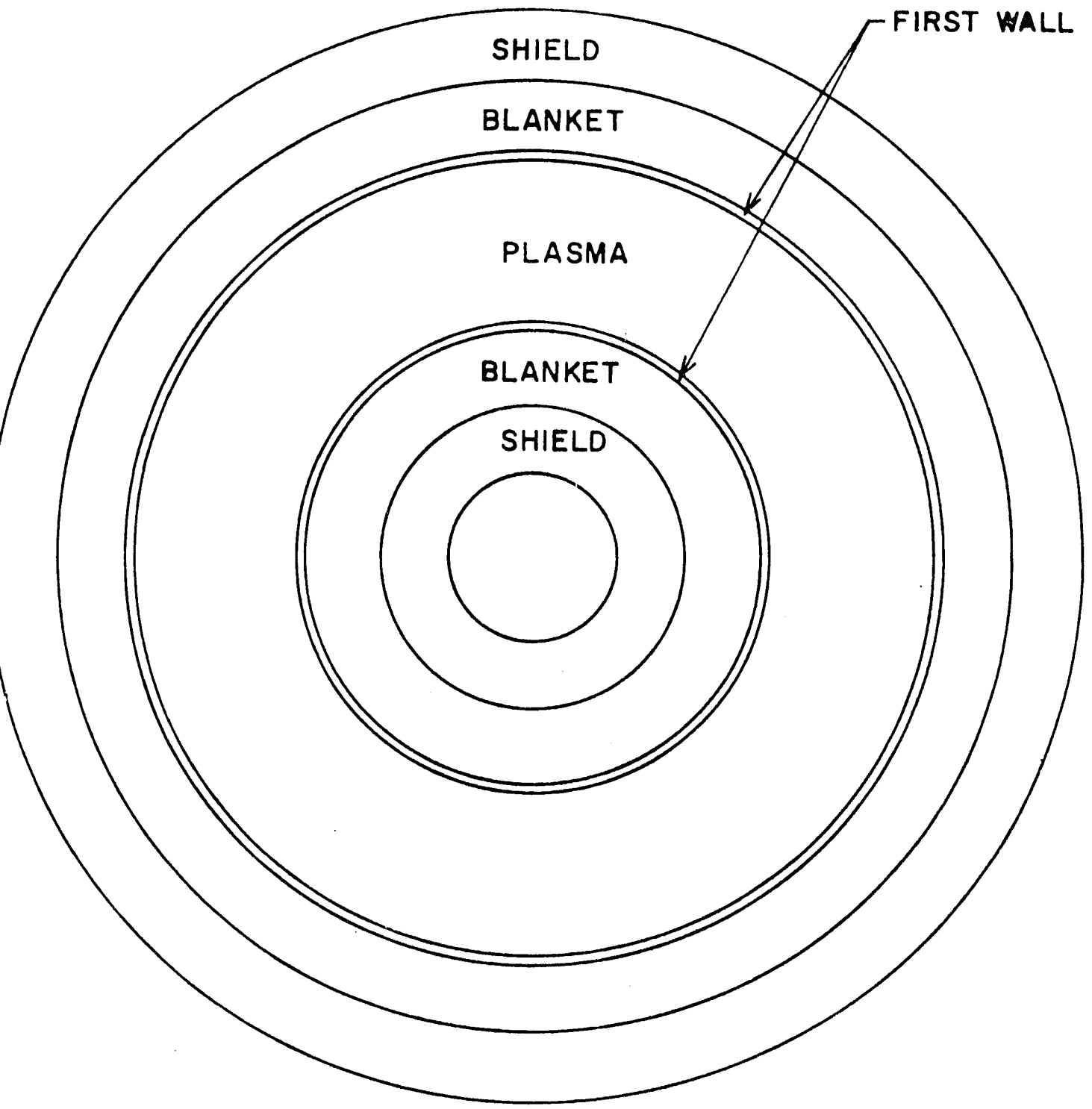
HORIZONTAL CUT THROUGH TOKAMAK MIDPLANE
FIRST WALL
SHIELD
BLANKET
PLASMA
BLANKET
SHIELD

Figure 5-2

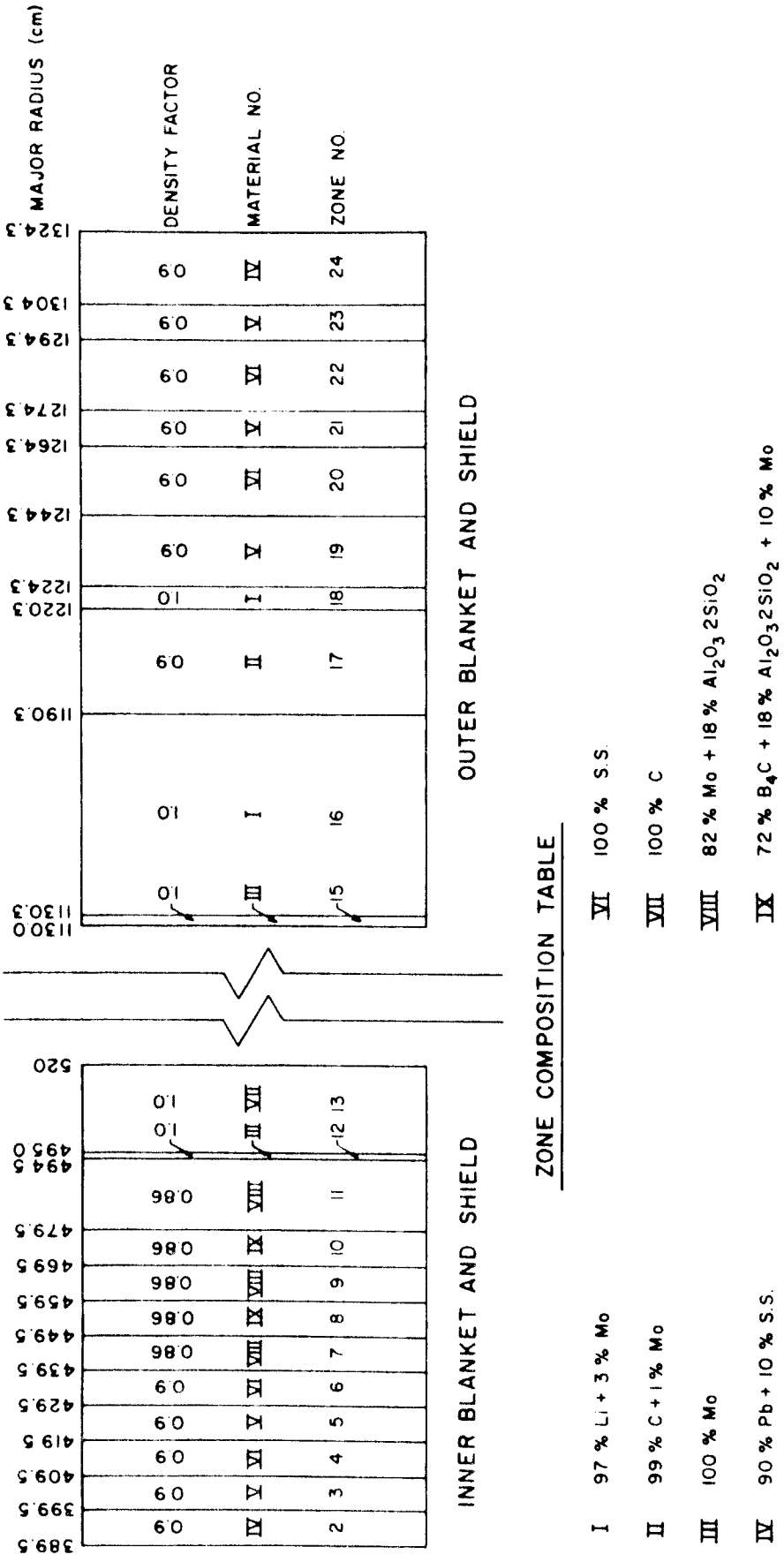
A SCHEMATIC OF THE UWMAK III BLANKET AND SHIELD
MAJOR RADIUS (cm)
DENSITY FACTOR
MATERIAL NO.
ZONE NO.
INNER BLANKET AND SHIELD
OUTER BLANKET AND SHIELD
ZONE COMPOSITION TABLE
I 97 % Li + 3 % Mo
II 99 % C + 1 % Mo
III 100 % Mo
IV 90 % Pb + 10 % S.S.
V 72 % B_4C + 10 % S.S. + 18 % $Al_2O_3 2SiO_2$
VI 100 % S.S.
VII 100 % C
VIII 82 % Mo + 18 % $Al_2O_3 2SiO_2$
IX 72 % B_4C + 18 % $Al_2O_3 2SiO_2$ + 10 % Mo

FIGURE 5-3

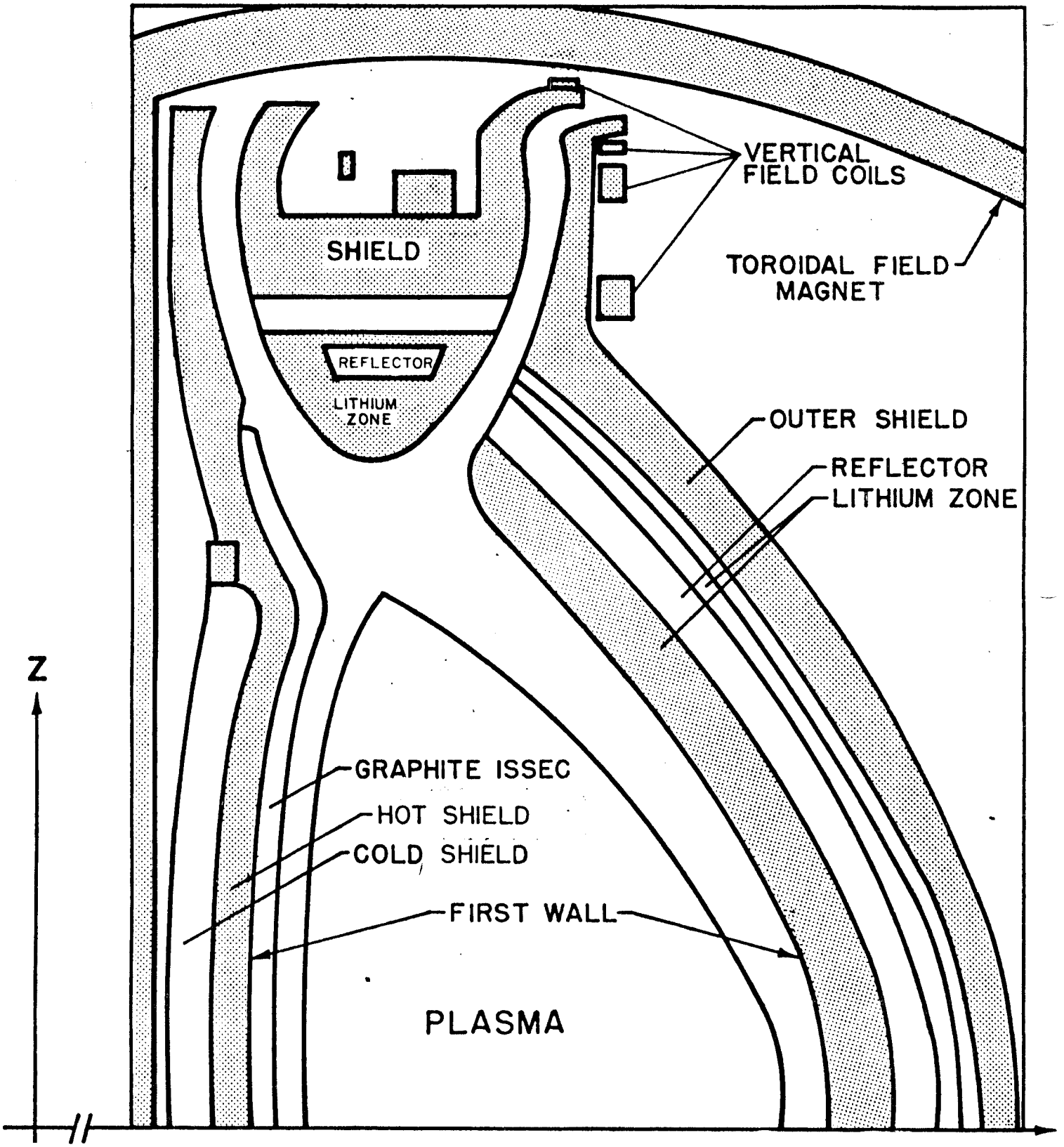

Figure 5-4

UWMAK-III Geometric Model Used for the Neutronics Calculation

Table 5-2

Nuclear Performance of UWMAK-III
Blanket Design (R-Z Geometry)

Breeding Ratio	1.25	
Energy Perfusion	21.1	
Power in Blanket	4075	
Power in Shield (MW)	90	
DPA Rate Per Year		
Inner Blanket First Wall	2.9	3.9*
Outer Blanket First Wall	18.8	16.5*
Helium Production Rate (appm/yr)		
Inner Blanket First Wall	10.8	12.5*
Outer Blanket First Wall	157.0	103.0*

* At Midplane

A summary of the results for the heat deposition per zone in the blanket region is given in Tables 5-3 and 5-4. The R-Z calculation indicates that 17.6 MeV per D-T neutron is deposited in the blanket and shield. It can be noted from Table 5-4 that the heat deposition in the outer blanket is 4 times that in the inner (including the ISSEC). This was only a factor of 2 in the x-y calculations.

Fig. 5-5 shows the variation of the neutron wall loading as a function of poloidal angle. As a result of the shifted neutron source, the wall loading has a maximum at the outer wall at about $\theta = 0°$. For ease of visualization, θ varies from 0° where the midplane intersects the inner blanket to 180° where the midplane intersects the outer blanket. This shows why the tritium breeding ratio of 1.25 is so much larger than the value from the x-y calculations. Neutrons tend to preferentially go towards the outer breeding blanket such that excessive parasitic absorptions in the inner blanket are avoided. This particular result can be obtained at essentially no expense by representing the source in (R-Z) coordinates, using one neutron group, and plotting the flux at the points where the first wall would be located. This simple approach gives results that match more elaborate and expensive calculations for the same cases. There is now, however, no restriction on the shape of the plasma cross section or on the neutron source distribution. From the figure, one can see that the wall loading varies substantially at different locations around the first wall.

Perhaps more relevant than wall loading is the variation of response functions like the atom displacement rate (in dpa/yr) and the helium production rate (in appm He/yr) in the first structural wall of TZM. These are shown in Fig. 5-6 and are the result of the full 46 neutron group, 21 gamma group, R-Z calculation. Again, the variations in θ are substantial. The relatively low values which occur when $\theta \lesssim 84°$ are caused by the graphite zone in front of the hot inner shield.

Thus, the representation of low aspect ratio toroidal CTR systems using (R) or (R-Z) coordinates allows one to adequately represent these systems using existing one and two-dimensional neutronics codes. Neutron wall loading distributions can be trivially calculated using one neutron group. In general, the inclusion of toroidal effects can have an important impact on the final results.

Table 5-3

Neutron and Gamma Heating Rates*
by Zone from x-y Geometry

Zone	Thickness (cm.)	Density Factor	Composition	Neutron Heating	Gamma Heating
2	10	0.9	90% Pb+10%SS	2.288-8	4.441-6
3	10	0.9	72%B_4C+10%SS+18%$Al_2O_3 2SiO_2$	3.212-5	8.076-6
4	10	0.9	90%Pb+10%SS	5.906-6	6.660-5
5	10	0.9	72%B_4C+10%SS+18%$Al_2O_3 2SiO_2$	4.644-4	1.161-4
6	10	0.9	100%SS	8.390-5	7.147-4
7	10	0.86	82%Mo+18%$Al_2O_3 2SiO_2$	1.694-4	3.704-3
8	10	0.86	72%B_4C+18%$Al_2O_3 2SiO_2$+10%Mo	5.037-3	4.302-3
9	10	0.86	82%Mo+18%$Al_2O_3 2SiO_2$	1.722-3	3.312-3
10	10	0.86	72%B_4C+18%$Al_2O_3 2SiO_2$+10%Mo	1.128-1	4.811-2
11	15	0.86	82%Mo+18%$Al_2O_3 2SiO_2$	4.381-2	7.678-1
12	0.5	1.0	100%Mo	3.336-3	6.608-2
13	25	1.0	100%C	1.654	5.689-1
14	610	0.0	Vacuum	0.0	0.0
15	0.3	1.0	100%Mo	2.677-2	2.283-1
16	60	1.0	97%Li+3%Mo	9.695	1.729
17	30	0.9	99%C+1%Mo	3.309-1	3.538-1
18	4	1.0	97%Li+3%Mo	1.414-1	1.275-2
19	20	0.9	72%B_4C+10%SS+18%$Al_2O_3 2SiO_2$	1.500-1	9.026-2
20	20	0.9	100%SS	1.566-3	1.935-2
21	10	0.9	72%B_4C+10%SS+18%$Al_2O_3 2SiO_2$	2.005-3	5.134-4
22	20	0.9	100%SS	3.468-5	4.407-4
23	10	0.9	72%B_4C+100%SS+18%$Al_2O_3 2SiO_2$	8.259-5	1.894-5
24	20	0.9	90%Pb+10%SS	2.103-7	1.255-7
				12.173	3.897

* All the heating rates are in MeV per D-T neutron

Table 5-4

Neutron and Gamma Heating Rates* by Zone from R-Z Toroidal Calculation

Zone	Neutron Heating	Gamma Heating	Total Heating/Zone
2	1.3481	0.6775	2.0256
3	0.0697	1.5886	1.6583
4	0.0841	1.0409	1.1250
5	0.0117	0.1781	0.1898
6	8.0960	1.7348	9.8308
10	0.3711	0.0809	0.4520
7	0.7874	0.1815	0.9689
8	0.3136	0.4979	0.8115
9	0.0300	0.0384	0.0684
36	0.0166	0.0424	0.0590
	11.1283	6.0610	17.1893

*All the heating rates are in MeV per D-T neutron

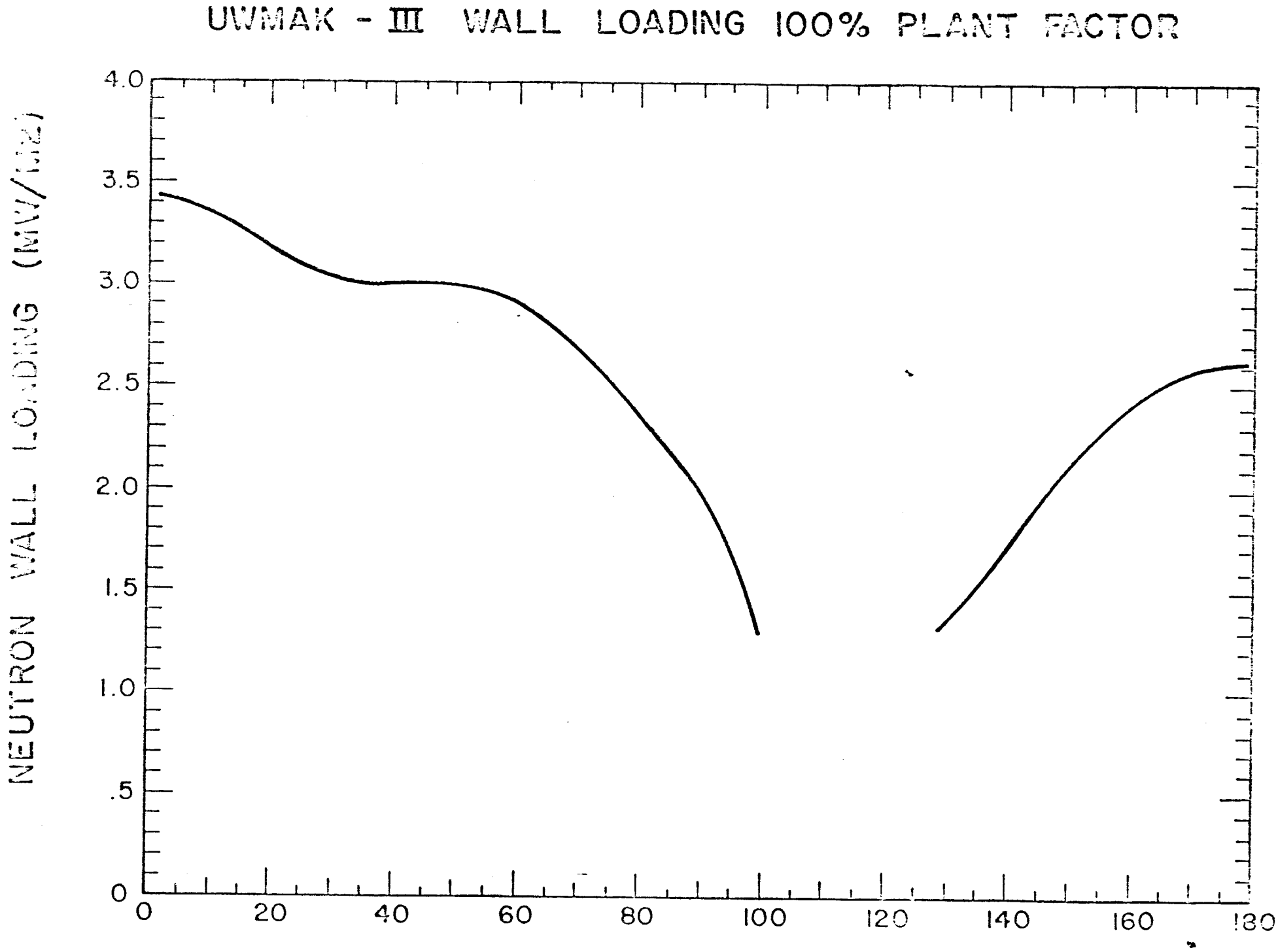
UWMAK - III WALL LOADING 100% PLANT FACTOR
NEUTRON WALL LOADING (MW/M2)
4.0
3.5
3.0
2.5
2.0
1.5
1.0
.5
0
0
20
40
60
80
100
120
140
160
180
POLOIDAL ANGLE (DEGREE)

Figure 5-5

Figure 5-6

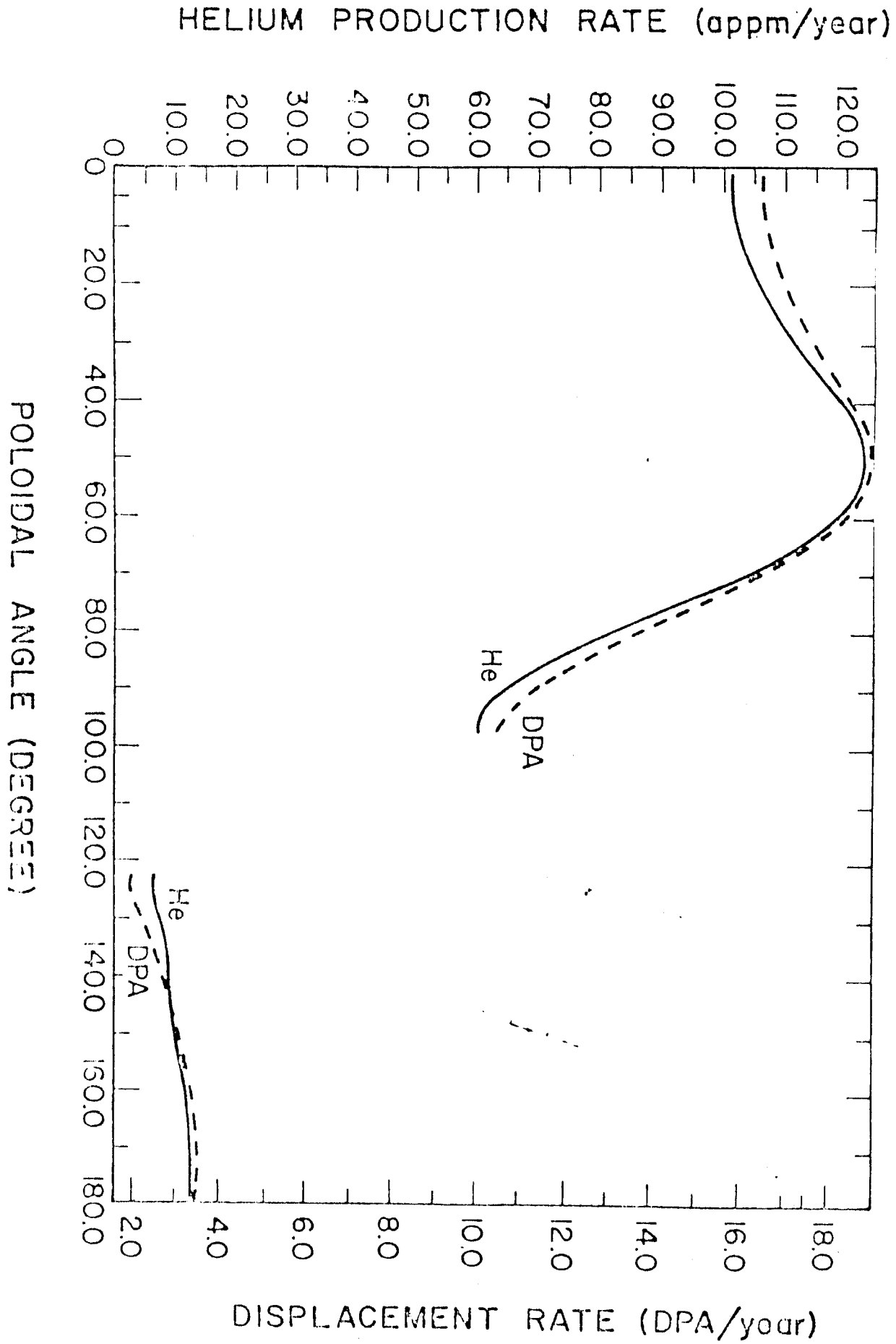
HELIUM PRODUCTION RATE (appm/year)
10.0
20.0
30.0
40.0
50.0
60.0
70.0
80.0
90.0
100.0
110.0
120.0
0
0
20.0
40.0
60.0
80.0
100.0
120.0
140.0
160.0
180.0
POLOIDAL ANGLE (DEGREE)
He
DPA
He
DPA
2.0
4.0
6.0
8.0
10.0
12.0
14.0
16.0
18.0
DISPLACEMENT RATE (DPA/year)

6. Thermal Hydraulics and Mechanical Design Aspects of the Blanket Design

The blanket design described in the previous section has three distinct components from a heat transfer viewpoint; the hot inner shield, the partial ISSEC of 25 cm graphite, and the outer breeding blanket. The neutronics calculations give the local neutron and gamma heating rates required as input to the heat transfer analysis.

The maximum allowable temperature in the graphite is not yet accurately defined. This temperature limitation may be set by any one of the following processes:

1. Evaporation process, causing the carbon vapor to be condensed on the panels in the cyropumps or causing impurity buildup in the plasma.

2. High temperatures inside the ISSEC, causing carbon transport.

3. Formation of hydrocarbons, particularly acetylene.

In this study and for reasons described in section 2, it is assumed that the maximum allowable surface temperature is 2000°C.

The heat deposited in the partial ISSEC zone will be transported to the front and back surfaces and radiated away. Thus, the maximum temperature will occur inside the graphite rather than at its surface. The heat transfer calculations based on the heating rates generated by the x-y geometry neutronics calculations show the temperatures in the ISSEC are within the specified limits if the graphite has a thermal conductivity comparable with 890S graphite. The surface temperature is $\lesssim$2000°C and the maximum temperature in the interior is ~2300°C. Recent neutronics calculations using R as the primary coordinate and thus including toroidal effects show that the heat deposition is reduced by about 25% compared with the x-y analysis. As such, the temperatures within the graphite will drop accordingly and nuclear grade graphite could be used without exceeding the specified temperature limits. The graphite curtain has no real temperature problems as calculations give its operating temperature as 1300°C.

The thermal energy in the ISSEC will be radiated away and this leads to high surface heating loads on the first structural walls. These are calculated to be 35 W/cm^2 on the TZM first wall of the inner hot shield and 25 W/cm^2 on the outer first structural wall.

Two of the most severe problems in the design of a lithium cooled Tokamak blanket are MHD problems and thermal recirculation problems. The MHD problems are caused by the circulation of electrically conducting lithium across magnetic field lines. The thermal recirculation problems are caused by the proximity of hot and cold lithium streams. The major feature of the outer blanket design in UWMAK-III is to minimize these two effects.

The base shape of a heat transfer unit is U-shaped, which is the same as in UWMAK-I.[1] This heat transfer cell design gives the lowest possible $\underline{V} \times \underline{B}$ value within the blanket and, therefore, minimizes MHD effects. However, this shape has to be modified to prevent heat transfer between adjacent legs of the cell. Fig. 6-1 shows a heat transfer cell for the UWMAK-III blanket. The width of the cell is 37 cm and there is a 10 cm wide static lithium zone in the middle of the cell which serves as thermal insulation. The high temperature in the middle of the static zone prevents heat transfer from the hot region toward the cold region. This design has a MHD pressure drop within the blanket of 60 psi. The important dimensions of the outer blanket are given in Table 6-1.

The lithium coolant pressure drop has been calculated including both effects described above and using the local magnetic field, $\underline{B}$, consisting of poloidal and toroidal components. The maximum coolant pressure on the first wall is only 70 psia and the pumping power required is just 2 MW. This shows the advantage of using the liquid metal coolant for the outer blanket only.

A two dimensional finite difference method has been used to calculate the temperature profile for a typical cell as shown in Fig. 6-2. The maximum temperature of the TZM structure is 1000°C and the exit temperature of the lithium to the power cycle is 980°C. The lithium velocity in the buffer zone is taken as zero for the heat transfer calculations although it will have a small velocity to facilitate tritium recovery.

The inner hot shield, or inner blanket, in UWMAK-III is cooled with helium. A 0.5m diameter feed tube is introduced between the TF magnets and connected to a manifold running in the toroidal direction. The surface heating load on the inner blanket is 35 W/cm^2 and, together with the space dependent volumetric heating from the neutronics analysis, leads to a coolant inlet temperature of 488°C and an outlet temperature of 870°C at 1000 psi pressure. These coolant conditions match the temperature of the helium coming from the secondary heat exchanger of the outer blanket cycle such that identical turbines and thermal energy storage can be used. This is discussed in Section 10.

The distribution of coolant tubes within the inner blanket are arranged to be inversely proportional to the heating rate so that the heat load on each coolant tube is approximately the same.

A large amount of Mo is used in the inner blanket for shielding reasons and most of this can be in the much less expensive form of powder. However, because both powdered Mo and B_4C are poor thermal conductors, we find that approximately 35% of the total Mo has to be in the form of fine sheet oriented to provide a conduction path to the TZM coolant tubes. The maximum allowable temperature in the B_4C and nonstructural Mo is assumed to be 1250°C.

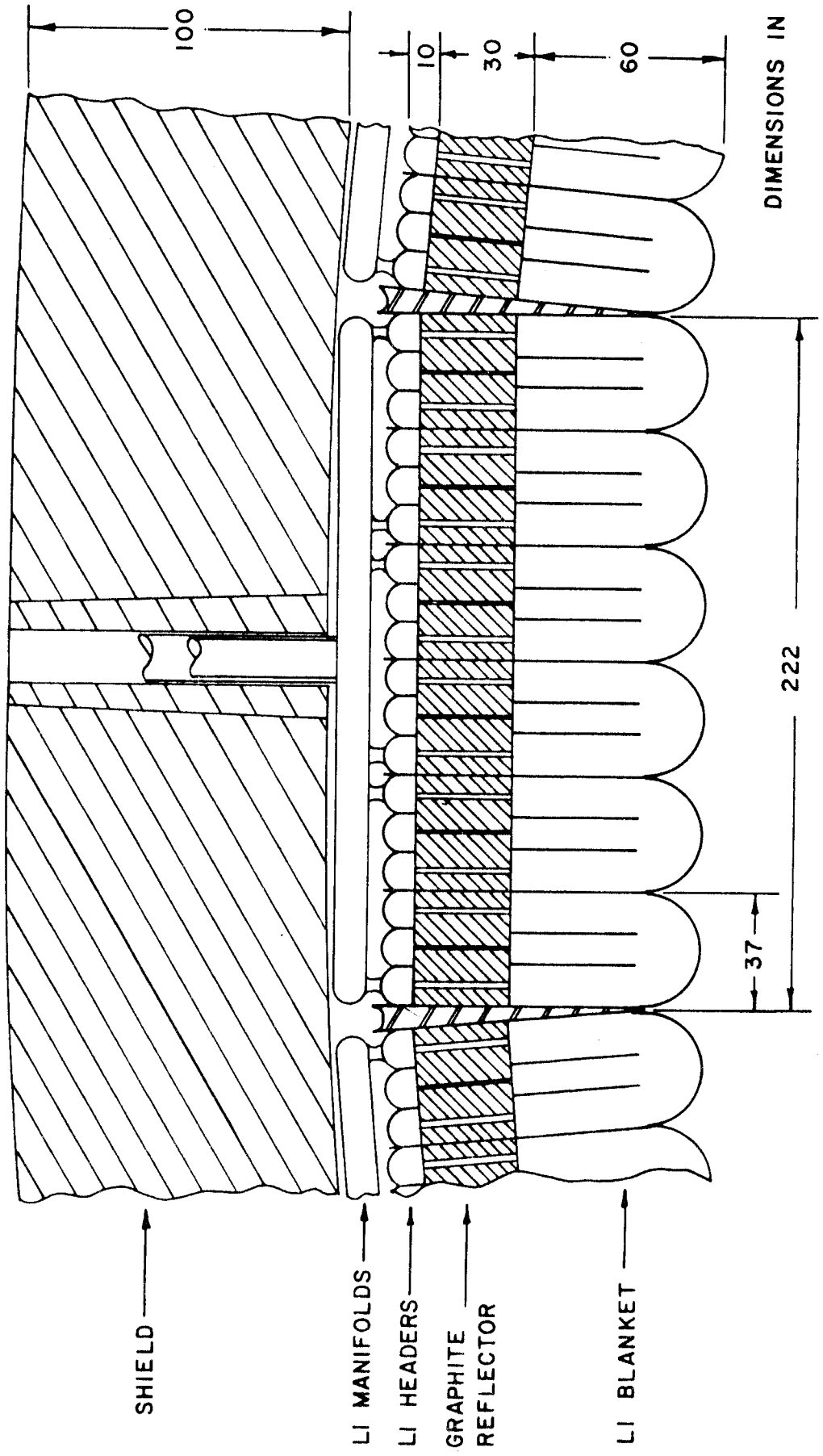

Fig. 6-1 Cross Section of Outer Blanket and Shield Viewed in the Toroidal Direction

TABLE 6.1

Important Dimensions of the Outer Blanket

Thickness of the First Wall	1.5 mm
Width of the U-Cell	37 cm
Width of the Lithium Gap	10 cm
U-Cell Wall Thickness	6 mm
Baffle Wall Thickness	2 mm
First Breeding Zone Thickness	60 cm
Refractory Zone Thickness	30 cm
Second Breeding Zone Thickness	10 cm
Percentage Structure in the Blanket	3%
Diameter of the Header	20 cm
Wall Thickness of the Header	2 mm
Diameter of the Feed Tube	50 cm
Wall Thickness of the Header	5 mm

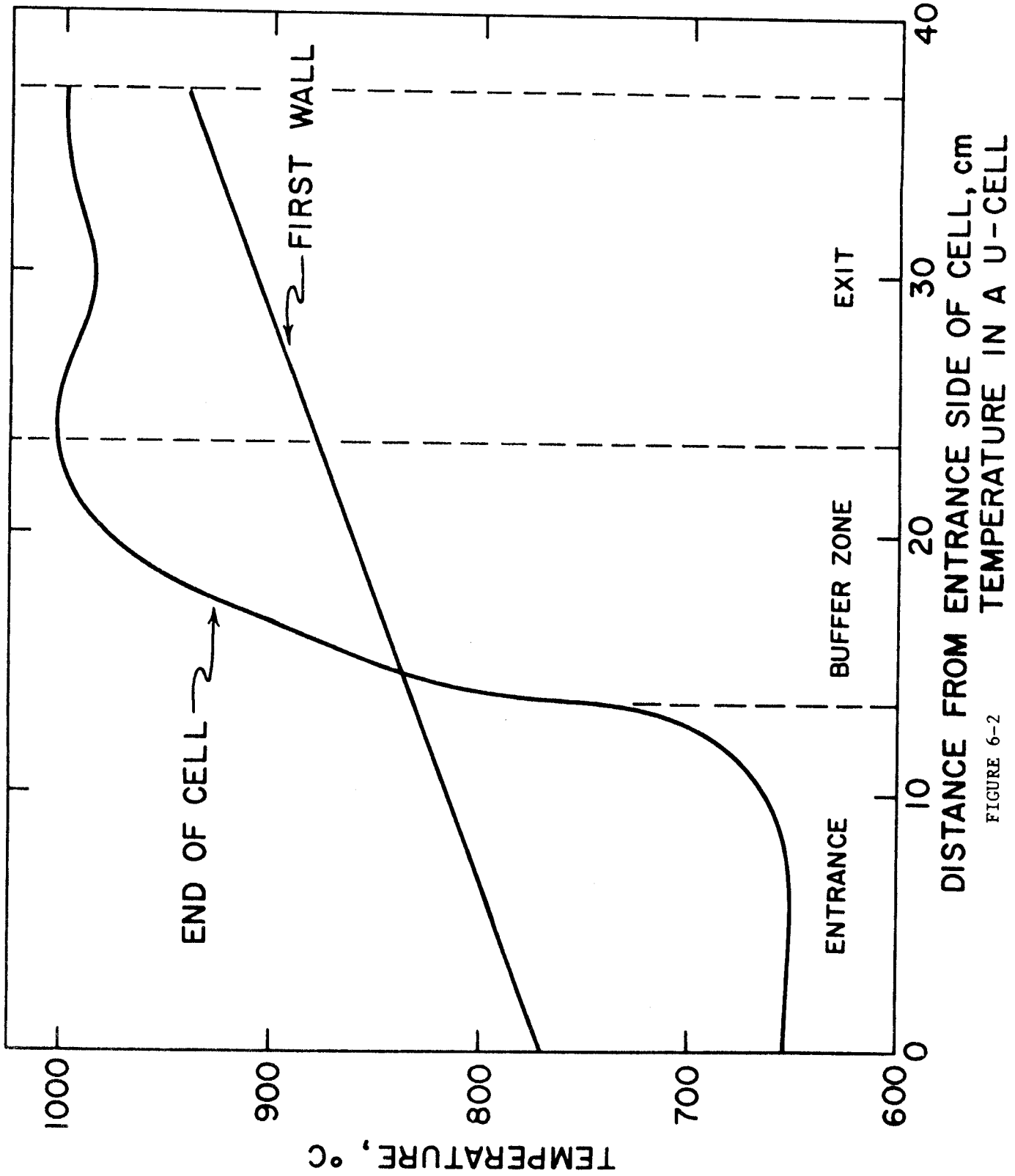

FIGURE 6-2 TEMPERATURE IN A U-CELL

Turning now to the mechanical design aspects, the blanket is divided into 18 equal modules. This is done to allow a blanket module to be taken out between the TF coils of which there are 18. Each module is further divided vertically into two regions. The region subtended by the angles $\pm$ 60° as measured from the plasma center, and which is assumed to have a lifetime of 1 1/2 years will be called region (A). The rest of the outer blanket consisting of the part extending to the first divertor slot and the central region between the divertor slots, which is assumed to have a lifetime of 3 years will be called region (B).

Each (A) region of an outer blanket module will have a skeletal frame shown in Fig. 6-3. This frame is divided into 8 trapezoidal cavities. An assembled section of the blanket consisting of six cells, fits into each cavity and is sealed to it. This design has the flexibility of allowing the removal of a single section or the removal of the whole frame with eight sections.

Region (B) will have a similar frame but the sections will be only 180 cm wide and will have six 30 cm wide cells.

Looking radially out from the plasma, the first 60 cm of the blanket contains lithium with a minimum amount of structure, the next 30 cm contain a TZM clad graphite reflector and the last 10 cm contain the lithium distribution headers. Holes in the graphite block allow the passage of lithium from the headers to the front wall and back. A toroidal view of an outer blanket section is shown in Fig.6-1 and a poloidal view in Fig. 6-4. The heavy wedge shaped material is part of the skeletal frame. It is wedge shaped to allow for poloidal and toroidal curvature. Blanket sections themselves are flat for ease of fabrication.

The entire outer blanket structural material is TZM with the possible exception of the skeletal frame. TZM displays superior properties in thin sheet form and is difficult to fabricate in heavy sections. The front wall material is 1.5 mm thick, the cell frame material is 2.5 mm thick, the partition and header material is 1.0 mm thick and the graphite cladding material is 0.5 mm thick. The skeletal frame thickness tapers from 5 cm thick at the heaviest section down to 0.5 cm, and is about 80 cm high.

TZM can be welded but the weld zone is recrystalized metal and its ductility and strength is affected. A preferable joining method is by brazing. Several high temperature brazing materials have been developed for TZM which have proven to be extremely good. For example, a 25% Ti, 3% Cr, Be brazing material has a liquidus temperature of 1110°C and a remelt temperature of 1700°C. Such a brazing material would be ideal for building up a blanket section, since certain parts can be brazed separately. The whole assembly then can be brazed together without effecting the pre-assembled joints. The final seal between the section and the frame can either be a braze or a weld joint. This region is not very highly stressed and suffers very little radiation damage.

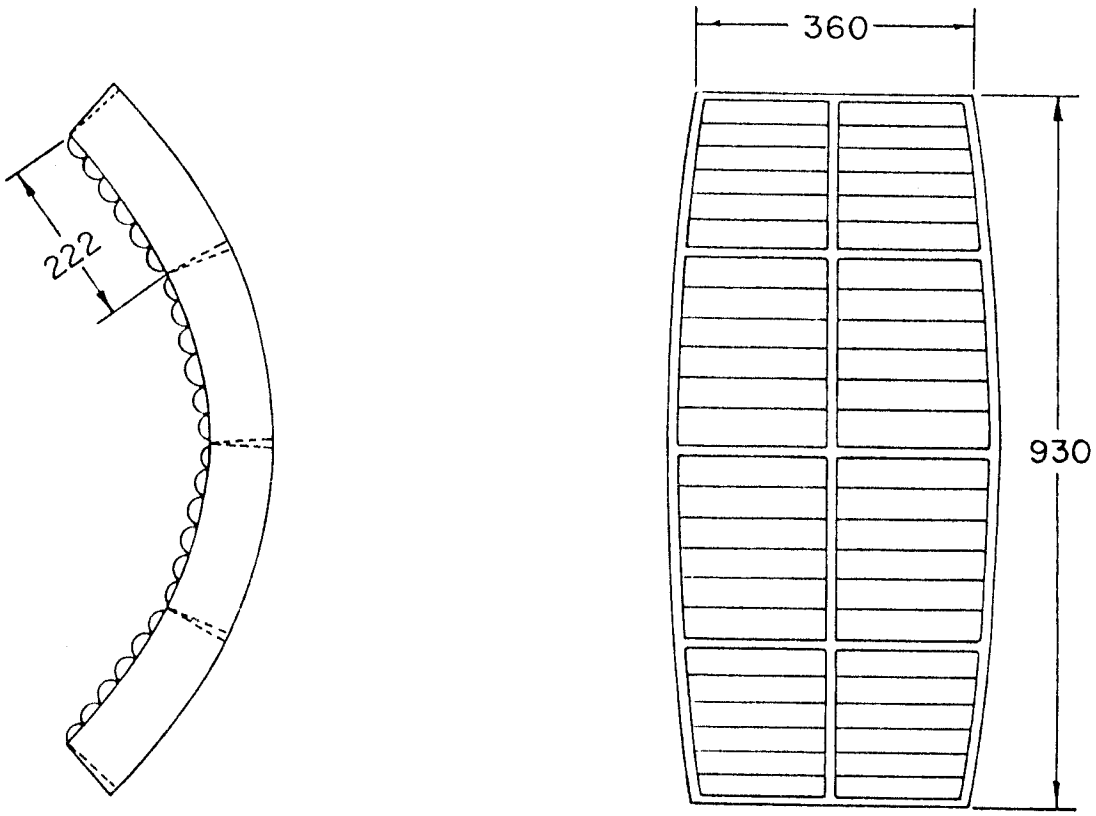

FIGURE 6-3 Skeletal Frame for Region (A) of Outer Blanket
(a) Side view in the toroidal direction
(b) Radial view from outside the blanket

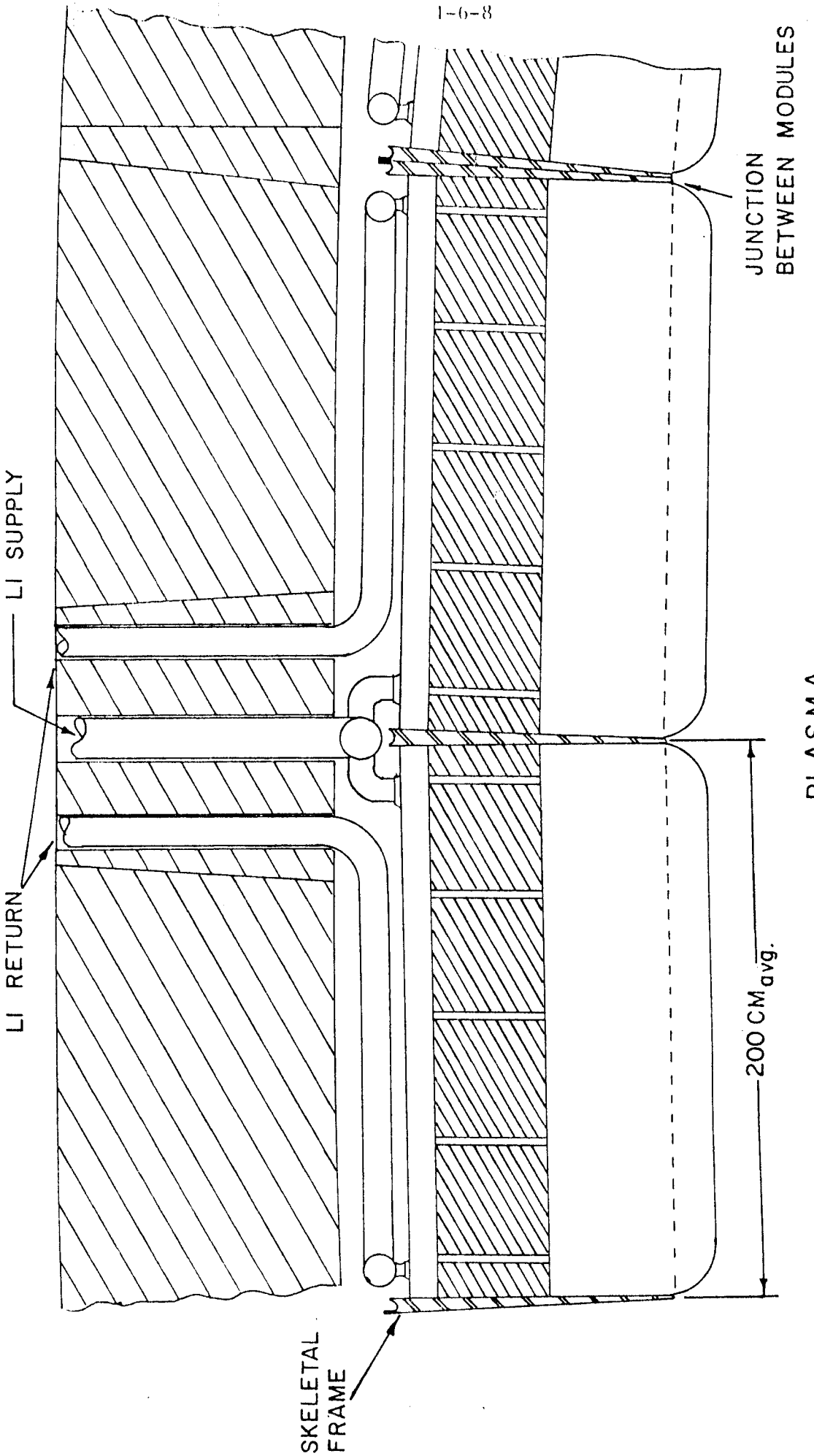

Fig. 6-4 - Cross Section of Outer Blanket and Shield Viewed in the Poloidal Direction

The skeletal frame material can either be TZM or niobium. The latter is easier to fabricate and weld in heavy sections but is not as strong. If the frame is made of niobium, the joint between the TZM section and the frame may present problems because of the difference in their coefficients of expansion.

The design of the inner hot blanket which is helium gas cooled is quite different from the outer blanket. A bank of TZM tubes joined together follows the graphite and essentially provides the seal for the plasma chamber on the inner wall. These tubes are 2 cm in diameter and extend for 12 m in the vertical direction. Additional tubes are provided further back with the number in each row progressively decreasing as a function of the energy deposited at that point. These tubes are embedded in layers of Mo and B_4C. Figure 6-5 shows a section through the inner blanket. Helium gas is supplied to the tubes from a manifold located between the inner divertor slot and the TF coil at the top and exhausts to a similar manifold at the bottom. The stresses in the front wall have been determined by simply adding the thermal and pressure stresses together. No attempt has been made to determine the effect of swelling or creep. A more thorough analysis using finite element codes can be made when more information is avialable on the swelling of TZM and other effects. Stress relieved TZM rolled sheet has a low value for tensile strength at 1000°C of 71,700 psi (5000 KG/cm^2). For recrystallized TZM sheet material at 1000°C, it is 28,680 psi (2014 Kg/cm^2). It is also interesting to note that a stress of 27,200 psi (1909 Kg/cm^2) will produce 0.2% creep in the material at 1000°C in three years. Based on this information, it was decided that a design stress of 10,000 psi (700 Kg/cm^2) would be satisfactory. This corresponds to a thickness of 1.5 mm. Even if 0.5 mm is lost to sputtering and blistering after three years, the stress will only rise to 14,000 psi (980 Kg/cm^2).

The inner shield is essentially a continuous cylinder subtending the inner legs of the TF coils and is composed of Mo and SS honeycomb structure filled with various materials. The weight of the inner shield is 2780 tonnes. It will be supported entirely on columns protruding between the TF coils and built into the floor of the containment building.

Central shield and blanket sections will be supported on structure also penetrating between the TF coils. Upper sections will be supported on the reactor containment building ceiling beams and the lower sections on the floor. Each of these blanket and shield sections weighs 900 tonnes or 50 tonnes per support.

The outer blanket module frames will be attached to reinforced plates which also compromise the wall of the outer divertor slot. These plates are attached to a shield support ring. At the same time, the blanket skeletal frames will also be supported on the shield as mentioned previously.

Although expansion joints for the blanket would be very beneficial, it is difficult to visualize an expansion joint which can subtend the entire plasma chamber including the vacuum plenum. At a temperature of 1000°C, the outer radius of the chamber will increase approximately 7 cm. This would present difficulties, especially if the blanket is attached to the shield which does

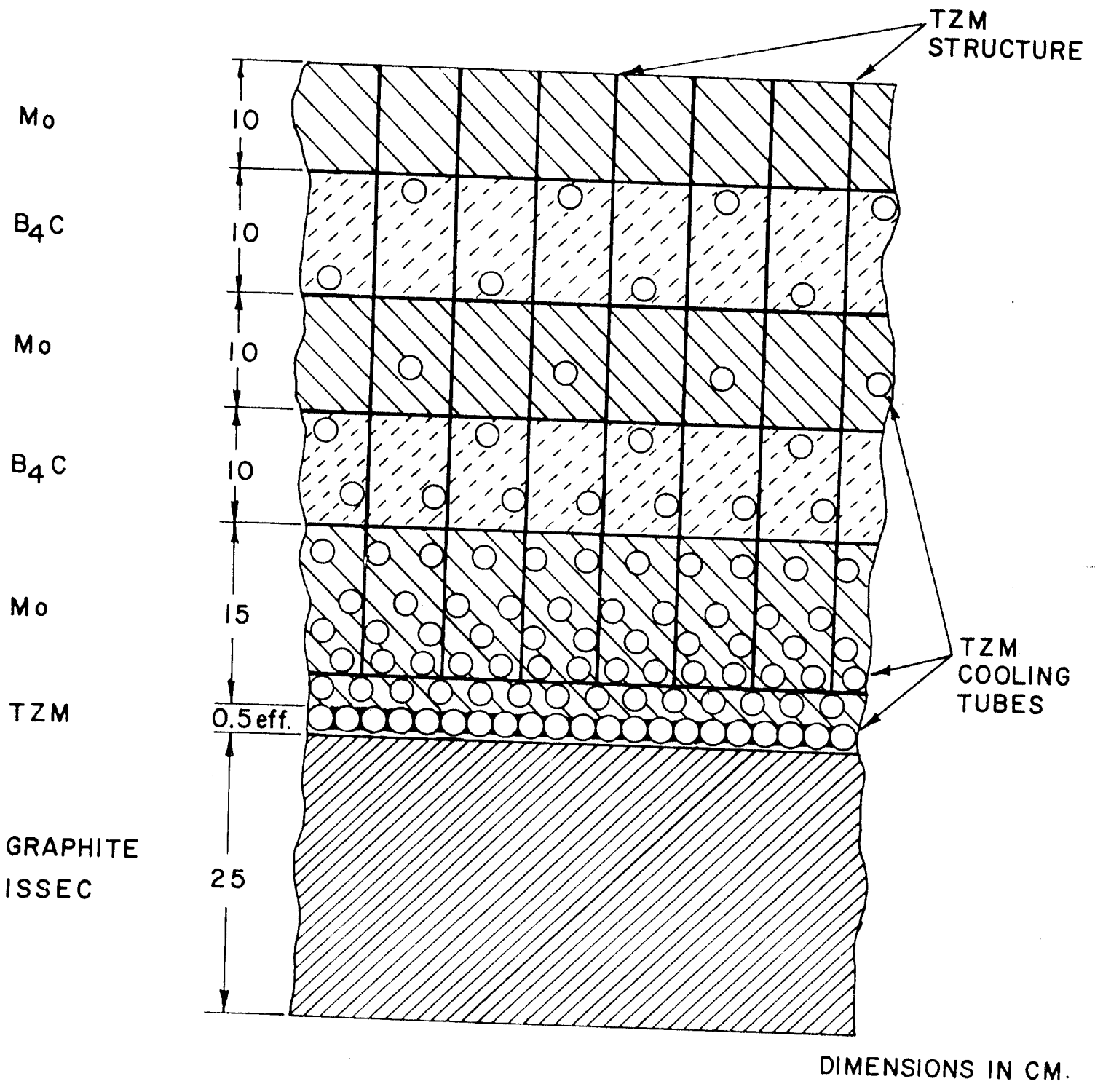
TZM
STRUCTURE
Mo
10
B4C
10
Mo
10
B4C
10
Mo
15
TZM
0.5 eff.
GRAPHITE
ISSEC
25
TZM
COOLING
TUBES
DIMENSIONS IN CM.
PLASMA

FIGURE 6-5

not get as hot. An alternative might be to design expansion joints into the shield without sacrificing efficiency. Some imaginative engineering will be needed to solve this problem.

For reasons to be discussed in section 9, parts of the blanket will be replaced every year and a half and others every three years.

In order to make the blanket accessible for servicing, the following functions must be performed:

1 - The plasma chamber and toroidal enclosure are brought up to atmospheric pressure.

2 - The lateral support structure between the TF coils has to be removed opening up a passage $\pm$ 8 m from the central plane. Simultaneously the blanket is drained of lithium.

3 - If there are RF waveguides in the module in question, they have to be disconnected and extracted.

4 - The VF coils which are in the way have to be retracted. They are supported on mechanical jacks.

5 - The outer lithium manifolds have to be disconnected and removed.

6 - The outer shield must be opened up and firmly secured.

The process for removing a blanket module having a one and a half year lifetime consists of grinding or plasma burning the weld sealing adjacent skeletal frames to each other, and then radially extracting the module between the TF coils. The backlegs of the TF coils are far enough apart as to allow radial extraction of an outer blanket module. Once the reactor is opened, then the rest of the module, namely the regions which are assumed to last three years become accessible. Removing these modules is harder, since it has to be done from the inside of the reactor.

Obviously, all this work has to be done with remote controlled tools by technicians in shielded capsules. We do not imply that any of these operations will be easy. The design and operation of the equipment needed to perform these functions will challenge the imagination of the best engineers.

Since an effort has been made to minimize the material in the blanket, it would seem that discarding the whole spent module is the best way to proceed. The spent modules will be crushed, compacted and stored in special rad-waste areas. The amount of material thus disposed of per year, averaged over three years is 164 tonnes of TZM and 472 tonnes of graphite. Replacement of the blanket modules will now consist of inserting and welding into place new modules. The process of closing up the reactor follows the functions enumerated above in reverse order.

7. The Tritium Systems on UWMAK-III

There are at least five aspects to the tritium problem in UWMAK-III: the recovery and reprocessing of tritium in the divertor and fueling cycle; the extraction of tritium from the breeding material and other heat transfer fluids; the containment of tritium in regions where the permeation rates are anticipated to be high; the recovery of tritium from the reactor building; and the loss of tritium to the enveronment in gaseous or agueous phases, as well as solid form waste. The routes along which tritium flows in UWMAK-III is shown schematically in Fig. 7-1.

The reactor building will have an inert atmosphere contained within an impermeable metal shell. The building system contains an emergency tritium cleanup system that will maintain a tritium pressure of 7.6×10^{-10} torr.

The largest amount of tritium is handled in the fueling and reprocessing cycle and is directly related to the small particle confinement time and low fractional burnup (see section 2). The temperatures of the piping and containment vessels, except within the torus, are very low and the tritium loss problem is minimal as long as the many joints and valves perform satisfactorily. However, the outer blanket power cycle operates at a very high temperature. Here the tritium bred in the lithium diffuses through the heat exchanger walls to the sodium and then to the helium. The pressure of tritium in the sodium loop is maintained at 7.6×10^{-10} torr; this ultimately becomes tritium pressure in the helium loop. Losses to the building environment at this point should be low (<1 curie/day).

In turn the tritium in the lithium must be maintained at a concentration such that diffusion into the sodium does not result in a tritium loss rate that exceeds the sodium cleanup system capacity. The tritium concentration in the lithium must also be low enough to prevent substantial leakage through the piping and valves.

We have designed a system which meets the above requirements. This system operates with a steady state tritium inventory in the lithium of 1 kg (2.08 ppm) and a leak rate into the sodium of 1256 curies/day. The sodium cleanup system will process this amount of tritium and maintain a tritium pressure over the sodium of 7.6×10^{-10} torr.

The solid fuel pellets are injected into the plasma at a rate of 1.63 kg of tritium and 1.085 kg of deuterium over the 30 minute burn time. This amounts to 74.4 kg of tritium and 49.6 kg of deuterium on a twenty-four hour basis. Of this quantity only 0.620 kg of tritium and 0.413 kg of deuterium are consumed. The unburned fuel and product helium ions are directed to a divertor plate where their energy is transferred to a stream of liquid sodium. The particles are then collected over a five hour period in cryopumps containing molecular sieves at cryogenic temperatures. The total inventory of tritium in the cryopumps after five hours is 15.5 kg. Two sets of cryopumps operate such that the one set collects hydrogen isotopes and helium while the second set is regenerated. The regenerated gaseous hydrogen isotopes and helium are freed from the molecular sieves by heating to 30°K. The gases released from the

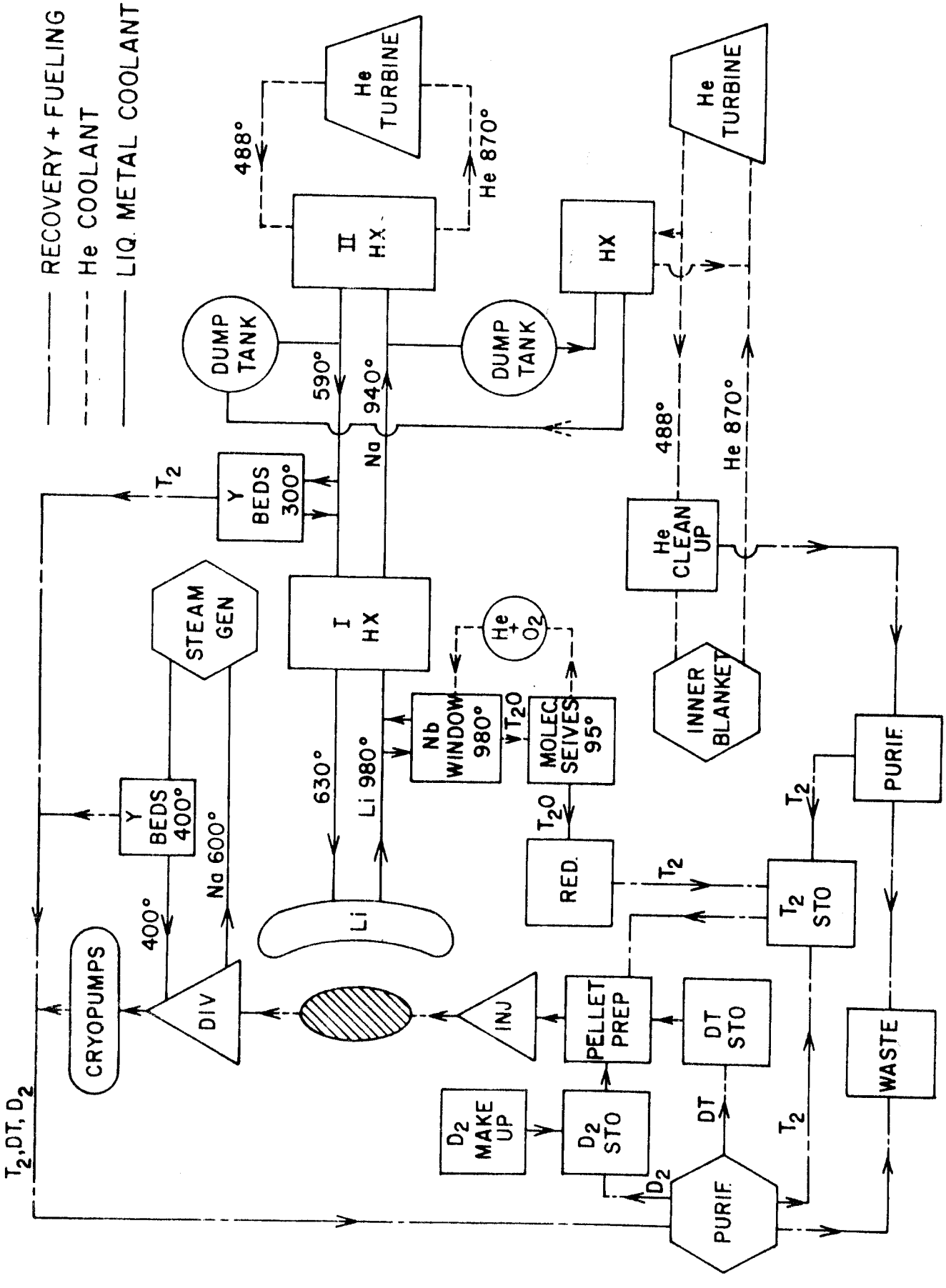

TRITIUM IN UWMAK III SYSTEM

cryopumps are to be purified by chromatographic stripping on molecules seives cooled to -131°C for the separation of all impurities except He, H_2 and HD. This hydrogen isotope stream is joined by other tritium streams and is fed to a cryoscopic fractional distillation apparatus based on a design developed by W. R. Wilkes.[14]

The extraction of the tritium bred in the liquid lithium in the outer blanket is removed using a niobium window. The liquid lithium is diverted to a niobium "window"[15] for the extraction of tritium. Niobium is particularly well suited for this purpose as it has a high permeability to hydrogen at these temperatures[16] and allows us to reduce the tritium concentration of the lithium to a level compatible with the subsequent tritium losses to the environment. Other methods for the extraction of tritium from lithium, such as yttrium beds, molten salt extraction, liquid alloy getters and fractional distillation, were considered but were not found to be as attractive.

However, the niobium window is not without its own problems. The oxygen level in the niobium must be less than 100 ppm or the lithium will erode the surface, and preferentially attack grain boundaries. Also carbon transport from the TZM will occur, causing embrittlement of the niobium. In addition, at 980° niobium will be subject to attack by oxygen and therefore some protective barrier is required. Palladium is the barrier of choice since it has a high hydrogen permeability. A palladium thickness of 0.001 cm deposited by electric deposition will give a coherent layer of suitable durability. This will require a total of 170 kg of palladium for the calculated surface area of the window.

Also, the mutual solubility of Nb and Pd is quite high and it is expected that the palladium will diffuse into the niobium, though there are no firm data for the rates of interdiffusion. Therefore we propose to introduce an intermediate yttrium layer to minimize the rates of diffusion so that a practical "window" lifetime can be achieved. Yttrium was chosen because it, along with the other IIIa elements and some of the rare earth metals, are among the few metals which do not form solid solutions with niobium. The required yttrium layer thickness is estimated to be 2500 Å. This will require a total of 2.0 kg of this element for the calculated surface area of the window.

The high temperatures in UWMAK-III creates a situation in which large amounts of tritium could leak through pipes. For example, the high temperature side of the lithium system is at 980°C and has a tritium pressure of 1.0×10^{-6} torr. The approximate pipe dimensions are 2×10^6 cm^2 area and 5 mm thickness. Assuming the downstream pressure is zero, the leak through such piping is 92 curies per day.

To protect the TZM from oxidation, the pipe is double walled using an outer pipe of stainless steel lined with ceramic insulating material. Since the temperature of the jacket is much lower and the permeability of the ceramic is very low, the release of tritium to the reactor building is vanishingly small.

The plant inventory of tritium is estimated to be 35.8 kg (Table 7-1). It should be noted that of this only 1.7 kg is in the breeding-recovery cycle.

The 34.1 kg in the refueling cycle includes 18.6 kg in reserve storage. The reason the refueling cycle inventory is so large is that more realistic, space-dependent plasma calculations were used in this study. The result is a fractional tritium burnup of only 0.8%, compared to 7.2% and 2.8% burnup calculated on the basis of the simpler plasma model used in UWMAK-I[1] and UWMAK-II.[2] Assuming 5% burnup, the refueling cycle tritium inventory would only be 5.5 kg and the total plant inventory would be 7.2 kg.

Table 7-1

Tritium Inventories (kg)

Cryopumps	7.75
Reprocessing	7.75
Storage	18.6
Outer Blanket - Li	1.0
Recovery - Li	0.666
Outer Blanket - Na	2.0×10^{-4}
Outer Blanket - Na (Y beds)	1.6×10^{-4}
Divertor - Na	6.0×10^{-4}
Divertor - Y beds	7.5×10^{-3}
Total	35.8 kg

8. Radioactivity and Afterheat in UWMAK-III

Induced radioactivity and afterheat are important aspects of fusion systems based on a neutron producing fuel cycle, and the analysis for UWMAK-III is particularly interesting because of the use of TZM rather than stainless steel as the primary structural material. The procedure for calculating radioactivity in the UWMAK-III system follows very closely that developed for UWMAK-I[1] and II[2]. Modifications have been made to account for the two dimensional characteristic of the UWMAK-III blanket as well as to incorporate more second order reactions.

The buildup of the total activity in the outer blanket including the inner blanket first wall is shown in Fig. 8-1. The rapid initial buildup is due to the production and saturation of the short half life isotopes ^{99}Mo ($T_{1/2}$ = 66 hr), ^{99m}Tc ($T_{1/2}$ = 6 hrs) and ^{91m} ($T_{1/2}$ = 16 min). The activity approaches a constant value after 1-2 months. If the blanket were to be left in for a long period of time (> ~5 yr) a slight decrease in activity would result due to the burn up of some of the parent nuclei over-riding the slow buildup of long lived nuclei. Fig. 8-2 also shows the buildup in the first breeding zone due to the large amount of material contained therein. However, the highest specific activity is, of course, in the first wall. The first wall and the first breeding zone are the major contributors with the reflector contribution only ~5% of the total.

The activity in the blanket after shutdown is of considerable interest not only from the point of view of radiation levels during the blanket change out or other maintenance, but also because of its implication in accident potential, recycling, and long-term radioactive waste. Fig. 8-2 shows the activity of the outer blanket and the inner blanket first wall following two years of operation. The activity levels at shutdown are of the same magnitude as in UWMAK-I and II but, because of the use of molybdenum (TZM) as a structural material, there are some significant differences in the time behavior of the activity following shutdown. In particular, it is seen that there is still a relatively slow decay of the activity for the first day or so, but following there is a relatively rapid decay requiring only 3 weeks for the activity to be down by a factor of 100. This contrasts to SS systems where the times are measured in years for this to take place. By about three years the short lived activities have died out and the activity has assumed its long-term value almost four orders of magnitude below the shutdown value. This long term activity is dominated by ^{93}Mo($T_{1/2}$ = 3 x 10^3 yr) and ^{93m}Nb($T_{1/2}$ = 14 yrs) with a small contribution from ^{99}Tc($T_{1/2}$ = 2 x 10^5 yr). This residual activity is higher than would be associated with a SS system but its effect is better put in perspective in the discussion of afterheat. It is seen that the first wall contributes about 25% of the activity at shutdown.

The buildup of the afterheat is shown in Fig. 8-3. As was the case with the radioactivity, saturation is seen to occur after about 3 weeks of operation. The major portion of the afterheat comes from the first breeding zones as expected.

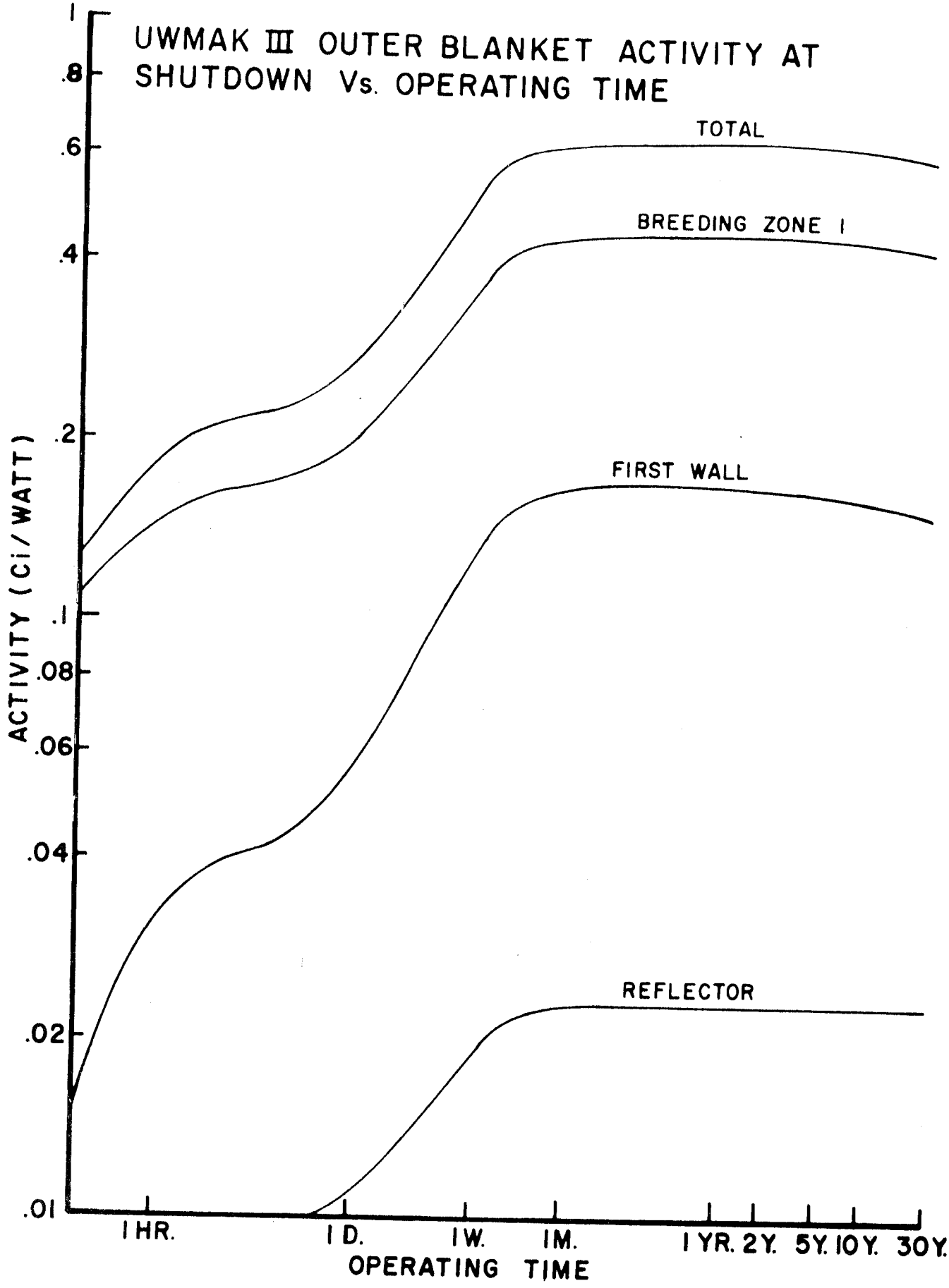
UWMAK III OUTER BLANKET ACTIVITY AT SHUTDOWN Vs. OPERATING TIME
TOTAL
BREEDING ZONE I
FIRST WALL
REFLECTOR
ACTIVITY (Ci/WATT)
1
.8
.6
.4
.2
.1
.08
.06
.04
.02
.01
1 HR.
1 D.
1 W.
1 M.
1 YR.
2 Y.
5 Y.
10 Y.
30 Y.
OPERATING TIME

FIGURE 8-1

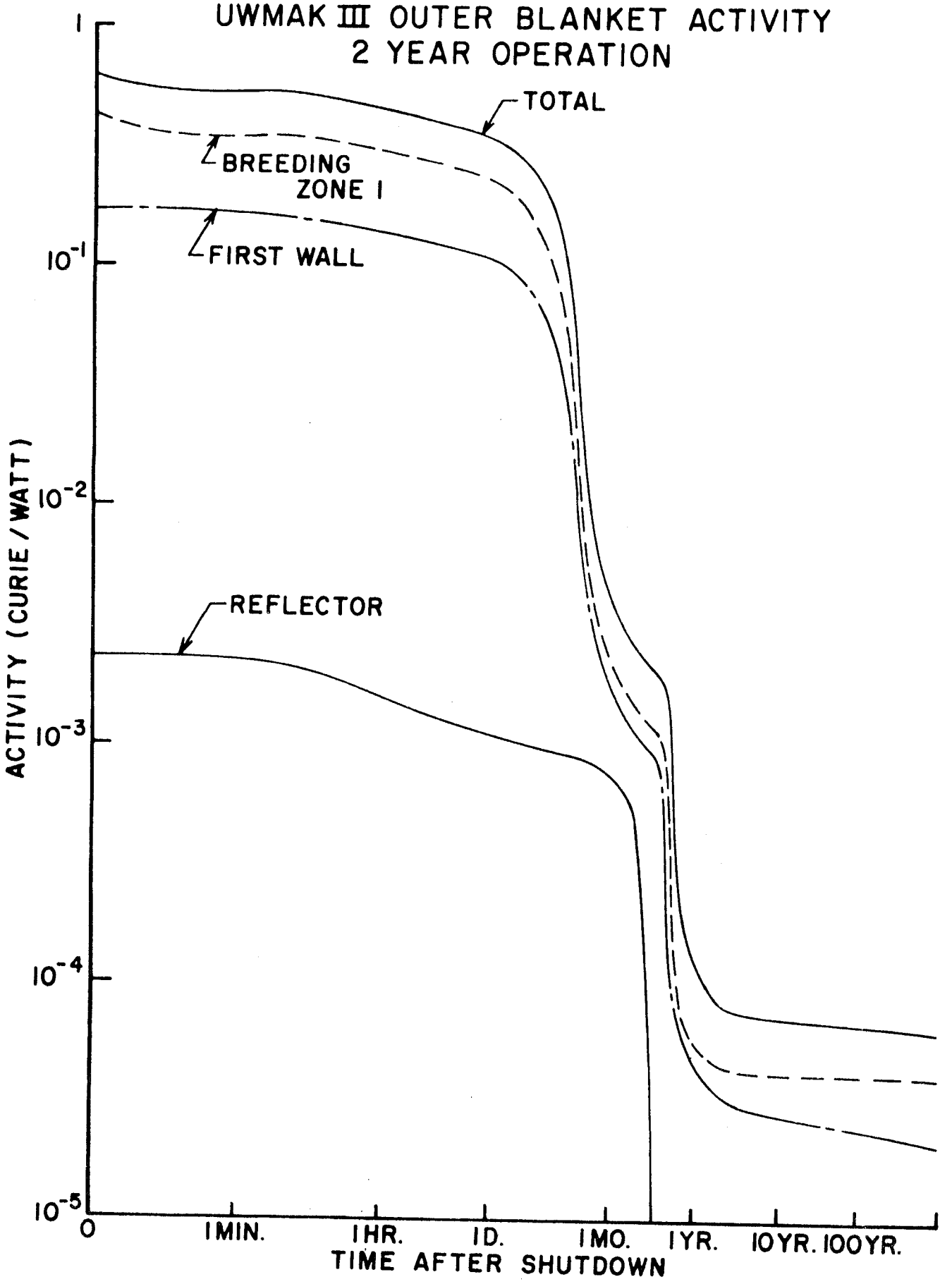
UWMAK III OUTER BLANKET ACTIVITY
2 YEAR OPERATION
TOTAL
BREEDING
ZONE I
FIRST WALL
REFLECTOR
ACTIVITY (CURIE / WATT)
1
10-1
10-2
10-3
10-4
10-5
0
1MIN.
1HR.
1D.
1MO.
1YR.
10YR.
100YR.
TIME AFTER SHUTDOWN

FIGURE 8-2

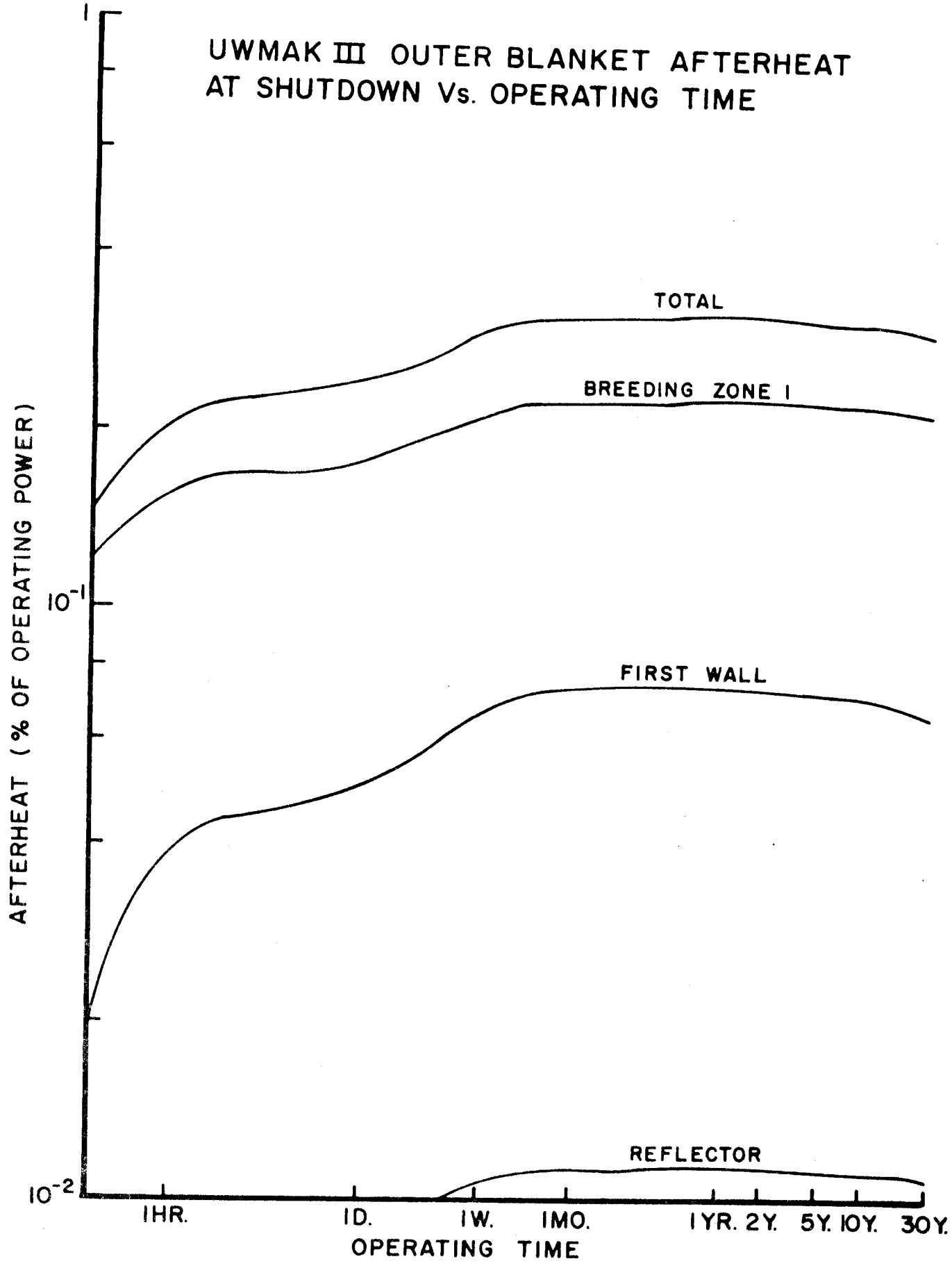
UWMAK III OUTER BLANKET AFTERHEAT
AT SHUTDOWN Vs. OPERATING TIME
TOTAL
BREEDING ZONE I
FIRST WALL
REFLECTOR
AFTERHEAT (% OF OPERATING POWER)
1
10^{-1}
10^{-2}
1HR.
1D.
1W.
1MO.
1YR.
2Y.
5Y.
10Y.
30Y.
OPERATING TIME

FIGURE 8-3

The decay of the afterheat following shutdown is shown in Fig. 8-4 for the case of 2 years of operation. Tritium is neglected. The sharp initial drop from 0.31% to 0.24% immediately following shutdown is due to the decay of very short lived ^{6}He ($T_{1/2}$ = 0.8 sec). The decay heat drops off more slowly than the activity, requiring 2 weeks to drop by a factor of ten and 1 month by a factor of 100. By the end of one year, however, the afterheat is approaching its long term value of approximately 10^{-6}% or a total heating of only ~50 watts. Although the activity is dominated by ^{93m}Nb and ^{93}Mo, because of the larger amount of energy in its decay, the afterheat at long times is primarily due to ^{99}Tc. This level of afterheat is greater than that expected for a SS system but less than that of a Nb based structure.

We have also calculated the "Biological Hazard Potential", or BHP, for UWMAK-III. BHP is defined as the activity in Curies/kw_{th} divided by the maximum permissible concentration (MPC) for general public exposure in Curies/km^3 of air as taken from 10CFR20, Appendix B, Table II, Column 2. The BHP is the volume of air required to dilute the activity per thermal kilowatt to MPC. It has proven to be a useful, if not definitive, way of making comparisons between systems and of making initial assessments of potential hazards of catastrophic events.

The BHP of the total blanket at shutdown after two years of operation is shown in Table 8-1. As is expected, the values are higher and are due primarily to the outer blanket. The BHP after two hundred years of decay is also shown and these values are reduced by a factor of 500 from the values at shutdown. It is clear that the major contribution comes from five relatively short lived isotopes and that the total BHP is of the same order as for the stainless steel first wall of UWMAK-I[1]. It should be noted that contributions for isotopes not listed explicitly in 10CFR20 have been included, and probably overestimate the total BHP.

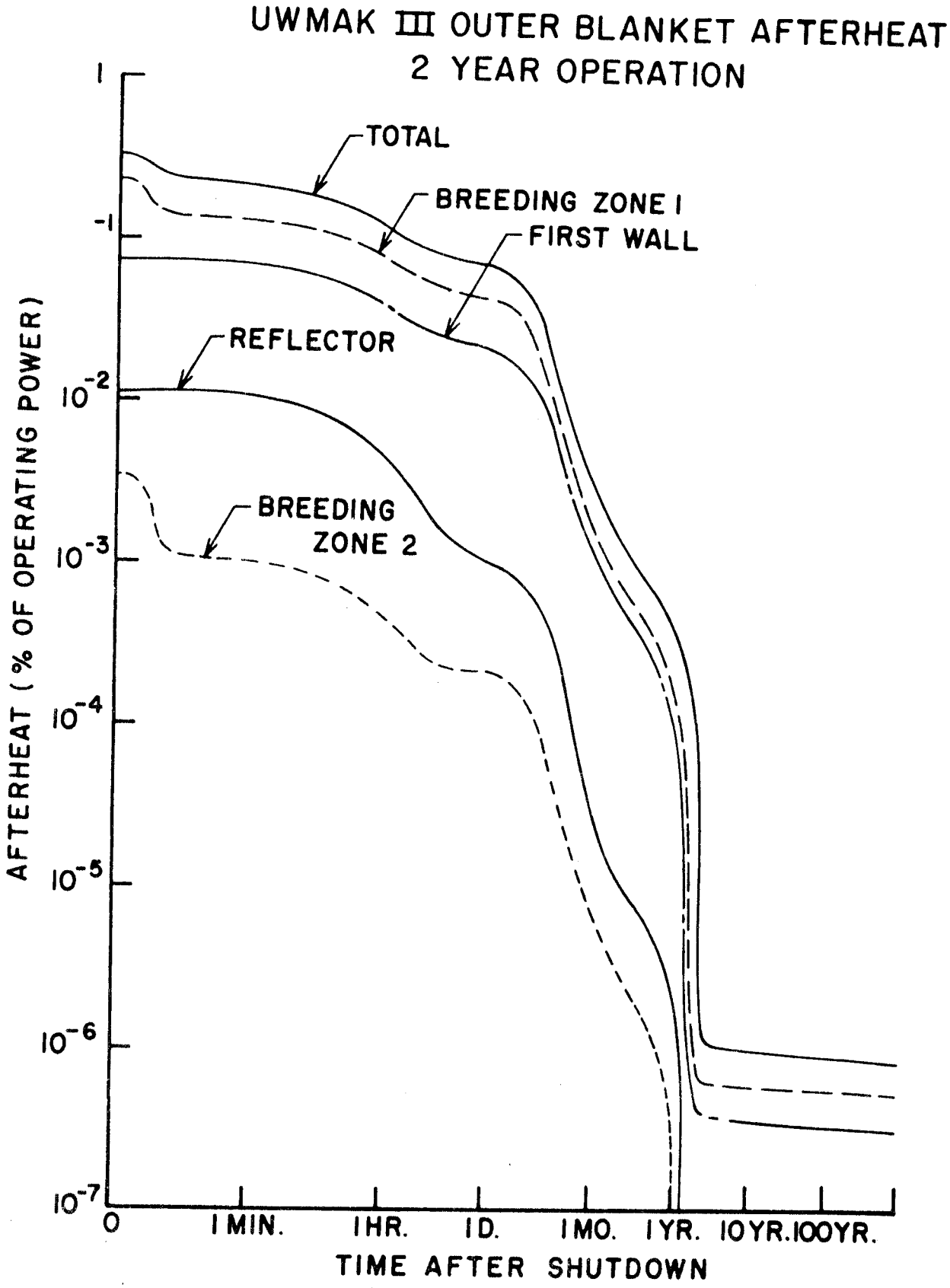
UWMAK III OUTER BLANKET AFTERHEAT
2 YEAR OPERATION
AFTERHEAT (% OF OPERATING POWER)
1
-1
10^{-2}
10^{-3}
10^{-4}
10^{-5}
10^{-6}
10^{-7}
TOTAL
BREEDING ZONE I
FIRST WALL
REFLECTOR
BREEDING
ZONE 2
0
1 MIN.
1 HR.
1 D.
1 MO.
1 YR.
10 YR.
100 YR.
TIME AFTER SHUTDOWN

FIGURE 8-4

TABLE 8-1

BHP OF DOMINANT ISOTOPES AT SHUTDOWN IN UWMAK - III
- TWO YEAR OPERATING TIME

ISOTOPE	BHP (km^3 air/kWth operating power)		
	OUTER BLANKET	HOT SHIELD	TOTAL
Nb 92^m	44.43	7.11	51.54
Zr 89	38.27	5.66	43.93
Nb 95^m	30.24	4.60	34.84
Mo 99	28.63	17.27	45.91
Nb 96	18.64	2.60	21.24
Nb 91^m	9.81	1.25	11.06
Te 101	1.46	1.49	2.95
Mo 101	1.46	1.57	3.03
Mo 95	1.60	.24	1.84
Zr 95	1.02	.16	1.18
Mo 91	1.01	.12	1.13
TOTAL (including other isotopes)	181.38	43.66	225.04

BHP OF DOMINANT ISOTOPES 200 YEARS AFTER SHUTDOWN
- TWO YEAR OPERATING TIME

Mo 93	.32	.15	.47
Nb 93^m	.01	~ 0	.01
TOTAL	.33	.15	.49

9. Materials

The choice of the molybdenum based alloy, TZM (99.4% Mo, 0.5% Ti, 0.1% Zr, 0.01% C), is governed in part by the basic philosophy of the UWMAK-III study, i.e., an advanced high temperature reactor, and in part on the assessment that TZM is the most attractive of the materials with the potential for high temperature (~1000°C) operation. On the other hand, it is fully anticipated that near term fusion systems and most likely the first demonstration reactors will use an austenitic stainless steel as the basic structural material. The reasons for this are presented in previous work,[1,2] where 316 stainless steel was the structural material chosen. Such systems have upper limits to the temperature that can be achieved such that the overall efficiency of the plant will be in the 35% range. To achieve still higher plant efficiencies, it is necessary to go to higher temperatures and this implies the use of either refractory metals (V, Nb, Mo or Ta) or nonmetals such as carbon or silicon carbide. The use of nonmetals as structural materials seems very difficult and the choice of TZM was based on a comparison of the metals and alloys which can potentially meet the necessary criteria.

At least ten different properties must be considered in deciding on a structural material for a fusion reactor. These are physical properties, mechanical properties, thermal properties, fabricability, neutronic properties, chemical compatibility with coolants, radiation damage, materials availability, interaction with tritium and cost. Obviously, no metal or alloy will satisfy all of these criteria and the ultimate choice of a CTR structural material will depend on the compromise between all of the ten properties mentioned above. At the present time there are only five metal systems seriously considered for CTR application and each has its own temperature range of importance. These are summarized below:

Low temperature (~200°C)	Aluminum alloys Austenitic steels
Medium temperature (200-600°C)	Austenitic steels Vanadium alloys
High temperature (600-1000°C)	Vanadium alloys Nb alloys Mo or Mo alloys

Three physical properties of metals are of major importance in fusion reactor technology. These are density, electrical resistivity, and vapor pressure. Table 9-1 summarizes these properties for the five systems considered here. The mass density is important with respect to dead weight loads of massive structures. This load is a complex function of yield or creep strength for a given internal and external pressure load and the mass of the structure depends roughly on the ratio of $\rho(T)/\sigma(T)$ where $\rho(T)$ is the density at a given temperature and ρ/σ are desirable. In the low temperature (<200°C) range, the Al alloys are best with Nb alloys clearly much worse. In the intermediate range (400-600°C), aluminum alloys are no longer applicable and V-20 Ti is clearly the best with 316 SS and TZM next. Finally in the high temperature range (600-1000°C), V and Mo alloys are the best while Nb-1Zr is clearly much worse.

Table 9-1

Selected Physical Properties of Potential CTR Structural Materials

Property	Al	Steel	V	Nb	Mo
Atomic Weight	27	~56	50.9	92.9	95.9
Melting Point °C	660	~1430	1900	2468	2620
Density (g/cm^3)	2.7	7.98	6.1	8.6	10.2
Atomic Density (10^{22} atoms/cm^3)	6.0	8.5	7.2	5.6	6.4
Electrical Resistivity					
($\mu\Omega$-cm) - 100°C	3.9	78	24	17	8
400°C	9	100	44	31	11
800°C		122	66	43	18
Vapor Pressure at Temperature (°C)					
10^{-7}_{-4} torr	800	900	1200	1920	1830
10^{-1}_{-1} torr	1150	1100	1810	2250	2350
10 torr	1660	1500	2050	3200	

There are five main mechanical properties that are of interest to fusion reactor designers: yield strength; high strain rate ductility; creep strength; fatigue life; and fracture toughness. These properties have been compared for Mo, TZM, Nb, 316 SS and aluminum and it is found that over the temperature of anticipated operation, molybdenum (or its alloys) has the highest yield strength, creep strength, and fatigue life of the metals compared. However, its ductility is low and its fracture toughness (ability to resist propogation of existing cracks, or those produced by fatigue or thermal cycling of the system) is about the same or slightly worse than for the other bcc metals.

As for thermal properties, a high value of thermal conductivity is required to minimize induced stresses in rigidly bound blanket components. Molybdenum clearly has the best combination of mechanical and thermal properties over all the temperature ranges, whereas the extremely high coefficients of Al and steel could present some problems.

A large heat capacity is desirable to minimize wide thermal fluctuation for given energy inputs and also to act as an energy reservoir in the event of an accident situation. Aluminum has the highest heat capacity for the low temperature region with Mo taking that honor for the intermediate and high temperature regimes. A summary of selected thermal properties for the materials under discussion is given in Table 9-2.

The important thermal figure of merit to consider is $[\frac{\alpha E}{k(1-\nu)}]$ where α is the thermal expansion coefficient, E is Young's modulus, K is the thermal conductivity, and ν is Poisson's ratio. These are listed in Table 9-3 for the material considered here. The materials fall into three distinct classes, those which have very low (but most desirable) values of the figure of merit (Al and its alloys), those with medium values of the figure of merit (Mo, Nb, and V), and those characteristic of very high values (stainless steels). This comparison shows that the stresses induced in Al are much lower than in the other systems (a factor of 3 lower than for steel). Within the refractory system, the order of increasing stresses is V, Mo, and Nb but the difference is not more than 15%.

We have also reviewed the area of fabricability for the various structural materials. This property is one of the most important and yet one of the most difficult material parameters to measure quantitatively. The final proof of whether a material is fabricable is the ability to construct both large and small components of varying shapes and thicknesses. Such structures should be crack-free and be able to maintain vacuum of high pressure loads.

There is no need to discuss the fabrication and joining of Al alloys and stainless steels. It is even relatively easy to fabricate pure V and Nb into complex shapes and tubes. However, joining of these last two metals is not easy and must be performed under closely controlled conditions to avoid interstitial pickup. The fabrication of V-Ti alloys is not easily accomplished and must be carefully controlled to avoid cracking in large angle bends.

Much of the development of the refractory metals and in particular the Mo alloys was initiated in the mid-to-late 1950's. At that time, the refractory metal industry was in the process of developing new alloys at the same time the aerospace industry was beginning to consider their use as primary structures. The original accent was on strength at temperature and not on fabricability. Alloying elements such as carbon, zirconium, and tungsten were used in ever

Table 9-2 - Selected Thermal Properties of Importance for CTR Materials

Property	Al	Steel	V	Nb	Mo
Thermal Conductivity (Cal/cm-sec ^{o}C)					
100°C	0.56	0.04	0.07	0.12	0.32
400°C	0.55	0.05	0.09	0.14	0.31
800°C		0.065	0.10	0.18	0.28
Coefficient of Thermal Expansion $^{o}C^{-1} \times 10^{-6}$					
100°C	25	16.5	9	7	5
400°C	30	17.5	10	7	5
800°C		19	11	9	6
Heat Capacity (Cal/gm ^{o}C)					
100°C	0.22	0.11	0.12	0.07	0.16
400°C	0.26	0.13	0.13	0.08	0.17
800°C		0.15	0.15	0.08	0.19

Table 9-3 - Figure of Merit for Thermal Stresses in Potential CTR First Wall Materials

	Temp. °C					
Material	25	200	400	600	800	1000
Mo	3620	3450	3250	3270	3250	2980
Nb	3810	3460	3230	3260	3580	3620
V	3490	3440	3430	3270	3100	
316 SS	27,700	24,300	21,400	18,100	16,300	
Al	1100	1200	1300	1400		

* $\left(\frac{\alpha E}{k(1-\nu)}\right)$, Newton per meter - watt. A number as low as possible is desired.

increasing amounts, until some of the alloys were so brittle that they could not be easily fabricated. It was at this point that most of the reports on the difficulty of fabricating refractory alloys began to emerge and many programs designed to use these alloys were modified or stopped.

Many improvements have been made in the last 15 years and many of the brittle and difficult to fabricate alloys have been eliminated. New improved processing and casting techniques are now used and the metals in general have lower ductile to brittle transition temperatures (DBTT) as a result of lower interstitial contents. This trend can be seen in the molybdenum industry, where alloys such as Mo-0.5 Zr, Mo-0.5 Ti, and TZM were created. For one reason or another, most of these alloys have been eliminated from major application with the exception of TZM. This alloy was initially difficult to fabricate and most of the forming was done at elevated temperatures. However, as the metal suppliers began to understand more about the metallurgy of the alloy, the forming temperature began to drop. Then with the advent of the Navy Sheet Rolling Program significant improvements were made in the formability of the alloy. As improvements were made in the alloy, the formation temperature began to drop until it is now at room temperature.

The TZM now produced is the product of technology developed as part of the Navy Sheet Rolling Program. This material was evaluated in the Structural Sheet Evaluation Program conducted at McDonnell-Douglas, and structures have been fabricated which have sharp angles of over 120° and where the panels are joined by welding. Thus, many molybdenum and TZM structures have been fabricated and successfully operated over the past 15 years and while joining large components of Mo alloys in the field will be difficult (as will the welding of Nb and V alloys), it will not be serious enough to remove Mo or TZM from consideration as a viable CTR structural material.

The neutronics aspects of a reactor material are critical if breeding ratios of one or greater are to be achieved. Five cross sections (or sets of cross sections) are important and these are: absorption (n,γ), neutron multiplication (e.g.,(n,2n)), hydrogen isotope gas production, helium gas production, and inelastic scattering. These reactions can lead to induced radioactivity, afterheat, and chemical changes in the host material.

Particular problems for Mo are its large number of isotopes and the fact that Mo has not been used as a major fission reactor material and therefore received little attention until now. The problem is that not all of the above cross sections have been measured for seven Mo isotopes and one must rely to a large degree on calculated values.

There are three general conclusions that can be drawn from an examination of the available nuclear data. (1) Aluminum is most desirable in the low energy neutron range (E<0.1 MeV). This element is followed by 316 SS, V, Mo, and Nb in order of increasing cross section. In fact, the Nb parasitic absorption cross section is 2 orders of magnitude higher than Al in this range. However, alloying elements may modify this conclusion. (2) The order of desirability is the same in the intermediate (0 to 1-3 MeV) range with the exception that V now has a lower parasitic cross section than 316 SS. (3) In the high energy regime (3-14 MeV), Mo actually has the lowest parasitic cross section followed by

Nb, V, Al and 316 SS in that order. The high energy cross sections are dominated by (n,p) and (n,α) reactions which are particularly bad for the Al and 316 SS system where they exceed the Li(n,T) values by factors of ~5. This competition not only removes a neutron which could have produced another tritium atom, but it does so at an energy where the Li-7 (n,T) reaction could give another neutron back to the system along with a tritium atom.

The (n,2n) reaction partially compensates for parasitic absorption and analysis indicates that the final breeding ratio is generally highest with V, about the same for Mo and stainless steel, and lowest for Nb when the same volume percent structure is used in a liquid lithium cooled blanket.

The gas production cross sections of all the refractory metals (V, Nb, Mo) are low compared with Al or stainless steel. This is advantageous, particularly for the case of helium production because this can lead to severe embrittlement.

The ability of structural materials to withstand the corrosive environment of high temperature coolants is essential. For fusion, only three coolants appear to be feasible at the present time: helium gas, liquid lithium, and lithium salts. It is found that aluminum can only be used with helium gas and it is severely attacked by liquid metals. Steels can be used up to the creep limit with helium and Li-Be-F, but studies have recently shown that excessive corrosion takes place in dynamic liquid lithium above 500°C[1].

Vanadium, niobium and molybdenum are all immune to liquid lithium for Li temperatures approaching half the melting point of the structure. However, V and Nb are susceptible to attack by the fluorine in Flibe salts. Vanadium and Niobium are both limited to 700°C and 800°C respectively. Since the solubilities of O_2, N_2 or C are so low in Mo, this metal can be safely used to 1000°C. In summary, the Mo or TZM system represents the best system from a chemical compatibility standpoint. This is also important with regard to the transport of radioactive elements around the coolant loops.

Tritium containment within the blanket is clearly important and this means that the metal should have a low diffusivity for hydrogen isotopes at the operating temperature of the metal. Figure 9-1 shows the variation of hydrogen diffusivity with temperature in five metal systems. It is clear that Mo and Al make effective diffusion barriers to tritium at their expected operating temperatures. The 316 SS has a diffusivity at 600°C about equal to that in Mo at 1000°C. However, the hydrogen diffusivity in Nb and V are much too high and tritium diffusion barriers would be required to prevent large amounts of tritium from diffusing into the reactor buildings.

Tritium Permeabilities in Potential CTR Materials

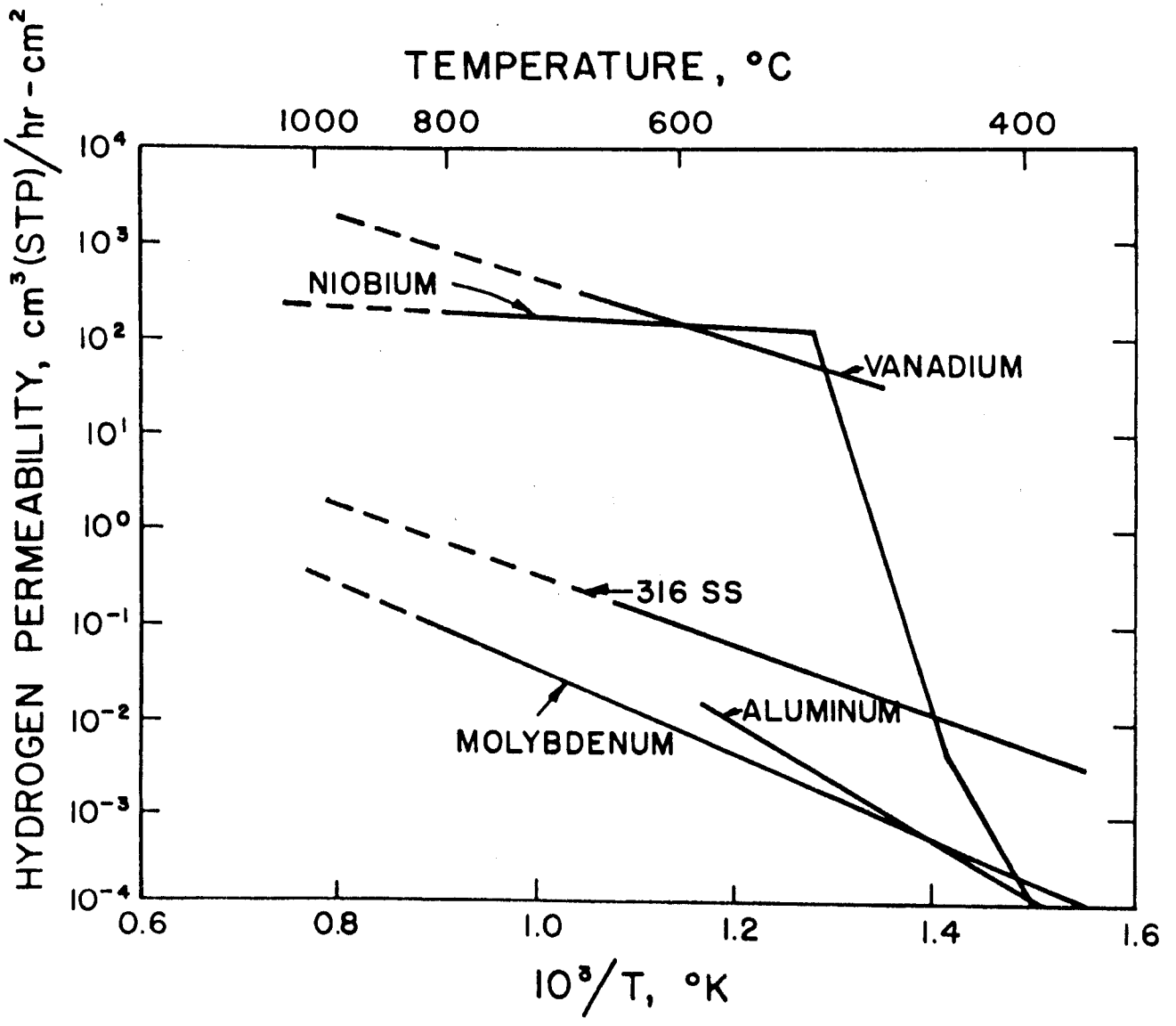

FIGURE 9-1

Up to this point we have considered the relative merit of TZM on the basis of 'normal' physical, thermal, and mechanical properties. The effect of neutron irradiation on those properties has also been assessed from the meager data in the literature and from the anticipated operating conditions in UWMAK-III. The poloidal variations in displacement damage and helium production are given in figure 5-6, and the anticipated temperature environment is given in figure 9-2. Figures 9-3 and 9-4 summarize the damage temperature regimes that will be experienced in the TZM after one year of operation at 80% P.F. It is noted that damage levels may approach 15 dpa per year at 750-950°C in the outer blanket and ~3 dpa per year at 950-1000°C in the inner blanket.

Analysis of all the data on swelling of Mo, TZM, and Mo-0.5 Ti from both ion and neutron bombardment[17] leads to the estimate that maximum swelling values in the outer blanket will be ~0.6 to 0.7% per year. A similar analysis of the meager mechanical property data reveals that if Mo (or TZM) is irradiated at the anticipated operating temperature, the total elongation may remain well above 1% for damage levels exceeding 20 dpa. It was also found that irradiation at high temperature actually increased the creep strength and increased the fatigue life of Mo or Mo alloys. Injection with helium and subsequent high temperature testing also failed to show any deleterious effects. Therefore it was concluded that a very conservative lifetime of ~25 dpa and 150 appm He could be attained.

Consideration of the behavior of carbon in the form of a curtain, ISSEC, or as a reflector revealed more strict restrictions than the TZM. It was shown that vacuum and sputtering properties of carbon in the plasma chamber could be considered quite satisfactory[21-25] and the major erosion mechanism may be the vaporation of carbon at high temperatures. The irradiation environment of the carbon in given in figures 9-5 and 9-6 which shows that damage levels may be as high as ~20 dpa per year at 1400-1700°C and ~12 dpa per year at 2100°C. The reflectors may experience damage levels up to 2.5 dpa per year at 900-1000°C. The helium generation could be as high as ~4000 appm per year at 1400°C and 1000 to 3000 appm per year at 2100 and 1800°C respectively. The high diffusivity of helium in carbon at these temperatures does not seem to represent a problem[22,23]. Nothing is known about the growth of carbon at temperatures above 1400°C but it should be less than measured values in the 1300-1400°C range[20]. However, the published data on some graphites irradiated in this range suggest that a lifetime of ~30 dpa may be limiting[18-20] and we have used that as a design value for UWMAK-III.

Analysis of the B_4C, stainless steel supports, Pb shield, copper in the VF coils, and superconducting material in the TF coils revealed no particular problem. However, a slight problem in the mylar insulation was discovered which indicated that it may reach its design lifetime in ~15 years. A more serious, but manageable problem was found in the Al stabilizer which doubled its resistivity at the 180° position every year. Periodic annealing to 270°K is necessary to remove this damage and could presumably be accomplished during maintenance outages.

A summary of the estimates of component lifetime in UWMAK-III due to radiation damage limitations is given in table 9-4. The design philosophy is to require access to the outer blanket every 18 months to change out the blanket modules which range from ±60° off the midplane. The carbon curtain will be changed at that time also. At every other maintenance, the rest of the outer blanket will be changed along with the ISSEC. The inner blanket will be considered a permanent structure with a 30 year lifetime.

Finally, it is felt that we have been very conservative in these estimates because of a lack of data in the appropriate temperature-damage regime. It is quite possible that longer lifetimes could be achieved which would reduce the amount of downtime and outflow of radioactive materials.

FIGURE I-9-2

Temperature Variations in UWMAK III Materials (Reactor Midplane)

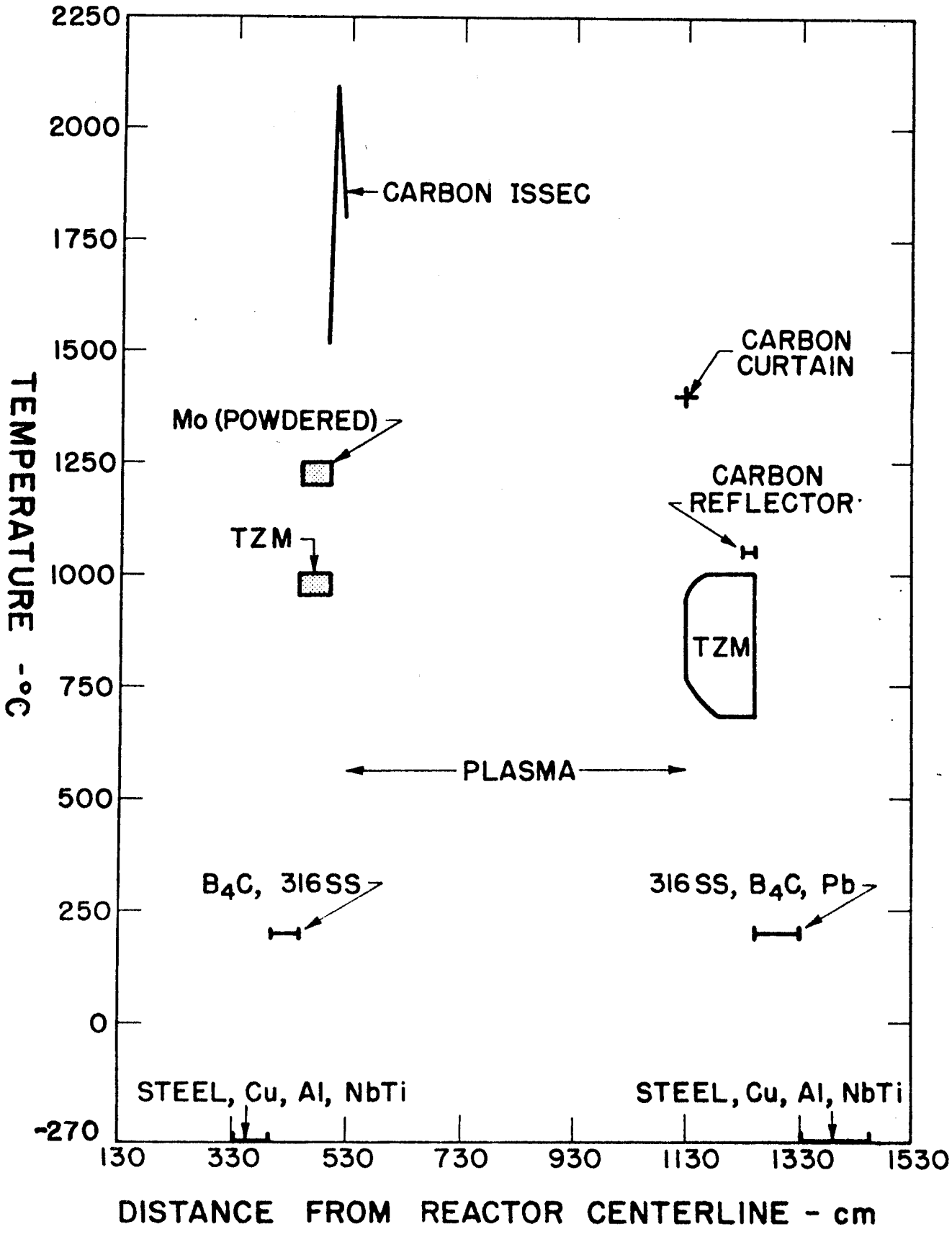

FIGURE I-9-3

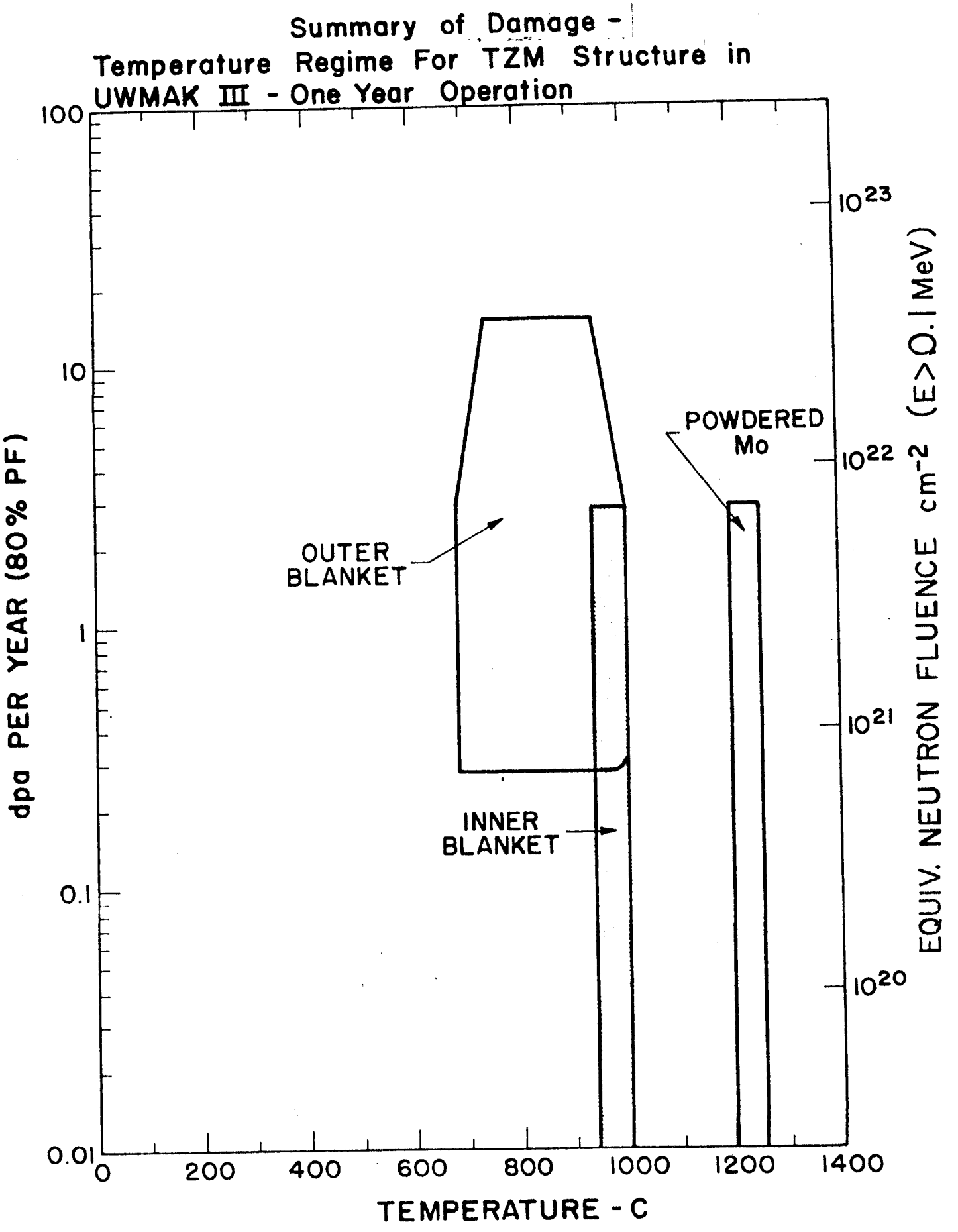
Summary of Damage - Temperature Regime For TZM Structure in UWMAK III - One Year Operation
dpa PER YEAR (80% PF)
EQUIV. NEUTRON FLUENCE cm⁻² (E>0.1 MeV)
TEMPERATURE - C
100
10
1
0.1
0.01
10²³
10²²
10²¹
10²⁰
0
200
400
600
800
1000
1200
1400
OUTER BLANKET
INNER BLANKET
POWDERED Mo

FIGURE I-9-4

Summary of Helium Gas Production Rates vs Temperature in TZM - One Year of Operation

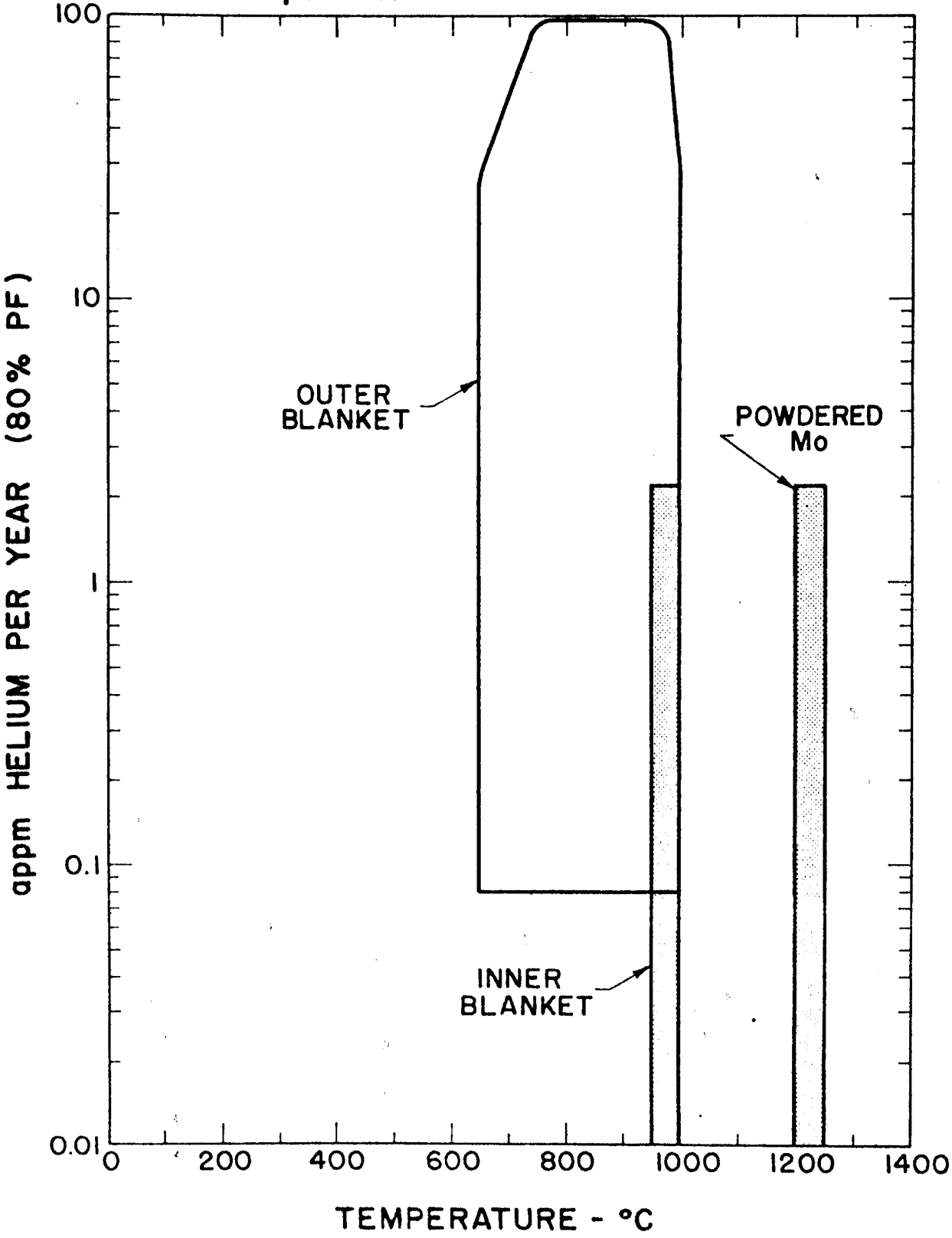

FIGURE I-9-5

Summary of Damage Temperature Regimes For One Year Operation in UWMAK - III - Carbon

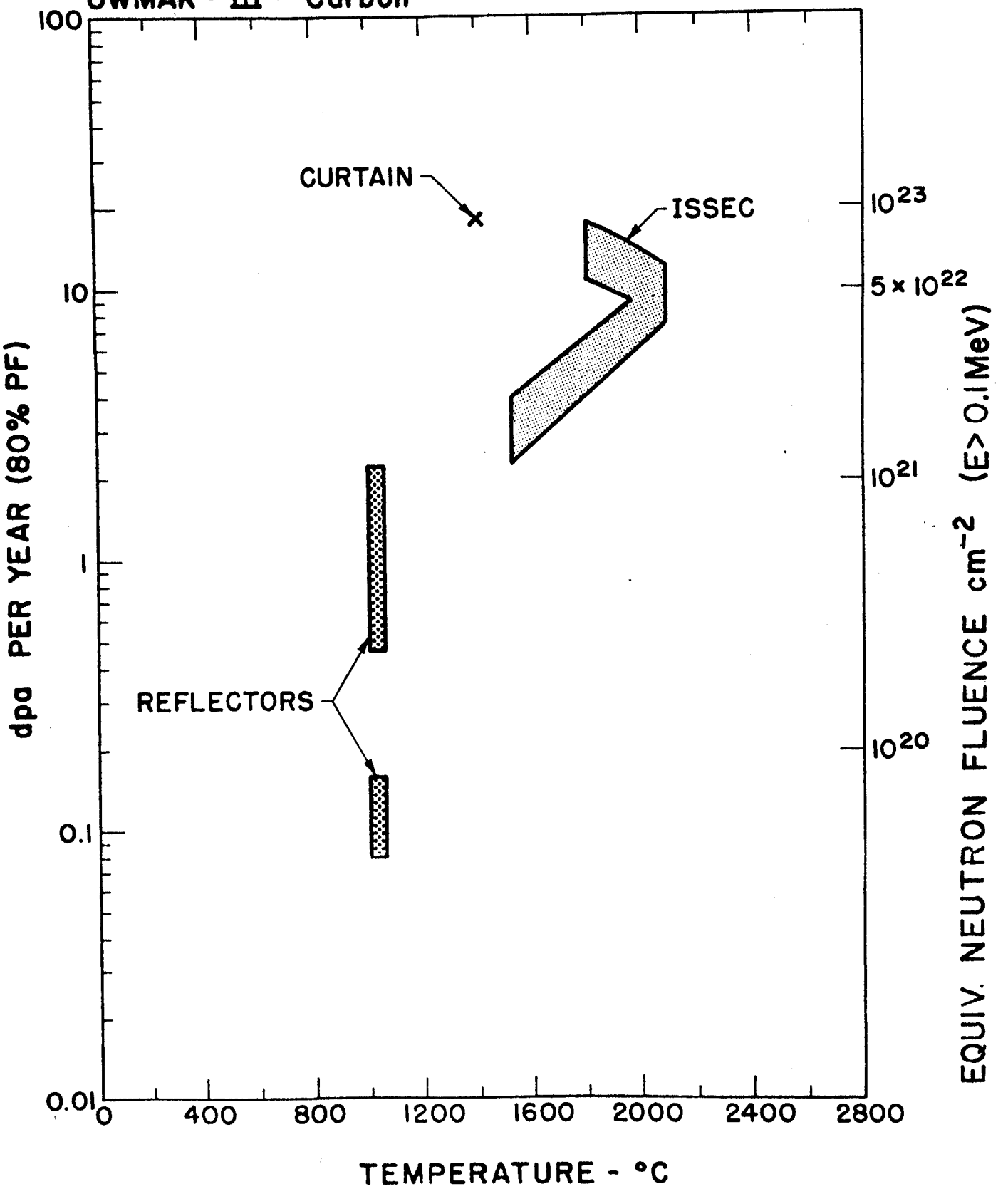

FIGURE I-9-6

Summary of Gas Production Rates vs Temperature in Carbon - One Year Operation

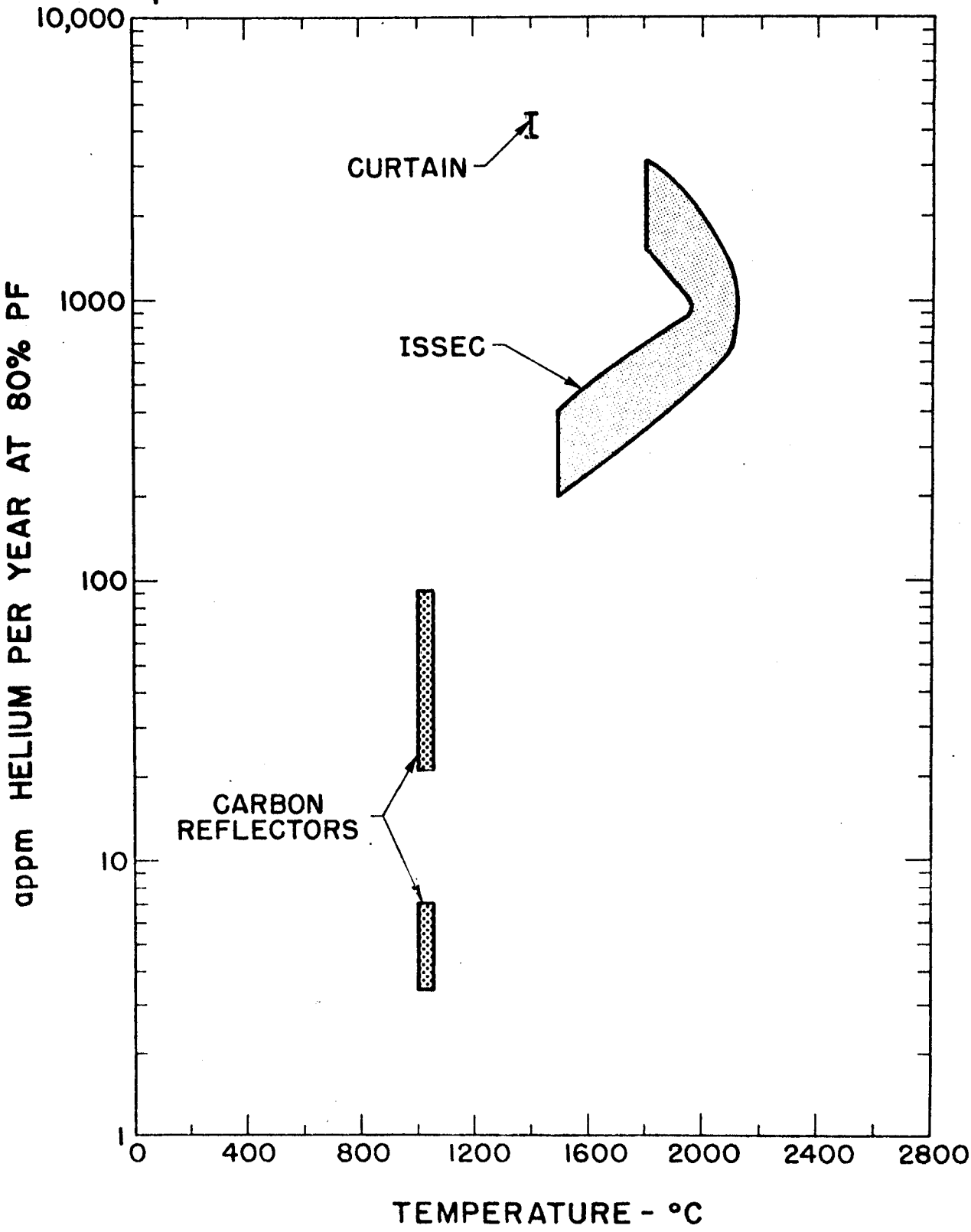

TABLE I-9-4

ESTIMATE OF COMPONENT LIFETIMES - UWMAK-III

Material	Design Criteria	Minimum Estimated Time to Reach Design Criteria-yr[a]
A) TZM	Swelling < 5%	
1) First Wall - Outer Blanket		7
2) First Wall - Inner Blanket		25
B) TZM		
1) First Wall - Outer Blanket	Total Elongation > 1%	> 1.5
2) First Wall - Inner Blanket		> 8
C) TZM First Wall - Outer Blanket	Wall Erosion < 10^{-2} cm	500
D) Carbon	Wall Erosion	
1) ISSEC	< 2.5 cm	40
2) Curtain	< 0.01 cm	55
E) Carbon	Growth Break Away Regime ($\Delta\ell$=0)	
1) ISSEC		> 3
2) Curtain		1.5
3) Reflector - Outer Blanket		> 3
E) Stainless Steel Inner Blanket	Uniform Elongation > 1%	> 30
F) Boron Carbon	$\Delta V/V_o$ < 5%	> 150
G) Copper Coil	$\Delta\rho/\rho$ < 1%	> 250
H) Al Stabilizer	$\Delta\rho/\rho$ < 100%	1
I) Super Conductor	$\Delta H_c/H_c$, $\Delta J_c/J_c$ and $\Delta T_c/T_c$ < 10%	> 50
H) Mylar	Exposure < 100 MRad.	15

a) 80% Plant Factor

10. Power Conversion System

The power conversion system for UWMAK-III has two distinct components, the power cycle associated with the heat deposited in the inner hot shield and the outer blanket, and the heat deposited in the divertor by particles diffusing from the plasma. The advanced power conversion system designed for the high temperature coolants of the inner hot shield and the outer blanket is based on a closed-cycle helium gas turbine system and yields a total power output of 1755 MW_e. The divertor power cycle is based on a conventional Rankine steam power cycle to utilize the 687 MW_t (average) in the divertor. The sodium coolant of the divertor plates leaves the reactor at 600°C and the total power output is 295 MW_e. The gross electrical power output is 2050 MW_e and the net electrical output is 1985 MW. This gives a net plant efficiency of 41.9%. A summary of system parameters is given in Tables 10-1 and 10-2.

The closed-cycle helium gas turbine offers the potential of high performance, low cost, fewer environmental effects, and would appear most suitable for integration (directly or indirectly) with advanced-design fusion reactors such as UWMAK-III. In addition to the attractive thermal efficiency, the helium gas turbine will be smaller in size (about one-quarter) compared to the steam turbine of the same output capacity, primarily because of a low overall expansion ratio (about 3:1 for the helium turbine compared to approximately 3000:1 for the steam turbine). Also, the closed-cycle helium gas turbine power system will be economically more adaptable to dry cooling, because heat rejection takes place over a temperature range much higher than the condenser temperature in a Rankine steam power system.

From the power utility viewpoint, a fusion power plant must be capable of delivering uninterrupted constant-output 60 Hertz ac power under normal operating conditions. This would require that the turbomachines operate at 3600 rpm, and that the operational characteristics of the power conversion systems must be adaptable to the existing power grids. Based on the power plant output level mentioned above, the two-zone blanket design, and the need to provide a reasonable system redundancy, turbomachinery unit capacity of approximately 500 to 600 MWe would be required.

The decision to have a helium-cooled inner blanket without tritium breeding and a lithium-cooled outer blanket with tritium breeding would mean that use of a primary heat exchanger to enable the containment and primary extraction of tritium within the lithium loop will be imperative (see Fig. 10-1 left and top diagram). If no intermediate loop is used, then the secondary loop of the primary heat exchanger and the inner blanket can be connected in series (Fig. 10-1 right and top), or in parallel (not shown) or separately (Fig. 10-1 right and bottom) with the helium gas turbine power systems. However, the need for secondary extraction and/or stringent containment of tritium and the need to store thermal energy using a liquid metal would require an intermediate sodium loop at a penalty of increased temperature drop between the lithium coolant and the helium turbine inlet. In this case again, the inner and the outer blankets can be connected in series (Fig. 10-1 right and middle), in parallel (Fig. 10-1 left and middle), or separately (Fig. 10-1 left

Table 10-1

POWER CYCLE PARAMETERS FOR UWMAK-III

OUTER BLANKET	
THERMAL POWER	2668MW
POWER CYCLE	Li-Na-He
Li-Na IHX AREA	5750 m^2
Na TEMPERATURES	590-940°C
Na-He IHX AREA	12300 m^2
He TEMPERATURE	488-870°C
POWER OUTPUT	1170MW
INNER BLANKET	
THERMAL POWER	1334MW
POWER CYCLE	He-DIRECT
HELIUM TEMPERATURES	488-870°C
HELIUM PRESSURE	1000 psi
Na-He HX-THERMAL STORAGE	6150 m^2
POWER OUTPUT	585MW

Table 10-2

POWER CYCLE PARAMETERS FOR UWMAK-III

DIVERTOR CYCLE	
THERMAL POWER	686MW
POWER CYCLE	Na-Steam
Na TEMPERATURES	400-600°C
STEAM GENERATOR AREA	6176m²
STEAM TEMPERATURE	538°C
STEAM PRESSURE	2400psi
POWER OUTPUT	295MW
PLANT POWER SYSTEM	
THERMAL POWER (CONTINUOUS)	4735MW
GROSS ELECTRICAL POWER	2050MW
NET ELECTRICAL POWER	1985MW
NET PLANT EFFICIENCY	41.9%

UWMAK-III POWER CONVERSION SYSTEM INTEGRATION SCHEMES

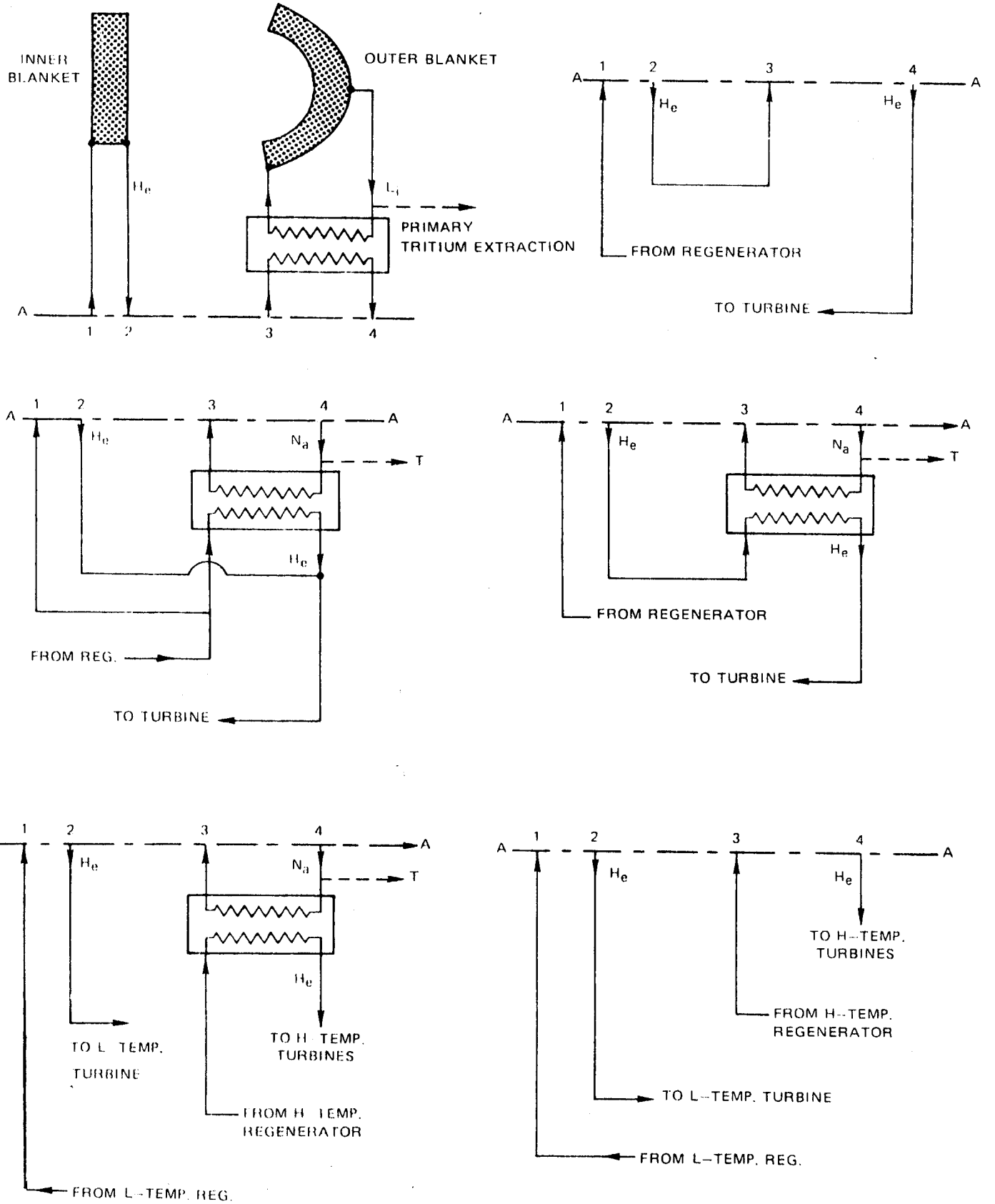

Figure 10-1

RO4-77-2

and bottom) with the helium gas turbine power systems. Since the inner blanket is "clean" from tritium, the separate connection scheme would be generally preferable. In this case, the split between the inner and the outer blanket loading must be controlled such that the number of gas turbine loops and their unit capacity to be selected would be acceptable from the economic and operational points of view.

The final reference design conditions for the baseline cycle configuration were selected based on interface problems and preliminary trade-off considerations. The temperature and pressure for the major cycle points are identified in the cycle flow diagram shown in Fig. 10-2. The turbine inlet temperature of 1600 F was selected essentially based on projected blanket capabilities with consideration given to the heat exchanger temperature drops and the projected turbomachinery technology. As pointed out earlier, the limiting factor is the blanket outlet temperature, and thus the selection of turbine inlet temperature involved more system constraints than trade-offs. The compressor inlet temperature of 110 F was selected based on the dry cooling tower requirement and reasonable precooler and intercooler designs; despite the dry cooling tower, use of intercooling for more than three points gain in cycle efficiency is justifiable considering the potential saving in power generation cost over the lifetime of the fusion plant vs the capital cost of the intercooler.

The selection of the turbine inlet pressure is largely based on component sizes and heat transfer considerations. As will be mentioned later, use of 1000 psia inlet pressure was mandatory for a turbomachinery unit capacity in the 500 to 600 MWe range. The overall pressure ratio of 2.8 (or 2.6 for turbine) was selected for a maximum cycle efficiency, and the intercooling pressure was selected so that the compressor work required will be a minimum. The regenerator effectiveness of 88 percent represents a compromise to accomodate the integration constraints yet generally provide a balance between the system performance and costs. Based on the operating conditions specified in Fig. 2, the cycle efficiency was estimated to be 43.9 percent, thus allowing an overall plant efficiency of greater than 40 percent.

As for the power system arrangement, a first glance at the thermal power rating of the UWMAK-III fusion reactor at 5000 MWt would suggest that between 3 and 6 units of helium turbomachinery would seem appropriate. Further examination of the inner (helium) and outer (lithium) blankets temperature capabilities and possible thermal power split would narrow down the number of inner and outer blanket turbomachineries to 1+2, 1+3, 2+4, and 2+6, using a direct-cycle for the inner blankets. After more detailed examination on blanket and turbomachinery design characteristics, the 1+2 system arrangement using three identical 585 MWe power conversion systems was selected, primarily based on the projected turbomachinery technology, and economic considerations.

The finalized system arrangement for the UWMAK-III fusion power plant is shown in Fig. 10-3. During each of the 30 minutes "burntime", the No. 1 and 2 power conversion systems will draw thermal energy from the outer blanket through the primary (lithium to sodium) and the secondary (sodium to helium) heat exchangers at a turbine inlet temperature of 1600°F, while the No. 3 power

REFERENCE-

DESIGN CLOSED-CYCLE HELIUM GAS TURBINE SYSTEM FOR UWMAK-III FUSION PLANT

THREE LOOPS NEEDED

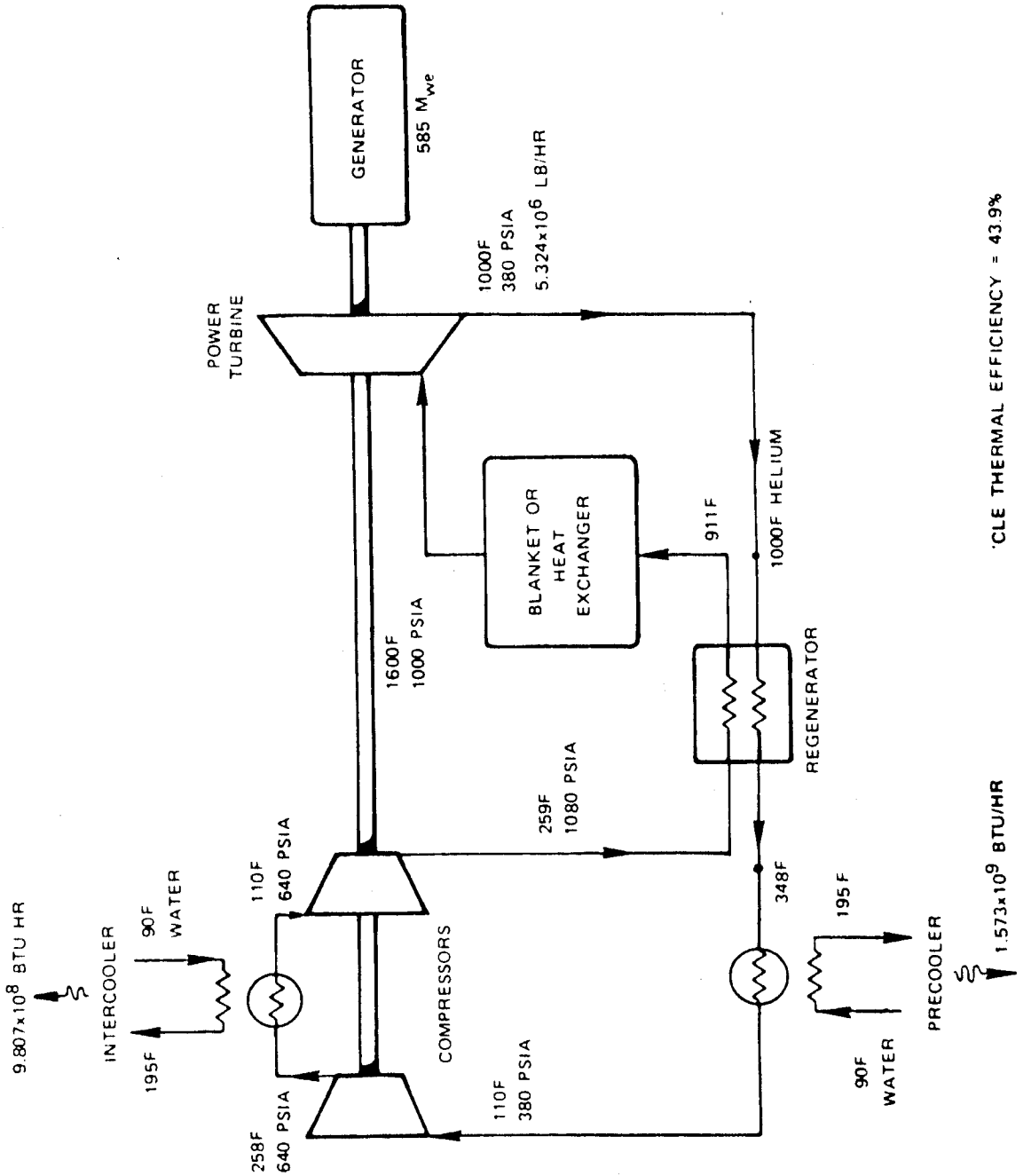

'CLE THERMAL EFFICIENCY = 43.9%

Figure 10-2

conversion system will be integrated directly with the inner blanket thus also operating at the same 1600F turbine inlet temperature. During this firing time, the sodium thermal storage system will be "charged" to store sufficient thermal energy to operate all three power conversion systems during the subsequent 1.5 minute "downtime". During the downtime,the thermal storage system will be "discharged" through the same sodium-helium heat exchanger to operate the No. 1 and No 2 power loops and a separate sodium-helium heat exchanger to operate the No. 3 unit. Although extraction of tritium will take place primarily in the lithium loop, any stringent restriction on the tritium level in the power conversion systems could require additional tritium extraction in the sodium intermediate loop. Operating temperatures and flow rates for key points in the inner and outer blanket transfer loops are also identified in Fig. 10-3.

Based on the foregoing discussions, the reference design 585-MWe turbomachinery (3 needed) for the UWMAK-III fusion power plant was based on a single-shaft, single-flow configuration at 3600 rpm shaft speed. This single-shaft turbomachinery can be coupled directly to the alternator to avoid overspeed, and generally represents a fairly compact design without serious penalties in the performance of the compressors. Generally speaking, the turbomachinery can be designed for either maximum efficiency or maximum output (per unit weight or volume) or somewhere between. The current design is for maximum efficiency based on 50 percent reaction at the mean diameter and a flow coefficient of approximately 0.5. Based on the unit capacity and rpm specified, the current design using one intercooler is regarded as the best compromise satisfying the power plant requirements and constraints.

The design data for the turbomachinery are summarized in Table 10-3, and Fig. 10-4 depicts the turbomachinery structure, including the arrangement of compressors and turbine, bearings and seals, and the overall dimensions. While conventional seals are regarded as sufficient for internal sealing, hermetic seals may be needed for the end seals. Because of the large flow area required at the turbine exit, an axial-flow flange design was adopted. The turbomachinery has the unique cost saving feature of employing the same constant hub diameter for the turbine and the compressors, all on the single shaft. The maximum diameter and blade length are 92.8 and 13.9 inches, respectively, and the stresses resulting from these configurations are regarded as well within the projected material capabilities.

In addition to the turbomachinery, similar detailed conceptual designs have been developed for the regenerator, precooler, and intercooler. A summary of the design details is given in Table 10-4.

The divertor power cycle to convert the heat carried to the collector plates by particle diffusion from the plasma is based on a conventional Rankine steam power cycle and uses the sodium coolant leaving the plate at 600°C. The steam conditions are 2400 psig at 1000°F with 1000°F reheat. The sodium returns at 400°C and the net output from this cycle is 295 MWe. This is a substantial improvement over previous designs[1,2] in which the use of liquid lithium to collect the particles limited the lithium outlet temperature to only 325°C. This limited the efficiency of the divertor cycle to only 25%. As such, the design here is much more compatible with the overall high performance of UWMAK-III.

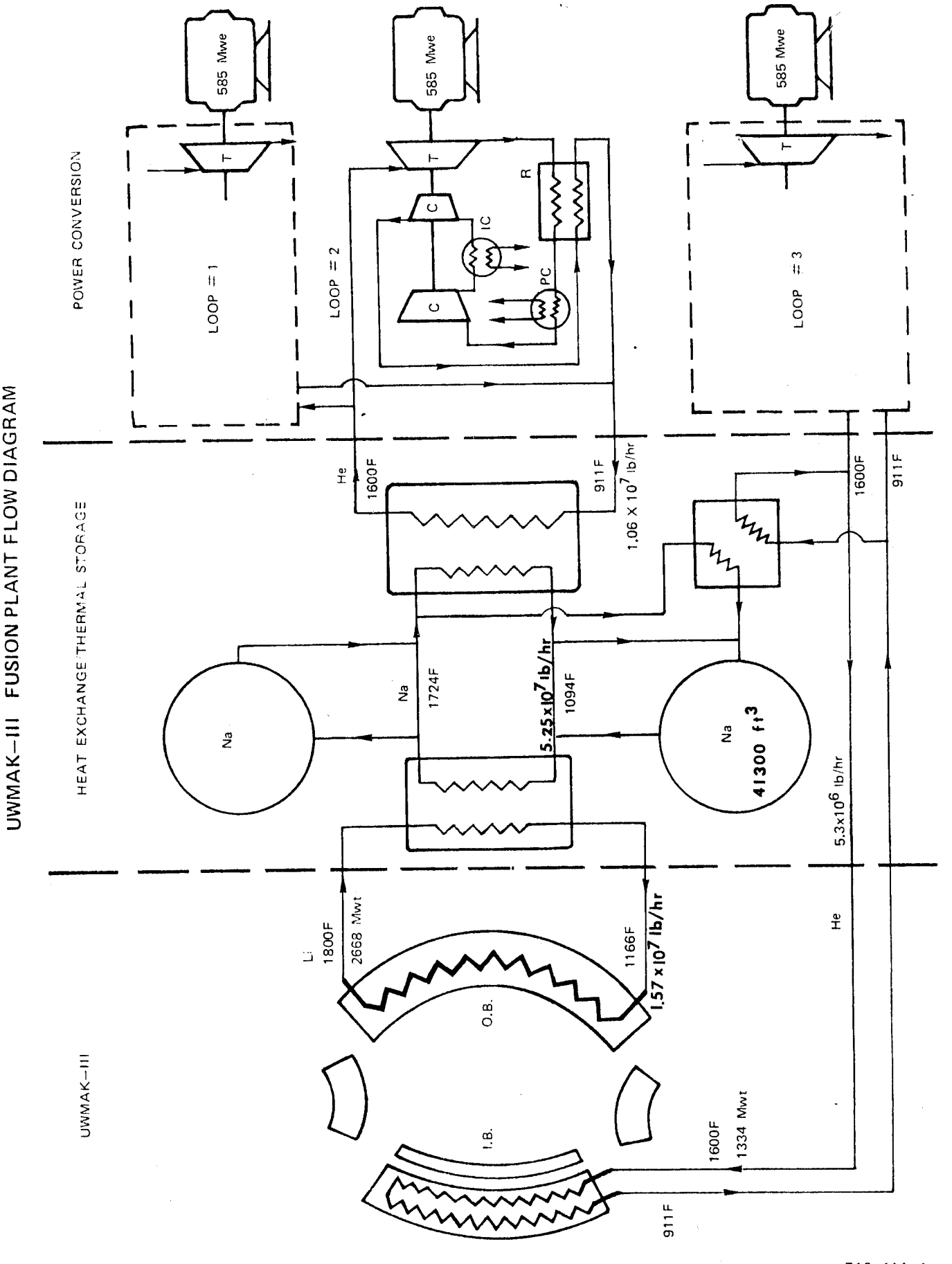
UWMAK-III FUSION PLANT FLOW DIAGRAM
POWER CONVERSION
HEAT EXCHANGE THERMAL STORAGE
UWMAK-III
585 Mwe
585 Mwe
585 Mwe
T
T
T
LOOP #1
LOOP #2
LOOP #3
C
C
IC
PC
R
He
1600F
911F
1.06 X 10^7 lb/hr
1600F
911F
Na
Na
Na
1724F
1094F
5.25x10^7 lb/hr
41300 ft^3
5.3x10^6 lb/hr
Li
1800F
2668 Mwt
1166F
1.57 x10^7 lb/hr
O.B.
I.B.
He
1600F
1334 Mwt
911F
R10-114-4

Figure 10-3

TABLE 10-3

CLOSED-CYCLE GAS TURBINE TURBOMACHINERY SUMMARY

Reference Design

585-Mwe Unit Output (3 units needed)

	Low Compressor	High Compressor	Turbine
Inlet Temperature - F	110	110	1600
Outlet Temperature - F	958	950	1000
Inlet Pressure - psia	980	940	1000
Outlet Pressure - psia	940	1080	340
Pressure Ratio	1.68	1.69	2.65
Efficiency (Adiabatic) - %	89	89	91
Number of Stages	10	10	9
Work per Stage - Btu/lb	18.6	18.9	75.1
Helium Flow - lb/sec	1472	1472	1472
Hub Diameter - in.	65	65	65
Inlet Tip Diameter - in.	79.7	73.9	79.8
Outlet Tip Diameter - in.	66.1	71.8	92.8
Wheel Speed, Hub - ft/sec	1021	1021	1021
Maximum Tip Speed	1351	1160	1458
Shaft Speed - rpm	3600	3600	3600

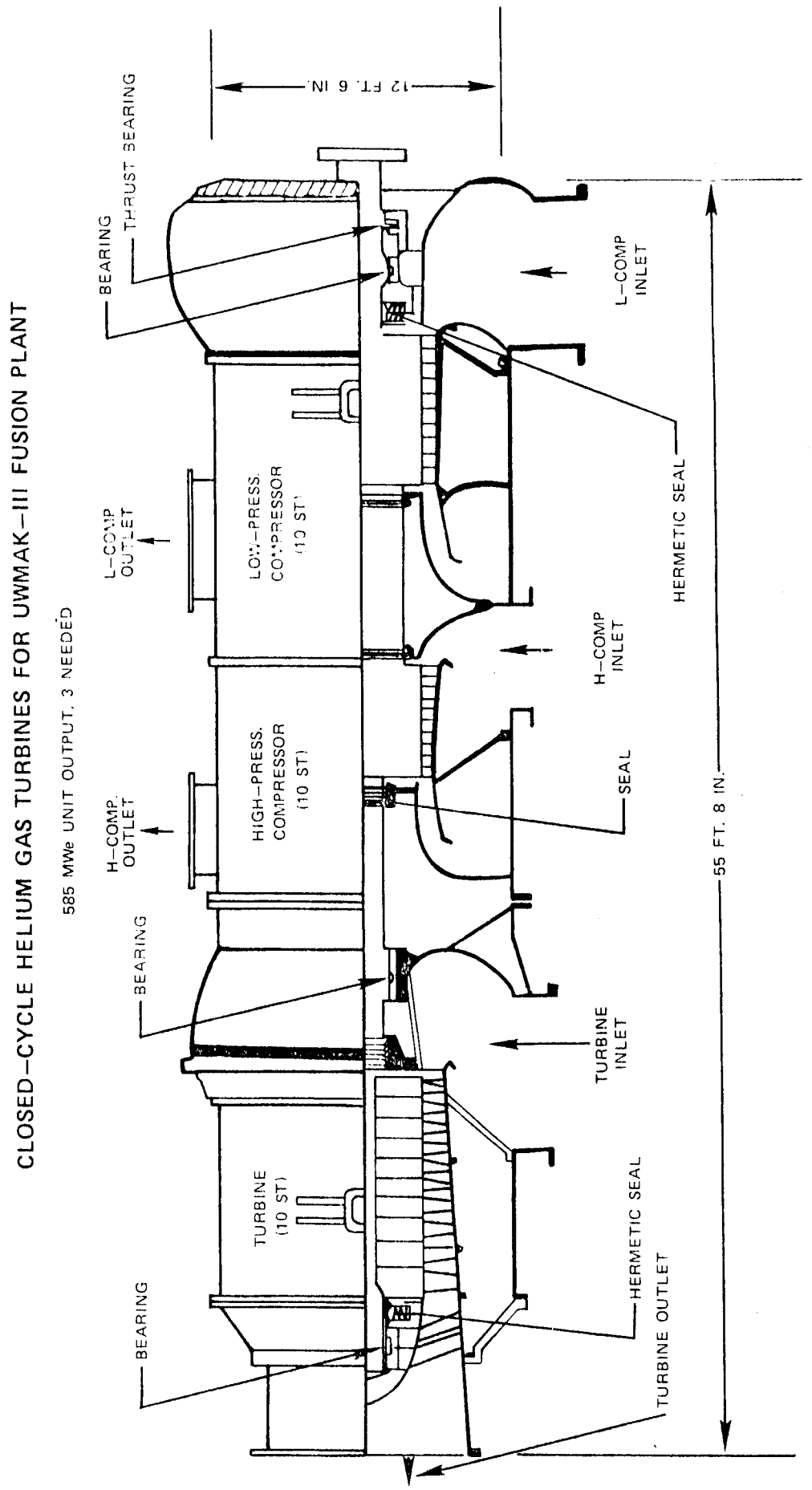

R10-106-7

Figure 10-4

TABLE 10-4

HEAT EXCHANGER DESIGN DATA SUMMARY

Reference Design

	Regenerator	Precooler	Intercooler
Heat Rate - Btu/hr	4.31×10^9	1.57×10^9	9.81×10^8
Flow Rate - lb/hr			
Hot Side (Helium)	5.39×10^6	5.39×10^6	5.39×10^6
Cold Side	5.39×10^6	1.9×10^7 water	6.3×10^6 water
Pressure Loss, $\Delta P/P$ - %			
Hot Side	2.8	1.3	1.1
Cold Side	1.0	---	---
Effectiveness - %	88	[illegible]	88
Overall Heat Transfer Coefficient - Btu/hr-ft^2-F	343	433	346
Heat Transfer Area - ft^2	1.41×10^6	0.99×10^6	5.97×10^5
Number of Heat Exchange Elements	150	150	150
Effective Tube Length - ft	58	30	31
Overall Shell Length - ft	75	43	44
Approximate Weight - ton	185	115	100

11. Plant Design for UWMAK-III

With the ever increasing successes in fusion development programs world-wide and with the hope of building commercial fusion power plants, the requirements of integrated plant design have begun to receive serious attention. The importance of the balance-of-plant should not be underestimated. For fission plants, the balance-of-plant amounts to over 85% of the plant capital cost. For fusion plants, this share may decrease somewhat. The fact remains, however, that the design of the balance-of-plant and construction planning have significant impacts upon the economic viability of fusion power plants. The conceptual design and the corresponding cost estimate play a major role in identifying the high-cost areas of the balance-of-plant and form the basis for development of design approaches with greater cost-effectiveness.

The arrangement of equipment and plant is based on the concept of identifying system functions and functional interrelationships and assigning these into modules. This forms the framework for definition of major buildings and functional requirements. These are: a reactor containment building containing the reactor and other components of the nuclear island; a hot cell for handling irradiated blanket segments; a reactor auxiliary building containing safety-related equipment and other equipment closely associated with the nuclear island; a heat exchanger building containing the heat exchange and transport equipment, (it also contains the thermal storage equipment); a turbine building containing the energy conversion equipment; a control building containing the central plant control equipment; a diesel generator building containing the diesel generators; a radwaste building containing the equipment for processing radioactive wastes; a helium storage building containing the equipment for storing high pressure helium and an inductive energy storage building containing equipment associated with magnet energy supply systems. The general plant layout is shown in Fig. 1-1.

The plant heat rejection system provides the heat sink for the power cycles, various components of the nuclear island and other plant equipment and rejects this waste heat to the atmosphere. Guidelines for the heat rejection system design are based on the concept of "zero water use". Consistent with this concept, dry cooling towers were selected for rejecting the plant heat to the atmosphere.

The use of a dry cooling tower also imposes some constraints on the performance of the energy conversion cycles. The minimum temperature obtained in the cycle with a dry tower is considerably higher than that obtained by a wet tower - the reason being that the dry tower approaches the dry bulb temperature. Also for economic reasons, the temperature drop for the dry tower is larger than for the wet tower. This has significant deleterious effects on the cycle efficiency. However, this sacrifice can probably be justified in locations where availability of water is scarce.

The replacement of the blanket segments from the outer blanket generates a large volume of solid radioactive wastes. A preliminary concept was developed for the removal, processing, storing and off-site disposal of the wastes. The guideline used to establish the concept is to reduce the specific activity of the

blanket to a sufficiently low level (200 Ci/cc) so that the shielding requirement during off-site transportation is reduced to a minimum.

The process block diagram is shown in Fig. 11-1 and the main considerations are as follows. The decay heat from the blanket at the time of the reactor shutdown is about 9 MWt; it is therefore necessary to circulate coolant to remove the decay heat. The decay heat is reduced by a factor of about 40 in seven days at which time gas cooling can take over. The lithium is drained from the cooling system. The modules are then transferred to the storage area for further decay.

The blanket will be held in the storage area for 3 years before processing for disposal. However, the frame attached to the blanket can be re-used and it will be separated from the blanket during the first six months in storage so that the frame can be welded to a new blanket module.

At the end of three years, the used blanket is transferred to the hot work shop where the large pieces will be cut into small pieces (1m x 2m) using a laser. The small pieces are then passed through a vacuum lock to the decontamination area which has an air atmosphere.

The annual blanket waste volume is 32 m^3 (1130 ft^3) and weighs 164 tonnes. Solidification is done by mixing the blanket fragments with cement. The waste will be shipped in 100 cu. ft. containers with 2-1/2 inch lead shielding. There will be 57 containers required annually. It may be more economical to use larger containers but shielding requirements and activity contents of the waste may limit the container size. However, no optimization was done in this study.

A first order consideration has been given to the plant electrical system to identify the major equipment associated with the main generation system and the system leading to the ultra high voltage (700 KV) switchyard. The study is also intended to define the major plant load centers and to identify the essential (Class 1E) loads related to plant safety.

Conceptual design studies were performed for the plant buildings and structures, and for the plant, equipment and piping arrangement. The structural design effort was confined to the major structures, viz, the containment building, hot cell, radwaste building, auxiliary building, heat exchanger building, and the turbine building. Only superficial consideration could be given to the plant equipment and piping arrangement.

The general plant arrangement and the internal arrangement of the buildings are patterned wherever possible after the generic concept developed by the Bechtel Corp. for fission reactor plants. The greatest effort was devoted to those areas unique to UWMAK-III, such as the containment building, the heat exchanger building, the turbine building, and the hot cell. Other buildings such as the control building, the radwaste building, etc., are similar to those in other nuclear plants, and their arrangements can be adopted readily to this plant.

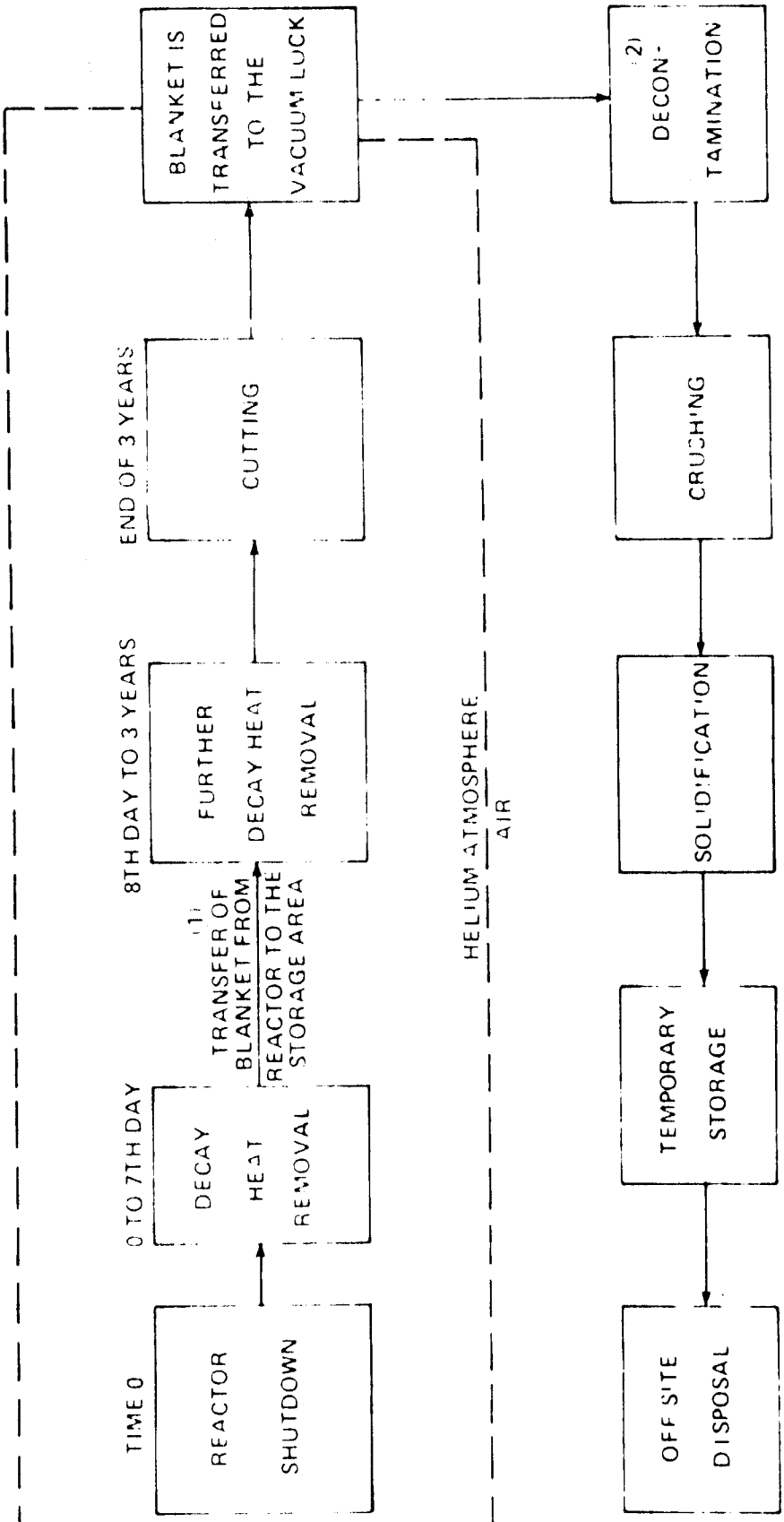

NOTE: (1) TRANSFER OF THE LARGEST BLANKET PIECE TAKES ABOUT 8 HOURS
(2) ANY LITHIUM LEFT IN THE BLANKET IS CONVERTED INTO LiOH AND THEN REMOVED

FIGURE 11-1
BLANKET PROCESS BLOCK DIAGRAM

The major features of the arrangement include the following: the containment building, which is centrally located relative to the outer buildings, is a reinforced concrete structure lined with stainless steel and has an inert environment to prevent lithium or sodium fire; the heat exchanger building, radwaste building, auxiliary building, hot cell, and the maintenance building are arranged around the containment building. This arrangement seems to have an advantage in handling blanket sections and radioactive wastes, and in arranging the reactor primary cooling piping between the containment building and the heat exchanger building. It also makes the plant layout very compact, with maximum utilization of space around the containment, by locating the reactor support systems and facilities close to the nuclear island. This is also expected to offer some economic advantage for piping, cabling and structural considerations. The peninsular arrangement of the Turbine Building orients the axes of the turbine-generators such that any missiles generated by the machines will not strike the containment building. Access corridors run the length of the turbine building and continue in the control building and the auxiliary building to provide accessibility to all equipment.

12. Survey of Materials Resource Implications of UWMAK-III

It is of interest to investigate the materials requirements of UWMAK-III type reactors to determine whether there might be major problems with regard to either reserves or procurement of specific elements. The reduced overall size of UWMAK-III compared with earlier studies[1,2] makes the requirements as summarized in Tables 12-1 and 12-2 correspondingly less. United States reserves and resources, together with U.S. 1974 production, are summarized in Table 12-3. Also listed are the requirements for a 10^6 MWe economy (500 reactors) of UWMAK-III type reactor systems. Of course, the requirements for a smaller economy of between 5 and 50 reactors will be proportionately smaller.

Of the many elements listed, some of the key ones include aluminum, lithium, molybdenum, niobium, chromium, copper and manganese. Each have a facet of their reserve and resource picture worth noting.

The United States has very limited bauxite reserves and imports over 90 percent of its bauxite supply. An adequate domestic supply of aluminum ore would require development of resources of high-alumina clays, anorthosite, alunite, and dawsonite, singly or in combination. The resources of aluminum in such materials are very large. The necessary technology is available for extraction from clays, anorthosite, and alunite, but energy costs and dollar costs would be above those of extraction of aluminum from bauxite. Mining of these three materials would be open cast, but no unusual environmental problems would be involved. Dawsonite production would be involved with oil shale production and would share the environmental and other problems facing the oil shale effort.

United States reserves of molybdenum are estimated by the U.S. Geological Survey at 3×10^6 tonnes and by the U.S. Bureau of Mines at 4×10^6 tonnes. The survey estimates identified marginal resources at 17.5×10^6 tonnes. These figures suggest that at prices somewhat higher than present prices, the UWMAK-III, 10^6MWe, requirements could be met but information on possible rates

Table XII-1

Materials Requirements - UWMAK-III Nuclear Island (Metric Tonnes)

Elements	Blanket: Initial Structure (a)	Blanket: Partial First Wall Replacement 19 Times-30 Yrs. (b)	Blanket: Balance First Wall Replacement 9 Times-30 Yrs. (c)	Balance of Plasma Chamber and Vacuum Plenum	Shield: Inner and Outer Shield	Shield: ISSEC Replacement 9 Times-30 Yrs. (d)	Magnets: T.F. Coils, Dewars and Cent. Struc.	Magnets: VF & OH Coils and Dewars	Shield, Blanket and Coil Support Structure	Vacuum Pumps	Total 30 Yrs.	Tonnes/MWe Based on 1595 MWe
Al					167.73		4623.56			20	4811.3	2.42
B					942.26						942.3	0.47
C	1039	9080.5	5049.35		494.33	2098.8					17,762.0	8.93
Cr				50	1128.63		23.8	71.4	300	35.2	1604.0	0.81
Nb							50	33			83.0	0.04
Cu							382.34	889		14.3	1285.6	0.65
He							18	13			31.0	0.02
Fe				165	3724.49		78.54	236	900	116.6	5310.2	2.66
Pb					3611.06						3611.1	1.82
Li	395										395	0.20
Ti	1.97	17.22	5.46	0.55	0.48		30.23	17			72.9	0.04
Mn				5	112.86		16.93	7.14	30	3.52	175.5	0.09
Mo	335.6	3107.95	987.56	99.33	1049.34						5599.8	2.82
V							6.35				6.4	0.003
Ni				30	677.18		14.28	43	180	21.12	965.6	0.49
Zr	0.43	3.76	0.93	0.12	0.10		10.58				15.9	0.01
TOTAL	1792	12,209.4	6043.3	350	11,908.5	2098.8	5254.6	1309.5	1500	210.3	42,676.6	21.50
COMPONENT WEIGHTS (MT)												
$Al_6Si_2O_{13}$					441.4						441.4	0.22
304 SS				250	5643.17		119	357	1500	176	8045.2	4.05
TZM	358	3128.92	944.22	100	86.67						4667.8	2.35
Mo					963.25						963.3	0.49
Al alloy 2219							4233			20	4253	2.14
Hi Purity Al							716.5				716.5	0.36
B_4C					1203.4					14.3	1203.4	0.61
Carb. St. 1020											998.3	0.50
Cu							95	889			126	0.06
NbTi							76	50				

(a) 18 Modules Plus 3 Spares
(b) 18 Partial Modules Replaced Every 1 1/2 Years Plus 3 Spares on Hand
(c) 18 Balance of Modules Replaced Every 3 Years Plus 3 Spares on Hand
(d) ISSEC Graphite Replaced Every 3 Years Plus 3 Spares on Hand

Table 12-2

Materials Requirements - UWMAK-III Balance of Plant (Metric Tonnes)

Element	Heat Exchangers: Li-Na[a]	Na-He[b]	Na-Steam[c]	Piping Li,Na He & Steam	Tritium Extraction System[d]	Thermal Flywheel Na Tanks	Li & Na Dump Tanks[e]	Li & Na Pumps	Containment Building Liner	Buildings	Energy Storage Unit	Turbine Machinery[f]	Generator and Exciters[g]	Regenerator Precooler Intercooler He-Steam	Miscell.	Total	Tonnes MWe Based 1981
Al												2.96				2.96	.001
Cr		79	60		0.4			120	222		81	30.72	50	32		675.1	0.3
Nb					9.26						7.5					16.75	.006
Cu											362		295			657	0.33
He		19		1.0							15				37.5(h)	72.5	0.037
Fe		261	197	33,796	1.3			396	733	78,486	269	230.9	1980	319.3		116,670	58.7
Mn		8	6	204				12	22	474	8	1.32		4.5		739.8	0.37
Mo	99.4	423		993	1.0	49.7	178.8	745				7.42	20			2517.3	1.27
Ni		47	36		0.24			72	133		49	68.56		19.2		425	0.21
Na		400	500	180		900										1980	1.00
Ti	0.50		2.3	5.5		0.27	1.0	4.1			4	3.56				21.2	0.01
Y					0.02											0.02	
Zr	0.10		0.5	1.2		0.06	0.22	1.0								3.08	.001
Pd					0.50											0.50	
Li	20			50												70	.035
Co												13.9				13.9	.007
Concrete										304,000m^3							
TOTAL	120	1237	801.8	35,230.7	12.72	950	180	1350	1110	78,960	795.5	359.3	2345	370.5	37.5	123,865	62.4
304SS		395	298		2.0			600						160		2565	1.29
316SS											400					400	0.20
Carb. St. 1020				34,000						78,960				215		113,175	57
IZM	100	426		1,000	1.0	50	180	750								2507	1.26
Cu											382					362	0.18
NbTi											11.5					11.5	0.006
Concrete										304,000m^3							

(a) 2 heat exchangers
(b) 6 " "
(c) 2 " "
(d) Material needed for 30 yrs of operation
(e) Li dump tanks and divertor Na dump tanks. Thermal flywheel tanks are used as dump tanks for the intermediate Na loop.
(f) Turbine is made of blades-UDIMET-700, Casing-INCONEL 718, disc- A-286, Compressors (2) are made of blades-PWA-IN-4017, casing and valves-ASTM A-487 2 1.4 Cr, 1 Mo, and disc-D6AC
(g) Silicon Steel 495 MT, Carbon steel 500, Copper 50, Cr.Mo.V. Stainless Steel 163, insulation 25.
(h) Liquid He in storage

Table 12-3

United States Production, Reserves and Resources of Metals Required for UWMAK-III

(metric tonnes x 10^6)

Metal	Requirement for 10^6 MWe	United States		
		Production-1974[1]	Reserves[2]	Resources[3]
Al	2.42	.40	~2.0	Very large
B	.47	.18	10.1	Very large
Cr	1.08	0	-	1.53
Nb	.06	0	.006	.07
Cu	.98	~1.59	85.0	100.0
Fe	60.28	50.0[4]	2,000.0[5]	10,000.0
Pb	1.82	.68	59.0	Large
Li	0.24	~.002	1.5	1.7
Mn	0.46	0	-	10.0
Mo	4.08	.06		
Ni	.67	.015	.20	16.0
Na	1.0	.200[6]	Unlimited	
Ti	.05	.29	34.0	29.0
Y	$<10^{-5}$	.00004	Probably large	
Zr	0.01	.07	10.0	No data
Pd	<0.001	0	0	Large[7]
Co	0.003	1,000	Included in resources	800,000

(1) Primary metal only.

(2) Metal in ores minable under current economic conditions.

(3) Metal in material judged available at prices up to 3X present prices.

(4) Fe content of domestically mined ores.

(5) Fe content of ore minable under current economic conditions.

(6) Metal only. Approximately 1 percent of total production of sodium minerals.

(7) Assumes development of newly discovered deposits in the Stillwater Complex, Montana

Data from U.S.G.S. (Prof. Paper 820, 1973), U. S. Bureau of Mines (Commodity Data Summaries, 1975), and J. D. Vine (Lithium, Trans. Amer. Nucl. Soc. 22 (1975)).

of production of molybdenum beyond the end of the century is not available. The current rate of production is only about 55,000 metric tonnes per year. Thus, molybdenum could be a serious problem because of procurement difficulties rather than resources.

If the chromite resources in the Stillwater Complex, Montana, are not used for other purposes, the UWMAK-III requirement could be met from that source, at prices probably not very much higher than present prices. Otherwise, the requirement might be met from domestic sources only by paying high prices for domestic chromite concentrates, probably 3X present prices or higher.

Niobium is a key element of the superconductor for the UWMAK-III coils. The requirement for niobium is approximately equal to the amount of niobium in ore blocked out by exploration of the Powderhorn Complex, Colorado, the only sizeable domestic resource. This is not a comfortable situation. Stockpiling of niobium in advance of use appears to be the only answer to the problem of procurement, unless new deposits can be discovered in the United States. The situation would be considerably more difficult if niobium were used as the structural material.

The copper requirement for UWMAK-III is small relative to the estimated reserves of 85×10^6 tonnes. However, these reserves will be about half depleted by the end of the century at present rates of production. Even now, domestic production is not quite equal to domestic consumption. The use of copper in fusion reactors will have to compete with conventional uses from available domestic supply, and it is not certain that present rates of domestic copper production can be maintained to the end of the century. Much will depend on success in discovering new deposits of copper during the next 25 years.

If it becomes necessary to draw on foreign sources of copper, the outlook for such supplies is fairly favorable. At least seven countries should be producing large amounts of copper during the first quarter of the 21st century - Peru, Mexico, Chile, Panama, Zambia, Zaire, and the Papua-New Guinea. Copper from the deep sea nodules should also have entered the market by that time.

World reserves of manganese are enormous, but the United States has no manganese reserves. At 3 times present prices, the UWMAK-III requirement could probably be met from off-grade resources in Maine, Arizona and Minnesota. The nodules of the deep sea basins are another potential source. Presumably the present dispute over jurisdiction of deep-sea mining will have been resolved.

Current reserves of nickel in the United States are too small to meet the UWMAK-III requirement and will be virtually exhausted by the end of the century. However, nickel deposits in the Duluth Complex, Minnesota, should be in production by the end of the century and should be able to supply the necessary amounts. Nickel won from the manganese nodules of the deep sea floors could be an alternative source.

Finally, the U.S. Geological Survey states that the identified resources of lithium in the United States likely to reach the marketplace by the year 2000 are scarcely adequate to meet the anticipated growth of the industry for conventional use and are grossly inadequate for the anticipated requirement for new energy-related uses. A search for new deposits is needed. The brines of western saline basins and certain types of clay deposits appear to offer the most promise.

13. Economic Analysis

a. Role of the Study

The role of an economic study for an early conceptual design such as UWMAK-III is to provide us with an indication of where the major cost areas might be in tokamak reactors. This helps guide future tokamak reactor studies and indicates areas where increased research and design effort can pay the greatest dividends. On the other hand, many parts of the UWMAK-III system, by the nature and scope of the study, remain undefined and this means that an accurate determination of absolute costs is extremely difficult. This is particularly true if one tries to compare fusion with power systems like fission reactors where the designs are known in much greater detail. Therefore, we place greater emphasis on the relative costs of key items in UWMAK-III than on any absolute figures.

It is also important to recognize that the economic analysis for UWMAK-III is specific to this system. That is, many of the items that have a strong impact on the results are governed by certain design choices peculiar to UWMAK-III. Different design choices can have very different effects on cost so that a generalization regarding the costs of tokamak reactors is not possible at this time. (As a specific example, one will note in the following sections that the estimated cost of high temperature refractory metal piping was a substantial cost driver. These costs would be sharply reduced if stainless steel has been chosen as the structural material.) The results reported here were obtained as part of a joint study by the Bechtel Corporation and the University of Wisconsin.

Turning to the estimating procedure itself, it is normal estimating practtice, when engineering is well defined, to derive the cost estimate by building up the cost item by item. In a less well defined study, where perhaps only 60 percent of the equipment is identified, this method can still be used, but a large portion of the cost must be based on allowances and factors. However, in a pre-conceptual estimate, such as the UWMAK-III study, where less definition is available, a different approach is necessary. The plant must be viewed as a series of systems which should be similar in content (but not necessarily in function) to systems in existing analogous plants, and the costs obtained by inductive reasoning using the costs of the analogous known systems. The estimate is thus derived by a macro, rather than micro, approach. There is still considerable margin for variation in the unknown systems, but the potential variation is diminished by using this composite systems approach.

Existing nuclear power plants are the most comparable source of pertinent data, and the cost estimate and schedule for UWMAK-III rely heavily on data from recent Bechtel Corporation power plant experience. The basis for the estimate is discussed and the resultant capital cost for the entire plant is summarized in part b of this section.

Parts c and d of this section are important because it is where we attempt to place the estimate of plant economics for UWMAK-III in persepctive by providing some comparison with estimates of electric power costs for other methods of generating electricity. We have asked how the costs developed for UWMAK-III compare with cost estimates developed by the same group for other, non fuel limited approaches to electric power generation. (It is important to maintain

consistency by using the estimates of a particular group since we find estimates by various groups, including costs developed with Federal Government guidelines, to vary widely.) Other approaches to electricity generation include fission breeder reactors, solar power, fuel cells, and coat fired MHD plants. Also included for reference are consistent estimates for light water reactors, coal fired steam plants and gas turbines. These systems, particularly LWR's and gas turbines, are not truly comparable because the fuel supply will no longer be available at the time advanced technologies like breeder reactors and fusion are ready to play a substantial role.

Of course, our main goal was to determine the key design decisions and cost items that most affect the economics of UWMAK-III. A discussion is given of design choices made at the beginning of the study which turned out, after the fact, to have more strongly affected the estimated costs than had been anticipated. From these considerations, one can draw conclusions regarding directions for future work.

b. Cost Estimate

The basis for the cost estimate involves many items. The facility under discussion is assumed to be a first generation model designed in a time when the major equipment functions have been successfully demonstrated. At that time industry will have developed the capability to produce the equipment, a capability which does not necessarily exist today. Development and first-of-a-kind costs are therefore not considered.

In general, the costs of the reactor plant equipment were developed by the University of Wisconsin and the balance of plant costs were determined by the Bechtel Corporation. The costs are in fourth quarter, 1975, dollars with no allowance for escalation.

The basis of the estimate is the plot plan, plan and elevation of the power block buildings (the main structures housing the reactor and power generation facilities), and a single-line electrical diagram. All of these were used as guides and, with the exception of building volumes and some quantities of concrete and lengths of main heat transfer piping, no quantity takeoffs were made. Fuller understanding of the engineering scope and extent and type of systems was provided in informal discussions with the engineering team.

The capital cost estimate is composed of field costs, engineering costs, a contingency allowance, owner's costs and interest during construction. The largest category, field costs, comprises the direct costs of permanent plant equipment and the indirect costs of temporary construction materials, supervision, etc., that are to be distributed across the entire facility.

Direct field costs are the costs for permanent plant equipment, materials, labor and subcontract items, and form the bulk of the field costs. These are derived from two basic sources: the bulk materials, and equipment. In general both are available from current and historic sources in a system and category format.

The major items of reactor equipment have been estimated by the University of Wisconsin and these have been included without comment. Items that lie in

the balance of plant category, e.g. cooling towers, have been estimated using current price guidelines from major manufacturers and current pricing data from within Bechtel. The costs of other equipment have been established as a function of the appropriate building.

The bulk of the mechanical equipment peculiar to UWMAK-III has been priced by the University of Wisconsin. Peripheral equipment such as pumps, condensers, and heating, ventilating and air conditioning equipment has been estimated by eliminating from an LWR mechanical account all those items related to a fission reactor and scaling up the remainder of the costs to the increased capacity.

The cooling tower was treated separately. Its duty corresponds to that of an equivalent 800 MWe LWR plant, except that the circulating flow is half and the temperature much higher. Its price is estimated to be 40 percent higher than that of an equivalent wet cooling tower.

Remote handling equipment was also treated separately and an allowance included, although little is known beyond the general function and certainly no equipment of the sort exists today.

There is a close correlation between the station load of a power plant and the cost of the electrical equipment. On a net basis UWMAK-III is more efficient than an LWR facility, but its equipment is more sophisticated. In sum, on a per-megawatt basis, UWMAK-III's electrical equipment is assessed to be 90 percent of that in an LWR plant, excluding the unique equipment for a fusion plant, and was estimated on this basis. To this base figure was added the estimated cost of the unique systems, the energy storage and inverter facilities and a low-voltate, cryogenic transmission system from the energy storage facility to the containment building.

The wage rate included is based on a craft mix and wage agreements as experienced in the Pacific Northwest, which is a representative area for the United States. Labor availability and consequent productivity is also affected by plant siting. For this study, labor productivity is again based on the Pacific Northwest experience and is generally regarded as good. Also, it is normal for a part of the work to be subcontracted, examples being earth work, cooling towers, insulation, and building finishings. In this respect a fusion plant is regarded as being normal and thus standard power plant relationships have been used.

Indirect costs can be a controversial part of any cost estimate. Previous UWMAK studies [1,2] have used the WASH 1230 report [26] as a guide to determining indirect costs. However, they are probably understated in WASH 1230, (20% of direct labor costs compared with 90% to 110% in Bechtel's experience). However, the different bases of the cost scope make comparisons difficult. For UWMAK-III, an approach consistent with Bechtel scope has been used.

The main categories of indirect costs and their approximate percentages for a typical fission facility are:

- Temporary construction facilities 15%
- Miscellaneous construction services (cleanup, maintenance of tools and equipment, material handling, guards, welder tests, etc.) 18%

. Construction equipment, tools, supplies and utilities	19%
. Field office costs (supervision, engineering, administration warehousing, field purchasing, medical and overhead)	42%
. Other (insurance, taxes and miscellaneous)	6%
	100%

In the UWMAK-III estimate, indirect costs are calculated at 100% of direct labor costs. The labor cost is not separately identified but is generally in the range of 20 to 25 percent of the total direct cost, and and average of 23% is assessed on the basis of a high bulk materials component, these being labor intensive. The resulting indirect costs are therefore 23% of total direct costs.

The engineering services provided include engineering costs, home office costs and fee. Engineering includes both preliminary and final designs, specifications, etc. Home office costs, which comprise estimating and scheduling services, procurement, start-up, quality assurance and project management, lie in the 50 to 60 percent range of engineering cost. Fee is normally a function of the total project cost and there are commonly accepted guidelines on appropriate schedules.

The sum of these three categories falls into the 12-22% range, which is historically consistent. The actual value is dependent on the complexity of the project. For Light Water Reactor plants, 12-15% is normal. For this study a figure of 16% of the total field costs has been used for engineering services because it is assumed that many of the problems lie in equipment and material specifications and in construction procedures, increasing the relative cost of engineering services.

Contingency is the sum of money added to an estimate to provide for items not specified in the engineering detail but which are known from experience to be a necessary part of a facility. Implicitly, it will be used, and it is not a drawdown fund to compensate for overruns or changes and additions to the project scope. Commonly used ranges for large complex facilities are from 15% of total construction costs for well defined projects to 30% or more for highly conceptual studies. As UWMAK-III is a first generation plant, there will be many problems unique to the facility and thus the contingency allowance has been set at 30%.

It is important to recognize that contingency provides for the unknown in the design only to the extent that the engineering is understood, and experience shows that it is quite difficult to assess the degree to which future processes are understood in the hardware sense. If the arrangement of the plant components contains major uncertainties, or the materials selected prove to be deficient, or the duty more severe than anticipated, or if additional major subsystems are required, then the scope of the engineering is inadequate and this is not covered by contingency.

Two final categories of cost include "Other Owner Costs" and "Interest during Construction". Other owner costs include the owner's general office and accounting costs, startup and operator training, spare part and inventory costs, and environmental impact studies. These costs lie in a range of 4%-12%,

and a figure of 8% has been selected as typical. This is based on the assumption that major equipment and start-up problems have been resolved and that environmental data acquisition and reports present no unusual concern.

As for interest during construction, we have taken the center of gravity of cash flow at the point where two thirds of the construction is complete, estimated from a proposed schedule to be three years from the plant fuel load date. Interest during construction is calculated at 8% of the total capital cost for three years. Escalation can be a difficult and tricky cost to include and it can distort the meaning of final results. For the purposes here, no provision is made for future escalation and estimates are based on fourth quarter, 1975, dollars.

A summary of the estimated capital costs for UWMAK-III is given in Table 13-1. The cost of electricity includes operating and maintenance costs, fuel costs, and the annual return on capital. The operating and maintenance costs include salaries, miscellaneous supplies and equipment, outside support services, miscellaneous and administrative costs, blanket rebuilding costs, and coolant makeup. These are estimated to be 1.5 mills/kWh.

The fuel costs are very small, estimated at 0.01 mills/kWh. UWMAK-III operates on a mixture of 50% deuterium and 50% tritium. The initial tritium inventory will be a substantial capital cost which has not been taken into account. However, after start of routine operation, a surplus of tritium will exist for which no credit has been allowed, so it has been assumed that tritium is available at zero cost. Deuterium is burned and lost in the operation of the plant, and an allowance for recycling is made.

The largest component of the electricity costs is the annual return on capital. The annual return on capital depends on many factors, particularly the financial structure of the utility and long-term interest rates. Consistent with recent experience, a 15 percent fixed charge rate is used.

c. A Perspective on Costs

To provide a perspective for evaluating the cost estimate for UWMAK-III, we show in fig. 13-1 the estimated cost of power for UWMAK-III in approximate relation to other base load plants. The systems have been arranged into three groups according to the time period when they will probably reach commercial operation. The figure has been developed using Bechtel Corporation experience and published reports adjusted where necessary to be comparable to UWMAK-III. Thus all costs are in present day dollars and include interest during construction, but exclude future escalation costs. The cost of power for each facility is divided into capital cost, fuel cost and operating and maintenance cost. The ranges of cost include the various types of facilities and differing site conditions. Coal was priced at $23 per ton and oil at $12 per barrel.

Escalation was not considered in the calculation because it would distort the basis of comparison, since its inclusion would entail some arbitrary assessment of when each type of plant is likely to be in commercial operation. However, excluding escalation introduces another bias resulting from neglecting the effect of escalating fuel prices. For fission plants scheduled for opera-

Table 13-1

CAPITAL COST SUMMARY

UWMAK III - 1985 MWe

Acct.	Item	Cost $ Millions	
	Direct Field Costs		
20	Land and Land Rights	1	
21	Structures & Site Facilities	568	
22	Reactor Plant Equipment	812	
23	Turbine Plant Equipment	561	
24	Electric Plant Equipment	280	
25	Miscellaneous Plant Equipment	60	
26	Special Materials	8	
	TOTAL DIRECT COST	2,290	
	Indirect Field Costs		
91	Construction Facilities and Services	530	
	TOTAL FIELD COST	2,820	
92	Engineering Services	450	
		3,270	
	Contingency	980	
	TOTAL ESTIMATED CONSTRUCTION COST	4,250	
93	Other Owner Costs	340	
94	Interest During Construction	1,100	
	TOTAL ESTIMATED CAPITAL COST: 4th Quarter 1975 Dollars	5,690	
	TOTAL CONSTRUCTION COST	2,140	$/KWe

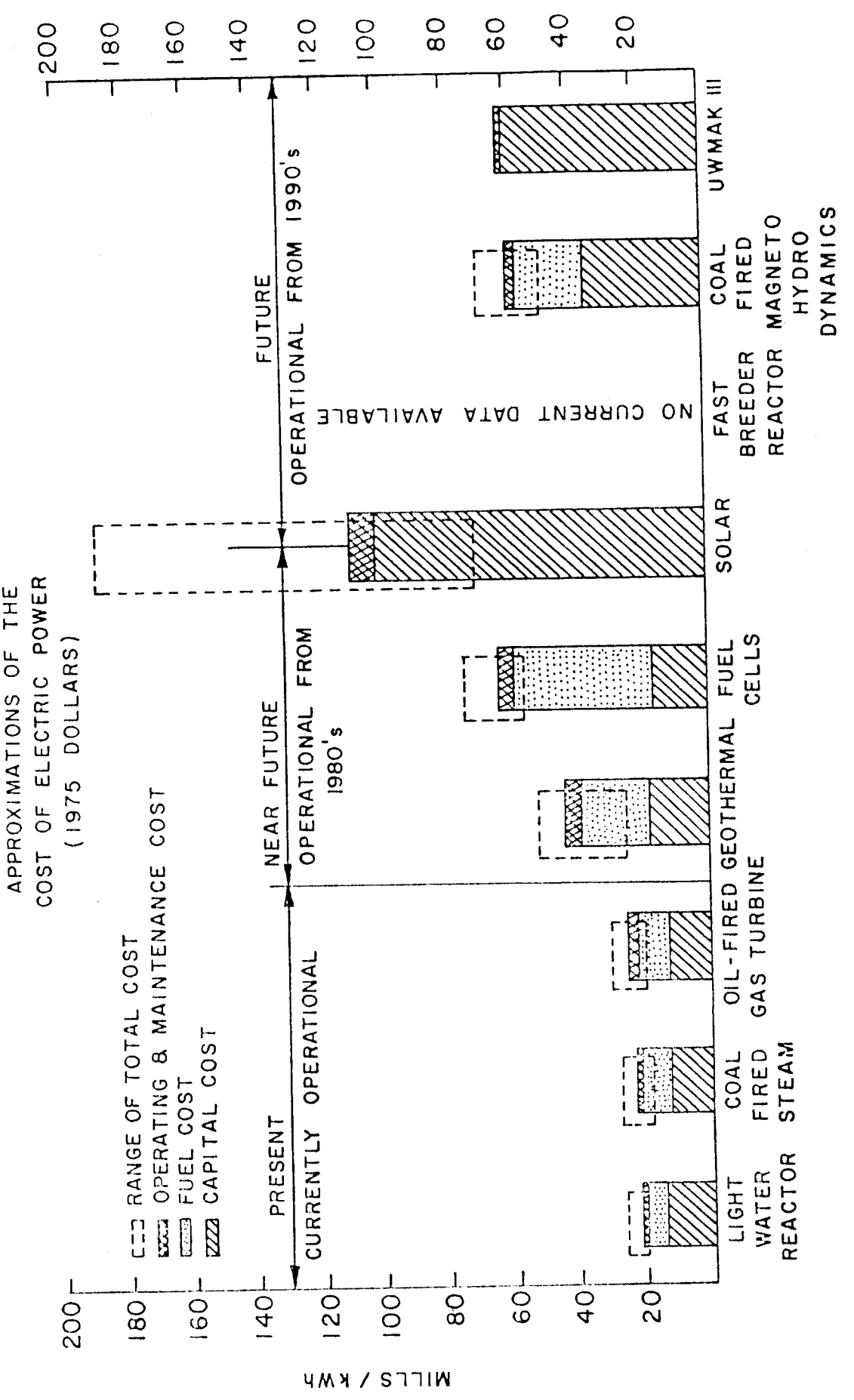
APPROXIMATIONS OF THE
COST OF ELECTRIC POWER
(1975 DOLLARS)
RANGE OF TOTAL COST
OPERATING & MAINTENANCE COST
FUEL COST
CAPITAL COST
PRESENT
CURRENTLY OPERATIONAL
NEAR FUTURE
OPERATIONAL FROM
1980's
FUTURE
OPERATIONAL FROM 1990's
NO CURRENT DATA AVAILABLE
MILLS / KWh
200
180
160
140
120
100
80
60
40
20
LIGHT WATER REACTOR
COAL FIRED STEAM
OIL-FIRED GAS TURBINE
GEOTHERMAL
FUEL CELLS
SOLAR
FAST BREEDER REACTOR
COAL FIRED MAGNETO HYDRO DYNAMICS
UWMAK III

Figure 13-1

tion in 1982, the cost of fuel might be from 6 to 12 mills/kWh on a 15 year levelized cost basis, depending on whether fuel costs escalate at 5% or nearer 10%. For coal-fired plants, the cost could be from 22 to 42 mills/kWh on the same basis. The higher figures represent approximately 29 percent of total generating costs for fission plants and about 56% for coal-fired plants, compared with roughly 21 percent and 36 percent respectively, for units starting up in 1978-79, but based on 1976 dollars. Further extrapolation would be difficult, but it is possible that fuel costs may continue to escalate faster than capital costs, gradually increasing the incentive for high capital/low fuel cost plants such as UWMAK-III.

Peak shaving and standby power systems are excluded from the comparison since criteria other than pure economic consideration govern their selection: reliability, simplicity or low capital costs are frequently the dominant factors. Hydro power is also excluded since the potential for a significant capacity increase in the continental U.S. is limited.

The source for all costs included on fig. 13-1 is the Bechtel Corporation and is based on cost estimates developed by Bechtel based either on direct experience or on a joint study. This provides the results with a consistency that is generally not possible since the basis for a cost estimate can differ widely among groups. The light water reactor and coal fired steam costs are based on Bechtel experience. The gas turbine estimate is based on a joint GE-NASA study. In the lower range are combined cycle gas turbine/steam plants, and in the higher range are closed cycle regenerative plants.

The cost estimate for geothermal power was developed by Bechtel in conjunction with input from the Pacific Gas and Electric Company. The lowest figures reflect Pacific Gas and Electric experience with their Geysers plants. However, the conditions are unique (relative cleanliness and high temperature with superheat). The high capital cost is a reflection of the relatively large steam turbine and cooling towers required for a low grade heat cycle. High temperature brine plants require more extensive equipment.

The costs for fuel cell and coal fired MHD plants were developed by Bechtel based on joint studies by General Electric Company and NASA. The fuel source for fuel cells is likely to be coal derived. Both high and low temperature fuel cells fall within the same approximate range with the former having the higher capital cost and lower fuel costs. The costs for coal fired MHD plants are for ones that include both open cycle, closed cycle inert gas and closed cycle liquid metal MHD plants. The open cycle is the least expensive, the liquid metal the most expensive and the inert gas is in the middle range.

The costs for central station solar power are based on studies by the Bechtel Corporation. The types of plants considered range from small solar ponds to large ocean thermal gradient powered plants. Also included at about the mid range are solar plants using heliostats focusing on a central tower furnace which powers a steam plant. To be comparable with other base load plants, the central tower system includes a heat storage system to accomodate night generation of power.

A major physical problem with land-based solar plants is the space required. A system designed to run on solar power for eight hours during the day and have sufficient thermal storage to carry a reduced night load would

require 3 1/2 to 4 square miles for 100 MWe. Further, unless summer loads are considerably higher than winter loads, the peak seasonal demand and generating capacity will be out of phase.

Ocean thermal gradient plants have neither of these problems. However, their overall efficiency is very low (in the order of 2% to 3%), and the environmental effects of transposing 4000 MWt of energy between the top and bottom of the ocean to generate 100 MWe have yet to be analyzed.

The perspective provided by Fig. 13-1 is that the electricity costs as developed for UWMAK-III appear to be comparable with estimates for central station solar power. The dashed boxes on Fig. 13-1 indicate a range of possible total costs but such a range has not been developed for UWMAK-III. This should be done by changing several of the key design choices, such as the choice of the primary structural material, and assessing the impact.

Fuel cells, with a low capital cost but a high fuel cost, appear to be the type of system ideally suited for peaking plants. Fusion and coal fired MHD are considered as base loaded plants because the capital costs make up a greater part of the electricity costs. The capital cost associated with the coal fired MHD system (approximately 40 mills/kWh) is higher than for coal fired steam because of the high temperature materials and cryogenic magnets associated with the MHD power cycle. The fuel costs add about a third to the electricity cost for both coal fired steam and coal fired MHD. In contrast, the fusion power costs are primarily related to capital costs while the fuel costs are only 1-2 mills/kWh. This is important if fuel costs escalate faster than capital costs. Past patterns of price behavior are a poor guide in predicting the future, but from an economics standpoint, if the scarcity of fuel is perceived to be greater than the scarcity of capital (not an unlikely event since fossil sources are finite, whereas capital sources are not) the cost of fuel will indeed rise faster than capital costs.

The solar estimates, which range from 70 to 200 mills/kWh, exceed those of all other systems. Further, solar power plants may not be feasible as base loaded systems except in the southwestern part of the U.S. because of this high load requirement during winter. Providing the energy storage capacity necessary for a base loaded plant in other parts of the country would roughly double the costs indicated in Fig. 13-1. (This does not detract from the positive role to be played by solar energy for space heating on homes and other buildings.)

The other potential base-loaded system not yet discussed is the Liquid Metal Fast Breeder Reactor (LMFBR). The LMFBR is the most highly developed of the non-fuel-limited power plants of the future, but consistent costs for this system were not available. Because it is found that costs vary widely depending upon the estimator, we did not feel it was appropriate to place a value not developed by Bechtel onto the Fig. 13-1. The only cost we will note is the relatively hard cost estimate for the Clinch River Breeder Reactor (CRBR) project.

The total estimated construction cost for CRBR is $891 million in 1974 dollars. (See ERDA Congressional Testimony, 1976.) We have used 4th quarter, 1975 dollars in this report and as discussed earlier, mid-1974 prices are to be escalated by 22% based on Bechtel escalation figures and the Handy Whitman Index. This would bring the CRBR estimated construction cost to $1.087 million

in the 4th quarter, 1975 dollars or $3105/kWe. Adding owner costs and interest during construction on the basis applied earlier gives a total estimated capital cost for CRBR of $1.455 billion, or $4157/kWe. The contribution to the cost of electricity from return on capital based on a 15% fixed charge rate is 89 mills/kWh. These costs do not include development costs, fuel costs, operating costs, or escalation beyond 1975. The plant is scheduled to operate in 1982.

The above costs are not strictly comparable because the CRBR is a demonstration plant and it is difficult to consistently estimate the cost of commercial plants from CRBR costs. This point has been made in a recent article by Levenson, Murphy and Zaleski.(27) However, Levenson, et al. do point out that demonstration plants (such as Shippingport) for light water reactors proved to be about twice as expensive as commercially built light water reactors like Dresden and Yankee. They also point out that "the cost of Shippingport, after normalization to 1974 conditions, is the same as the estimated cost of CRBR with a 15 percent contingency". If one infers that fast breeder reactors will experience a similar cost reduction on commercialization, then a commercial LMFBR will cost about $2000/kWe and will have electricity costs in the range of 45-55 mills/kWh, (1975 dollars). This result is in basic agreement with current reports by the French for the costs of Superphenix, a 1200 MWe LMFBR which will follow the French demonstration LMFBR, Phenix. The electricity costs for Superphenix are projected to be approximately double the costs of light water reactors. Lower costs than these will mean the commercial LMFBR's will have to be less than half the costs of demonstration fast breeder reactors. The costs for CRBR are summarized in Table 13-2.

d. Analysis of UWMAK-III Costs

The detailed costs summarized in part b have been analyzed to understand which items were keys to determining the costs. The unanticipated result is that the cost of high temperature refractory metal piping is critical while the cost of the toroidal field magnet system is relatively less important. This last result is crucial because it is opposite from the accepted folklore that the magnet costs are the primary factor in determining fusion plant costs.

The piping costs were high because it is necessary to protect refractory metals from the atmosphere to avoid oxide formation and hydrogen embrittlement Importantly, this is a general characteristic of refractory metals and is not specific to the use of molybdenum based alloys. The cost estimate developed for such pipe in the primary system is approximately $35,000/ft. As such, about a quarter of the nuclear island costs and about a third of the closed cycle helium gas turbine plant equipment costs were for pipe. It will be of great interest to redesign UWMAK-III (a relatively small unit physically with R = 8m) using a lower technology structural material such as 316 stainless steel. Clearly, the absolute costs will be reduced significantly and it is important to determine just how much.

An important auxiliary result is the breakdown by major category of the total costs. The direct costs are 40% of the total costs. Since all indirect costs are computed as a percentage of direct costs, every saving of $1 in direct costs means a savings of $2.50 in total costs. Therefore, a substantial reduction in piping costs (part of direct costs) will have a multiple effect on total estimated costs.

Table 13-2

Estimated Capital Costs for 350 MW_e CRBR

(4th Quarter, 1975 Dollars)

(In Millions of Dollars)

Total Estimated Construction Costs ($891 million*(1974 dollars) + 22% escalation to 1975)	$1,087
Other Owner Costs	87
Interest During Construction	261
Total Estimated Capital Costs	$1,435
Total Construction Costs ($/kWe)	$3,105/kWe
Total Capital Costs ($/$kW_e$)	$4,100/kWe

Estimated Electricity Costs for CRBR

	(mills/kWh)
A. Operation and Maintenance	1
B. Fuel	--
C. Return on Capital	89
Total Estimated Electricity Cost	90 mills/kWh

* 1976 ERDA Congressional Testimony

The direct costs in UWMAK-III were divided as follows: 25% for buildings, 35% for the reactor plant equipment (nuclear island), 25% for the turbine plant, 12% for the electric plant equipment, and 3% for remaining miscellaneous items. Therefore, the nuclear island is 35% of the direct costs while the balance of the plant is 65%. The toroidal field magnets were estimated to be 10% of the reactor plant equipment costs or just 3.5% of the total direct costs. This is much lower than anticipated and leads us to conclude that we can afford to pay for higher magnetic field.

This result has some very important implications. In particular, it has an implication for the size of tokamak reactors. There are two reasons one would build a tokamak large. The first is to improve the confinement time of the plasma and the second is to keep the neutron wall loading to a prescribed but low value. A wall loading constraint at some level (high or low) is applicable to all magnetic approaches to fusion and is not specific to tokamaks. On the other hand, increasing the size to improve confinement time is more peculiar to closed line devices like tokamaks than it is to an open-ended system like a mirror machine. However, almost all theories, as well as experience, indicated the confinement time improves with magnetic field. Therefore, within a given wall loading constraint, tokamaks can be made as small as possible by increasing the magnetic field. The cost penalty on the coils will not be overwhelming whereas keeping the size small will lower the costs of buildings, piping, blanket system and so on.

Turning to the role of the structures in this design, the building costs were about a quarter of the direct costs and the reactor building was approximately a third of the total building costs. Future designs of the reactor building should therefore aim for a highly optimized design. A constraint is the apparent need for access to a tokamak from both the side and the top. This leads to a tall, large diameter building for UWMAK-III. However, further examination may allow for improvements.

The choice of power conversion cycle also merits further careful study. The cost of a closed cycle helium plant appears to be in the same range as a steam cycle (about $140/kWe for the turbogenerator island). In this case, the determining factor in the choice of the cycle would be the power conversion efficiency and since capital costs are relatively high, the choice of an efficient power cycle is very important. There are indications from other studies that advanced steam cycles can produce comparable efficiencies at lower costs compared to closed cycle helium gas systems. (See "Study of Advanced Energy Conversion Techniques for Utility Application Using Coal or Coal Derived Fuels", Oral Briefing on Results of Task II, General Electric Co., February 10, 1976.)

Lastly, a comment about the intermediate loop. We have felt that the use of liquid lithium as the primary coolant would necessitate the use of an intermediate loop to isolate the primary coolant from the turbine cycle. This entails an added heat exchanger, an extra building, and added pipe length. The intermediate sodium loop in UWMAK-III is about 15% of the nuclear island cost. The development of a blanket design and cooling systems that can eliminate the need for the intermediate loop will thus lead to a potential savings in total direct costs. An example of such a blanket system is the use of Li_2O particles in a

moving bed similar to those used in the chemical industry.[28] Combined with the lower costs associated with a material like stainless steel, such a system will be less expensive than the UWMAK-III design employing TZM and thus should be investigated.

In sum, the economic analysis of UWMAK-III has shown that costs can be determined by certain key design decisions made early in a reactor study. For this system, the choice of a refractory metal alloy caused piping costs to be a main cost driver. It has been found that magnet costs are not dominant and that it will make good sense to increase magnetic fields to achieve the required plasma confinement time. One can then design the reactor in a minimum size consistent with other design constraints. It is also found that the need for an intermediate loop results in increased costs. Yet this loop is required only for certain choices of coolant and breeder materials and may be eliminated with alternative blanket designs. Thus, there are many avenues open for reducing the cost of tokamak systems below those of UWMAK-III. Finally, a cost comparison shows UWMAK-III costs to be in the same range as those projected for other advanced energy systems. As noted earlier, directly comparable LMFBR costs were not available for inclusion here but estimates based on the analyses of others indicate that these costs will be in approximately the same range.

14. Remarks

This concludes a general overview of the UWMAK-III conceptual power reactor study. It should be noted again that the primary purpose of this research is to investigate the potential technological problems which will be presented by fusion reactors, to investigate self-consistently the anticipated conditions in such reactors, to develop and investigate potential solutions to problems uncovered, and to provide a guide for further research. The chapters to follow give a detailed description of the analysis and design on each topic relevant to this reactor study. The general conclusions that have been reached are summarized in Chapter XIV, a section which directly complements this overview.

References for Section I

1. B. Badger, M. A. Abdou, R. W. Boom, R. G. Brown, T. E. Cheng, R. W. Conn, J. M. Donhowe, L. A. El-Guebaly, G. A. Emmert, G. R. Hopkins, W. A. Houlberg, A. B. Johnson, J. H. Kamperschroer, D. Klein, G. L. Kulcinski, R. G. Lott, C. W. Maynard, A. T. Mense, G. R. Neil, E. Normand, P. A. Sanger, W. E. Stewart, T. Sung, I. Sviatoslavsky, D. K, Sze, W. F. Vogelsang, L. J. Wittenberg, T. F. Yang, W. D. Young, A Wisconsin Toroidal Fusion Reactor Design, UWMAK-I, Nucl. Eng. Dept. Report UWFDM-68 (Univ. of Wisconsin) Vol. I (November 1974).

2. B. Badger, R. W. Conn, G. L. Kulcinski, M. A. Abdou, R. W. Boom, G. A. Emmert, J. W. Davis, Y. Eyssa, S. Ghose, M. Hilal, J. Kesner, W. Lue, C. W. Maynard, A. T. Mense, J. Scharer, T. Sung, I. Sviatoslavsky, D. K. Sze, W. Vogelsang, L. Wittenberg, T. Yang, J. Young, W. D. Young, A Conceptual Tokamak Reactor Design, UWMAK-II, Nucl. Eng. Dept. Report UWFDM-112, (November 1975).

3. R. W. Conn, G. L. Kulcinski, H. Avci, M. El-Maghrabi, Nuclear Technolgy 26, (1975) 125.

4. See several University of Wisconsin Reports - G. L. Kulcinski, R. W. Conn, H. Avci, D. K. Sze, UWFDM-127; R. W. Conn, D. K. Sze, UWFDM-128, G. L. Kulcinski, H. Avci, UWFDM-135.

5. H. Segal, T. G. Richard, "Low Temperature Resistance Studies on Cyclically Strained Aluminum," Proc. Cryogenic Eng. Conf. (Kingston, Ca., July 1975) to be published in Advances in Cryogenic Engineering (Vol. 21)

6. J. Adam et al. "Wave Generation and Heating on the ST Tokamak at the Fundamental and Harmonic Ion Cyclotron Frequencies," Plasma Physics and Controlled Nuclear Fusion Research 1974 (Tokyo Conf., IAEA, Vienna, 1975) 1, 65.

7. R. W. Conn, J. Kesner, Nuclear Fusion 15 (1975) 775.

8. G. L. Kulcinski, R. W. Conn., G. Lang, Nuclear Fusion 15 (1975) 327.

9. R. Behrisch, H. Roth, M. Bodansky, Max Planck Institute for Plasmaphysik, Garching, private communication.

10. G. Hopkins, Trans. Amer. Nucl. Soc. 21 (1975) 57.

11. A. T. Mense, G. A. Emmert, J. Callen, Nuclear Fusion 15 (1975) 703.

12. R. Moses, W. Young, "Analytic Expression for Magnetic Forces on Sectored Toroidal Coils," 6th Symposium on Eng. Problems of Fusion Research (San Diego, November 1975).

13. D. Cornish, private communication.

14. W. R. Wilkes, "Separation of Hydrogen Isotopes for Tritium Waste Removal", Proc. Symp. on Tritium Technology Related to Fusion Reactor Systems (ERDA-50, p. 113, 1974).

15. J. S. Watson, "An Evaluation of Methods for Recovering Tritium from the Blanket or Cooling Systems of Fusion Reactors", Oak Ridge National Lab. Report, ORNL-TM-3794 (July 1972).

16. R. M. Barrer, Diffusion in and Through Solids (Cambridge University Press, 1941).

17. D. Schmunk, G. L. Kulcinski, "Survey of Irradiation Data on Molybdenum", University of Wisconsin Report, UWFDM-161 (Sept. 1976).

18. W. J. Gray, W. C. Morgan, "High Temperature Graphite Irradiations: 550 to 1450°C", Battelle Pacific Northwest Laboratories Report, BNWL-1672 (1972).

19. M. Van den Berg, M. R. Everett, A. Kingsbury, "The Relationship Between Irradiation Temperature and Dimensional Changes of Nuclear Graphite", 12th Biennial Conf. on Carbon (University of Pittsburgh, 1975).

20. W. C. Morgan, E. M. Woodruff, W. J. Gray, "Irradiation Behavior of Graphite at Very High Temperature", in 2nd National Topical Meeting on Controlled Fusion Technology (Richland, Wash., Sept. 1976), to be published.

21. R. Behrisch, B. B. Kadomtsev, in Plasma Physics and Controlled Nuclear Fusion Research 1974 (IAEA, Vienna, 1975), Vol. II., p. 229.

22. J. B. Holt et al., "Helium Generation and Diffusion in Graphite", same conference as reference 20.

23. S. K. Erents, C. M. Braganza, G. M. McCracken, "Methane Formation During the Interaction of Energetic Protons and Deuterons with Carbon", J. Nucl. Mat. (in press).

24. M. Balooch, D. R. Olander, J. Chem. Phys. 63, 4772 (1975).

25. G. Lang, V. L. Holmes, Nucl. Fusion 16, 162 (1976).

26. United Engineers and Contractors, "Pressurized Water Reactor Plant, 1000 MW_e Central Station Power Plants - Investment Cost Study", AEC Report, WASH-1230 (1971) Vol. I.

27. M. Levenson, P. M. Murphey, C. P. L. Zaleski, Nuclear News 19, 54 (1976).

28. D. K. Sze, E. M. Larsen, E. T. Cheng, R. G. Clemmer, Trans. Amer. Nucl. Soc. 22, 21 (1975).

II. Plasma Analysis for UWMAK-III

Noncircular cross sections offer the potential for achieving higher values of total β (the ratio of plasma to magnetic field pressure) compared with circular plasmas of equal poloidal beta, β_θ, and safety factor, q. The scaling is

$$\beta = \beta_\theta \left(\frac{S}{qA}\right)^2$$

where A is the aspect ratio and S is the plasma shape factor defined as the plasma cross sectional perimeter divided by the perimeter of the largest inscribed circle. From a reactor point of view, this effective increase in β translates into a lower value of the required toroidal magnetic field and therefore to lower cost. Alternatively, with the same magnetic field as in a circular device, it means the device will generate more power.

As described in the Overview, a primary objective in the UWMAK-III study is to decrease the overall reactor size compared with earlier studies while still designing for the same thermal power output of 5000 MW. The reduction in size will translate into reductions in costs and therefore improved economics. The use of a noncircular plasma allows us to design a small 5000 MW_{th} reactor system without having to increase the maximum toroidal field at the magnet beyond the 8 to 9 T range compatible with the use of NbTi superconductor.

Of course, the potential benefits of noncircular tokamaks will only be realized if an equilibrium plasma can be made which is stable at similar values of β_θ and q as those achieved in circular machines. If, for example, q must be increased for a noncircular plasma to maintain stability, the desired increase in β will not come about.

Therefore, the equilibrium and stability of the plasma cross section in the UWMAK-III design is crucial and Section A of this chapter describes our study on this subject. Of particular relevance is that we consider noncircular plasma shapes that are bounded by a separatrix. This provides the device with a double null poloidal divertor. The analysis also assumes discrete external coils and does not require a conducting shell.

In Section B, the design of the ohmic heating system and the determination of the reactor burn cycle is discussed. This is followed in Section C by an analysis of RF heating of a reactor grade plasma. In particular, we have considered which modes hold the greatest potential for reactor application and, having made a choice, go on to examine plasma heating to ignition using RF. Particular attention is also given to the design of the wave launching structure.

The analysis of heating is followed in Section D by an evaluation of the expected plasma operating conditions during the steady burn period. Both a global and a space dependent plasma simulation program have been used and significant differences are found between these procedures.

II-A. Plasma Design for UWMAK-III

1. MHD Equilibrium and Stability Theory

General Considerations

Future tokamaks and particularly tokamak power reactors will require discrete external coils rather than a conducting shell to keep the plasma in equilibrium. The required vacuum vertical field generated by such coils can be estimated in many ways. For example, a virtual shell can be placed around the plasma and, at equilibrium, one can replace the resulting image currents by a set of discrete coils.[1] One then iterates on this procedure until a new equilibrium configuration is determined using only discrete coils. Alternatively, one can estimate the required vacuum field strength on the midplane by using the formula[2,3] for circular tokamaks,

$$B_{\perp} = \frac{\mu_o I_\phi}{4\pi R} \left(\ln \left(\frac{8R}{a}\right) + \frac{\ell_i}{2} + \overline{\beta_\theta} - \frac{3}{2} \right)$$

where

$$\ell_i = \frac{1}{\pi a^2 B_\theta^2(a)} \int_o^a B_\theta^2(r)\, 2\pi r dr \quad .$$

The currents and locations of the external coils must then be adjusted until an equilibrium is found which satisfies additional constraints placed on the size and shape of the plasma and the decay index of the vacuum field. We find this second method more convenient to use in connection with studies on systems that include a poloidal divertor.

The equilibrium vertical field required for a non-circular, elliptical plasma of small eccentricity and uniform current density is[4]

$$B_{\perp} = \frac{\mu_o I_\phi}{4\pi R_o} \left\{ \ln \frac{8R_o}{a} + \overline{\beta_\theta} - \frac{5}{4} - \frac{R-R_o}{R_o} \left[\frac{3}{4} \ln \frac{8R_o}{a} - \frac{17}{16} + \frac{R_o^2}{a^2} \left(1 - \frac{b}{a}\right) \right] \right\} \qquad (1)$$

where R_o is the major radius, 2a is the plasma width, 2b is the plasma height and the average poloidal beta is defined as

$$\overline{\beta_\theta} = \frac{\langle P \rangle}{\frac{B_\theta^2}{(2\mu_o)}} \quad . \qquad (2)$$

The shift of the magnetic axis from the geometrical center is an important quantity and, in the large A limit, is approximately given by

$$\Delta_m = \frac{4\pi a^2}{2\mu_o I_p} B_\perp \quad . \tag{3}$$

Another important quantity is the decay index of the transverse field. For non-circular cross section and small β_θ, the decay index is given by

$$n = \frac{3}{4} \frac{\ln \frac{8R_o}{a} - \frac{17}{12}}{\ln \frac{8R_o}{a} + \overline{\beta_\theta} - \frac{5}{4}} + \frac{\frac{R_o^2}{a^2}(1 - \frac{b}{a})}{\ln \frac{8R_o}{a} + \overline{\beta_\theta} - \frac{5}{4}} \tag{4}$$

and we require $n > 0$ at the magnetic axis for stability with respect to radial and vertical displacements.[5] The condition $n > 0$ is valid only for $\frac{b}{a}$ small and R_o/a large, but it is sufficient for our purposes to know the field at the magnetic axis in order to estimate the current in the external coils.

MHD Equilibrium Calculations

The MHD equilibrium for an axisymmetric system can be determined by solving the usual equation for the flux function Ψ which satisfies

$$X \frac{\partial}{\partial X} \left(\frac{1}{X} \frac{\partial \psi}{\partial X} \right) + \frac{\partial^2 \psi}{\partial Z^2} = -X J_\phi \quad , \tag{5}$$

where

$$J_\phi = X \frac{dp}{d\Psi} + R_o B_o^2 g \frac{dg}{d\Psi} \quad . \tag{6}$$

The magnetic field has been decomposed into poloidal and toroidal components using

$$\vec{B} = B_o \left[f(\psi) \vec{\nabla\phi} X \vec{\nabla\psi} + R_o g(\psi) \vec{\nabla\phi} \right] \quad . \tag{7}$$

The coordinates R, ϕ and Z are the axisymmetric coordinates, ϕ is the ignorable variable and X is the distance from the symmetric axis. ψ represents an arbitrary surface label and Ψ is the poloidal flux inside a magnetic surface.

The MHD study group[6] at the Princeton Plasma Physics Laboratory has developed a general computational program to solve equation (5) in which the plasma boundary is determined self consistently with the location of external coils. A square of arbitrary size is used as an outer boundary for the problem and the boundary conditons on this border are fixed by specifying the current in the external coils. As such, the procedure does not require the use of a conducting external boundary. The plasma boundary can be fixed by a limiter or a separatrix. The program evaluates $q(\Psi)$, $\beta_\theta(\Psi)$ and β_θ from the formulae:[7,8]

$$q(\psi) = \frac{f}{2\pi} \oint \frac{dl}{|\nabla\Psi| X} \quad , \tag{8}$$

$$\beta_\theta(\psi) = \frac{2\pi P}{\left\langle \frac{|\nabla\Psi|^2}{R^2} \right\rangle} \tag{9}$$

$$\overline{\beta_\theta} = \frac{\int P \frac{dv}{d\Psi} d\Psi}{\int^{\Psi} P \frac{dv}{d\Psi} d\Psi - R_o^2 B_o^2 \int^{\Psi} vg \frac{dg}{d\Psi} \left\langle \frac{1}{X^2} \right\rangle d\Psi} \tag{10}$$

Here,

$$V = 2\pi \int^{\Psi} d\Psi \oint \frac{X dl}{|\nabla\Psi|} \quad , \tag{11}$$

and

$$\frac{dv}{d\Psi} = 2\pi \oint \frac{dl}{|\nabla\Psi|} \quad . \tag{12}$$

The non-linear equation (5) is solved by prescribing the functions $P(\Psi)$ and $g(\Psi)$ in equation (6). For the case of a reactor size system, the form of these functions has a significant effect on the equilibrium and stability of the plasma warrants some discussions. If we choose

$$P(\Psi) = P_o \left(\frac{\Psi_* - \Psi}{\Psi_* - \Psi_o} \right)^{\alpha_1} \tag{13}$$

and

$$g(\Psi) = \left[1 - g_p \left(\frac{\Psi_* - \Psi_o}{\Psi_* - \Psi_m} \right)^{\alpha_2} \right] \quad , \tag{14}$$

the plasma current, $j_\phi(\Psi)$, has the form

$$j_\phi(\Psi) = -\frac{X P_o \alpha_1}{\Delta\Psi}\left(\frac{\Psi_* - \Psi}{\Delta\Psi}\right)^{\alpha_1 - 1} + \frac{\alpha_2 R_o^2 B_o^2}{\Delta\Psi X} g_p \left(\frac{\Psi_* - \Psi}{\Delta\Psi}\right)^{\alpha_2 - 1}$$

$$+ \frac{\alpha_2 R_o^2 B_o^2}{\Delta\Psi X} g_p^2 \left(\frac{\Psi_* - \Psi}{\Delta\Psi}\right)^{\alpha_2 - 1} , \qquad (15)$$

where $\Delta\Psi = \Psi_* - \Psi_m$ and Ψ_*, Ψ_m are the flux at the plasma surface and magnetic axis. The constant g_p is varied until Ψ converges. On the other hand, if one chooses α_1 and $\alpha_2 = 1$, $P(\Psi)$ and $g(\Psi)$ are independent of Ψ and $j_\phi(\Psi)$ is given by

$$j_\phi(\Psi) = -\frac{X P_o}{\Delta\Psi} + \frac{R_o^2 B_o^2}{X\Delta\Psi} g_p + \frac{R_o^2 B_o^2}{X\Delta\Psi}\left(\frac{\Psi_* - \Psi}{\Delta\Psi}\right)^2 g_p . \qquad (16)$$

Thus, $j_\phi(\Psi)$ is nearly a linear function of R when $g_p < 1$. This however is not a desirable profile and does not appear to be consistent with present tokamak experiments. If we set $\alpha_1 = 2$ and $\alpha_2 = 1$, then

$$j_\phi(\Psi) = -\frac{X P_o}{\Delta\Psi}\left(\frac{\Psi_* - \Psi}{\Delta\Psi}\right) + \frac{R_o^2 B_o^2}{X\Delta\Psi} g_p + \frac{R_o B_o}{X\Delta\Psi}\left(\frac{\Psi_* - \Psi}{\Delta\Psi}\right)^2 g_p \qquad (17)$$

The current profile is now nearly parabolic in r. However, for $\overline{\beta_\theta} > 2.0$, it is found that the safety factor becomes less than 1 near the magnetic axis. After further study, we find that values of α_1 and α_2 in the neighborhood of 1.4 are optimum.

Stability Analysis

The stability of the plasma with respect to rigid motions (vertical and radial displacements and flipping), localized interchange modes of both the resistive and ideal types, and general kink modes have each been considered.

a. Rigid Motions

We have found that one can often obtain large elongated plasma of approximately elliptical shape with $\frac{b}{a} > 2$ and $S \tilde{-} 1.8$ for which $q(\Psi) > 1$ and the plasma is stable against localized modes but which nevertheless has the wrong curvature associated with the vacuum vertical field. It is therefore unstable to rigid displacements and it is typically a major effort to arrange the external coils such that the decay index, n, at the magnetic axis, R_m is greater than zero.

A detailed study has recently been made by Rebhan.[9] The necessary and sufficient criteria for stability with respect to any arbitrary rigid perturbation b_ξ are given as

$$\oint \frac{R\Psi_z}{|\nabla\Psi|} P_z^* \, dl + \frac{1}{2\pi} \int_s \vec{B} \cdot \vec{b}_\xi \vec{e}_\xi \cdot d\vec{s} = 0 \tag{18}$$

$$\oint \frac{R\Psi_R}{|\nabla\Psi|} P_R^* \, dl \geq 0 \tag{19}$$

and

$$\oint \frac{R(R\Psi_z - Z\Psi_R)}{|\nabla\Psi|} (R P_z^* - Z P_R^*) dl \geq 0 \quad . \tag{20}$$

P* represents the equilibrium pressure while subscripted values of Ψ and P imply derivatives. These general criteria can be evaluated numerically, and the stability can be cast in terms of critical values for the parameters, $e_{cr} \equiv \frac{b}{a}$, and q. Assuming a parabolic pressure profile, elliptical flux surfaces with triangular deformation, and constant values of P (Ψ) and g(Ψ)g (Ψ), Rebhan obtained the critical value of q, designated q_h, for stability with respect to horizontal displacement as

$$\lim_{A \to \infty} q_h = \frac{1}{\sqrt{2}} \quad . \tag{21}$$

He also found critical q value, denoted by q_f, for stability against flipping of the plasma ring as

$$\lim_{A \to \infty} q_f = 1 \quad . \tag{22}$$

The values of q_h and q_f tend to decrease as A decreases. The plasma is stable if q is greater than q_h and q_f. The existence of a critical q is to be expected from the fact that horizontal displacement and flipping are special kink modes and q must be kept above one to satisfy the Kruskal-Shafranov limit[10,11] and obtain stability with respect to other kink modes. As such, no additional precautions need be taken. The criterion (18) can be reduced to

$$C_{vert} = \oint \left\{ \frac{1}{R|\nabla\Psi|} \left[-\Psi_R \Psi_{RR} + \frac{\Psi_Z \Psi_R}{R} + \Psi_R \Psi_{RZ} \right] + Y \right\} \Psi_z \, dl \geq 0 \tag{23}$$

for vertical displacements, where $y = (\vec{e}_\theta \times \vec{n})\cdot\vec{b}_\xi$.

b. Localized Modes

The criteria for stability with respect to the localized interchange modes are,[12,13] for idealized modes,

$$D_I = D + H - \frac{1}{4} < 0$$

and for resistive modes,

$$D_R = D + H^2 < 0$$

The parameters D and H are defined by

$$D \equiv \frac{\langle B^2/|\nabla V|^2\rangle}{\Lambda^2}\left[J'\phi'' - I'\Psi'' + \frac{\langle \sigma B^2\rangle}{\langle B^2\rangle} + P'^2\left\langle\frac{1}{B^2}\right\rangle + \left\langle\frac{\sigma^2 B^2}{|\vec{\nabla}V|^2}\right\rangle - \frac{\langle \sigma B^2/|\vec{\nabla}V|^2\rangle^2}{\langle B^2/|\vec{\nabla}V|^2\rangle}\right]$$

$$H \equiv \frac{\langle B^2/|\vec{\nabla}V|^2\rangle}{\Lambda}\left[\frac{\langle \sigma B^2/|\vec{\nabla}V|^2\rangle}{\langle B^2/|\vec{\nabla}V|^2\rangle} - \frac{\langle \sigma B^2\rangle}{\langle B^2\rangle}\right],$$

where $\Lambda \equiv \phi'\Psi' - \Psi'\phi'$ and $\sigma \equiv \vec{J}\cdot\vec{B}/B^2$. ϕ and Ψ are the toroidal and poloidal field flux functions and J and I and the toroidal and poloidal current fluxes, respectively. Primes denote derivatives with respect to the volume, V, and brackets denote field line averages.

c. General Kink Modes

The stability with respect to kink modes may be insured by examining the q values and β. If the safety factor $q > 1$, the well-known Kruskal-Shafranov limit[10,11] is that all "m" modes are stabilized and the critical β for stability is $\beta = \epsilon^2$, where $\epsilon = \frac{a}{R}$, the inverse aspect ratio. A detail stability study by Freidberg[16] based on a sharp boundary model shows that the critical β_θ increases due to ellipticity and decreases due to triangularity. A value of this critical beta will be estimated from the results of Freidberg and used to estimate the stability against kink modes of the specific examples discussed next.

2. Calculations for UWMAK-III

The main guidelines for the plasma design in UWMAK-III were that the plasma should have a shape factor of approximately 1.6 with a major radius between 8 and 9m, and magnetic field on axis in the vicinity of 4T. For a 5000 MW_t system, this would lead to an average neutron wall loading of $\sim 2 MW/m^2$ and would leave adequate core space for the transformer winding without exceeding a maximum field in the machine throat of about 8T. Such a plasma achieves a dramatic reduction in system volume compared with earlier studies and this was described quantitatively in the overview. It was also required that the plasma be bounded poloidally by a separatrix with null points alone and below the median plane to provide an appropriate design for a divertor system.

A list of the characteristic parameters finally developed for the UWMAK-III reactor system is given in table II-A-1. For this large system, the vacuum field calculated from Eqn. (3) is $B_\perp = 0.77T$ and the shift of magnetic axis calculated from Eqn. (3) is $\Delta_m = 1.85m$. The decay index for mildly elliptical cross-sections is 0.34. The external coils were arranged in such a way that $B_\perp = 0.77T$ and $n > 0$ at $R_m = 10.0m$.

Fig. II-A-1 is a detailed flux plot for the equilibrium plasma in UWMAK-III and Fig. II-A-2 shows the vacuum vertical field. Table II-A-2 is a list of the locations and the currents in all the discrete external vertical field coils. As can be seen, the plasma cross-section is vertically elongated with two stagnation points on the boundary that are symmetrically located above and below the median plane, as required for a poloidal divertor. The stagnation points are fixed by the coil D_o. For reasons related to the blanket design discussed in Chapter 5, we have required that the plasma surface intersect the midplane at $R_1 = 5.4m$ and $R_2 = 10.8m$. The stagnation point has been placed at a height above the midplane such that $b \tilde{-} 2a$.

Two virtual limiters were placed at R=5m and R=11.5m to specify the initial size of the plasma at the beginning of the calculation. The parameters α_1 and α_2 were initially set at 1.4 for the reasons discussed in section 1. The calculational sequence is to vary the locations and the currents in the external coils and the peak pressure, P_o, until an equilibrium is found with $\beta_\theta \tilde{=} 2.2$, $q(\Psi) > 1$ and the decay index $n > 0$. The parameters α_1 and α_2 are then varied until an optimum solution is found.

The two dimensional toroidal current density distribution is shown in Fig. II-A-3 while the pressure and current profiles are shown in Fig. II-A-4 as a function of R on the midplane. The magnetic axis is at ~9.0m, which is a shift outward from the geometric center of 0.9m. The toroidal current, j_ϕ, peaks at $R_j = 10.0m$ and we refer to this location as the toroidal current axis. It is interesting to note that the current axis is shifted outward beyond the magnetic axis by about 1m. The vacuum vertical field at R_m=9.0 is $B_\perp \tilde{=} 0.7$ T. This last value shows that formula (3) gives a reasonably accurate prediction for $B_\perp$ and is useful as an initial guess.

Turning now to the stability problems, the vacuum field for UWMAK-III shown in Fig. II-A-2 has good curvature to the right of the magnetic axis and bad curvature to the left. It seems clear that only for circular or mildly non-circular plasmas can the vacuum field have good curvature throughout the entire plasma cross-section. However the decay index criterion n>0 is valid for circular plasmas of large aspect ratio. In general, it will be necessary to calculate detailed spectra in order to understand the plasma stability with respect to small perturbations using a ΔW formulation. This will be possible only when a ΔW code becomes operational.[15]

Table II-A-1

Plasma Parameters of UWMAK-III

R_o = 8.1 m	I_p = 15.8 MA
B_o = 4.05 T	$\overline{\beta_\theta}$ = 2.2
R_{in} = 3.75 m	$q_* \cong 3.5$
B_{max} = 8.75 T	$q_o \cong 1.0$
R_m = 9.0 m	a = 2.7 m
R_j = 10.0 m	b $\cong$ 5.4 m
Δ_m = 0.8 m	S $\cong$ 1.6
Δ_j = 1.2 m	b/a = 2.0

Table II-A-2

External Coil Parameters of UWMAK-III

	Z(m)	R(m)	I(MA)
D_o	9.0	6.8	15.50
D_1	0.0	3.9	.40
D_2	1.0	3.9	.40
D_3	4.5	4.0	2.00
D_4	5.5	4.6	-0.60
D_5	9.0	3.9	-1.2
D_6	9.5	5.9	-2.2
D_7	13.0	6.8	-1.30
D_8	11.7	8.3	-4.30
D_9	9.9	8.5	-3.00
D_{10}	10.0	8.8	-1.53
D_{11}	9.3	8.8	-1.65
D_{12}	9.9	8.8	-1.10
D_{13}	7.7	8.9	-1.60
D_{14}	7.5	9.3	-1.62
D_{15}	7.3	10.8	-1.55
D_{16}	6.8	11.8	-1.60
D_{17}	5.3	12.8	-1.65
D_{18}	4.3	13.0	-1.65
D_{19}	2.3	13.5	-1.52
D_{20}	0.0	13.5	-1.52

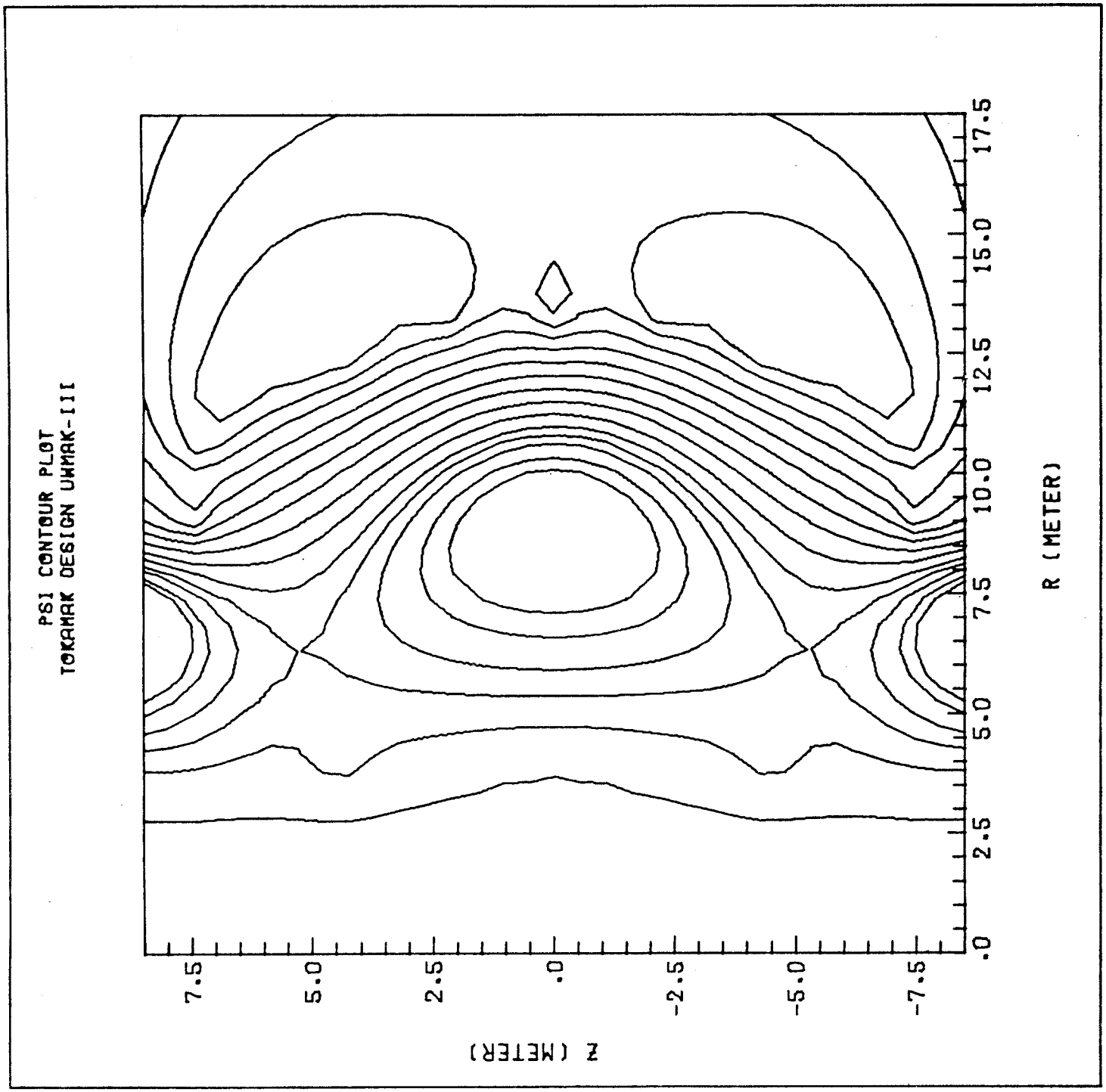
PSI CONTOUR PLOT
TOKAMAK DESIGN UWMAK-III
Z (METER)
7.5
5.0
2.5
.0
-2.5
-5.0
-7.5
R (METER)
.0
2.5
5.0
7.5
10.0
12.5
15.0
17.5

FIGURE II-A-1

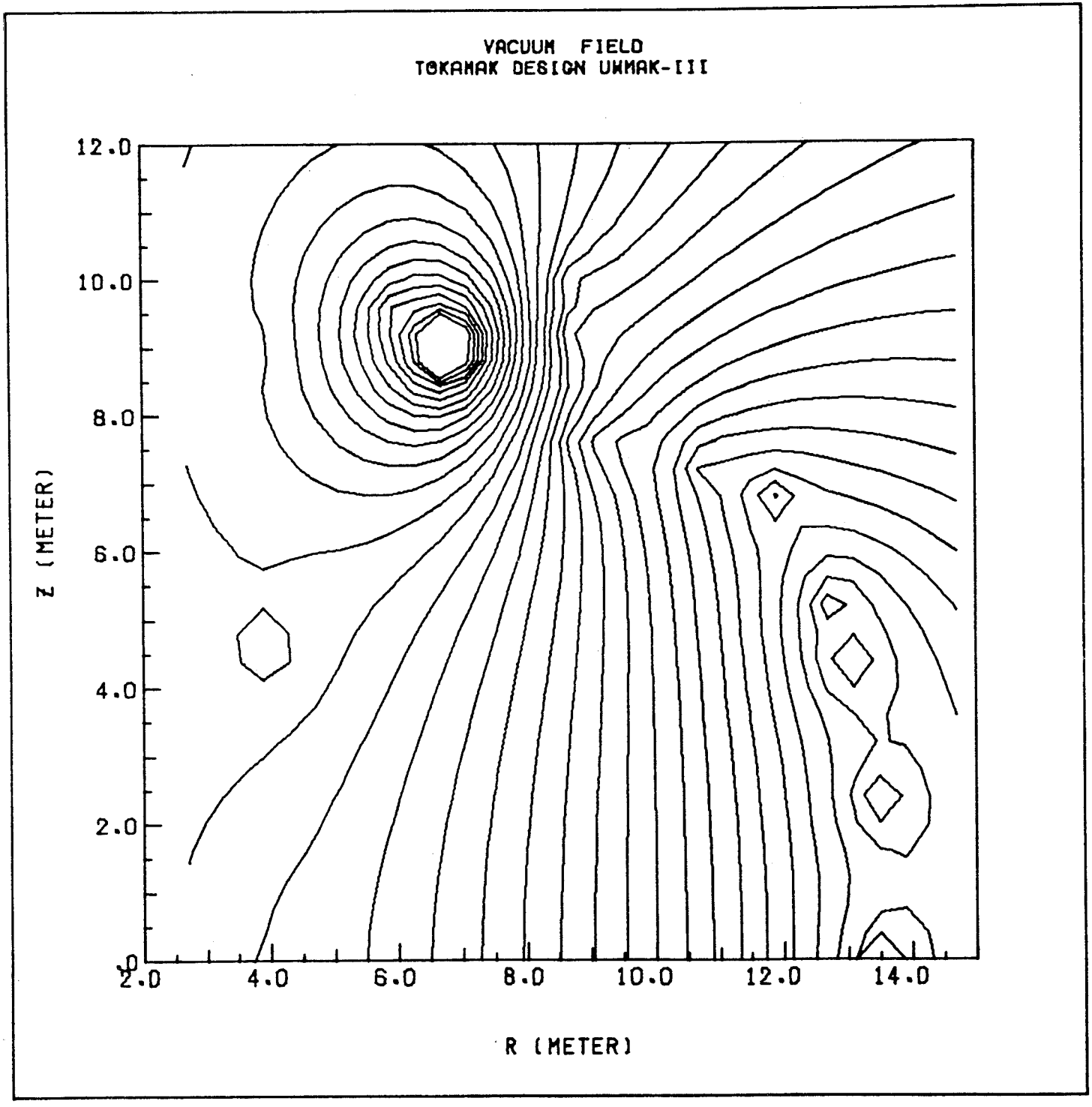
VACUUM FIELD
TOKAMAK DESIGN UWMAK-III
12.0
10.0
8.0
6.0
4.0
2.0
0
Z (METER)
2.0
4.0
6.0
8.0
10.0
12.0
14.0
R (METER)

FIGURE II-A-2

CURRENT CONTOUR
TOKAMAK DESIGN UWMAK-III
Z (METER)
7.5
5.0
2.5
.0
-2.5
-5.0
-7.5
R (METER)
.0
2.5
5.0
7.5
10.0
12.5
15.0
17.5

FIGURE II-A-3

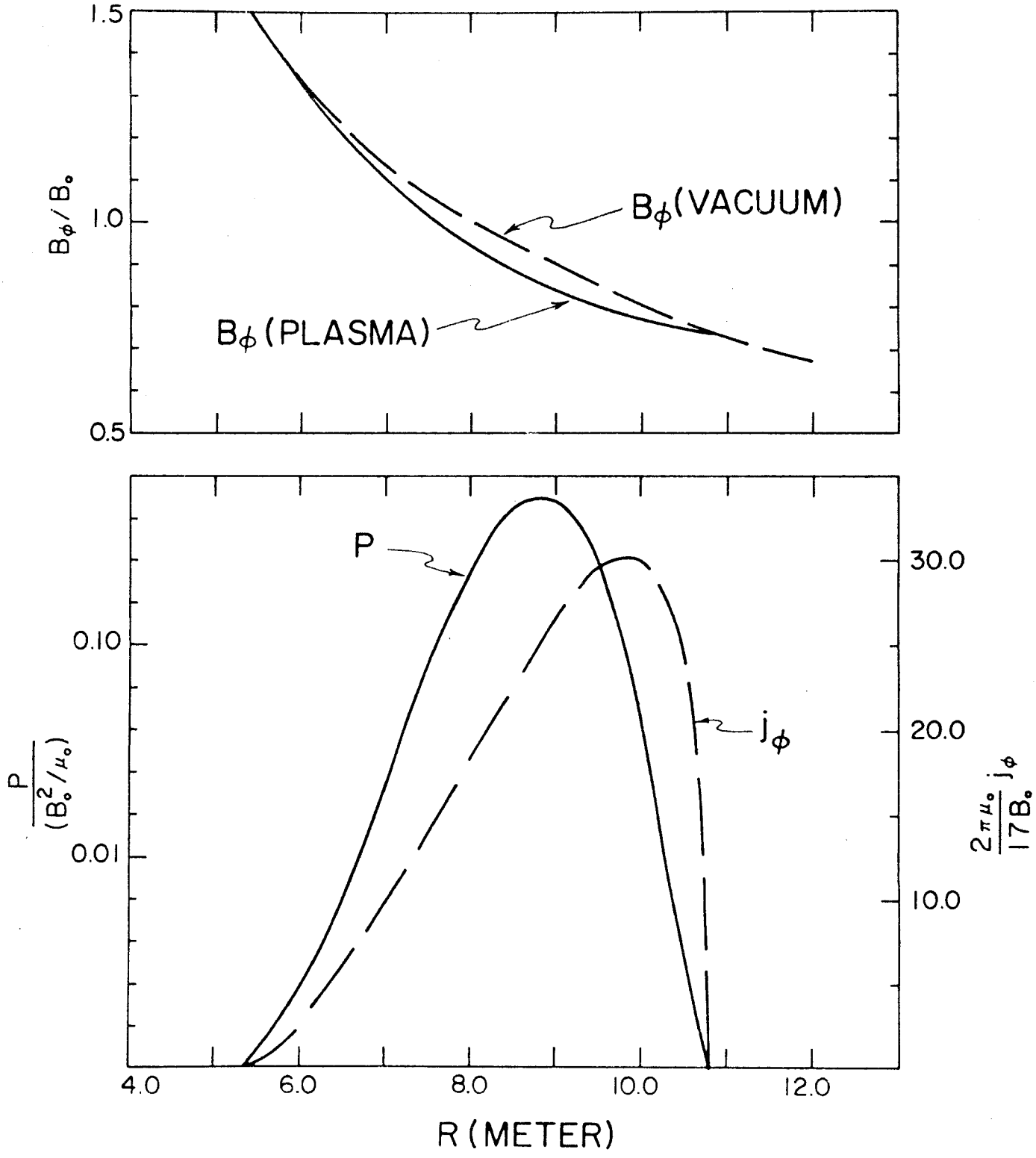
1.5
1.0
0.5
$B_\phi / B_\circ$
B_ϕ(VACUUM)
B_ϕ(PLASMA)
P
j_ϕ
0.10
0.01
$\frac{P}{(B_\circ^2/\mu_\circ)}$
30.0
20.0
10.0
$\frac{2\pi\mu_\circ}{17B_\circ} j_\phi$
4.0
6.0
8.0
10.0
12.0
R (METER)

FIGURE II-A-4

One important observation which can be made is that the large triangularity of the plasma shape is a result of forcing the vertical field to have good curvature in the region to the right of the magnetic axis. The decay index n is small but positive. To obtain larger values of n would require a reduction in the height to width ratio, $\frac{b}{a}$, and shape factor S, i.e., a reduction in the ellipticity. When n becomes negative, the triangularity is reduced and the plasma becomes more and more elliptical. This agrees with many theoretical predictions that vertically elongated plasma cross-sections with large triangularity are more stable[9,14,16]. Obviously the plasma will be more stable when n becomes larger until it reaches some maximum n value. The present plasma for UWMAK-III gives an elongation factor, e = 2 and a shape factor, S = 1.6. Since the vacuum vertical field is nearly parallel at the outer region of the plasma, it will begin to curve in the wrong direction if one tries to increase e and S further. Therefore, using the criterion $n > 0$, the values e = 2 and S = 1.6 are the upper limits we can use for the UWMAK-III case.

The stability of the plasma against radial displacements and flipping is insured by the fact that $Q(\Psi)$ is greater than q_h and q_f. To test for stability to vertical displacements, we consider a flux surface in the neighborhood of the magnetic axis for which e = 1.4 and $\beta_\theta = 1.2$. The corresponding value of e_{cr} is approximately 1.5 using the results in Ref. 10. Therefore $e < e_{cr}$ and the plasma is stable with respect to vertical displacements.

The stability criteria D_I and D_R are given by the solid curve and dashed curve, respectively, in Fig. II-A-5. The values of D_I and D_R are negative implying that localized modes are stable. Negative values of D_R provide strong stabilization for the tearing mode. The surface ψ=-0.13 is a flux surface near the magnetic axis while ψ=-0.054 is the surface closest to the separatrix.

The critical β value estimated from Ref. 15 is 0.047 for an aspect ratio of 3, an elongation factor, e, of 2, and $\overline{\beta_\theta} = 1$. If we take q = 3.5 at the flux surface closest to the separatrix, we find

$$\beta = \left(\frac{S}{Aq}\right)^2 \overline{\beta_\theta} \simeq 0.032$$

for UWMAK-III and this is less than the critical β.

The toroidal field in the vacuum and in the plasma are shown by dashed and solid curves in the upper part of Fig. II-A-6. The diamagnetic effect is small, about 7%. The value of B_ϕ at the magnetic axis is reduced by 0.25 T. This means higher powers are needed when RF heating is used. As useful information for the RF heating studies discussed in section C of this chapter, we present in Fig. II-A-6 the resonance surfaces (i.e. the contours of constant $|B|$) as solid curves and the flux surfaces as dashed curves.

In summary, the UWMAK-III non-circular plasma shape is in stable equilibrium using discrete external coils and is bounded by a separatrix with two null points above and below the median plane. This design therefore yields the advantages of noncircularity without theoretically sacrificing stability.

II-A-15

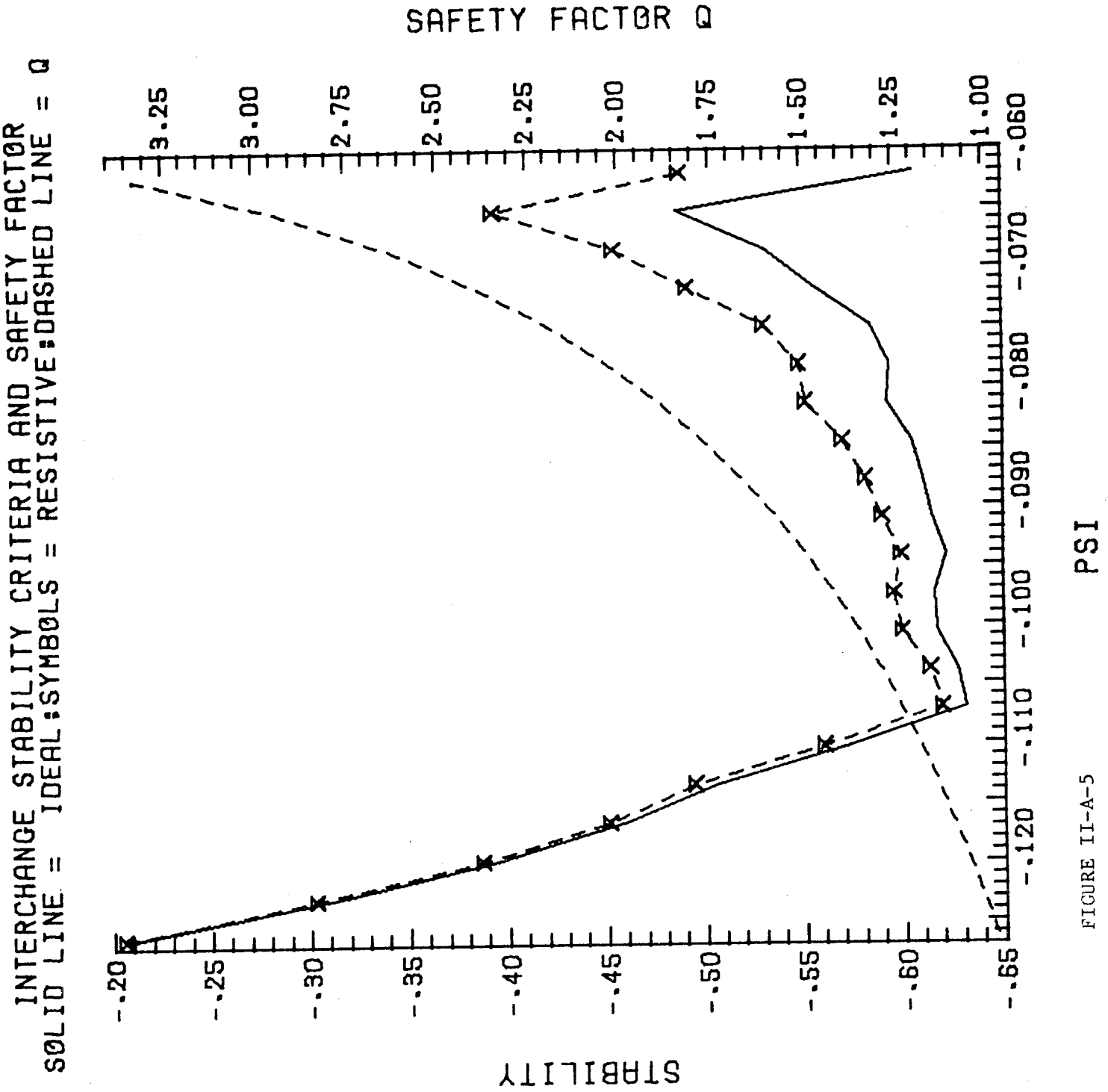

FIGURE II-A-5

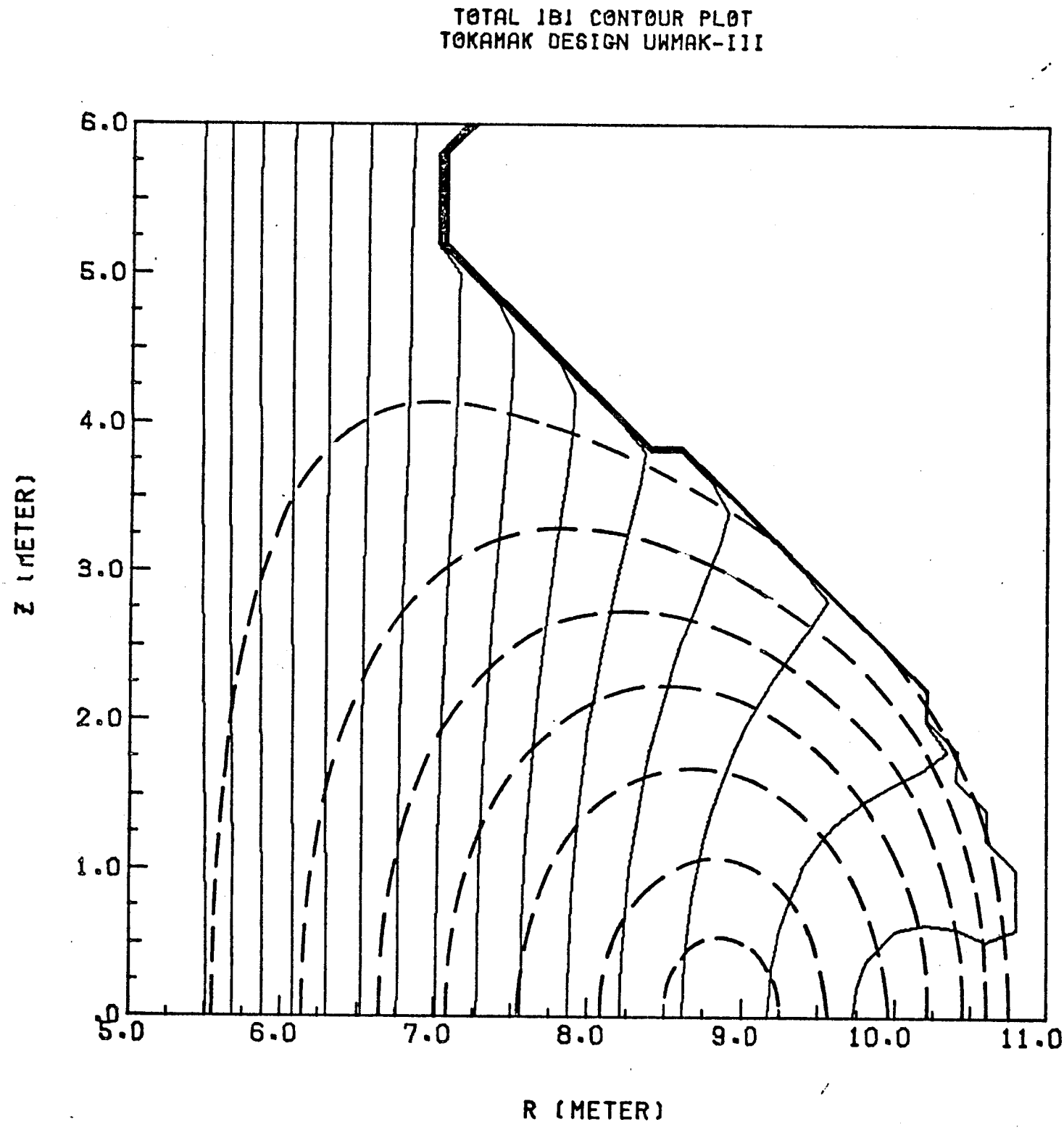
TOTAL |B| CONTOUR PLOT
TOKAMAK DESIGN UWMAK-III
6.0
5.0
4.0
3.0
2.0
1.0
0.0
Z (METER)
5.0
6.0
7.0
8.0
9.0
10.0
11.0
R (METER)

FIGURE II-A-6

References for Section II-A

1. Y. Suzuki, A. Kameayui, H. Ninomya, M. Masuzaki, and H. Toyama, Proc. 5th Conf. on Plasma Physics and Controlled Nuclear Fusion Research, (IAEA, Vienna, 1975) Vol. I, p. 411.

2. V. D. Shafranov, Review of Plasma Physics, (Consultants Bureau, New York, (1966), Vol. 2, p. 103.

3. John M. Greene, John L. Johnson, and Katherine Weimer, Phys. Fluids, Vol. 14, 671 (1971).

4. V. S. Mukhovatov, V. D. Shafranov, Nuclear Fusion 11, 605 (1971).

5. S. Yoshikawa, Phys. Fluids 7, 278 (1964).

6. M. S. Chance, R. L. Dewar, A. H. Glasser, J. M. Greene, R. C. Grimm, S. C. Jardin, J. L. Johnson, B. Rosen, G. W. Sheffield, and K. E. Weimer, Proc. 5th IAEA Conf. on Plasma Phys. and Cont. Nucl. Fus. Research, (IAEA, Vienna, 1975) Vol. I, p. 463.

7. Katherine Weimer, private communication.

8. L. E. Zakharov and V. D. Shafranov, Sov. Phys. Tech. Phys. 18, 151 (1973).

9. E. Rebhan, Nuclear Fusion, 15, 277 (1975).

10. M. D. Kruskal, J. L. Johnson, M. B. Gottlieb, and L. M. Goldman, Phys. Fluids, 1, 421 (1958).

11. V. D. Shafranov, Plasma Physics and the Problem of Controlled Thermonuclear Reactions, (Pergamon, Oxford, 1969), Vol. 2, p. 197.

12. J. L. Johnson, J. M. Greene, Plasma Physics 9, 611 (1967).

13. A. H. Glasser, J. M. Greene, J. L. Johnson, submitted to Physics of Fluids.

14. J. P. Freidberg, W. Grossmann, Los Alamos Scientific Laboratory Report, LA-UR-75-416 (1973).

15. R. C. Grimm, J. M. Greene, and J. L. Johnson, to be published in Computational Physics, Vol. 16.

16. K. E. Weimer, E. A. Frieman and J. L. Johnson, Plasma Phys. 17, 645 (1975).

II-B. Startup

The design of the transformer used to drive the plasma current during startup and burn is based on the same philosophy as set forth in previous reports.[1] The plasma is a single turn secondary of the air core coupled transformer. Startup flux necessary to bring the plasma to full current is provided by the divertor coils assisted by the transformer. At the end of startup the divertor currents remain fixed and the flux necessary for sustaining the plasma current during the burn is provided by the transformer, since the bootstrap current is not assumed to exist. Table II-B-1 outlines the full reactor cycle for UWMAK-III.

The locations of and relative currents carried in the transformer coils were determined using the same method as was used in our previous designs. However, instead of generating a flux surface by placing one filamentary loop at the major radius of the plasma magnetic axis, it was necessary to generate the flux line using several filaments placed in a vertical line located closer to the centerline; this was necessitated by the fact that the major radius has been reduced from earlier designs while the height of the TF coils has not been reduced significantly. Thus an almost vertical field line is necessary for determining surface currents (transformer currents). This flux line closes on itself at a very large major radius; the path length of the line is very large. Since mathematically one would like to distribute current uniformly over the entire line, termination of the transformer currents at a height of 20 meters from the midplane removes a very substantial part of the designed distribution. This in turn allows the leakage fields in the region of the plasma to be so high as to necessitate extra coils on the outside of the plasma ring whose function is to compensate for these leakage fields. Having generated a suitable flux line, surface currents were determined using

$$\Delta I = H \, \Delta S$$

where ΔS is a distance measured along the field line. Values of ΔI were then lumped into discrete currents which yield fixed ratios of the transformer currents to the current carried in the first coil T1.

During startup the plasma current is assumed to rise in a linear fashion following linear changes in the divertor and transformer currents. The startup period is taken to be 15 seconds. For this design the divertor currents will provide approximately 96% of the necessary startup flux, with the transformer providing the remaining amount. This is a significant reduction in transformer startup flux from previous designs because of the reduction of self-annihilation of divertor flux; i.e., better coupling of the poloidal field due to the divertor currents through the disk of radius R_o. A list of all transformer coils together with the currents in these coils are listed in Table II-B-2 and the location of OH and VF coils are shown in Fig. II-B-1. The total flux change required per cycle is 254 v-sec.; startup requires 147 v-sec and the burn requires 107 v-sec. The transformer produces 113 v-sec and the divertor produces the remainder.

To determine whether the plasma will act as an inductive or resistive load, estimate the self-inductance of the plasma by

$$L_p = \Phi_p / I_p \tag{1}$$

where Φ_p is the flux through the disk of radius R_o and I_p is the total plasma current. This gives

$$L_p \simeq 9.25 \times 10^{-6} \text{h}. \tag{2}$$

The voltage transient equation during startup and shutdown is

$$L_p \frac{dI_p}{dt} + R_p I_p = \text{Vexternal} \tag{3}$$

where

$$R_p = \frac{2\pi R_o}{\pi a^2} \eta \, . \tag{4}$$

The plasma is inductive if

$$R_p I_p << L_p \frac{dI_p}{dt} \tag{5}$$

For a 15 second startup and assuming a linear plasma current rise,

$$R_p << 6.17 \times 10^{-7} \text{ ohms},$$

so that

$$\eta << 5.52 \times 10^{-5} \text{ohms-cms},$$

or

$$T_e >> 125 \text{ eV}.$$

Joule heating is expected to attain this temperature within a second or two, so that the plasma can be considered as an inductive load during startup. The inductance is assumed to change very little during this time due to rapid soak of the poloidal field into the blanket.

Once transformer coil locations and relative magnitudes of currents were determined, placement of the compensating coils was determined to minimize the leakage field. This was done using an arbitrarily high normalization of the current in coil T_1.

The volt-second requirement for the burn phase was determined using the space-time plasma code described in Section II-D. The conductivity is determined by

$$\sigma = \sigma^*_{sp} \frac{\{1-0.95(\frac{r}{a}) + 1.95 (\frac{r}{a})^{1/2}\}}{1 + \nu_{eff}/\omega_{be}} \quad (6)$$

where σ^*_{sp} is the Spitzer conductivity corrected for Z_{eff}; ν_{eff} is the effective collision frequency; and ω_{be} is the electron bounce frequency. From this and the plasma current profile, the voltage drop, averaged over the plasma cross section, was determined to be 0.059 volts. This gives 107.1 volts-seconds to be provided by the transformer during the burn.

Based on maximum power limitations, the times required for shutdown and recharging, or recocking, the transformer to its initial value have been reduced to 20 seconds each. Allowing for 15 seconds of RF heating and 50 seconds for pumpout and refill of the chamber (which includes the 20 second recock time), we were able to reduce total down time to 100 seconds. For a fixed duty factor of 94.74%, this allowed a reduction of the burn necessary from 90 minutes to 30 minutes. This will have a beneficial effect in terms of the plant thermal inertia.

The periods for pumpout and recocking the transformer have been combined in this design to reduce the plant down time. At the beginning of the pumpout phase, hydrogen gas is injected into the chamber to cool the plasma. The density of hydrogen at this time is approximately 3.54×10^{14} molecules/cm^3, corresponding to 10^{-2}torr. The electron impact ionization cross section at 20 eV is about 3×10^{-17}cm^2. This gives a mean free path of approximately 95 cm. The electric field set up during the 20 second recock time will be approximately 1 mV/cm.

The average energy of an electron, accelerated by this field for 100 cm is on the order of 0.1 volts, far below threshold energy for ionization. However, as the hydrogen gas is pumped out, the mean free path is longer and it is assumed that at the minimum pressure of 10^{-8} torr, all the remaining hydrogen will be ionized. Assume that the divertor currents, which at this time are normally at zero, are turned on to a level sufficient to divert the particles to the wall after an average of one circuit around the torus. The density of hydrogen at a pressure of 10^{-8} torr is approximately 3.54×10^8 per cm^3. After one circuit around the torus, a proton will have about 5 eV energy, giving an approximate total energy content of .75 Joule. The energy flux to the wall under these conditions is negligible.

The programming of each of the transformer coils is similar to that of coil T1 which is shown in Fig. II-B-2, along with the plasma current wave form. Shown in Fig. II-B-3 is the power requirement during the cycle, and in Fig. II-B-4, the energy stored in the poloidal magnetic fields of the plasma, divertor, and transformer currents. With this system we propose to take 500 MW off the grid during the startup phase. The other 413 MW (peak) is

provided from a separate energy storage unit. This unit is recharged during the rest of the cycle. The other large power demand of the system is the RF heating power which is required after the startup phase so that it will not be additive to the 913 MW peak load.

References for Section II-B

1. B. Badger et al., "UWMAK-I, A Wisconsin Toroidal Fusion Reactor Design," UWFDM-68, Vol. I, and "UWMAK-II, A conceptual Tokamak Reactor Design,"UWFDM-112 Dept. of Nuclear Engin. Univ. of Wis.

Table II-B-1

UWMAK - III REACTOR CYCLE

Time(Sec).	Phase
0-15	Startup: Plasma and divertor currents rise to full value; transformer currents begin to drop.
15-30	RF Heating: Plasma and divertor currents at full value; transformer currents continue to drop.
30-1830	Burn: Transformer currents drop to maximum negative value.
1830-1850	Shutdown: Plasma and divertor currents drop to zero; transformer currents rise to provide negative startup flux.
1850-1890	Pumpout and recharge: First 20 seconds, hydrogen gas pumped into cool plasma, residual gas pumped out. Final 20 seconds; transformer currents reset to initial values.
1890-1900	Final pumpout and refill: Chamber purged and refilled with fresh fuel.

Table II-B-2

TRANSFORMER PROGRAMMING

(All Currents in MA)

Coil Number	R(m)	±Z(m)*	Initial Current	Current -End of Startup	Current -End of Plasma Burn
T1	2.502	1.0	4.0528	3.5463	-5.1528
T2	2.508	3.0	4.0376	3.5330	-5.1336
T3	2.522	5.0	3.9900	3.4901	-5.0956
T4	2.546	7.0	3.9168	3.4273	-4.9798
T5	2.591	9.0	3.8034	3.3281	-4.8356
T6	2.675	10.997	3.5917	3.1428	-4.5665
T7	2.854	12.989	3.2211	2.8185	-4.0953
T8	3.227	14.950	2.5632	2.2429	-3.2590
T9	3.857	16.844	1.7693	1.5482	-2.2497
T10	4.725	18.643	1.1418	0.9991	-1.4516
T11	5.489	19.932	0.4159	0.3639	-0.5287
T12	19.0	5.0	0.1588	0.1390	-0.2019
T13	9.0	10.5	0.1512	0.1323	-0.1923

Divertor

Coil Number	R	±Z(m)*	I(MA)
D0	6.8	9.0	15.50
D1	3.9	0.0	.40
D2	3.9	1.0	.40
D3	4.0	4.5	2.00
D4	4.6	5.5	-0.60
D5	3.9	9.0	-1.20
D6	5.9	9.5	-2.20
D7	6.8	13.0	-1.30
D8	8.3	11.7	-4.30
D9	8.5	9.9	-3.00
D10	8.8	10.0	-1.53
D11	8.8	9.3	-1.65
D12	8.8	9.9	-1.10
D13	8.9	7.7	-1.60
D14	9.3	7.5	-1.62
D15	10.8	7.3	-1.55
D16	11.8	6.8	-1.60
D17	12.8	5.3	-1.65
D18	13.0	4.3	-1.65
D19	13.5	2.3	-1.52
D20	13.5	0.0	-1.52

*For each coil at location (R,Z), there is a similar coil at (R-Z) for Z = 0.

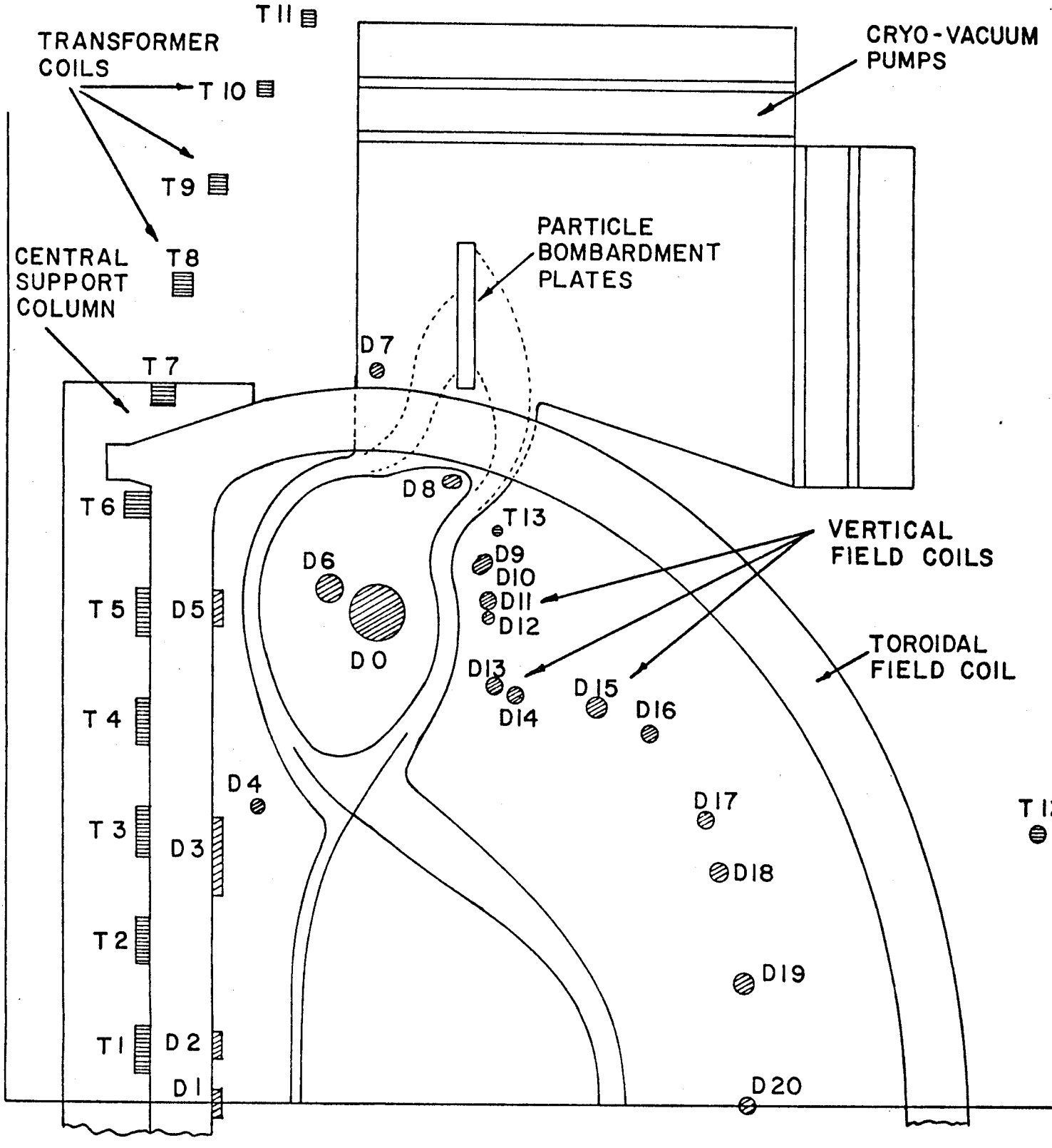

FIGURE II-B-1

UWMAK-III Divertor and Transformer Coils

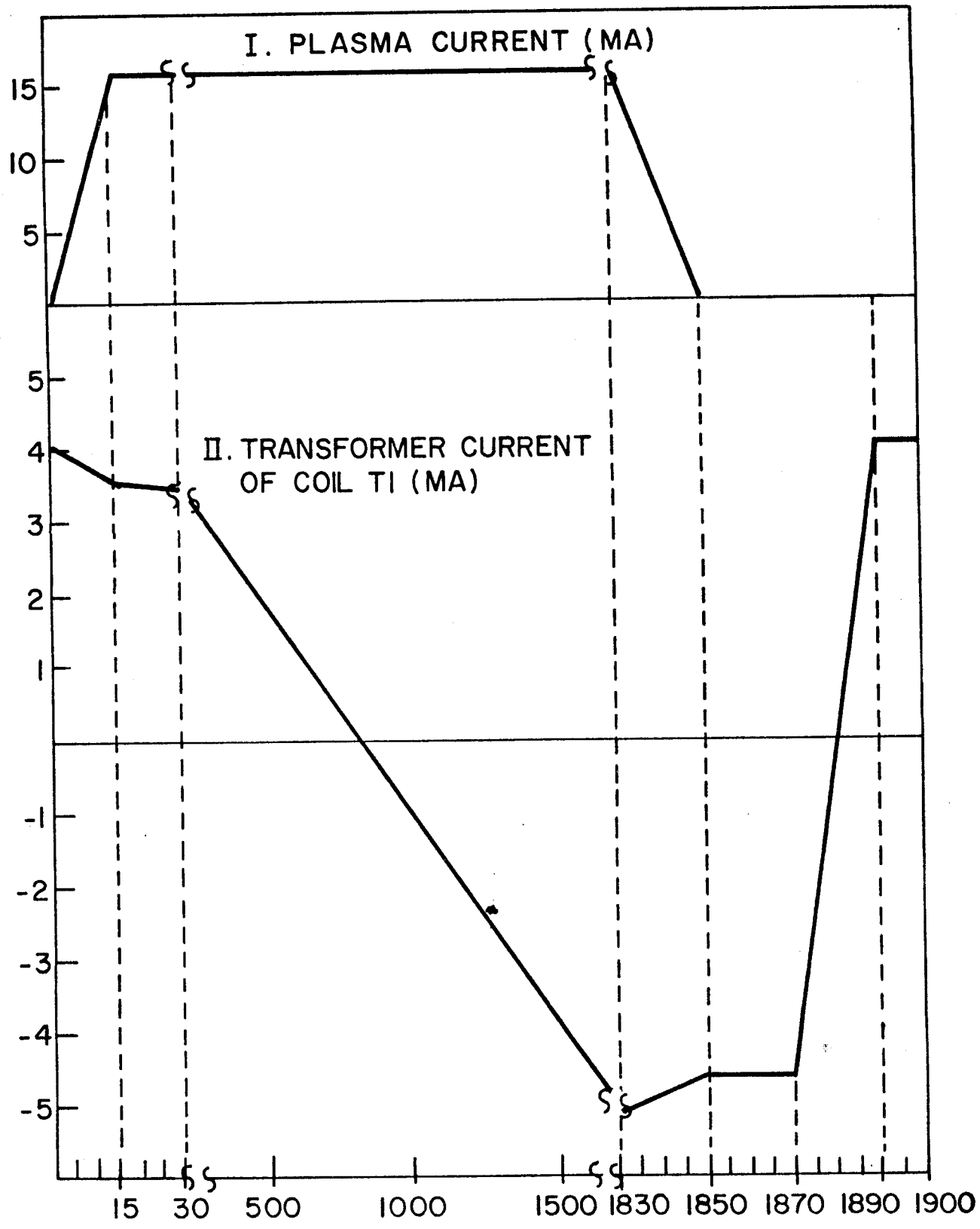
I. PLASMA CURRENT (MA)
15
10
5
5
4
3
2
1
II. TRANSFORMER CURRENT
OF COIL TI (MA)
-1
-2
-3
-4
-5
15
30
500
1000
1500
1830
1850
1870
1890
1900
TIME (SEC)

FIG. II-B-2

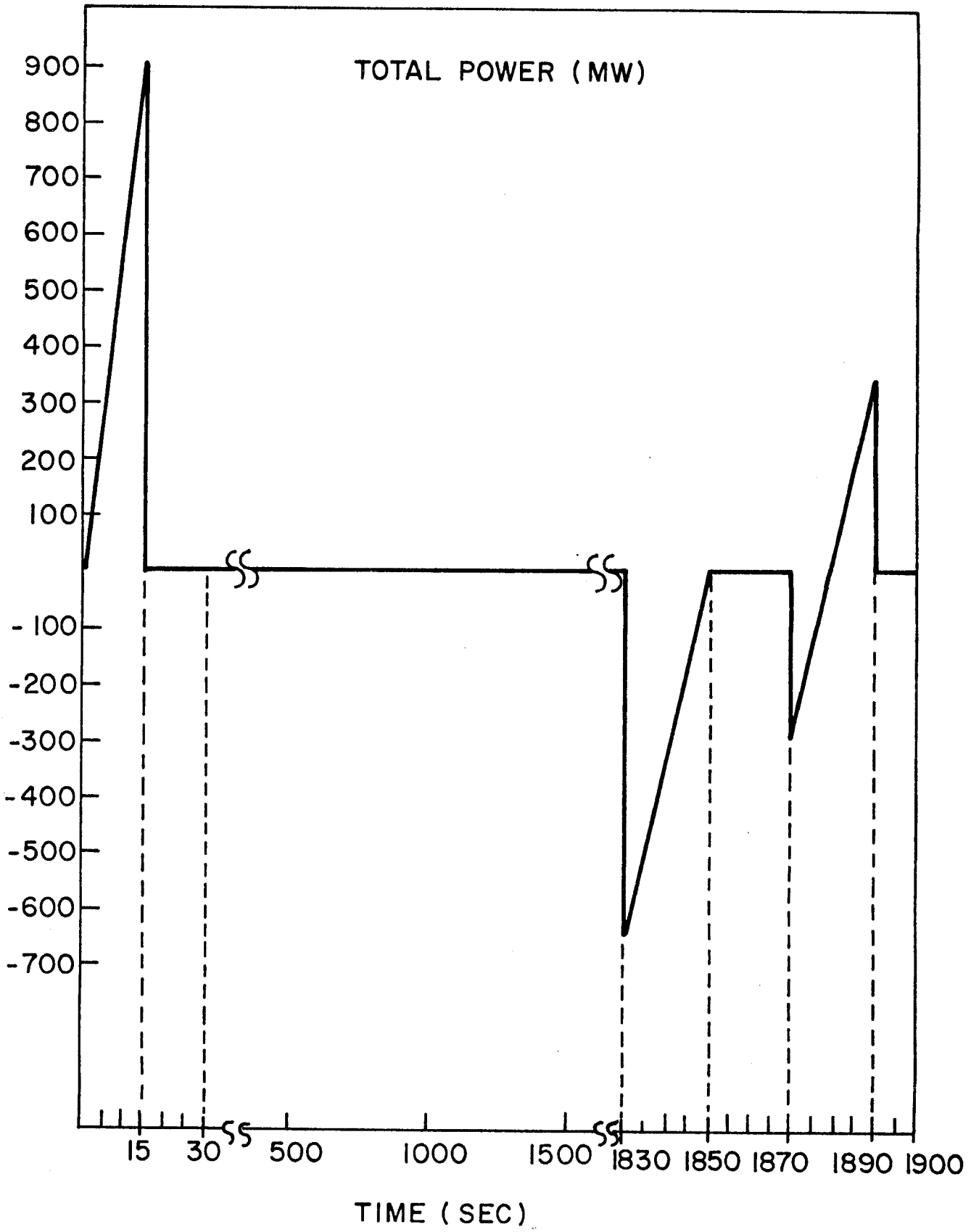
TOTAL POWER (MW)
900
800
700
600
500
400
300
200
100
-100
-200
-300
-400
-500
-600
-700
15
30
500
1000
1500
1830
1850
1870
1890
1900
TIME (SEC)

FIG. II-B-3

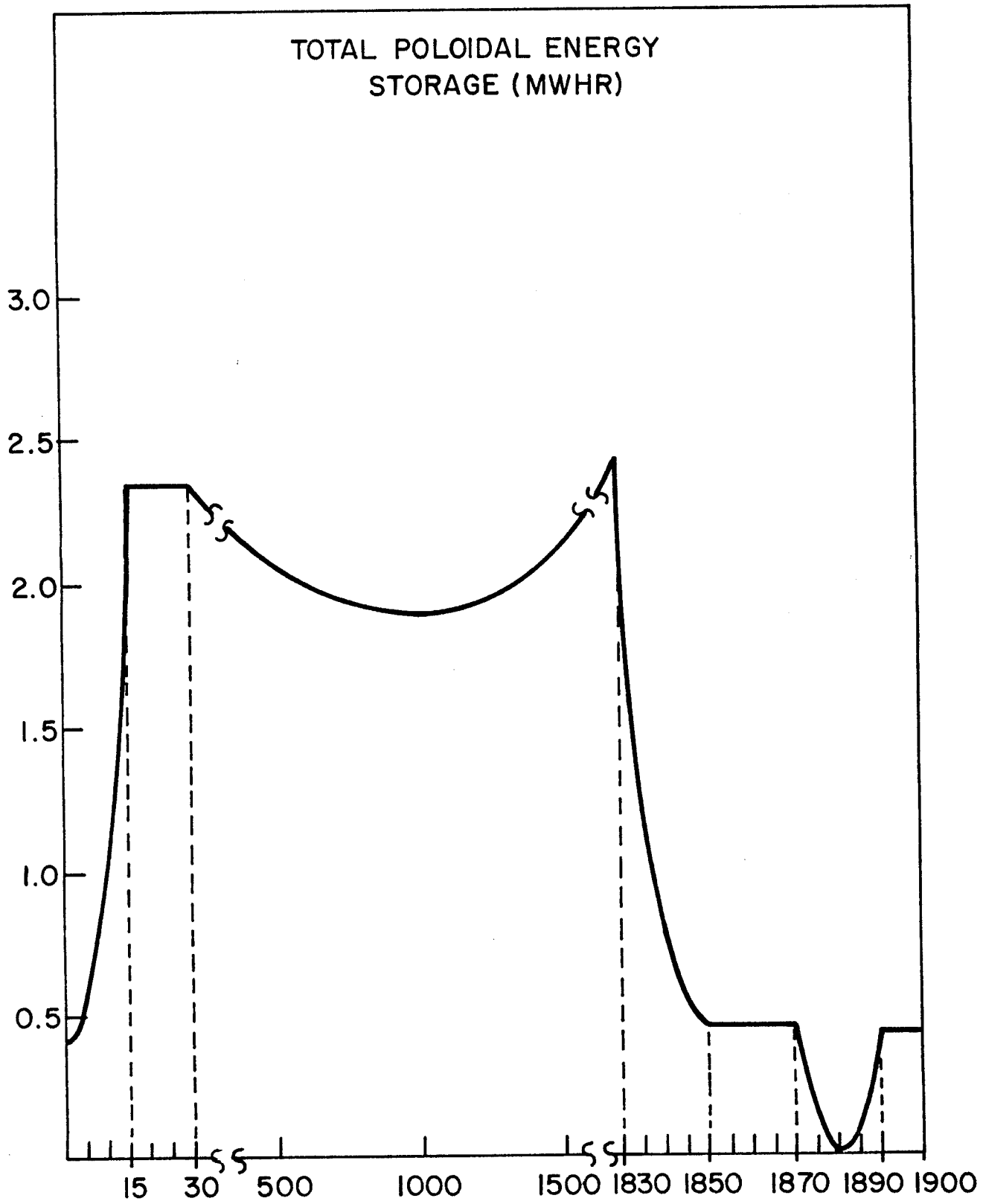
TOTAL POLOIDAL ENERGY
STORAGE (MWHR)
3.0
2.5
2.0
1.5
1.0
0.5
15
30
500
1000
1500
1830
1850
1870
1890
1900
TIME (SEC)

FIG. II-B-4

II-C. The RF Supplementary Heating System in UWMAK-III

II-C-1. Introduction to Magnetosonic Wave Heating in Tokamaks

Several supplementary RF heating wave modes are currently being considered to ignite a tokamak reactor. They are (1) fast magnetosonic waves at $\omega = 2\omega_{cD}$, $\omega = \omega_{cD}$ (ω_{cD} is the deuteron ion cyclotron frequency) and the two-ion hybrid resonance $\omega = \omega_{2IHR}$ (2) lower hybrid waves at $\omega \approx \omega_{pi}$, and (3) low frequency Alfvén waves $\omega << \omega_{cD}$. Because of the potential for generation of large amounts of RF power, accessibility of the wave and energy deposition in the plasma core, and direct heating of the ions, we have decided to concentrate on the fast magnetosonic wave. Earlier theoretical works by Adam and Samain[1], Perkins[2], and Weynants[3] have presented the basic wave propagation properties and absorption mechanisms. The operative absorption mechanisms are cyclotron harmonic damping of the wave by the ions and electron Landau and transit-time damping of the wave by the electrons. Stix[4] has shown that, for TFTR parameters, when cross terms in the dielectric tensor are included in the electron damping calculation, the net electron damping is Landau damping and has a value which is half that for the transit time term considered separately. We have found from computational studies that this is generally the case for reactor oriented machines.

We now present a brief derivation of the fast magnetosonic wave hot plasma dispersion relation. Assuming an $e^{-i\omega t + i\bar{k}\cdot\bar{r}}$ Fourier component of wave quantities, the wave equation is obtained as $\bar{k} \times (\bar{k} \times \bar{E}) + (\omega/c)^2 \bar{\bar{K}} \cdot E = 0$ where $\bar{\bar{K}}$ is the dielectric tensor as defined in Stix.[5] By noting that in the magnetosonic regime the Bessel function argument $\lambda_j = k_\perp^2 \rho_j^2/2$ is small for both ion and electron terms, one can obtain a tractable dispersion relation in which first-order finite gyroradius effects are included by expanding to first order in λ_j. Further, the K_{zz} component of the dielectric tensor is so large compared to other elements involving the z component that the dispersion relation can be obtained to a very good approximation by expanding the 2 x 2 minor of the K_{zz} component. The dispersion relation then becomes ($k_\perp = k_x$, $k_\parallel = k_z$) to the fourth order in $k_\perp$

$$\begin{vmatrix} (\omega/c)^2 K_{xx} - k_\parallel^2 & (\omega/c)^2 K_{xy} \\ (\omega/c)^2 K_{yx} & (\omega/c)^2 K_{yy} - k_\parallel^2 - k_\perp^2 \end{vmatrix} = 0 \qquad (1)$$

where

$$K_{xx} = 1 + \sum_{\alpha=i,e} (\omega_{p\alpha}^2/2\omega k_\parallel v_\alpha)(Z_1^\alpha + Z_{-1}^\alpha) - k_\perp^2 \sum_{\alpha=i,e} (\omega_{p\alpha}^2 v_\alpha/4\omega k_\parallel \Omega_\alpha^2)(Z_1^\alpha + Z_{-1}^\alpha - Z_2^\alpha - Z_{-2}^\alpha),$$

$$K_{yy} = K_{xx} + k_\perp^2 \sum_{\alpha=i,e} (\omega_{p\alpha}^2 v_\alpha/\omega k_\parallel \Omega_\alpha^2)\left[Z_0^\alpha - 1/2(Z_1^\alpha + Z_{-1}^\alpha)\right],$$

$$K_{xy} = -K_{yx} = -i \sum_{\alpha=i,e} (\omega_{p\alpha}^2/2\omega k_\parallel v_\alpha)(Z_1^\alpha - Z_{-1}^\alpha) + ik_\perp^2 \sum_{\alpha=i,e} (\omega_{p\alpha}^2 v_\alpha/4\omega k_\parallel \Omega_\alpha^2)(2Z_1^\alpha - 2Z_{-1}^\alpha - Z_2^\alpha + Z_{-2}^\alpha)$$

and Z_ℓ^α denotes the Fried and Conte Plasma dispersion function $Z((\omega + \ell\Omega_\alpha)/k_{||}v_\alpha)$. The dispersion relation then includes wave absorption due to finite ion gyro-radius effects, cyclotron damping, and electron transit-time damping (a factor of 2 greater than the resulting Landau damping obtained from the 3 x 3 dispersion relation).

The power absorbed by the ions and electrons per unit volume can be obtained in the weak damping limit in a manner following Stix[4] as $p = \omega\bar{E}^* \cdot (\bar{\bar{K}}^a \cdot \bar{E})/2 (\text{watt/cm}^3)$ where $\bar{\bar{K}}^a$ is the anti-Hermitian part of the dielectric tensor. The finite ion gyroradius damping term becomes

$$p_i = \pi^{1/2}\varepsilon_o\omega_{pi}^2(\text{Re}\lambda_i)^{\ell-1}|E_+|^2 e^{-((\omega - \ell\omega_{ci})/k_{||} v_i)^2/4k_{||} v_i} \qquad (2)$$

and the electron Landau damping term can be written

$$p_e = \pi^{1/2}\varepsilon_o(\omega_{pe}/\omega_{ce})^2 k_\perp^2 |E_y|^2 v_e e^{-(\omega/k_{||} v_e)^2/4k_{||}} \qquad (3)$$

In the above equations, ℓ is the harmonic number $\omega = \ell\omega_{ci}$, E_+ is the left hand circularly polarized electric field component rotating in the sense of the ions, and E_y is the rectangular component of the electric field. $|E_+| = |1-\chi||E_y|$, where $\chi = iE_x/E_y$ is the polarization factor.

The ion cyclotron harmonic absorption term occurs in a region of finite width in the tokamak minor cross section due to the thermal effects and the 1/R variation of the toroidal magnetic field. For the second harmonic, this width is $\Delta = k_{||} v_i R/\omega_{ci}$. It is further assumed that the energy deposited in the slab is uniformly distributed over the circular flux surface intersecting the radial element on the slab due to the rotational transform. After making this calculation, one can obtain the variation of the ion heating profile with plasma radius as

$$\langle p_i \rangle = \varepsilon_o(\omega_{pi}^2/\omega_{ci})(R/r)\ \text{Re}(\lambda_i)^{\ell-1}|E_+|^2/4\ell \qquad (4)$$

where the brackets indicate that it has been averaged over the flux surface. Note that this provides strong peaking of the energy deposition to the ions at the plasma core. By integration over the tokamak cross section these equations are adapted to a time-dependent model for the startup calculation in UWMAK-III.

The last point is the existence of toroidal eigenmodes for the tokamak as predicted by Adam and observed experimentally on ST.[6] These modes are beneficial in that they enhance the plasma loading of the wave launching structure and allow efficient heating of the plasma. Indeed, in smaller devices such as ST, the eigenmodes are well separated but for large reactor

machines such as UWMAK-III the density of toroidal eigenmodes in the frequency domain becomes a near continuum. Stix,[4] Swanson and Ngan[7] and Scharer et al.[8] have indicated that when toroidal, poloidal, and radial eigenvalues are varied, the spacing between modes may be as small as one part in 60,000 of the magnetosonic wave frequency. This means that eigenmodes will always be available to heat the plasma but the cumulative effect of all excited modes on the loading of the launching structure and heating efficiency is a subject which will require much further study before a conclusion can be reached. Swanson and Ngan[7] have indicated that the overlapping density of eigenmodes enhances the mode conversion to ion Bernstein modes but Scharer et al.[8] have shown that the introduction of large $k_{//}$ in the wave can minimize this effect. Thus, the heating rates used in this startup calculation might be considered as a simplistic model with wave penetration due to plasma profile effects at the edge, the influence of the dense eigenmode structure and the resultant velocity distributions of heated particles on the net heating rates subjects of further investigation.

II-C-2. Reactor Startup Utilizing Supplementary Fast Magnetosonic Wave Heating

We now adapt the heating equations from the previous section to a time dependent model of heating at the second harmonic of the deuteron ion cyclotron frequency. For the ions we assume a parabolic density and temperature profile given by

$$n_i = 2n_o(1-(r/a)^2) \text{ and } T_i = 2T_o(1-(r/a)^2)$$

where a is the plasma radius. By integrating eq. (4) over the plasma volume we can determine the power delivered to the ions as

$$P_{ti} = \int \langle p_i \rangle r \, dr \, d\theta \, dz$$

$$P_{ti} = \frac{((4.84\times10^{-11})n_o R^2 T_o a|E_+|^2}{B_o^3} \quad \text{watts}$$

where B_o is in Gauss, T_o in keV, n_o in cm^{-3} and $|E_+|$ in V/m which is assumed uniform over the cross section.

For the electron heating we assume a density and temperature profile for the ions as given above and for the electrons given by

$$n_e = 2n_1(1 - (r/a)^2) \text{ and } T_e = 2T_1 (1 - (r/a)^2).$$

The electric field polarization is related by

$$E_y = E_+(1 + 6.94 \times 10^{-23} n_i^2 T_e B_o^{-2})$$

where T_e is measured in keV, n_i in cm^{-3} and B_o in Gauss.

The electron power absorption per unit volume becomes

$$p_e = (8\, n_o n_i e^2\, |E_+|^2/\varepsilon_o B_o^2 M c^2 k_{||})(\pi m \kappa T_1)^{1/2} \exp\left[\frac{-2\, e^2 B_o^2 m}{k_{||}^2 \kappa T_e M^2}\right] x$$

$$\left[(1-r^2/a^2)^{5/2} + \frac{5.53\times10^{-19}(1-(r/a)^2) n_o^2 T_o}{B_o^2}\right] \text{ (watts/cm}^3\text{)}. \qquad (5)$$

We then integrate this over the plasma volume, inserting the average electron temperature over the cross section in the exponential Landau term and obtain

$$P_{te} = 3.28\times10^{-26} n_o n_1 |E_+|^2\, T_1^{1/2} \exp[-6.64\times10^{-9} B_o^2 T_1^{-1}] R a^2 B_o^{-2} \quad x$$

$$\left[\frac{1}{7} + \frac{5.53\times10^{-19} n_o^2 T_o}{13\, B_o^2}\right] \text{ watts} \qquad (6)$$

where R and a are measured in cm.

At the end of the 15 sec ohmic heating phase, the electrons and ions reach a temperature of 1.8 keV. During this phase, the neutral and charged particle flux to the wall is considerable. The waveguide feeds could be protected from the plasma when the RF heating is shut off by a 1 m movable blanket. At the end of the ohmic heating cycle, the magnetosonic wave heating is turned on. We first consider a constant injected power of 40 MW, most of which is deposited with the ions. Fig. II-C-1 illustrates the ion and electron temperatures during the startup cycle using the global energy balance model described in section II-A. After 8 seconds the plasma reaches ignition and if the injected power is left on for 12 secs, the plasma reaches the equilibrium temperature of T_i = 19 keV and T_e = 23 keV in 15 secs.

As an alternative case, we consider a constant heating power of 200 MW. Fig. II-C-2 shows that ignition is reached after 1.32 secs and the magnetosonic wave heating is turned off after 1.36 sec. In this case, the ions are driven to a temperature 450 eV greater than that of the electrons during the magnetosonic wave heating phase. It can be seen that the ions begin to cool after extinguishing the supplementary heating but the alpha heating contribution is larger than the loss terms so that the plasma continues to heat and reaches equilibrium in 15 secs. In this case, it is important that the ions are heated sufficiently greater than the electrons so that during the drop in ion temperature, the plasma continues to heat and reach reactor equilibrium.

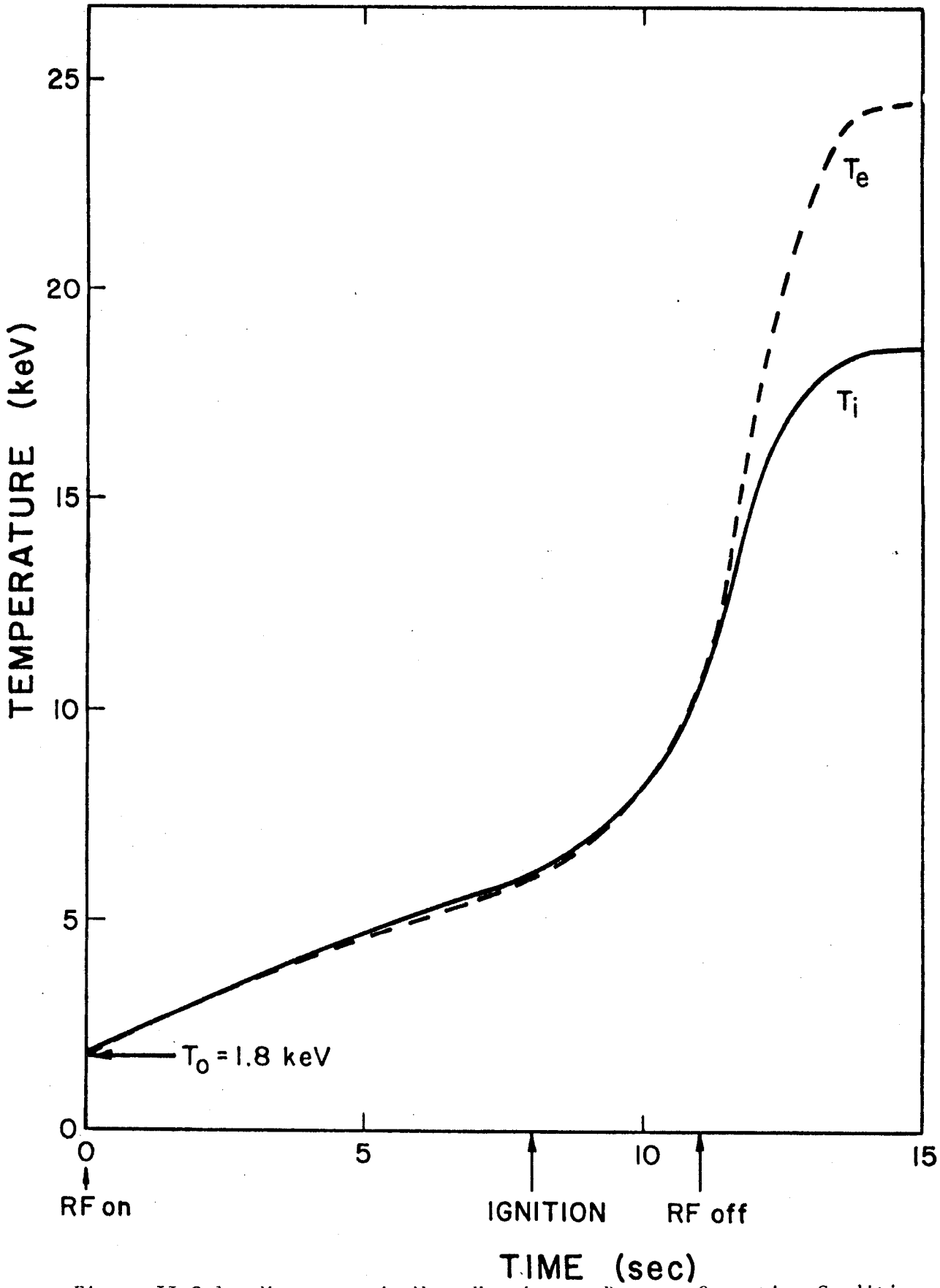

Figure II-C-1 - Magnetosonic Wave Heating to Reactor Operating Conditions
P_{RF} = 40 MW

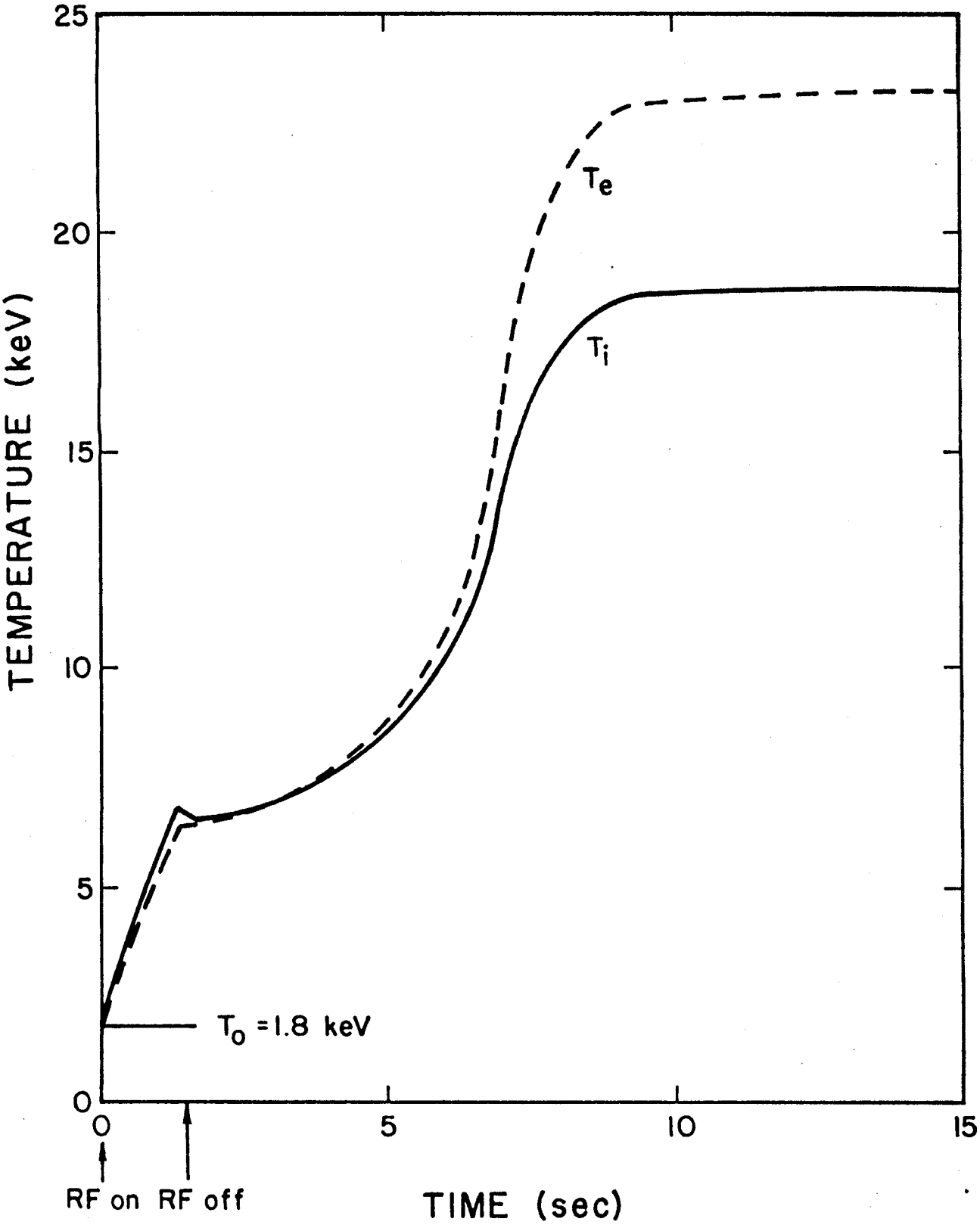

Figure II-C-2 - Magnetosonic Wave Heating to Reactor Operating Conditions
P_{RF} = 200 MW

In both cases, the net energy given to the plasma by the magnetosonic wave heating system is within a factor of 2. Even though the ions absorb most of the heating power, the ion-electron equilibration time is sufficiently short so that the electron temperature follows the ion temperature to ignition. Only if there is a mechanism which destroys the ion heating by the electrons would it be necessary to consider plasma heating, which deposits its energy within the ions, with the present trapped particle scaling laws.

II-C-3. Conceptual Magnetosonic Wave Launching System

In order to heat the plasma by fast magnetosonic wave eigenmodes, a suitable launching structure located in the torus wall must be devised. It must be capable of handling 200 MW of power at 60 MHz for a startup period of 15 seconds. It must have the property that the RF fields excited have a toroidal magnetic field with an orthogonal electric field as shown in Fig. II-C-3a. It must also excite desirable modes which lead to energy deposition near the plasma core. An ideal system would have a spectrum which excites lower order poloidal m values since higher order m values cause the finite ion gyroradius heating to peak further towards the plasma edge, leading to edge heating rather than core heating. In order to excite only low m numbers, the source distribution would have to cover most of the poloidal circumference. A further problem is caused by the fact that for large tokamaks such as UWMAK-III, the minor circumference is large compared to a free space wave length $2\pi a > \lambda_o$. This introduces phase shifts of a wave traveling in the poloidal direction which contribute to a higher order poloidal spectrum and reduced efficiency. A possibility for overcoming this is to introduce external circuit phase shifts which correct for the natural phase shift of the wave as it travels in the poloidal sense.

A further possible plasma consideration in the design of the launching system is the fact that many eigenmodes can be excited at a given frequency. Weynants[9] and Swanson and Ngan[7] have indicated that magnetosonic wave modes propagating towards the core from the high field region can undergo mode conversion to the ion Bernstein mode which could lead to electron heating or reflected power from the plasma back towards the source. Scharer et al.[8] have shown that the region of confluence between the fast magnetosonic mode and the ion Bernstein mode can be made very small by the excitation of modes with $k_{||}$ sufficiently large compared to the free space wavenumber k_o. This can minimize the mode conversion from the magnetosonic wave. Further, as shown in eqn. (5), the relative amount of electron Landau damping obtained by the magnetosonic mode can be increased by making $\omega/k_{||} v_e \sim 1$. Thus, if startup requires a more detailed consideration of the wave modes' initial deposition of energy to the ions and electrons, the potential of varying the wavenumber parallel to the magnetic field provides a possibility for tuning the relative energy deposition to ions and electrons. A drawback of the higher $k_{||}$ excitation spectrum is that the field intensity between the torus wall and plasma edge will be evanescent causing a reduction in heating efficiency. Cato et al.[10] have considered a poloidal hoop to excite RF fields in a tokamak reactor. The hoop would have to be made from a series of short sections driven to provide uniform phase excitation in the poloidal sense as shown in Fig. II-C-3c. The main problems that have to be worked out are the impurity contribution caused by its proximity to the discharge and the required coaxial insulators.

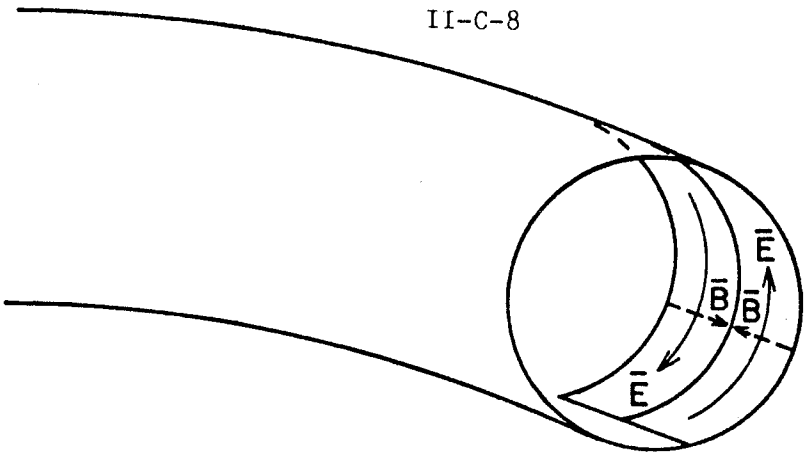

a) IDEALIZED MAGNETOSONIC WAVE FIELD SOURCE DISTRIBUTION:
$k_{||}$ = 6-10 m^{-1} AND DOMINANT $m = 0, \pm 1, \pm 2$ EXCITATION

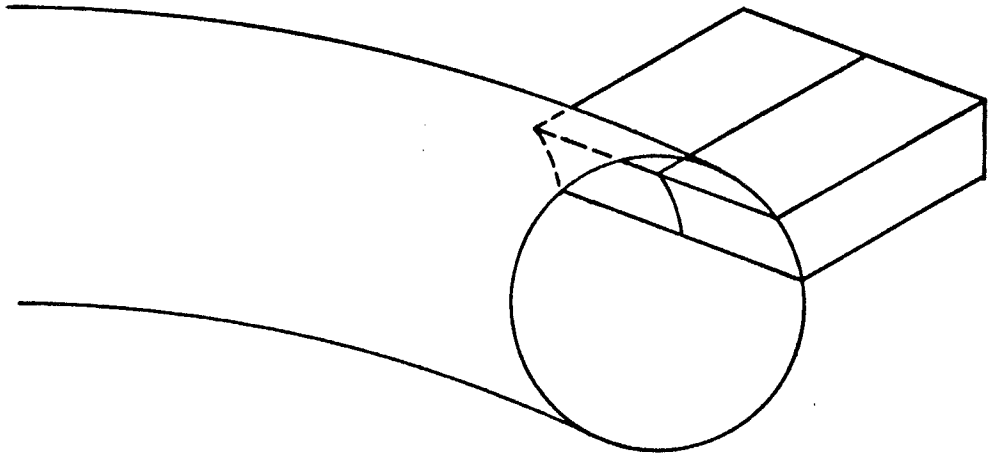

b) EXCITATION BY MEANS OF STANDARD WAVEGUIDES

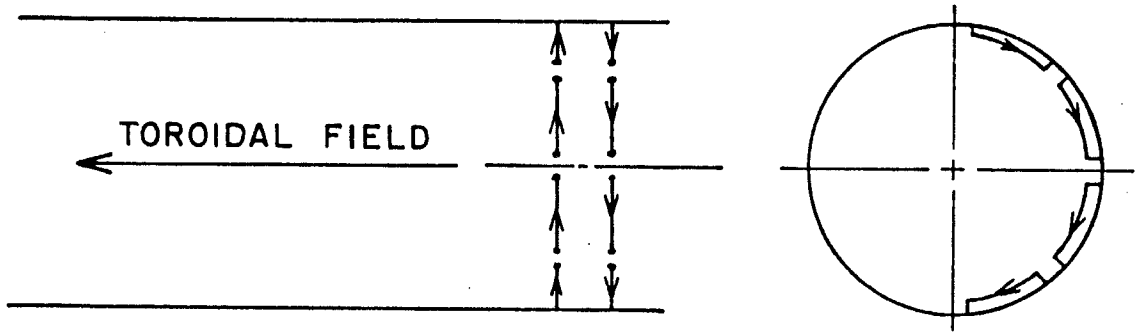

c) HOOP EXCITATION

Figure II-C-3 - Considerations for Magnetosonic Wave Heating Launching Structure

A standard rectangular waveguide launcher flush mounted in the wall as shown in Fig.II-C-3b introduces new spectral excitation problems since its toroidal dimension must be larger than half a free space wavelength for propagation of the dominant TE_{10} mode. As noted in the later sections, this can be overcome by using an array of smaller waveguides, possibly filled with high dielectric ceramic which reduces the dimension of the guide and excites larger $k_{\parallel}$ values. If a small excursion of conducting material into the torus can be tolerated, a strip line located over ceramic dielectric inside a rectangular guide could be envisioned which does not have a cut-off limitation due to small aperture size. The conducting strip would have to be coupled to the torus by making a small loop which is electrically connected to the bottom of the guide.

The constraints on the design of the RF power system are as follows: It is assumed that up to 200 MW are provided by as many as twelve separate feed systems with a minimum capability of 17 MW/feed. These feeds are placed in pairs located toroidally around the device. A single unit is shown in Fig. I-2 of the overview. This puts a constraint on the minimum cross-sectional area of the feed so that the field strengths remain below the breakdown level. While the magnitude of electric field strengths for 60 MHz breakdown in a tokamak environment are not precisely known, several estimates are indicated in the literature. Hooke et al. have indicated privately that a 25 MHz, 10 kV/cm RF field on ST did not give rise to breakdown while Weynants[9] assumes a maximum field strength of 30 V/cm in the plasma in his magnetosonic wave heating calculations. In UWMAK-III, we adopt the criteria that the RF field be held to a maximum of 3 kV/cm in the RF feeds during startup. It would be preferable if the startup neutral pressure outside the plasma confinement region was below 10^{-5} Torr, but 10^{-4} Torr is all that can be accommodated given the large device size, pumping capacity and limited pumping area.

A further condition that will require considerable theoretical and experimental effort is the plasma loading impedance on the launching structure. Of particular interest is the effect of a near continuum of eigenmodes excited at different levels on the input impedance. A simplified model indicates that the input resistance related to absorption mechanisms for the modes will effectively be in parallel, indicating a low value for the resistive part of the input impedance. If the wave impedance of the RF feeds is low, this will allow a more easily obtained match for the supplementary heating system to the plasma. Both ridged waveguide and dielectric filling contribute to a reduction in the wave impedance in the RF feed system.

Another aspect of the generation of 60 MHz RF power at 10 MW levels is the necessary development. A small to moderate development would be required to advance the state of RF generation from current 1 MW CW levels/tube to 10 MW levels. Other problems would involve details of the matching and feed design that could be incorporated in the UWMAK-III configuration.

The design of the waveguide feed is obtained subject to the following conditions: (1) each element of the launching structure must be capable of supplying 17 MW of power with a maximum electric field strength of 3 kV/cm. (2) The ratio of wave frequency to cutoff frequency of the feed must be greater than 1.2 in order that the attenuation in the guide due to skin effect is not too large. If we require that the feed be a vacuum region then one can consider

two types. In all cases due to a lower cost of fabrication, it is advisable to consider a copper coaxial line running most of the distance from the RF source to the torus with a 1 m diameter. A coaxial to waveguide transition could be made near the torus wall.

If the neutron and plasma flux to the launching aperture during startup dictate a vacuum filled waveguide, the following designs can be considered. A rectangular guide with a ratio of wave frequency to cutoff frequency of $f/f_c = 1.2$ for the TE_{10} mode. This would require a toroidal inner dimension of 3 m and a poloidal dimension of 1.5 m as shown in Fig. II-C-4. A waveguide of this size with the imposed maximum field intensity of 3 kV/cm would have a theoretical power injection energy capability of 500 MW and a wave impedance of 190 ohms. In order to reduce the toroidal extent of the guide for improved wave penetration and heating, a ridged waveguide[11] can be considered. This reduces the mode conversion potential and provides a means of determining the fraction of wave power initially deposited in the ions vs the electrons. The H-shaped guide would have the inner dimensions of 1 m high by 1 m wide with a gap width of 8.7 cm which is 50 cm in extent as shown in Fig.II-C-4. The wave impedance of the dominant TE_{10} mode is 70 ohms and the theoretical power carrying capability is 30 MW.

If neutron and plasma heating of the guide aperture during startup are not too severe, a guide which is partially or fully filled with a dielectric medium can be considered. Alumina ceramic (Al_2O_3) has a relative dielectric constant of $\varepsilon_r = 8$, a loss tangent of 10^{-4}, and a maximum temperature of operation of 1500-1900°C. A ridged waveguide which is filled with ceramic 50 cm wide by 50 cm high with a 10 cm gap can be designed as shown on Fig. II-C-4. The wave impedance is 40 ohms and a theoretical power transfer of 60 MW can be obtained.

II-C-4. Discussion

It is evident from the previous discussion that several alternatives for the design of magnetosonic wave launching structures exist. Much further analytical work in relating a given wave source distribution on the torus wall to the heating deposition profiles in the plasma is required. However, with the analysis that has been done to date we put forth a recommendation.

From the plasma point of view, we propose a wave source distribution that goes half way around the minor cross section on the outside edge. A second source located very close to the first but shifted in phase by 180° is proposed in order to set up short wavelengths $\lambda \sim 1$ m in the toroidal sense.

From a materials point of view under reactor conditions, we choose a vacuum-filled flush mounted waveguide array due to the absence of insulator material exposed to the neutron flux, structural rigidity, and relative remote location from the fusion plasma. A molybdenum ridged waveguide is recommended for the last 2 meters of each RF feed. This is due to its high conductivity (2×10^5 mhos/cm @ 20°C) comparable to copper and high operating temperature. Its conductivity is about six times lower at an operating temperature of 800°C and it is expected to have considerable resistance to material changes under neutron bombardment.

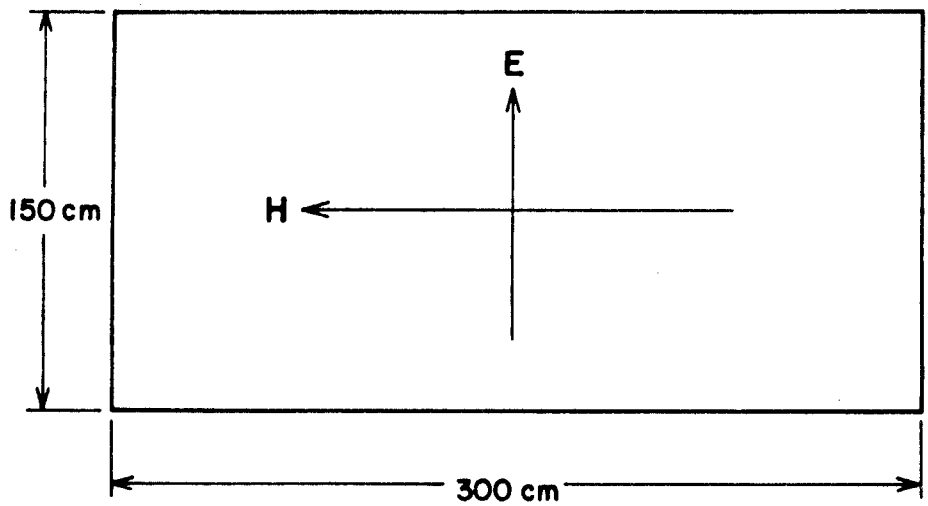

a) STANDARD RECTANGULAR WAVEGUIDE

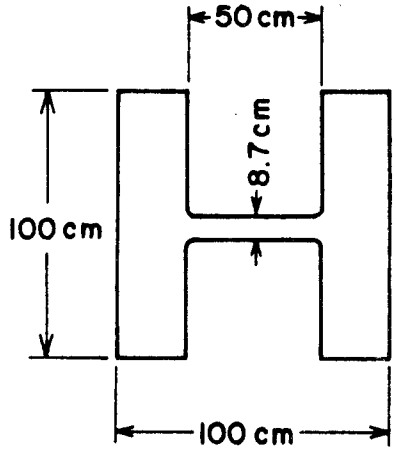

b) RIDGED WAVEGUIDE

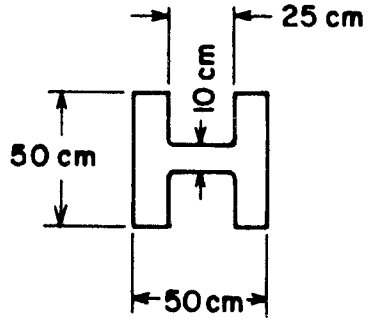

c) RIDGED WAVEGUIDE WITH CERAMIC ($\epsilon_r = 8$) FILLED DIELECTRIC

Size Comparison of Te_{10} Waveguide Feeds for 60 MH_Z RF

Figure II-C-4

Taking the above considerations into account we then have a feed system which is made up of 12 1 m x 1 m ridged waveguides arranged in two strips around the outside of the inner cross section as shown in Fig. II-C-5.

While the above is optimum for plasma physics considerations, it presents obvious problems from the viewpoint of vertical field coil placements and access. This added complexity led us to attempt the design approach shown in Fig. II-C-3b. This was used as the basis in locating the equilibrium vertical field coils used in the MHD analysis described in Section II-A. Again, while we have used this as the base case and shown this layout in Fig. 1-2 of the Overview, we reiterate that the wavelaunching system fanned in the poloidal sense as shown in Fig. II-C-5 would be preferable from the point of view of wave heating of the plasma core.

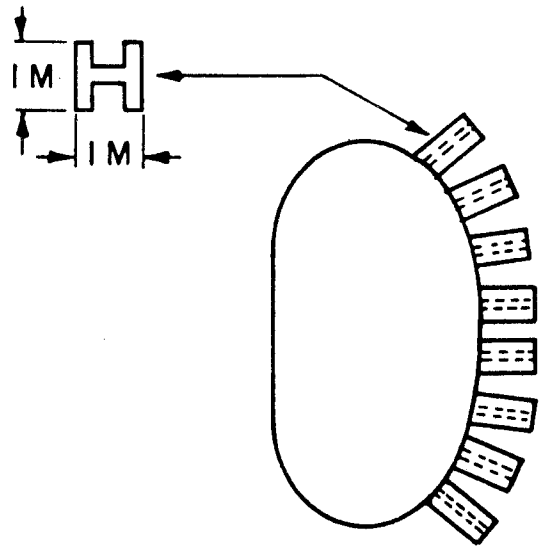

CROSS SECTION VIEW

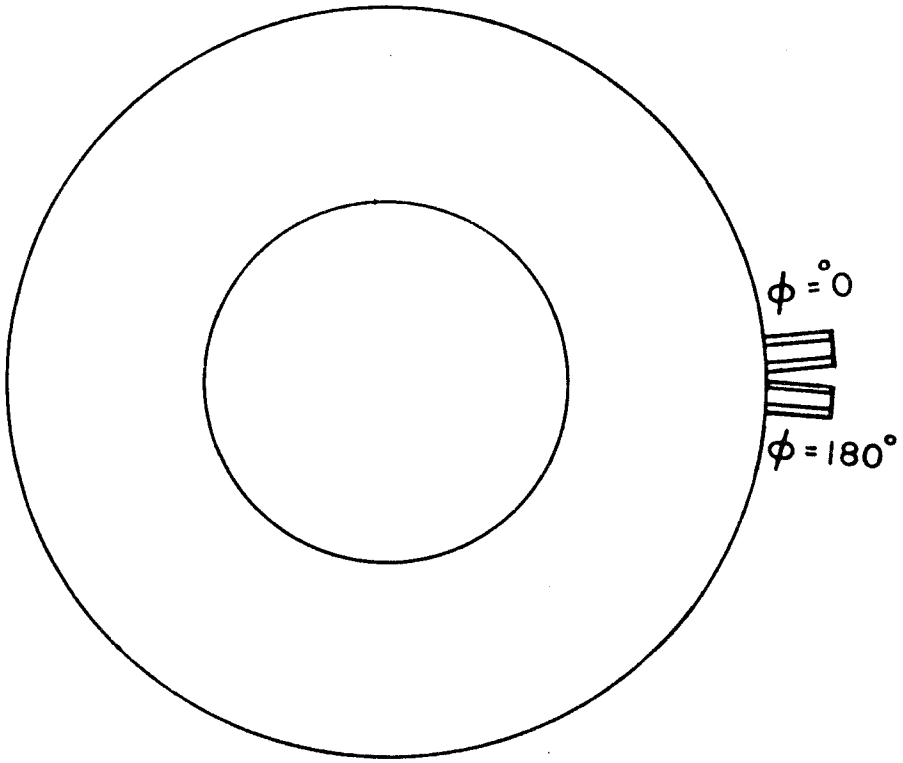

TOP VIEW
CROSS SECTION

Schematic of a Conceptual Magnetosonic Wave Launching System

Figure II C-5

References for Section II-C

1. Adam, J. and Samain, A. "Chauffage par Absorption Cyclotronique." Rapport du Groupe d'etude du Chauffage d'un Plasma, Confine dans une Configuration Magnetique du Type Tokamak. Report EUR-CEA-FC-579.

2. Perkins, F. W., "Hydromagnetic Wave Heating of Tokamak Plasmas," Symposium of Plasma Heating and Injection, (Varenna, 1972).

3. Weynants, R. R., "Ion Heating at Twice the Ion Cyclotron Frequency in Reactor Oriented Machines", Phys. Rev. Letters 33, 78 (1974).

4. Stix, T. H., "Fast-Wave Heating of a Two-Component Plasma", Princeton University, Plasma Physics Laboratory MATT-1113..

5. Stix, T. H., The Theory of Plasma Waves, McGraw-Hill, New York 1962.

6. Adam, J., Chance, M., Eubank, H., Getty W., Hinnov, E., Hooke, W., Hosea J., Jones, F., Perkins, F., Sinclair, R., Sperling, J., Takahasi, H. "Wave Generation and Heating in the ST Tokamak at the Fundamental and Harmonic Ion Cyclotron Frequencies", Proc. 5th International Conf. on Plasma Physics and Controlled Fusion Research (Tokyo, 1974) IAEA-CN-33/G1-2.

7. Swanson, D. G. and Ngan, Y. C., "Warm Plasma Effects on Fast Alfven Wave Cavity Resonances." Phys. Rev. Lett. 35, 517 (1975).

8. Scharer, J. E., Mau, T. K., Blackfield, D. T., Mc Vey, B. D., "Fast Magnetosonic Wave Heating at the Second Ion Cyclotron Harmonic in Tokamak Plasmas," Proc. Seventh European on Controlled Fusion and Plasma Physics, p. 145, Lausanne, Switzerland, September, 1975.

9. Weynants, R. R., "A High-Temperature, High Density Reduction of Harmonic Ion-Cyclotron Heating Efficiency", Symposium on Plasma Heating in Toroidal Devices, (Varenna, September, 1974).

10. Cato, J. E., Kristiansen, M., and Hagler, M. O., "Some Engineering Problems of Low-Frequency Heating of Fusion Reactors," Nuclear Fusion 12, 345-352 (1972).

11. Cohn, Seymour, B., "Properties of Ridged Wave Guide", Proc. I.R.E., 35, 783-788 (1974).

II-D. Plasma Burn Analysis

The equilibrium plasma conditions for UWMAK-III have been studied by using both a global plasma energy balance model and a more sophisticated space-time tokamak code. In both cases, thermal equilibria are found which produce 5000 MW_{th} of power. In the latter case, however, the average ion and electron temperatures and the plasma β_θ are found to be significantly lower than those predicted by the global model because the temperature and density profiles are sharply peaked at the axis of the torus.

The global model described previously[1] was modified to include the effects of non-circularity. In the space dependent transport code, however, the fluid equations are written in cylindrical geometry and we have therefore represented the UWMAK-III plasma as circular plasma with a cross-sectional area and major radius equal to the non-circular UWMAK-III plasma such that the total volume is preserved.

The plasma transport coefficients are assumed to follow microinstability theory, as summarized in reference 2, since this corresponds to a pessimistic assumption and is most likely a "worst case" approach. The fraction of trapped particles which is an important parameter in the transport coefficient was evaluated consistent with the non circular geometry.

In both the space dependent and space independent calculations, the plasma is assumed to be essentially free of impurities. This follows simply from the assumption that in the presence of turbulence, high Z impurities will be transported out of the plasma with the same diffusion coefficient as the plasma itself. With this assumption, one can set the flux of high Z impurities leaving the plasma equal to the impurity reflux:

$$-D\frac{\partial n_z}{\partial r} = -S(1-\eta)D\frac{\partial n_{DT}}{\partial r} + \frac{aS_n}{8}\overline{n_{DT}^2\langle\sigma v\rangle} + Sn_{DT}(a)n_n\langle\sigma v\rangle_{cx}\lambda_{cx} \qquad (1)$$

where D is the diffusion coefficient, n_z is the density of high Z impurities, $n_{D(T)}$ is the density of plasma ions, n_n is the density of neutrals at the plasma edge, S is the D-T sputtering yield (of order .01), η is the divertor unload efficiency (of order .99), $\langle\sigma v\rangle_{cx}$ is the charge exchange cross section at the plasma edge, λ_{cx} is the charge exchange mean free path at the plasma edge, and S_n is the sputtering coefficient for neutrons ($\sim 10^{-4}$). The first term on the right represents sputtering by plasma ions diffusing out of the plasma core and it is the dominant term. The second and third terms represent neutron and charge exchange neutral sputtering respectively. By setting $\frac{\partial n}{\partial r} \propto \frac{\bar{n}}{a}$, one finds

$$\frac{\bar{n}_z}{\bar{n}_{DT}} \approx S(1-\eta) \approx 10^{-3} \text{ to } 10^{-4}$$

Therefore, we have assumed that the plasma is essentially free of impurities.

The global plasma energy balance model, the space-time model and the operating plasma parameters for UWMAK-III are described in the following section.

II-D-1. Global Balance Model for Plasma

The space dependent electron and ion energy conservation equations may be written as

$$\frac{\partial n_e T_e}{\partial t} = 4.28 \times 10^{-11} n_e n_i \frac{(T_i - T_e)}{T_e^{3/2}} + \frac{1}{1.5r} \frac{\partial}{\partial r} (r n_e \chi_e \frac{\partial T_e}{\partial r}) - \frac{1}{r} \frac{\partial}{\partial r} (r n_e V_e T_e)$$

$$+ 4.17 \times 10^{15} \{n_D n_T \langle\sigma v\rangle U_{\alpha e} + \underline{E} \cdot \underline{J} + P_{inj}(U_{be} + f(\frac{E_\alpha}{E_b}) U_{\alpha e})$$

$$- P_I - P_B - P_S - P_L - P_R\} \qquad (2)$$

and

$$\frac{\partial n_i T_i}{\partial t} = -4.28 \times 10^{-11} n_i n_e \frac{(T_i - T_e)}{T_e^{3/2}} + \frac{1}{1.5r} \frac{\partial}{\partial r} (r n_i \chi_i \frac{\partial T_i}{\partial r}) - \frac{1}{r} \frac{\partial}{\partial r} (r n_i V_i T_i)$$

$$+ 4.17 \times 10^{15} \{n_D n_T \langle\sigma v\rangle_{DT} U_{\alpha i} + P_{cx} + P_{inj}(U_{bi} + f(\frac{E_\alpha}{E_B}) U_{\alpha i})\} \qquad (3)$$

$T_{e,(i)}$ is the electron (ion) temperature (eV), B_θ is the poloidal magnetic field (gauss), $n_{e,(i)}$ is the electron (ion) density (cm^{-3}), V_i is the ion velocity (cm/ms), J is the toroidal current density (amp/cm^2), E is the toroidal electric field (volt/cm), r is the radius (cm), t is time (ms), $\chi_{e,(i)}$ is the electron (ion) thermal diffusivity (cm^2/ms), η_{NC} is the neoclassical resistivity (ohm-cm), D is the diffusion coefficient (cm^2/ms), $U_{bi,(e)}$ is the fraction of alpha energy going to ions (electrons), and f is the fraction of deuterons in the neutral beam which undergo fusion as they slow down in a tritium target plasma. P_B, P_S, P_L, and P_R represent bremsstrahlung, synchrotron, line and recombination radiation, respectively (watts), P_{cx} is the energy loss due to charge exchange (watts), and S is the source of cold plasma ($cm^{-3}ms^{-1}$) due to a cold plasma source or neutral particle reflux.

The neoclassical resistivity η_{NL} is given by [3]

$$\eta_{NL} = 0.0103 \frac{\ell n\Lambda}{T_e^{3/2} f_T} \left(\frac{.457\ Z_{eff}}{1.077 + Z_{eff}} + .29\ Z_{eff}\right) \text{ohm-cm} \tag{4}$$

with

$$f_T = 1 - \{1.95\sqrt{\frac{r}{R}} + .95(r/R)\}/(1 + \nu^*) \tag{4a}$$

and

$$\nu^* = 6.92 \times 10^{-14} Z_{eff} \frac{R^{3/2} B_T n_e \ell n\Lambda}{\sqrt{r}\ B\ T_e^{\ 2}} \tag{4b}$$

$$Z_{eff} = \frac{\sum_j n_j Z_j^2}{n_e} . \tag{5}$$

R is the toroidal major radius (cm), $\ell n\Lambda$ is the coulomb logarithm, f_T is the correction to the resistivity due to particle trapping, and ν^* is the ratio of collision frequency to bounce frequency. The impurities are assumed to radiate according to the formula [4,5]

$$P = P_L + P_R = P_B \left(\frac{37.9\ n_z Z^4}{Z_{eff} n_e T_e} + \frac{860\ n_z Z^6}{Z_{eff} n_e T_e^{\ 2}}\right). \tag{6}$$

Here n_z is the density (cm^{-3}) of impurities in charge state Z and W_B is the bremsstrahlung radiation ($watts/cm^3$),

$$P_B = 1.52 \times 10^{-32} n_e^{\ 2} T_e^{\ 1/2} . \tag{7}$$

Synchrotron radiation is taken as [25]

$$P_s = 1.6 \times 10^{-28} \left(1 - 0.0305 \frac{R}{a}\right)^3 B_T^{5/2} \sqrt{\frac{n_e}{a}}\ T_e^{2.1} \tag{8}$$

At low temperatures, eqn. (6) becomes inaccurate and in that case, the formula of Hinnov(7) has been used,

$$P_L = 1.2 \times 10^{-32} n_z n_e \tag{9}$$

Which is approximately correct for impurities with three or more electrons remaining. In calculations, the smaller value from eqns. (6) and (9) is used.

In the global energy balance model, the radial dependence is eliminated as follows:

The conduction terms:

$$\frac{2}{3} \frac{\partial}{\partial r} rn\chi \frac{\partial T}{\partial r} \rightarrow \frac{nT}{\tau_c}$$

where $\tau_c = a^2/4D$

The convection terms:

$$\frac{1}{r} \frac{\partial}{\partial r} (rnVT) \rightarrow \frac{nT}{\tau_D}$$

where $\tau_D = \frac{a^2}{4D}$

The other terms are evaluated by assuming parabolic temperature and density profiles. The average density is then computed from

$$\bar{n} = \frac{2\int_0^a n(r) r dr}{a^2} \tag{10}$$

and the average temperature is defined as

$$\bar{T} = \frac{\int_0^a n(r)T(r)rdr}{\int_0^a n(r)rdr} \tag{11}$$

For a non-circular plasma, we define a shape factor, S, as

$$S = \frac{\text{circumference of plasma}}{\text{circumference of inscribed circular plasma}} .$$

The stability factor, q, is

$$q = \frac{S}{A} \frac{B_T}{B_\theta} \tag{12}$$

where A is the aspect ratio based on the small plasma minor radius, B_T is the toroidal magnetic field and B_θ is the poloidal field at the plasma edge. The equation for poloidal beta is

$$\beta_\theta = 2\mu_o \sum_j n_j T_j / B_\theta^2$$

where the summation includes the ions, electrons and alphas. B_θ may be eliminated in favor of q to yield

$$\beta_\theta = 2\mu_o \frac{A^2 q^2}{S^2 B_T^2} \sum_j n_j T_j$$

For a given β_θ, this equation is used to obtain the electron density that is inserted in the expressions for the transport coefficients.

II-D-2. Fluid Model of Tokamak Plasma

The space-time model solves the energy balance equations (2) and (3) in cylindrical geometry self-consistently with a diffusion equation for ion density and allows for electric and magnetic field diffusion. It also takes account of recycling, the transport of neutrals for liner sputtering, and the stripping, radiation, and diffusion of the neutrals. The diffusion equation and Faradays, Amperes and Ohms Laws may be written as follows

$$\frac{\partial n_i}{\partial t} = -\frac{1}{r} \frac{\partial}{\partial r}(r n_i V_i) \tag{13}$$

$$n_i V_i = -D \frac{\partial n_i}{\partial r} \tag{14}$$

$$\frac{\partial B_\theta}{\partial t} = 10^5 \times \frac{\partial E}{\partial r} \tag{15}$$

$$\frac{\partial J}{\partial t} = 7.96 \times 10^4 \frac{1}{r} \frac{\partial}{\partial r}\left(r \frac{\partial E}{\partial r}\right) \tag{16}$$

$$E = \eta_{NC} J \tag{17}$$

In addition, charge neutrality is imposed on the plasma

$$n_e = n_i + 2n_\alpha + \sum_i n_{Z_i} Z_i . \tag{18}$$

This set of differential equations (2), (3) and (13)-(17) is solved using a symmetric Cranck-Nicholson method in which the equations are linearized and transformed into an implicit set of difference equations.[8]

The transport coefficients (D, χ_e, χ_i) are treated implicitly and are assumed to vary in functional form as the plasma changes in collisionality. The high collisionality regime reflects pseudoclassical scaling[9] and, as the plasma heats, the transport is assumed to be caused by turbulence, passing successively into regimes dominated by the presence of the trapped electron mode,[10] the trapped ion mode[11] and the collisionless trapped particle interchange mode.[12] Transport coefficients based on estimates of the linear growth rates for these modes have been summarized by Dean et al.[2] In the trapped electron regime, the relationship between χ_i and χ_e is not known. Rather than optimistically assuming χ_i remains neoclassical in this regime, we have taken $\chi_i = \varepsilon\chi_e$ where ε is the local inverse aspect ratio.

To allow for a general variation of the transport coefficients, the general form

$$D,\ \chi_e,\ \chi_i = C\ T_e^{S1}\ T_i^{S2}\ n_i^{S3}\ B^{S4}(\nabla n)^{S5}(\nabla T)^{S6}(\nabla q)^{S7}(1 - T_e/T_i)^{S8} \qquad (19)$$

is used in which the coefficients C and S1, S2 . . . , for D, χ_e, or χ_i are determined by the dominant mode present.

A three dimensional neutral particle transport model has been developed to determine both the spectrum of charge exchange neutrals that impinge on the liner and the loss of plasma energy due to charge exchange. A slab geometry is used since the thickness of the region which neutrals penetrate is much smaller than the plasma minor radius. In this model, the ions diffusing from the plasma and the charge exchange neutrals can be recycled at the plasma edge as cold H_2. In this case, the H_2 molecules are assumed to dissociate in the outer plasma layer and give rise to Franck-Condon neutrals of 5-10 eV which then penetrate isotropically into the plasma. These neutrals are either ionized by electron or ion impact ionization, suffer a charge exchange which isotropically produces a neutral at the local ion temperature, or escape from the plasma. Particles converted to secondary neutrals by charge exchange continue to be treated for up to 10 generations.

II-D-3. Plasma Burn Conditions

In utilizing the code to produce thermal equilibria, we have the liberty of using relatively long time steps since errors in the approach to equilibria are of no consequence. The program appears to approach the same solution from different initial conditions which leads one to believe without general proof that the solutions are unique.

Plasma thermal equilibria are a function of machine parameters (minor radius, major radius, toroidal magnetic field, plasma current) as well as the particle source profile and the boundary conditions. In order to maintain a density balance in the plasma, a source of D and T must be used to replenish the plasma

lost by convection and D-T burnup. We have assumed that there is a flat particle source profile (independent of radius) since there is no detailed knowledge available on this subject.

The boundary conditions used reflect the presence of a divertor at the plasma edge. We define characteristic lengths for the ion and electron temperatures and for the density as follows:

$$L_i = T_i/\nabla T_i \tag{19a}$$

$$L_e = T_e/\nabla T_e \tag{19b}$$

$$L_n = n/\nabla n \tag{19c}$$

As is discussed in an earlier report,[13] the density and electron temperatures are expected to fall off rapidly in the divertor zone (which has a 50 cm width). Therefore, we have taken $L_e = L_n = 50$ cm. For the ion temperature, which we expect to remain approximately constant in the divertor zone, we have used $L_i = 10^3$cm.

The results from the code are relatively insensitive to the plasma current and q since ohmic heating is negligible at the temperatures of the reactor and the poloidal magnetic field does not enter into trapped ion mode scaling, which dominated the transport processes. Therefore, to be consistent with MHD calculations, we have chosen q at the plasma edge to be 2.7. This gives a corresponding plasma current from eqn. (12) of

$$I = 5S^2 B_T a/A\ q\ \text{(amperes)} = 15.8 \times 10^6\ \text{Amperes} \tag{20}$$

In the equilibrium solution of the space dependent calculations, the average temperature of ions and electrons is 11.4 and 11.9 keV, respectively, the poloidal beta is 1.65, and $n\tau_E$ is 1.3×10^{14}cm^{-3}-s. The reason for the low values of temperature, beta and $n\tau_E$ is that the equilibrium profiles are quite peaked compared to the usual assumption of a uniform or parabolic profile implicit in the use of global energy balance models. The profiles are shown in Fig. II-D-1.

The plasma and magnetic field parameters are listed in Tables II-D-1, II-D-2, and II-D-3. The energy confinement time is 1.6 sec while the particle confinement time is 0.55 sec. The fractional burnup is a very low 0.83% and the fueling rate for D and T atoms is 1.43×10^{21}/sec. This low fractional burnup and correspondingly high fueling rate results because the diffusion of particles from the plasma is governed by the diffusion coefficient at the plasma edge. The edge condition associated with the use of a divertor implies a very low density and therefore a quite collisionless plasma. In turn this leads to a large diffusion coefficient assuming microinstability scaling. The surface heat load due to bremsstrahlung and synchrotron radiation is 3.95 W/cm^2 and, since the divertor is 99% efficient, the heat load due to particles on the wall is only 0.51 w/cm^2. Since the radiation losses are relatively small, the heat load to the divertor is large, being 725 MW.

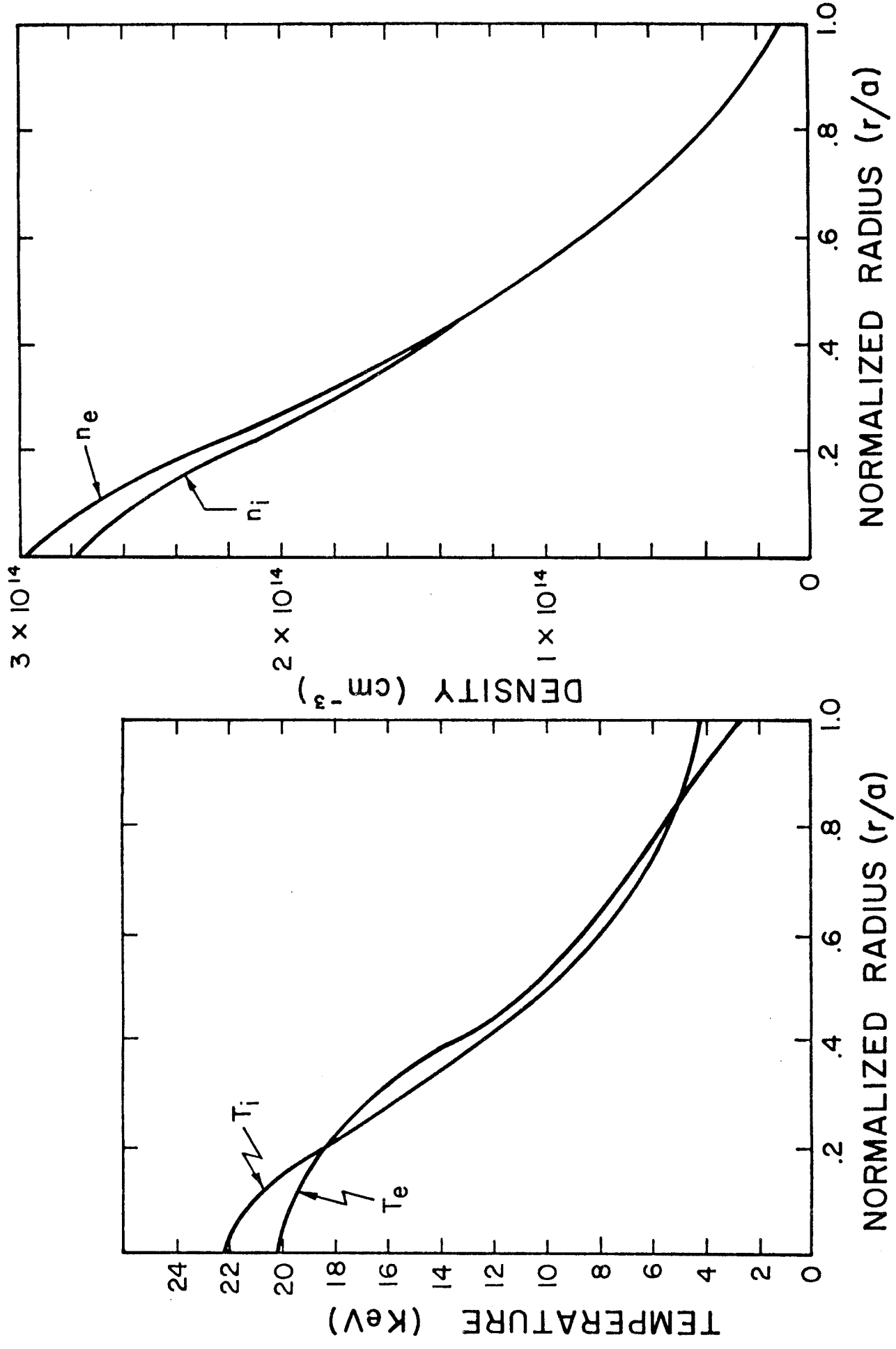
TEMPERATURE (keV)
0
2
4
6
8
10
12
14
16
18
20
22
24
T_i
T_e
.2
.4
.6
.8
1.0
NORMALIZED RADIUS (r/a)
DENSITY (cm^{-3})
0
1×10^{14}
2×10^{14}
3×10^{14}
n_e
n_i
.2
.4
.6
.8
1.0
NORMALIZED RADIUS (r/a)

FIGURE II-D-1

Table II-D-1

Plasma Parameters for UWMAK-III

	Space-Time	Point Model
Mean Ion Temperature (keV)	11.4	18.4
Mean Electron Temperature (keV)	11.9	22.9
Mean Ion Density (cm^{-3})	7.9×10^{13}	6.46×10^{13}
Mean Electron Density (cm^{-3})	8.1×10^{13}	6.86×10^{13}
Mean Alpha Density (cm^{-3})	8.8×10^{11}	1.9×10^{12}
Plasma Current (MA)	15.6	15.7
Stability Factor at Plasma Edge, q(a)	2.7	2.69
Plasma Width (m)	2.7	2.7
Plasma Height (m)	5.4	5.4
Radius of Equivalent Volume Circular Plasma (m)	3.83	---
Major Radius (m)	8.1	8.1
Axial Toroidal Magnetic Field (kG)	40	40
Plasma Volume (m^3)	2370	2360
Electron Poloidal Beta, β_θ^e	0.69	1.05
Total Poloidal Beta, β_θ	1.65	2.3
Total Toroidal Beta, β_ϕ	.058	.083
Energy Content of Plasma (GJ)	1.32	1.63
Wall Surface Area (m^2)	1600	1600
Particle Confinement Time (sec)	0.547	3.33
Energy Confinement Time (sec)	1.64	1.66
$\bar{n}_e \tau_E$	1.33×10^{14}	1.14×10^{14}
Fractional burnup, f_b	0.83%	5.9%
Voltage Around Torus (volts)	0.059	

Table II-D-2

Power Parameters

Energy per Fusion (MeV)	21.7
Thermal Power During Burn (MW)	5000
Average Power Density in Plasma (MW/m^3)	1.72
14 MeV Neutron Production Rate (sec^{-1})	1.44×10^{21}
Power to Wall (MW)	71.3
Radiation (MW)	63.2
Particles (MW)	8.1
Surface Wall Loading (MW/m^2)	0.44
Power to Divertor (MW)	725

Table II-D-3

Fueling Parameters

Tritium (deuterium) Consumption Rate	1.94×10^{21}/sec
Tritium Burnup Rate	.62 kg/day
Deuterium Burnup Rate	.413 kg/day
Particle Leakage Rate (D+T+α)	3.44×10^{23}/sec
Fueling Rate	
Deuterium	49.8 kg/day
Tritium	74.7 kg/day

References for Section II-D

1. R. W. Conn, J. Kesner, "The Potential of Driven Tokamaks as Thermonuclear Reactors," Nuclear Fusion, 15 (1975) 775

2. S. O. Dean et al. "Status and Objectives of Tokamak Systems for Fusion Research," U. S. Atomic Energy Commission, WASH-1295 (1974).

3. R. Hazeltine, F. Hinton, M. Rosenbluth, Phys. Fluids, 16, (1973) 1645.

4. A. P. Vasil'ev, G. G. Dologov-Salev'ov, V. I. Kogan, Nuclear Fusion Suppl., pg. 2 (1962) 655.

5. G. R. Hopkins, "Impurity Radiation Loss Mechanism for Fusion Reactor Plasmas," General Atomic Co. Report, G.A. 12374 (Oct. 1972).

6. T. F. Yang et al., "The Calculation and Parametric Study of Synchrotron Radiation Loss for Tokamak Reactors," Nucl. Eng. Dept. Report UWFDM-49, University of Wisconsin (1973).

7. E. Hinnov, Plasma Physics 14, (1972) 755, See also Princeton Plasma Physics Lab. Report. MATT-777 (1970).

8. M. M. Widner, R. A. Dory, Bull. Am. Phys. Soc. 11(1970)1418. See also Oak Ridge National Lab. Report, ORNL-TM-3498 (1971).

9. L. Artsimovich, J.E.T.P. Letts. 13 (1971) 70.

10. B. B. Kadomtsev, O. P. Pogutse, Nuclear Fusion 11 (1971) 67.

11. B. B. Kadomtsev, O. P. Pogutse, Sov. Phys. Dokl. 14 (1969) 470.

12. J. D. Callen, B. Coppi, R. Dagazlan, R. Gajewski, D. J. Sigmar, in Plasma Physics and Controlled Nuclear Physics Research (Proc. Madison Conf., June 1971)(IAEA, Vienna 1972) Vol. II, Pg. 51.

13. B. Badger, et al., "UWMAK-II, A Conceptual Tokamak Reactor Design," University of Wisconsin Nuclear Engineering Dept. Report UWFDM-112, (1975).

III. Divertor and Vacuum Pumping

III-A. Divertor Magnetic Field Design

UWMAK-III utilizes a double-null poloidal divertor in order to protect the first wall from charged particle bombardment and the consequent buildup of impurities in the plasma. The divertor also possesses the desirable property of establishing a boundary for the magnetically confined plasma and, with proper programming of the divertor and transformer currents during startup, can produce an expanding magnetic limiter. The large stored poloidal magnetic energy in the reactor size plasmas requires that the plasma current be brought to its full value rather slowly (~15 seconds). In order to maintain reasonable values of q, the MHD stability factor, during this time, it is necessary to have a small plasma initially and let the radius expand during the current rise, keeping the current density approximately constant. The programmed divertor is a way of doing this without having metallic surfaces in contact with the plasma.

The UWMAK-I[1] and UWMAK-II[2] divertors were designed using a filamentary model[1] to calculate the flux surfaces. This model is acceptable for determining approximate values for the divertor currents and their locations. The next level of sophistication is to use a free boundary MHD equilibrium code where the divertor currents play a crucial role in determining the MHD equilibrium. This has been done for UWMAK-III and is described in Section II-A of this report. In this section, we describe the magnetic field geometry in the scrape-off zone and discuss how particles get to the collectors. Section III-B describes the vacuum pumping system and Section III-C describes the particle collectors.

The UWMAK-I and UWMAK-II divertors used a flowing liquid lithium film to collect the particles. These plates were placed inside the toroidal field magnets, as shown in Fig. III-A-1 for UWMAK-II. The major drawback, especially for UWMAK-II, was that the power density on the collectors was large because of the small transverse dimension of the plasma beam at the collector. The heat transfer problems caused by this were tremendous. This problem becomes worse for a smaller size reactor of the same power level. Furthermore, space becomes a problem when the plasma is vertically elongated as in UWMAK-III. (See Fig. III-A-2).

We decided in UWMAK-III to design the divertor with the particle collectors outside the toroidal field coils. This allows us to fan the field lines and reduce the power density on the collectors. Furthermore, it allows us to place the cryopumps in close proximity to the collectors for maximum pumping efficiency. Combining this with the relatively small flow conductance back through the slots to the plasma, we expect that there will be little back-streaming of neutrals and impurities.

The particles get from the plasma to the collectors by following magnetic field lines into the fringing region of the toroidal field coils. These field lines get "caught" in the poloidal component of the fringing toroidal field and pass through the gaps.

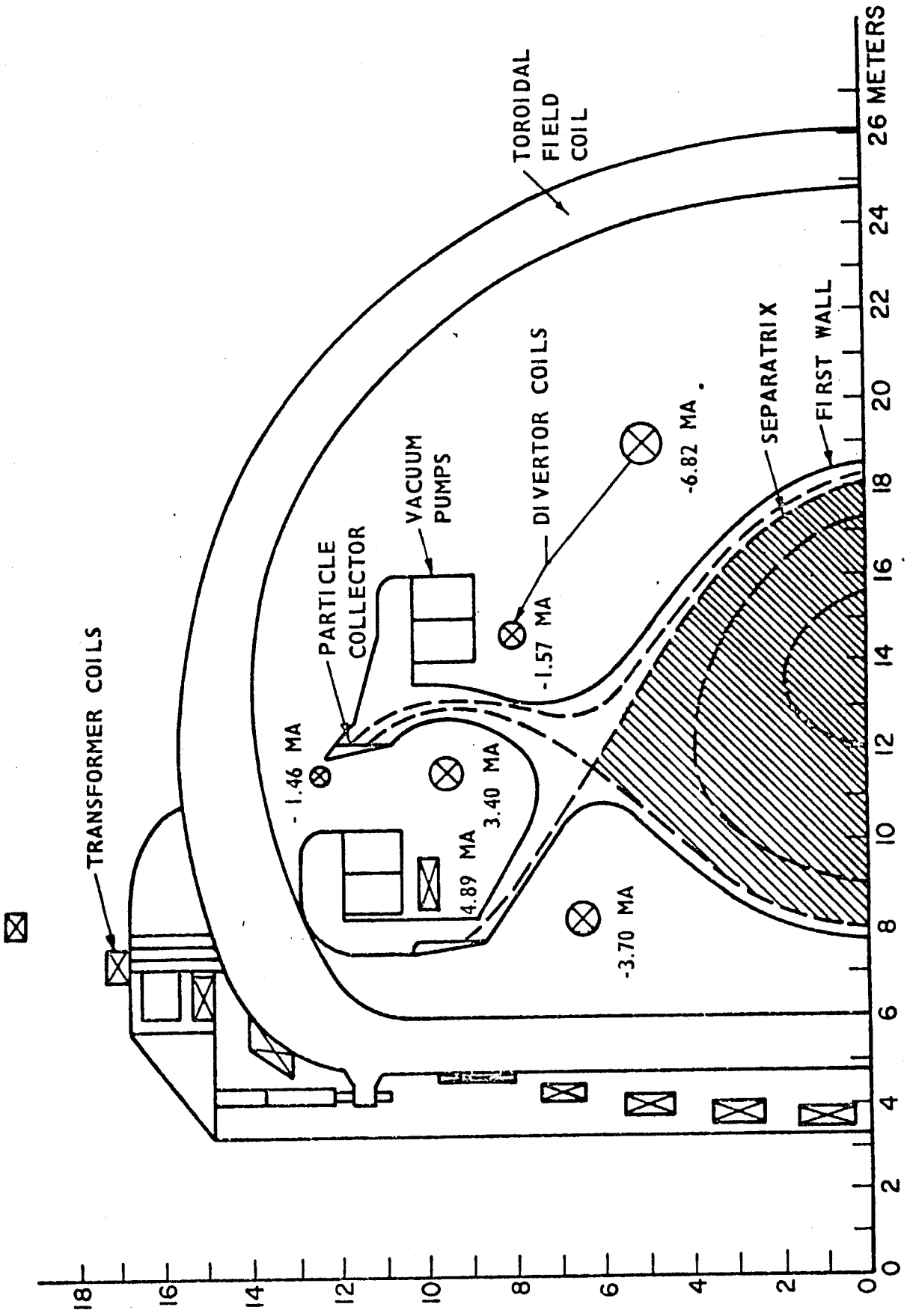
UWMAK - II POLOIDAL DIVERTOR
TRANSFORMER COILS
TOROIDAL FIELD COIL
PARTICLE COLLECTOR
VACUUM PUMPS
DIVERTOR COILS
SEPARATRIX
FIRST WALL
-1.46 MA
3.40 MA
4.89 MA
-1.57 MA
-6.82 MA
-3.70 MA
26 METERS
0
2
4
6
8
10
12
14
16
18
20
22
24

FIGU III-A-1

CROSS SECTION VIEW OF UWMAK III

FIGURE III-A-2

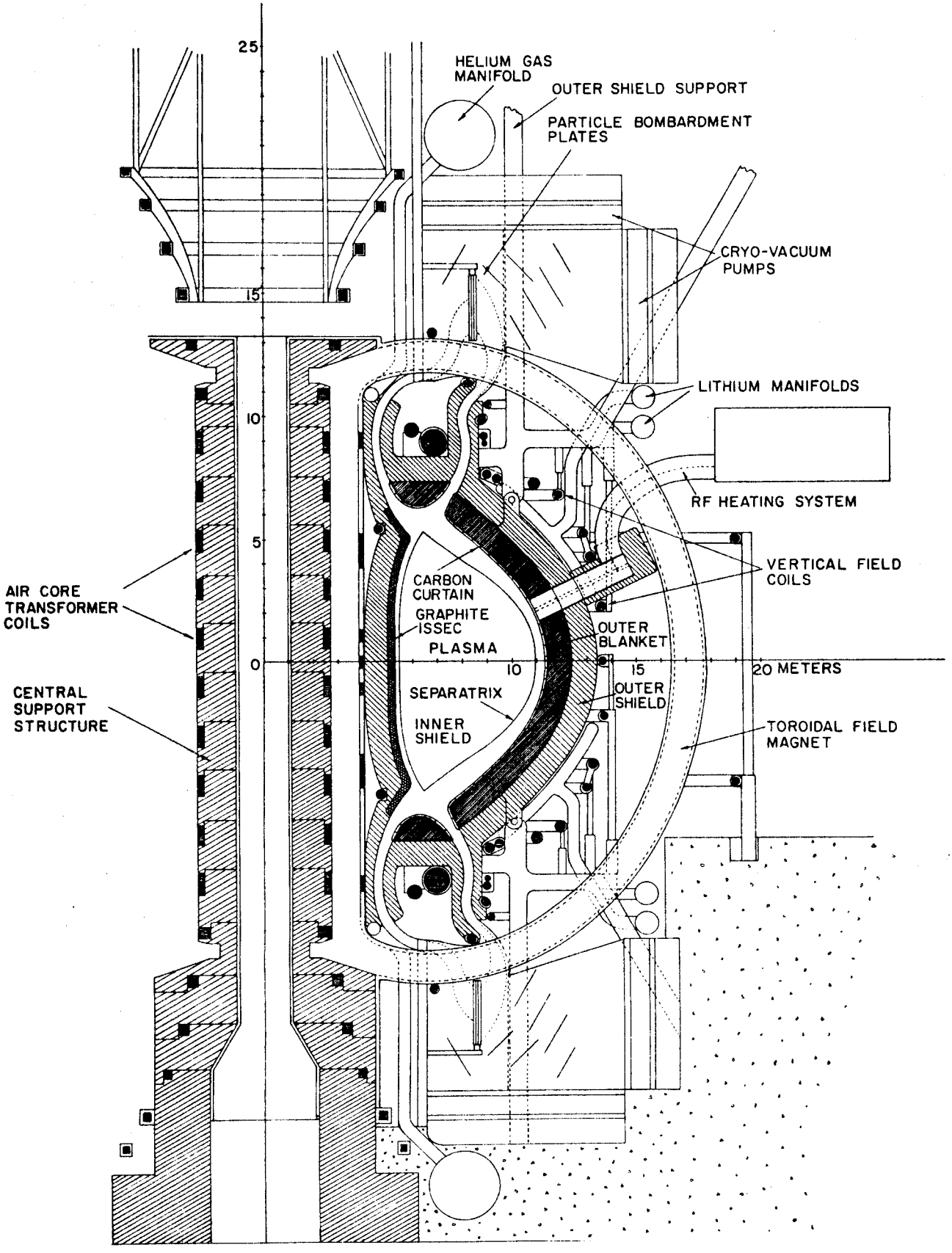

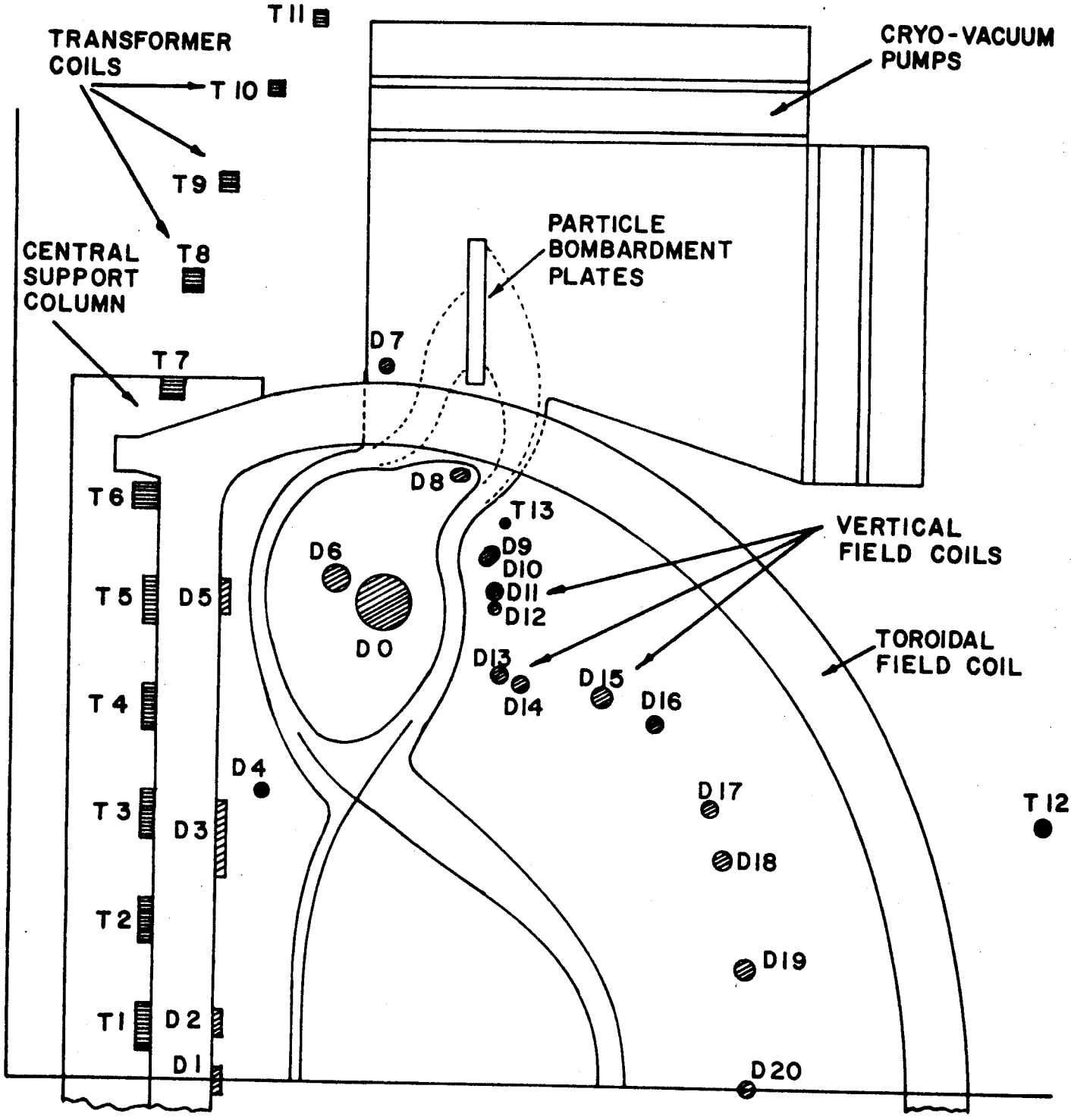

FIGURE III-A-3 - UWMAK-III Poloidal Divertor

To see how this occurs, consider first a discrete coil cylindrical solenoid as shown in Fig. III-A-4. Around each coil there is a separatrix. Field lines (A) inside the separatrix encircle their respective coil; some of them will intercept the coil structure because of the finite dimensions of the windings. Field lines (B) inside the solenoid but outside the separatrix deflect outwards near the gap but return to the interior of the solenoid. Some of them intercept the coil structure only if the separatrix also intercepts the structure.

Let us now introduce an external magnetic field transverse to the solenoid axis. The resulting flux plot near the coils is shown qualitatively in Fig. III-A-5. All field lines (B) are now carried towards the coils and eventually pass through the gaps if the separatrix lies outside the coil dimensions. If these field lines are carrying particles, as in the scrape-off zone of a divertor, then the particles get through the gaps and do not bombard the surfaces of the coil.

Let us now apply these rather "idealized" concepts to the tokamak reactor where we have discrete toroidal field coils and an axisymmetric poloidal field. Near the TF coils the poloidal field is outwards in some locations and inwards at others. The resultant path of field lines which originates in the scrape-off zone near the plasma is shown qualitatively in Fig. III-A-6 from three different perspectives. The UWMAK-III divertor utilizes this behavior of the magnetic field to carry particles through the gaps between the TF coils to the particle collectors.

The surfaces of the magnets will experience direct charged particle bombardment if the separatrix around the coils intercepts the surface or if the particles can cross-field drift (due to curvature and ∇B drifts) to field lines that intercept the surface. The latter effect is not considered to be important since the particles can only drift a distance of the order of the gyroradius while traversing a distance along the field lines equal to the radius of curvature of the field. The fields are strong (toroidal field = 4T, poloidal field ~1T) and the gyroradius is small ($\lesssim$ 1 cm) so this effect can be ignored. Calculation of the location of separatrix requires extensive 3D field line computer calculations. This has not yet been done for UWMAK-III, but we are preparing to do this work. We have done similar calculations for UWMAK-I and II[3]; in those cases, the coils were protected except near the inner leg of the "D". This leads us to believe the method described will work for UWMAK-III. If the coils suffer some charged particle bombardment, one can place particle collectors on the surface of the magnets, or at other strategic locations, to protect the magnets from erosion and heat input.

The location of the particle collector plates is shown in Fig. III-A-2 and III-A-3. This is based on the assumption that the coils are protected by the magnetic field against bombardment. This arrangement requires two collectors back-to-back to receive the flux from the inner and outer scrape-off zones. The particles from the inner scrape-off zone pass by the supports for the portion of the blanket and shield directly above and below the plasma.

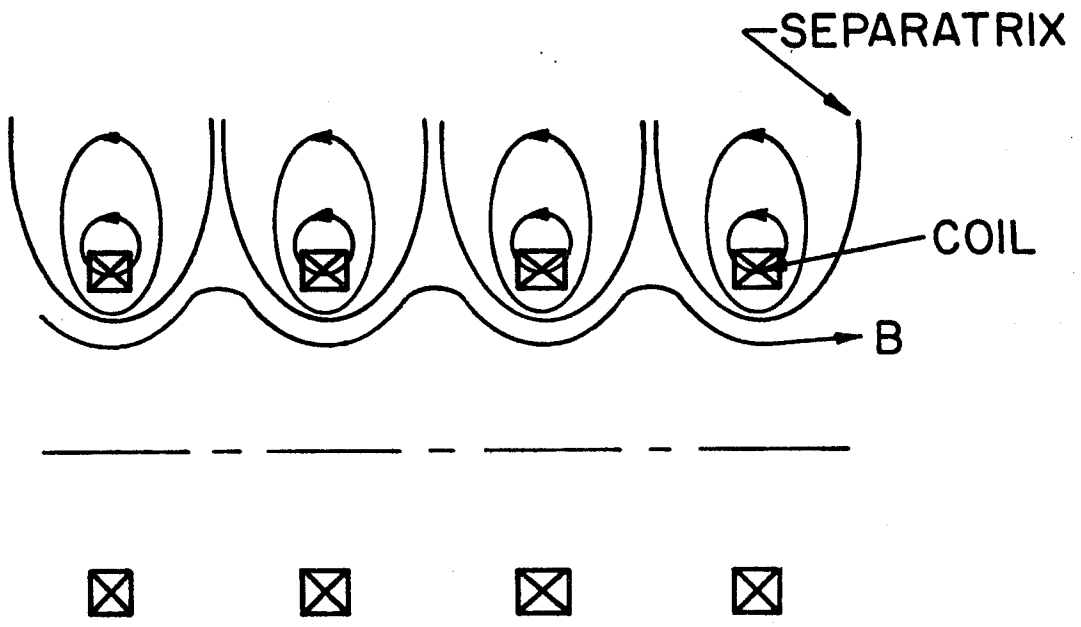

Fig. III – A – 4

Magnetic Field of a Solenoid

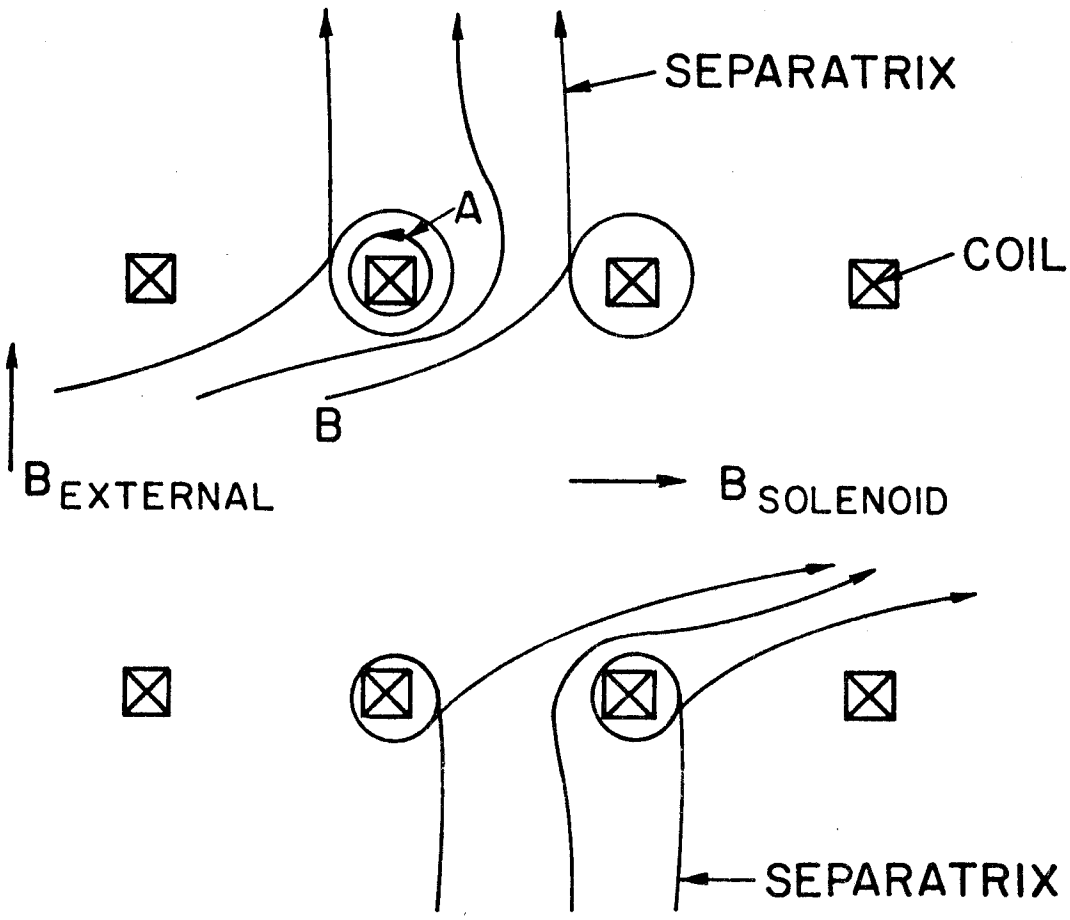

Fig. III - A - 5

Effect of a Transverse Field

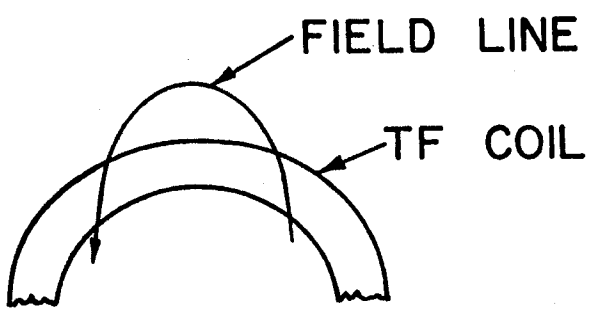

SIDE VIEW

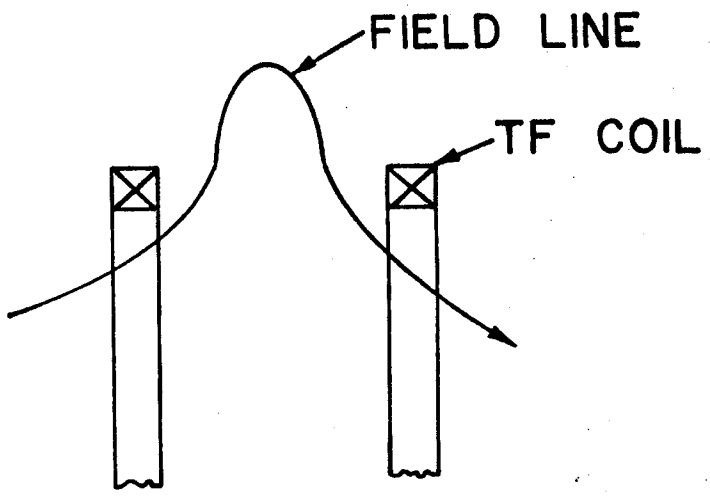

END VIEW

(cant of the TF coils not shown)

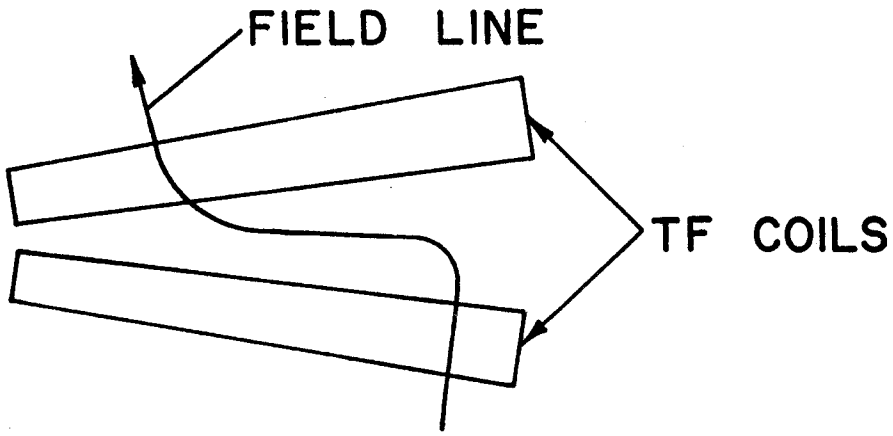

TOP VIEW

Fig. III - A - 6

Diverted Field Line Near TF Coils

These supports are guarded against charged particle bombardment by two parallel currents as shown in Fig. III-A-7. The line currents create a separatrix and thereby divert the field around the supports as shown in Fig. III-A-8. The required current to guard the supports is 1.9 MA per support. Because of the location behind the blanket and shield, this can be a superconducting current.

References for Section III-A

1. B. Badger et al., "UWMAK-I, A Wisconsin Toroidal Fusion Reactor Design," UWFDM-68, Vol. I, Dept. of Nuclear Engineering, Univ. of Wisconsin.

2. B. Badger, et al., "UWMAK-II, A Conceptual Tokamak Reactor Design," UWFDM-112, Dept. of Nuclear Engineering, Univ. of Wisconsin.

3. T. F. Yang, "A Direct Energy Conversion Scheme for a Tokamak with a Poloidal Divertor," Bull. of the APS, 18, 1303 (1973).

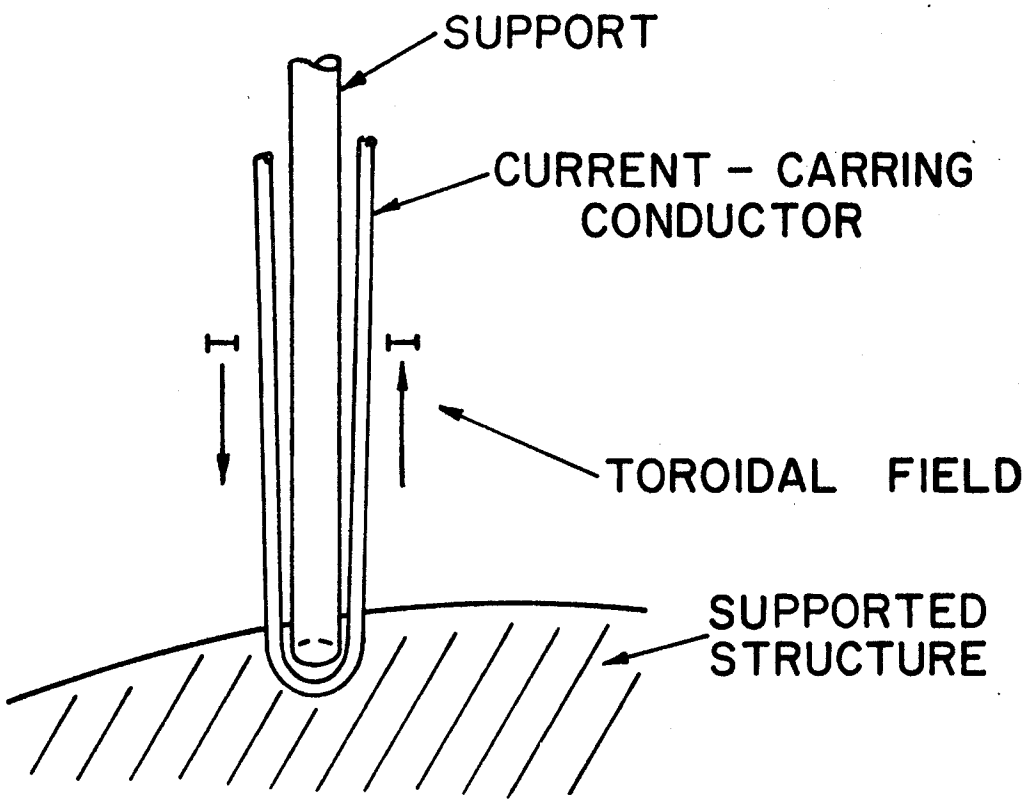

Fig. III-A-7

Magnetic Guarding of the Support

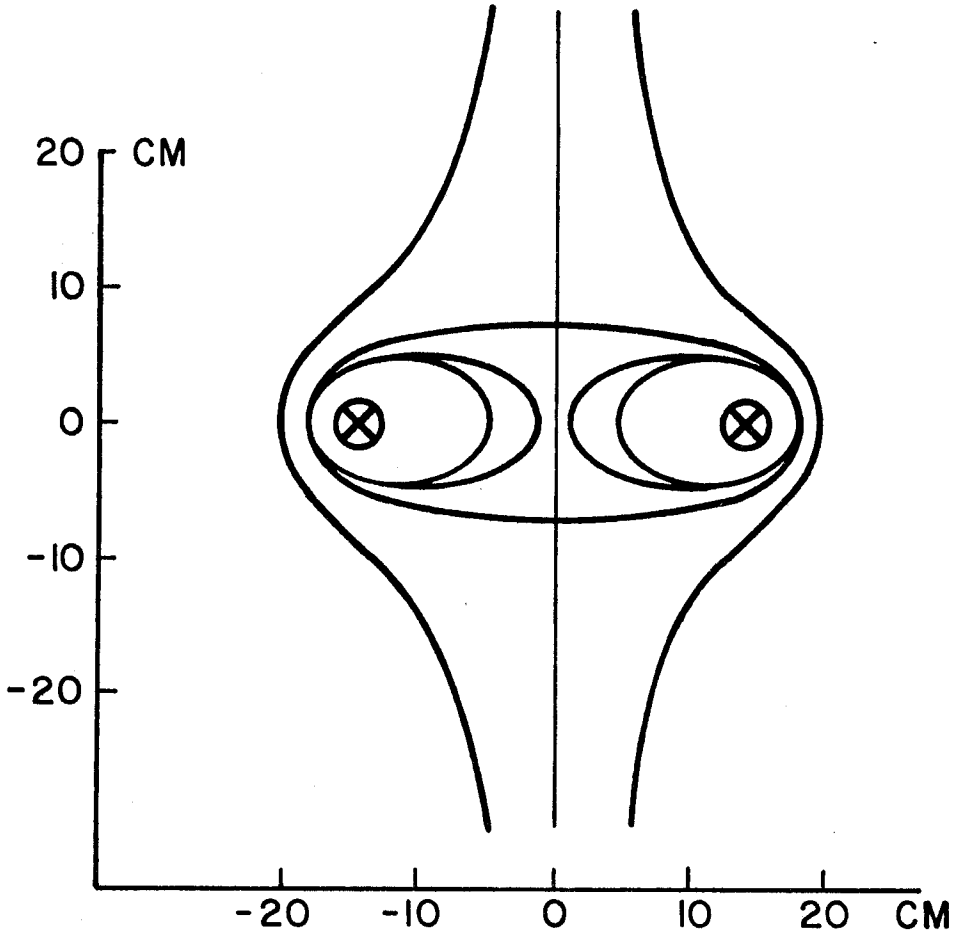

Fig. III - A - 8

Magnetic Guarding of Supports

III-B Primary Vacuum Pumping System

III-B-1 General Description

The main function of the primary vacuum system is to remove the unburned fuel during the burn cycle maintaining the plasma chamber surrounding the plasma confinement zone at a pressure of $1x10^{-4}$torr or better. A secondary function, but equally as important, is to pump the chamber down to a relatively high vacuum between burn cycles in order to clean and condition the chamber surfaces.

In both UWMAK-I and UWMAK-II, flowing liquid lithium surfaces were used in the divertor region to both thermalize and pump the diverted particles. It was assumed that about 90% of the D & T ions would combine chemically with the lithium to form a hydride, while 50% of the α particles would be mechanically trapped and swept out before diffusing back from the lithium stream.

The smaller physical size of UWMAK-III, while producing the same thermal output as its two predecessors, causes the thermal load in the divertor zone to be substantially increased. Although it is felt that lithium trapping surfaces would work under the condition of UWMAK-I & II, they would be difficult or impossible to implement in UWMAK-III in the same way. It was therefore decided to extend the divertor system in UWMAK-III such as to allow the particle to exit between the magnets from the toroidal enclosure and be collected externally where more space is available. But even here, the temperature restraints of a lithium surface imposed by its melting points and its vapor pressure made the usefulness of such a system doubtful. It was therefore decided to do away with lithium surfaces altogether and to design a radically new system thermalizing and collecting the particles.

Eliminating the lithium surfaces puts a tremendous burden on the primary vacuum system which now must have a capacity an order of magnitude larger than previously needed. However, with the particles diverted out of the toroidal enclosure, more space is available for the placement of vacuum pumps.

A cooled sacrificial TZM sheet, designed to be replenished at frequent intervals is used to thermalize the particles. The vacuum chamber walls and radiation baffles will be cooled to essentially room temperature. The recombined molecules of D_2, T_2 and DT which will cool down to 300K will be pumped by cryo-pumps similar to those used in UWMAK-II.

III-B-2 Primary Vacuum Pump Layout

A pumping scheme for a fusion reactor is complicated by the fact that twice as many pumps as needed in normal operation have to be provided, to allow one half of them to be recycled while the other half is on line. For anyone even remotely familiar with vacuum systems, this implies low conductance gate valves, heaters, back up pumps and a maze of ducts and vacuum lines.

It is true that all of these things are needed, but a system such as UWMAK-III lends itself rather nicely to a simple design. We envisage that the cryo-pumps will be rectangular in shape and will cover about 65% of the available space. The total pumping area will be 1600m^2, with only one half of it in use at one time.

The pumps will be arranged in even numbers, covering the horizontal and vertical space available in the vacuum plenum. Figure III-B-1 shows the location of the vacuum pumps on the upper half of the reactor and Figure III-B-2 shows pump layout on the horizontal plane. Sliding plates will act as gate valves and will be sealed with conventional elastomer seals. The seals will be shielded from neutrons but will suffer damage from scattered gammas and will have to be replaced periodically. Each sliding plate will serve a pair of pumps, one on-line and the other being regenerated. During change-over, the plate is moved to seal the saturated pump while exposing a freshly regenerated one to the chamber plenum. The back end of the pumps will have a similar gate plate arrangement operating in reverse of the front gate plate. The rear plate isolates the pump on line from the common pump-out plenum while opening the pump being regenerated to it. This scheme will provide essentially no pumping impedance, will save on space and requires no extrapolation of present day vacuum technology.

III-B-3 Primary Vacuum System Capacity and Base Pressure

As in UWMAK-II, the cryo-pump design is based on a type manufactured by Excalibur Corp., Waltham, Mass., and consists of a molecular sieve bonded to a metal substrate with two sets of chevron-shaped metal baffle surfaces in front. The chevron surface farthest from the molecular sieve is cooled to 80K, the next one to 20 K and the molecular sieve panel to 5K. Condensable gases or vapors will condense on the 80K and 20K chevron surfaces, while hydrogen isotopes as well as helium are adsorbed on the 5 K molecular sieve surface.

Cryo-sorption on this panel is not dependent merely on the vapor pressure-temperature curves for the gases being pumped. Helium for example, is held by surface attraction forces and further immobilized by the condensing deuterium and tritium, even though the 5 K is above its boiling point.

The advertised pumping speed for pumps of this type for hydrogen isotopes is ~10 liters/sec. cm^2 and is definitely flow limited by the chevron plates and the mounting flanges. It is readily conceded that the pumping speed could be increased to 15 liters/sec.cm^2 with a combination of a more efficently designed mounting flange and, perhaps, with a less efficient baffle system. This, of course, implies a higher rate of cryogen use, but may be justified in order to increase the pumping capacity. The pumping speed for helium is roughly 75% of hydrogen and for air, ~5% of hydrogen.

If we assume a pumping speed for D & T of 13 liters/sec.cm^2, the pumping capacity of the system will be

$$S^{\circ}_{D,T} = 800\times10^{4}\text{cm}^2 \times \frac{13 \text{ liters}}{\text{sec.cm}^2} = 1.04\times10^{8}\text{liters/sec.}$$

CROSS SECTION VIEW OF UWMAK III

FIGURE III-B-1

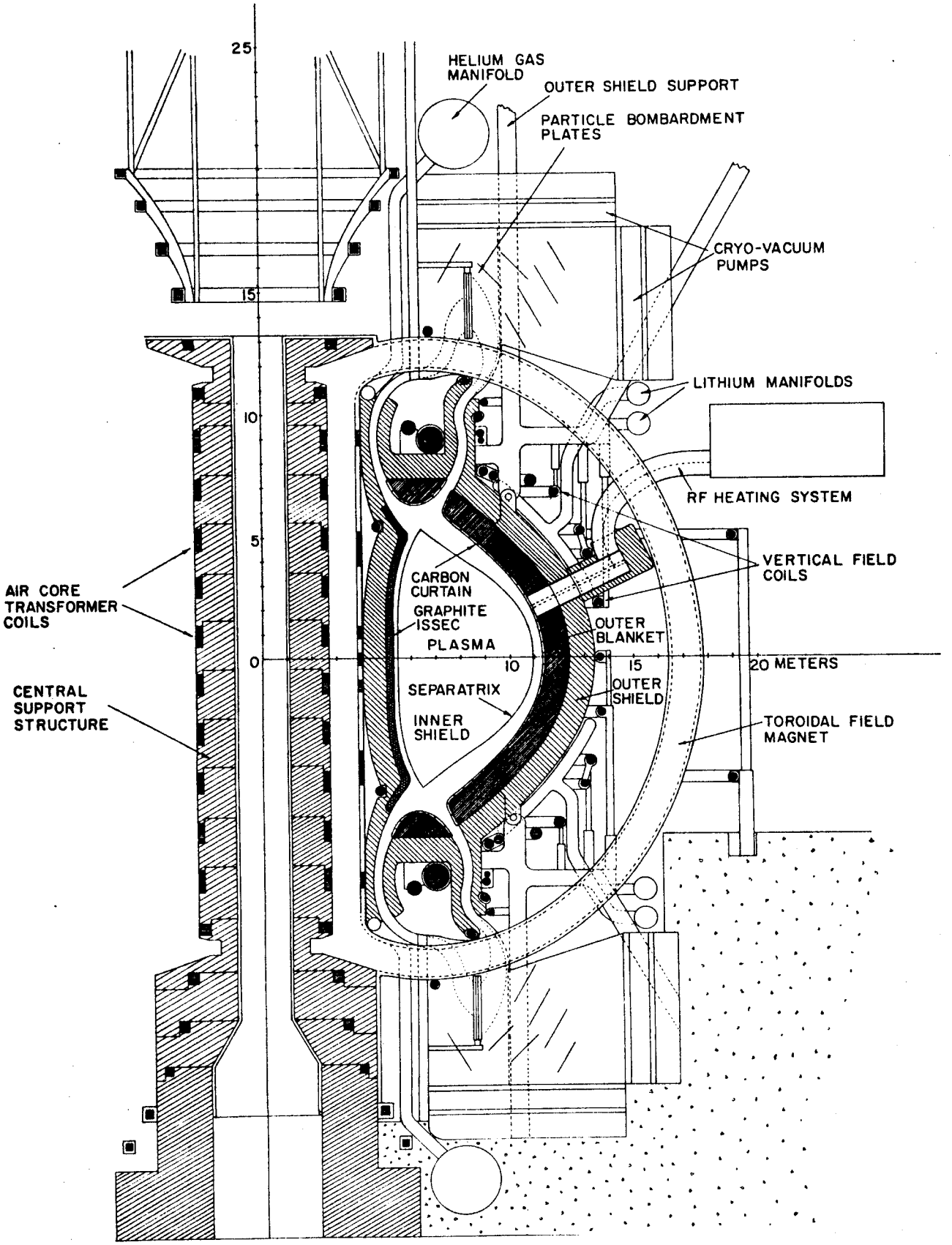

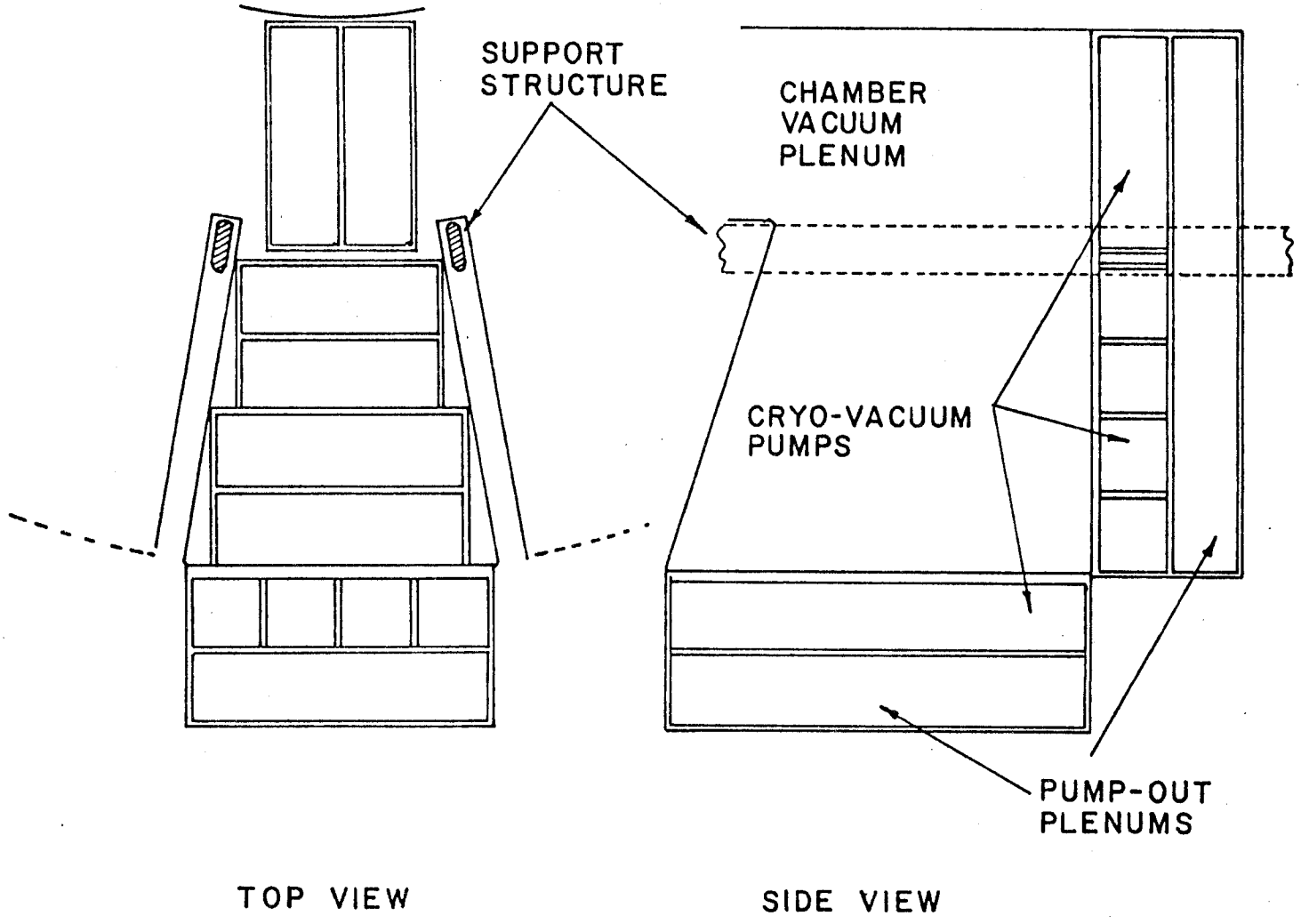

FIGURE III-B-2

Vacuum Pump Layout

$$S^{\circ}_{He} = 7.8 \times 10^{7} \text{ liters/sec}$$

$$S^{\circ}_{air} = 5.2 \times 10^{7} \text{ liters/sec}$$

The particle flux in the divertor zone is 3.15×10^{4} torr-liters/sec of D & T ions and 1.57×10^{3} torr-liters/sec of He ions, both at 588K. Cooled to 300K and recombined in molecular form, this is a throughput of 8.035×10^{3} torr liters/sec of D & T and 8.01×10^{2} torr liters/sec of He.

The base pressure that might be expected is then:

$$P^{\circ}_{D\&T} = \frac{8.03 \times 10^{3} \text{ torr liters sec}}{\text{sec. } 1.04 \times 10^{8} \text{ liters}} \approx 8 \times 10^{-5} \text{ torr}$$

$$P^{\circ}_{He} = \frac{8.01 \times 10^{2} \text{ torr liters}}{\text{sec } 7.8 \times 10^{7} \text{ liters}} \approx 1 \times 10^{-5} \text{ torr} \quad .$$

The toroidal magnet enclosure will be evacuated to a pressure of about 75 torr. The reactor containment building will be filled with helium at slightly less than an atmosphere of pressure and it is therefore safe to assume that the toroidal magnet enclosure will contain primarily helium gas. If we assume a leak rate per seal of about 0.02 liters/sec, which is consistent with a high vacuum seal in a vessel of this type, the total leak rate for 18 seals will be 0.36 liters/sec, or 27 torr liters/sec. This amounts to about 4% of the helium throughput and will not appreciably change the helium partial pressure.

III-B-4 Cryogenic Requirements

The heat load imposed on a cryo-pump by the gas being pumped is a tiny percentage of the total load, which is dominated by heat leaks to the cryo-panel. It is therefore entirely reasonable to extrapolate the cryogen requirement of a cryo-pump strictly on the basis of area.

Using data supplied by the Excalibur Corp., we find that the cryo-pumps will require about 65,000 liters/day of liquid helium and an additional 550,000 liters/day of liquid nitrogen. These values take into account the higher rate of cryogen consumption because of the higher pumping speed assumed. The 20K chevron panels are cooled by boil-off helium gas coming from the 5 K panels and therefore do not require a separate coolant.

The refrigeration needed to supply this amount of cryogenic fluid is 7.3KW at 4.2K and 1 MW at 77K. The combined power needed at 300K is 6.2MW.

III-B-5 Chamber Evacuation and Cleanup

Between burn cycles, the plasma chamber is backfilled with hydrogen gas to a pressure of $1x10^{-2}$torr and immediately pumped down to ~$1x10^{-8}$torr in order to clean and condition the chamber surfaces.

During the burn cycle, the ions follow flux lines through the divertor slots and the throughput is then essentially independent of the conductance of the slots. But during pumpdown, the speed of evacuation will depend on the conductance of the divertor slots, where flow in the molecular regime is dominated by the collisions of the molecules with the walls of the ducts.

For hydrogen molecules at an average temperature of 600K, the conductance of the divertor slots has been estimated to be ~$5x10^6$ liters/sec. The effective pumping capacity of the system is then,

$$\frac{1}{S} = \frac{1}{C} + \frac{1}{S_p} \quad \text{where } S_p \text{ is the pumping speed.}$$

$$\frac{1}{S} = \frac{1}{5x10^6} + \frac{1}{1x10^8}$$

$$S = 4.7 \times 10^6 \text{ liters/sec.}$$

The volume of the chamber is $2210m^3$, and the time to evacuate it from $1x10^{-2}$ torr to $1x10^{-8}$ torr can be obtained from:

$$p = p_o e^{-\frac{st}{v}}$$

where p is the final pressure
p_o is the initial pressure
t is time
v is chamber volume
s is the effective pumping speed.

Solving for t we get,

$$t = \frac{v}{s} \ln \frac{p_o}{p} \quad .$$

The time needed to evacuate the chamber is

$$t = \frac{2210x10^3 \text{liters sec}}{5 \times 10^6 \text{ leters}} \ln \frac{1x10^{-2}}{1x10^{-8}}$$

$$t \tilde{\sim} 6.5 \text{ sec.}$$

The volume of the vacuum plenum itself is $5260m^3$ but its evacuation is governed by the pumping speed of the vacuum system only. The total evacuation of the chamber and vacuum plenums to $1x10^{-8}$torr will be accomplished in less than 10 seconds.

III-B-6 Cryo-pump Regeneration

Saturation of the molecular sieve with D & T molecules is observed when 300 cm^3(STP) are absorbed per gram of molecular sieve at 77K. Performance is greatly enhanced at 5K. The amount of molecular sieve in the pumps on line is about 2000 Kg covering the panels to a depth of 3mm.

If we assume that the pumps will be regenerated every five hours, then the amount of gas collected in that period by the cryopumps is

2×10^5liters(STP) of D & T

2×10^4liters(STP) of He

and the amount absorbed by the molecular sieve is 100 cm^3(STP)/gm of D&T and 10cm^3(STP)/gm of He. This is still a long way from saturation at a temperature of 5K.

To regenerate the pumps, they are valved off from the plasma chamber and then opened up to the regeneration plenum. The molecular sieve is then warmed up to ~20K, and the other chevron panels to 40K and 100K respectively.

Large amounts of gas will be immediately liberated and will have to be pumped out. Regeneration need not take place at a very low pressure. A pressure of 70-100 torr would be quite satisfactory. At this pressure, dry compressors such as those built by Ingersoll Rand and others would be used to pump the gasses from the cryo-pumps and deliver them to the distillation columns at about one atmosphere, where isotope separation will take place. The gasses will not be oil contaminated and will not require any prior treatment before distillation. The gas temperature will still be low and will therefore save on the cryogenic refrigeration needed in the distillation column.

The time it will take to regenerate the pumps will be determined by the capacity of the dry compressors. A $6.7x10^3$liters/minute dry compressor will regenerate the pumps in one hour, which seems to be a reasonable time. Taking into account warm up and cool down, the cryo-pumps can be ready to be used again in an hour and a half.

III-B-7 Additional Vacuum Systems

The RF waveguides in UWMAK-III, of which there are twelve, will need separate vacuum pumps to insure a reasonably high vacuum within them to prevent arcing during start up. The conductance of an RF waveguide for hydrogen at 600K is about $2x10^4$liters/sec. Although the volume of the waveguide is small, since it is at the end of the line relative to the primary vacuum system its pressure will be higher than the system pressure.

It is therefore planned that each RF waveguide will have a single cryo-pump of $\sim 0.64 m^2$, with a pumping speed of 8.3×10^4 liters/sec for D&T. The pumps will be on during startup and will maintain a pressure of 2×10^{-5} torr in the waveguide. During the burn cycle, the pumps will be valved off to conserve cryogenic fluid.

The toroidal magnet enclosure will be evacuated to a pressure of ~75 torr. This pressure range was picked in order to avoid electrical breakdown. There are three primary reasons for an evacuated toroidal enclosure:

1. To collect any tritium diffusing from the plasma chamber
2. To prevent a lithium fire by excluding oxygen
3. To reduce the pumping load on the primary vacuum system due to leaks through the plasma chamber.

If we assume a leak rate through the toroidal enclosure vacuum wall of 10 liters/sec for each seal, the throughput will be 180 liters/sec or 1.37×10^5 torr liters/sec. The pumping speed needed to maintain a pressure of 75 torr is 1.8×10^3 liters/sec for helium. The volume of the toroidal enclosure is $6500 m^3$. The time it would take to evaluate it from atmospheric pressure to 75 torr is ~2.3 hours.

We expect to use dry vacuum compressors similar to those used for regenerating the cryo-pumps to evaluate the toroidal enclosure. Such dry compressors can be built in rather large capacity and are capable of continuous operation for sustained periods at those pressures. The main advantage is that the effluent will not be contaminated with oil and can be readily processed for tritium extraction.

III-C. The Particle Collector Plates

The particle collector plates in UWMAK-I and II consisted of a flowing lithium film to absorb both the D,T particles and the associated thermal energy. This design is not suitable for UWMAK-III due to the very large thermal load carried on the plates. The average thermal load in UWMAK-I was 1.0 MW/m^2. This load increased to 3 MW/m^2 in UWMAK-II, with the peak load estimated to be around 30 MW/m^2. The lithium temperature can only vary from 186°C (its M.P.) to 350°C (the B.P. at the plasma chamber pressure at 10^{-5} torr). With this very small coolant temperature rise available, and with the intense thermal load, the heat transfer problem becomes almost insurmountable.

The design philosophy for the particle collector plates in UWMAK-III has been completely changed. The pumping and heat transfer problems have been decoupled. The vacuum pumping capacity has been increased by more than one order of magnitude to compensate for the loss of pumping by the lithium film. The sole purpose of the collector plates is now to slow down the particles and convert their kinetic energy to thermal energy. A coolant is now required to transfer the thermal energy to a power conversion system. The vacuum pumping aspect has been discussed in the previous section. The mechanical design and the heat transfer problem in the collector plates will be discussed in the following section.

III-C-1. Mechanical Design

The main structure of the collector plate will consist of a bank of tubes which form the coolant passages. To avoid excessive sputtering due to incident high energy particles, a thin sheet of TZM is used to cover the main plate. Good thermal contact between the sheet and the plate is maintained by means of a liquid lithium film which fills the void between them. The main sheet of TZM acts as a sacrificial wall provided against particle sputtering and will be designed to allow frequent replacement. One of the most important questions is then, how often does the sacrificial wall have to be replaced. A schematic drawing of the particle collector plate is shown in Figure III-C-1.

The location of the collector plate is outside the toroidal magnet enclosure between the magnet, at a major radius of 7 meters. There are 36 collector plates, each 1.14 m wide and 3 m high giving a total surface area of 123 m^2. The sacrificial wall is 0.1 mm thick, weighing a total of 125 Kg per replacement.

The erosion due to physical sputtering by many types of species may be calculated by[1]

$$d(t) = S\phi \frac{t\ A_w}{N_o\ \rho}$$

FIGURE III - C - 1

SCHEMATIC DRAWING OF THE COLLECTOR PLATE DESIGN FOR UWMAK III

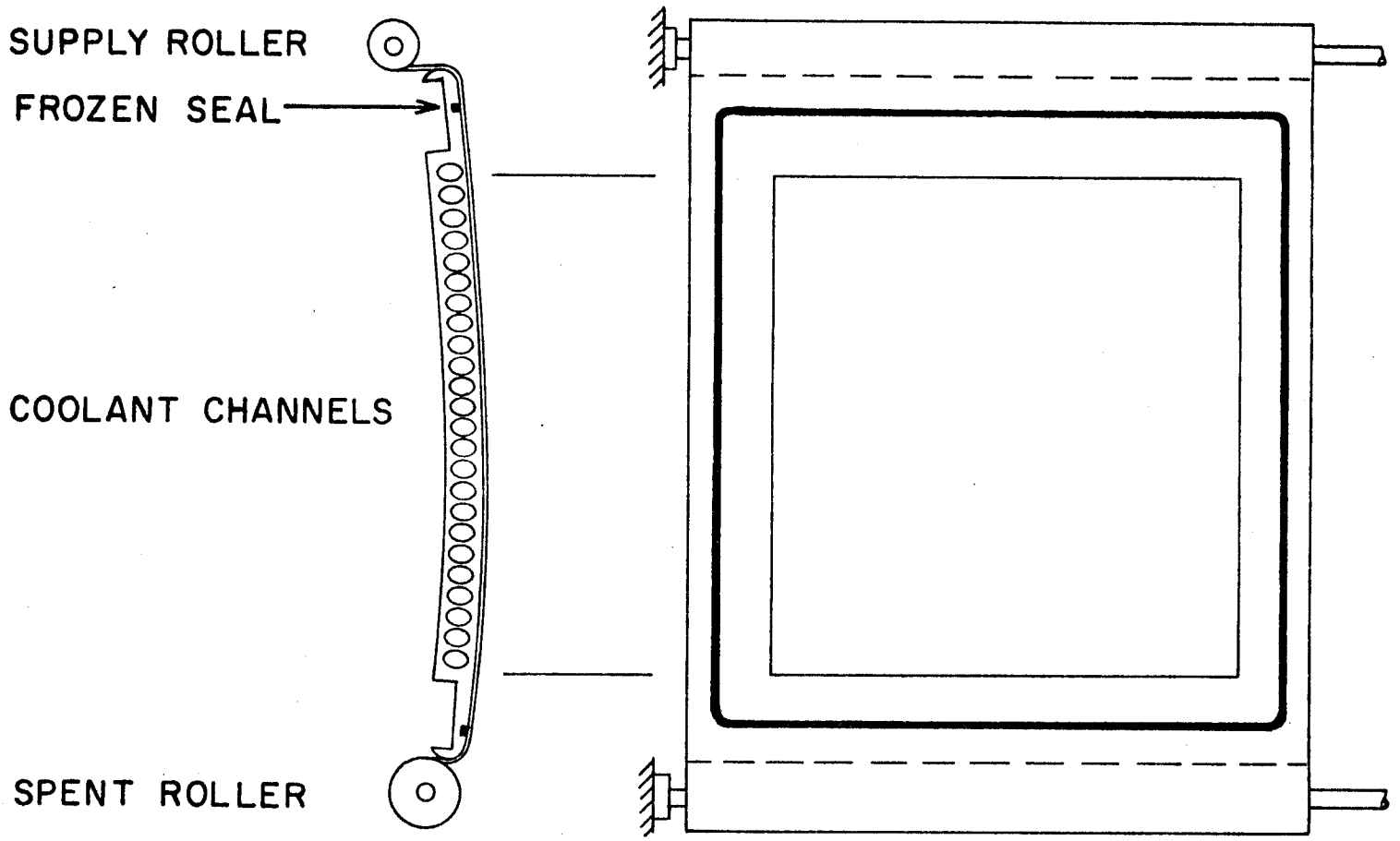

where S is the sputtering yield in atoms per particle

ϕ is the flux of bombarding particles

A_w is the atomic weight of the material

t is the irradiation time

N_o is the Avogardo's number

ρ is the density of the wall material

For the interaction of TZM with D,T particles, S is about .005. The particle flux is 5.2×10^{23}. The erosion rate from the sacrificial wall is .041 cm^3/sec, at 1490 g/hr. Assuming that 20% of the sacrificial wall material can be eroded, the time between replacements is 17 hrs. The material required for the sacrificial wall is 180 Kg/day.

Since the sacrificial wall has to be replaced frequently, a periodic automatic replacement process is envisaged which is shown schematically on Fig. III-C-1. The thin TZM sheet is fed from a supply roller and taken up on a spent roller. A frozen lithium seal is provided on the periphery of the plate to prevent lithium from leaking out. After a TZM sheet has been in service for 17 hours, the peripheral seal is melted and the sheet advanced until new material covers the plate. The seal is then allowed to solidify again. This process can be carried out during a burn cycle with no downtime for the reactor. A cross section of the collector plate is shown in Fig. III-C-2.

III-C-2. Tritium Diffusion Considerations

The energetic D,T particles impinging on the collector plate will bury themselves to a certain depth. While most of the tritium atoms will diffuse back into the vacuum, are recombined and pumped away as T_2 molecules, a small fraction will stay in the TZM sheet and are eventually trapped in the spent roller. It is important to estimate the amount of tritium which is lost in this way.

The diffusion model is illustrated on Fig. III-C-3, with δ as the penetration depth of the tritium particles, and L the thickness of the sacrificial wall. The diffusion equations and the boundary conditions are:

Region I -

$$D\nabla^2 C + G = 0 ,$$

$$C = C_s \text{ at } x = -\delta,$$

$$\frac{\partial c}{\partial x}\Big]_o \text{ (region I)} = \frac{\partial c}{\partial x}\Big]_o \text{ (region II)} ,$$

$$C]_o \text{ (region I)} = C]_o \text{ (region II)}.$$

FIGURE III - C - 2

CROSS SECTION OF COLLECTOR PLATE

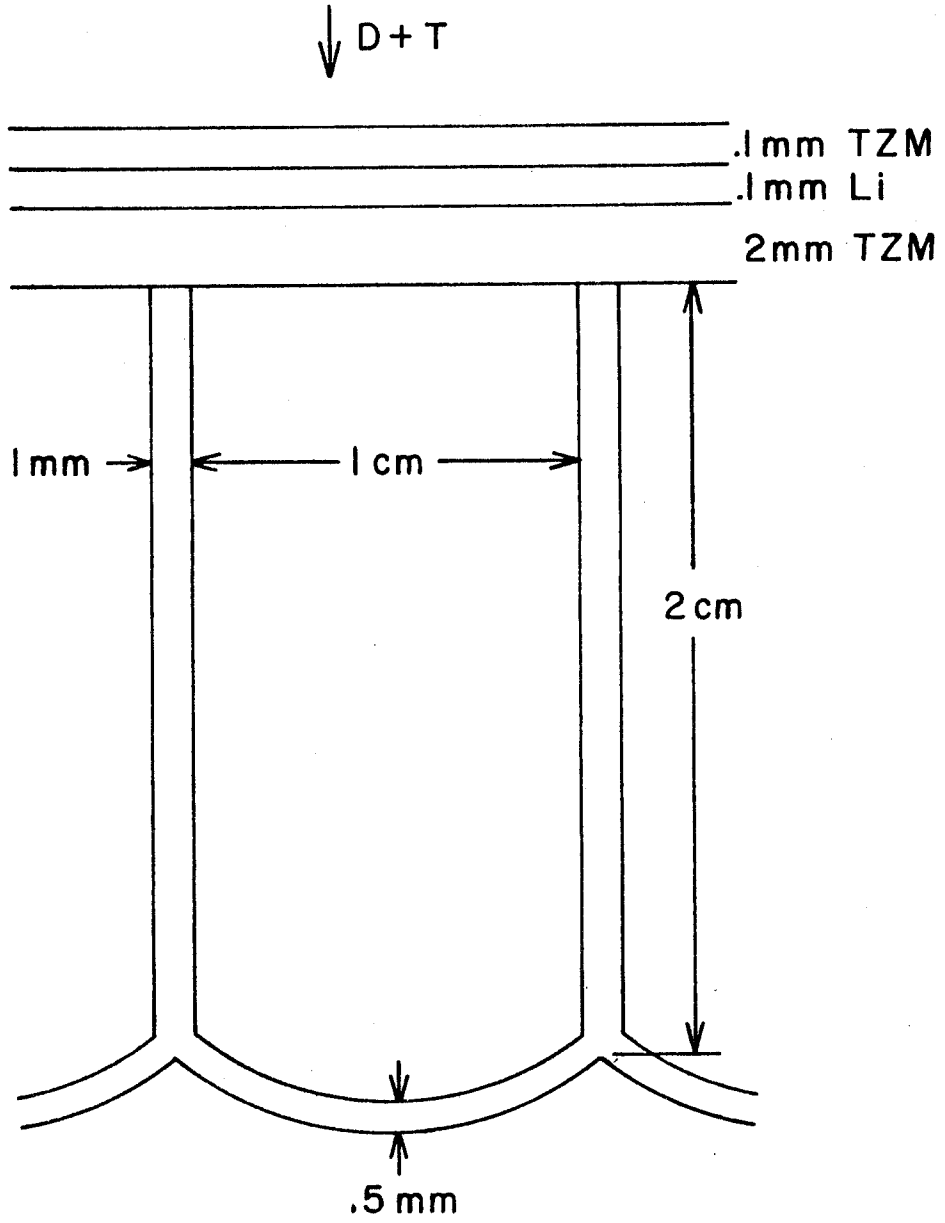

FIGURE III - C - 3

DIFFUSION MODEL

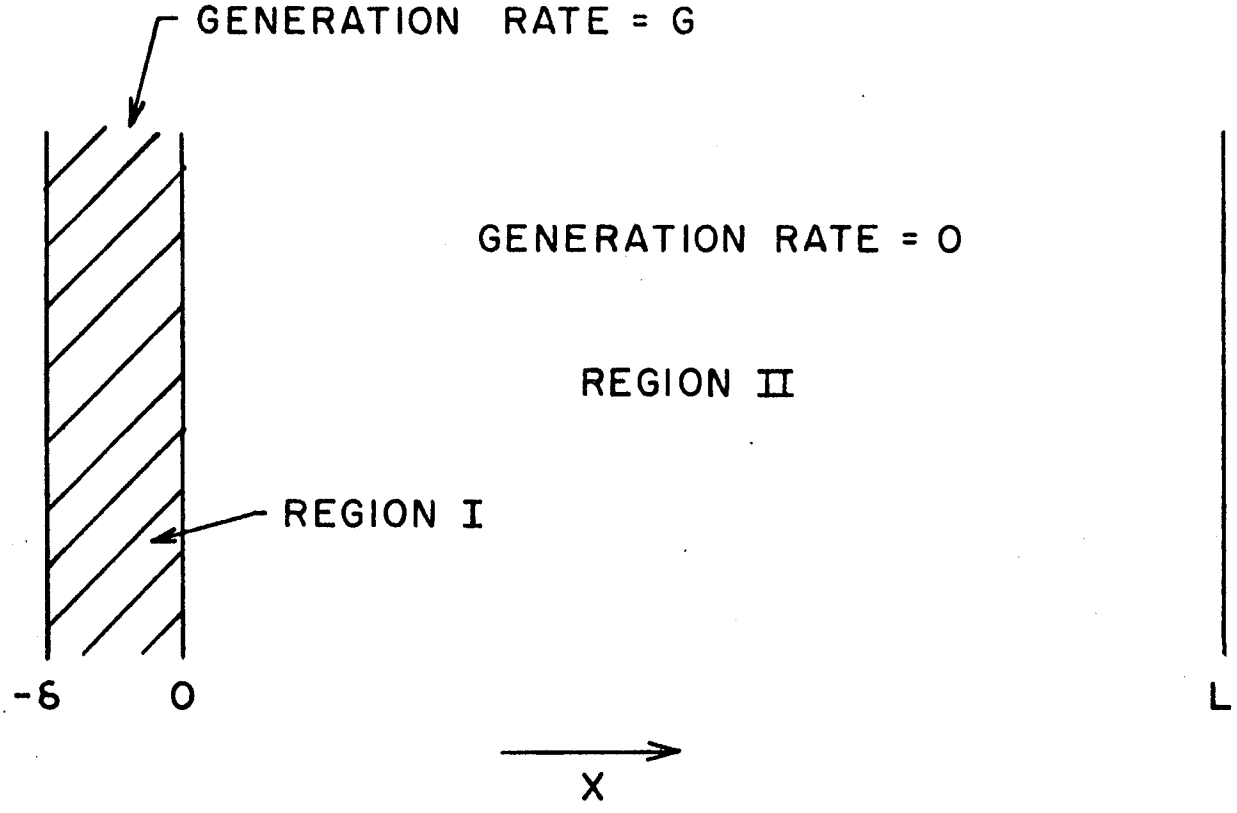

Region II -

$$D\nabla^2 C = 0 ,$$

$$C = C_L \text{ at } x = L .$$

The solution is:

Region I -

$$C = \frac{G}{2D}(\delta^2 - x^2) - \frac{G\delta^2(x+\delta)}{2DL(1+\delta/L)} + \frac{C_L - C_S}{L+\delta}x + \frac{C_S L + C_L \delta}{L+\delta}$$

Region II -

$$C = -\frac{G\delta^2(x-L)}{2DL(1+\delta/L)} + \frac{C_L - C_\delta}{L+\delta}x + \frac{C_\delta L + C_L \delta}{L+\delta}$$

The tritium concentration per unit area of wall is

$$C^* = \int_{-\delta}^{o} C\,dx)\text{region 1} + \int_{o}^{L} C\,dx)\text{ region II}$$

$$= \frac{G\delta^2 L}{4D}\left[\frac{4}{3}\frac{\delta}{L} - \left(\frac{\delta}{L}\right)^2 \frac{1}{1+\delta/L} + \frac{1}{1+\delta/L}\right]$$

$$\cong \frac{J\delta L}{4D} + \frac{C_L + C_S}{2} L \qquad \text{if } \delta/L << 1$$

where J = incident particle flux ($J/\delta = G$)

$L \cong$ thickness of the wall

δ = penetration depth

D = diffusivity

C_L, C_S = concentrations maintained at back and front of the wall, respectively.

The first term is due to supersaturation and the second term is the saturation contribution.

The individualterms in the solution can be estimated as:

1. Particle Flux

$$J = 5.2 \times 10^{23} \text{ atom/sec}/123 \text{ m}^2 = 4.2 \times 10^{17} \text{ atom/sec-cm}^2$$

2. Solubility

From Smithel's Handbook on Metals[2], solubility of H_2 in Mo is:

$$\text{Log } S/P^{1/2} = -1370/T - .671 + 1.440$$

S = solubility

T = deg K

P = atmospheres

This may be rearranged as

$$S = K_s\sqrt{P}$$

and $$K_s = 3.2 \times 10^{19} \exp[\frac{-6310}{RT}] \frac{\text{atoms}}{\text{cm}^3 \text{Atm}^{1/2}}$$

3. Diffusivity D: This must be estimated from the permeability.

The permeability relationship is

$$J_{\text{particles}} = K_p \frac{(\sqrt{p_1} - \sqrt{p_2})}{x}$$

where x = plate thickness between points 1 and 2 . In our case, it is conservative to assume that the permeability is diffusion controlled, so that the flux must also be given by

$$J = \frac{D(C_1 - C_2)}{x} = \frac{DK_s(\sqrt{p_1} - \sqrt{p_2})}{x}$$

so that $$D = K_p/K_s$$

From Smithel's Handbook,[2] the permeability is given as

$$K_p = 9.3 \times 10^{-4} \, e^{-20,200/RT} \text{ cc(STP) sec}^{-1}\text{cm}^{-1}(\text{mmHg})^{-1/2}$$

which may be converted to

$$K_p = 1.37 \times 10^{18} \, e^{-20,200/RT} \text{ atom}\cdot\text{sec}^{-1}\text{cm}^{-1}\text{Atoms}^{-1/2}$$

Consequently, D is given by

$$D = K_p/K_s = 4.27 \times 10^{-2}\ e^{-13,900/RT}\ cm^2/sec.$$

With the individual terms so obtained, the tritium content in the sacrificial wall can be calculated. This is the steady state tritium content in the sacrificial wall and is presumed to be lost to the spent roller whenever the wall is changed, or once every 17 hours. The tritium diffusion results are shown on Table III-C-1.

Table III-C-1

Tritium Diffusion Results in Collector Plates

T(°C)	Super Saturation atom/cm^2	Saturation atom/cm^2	Total atom/150m^2	Total grams
1000	5.8×10^{13}	1.4×10^{12}	7.3×10^{19}	3.2×10^{-4}
1100	3.9×10^{13}	1.6×10^{12}	5×10^{19}	2.2×10^{-4}
1200	2.8×10^{13}	1.9×10^{12}	3.7×10^{19}	1.4×10^{-4}

If the sacrificial wall is at 1000°C, the total amount of tritium trapped in the roller is only 4.5×10^{-4} grams/day.

III-C-3. MHD and Heat Transfer Calculations

The MHD effects on pressure drop have been discussed in References 3 and 4. This pressure drop can be classified into two categories: the Hartmann and end-of-loop effects.(3) The Hartmann pressure gradient arises in fully-developed laminar flow with a uniform transverse magnetic field, while the end-of-loop effect is caused by gradients of $[\underline{V} \times \underline{B}]$ in the flow direction. The pressure drops caused by those two effects can be calculated by the following two equations; the total pressure drop equals the sum of the two effects.

The Hartmann pressure gradient is given by,

$$-\frac{dp}{dx} = \frac{VB_\perp^2 \sigma \omega t \omega}{a(1 + c)} \quad ,$$

and the end of loop pressure drop is given by

$$\Delta p = k_{PIE} \frac{\sigma b}{V_{av}} \Delta(V^2 B_\perp^2),$$

where c is the wall conductive ratio, $\sigma\omega t\omega/\sigma a$

a is the half-width of the cooling channel

$\sigma\omega$ is the electrical conductance of the wall material

$t\omega$ is the wall thickness

V is the velocity

b is the half-width of the cooling channel in a direction normal to $B_\perp$

k_{PIE} is the geometry coefficient as shown on Figs. III-C-4 and III-C-5.

The magnetic field along the collector plate is calculated in the previous section and is shown on Fig. III-C-6.

The geometry of the collector plate and the coolant channel has been shown on Fig. III-C-1 and III-C-2. The heat flux on the surface is 5.87 MW/m^2. With these calculations, the MHD effects can be calculated and the results are shown on Table III-C-2. The total pressure drop is 100 psi.

The MHD effects on heat transfer have been estimated by Hoffman and Carlson.[37] For a Hartmann flow, the following equation can be used

$$\frac{hD_h}{k} = 12.0$$

where h is the heat transfer coefficient

D_h is the hydraulic diameter

k is the thermal conductivity

The steady state temperature calculation can thus be performed and the results are listed on Table III-C-2. The coolant exit temperature is 600°C, compared to 300°C for UWMAK-I design.[1] This coolant will then be fed to a steam generator. This is discussed in Chapter IX.

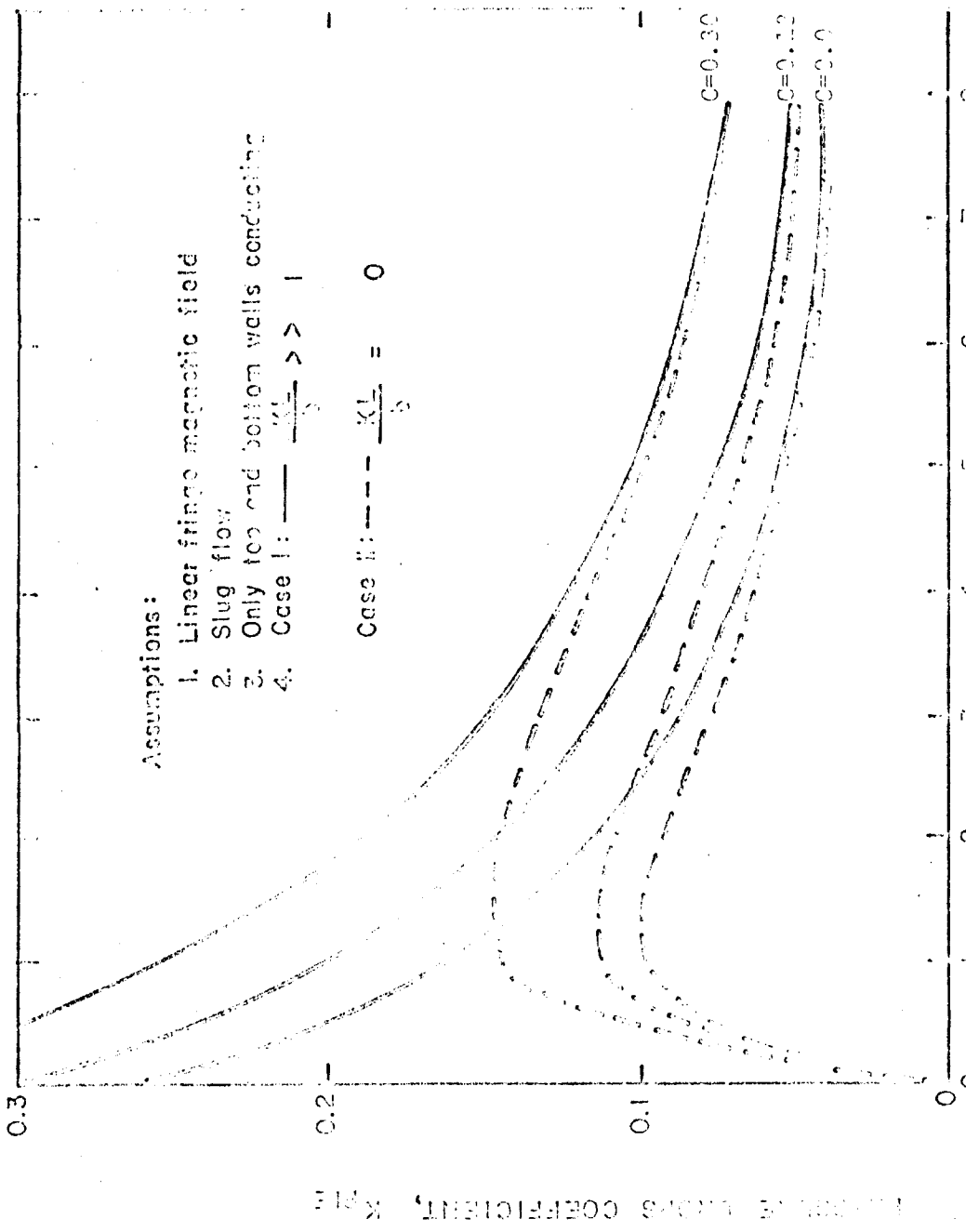

FIG. **III-C-4** PRESSURE DROP DUE TO ENTRANCE OR EXIT EDDY CURRENTS.

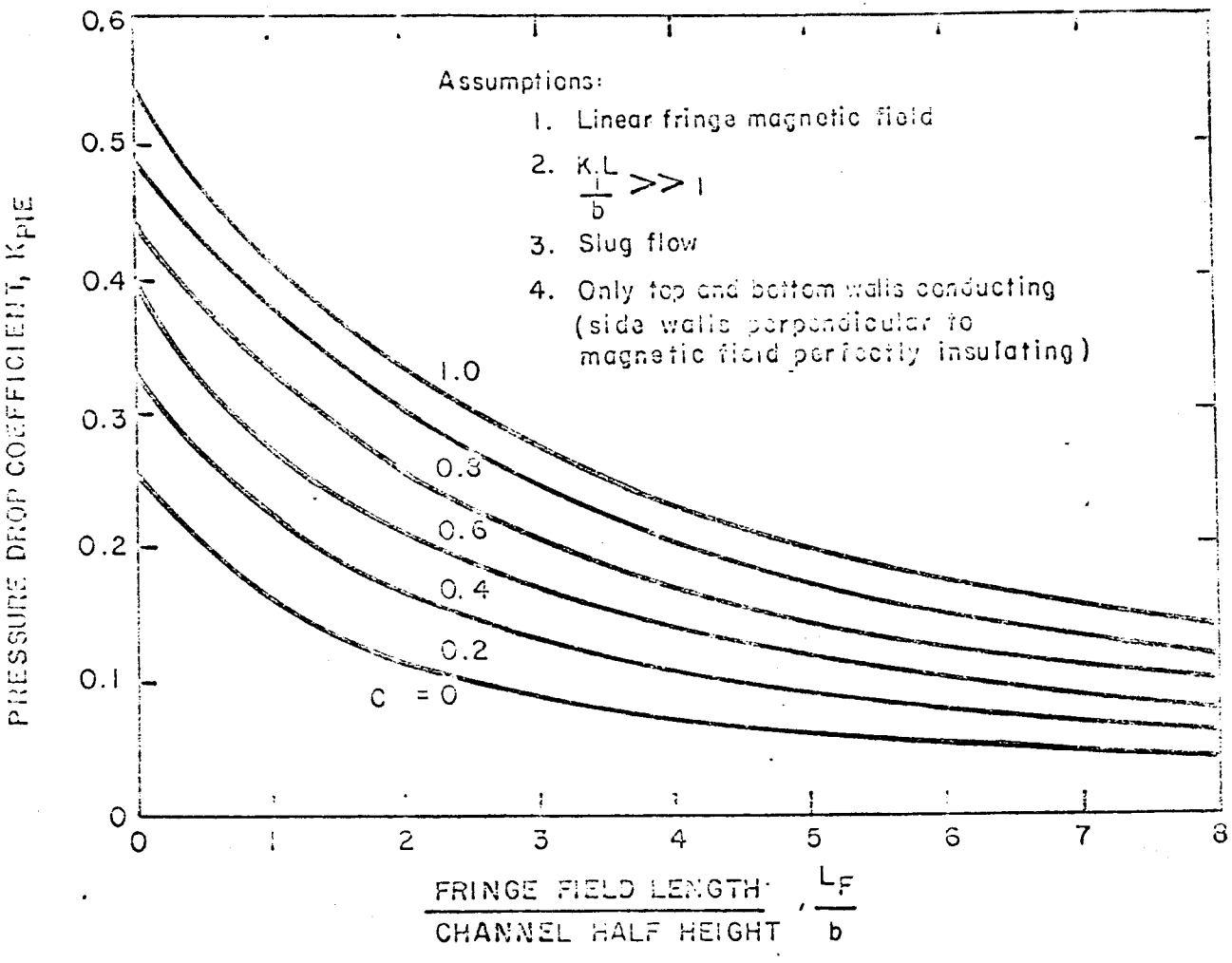

FIG. III-C-5 PRESSURE DROPS DUE TO ENTRANCE AND EXIT EDDY CURRENT FOR LINEAR FRINGE MAGNETIC FIELDS SEPARATED BY A LONG REGION OF UNIFORM MAGNETIC FIELD.

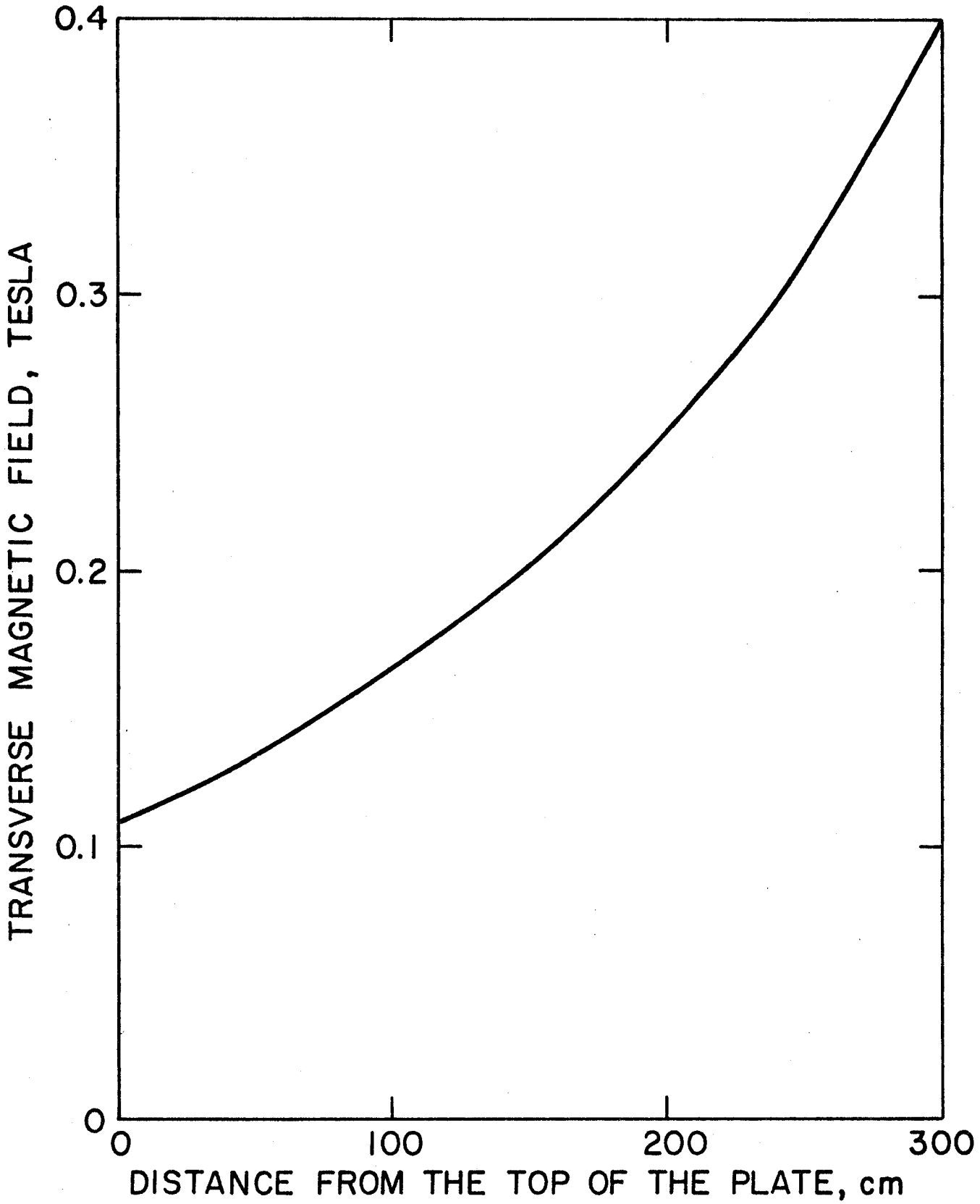

FIGURE III - C - 6 MAGNETIC FIELD ALONG A COLLECTOR PLATE

Table III-C-2

Summary of the Collector Plates Calculations

Thermal Load	725 MW
Total Area	123 m^2
Sacrificial Wall Thickness	.1 mm
Sacrificial Wall Replacement Rate	Once Every 17 Hours
Structure Material	TZM
Structure Temperature	680 to 880°C
Coolant	Na
Coolant Temperature	400 to 600°C
Coolant Flow Rate	3.12×10^6 Kg/hr
Coolant Velocity	4.27 m/sec
Maximum Magnetic Field	0.4 Tesla
Pressure Drop	100 psi
Pumping Power	1 MW

References for Section III-C.

1. University of Wisconsin Fusion Feasibility Study Group, "UWMAK-I, A Wisconsin Toroidal Fusion Reactor Study" (March 1974).

2. C. J. Smithel , "Metal Reference Book," Plenum Press, N. Y., 1967.

3. M. A. Hoffman and G. A. Carlson, "Calculation Techniques for Estimating the Pressure Losses for Conducting Fluid Flows in Magnetic Fields," USAEC Report UCRL-51010, 1971.

4. G. W. Sutton and A. Sherman, Engineering Magnetohydrodynamics, McGraw Hill, N. Y., 1956.

IV. Magnet System

The material in this chapter covers the design of the magnets and the associated equipment and supporting structures. Included are the toroidal field magnets, the ohmic-heating magnets, the vertical field magnets and the magnetic energy storage system used to limit the pulsed power demands on the electric utility power system. In all cases, including the external magnetic energy storage system, all of the magnets are superconducting and are fully cryogenically stabilized. TiNb superconducting filaments are processed in an OFHC copper matrix for convenience but stabilized with high-purity aluminum in the case of the toroidal field magnets. The vertical field and ohmic-heating magnets use cold worked OFHC copper for both stabilizer and structure with some stainless steel used in addition in the more highly stressed vertical field magnets. Details of the design factors, construction and assembly techniques, heat losses, and power requirements are included.

The toroidal field coils have a modified constant tension "D" shape, corrected for the field variation due to the finite number (18) of coils.[4] The embedded conductor in a solid "D" shaped alloy aluminum former is used to minimize the material requirements while providing maximum strength and stiffness. This construction was described in detail in the UWMAK-I report.[1] The cold central structure and the secondary vacuum wall used in the UWMAK-II[2] design are retained.

The vertical field coils are constructed inside the toroidal field magnets as they were in UWMAK-II.[2] The maximum stored energy in these coils is less than in UWMAK-II primarily due to the increased magnetic field utilization for non-circular plasmas. A 4-element conductor introduced by D. Cornish[3] has been modified to accomodate the requirements of both the vertical field magnets and the ohmic heating magnets. The improved cooling afforded by this design has allowed an increase in the current density at full cryogenic stability and this fact coupled with smaller diameter coils results in a less expensive set of magnets.

IV-A. Toroidal Field Magnets

In this section we describe the design of the toroidal field magnets. The design philosophy is unchanged from that of UWMAK-I[1] and UWMAK-II,[2] that is, the need for full cryogenic stability and reliable solid structures. The design is a slightly modified constant tension "D" shaped toroid producing a magnetic field of 4.05 tesla at a radius of 8.1 meters, the plasma center.

The vertically elongated plasma and a new blanket removal scheme coupled with only 18 toroidal field magnets instead of the 24 used in UWMAK-II permits the use of much smaller TF magnets. The inside surface of the outer leg is at 16.5 m as shown in Fig. IV-A-1. The shape of the constant tension "D" naturally accomodates a vertically elongated plasma. In this case, the plasma, blanket, shield and divertors would fit within a "D" shape based on a 1/R

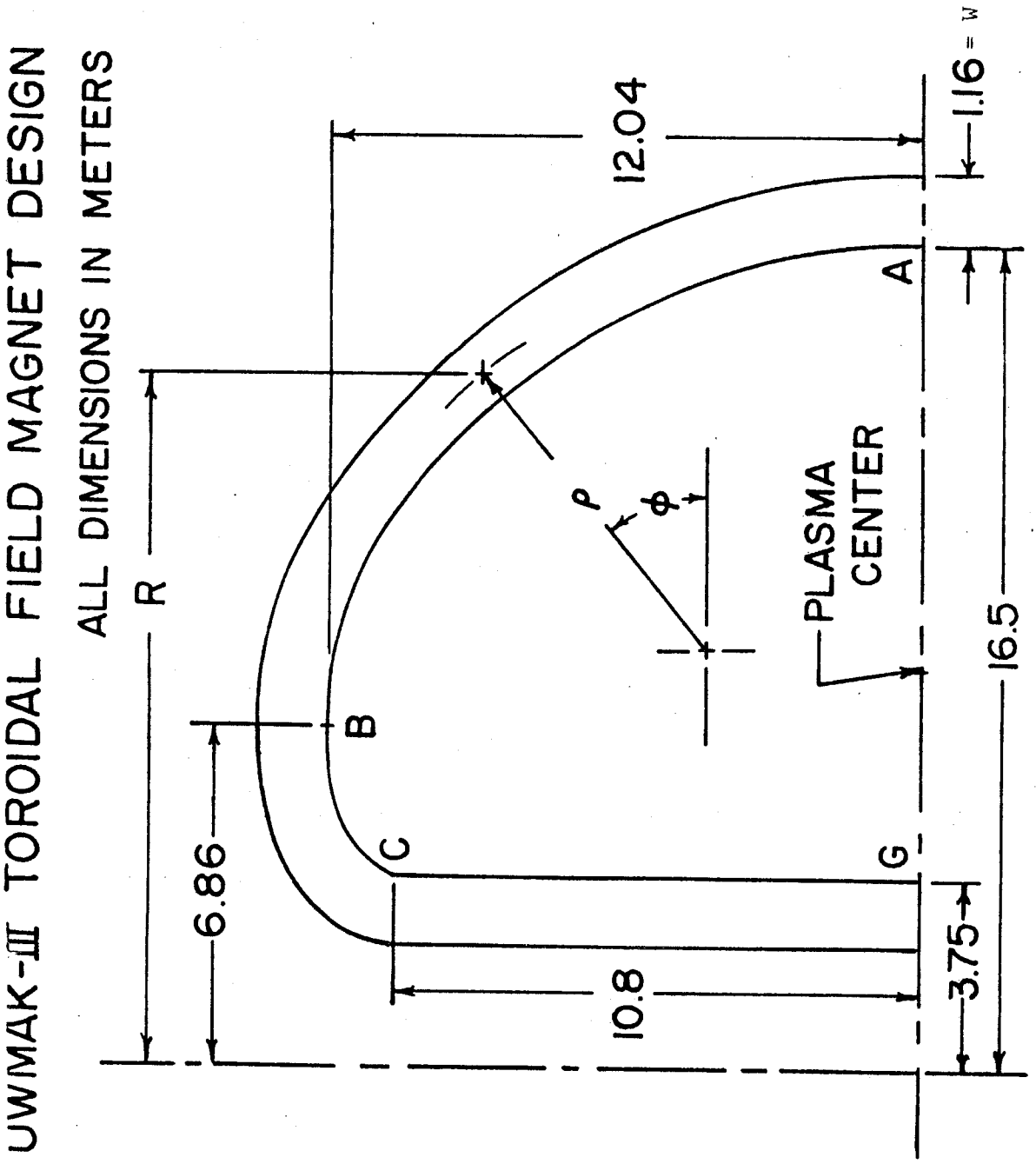

FIGURE IV-A-1
"D" Shaped Toroidal Field Magnet Design

field variation i.e. a field variation produced by a continuously wound toroid. However, since the local fields near the 18 individual windings are higher due to sector caused field perturbations, the resultant specific "D" shape which becomes vertical at the desired position on the inside leg is not high enough to clear the interior structure. Figure IV-A-1 shows the shape of the modified "D" chosen for additional height. From point A to point C the magnet has a constant tension shape. For a continuously wound toroid, the shape A to C could be described by a radius of curvature ρ proportional to the radial distance from the axis of the toroid, as

$$\rho = KR \tag{1}$$

For sectored toroidal coils, such as those used in UWMAK-III one should correct for the local perturbations of the magnetic field due to the flux leakage between the finite number of finite coils. An analytic expression for the radius of curvature ρ from work by R. Moses and W. Young[4] is

$$\rho = KR \left[\frac{1}{1 + \frac{1}{N}\left(\cos\phi + \frac{R}{\rho} \ln \frac{1.284R}{CN}\right)}\right] \tag{2}$$

where: (see Fig. IV-A-1)

K = a constant directly proportional to the design tensile force and inversely proportional to the square of the total current in a coil

R = distance from major toroid axis

N = number of discrete magnets in the toroidal field system

ϕ = angle from midplane to a normal vector

C = radius of TF coil cross section if the "D" magnet has a round cross section or it is approximately $W/\sqrt{\pi}$ if the cross section is a square of width W. (W is shown in Fig. IV-A-1).

Solving Eq. (2) for a square cross section gives:

$$\rho = \frac{R\left[K - \frac{1}{N} \ln \frac{2.276R}{WN}\right]}{1 + \frac{\cos\phi}{N}} \quad . \tag{3}$$

Eq. (3), although approximate, gives results that agree within a few percent to values found by much more difficult to use iterative procedures discussed in references 6 and 7.

The support system to accomodate the discontinuity at point C is discussed in detail in Section IV-A-4-a.

A lack of circumferential space around the central core does not allow extra discs per sector to provide the redundancy and reliability possible in the UWMAK-II design.(2) Redundancy is provided, however, by sizing the aluminum conductors such that a current of 10,909 A in the conductors of 14 disks of one magnet would provide the necessary field and still be cryogenically stable with a heat transfer coefficient of 0.35 watts/cm^2 into 4.2 K liquid helium. Normal operation will be with all 16 disks operating at 88% design current with a 0.24 W/cm^2 required heat transfer coefficient. As in the UWMAK-II design, provision is made to disconnect and isolate the conductors in case it is desirable to operate without a disc. This can be done without warm up and disassembly. The stress analysis was carried out using 16 disks and a design stress level of 3.11×10^8 N/m^2 (45,000 psi) in the 2219-T87 aluminum alloy was taken.

IV-A-1. Specifications

Table IV-A-1 lists the specifications of the toroidal field magnets and compares them to those of the designs for UWMAK-I(1) and UWMAK-II.(2)

IV-A-2. Materials

UWMAK-III is designed with aluminum alloy structure and aluminum stabilized composite conductor in contrast to the stainless-steel structure and copper stabilizer used in UWMAK-I and II. The result is a saving in weight and cost.

It has long been recognized that an aluminum stabilizer could be attractive because of its potential lower resistivity and reduced magneto-resistance. However aluminum has not been used because of its low yield stress of 2~4000 psi and large resistivity increases with strain. Our decision to use an aluminum matrix conductor is based on experiments of Boom(10) and Segal(5) which are beginning to show that under some circumstances the resistivity of over-strained aluminum will not increase excessively. These experiments involve mechanically reinforced high purity aluminum wires which have been cyclically strained to values of $\varepsilon \sim 0.1\%$, see Fig. IV-A-2. Translating from RRR, residual resistivity ratio, to resistivity, the data plotted in Fig. IV-A-2 indicate that for 2000 strain cycles the resistivity of high purity aluminum may be less than ρ_0 (B=0) $\approx 1.7 \times 10^{-9}$ Ω cm which is 1/6 the OFHC copper resistivity used in previous designs. This aluminum resistivity will saturate in high fields to about 7×10^{-9} Ω cm compared to $\sim \times 10^{-8}$ Ω cm for copper at 8 T. (Copper does not saturate but obeys the empirical equation $\rho \sim 10^{-8}$ (1 + B/2) Ωcm, where B is in tesla). We have used $\rho = 10^{-8}$Ω cm everywhere for the aluminum stability calculations.

Worzala(11) has noted one possible reason for this newly found aluminum insensitivity to excess strain. With electron microscopy he has seen evidence for the development of "easy glide slip planes" in the cycled samples. It is possible that easy glide slip planes at low temperature would not necessarily continue to generate new dislocation tangles with repeated strain cycling and therefore could be responsible for a saturation resistivity which is <u>independent</u> of strain at an unexpectedly low value of resistivity.

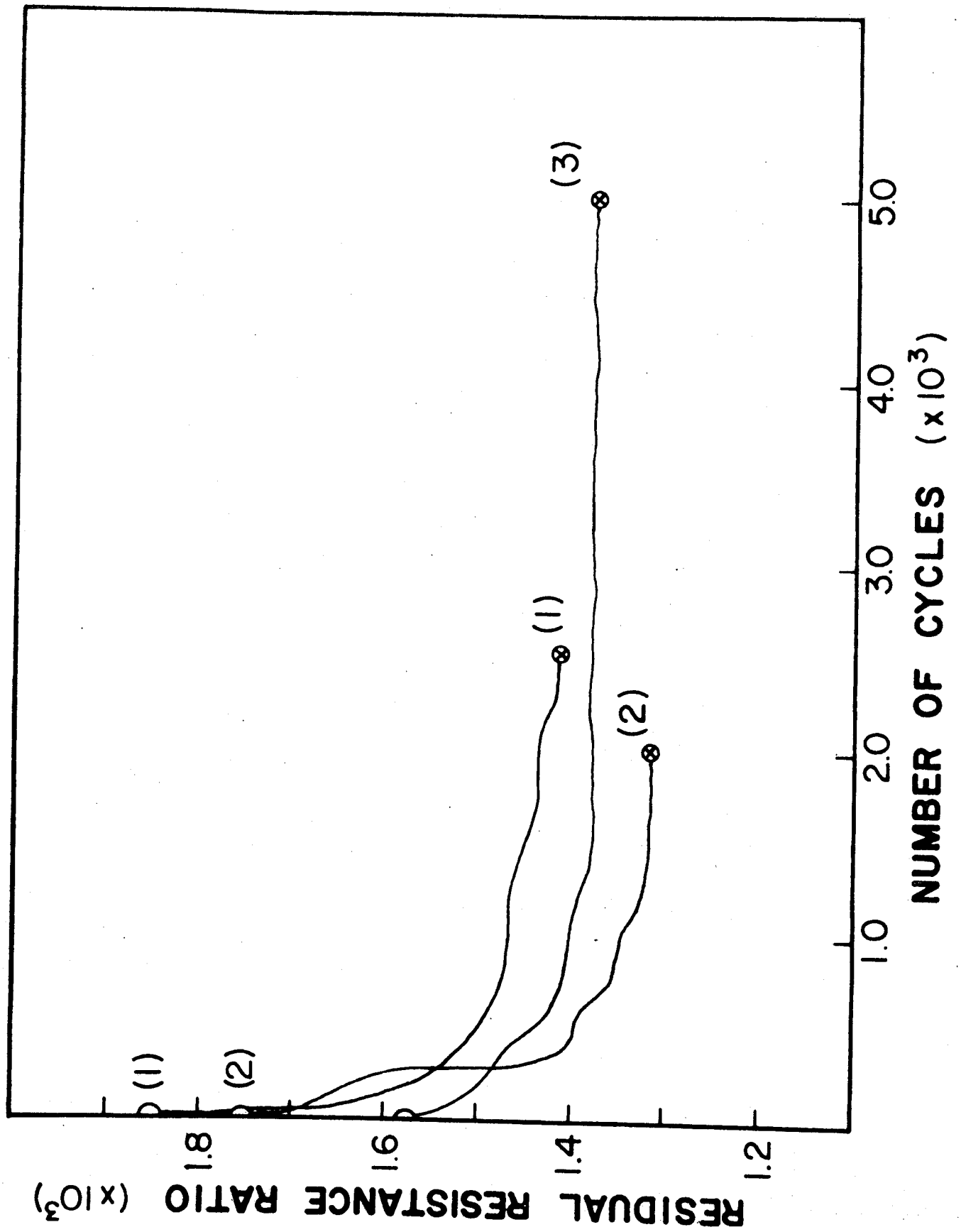

Figure IV-A-2 Change in the residual resistance ratio with the number of strain cycles to 0.1% strain for reinforced elastic samples. Test condition: 4.2 K and B = 0.

Table IV-A-1

Specifications of Toroidal Field Magnets

	UWMAK-I	UWMAK-II	UWMAK-III
a. Field Specifications			
On-axis field, B_o	3.83T @ 13m	3.67T[(a)] @ 13m	4.05T @ 8.1m
Field at inside turn of far edge (point A)	2.42T @ 20.5m	1.91T @ 25M	1.99T @ 16.5m
Maximum field at the conductor, B_m (point C)	8.66T @ 5.75m	8.30T @ 5.75m	8.75T @ 3.75m
Field Ripple along the far edge of the plasma	20%	0.05%	≈ 1%
Total electromagnetic energy stored in TF coils	44 MWh	62 MWh	30 MWh
b. Design Stress			
Maximum design stress in 316 stainless steel at 4.2K for UWMAK-I and II or in 2219-T87 aluminum at 4.2K for UWMAK-III	$4.14 \times 10^8 N/m^2$ (60,000 psi)	$4.14 \times 10^8 N/m^2$ (60,000 psi)	$3.11 \times 10^8 N/m^2$ (45,000 psi)
Design strain	$\leq$ 0.002	$\leq$ 0.002	$\leq$ 0.0038
c. Magnet Components			
Number of magnets	12	24	18
Number of discs per magnet	34	19	16
Number of conductor turns per disc. In UWMAK-III the two end discs have no turns on outer surface	60 (30 each side)	58 (29 each side)	64 (32 each side)
Conductor current	10,212 Amp	9,065A @ 19 discs 10,131A @ 17 discs 11,482A @ 15 discs	9,545A @ 16 discs 10,909A @ 14 discs
Disc cross section (see Figure III-A-2)	5 x 93 cm	5 x 98 cm	5 x 116 cm
Superconductor composite: TiNb in copper matrix, filament diameter = 0.038 cm, twisted every 30 cm	600 filaments	500 filaments	182 filaments
Stabilizer cross section, copper in UWMAK-I and II, aluminum in UWMAK-III	2.99 cm wide x 2.00 cm thick on inside turn, tapers to 1.10x1.60 cm on outermost turn	2.87 cm wide x 190 cm thick on inside turn, tapers to 1.70 x 1.13 cm on outermost turn	1.5 x 1.5 cm
Average stabilizer to superconductor ratio (volumetric)	29:1	30:1	19:1

Table IV-A-1 (continued)

	UWMAK-I	UWMAK-II	UWMAK-III
Insulation between conductor and stainless steel disc	0.10 cm reinforced epoxy	0.10 cm reinforced epoxy	0.05 cm reinforced epoxy
Spacer between discs	0.64 cm thick micarta, covering 50% of the area		
Aluminum alloy bolts to fasten the discs together against slipping, 2.54 cm diameter	1670	2630	1250
Lateral support between the magnet and dewar: reinforced epoxy struts on each side of cross section	8500 cm^2	5500 cm^2	3500 cm^2
Each magnet weight	900 Mt[(b)]	710 Mt	174 Mt
d. Total materials required in magnet system			
TiNb alloy superconductor	104 Mt	164 Mt	76 Mt
Stabilizer material	4890 Mt Cu	8000 Mt Cu	717 Mt Al
Structural disc material	4500 Mt	7230 Mt	2290 Mt
Dewars	932 Mt (including core dewar)	941 Mt (removable portion only)	730 Mt (alumimum) 119 Mt (SS)
Reinforced epoxy in discs	264 Mt	395 Mt	43 Mt
Micarta spacers between discs	147 Mt	255 Mt	108 Mt
Reinforced epoxy struts in dewars	12 Mt	16 Mt	10 Mt
Aluminum alloy bolts to assemble discs	55 Mt	95 Mt	34 Mt
Cryogenic insulation	516,000 m^2	850,000 m^2	503,000 m^2
Liquid helium inside dewars	100,000 liters	160,000 liters	144,000 liters

(a) T ≡ Tesla = 10^4 Gauss

(b) Mt ≡ Metric ton = 10^3kg.

The difference between these findings and earlier aluminum experiments is that they dealt with unsupported samples which were strained beyond the aluminum yield point. Such samples became plastically deformed and would continue to increase in resistivity. Our experiments are realistic engineering tests of supported samples. The gross structure of a magnet must be mechanically elastic, otherwise a magnet would tear itself apart. Any conductor, copper or aluminum, in effect is bonded to the steel or alloy structure and must strain and then recover to its exact initial location according to the stress-strain characteristics of the elastic support element. Based on the present experiments 7×10^{-9} Ω cm at any field could be used for strains up to 0.1%. We design to 0.4% strain and have used $\rho = 10^{-8}$ Ω cm, which admittedly is an extrapolation of our data. Work in progress at Wisconsin will verify the exact value to be used; however the case for using highly strained but reinforced aluminum seems to be good enough at this time to utilize in the UWMAK-III magnet design.

The structure of 2219 aluminum alloy is an excellent match for the aluminum matrix conductor. There would be no contraction stresses between the conductor and solid D former on cool down, which, among other advantages puts a minimum shear strain on the epoxy bonding agent. This alloy was selected for its strength, ability to be welded and heat treated and its ability to be formed at a reasonable cost. The use of 2219 for structure also would eliminate the need for the chromium in stainless steel which has been replaced. The cost and weight of the TF coil system is reduced to one half the SS-Cu cost and weight. The only penalty is that a slightly larger volume is needed since the design stress for elastic 2219 is 45000 psi while for steel it was 60000 psi. For large units such as UWMAK-III, space is available; for smaller experimental units other higher stress level support material might be utilized.

IV-A-3. Construction Techniques

The conductor will consist of filaments of TiNb which have been codrawn in a matrix of copper on a 1 to 1 ratio by volume, twisted to a pitch length of 30 cm, flattened into a rectangular strip, and then continuously cast into a stabilizer of high purity aluminum. A resistivity ratio of 250 was chosen for the aluminum by considering the cyclic strain level of 0.0038 to which the stabilizer will be subjected each time the toroidal fields are shut down for repairs or for system adjustments. Since the magneto-resistivity of the aluminum saturates in a low magnetic field, a constant cross section conductor is adequate throughout as shown in Fig. IV-A-3. The excellent thermal and electrical conductivity of aluminum permits a smaller conductor cross section and the lower strength of the aluminum alloy structural material requires a greater cross section in the disc so therefore there is more space available for the lands between conductors and for the clamping bolts. As shown in Fig. IV-A-3,

DETAIL OF UWMAK-III T.F. MAGNET CROSS SECTION

ALL DIMENSIONS IN CM

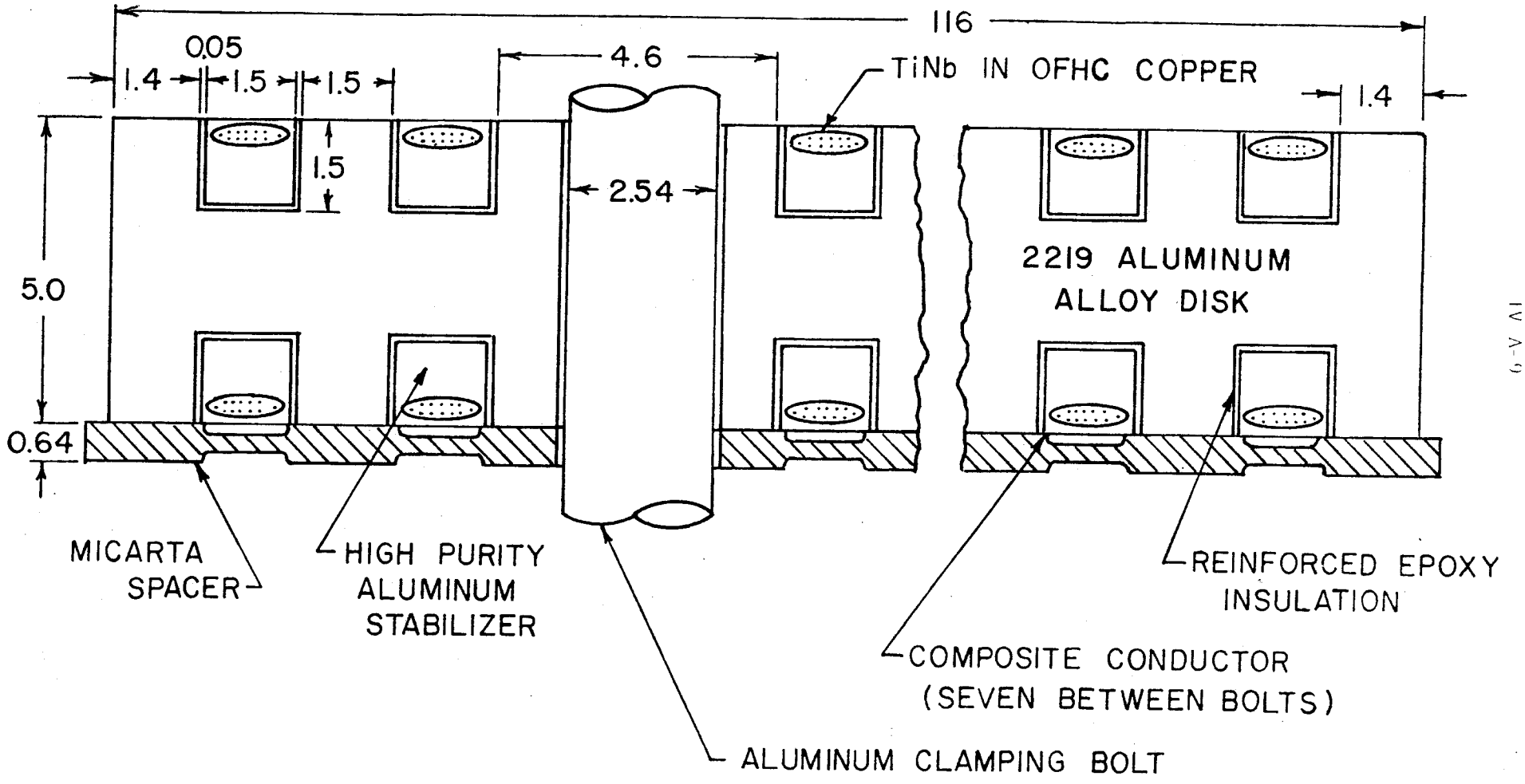

FIGURE IV-A-3

the lands between conductors are square and five of the lands have been increased to 4.6 cm wide to easily accomodate the 2.54 cm diameter clamping bolts. In consultation with J. Davis and A. Brown[12] from McDonnell-Douglas Corp., a manufacturing technique was developed and is described as follows.

1. The cross section shown in Fig. IV-A-3 will be extruded slightly oversize from 2219 aluminum alloy. A section 20 m long will be cut from the extrusion to form the inner straight leg of a disc as shown in Fig. IV-A-1. Similarly a piece 42 m long will be cut and used, after bending in the plane of the extrusion, for the curved outer portion from C to A to C' where C' is the mirror image position for C. The in-plane bending into this form will produce changes in thickness but the original oversize will accomodate this change.

2. Connections between these two segments of the "D" will be made by using forged transition sections of the same material as used in the extrusions. The top transition section is shown in Fig. IV-A-4. This piece is forged to a thickness slightly greater than 5 cm thick in the region containing the grooves for the conductors and slightly greater than 5.635 cm thick in the portion which will be keyed into the central core structure. Since the extruded portions will have parallel conductor grooves which are aligned on both surfaces, the upper transition section shown in Fig. IV-A-4 will contain the groove pattern necessary to allow a continuous conductor to be inserted in one face, starting at point E on the upper transition section, pass through the disk at point M and then be wound continuously outward on the rear face and emerge at point F. The lower transition section will be similar except the grooves will be parallel as they are in the extrusions.

3. After welding the two extrusions and the two transition sections together to form a "D" shaped disc, the disc will be heat treated to a T87 condition and then machined to size and the grooves cleaned up to accept the conductor.

4. The insulation and placement of the conductor and the curing of the adhesive insulation are fully described in the UWMAK-I report.[1]

5. The assembly of the discs into a magnet is changed from that previously described, the change being made to accomodate the change from stainless steel to aluminum discs. When using stainless steel discs and micarta spacers with aluminum clamping bolts, as was done in UWMAK-I and UWMAK-II, the thermal contraction of the materials in going from room temperature to 4.2K resulted in a slight increase in the clamping force. This occurred since the aluminum bolts contract more than the combined shrinkage of the stainless steel plus micarta. With aluminum discs, however, the clamping force will be reduced upon

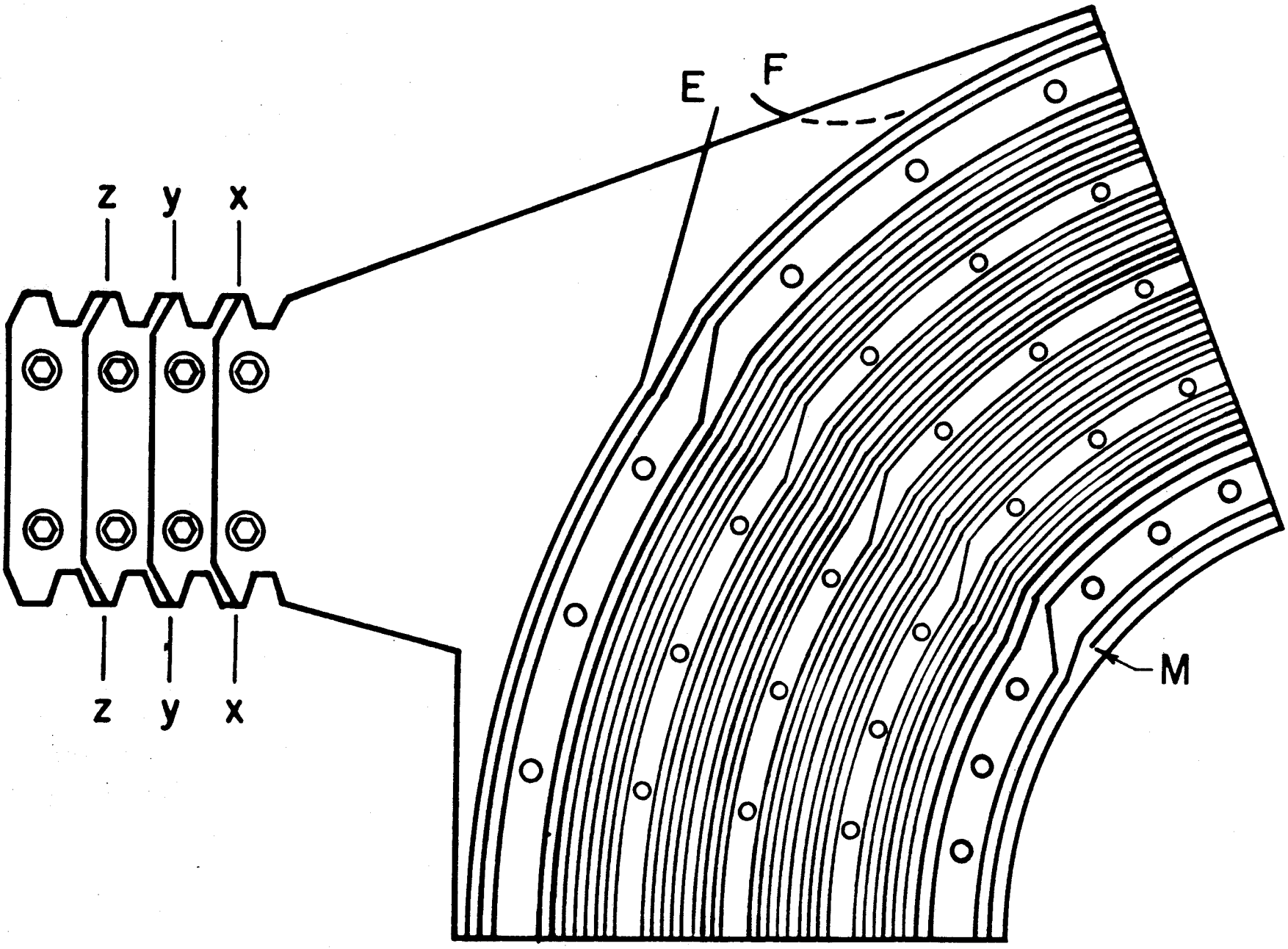

FIGURE IV-A-4

Forged Transition Section for Toroidal Field Magnet Discs

cooling due to the differential excess contraction of micarta. To maintain the required clamping between discs, Belleville washers (conical disc springs) will be used at each end of each aluminum clamping bolt. These can be seen in Fig. IV-A-5. To permit these washers to be mounted in a minimum space, the decision was made to eliminate the conductors on the outer surfaces of the outer discs. Thus, there are a total of 64 turns on each of 14 discs and 32 turns on each of two discs for a total of 960 turns per magnet.

With all conductor grooves parallel and aligned on the two surfaces of each disc only a single shape micarta spacer need be used. Each spacer will be placed over 5 clamping bolts used in each pattern with a total of 250 spacers being used per disc. Thus, there are 1250 bolts used per magnet with center to center spacing of approximately 23 cm each way.

The cross section of the assembled magnet is shown in Fig. IV-A-5 The inner dewar wall is assembled against micarta spacers to a tight fit around the magnet. A series of reinforced epoxy struts between inner and outer dewar walls provides lateral support to the magnet. This portion of the support system is unchanged in concept from that in UWMAK-II[2] and will not be repeated here.

IV-A-4. General Restraints and Design Factors

The design procedure and stress analysis for the "D" shaped toroidal field magnets was discussed in detail in the UWMAK-I report.[1] Other than the modification for the finite number of finite size coils introduced in Section IV-A of this report and the few changes described in the following section, most of the description in the UWMAK-I report applies equally well here.

IV-A-4-a. Vertical and Radial Support Structure

A thin "D" shaped magnet, the shape of which has been corrected for field perturbations, should be free of bending stresses. It is assumed that support is provided by a central steel structure which keeps the inner vertical leg straight to the point of tangency with the curved outer leg of the "D". The finite wall thickness in an actual magnet requires a redesign of the central core in order to reduce the amount of bending produced in the portion of the magnet just above or below the straight position. Purcell[7] discusses these peak stresses and their causes.

Since the "D" shaped magnet being discussed here is not tangent at point C, a modified support system is required at point C. (See Fig. IV-A-1) In Fig. IV-A-6, the constant total tensile force T, which would have been in equilibrium with the remaining dotted portion of a complete "D" magnet, must be provided for in another manner. The vertical component of T or $T_V = T \sin\theta$ can be carried in tension by the vertical inner leg of the magnet from C to G. The horizontal component of T or $T_H = T \cos\theta$ will be directed radially outward on an inner structure and will tend to create tension in such a structure. In Fig. IV-A-7 an inner structure is shown which consists of an inner shell to support the radially inward loading from the vertical leg of the magnet and an inner ring keyed to the magnet at point C to carry the outward load T_H. The obvious disadvantage of this support system is that the shell tends to deflect radially inward under its loading while the ring tends to deflect radially outward. If the ring and shell are not joined together the vertical leg of the magnet suffers a large shear force at the intersection. If they are joined together, the ring will experience a clockwise

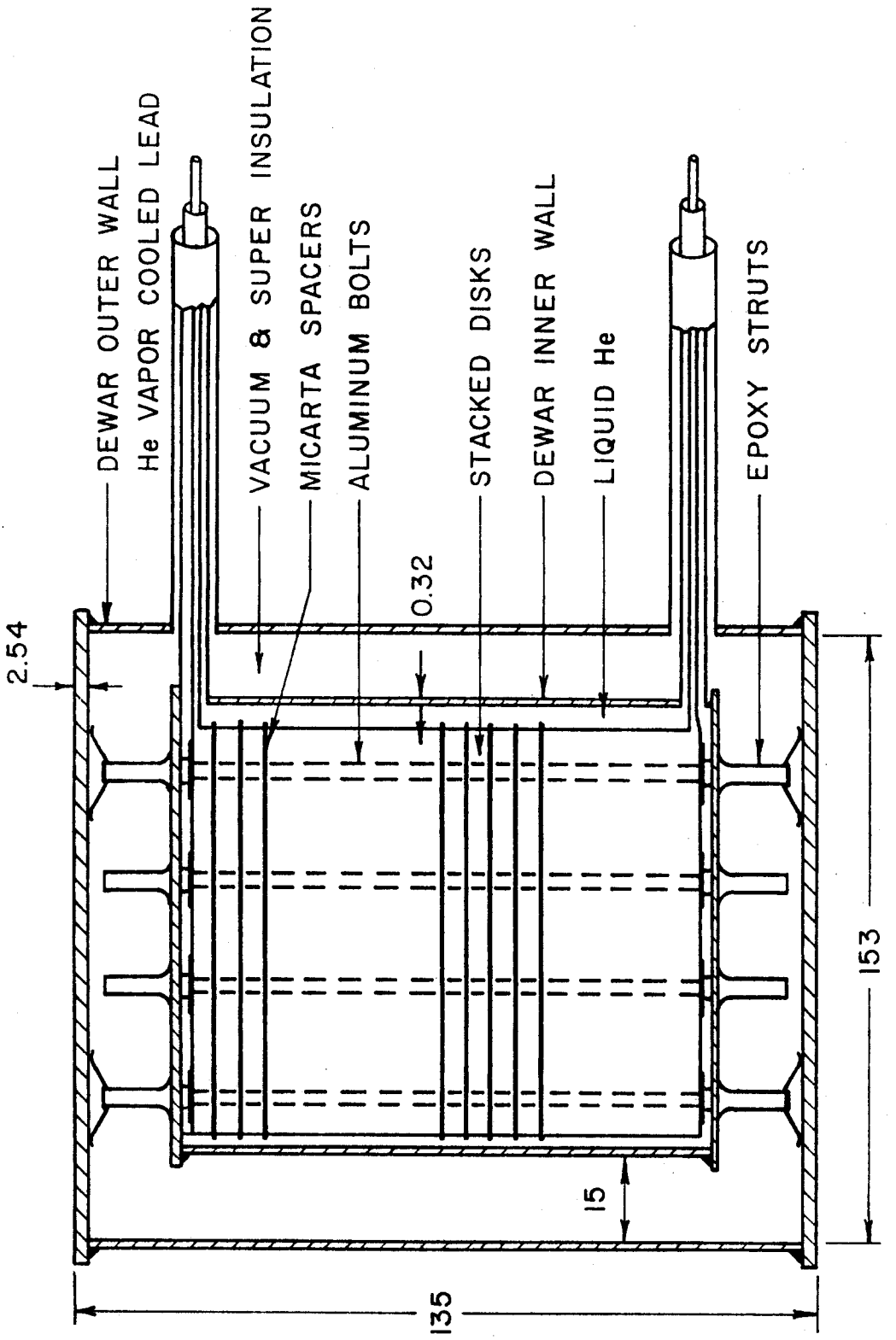

FIGURE IV-A-5

Cross Section of Toroidal Field Magnet

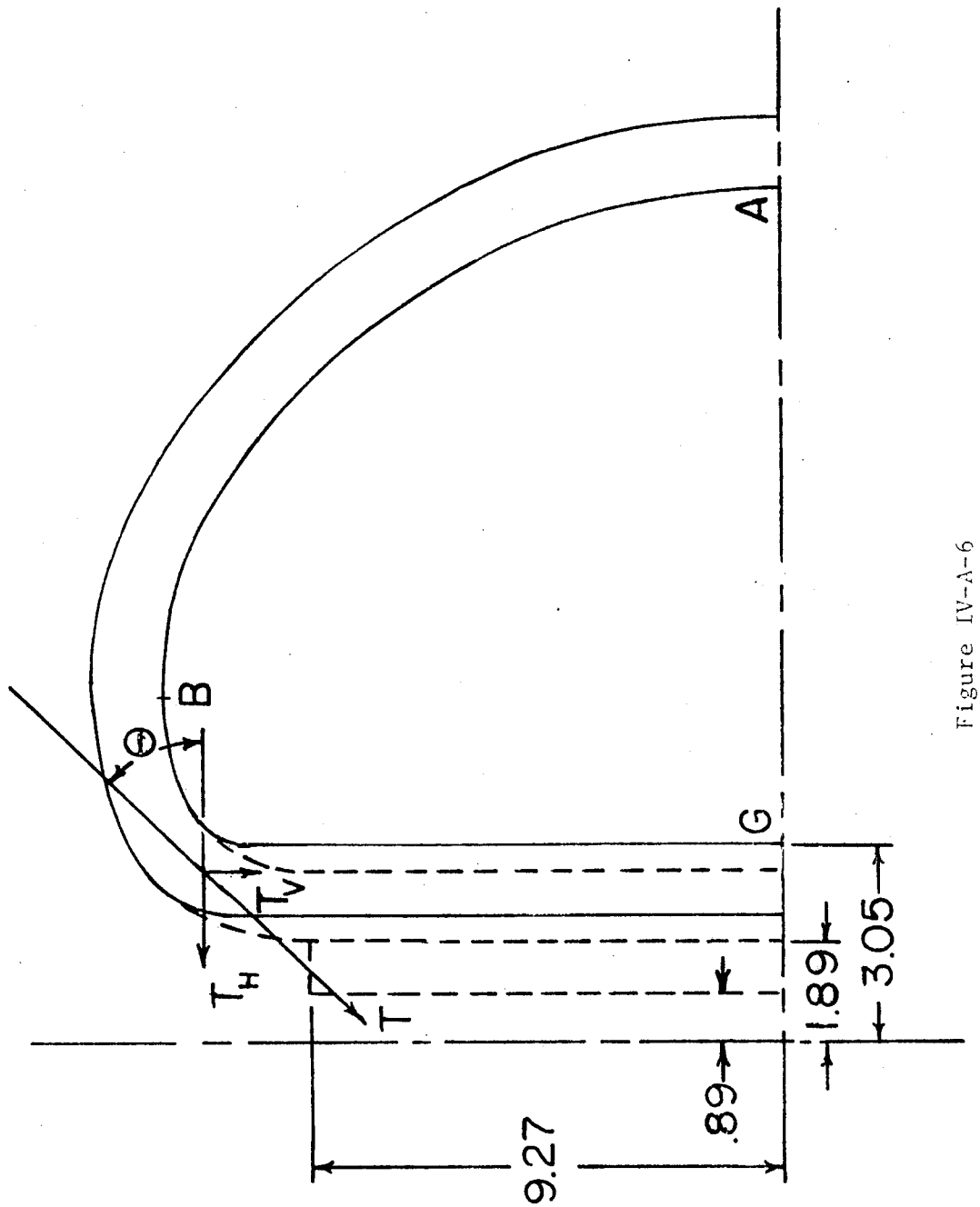

Figure IV-A-6
Loads in "D" Shaped Toroidal Field Magnet

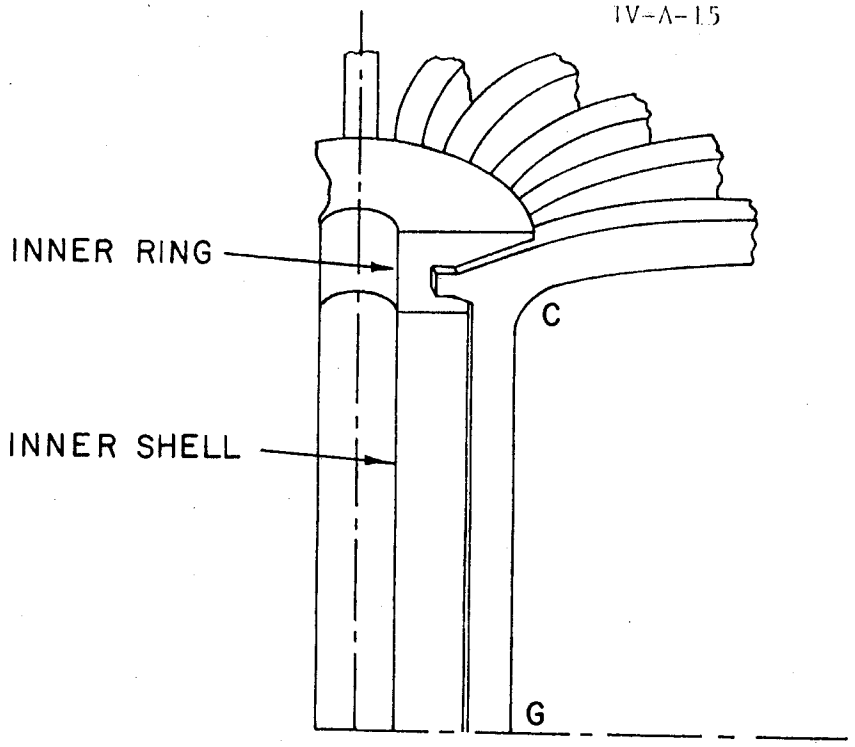

FIGURE IV-A-7

Inner Support Structure for Toroidal Field Magnets

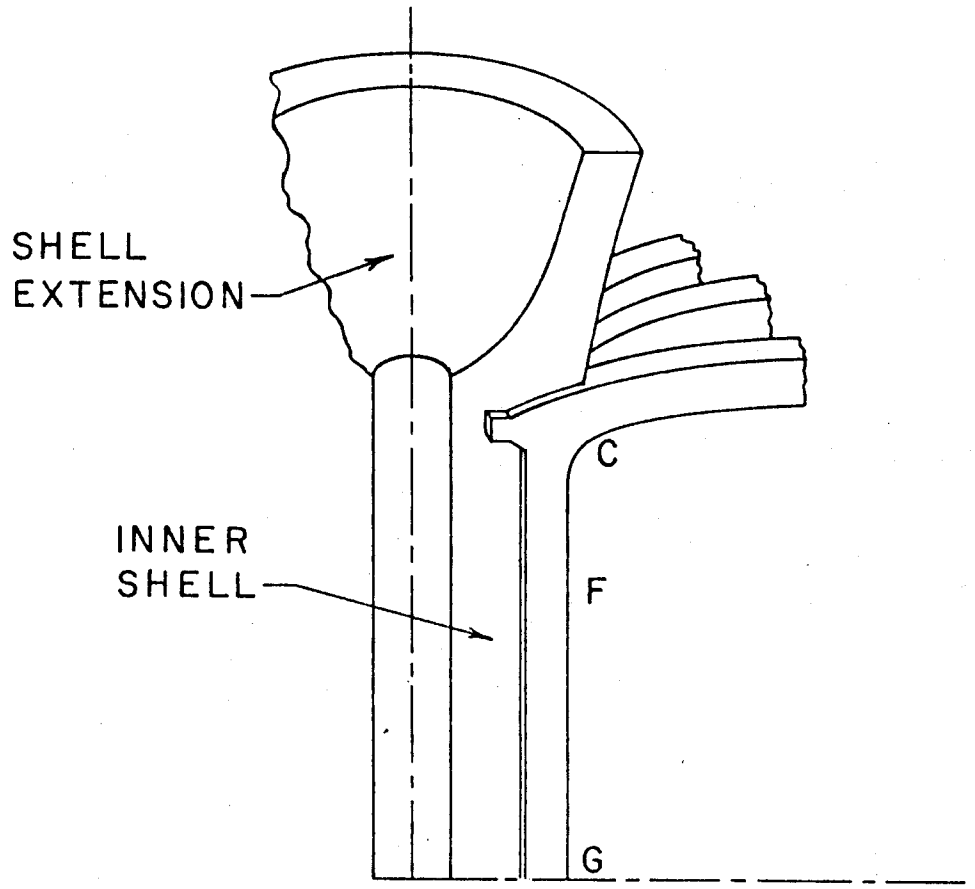

FIGURE IV-A-8

Modified Inner Support Structure for Toroidal Field Magnets

rotation which bends the magnet at point C creating tension on the inner surface where the tensile stresses are already the largest in the entire magnet.

An improvement on this support system is shown in Fig. IV-A-8. The inner leg of the magnet is subjected to lower tensile stresses than the remainder of the magnet since T_V is less than T. By properly shaping the inner shell and supporting the force T_H by a flared inner shell extension which extends upward beyond the attachment point of the magnet the rotation at point C can be controlled and in fact can be made to be counterclockwise to more evenly distribute the tensile stresses in the vicinity of point C. This of necessity creates bending in the vertical leg of the magnet in the vicinity of point F but the lower tensile load in this region will permit some bending without exceeding the design stresses. A detailed analysis of this type of structural support system is being undertaken and the results will be published at a later date.

Keying of the "D" shaped toroidal field magnet to the cantilever extensions of the central support structure poses some problems primarily caused by lack of space. Figure IV-A-4 shows one possible design in which eight work hardened alloy aluminum keys are inserted by a mechanically actuated linkage to key the magnets to the inner structure. Circumferential space limitations require that the two outer disks terminate at section XX, the next two at section YY and the next two at section ZZ. The keyed portion of each disc is as thick as the portion containing the conductors plus the micarta spacer thickness and the discs are bolted together as shown. Since the bolts, the keys, the discs and the inner support structure are all made of aluminum, the differential shrinkage problems are largely eliminated.

The central support structure, which is best shown in Fig. IV-A-9 is a massive axisymmetric aluminum cylinder. It carries the 18 cantilever extensions keyed to the toroidal field magnets and also flares out of the top and bottom to support the ohmic heating coils in those regions. Only six of the ohmic heating coils will contain interleaved structural materials since most of them will be embedded within and supported by the central cylinder. The central cylindrical support structure, the ohmic heating coils and the vertical straight portions of all of the toroidal field magnets will be maintained at 4.2 K.

IV-A-4-b Radiation Damage to the Toroidal Field Magnets

The radiation level on the magnet components is about four orders of magnitude less than for UWMAK-I. In that case at 3×10^{-4} dpa/year we allowed for extra copper and for extra cooling surface and planned for room temperature anneals every ten years. For UWMAK-III, in contrast, the dpa rate on the front surface of the magnet is 1.6×10^{-8} dpa/year. For $10^{-8}\Omega$cm aluminum it would require 10^{-6}dpa to change the resistivity by 10%. The damage to insulators, which was not considered a serious problem for UWMAK-I, is negligibly small for UWMAK-III. Therefore we expect up to 40 years of operation without any anneals.

CROSS SECTION VIEW OF UWMAK III

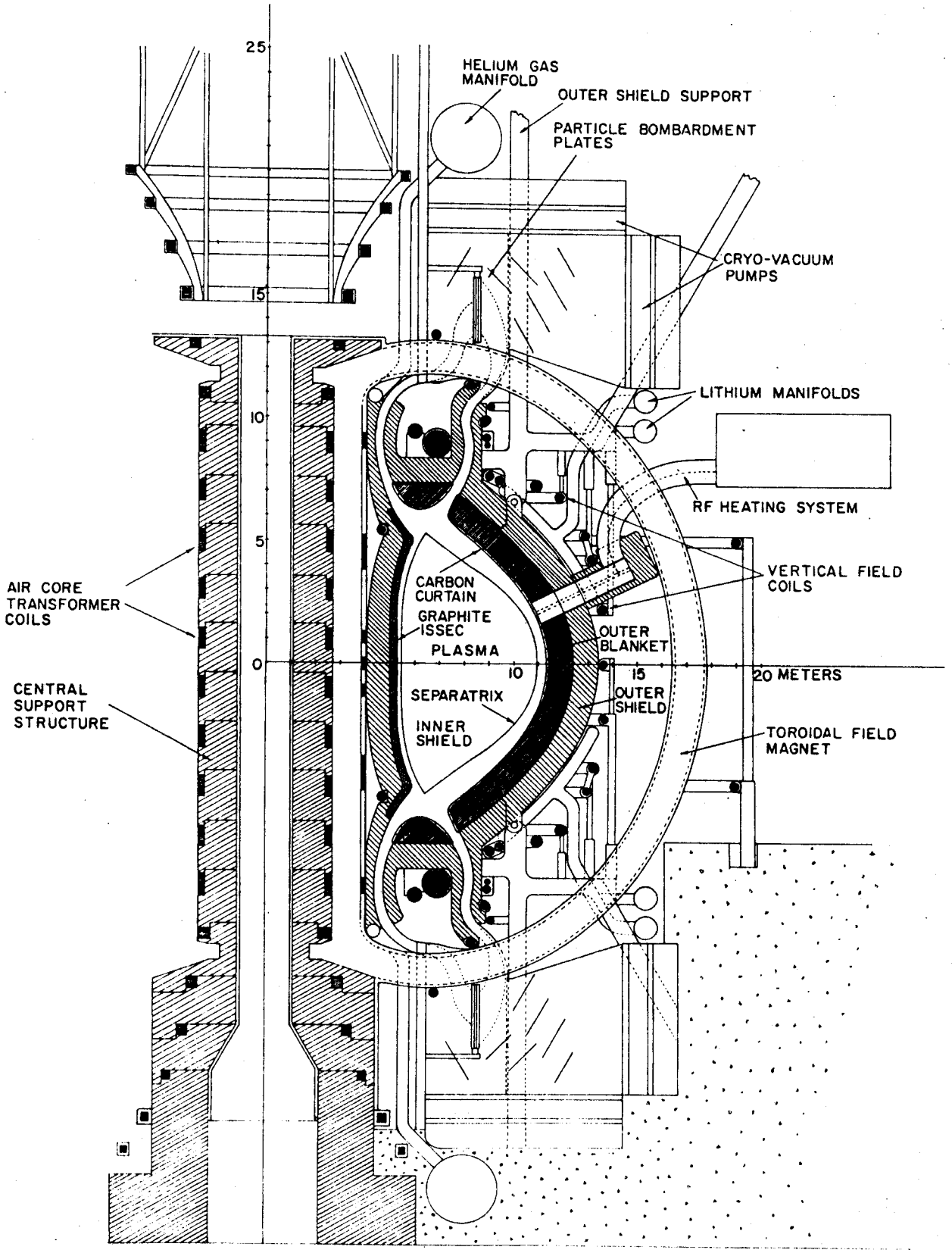

Figure IV-A-9

IV-A-4-c Dewars

The dewars in UWMAK-III are fairly conventional. The liquid helium barrier will be a 3 mm 304 stainless steel sheet material which will enclose each magnet completely. This implies that the container will also enclose the TF coil attachment extension. Here the material can be thinner, ~1 mm, and will be formed to fit snuggly around the notched extension and welded in place.

There is no question of the advantage of having individual vacuum dewars for each TF coil. Although the inner legs of the TF coils are enclosed in a common dewar, it would still be possible to have inside the common dewar an additional separate vacuum system for each coil. The vacuum barrier at the inner leg can be of a thin aluminum alloy material formed similarly to the stainless steel sheet and fitting on top of it in the TF coil attachment area and at the inner leg facing the central support structure. No insulation will be needed here since all the components, including the central support structure will be at 4.2 K. In the region where this condition does not exist; such as in the curved portion of the TF coils, the aluminum dewar is gradually increased in thickness to 2.5 cm and is separated from the inner dewar by 15 cm. This space is filled with superinsulation and epoxy struts which are needed for lateral stability as previously discussed.

Clearly, at some point there has to be a joint between the individual aluminum dewars and the common dewar surrounding the inner legs of the TF coils. This can be accomplished by welding the two together where they join at the top and bottom.

It has to be kept in mind that both helium containment and the vacuum dewars have to support an atmospheric loading. This is not a problem in the sidewalls, since the epoxy struts and lateral support structure can be designed to contain the atmospheric loading. On the inner and outer peripheries, however, where struts are not needed, additional reinforcing will have to be provided for this purpose.

The amount of material needed for the TF coil dewars is 119 MT of stainless steel and 730 MT of aluminum alloy.

Sixteen of the 26 OH coils are built into the central support structure. These coils will have individual helium dewars but will not require vacuum dewars. In addition seven of the VF coils are contained within the common dewar surrounding the straight legs of the TF coils. These too will have individual helium dewars but will share the vacuum of the common dewar.

The rest of the VF and OH coils will have conventional helium and vacuum dewars. Approximately 90 MT of stainless steel and 500 MT of aluminum alloy will be needed for the VF and OH coil dewars.

IV-A-5 Lateral Support and Structural Safety

The UWMAK-II report[2] described in detail the use of a continuous wall between the toroidal field magnets. This wall provides both a secondary vacuum barrier and a lateral support system for the toroidal field magnets in case

of an accident causing the loss of current in one or more of the 18 toroidal field magnets. Figure IV-A-10 shows such a wall and the reader is referred to the UWMAK-II report[2] for the details of design and construction. One detail that is changed is the addition of the Belleville washer to the clamping system. This change is shown in Fig. IV-A-11. The conical spring caps at the outer ends of 10% of the fiberglass epoxy struts are designed to support the transverse loading due to the pulsing of the vertical field and ohmic heating coils and to provide the lateral stiffness needed for magnetoelastic stability of the toroidal field magnets. Under an accident condition where one or more of the toroidal field magnets have lost current, the conical disk spring provides a cushioned deformation and allows the other 90% of the struts to carry their share of the lateral loading. For details and design data see Ref. 2.

IV-A-6 Magnet Safety and Protection

The problem of magnet safety and protection is addressed in this section. We consider the case in which one TF coil develops a problem which requires that its current be discharged as soon as possible. Typically this could be caused by losing vacuum, losing helium, shorting a coil to ground, developing a local hot spot, developing an open circuit or other. It is our intention that the design of the UWMAK coils is such that the following protective scheme will be available.

1. Each TF coil is in a separate dewar so that only the bad coil needs to be discharged.

2. Normally all coils would be operated in series with one three-phase Graetz bridge power supply. In case of a fault in one coil automatic shorting switches would short out all coils individually so that the power supply would be across only the bad coil. The power supply which was set at a few volts positive to balance lead losses would be immediately switched to -10,000 volts. The 9,545 A current in the bad coil would then decay linearly to zero since a Graetz bridge provides an almost constant voltage independent of current level. In fact, the voltage rises slightly at lower currents. Thus the decay is superior to using a simple dump resistor with its exponential L/R decay time.

3. The other coils absorb the coupled flux from the discharged coil by increasing their currents, mostly in the nearest neighbors. It is important to initially design for extra current capacity and extra cooling so that the added current will not drive a TF coil normal.

4. The penalty for using this scheme is three-fold. First, every TF coil and the leads must be designated for 10 kV. Some variation of complete insulator coverage of the stainless former seems necessary. Second, the over-rated power supply would cost about $\$2 \times 10^6$, which however, adds only 1.5% to the Tokamak magnet system costs. Third, all coils must be designed to withstand the overcurrent and unbalanced forces developed during the shutdown of one coil.

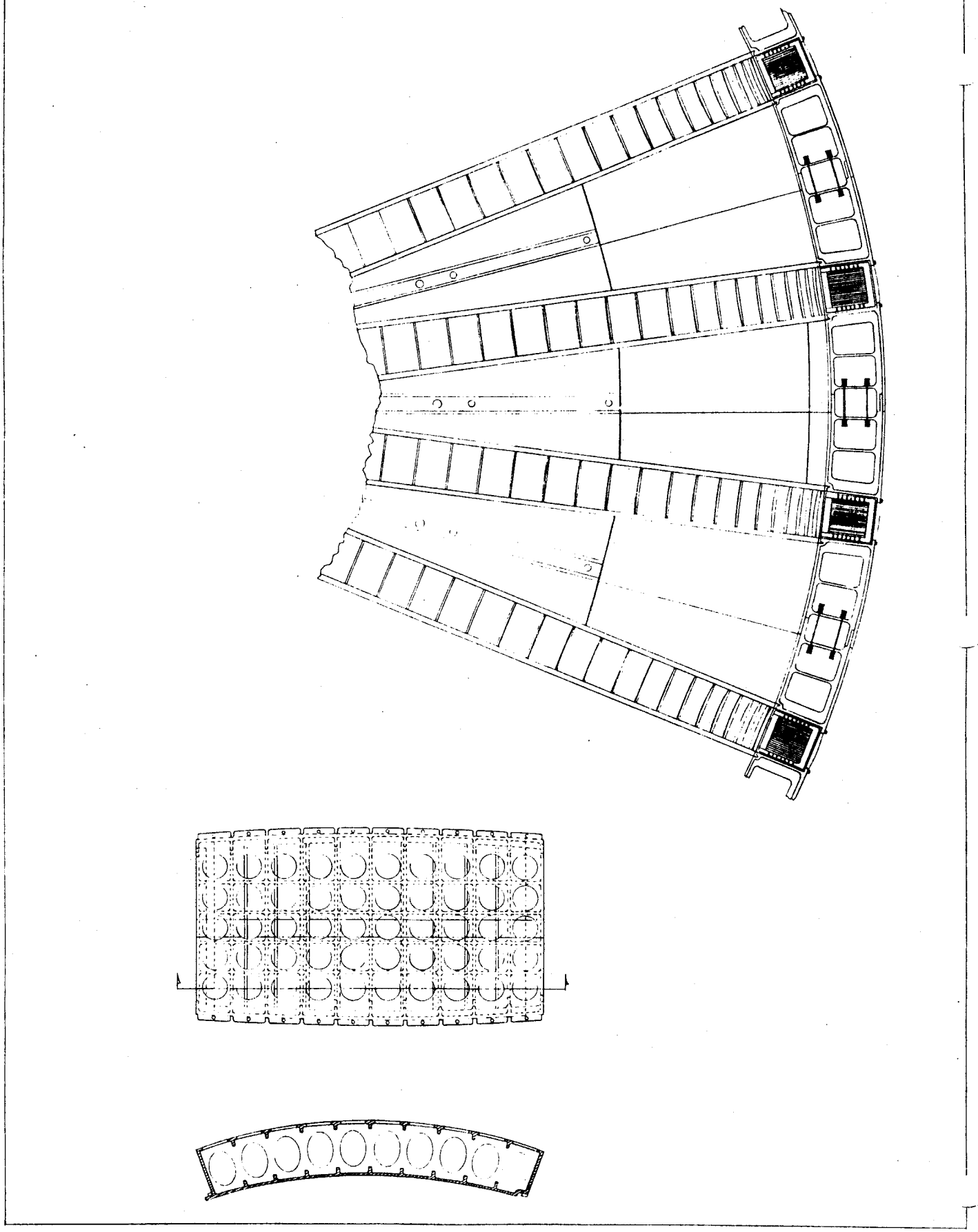

Figure IV-A-10 Secondary Vacuum Shell and Lateral Support

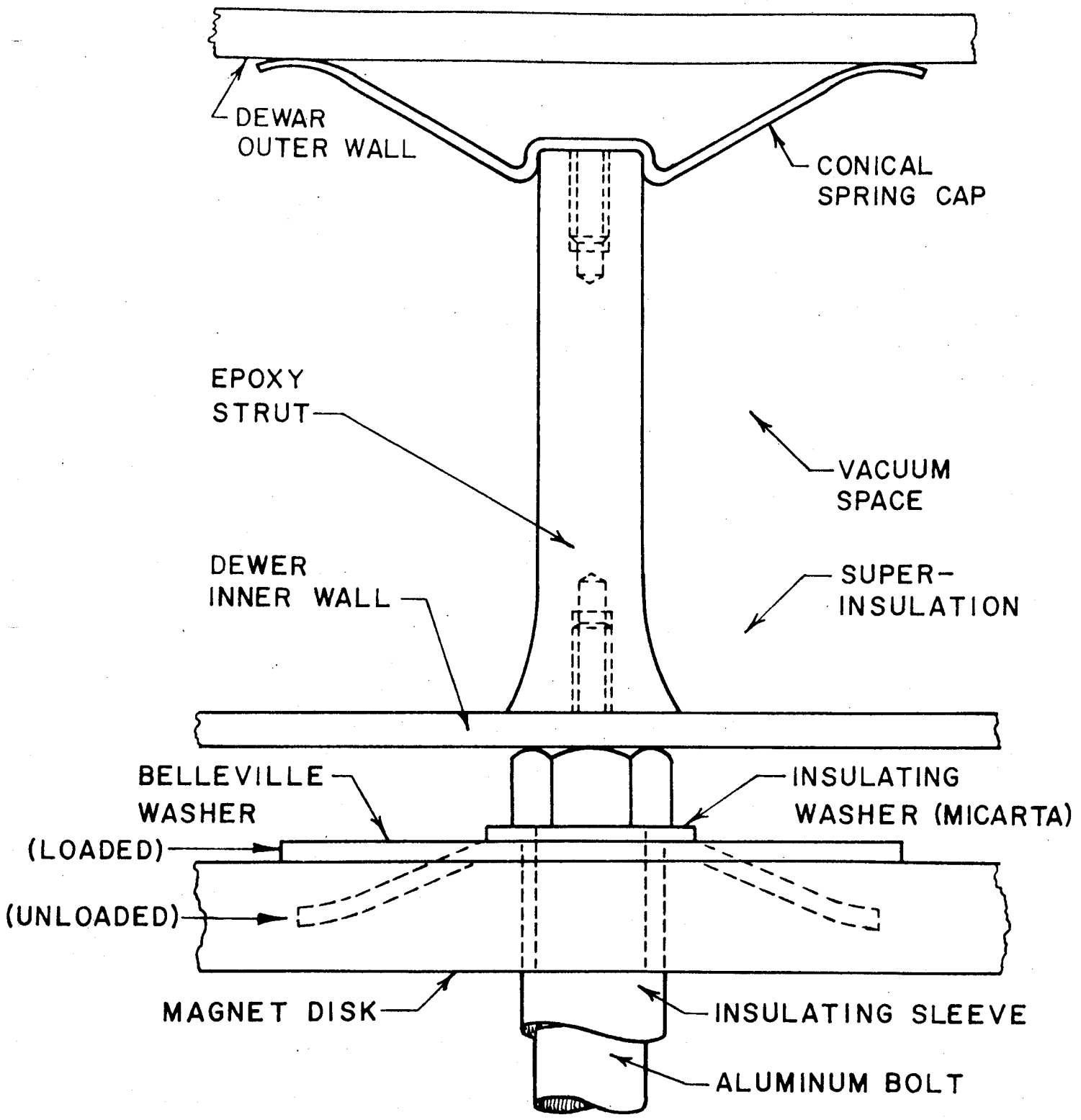

Figure IV-A-11

Lateral Load Bearing Epoxy Strut

Detailed temperature rise calculations and discharge times are found below. The coupling provided by the other TF coils reduces the energy per coil which must be removed to about 20% of the per coil energy. Note also that the gross flux in the TF system changes very little due to dropping one coil, largely removing general eddy current forces and losses.

As a reference point let us consider the circuit of Fig. IV-A-12 during shutdown. Here we restrict the component to ground voltage drop to 5 kV; hence, the converter voltage is limited to 10 kV. As mentioned above, because of the shorting switches, the power supply would discharge only the faulty coil and take advantage of inductive coupling to transfer most of the energy directly to the rest of the TF magnet.

To simplify the inductance computations for UWMAK-III we take 18 circular coils of radius a = 9.2m arranged to form a toroid of major radius R = 10.1m. Each coil has 960 turns of copper stabilized TiNb superconductor carrying 9545 A. The inductance of the TF magnet as a whole is L = 2370 H, and the stored magnetic energy is 1.08×10^{11} J.

The self inductance of a single coil is 33 h. If a 10 kV back emf were applied to one of the coils and the current in the rest of the magnet were held fixed by an external power supply, it would take 32 seconds to shut down the coil. Here 1.5×10^9 J or about 1.4% of all the energy in the TF system would be removed by the 10 kV power supply. A smaller amount of energy would be extracted from the rest of the magnet.

By placing each individual coil in persistant mode even more energy is transferred directly from the failing coil to the rest of the TF system. Approximate values of the coil-to-coil mutual inductances were obtained using the tables of Grover.[17] The circuit equations for Fig. IV-A-12 were solved to give the current increases in coils 2 through 18. Under these conditions the apparent inductance of coil 1 is $L_o \tilde{} 27$h as compared to 33 h for the self inductance. The energy removed via coil 1 is now 1.23×10^9 J. When a voltage of 10 kV is applied to the failing coil, it takes 26 sec to reduce the current to zero. This is far superior to the 38 min needed to discharge all coils in series. It is even much better than an expensive scheme of having a 10 kV converter for each sector to discharge all coils together in 5 min. For the rest of our discussion we take a single coil discharge time of 32 seconds and examine the adiabatic heating of that coil and the current and force changes in ne rest of the TF magnet.

There are 4×10^7 g of aluminum in each sector. If all coils were in separate persistent circuits and the power supply did not extract energy, the failing coil would absorb 1.5×10^9 J. If this energy were uniformly distributed throughout the aluminum the temperature rise would be

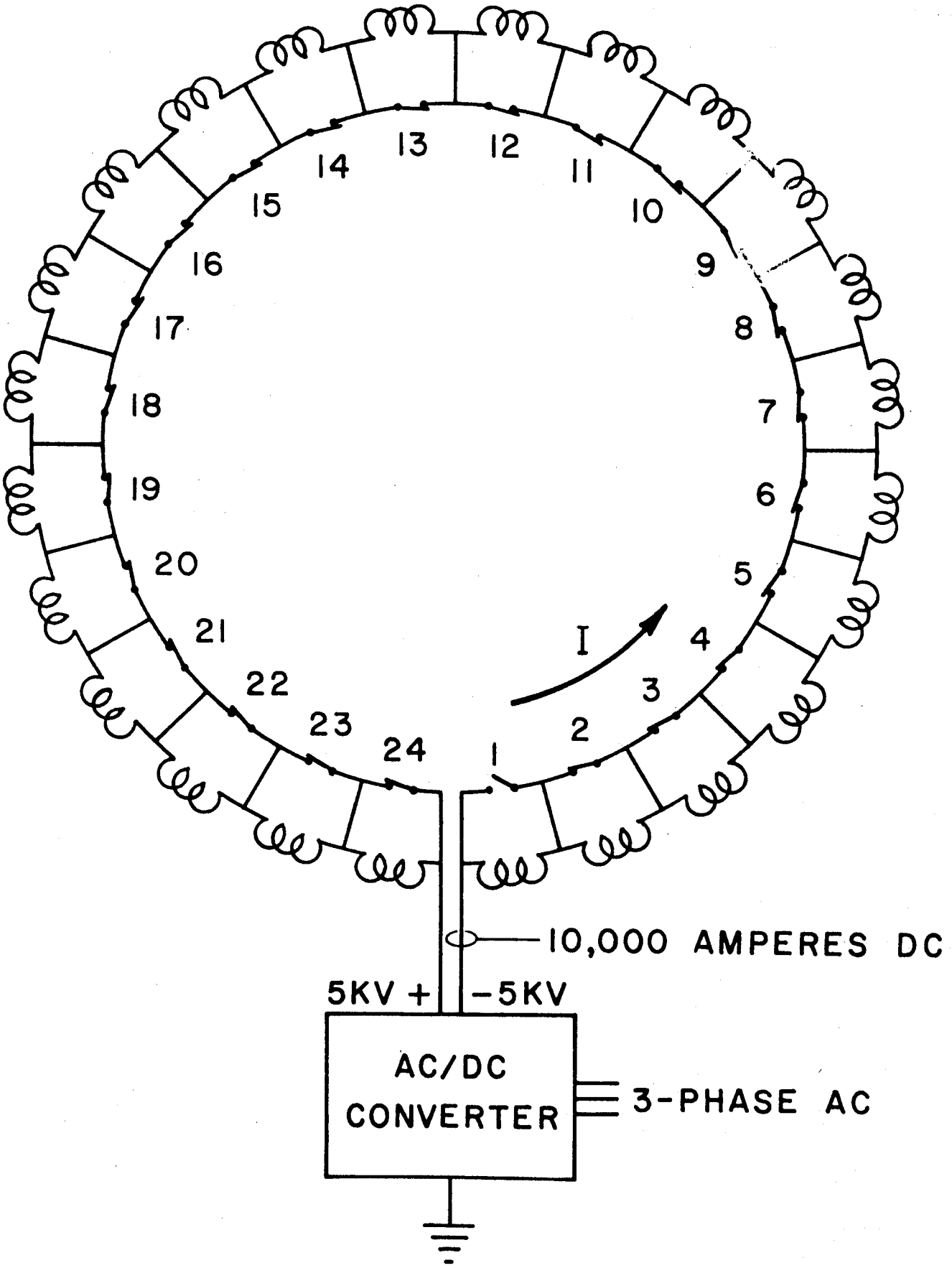

FIGURE IV-A-12

TF Coils Shown Shorted for Rapid Discharge of Faulted Coil

$$\int_{4K}^{T} c\,dT = \frac{\Delta W}{m} \simeq 37.5 \text{ J/g} \qquad (4)$$

$$\Rightarrow T \simeq 120 \text{ K.}$$

A more serious problem occurs when energy is deposited in a small fraction of the conductor. As an example T would exceed 300 K if the ΔW above went into less than 25% of the aluminum of one coil.

If a small portion of a coil is normal as in the case of a local lack of coolant, one should know the adiabatic temperature rise of the region during the 26 second "powered shutdown" described above. Various parameters are defined as follows:

$c(T)$ = specific heat of high purity aluminum

$\rho(T)$ = electrical resistivity

D = mass density

t_{dis} = discharge time

$J(T) = J_{max}(1-t/T_{dis})$ current density

The rate of change of temperature with respect to time is

$$\frac{dT}{dt} = \frac{J^2\rho}{cD} \quad . \qquad (5)$$

This leads to the integral relationship

$$D\int_{4K}^{T_{max}} \frac{c}{\rho}\,dT = \int_{o}^{t_{dis}} J^2 dt \qquad (6)$$

$$= \frac{1}{3} J_{max}^2\, t_{dis} \quad .$$

For a 1.5 x 1.5 cm conductor carrying 9,545 A, J_{max} is 4242 amp/cm^2. Equation (6) was solved to give

$$T_{max} \simeq 40 \text{ K.} \qquad (7)$$

Consequently if the early stages of a fault are detected a coil could be shut down before any portion of it exceeded 40 K.

For the above technique to work it is vital to preserve the integrity of the stabilizer. If it were partially destroyed or broken, the resistance and density terms in Eq. (6) would no longer be valid and drastic temperature rises could result.

IV-B Vertical Field and Ohmic Heating Coils

In this section, we will describe the steps used in the design of the superconducting vertical field coils and the ohmic heating coils. The periodic cycling of these magnets through the 1935 second reactor cycle, which includes a short rise time of 15 seconds during startup, poses problems which make the design of these coils quite different from that used for the toroidal field magnets. Lower values of magnetic loading reduce the emphasis on reinforcement; the main emphasis now is on conductor design for full cryogenic stability and low ac losses.

IV-B-1 Specifications

IV-B-1-a Description and Specifications

As with all designs associated with highly reliable power generation equipment, complete cryogenic stability for life-time reliability is our guiding philosophy. The rise time mentioned above is similar to that encountered in the design of a pulsed energy storage dipole magnet designed by the University of Wisconsin and the Fermi National Laboratory.[8] The conductors used in the vertical field coils and the ohmic heating coils for the UWMAK-II design[2] were based on the conductor designed for the Fermi Lab. Cornish[3] has been concerned with similar problems and has proposed a conductor which should have lower losses and a lower construction cost. The design of the vertical field coils and the ohmic heating coils for UWMAK-III are based on his concept and the details of design are covered in section IV-B-2.

The Cornish design uses work hardened copper as both stabilizer and structure. To provide a maximum cooling surface each conductor is manufactured in four pieces and the individual portions soldered together with side groves on half of the pieces providing the internal cooling chambers. In the present application the magnetic loading required additional strength in many of the coils but for reasons of economy of design, testing, and construction it was decided to use a single basic size element for all coils. The conductor type 1 consists of four copper sections, one of which contains the superconductor. Conductor type 2 replaces one of the copper sections with a stainless steel section but maintains the same geometry. Conductor type 3 replaces the two outer sections of copper with a stainless steel section which varies in thickness according to the amount of reinforcement which is necessary. These conductor types are shown in Fig. IV-B-1. Sixteen of the ohmic heating coils are housed inside the central structure supporting the toroidal field magnets and require no additional reinforcement. See Fig. IV-A-9. The remaining ten coils are reinforced as necessary. The general specifications of the vertical field and ohmic heating coils are given in Table IV-B-1.

To reduce the ac losses described later, the superconducting filaments are extruded with cupronickel in an OFHC copper matrix, drawn to size, twisted, and finally formed into a square cross section. All conductor sections containing the superconductors will have the same size in all the coils but the number of TiNb filaments will depend upon the current being carried and the maximum ambient field at the given coil location.

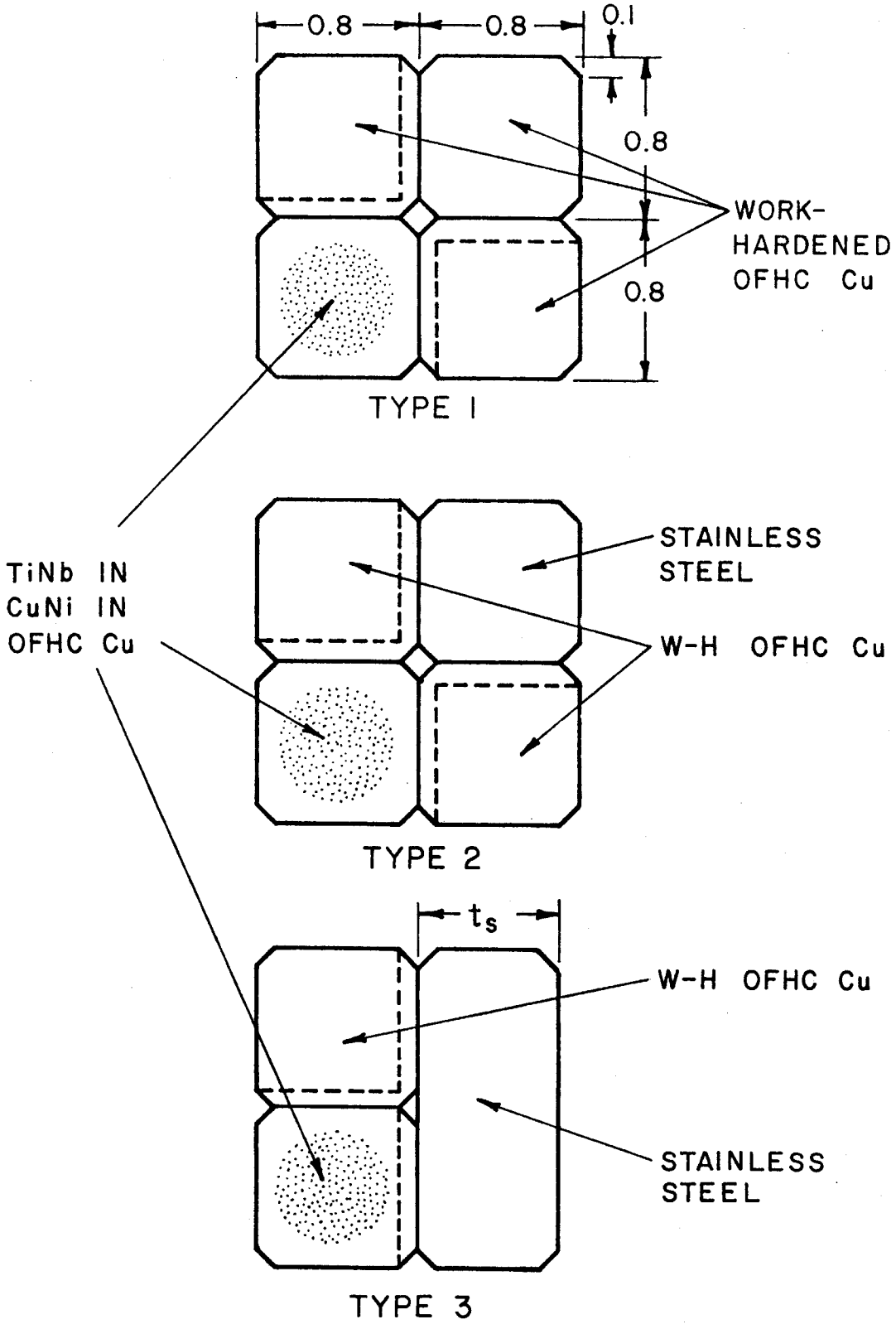

FIGURE IV-B-1

Conductor Cross Sections for Vertical Field and Ohmic Heating Coils

TABLE IV-B-1

General Specifications for the Vertical Field

and the Ohmic Heating Coils

(1) Conductor TiNb + CuNi sleeve + work hardened OFHC copper stabilizer, fully cryogenically stabilized

(2) Conductor current in Type 1 = 14,160 to 14,520 A
Conductor current in Type 2 = 10,390 to 11,110 A
Conductor current in Type 3 = 4,340 to 6,750 A

(3) Conductor current density in Type 1 = 4880 to 5320 A/cm^2
Conductor current density in Type 2 = 3120 to 3850 A/cm^2
Conductor current density in Type 3 = 1410 to 3580 A/cm^2
(based on gross coil area)

(4) Conductor size in Type 1 = 1.6 cm x 1.6 cm
Conductor size in Type 2 = 1.6 cm x 1.6 cm
Conductor size range in Type 3 = 1.6cm x 0.951cm to 1.6cm x 2.09 cm
(this includes the bonded stainless steel reinforcement in Types 2 and 3.)

(5) TiNb - CuNi- Cu composite subsection: 0.80 cm x 0.80 cm with 34 to 182, 0.038 cm diameter filaments, twisted every 30 cm.

(6) Copper to superconductor ratio = 6.03 to 33.2

(7) Design stress at 4.2K: $1.24 \times 10^8 N/m^2$ (18,000 psi) in 10% cold reduced OFHC copper, $2.11 \times 10^8 N/m^2$ (30,600 psi) in 316 stainless steel in conductor types 1 and 2.
$2.07 \times 10^8 N/m^2$ (30,000 psi) in 10% cold reduced OFHC, $3.51 \times 10^8 N/m^2$ (50,900 psi) in 316 stainless steel in conductor Type 3.

(8) Spiral wrapped with 0.1 cm thick fiberglass reinforced epoxy over 50% of the surface. Alternate conductors wrapped to produce a spacing of 0.1cm in both vertical and radial directions for the layer wound coils.

(9) Design limits temperatures to 5.2 K in a 4.2K bath for all normal situations.

(10) Total TiNb superconductor required = 64.5 Mt

(11) Total copper required = 1331 Mt

(12) Total 316 SS reinforcement required = 436 Mt

(13) Total insulation for wrapping conductors = 26 Mt

IV-B-1-b Comparison with UWMAK-I and UWMAK-II

In the UWMAK-I design the vertical field coils were placed outside the toroidal field magnets for ease of construction and repair. For the UWMAK-II report it was shown that a large reduction in stored energy and magnet cost could be accomplished by winding the vertical field coils in place inside the "D" shaped toroidal field magnets. The same approach is used in the present design. A major change is in the number of vertical field magnets used to properly shape the plasma and divert the charged particles. There were 12 such coils in the UWMAK-II design and there are 41 in the present design. Table IV-B-2 lists various parameters to give an overall comparison of the poloidal field coils in the three UWMAK designs.

IV-B-2 Design Factors

IV-B-2-a Design for External Stability

For the reliability required of a commercial power generating plant we have chosen to design the conductor for full cryogenic stability. The conductor proposed by D. Cornish[3], four segments of cold reduced copper soldered together on 50 percent of their adjoining surfaces is used. The remaining 50 percent of the adjoining surfaces is devoted to the internal cooling passages shown in Fig. IV-B-1. The combined lateral channels provided by these grooves and the longitudinal channels provided by the beveled corners give excellent cooling characteristics and permit higher current densities than in previous UWMAK designs. Present plans call for layer wrapped coils of either round or rectangular cross section made up of these conductors. To provide insulation between conductors and also to provide surface cooling on the outer surface of each conductor, a spiral wrap of B-cured fiberglass reinforced epoxy tape will cover 50% of every other conductor. This technique will slow down the coil winding process since only half the conductor will be wrapped and in an intermittent fashion requiring manual control. However, only one element is being wound on the coil form and the process provides for positive cooling channels. Alternatives involve insulation between layers and adjacent turns which would also have to be manually placed. Cornish did not plan to use any structural material other than the strain hardened OFHC copper which also acts as the stabilizer. In the present application, however, the loads are great enough in some coils so that stainless steel reinforcement is necessary. To maintain the advantage of winding a single conductor on the coil form, the stainless steel reinforcement is soldered into the conductor in place of a portion of the copper.

In the type 2 conductor shown in Fig. IV-B-1, the stainless steel replaces the ungrooved copper segment diagonally opposite the segment containing the superconductor. In this configuration the two grooved copper segments act as stabilizer and structure. In the type 3 conductor a single stainless steel reinforcing band replaces the two outer copper segments necessitating the placement of grooves on one surface of the copper segment which contains the superconductor. By placing the stainless steel bands on the outside of the conductor

TABLE IV-B-2

Poloidal Field Magnets in UWMAK-I, UWMAK-II and UWMAK-III

	UWMAK-I	UWMAK-II	UWMAK-III
Vertical field coil positions	outside "D" magnet	inside "D" magnet	inside "D" magnet
Ohmic heating coil positions	6 inside central core; 4 outside	16 inside central core; 2 outside	16 inside central core; 10 outside
Number of vertical field coils	8	12	41
Maximum tension	4.57×10^8 N (1.02×10^8 lbf)	2.44×10^7 N (5.48×10^6 lbf)	9.47×10^7 N (2.13×10^7 lbf)
Maximum current	24.5 MA[a]	6.8 MA	15.5 MA
Maximum field	7.59 T	5.72 T	8.6 T
Maximum dB/dT	.076T/sec (100 sec rise time)	0.57T/sec (10 sec rise (time)	0.57T/sec (15 sec rise time)
Maximum stored energy of the poloidal field	16 MWh[b] $\hat{=}$ 57.6×10^9 J	2.9 MWh = 10.4×10^9 J	2.46 MWh = 8.86×10^9 J
Maximum total current	128 MA	58 MA	152 MA
Total eddy current loss		14.71 KWh/charge	0.25 KWh/charge
Total coupling loss		0.18 KWh/charge	0.16 KWh/charge
Total hysteresis loss	not calculated	0.24 KWh/charge	0.46 KWh/charge
Total conduction loss		850 watts	1600 watts
Total thermal radiation loss		312 watts	231 watts
Total lead loss		2800 watts.	6730 watts

(a) MA $\equiv$ Mega-Ampere = 10^6 A

(b) MWh $\equiv$ Mega-Watt-hour = 3.6×10^9 J

the radial compressive stress in the interlayer insulation is reduced to a minimum a. the inner copper segments are subjected to a small residual compression due to the curvature imposed.

Some care will be required when winding the type 2 conductor since the principal axes are not paralled to the edges of the conductor. Since the problem is recognized it can be overcome by proper winding techniques.

Cryogenic stability requires that the heat which would be dissipated in the stabilizer, in the event that the superconductor goes normal, be transfered by the cooled surfaces without a loss in the surface heat transfer capacity.

$$I^2\rho_s/a_s \leq qp \qquad (1)$$

where

I = the current flowing in the stabilizer

ρ_s = resistivity of the stabilizer in the ambient field

a_s = effective cross-sectional area of the stabilizer

q = surface heat transfer coefficiant

p = effective cooled perimeter of the stabilizer.

The resistivity of 10% cold reduced OFHC copper is taken as $1.86 \times 10^{-10}\ \Omega$ m at 300K[3] and the resistivity ratio as 110 at zero field. The resistivity ratio varies from the value of 110 at zero field to 30 at 9 tesla.[3] For the ungrooved copper portion of the conductor the effective cross-sectional area is 0.62 cm^2 and the effective cooled perimeter is 1.483 cm. For the grooved copper portion the effective cross-sectional area is 0.485 cm^2 and the effective cooled perimeter is 2.123 cm.

Using $q = 0.3\ W/cm^2$ the current carried by each conductor can be calculated and the number of turns established for each coil. At this stage in the design, the strength of the coil can be determined and a decision made as to whether reinforcement is necessary.

IV-B-2-b Stress Analysis and Reinforcement

The strength of a conductor is based upon the load necessary to cause yielding of all elements of the cross section. The design load is taken as 60% of this yielding load. For the 10% cold reduced OFHC copper $\sigma_y = 20{,}685 N/cm^2$ (30,000 psi). For the stainless steel reinforcement $\sigma_y = 69{,}000 N/cm^2$ (100,000 psi). Since the ratio of the modulus of elasticity of the stainless steel to that of the copper is 1.70 it is possible under some conditions to yield the copper without exceeding 60% of the load required to yield both the copper and stainless steel. This would occur in the designs presented if the required thickness of the stainless steel band of the type 3 conductor exceeds 0.915 cm. For these cases the strain at which the copper yields, $\varepsilon = 0.0017$, is set as a limit and the stress in the stainless steel limited to 35,100 N/cm^2 (50,900 psi). Table IV-B-3 gives the parameters of the vertical field coils and Table IV-B-4 those of the ohmic heating coils. Figure IV-B-2 shows the location of the several coils. Coil VF 7 is wound with 4 type 3 conductors in parallel in order to keep the charging and discharging voltages to an acceptable level.

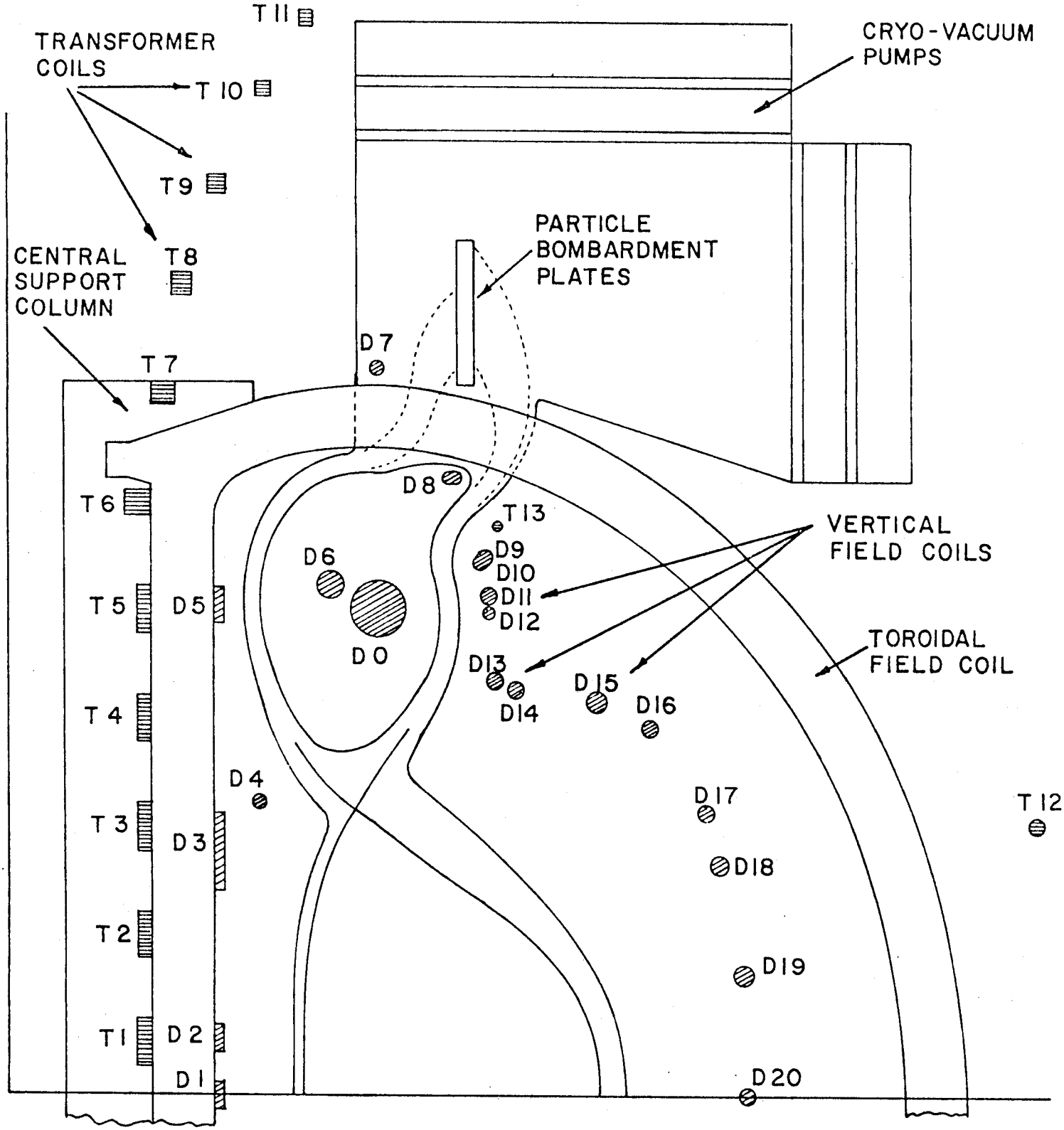

FIGURE IV-B-2

Locations of Vertical Field and Ohmic Heating Coils

TABLE IV-B-3

Physical Parameters of the Vertical Field Coils

Coil	D1	D2	D3	D4	D5	D6	D0	D7	D8	D9
R(m)	3.90	3.90	4.00	4.60	3.90	5.90	6.80	6.8	8.3	8.6
Z(m)	0.00	1.00	4.50	5.50	9.00	9.50	9.00	13.3	11.3	9.9
Maximum Current (MA)	-0.40	-0.40	2.00	-0.60	-1.20	2.20	15.50	-1.3	4.3	-3.0
Maximum B (tesla)	1.8	1.8	1.9	1.7	3.1	6.5	8.6	3.1	5.0	3.7
Maximum tension (10^6N)	-1.08*	-1.08	-1.88	-1.01	-6.59	36.4	-55.6 (+94.7)**	2.38	13.0	37.0
Conductor type***	2	2	1	1	3	3	3	1	2	3
Thickness of stainless steel for type 3 (cm)	-	-	-	-	0.296	0.940	0.172	-	-	0.87
Number of SC filaments per conductor	64	64	88	80	45	64	182	94	80	45
Number of turns	36	36	142	42	198	482	942****	102	528	520
Magnet cross section, radius (cm)	10.0	10.0	10.0	6.2	10.0	21.9	46.8	9.7	22.0	22.3
or radial width (cm) x height(cm)	x 10.4	x 10.4	x 41.0		x 40.3					
Material Quantities (MT)										
TiNb	0.036	0.036	0.197	0.062	0.137	0.722	18.5	0.259	1.396	0.805
Copper	1.47	1.47	7.91	2.69	5.38	19.81	178.4	9.97	47.30	32.18
Stainless Steel	0.43	0.43	---	---	1.81	21.16	34.82	---	13.83	30.74
Insulation	0.02	0.02	0.10	0.03	0.11	0.51	3.52	0.12	0.77	0.74

* Negative value means the coil is under compression

** Coil D0 was designed for a self field tension of 94.7 x 10^6N

*** For a discussion of the three types of conductors see section IV-B-1-a

**** Coil D0 is to be wound with 4 type 3 conductors per turn

Table IV-B-3 (Cont.)

Physical Parameters of the Vertical Field Coils

Coil	D10	D11	D12	D13	D14	D15	D16	D17	D18	D19	D20
R(m)	8.80	8.80	8.80	8.90	9.30	10.80	11.80	12.80	13.00	13.50	13.50
Z(m)	10.00	9.30	9.00	7.70	7.50	7.30	6.80	5.30	4.30	2.30	0.00
Maximum Current (MA)	-1.53	-1.65	-1.10	-1.60	-1.62	-1.55	-1.60	-1.65	-1.65	-1.52	-1.52
Maximum B (tesla)	3.7	4.7	4.7	4.5	2.6	2.6	2.2	2.4	2.6	2.4	2.4
Maximum Tension (10^6N)	17.8	24.3	17.0	29.0	9.54	10.08	4.12	6.11	6.45	7.65	10.04
Conductor Type***	3	3	3	3	3	3	2	3	3	3	3
Thickness of stainless steel for type 3 (cm)	0.805	0.942	1.030	1.290	0.343	0.392	---	0.151	0.159	0.283	0.436
Number of SC filaments per conductor	45	48	48	45	45	45	68	45	45	45	45
Number of turns	266	320	210	304	262	254	154	258	266	236	236
Magnet cross section, radius (cm) or radial width (cm) x height (cm)	15.7	17.9	14.8	19.0	13.3	13.3	11.9	12.1	12.3	12.3	13.1
Material Quantities (MT)											
TiNb	0.418	0.539	0.340	0.476	0.409	0.490	0.490	0.563	0.581	0.546	0.546
Copper	16.30	19.60	12.87	18.85	16.97	19.11	18.98	23.00	24.09	22.19	22.19
Stainless Steel	14.86	20.90	15.04	27.59	6.61	8.50	5.56	3.94	4.32	7.12	11.00
Insulation	0.40	0.50	0.34	0.53	0.36	0.41	0.31	0.45	0.47	0.46	0.48

***For a discussion of the three types of conductors see section IV-B-1a

Table IV-B-4

Physical Parameters of the Ohmic Heating Coils

Coil	T1	T2	T3	T4	T5	T6	T7	T8	T9	T10	T11	T13	T12
R(m)	2.502	2.508	2.522	2.546	2.591	2.675	2.854	3.227	3.857	4.725	5.489	9.0	19.0
Z(m)	1.0	3.0	5.0	7.0	9.0	10.997	12.989	14.950	16.844	18.643	19.932	10.5	5.0
Maximum Current (MA)	5.15	5.13	5.10	4.98	4.84	4.57	4.10	3.26	2.25	1.45	0.53	0.19	0.20
Maximum B (tesla) **	5.34	5.31	5.28	5.18	5.06	4.71	4.67	4.01	3.03	2.56	1.32	0.93	0.74
Maximum tension (10^6N) **	21.9	21.7	21.4	20.7	19.8	18.1	15.2	10.4	5.4	2.3	0.32	0.92	-0.26*
Conductor type ***	1	1	1	1	1	1	1	2	2	1	1	3	1
Thickness of stainless steel for type 3 (cm)	--	--	--	--	--	--	--	--	--	--	--	0.32	--
Number of SC filaments per conductor	120	120	120	120	120	120	120	82	72	92	78	34	70
Number of turns	496	494	490	474	456	418	374	362	230	108	36	26	13
Magnet cross section radius (cm)	25	25	25	25	25	35	33	33	26	18	10	9	7
or radial width (cm)xheight (cm)	x 60	x 60	x 60	x 55	x 53	x 35	x 33	x 33	x 26	x 18	x 10		
Material Quantities (MT)													
TiNb	.594	.594	.594	.577	.566	.538	.510	.381	.258	.185	.062	.034	.067
Copper	17.84	17.82	17.71	17.34	16.99	16.09	15.38	12.61	9.57	7.34	2.84	3.55	1.68
Stainless Steel	--	--	--	--	--	--	--	3.69	2.83	--	--	--	0.59
Insulation	0.20	0.20	0.20	0.20	0.20	0.20	0.20	0.20	0.15	0.09	0.03	0.03	0.04

* Negative value means the coil is under compression

** Conductors were designed for the maximum combination of loadings produced by fields from self field, the remaining ohmic heating coils, and the vertical field coils and plasma.

*** For a discussion of the three types of conductors see Section IV-B-1-a

IV-B-2-c Design for Internal Stability

The internal stability is concerned with the number and size of the superconducting filaments used in each conductor. The maximum power dissipated in the superconductor occurs when one half the current is flowing in the superconductor. Under this condition the power dissipated in the superconductor filaments is one quarter the power which would be dissipated in the stabilizer were the stabilizer carrying all of the current. To assure that the power dissipated in the superconductor filament can be transmitted to the stabilizer without excessive temperature rise the following inequality must be satisfied

$$\frac{1}{4N} (I^2 \rho_s / a_s) \leq 8\pi K_{se} (\bar{T} - T_o), \qquad (2)$$

where

I = the total conductor current

K_{sc} = thermal conductivity of TiNb = 0.5 MW/cm-K

$\bar{T}$ = average temperature of a superconductor filament $\leq$ 5.2K

T_o = average temperature of the copper = 4.7K

Using this condition for the present design the number of filaments required is approximately 18 in the several coils. The actual number used is arbitrarily chosen much larger for ease of twisting and fabrication. The number of filaments shown in Tables IV-B-3 and IV-B-4 is based on a filament diameter of 0.038 cm and superconductor critical current densities based on data by Wohllenden.[9] The greater number of filaments provided will more than compensate for the thermal resistance of the thin layer of cryo-nickel placed around each superconductor filament so the internal stability is more than adequate.

IV-B-2-d Coil Winding

The majority of the ohmic heating coils will be built inside the torus center-core cold structure. They can be wound into the central core as the construction of the core proceeds. The winding of the remaining ohmic heating coils can be done elsewhere and they can be added at the appropriate time. The problems associated with building the vertical field coils are more difficult since they are inside the "D" shaped toroidal field magnets. It is obvious from viewing Fig. IV-A-9 that the logistics of assembling the vertical field magnets, the blanket, the shields and the vacuum chambers is formidable. For the vertical field magnets, the inner dewar and support structure would be constructured first and then a winding track and coil tensioner placed inside the toroidal field magnets. The use of just one integral conductor-structure with the insulation prewrapped around it makes the coil winding much simpler than would the case of separate layers of conductor, insulation and structure bands; i.e., only one tensioner is necessary. The exception to this is VF7 in which four normally reinforced conductors are wound in parallel. To more perfectly match the inductances of these four conductors they will be transposed at the end of each layer of the winding process. In order to reduce the dewar surface area and to reduce the maximum fields present at the conductors the majority of the vertical field coils will be wound in such a way as to produce as nearly a round cross section to the coil as is possible. Exceptions to this rule are coils VF1, VF2, VF3, and VF5 which are rectangular in cross

sections due to space limitations.

IV-B-2-c Dewars and Supports for the Divertor Coils

The dewar structure for the divertor coils will be similar to that used for the "D" magnets. The inner vessel consists of 3 mm stainless steel sheets in tight contact with the magnet through micrata spacers. There will be a 15cm vacuum space between the inner and outer vessels, where about 1/3 of the volume is filled with superinsulation. The thickness, t, of the alloy aluminum outer vessel is dependent upon the size of the magnet through

$$t > D \sqrt[3]{\frac{p}{KE}} \qquad (3)$$

where

K = a geometric constant = 2.2 for infinite vessel as is the case here (R>>D)

p = loading pressure = 101 x 10^3 N/m^2 (14.7 psi)

E = modulus of elasticity of alloy aluminum = 6.90 x 10^{10} N/m^2 (10x10^6psi)

D = dewar diameter = magnet diameter + 30 cm

The thickness ranges from 4mm to 11mm. All the dewar and magnet assembly will be supported by some vertical structure penetrating through the vacuum chamber between the toroidal field magnets. This structure is sized to provide the necessary centering and vertical loads on each magnet (see Fig. IV-A-9).

IV-B-3 AC Losses in Divertor and Transformer Coils

The operating cycle of the reactor requires charging and discharging of the vertical field and ohmic heating coils. During the 15 sec plasma current rise time the vertical field coils are charging while the ohmic heating coils are discharging. Substantial ac losses are produced in the copper stabilizer as well as in the superconducting filaments by these rapid current (and thus field) variations. The plasma current turn-off and transformer reset time are smaller than in the current rise stage. The ac losses in each cycle are induced from the following mechanisms:

a) eddy current loss in the normal metal

b) multifilament coupling loss

c) hysteresis loss in the superconducting filaments

IV-B-3-a Eddy Current Loss

The use of a much smaller conductor cross section with better cooling and the use of a stabilizer with higher resistivity, i.e., 10% cold reduced OFHC copper, has reduced the eddy current losses in the UWMAK-III design to negligible amounts. Table IV-B-2 shows that estimated values of this loss have been reduced from 14.71 KWh/charge in UWMAK-II to 0.25 KWh/charge in UWMAK-III.

IV-B-3-b Coupling Loss

The higher resistivity and the smaller cross section reduce the coupling losses from those in the UWMAK-II design but it is still necessary to use a Cu-Ni sheath around each superconductor filament. While no formal optimization was carried out, the thickness of the Cu-Ni sheath was finally set at 0.002 cm. With the smaller amount of stabilizer in this design a thicker sheath reduces the external stability and with a thickness of 0.002 cm the coupling loss for the vertical field magnets totals 0.16 kWh/charge with the twist pitch maintained at 30 cm.

IV-B-3-c Hysteresis Loss

The hysteresis losses in the UWMAK-III design are somewhat larger than those in the UWMAK-II design only by virtue of the greater number of coils. The total hysteresis loss is up to 0.46 kWh/charge in the vertical field coils from the previous value of 0.24.

IV-C Refrigeration

In this section the major sources of heat input to the magnets will be identified and estimates made of the refrigeration necessary to accomodate these losses.

IV-C-1 Heat Losses

The major sources of heat flow into the magnets are itemized as follows:

a. Thermal radiation loss: The outer surface and the side surfaces of the outer legs of the toroidal field coils are facing room temperature surfaces while the inner surface is facing the outer warm surfaces of the shields and other components. Assuming an average radiation loss of 7.5 MW/cm^2 and using a total surface area of $5000m^2$ this loss is 375 watts.

   A total of $3080m^2$ of surface area of the vertical field coils and ohmic heating coils will suffer similar losses to those in the toroidal field magnets or a loss of 231 watts.

b. Conductive loss: These are $3500cm^2$ of cross section of reinforced epoxy struts on each side of each toroidal field magnet with only 10% of the struts in contact in normal operation. Each strut is 15 cm long and the assumed conductive loss from 300K to 4.2K is 1700 mW/cm. The total loss is then (3500x2)x0.1x1.70x18÷15=1430 watts. Similar losses in the vertical field coils and ohmic heating coils total 1600 watts.

c. Resistive losses in conductor joints: Losses from this source are estimated to be 300 watts total in all magnets.

d. Lead losses: If we allow 5 mW/A for well designed vapor cooled leads the losses are evaluated as follows.

   1. Toroidal field magnets
      2x9545x18x0.005 = 1718 watts

2. Vertical field coils: In the 40 coils the average current carried by the vertical field coil conductors is 8500 A
   2x8500x40x0.005 = 3,400 watts
3. Ohmic heating coils: In the 26 coils the average conductor current is 12,800 A.
   2x12,800x26x0.005 = 3,330 watts

e. Nuclear Heating: The nuclear heating of the magnets is calculated to be 600 watts. See section V-C.

f. AC Losses: The ac losses were calculated in section IV-B-3 for the vertical field and ohmic heating coils and are;
   Eddy current loss = 0.25 KWh/charge = 500 watts
   Coupling loss = 0.16 KWh/charge = 320 watts
   Hysteresis loss = 0.46 KWh/charge = 920 watts
   The ac losses in the toroidal field magnets are much smaller and are neglected. The total ac losses are 1740 watts.

g. Transfer line and storage tank losses: These losses are estimated to be about the same as calculated in the UWMAK-I[1] report or 800 watts.

The total magnet system heat leak is 15,524 watts at 4.2K. The total power at room temperature to run the refrigerators is about 15,524x300 = 4.66 MW.

IV-C-2 Refrigerators

Ten 3 kW refrigerators are proposed with seven in operation and three in reserve. 300,000 liters of liquid helium in storage could supply the refrigeration for 12 hours of operation with no liquifiers in operation. This helium refrigeration capacity includes the requirements for the vacuum cryopumps, 7.3 kW at 4.2K (see section III-B-4).

IV-D Power Supplies

IV-D-1 Toroidal Field Magnets

The total energy stored in the "D" shaped toroidal field magnets is found by integrating the magnetic energy density, $B^2/2\mu_o$ over the volume of the torus. This gives 30 MWh or 108 GJ. The inductance, L, of the toroidal magnet system is found from $108 \times 10^9 J = 1/2\ L(9545)^2$ or $L \approx 2371$ henries. Assuming a 24 hour charging time, the voltage rating of the power supply will be 262 volts. An ac/dc bridge rated at 2.5 MW is required for the power supply for the toroidal field magnets.

IV-D-2 Vertical Field and Ohmic Heating Coils

Figure IV-D-1 shows the plasma current and the current in coil T1 of the ohmic heating system. The form of the time variation in current in the remaining coils in the ohmic heating system is the same as that in coil T1. Figure IV-D-2 shows the time variation in the total power being supplied to the poloidal system and Figure IV-D-3 shows the time variation in stored energy. If we assume a reasonable limit of 500 MW of three-phase power supplied from a converter connected to an electrical utility system the remaining 413 MW of peak power required at the 15 second position must be supplied from an energy storage unit. For the amount of energy storage

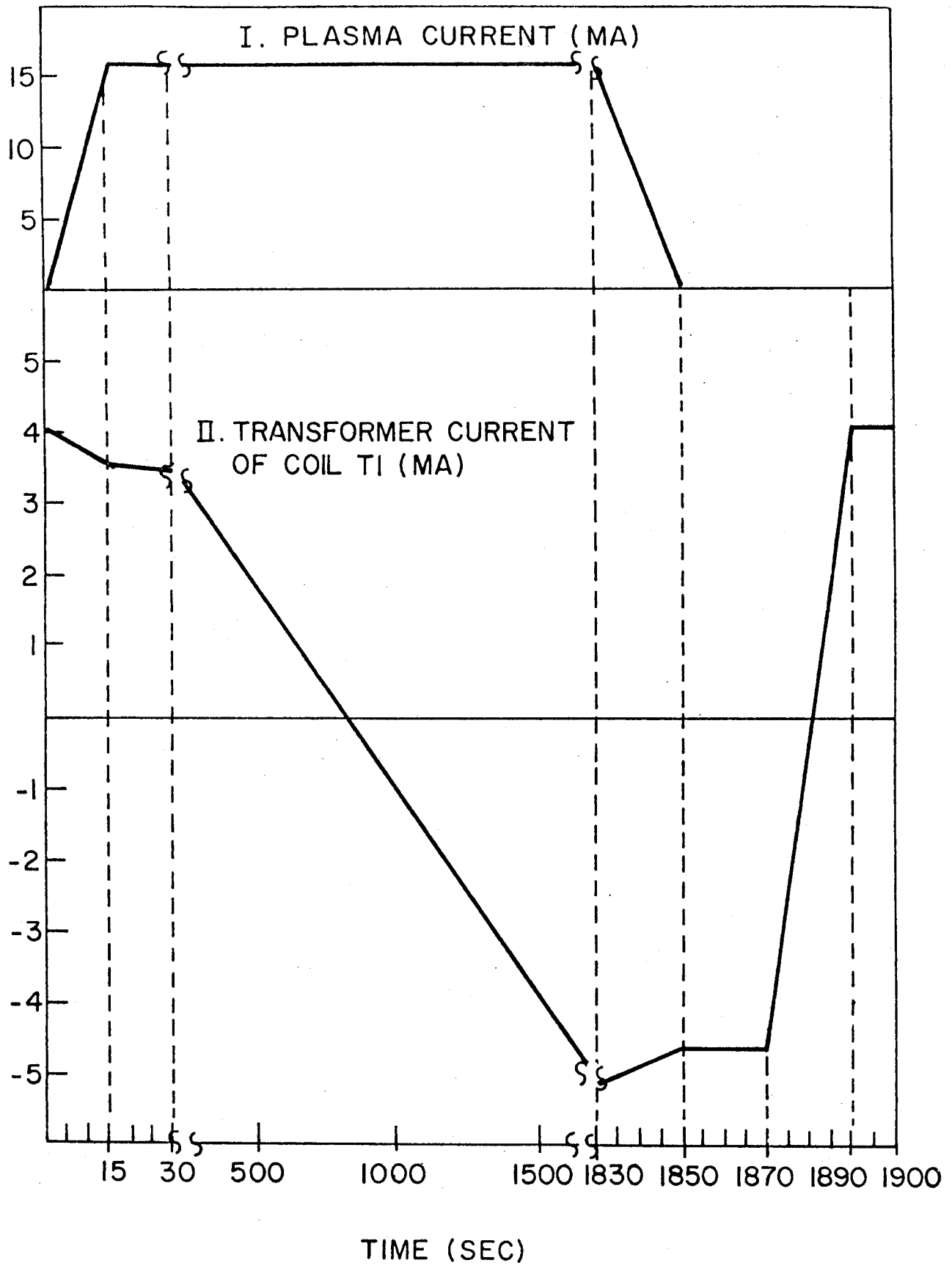

FIGURE IV-D-1

Time Variation of Plasma Current and a Representative Transformer Coil Current

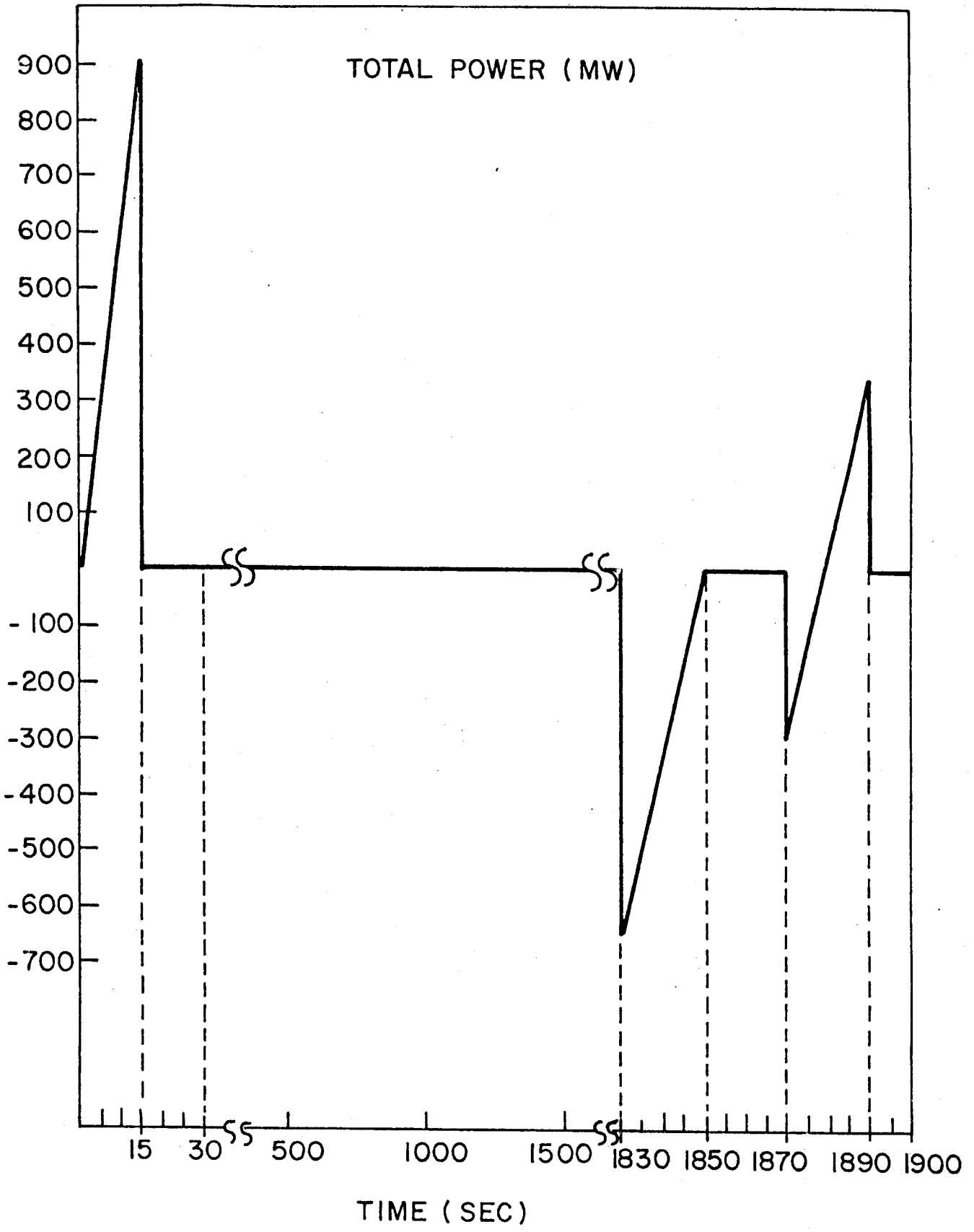

FIGURE IV-D-2

Time Variation of Total Power Supplied to the Poloidal Coils

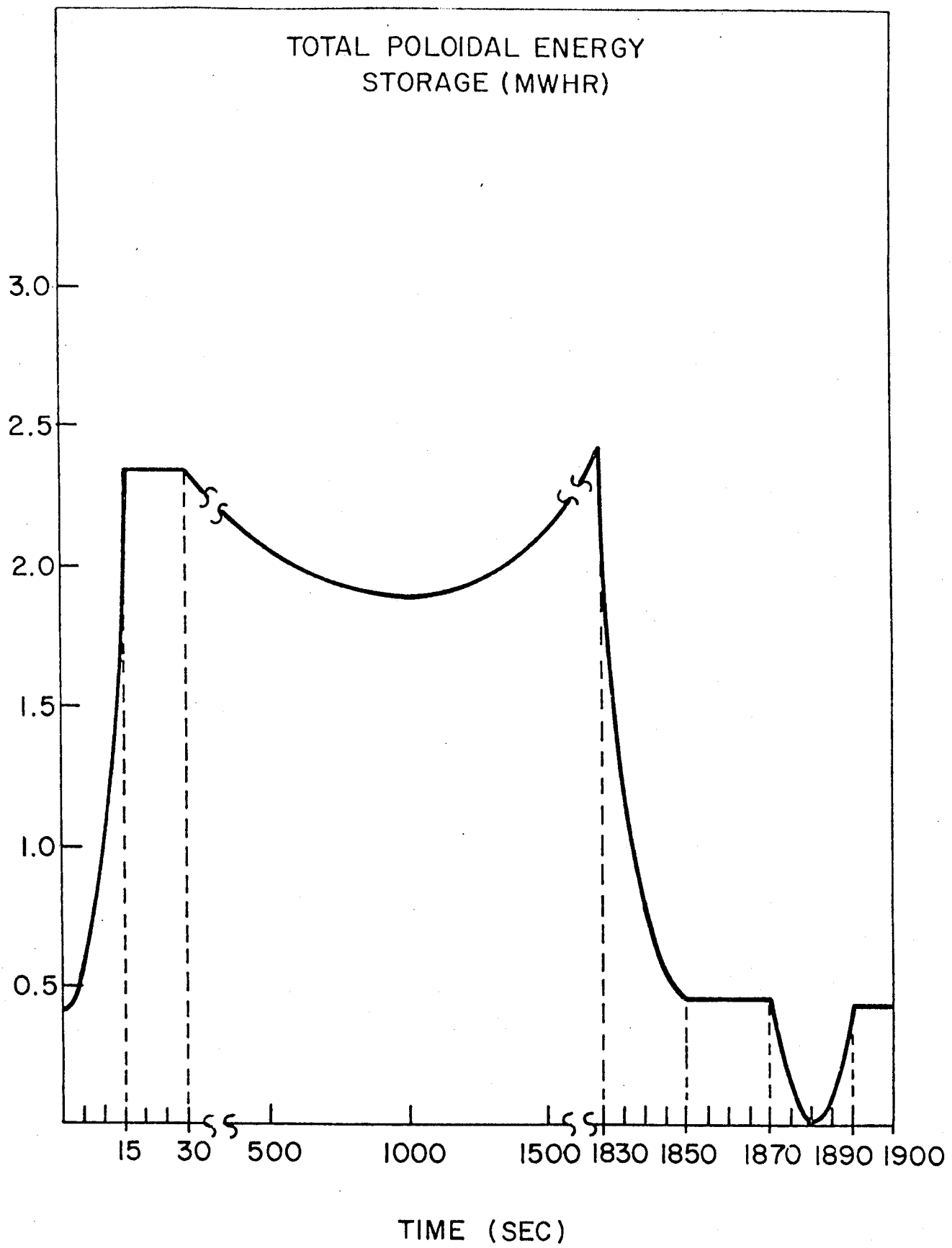

FIGURE IV-D-3

Time Variation in Total Stored Energy in the Poloidal Fields

required, the maximum rate at which energy is extracted from the unit, and the shape of the power pulses, we believe that a superconductive magnetic energy storage unit is the one best suited for this purpose. The maximum energy withdrawn can be estimated by referring to the first peak in the power curve in Figure IV-D-2 and evaluating the area under this curve above the 500 MW level as $413 \times (\frac{413}{913} \times 15) \times \frac{1}{2} \times \frac{1}{3600} = 0.39$ MWh. We assume that it is reasonable to withdraw 0.39 MWh from a 1 MWh unit so the superconductive energy storage dipole designed for the Fermi National Laboratory[8] is appropriate for this purpose.

Recent work at Wisconsin[13] on the interface components of such a system has led to circuits which minimize the disturbance to an electric utility from peak power pulses.

Figure IV-D-4(b) shows the pulsed power and current required by the poloidal field coils for a representative fusion reactor. For the UWMAK-III design, the power demand P_T rises linearly to about 913 MW in 15 seconds ($t=T_2$) and thereafter drops to a very low level. The cycle repeats with a period of 31.7 minutes.

Figure IV-D-4(a) shows the basic arrangement to supply such a pulsed load from two converters #1 and #2 in parallel. A large power system might be able to supply up to 500 MW without exceeding the allowable electrical system frequency deviation and attendant voltage fluctuations. The converter #1 in Fig. IV-D-4(a) supplies this power P_1 from the three-phase power system directly to the load. The rest of the power P_2 is supplied by converter #2 through the Superconductive Inductor Energy Storage Unit shown in Fig. IV-D-5. The storage inductor L_s is charged slowly from the three-phase power system through the Power Source Converter PSC (Fig. IV-D-5).

The converters 2' and 2 together with the capacitor bank form a dc/ac/dc double conversion sub-unit.[14] This subunit and the converter #1 may operate in parallel to supply the shared load L_o.

The circuit arrangement for the storage inductor and the dc/ac/dc conversion sub-unit are shown in Fig. IV-D-5. DC power is drawn out of the storage unit, converted to ac, rectified back to dc and is finally supplied to the load. The capacitor bank shown provides the Q (reactive volt-amperes) required for the commutation of both converters 2' and 2. The commutation frequency can be varied over a wide range by the proper choice of capacitors. The power required from the three-phase source through the PSC is the power averaged over the period of repetition (about 1/2 hour); thus, the three-phase power system is required to deliver only a small and fairly constant power corresponding to the pulsed power P_2. P_2 may be made any fraction of the total power P_T by proper design. Correspondingly, W_2 may be made any fraction of the total W_T pulsed energy requirement. Clearly, reduction of the resultant power pulses and correspondinging voltage fluctuations is a matter of design economics.

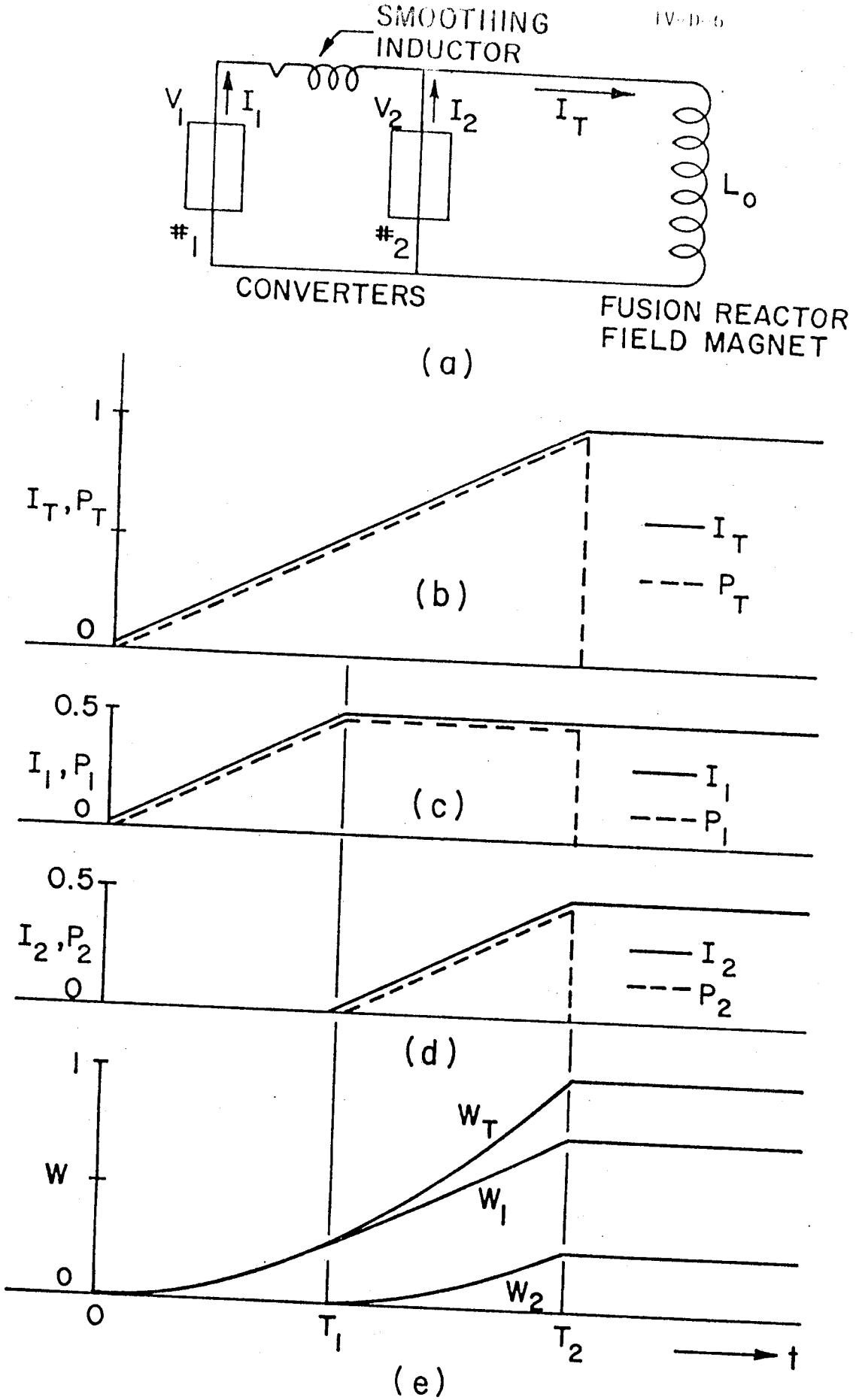

Fig. IV-D-4 REPRESENTATIVE FUSION REACTOR PULSED LOAD CHARACTERISTICS

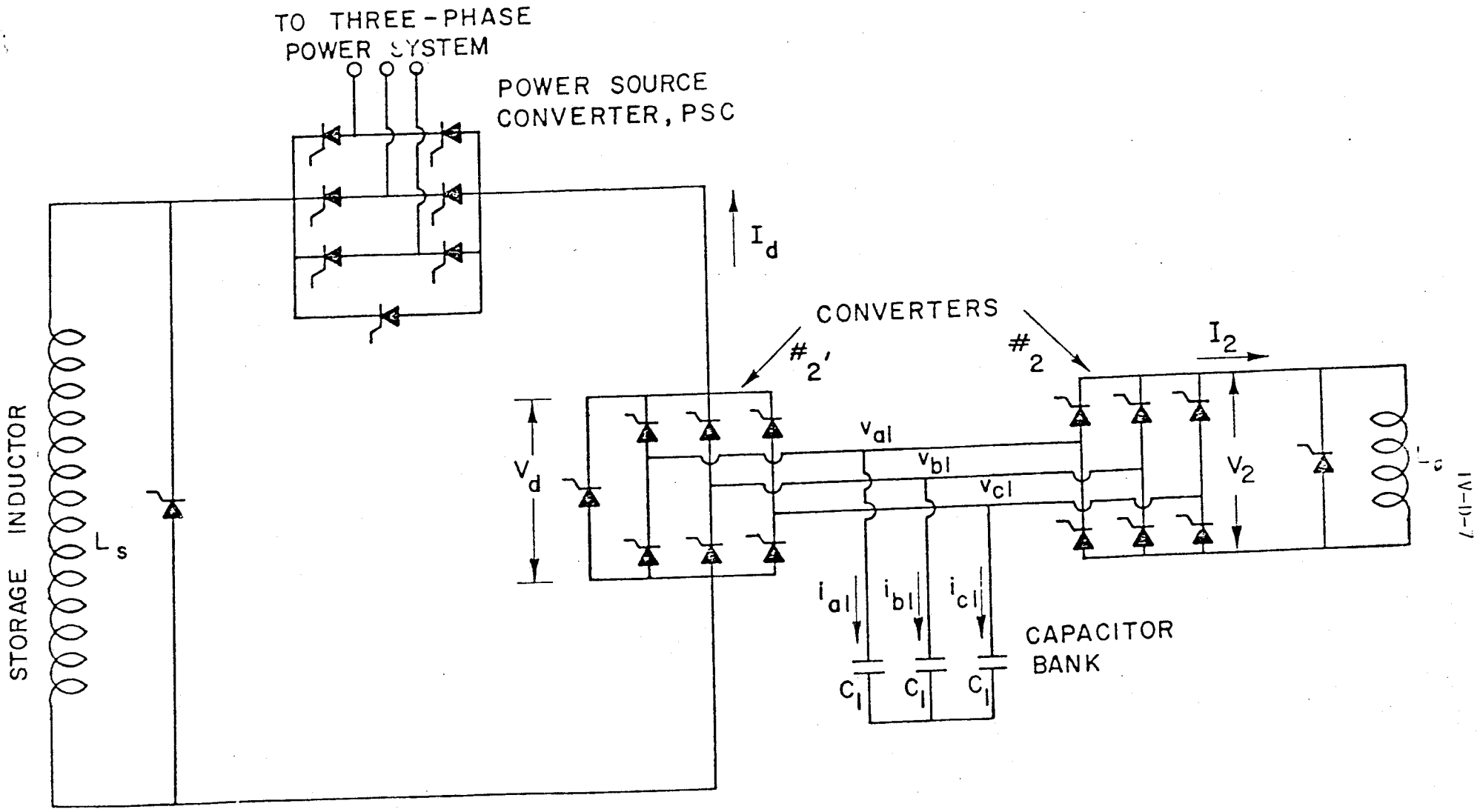

Figure IV-D-5

CIRCUIT DIAGRAM OF SUPERCONDUCTING ENERGY STORAGE INDUCTOR UNIT L_s
AND THE DC/AC/DC DOUBLE CONVERSION SUB-UNIT

IV-D-3 Design of Energy Storage Inductor

For UWMAK-III the stored energy is 1 MWh (3.6×10^9 J) of which only 39% (W_2, Fig. 1(e)) is cycled in and out of storage. The storage magnet L_s is a short solenoid whose diameter to length ratio is about 3:1 for optimum economy in storage. The conductor is a 38:1 copper to TiNb cryogenically stable strip wound bifilarly with stainless-steel reinforcement strips. The overall construction is a stack of double pancake coils separated with micarta slats, all very similar to the NAL bubble chamber magnet.[15] AC losses have been calculated to be less than 0.02% of the 1 MWh stored energy. Calculations have also shown that no filament temperature during pulsing will exceed 5.0K. The other more routine losses: leads, mechanical supports and thermal radiation account for 3370 kJ or 0.1% of the stored energy. It is thus seen that the reliability of a cryogenically stable magnet can be obtained without an energy loss penalty; if the repetition rate were higher, then more complicated magnets, with flux shields[16] or with less stable ac composite conductors, might be needed.

IV-E. Cost Estimate

IV-E-1 Toroidal Field Magnets

Material	Costs-10^6
Conductor	10.72
Discs with installed conductors	11.66
Epoxy insulation	0.59
Aluminum alloy bolts	0.20
Micarta spacers	1.10
Helium dewars	1.78
Vacuum dewars	4.38
Super insulation	0.45
Central support structure	5.40
Assembly and erection, including superinsulation	36.00
Cast aluminum secondary vacuum wall and lateral support structure	5.00
Total	$77.28

IV-E-2 Vertical Field Coils

Material	Costs-10^6
Conductor	10.78
Epoxy fiberglass	.04
Superinsulation	.27
He dewars	2.00
Vacuum dewars	4.00
Assembly and erection	3.74
Total	$20.83

IV-E-3 Ohmic Heating Coils

Material	Costs-10^6
Conductor	$4.34
Epoxy fiberglass	.22
Assembly and erection	1.42
Total	$5.98

IV-E-4 Refrigeration System

Material		Costs-10^6
Ten 3 kW refrigerators @ $583,000/kW		$17.5
Liquid helium inventory		
"D" magnet	144,000	
Vertical field and ohmic heating coils	100,000	
Storage	300,000 liters	
Total	544,000 l @ $3/liter =	1.63
		$19.13

IV-E-5 Power Supplies and Energy Storage Magnet

a. Toroidal field magnets.

An ac/dc bridge rated at 2500 kW is needed. Assuming a cost of $40/kW, the total capital cost of this power supply is $2.00 x 10^6.

b. Vertical field and ohmic heating coils.

The ac/dc bridge which provides 500 MW of peak power to the poloidal coils directly from the ac utility system is priced at $20/kW due to the short pulse duration. This cost is $10 x 10^6. The superconductive energy storage unit of 1MWh size is estimated to cost $15 x 10^6.(8) The dc/ac/dc conversion bridge discussed in section IV-D-2 is rated at 413 MW but costs only $15/kW or $6.2 x 10^6. The power source converter to charge the storage unit has a negligible cost.

The total power supply cost is $33.2 x 10^6.

IV-E-6 Entire Magnet System

The total cost of the magnets, refrigeration system, and the power supplies is estimated to be (77.3 + 20.8 + 6.0 + 19.1 + 33.2) x 10^6 = $156.4 x 10^6.

References for Chapter IV

1. B. Badger et al., "UWMAK-I, A Wisconsin Toroidal Fusion Reactor Design," UWFDM-68, Nuclear Engr. Dept., Univ. of Wisconsin (Nov. 1973) Vol. I.

2. B. Badger et al., "UWMAK-II, A Conceptual D-T Fueled,Helium Cooled, Tokamak Fusion Power Reactor Design, Fusion Technology Program," UWFDM-112, Nuclear Engr. Dept., Univ. of Wisconsin (May 1975).

3. D. Cornish, private Communication.

4. R.W. Moses, Jr. and W.C. Young, "Analytic Expressions for Magnetic Forces on Sectored Toroidal Coils," Presented at the Sixth Symposium on Engineering Problems of Fusion Research, November 17-21, 1975 at San Diego, Calif.

5. H. R. Segal and T. G. Richard, "Low Temperature Resistance Studies on Cyclically Strained Aluminum," Presented at the 1975 Cryogenic Engineering Conference, Kingston, Ont.

6. J. File and G.V. Sheffield, "A Large Superconducting Magnet for Fusion Research," Proceedings of the Fourth International Conference on Magnet Technology, Brookhaven, 1972.

7. J. R. Purcell et al., "Tokamak Experimental Power Reactor Studies Report, ANL/CTR-75-2, Argonne National Laboratory, June, 1975.

8. "Cryogenic Energy Storage System Design Report," Fermi National Laboratory Report FN-264, 8000.00 in collaboration with the University of Wisconsin, Oct. 1974.

9. K. Wohlleben, "Influence of Proton Irradiation on the Critical Current Density $j_c(B,T)$ of NbTi," Jour. of Low Temperature Physics, Vol. 33, Nos. 3/4, 1973.

10. R.W. Boom, et al., "Aluminum Composite Conductors," A.P.S. Bulletin, Series II, Vol. 17, No. 12, p. 1195, 1972.

11. F.J. Worzala, private communication.

12. J. Davis and A. Brown, private communication.

13. H.A. Peterson, et al., "Energy Storage and Switching for Tokamak Fusion Reactors," Invited paper for the Energy Storage for Fusion Devices Section of the American Nuclear Society, Winter Meeting, San Francisco, Nov. 16-21, 1975.

14. H.A. Peterson, et al., "Superconductive Inductor-Converter Units for Pulsed Power Loads," Intl. Conf. on Energy Storage Compression and Switching, Torino, Italy, Nov. 5-7, 1974.

15. J. R. Purcell and H. Desportes, "The NAL Bubble Chamber Magnet," Proceedings of the 1972 Applied Superconductivity Conference, p. 246, Annapolis, Maryland.

16. R.W. Moses, Jr. and J.K. Ballou, "Inductive Shielding for Pulsed Energy Storage Magnets," IEEE Transactions on Magnetics, Vol. MAG-11, No. 2, p. 43, March, 1975.

17. F. W. Grover, Inductor Calculations (Dover Pub. Inc., N.Y., 1946).

V. Blanket Design and Neutronics Analysis

V-A. Design Philosophy and Requirements

UWMAK-III is intended to typify an advanced reactor which would be built by a mature fusion industry. As such, its design emphasizes economic criteria and concommittant sophistication in contrast to our earlier UWMAK I and II designs[1,2] which emphasized state of the art technology. In order to improve the economics of the system, the physical size of the plant must be reduced as a means of controlling capital costs. As has already been described, the magnets are more effectively used by the noncircular plasma. However, the full benefit of size reduction can only be realized by reducing the chamber volume. An additional significant economic gain can be realized by operating the system at higher temperatures than in our previous designs.

The higher temperature operation essentially dictates the use of a refractory metal for the structure. The molybdenum alloy TZM has been chosen for UWMAK-III. The reasons for this choice are given in Chapter IX on materials and radiation damage. From a neutronics standpoint, this is a very acceptable choice.

Other than fixing the structural material, the detailed design is not greatly affected by the higher temperature operation. However, the small chamber size for the same power level of 5000 MW_t as in references 1 and 2 results in an increased average wall loading. Wall exposure is one of the limiting design constraints and at the proposed loading would result in unacceptably short wall life in our earlier designs. To overcome this problem, the structural wall must either be protected or designed for rapid replacement. Both approaches have been employed in UWMAK-III.

The inside of a torus in the poloidal direction is the most difficult part of a tokamak to replace because there is little access space. Thus a thick graphite wall (region 12 in Fig. V-1) is introduced in front of the vacuum wall (region 13 in Fig. V-1) which acts to soften, reflect, and attenuate the neutrons incident from the plasma in the manner described in reference 3. This ISSEC zone (Internal Spectral Shifter and Energy Converter) reduces both the displacement and helium production rates in the first structural wall (region 13 in Fig. V-1) and thus increases the wall life for this zone. The ISSEC zone is not actively cooled but radiates heat to the first structural wall behind it and also to the first wall on the outer portion of the plasma chamber. The inner blanket is further simplified by use of helium cooling. The absence of flowing liquid lithium eliminates the problem of the high pressure drop that results from using a liquid metal coolant in the high magnetic field region. The absence of lithium also alleviates tritium removal problems by eliminating the need for this function in the inner blanket. Finally, the inner blanket and shield is consciously designed to be as thin as feasible to allow for a lower aspect ratio and to allow higher magnetic fields in the plasma for the same magnetic field at the coil.

The ISSEC cannot be extended around the chamber since it would result in problems in achieving adequate tritium production. For this reason and because one has relatively easy access to the outer blanket and shield (zones 1, 2, 3, 4, 7, 8, 9, 10 of Figure V-1) the outer blanket system is designed for convenient replacement. This is discussed in detail in Chapter VI, section E. Experience with the UWMAK-I and UWMAK-II designs indicates that resource limitations make use of Be as a neutron multiplier undesirable. This leads to the choice of a liquid lithium cooled system for the outer blanket to achieve adequate breeding without a contribution from the inner blanket. The choice of zone thickness is made on the basis of results from a series of one dimensional calculations. The final structural details are chosen on the basis of heat transfer and mechanical design (Chapter VI).

The higher wall loading emphasizes the importance of geometrical effects and has dictated a more intense study of the neutron transport in UWMAK-III. This includes both one and two dimensional S_n calculations as described in the next section.

V-B. Blanket and Shield Calculations

V-B-1. Neutron Source Distribution

Both the plasma and the chamber are noncircular and the magnetic axis which serves at the plasma axis, is not at the geometrical center of the plasma. The neutron source distribution is proportional to the square of the ion density and has been approximately represented as a function of x and y in a vertical plane through the torus as

$$S(x,y) = S(0,0)\ [1 - (\frac{x - 50}{200})^{2\,3}]\ \ [1 - (\frac{y}{580})^{2\,3}]\ ,\ -150 \leq x \leq 250;$$

and $$S(x,y) = S(150,y)\ [0.01\ x + 2.50],\ -250 \leq x \leq -150.$$

This is shown in Figure V-2 and the source peak is centered vertically but is shifted 50 cm toward the outside of the torus from the plasma center at 8.1m.

V-B-2. Nuclear Data

The neutron transport and gamma production cross sections were obtained as a coupled set of 100 neutron groups and 21 gamma groups produced for EPR calculations.[4] This data set was generated with the AMPX modular code system[5] from the nuclear data in ENDF/B-IV. The only exception is Mo where evaluation of the cross sections are based on ENDF/B-III data. The cross sections wereweighted with a 1/E spectrum for $E_n > 0.345$ eV and with a Maxwellian distribution for $E_n \leq 0.345$ eV. The gamma interaction cross sections were uniformlyweighted.

Due to costs and computer memory limitations, the one hundred neutron group cross sections were collapsed to 46 groups keeping the same fine group structure above 2 MeV as in the original set. The 46 group structure is shown in Table V-1 and is the same as that used in earlier designs.[1,2]

The gamma production cross sections for Mo at the time of the calculations were unfortunately not available. Niobium gamma production data was substituted for the missing Mo data and the effect of this substitution will be discussed below. The 21 group structure for the gamma interaction cross sections used in these calculations is shown in Table V-2.

Neutron kerma factors were generated using the MACK program[6] based on data in ENDF/B-III. The gamma kerma factors were calculated using the MUG[7] code and ENDF/B-III data.

FIGURE V-1
BLANKET MODEL USED FOR TWO-DIMENSIONAL NEUTRONICS ANALYSIS OF UWMAK-III

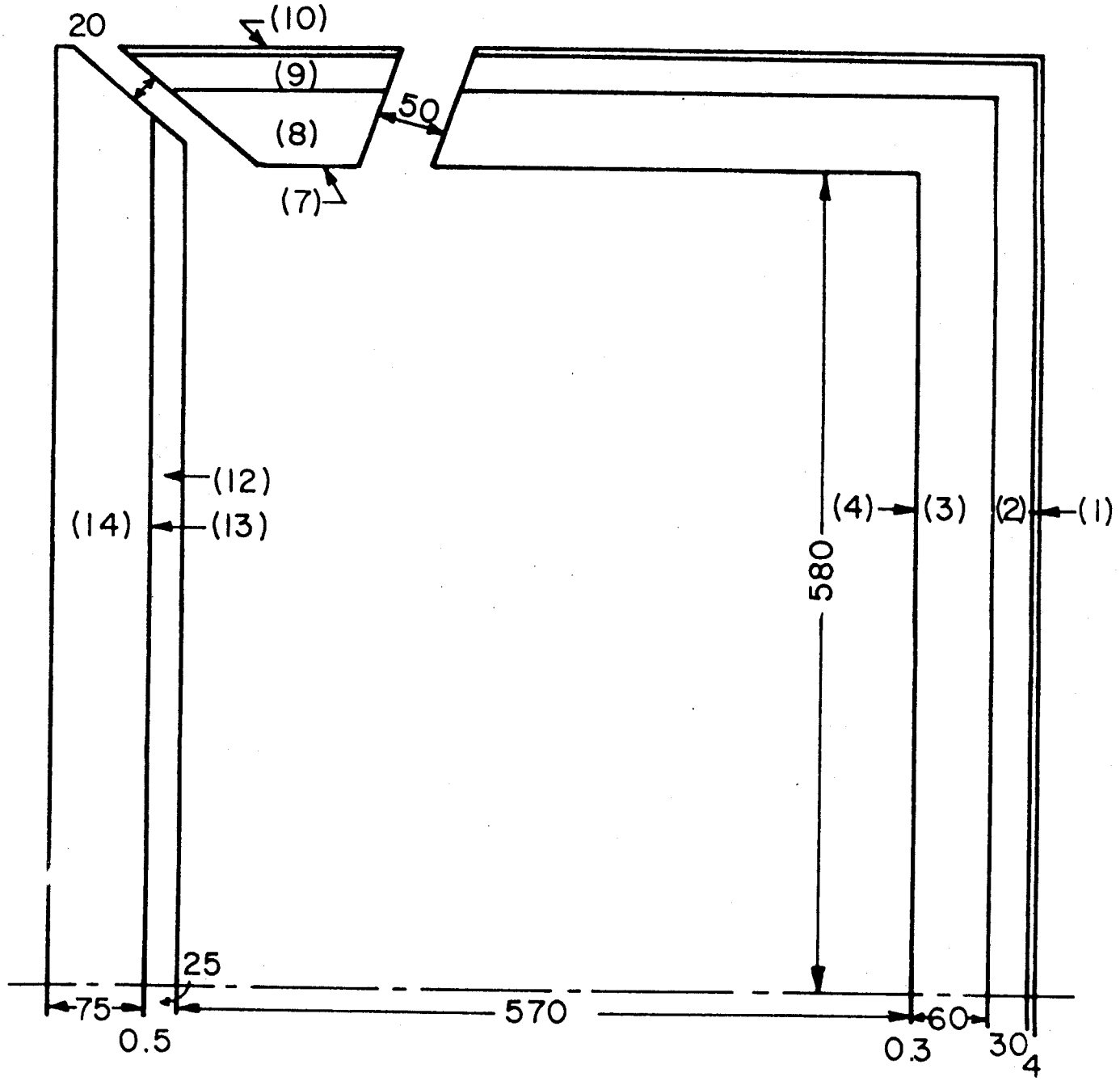

ZONE	COMPOSITION	ZONE	COMPOSITION
1, 3,..8, 10	97% Li + 3% Mo	4, 7, 13 -	Mo
2, 9	99% C + 1% Mo	12	C
14	40% B_4C+60%Mo (DENSITY FACTOR .95)		

V-B-3. One Dimensional Calculations

One dimensional neutron transport calculations for Tokamak reactors have typically been based on an infinite cylinder by considering a vertical cut through the torus. This results in the problem shown schematically in Fig. V-3 where the central zone contains the plasma and thus the neutron source. The first zone surrounding the plasma is the first structural wall while the second is the blanket containing the breeding and cooling materials and these are followed by reflector and shielding zones. This calculational model is expected to be acceptable only when the system has poloidal symmetry and a high aspect ratio.

Actually, the UWMAK-III design employing the ISSEC concept, a noncircular plasma and blanket and shield, and a low aspect ratio, differs greatly from the type of system for which the conventional calculational model is appropriate. However, a suitable calculational model can be obtained by considering a horizontal cut through the torus at the midplane. A general schematic for this representation is shown in Figure V-4 where the system must now have toroidal symmetry but not necessarily poloidal symmetry. A lack of poloidal symmetry is represented apprixmately by a difference in composition and/or thickness between the inner and outer blankets and shields. The resulting one dimensional calculational model treats the zones as shells of infinite height. This takes the low aspect ratio into account properly and, for a vertically elongated plasma as in UWMAK-III, may represent the midplane results very well. This is implemented using the cylindrical option of the S_n computer program ANISN[8] with a minor programming change.

Following a simple parameter survey to maximize the tritium production rate, the UWMAK-III design was modeled as shown schematically in Figure V-5. On the left is the inner most shield starting at a major radius of 389.5 cm, the inner structural wall is at 495 cm, and the ISSEC ends at 520 cm. The plasma is centered at 810 cm but the source peaks at 890 cm in the 1-D study based on a better plasma calculation than the earlier 50 cm shift, and the outer blanket and shield occupy the region between 1130 and 1324 cm. The outer structural wall is 0.15 cm thick TZM which is adequate for the stresses in the low pressure liquid lithium system. The inner blanket is mostly solid materials cooled with helium. The high pressure required by the gas coolant results in the need for a 0.25 cm TZM wall as the first structural wall of the inner blanket. The liq

lithium zones are 60 cm and 10 cm thick respectively, for tritium production in the actual design. However, the calculations and figures presented here treat the second lithium bearing zone as only 4 cm thick. The performance of the actual blanket will exceed the calculated results but only by a trival amount. The TZM in these zones is estimated on structural grounds to be 3% by volume. The results are only moderately sensitive to the volume percent of structure and small changes would be tolerable. Graphite with 1% TZM structure is used in a 30 cm thick reflector zone for the outer blanket region.

The ISSEC concept is implemented by placing a 25 cm graphite zone in front of the first structural wall of the inner blanket. This protects the wall by reducing the dpa and gas production rates. This is discussed in the next section. In addition, some neutrons are reflected to the outer blanket to aid the breeding of tritium and energy. The inner blanket is simply a hot shield consisting of a mixture of TZM, B_4C and $Al_2O_3SiO_2$ as a binder. The outer shield composition and thickness is based primarily on earlier studies done by Abdou and Maynard. The inner shield has been adjusted to the design requirement for energy attenuation and the last zone of the shield is primarily lead to remove the residual secondary gamma flux.

Summary results of S_4-P_3 calculations are given in Tables V-3 and V-4 for the tritium production and heating rate/zone. The distribution of the tritium production, heating, and energy attenuation for the inner and outer zones are shown on Figures V-6, V-7 and V-8, respectively. The breeding ratio of 1.27 is quite satisfactory. However, this is expected to be higher than the actual value. The calculational model is best at the midplane and accounts for neither the curvature of the media in the poloidal direction nor the finite height of the source distribution. A two dimensional calculation is described in another subsection which partly accounts for these effects (See Appendix A).

The total energy deposition per D-T neutron in the blanket and shield is approximately 16 MeV. This is 0.49 MeV and 1.99 MeV less than in the UWMAK-I and UWMAK-II designs, respectively. This decreased energy production relative to UWMAK-I is primarily related to the reduced tritium production rate in the present design since the ^6Li tritium producing reaction is highly exothermic. Although UWMAK-II has an even lower breeding ratio, its energy production is still slightly better than the current case since almost all breeding is achieved with the ^6Li reaction with the neutron multiplication coming from the (n,2n) reaction in Be, which has a low Q value. The energy production is actually expected to be somewhat less than 16 MeV since this value was calculated by adding the neutron and gamma heating. The gamma heating is expected to be lower in the molybdenum containing zones because preliminary information indicates the actual gamma production cross sections of molybdenum are lower than those of niobium.

It can be noted from Table V-4 that the heating rates in the inner and outer blankets are predicted to be in the ratio of 1 to 3.7. The calculational model undoubtedly overestimates this ratio but it should be approximately correct

at the midplane. This shows the kinds of effects which can result from toroidal geometry. The effect is advantageous for the tritium production and for the inner first wall life. In addition, note that the dpa rate behind the ISSEC is only one ninth the dpa rate in the outer wall. The wall life is enhanced proportionately.

The energy attenuation in the shielding zone is shown in Figure V-8. From these results the heat load to the cryogenic system of the magnets will be 0.6 KW which is reasonable for the refrigeration system.

V-B-4. Two Dimensional Calculations

The chamber and neutron source distribution shown in Figs V-1 and V-2 can be represented realistically with the xy geometry option of the two dimensional S_n program DOT[9]. However, unlike the earlier calculational model, the toroidal curvature is not accounted for here. The calculations employ 46 neutron energy groups, 21 gamma energy groups, and 16 directions. Table V-5 gives the results for the tritium production by zone. The overall production per source neutron is 1.076. Although this is considerably less than the result from the one dimensional model, it is still adequate and accounts for the lack of inner blanket breeding and for leakage. Further, it is expected to be a lower bound since the toroidal effect should increase the total outer blanket contribution.

More generally, integral type quantities are expected to fall between the 1-D model and the xy geometry 2-D model results. Thus the total energy deposition in the outer blanket is 3.7 times that in the inner blanket from the 1-D calculation. The 2-D calculation yields 2 for the same quantity. The lowest order effect of toroidal geometry is the increase in the volume of the outer zones thus tending to push the results toward those of the 1-D model.

The trend of average quantities and maxima of densities are more difficult to predict in going from one model to the other. The 1-D model result for the energy per D-T neutron is 16.1 MeV while the corresponding 2-D result is 18.2 MeV The increase is primarily due to added gamma heating in the inner blanket caused by the relatively larger amount of structural material implied by the 2-D model. Since this is not actually the case, the correct result is somewhat less than 18 MeV. It should be noted that the gamma heating in TZM should be less than is predicted by the Niobium gamma production data which was substituted, thus both figures should be reduced. The details of the energy production by zone are given in Table V-6.

The complicated variation of the tritium production as one goes around the outer blanket in the poloidal direction at various distances from the first wall is shown in Fig. V-9A and V-9B. The reaction rates per D-T neutron for the tritium producing reactions in ^6Li and ^7Li are designated as T_6 and T_7 respectively. The lines along which results are shown are numbered 1, 2, and 3 in the schematics in a lower corner of each Figure. Lines 1, 2 and 3 are respectively at depths of 3, 33 and 57 cm in the outer blanket. The general trend is a decrease as one proceeds along the blanket starting from the mid-plane. T_6 varies less since these reactions are induced primarily by thermal

or epithermal neutrons some of which have been reflected from the ISSEC and other walls. The T_7 variation reflects the effects of both flux and spectrum variation and is probably not too important. The more dramatic variation shown in Fig. V-9B is caused by the divertor slots. As the reaction rate may correlate fairly well with radiation damage, this variation indicates the need for careful placement and shaping of the slots and ISSEC to protect the walls, particularly on the inner blanket side.

The displacements per atom (dpa) from the 1-D model are 9.3 to one from the outer to inner first walls. This provides a measure of the protection provided the inner wall by the geometry and the ISSEC. The 2-D results for the dpa rate at various distances along the outer and inner walls from the midplane are shown on Fig. V-10. The dpa rate drops appreciably from the midplane values and the protection afforded the inner wall is about a factor of six. The actual protection will, as far as dpa rate, is concerned lie somewhere between the 1-D and 2-D results, i.e. in the range 6-9. Due to the softer spectra behind the ISSEC, the Helium gas production in the wall will be only 1/24 of the outer first wall value. This will tend to reduce the radiation damage still further. This is considered in detail in chapter IX.

V-C Non Uniform Neutron Wall Loading

The complete two dimensional R-Z geometry calculation using DOT has not been carried out at this point due to the expense of such a problem, although the results have generally been bounded by our 1 and 2-D calculational models. To obtain some insight into the toroidal geometry effect without the full expense of the complete problem, a special R-Z geometry problem has been carried out to determine the wall loading. This is shown schematically in Figure V-11 where the source boundary cross section in the R-Z plane is the inner curve. The medium is treated as a vacuum with vacuum boundary conditions at the top, left and right boundaries and a reflecting condition along the lower boundary.

The energy flux or wall loading is obtained along the curve labeled first wall. The resulting wall loading in MW/m^2 is plotted against the height above the midplane in Figure V-12. The average wall loading is 1.91 MW/m^2 and the maximum is 2.37 MW/m^2. In interpreting these results, it should be kept in mind that the actual area of the outer wall is much greater than that of the inner wall and that the inner wall will in fact be behind the ISSEC. (See Appendix A for two dimensional toroidal geometry analysis).

V-D Biological Shielding

The shield discussed in the earlier sections of this chapter has been designed primarily to protect the magnets. It will also do a very reasonable job of protecting other equipment but special shields will undoubtedly be needed for special purposes in the regions near the reactor. However, the radiation outside the reactor during operation is still much too intense for personnel. The rules for allowed radiation levels in work areas and legally allowed exposures are those given in Title 10, code of Federal Regulations, Part 20[11]. The key limit for our purposes is the 5.0rem per year or 2.5 mrem per hour. The biological shield will consist of concrete walls surrounding the entire nuclear island, 225cm thick.

TWO DIMENSIONAL NEUTRON SOURCE DISTRIBUTION

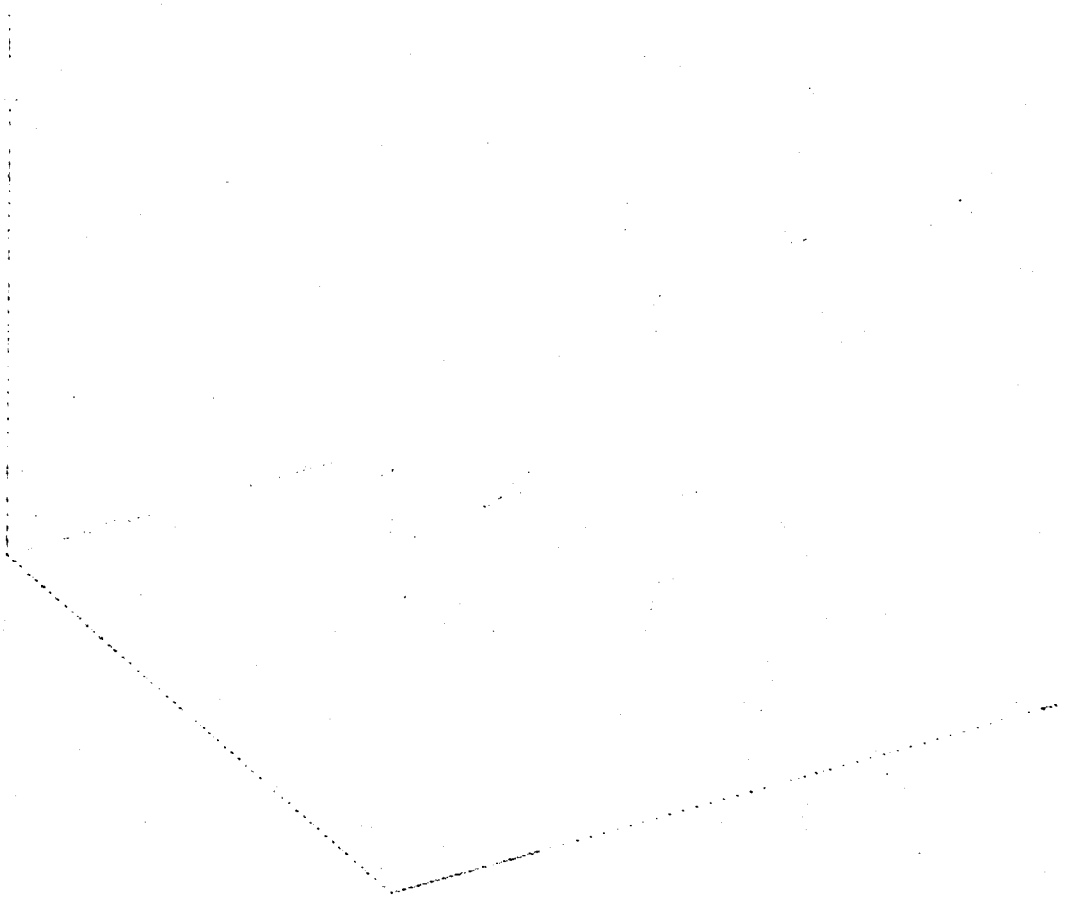

FIGURE V-2

TWO DIMENSIONAL NEUTRON SOURCE DISTRIBUTION

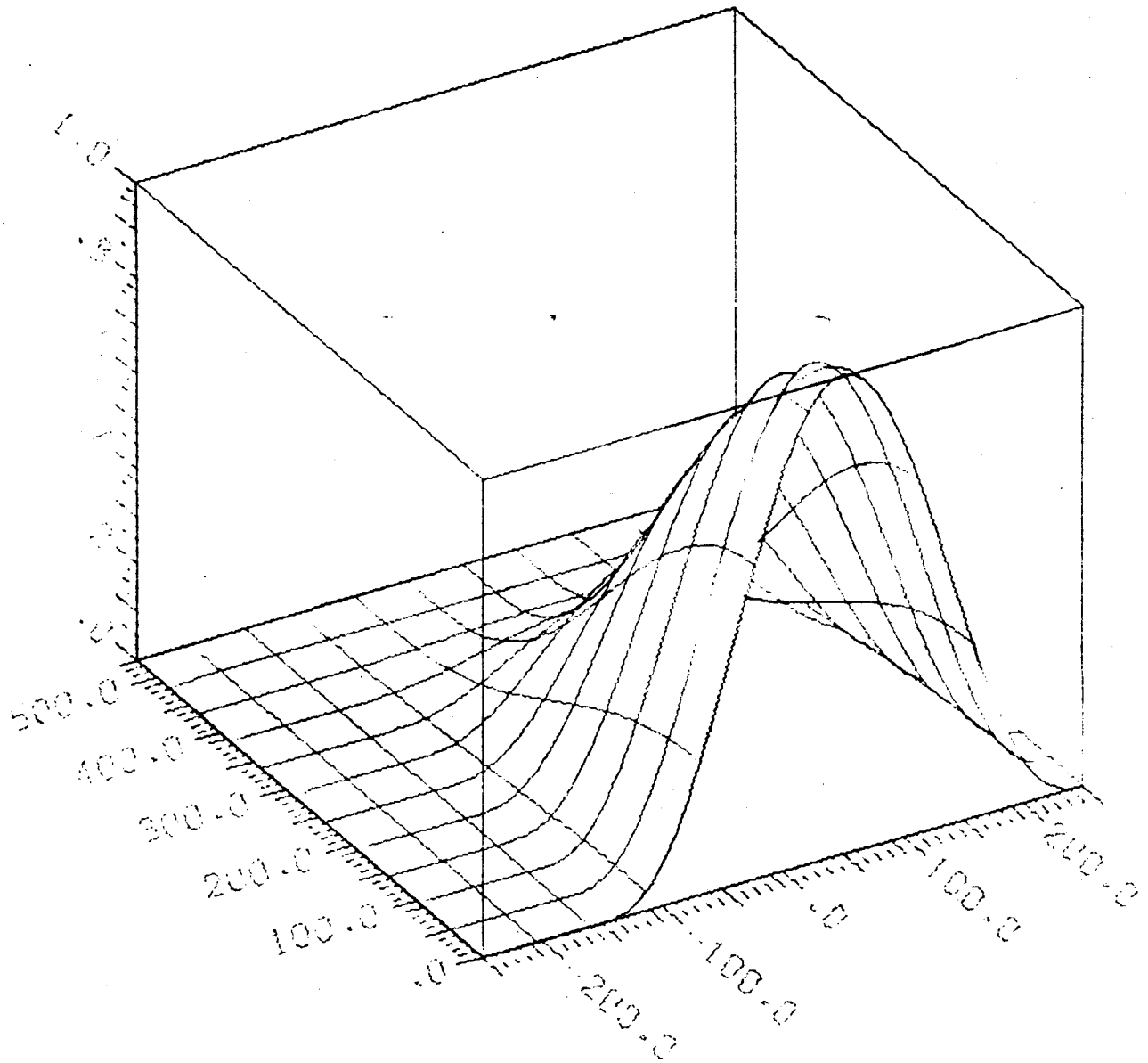

FIGURE V-2

VERTICAL CUT THROUGH TOKAMAK

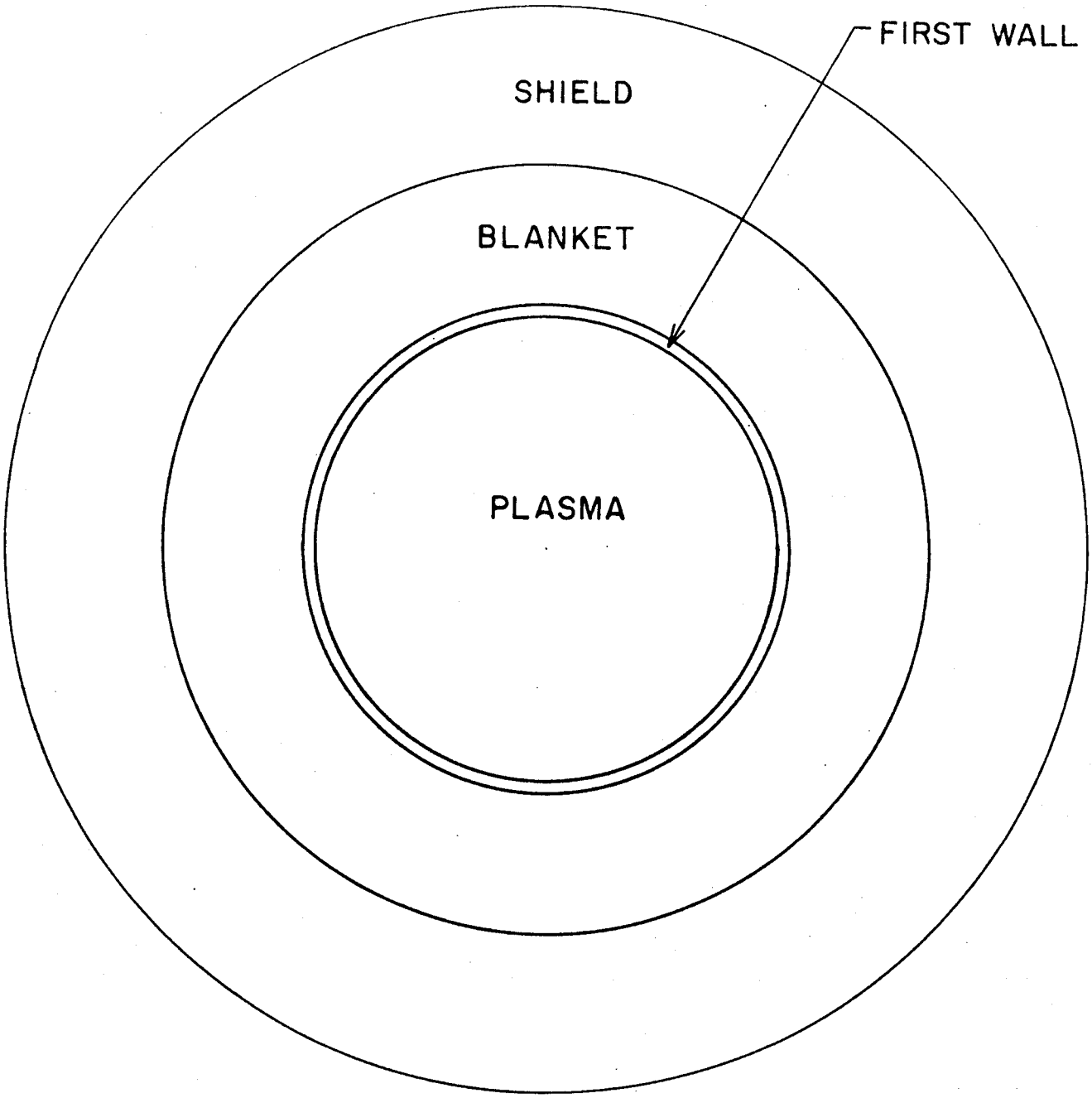

FIGURE V-3

HORIZONTAL CUT THROUGH TOKAMAK MIDPLANE

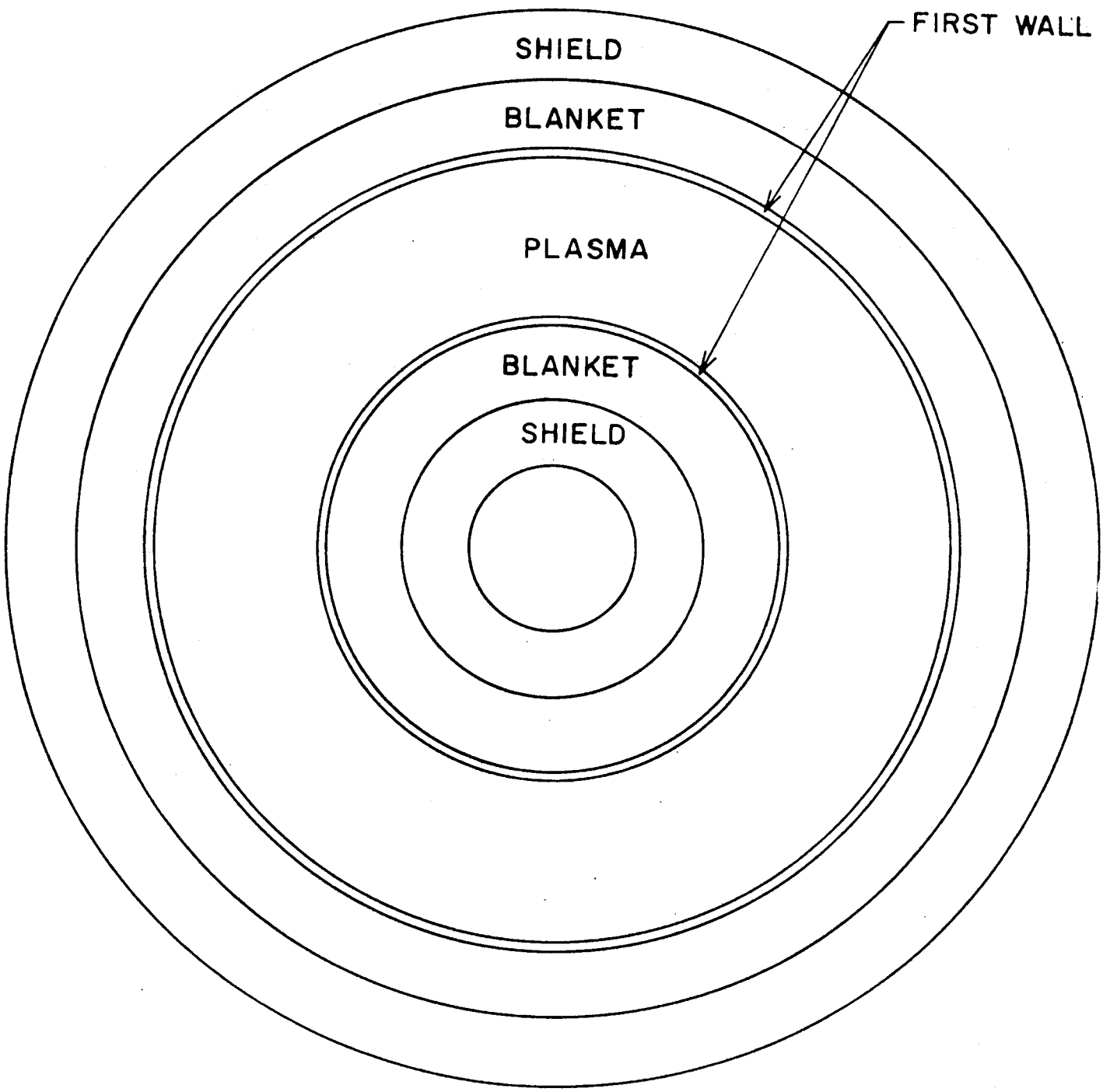

FIGURE V - 4

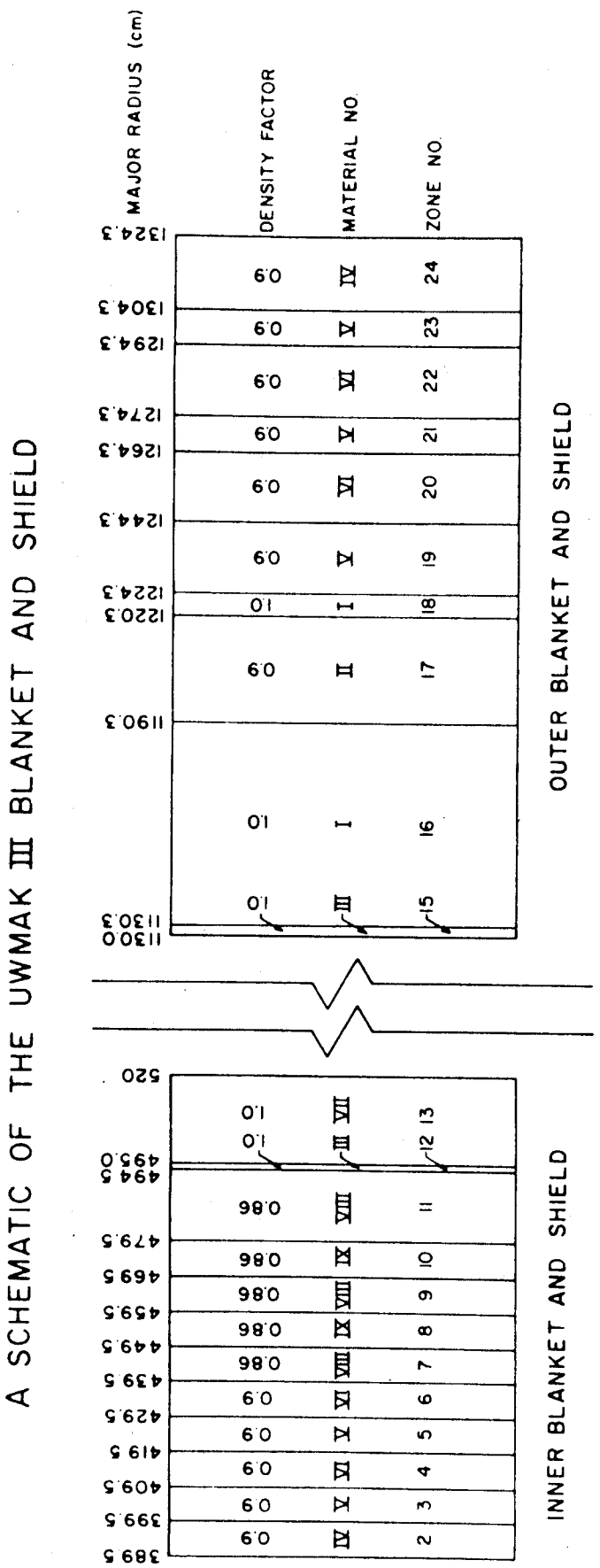
A SCHEMATIC OF THE UWMAK III BLANKET AND SHIELD
MAJOR RADIUS (cm)
DENSITY FACTOR
MATERIAL NO
ZONE NO
OUTER BLANKET AND SHIELD
INNER BLANKET AND SHIELD
ZONE COMPOSITION TABLE
I 97 % Li + 3 % Mo
II 99 % C + 1 % Mo
III 100 % Mo
IV 90 % Pb + 10 % S.S.
V 72 % B_4C + 10 % S.S. + 18 % $Al_2O_3 2SiO_2$
VI 100 % S.S.
VII 100 % C
VIII 82 % Mo + 18 % $Al_2O_3 2SiO_2$
IX 72 % B_4C + 18 % $Al_2O_3 2SiO_2$ + 10 % Mo

FIGURE V-5

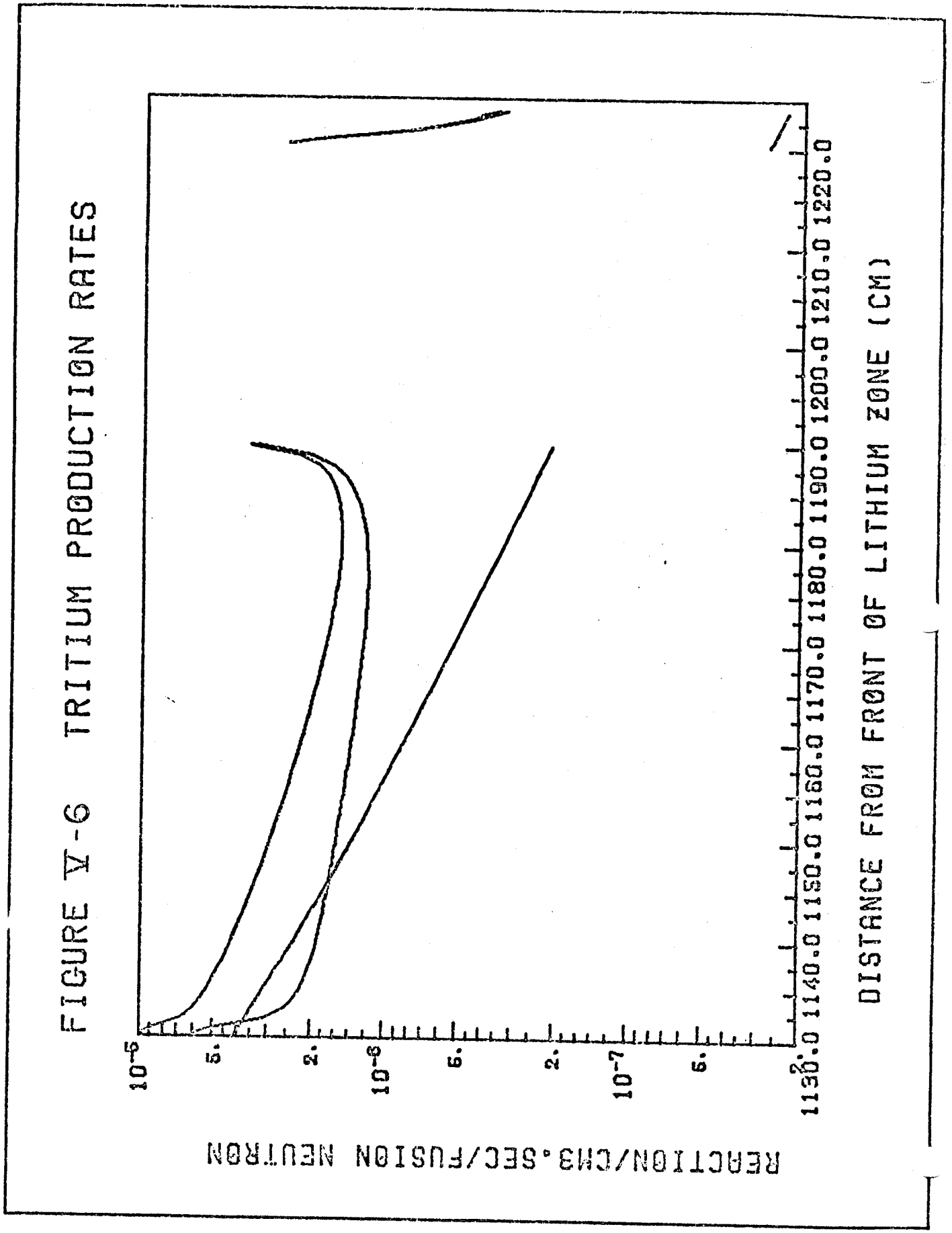
FIGURE V-6 TRITIUM PRODUCTION RATES
REACTION/CM3.SEC/FUSION NEUTRON
10⁻⁵
5.
2.
10⁻⁶
6.
2.
10⁻⁷
6.
1130.0 1140.0 1150.0 1160.0 1170.0 1180.0 1190.0 1200.0 1210.0 1220.0
DISTANCE FROM FRONT OF LITHIUM ZONE (CM)

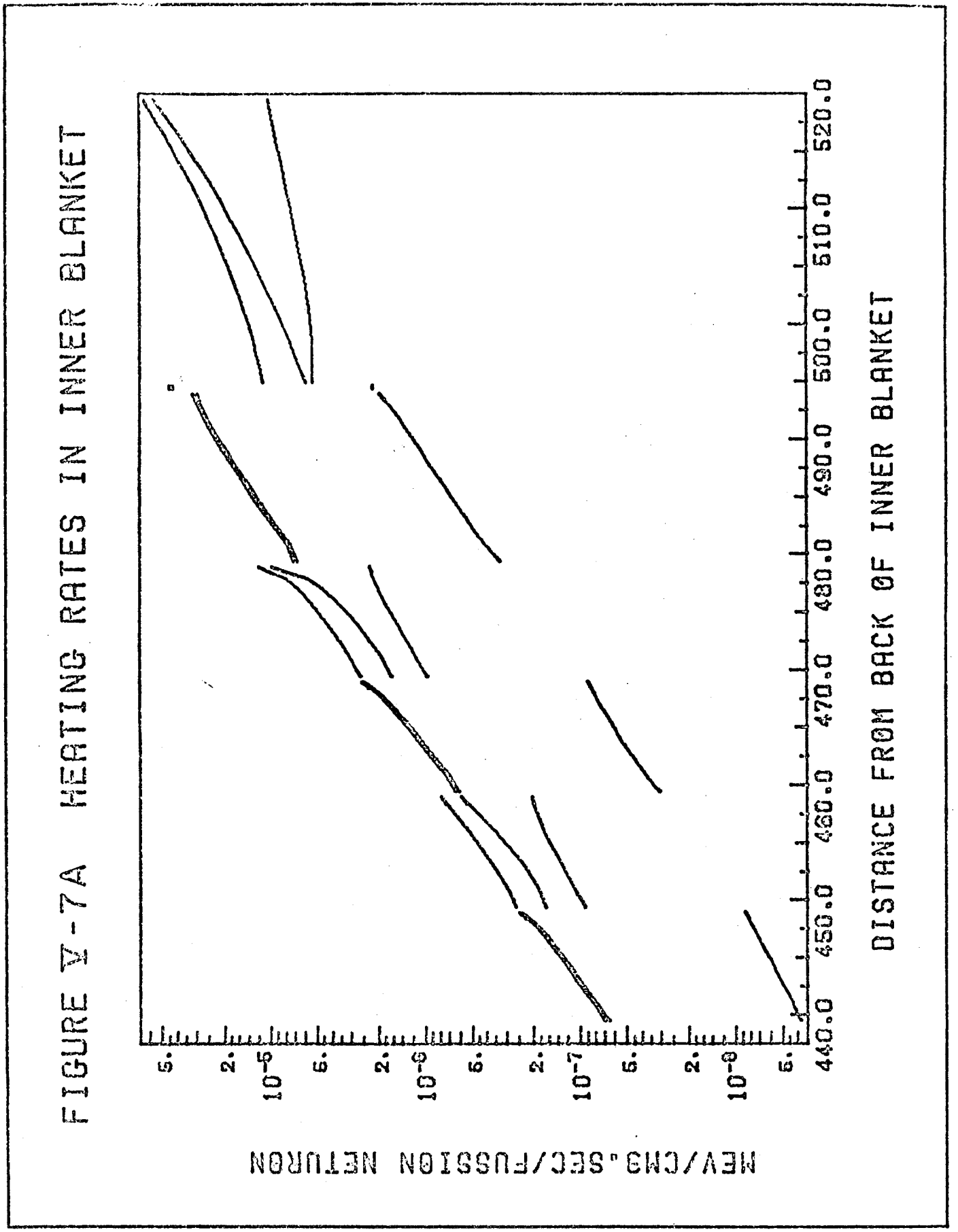
FIGURE V-7A HEATING RATES IN INNER BLANKET
MEV/CM3.SEC/FUSION NEUTRON
5.
2.
10-5
5.
2.
10-6
5.
2.
10-7
5.
2.
10-8
5.
440.0
450.0
460.0
470.0
480.0
490.0
500.0
510.0
520.0
DISTANCE FROM BACK OF INNER BLANKET

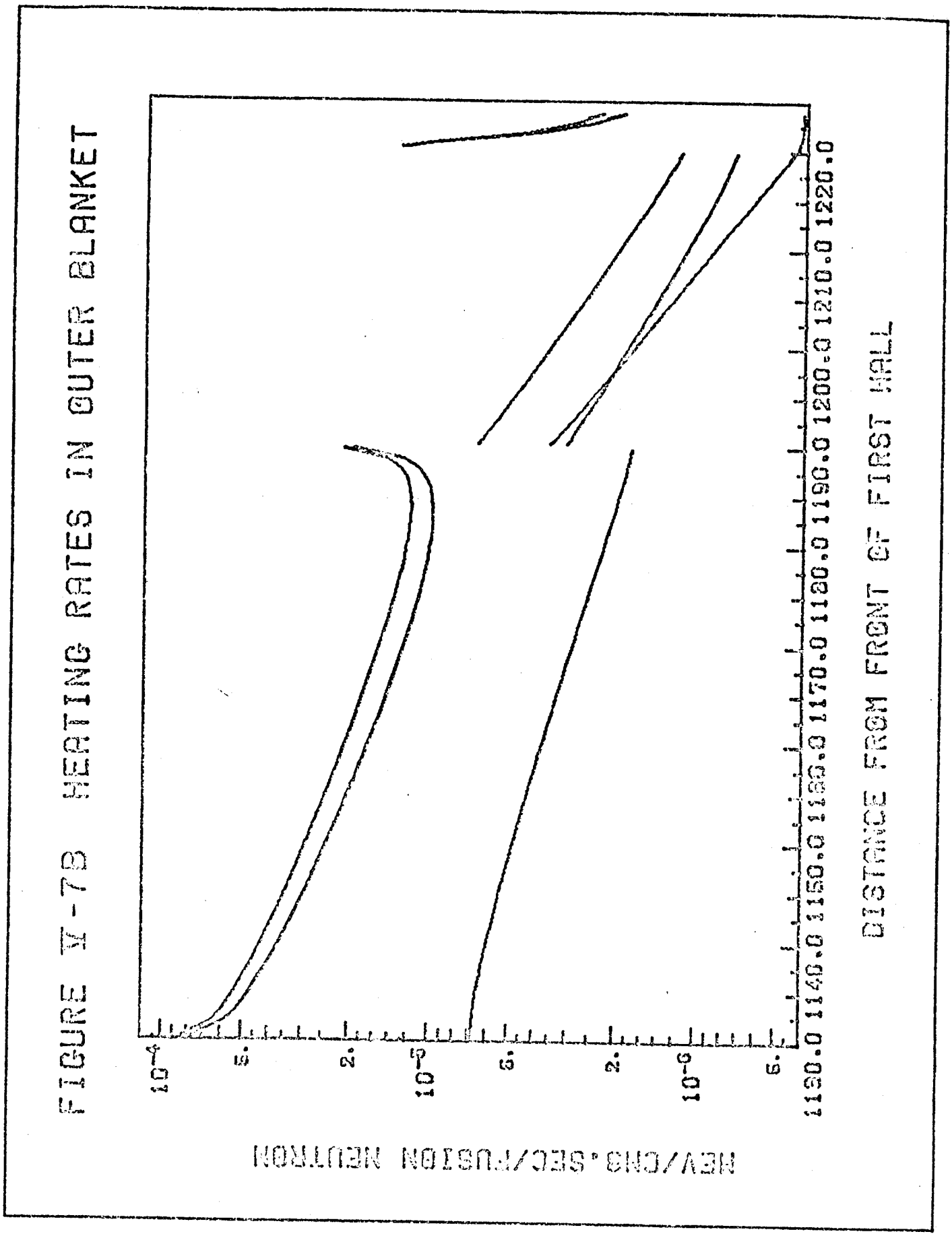
FIGURE V-7B HEATING RATES IN OUTER BLANKET
MEV/CM3.SEC/FUSION NEUTRON
10⁻⁴
5.
2.
10⁻⁵
5.
2.
10⁻⁶
5.
1130.0 1140.0 1150.0 1160.0 1170.0 1180.0 1190.0 1200.0 1210.0 1220.0
DISTANCE FROM FRONT OF FIRST WALL

ENERGY ATTENUATION IN OUTER SHIELD

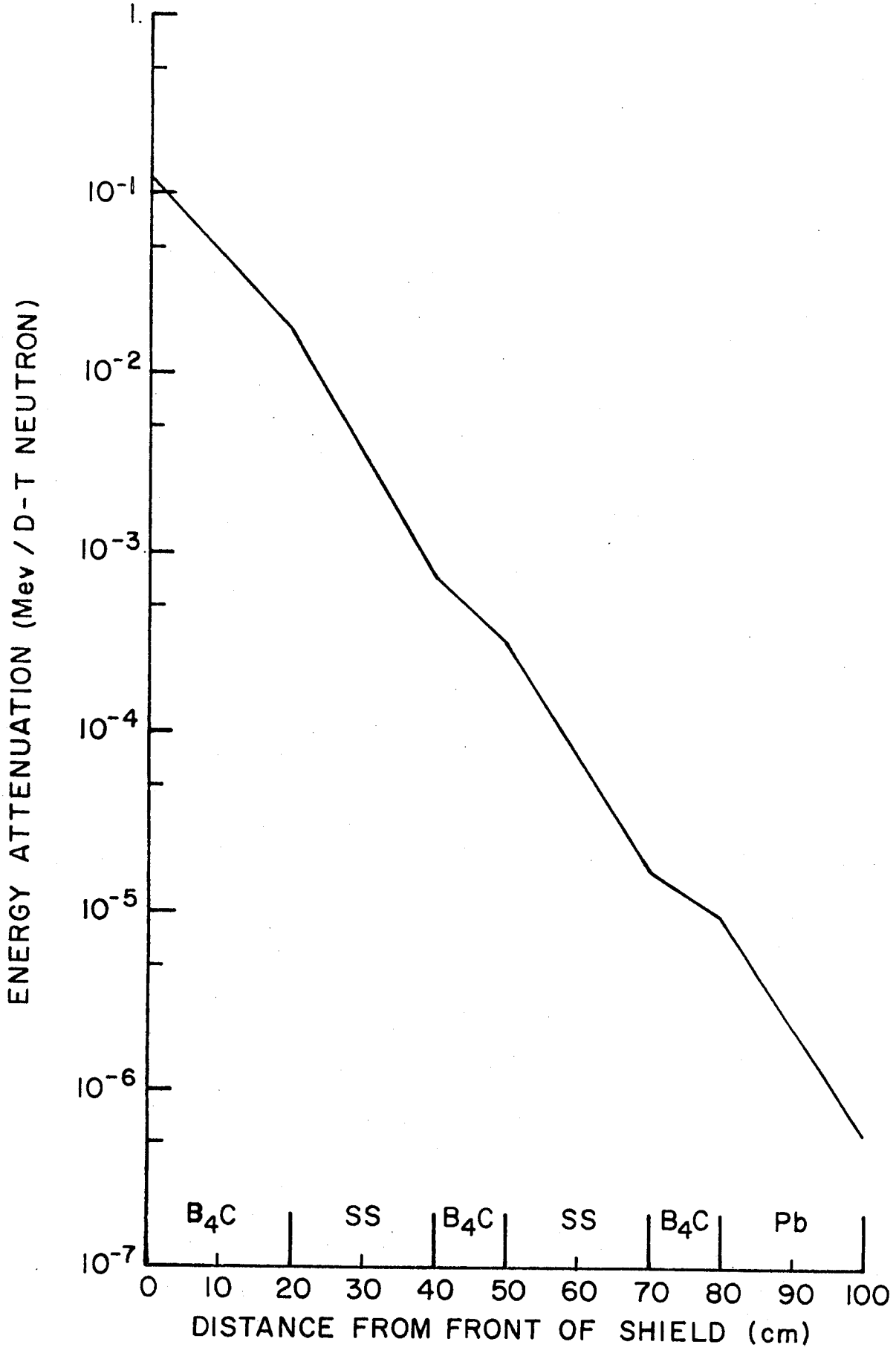

FIGURE II-9A

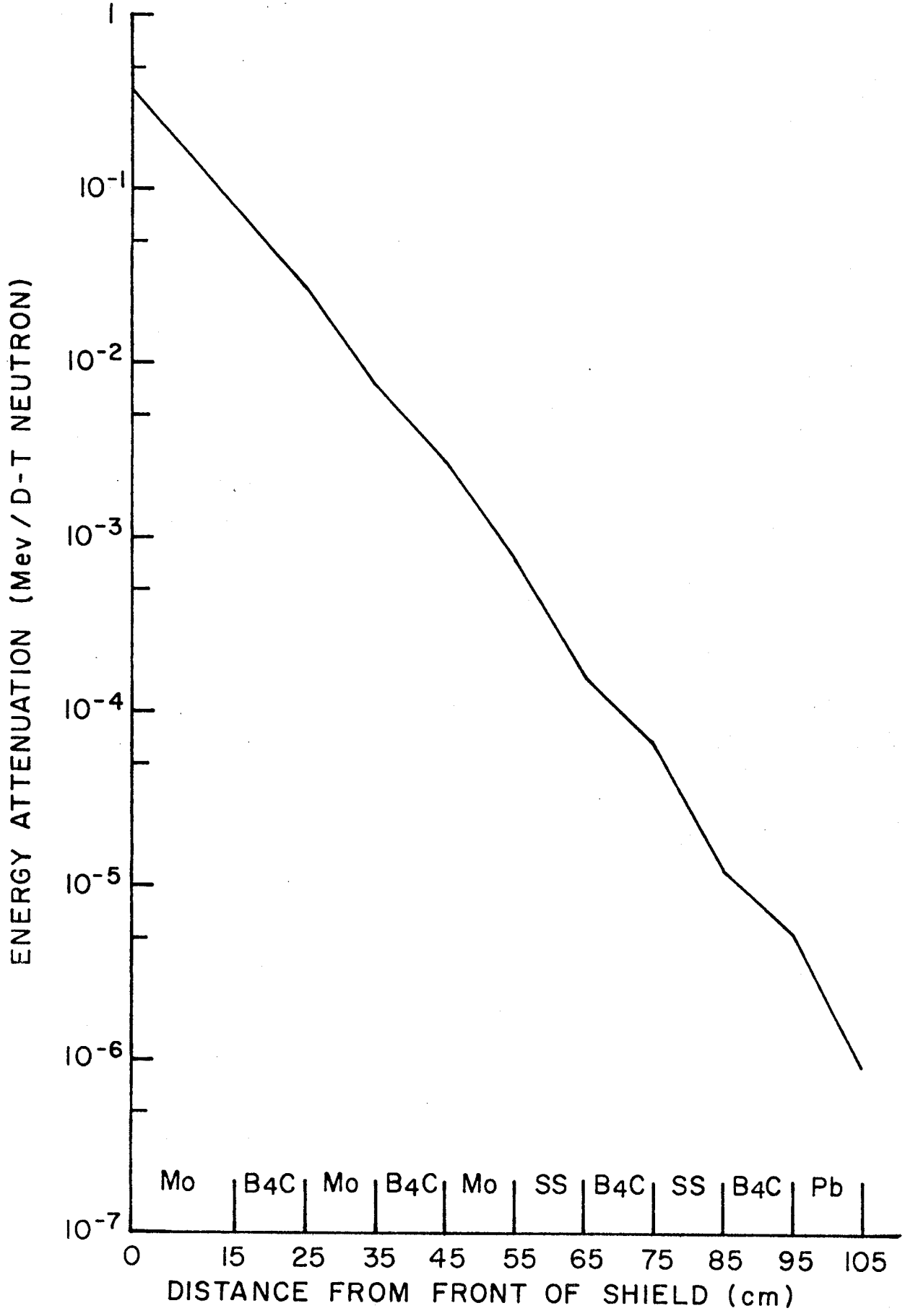
ENERGY ATTENUATION IN INNER SHIELD
ENERGY ATTENUATION (Mev / D-T NEUTRON)
1
10-1
10-2
10-3
10-4
10-5
10-6
10-7
Mo
B4C
Mo
B4C
Mo
SS
B4C
SS
B4C
Pb
0
15
25
35
45
55
65
75
85
95
105
DISTANCE FROM FRONT OF SHIELD (cm)

FIGURE V - 8B

FIGURE X - 9A

TRITIUM PRODUCTION RATES

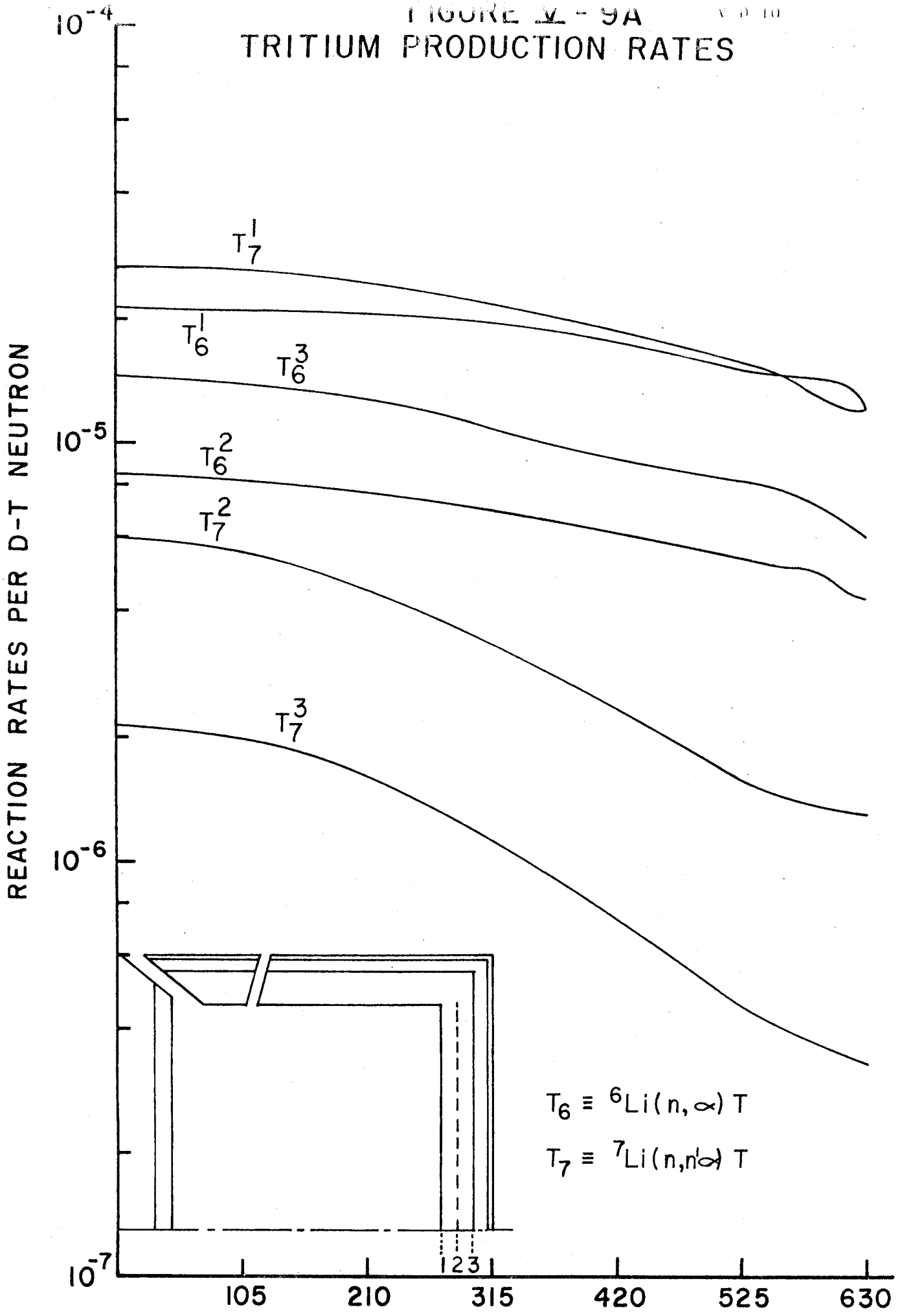

FIGURE X - 38

TRITIUM PRODUCTION RATES

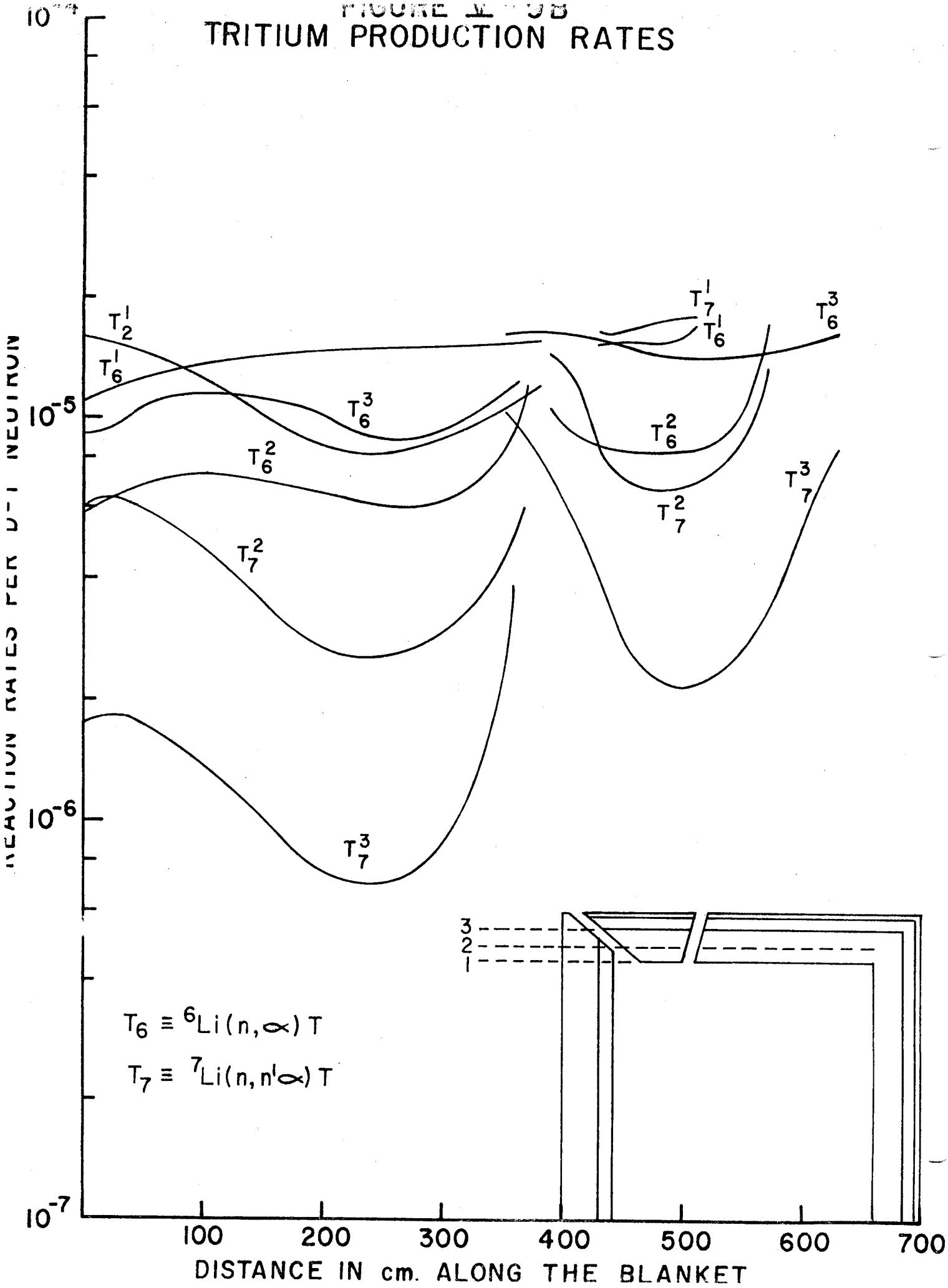

FIGURE V-10

DPA IN FIRST WALL, IN FRONT AND BEHIND ISSEC

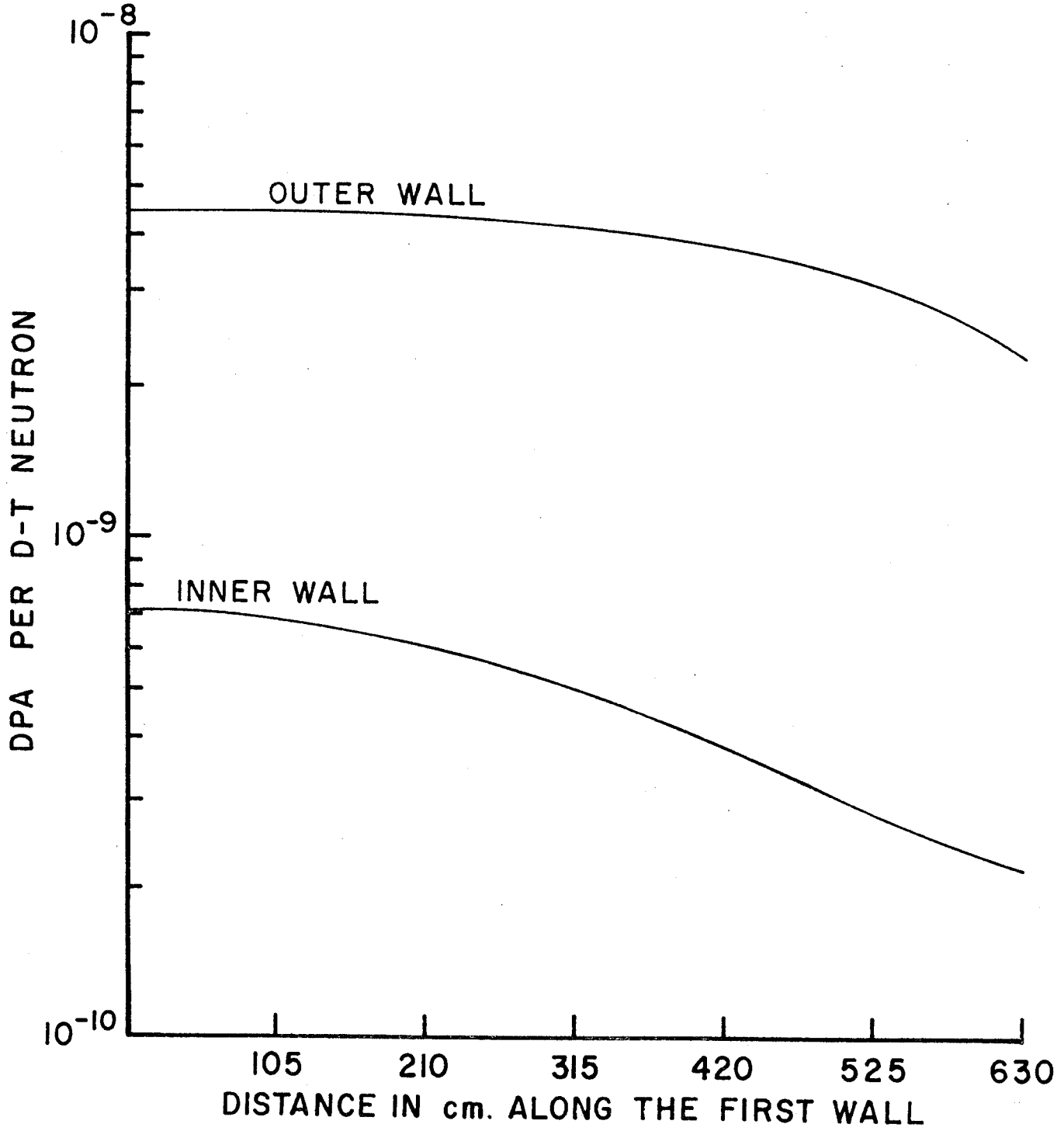

UWMAK III CROSS SECTION FOR R-Z FIRST WALL CALCULATION

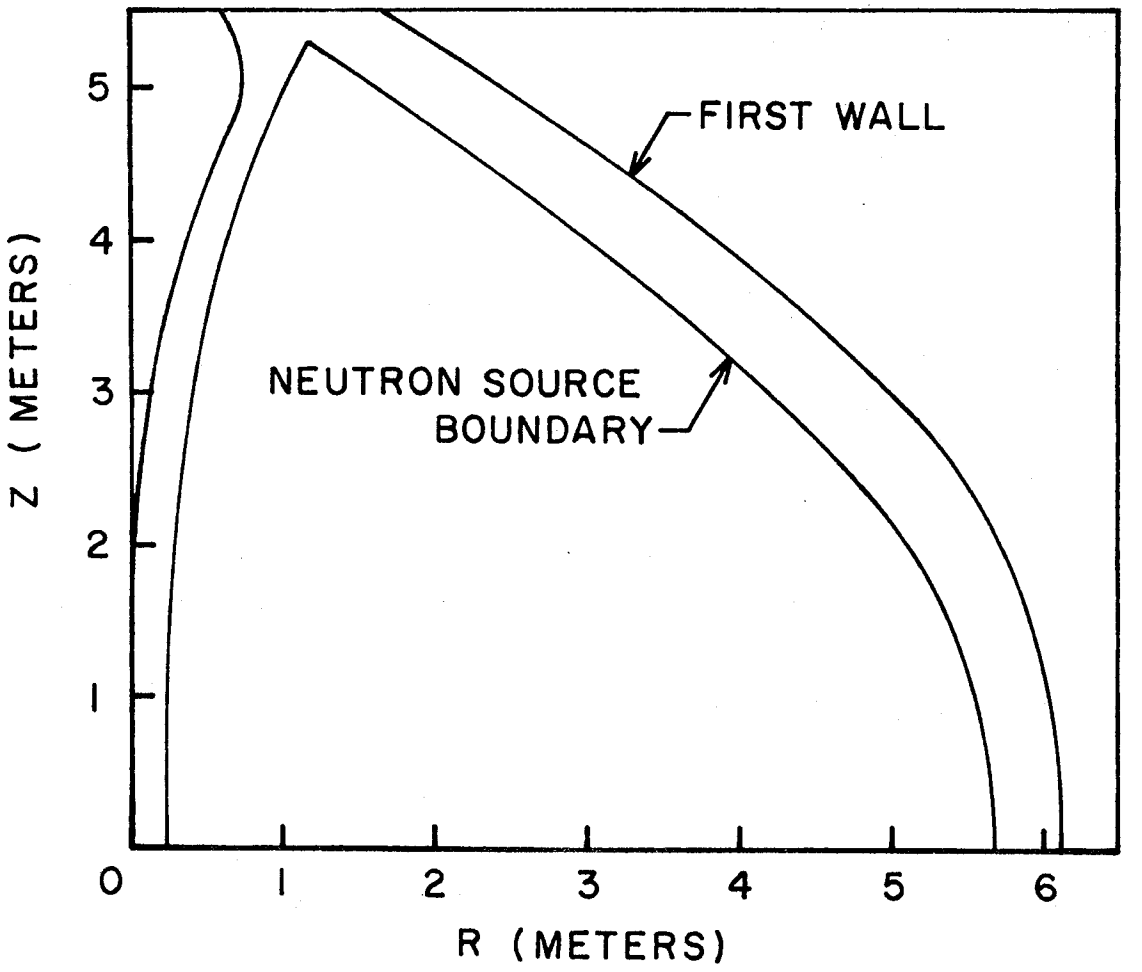

FIGURE V-11

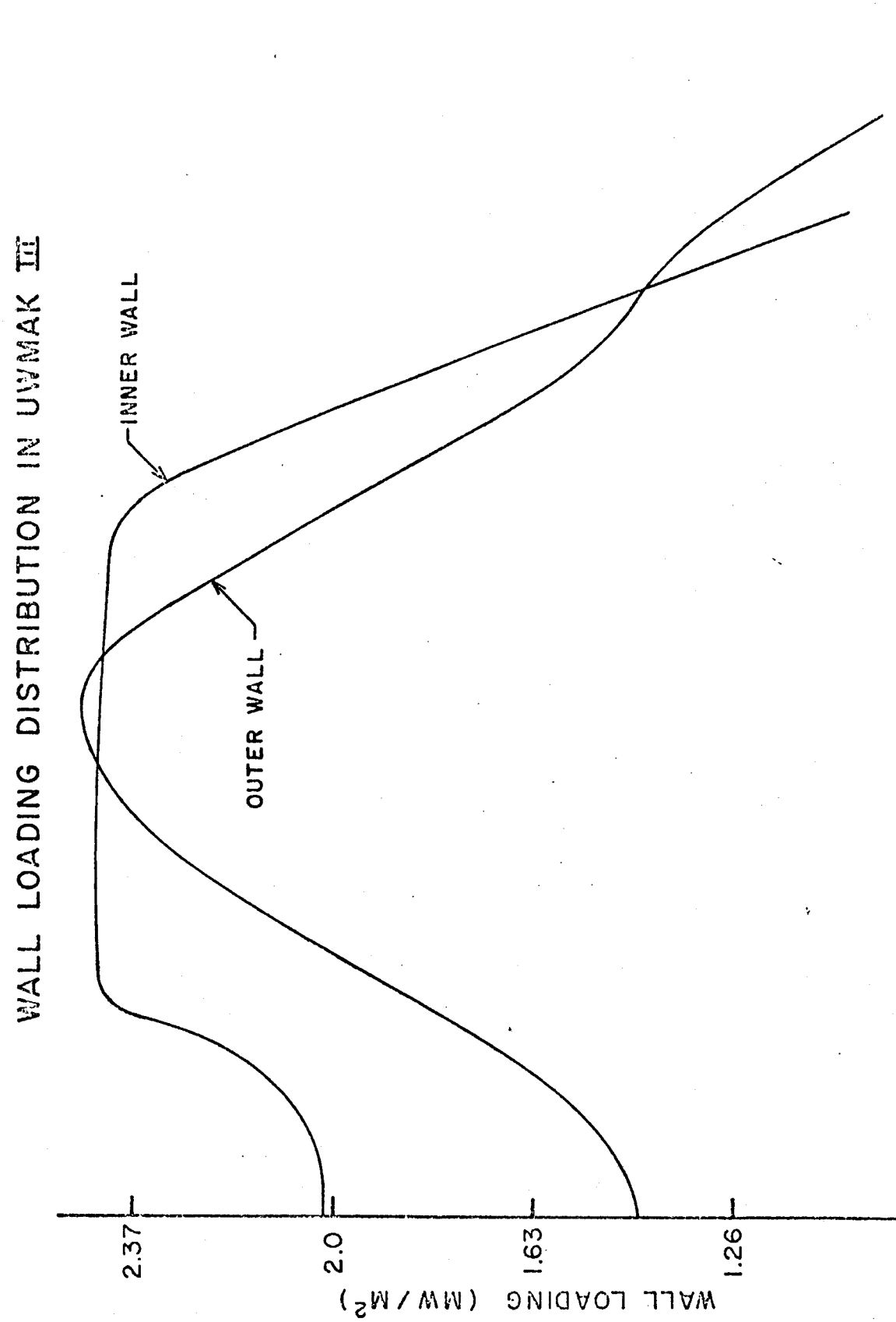
WALL LOADING DISTRIBUTION IN UWMAK III
INNER WALL
OUTER WALL
WALL LOADING (MW/M²)
2.37
2.0
1.63
1.26
0.89
0
1
2
3
4
5
6
HEIGHT ABOVE MIDPLANE (METERS)

FIGURE V-12

TABLE V.1

Neutron 46 Multigroup Structure in eV

Group	Group Limits E(Top)	E(Low)	E(Mid-Point)
1	1.4918 (+7)	1.3499 (+7)	1.4208 (+7)
2	1.3499 (+7)	1.2214 (+7)	1.2856 (+7)
3	1.2214 (+7)	1.1052 (+7)	1.1633 (+7)
4	1.1052 (+7)	1.0000 (+7)	1.0526 (+7)
5	1.0000 (+7)	9.0484 (+6)	9.5242 (+6)
6	9.0484 (+6)	8.1873 (+6)	8.6178 (+6)
7	8.1873 (+6)	7.4082 (+6)	7.7977 (+6)
8	7.4082 (+6)	6.7032 (+6)	7.0557 (+6)
9	6.7032 (+6)	6.0653 (+6)	6.3843 (+6)
10	6.0653 (+6)	5.4881 (+6)	5.7767 (+6)
11	5.4881 (+6)	4.9659 (+6)	5.2270 (+6)
12	4.9659 (+6)	4.4933 (+6)	4.7296 (+6)
13	4.4933 (+6)	4.0657 (+6)	4.2795 (+6)
14	4.0657 (+6)	3.6788 (+6)	3.8722 (+6)
15	3.6788 (+6)	3.3287 (+6)	3.5038 (+6)
16	3.3287 (+6)	3.0119 (+6)	3.1703 (+6)
17	3.0119 (+6)	2.7253 (+6)	2.8686 (+6)
18	2.7253 (+6)	2.4660 (+6)	2.5956 (+6)
19	2.4660 (+6)	1.8268 (+6)	2.1464 (+6)
20	1.8268 (+6)	1.3534 (+6)	1.5901 (+6)
21	1.3534 (+6)	1.0026 (+6)	1.1700 (+6)
22	1.0026 (+6)	7.4274 (+5)	3.726 (+5)
23	7.4274 (+5)	5.5023 (+5)	6.4648 (+5)
24	5.5023 (+5)	4.0762 (+5)	4.7892 (+5)
25	4.0762 (+5)	3.0197 (+5)	3.5480 (+5)
26	3.0197 (+5)	2.2371 (+5)	2.6284 (+5)
27	2.2371 (+5)	1.6573 (+5)	1.9472 (+5)
28	1.6573 (+5)	1.2277 (+5)	1.4425 (+5)
29	1.2277 (+5)	6.7379 (+4)	9.508 (+4)
30	6.7379 (+4)	3.1828 (+4)	4.9604 (+4)

Table V.1 (cont.)

Group	Group Limits E(Top)	E(Low)	E(Mid-Point)
31	3.1828 (+4)	1.5034 (+4)	2.3431 (+4)
32	1.5034 (+4)	7.1017 (+3)	1.1068 (+4)
33	7.1017 (+3)	3.3546 (+3)	5.2281 (+3)
34	3.3546 (+3)	1.5846 (+3)	2.4696 (+3)
35	1.5846 (+3)	7.4852 (+2)	1.1666 (+3)
36	7.4852 (+2)	3.5358 (+2)	5.5105 (+2)
37	3.5358 (+2)	1.6702 (+2)	2.6030 (+2)
38	1.6702 (+2)	7.8893 (+1)	1.2296 (+2)
39	7.8893 (+1)	3.7267 (+1)	5.8080 (+1)
40	3.7267 (+1)	1.7603 (+1)	2.7435 (+1)
41	1.7603 (+1)	8.3152 (+0)	1.2959 (+1)
42	8.3153 (+0)	3.9279 (+0)	6.1216 (+0)
43	3.9279 (+0)	1.8554 (+0)	2.8917 (+0)
44	1.8554 (+0)	8.7643 (-1)	1.3659 (+0)
45	8.7643 (-1)	4.1399 (-1)	6.4521 (-1)
46	4.1399 (-1)	2.2000 (-2)	2.1800 (-1)

TABLE V.2

Gamma 21 Multigroup Structure in MeV

Group	Group Boundaries E(Top)	E(Low)	E(mid-Point)
1	1.2E01	1.4E01	1.30E01
2	1.0E01	1.2E01	1.10E01
3	8.0E00	1.0E01	9.00E00
4	7.5E00	8.0E00	7.75E00
5	7.0E00	7.5E00	7.25E00
6	6.5E00	7.0E00	6.75 E00
7	6.0E00	6.5E00	6.25E00
8	5.5E00	6.0E00	5.75E00
9	5.0E00	5.5E00	5.25E00
10	4.5E00	5.0E00	4.75E00
11	4.0E00	4.5E00	6.25E00
12	3.5E00	4.0E00	3.75E00
13	3.0E00	3.5E00	3.25E00
14	2.5E00	3.0E00	2.75E00
15	2.0E00	2.5E00	2.25E00
16	1.5E00	2.0E00	1.75E00
17	1.0E00	1.5E00	1.25E00
18	4.0E-01	1.0E00	7.00E-1
19	2.0E-01	4.0E-01	3.00E-1
20	1.0E-01	2.0E-01	1.50E-1
21	1.0E-02	1.0E-01	5.00E-2

TABLE V.3

Tritium Production Rates* from One Dimensional Calculation

Zone	$^{6}Li(n,\alpha)T$	$^{7}Li(n,n'\alpha)T$	Total/Zone
16	0.7141	0.5187	1.2328
18	0.0265	0.0006	0.0271
Total			1.2699

*Reactions Per 14 MeV D-T Neutron

TABLE V-4

Neutron and Gamma Heating

by Zone (in Units of MeV per D-T Neutron)

Zone	Thickness (cm)	Density Factor	Composition	Neutron Heating	Gamma Heating
2	10	0.9	90%Pb+10%SS	2.288-8	4.441-6
3	10	0.9	72%B_4C+10%SS+18%$Al_2O_3 2SiO_2$	3.212-5	8.076-6
4	10	0.9	90%Pb+10%SS	5.906-6	6.660-5
5	10	0.9	72%B_4C+10%SS+18%$Al_2O_3 2SiO_2$	4.644-4	1.161-4
6	10	0.9	100%SS	8.390-5	7.147-4
7	10	0.86	82%Mo+18%$Al_2O_3 2SiO_2$	1.694-4	3.704-3
8	10	0.86	72%B_4C+18%$Al_2O_3 2SiO_2$+10%Mo	5.037-3	4.302-3
9	10	0.86	82%Mo+18%$Al_2O_3 2SiO_2$	1.722-3	3.312-3
10	10	0.86	72%B_4C+18%$Al_2O_3 2SiO_2$+10%Mo	1.128-1	4.811-2
11	15	0.86	82%Mo+18%$Al_2O_3 2SiO_2$	4.381-2	7.678-1
12	0.5	1.0	100%Mo	3.336-3	6.608-2
13	25	1.0	100%C	1.654	5.689-1
14	610	0.0	Vacuum	0.0	0.0
15	0.3	1.0	100%Mo	2.677-2	2.283-1
16	60	1.0	97%Li+3%Mo	9.695	1.729
17	30	0.9	99%C+1%Mo	3.309-1	3.538-1
18	4	1.0	97%Li+3%Mo	1.414-1	1.275-2
19	20	0.9	72%B_4C+10%SS+18%$Al_2O_3 2SiO_2$	1.500-1	9.026-2
20	20	0.9	100%SS	1.566-3	1.935-2
21	10	0.9	72%B_4C+10%SS+18%$Al_2O_3 2SiO_2$	2.005-3	5.134-4
22	20	0.9	100%SS	3.468-5	4.407-4
23	10	0.9	72%B_4C+100%SS+18%$Al_2O_3 2SiO_2$	8.259-5	1.894-5
24	20	0.9	90%Pb+10%SS	2.103-7	1.255-7
				12.173	3.897

TABLE V.5

Tritium Production Rates* From Two Dimensional Calculation

Zone	$^{6}Li(n,\alpha)T$	$^{7}Li(n,n'\alpha)T$	Total/Zone
1	0.0253	0.0007	0.0260
3	0.5340	0.3684	0.9024
8	0.0771	0.0602	0.1373
10	0.0074	0.0009	0.0083
Total	0.6438	0.4302	1.0740

*Reactions per 14 MeV D-T Neutron

TABLE V.6

Heating Rates* From Two Dimensional Calculation

Zone	Neutron Heating	Gamma Heating	Total/Zone
1	0.1300	0.0139	0.1439
2	0.2630	0.3467	0.6097
3	6.9701	0.5960	7.5641
4	0.0195	0.0759	0.09564
7	0.0014	0.0059	0.0073
8	1.0796	0.0819	1.1615
9	0.2083	0.0955	0.3038
10	0.0460	0.0046	0.0506
12	2.4505	0.660	3.1105
13	0.0038	0.209	0.2128
14	0.6744	4.233	4.9074
Total	11.8466	6.3204	18.1670

*All the heating rates are in MeV per 14 MeV D-T neutron

References for Section V.

1 B. Badger, et al., "A Wisconsin Toroidal Fusion Reactor Design", UWFDM-68, Univeristy of Wisconsin (1973).

2 Fusion Technology Program, "UWMAK-II, A Conceptual D-T Fueled, Helium Cooled, Tokamak Fusion Power Reactor Design," May 1975 UWFDM-112.

3 R. W. Conn and G. L. Kulcinski, "The ISSEC Fusion Blanket Design Concepts," Trans. Am. Nucl. Soc., 21, 49 (1975).

4 D. M. Plaster, R. T. Santoro, and W. E. Ford III, "Coupled 100 Group Neutron and 21 Group Gamma Ray Cross Section for EPR Calculations," ORNL-TM-4872. (April, 1975).

5 N. M. Greene, et al. AMPX: A Modular Code System for Generating Coupled Multigroup Neutron-Gamma Libraries from ENDF 1B, ORNL-TM-3706, Oak Ridge National Laboratory.

6 M. Abdou, C. W. Maynard, and R. Q. Wright, "MACK: A Program to Calculate Neutron Energy Release Parameters (Fluence to Kerma Factors) and Multigroup Neutron Reaction Cross Sections From Nuclear Data in ENDF Format", ORNL-TM-3994.

7 J. R. Knight and F. R. Mynatt, "MUG: A Program for Generating Multigroup Photon Cross Sections" CTC-17 (January 1970).

8 Jr. W. W. Engle, "A User Manual for ANISN", L'-1973, Oak Ridge National Laboratory.

9 F. R. Mynatt, et al., "The DOT-III Two Dimensional Discrete Ordinates Transport Code", ORNL-TM-4280 Sep. 1973.

10 M. A. Abdou, C. W. Maynard, "Nuclear Design of the Magnet Shield for Fusion Reactors," FDM-98 University of Wisconsin (1973).

11 Title 10, Atomic Energy Rules and Regulations, Chapter 1, Atomic Energy Commission, Part 20 Standards for Protection Against Radiation, Federal Register, U. S. Government Printing Office, October 25, 1974.

VI. Thermal Hydraulics

The blanket of UWMAK-III can be divided into three regions, as can be seen in Fig. VI-1. The first region is the partial ISSEC, which is simply a layer of graphite, 25 cm thick. The purpose of this region is to protect the second region, or the inner blanket, which is behind the ISSEC. Access for repair and replacement of the inner blanket is limited due to the toroidal shape of a Tokamak. The purpose of the ISSEC is to reduce radiation damage to the inner structure so that it can last the life of the reactor. The third region is the outer blanket which is more conventional.

The principle of the ISSEC is to let a non-structural material effect the neutron spectrum but not be structure. Therefore, it is not actively cooled. The thermal energy generated within it will be thermally radiated to the outer and inner blankets. This effect will significantly increase the surface heat load on both inner and outer first walls. The inner blanket is helium cooled to avoid excessive MHD problems associated with using lithium as a coolant in this region where the magnetic field is high and access is limited. The outer blanket is lithium cooled to provide adequate breeding.

The thermal hydraulics problem for the three regions will be discussed separately.

VI-A. The Partial ISSEC

The heat generating rate in the graphite is obtained from neutronic calculations as shown in Fig. VI-A-1. This thermal energy will be conducted to the surface and radiated to the outer and inner blakets. Since the burn time of the plasma is much longer than the down time, only steady state temperature in the ISSEC is needed.

The ISSEC is 25 cm thick. The thickness is set by the requirement that the inner blanket structure last about the life of the reactor.[1] The outer blanket is protected by a carbon curtain, which forms a radiation shield. The purpose of the curtain has been discussed in Chapter II. A finite difference, steady state heat transfer program is used to calculate the temperatures in the ISSEC and the curtain, as a function of the thermal conductivity of graphite. The results are shown on Figs. VI-A-2 and VI-A-3 for two different values of thermal conductivity of the graphite.

The maximum allowable temperature in the graphite is yet to be defined. This temperature limitation may be set by any one of the following processes:

1. Evaporation process, causing the carbon vapor to be condensed on the cryogenic pump panels.

2. Evaporation process, causing the impurity build up in the plasma.

3. High temperature inside the ISSEC, causing carbon transport within the ISSEC.

Fig. VI - 1 CROSS SECTION VIEW OF UWMAK III

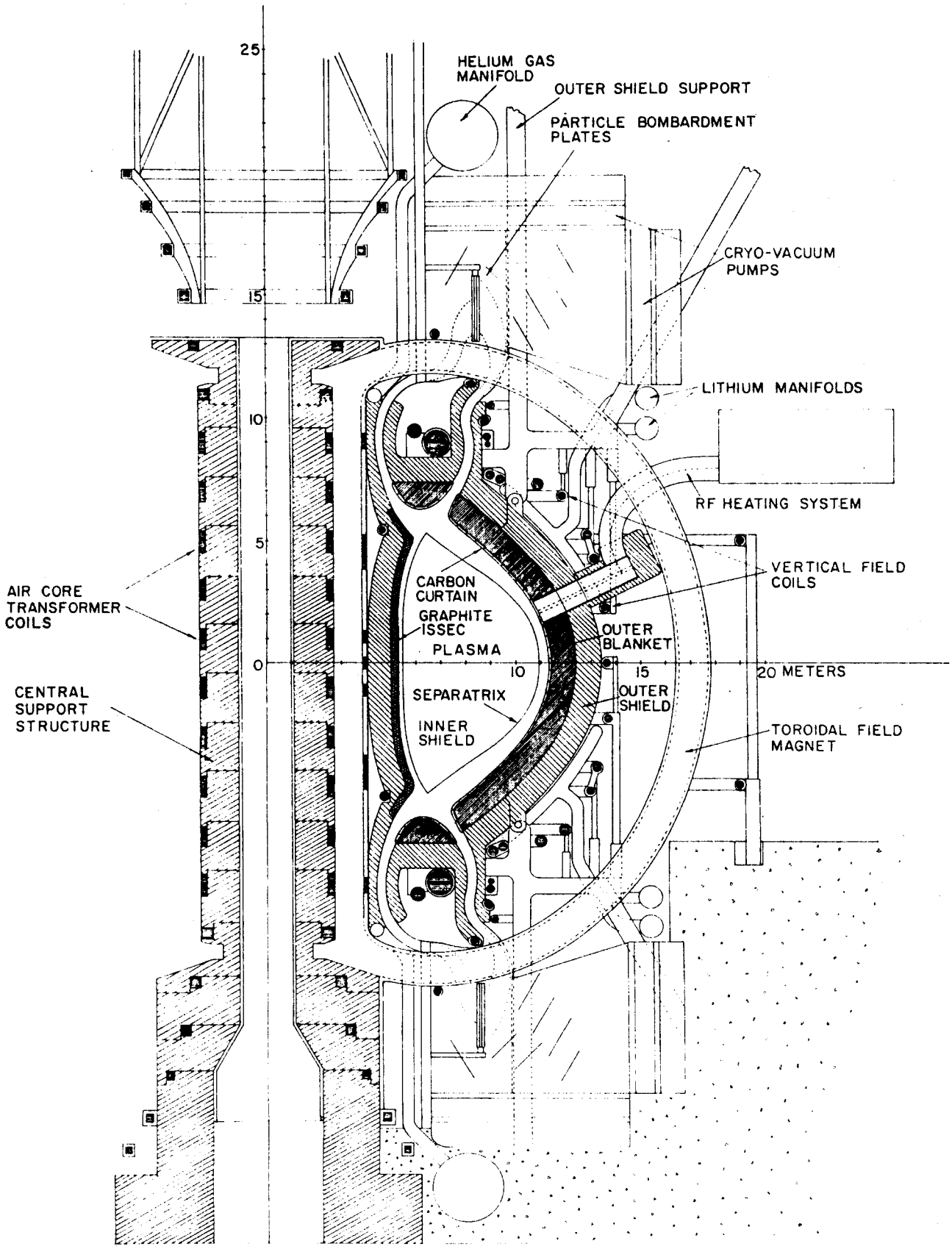

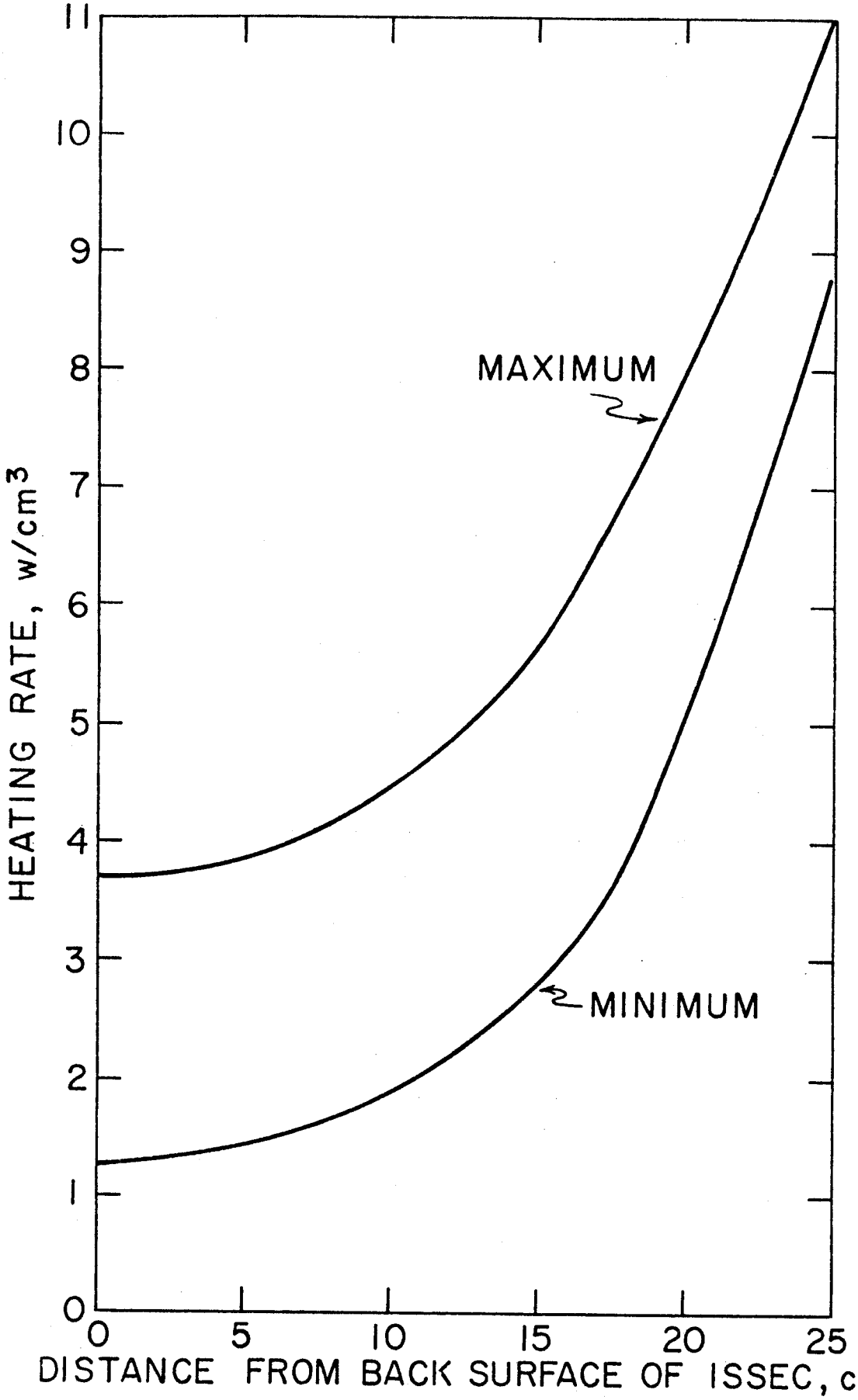

FIGURE VI-A-1 HEATING RATE IN THE ISSEC

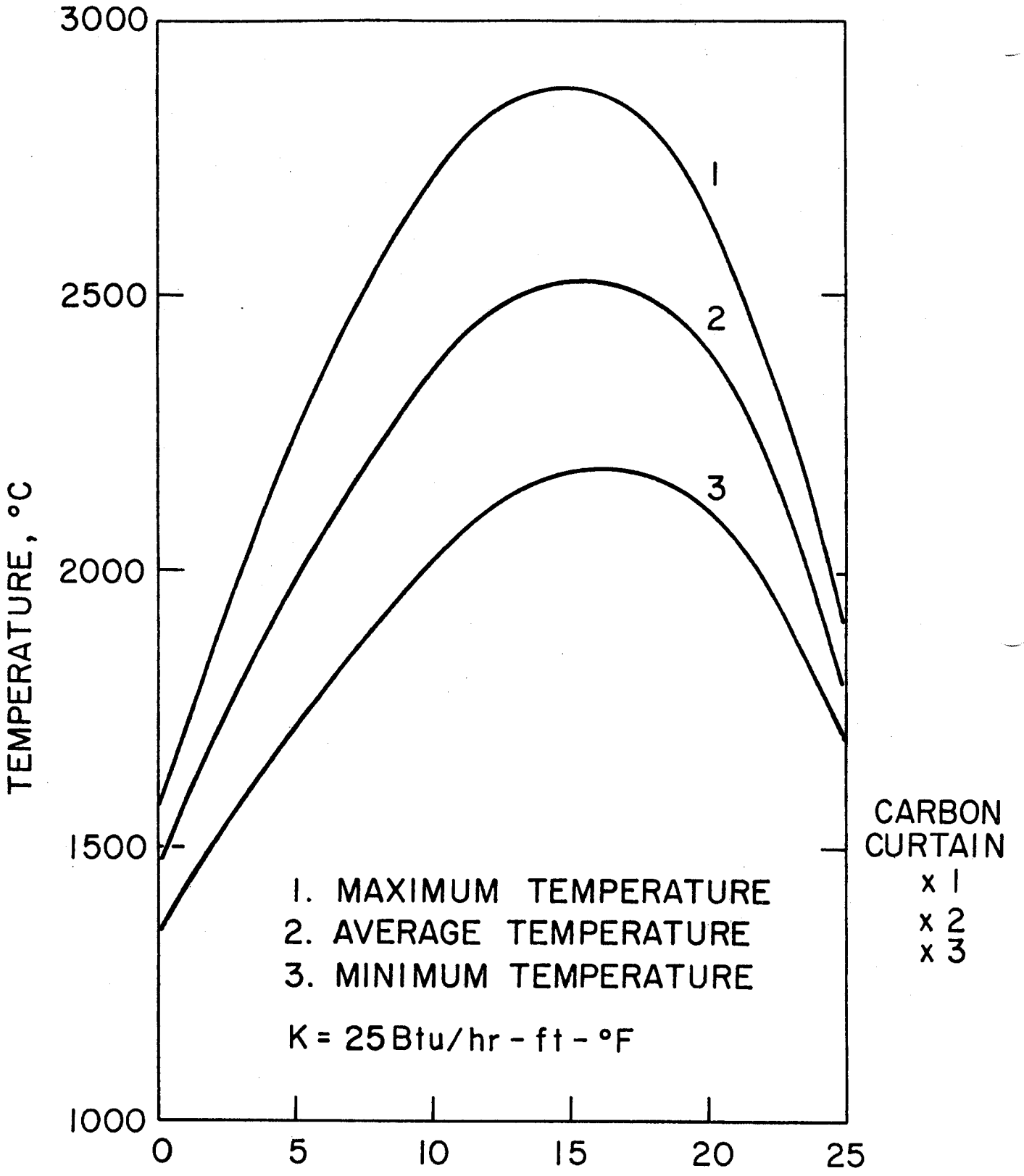

FIGURE VI-A-2 TEMPERATURE OF THE ISSEC AS A FUNCTION OF DISTANCE FROM THE BACK WALL

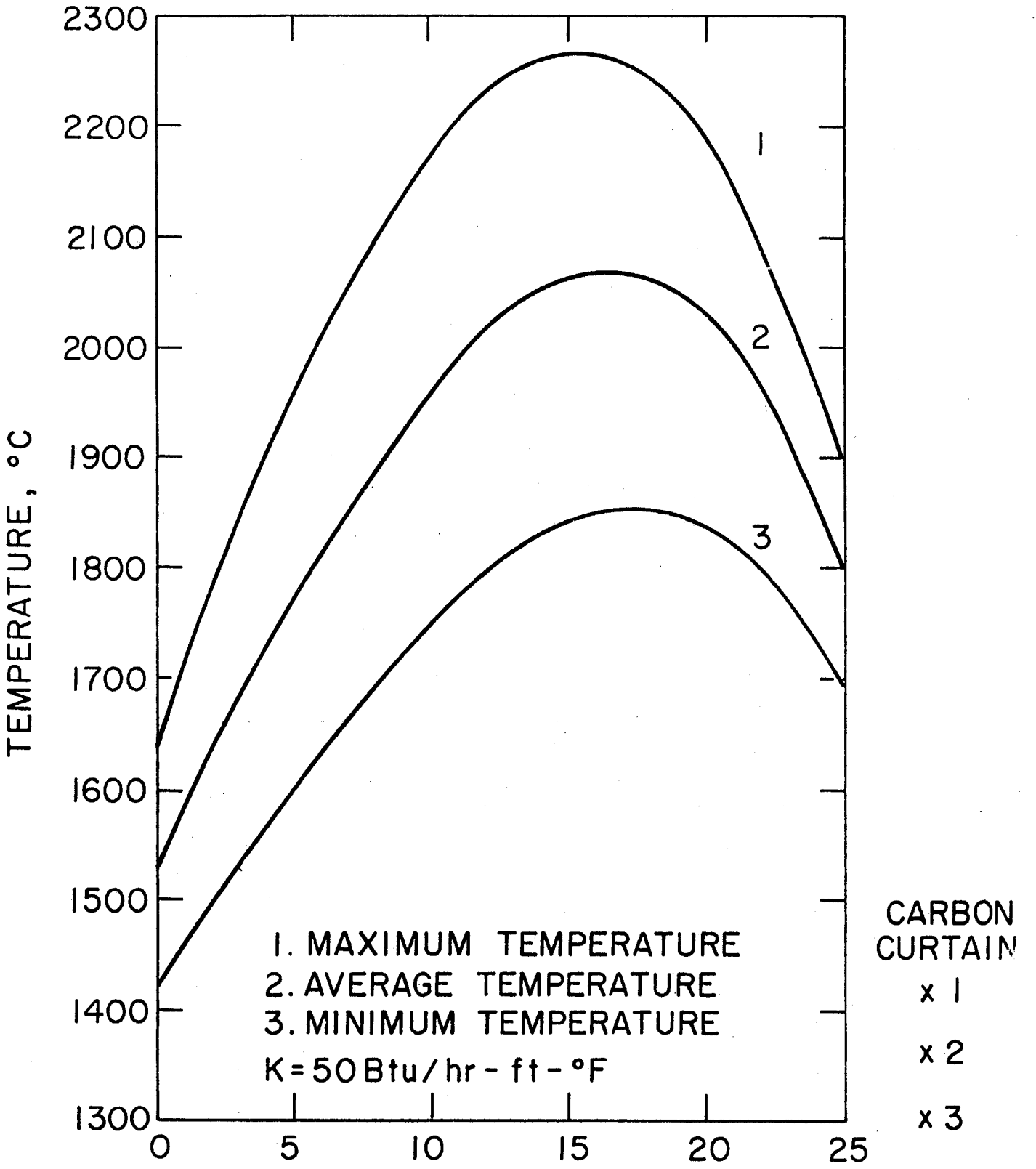

FIGURE VI-A-3 TEMPERATURE OF THE ISSEC AS A FUNCTION OF DISTANCE FROM THE BACK WALL

For the purpose of this study, it is assumed that the maximum allowable temperature on the surface of the ISSEC is 2000°C. This temperature limits the rate of the first two processes. The maximum temperature inside the ISSEC controls the rate of the third process, and is assumed to be 2300°C. It should be emphasized here that all those temperature limitations are based on our best estimates only. Experimental work will be needed to determine those temperatures more exactly.

The temperatures shown on Fig. VI-A-2 are for nuclear grade graphite. It can be seen clearly that the temperature inside the ISSEC far exceeds 2300°C. Therefore, a gap may develop inside the ISSEC which will further retard heat transfer and raises the temperature even higher. How soon this gap will develop is yet to be determined. For graphite with a higher thermal conductivity, i.e. 890S graphite, the temperatures are shown in Fig. VI-A-3 and are within the set limit. The temperatures on the curtain are all reasonably low.

New neutronic calculations which take into acccount the actual toroidal geometry show that the heat generation rate inside the ISSEC is reduced by 25%. This will reduce the high temperature in the graphite. Heat transfer calculation from this new information will be performed in the near future.

The thermal energy generated in the ISSEC will be radiated either to the inner blanket, or to the graphite curtain, and then to the outer blanket. This significantly increases the surface heating load of the blanket. The surface heating loads are 35 W/cm^2 and 25 W/cm^2, on the inner and outer blankets, respectively. This high thermal wall loading would make a stainless steel blanket difficult to design due to the resulting high thermal stress.

VI-B. Outer Blanket

The outer blanket of UWMAK-III is lithium cooled. This is needed to provide enough tritium breeding in order to compensate for the non-breeding inner blanket. The MHD problems are much less severe for a lithium cooled outer blanket because of the lower magnetic field in this region and easier access.

Two of the most severe problems in the design of a lithium cooled Tokamak blanket are MHD problems and thermal recirculation problem.[2] The MHD problems are caused by the circulation of electrically conducting lithium across magnetic field lines. The thermal recirculation problems are caused by the proximity of hot and cold lithium streams. The major feature of the outer blanket design in UWMAK-III is to minimize these two effects.

The base shape of a heat transfer unit is U-shaped, which is the same as in UWMAK-I.[3] This heat transfer cell design gives the lowest possible $\underline{V} \times \underline{B}$ value within the blanket and, therefore, minimizes MHD effects. However, this shape has to be modified to prevent heat transfer between adjacent legs of the cell. Figure VI-B-1 shows a heat transfer cell for the UWMAK-III blanket. The width of the cell is 37 cm, which is possible due to the very low pressure within the blanket. There is a 10 cm wide static lithium zone in the middle of the cell which serves as thermal insulation. This insulating effect is

possible due to the high neutron heat generation rate within the lithium. This neutron heat generation results a temperature profile which provides the insulating effect in spite of the high thermal conductivity of the lithium. The high temperature in the middle of the static zone prevents heat transfer from the hot region toward the cold region. The introduction of the static zone increases the volocity over that of the basic U-shape geometry. This buffer zone also provides a thick passage for eddy currents. This increases the MHD pressure drop within the blanket significantly over that of a U-shaped geometry. This is necessary for improved heat transfer characteristics. The effect of the static lithium zone or heat transfer and MHD problems will be discussed in greater detail later in this chapter.

Figure VI-B-2 shows the supply, discharge and the distribution system for the outer blanket. Each of the outer blanket modules has an independent lithium supply and return tube. Each feed tube is connected to supply heaters. Each supply heater feeds a U-shaped cell for the length of the blanket module. The discharge system of the blanket is completely symmetric to the supply system.

The important dimensions of the outer blanket are tabulated on Table VI-B-1.

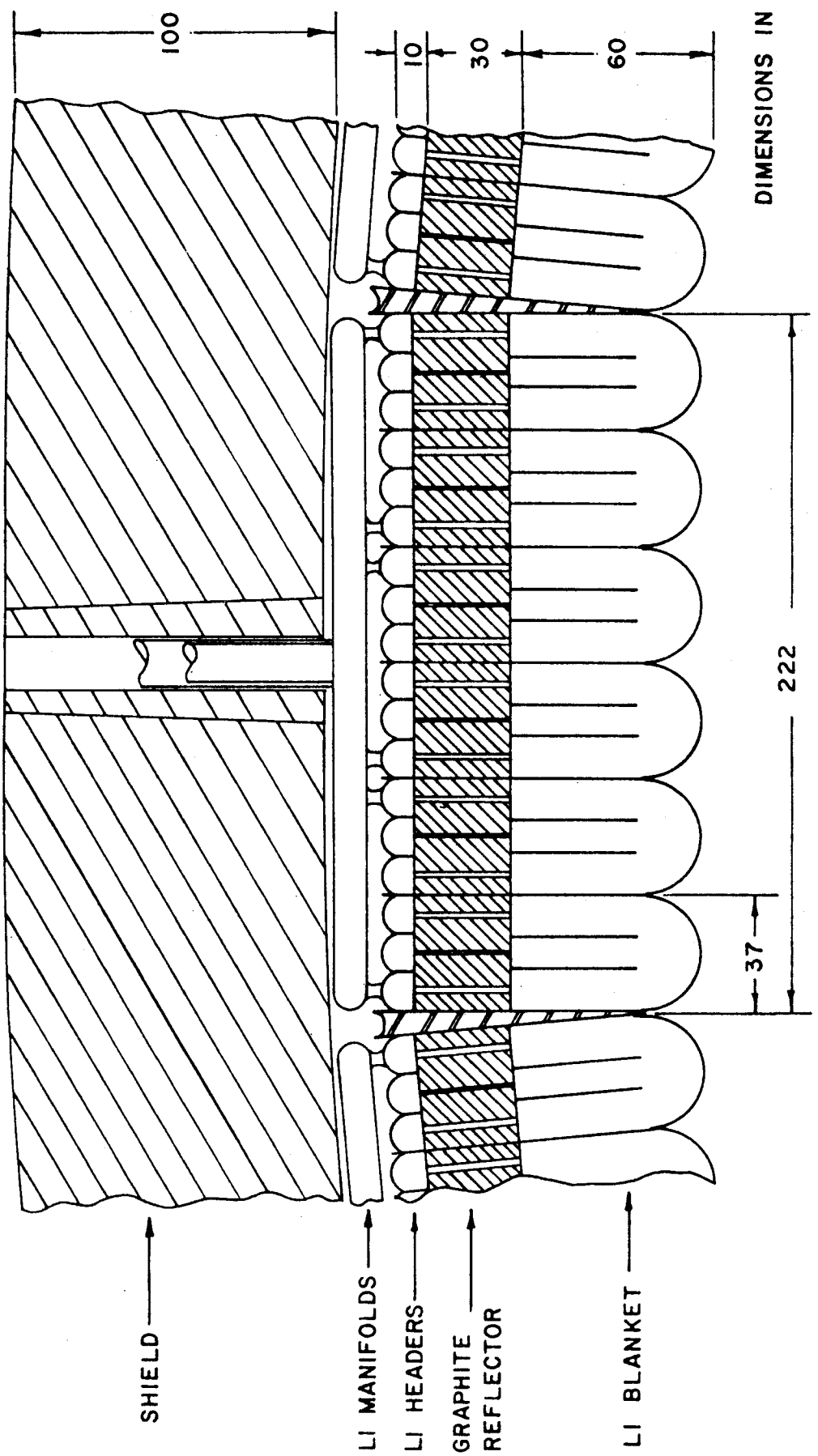

Fig. VI-B-1 Cross Section of Outer Blanket in the Toroidal Direction

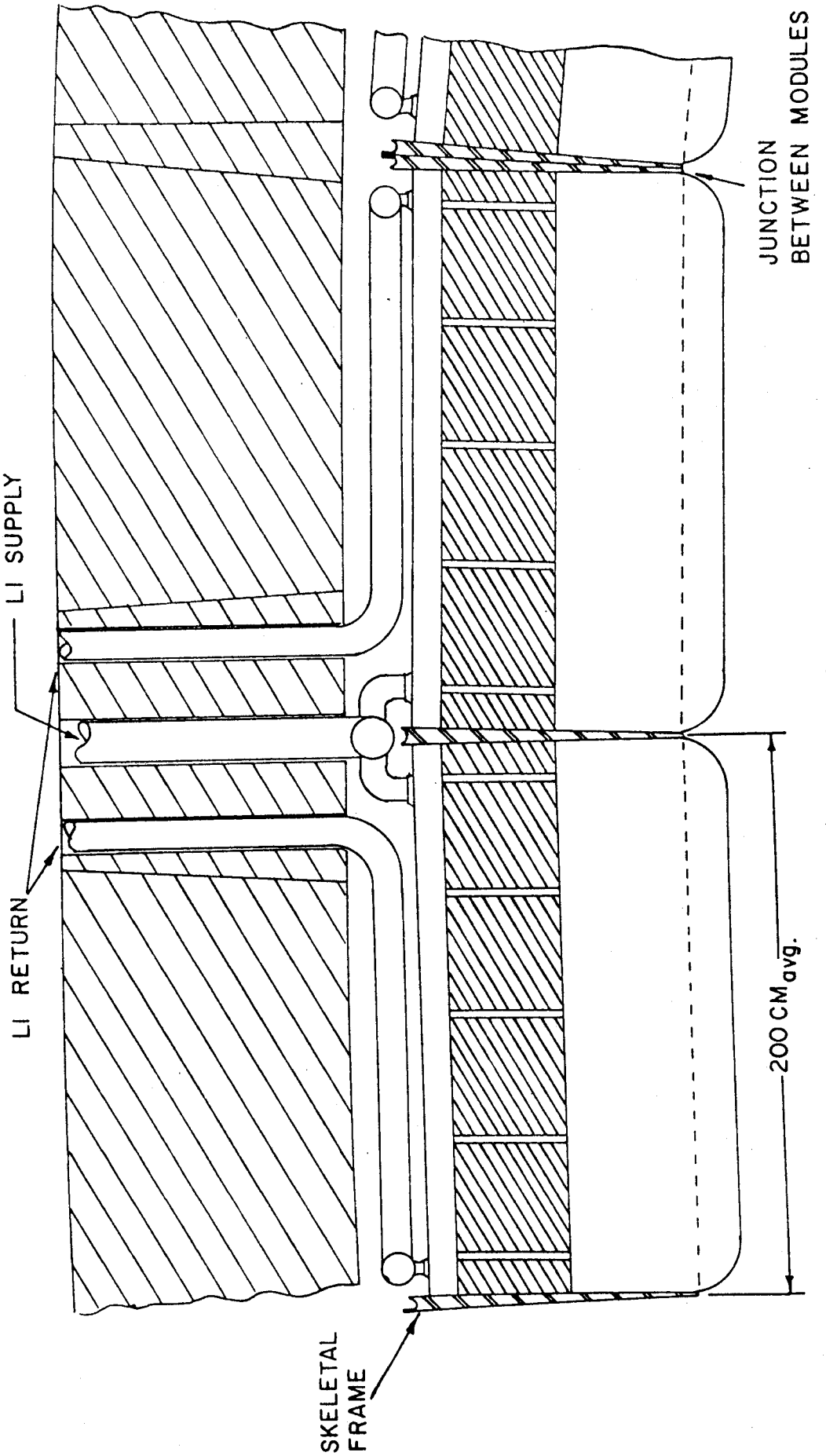

Figure VI-B-2. Cross Section of Outer Blanket in the Poloidal Direction

TABLE VI-B-1

Important Dimensions of the Outer Blanket

Thickness of the First Wall	1.5 mm
Width of the U-Cell	37 cm
Width of the Lithium Gap	10 cm
Cell Frame Thickness	2.5 mm
Baffle Wall Thickness	1 mm
First Breeding Zone Thickness	60 cm
Reflector Zone Thickness	30 cm
Second Breeding Zone Thickness	10 cm
Percentage Structure in the Blanket	3%
Diameter of the Header	20 cm
Wall Thickness of the Header	2 mm
Diameter of the Feed Tube	50 cm
Wall Thickness of the Header	5 mm

VI-B-2. MHD Calculations

The magnetohydrodynamic effects on the coolant are two fold. The eddy current generated by the $\underline{V} \times \underline{B}$ effect will retard the motion of the flow and cause an additional pressure drop. This pressure drop can be extremely large, as shown in refs. 3 and 4. The second effect is the retardation of heat transfer due to the suppression of turbulence. This effect is not too critical because lithium is a good heat transfer medium and conduction is sufficient to spread the heat. This section deals with the MHD effect on the pressure drop through the blanket. Heat transfer will be assumed to be by conduction only and will be discussed in the next section.

The MHD effects on pressure drop of an electrically conducting medium flowing across magnetic field lines have been previously discussed[3,4,5]. These pressure drops will be classified into two categories:[4] the Hartmann and end-of-loop effects.

The Hartmann pressure gradient arises in fully-developed laminar flow with a uniform transverse magnetic field. For such a flow between parallel plates, in a uniform magnetic field normal to the plates, the pressure gradient is given by the following equation:[5]

$$-\frac{dP}{dx} = \frac{\mu v}{a^2}\left[\frac{H_\perp^2 \tanh H_\perp}{H_\perp - \tanh H_\perp} + \frac{H_\perp^2 C}{1+C}\right] \qquad \text{(VI-1)}$$

where C = wall conductance ratio, $\sigma_w t_w / a\sigma$

a = channel half-width

σ_w = electrical conductivity of the wall material

t_w = wall thickness

μ = viscosity

v = velocity

H = Hartmann number $\equiv aB_\perp\sqrt{\sigma/\mu}$

$B_\perp$ = transverse magnetic field

When the fluid is in a channel with a conducting wall and under large magnetic fields ($H \gg 1 + 1/C$), the last term of Equation VI-1 dominates giving

$$-\frac{dP}{dx} = \frac{vB_\perp^2 \sigma_w t_w}{a(1 + C)} \qquad \text{(VI-2)}$$

If the wall is strong enough to withstand the pressure and the corrosion of the lithium, the value of C is usually on the order of 10^{-2} or larger; hence, Eqn. (VI-2) is an excellent approximation in the present range of Hartmann numbers ($H \approx 10^5$).

Hoffman and Carlson[4] have given useful approximate formulas for the Hartmann pressure gradient in rectangular and circular ducts. In the region of interest here, namely $H \gg 1 + 1/C$, their results are closely represented by Eqn. (VI-2) provided that we generalize the definition of "a" as follows:

a = mean half-width of the flow cross section in the direction of $B_\perp$.

The end-of-the loop effects are caused by gradients of [$\underline{v}$ x $\underline{B}$] in the flow direction. The resulting pressure drops are given approximately by the following generalization of Eqn. (16), Ref. 4:

$$\Delta P = K_{PIE} \frac{\sigma_{bav}}{v_{av}} \Delta(v^2 B_\perp^2) \qquad \text{(VI-3)}$$

Here b = mean half-width of the local cross section in the direction normal to $B_\perp$

av = arithmetic mean of the values for the initial and final cross sections.

The coefficient K_{PIE} has been presented by Hoffman and Carlson[4] for flows in tubes and ducts with varying $B_\perp$; the results are summarized in Figs. VI-B-3 and VI-B-4. We will use the same plots here to estimate K_{PIE} for changes of velocity and channel width; in this estimation L_F is taken as the downstream length of the region of varying $vB_\perp$.

The lithium coolant pressure drops are calculated from eqns. VI-2 and VI-3. The results are summarized in Table VI-B-2. The calculations are based on the local magnetic field $\underline{B}$, consisting of the poloidal and toroidal components. The maximum coolant pressure on the first wall is 84 psia. The pumping power needed is only 2 MW.

VI-B-3. Heat Transfer Calculations

The outer blanket configuration which was chosen for UWMAK-III is characterized by a buffer zone of near static lithium located between the coolant channels. The lithium velocity in the buffer zone will be sufficient for tritium recovery, but will be considered static in heat transfer calculations.

A two dimensional, finite difference method is used to calculate the temperature profile in the cell. A temperature rise of the coolant through the blanket is assumed. The heat generation rate as a function of distance from the first wall is obtained from neutronic calculations, and is shown on Fig. VI-B-5 for two locations in the blanket. The velocity of the lithium can be calculated from this information. The following energy balance equation can then be written for the finite difference zone j:

$$\sum_i C_{ij}(T_i - T_j) + V\rho C_p(T_{j-1} - T_j) + q_j = 0$$

in which C_{ij} is the conductance between zone i and j

$$(\equiv \frac{KA}{x})$$

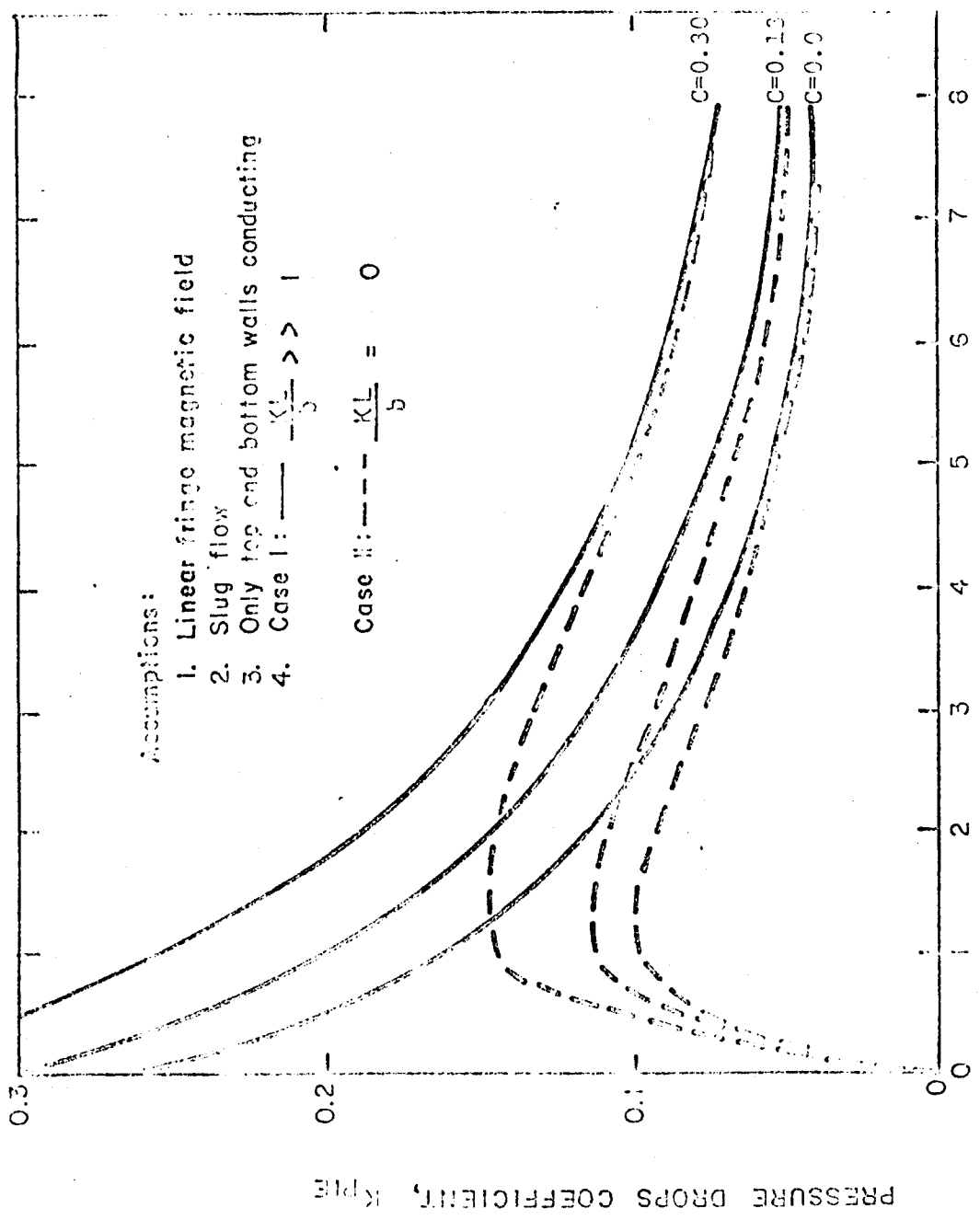

FIG. VI-B-3. PRESSURE DROP DUE TO ENTRANCE OR EXIT EDDY CURRENTS.

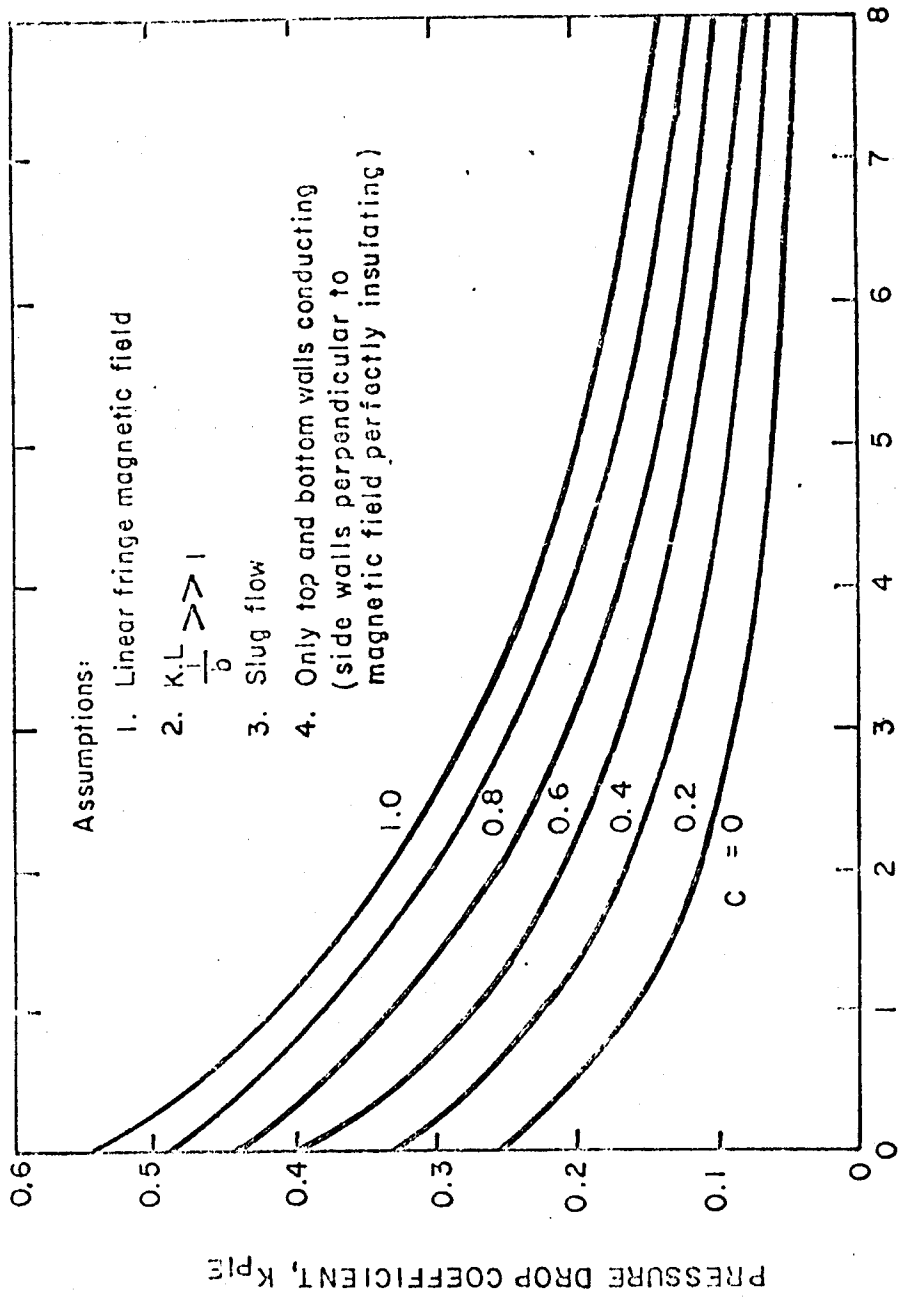

FIG. VI-B-4. PRESSURE DROPS DUE TO ENTRANCE AND EXIT EDDY CURRENT FOR LINEAR FRINGE MAGNETIC FIELDS SEPARATED BY A LONG REGION OF UNIFORM MAGNETIC FIELD.

Table VI-B-2

Summary of MHD Pressure Drop Calculations

Average Surface Area/Module	22 m^2
Average Thermal Load/Module	53.54 MW
Volumetric Coolant Flow Rate/Module	.076 m^3/sec
Diameter of Feed (Discharge) Tube	50 cm
Velocity in Feed (Discharge) Tube	.39 m/sec
Pressure Drop in Feed (Discharge) Tube	26.5 psi
Pressure Drop in Headers	1 psi
Velocity in U-Cell	.01 m/sec
Pressure Drop in U-Cell	60 psi
Total Pressure Drop	114 psi
Maximum First Wall Pressure	84 psia
Total Circulating Power	2 MW

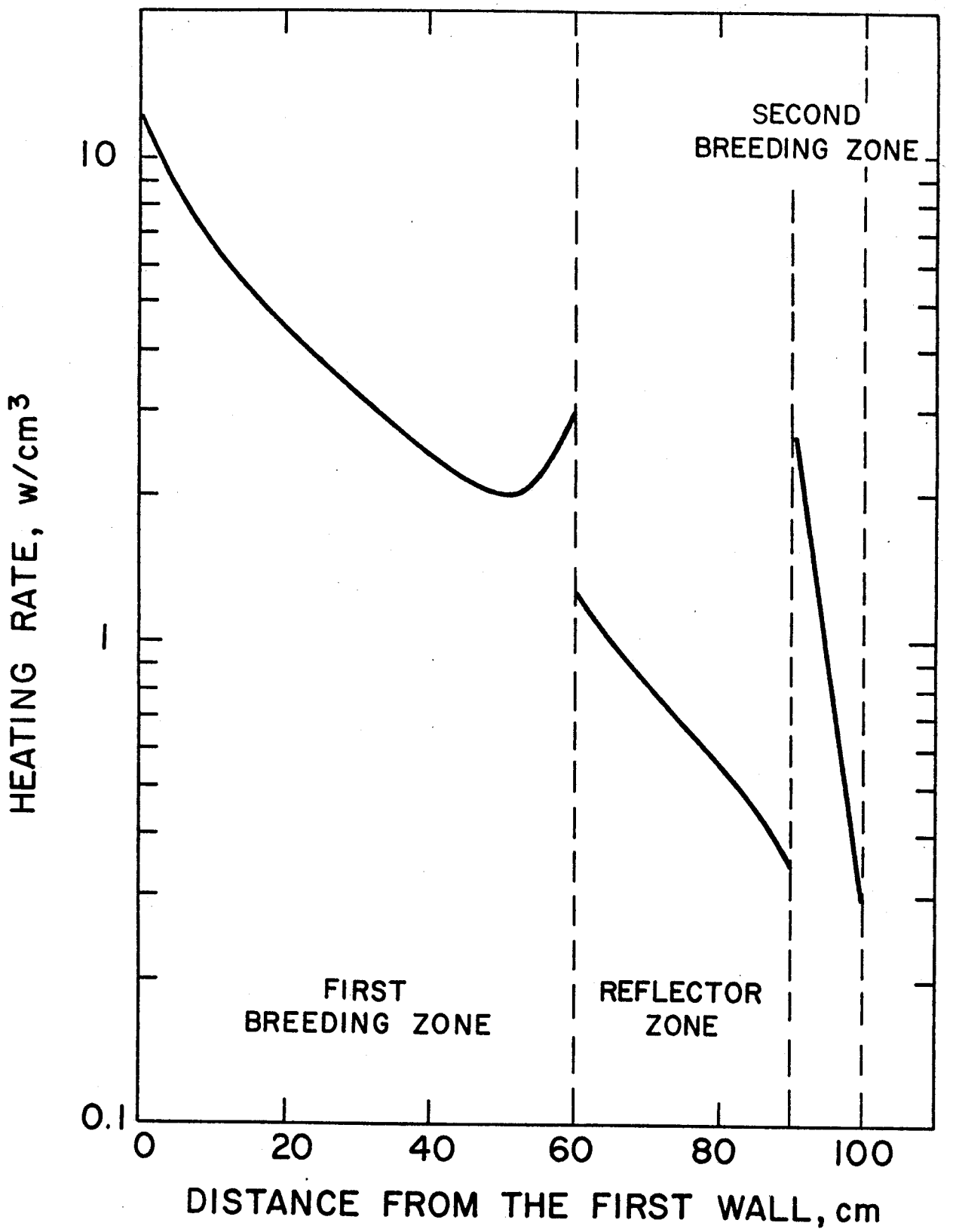

FIGURE VI-B-5 HEATING RATES IN OUTER BLANKET

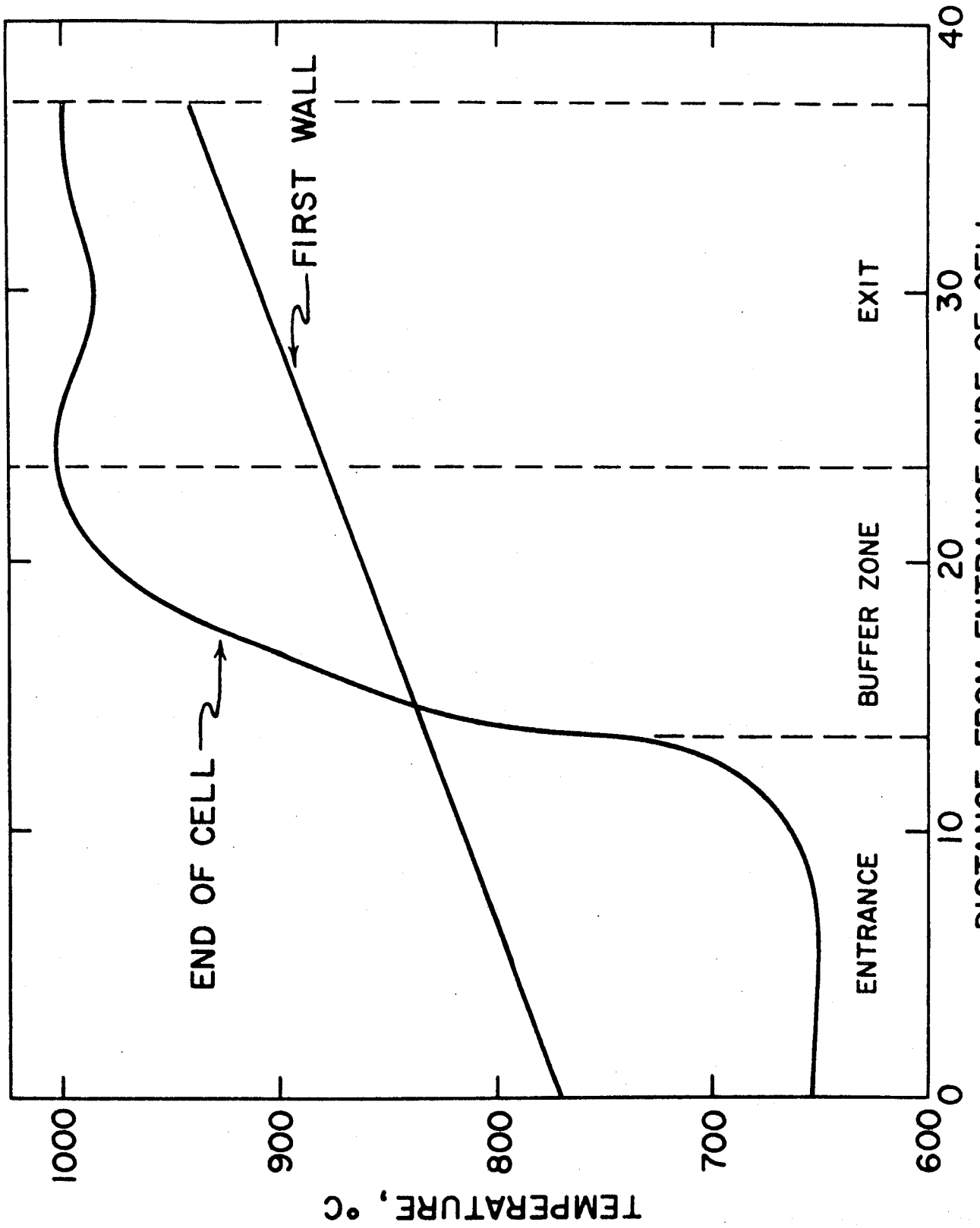

FIGURE VI-B-6 TEMPERATURE IN A U-CELL

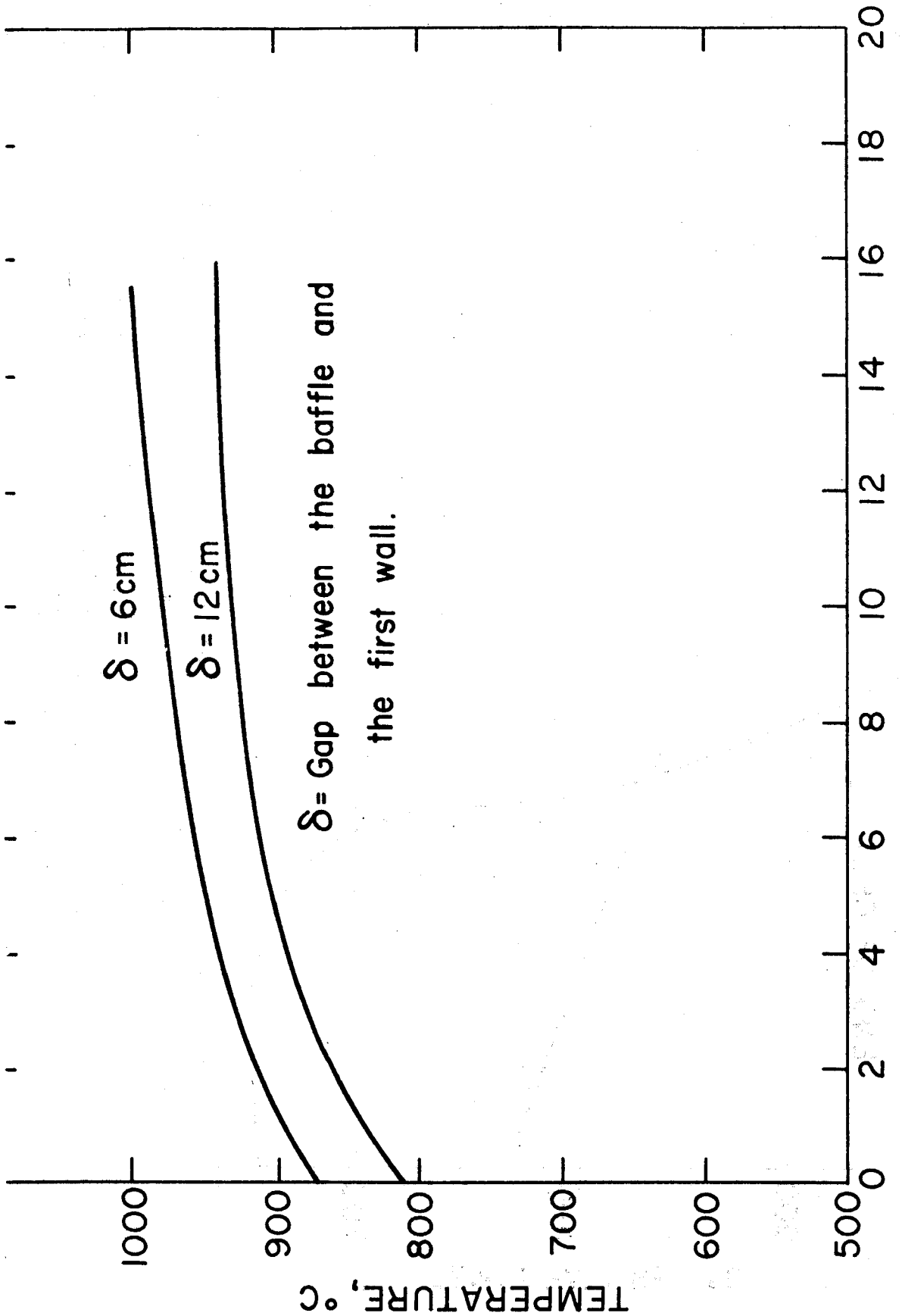

FIGURE VI-B-7 LITHIUM EXIT TEMPERATURE AS A FUNCTION OF BUFFER ZONE THICKNESS

VI-C. Inner Blanket

A cross section of the UWMAK-III inner blanket is shown in Fig. VI-C-1. A 0.5 m diameter feed tube is introduced between the TF magnets. This large feed tube connects with a manifold running in the toroidal direction immediately inside the magnets, to take advantage of the relatively abundant space there. Each inner blanket module will have 11 supply tubes coming from the large manifold and feeding smaller manifolds located at 11 points throughout the depth of the blanket. These small manifolds supply coolant to 11 rows of tubes which run the full height of the blanket as shown in Fig. VI-C-2. Each cooling tube has an inside diameter of 1.8 cm and a wall thickness of 0.1 cm. A bank of 86 cooling tubes joined together form the first wall. The rest of them cool the interior of the blanket.

The surface heating load on the first wall of the inner blanket is 35 W/cm^2. The volumetric heating rate within the blanket is obtained from neutronic calculations and is shown in Fig. VI-C-3. The coolant inlet and outlet temperatures are 488°C and 870°C, respectively. The pressure of the helium is 1000 psi (70 Kg/cm^2). These coolant conditions match the temperature of the helium coming from the secondary heat exchanger of the outer blanket so that identical turbines and thermal storage units can be used. The coolant from the inner blanket will be fed directly to a gas turbine. The sodium from the secondary loop of the outer blanket will supply the energy to heat the helium gas during plasma downtime. This will be discussed in more detail in Section VI-D.

The heat transfer characteristics of a gas in a tube are well established. The heat transfer coefficient can be calculated from the following equation:

$$\frac{hD}{K} = 0.023 \left(\frac{Dv\rho}{\mu}\right)^{0.8} \left(\frac{C_p \mu}{K}\right)^{0.3} \qquad \text{(VI-3)}$$

in which h is the heat transfer coefficient

D is the diameter of the tube

K is the thermal conductivity

v is the velocity

ρ is the density

μ is the viscosity

C_p is the specific heat

and the maximum temperature of the structure can be calculated from

$$[T_{max} - T_c]_{max} = \dot{q}/h \qquad \text{(VI-4)}$$

Fig. VI -C-1 CROSS SECTION VIEW OF UWMAK III

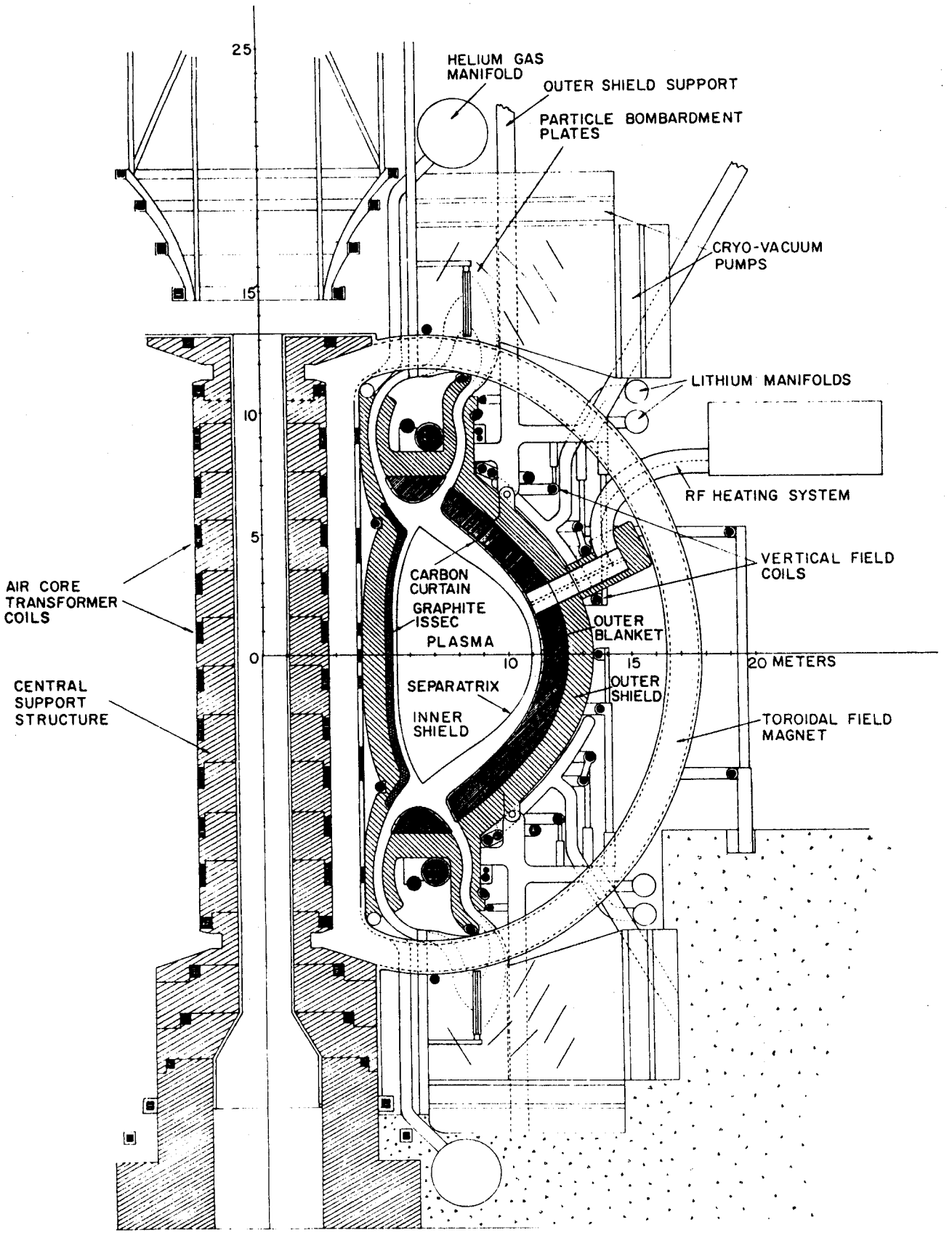

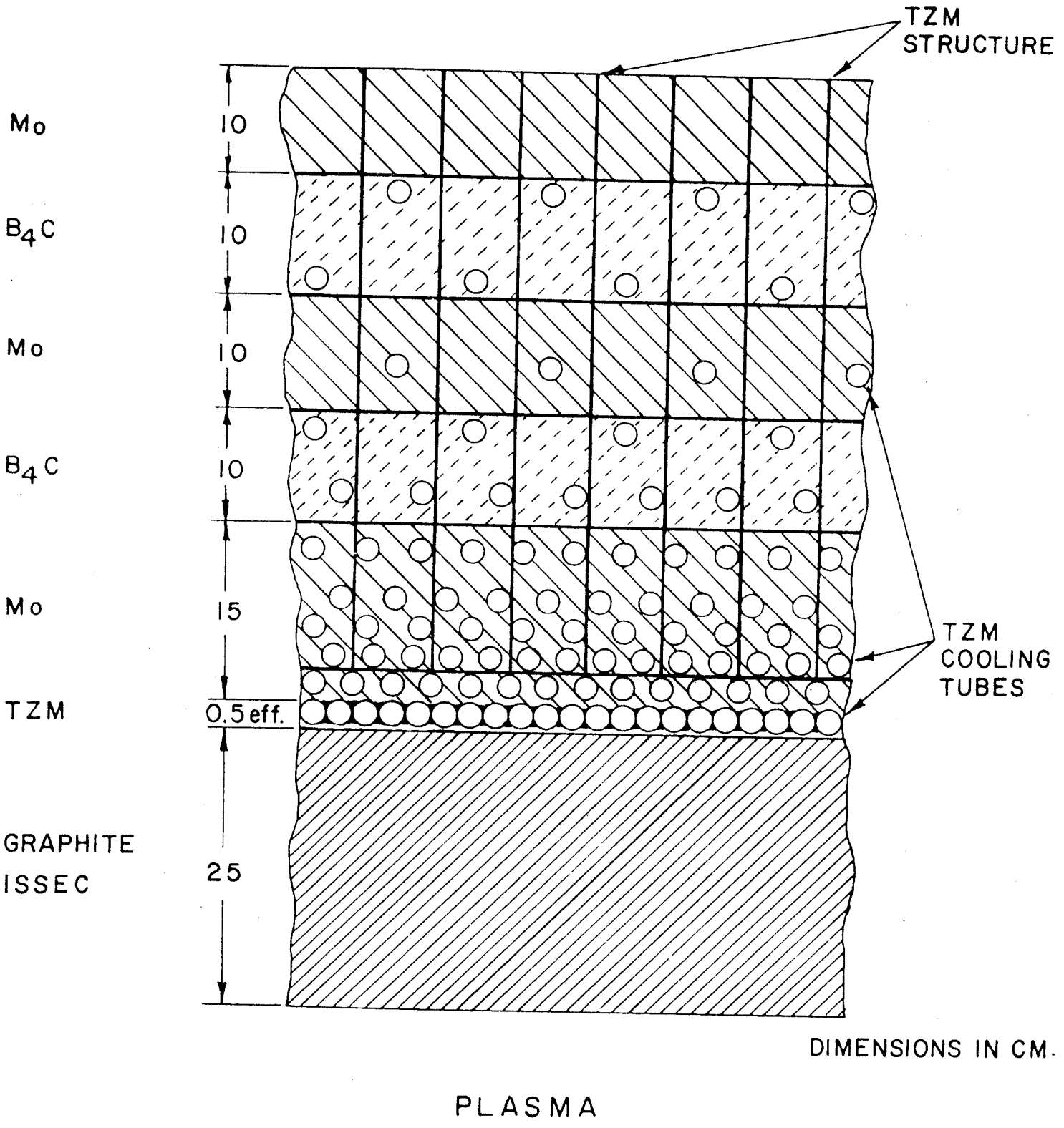

Fig. VI-C-2 Cross Section of Inner Blanket

FIGURE VI-C-3

HEATING RATE IN INNER BLANKET

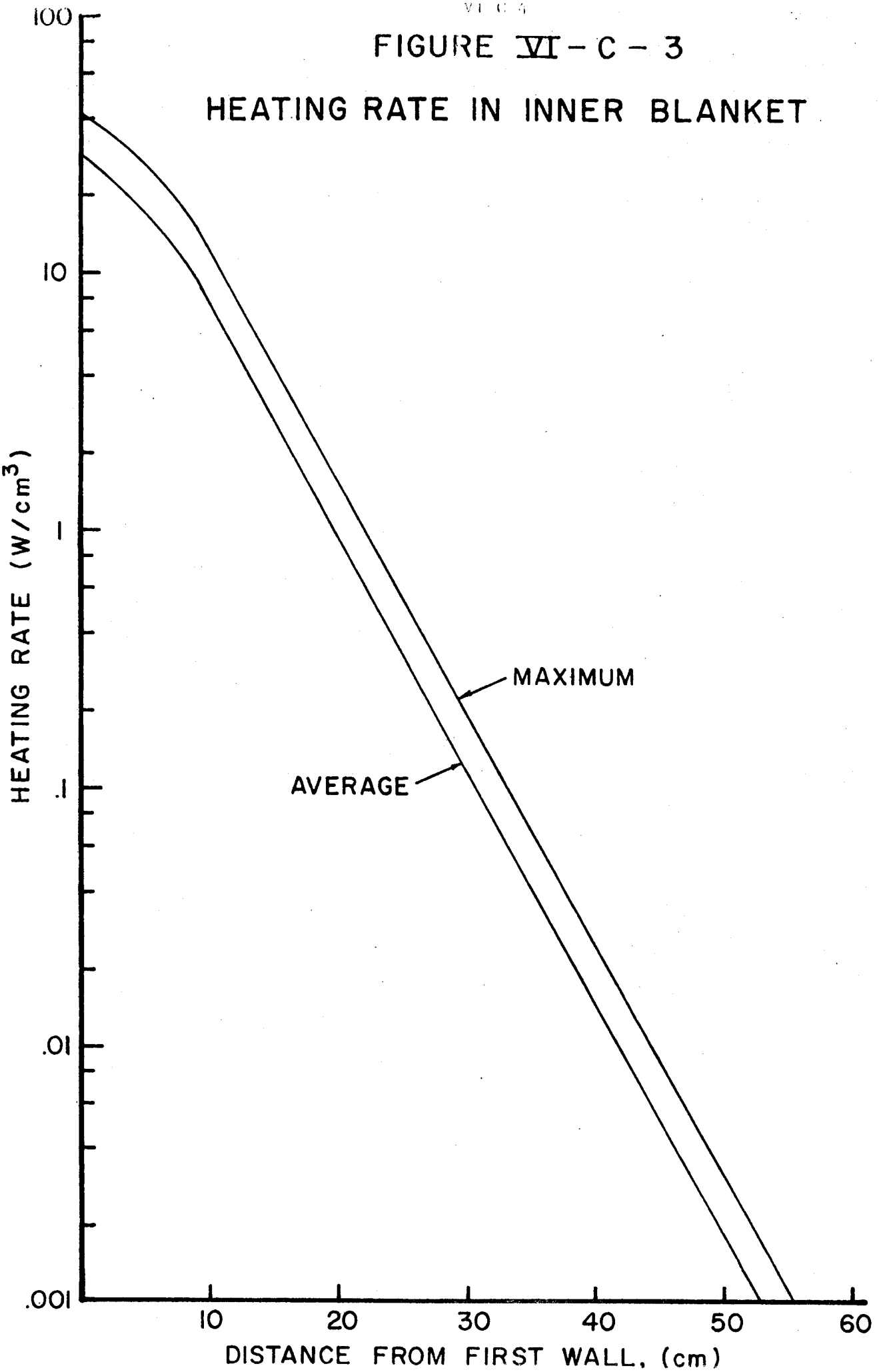

in which T_{max} is the maximum tube temperature

$T_{c\,max}$ is the maximum coolant temperature

q is the maximum surface heating level.

The first wall temperature thus calculated varies from 616°C to 998°C from the supply side to the return side of the coolant.

The distribution of the coolant tubes within the inner blanket is arranged to be inversely proportional to the energy generation rate as shown on Fig. VI-C-2 so as to make the heating load on each coolant tube approximately the same. The coolant tube distribution is schematically shown in Fig. VI-C-2. It should be noted that the blanket region is much thicker than actually needed, based on the heating curve in Fig. VI-C-3. The heat generation rate in the last 20 cm of the blanket is so small that it becomes very inefficient to recover it. This is, however, a first iteration of such a blanket design and the thickness of the blanket was decided from neutronic considerations before the heat transfer results where available.

A large amount of molybdenum is used in the inner blanket for neutronic purposes. Most of the Mo can be assumed to be in powder form, which is much less expensive than structural TZM. Both powdered Mo and B_4C are poor thermal conductors. Therefore, a certain amount of Mo has to be used to furnish the conduction path for the thermal energy. The maximum allowable temperature in the B_4C and non-structure Mo is assumed to be 1250°C[6]. The apparent thermal conductivity of the blanket is assumed to be

$$K_A = x_s K_{Mo}$$

where K_A is the apparent thermal conductivity of the mixture in the inner blanket.

x_s is the fraction of structural TZM

K_{Mo} is the thermal conductivity of M.

A simple thermal analysis shows that 35% of the total Mo in the inner blanket has to be in the form of fine sheet oriented to provide the needed heat conduction path.

The important results of the thermal hydraulic design for the inner blanket of UWMAK-III are listed in Table VI-C-1.

Table VI-C-1

Summary for Thermal Hydraulic Design of the Inner Blanket

Thermal Load	1334 MW
He Flow Rate	2.43×10^6 Kg/hr
Inlet He Temperature	488°C
Outlet He Temperature	870°C
He Pressure	1000 psi
No. of Coolant Tube	7780
Length of Coolant Tube	11 m
I.D. of Coolant Tube	1.8 cm
Coolant Tube Wall Thickness	.1 cm
Total Tube Surface Area	5791 m^2
Thermal Load on Tube Surface	23 w/cm^2
Maximum Temperature on Tube	1000°C
Maximum Temperature in the Blanket	1250°C

VI-D. Thermal Storage and Heat Exchanger Systems

The thermo-mechanical system connecting the fusion reactor with the power conversion system has to perform the following functions:

1. Transfer the thermal energy from the reactor coolant to the working fluid of the power conversion unit.

2. Contain the tritium within the reactor coolant.

3. Protect the reactor from the high pressure working fluid of the power conversion unit.

4. Change the pulsed energy output of a Tokamak reactor to continuous power fed to the power conversion unit.

All four functions have to be performed for the outer blanket. A sodium intermediate loop and a Li-Na and Na-He heat exchanger are used to accomplish the first three functions. A sodium storage tank is used as a thermal fly-wheel to smooth out the reactor energy output. The first three functions do not apply to the inner blanket which does not breed tritium and has helium coolant, the same as the working fluid of the turbine machinery. Coolant from the outer blanket supplies the energy storage for the inner blanket as well as the outer, since it is difficult to store a large amount of high pressure helium. The complete flow diagram of the coolants between the UWMAK-III reactor and the power conversion system is shown in Fig. VI-D-1.

The lithium from the outer blanket will be fed to a Li-Na intermediate heat exchanger. The sodium then is fed to a Na-Ne heat exchanger. A small amount of the sodium, however, is diverted to a thermal storage unit. This sodium is used to feed the Na-He heat exchanger during the time when the plasma is down. The same thermal storage unit is used to feed a Na-He exchanger for the inner blanket system. The coolant from the divertor has its own thermal storage unit. That coolant is fed directly to a steam generator.

Two Li-Na heat exchangers are used to transfer the energy from the outer blanket. However, because of the larger surface area needed, six Na-He heat exchangers are used, four for the outer blanket and two for the inner blanket.

The fusion reactor blanket is made of TZM, while the turbine machinery is primarily made of stainless steel. The Na-He heat exchanger is the transition where the two metals meet. The helium is on the shell side of the heat exchanger, which is made of S. S. protected by thermal insulation from the hot helium, while the tubes are made of TZM which contain the sodium. This unusual design prevents the metal to metal joint from exposure to a liquid metal. In this way, various corrosion problems are avoided.

The important dimensions of the two heat exchangers are tabulated in Table VI-D-1. It should be kept in mind that the exchanger designs have not been optimized.

References

1. G. L. Kulcinski, R. W. Conn, H. I. Avci, D. K. Sze, "Protection of CTR Metallic First Walls by Neutron Spectral Shifting" FDM 127, (June, 1975).

2. B. Badger, et al., "UWMAK-I, A Wisconsin Toroidal Fusion Teactor Design," UWFDM-68, (Nov. 1974).

3. D. K. Sze, W. E. Stewart, "Lithium Coding for a Low-β Tokamak Reactor" Procedings of Texas Symposium on the Technology of Controlled Thermal Nuclear Fusion Experiments and Engineering Aspects of Fusion Reactors, Nov. 1972.

4. M. A. Hoffman and G. A. Carlson, "Calculation Techniques for Estimating the Pressure Losses for Conducting Fluid Flows in Magnetic Fields," USAEC Report UCRL-51010, 1971.

5. Sutton, G. W., and A. Sherman, Engineering Magnetohydrodynamics, McGraw Hill, N.Y., 1956.

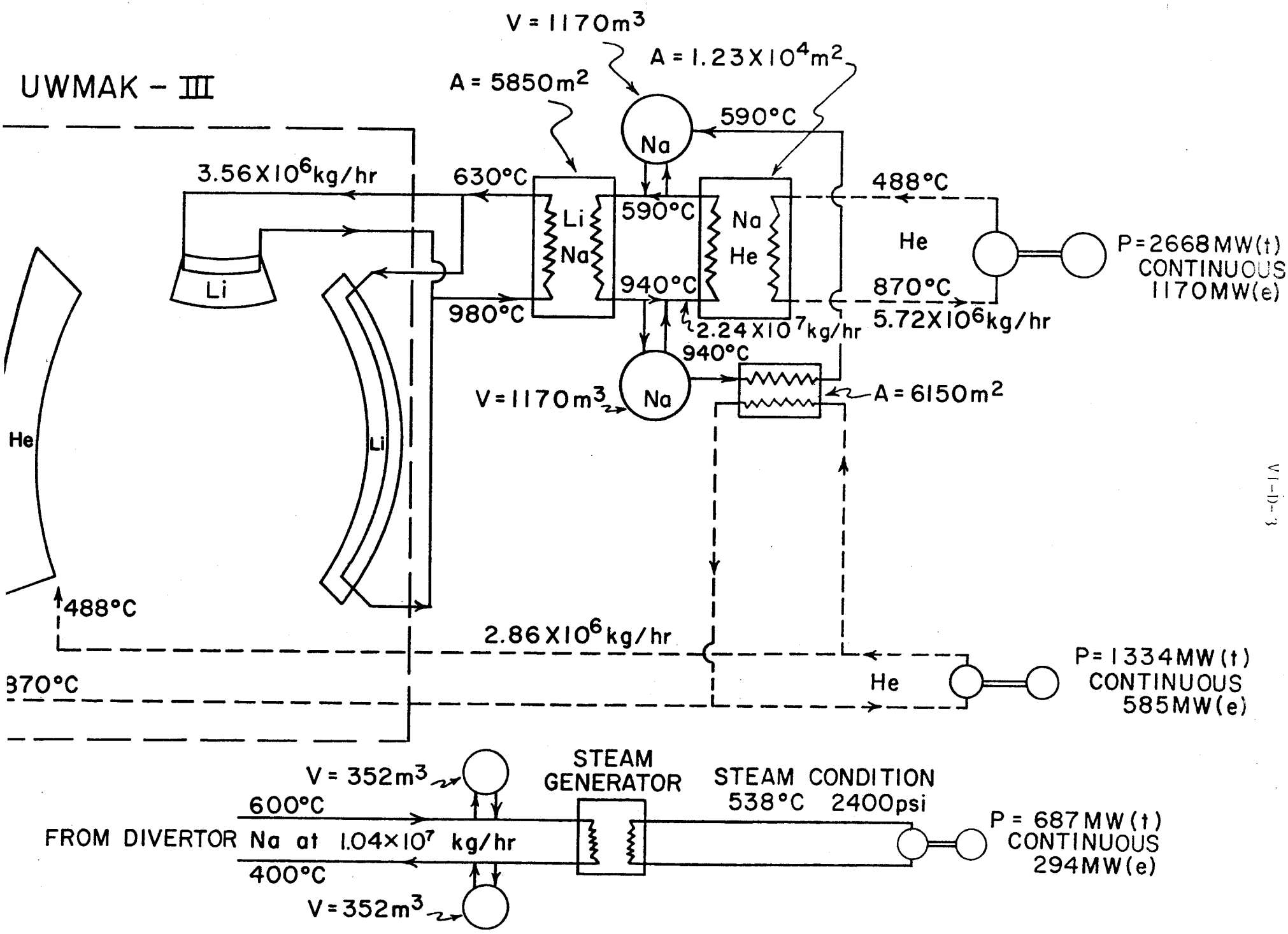

Fig. VI-D-1 Flow Diagram for UWMAK-III

Table VI-D-1

Dimensions and Performances of Heat Exchangers

	Li-Na	Na-He
Shell Side	Na	He
Tube Side	Li	Na
No. of Tubes	4982 cm	8498 cm
Pitch	2.69 cm triangular	4 cm square
Tube O. D.	2.06 cm	2.06 cm
Tube Thickness	.087 cm	.089 cm
Tube Length	8.92 m	5.6 m
Heat Transfer Area	2875 m^2	3073 m^2
I. D. of Shell	2.54 m	4.16 m
h) Tube Side	2.35 w/cm^2-°C	2.06 w/cm^2°C
h) Shell Side	3.42 w/cm^2-°C	.3 w/cm^2°C
Thermal Load	1445 MW	667 MW

VI-E. Mechanical Design of Blanket and Shield

VI-E-1. General Description of Blanket

There are two distinct blanket designs in UWMAK-III. The breeding blanket which covers the central and outer regions of the plasma chamber, hereon referred to as the outer blanket, and the inner, non-breeding blanket, sometimes called the hot shield.

The outstanding features of the outer blanket are that it is made of TZM, that it is a low pressure liquid lithium cooled structure designed to contain a large quantity of lithium with a minimum amount of structural material, and that it is designed to minimize the effect of energy loss due to heat exchange between the hot and cold lithium streams.

The front wall of the outer blanket consists of semi-cylindrical cells, 37 cm wide and from 1-2 m long, depending on the location in the plasma chamber. Each cylindrical cell is attached to a rectangular framework of flat sheets terminating in the lithium distribution headers. Six of these cells are joined together and are called a section. A section is 222 cm wide.

Circumferentially, the blanket is divided into 18 equal modules. This is done to allow a blanket module to be taken out between the TF coils, of which there are 18. Each module is further divided vertically into two regions. The region subtended by the angles $\pm$ 60° as measured from the plasma center, and which is assumed to have a lifetime of 1 1/2 years, will be called region (A). The rest of the outer blanket consisting of the part extending to the first divertor slot and the central region between the divertor slots, which is assumed to have a lifetime of 3 years, will be called region (B).

Each region (A) of an outer blanket module will have a skeletal frame as shown in Fig. VI-E-1. This frame is divided into 8 trapezoidal cavities. An assembled section of the blanket consisting of six cells, fits into each cavity and is sealed to it. This design has the flexibility of allowing the removal of a single section or the removal of the whole frame with eight sections.

Region (B) will have a similar frame but the sections will only be 180 cm wide and will have six 30 cm wide cells.

Looking radially out from the plasma, the first 60 cm of the blanket contain lithium with a minimum amount of structure, the next 30 cm contain a TZM clad graphite reflector and the last 10 cm contain the lithium distribution headers. Holes in the graphite block allow the passage of lithium from the headers to the front wall and back. A toroidal view of an outer blanket section is shown in Fig. VI-E-2 and a poloidal view in Fig. VI-E-3. The heavy wedge shaped material is part of the skeletal frame. It is wedge shaped to allow for poloidal and toroidal curvature. Blanket sections themselves are flat for ease of fabrication.

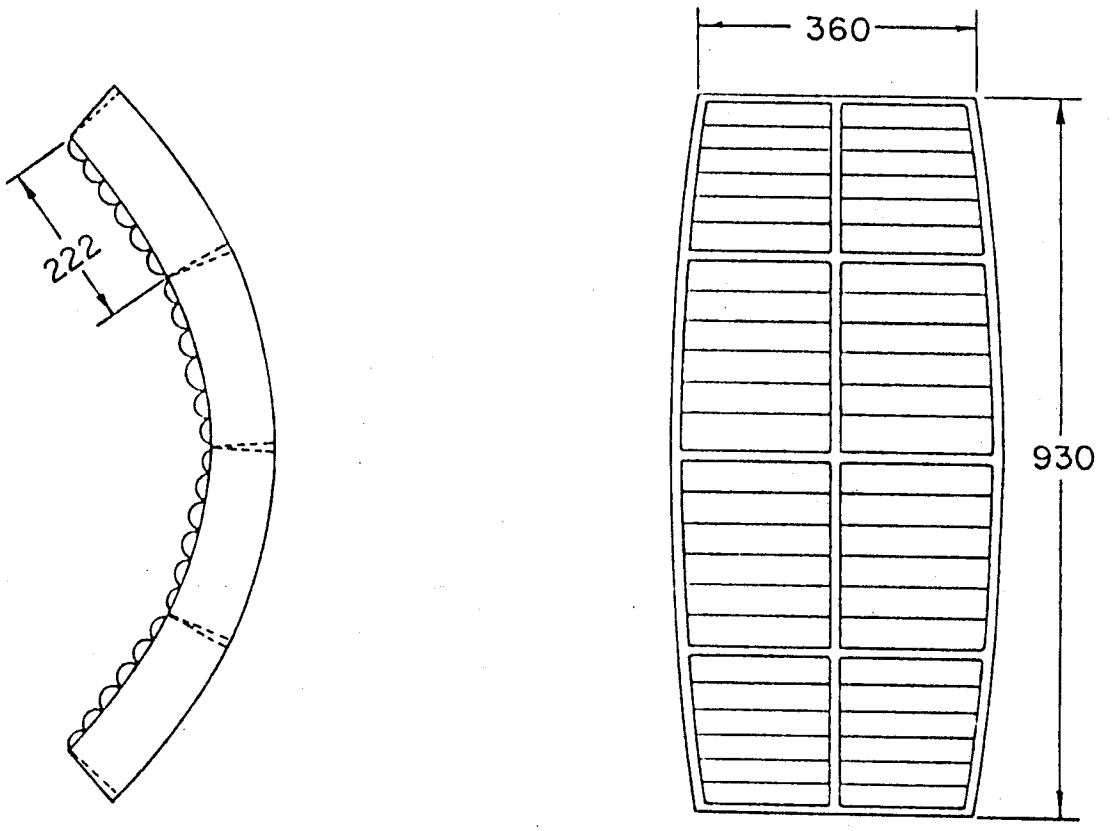

Fig. VI-E-1 Skeletal Frame for Region (A) of Outer Blanket
(a) Side view in the toroidal direction
(b) Radial view from outside the blanket

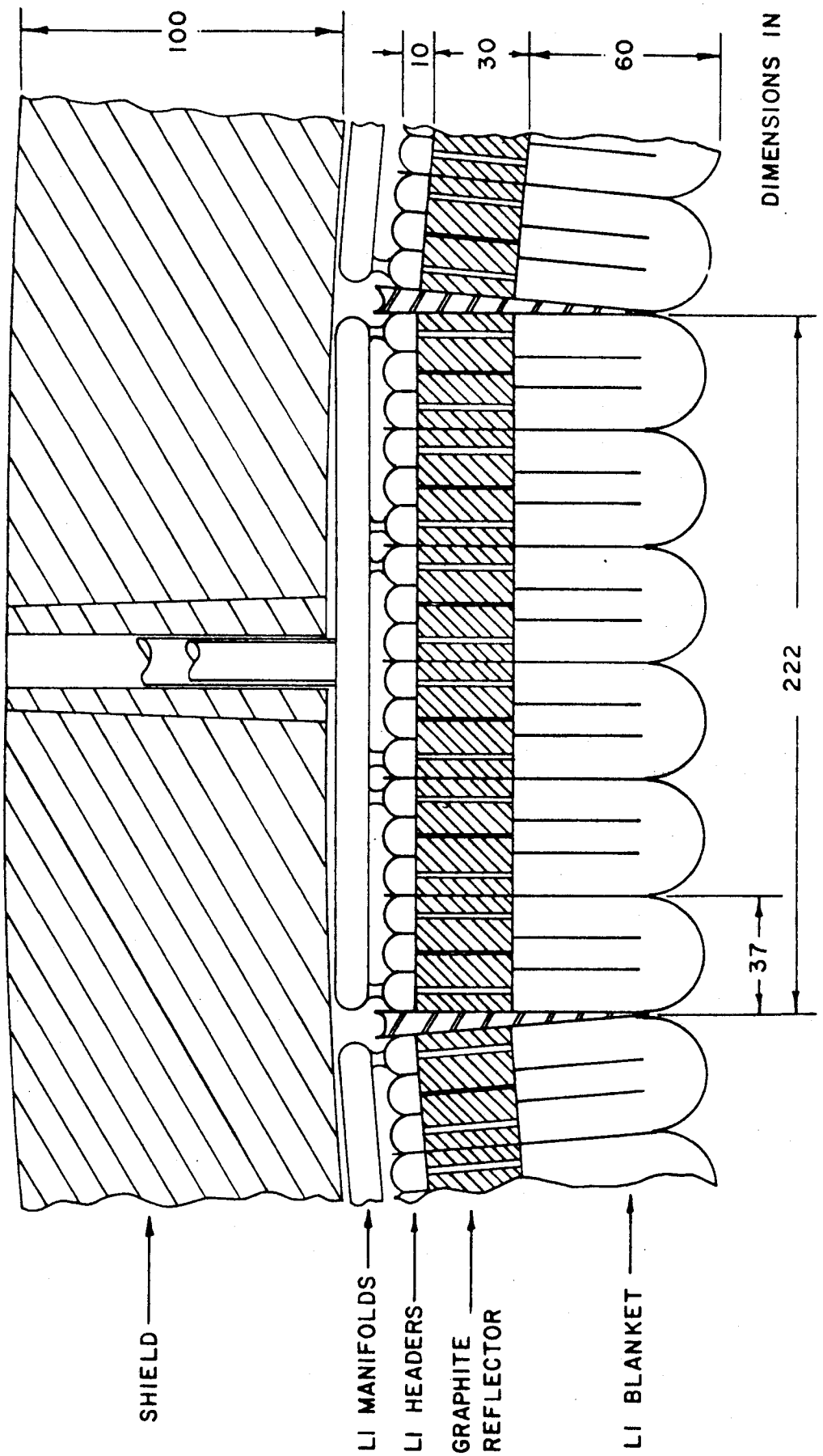

Fig. VI-E-2 Cross Section of Outer Blanket and Shield Viewed in the Toroidal Direction

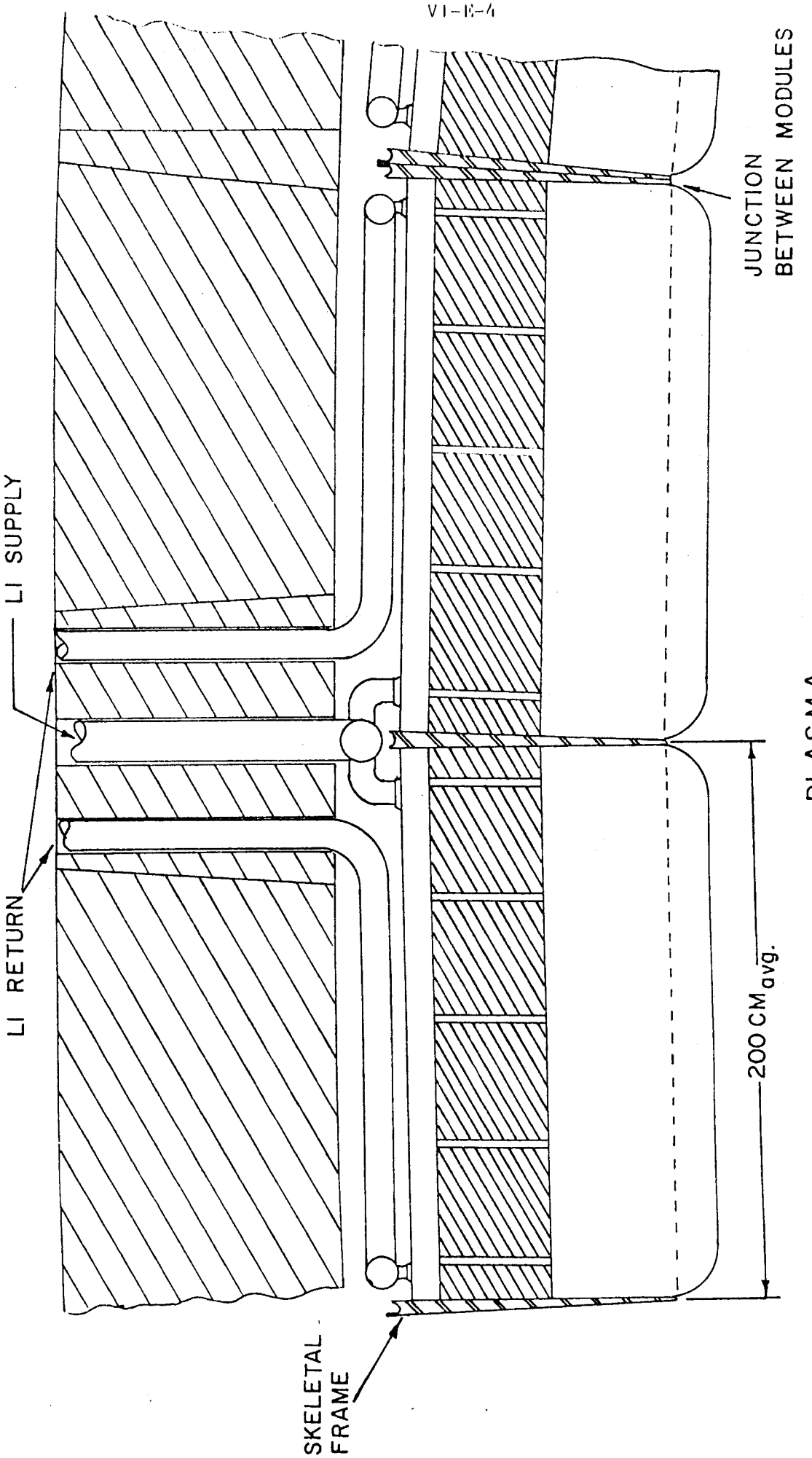

Fig. VI-E-3 Cross Section of Outer Blanket and Shield Viewed in the Poloidal Direction

It will be noticed that the blanket cell on either side of the graphite block is divided into three parts. The two end headers are supply and return headers while the one in the middle is a buffer. The middle header has a very slow flowing stream of lithium and from the heat transfer standpoint is essentially static. Direct heat exchange between the cold supply and the hot return headers is almost eliminated. Similarly, the region between the baffles in each blanket cell serves the same purpose. It provides additional lithium for breeding and energy conversion, serves as a buffer between the hot and cold lithium streams, but for all practical purposes does not take part in cooling the front wall.

Headers of adjacent cells are also arranged to minimize energy transfer. In this way headers which are in contact with each other are like headers (i.e. either supply or return). Besides minimizing energy transfer, this scheme reduces thermal stresses.

The whole outer blanket is fabricated from TZM, with the possible exception of the skeletal frame. TZM displays superior properties in thin sheet form and is difficult to fabricate in heavy sections. The front wall material is 1.5 mm thick, the cell frame material is 2.5 mm thick, the partition and header material is 1.0 mm thick and the graphite cladding material is 0.5 mm thick. The skeletal frame thickness tapers from 5 cm thick at the heaviest section down to 0.5 cm, and is about 80 cm high. Distribution of material in the outer blanket is given in Table VI-E-1.

Table VI-E-1

Distribution of Material in Outer Blanket (Tonnes)

	Region (A) 1 1/2 Yr Life	Region (B) 3 Yr Life
Front Wall (TZM)	17.3	9.8
Cell Frame (TZM)	67.1	38.8
Partitions (TZM)	18.6	10.6
Graphite Cladding (TZM)	16.1	8.7
Headers (TZM)	17.4	8.9
Frame (TZM or Niobium)	52.2	40.1
Graphite	550	317
Lithium	250	145
TOTAL	989	579

TZM can be welded, but the weld zone is recrystalized metal and its ductility and strength are impaired. A preferable joining method is by brazing. Several high temperature brazing materials have been developed for TZM which have proved to be extremely good. For example, a Ti-25% - 3% Be brazing material has a liquidus temperature of 1110°C and a remelt temperature of 1700°C.

Such a brazing material would be ideal for building up a blanket section, since certain parts can be brazed separately then the whole assembly brazed together without effecting the pre-assembled joints. The final seal between the section and the frame could be either a braze or a weld joint. This region is not very highly stressed and suffers very little radiation damage.

The skeletal frame material can either be TZM or niobium. The latter is easier to fabricate and weld in heavy sections but is not as strong. If the frame is made of niobium, the joint between the TZM section and the frame may present problems because of the difference in their coefficients of expansion.

The design of the inner blanket which is helium gas cooled is quite different from the outer blanket. The surface facing the plasma is a slab of graphite 25 cm thick. Its purpose is to shift the neutron spectrum in order that the inner blanket will suffer less radiation damage. The graphite is attached to a bank of TZM tubes joined together. These tubes provide the seal for the plasma chamber on the inner wall. They are 2 cm in diameter and extend for 12 m in the vertical direction. Additional tubes are provided further back with the number in each row progressively decreasing as a function of the energy deposited at that point. These tubes are embedded in layers of Mo and B_4C. Figure VI-E-4 shows a section through the inner blanket.

Helium gas is supplied to the tubes from a manifold located between the inner divertor slot and the TF coil at the top and exhausts to a similar manifold at the bottom as shown in Fig. VI-E-5.

VI-E-2. Blanket Stresses

The stresses in the front wall have been determined by simply adding the thermal and pressure stresses together. No attempt has been made to determine the effect of swelling or creep. A more thorough analysis using finite element codes can be made when more information is available on the swelling and other effects of TZM.

The thermal stress in a plate heated from one side is:

$$\sigma_{th} = \pm \frac{\alpha}{2} \frac{E}{(1-\nu)} \Delta T$$

where α = coefficient of expansion
E = modulus of elasticity
ν = Poisson's ratio
ΔT = temperature drop across the plate

For TZM at 1000°C these values are:

$\alpha = 6.7 \times 10^{-6} {}^{\circ}C^{-1}$
$E = 39.6 \times 10^{6}$ psi (2.76×10^{6} Kg/cm^2)
$\nu = 0.32$

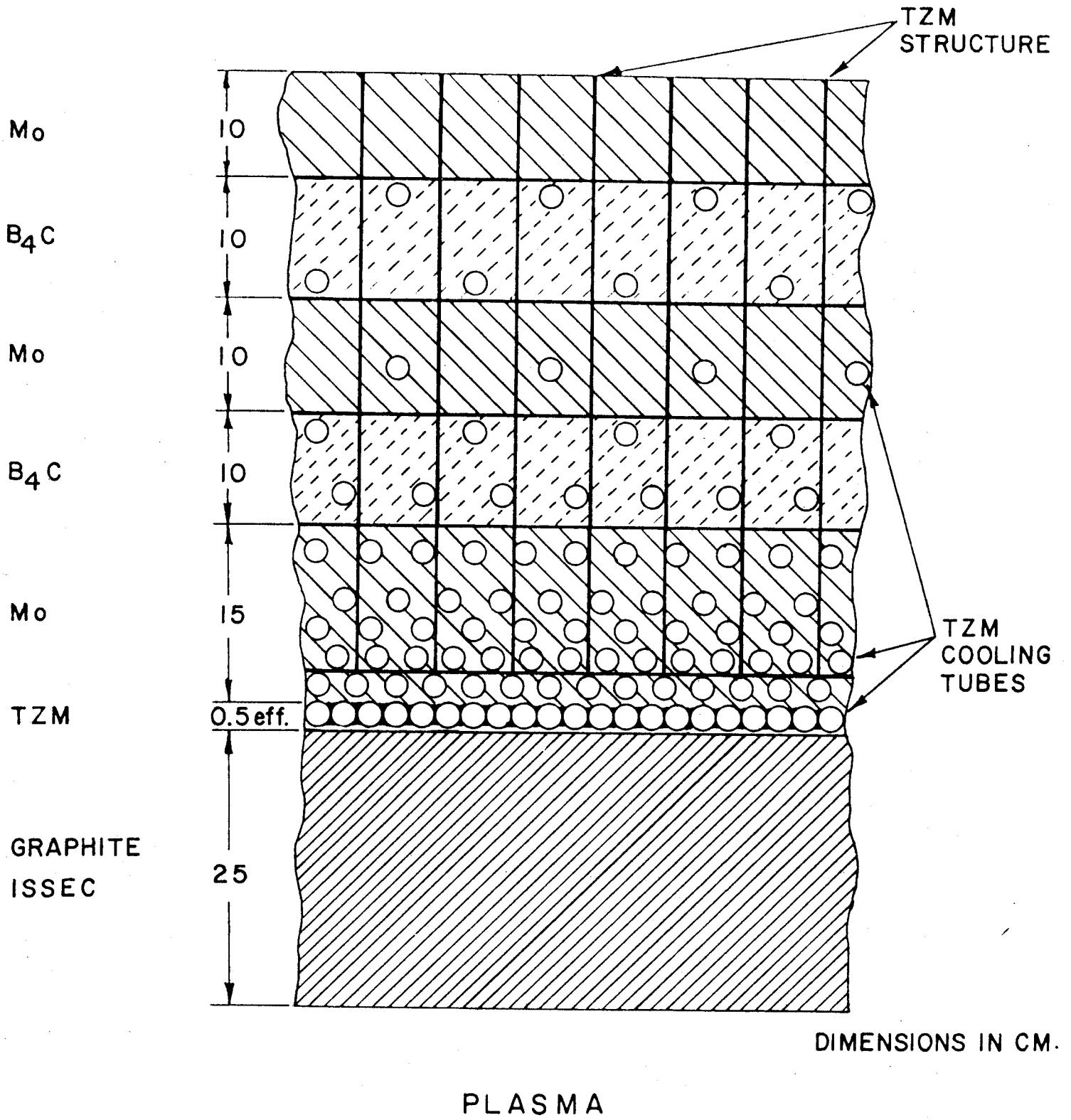

Fig. VI-E-4 Cross Section of Inner Blanket

The temperature drop across the plate due to the surface wall loading W_s and the neutron wall loading W_n is given by

$$\Delta T = \frac{1}{k} \left(W_s + \frac{W_n}{2} t\right)t$$

where k is the thermal conductivity and t the thickness of the plate. Substituting ΔT in the thermal stress equation gives

$$\sigma_{th} = \pm \frac{\alpha}{2} \frac{E}{k(1-\nu)} \left(W_s + \frac{W_n}{2} t\right)t$$

Based on a surface wall loading W_s of 25 watts/cm^2, a neutron heating rate W_n of 8 watts/cm^3, and k for TZM at 1000°C of 0.25 cal/cm,sec,°C, the thermal stresses were calculated for thicknesses ranging from 0.05 mm to 6 mm.

Hoop stress in a thin walled cylindrical structure is given by

$$\sigma_h = \frac{pr}{t}$$

where p = pressure
r = internal radius
t = wall thickness

The operating pressure of the outer blanket is 50 psi (3.5 Kg/cm^2). The hoop stress was based on a pressure of 75 psi (5.3 Kg/cm^2) and a thickness range from 0.05 mm to 6 mm. Both the hoop and thermal stresses are tensile on the side of the front wall facing the lithium and are therefore additive. On the side facing the plasma, the thermal stress is compressive and is therefore subtracted from the hoop stress. The values for thermal stress, hoop stress and maximum stress are given in Table VI-E-2. A curve of the maximum stresses as a function of material thickness is given in Fig. VI-E-6.

Since thermal stresses are small in a material such as TZM and the hoop stresses dominate, the curve does not have a minimum for the range of thickness used.

Stress relieved TZM rolled sheet has a yield value taken from a scatter band for tensile strength at 1000°C of 71,700 psi (5000 Kg/cm^2). For recrystallized TZM sheet material at 1000°C it is 28,680 psi (2014 Kg/cm^2). It is also interesting to note that a stress of 27,200 psi (1909 Kg/cm^2) will produce 0.2% creep in the material at 1000°C in three years. (1)

Based on this information, it was decided that a design stress of 10,000 psi (700 Kg/cm^2) would be satisfactory. This corresponds to a thickness of 1.5 mm. Even if 0.5 mm is lost to sputtering and blistering after three years, the stress will only rise to 14,000 psi (980 Kg/cm^2).

Table VI-E-2

Front Wall Stresses

Material Thickness (cm)	Thermal Stress[a] σ_h (psi)	Hoop Stress[b] σ_h (psi)	Maximum Stress σ_{max}[c] (psi)	Kg/cm^2
.05	± 191	27,750	27,941	1,950
0.1	± 385	13,875	14,260	995
0.15	± 582	9,250	9,832	686
0.20	± 782	6,937	7,719	538
0.25	± 985	5,550	6,535	456
0.30	±1191	4,625	5,816	406
0.35	±1400	3,964	5,364	374
0.40	±1612	3,469	5,081	354
0.45	±1827	3,083	4,910	342
0.60	±2490	2,313	4,803	335

(a) Surface wall loading W_s = 25 watts/cm^2, neutron wall loading W_n = 8 watts/cm^2

(b) Pressure = 75 psi (5.3 Kg/cm^2)

(c) Maximum stress is tensile on the inside surface of the front wall facing the lithium coolant.

CROSS SECTION VIEW OF UWMAK III

FIGURE VI-E-5

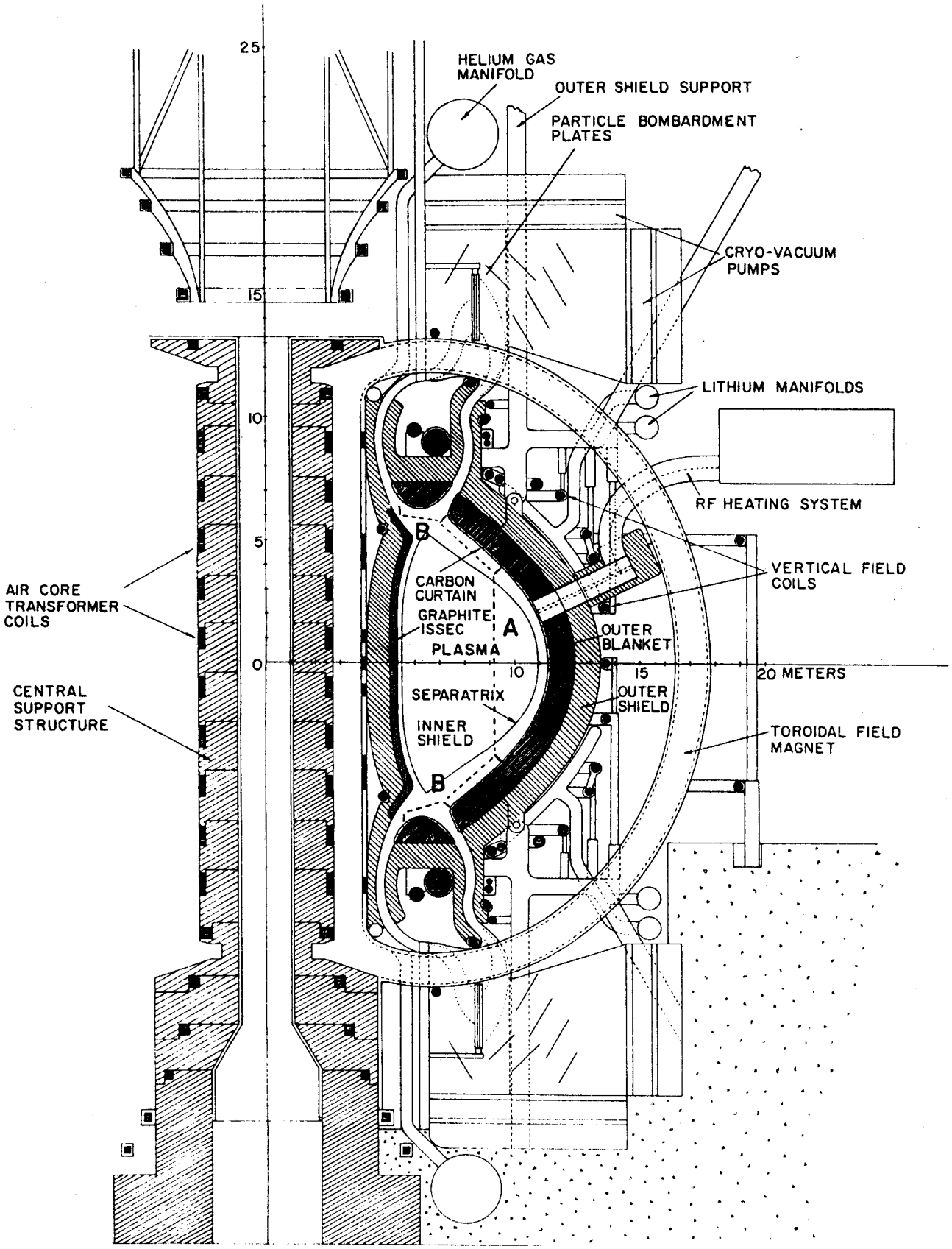

Although the plasma chamber will be surrounded by an environment of ~70 torr, it will nevertheless be subjected to atmospheric loading during testing periods and in the event of a failure in the secondary vacuum system. A cursory look at the stiffness of the structure indicates that it can withstand an atmospheric loading. However, it might be prudent to utilize the enormous stiffness of the shield to aid in the support of the blanket. This can be accomplished with bolts that penetrate the shield and fasten to the skeletal frame of the blanket.

VI-D-3. Shield Design

The shield in UWMAK-III is made up of alternating layers of different materials as discussed in Chapter V. Materials such as B_4C, Mo powder and lead are cast into a structure of either TZM or stainless steel.

The central and outer shields will have B_4C, stainless steel and Pb in them. The B_4C is in powder form, is mixed with 18% molten aluminum silicate ($Al_6Si_2O_{13}$) and cast in the stainless steel structure. The structure comprises 10% of the layers in both cases.

The inner shield is divided into two parts, a cooled warm shield (referred to as inner blanket in Section VI-E-1) which has Mo powder cast with aluminum silicate into TZM structure, and a cold shield which will primarily consist of B_4C cast as previously stated and alternating with thick layers of stainless steel, terminating in a 10 cm layer of lead.

Construction of all these shields can be in the form of preshaped H beams of either TZM or stainless steel, welded together with the resulting spaces filled either with B_4C, Mo or Pb. The heavy stainless steel zones can be made of preshaped plates welded together or they can be castings.

Both inner and outer shields will have cooling tubes running throughout. Helium gas will be used to cool the shield.

The outer shield has been designed to open up clam-shell-wise similar to the design of UWMAK-II. A small wedge shaped section of the shield has to be removed at the junction between the two shield modules at mid-plane. The junctions between the shield modules fall directly beneath each TF coil instead of between them. In this way the end of the shield modules protrudes out between the TF coils when the shield is in the open position. Figure VI-E-5 shows how the outer shield is hinged at about $\pm$ 60° from the plasma center. Separating at mid-plane, the two shield halves swing open exposing the outer blanket for servicing or replacement.

Table VI-E-3 gives the material quantities in the shield.

Table VI-E-3

Mass of Material in the Shield (Tonnes)

Material	Outer Shield	Central Shield	Inner Shield
TZM (structure)			87
Mo powder			963
SS (structure)	563	87	90
SS plate	3,766	600	576
B_4C	818	133	254
$Al_6Si_2O_{13}$	256	42	145
Pb	2,750	435	432
Graphite			233
TOTAL	8,153	1,297	2,780

VI-E-4. Blanket and Shield Supports

The inner shield is essentially a continuous cylinder subtending the inner legs of the TF coils. As described in the previous section, it is composed of Mo and SS structure filled with various materials. The weight of the inner shield is 2780 tonnes. It will be supported entirely on columns protruding between the TF coils and built into the floor of the containment building.

Central shield and blanket sections will be supported on structure also penetrating between the TF coils. Upper sections will be supported on the reactor containment building ceiling beams and the lower sections on the floor. Each one of these blanket and shield sections weighs 900 tonnes or 50 tonnes per support.

Similarly, the upper and lower halves of the outer shield will be supported on massive structure also penetrating through the TF coils and through radial slots in the vacuum plenums. They also anchor into the floor and the ceiling of the containment building. Immediately inside the TF coils, the structure is attached to a continuous ring which runs the circumference of the toroid. Supports from this ring hold the fixed section of the outer shield. The ring also contains the hinges on which the movable outer shield is supported. As can be seen from Fig. VI-E-5, the outer shield support ring also has diagonal braces anchored into the ceiling and the floor. These braces support some of the

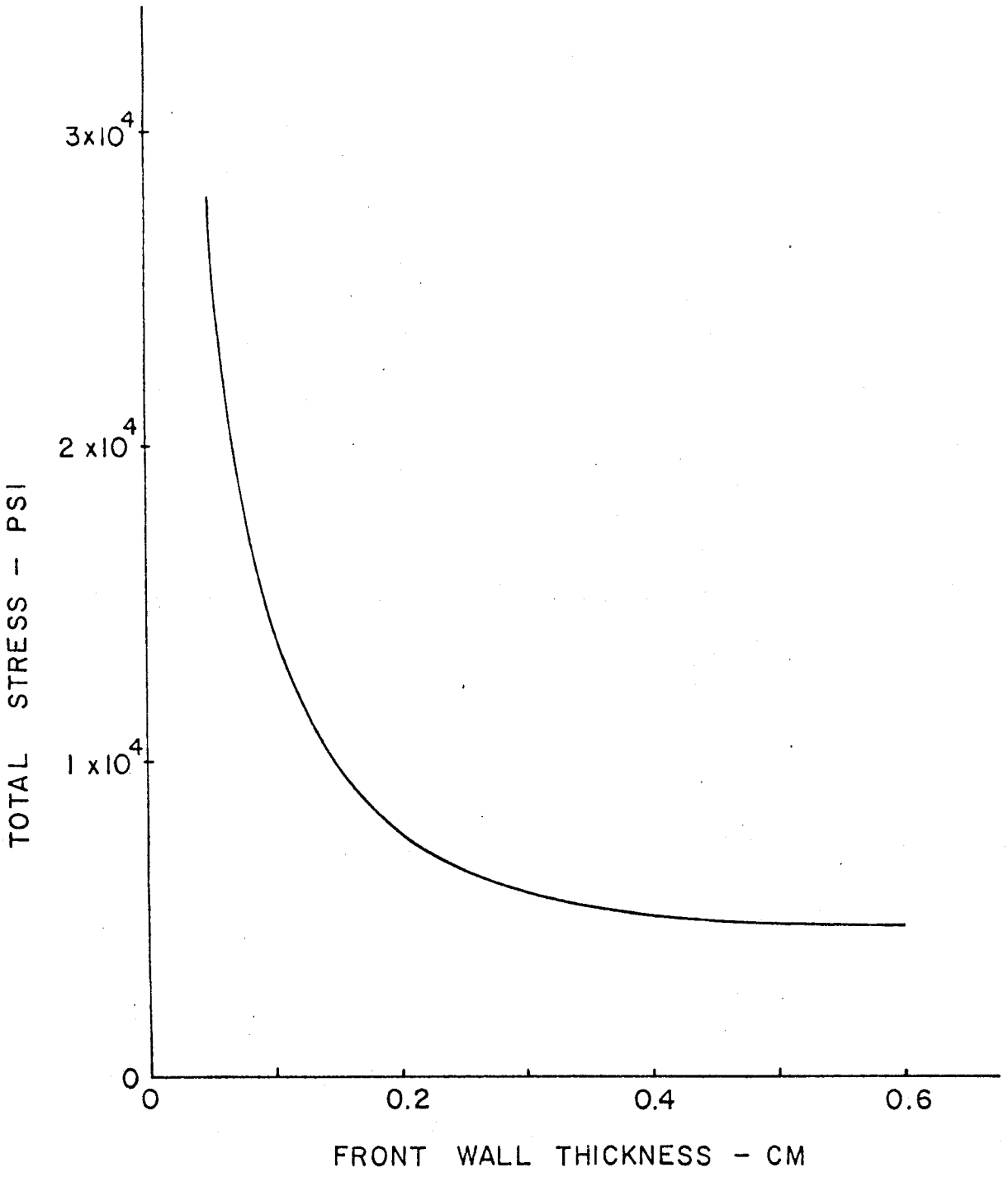

Fig. VI-E-6 Sum of Thermal and Pressure Stresses in the Front Wall as a Function of Thickness

VF coils and also contribute to the torsional restraint of the shield support ring. The total load on the roof from the outer blanket and shield if shared equally with the floor is 4400 tonnes, or 245 tonnes per each support.

The outer blanket module frames will be attached to reinforced plates which also compromise the wall of the outer divertor slot. These plates are attached to the shield support ring. At the same time, the blanket skeletal frames will also be supported on the shield as mentioned previously.

Although expansion joints for the blanket would be very beneficial, it is difficult to visualize an expansion joint which can subtend the whole plasma chamber, including the vacuum plenum. At a temperature of 1000°C, the outer radius of the chamber will increase approximately 7 cm. This would present difficulties, especially if the blanket is attached to the shield which does not get as hot. A solution might be to design expansion joints into the shield without compromising its efficiency. Some imaginative engineering will be needed to solve this problem.

VI-D-5. Blanket Replacement

We have mentioned earlier that certain parts of the blanket will be replaced every year and a half and others every three years.

In order to make the blanket accessible for servicing, the following functions must be performed:

1 - The plasma chamber and toroidal enclosure are brought up to atmospheric pressure.

2 - The lateral support structure between the TF coils has to be removed, opening up a vertical passage $\pm$ 8 m from the central plane. Simultaneously the blanket is drained of lithium.

3 - If there are RF waveguides in the module in question, they have to be disconnected and extracted.

4 - The VF coils which are in the way have to be retracted. They are shown supported on mechanical jacks in Fig. VI-E-5.

5 - The outer lithium manifolds have to be disconnected and removed.

6 - The outer shield must be opened up and firmly secured.

The process for removing a blanket module which has a 1 1/2 year lifetime, consists of grinding or plasma burning the welds sealing adjacent skeletal frames to each other, and then radially extracting the module between the TF coils. The backlegs of the TF coils are far enough apart as to allow radial extraction of an outer blanket module. Once the reactor is opened, the rest of the blanket module, namely the regions which are assumed to last three years, become accessible. Removing these modules is harder, since it has to be done from the inside of the reactor.

Obviously all this work has to be done with remote controlled tools by technicians in shielded capsules. No one pretends that any of these operations will be easy. The design and operation of the equipment needed to perform these functions will challenge the imagination of the best engineers in the country.

Since an effort has been made to minimize the material in the blanket, it would seem that discarding the whole spent module is the best way to proceed. The spent modules will be crushed, compacted and stored in special rad-waste areas. The amount of material thus disposed of per year, averaged over three years is 164 tonnes of TZM and 472 tonnes of graphite.

Replacement of the blanket modules will now consist of inserting and welding new modules into place. The process of closing up the reactor follows the functions enumerated above in reverse order.

References for Section VI-E

(1) Arc-cast molybdenum base TZM alloy: properties and applications. Janet Z. Briggs, R. Q. Barr, High Pressure, 1971, vol. 3, pp. 363-409.

VII. The Tritium System

VII-A. Introduction

The routes along which tritium flows throughout the UWMAK-III installation are shown schematically in Figure VII-1. These include the recovery and reprocessing of tritium in the fueling cycle, the extraction of tritium from the heat transfer fluids, the containment of tritium in regions where permeation rates are anticipated to be high, the emergency recovery of tritium from the building environment and the loss of tritium to the environment in gaseous and aqueous phases as well as in solid form as waste. The philosophy and basis for the selection of tritium recovery and cleanup systems are discussed in the next section.

VII-B. Basis for Design and Calculations

VII-B-1. Design Considerations

The reactor building will have an inert atmosphere (Chap. XI Sec. F) contained within an impermeable metal shell. The building system contains an emergency tritium cleanup system that will maintain a tritium pressure of 7.6×10^{-10} torr. The largest amount of tritium is handled in the fueling and reprocessing cycle. However, the temperatures of the piping and containment vessels, except within the torus, are very low and the tritium loss problem is minimal as long as the many joints and valves perform satisfactorily. However, the outer blanket power cycle operates at a very high temperature. Here the tritium bred in the lithium diffuses through the heat exchanger walls to the sodium and then to the helium. The pressure of tritium over the sodium is maintained at 7.6×10^{-10} torr. This ultimately becomes the tritium pressure in the helium loop. Routine losses of tritium to the building environment from the sodium and helium heat transfer fluids are low (<1 curie/day).

In turn the tritium in the lithium must be maintained at a concentration such that diffusion into the sodium does not result in a tritium loss rate that exceeds the sodium cleanup system capacity. The tritium concentration in the lithium must also be low enough to prevent substantial leakage through the piping and valves.

We have designed a system which meets the above requirements. This system operates with a steady state tritium inventory in the lithium of 1 kg (2.08 ppm) and a leak rate into the sodium of 1256 curies/day. The sodium cleanup system will process this amount of tritium and maintain a tritium pressure over the sodium of 7.6×10^{-10} torr. For a comparison and detailed study of tritium leak mechanisms in other CTR systems see Kabele, et al.[1]

VII-B-2. Permeation Behavior

The permeation of tritium through a wall is expected to follow a square root dependence[2] on the tritium pressure. However, recent experiments[3,4] indicate that at low pressures (<1 torr) the dependence is close to linear. These results

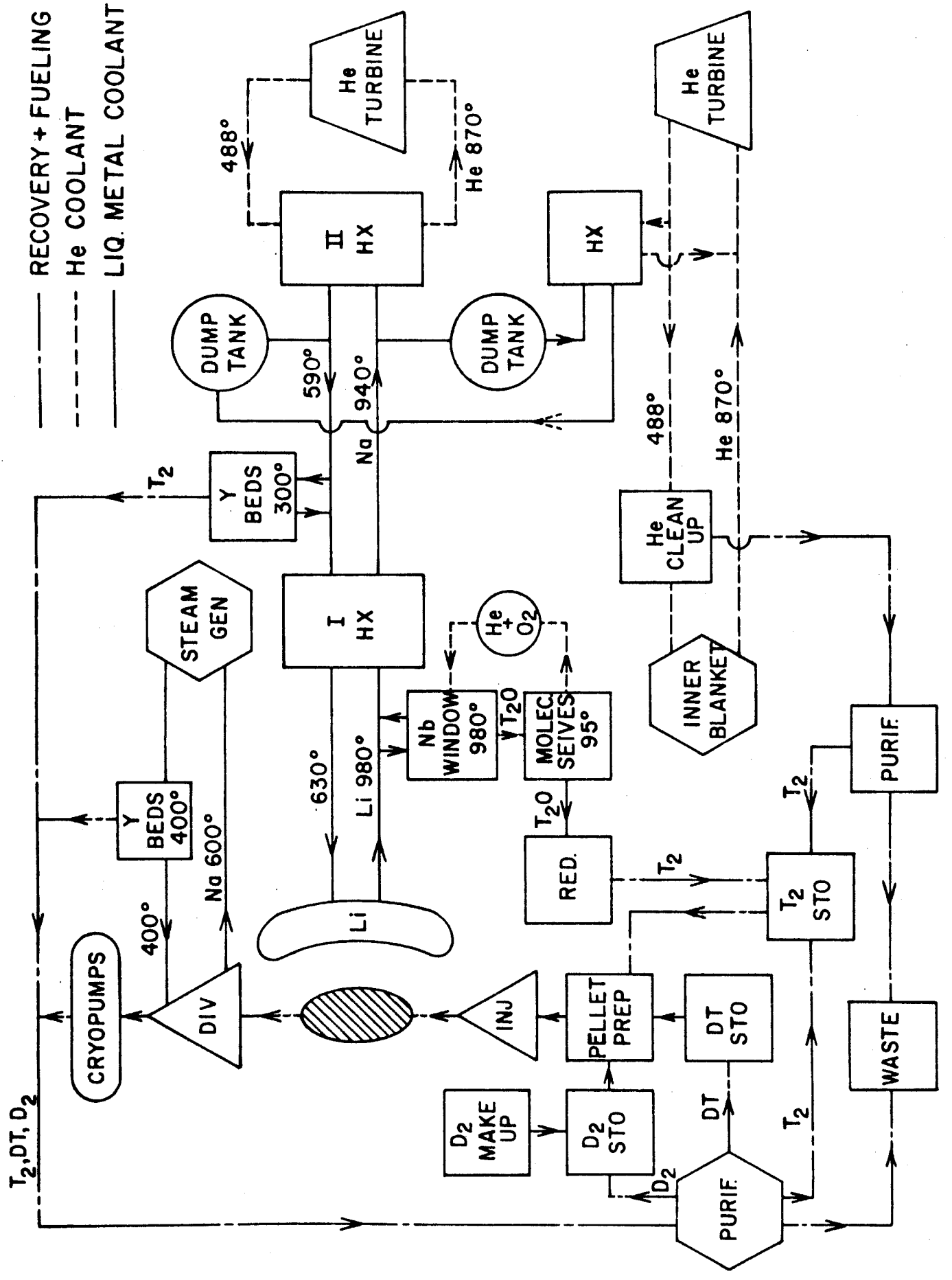

Fig. VII-1 TRITIUM IN UWMAK III SYSTEM

seem to indicate that inefficient surface desorption is the rate limiting step in the permeation process. However, if the surfaces are clean and a mechanism is provided for removal of tritium from the downstream surface, the square root law still should be valid. Thus, in those instances in which either oxygen-containing helium or liquid sodium is present on the downstream side of the wall, the square-root dependence of the permeation is probably the best model to use. In other cases the square-root dependence represents a worst case analysis. In this report we have consistently used the square-root dependence in the permeation calculations. The data upon which the calculations are based are found in Table VII-1.

VII-C. Recovery and Reprocessing of Tritium from the Fueling Cycle

VII-C-1. Injection, Divertor and Cryopump

The solid fuel pellets (Chap. II, Sec. D) are injected into the plasma at a rate of 1.63 kg of tritium and 1.085 kg of deuterium over the 30 minute burn time (Chap. II, Sec. D). This amounts to 74.4 kg of tritium and 49.6 kg of deuterium on a twenty-four hour basis. Of this quantity only 0.620 kg of tritium and 0.413 kg of deuterium are consumed. The unburned fuel and product helium ions are directed to a divertor plate (Chap. III, Sec. C) where their energy is transferred to a stream of liquid sodium. The particles are then collected over a five hour period in cryopumps (Chap. III, Sec. C) containing Linde 5A molecular Sieves at cryogenic temperatures. The total inventory of tritium in the cryopumps after five hours is 15.5 kg. Two sets of cryopumps operate such that the one set collects hydrogen isotopes and helium while the second set is regenerated. The regenerated gaseous hydrogen isotopes and helium are freed from the molecular sieves by heating to 30°K. The gases are then passed to the refueling cycle for purification and pellet preparation.

VII-C-2. Purification and Storage

The gases released from the cryopumps contain in addition to the unburned D_2, T_2, T, and HT, the following impurities: He, HD, H_2, Ar, N_2, O_2, and hydrocarbons. The impurities must be removed before the fuel is injected (as solid pellets) back into the plasma. We propose the utilization of chromatographic stripping by the use of molecular sieves cooled to -131°C [10] for the removal of all impurities except He, H_2 and HD.

The off-gas from the purifier will now contain the molecular species D_2, DT, T_2, HD, HT plus some helium, which is produced in the fusion reaction at the rate of 0.83 kg/day. Since the maximum desirable level of He in the fuel is about 5 atom per cent, the maximum permissible level in one day's fueling is about 10 kg in UWMAK-III. The helium is separated in the fuel preparation step, because the D-T mixture has to be liquified to prepare the frozen fuel pellets and the helium gas is simply pumped off. All the fueling in UWMAK-III is done by injection of solid frozen DT pellets. In addition, about 1 g of protium is produced per day from nuclear reactions in the structural first wall. The maximum desirable level is about 2 kg of protium in one day's fueling. To maintain an acceptable protium level in the fuel, 0.1% of the recycled fuel stream from the purifier is passed to a cryogenic distillation unit [11,12,13] and the HD is removed.

Table VII-1

Parameters and Relationships Used in Calculations

1. Relationship used for calculation of permeation rate, V,[2] is

$$V = \frac{A \times 10^{-5} \times C \times e^{-E_A/RT} \times (p_1^{1/2} - p_2^{1/2})}{X\sqrt{3}}$$

where $\sqrt{3}$ corrects for isotope effect and

A = area

C = permeability constant for given metal

E_A = activation energy for permeation

T = temperature °K

p_1 = upstream gas pressure

p_2 = downstream gas pressure

X = wall thickness

2. Permeation parameters*

a. Lithium-sodium heat exchangers (2)	Total area = 5.75×10^7 cm^2
	Wall thickness = 0.89 mm
	Av. temp.† = 1058°K
	$p_1 = 2.20 \times 10^{-7}$ torr
	$p_2 = 9.6 \times 10^{-11}$ torr
	C for Mo[5] = 930 $\frac{\text{cc(STP)mm}}{\text{cm}^2\text{hrs atm}^{1/2}}$
	E_A[5] = 21.5 Kcals/mole
b. Sodium-helium heat exchangers (4) (outer blanket)	Total area = 123×10^8 cm^2
	Wall thickness = 0.89 mm
	Av. temp. = 1038°K
	$p_1 = 7.6 \times 10^{-10}$ torr
	$p_2 = 7.6 \times 10^{-10}$ torr

*Wall material is TZM for all the heat exchangers and divertor plate. Data for molybdenum were used.

†Average temperature of lithium and sodium.

Table VII-1 continued

c. Sodium-helium heat exchangers (2) (inner blanket)	Total area = 6.16×10^{7} cm^2 Wall thickness = 0.89 mm Av. temp. = 1038°K $p_1 = 7.6 \times 10^{-10}$ torr $p_2 = 7.6 \times 10^{-10}$ torr
d. Divertor plates - sodium	Total area = 1.5×10^{6} cm^2 Wall thickness = 2.1 mm Temp. = 1273°K $p_1 = 4.6 \times 10^{-5}$ torr $p_2 = 8.0 \times 10^{-6}$ torr
e. Piping - Li	Total area = 400 meters^2 Wall thickness = 5 mm Temp. = 1253°K (hot leg) 903°K (cold leg)
f. Sodium-steam heat exchanger (material SS-304)	Total area = 5×10^{7} cm^2 Wall thickness = 1.5 mm -1.8 mm (double walled) Av. temp. = 773°K

3. Sieverts constants (units, torr$^{1/2}$/atom fraction)

   a. Sodium K_s [6] = 2.8×10^{4} (independent of temperature)

   b. Lithium[7] $\log_{10} K_s = 4.591 - 2809/T$

4. Equilibrium pressure over yttrium bed[8,9]

$$\log P = 10.52 = \frac{11,869}{T}$$

where P is the pressure of hydrogen over the composition range

$YH_{1.8} - YH_{0.8}$ in torr

Table VII-1 continued

5. Coolant parameters

Coolant	Flow Rates (kg/hr)	Inventory (kg)
Li	7.12×10^6	4.8×10^5
Na (outer blanket)	2.38×10^7	1.3×10^6
Na (divertor)	1.07×10^7 Kg/hr	3.2×10^5
He* (outer power cycle)	4.8×10^6	10.9×10^3
He* (inner power cycle)	2.4×10^6	5.45×10^3

*Pressure is 1000 psi at turbine.

The fuel cycle will require storage because of the cyclic nature of the burn and the need to have a reserve capacity of fuel. For the large amounts of D_2, T_2, and DT involved in this system, two types of storage are feasible, namely liquid storage as D_2O, T_2O, and DTO and gas storage in pressure tanks. Liquid storage as T_2O occupies less volume and requires a reduction step, but the main concern with this method of storage is related to biological risks if a leak should occur. The seriousness of this potential problem needs further study. Most industrial experience with hydrogen storage has been in a metal pressure tank.[14] For tritium storage, an austenitic stainless steel tank would be used and the contents kept near atmospheric pressure so that the mechanical strain and tritium embrittlement of the container are minimized and the long-term integrity of the tank assured. We propose storage of the fuel in a pressurized tank. The tritium inventory in reserve storage is 18.6 Kg, which corresponds to six hours of fueling.

VII. D. Recovery of Tritium from Heat Transfer Fluids

VII-D-1. Metals

a. Outer Blanket

(i) Liquid lithium - The primary energy deposition and tritium production site is in the outer liquid lithium blanket (Chap. VI, Sec. B). Here the neutrons react with lithium to produce tritium and helium. The total mass of lithium in the blanket is 4.8×10^5 kg which at 980°C has a density of 0.44 g/cc and thus occupies a volume of 964 m^3. The steady state concentration of tritium in the blanket will be 2.08 ppm. An additional reservoir (UWMAK-I, Vol.II, Sec.I)[15] of sufficient volume to contain all the liquid lithium is available in the event of a plant shutdown. This reservoir has a wall thickness of 1.43 cm and is heated to ensure that the lithium remains liquid. Tritium diffusion through the walls is tolerably low under these conditions.

The liquid lithium is circulated through the system at a rate of 7.12×10^6 kg/hr. Five percent of the lithium is diverted to a niobium "window"[16] for the extraction of tritium. Niobium is particularly well suited for this purpose as it has a high permeability to hydrogen at these temperatures[17] and allows us to reduce the tritium concentration of the lithium to a level compatible with the subsequent tritium losses to the environment.

The niobium "window" is of heat exchanger design (Chap. VI, Sec. B) with liquid lithium flowing through niobium tubes of wall thickness 0.38 mm and helium containing 10^{-2} torr oxygen flowing past the tubes at a flow rate of 4.1×10^3 ℓ/hr. The total surface area will be 1.47×10^7 cm^2. Calculations have shown that diffusion of tritium from the bulk of the lithium to the wall surface will not be the rate determining step in the permeation process. The oxygen in the helium should rapidly react with the tritium atoms on the catalytic metal surface to yield T_2O.

The five percent bypass of lithium into the "window" system reduces the total tritium concentration from 2.08 ppm to 2.04 ppm and removes 0.666 kg of tritium in a 24 hour period.

The fabrication of the desired window will require considerable development. The oxygen level in the niobium must be less than 100 ppm or the lithium will erode the surface and preferentially attack grain boundaries.[18] Also carbon transport from the TZM will occur,[19] causing embrittlement of the niobium. In addition, at 980° niobium will be subject to attack by oxygen and therefore some protective barrier is required. Palladium is the barrier of choice since it has a high hydrogen permeability.[16,17] A palladium thickness of 0.001 cm deposited by electrodeposition[18,20] will give a coherent layer of suitable durability. This will require a total of 170 kg of palladium for the calculated surface area of the window.

Even though palladium oxide is thermodynamically unstable and the oxygen concentration is low, some transport of palladium oxide from the window surface will occur. However, we do not expect this to be a serious problem as extrapolating from what data[21] exist we calculate a lifetime for the palladium layer of 28 years; essentially the same as the plant lifetime. It is also conceivable that counter diffusion of oxygen through the palladium could occur. However, in this system, diffusion of tritium through the niobium metal should inhibit this process. The mutual solubility of the two metals is quite high[22] and it is expected that the palladium will diffuse into the niobium, though there are no firm data for the rates of interdiffusion. Therefore we propose to introduce an intermediate yttrium layer to minimize the rates of diffusion so that a practical "window" lifetime can be achieved. Yttrium was chosen because it, along with the other IIIB elements and some of the rare earth metals, are among the few metals which do not form solid solutions with niobium.[22] The required yttrium layer thickness is estimated to be 2500 Å. This will require a total of 2.0 kg of this element for the calculated surface area of the window.

The permeability of yttrium to hydrogen is unknown, although it is expected to have a permeability similar to zirconium. We estimate the permeability of the 2500 Å yttrium layer to be the same as the 0.38 mm niobium wall. This estimate was used to calculate the required "window" surface area.

Assuming that a "window" can be successfully constructed to these specifications we would expect the lifetime to be 10 years and therefore a change out would be required twice during the lifetime of the plant. The design includes additional reserve "window" modules (10% of the capacity) so that a tube failure would not require a plant shutdown but only a switch to a reserve "window" module.

The T_2O recovered from the "window" will be collected on Linde 5A molecular sieves at 95°. One bed will contain 460 kg of sieves with a capacity of 2.5 kg of T_2O. The gaseous T_2O will be regenerated by heating the bed to 200°C. This will then pass over uranium[23,24] metal or an alternate active metal, to reduce the T_2O to T_2 under conditions in which the metal hydride will not form. Again a dual system will be employed so while one reduction bed is operating, the spent bed is being regenerated. To process 2.5 kg of T_2O, 13.5 kg of uranium will be required. The tritium so generated will be pumped into the tritium high pressure reservoir and then to the pellet preparation equipment.

Other methods for the extraction of tritium from lithium, such as yttrium beds, molten salt extraction, liquid alloy getters, and fractional distillation were considered. The yttrium bed[25,26] will not reduce the tritium level in the lithium to the desired concentration under the temperature and tritium pressures of this design. The extraction of tritium from liquid lithium via liquid metal alloy getters[27] is attractive, although more data on the mutual solubilities of lithium and alloy are required. Similarly, although the extraction of tritium with a molten potassium chloride-lithium chloride mixture[28,29] has shown potential, the utility of this technique will depend upon the development of a suitable method for the recovery of the tritium from the salt mixture. Finally, vapor pressure measurements of deuterium species Li_2D, LiD and D_2 over liquid lithium[30] at 973° suggests that a fractional distillation technique might be a useful route to separation of hydrogen isotopes from the bulk lithium since Li_2D is reported to become the important gas phase species at elevated tempertures. However, the comparable tritium system species has not been observed at this point.

There are several problems which have not been thoroughly considered. One is a lithium purification system for the removal of corrosion products, radioactive species other than tritium and any lithium oxygen species. Since the lithium is already at 980° it may be that vapor phase transport of the lithium under reduced pressure to a cooler surface at least would reduce the concentration of less volatile contaminants. In this kind of process only 1% of the lithium stream would be diverted for this purpose. The reservoir from which the lithium would be distilled would contain the less volatile components and with time would have to be removed for disposal.

The other problem relates to the production of helium in the lithium breeding blanket. For every mole of tritium produced one mole of helium will be produced and whereas the tritium will be continuously removed, the helium will accumulate. Since the helium is essentially insoluble in the liquid lithium and imperable to the TZM walls it gradually will collect as bubbles and will have to be vented. This will require an additional cleanup system for removal of tritium from the vented helium.

The whole tritium, deuterium purification, storage, and pellet preparation should be in an isolated self-contained inert atmosphere structure within the hull of the building. This is for the following safety reasons: (1) the high concentration of tritium in the system, and (2) the potential for an explosive hydrogen-oxygen reaction should the external metal shell be breeched. Of course in the latter case, the reaction of oxygen with hot lithium, niobium and molybdenum would be of greater concern simply because of the amounts of these materials present.

(ii) Sodium - The liquid lithium-sodium intermediate heat exchangers act as a buffer between the tritium bearing lithium and the helium which will drive the turbines. These heat exchangers consist of TZM tubes with a wall thickness of 0.89 mm and a total area of 5.75×10^7 cm^2. Under the conditions of the system the tritium concentration on both sides of the heat exchanger will be 7.6×10^{-10} torr. The tritium concentration will be reduced by reaction with yttrium metal on the "cold" leg of the heat exchanger. The "cold" sodium will initially pass through a regenerative heat exchange (Chap. VI, Sec. B) to reduce its temperature to 200° and then to the yttrium beds containing 0.020 kg of 0.10 mm yttrium foil. It is calculated that the tritium concentration in the sodium will be reduced by 10% by reaction with the yttrium. The exiting sodium will again pass

through the regenerative heat exchanger to raise the temperature to 590° after which the sodium will rejoin the main sodium loop. The yttrium beds are also operated in tandem so that one set is extracting while the other set is being regenerated. Each set contains a total of .020 kg of yttrium foil. In the regeneration process the yttrium sheets are heated to 500°C to thermally decompose the yttrium hydride formed. The composition of the yttrium hydride ranges from a low of $YT_{0.8}$ to a maximum of $YT_{1.8}$, so the capacity of the yttrium bed is one mole of tritium per mole of yttrium. However, there will always be a constant tritium inventory in these beds amounting to 0.8 mole of tritium per mole of yttrium. This gives us a tritium inventory in the yttrium beds of 1.0×10^{-4} kg. As the tritium decays to ^3He with subsequent formation of bubbles which degrade the mechanical strength of the foil, (26) the lifetime of the beds is estimated to be 5 years.

Associated with this sodium stream are two dump tanks which constitute a thermal flywheel (Chap. VI, Sec. B). One dump tank is on the high temperature side and one on the low temperature side. They are constructed of TZM, have a wall thickness of 1.43 cm, and will be heated to maintain the sodium up to temperature. The diffusion of tritium through the walls will be negligible.

Like lithium, the liquid sodium requires continuous purification to remove corrosion products and oxide species. Again 1% of the stream could be diverted and the impurities cold-trapped as in the LMFBR(FFTF).(31)

VII-D-2. Divertor Cycle

The energy from the divertor panel is transported to a steam generator and then to a turbine generator (Chap. III, Sec. C). The hot leg of this cycle is 600° and the cool leg 400°. The tritium diffusion through the Mo metal divertor panel and the stationary lithium-thermal-contact-layer to the liquid sodium heat transfer fluid has been estimated to be 14.65 grams/day. This tritium concentration is reduced to 2.00×10^{-3} ppm by passing the entire sodium stream through yttrium beds operating in tandem. These beds will contain 2.17 kg of yttrium. When the plant is shut down this sodium will be bypassed to the sodium dump tanks for storage.

VII. E. Tritium Recovery and Control in Other Systems

VII-E-1. Leaks in Piping

The high temperatures in UWMAK-III create a situation in which large amounts of tritium could leak through pipes. For example, the high temperature side of the lithium system is at 980°C and has a tritium pressure of 1.0×10^{-6} torr. The approximate pipe dimensions are 2×10^6 cm^2 area and 5 mm thickness. Assuming the downstream pressure is zero, the leak through such piping is 92 curies per day.

To control such leaks, the lithium pipes are double walled. An outer pipe of stainless steel is lined with ceramic insulating material. Since the temperature of the jacket is much lower and the permeability of the ceramic is very low, the release of tritium to the reactor building is vanishingly small.

Federal regulations require that welds on piping be inspected. The jackets must either be removable or there must be provisions made for remote inspection.

VII-E-2. Shields

Tritium is produced from ^{10}B and ^{11}B in the boron carbide contained in the outer blanket shield and the inner blanket cold shield at a rate of 0.18 g/day in the outer shield and 2.2×10^{-4} g/day in the inner shield. At the low temperature of the shields (<150°C), the tritium produced will not diffuse through the pipes carrying the helium coolant. Unless some system is designed to sweep helium gas through the outer shield, the tritium will gradually build up.

VII-E-3. Helium Turbine Seals

In this design, the tritium levels in the helium coolant are controlled so that small amounts of tritium are permitted to leak through the turbine seals into the reactor building. If the leaks became a problem, the seals could be covered and a sweep gas passed over them.

VII-E-4. Tritium Cleanup from the Reactor Buildup

There now exist commercially available systems[32-35] that are capable of processing large volumes of gas to maintain a tritium pressure of less than 1×10^{-9} atm. These systems oxidize a mixture of tritium and hydrogen to T_2O and H_2O and the oxides are collected on molecular sieves at liquid nitrogen temperature. Recent results[34,35] indicate the oxidation catalysts are orders of magnitude more efficient than required for routine performance. More hydrogen can be added to the effluent and the process can be repeated. Thus, in a typical example, gas containing T_2 at 1000 ppm is purified to 1 ppm, 999 ppm of H_2 is added, and the gas is reprocessed to 1 ppb tritium. In this design, the amount of isotopic dilution is increased from 10^3:1 to 10^6:1. The system is designed to maintain a tritium pressure (including T_2, DT, DTD and T_2O of 1×10^{-12} atm (7.6×10^{-10} torr).

VII-F. Tritium Inventory

The plant inventory of tritium is estimated to be 35.8kg (Table VII-H-4). It should be noted that of this only 1.7 kg is in the breeding-recovery cycle. The 34.1 kg in the refueling cycle includes 18.6 kg in reserve storage. The reason the refueling cycle inventory is so large is that more realistic, space-dependent plasma calculations were used in this study (Chap. II, Sec. D). The result is a fractional tritium burnup of only 0.8%, compared to 7.2% and 2.8% burnup calculated on the basis of the simpler, point-source plasma model used in UWMAK-I[36] and UWMAK-II[37,38]. Assuming 5% burnup, the refueling cycle tritium inventory would only be 5.5kg and the total plant inventory would be 7.2kg.

VII. G. Summary and Conclusions

VII-G-1. The uncontrolled release of tritium to the environment is minimal, being less than one curie per day, including liquid and gaseous forms of tritium.

VII-G-2. The steady state plant inventory (Table VII-H-4) of tritium is 35.8 kg, the major portion being in the refueling cycle. The large inventory is due to the more realistic, space dependent plasma model used in this study.

VII-G-3. The tritium recovery system from the breeding lithium blanket is a niobium "window" coated with thin layers of yttrium and palladium. The tritium is collected as T_2O.

VII-G-4. Yttrium beds are used to clean up tritium from sodium coolant loops.

VII-G-5. The reactor building contains a cleanup system to remove accidentally released tritium.

VII. H. Appendix

Table VII-H-1

Tritium Flow Rates

	kg/day	
	Tritium	Deuterium
Feed	74.4	49.6
Burn	0.620	0.413
Divertor cryopumps	73.8	49.2
Breed	0.666	----
D_2 makeup	----	0.444
Produced in inner blanket	1.2×10^{-4}	----
Produced in inner cold shield	1.8×10^{-4}	----

Table VII-H-2

Tritium Leak Rates

	Curies/day
Outer Blanket	
Li to Na	1256
Na to He	<1
Na to He (inner blanket)	<1
Inner Blanket	
To He coolant	1200
To Reactor Building	
Total	<100
Divertor	
To Na coolant	1.5×10^{5}
To steam	<<1

Table VII-H-3

Tritium Recovery

	g/day	
	Tritium	Deuterium
Divertor-Cryopumps	7.4×10^{4}	5.0×10^{4}
Outer Blanket (Li-Nb Window)	666	
Outer Blanket (Na-Y Beds)	0.126	
Divertor Coolant (Na-Y Beds)	14.6	9.8
Inner Blanket He Cleanup	0.12	
Building	1.00×10^{-2}	

Table VII-H-4

Tritium Inventories

	kg
Cryopumps	7.75
Reprocessing	7.75
Storage	18.6
Outer Blanket-Li	1.0
Recovery-Li	0.666
Outer Blanket-Na	2.0×10^{-4}
Outer Blanket-Na (Y beds)	1.6×10^{-4}
Divertor-Na	6.0×10^{-4}
Divertor-Y beds	7.5×10^{-3}
Total	35.8

VII. H. References for Section VII

1. T. J. Kabele, A. B. Johnson and L. R. Mudge, "Definition of Source Terms for Tritium Evolution from CTR Systems", Paper H-1, Int. Conf. on Radiation Effects and Tritium Technology for Fusion Reactors, Gatlinburg, Tenn., U.S.A., Oct. 1-3, 1975.

2. R. W. Webb, Permeation of Hydrogen Through Metals, NAA-SR-10462, July 1965.

3. C. W. Kuelher, R. C. Axtmann, E. F. Johnson, "Permeation of Hydrogen Through 304 Stainless Steel and Its Importance to Tritium Control in Fusion Reactor Systems", Paper M-5, Int. Conf. on Radiation Effects and Tritium Technology for Fusion Reactors, Gatlinburg, Tenn., U.S.A., Oct. 1-3, 1975.

4. G. M. McCracken and D. H. Goodall, "Experimental Measurements of the Permeation of Hydrogen Isotopes in Lithium Filled Niobium Cells", Paper M-1, Int. Conf. on Radiation Effects and Tritium Technology for Fusion Reactors, Gatlinburg, Tenn., U.S.A., Oct. 1-3, 1975.

5. R. E. Stickney in The Chemistry of Fusion Technology, P. Gruen, Ed., Plenum Press, New York, 1975, p. 305.

6. A. C. Whittingham, "The Liquid Sodium-Hydrogen System: Equilibrium and Kinetic Measurements in the 610-677K Temperature Range", RD/B/N2550, 1974 and references therein.

7. V. A. Maroni, E. J. Cairns, F. A. Cafasso, "A Review of the Chemical, Physical, and Thermal Properties of Lithium that are Related to the Use in Fusion Reactors", ANL-8001, March, 1973.

8. W. M. Mueller, J. P. Blackledge, and G. G. Libowitz, Metal Hydrides, Academic Press, New York, 1968, p. 453.

9. P. F. Adams and P. Hubberstey, "Hydrogen Isotope Removal from Liquid Lithium: Use of Yttrium Sponge as a Getter", Paper I-5, Int. Conf. on Radiation Effects and Tritium Technology for Fusion Reactors, Gatlinburg, Tenn., U.S.A., Oct. 1-3, 1975.

10. C. J. Kershner, Tritium Effluent Critical Progress Report, Monsanto Research Corporation, Mound Laboratory Report MLM-2146(LD), July 1974.

11. W. R. Wilkes, "Separation of Hydrogen Isotopes for Tritium Waste Removal", Proc. Symp. on Tritium Technology Related to Fusion Reactor Systems, Miamisburg, Ohio, Oct. 2, 1974. ERDA-50, p. 113 (1975).

12. W. R. Wilkes, "Hydrogen Isotope Distillation in a Fusion Reactor System", ANS Meeting, Sept. 27-Oct. 1, 1974, Washington, D.C.

13. W. R. Wilkes, "Hydrogen Isotope Separation for a TOKAMAK Experimental Power Reactor", Paper H-10, Int. Conf. on Radiation Effects and Tritium Technology for Fusion Reactors, Gatlinburg, Tenn., U.S.A., Oct. 1-3, 1975.

14. L. J. Wittenberg, et al., "Evaluation Study of the Tritium-Handling Requirements of a Tokamak Experimental Power Reactor," Mound Laboratory Monsanto Research Corp., Miamisburg, Ohio, Report MlM-2259, Nov. 1975.

15. B. Badger, et al., Fusion Feasability Study Group, "UWMAK-I, A Wisconsin Toroidal Fusion Reactor Design", Vol. II, Nuclear Engineering Department, Report UWFDM 68, Vol. II (May 1975), Chap. I.

16. J. S. Watson, An Evaluation of Methods for Recovering Tritium from the Blanket or Cooling Systems of Fusion Reactors, ORNL-TM-3794, July 1972.

17. R. M. Barrer, Diffusion in and Through Solids, Cambridge University Press, 1941, p. 168, and references therein.

18. J. Davis, McDonald-Douglass, St. Louis, private communication.

19. D. L. Smith and K. Natesan, Nucl. Tech., 22, 392 (1974).

20. S. D. Cramer, C. B. Kenahan, R. L. Andrews, and D. Schlain, "Electrodeposition of Thick Coatings of Platinum and Palladium on Refractory Metals from Aqueous Electrolytes", U. S. Bureau of Mines Report, RI-7016, September 1967.

21. W. L. Phillips, "The Oxidation of Platinum Metals in Air", ASM Trans. Quart., 57, 33-37 (1964).

22. M. Hanson, The Constitution of Binary Alloys, 2nd Ed., McGraw-Hill, New York, 1958.

23. J. H. Owen and D. Randall, "Equilibrium and Kinetics Studies of Systems of Hydrogen Isotopes, Lithium Hydrides, Aluminum, and $LiAlO_2$", Paper J-3, Int. Conf. on Radiation Effects and Tritium Technology for Fusion Reactors, Gatlinburg, Tenn., U.S.A., Oct. 1-3, 1975.

24. K. Tanaka, It. Kudo, H. Amano, "Tritium Recovery From a Fusion Reactor of Lithium Oxide Blanket", Paper I-4, Int. Conf. on Radiation Effects and Tritium Technology for Fusion Reactors, Gatlinburg, Tenn., U.S.A., Oct. 3, 1975.

25. L. J. Wittenberg in A Wisconsin Toroidal Fusion Reactor Design, Univ. of Wisconsin UWFDM-68.

26. L. J. Wittenberg, private communication.

27. J. L. Anderson, D. H. W. Carstens, and R. M. Alire, "CTR Related Research at LASL: Tritium Diffusion in Lithium and a Study of Liquid-Liquid Schemes for Tritium Separations", Paper J-1, Int. Conf. on Radiation Effects and Tritium Technology for Fusion Reactors, Gatlinburg, Tenn., U.S.A., Oct. 1-3, 1975.

28. V. A. Maroni, E. Veleckis, "Chemical Processing of Lithium for Fusion Reactors", ALCHE Meeting, Detroit, Mich., U.S.A., June 1973.

29. V. A. Maroni, R. D. Wolson and G. E. Staahl, Nucl. Tech., 25, 83 (1975).

30. H. R. Ihle and C. H. Wu, "Experimental Determination of the Partial Pressures of D_2, LiD, and Li_2D in Equilibrium with Dilute Solutions of Deuterium in Liquid Lithium", Paper K-1, Int. Conf. on Radiation Effects and Tritium Technology for Fusion Reactors, Gatlinburg, Tenn., U.S.A., Oct. 1-3, 1975.

31. G. Bluhm, Westinghouse-Hanford, private communication.

32. C. J. Kerschner, "Tritium Control Project at Mound Laboratory", Proc. Symp. on Tritium Technology Related to Fusion Reactor Systems, Miamisburg, Ohio, Oct. 2, 1974.

33. W. A. Swansiger and L. A. West, "Current Sandia Programs and Laboratory Facilities for Tritium Research", Proc. Symp. on Tritium Technology Related to Fusion Reactor Systems, Miamisburg, Ohio, Oct. 2, 1974.

34. P. D. Gildea, "Containment and Decontamination Systems Planned for the Tritium Research Laboratory Building at Sandia Laboratories, Livermore", Paper H-7, Int. Conf. on Radiation Effects and Tritium Technology for Fusion Reactors, Gatlinburg, Tenn., U.S.A., Oct. 1-3, 1975.

35. C. J. Kerschner, private communication.

36. B. Badger, et al., Fusion Feasibility Study Group, "UWMAK-I, A Wisconsin Toroidal Fusion Reactor Design", Nuclear Engineering Department UWFDM-68, Univ. of Wisconsin, March 15, 1974.

37. B. Badger, et al., Fusion Feasibility Study Group, "UWMAK-II: A Conceptual Tokamak Fusion Reactor Design", Nuclear Engineering Department Report, UWFDM 112, Univ. of Wisconsin (November 1975).

38. R. W. Conn, et al., "Major Design Features of the Conceptual D-T Tokamak Power Reactor: UWMAK-II. Plasma Physics and Controlled Nuclear Fusion Research 1974, (IAEA Vienna, 1975), Vol. III, p. 497.

VIII. Radioactivity and Afterheat

VIII-A. Method of Calculation

The procedure for calculating radioactivity and afterheat in the UWMAK-III system follows very closely that developed for UWMAK-I[1] or II.[2] Modifications have been made to account for the two dimensional characteristic of the UWMAK-III blanket as well as to incorporate more second order reactions. Basically the procedure is to break the various zones of the blanket e.g. first wall, first breeding zone, reflector etc., into one or more regions and use the average set of group fluxes obtained from the neutronics calculations as input parameters. Cross sections are obtained primarily from the BNL model calculations[3] supplemented by data from the ENDF tapes, BNL 325 and other literature sources. These cross sections are processed by MACK[4] when appropriate to obtain the group cross sections for use in the calculations. No attempt has been made to allow for self-shielding in the resonance region. Where reactions can lead to isomeric states and no experimental information is available the reactions are assumed to go with equal probability to the two states. Figure VIII-1 shows the geometry used in the calculation along with the composition of the various zones. Tables VIII-1 and VIII-2 present the reactions considered in the calculation. Because of the complexity of the geometry of the blanket and the need to approximate it for the purposes of calculation, the results presented are not completely consistent with those which would be obtained for a detailed calculation in exact geometry. However the calculations along the midplane of the system should be quite reasonable and the total activity presented here should be reasonably close to that of the actual system, certainly within a factor of 2. The trends with time should be good and a slight renormalization would remove most discrepancies in magnitude.

VIII-B. Outer Blanket and First Walls

VIII-B-1 Activity Build Up During Operation

The build up of the total activity in the outer blanket including the inner blanket first wall is shown in figure VIII-2. The rapid initial buildup is due to the production and saturation of the short half life isotopes ^{99}Mo ($T_{\frac{1}{2}}$=66 hr), ^{99m}Tc ($T_{\frac{1}{2}}$= 6 hrs) and ^{91}Mo (T 1/2 = 16 min). The activity approaches a constant value after 1-2 months. If the blanket were to be left in for a long period of time ($\gtrsim \sim 5$ yr) a slight decrease in activity would result due to the burn up of some of the parent nuclei over-riding the slow buildup of long lived nuclei. Figure VIII-2 also shows the buildup in the various zones of the blanket. It is seen that the largest contributor is the first breeding zone due to the large amount of material contained therein. However the highest specific activity is, of course, in the first wall. The first wall and the first breeding zone are the major contributors with the reflector contribution only $\sim$ 5% of the total.

UW/MAK III BLANKET AND SHIELD REPRESENTATION

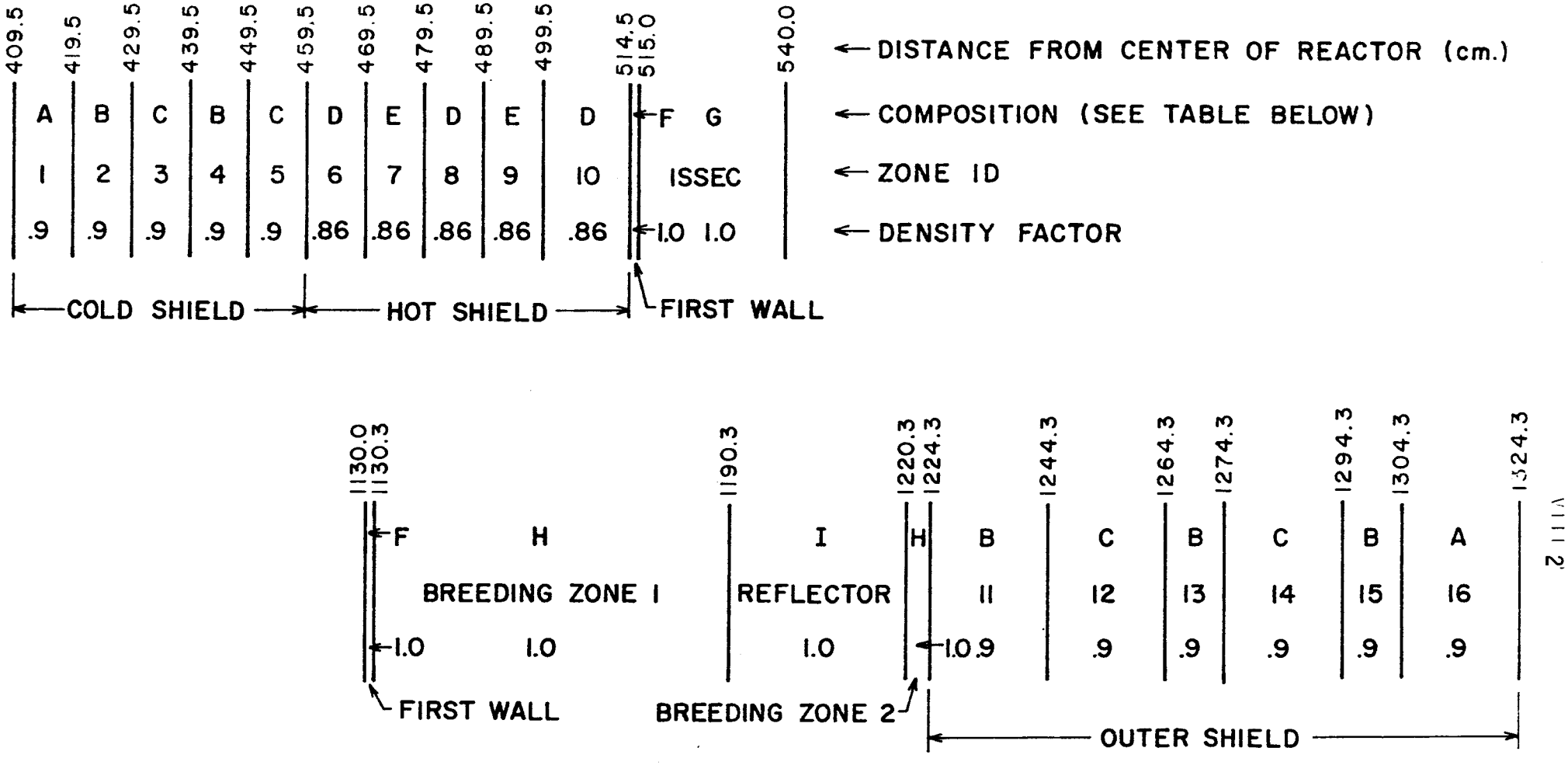

MATERIALS (VOLUME PERCENT)

A - 90 % Pb + 10 % S.S.

B - 72 % B_4C + 10 % S.S. + 18 % $Al_2O_3 2SiO_2$

C - 100 % S.S.

D - 82 % TZM + 18 % $Al_2O_3 2SiO_2$

E - 72 % B_4C + 10 % TZM + 18 % $Al_2O_3 2SiO_2$

F - 100 % TZM

G - 100 % C

H - 97 % Li + 3 % TZM

I - 99 % C + 1 % TZM

FIGURE VIII-1

TABLE VIII - 1

NEUTRON REACTIONS INVOLVING INITIAL ISOTOPES - BLANKET

I.	TZM		
	Mo	100	(n,γ), (n,2n), (n,p), (n,D), (n,α)
	Mo	98	(n,γ), (n,2n), (n,p), (n,D), (n,α)
	Mo	97	(n,γ), (n,2n), (n,p), (n,D), (n,T), (n,α)
	Mo	96	(n,γ), (n,2n), (n,p), (n,D), (n,α)
	Mo	95	(n,γ), (n,2n), (n,nα), (n,p), (n,D), (n,T), (n,α)
	Mo	94	(n,γ), (n,2n), (n,nα), (n,p), (n,np), (n,T), (n,α)
	Mo	92	(n,γ), (n,2n), (n,np), (n,p), (n,α)
	Zr	96	(n,γ), (n,2n), (n,p), (n,α)
	Zr	94	(n,γ), (n,2n), (n,p), (n,D), (n,α)
	Zr	92	(n,γ), (n,2n), (n,p), (n,D), (n,T), (n,α)
	Zr	91	(n,γ), (n,2n), (n,p), (n,D), (n,T), (n,α)
	Zr	90	(n,γ), (n,2n), (n,p), (n,np), (n,α)
	Ti	50	(n,γ), (n,2n), (n,p), (n,np), (n,α)
	Ti	49	(n,γ), (n,2n), (n,p), (n,np), (n,T), (n,α)
	Ti	48	(n,γ), (n,2n), (n,p), (n,np), (n,α)
	Ti	47	(n,γ), (n,2n), (n,nα), (n,p), (n,np), (n,α)
	Ti	46	(n,γ), (n,2n), (n,nα), (n,p), (n,np), (n,α)
II.	B_4C		
	C	13	(n,γ)
	C	12	(n,γ), (n,n3α), (n,α)
	B	11	(n,γ), (n,2n), (n,p), (n,T), (n,α)
	B	10	(n,γ), (n,p), (n,D), (n,α), (n,2α)
III.	Li		
	Li	7	(n,γ), (n,α2n), (n,2n), (n,D)
	Li	6	(n,γ), (n,α2n), (n,p), (n,α)
IV.	C		
	C	13	(n,γ)
	C	12	(n,γ), (n,n3α), (n,α)

TABLE VIII - 2

NEUTRON REACTIONS INVOLVING TRANSMUTATION PRODUCT ISOTOPES - BLANKET

I.	TZM		
	Tc	99	(n,γ), (n,2n), (n,p), (n,np), (n,T), (n,α), (n,nα)
	Mo	99	(n,γ), (n,2n), (n,p), (n,D), (n,T), (n,α)
	Mo	93	(n,2n), (n,p), (n,np), (n,T), (n,α)
	Nb	94	(n,γ), (n,2n), (n,p), (n,np), (n,T), (n,α)
	Nb	93	(n,γ), (n,2n), (n,nα), (n,p), (n,np), (n,T), (n,α)
	Nb	92	(n,2n) (n,p), (n,np), (n,T), (n,α)
	Zr	95	(n,γ), (n,2n), (n,p), (n,np), (n,T), (n,α)
	Zr	93	(n,γ), (n,2n), (n,p), (n,np), (n,T), (n,α)
	Y	91	(n,γ), (n,2n), (n,p), (n,D), (n,T), (n,α)
	Y	90	(n,γ), (n,2n), (n,p), (n,np), (n,T), (n,α)
	Y	89	(n,γ), (n,2n), (n,p), (n,np), (n,α)
	V	51	(n,γ), (n,2n), (n,nα), (n,p), (n,T)
II.	B_4C		
	Be	9	(n,γ), (n,T), (n,α)
III.	C		
	Be	9	(n,γ), (n,T), (n,α)
	Li	7	(n,γ), (n,α2n), (n,2n), (n,D)
	Li	6	(n,γ), (n, 2n), (n,p), (n,α)

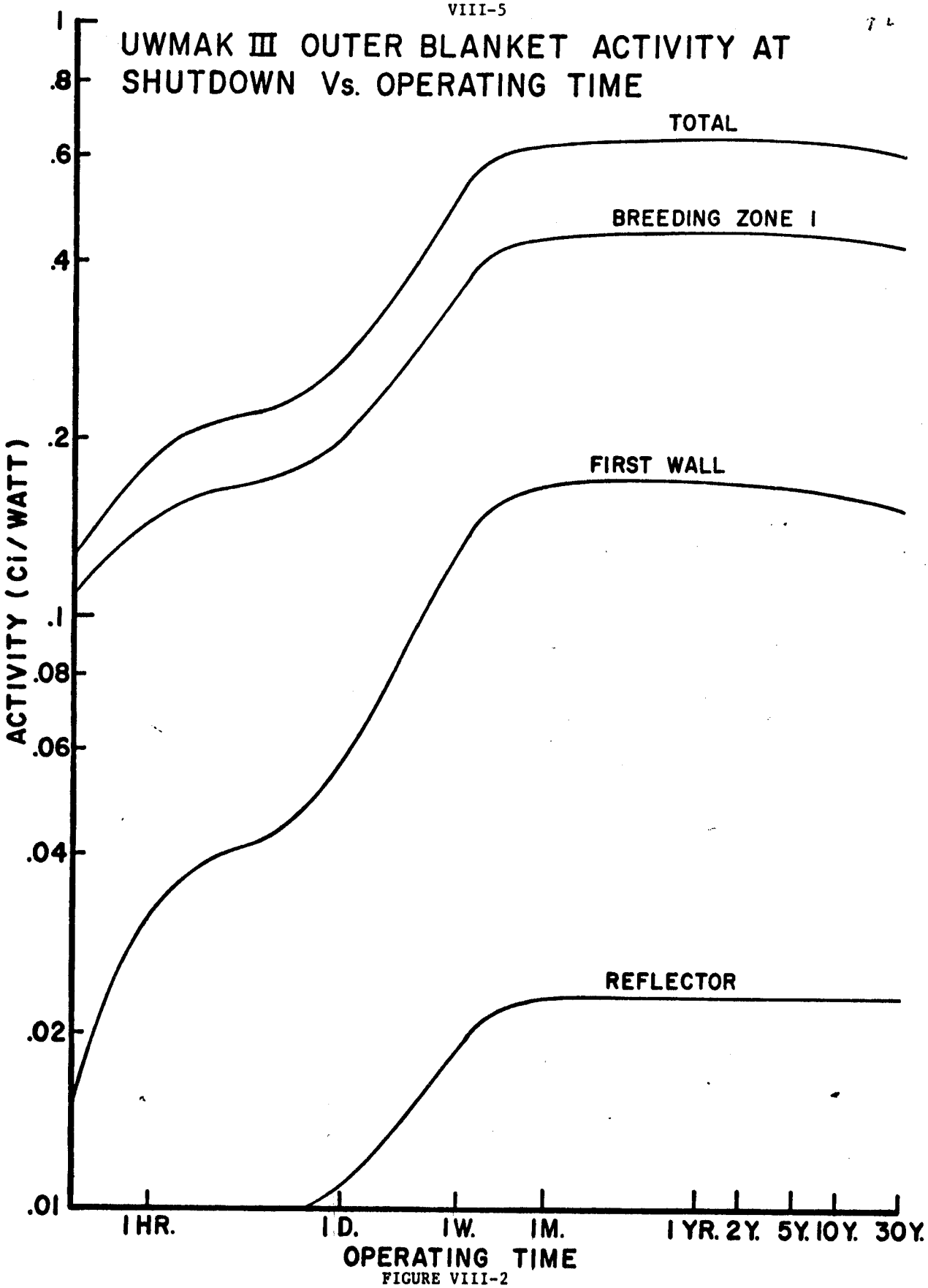

FIGURE VIII-2

VIII-B-2 Spatial Distribution of Activity

Because of the two-dimensional nature of the blanket, it is useful to obtain a feel not only for the spatial distribution of activity through the blanket but also around the surface of the blanket. Figure VIII-3 shows the specific activity at shutdown in the first wall as a function of position around the first wall. This particular calculation is based on a two-dimensional rectangular cylinder but nevertheless should provide an appreciation for the contribution from the different sections. As expected in the calculation the activity drops going away from the mid plane of the reactor. There is a large change going past the divertor slots corresponding to a transition from a first wall behind the ISSEC in the inner blanket to a first wall facing the plasma in the remainder of the system. Clearly the major portion of the activity comes from the outer blanket and is concentrated near the midplane of the outer blanket. For comparison, the average specific activities in the first wall of the UWMAK-I and II are shown on the same figure. Since both of these systems are circular cylinders in the model, their activities are constant. The effects of the shifted plasma center and of the ISSEC on the distribution are clearly apparent.

Figure VIII-4 shows the spatial distribution of activity through the outer blanket at shutdown for two years of operations. The highest level of specific activity comes from the first wall with a drop of over a factor 25 going into the first breeding zone.

VIII-B-3 Activity after Shutdown

The activity in the blanket after shutdown is of considerable interest not only from the point of view of radiation levels during the blanket change out or other maintenance, but also because of its implication in accident potential, recycling, and long-term radioactive waste. Figure VIII-5 shows the activity of the outer blanket and the inner blanket first wall following two years of operation. The activity levels at shutdown are of the same magnitude as UWMAK-I and II but because of the use of molybdenum (TZM) as a structural material, there are some significant differences in the time behavior of the activity following shutdown. In particular, it is seen that there is still a relatively slow decay of the activity for the first day or so, but following there is a relatively rapid decay requiring only 3 weeks for the activity to be down by a factor of 100. This contrasts to SS systems where the times are measured in years for this to take place. By about three years the short lived activities have died out and the activity has assumed its long-term value almost four orders of magnitude down from the shutdown value. This long term activity is dominated by $^{93}Mo(T_{\frac{1}{2}} = 3 \times 10^3$ yr) and $^{93m}Nb(T_{\frac{1}{2}} = 12$ yrs) with a small contribution from $^{99}Tc(T_{\frac{1}{2}} = 2 \times 10^5$ yr). This residual activity is higher than would be associated with a SS system but its effect is better put in perspective in the later section on afterheat. It is seen that the first wall contributes about 25% of the activity at shutdown.

The relative contribution of the major contributors to the activity following two years of operation is shown in Figure VIII-6. The activity at shutdown is due primarily to two isotopes, $^{99}Mo(T_{\frac{1}{2}} = 66$ hrs) and $^{99m}Tc(T_{\frac{1}{2}} = 6$ hrs) with $^{91}Mo(T_{\frac{1}{2}} = 15.5m)$, ^{101}Mo, and ^{101}Tc contributing about 21%. These latter

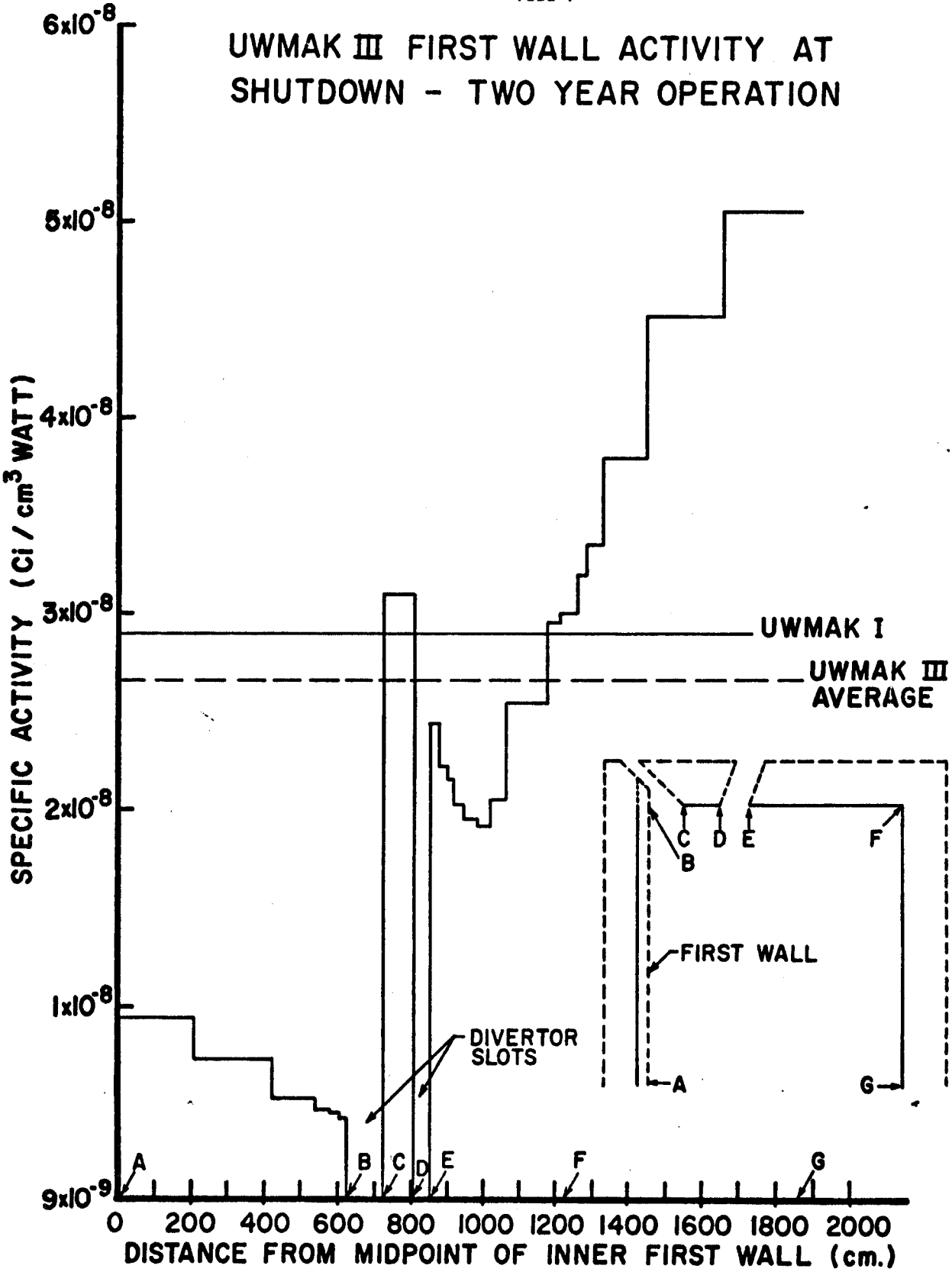

FIGURE VIII-3

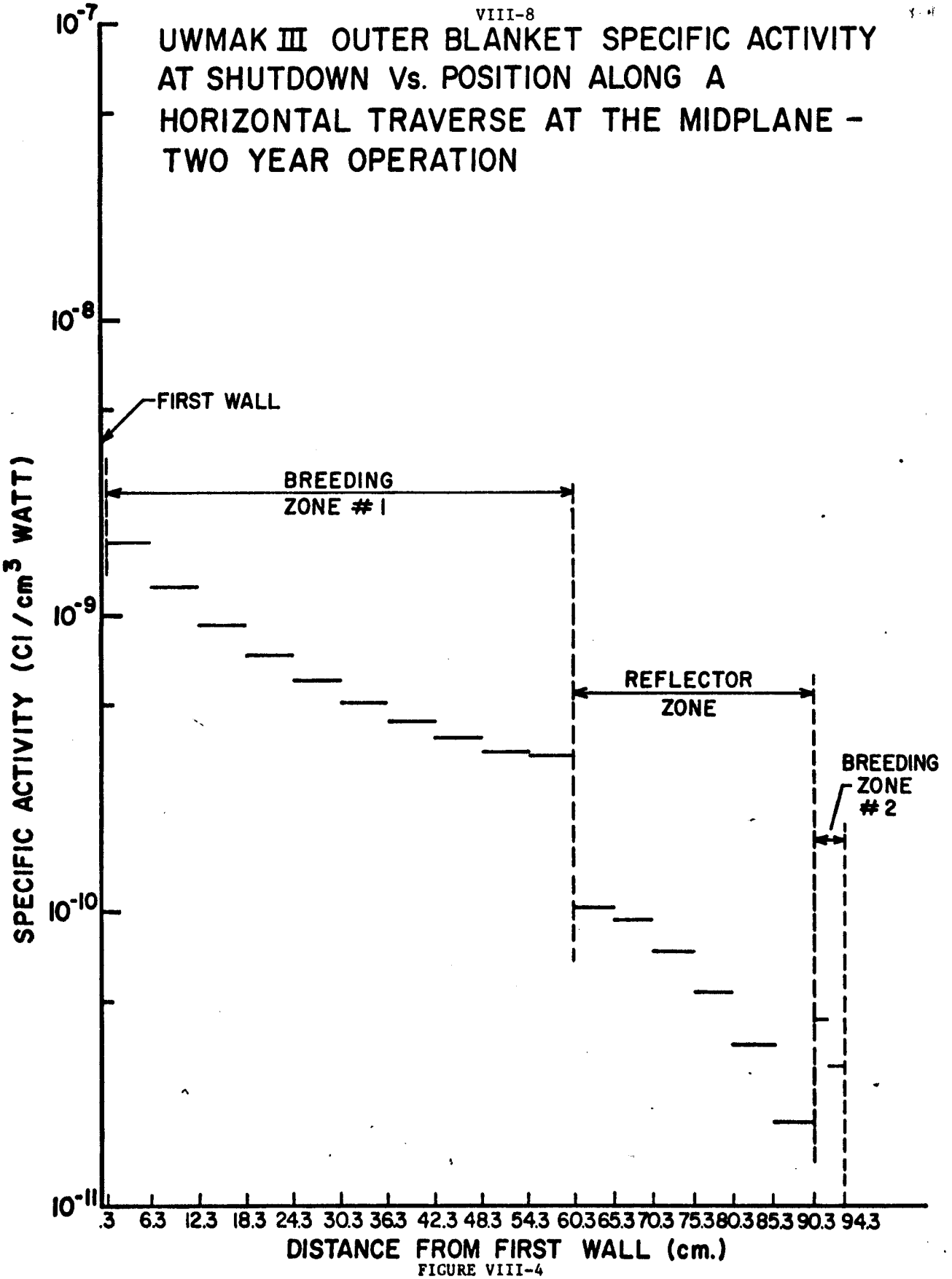

FIGURE VIII-4

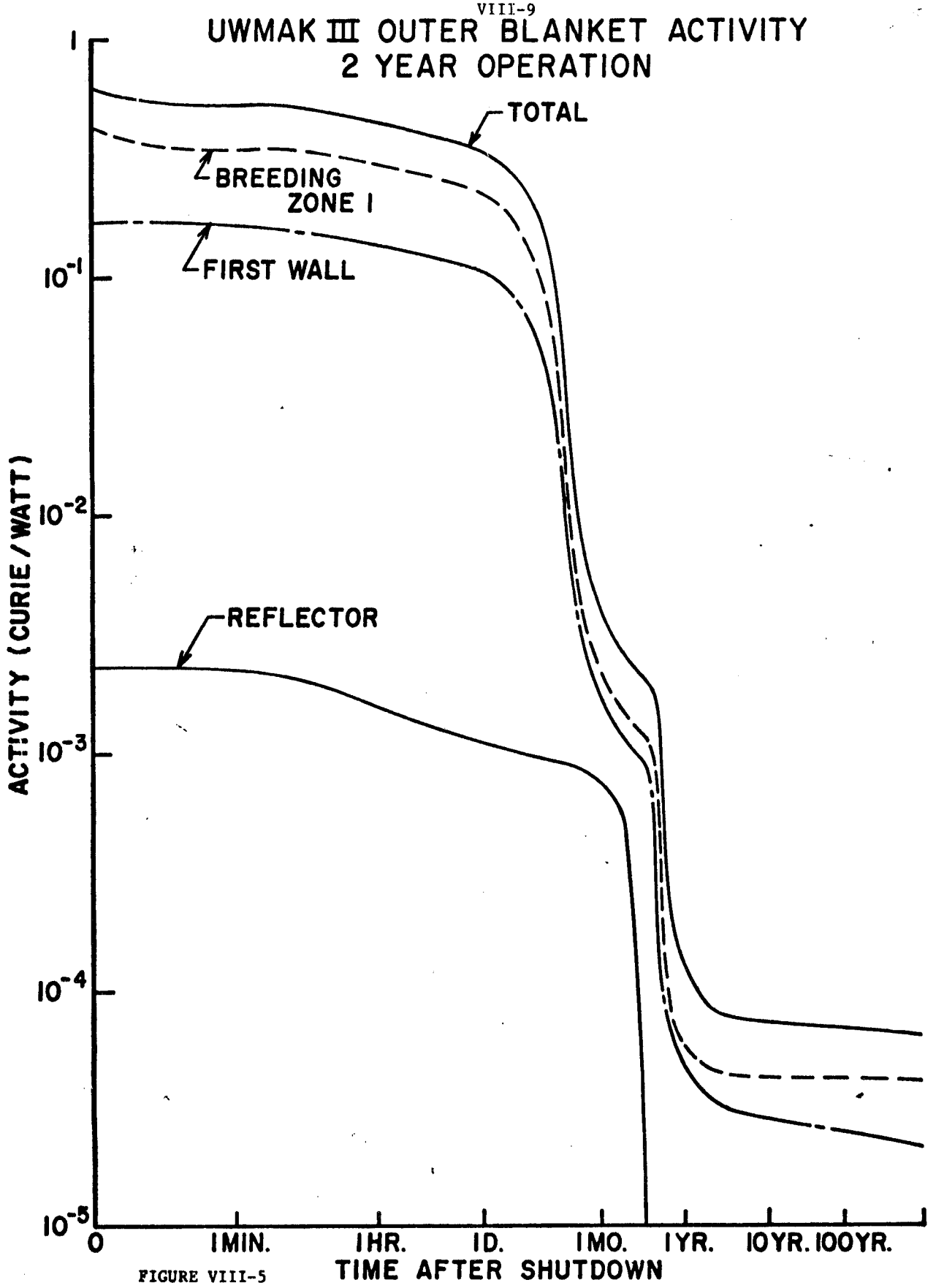

FIGURE VIII-5

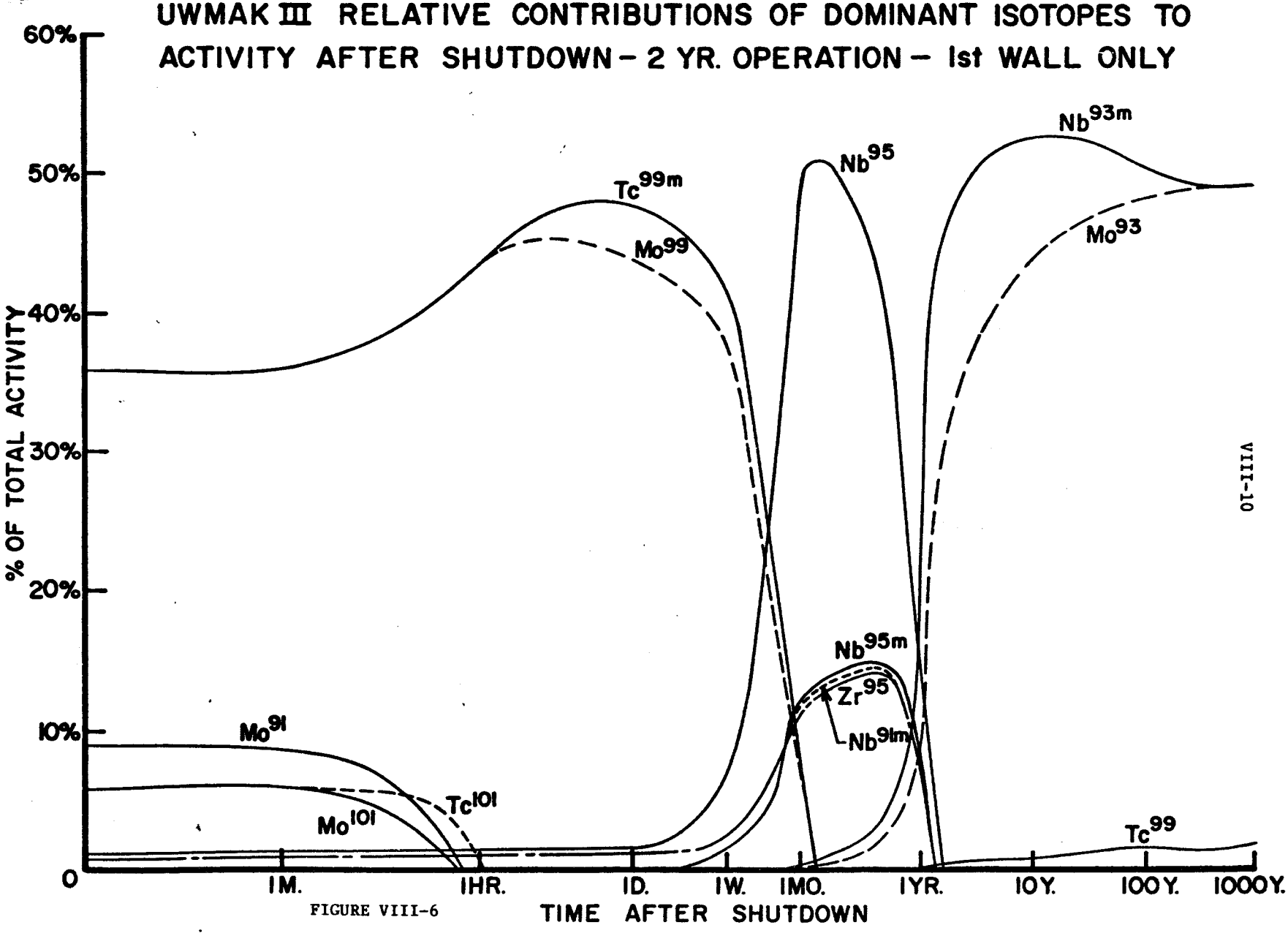

FIGURE VIII-6

isotopes decay quickly with ^{95}Nb becoming the next dominant contributor. As mentioned previously, the long term activity is dominated by ^{93}Mo, ^{95m}Nb, and ^{99}Tc with the latter surving the longest.

VIII-B-4 Afterheat

The afterheat is calculated using the same procedures as in UWMAK-I and II. The activity calculations in the previous section are used as a source term and the energy of the disintegration is taken to be deposited at the site of the disintegration. Because of the different decay energies of the different isotopes, the afterheat curves (while having shapes qualitatively similar to activity) will be somewhat different.

The build up of the afterheat is shown in Figure VIII-7. As was the case with the radioactivity, saturation is seen to occur after about 3 weeks of operation. The major portion of the afterheat comes from the first breeding zone as expected.

The decay of the afterheat following shutdown is shown in Figure VIII-8 for the case of 2 years of operation. Tritium is neglected. The sharp initial drop from 0.31% to 0.24% immediately following shutdown is due to the decay of very short lived ^{6}He ($T_{\frac{1}{2}}$ = 0.8 sec.). The decay heat drops off slightly slower than the activity requiring 2 weeks to be down by a factor of ten and 1 month for a factor of 100. By the end of one year, however, the afterheat is approaching its long term value of approximately 10^{-6}% or a total heating of only $\sim$ 50 watts. Although the activity is dominated by ^{93m}Nb and ^{93}Mo, because of the larger amount of energy in its decay, the afterheat at long times is primarily due to ^{99}Tc. This level of afterheat is greater than that expected for a SS system but less than that of a Nb based structure.

VIII-C. Hot Shield

The hot shield is that portion of the inner blanket behind the ISSEC and the wall immediately adjacent to it. These regions have already been taken into account in section B. As it must operate at an elevated temperature it is constructed of the same structural material as the outer blanket i.e. molybdenum (TZM). To absorb thermal neutrons B_4C is added and to improve fabricability of the large molybdenum regions, $AlSiO_2$ has been added. The composition and zone sizes are shown in Figure VIII-1.

Figure VIII-9 shows the buildup of activity in the hot shield. The curves are similar in shape to those of the outer blanket rising rapidly and saturating after $\sim$ 2 weeks. By far the largest contribution comes from the region nearest the plasma, i.e. zone 10, which contributes 95% of the activity. The next largest contributor is the second molybdenum zone which contributes only 3.5%.

The total activity of the hot shield at shutdown after one month of operation is $\sim$ 0.35 Ci/watt. This is to be compared with the activity of the outer blanket of about 0.63 Ci/watt having a total activity of about 1 Ci/watt at shutdown.

The activity in the hot shield following shutdown for two years of operation is shown in Figure VIII-10. The drop in activity immediately after shutdown is less than a factor of two for the first day. By the end of a month however it is

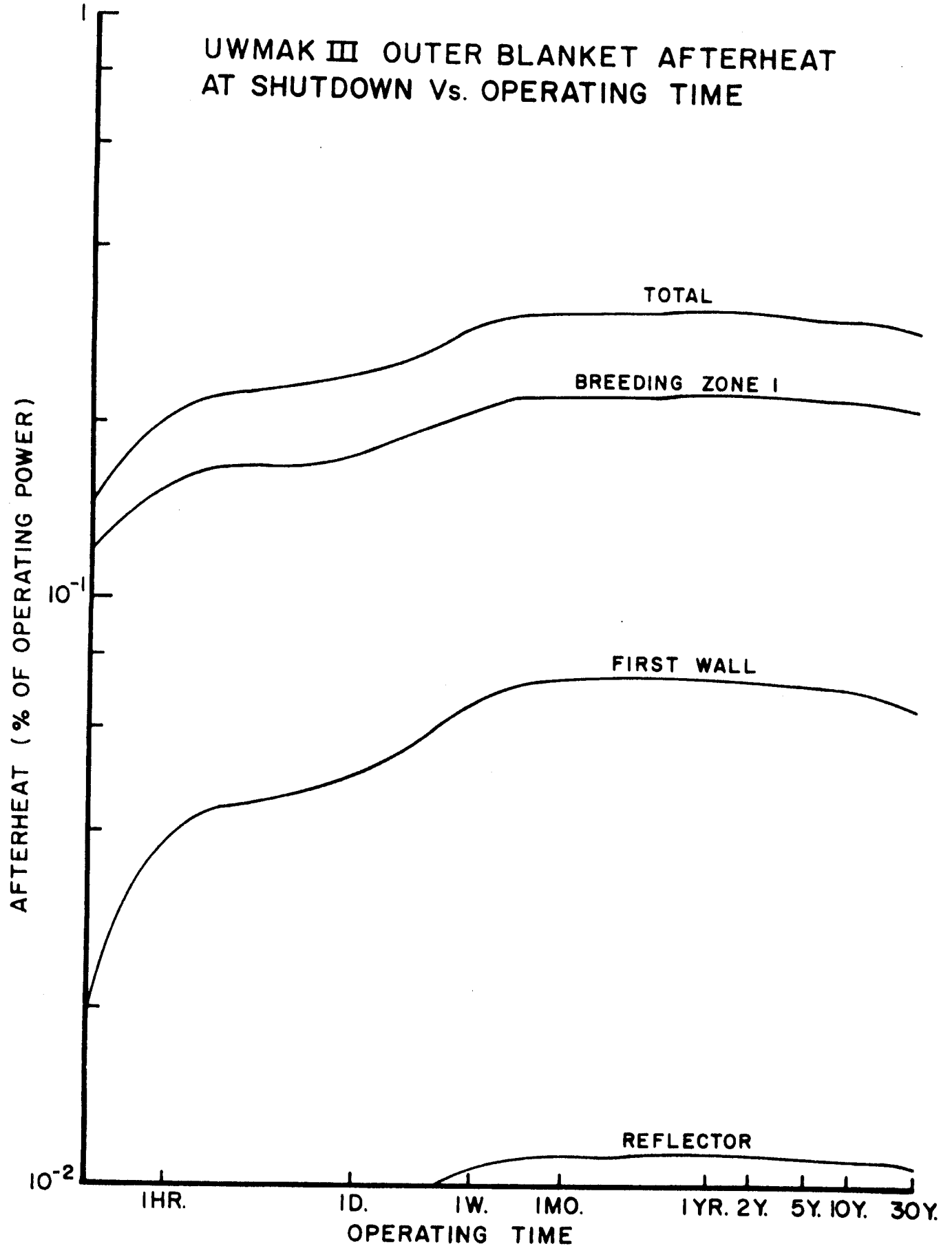

FIGURE VIII-7

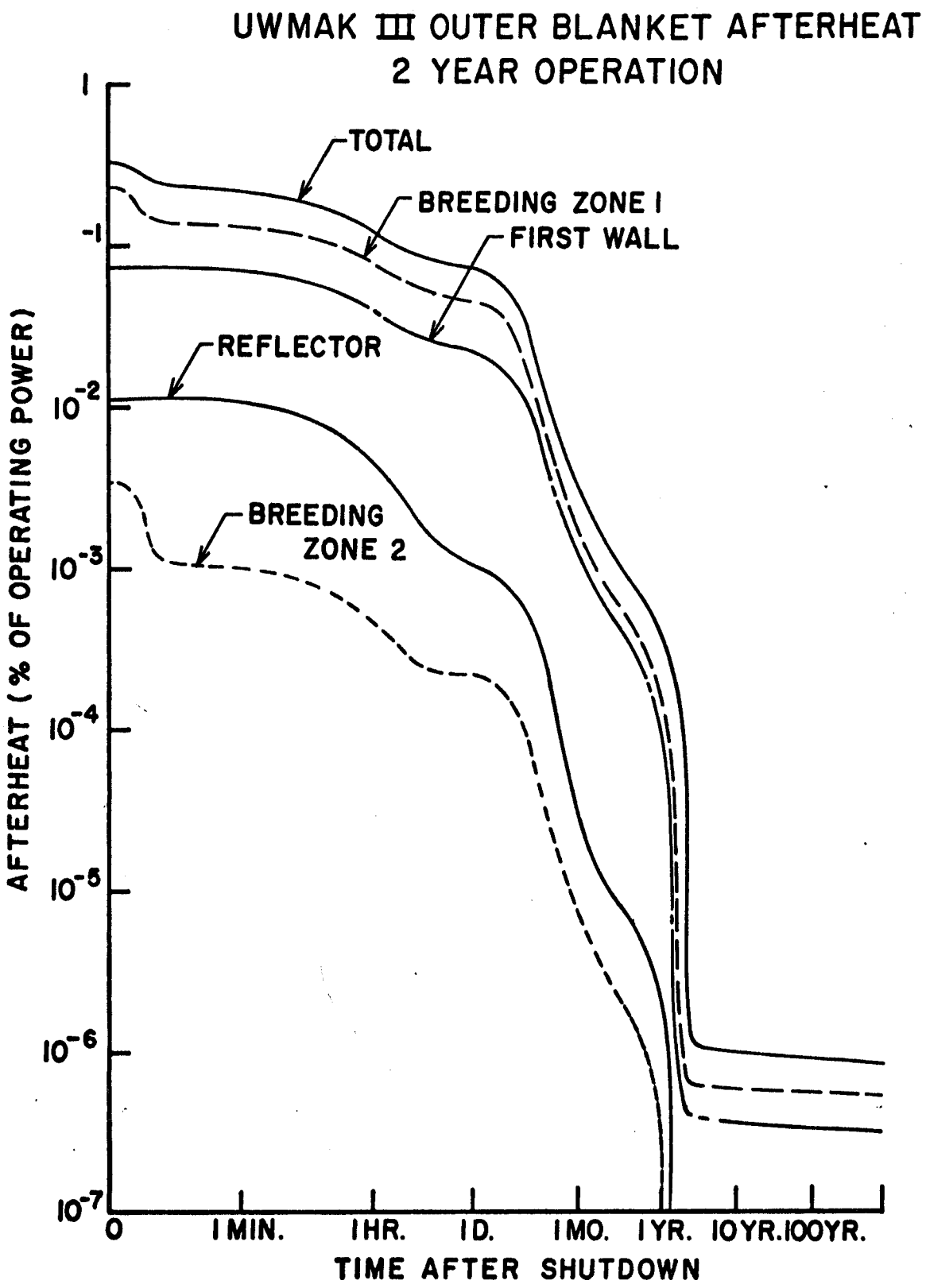

FIGURE VIII-8

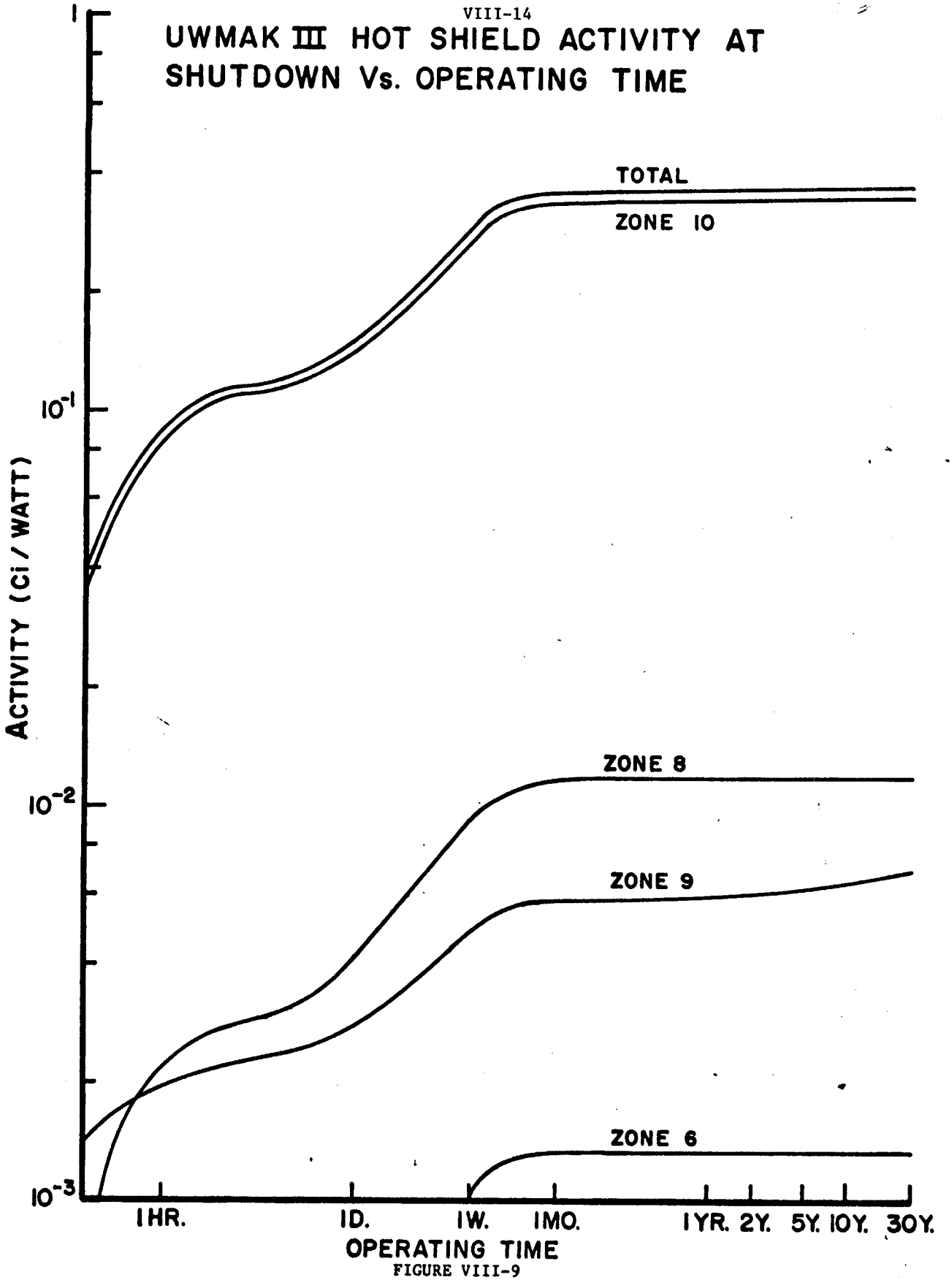

FIGURE VIII-9

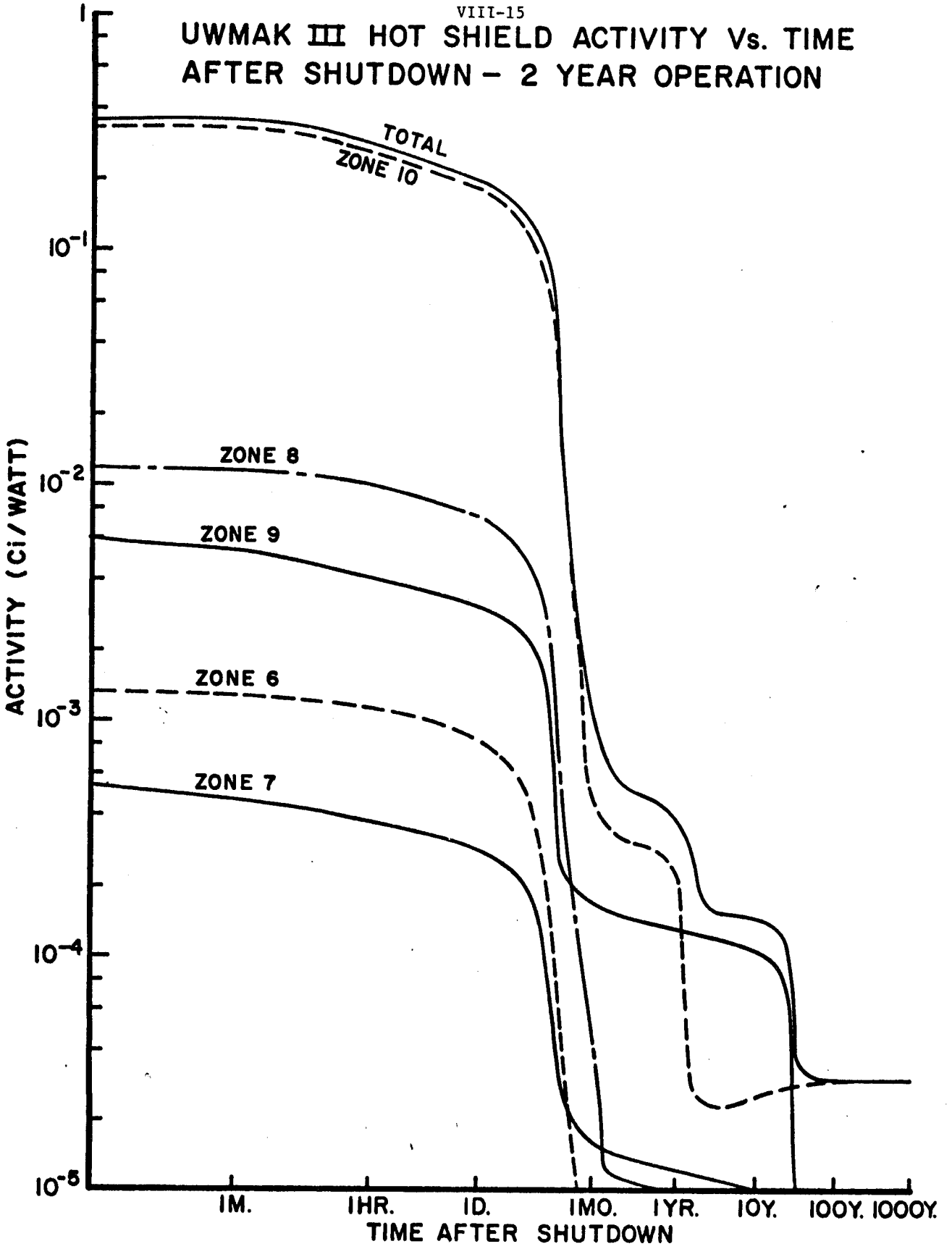

FIGURE VIII-10

down by a factor of 300. For the first year the major contributor to the activity is the first molybdenum zone (10). From then until about 20 years the first B_4C region (zone 9) is the primary contributor. The reason for this is the tritium produced from the boron via (n, T) reactions. Whereas in the outer blanket tritium is bred in the molten lithium and is subject to constant removal, in the shield regions of the reactor there are no plans to remove the relatively small amount of tritium produced. Since it is not removed but remains in place it is treated like any other activity in the shield. The long lived activity is again ^{93m}Nb, ^{93}Mo and ^{99}Tc. We see on this plot for the first time the increase of activity from ^{93m}Nb at times 5 - 50 years after shutdown. This is due to the ^{93m}Nb ($T_{1/2}$ = 12y) coming into secular equilibrium with its parent ^{93}Mo ($T_{1/2}$ = 3 x 10^3 yrs.).

The afterheat of the hot shield following two years of operation is shown in Figure VIII-11. The value at shutdown is $\sim$ 0.17% of the operating power. This may be compared with 0.31% from the outer blanket giving an initial afterheat following shutdown of 0.48% of the operating power. The shape of the curve follows that of the outer blanket with the major qualitative difference being the addition of the decay heat due to tritium which appears as a significant contribution in the 1-20 year period. The long term afterheat is again quite low being $\sim$ 3 x 10^{-7}% of the operating power.

VIII-D. Outer Shield and Cold Inner Shield

The build up of activity as a function of operating time for the outer shield and cold inner shield is shown in Figures VIII-12 and VIII-13. Since the structural material in these regions is stainless steel rather than molybdenum the shape of the curves is qualitatively quite different. The build up after the initial quick rise is much more gradual and saturation is not approached until the shield has been operated for very long times ($\sim$ 20 yrs.). As is expected most of the activity in the shield is due to the regions closest to the plasmas. The difference in the way the activity builds up for short operating times in several of the zones, for example zones 4 and 5 in the cold shield or zones 11 and 12 in the outer shield, is due to the presence of aluminum silicate in the B_4C containing regions. The rapid build up being due to ^{28}Al ($T_{1/2}$ = 2.2 min.).

The decay of the activity following shutdown for 2 year operation of the cold shield and the outer shield is shown in figures VIII-14 and VIII-15. The activity in the outer shield is higher than that of the cold shield and both have decay curves typical of that seen for 316 SS in previous designs i.e., a slow drop off for the first year and dropping by a factor of 100 by the end of ten years.

The afterheat following the same period of operation is shown in figures VIII-16 and-VIII 17. The afterheat drops off more quickly than the activity, being down a factor of 100 after one year of decay, over 3 orders of magnitude after 10 years and over seven orders of magnitude after 100 years.

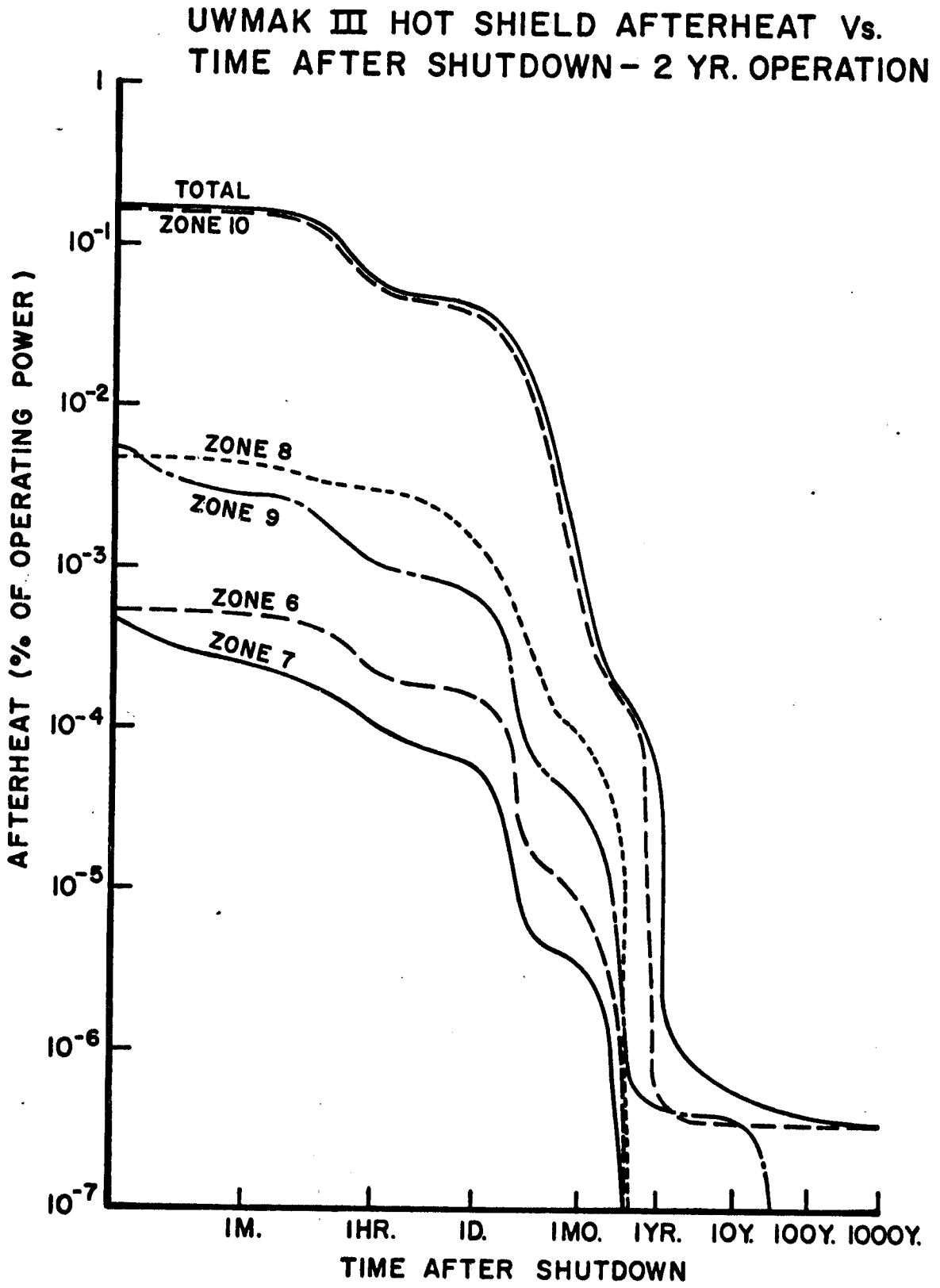

FIGURE VIII-11

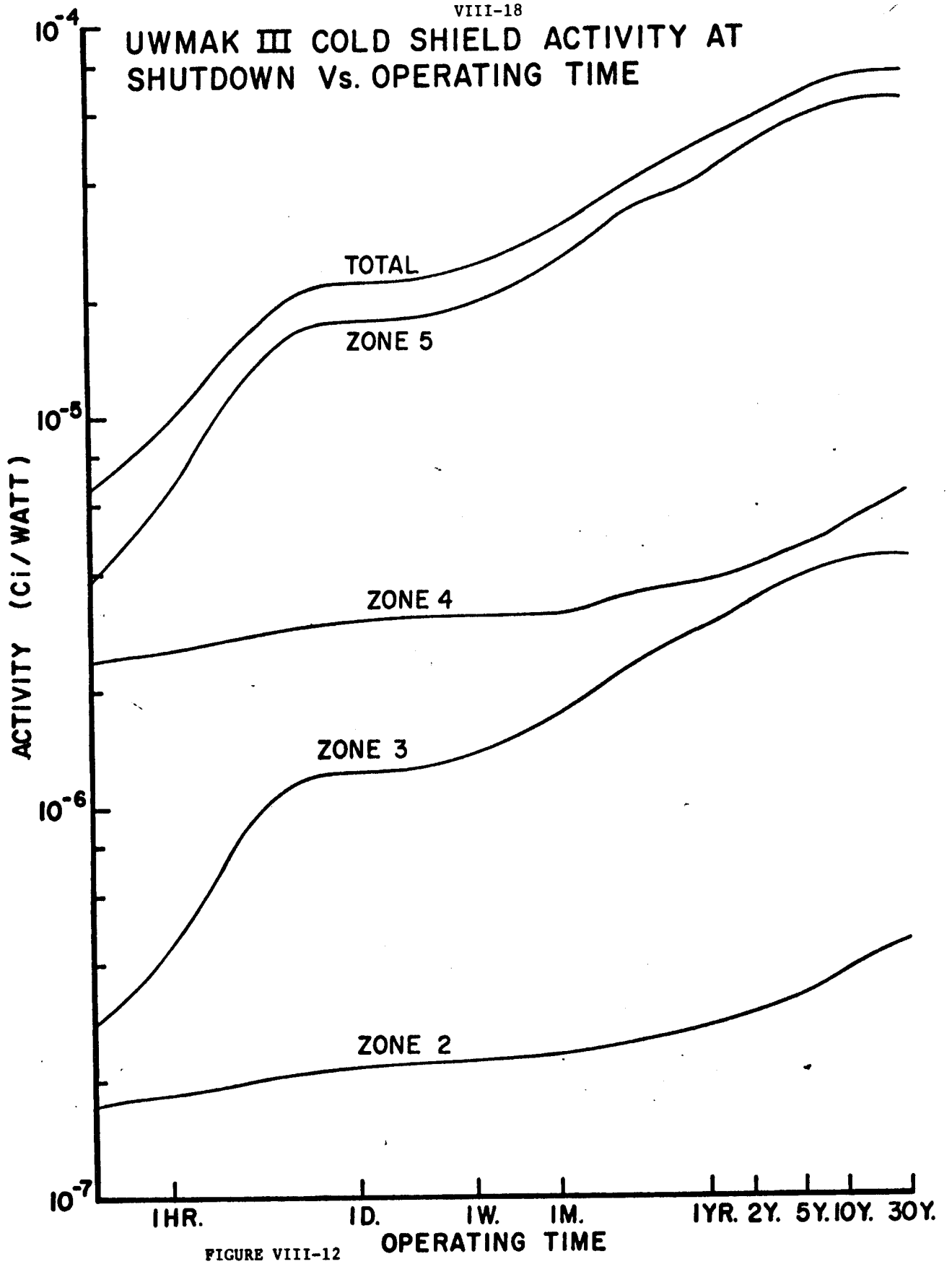

FIGURE VIII-12

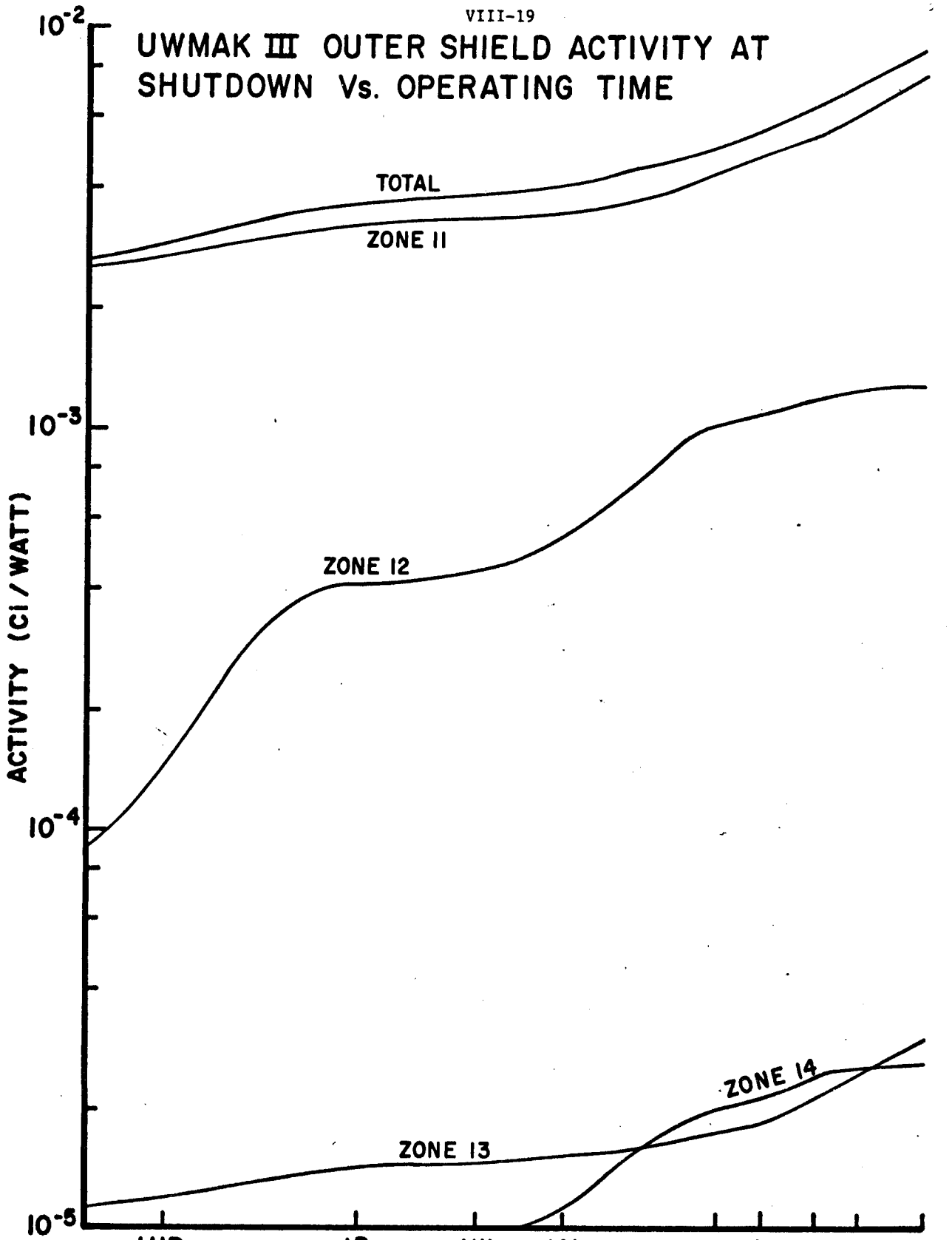

FIGURE VIII-13

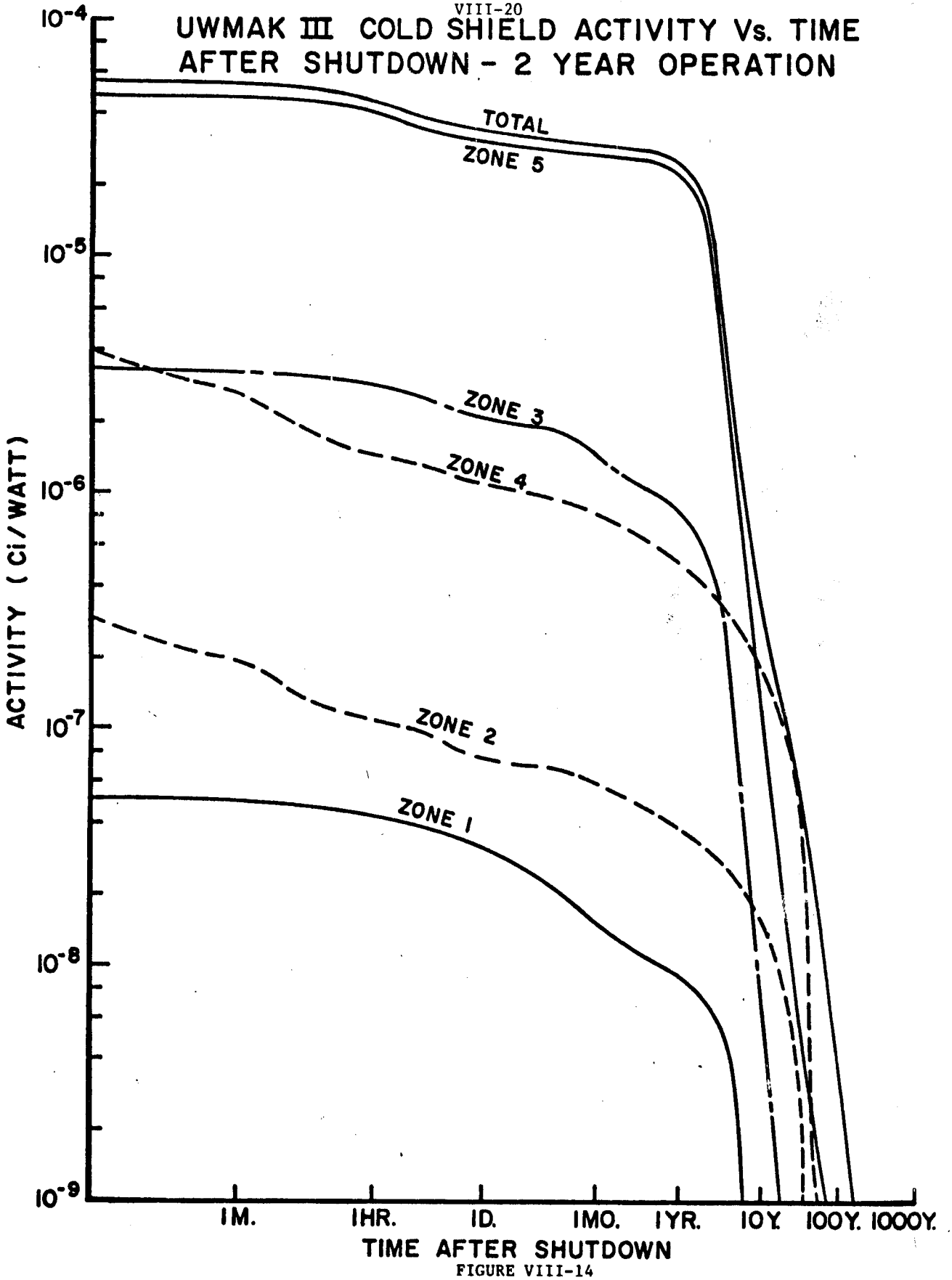

FIGURE VIII-14

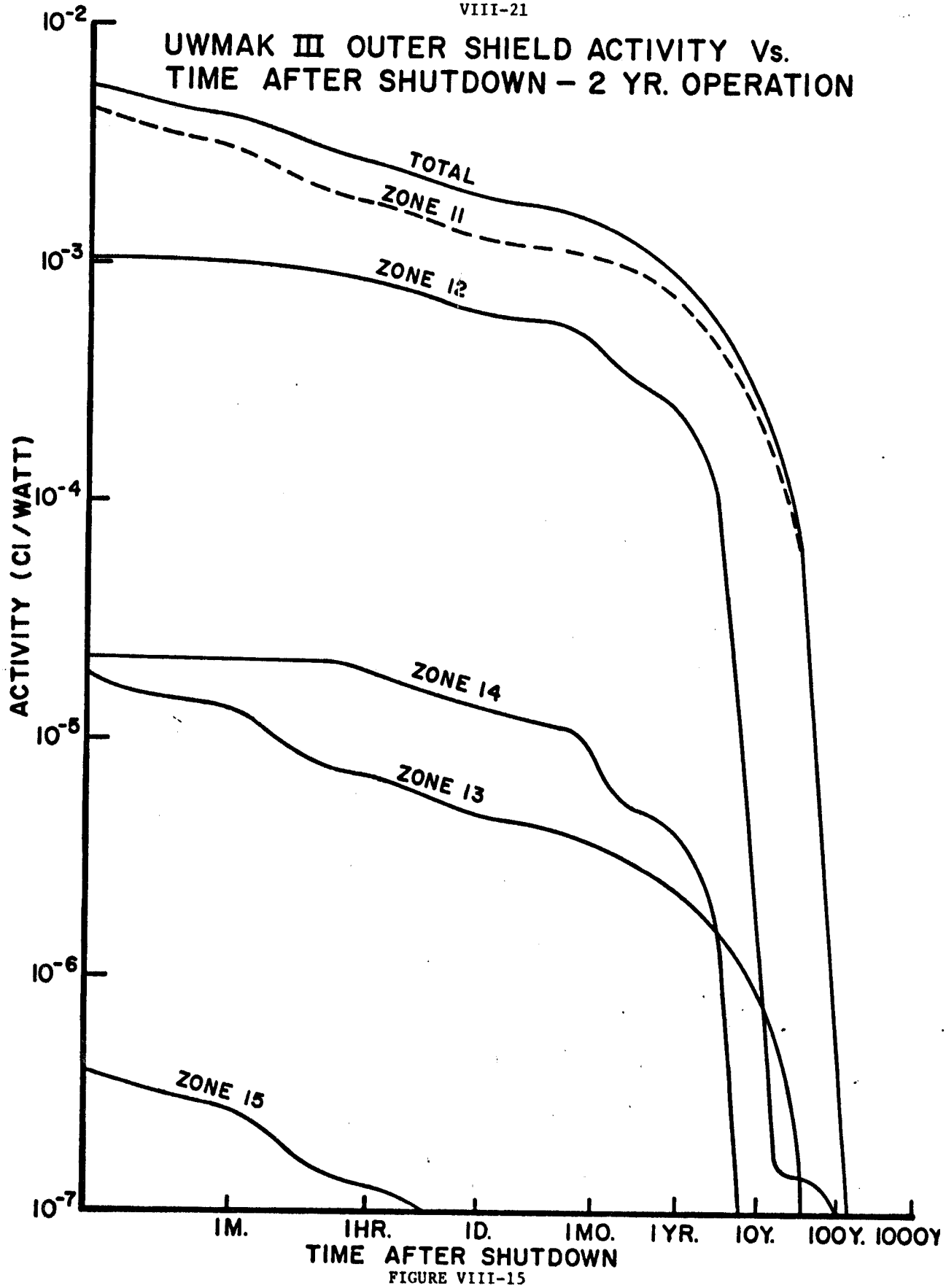

FIGURE VIII-15

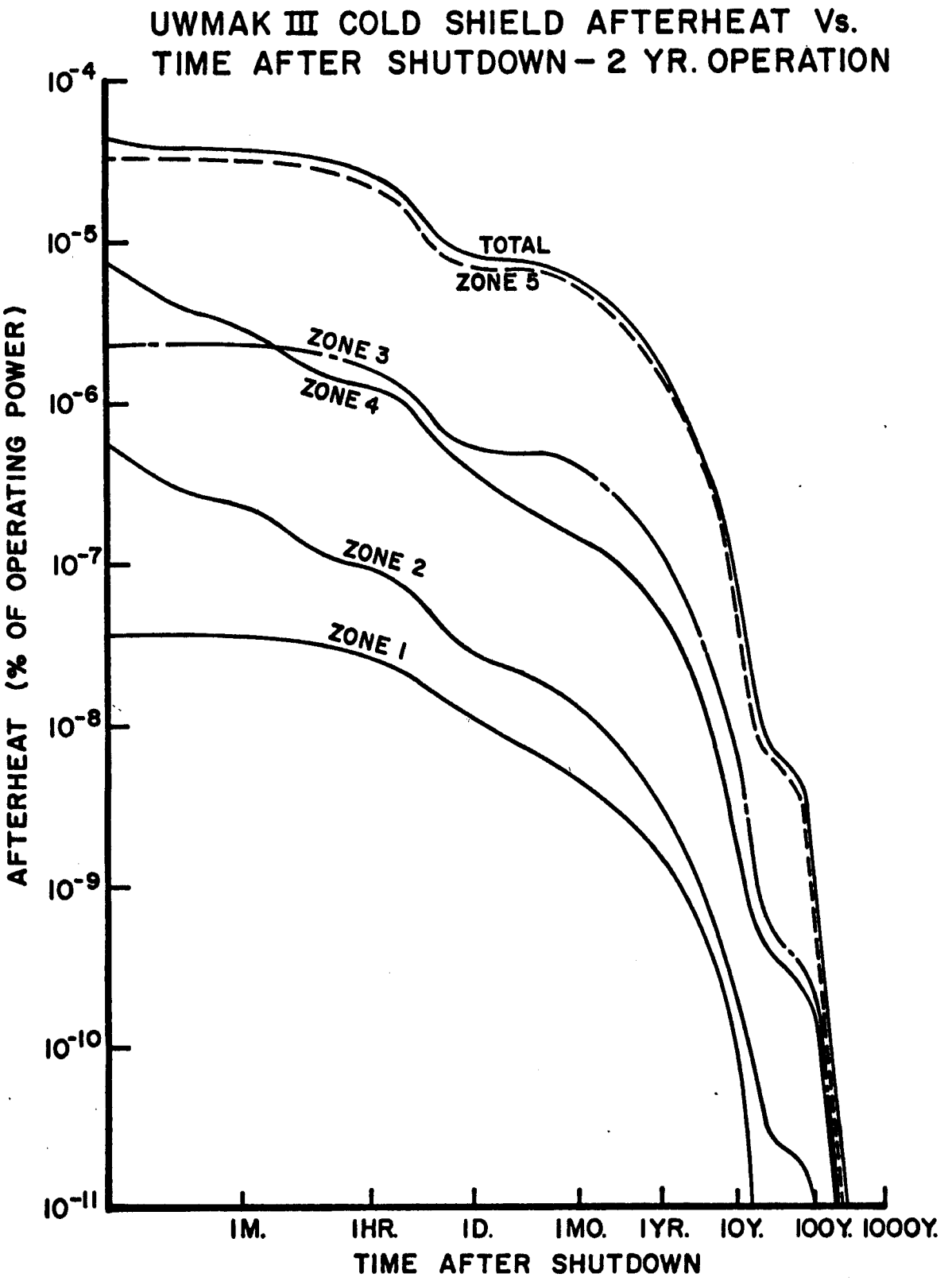

FIGURE VIII-16

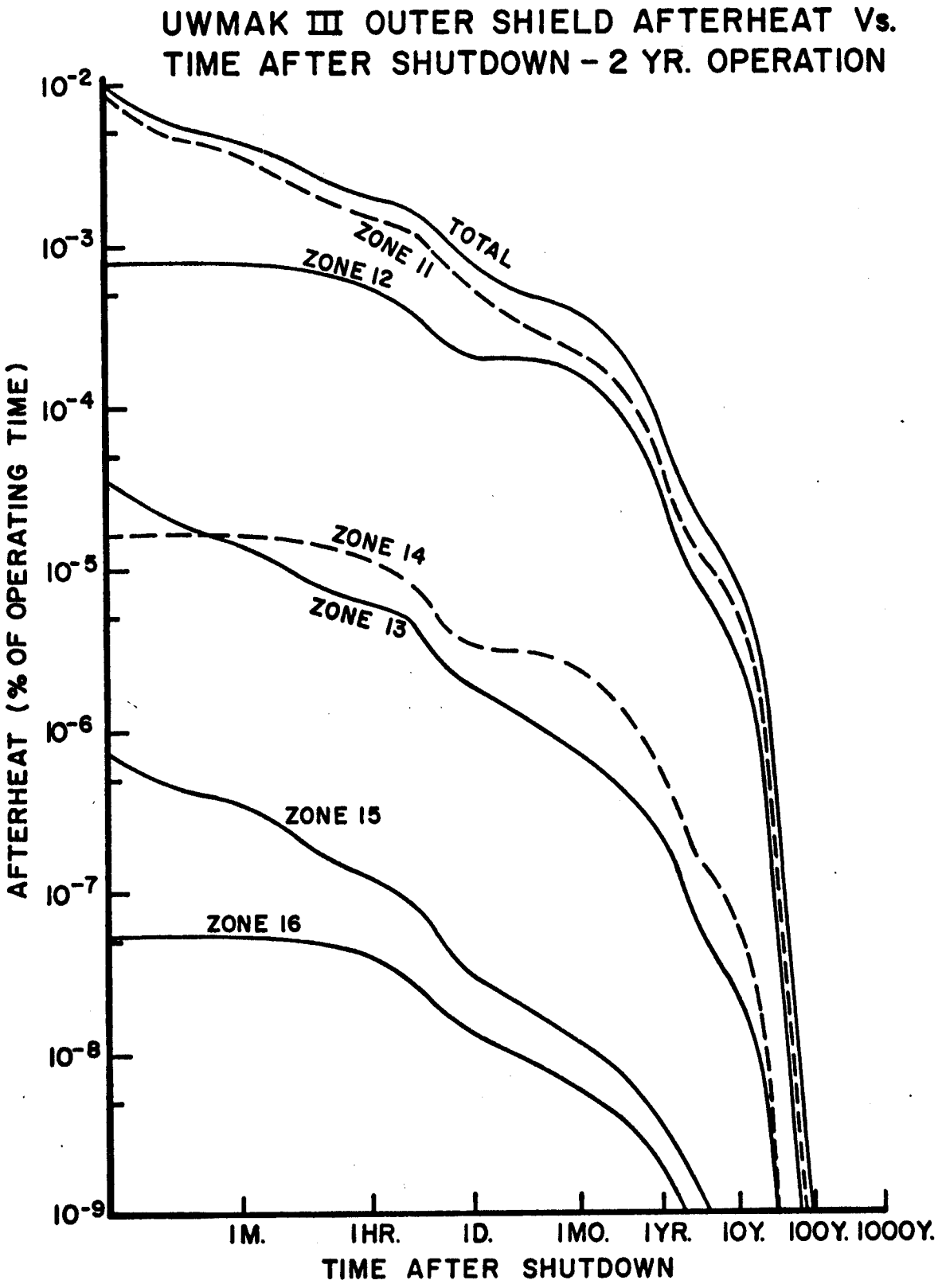

FIGURE VIII-17

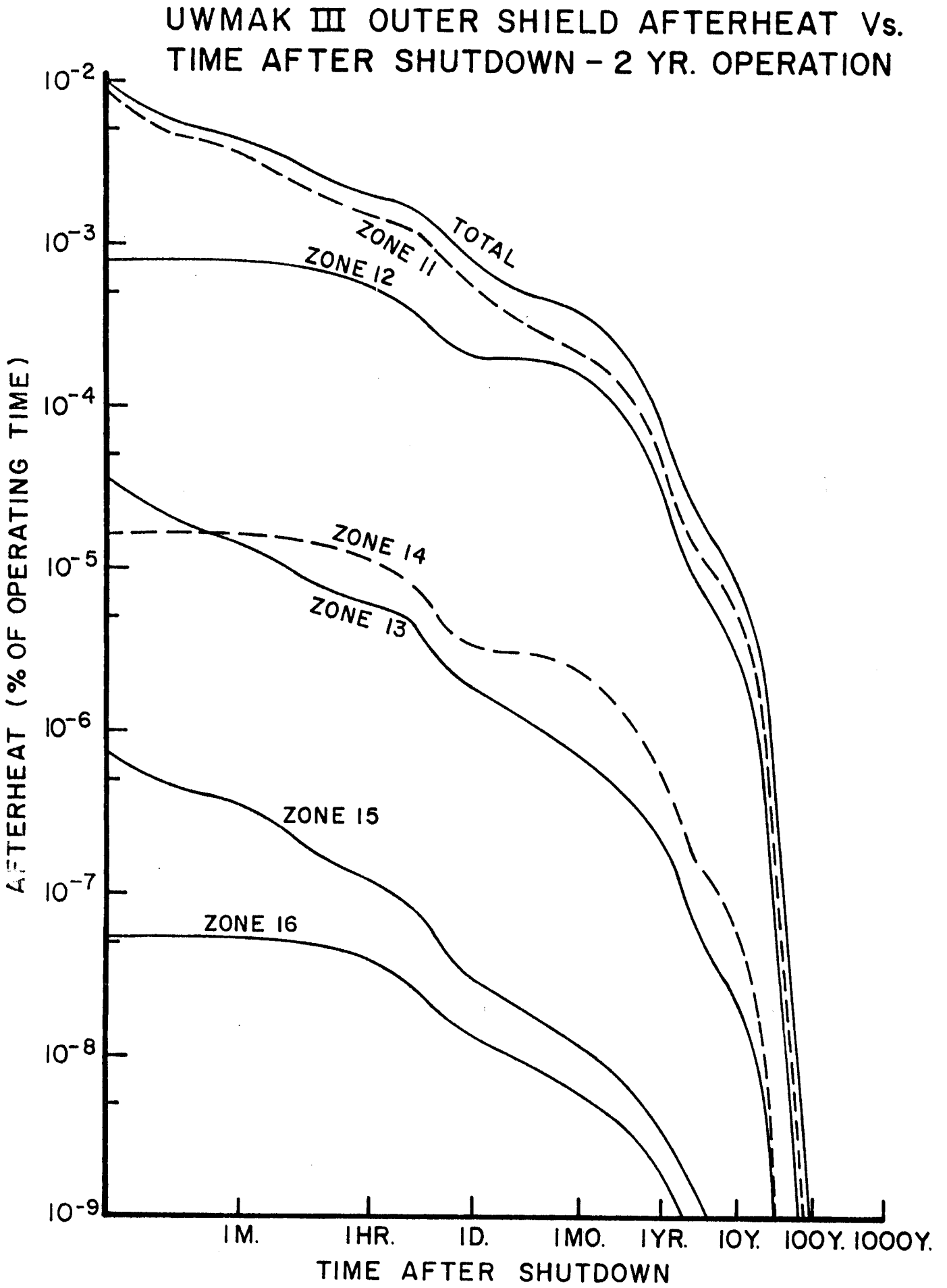

FIGURE VIII-17

VIII-E. Nature of Activity

As with the previous designs, UWMAK-I[1] and II[2] we have chosen to follow Steiner[5] and calculate the "Biological Hazard Potential" (BHP) for this reactor. BHP is defined as the activity in Curies/kw_{th} divided by the maximum permissible concentration(MPC) for general public exposure in Curies/km^3 of air as taken from 10CFR20, Appendix B, Table II, Column 2. The BHP is the volume of air required to dilute the activity per thermal kilowatt to MPC. It has proven to be a useful, if not definitive way, of making comparisons between systems and of making initial assesments of potential hazards of catastrophic events.

The BHP of the significant isotopes in the UWMAK-III first wall at shutdown after two years of operation are shown in Table VIII-3. It is clear that the major contribution comes from five relatively short lived isotopes and that the total BHP is of the same order as for the stainless steel first wall of UWMAK-I[1]. It should be noted that contributions for isotopes not listed explicitly in 10CFR20 have been included and probably overestimates the total BHP.

The BHP of the total blanket at shutdown after two years of operation is shown in Table VIII-4. As is expected the values are higher and are due primarily to the outer blanket. The BHP after two hundred years of decay is also shown and are reduced by a factor of 500 from the values at shutdown.

TABLE VIII - 3

UWMAK-III BHP FOR DOMINANT ISOTOPES IN FIRST WALL
AT SHUTDOWN - TWO YEAR OPERATING TIME

ISOTOPE	BHP (km^3 air/kWth operating power)
Nb 92^m	18.39
Zr 89	16.67
Nb 95^m	13.11
Mo 99	8.52
Nb 96	8.30
Nb 91^m	4.59
Tc 101	.32
Mo 101	.32
Nb 95	.69
Zr 95	.44
Mo 93	.12
Tc 99^m	.12
Mo 91	.50
Y 88	.12
TOTAL	72.55

TABLE VIII - 4

BHP OF DOMINANT ISOTOPES AT SHUTDOWN IN UWMAK - III
- TWO YEAR OPERATING TIME

ISOTOPE	BHP (km^3 air/kWth operating power)		
	OUTER BLANKET	HOT SHIELD	TOTAL
Nb 92^m	44.43	7.11	51.54
Zr 89	38.27	5.66	43.93
Nb 95^m	30.24	4.60	34.84
Mo 99	28.63	17.27	45.91
Nb 96	18.64	2.60	21.24
Nb 91^m	9.81	1.25	11.06
Tc 101	1.46	1.49	2.95
Mo 101	1.46	1.57	3.03
Mo 95	1.60	.24	1.84
Zr 95	1.02	.16	1.18
Mo 91	1.01	.12	1.13
TOTAL (including other isotopes)	181.38	43.66	225.04

BHP OF DOMINANT ISOTOPES 200 YEARS AFTER SHUTDOWN
- TWO YEAR OPERATING TIME

Mo 93	.32	.15	.47
Nb 93^m	.01	$\sim$ 0	.01
TOTAL	.33	.15	.49

REFERENCES FOR CHAPTER VIII

1. B. Badger, et al., "UWMAK-I - A Wisconsin Toroidal Fusion Reactor Design", University of Wisconsin Fusion Design Memo, UWFDM-68, Madison, Wisconsin (1974).

2. B. Badger, et al., "UWMAK-II - A Conceptual Tokamak Reactor Design", University of Wisconsin Fusion Design Memo, UWFDM-112, Madison, Wisconsin (1975).

3. S. Pearlstein, "Neutron Induced Reactions in Medium Mass Nuclei", Journal of Nuclear Energy 27, 81 (1973).

4. M. A. Abdou, C. W. Maynard, and R. Q. Wright, "MACK: A Program to Calculate Neutron Energy Release Parameters (Fluence-to-Kerma Factors) and Multigroup Neutron Reaction Cross Sections from Nuclear Data in ENDF Format", University of Wisconsin Fusion Design Memo, UWFDM-37, Madison, Wisconsin (1974).

5. D. Steiner and A. P. Fraas, "Preliminary Observations on the Radiological Implications of Fusion Power", Nuclear Safety 13, 353 (1972).

IX. Radiation Damage and Materials

IX-A. Introduction

The design philosophy of UWMAK-III is to consider an advanced reactor concept that may be representative of the time period beyond ~2020. It is fully expected that, from the materials standpoint, austenitic steels will play the predominate role in the reactors constructed from 1980 to at least the first commercial reactor. However, these steels have upper operating temperature limits which may limit overall efficiencies to ~32-38%. In order to exceed these efficiencies it will be necesary to go to higher temperatures and this means we must use either the refractory metals (V, Nb, Mo, or Ta) or non-metals such as carbon or SiC. As is evidenced by the overview of this report, we have chosen TZM, a titanium-zirconium alloy of molybdenum for our advanced reactor design. We have also used considerable amounts of carbon to enhance the operating temperatures and extend the first wall lifetime and the potential plasma burn time. The reasons for these choices will be outlined in section B of this chapter.

Special consideration must be given the irradiation behavior of Mo because of the key role the structural material has with respect to plant costs. This topic will be discussed, to at least the detail which present data allows, in section C. The last section in this chapter will examine how the materials of UWMAK-III behave in the reactor environment. Primary emphasis is again given to TZM. The reader is also referred to Chapter XIII for radioactivity and afterheat characteristics of this system, Chapter XII for the materials resource question and Chapter XIII for the economic considerations of UWMAK-III.

IX-B. Reasons for the Choice of TZM for UWMAK-III

The choice of a structural material for fusion reactor blankets is a very complicated one. At least ten different properties must be considered, any one of which could eliminate the metal (or its alloys) from serious considerations. These areas are listed below, not necessarily in the order of importance.

Physical properties
Mechanical properties
Thermal properties
Fabricability
Neutronic behavior
Compatibility with coolants
Interaction with tritium
Radiation damage
Availability to country concerned
Cost

The basic function of a blanket structural material is to provide the proper vacuum environment for the plasma and to contain the coolant while being inert to the plasma and not interfering with the production of tritium. It should do this at as high a temperature as possible (to increase the plant efficiency)

and not have its properties significantly degraded in the intense radiation environment. The cost of the material should be low and it should be easily fabricated and joined, perferably in the 'field'. The reserves of the structural material should be adequate to construct hundreds, if not thousands of plants over several generations. The reserves should be readily accessible to all nations who wish to base their electrical generating industry on the fusion concept. The structural material should retain its integrity over long periods of time in a sometimes chemically corrosive media and not represent a safety hazard in itself if severe accidents were to befall the reactor. Finally, the inevitable absorption of neutrons should not produce long lived isotopes which need to be monitored for centuries to come.

Obviously, there is no metal or alloy which will satisfy all of these criteria and the ultimate choice of a CTR structural material will depend on a compromise between all of the nine properties previously mentioned. At the present time there are only 5 metal systems seriously considered for CTR application and each has its own temperature range of importance. These are summarized below:

Low temperature (~200°C)	-	Aluminum alloys* Austenitic Steels
Medium temperature (200-600°C)	-	Austenitic Steels Vanadium alloys
High temperature (600-1000°C)	-	Vanadium alloys Nb alloys Mo or Mo alloys

We will try to compare the five systems as much as possible on the same basis. However, due to a lack of data in some areas, we will occasionally have to fall back on a comparison of the base metals Al, Fe, V, Nb and Mo. As more information becomes available one can update this work to get a more refined comparison.

The choice of the particular Al, V, Nb, and Mo alloys is somewhat arbitrary, but they appear to be consistent with much broader studies of CTR structural materials. Here we will use 2024 series Al, 316 stainless steel, V-20 Ti, Nb-1Zr, and TZM† as representative alloys of the basic metals.

IX-B-1 Physical Properties

Among the many properties of metals there are only three physical properties which are of major importance in fusion reactor technology. There are:

---

*Coolant outlet temperatures may be higher if ceramic liners can be used[1]

† 0.5% Ti, 0.08% Zr, 0.03% C, Balance Mo

a. density
b. electrical resistivity
c. vapor pressure

Table IX-B-1 summarizes these properties for the 5 systems considered here.(2)

The mass density is important with respect to dead weight loads of massive structures. The allowable load is a complex function of yield or creep strength for a given internal and external pressure load. The mass of the structure depends roughly on the ratio of $\rho(T)/\sigma(T)$ where $\rho(T)$ is the density at a given temperature and $\sigma(T)$ is either the yield or creep rupture strength at temperature T. Obviously low values of ρ/σ are desirable. Figure IX-B-1 shows how this ratio varies with temperature for the alloys considered here. In the low temperature (<200°C) range the Al alloys are best with Nb alloys clearly much worse. In the intermediate range (400-600°C) aluminum alloys are no longer applicable and V-20Ti is clearly the best with 316 SS and TZM next. Finally in the high temperature range (600-1000°C) V and Mo are the best while Nb1Zr again has a very high density to yield strength ratio.

If we calculate the ratio of the density divided by the creep-rupture strength of the alloys after 10,000 hours at typical operating temperatures, we can get a relative feeling about the minimum mass required to balance the mechanical forces. These ratios are given below.

Alloy	Anticipated Operating Temperature °C	ρ/σ_r (g/MPa-cm^3) x 10^{+2}
Nb1Zr	1000	12
316 SS	600	5.5
Vanstar-7*	700	3.8
TZM	1000	3.4
2024 Al(T-4)	200	1.3

This basis of comparison shows that at the anticipated maximum operating temperatures Al alloys require less mass than TZM, Vanstar-7, 316 SS, and Nb-1Zr in that order. The Nb alloys show up particularly bad in this respect because of their low creep strengths.**

The electrical conductivity of the first walls should be as low as possible to reduce losses set up by the varying magnetic fields in tokamaks. Provisions will certainly be made to interrupt major closed loops, but localized circuits can be present. Aluminum is clearly the worst material here for the low temperature range while molybdenum alloys have the lowest resisitivities at intermediate and high temperatures (Fig. IX-B-2). Steel has the advantage with respect to this property.

Finally, the vapor pressure of the metals should be as low as possible, but certainly below 10^{-7} to 10^{-5} torr during operation. The only materials where this is even a remote problem is for steel and V. They would have to reach temperatures of ~900 and 1200°C respectively which is ~300-400°C above their maximum operating temperature as determined by mechanical property considerations, before pressures of 10^{-7} torr would be reached.

* Composition, V-9Cr-3Fe-1.3Zr-0.05C

**One might use higher strength Nb alloys but most of them contain high percentages of W or Hf, the latter being bad from neutronics and the W is undesirable because of resource and cost considerations.

Table IX-B-1

Selected Physical Properties of Potential CTR Structural Materials (a)

Property	Al	Steel	V	Nb	Mo
Atomic Weight	27	~56	50.9	92.9	95.9
Melting Point °C	660	~1430	1900	2468	2620
Density (g/cm^3)	2.7	7.98	6.1	8.6	10.2
Atomic Density (10^{22} atoms/cm^3)	6.0	8.5	7.2	5.6	6.4
Electrical Resistivity					
($\mu\Omega$-cm) - 100°C	3.9	78	24	17	8
400°C	9	100	44	31	11
800°C		122	66	43	18
Vapor Pressure at Temperature (°C)					
10^{-7} torr	800	900	1200	1920	1830
10^{-4} torr	1150	1100	1810	2250	2350
10^{-1} torr	1660	1500	2050	3200	

(a) Most of this information comes from reference 2 and the rest from handbooks.

FIGURE IX-B-1 – A Measure of Mass Required to Withstand Internal Coolant and External Vacuum Loads For CTR Materials

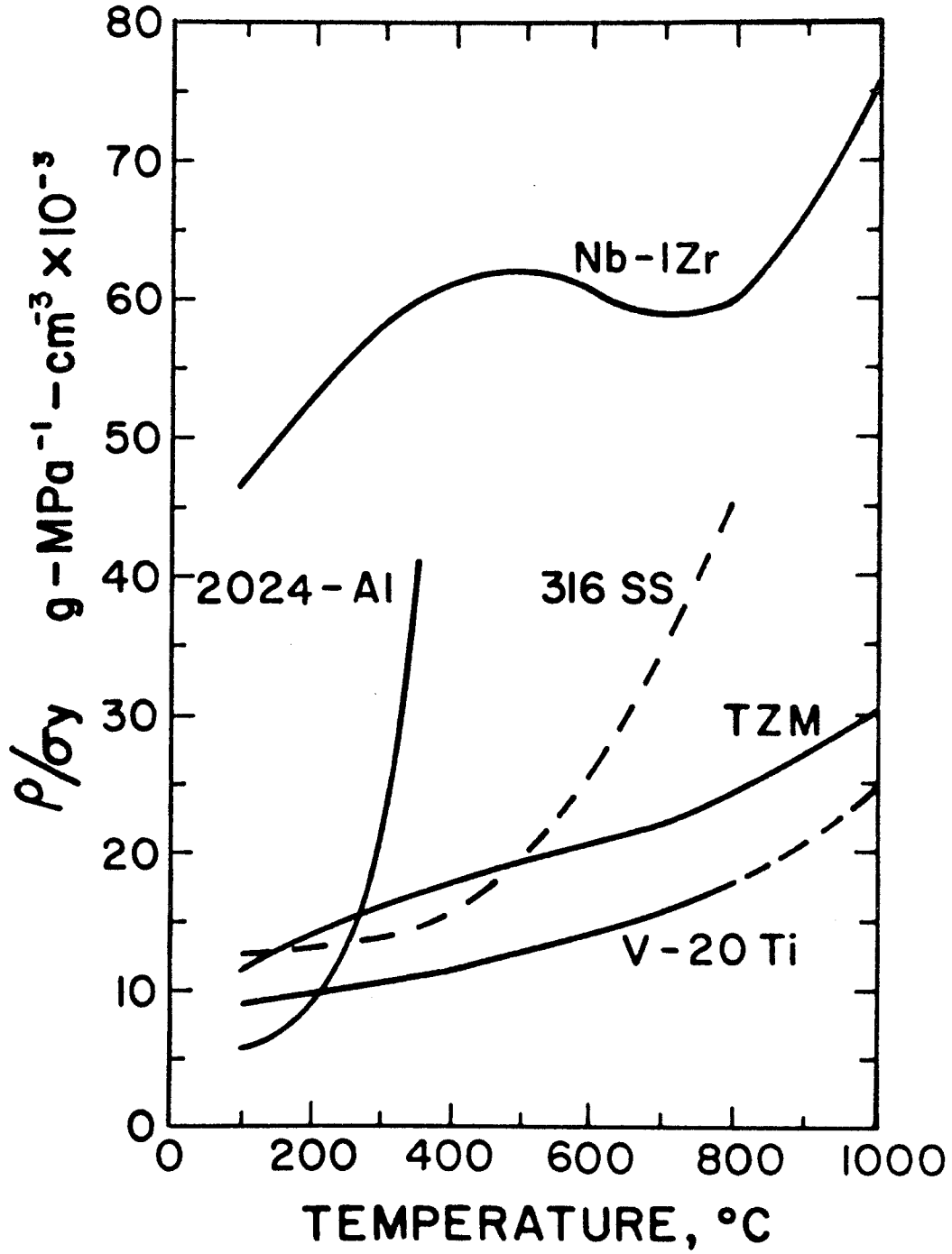

FIGURE IX-B-2 – Electrical Resistivity of CTR Materials

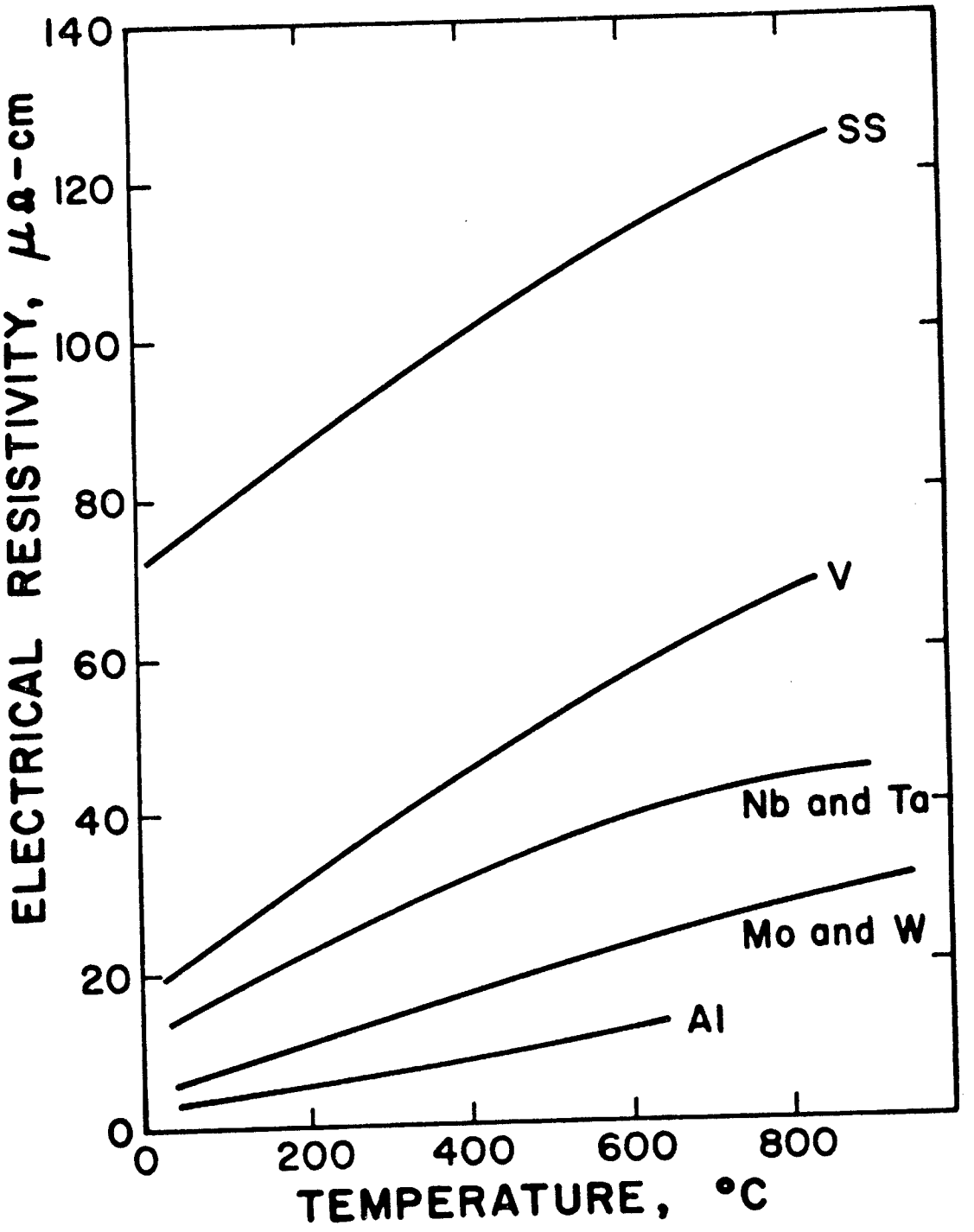

IX-B-2. Mechanical Properties

We will only compare the unirradiated properties in this section and radiation effects will be investigated later. There are 5 main properties that are of interest to fusion reactor designers.

a. yield strength
b. ductility
c. creep rupture strength
d. fatigue life
e. fracture toughness

The fracture toughness is of lesser importance at high temperatures and rather difficult to analyze for all the materials involved. Therefore, we will not cover that property here but it should be included in future assessments when the procedures for analysis become more refined.

Figures IX-B-3 to 7 summarize how Mo and Mo alloys compare to the other metals with respect to yield strength, ductility, creep strength, and fatigue respectively. The yield strength curves show that TZM is superior to all of the metal systems considered, at least up to 1200°C. Stainless steel and V-20Ti have very good properties up to ~600°C whereafter the yield strength of the steel drops off rather rapidly. Even pure Mo has respectable strength up to 1000°C in contrast to pure V or Nb. Alloying Nb with Zr helps its corrosion resistance but does not increase its yield strength appreciably. Finally, at temperatures of 200°C and lower, aluminum alloys are very strong and could be considered for fusion reactors. However, this advantage drops off very rapidly above 300°C and the radiation damage resistance of that system is notoriously low.[10]

Ductility is a measure of a material's ability to deform without failure. It can be measured in a variety of ways ranging from bend angle in a ductile-to-brittle transition test to total elongation at failure in a tensile test. In general, materials with large bend angles at low temperature or high tensile elongations are referred to as being ductile. Figure IX-B-4 compares the tensile elongation of V-20Ti,[3] Nb,[11], TZM[12], 2024 Al (T-4)[13] and stainless steel[14] as a function of temperature. From this figure it can be seen that all of the metals have adequate elongation at room temperature, the lowest being TZM molybdenum with 16%. All five metals experience an initial decrease in elongation followed by a very rapid increase in elongation to above that at room temperature. In the case of TZM, the elongation drops from 16 to 3%, for V-20Ti it drops from 27 to 10%, for Nb it drops from 37 to 21%, for 316 SS the ductility reaches a low of 28% from a room temperature value of 34%, and finally, 2024 Al drops from 20% to 19%. From this comparison we see that TZM has the lowest tensile ductility of all the alloys and unfortunately it occurs in its normal operating range of 600-1000°C.

FIGURE IX-B-3

Effect of Temperature on Yield Strength of Potential CTR Materials

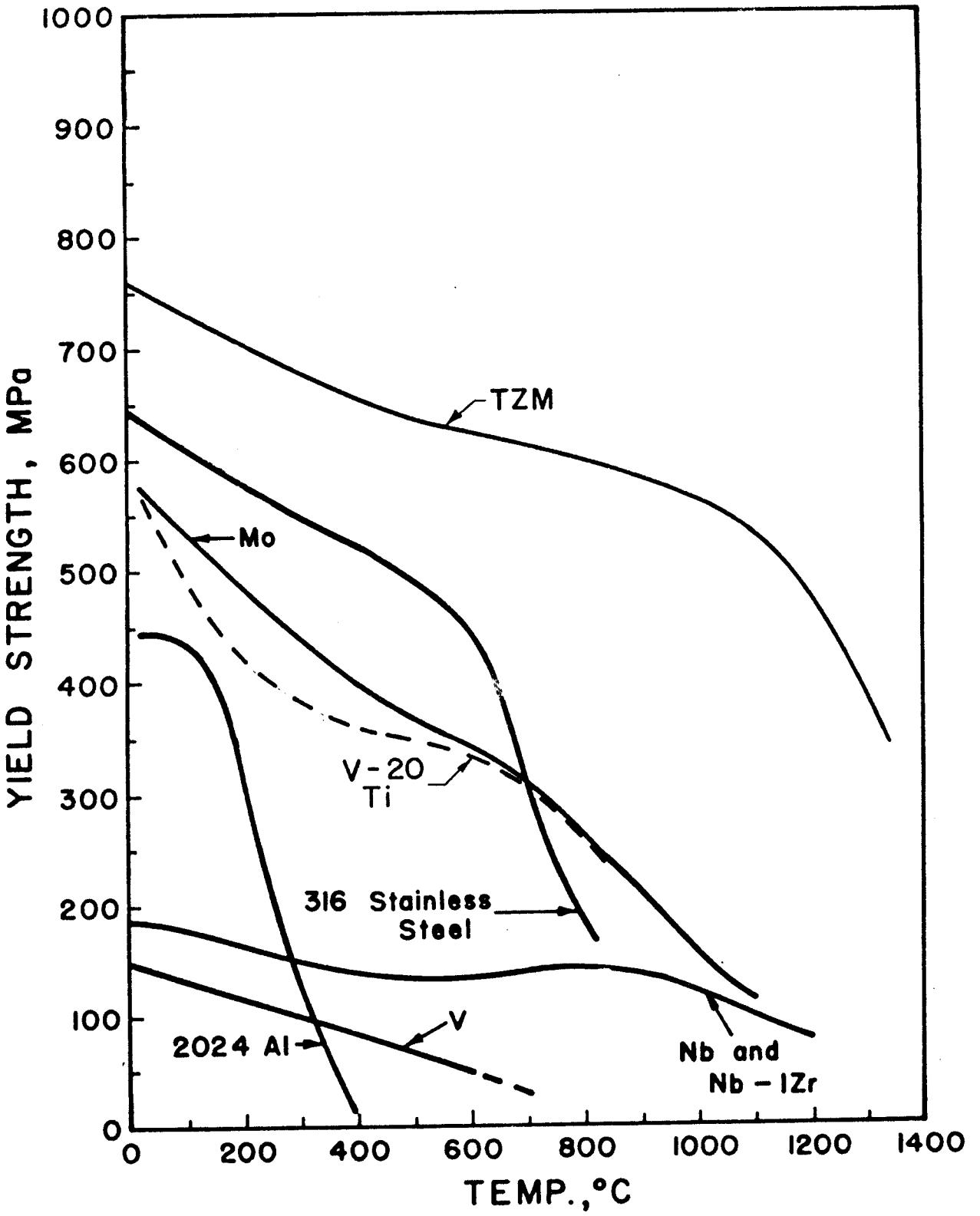

Figure IX-B-4
TENSILE DUCTILITY OF SEVERAL CTR MATERIALS IN THE FULLY ANNEALED CONDITION

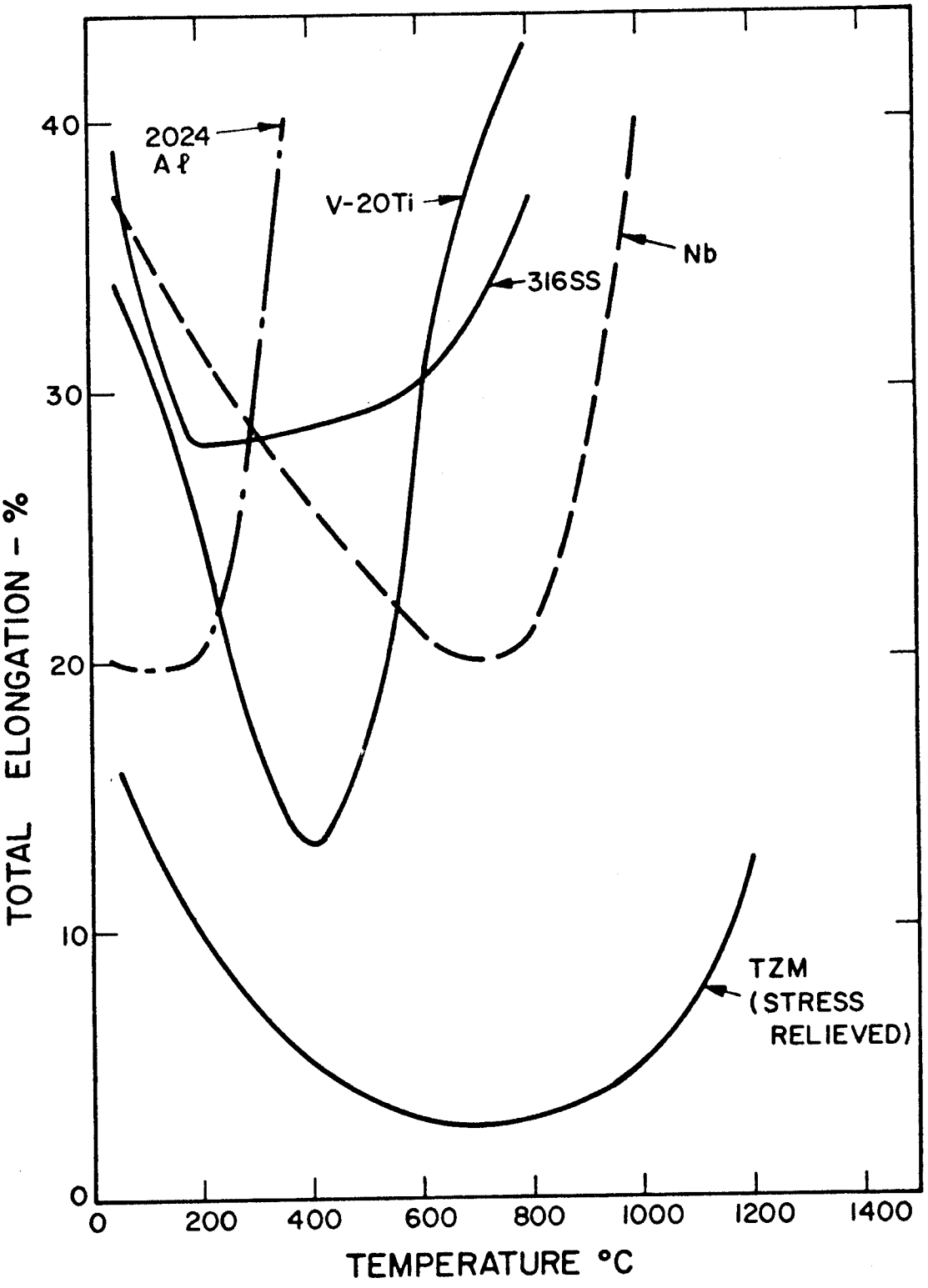

In our comparison of the tensile ductility of the various candidate materials it should be noted that all of the metals are in the fully annealed condition except TZM which is in the stress relieved condition. Fully annealed TZM (or Mo) has a ductility close to that of niobium. Unfortunately one cannot use annealed molybdenum because of a phenomenon called ductile-to-brittle-transition temperature, or DBTT for short. Molybdenum and its alloys (TZM), like other BCC metals, experience a temperature range below which a ductile material acts as a brittle one. In the case of the group VI-A metals (chromium, molybdenum, and tungsten) this temperature is above room temperature while for the group V-A metals (tantalum, niobium, and vanadium) it is below room temperature. This temperature, however, is not fixed but can be raised or lowered depending upon chemistry or microstructure. For example, it is known that the interstitial elements such as C, O, H, and N have a significant effect on this temperature and that the DBTT can be raised as the impurities are increased[15-17] (see Figure IX-B-5a and b).

One way of increasing the tolerance for these interstitial elements is to alloy with gettering elements such as Ti or Zi which are effective in tying up large concentrations of interstitials. This was one of the reasons for creating the molybdenum alloy TZM (Mo-0.5Ti-0.08Zr). Another way of lowering the DBTT is through the use of cold work. Cold working is a process by which a metal is deformed below its recrystallization temperature thereby creating a heavy dislocation microstructure. This microstructure results in a lower transition temperature because it tends to increase the metal's tolerance for interstitials. Figure IX-B-6 shows the effect of cold working on the DBTT of Mo[18] From this figure it can be seen that it takes about 70% cold work below the transition temperature to reduce the DBTT to below 20°C It is for this reason that molybdenum is supplied in the cold worked and stress relieved condition.

Subsequent fabrication can also effect the transition temperature. Lessman[19] found that welding the niobium alloy Cb-752 (Nb-10W-2.5Zr) increased this temperature from -160° to -45°C. The reason for this increase is probably due to interstitial contamination and larger grain sizes in the weld zone. Subsequent post weld heat treatment will lower the DBTT but not to the unwelded state. Molybdenum also experiences the same shift in DBTT but since this transition temperature was near room temperature, the shift appears to be more dramatic. Because of its potential for cracking, one would like to consider using molybdenum in the welded condition. The approaches one should use in joining molybdenum will be discussed in a later section.

Up to this point we have discussed what influences the DBTT but there are several questions which may arise. For example, how can one get 40-50% elongation in a brittle material? The answer is the DBTT is dependent upon the strain rate and the stress state. As long as a material is in pure tension and the strain rate is slow enough the material will be ductile. If instead of tension, the material is subjected to a bending mode (biaxial stresses) it will act like a brittle material.

FIGURE IX-B-5a EFFECT OF CARBON ON DBTT OF POTENTIAL CTR REFRACTORY STRUCTURAL MATERIALS

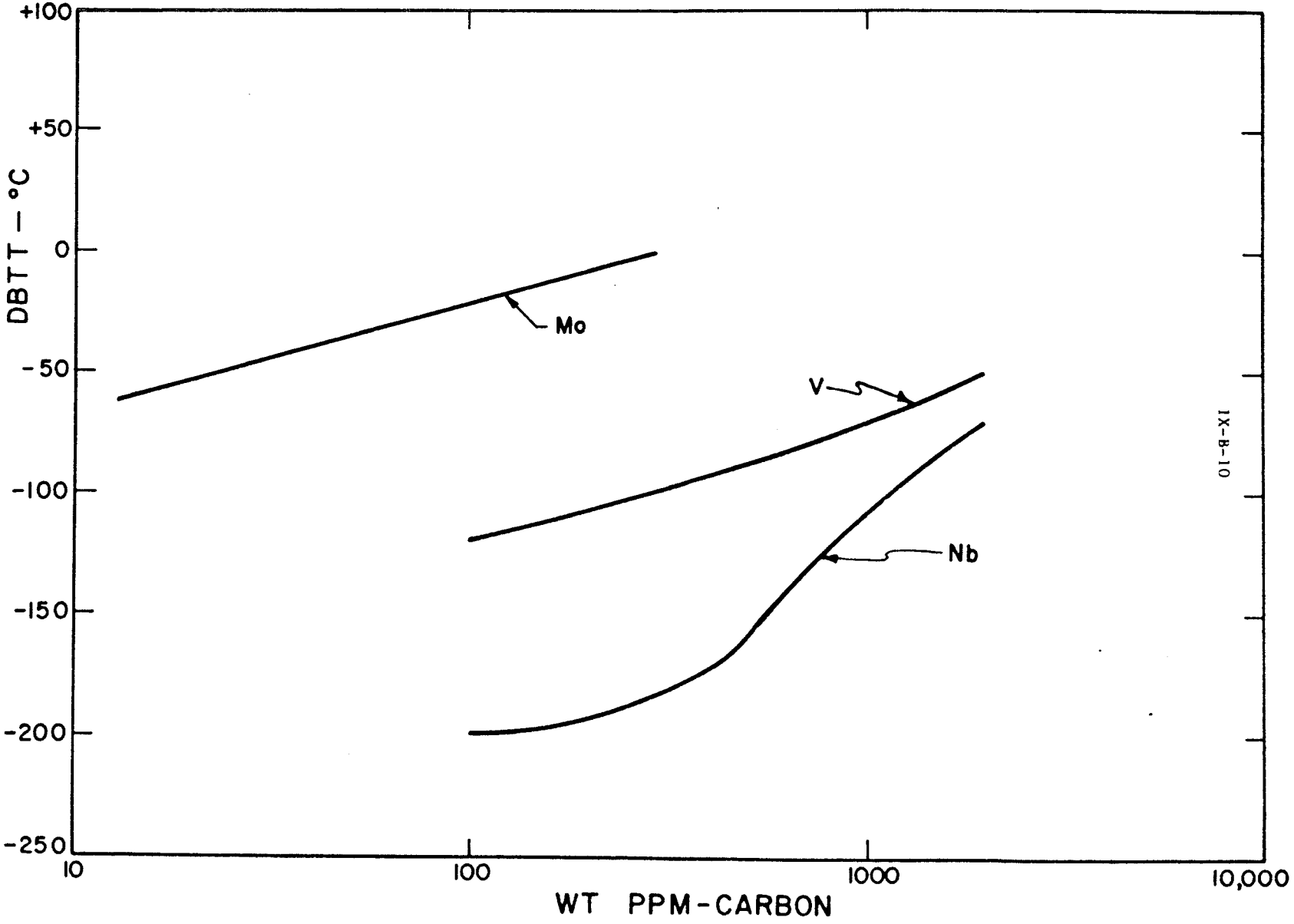

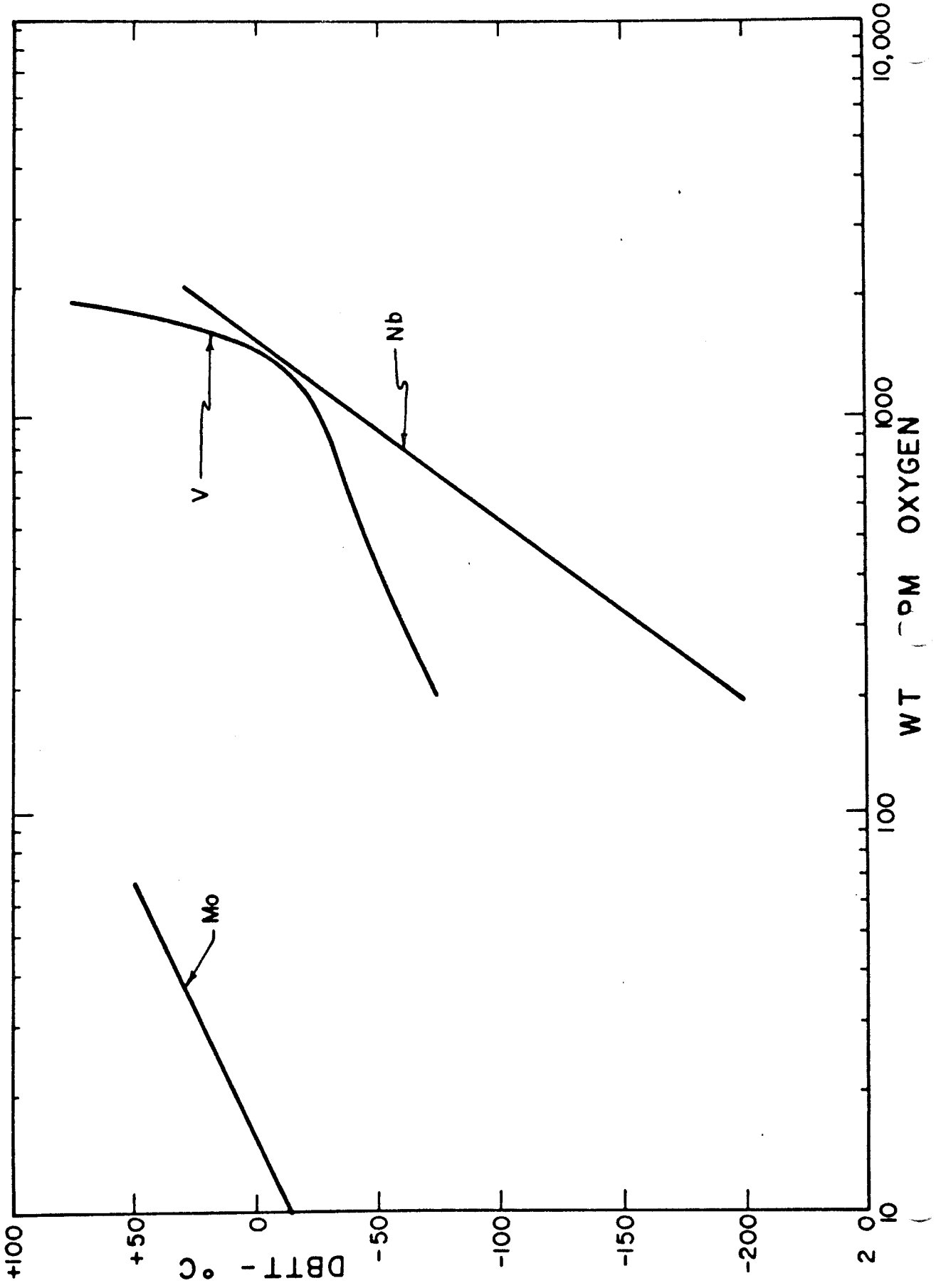

FIGURE IX-B-5b EFFECT OF OXYGEN ON DBTT OF Mo, Nb and V.

FIGURE IX-B-6

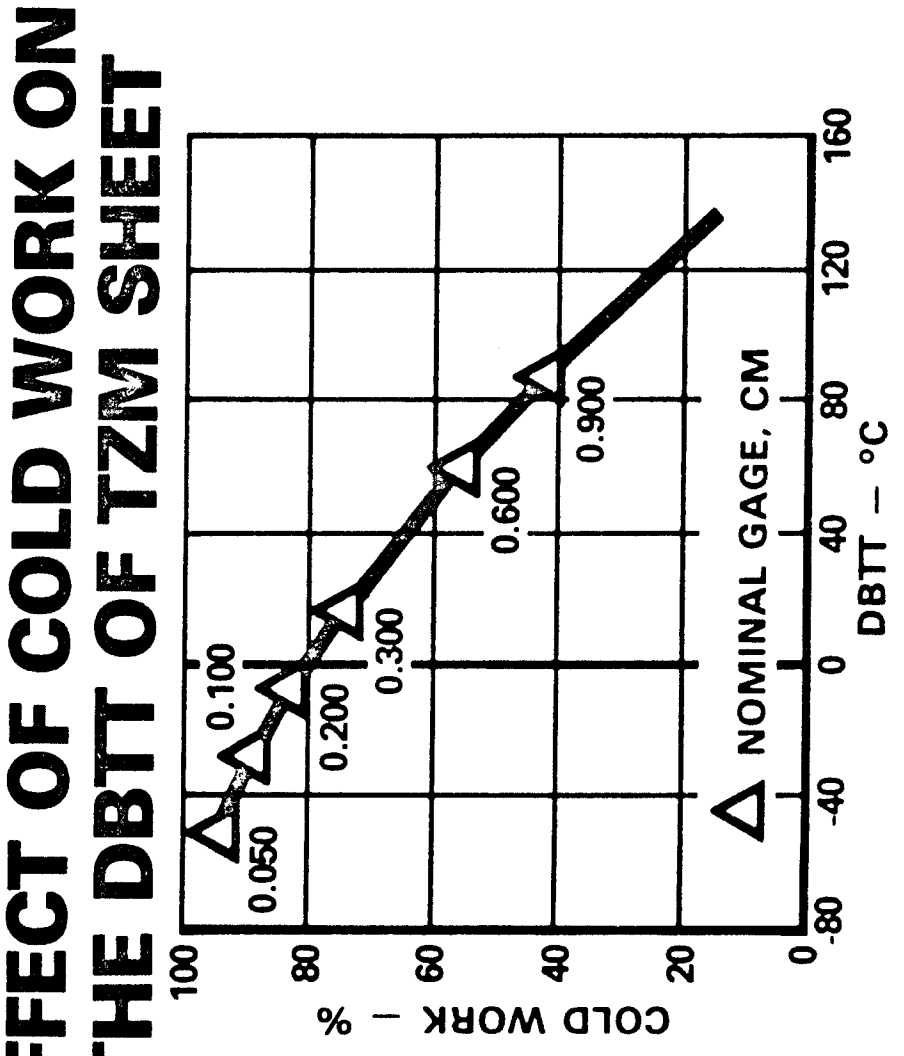
EFFECT OF COLD WORK ON
THE DBTT OF TZM SHEET
COLD WORK — %
100
80
60
40
20
0
-80
-40
0
40
80
120
160
DBTT — °C
NOMINAL GAGE, CM
0.050
0.100
0.200
0.300
0.600
0.900

Figure IX-B-7 displays the creep rupture life of five potential CTR alloys at their anticipated operating temperatures.[20-24] The data is given out to 10,000 hours. Again it is seen that TZM is far superior to V or Nb alloys at its operating temperature of 1000°C. The TZM is even more than a factor of 2 stronger than 316 SS at 600°C and ~50% stronger than 2024 (T-4) Al at 200°C. The creep rupture life of Nb-1Zr is a factor of four times lower than TZM at 1000°C which is another way of saying that for the same coolant and blanket design, much more Nb will be required to withstand the mechanical stresses.

The failure of materials can occur at stresses considerably below the ultimate tensile stress if the member is subject to cyclic loading. Such loading is probably more characteristic of fusion power plants than fission reactors because of the pulsed nature of the D-T burn in tokamaks, pinch devices, laser and e-beam reactors. There are many factors which influence the fatigue life; temperature, method of loading, (tension, compression, tension-compression, etc.), surface roughness, cold working, microstructure, and grain size to mention a few.

There have been some attempts to predict fatigue life from other mechanical properties such as ultimate tensile strength (σ_{uts}), Youngs Modulus (E) and reduction in area (RA). These properties have been incorporated into an empirical relationship to predict the total strain at failure ($\Delta\varepsilon_t$).[25]

$$(\Delta\varepsilon_t) = 3.5 \frac{\sigma_{uts}}{E\, N_f^{0.12}} + \frac{D^{0.6}}{N_f^{0.6}} \qquad \text{(IX-B-1)}$$

where N_f is the number of cycles to failure

D is the ductility coefficient given as

$$\ell n\left[\frac{100}{100\text{-R.A.}(\%)}\right]$$

At low strains where no yielding occurs, this relationship predicts that the fatigue life is governed by the strength of the material while at high strain ranges the fatigue is governed by the ductility of the material (Fig. IX-B-4). It is evident at low strain levels the parameter $(\sigma)/E$ is important and we have listed this ratio for the alloys at their maximum temperature of operation.

Alloy	T°C	$(\frac{\sigma_{ys}}{E})$
Al-2024	200	4.6×10^{-3}
316 SS	650	2.4×10^{-3}
V-20Ti	800	2.7×10^{-3}
Nb-1Zr	1000	1.6×10^{-3}
TZM	1000	1.1×10^{-3}

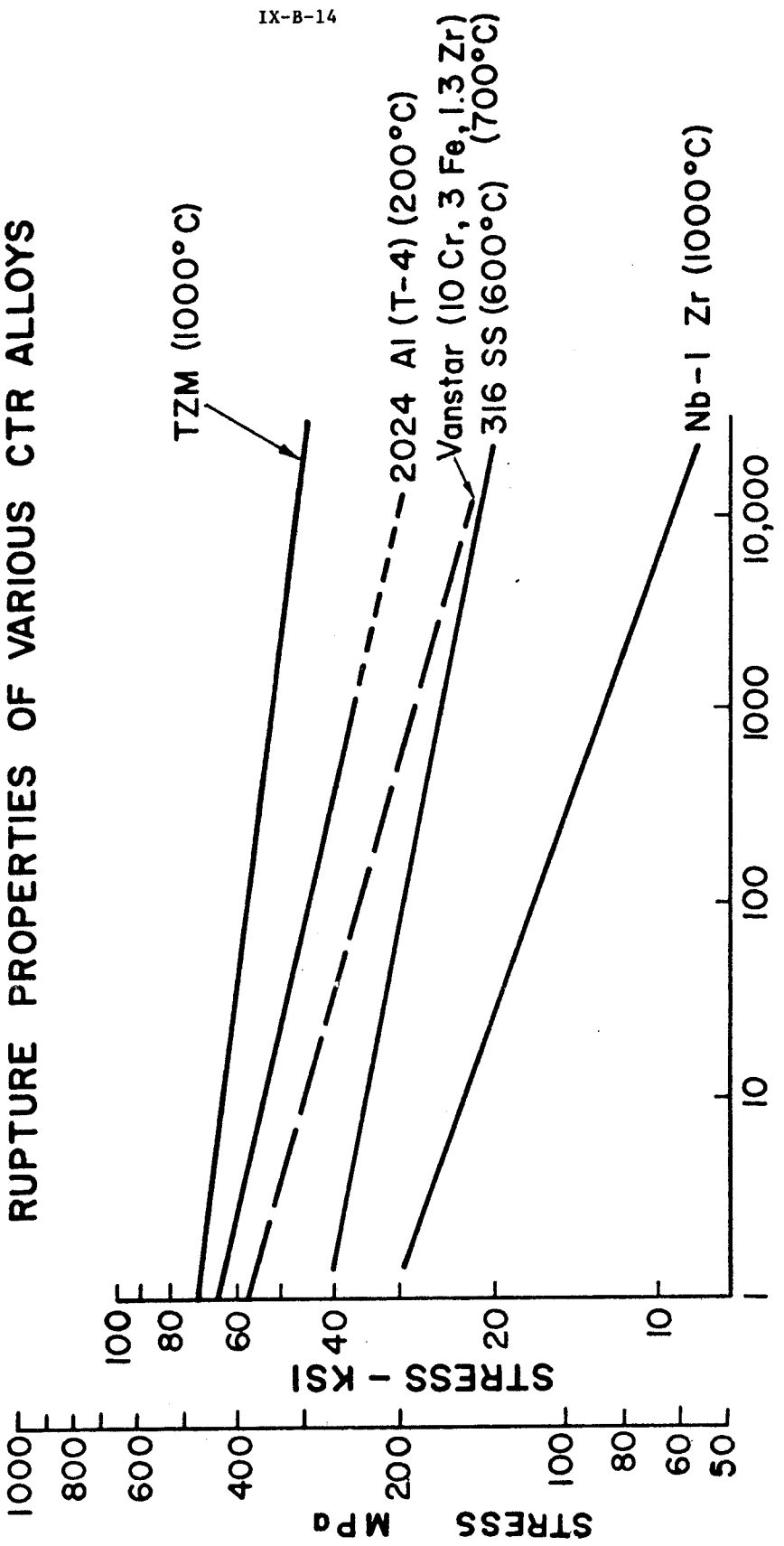
RUPTURE PROPERTIES OF VARIOUS CTR ALLOYS
TZM (1000°C)
2024 Al (T-4) (200°C)
Vanstar (10 Cr, 3 Fe, 1.3 Zr) (700°C)
316 SS (600°C)
Nb-1 Zr (1000°C)
TIME — HOURS
1
10
100
1000
10,000
STRESS — KSI
100
80
60
40
20
10
STRESS MPa
1000
800
600
400
200
100
80
60
50

FIGURE IX-B-7

This qualtitative comparison along with the ductility values shows that for a fixed number of cycles to failure, the steel and Al alloys should be able to withstand the largest strains while TZM will fail at the lowest. Stated another way, for a fixed strain, the fatigue life for 316 and Al will be the longest and it will be the shortest for TZM.

Figure IX-B-8 summarizes what data is available on the fatigue properties of 2024 Al(30°C)[26], 316 SS (600°C)[27], and TZM (1000°C)[28]. The conclusion that one can draw from this information is that since tokamaks will undergo approximately 5000 cycles per year (or more), the strain during the startup or shutdown should be limited to less than 0.2% for TZM, less than 0.3% for 2024 Al, and <0.5% for 316 SS.

One element that is missing in this analysis is the magnitude of the strain induced by a given fluctuation in heat load or pressure surge in the coolant. A more complete analysis would include the thermal properties and show that the strains induced in the refractory metals will be far less than in steel because of the high thermal expansion coefficient in the latter material. Therefore, the fatigue life may actually be longer for the refractory metals at typical operating conditions.

To summarize the mechanical property data we find that TZM is the most desirable material in the 600-1000°C temperature range followed closely by V alloys in the 600-800°C region. Nb-Zr alloys are not very attractive because of their low tensile and creep strengths. At the lower temperatures the Al alloys seem to be definitely competitive from a mechanical property standpoint.

IX-B-3. Thermal Properties

There are two main properties of interest here (thermal conductivity and thermal expansion) and one of secondary importance (heat capacity). Representative quantities are listed in Table IX-B-2 for the pure metals. Figures IX-B-9 to 11 represent the properties of these materials graphically.

Qunatitatively, a high value of thermal conductivity is required to reduce temperature gradients and to keep the maximum temperature of the structure close to the coolant temperature. In this respect, Al is superior in the low temperature regime, while Mo is much preferred over the intermediate and high temperature ranges.

Low values of thermal expansion coefficients are also desirable to minimize induced stresses in rigidly bound blanket components. Molybdenum is clearly superior over all the temperature ranges whereas the extremely high expansion coefficents of Al and steel could present some problems.

FIGURE IX-B-8 TYPICAL FATIGUE LIFE OF SELECTED CTR MATERIALS

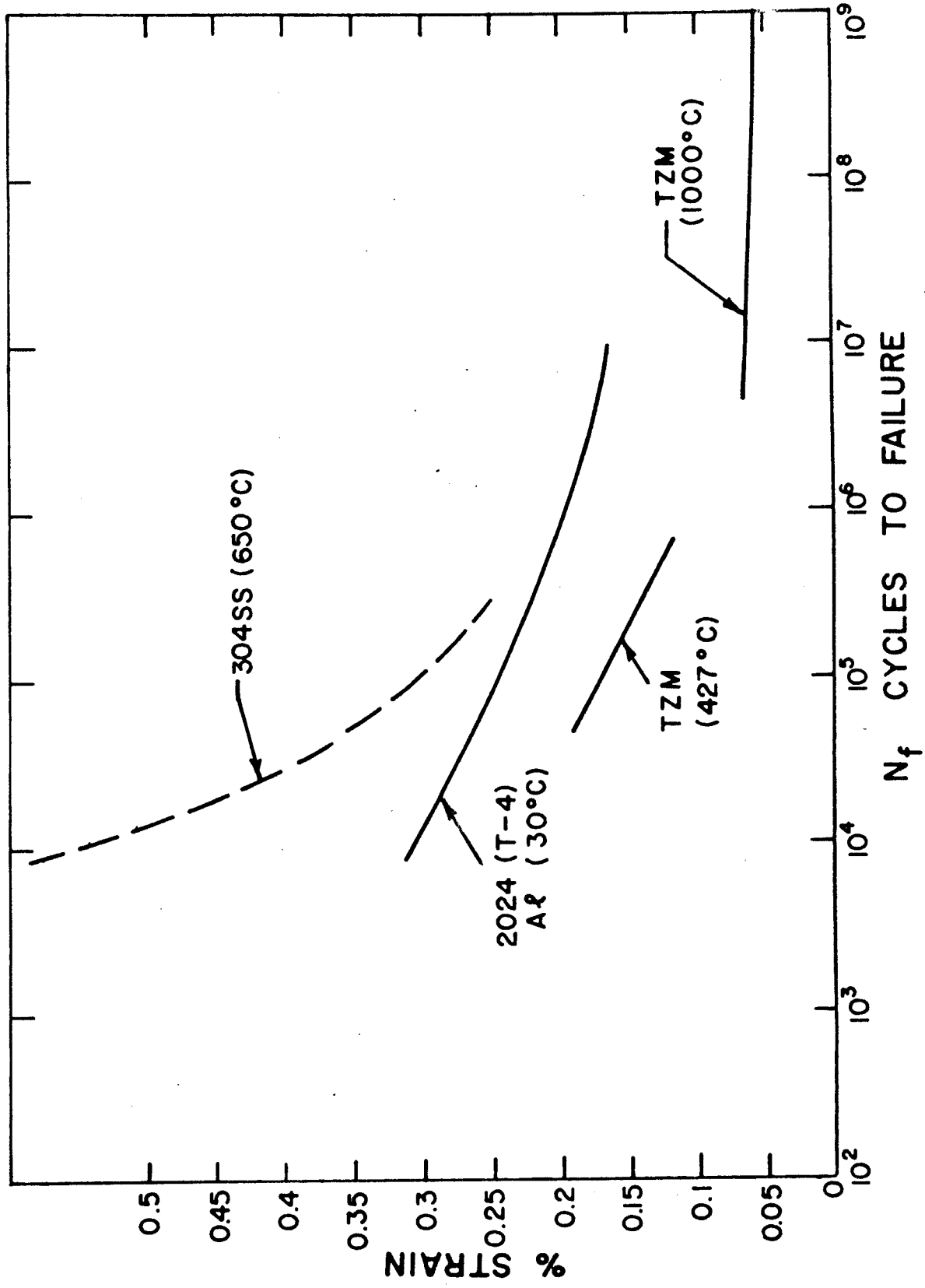

Table IX-B-2

Selected Thermal Properties of Importance for CTR Materials (a)

Property	Al	Steel	V	Nb	Mo
Thermal Conductivity (Cal/cm-sec °C)					
100°C	0.56	0.04	0.07	0.12	0.32
400°C	0.55	0.05	0.09	0.14	0.31
800°C		0.065	0.10	0.18	0.28
Coefficient of Thermal Expansion $°C^{-1} \times 10^{-6}$					
100°C	25	16.5	9	7	5
400°C	30	17.5	10	7	5
800°C		19	11	9	6
Heat Capacity (Cal/gm °C)					
100°C	0.22	0.11	0.12	0.07	0.16
400°C	0.26	0.13	0.13	0.08	0.17
800°C		0.15	0.15	0.08	0.19

(a) Most values in this table come from Reference 2 along with a few data points from handbooks.

FIGURE IX-B-9— Thermal Conductivity — CTR Materials

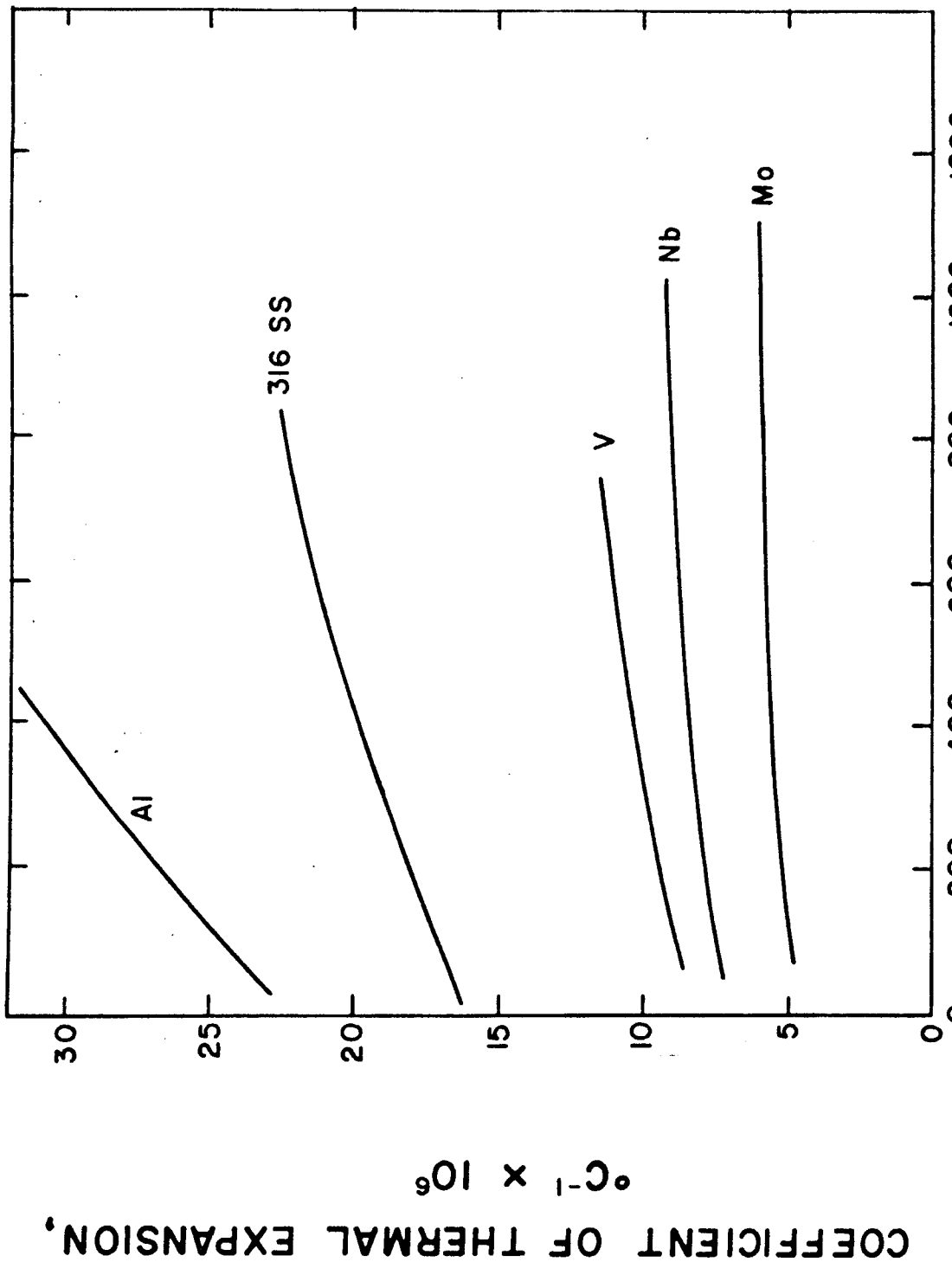

FIGURE IX-B-10—Coefficient of Thermal Expansion FOR CTR MATERIALS

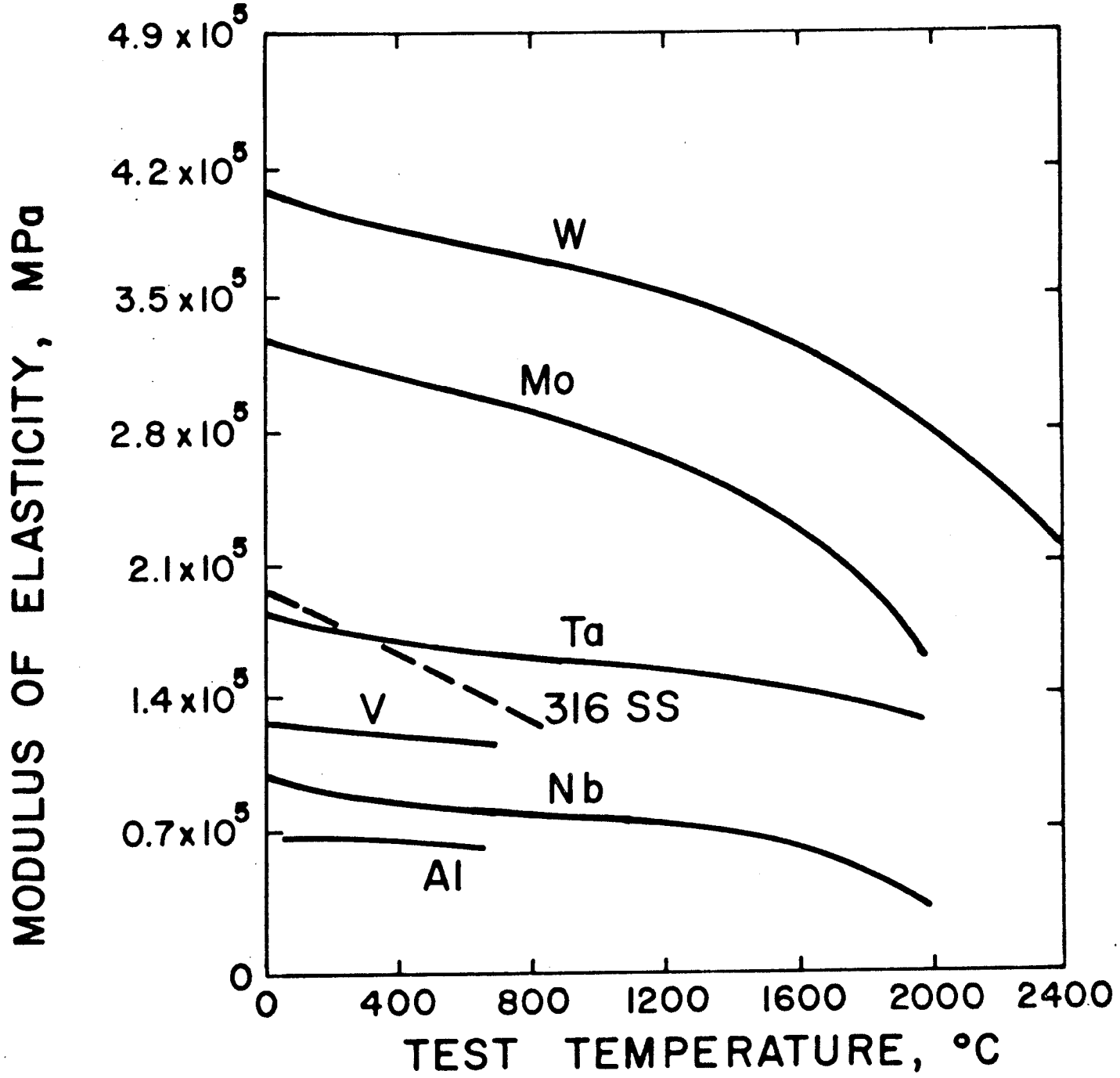

FIG. IX-B-11. MODULUS OF ELASTICITY FOR CTR MATERIALS

A large heat capacity is desirable to minimize wide thermal fluctuations for given energy inputs and also to act as an energy reservoir in the event of an accident situation. Aluminum has the highest heat capacity for the low temperature region with Mo taking that honor for the intermediate and high temperature regimes. However, when one calculates the energy required to cause melting the situation is somewhat different. Representative values are given below and show that the problem is most severe for Al. It is calculated that under adiabatic conditions only 120 cal/g will raise Al alloys from their normal operating temperature to the melting point. Unfortunately, the relative problem is even worse than indicated by the calculations because there is very little change of Al losing heat by radiation while this loss mechanism would definitely increase the energy required to cause melting in the other alloys.

The Energy Required to Produce Melting of Various CTR Structures

Metal	Maximum Operating Temperature °C	Melting Point °C	Approximate Energy Required to Produce Melting From Operating Conditions[a] cal/g
Al	200	660	120
316 SS	600	1550	145
V	700	1900	180
Nb	1000	2415	140
Mo	1000	2610	320

(a) Assuming rapid energy deposition with no heat leakage

One way to illustrate how these thermal properties can effect the stress state in a material is to consider the first wall in the CTR blanket. A high surface heat load (~10 watts/cm^2) can be incident on it from plasma radiation or particle leakage while nuclear heating can amount to 10 watts/cm^3 or more. This energy must be transmitted through the first wall into the coolant. The transfer of this energy is associated with temperature gradients which in turn set up differential expansion across the first walls. The stresses generated by this expansion can be calculated by the following expression,

$$\sigma = \pm \frac{\alpha}{2} \frac{E}{(1-\nu)} \Delta T \qquad \text{(IX-B-2)}$$

where $\Delta T = \frac{1}{k} [W_s t + \frac{W_n}{2} t^2]$

α = thermal expansion coefficient
E = Youngs modules
ν = Poissons Ratio
k = thermal conductivity
W_s = surface heat load watts/cm^2
W_n = volumetric heating rate, watts/cm^3
t = thickness of first wall
(+) is tension
(-) is compressive

The important thermal figure of merit to consider is then $[\frac{\alpha E}{k(1-\nu)}]$ which is listed in Table IX-B-3 for the materials considered here. The materials fall into 3 distinct classes: those which have very low values of the figure of merit (Al and its alloys), those with medium values of the figure of merit (No, Nb, and V) and those characteristic of very high values (stainless steels). This comparison shows that the stresses induced in Al are much lower than in the other systems (a factor of 3 lower than the refractories and a factor of 13 to 25 lower than for steel). Within the refractory system, the order of increasing stresses is V, Mo, and Nb but the difference is not more than 15%.

Perhaps a more meaningful comparison would be the ratio of the induced stress to the yield strength or the creep strength at that temperature. This ratio is given in Tables IX-B-4 and 5 and Figure IX-B- 12 takes into account both the stress induced by thermal gradients along with the ability of the metal to withstand such stress at temperature (irradiation effects are not included here).

The calculations reveal that in the low temperature range, the 2024 Al alloy has the best combination of thermal and strength parameters. However in the intermediate temperature range TZM is clearly best, followed closely by V-20Ti and pure Mo. The Nb, Nb1Zr, V, and 316SS systems are clearly inferior to Mo in the intermediate regime. The TZM system also retains its advantage at the highest temperatures and at a 1000°C (where V-20Ti is not expected to have sufficient creep strength) it has an overall figure of merit which is twice as good as pure Mo and three times that for the Nb system. The case for TZM is even more favorable when one considers the creep properties as shown in Table IX-B-5. For example, TZM is a factor of ~ 5 better than the Nb1Zr alloy at 1000°C and twice as good as Vanstar-7 at 700°C.

Table IX-B-4

Figure of Merit for Thermal Stresses in Potential CTR First Wall Materials *

	Temp. °C					
Material	25	200	400	600	800	1000
Mo	3620	3450	3250	3270	3250	2980
Nb	3810	3460	3230	3260	3580	3620
V	3490	3440	3430	3270	3100	
316 SS	27,700	24,300	21,400	18,100	16,300	
Al	1100	1200	1300	1400		

*$[\frac{\alpha E}{k(1-\nu)}]$, Newtons per meter - watt, a number as low as possible is desired.

Ratio of Thermal Figure of Merit to Yield Strength of Potential CTR Materials *

Units of 10^{-6} m-Watt^{-1}

Temp. °C	25	200	400	600	800	1000
Material						
Mo	6.4	7.1	8.3	9.6	12.5	20
TZM	4.0	5.2	5.8	6.7	7.8	10.3
Nb(Nb1Zr)	21	21	23	23	25	31
V	24	30	40	65	~200	-
V-20Ti	5.5	6.0	7.0	8.0	9.4	-
316 SS	44	42	40	40	93	-
2024 Al	2.5	3.8	87	-	-	-

* $[\frac{\alpha E}{k(1-\nu)\sigma_y}]$ Meter per watt, low numbers are desirable.

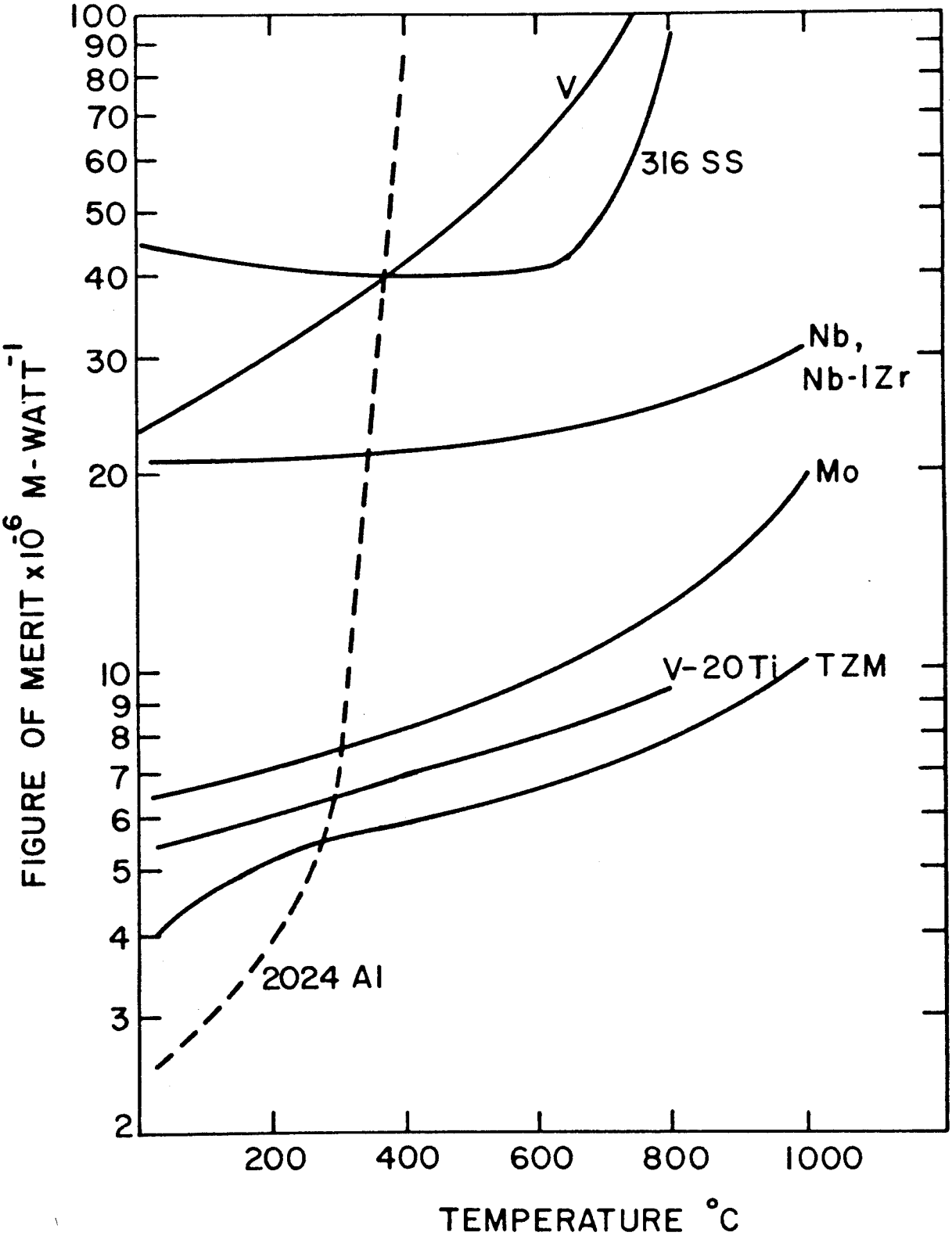

FIG. IX-B-12. THERMAL STRESS FIGURE OF MERIT-CTR MATERIAL USING YIELD STRENGTH

Table IX-B-5

Ratio of Thermal Figure of Merit to Creep Strength[a] at the Highest Temperature of Operation

System	Maximum Anticipated Operating Temp. °C	$\left(\frac{\text{Figure of merit}}{\sigma_{creep}}\right)_T$[b]
TZM	1000	9.8
Nb1Zr	1000	53
Vanstar-7	700	19
316 SS	600	120
2024 Al	200	17

(a) Creep rupture life at 10,000 hrs.

(b) m-watt^{-1}, low numbers are desirable.

Hence, it is concluded that for the intermediate and high temperature operation range the Mo-TZM system is far superior to the 316 SS, V and Nb system and slightly better than the V-20Ti alloy with respect to thermal stresses. This, coupled with its excellent high temperature creep resistance, is a strong point in favor of considering Mo for CTR blanket structures.

IX-B-4. Fabrication

This property is one of the most important and yet one of the most difficult materials parameters to measure quantitatively. The final proof of whether a material is fabricable is the ability to construct both large and small components of varying shapes and thicknesses. Such structures should be crack free and be able to maintain vacuum or high pressure loads.

There is certainly no need to discuss the fabrication and joining of Al alloys and stainless steels. It is even relatively easy to fabricate pure V and Nb (and Nb1Zr) into complex shapes and tubes. However, joining of these last two metals is not easy and must be performed under closely controlled conditions to avoid interstitial pickup.[29,30] The fabrication of V-Ti alloys is not easily accomplished and must be carefully controlled to avoid cracking in large angle bends.

Since the major objective of this section is to discuss the usefulness of Mo and its alloys in CTR environments, we will spend the rest of this subsection on that topic. However, the reader must constantly remember that considerable difficulties also exist for the Nb and V systems.

Much of the development of the refractory metal alloys and in particular the Mo alloys, was initiated in the mid-to-late 1950's. At that time, the refractory metal industry was in the process of developing new alloys at the same time the aerospace industry was beginning to consider their use as primary structures. The original accent was on strength at temperature and not on fabricability. Alloying elements such as carbon, zirconium, and tungsten were used in ever increasing amounts, until some of the alloys were so brittle that they could not be easily fabricated. It was at this point in time that most of the reports on the difficulty of fabricating refractory alloys began to emerge and many programs designed to use these alloys were modified or dropped.

While most scientists and engineers remember the problems in refractory metals, few recognize the improvements that have been made in the last 15 years. Many of the brittle and difficult to fabricate alloys have been eliminated. New improved processing and casting techniques are now used and the metals in general have lower DBTTs as a result of lower interstitial contents. This trend can be seen in the molybdenum industry where alloys such as Mo-0.5 Zr, Mo-0.5 Ti, TZM, and TZC were created. For one reason or another,most of these alloys have been eliminated from major application with the exception of TZM. This alloy was initially difficult to fabricate and most of the forming was done at elevated temperatures. However, as the metal suppliers began to understand more about the metallurgy of the alloy, the forming temperature began to drop. Then, with the advent of the Navy Sheet Rolling Program,[31]

significant improvements were made in the formability of the alloy. This trend can be seen in Fig. IX-B-13.[18] Up to 1963 all corrugation was done at 300°C, however, as improvements were made in the alloy, this temperature began to drop until it is now at room temperature.

It is at this time that we should introduce the concept of old TZM vs new TZM. Old TZM is the material that was used before the Navy Sheet Rolling Program[31] and is the material most people think of when molybdenum is mentioned. This material required elevated temperatures for forming and in general was difficult to fabricate. The old TZM was used on the ASSET flight vehicle[32] and on the Dynasoar[33]. A typical ASSET panel is shown in Figure IX-B-14a. From this figure it can be seen that the panel is essentially riveted and that the corrugations have large, generous radii.

The new TZM is the product of the technology that was developed on the Navy Sheet Rolling Program. This material was evaluated on the Structural Sheet Evaluation Program conducted at McDonnell[34] and the resultant structure that was produced is shown in Figure IX-B-14b. From this figure it can be seen that the corrugations have sharp angles of over 120° and that the panels are joined by welding. A summary of the programs that have fabricated molybdenum into structure is shown in Table IX-B-6. From this table it can be seen that many molybdenum and TZM structures have been fabricated and successfully operated over the past 15 years. The fabrication is not as easy as steel and will require an understanding of the material. For example, TZM can be formed, free of cracks, provided adequate preparation of the sheet surface and edges are made and the material has the proper microstructure. Studies have revealed that surface contamination can effect formability. Figure IX-B-15 shows that if a small layer of surface is chemically removed, the DBTT can be significantly lowered.[18]

Since TZM is supplied in the cold worked and stress relieved conditions to keep a low DBTT, it becomes obvious that any shearing or blanking of a part will result in laminations. In subsequent forming, these laminations will propagate. Therefore, in forming one would like to have a edge free of lamination. Such edges can be obtained by abrasive or band sawing the blanket prior to forming. These are an example of the precautions that should be taken if TZM is to be successfully formed.

Once all the components are formed, the key question becomes how to provide a joint. There are a variety of ways this can be done ranging from welding to brazing.

There is considerable controversy about the viability of successfully joining Mo. For example in a recent report, A. P. Fraas[39] stated:

> "Molybdenum and tungsten do not appear suitable [for CTR application] because over 50 years of effort has failed to yield a method for making ductile welds in either of these materials, and research into the reasons for the brittle welds indicated that the problems are fundamental and it is highly unlikely that it will be resolved satisfactorily."

However, this statement seems to ignore the previously stated progress in the field over the past 15 years (Figures IX-B-13, 14, and 15 and Table IX-B-6).

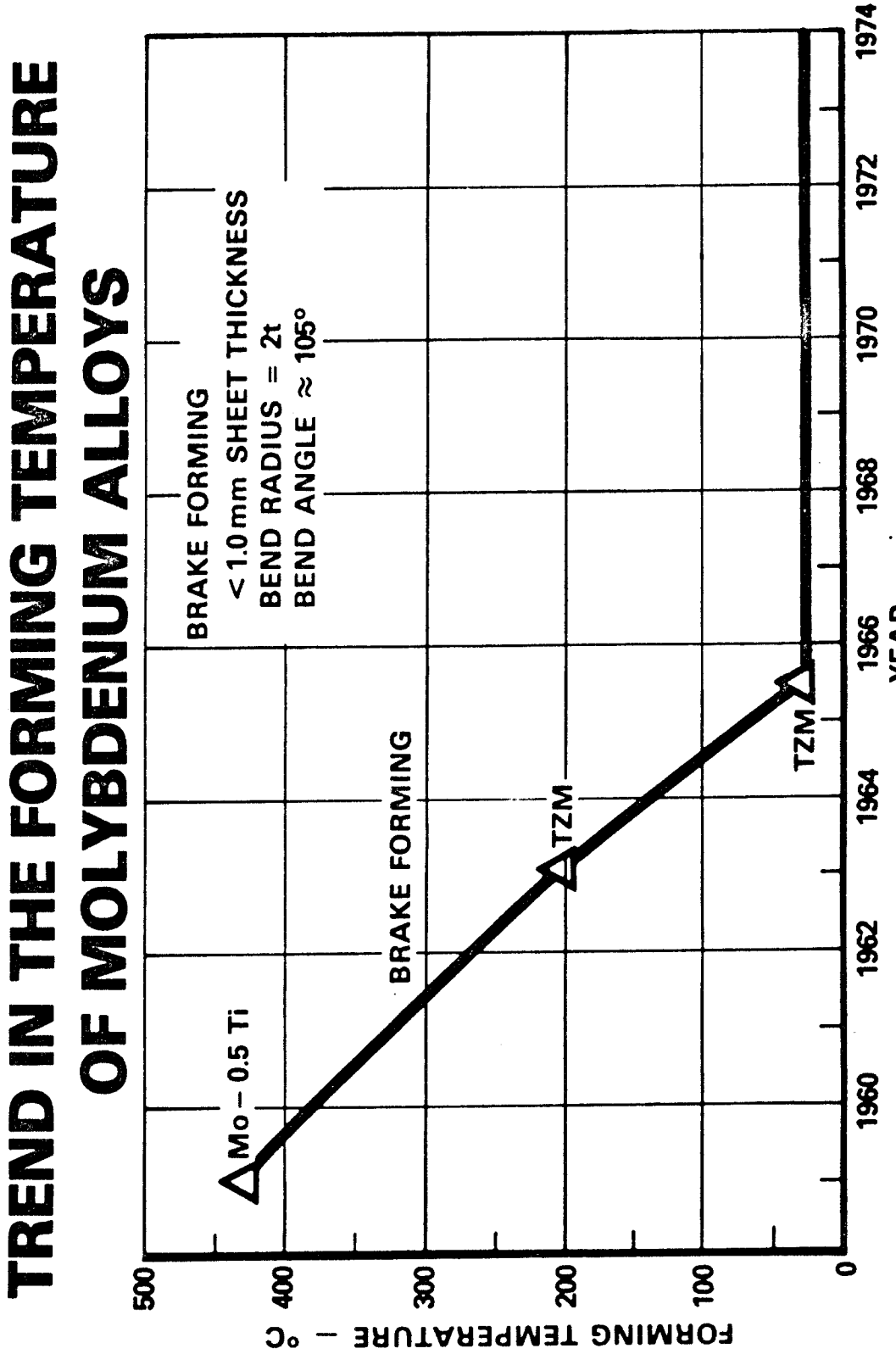
TREND IN THE FORMING TEMPERATURE OF MOLYBDENUM ALLOYS
BRAKE FORMING
< 1.0 mm SHEET THICKNESS
BEND RADIUS = 2t
BEND ANGLE ≈ 105°
Mo – 0.5 Ti
BRAKE FORMING
TZM
TZM
FORMING TEMPERATURE – °C
500
400
300
200
100
0
1960
1962
1964
1966
1968
1970
1972
1974
YEAR

FIG. IX-B-13

TYPICAL AIR FRAME COMPONENT

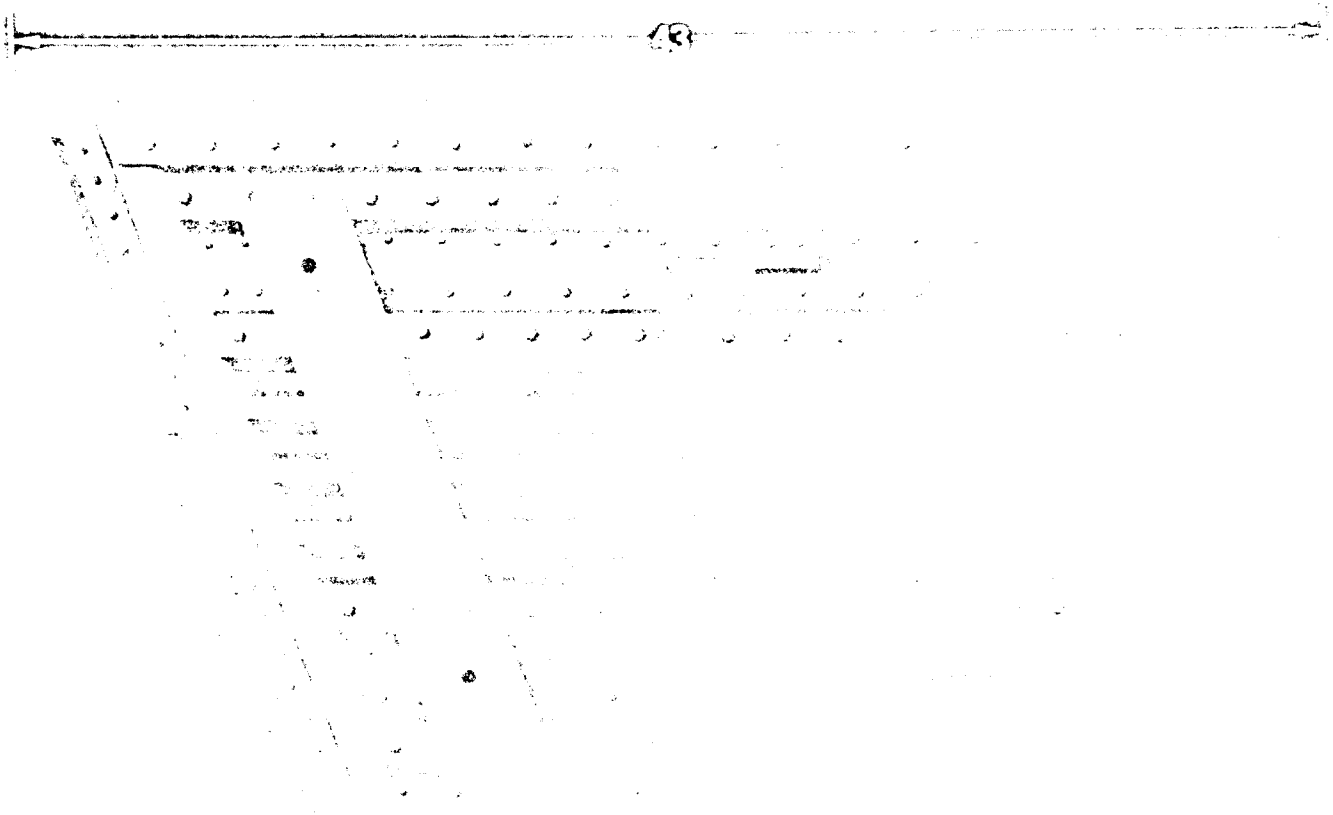

ALL DIMENSIONS IN CM

FIGURE 14-a

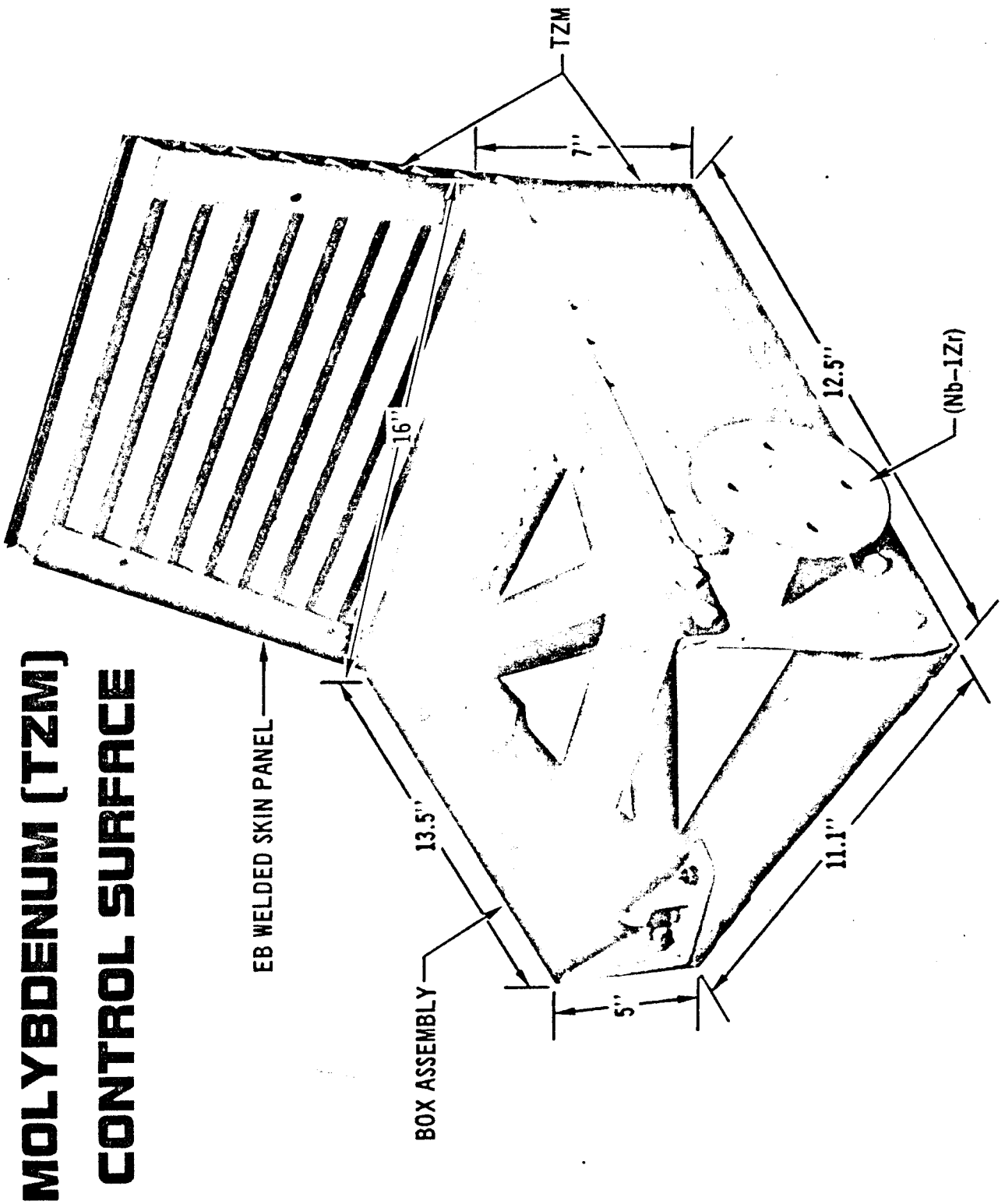

FIGURE IX-B-14b

TABLE IX-B-6

Summary of Major Studies Which Have Used Molybdenum

Program Name	Structure	Joining Approach	Reference
Dynasoar	Panel	Rivet	Boeing[33]
ASSET	Panel	Rivet	MDC[32]
TZM Sheet Evaluation Program	Control Surface	Weld/Mechanical	MDC[34]
Advanced Test Reactor	Electrodes/Tubes/Connectors	Weld	Solor[35]
DART	Fuel Can, Impact, Capsules	Weld	LASL[36]
Molten Salt Reactor Program	Tubes, Tanks	Weld	ORNL[37]
Potassium Turbo-alternator Design Study	Torque Tube and Shafts	--	G.E.[38]

For example, a recent Los Alamos Scientific Laboratory report[40] states:

"Past experience at LASL with electron bombardment welding of molybdenum and its alloys indicate that the aforementioned concern is unfounded, provided a series of straightforward precautions are evoked. These precautions are summarized below.

* Arc-melted material should be used exclusively. Pressed and sintered molybdenum is too porous and impure to render strong defect-free welds.

* Extreme care should be exercised in maintaining a pure and inert environment during the welding.

* Proper pre-treatment and post-treatment (stress relief, joint design, preheating) procedures should be adopted.

These procedures generally do not present insurmountable problems and are in fact similar to joining procedures employed for most refractory metals.

The experience at LASL with molybdenum welding, although on a small scale relative to the CTR requirement, has been diverse and in most cases routine: molybdenum welds made on irradiation capsules (R. Krakowski, Thermionics Program), high-temperature rock penetrators (J. Rowley, Subterrene Program), thermal radiation shields and insulation (W. Turner, Decomposed Ammonia Radioisotope Thruster-DART). The final report for DART[5] documents a specific experience with molybdenum. For a given application the welding of molybdenum has been so routine that detailed fabrication reports were not warranted.

Of particular note in Reference 5 (p. 8)* is the statement:

"Weldability varies inversely with impurity level. It is always beneficial to preheat molybdenum into the ductile range prior to welding, but microcracking upon subsequent cooling can be avoided only if the level of impurities is low."

Given proper purity control, the weldability of both molybdenum and TZM appears facile. Although additions of titanium and zirconium to molybdenum in small amounts (<1 w/o) appear to have no significant influence on weldability, other benefits are accrued by alloying (see p. 8 of Reference 5).

The foregoing documentation is not presented to indicate that electron beam welding of molybdenum and its alloys is as easy as TIG welding a 300-series stainless steel. However, the problems associated with the former system are of a degree to allow good weldments to be achieved routinely."

* of reference 36

EFFECT OF SURFACE REMOVAL ON FORMABILITY OF TZM SHEET

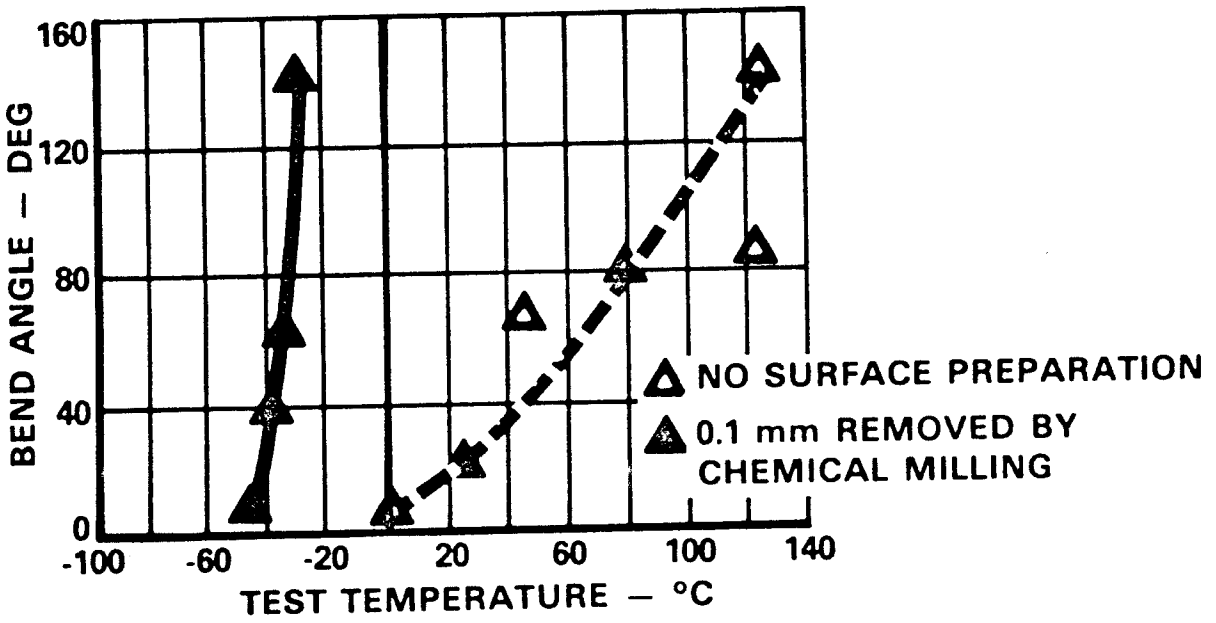

FIG. IX-B-15

This report also goes on to say,

> "(the) anticipated difficulties in achieving good molybdenum welds are not severe enough to warrant exclusion of it as a candidate structural material in the CTR."

Additional procedures for the welding of TZM can be found in a report by Hanks[41].

After studying the literature, we come to the conclusion that the pessimism over joining Mo is given too much credence and the shear weight of experimental evidence does not support such conclusions. Therefore, while we realize that welding large components of Mo alloys in the field will be difficult (as will the welding of Nb and V alloys), it will not be serious enough to remove it from consideration as a viable CTR structural material.

Another approach which has successfully been used to join molybdenum is brazing. Brazing is one of the classic joining techniques and molybdenum has been successfully brazed in the electronic industry for many years. These joints, however, do not require high strength nor do they have to contend with the CTR environment. If brazes are to be used in a CTR, the melting point of the braze must be above the operating temperature of the component, in this case 1000°C. In addition, the braze must not embrittle the structure after long periods of exposure, it must be compatible with the coolants, it must not interfere with breeding, it should possess sufficient strength and ductility to be used in a structural joint. From the large number of brazes that have been used on TZM we have selected 5 which appear to offer potential. These brazes are presented in Table IX-B-7. From this table it can be seen that all of these brazes have melting temperatures above the service temperature of the component. Further work will have to be done to determine their structural performance, but at this time the Ti-Cr-Be braze appears to have the most promise.

IX-B-5 Neutronics

The neutronics aspects of a reactor material are critical if breeding ratios of one or greater are to be achieved. There are five cross sections (or sets of cross sections) which are important

a.) Absorption (n,γ)
b.) Neutron multiplication $(n,2n)$
c.) Hydrogen isotope gas production $(n,p),(n,n'p),(n,D)$
d.) Helium gas production $(n,\alpha),(n,n'\alpha)$
e.) Inelastic scattering (n,n')

These reactions lead to three other consequences which could result in modified performance for a fusion reactor. They are:

i) Induced radioactivity
ii) Afterheat
iii) Chemical changes in the host material.

BRAZE ALLOYS SUCCESSFULLY USED ON TZM

COMPOSITION	LIQUIDUS TEMPERATURE(°C)	REMARKS
Ti-25% Cr-3% Be	1110	REMELT TEMPERATURE ABOUT 1700°C AFTER DIFFUSION TREATMENT (980°C, 8h + 1040°C, 16h + 1095°C, 8h + 1120°C, 40h). NORTHROP (STONE et al., 1967) PRODUCED DUCTILE CLOSED-CELL HONEYCOMB FOR STRUCTURAL AND HEAT-SHIELD APPLICATIONS THAT HAD SERVICE CAPABILITY AT 1600°C.
PALLADIUM	1146	NARMCO WORK ON EXOTHERMIC BRAZING (LONG, 1966).
Co-21% Cr-21% Ni-8% Si-3.5% W-0.8% B-0.4%C	1190[a]	SOLAR ROCKET NOZZLE(SOLAR DIV., 1963).
Ti-49% Zr-2% B	1250	FUEL SUBASSEMBLIES FOR ARGONNE ADVANCED RESEARCH REACTOR (KOLBA et al., 1968).
Ni-7% Si-5% Cr-4% Co-1% W-1% B	1250[a]	DISSIMILAR-METAL BRAZES BETWEEN TZM AND THE NICKEL-BASE SUPERALLOYS HASTELLOY X AND RENE' 41(PATTEE et al., 1968).
Pd-40% Ni	1300[a]	DISSIMILAR-METAL BRAZES BETWEEN TZM AND THE NICKEL-BASE SUPERALLOY HASTELLOY X AND THE COBALT-BASE SUPERALLOY L605 (PATTEE et al., 1968).

a – BRAZING TEMPERATURE

TABLE IX-B-7

Two problems for Mo are its large number of isotopes (seven) and the fact that Mo has not been used as a major fission reactor material and therefore received little attention until now. The problem is that not all of the above cross sections have been measured for the 7 Mo isotopes and we must rely to a large degree on calculated values if we are to obtain any quantitative information. Fig. IX-B-16 is a plot of the parasitic absorption cross section (items a,c,d,e above) for Al, 316SS, V, Nb, and Mo.[42-43] These cross sections do not include the (n,2n)cross sections because they are actually beneficial in that they result in neutron multiplication.

There are three general conclusions that can be drawn from Figure IX-B-16

1.) Aluminum is most desirable in the low energy neutron range (E~0.1 MeV). This element is followed by 316SS, V, Mo, and Nb in order of increasing cross section. In fact, the Nb parasitic absorption cross section is ~2 orders of magnitude higher than Al in this range. However alloying elements may modify this conclusion.

2.) The order of desirability is essentially the same in the intermediate (0.1-3 MeV) range with the exception that V now has a lower parasitic cross section than 316SS.

3.) In the high energy regime (3-14 MeV) Mo actually has the lowest parasitic cross section followed by Nb, V, Al and 316SS in that order. The high energy cross sections are dominated by (n,p) and (n,α) reactions which vary by factors of ~5. This competition not only removes a neutron which could have produced another tritium atom, but it does so at an energy where the Li-7 (n,T) reaction could give another neutron back to the system along with a tritium atom.

The (n,2n) reaction (Figure IX-B-17) partially compensates for this parasitic absorption but the extra neutron usually has energy below the $Li^7(n,T)n'He$ threshold. This means that the number of potential tritium atoms bred by the initial neutron is not twice what it was before the (n,2n) reaction, but something less than two. An idea of the importance of the net effect is illustrated by a calculation by Cheng[44] in which the breeding ratio was calculated for a liquid lithium system with varying amounts and types of structural materials, (Figure IX-B-18). The breeding ratio was consistently highest for the V system and 5% of structure reduced the zero structure value by the following amounts, V(5%), SS(10%), Mo(13%), Nb(13%). It is anticipated that the results for Al would be between V and SS.

The gas production cross sections for the potential CTR materials are displayed in Figures IX-B-19a and 19b. The (n,α) cross section for a fusion neutron spectrum is quite high (>100 mb) for both Al and stainless steel. Helium production rates of 200 to 400 appm/year are not uncommon.[45] The (n,α) cross sections for the refractory metals are reduced by a factor of 5 to 10 with Nb having the lowest helium production rate, followed by Mo and then V. The production of helium atoms is especially detrimental because they tend to end up on grain boundaries at high temperature and can cause severe embrittlement.

The hydrogen production cross section for Al and 316SS are also quite high but the end result is not expected to be so serious in the steel as hydrogen can easily diffuse out of it at high temperatures. The situation for Al is not so clear because the solubility is <<1 appm. Again, the refractory metals have low (n,p) cross sections with Mo having the lowest of the group.

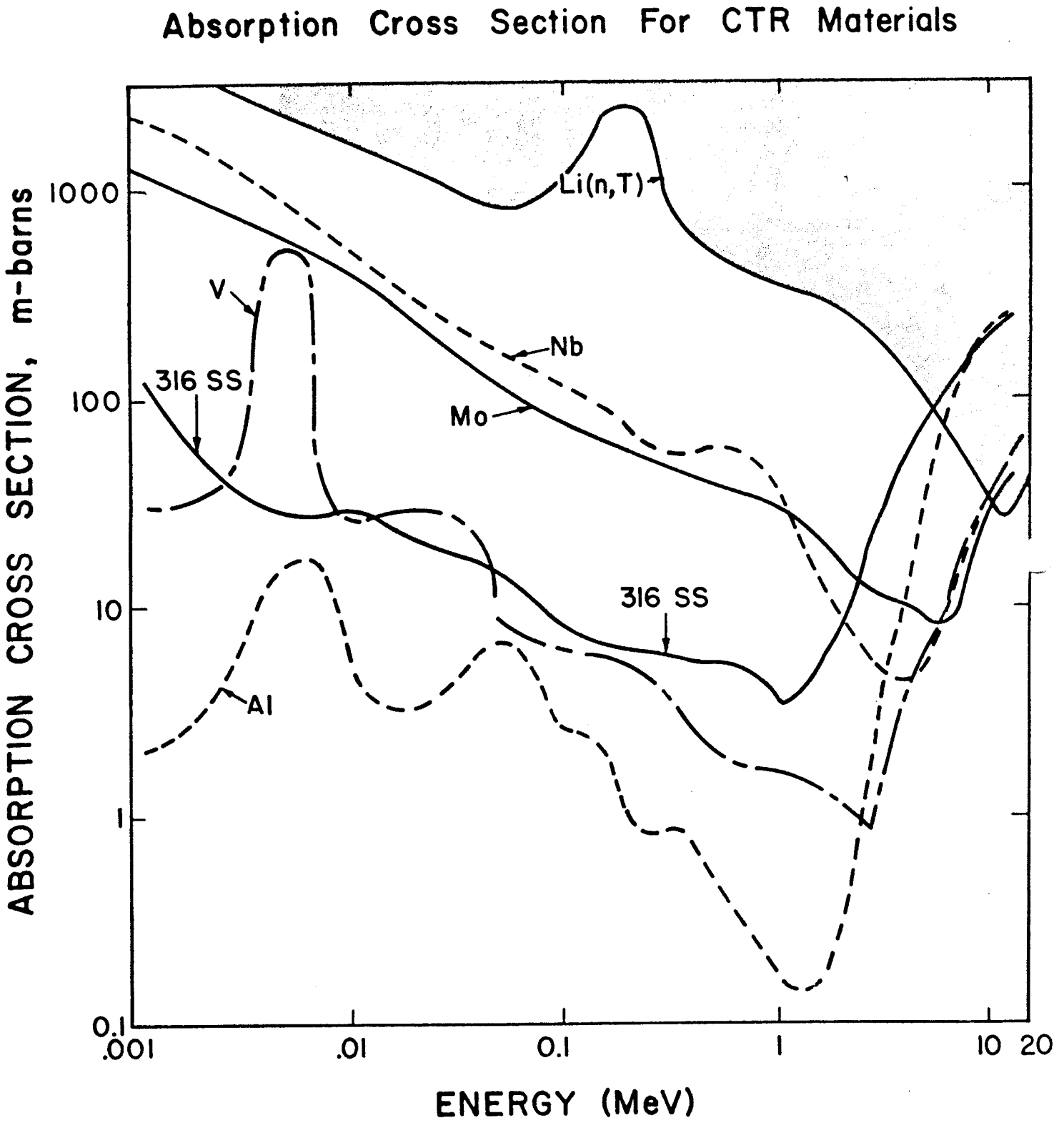
Absorption Cross Section For CTR Materials
ABSORPTION CROSS SECTION, m-barns
1000
100
10
1
0.1
.001
.01
0.1
1
10
20
ENERGY (MeV)
Li(n,T)
V
316 SS
Nb
Mo
316 SS
Al

FIG. IX-B-16

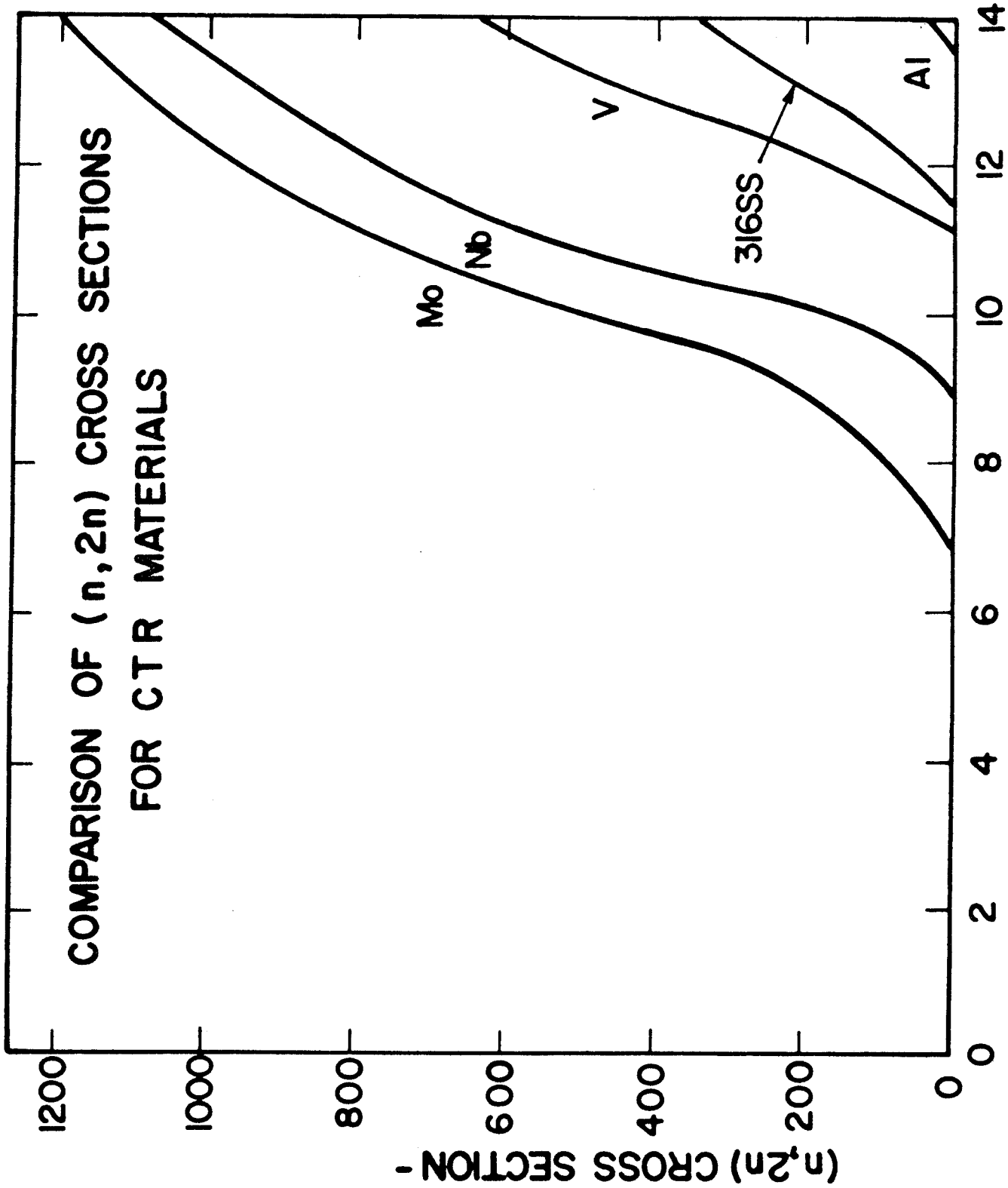
COMPARISON OF (n,2n) CROSS SECTIONS
FOR CTR MATERIALS
Mo
Nb
V
316SS
Al
(n,2n) CROSS SECTION - mb
0
200
400
600
800
1000
1200
0
2
4
6
8
10
12
14
E_n - MeV

FIG. IX-B-17

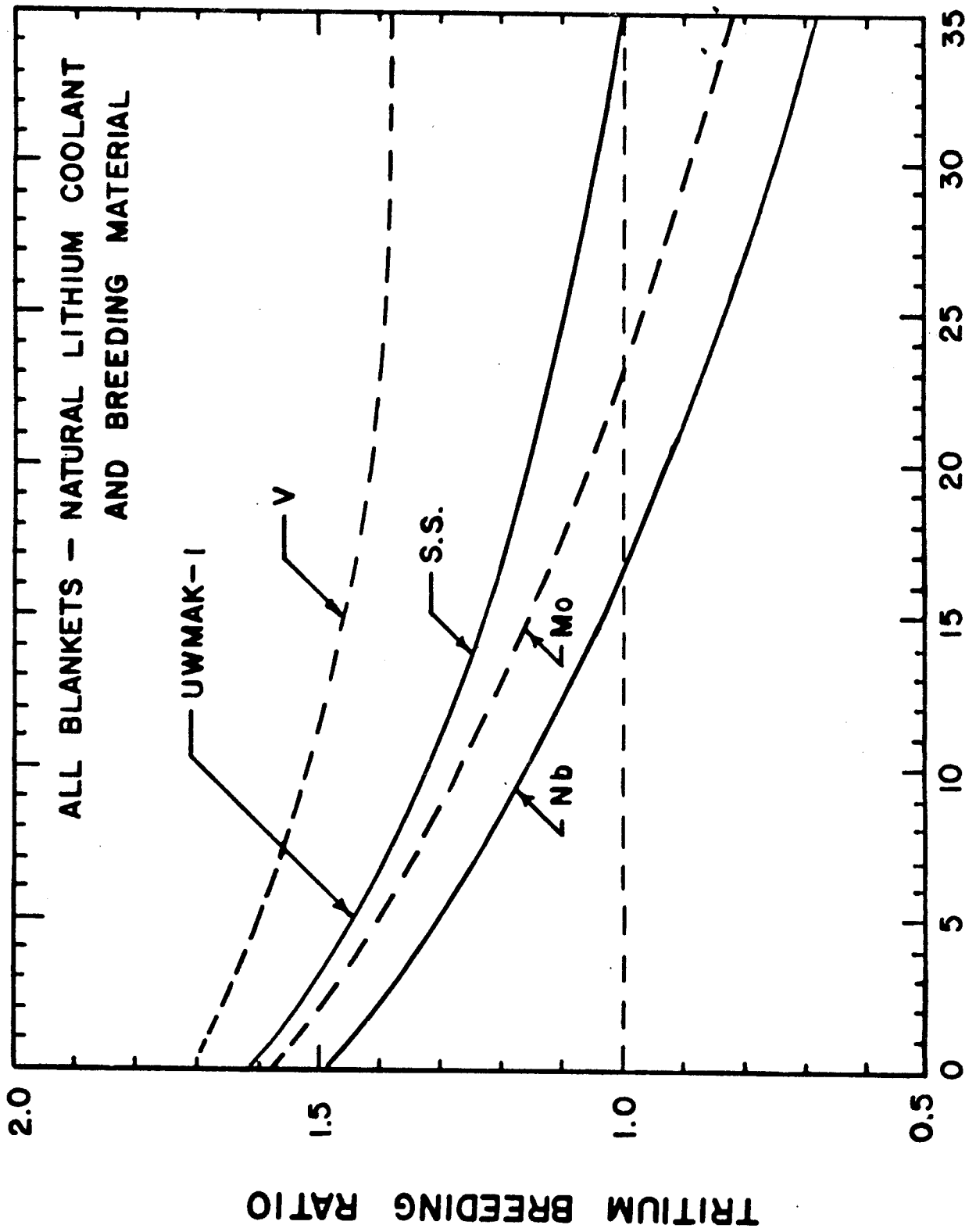

FIGURE IX-B-18

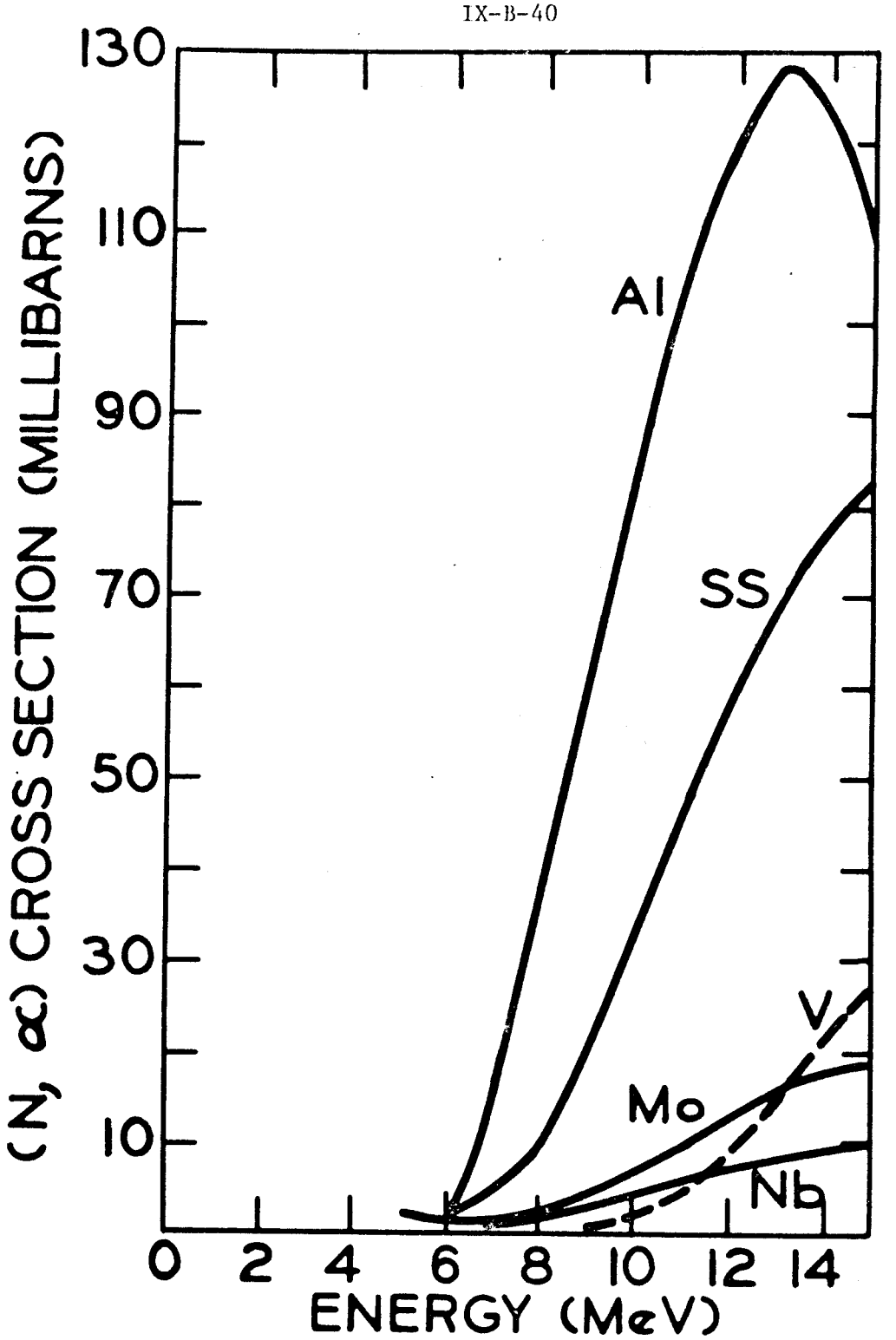

FIG. 19a COMPARISON OF THRESHOLD (N, α) CROSS SECTIONS FOR 316 SS, V, Nb, Mo AND Al

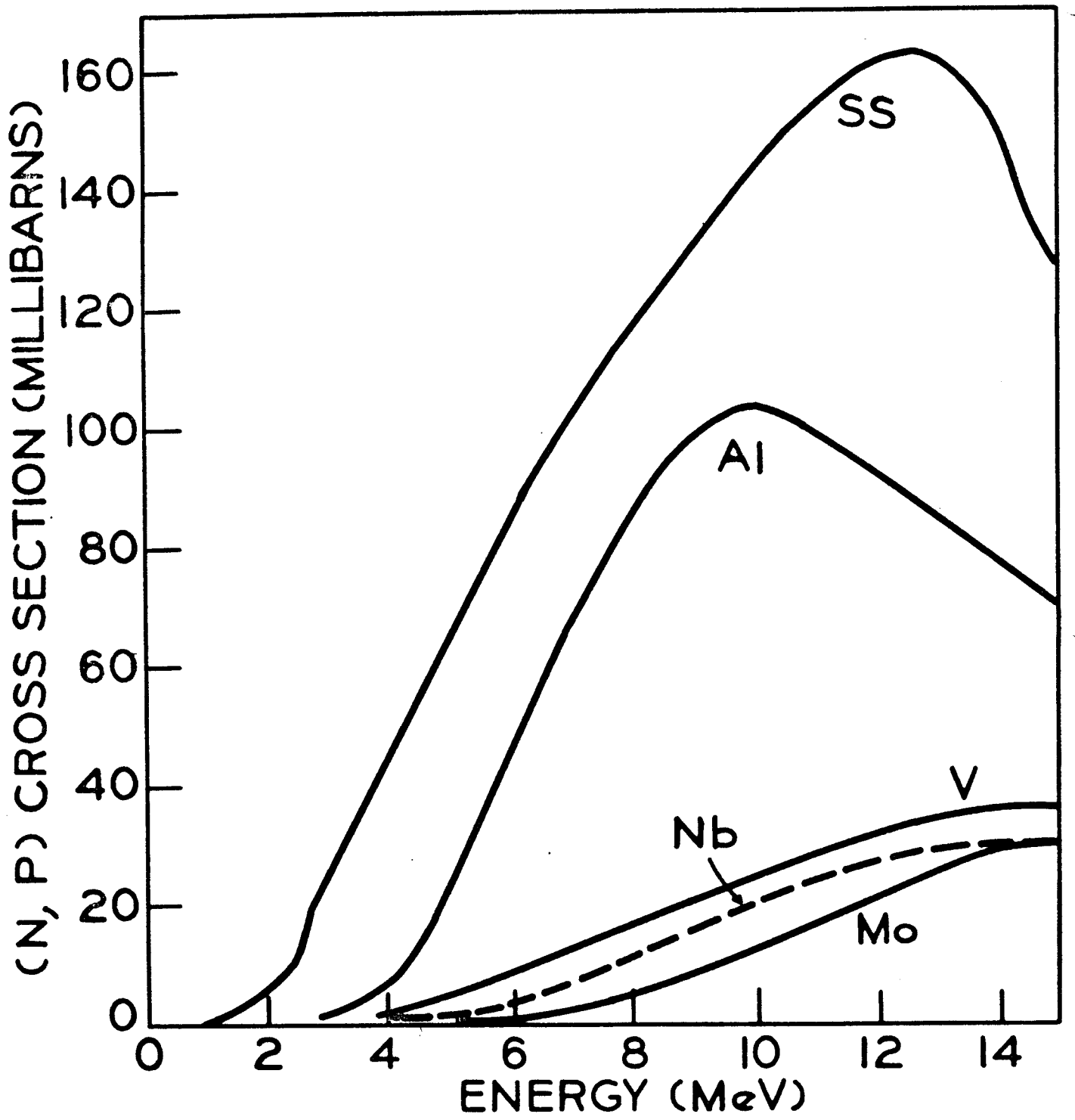

FIG. 19b COMPARISON OF THRESHOLD (N, P) CROSS SECTIONS FOR 316 SS, V Nb, Al AND Mo

The amount of radioactivity induced in TZM, Nb 1Zr, V-20Ti, 316SS and 2024 Al* by a typical CTR neutron spectra is given in Table IX-B-8 and the decay of the activity is plotted in Figure IX-B-20. The important points from this comparison are

- All of the materials have ~0.8-5 curies per watt induced in them by 2 years of irradiation at 1.25 MW/m^2.
- The following approximate times are required for the activity to decay by a factor of 10, V-20 Ti (20 minutes) 2024 Al (1 day), TZM and Nb-1Zr (10-20 days) and 316SS (2 years).
- The activity after 1 year decay is (in decreasing order) 316SS, Al 2024, V-20, Ti, TSM, and Nb-1Zr. The spread in activities is a factor of $\sim 10^3$.
- The activity of V-20 Ti decays to inconsequential levels after 100 years while the activity of the TZM structure is a factor of ~5 higher than for 316 SS.

The major isotopes contributing to the activities after 100 years of decay are listed in Table IX-B-9. As might be expected the V-20Ti has no long lived isotopes with $t_{1/2} > 1$ year. It is also noted that the Cu, Si, Fe, and Zn alloying elements in 2024 Al do not contribute to the long lived activity, it is dominated by the Al-26 decay. The only very long lived isotopes in the 316SS system is Ni-59 ($t_{1/2}$ = 80,000 years) and Mo-93 from the Mo alloying additions ($t_{1/2}$ = 10,000 years) The Mo-93 is dominant and holds the radioactivity of the steel to $\sim 10^{-4}$ curies/watt for several thousand years.

There is only one major isotope in the Nb-1Zr system which accounts for the activity beyond 100 years, Nb-94 ($t_{1/2}$ = 20,000 years). The Nb-94 isotope will undoubtedly be dominating for 50,000 years or so after shutdown and is a liability for the Nb system. TZM also has a major long lived isotope in Mo-93 ($t_{1/2}$) = 10,000 years whose activity after 100 years levels out at 2×10^{-4} curie/watt. Even though the Mo system will have a specific activity of ~400 times that of Nb-94, the absolute value for a large reactor ($\sim 10^6$ curies) is divided by a large mass so that the specific activities is only a few millicuries per cm^3 after 100 years.

A measure of the hazard potential represented by these isotopes can be obtained by calculating the biological hazard potential (BHP) which is simply the amount of radioactivity produced divided by the maximum permissible concentration of each isotope which produces that radioactivity. Representative values (all normalized to a MW_t of energy generated) are listed in Table IX-B-10 and Figure IX-B-21 for a 2 year operation time. The BHP of each of the alloy is given at reactor shutdown, and as a function of time after shutdown. The specific isotopes governing the long time behavior of the element are given in Table IX-B-9. Note that TZM has the highest BHP at shutdown followed by 316SS, Al-2024, Nb-1Zr and V-20Ti in that order. After 1 year of decay, the order has changed to 316SS, 2024 Al, V-20Ti, TZM and Nb-1Zr in order of decreasing values. It is clear from this kind of consideration that the V system represents no significant hazard after 100 years. The Mo, Nb and Al systems represent only a moderate problem and 316SS requires more attention.

*Note that only the alloying elements of Cu and Mg were used here, normal impurities such as Fe were not included.

Typical Results of Activation in CTR Materials (a)(b)

SYSTEM	ACTIVITY (Ci/watt)		
	t=0	1y	100y
Al-2024	0.9	3×10^{-3}	9×10^{-8}
316 SS	1.1	0.2	5×10^{-5}
Nb+1Zr	4.4	2×10^{-5}	6×10^{-7}
V+20Ti	1.2	3×10^{-3}	$< 10^{-36}$
Mo (TZM)	4.1	5×10^{-4}	2×10^{-4}

a) 2 years operation 1.25 MW/m^2 wall loading

b) Reference 46

TABLE IX-B-8

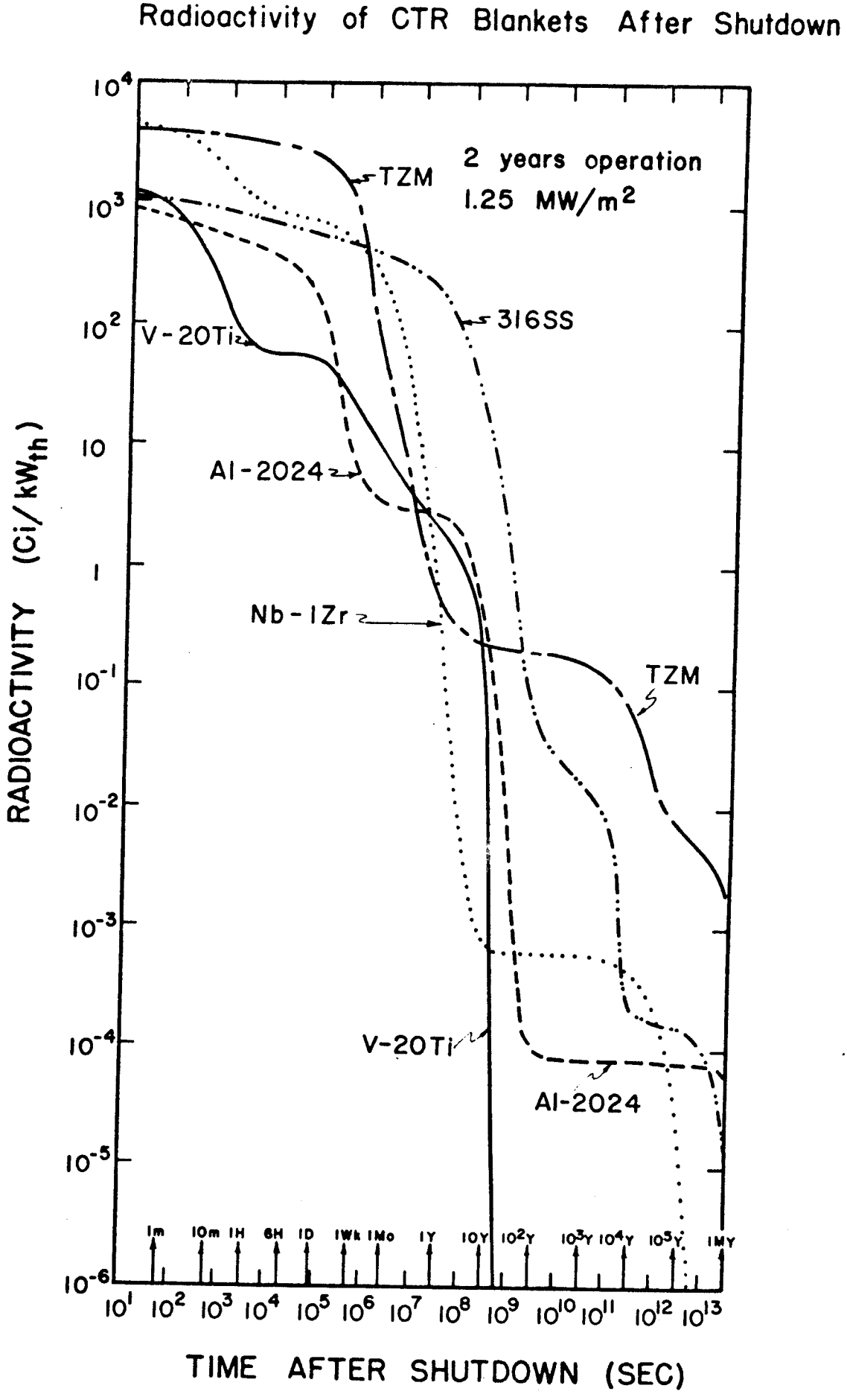

Figure IX-B-20

Table IX-B-9

Major Long Lived Radioisotopes in CTR Materials, 2 Year Operation

System	Isotope	$t_{1/2}$ (Yr.)	100 Yr. BHP (km^3 AIR/MW_t)
Al-2024	Al-26	735,000	0.9
316 SS	Ni-63	92	300
	Mo-93	10,000	0.01
	Ni-59	80,000	0.002
	Tc-99	215,000	0.1
V-20Ti	None	-	-
Nb-1Zr	Nb-94	20,000	0.4
	Zr-93	1,100,000	0.001
Mo(TZM)	Mo-93	10,000	0.5
	Nb-94	20,000	0.0002
	Tc-99	215,000	5

TABLE IX-B-10

TYPICAL RESULTS OF ACTIVATION IN CTR MATERIALS

SYSTEM	BHP (km^3 air/MW_t)		
	t = 0	t = 1y	t = 100y
Al (2024)	73,000	3,000	0.9
316 SS	156,000	50,000	300
Nb-1Zr	39,000	10	0.4
V-20Ti	27,000	1400	~0
TZM	391,000	200	5

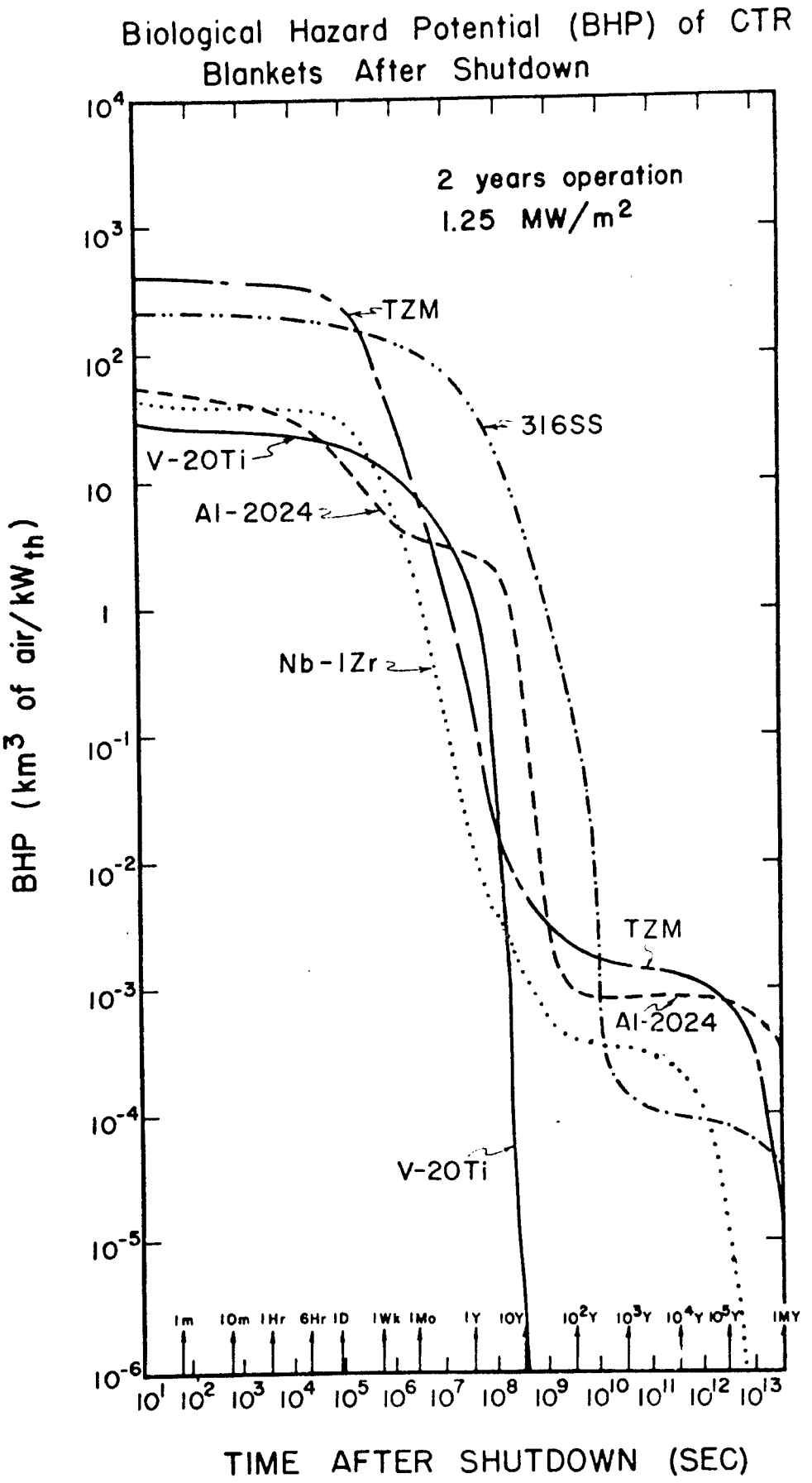

Figure IX-B-21

The radioactivity described above can produce afterheat which decays in the manner shown in Figure IX-B-22. Table IX-B-11 also contains a few values for the afterheat at shutdown and after 1 and 100 years of decay. This type of comparison shows that at shutdown the V-Ti alloy has the highest afterheat level. However, V-20Ti afterheat drops by 3 orders of magnitude in a year. At that time, 316 SS has the largest afterheat followed by 2024-Al, V-20Ti, TZM and Nb-1Zr. The afterheat in 316SS continues to drop with time whereas that associated with Nb and Mo saturates because of long lived isotopes. At 100 years after shutdown, TZM has an afterheat level of ~4×10^{-6}% while 316SS, Nb-1Zr, and 2024-Al are in the 1-8×10^{-7}% range.

The afterheat numbers can be put into more perspective by considering the maximum afterheat density in the first wall. Representative heat generation rates in watts/cm^3 for a 5000 MW_{th} reactor are given below (for wall of $1.13 \times 10^7 cm^3$)

Maximum Afterheat Density - Watts/cm^3 *

	t = 0	1 Hour	1 Week	1 Year	100 Years
TZM	0.52	0.26	0.05	3×10^{-4}	7×10^{-5}
Nb-1Zr	0.35	0.35	0.21	3×10^{-6}	1×10^{-7}
V-20Ti	0.30	0.12	0.02	8×10^{-4}	$<10^{-37}$
2024-Al	1.03	0.63	3×10^{-3}	1.5×10^{-3}	3×10^{-7}
316SS	0.57	0.39	0.12	0.04	5×10^{-7}

It is clear from this consideration that there is very little distinction between all the alloys for the first hour after shutdown. The values of 0.1 to 0.8 watts/cm^3, while not neglible, are not too difficult to handle with normal convection or conduction. Even under adiabatic conditions (a very pessimistic case) the rate of temperature increase is on the order of 1°C per second which could presumably be controlled by emergency cooling after a few minutes.

Finally, the neutronic reactions can often lead to transmutations which can change the chemical composition of the host material. Table IX-B-12 shows how the composition of major metals can change with fluence. One potential problem could occur in Al where Si is produced at a rate of approximately 0.004%/year per MW/m^2 and the solubility limit is only 0.06% at 200°C.[47] The production of Zr at the rate of ~0.15% per MW/m^2 per year could also be a problem if the wall loading was as high as 2 MW/m^2. The V-20Ti, 316SS and Mo systems all have rather inconsequential transmutations and seem to present no particular problem from the aspect of phase changes.

* For First Wall Only

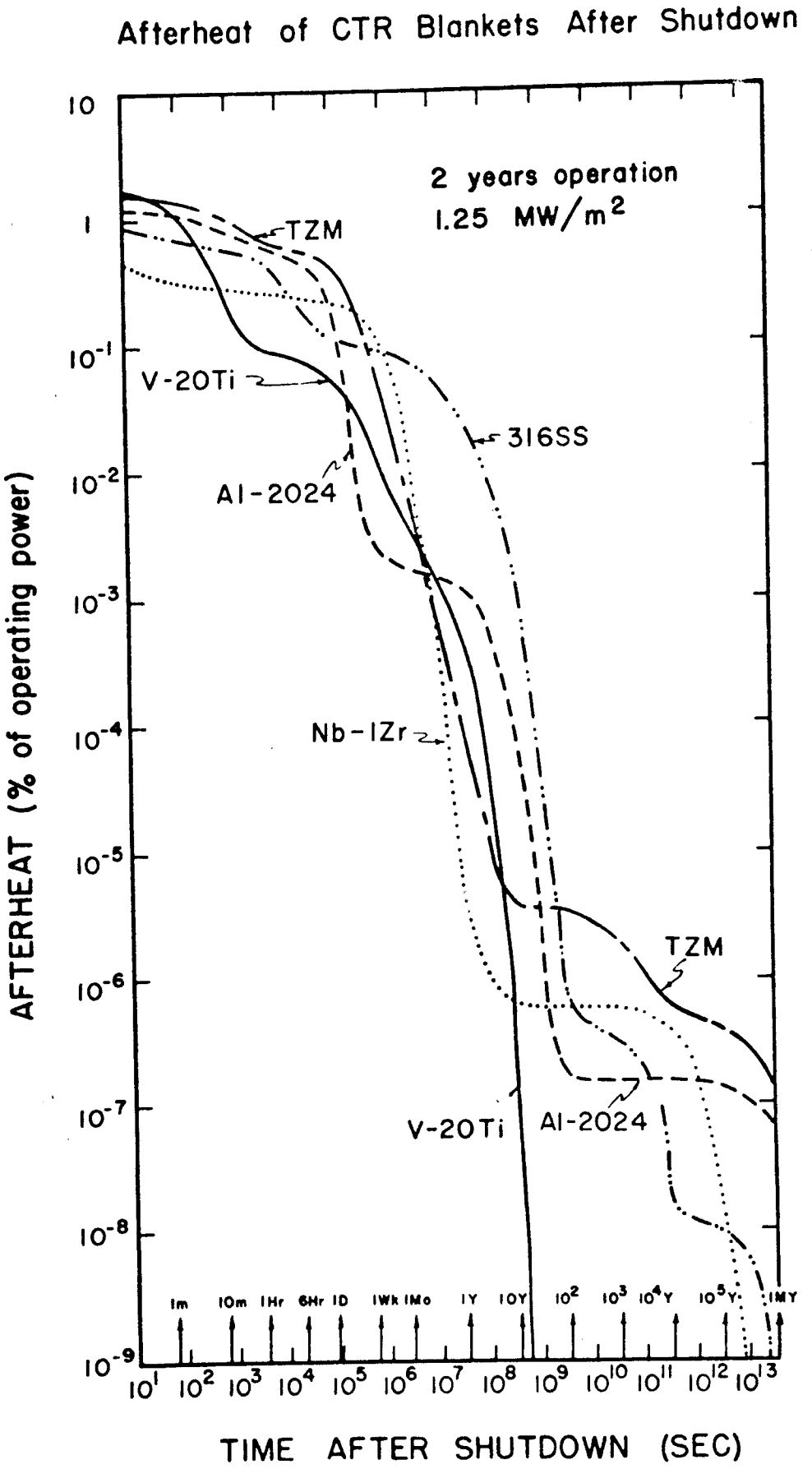

Figure IX-B-22

TYPICAL RESULTS OF ACTIVATION IN CTR MATERIALS

SYSTEM	AFTERHEAT (%)		
	t=0	1y	100y
Al-2024	1.1	1×10^{-3}	1.8×10^{-7}
316 SS	0.9	0.03	8×10^{-7}
Nb-1Zr	0.45	8×10^{-6}	6×10^{-7}
V-20Ti	1.5	7×10^{-4}	$<10^{-37}$
TZM	1.4	2×10^{-4}	3×10^{-6}

TABLE IX-B-11

Table IX-B-12

Major Chemical Changes in CTR Materials Due to Transmutations[a]

System	Transmutation	At % / Yr-Mw/m^2	Approx. At % Solubility at 0.4 Tm
		At %	
Al	Mg	0.040	4
	Si(b)	0.004	0.006
316 SS	Mn	0.12	60
	V	0.02	20
	Ti	0.005	~3
V	Cr	0.013	S. Soln
	Ti	0.008	70
Nb	Zr	0.07	10
Mo	Tc	0.04	?
	Ru	0.003	?

(a) Model used for Radioactivities, BHP and Afterheat Calculation in Tables IX-B-9, 10, & 11.
(b) Could represent problems in pure Al, but is not of importance in aluminum alloys.

IX-B-6. Chemical Compatibility

The ability of structural materials to safely operate in the corrosive environment of a CTR is absolutely essential. The primary problems come from the high temperature coolants such as liquid lithium, lithium salts, or contaminants in high pressure helium. We can only cover a few general features here and the reader is referred to references 48-50 for further information.

The most probable coolant in a high temperature-large power reactor is liquid lithium (at least with the present state of technology). There are two properties of the liquid metal-structural system which are of interest -

(a) solubility of the metal in liquid lithium at the maximum operating temperature.

(b) the impurity transfer between the structural metal and the liquid.

We exclude from this discussion Al because of its high solubility in lithium.(51) The situation with respect to austenitic steel has been reviewed elsewhere(52) and only a few pertinent points will be mentioned here. Below 400°C, ferrous alloys are resistant to lithium corrosion. At higher temperatures, (700-800°C) steels are decarburized(53) and Ni is selectively leached from the alloy and the lithium penetrates into the metal.(54) The penetration values range from 0.0013 cm in 160 hours at 538°C to 0.010 cm in 1000 hr at 650°C. Recent work at Tokai has revealed that weight losses of ~1.2 mg/cm^2 per 1100 hour exposure at 600°C can occur.(55) It is generally concluded that for long term operation in flowing lithium without significant weight loss, the temperature of the steel should be maintained below 500°C.(52)

The situation is much better for the refractory metals in that they are relatively insoluble in high temperature lithium. This is exhibited in Figure IX-B-23 where the typical solubilities of Mo, Nb and V are plotted as a function of temperature in high purity lithium. This data shows that even at 1000°C the solubility of Nb is <50 ppm (wt) and that for Mo is <20 ppm. The solubility of V at a typical operating temperature of ~800°C is also <50 ppm by weight. To give some perspective to these numbers one should note that in UWMAK-III the total lithium inventory is ~4 x 10^5 kg and the weight of the Mo structure is ~3.5 x 10^5 kg. If as much as 20 appm is dissolved into the lithium then ~5 kg of the molybdenum structure would be in the coolant. This is only 2 x 10^{-2}% of the total structure and hence would represent no serious problems. However, one should not forget that this dissolved structural material will become activated and could easily be released into the environment if the coolant were to escape the reactor and catch fire. Hence, there is an incentive to keep the solubility as low as possible from a radioactive hazard standpoint.

The next problem is the potential interstitial impurity atom transfer from the coolant to the metal or from the metal to the coolant. Smith and Natesan(56) have reviewed the available data for the Li-(Nb,V, Mo, Cr, Zr, and Ti) system with respect to carbon, oxygen and nitrogen. The following general conclusions were drawn:

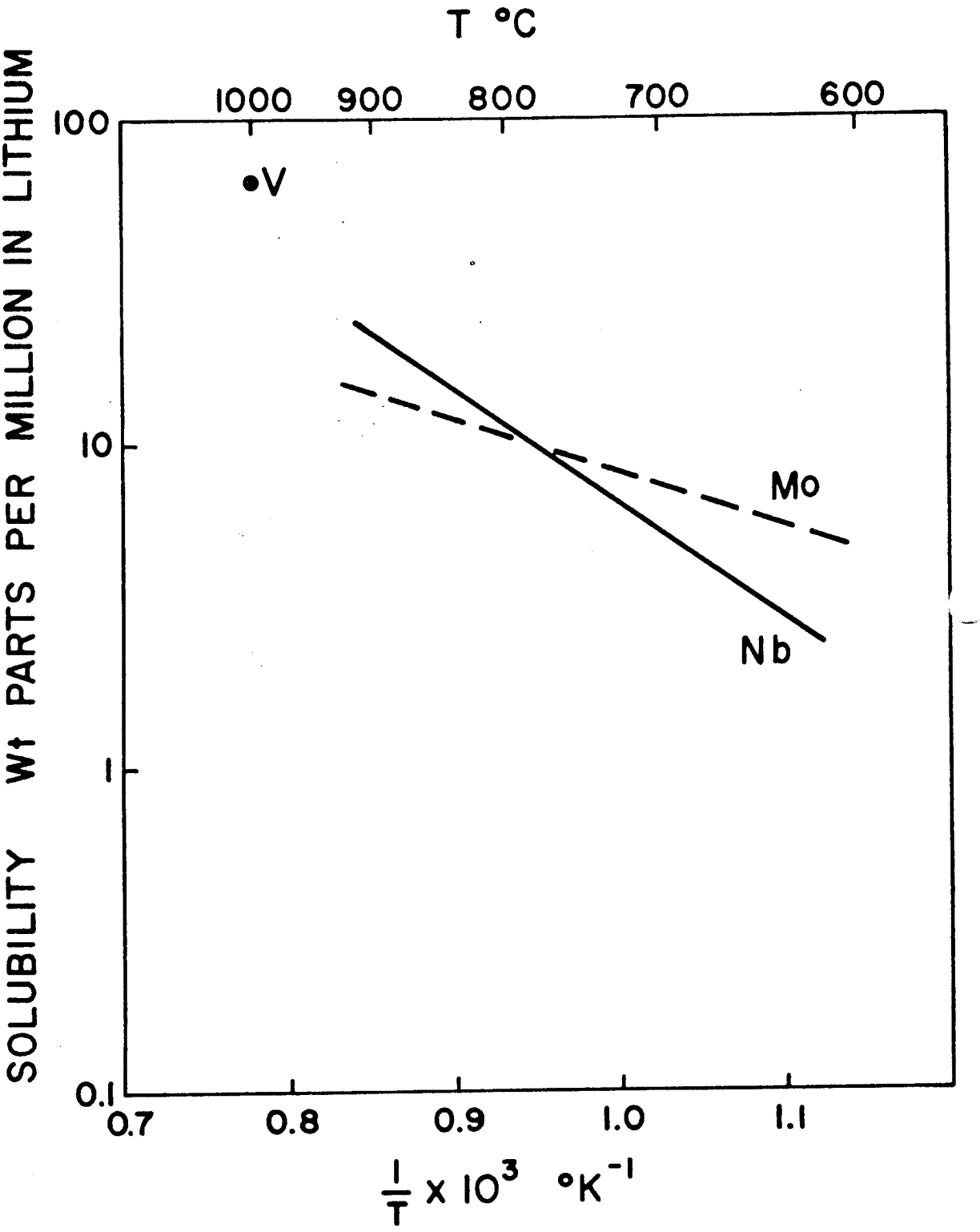

FIGURE IX-B-23 SOLUBILITY OF REFRACTORY METALS IN LITHIUM

(1) Lithium will tend to extract oxygen from Mo, Nb and V over a wide range of temperatures. However, if Zr is added as an alloying element it can actually reverse the flow of oxygen and significant impurity contamination can occur over the temperature range 600-1000°C. The addition of Ti or Cr to the refractories has little effect (see Fig. IX-B-24).

(2) Pure Nb and V (as well as their alloys with Zr and Ti) will be subject to high rates of nitrogen contamination in lithium which contains more than 0.001 weight ppm of nitrogen. This is a very serious problem because techniques to maintain such low levels of nitrogen will be very expensive to install and maintain. Molybdenum, on the other hand, will actually be purified of nitrogen over the 600-1000°C temperature range. If substantial amounts of Zr and Ti are added to Mo, internal nitriding could occur, but if the concentrations of these alloying elements are kept to a few percent or less, there should be no serious problems. (In fact, the Ti and Zr are added to product internal carbides and nitrides for strengthening reasons.)

(3) The situation with respect to carbon is much the same as for nitrogen except that the addition of Cr to the base refractory metals will induce carburization. (Figure IX-B-24). Another way of stating the conclusions of the above study is that pure Mo will not be contaminated in lithium by O, N, or C over the 600-1000°C temperature range. The addition of small amounts of Zr and Ti will be beneficial in that they will combine with impurities and form carbides, nitrides or oxides inside the metal and increase the strength properties. Large amounts (>5-10%) of Ti or Zr will be counterproductive and should be avoided.

In summary, Nb and V will not be contaminated by oxygen but they could be quite subject to nitrogen and carbon contamination. Alloying with Ti or Zr will make matters worse. This extreme sensitivity to nitrogen and carbon levels in the lithium is one reason why dissimilar metals, such as steel, cannot be used in the same coolant loop which contains Nb or V.

Figure IX-B-25 gives one an idea of how stable the nitrides and carbides of these refractory metals are with respect to the impurity levels in lithium. The minimum carbon concentrations attainable in cold trapped systems are also given. The first observation is that simple cold trapping will prohibit Li_3N or Li_2C_2 formation, but it will not be sufficient to prevent the formation of refractory metal nitrides or carbides. The one exception to the latter statement is that the formation of Mo_2C can be prevented below 700°C by cold trapping. It is also seen that hot trapping with Ti or Zr will be necessary to prevent formation of the nitrides and carbides of refractory metals.

The overall conclusion that we draw with respect to compatibility of the refractory metals in reactor grade lithium is -

(1) Mo is by far the most desirable material and small additions of Ti and Zr will not reduce this quality.

(2) V and Nb are subject to high contamination rates in reactor lithium unless the concentrations of the impurities can be maintained to much less than

FIGURE IX-B-24 TEMPERATURE DEPENDENCE OF THE EQUILIBRIUM DISTRIBUTION COEFFICIENTS FOR INTERSTITIAL ELEMENTS BETWEEN SELECTED REFRACTORY METALS AND LITHIUM

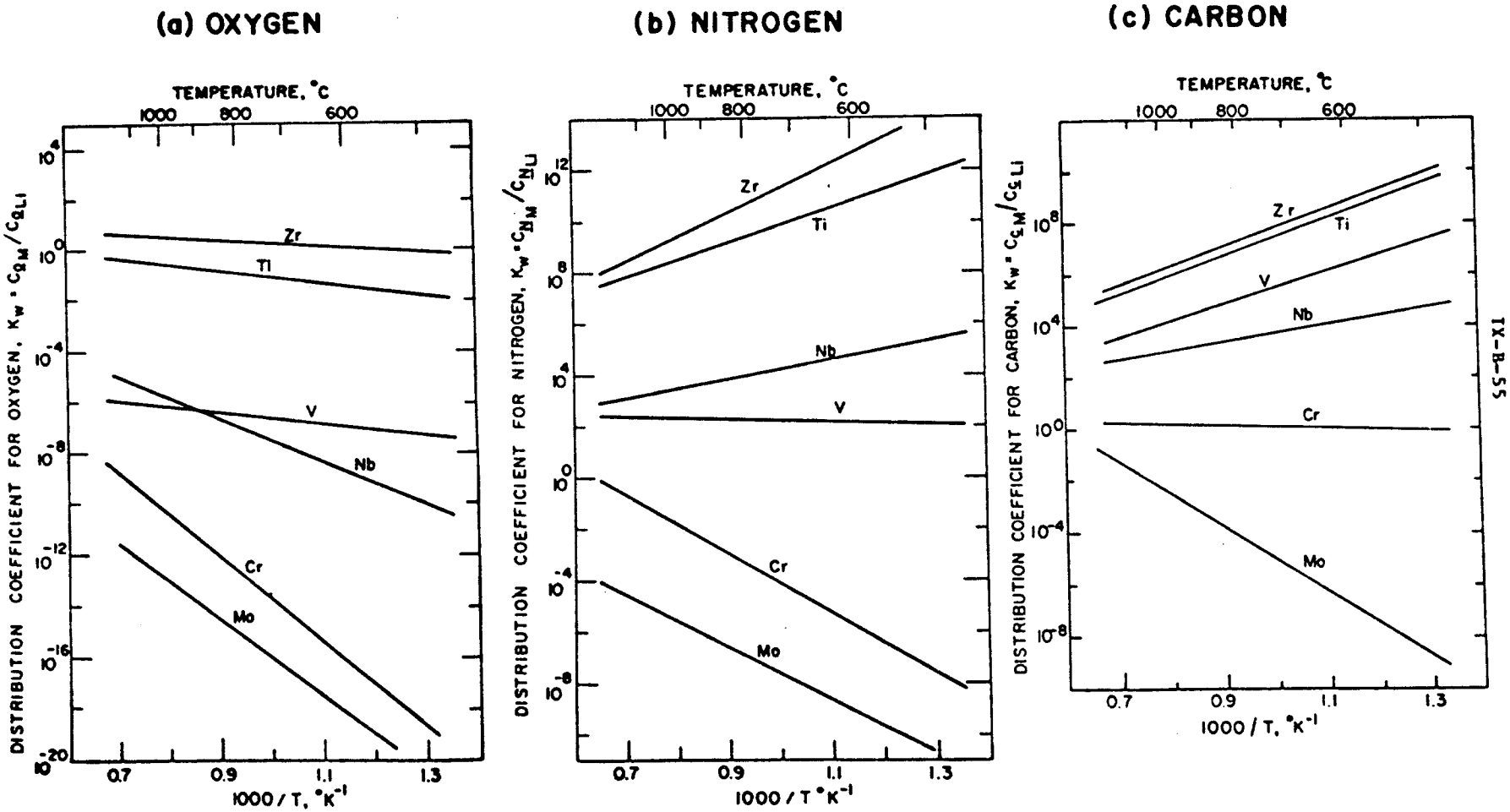

FIG. IX-B-25 TEMPERATURE DEPENDENCE OF THE INTERSTITIAL CONCENTRATIONS IN LITHIUM AT WHICH SELECTED REFRACTORY METAL COMPOUNDS ARE STABLE.*

a) NITROGEN

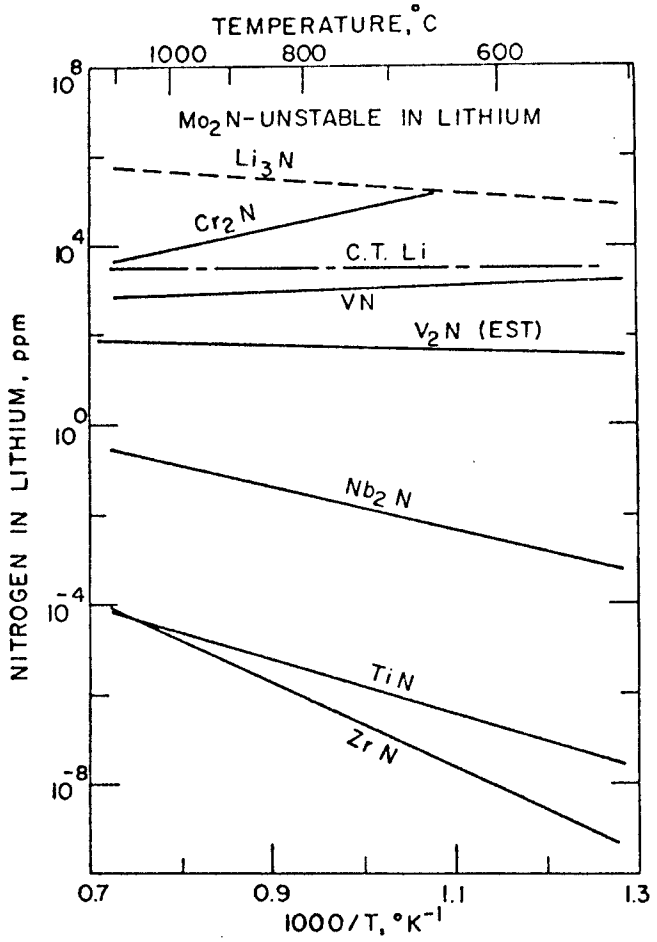

b) CARBON

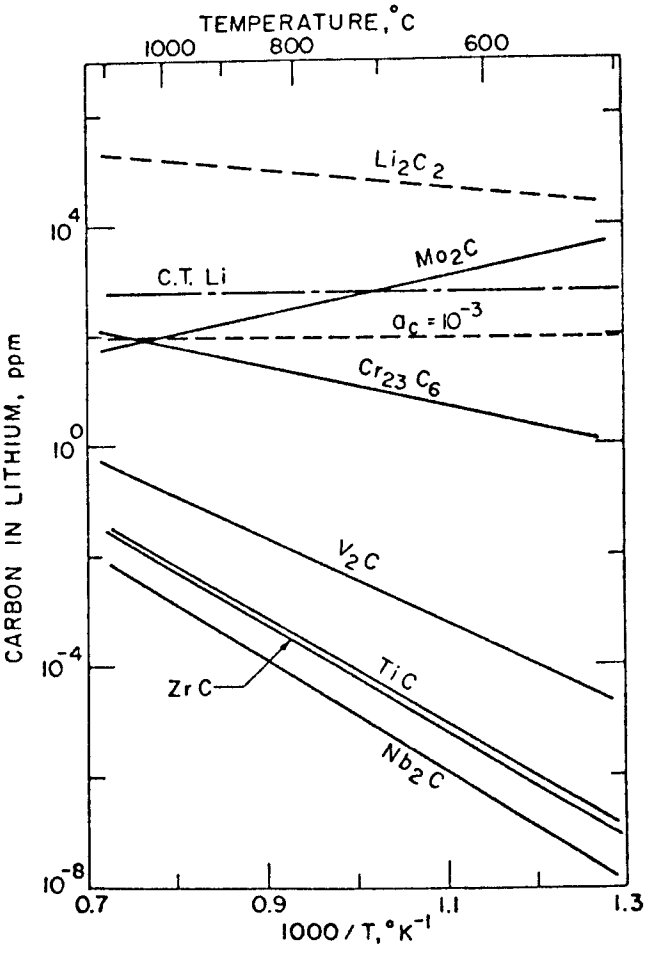

* COMPOUNDS ARE STABLE ABOVE THE GIVEN LINES.

1 part per million. This is an exceedingly difficult job and one may have to accept contaminated V and Nb (with the appropriate increase in DBTT) as a penalty for using these metals in lithium.

The next area to consider is the compatibility of the metals (or alloys) in question with high temperature and high pressure helium. To be more specific, since helium gas itself is inert, we must consider the compatibility of the metals with the impurities in the helium (O_2, N_2, C containing molecules, and hydrogen).

The integrity of Al and steel alloy systems depends on the development of an adherent, protective film. This film is Al_2O_3 in the Al alloys and chromium oxide for the steels. Hence, such metals are not significantly effected by oxidizing atmosphere, but they are sensitive to reducing environments. Westerman has analyzed the situation for 316 stainless steel subjected to 650°C helium containing 10^{-2} torr oxygen partial pressures.(57) He concluded that no deleterious effects should occur and that one could safely use 316 SS in that environment. The reader is urged to read that report for the details of his analysis.

We have no information on the compatibility of Al with trace impurities in helium but see no reason why it could not be used with such a coolant to temperatures of 200-300°C.

Unlike the Al and stainless steel systems, the refractory metals do not form adherent, protective films in the presence of O, N or C impurities. One must also be careful about separating the response of Mo and its alloys from the Nb and V system because the solubilities for interstitial elements are quite different. The effect of alloying elements must also be examined because they can have a much different affinity for contaminants than the base metal.

There are several points to consider in this type of analysis -

(1) Source of Contamination

- (a) initial helium charge and make up
- (b) adsorbed on surface
- (c) in-leakage via molecular flow
- (d) in-leakage by surface diffusion
- (e) component outgassing
- (f) in-leakage from secondary coolant system

(2) Level of Impurities in the Metal

- (a) surface reaction rate
- (b) bulk diffusion rate
- (c) solubility
- (d) alloy effect

(3) Sensitivity of metal (or alloy) to impurities

The first area is design dependence and obviously not a topic for this report except for an indication of anticipated levels. The last two areas are material dependent and we will make a few observations about the Nb (which is similar to the V system) and the Mo system.

There seems to be two basic approaches to the source of contaminants. The first one has been clearly stated by J. DeVan[58] who points our that in previous experimental loops (59-60) severe oxygen contamination occurred in loops where the oxygen content was maintained at $\leq$ 1 wt ppm. This is supported by further work which concluded that the total residual gas pressure must be maintained below 10^{-6} torr to avoid serious deterioration of the mechanical properties of Nb-1Zr in periods as short as months at 600°C and weeks at 1000°C.[61] DeVan uses thermodynamic arguments to point out that if a helium loop operated at a pressure of 50 atmospheres, then holding the partial pressure to less than 10^{-6} torr means control to less than 2 parts per trillion (2×10^{-6} ppm), a rather difficult job to say the least. A similar analogy could be constructed for V. DeVan's arguments rest on the fact that the metal will quickly come to equilibrium with the gas and that there is an infinite source of this low concentration of impurities.

Charlot and Westerman[62] point out that item 1a above contributes only a small amount of contamination due to the initial charge of helium (on the order of a few ppm or less) and that items 1b, 1d, and 1e can also be small. The big question is whether item 1c can be controlled so that (for the case of the PPPL system with a Nb-1Zr blanket) the oxygen leakage can be kept below 100 micrograms per unit of reaction time (typically on the order of a few seconds at ~1000°). There is no way to answer this question short of a full scale test loop but until such impurity control can be demonstrated, the authors are inclined to assume constant contamination levels of ~1 ppm.

The amount of impurities that can be dissolved in a metal depends on reaction rate at the surface and the rate at which the impurities can penetrate the metal. Charlot and Westerman[62] estimate that both steps can be accomplished at 1000°C in one week for oxygen and 12 weeks for nitrogen atoms in Nb. Because of the lower diffusivity of oxygen (as well as nitrogen and carbon) in Mo, this process make take as long as 2 years at 1000°C. Therefore, one concludes that for the Nb and V system at 1000 and 800°C respectively, the metals can be sufficiently contaminated in times short compared to reactor wall lifetimes. The rate of contamination in Mo would be much slower and could require times comparable to the first wall life (~2 years).

The next concern is the terminal solubility of the interstitial impurities in the Nb(V) system and the Mo system. Figures IX-B-26 and IX-B-27 show how the O, N, and C terminal solubilities vary with temperature. This information coupled with that in the literature is summarized below for three metals (Mo,Nb,V) at their anticipated operating temperatures.

Terminal Solubility wt ppm[63]

	Temp.°C	C	O	N
Mo	1000	0.4	15	3
Nb	1000	8	3500	380
V	800	2000	9000	

In general, the solubility of the O, N, and C atoms is much higher in Nb or V than in Mo. The ratio varies from a factor of 20 to 200 higher in the Nb system are from 500 to 1000 times higher for the V system. The general conclusion here is that Mo tends to absorb for less interstitial impurity atoms than the Nb or V system.

The final question is:"How sensitive are the materials properties to changes in the interstitial impurity content"? Of the two major mechanical property effects, yield strength and DBTT increases with increasing interstial content, the latter is more important.

We have plotted the DBTT for the three metals as a function of oxygen and carbon content in Figures IX-B- 5a and IX-B- 5b. The important point to note here is that while Mo absorbs far less interstitial impurities, it is also much more susceptible to those elements. If the impurities are present in levels higher than the terminal solubility, they will precipitate in the metal matrix making it very strong but quite brittle.

The last compatibility question to address is that associated with the use of lithium salts such as $LiF-B_eF_2$. DeVan[58] has investigated this area and we will simply summarize some of his remarks. First of all, Mo, Ni - Mo alloys and graphite are very corrosion resistant toward $LiF-B_eF_2$ salt mixtures.[64] Niobium and iron based alloys are less resistant to attack by fluoride salts[65] but may be suitable for operation in $LiF-BeF_2$ in the range 600-700°C provided the purity of the salt is kept high. There are no reported tests of V in fluoride salt mixtures,but on the basis of free energy considerations, V would be expected to undergo considerable reactions even with fluoride mixtures of relatively low oxidizing potential.

The above analysis applies to a non radiation environment in the absence of magnetic fields. The production of free radicals of fluorine or HF^- by the intense radiation could increase the corrosion rate. The generation of low voltages by moving an electrically conducting fluid through a magnetic field

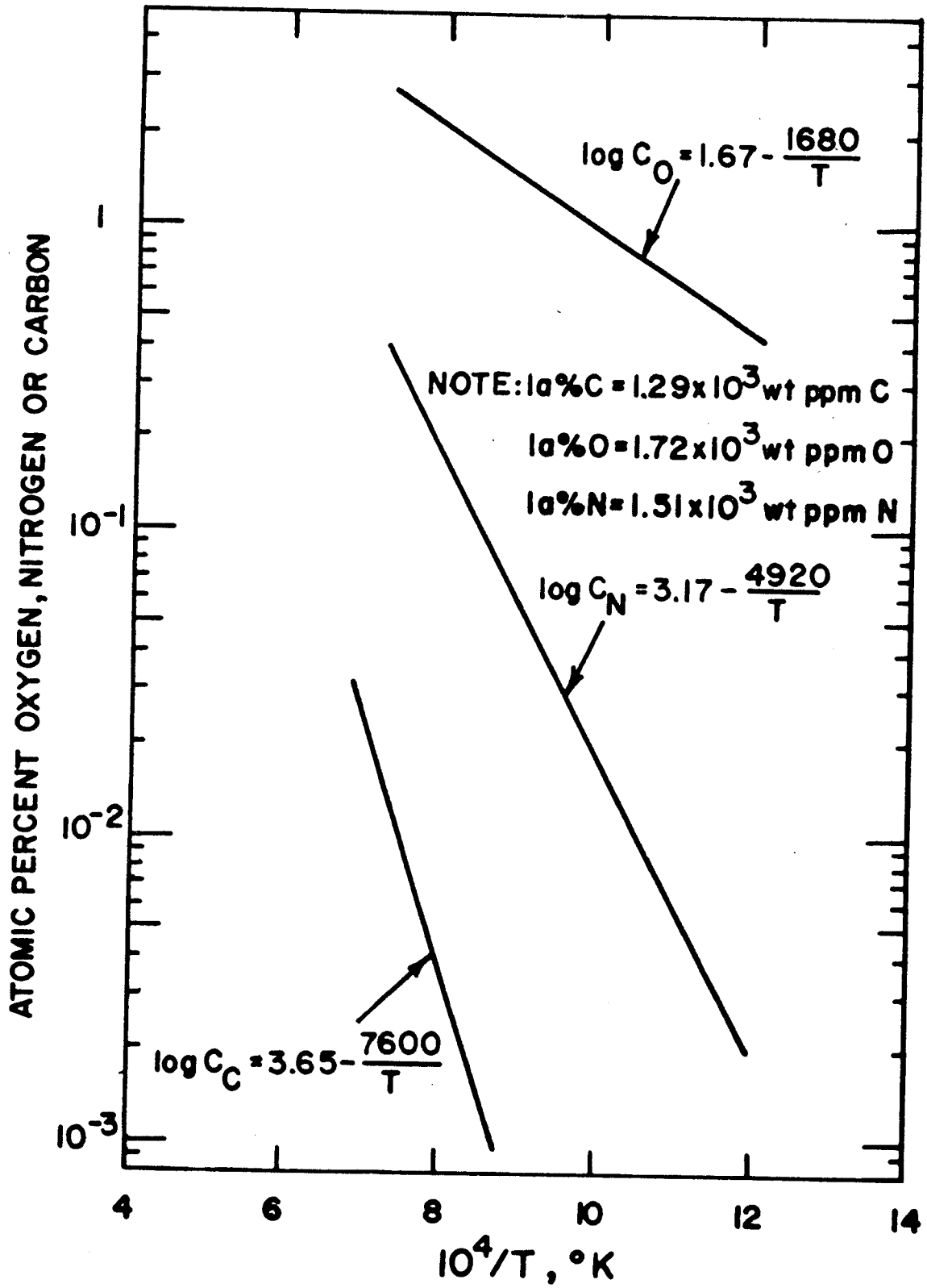

FIGURE IX-B-26—HIGH TEMPERATURE TERMINAL SOLUBILITIES OF OXYGEN, NITROGEN AND CARBON IN NIOBIUM

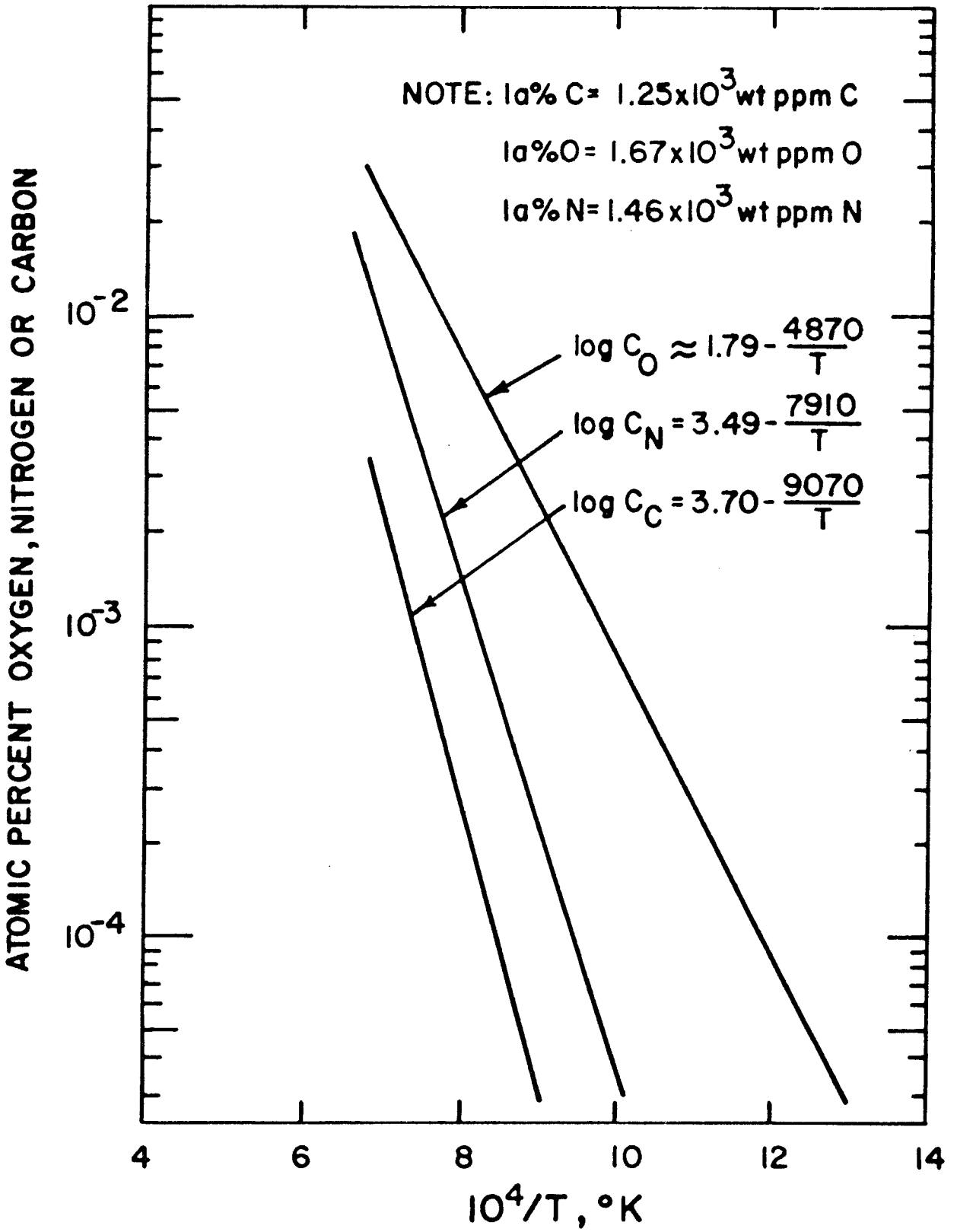

FIGURE IX-B-27 — HIGH TEMPERATURE TERMINAL SOLUBILITY OF OXYGEN, NITROGEN AND CARBON IN MOLYBDENUM

could also promote galvanic corrosion. Both of these effects need to be examined before more conclusive statements can be made. However, at this time it appears that Mo is far superior to the Nb and V system for use at high temperatures with Li-F-Be salts.

We have summarized, in Figure IX-B-28, the situation with respect to the useful temperature range for the five alloy systems considered here. The approximate mechanical property limit is given as a dotted line at onehalf the melting point. Examination of Figure IX-B-28 shows that the Mo system has a much wider potential temperature range than for the Nb or V systems, especially due to interstitial impurity atom pick up from helium gas and with regard to molten salt operation. The steels appear to be useful up to their mechanical property limit in helium gas and molten salts but will probably be limited to ~500°C due to selected teaching of certain alloying elements in dynamic lithium. Finally, Al alloys will probably be limited to helium coolants as their compatibilities with liquid metals is notoriously bad. The maximum operating temperature of the Al will probably be in the 200°C range.[69]

The last area of concern is the interaction between the structural material and hydrogen isotopes which are quite abundant in a fusion reactor environment. There are basically three items of concern here,

A.) The solubility of hydrogen isotopes in the structural material. This is important in terms of increasing the tritium inventory, complicating maintenance, and potential side effects of the decay of tritium into helium inside of the metal matrix.

B.) The release of tritium to the environment. In this regard the permeability of the metal to the hydrogen isotopes should be low. If it is too high then special containment facilities will have to be built to reduce the leakage to the reactor building.

C.) The effect of hydrogen on the mechanical properties of the structural metals. This is most important to processes which involve crack propagation

The solubility of hydrogen in metals depends mainly on the temperature and partial pressure of hydrogen in the environment. We have plotted, in Figure IX-B-29[70] the equilibrium solubilities of hydrogen in Mo, Nb, V, and 316SS as a function of temperature. (The solubility of Al is much less than 0.01 appm at ~ 200°C.) For a given background partial pressure of tritium we see that the Nb and V systems will absorb almost a thousand times more hydrogen than picked up by Mo. Furthermore the slope of the solubility temperature plot is positive for Mo and negative for Nb and V meaning that the location of the maximum hydrogen concentration in the blanket materials will be different for these two metal systems.

The major source of tritium to be absorbed into the metal is from the background pressure in the plasma chamber. It is estimated that this varies from $\sim 10^{-5}$ torr during operation to $\sim 10^{-2}$ torr during the refilling stage. In contrast the partial pressure of tritium in Li between 700-1000°C is ~ 6×10^{-9} to 6×10^{-8} torr for a 1 appm concentration.[71] This partial pressure scales as $(\text{concentration})^2$ so that even at 10 appm the tritium partial pressure from the Li would be less than that from the plasma. If we chose a worst case of 10^{-2} torr background partial pressure of tritium then the calculated maximum tritium concentrations in the four metal systems is as given below.

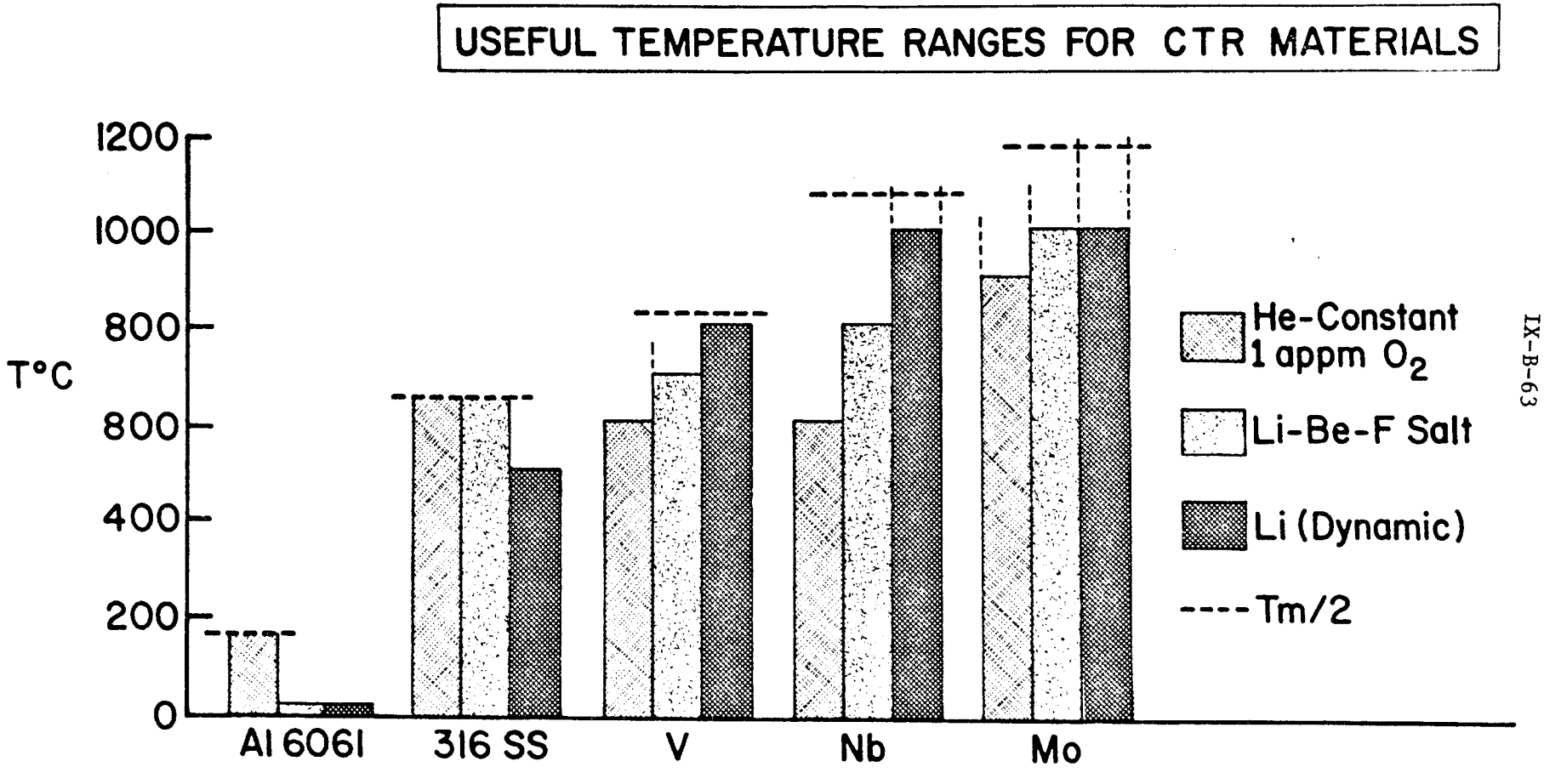

IX-B-63

FIG. IX-B-28

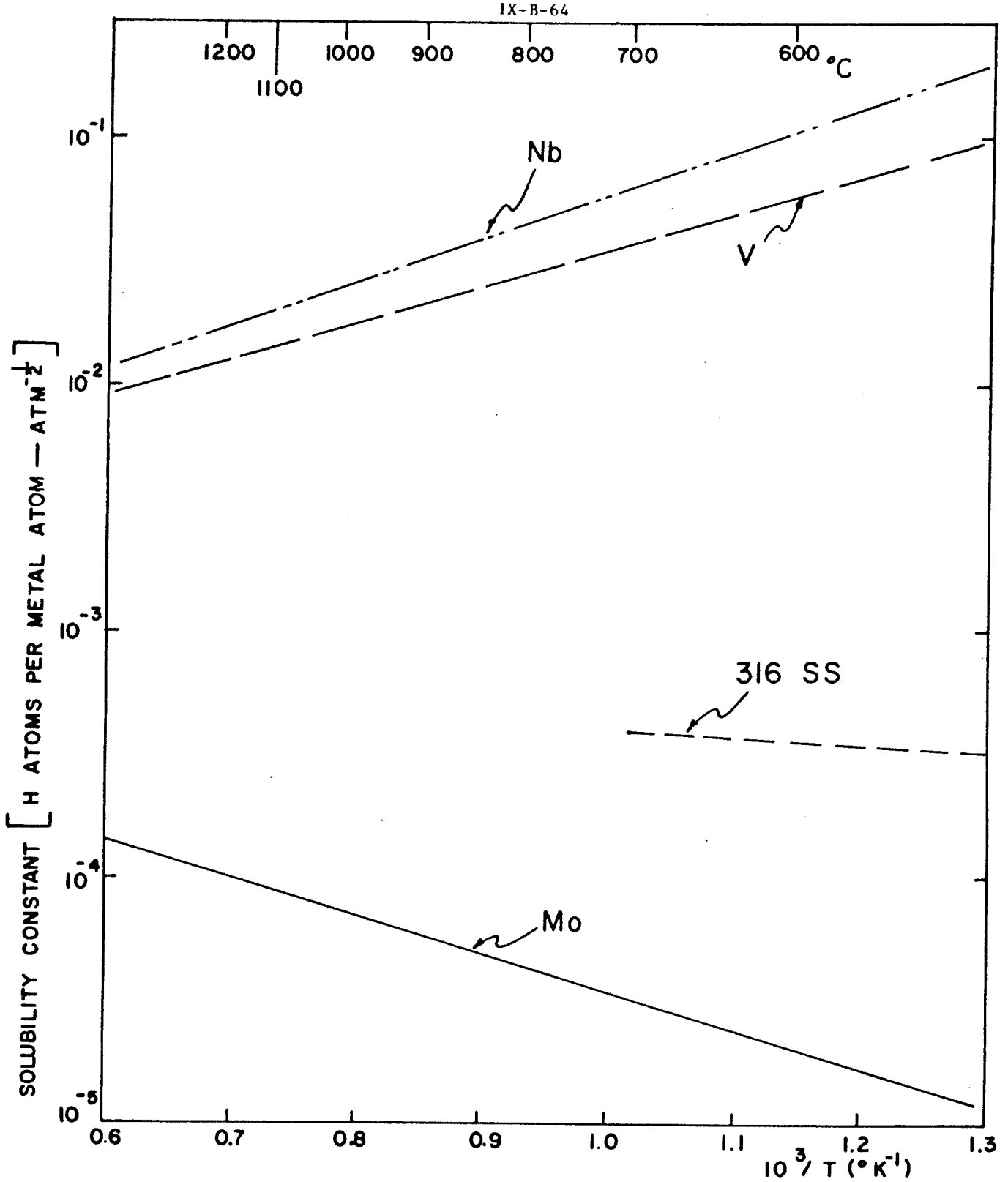

FIGURE IX-B-29 EQUILIBRIUM SOLUBILITY OF HYDROGEN IN SELECTED CTR MATERIALS

System	Operational Temperature Range °C	Atomic Hydrogen[a] Concentration -ppm
Nb	600-1000	400-100
V	600-800	200-100
316SS	500-650	1-1.5
Mo	600-1000	0.07-0.3

a) for 10^{-2} torr partial pressure tritium

The significance of the above numbers can be appreciated if one calculates the inventory and potential tritium concentrations in a typical blanket design. For example, if we assume a chamber wall area of $3000m^2$ and a wall thickness of 2mm (volume = $6x10^6cm^3$) then the following maximum inventories of tritium in the structural first wall might be achieved

Metal	T_2 inventory[a] (g)
Nb	400
V	30
316SS	3
Mo	0.3
Al	<<0.1

a) based on average concentrations of tritium over the operating temperature range.

It is obvious from these numbers that Nb could accumulate enough tritium to become a hazard during maintenance and during potential accident conditions. Al,Mo and steel represent little problem and V is somewhat in between.

Another problem to worry about is the decay of tritium into helium. If we assume a $t_{\frac{1}{2}}$ of 12.3 years, the decay constant is $5.63x10^{-2}$ per year. The helium production rate by this mechanism is compared to the helium produced by neutronic reactions in the table below.

TABLE IX-B-13

Helium Production Rates in Potential CTR First Wall Materials

Element	appm He per year-neutronic[a]	Maximum appm He per year, T_2 decay[b]	appm He/yr total
Nb	19	23	42
V	45	11	56
316 SS	160	<0.1	~160
Mo	37	<0.01	~37
Al	265	<<0.01	~265

a) per/MW/m^2, 80% P.F.
b) assuming all hydrogen in metal is tritium at terminal solubility level.

The major effect is again in Nb and Table IX-B-13 shows that the helium production rate due to T_2 decay in Nb can be as much as that produced by neutronic reactions. This fraction produced by tritium decay drops to about 20% for V and is negligible for the other three systems considered. The net effect for Nb is that it loses its lower helium production advantage over Mo and makes the helium production about the same in both metallic systems.

The release of tritium to the environment is a topic of grave concern to the fusion community. In order to estimate how the various metals compare in this area one should calculate the flux of atoms through the pipe walls of the flux of the primary coolant or the tritium collection system. Of course one could always use a double walled construction but then one must be concerned with the escape of tritium through the heat exchanger first walls. Again permeability is a very important parameter.

The hydrogen permeability for the five metal systems studied here is given in Figure IX-B-30. The Nb and V systems have very high permeabilities followed by 316SS, Al and Mo in that order. To get a feeling for the importance of these parameters the following illustrative calculation for liquid Li was made. Assume that we have 10 appm tritium in a lithium coolant which is contained in a 5 mm thick piping system that has a surface area of 1,000m^2. The partial pressure of the tritium outside the pipes is assumed to be zero and using the maximum anticipated operating temperatures we calculate the following tritium leakage rates.

Piping Material	Maximum Operating Temp°C	T_2 leakage Rate-g/year
V	800	58,000[a]
Nb	1000	31,000[a]
Mo	1000	23
316SS	650	7

a) These numbers are obviously too high as they approach the production rate.

It is fairly evident from the data above that both V and Nb systems present a potential problem of tritium leakage into the environment. This may be alleviated by coatings (which must yet be found) or by expensive double walled pipe constructions. The latter solution is more likely because all refractory metals must be protected from air at high temperature. This may even be required for the steel systems. Nevertheless, the use of Mo as a blanket structural material and for primary coolant piping at very high temperatures will represent a better choice than V or Nb.

IX-B-7 Radiation Damage

To be covered in Section C.

IX-B-8 Availability

To be covered in Chapter XII.

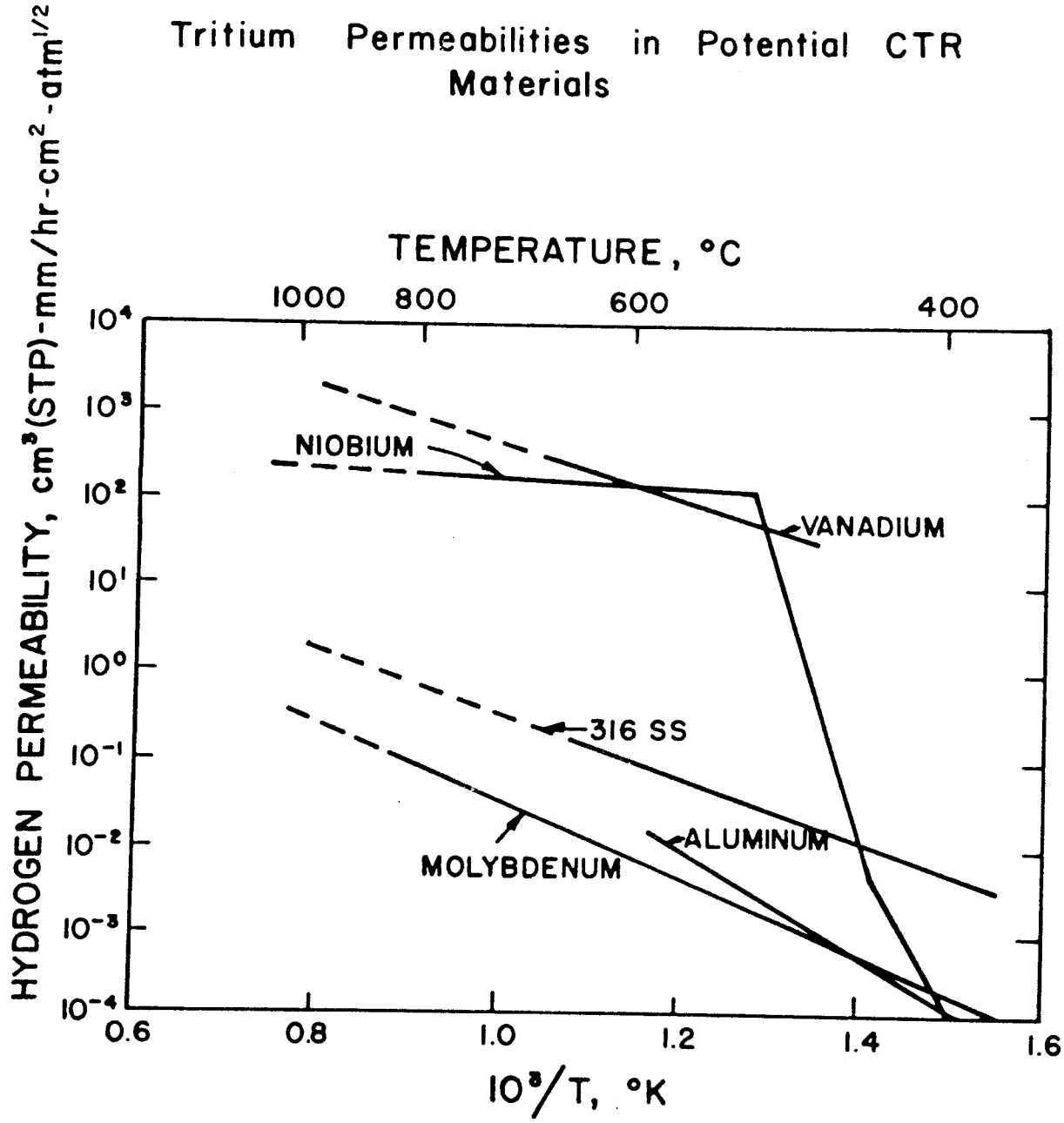
Tritium Permeabilities in Potential CTR Materials
TEMPERATURE, °C
1000
800
600
400
HYDROGEN PERMEABILITY, cm³(STP)-mm/hr-cm²-atm^1/2
10⁴
10³
10²
10¹
10⁰
10⁻¹
10⁻²
10⁻³
10⁻⁴
NIOBIUM
VANADIUM
316 SS
ALUMINUM
MOLYBDENUM
0.6
0.8
1.0
1.2
1.4
1.6
10³/T, °K

FIG. IX-B-30

IX-B-9 Costs

To be covered in Chapter XIII.

IX-B-10 Summary

Taking all of the above factors into account we came to the conclusion that for advanced (temperatures up to 1000°C) fusion reactors, Mo (or TZM) is clearly superior to other metals with respect to the following properties.

Mechanical Strength
Compatibility with potential coolants
Containment of tritium
Availability
and Cost

The response of Mo is roughly the same as that of V and Nb with respect to

Physical
Thermal
Neutronic
and Radiation damage considerations.

The biggest drawback of Mo is its difficult (but not impossible) joining characteristics, especially in the field. The solution of this problem will make Mo the most favored material for high temperature CTR applications.

References

1. J. R. Powell, F. T. Miles, A. Aronson, W. E. Winsche, and P. Bezler, BNL-18439, (1973).

2. M. V. Davis, ANL/CTR-72-01, Dec. (1972).

3. F. L. Yagee, Vanadium Alloys Meeting, Germantown, MD., April, (1970).

4. Unpublished data, V. Bates, Fansteel, Inc. (1968).

5. K. S. Hirahashi, K. Fukaya, Y. Katano, to be published.

6. Nuclear Systems Materials Handbook, Vol. 1, part I, Group 1, Section 5, Property Code 2101, p. 10, TIP-26666.

7. Military Standardization Handbook, MIL-HDBK-5B, August (1974).

8. Schmidt, F. F., Ogden, H. R., "Engineering Properties of Molybdenum and Molybdenum Alloys" DMIC Report 190, 1963 Battelle Memorial Institute.

9. Unpublished data, McDonnell-Douglas Corporation.

10. K. Farrell and J. J. Houston, to be published Int. Conf. on Radiation Effects and Tritium Technology for Fusion Reactors, Gatlinburg, Tennessee, Oct. (1975).

11. Unpublished data, V. Bates, Fansteel, Inc.(1968).

12. Briggs, J. Z., Barr, R. Q., Arc-Cast Molybdenum Base TZM Alloy: Properties and Applications," Paper presented at 7th Plansee Seminar, 1971, Reutte, Austria.

13. Military Standardization Handbook, MIL-HDBK-5B, August 1974.

14. Nuclear Systems Materials Handbook, Vol. 1, Part 1, Group 1, Section 4. Property Code 2105, p. 10.

15. B. A. Loomis, and O. N. Carlson in Reactive Metals (metallurgical Society Conferences, Vol. 2), Interscience, New York-London, 1959, p. 227.

16. L. E. Olds, and G. W. P. Rengstorff, Trans. AIME, 206 150, 1956.

17. A. G. Imgram, E. S. Barlett, and H. R. Odgen, Trans. AIME, to be published.

18. J. W. Davis, unpublished Results.

19. Lessmenn, G. G., NASA-Cr-1608, (1970).

20. Houck, J. A., Physical and Mechanical Properties of Molybdenum and Molybdenum Based Alloys, DMIC Report 140, 1960, Battelle Memorial Institute.

21. Alcoa Research Laboratory Data Sheet 2024-T4 Products, September 1957.

22. F. W. Wiffen, Vanadium Alloys Meeting, Germantown Md., April (1970).

23. Air Force Report AFML-TR-68-115.

24. Columbium Tantalum and Tungsten Alloys, Wahchang Corp. (1968).

25. A. S. Tetelman and A. J. McEvily, Jr., Fracture of Structural Materials, J. Wiley & Sons Inc., New York, (1967), p. 377.

26. Military Standardization Handbook, NIL-HDBK-5B, August (1974).

27. C. R. Brinkman, J. M. Beeston, and G. E. Korth, ANCR-1096, Feb. (1973).

28a. D. J. Michel, to be published.

28b. Honeycutt, C. R., Sawyer, J. C., Determination of Electron Temperature Fatigue Data on Refractory Alloys in Ultra-High Vacuum, 5th and 6th Quarterly Report Nasa-CR-54775 and 54983.

29. Loomis, B. A. Carlson, O. N., Reactive Metals, Interscience 1969, p. 227.

30. H. R. Hietz, Colombium, ASM 1959 and see also "Hydrogen Effect on Refractory Metals," W. T. Chandler, R. J. Walter, page 222, Refractory Metal Alloys Metallurgy and Technology, Plenum 1968.

31. L. M. Bianchi, et al., AD-458529, (1964).

32. AMFL-TR-65-31, (1965 (7 volumes).

33. W. Cowie, SEG-TDR-64-19, (1964).

34. R. E. Jackson, B008-6, Sept. (1966).

35. W. P. McGregor and H. Marquez, Welding Design and Fabrication, p. 82, April, (1970.

36. K. C. Cooper, W. C. Turner, LA-5017-MS (Dec. 1972).

37. J. R. D. Steifano, A. J. Moorehead, ORNL-4874, Dec. (1972).

38. NASA-CR-1586, June (1970).

39. A. P. Fraas, ORNL-TM-4949, Nov. 1975.

40. R. A. Krakowski, W. V. Green, and W. C. Turner, LA-UR-73-505, March, (1973).

41. G. S. Hanks, LA-DC-11124 (1970).

42. M. K. Drake, BNL-50279, 1970, See also G. Ozer and D. Garber, BNL-17541, 1973.

43. S. Pealstein, J. Nucl. Eng. 27, 81, (1973).

44. E. Cheng, unpublished Results.

45. G. L. Kulcinski, D. G. Doran, and M. A. Abdou, To be published ASTM-STP-570, (1972).

46. T. K. Sung., unpublished results.

47. W. D. Treadwell and R. Walk, Helv. Chim, Acta, 25, (161), 1154, (1942).

48. E. J. Cairns, F. A. Catasso, and V. A. Maroni, p. 91 in The Chemistry of Fusion Technology, ed. D. M. Gruen, Plenum Press, 1972.

49. D. L. Smith and K. Natesan, J. Nucl. Tech. Vol. 22, 392, 1974.

50. J. H. DeVan, p. 25 in "Fusion Reactor First Wall Materials," ed. L. C. Ianniello, Wash 1206-1972.

51. F. I. Shamrai, and P. Ya Sal'dau, IZV. Akademii Nauk SSST, Seriya Khimi, No. 3, 631, 1937.

52. B. Badger et al., "A Wisconsin Tokamak Reactor Design," UWFDM-68, Vol. 1, Chapter IV, 1973.

53. J. H. DeVan, J. E. Selle, and A. E. Morris, "Review of Lithium-Iron Base Alloy Corrosion Studies," ORNL-TM-4927, (To be published).

54. W. W. Gill et al., AIChE, 6(1), 139, 1960.

55. I. Nihei, I. Sumiya, Y. Fukaya, and Y. Yamazaki, To be published.

56. D. L. Smith and K. Nateson, J. Nucl Tech. Vol. 22, 392, 1974.

57. R. E. Westerman, "Compatibility of Stainless Steel with Oxygen Contaminated Helium," UWFDM-117, Oct. 1974.

58. J. H. DeVan, p. 25 in "Fusion Reactor First Wall Materials," ed. L. C. Ianniello, Wash-1206, 1972.

59. J. F. Hogan, E. A. Limoncelli, and R. E. Cleary, TIM-901, Pratt-Whitney Aircraft, CANEL (Aug. 1965).

60. E. A. Limoncelli, TIM-824, Pratt-Whitney Aircraft, CANAL (Nov. 1965).

61. W. M. Phillips, p. 197-217 in Corrosion by Liquid Metals (Edited by Weeks and Draley), Plenum Press, New York, 1970.

62. L. A. Charlot and R. E. Westerman, BNWL-1842, July 1974.

63. The values in this table are obtained equations based on data from a multitude of references in Reference 49.

64. J. L. Henry, S. A. O-Hare, R. A. McCune, and M. P. Krug, J. Less Common Metals 25, 39, 1971.

65. G. M. Adamson Jr., R. S. Crouse, and W. D. Manly, "Interim Report on Corrosion by Zirconium-Base Fluorides" ORNL-2330, January 1961.

66. J. DeVan "Effect of Alloying Elements on Corrosion Behavior of Ni-Mo Alloys in Fused Fluoride Mixtures," ORNL-TM-2021, Vol. 1, May 1969.

67. J. W. Kroger and A. P. Litman, "Compatibility of Mo Based Alloy TZM with $LiF-BeF_2-ThF_2-UF_4$ at 1100°", ORNL-TM-2724 (Dec. 1969).

68. R. C. Schulze, et al., "INOR-8-Graphite-Fused Salt Compatibility Test," ORNL-3124, June 1961.

69. G. L. Kulcinski, et al. in Proceedings of Low Activity Fusion Materials Workship, San Francisco, Feb. 1976, to be published.

70. R. E. Stickney, p. 241, in The Chemistry of Fusion Technology, Plenum Press, New York, 1972.

71. V. Maroni, to be published.

IX-C.) General Radiation Effects

The purpose of this section is to document the data which will be used to analyze the behavior of material in UWMAK-III. A thorough and complete listing of all the previous work is obviously beyond the scope of this report so we will concentrate on those damage regions (in dpa and temperature) which may be typical of UWMAK-III operation. Some of this information has already been discussed in UWMAK-I[1] and UWMAK-II[2] (i.e., damage in carbon, B_4C , 316SS, mylar, TiNb, Cu, and Al) so only the most pertinent information will be repeated here. Since the use of Mo is unique to this design, we will spend some time on outlining what has been previously reported for radiation damage to this element.

IX-C-1.) Molybdenum or Its Alloys

This treatment will be divided into four sections; a) the neutronic behavior, b) prior irradiation studies, c) bulk effects, and d) surface effects. Again, in many cases we will have to rely on information for pure Mo to represent TZM, but hopefully we can point out where future work is required.

IX-C-1-a.) Neutronic Behavior

The displacement cross sections for TZM will be assumed to be the same as for pure Mo. These have been reported elsewhere[3] and summarized in Table IX-C-1 in the 46 energy group structure used for most of our calculations. We have also listed the (n,α) and (n,P) cross sections as calculated by Pearlstein.[4] The displacement energy threshold used here is 37 eV[5] and the displacement function used is similar to that recommended by the IAEA working group on damage analysis.[6]

IX-C-1-b.) Prior Irradiation Studies

A summary of all the known irradiation studies up to 1975 on Mo or Mo alloys is given elsewhere.[7] Here we will try to quote only the general conclusions of that study and will not attempt to duplicate the complete bibliography.

In general, there have been relatively few irradiation studies of Mo and its alloys compared to steels and even Al alloys. However there seems to be as much or more radiation damage analysis on the Mo system as the Nb system and certainly more than on the V system. The first work was reported in 1956 and up to Fall of 1976, some 300 individual studies have been uncovered. The bulk of the studies (71%) have been performed with neutrons, 13% with electrons, 19% with heavy ions, 3% with helium atoms and 3% with hydrogen isotopes (note we are not counting all of the sputtering work on Mo which would comprise a much larger field of data). A chronological listing of the studies is given in table IX-C-2. Note that the data for 1976, and to some extent 1975, should be considered incomplete due to the lag in publication and abstracting. Normally, the electron studies are aimed at low temperature (<<RT) basic defect studies

Table IX-C-1
Summary of Mo Reaction Cross Sections Used in UWMAK-III Studies

Energy Group	Upper Energy - eV	dpa	Cross Sections - barns (n,α)	(n,p)
1	1.4918 (+7)	1751	1.7889-02	2.9288-02
2	1.3499 (+7)	1670	1.5131-02	2.5342-02
3	1.2214 (+7)	1557	1.1656-02	2.0422-02
4	1.1052 (+7)	1461	8.3124-03	1.5251-02
5	1.0000 (+7)	1362	5.6304-03	1.0613-02
6	9.0484 (+6)	1281	3.7083-03	7.1084-03
7	8.1873 (+6)	1254	2.4212-03	4.6820-03
8	7.4802 (+6)	1156	1.5959-03	3.1166-03
9	6.7032 (+6)	1108	1.0670-03	2.0812-03
10	6.0653 (+6)	1048	7.7087-04	1.4167-03
11	5.4881 (+6)	965	4.5817-04	9.8249-04
12	4.9659 (+6)	916	2.8378-04	6.6659-04
13	4.4933 (+6)	887	1.9906-04	4.8596-04
14	4.0657 (+6)	843	1.4553-04	3.4228-04
15	3.6788 (+6)	780	9.6803-05	2.9649-04
16	3.3287 (+6)	759	6.9288-05	1.0918-04
17	3.0199 (+6)	741.1	5.2082-05	4.1220-05
18	2.7253 (+6)	711.9	4.2728-05	2.0038-05
19	2.4660 (+6)	639.2	1.3812-05	4.7870-06
20	1.8268 (+6)	534.6	3.5189-07	3.4769-07
21	1.3534 (+6)	442.1	0	0
22	1.0026 (+6)	378.4	0	0
23	7.4274 (+5)	342.6		
24	5.5023 (+5)	287.3		
25	4.0762 (+5)	247.6		
26	3.1097 (+5)	201.2		
27	2.2371 (+5)	164.8		
28	1.6573 (+5)	128.9		
29	1.2277 (+5)	93.5		
30	6.7379 (+4)	44.5		
31	3.1828 (+4)	20.1		
32	1.5034 (+4)	13.8		
33	7.1017 (+3)	6.7		
34	3.3546 (+3)	3.6		
35	1.5846 (+3)	2.2		
36	7.4852 (+2)	1.9		
37	3.5358 (+2)	1.1		
38	1.6702 (+2)	2.0		
39	7.8893 (+1)	8.0		
40	3.7267 (+1)	1.4		
41	1.7603 (+1)	.41		
42	8.3153 (+0)	.19		
43	3.9279 (+0)	.23		
44	1.8554 (+0)	.33		
45	8.7643 (-1)	.48		
46	4.1399 (-1)	1.0		

Table IX-C-2

Number of Papers or Reports on Radiation Damage in Mo as a Function of Time and Irradiation

	n	p	α	e^-	HI	d	TOTAL
1955							
56	1						1
57	1						1
58	2						2
59	1						1
1960	8						8
61	3						3
62	6	1	1	2			10
63	4						4
64	4				1		5
65	12			1	1		14
66	2			1			3
67	10				1		11
68	7				1		8
69	16			2			18
1970	9			3			12
71	19	1		1	7		27
72	13		2	8	3	1	27
73	16		2	3	1	1	23
74	12	2	3	4	1		22
75*	12			2	4		18
76*	12			3	7		25
	170	4	8	30	27	2	240

n = Neutron
p = Proton
α = Alpha Particle
e^- = Electron
HI = Heavy Ion
d = Deuteron

* Data for these two years should be considered incomplete due to lag in publication and abstracting.

and will be of limited use in assessing high temperature effects. The heavy ion studies are primarily aimed at void studies and we have only quoted light ion ($Z \leq 2$) studies when they pertain to blistering studies.

We have further analyzed the neutron radiation damage work with respect to type of property measured and temperature of irradiation. This is given is table IX-C-3. While the effects of neutron irradiation below stage III (<150°C) are of fundamental interest, they again tend to shed little light on reactor behavior. In fact, only those tests above ~450°C are of major interest to a reactor designer. Since resistivity recovery is also of minor importance, this leaves us with only 117 studies. Of that work only 24 studies have measured mechanical properties and 54 studies have been concerned with dimensional changes.

Finally, it may be of interest to the reader to note that ~ 70% the property measurements were made by scientists in the US and UK with Russia, France, Japan, Belgium and the Netherlands comprising another 27%. Similarly, 73% of the mechanical property studies were made in the US and UK and practically all of the high temperature neutron studies were performed in the US and UK.

IX-C-1-c) Bulk Effects

i) Dimensional Stability

The main problem of concern here is the swelling produced by the production of voids although it has been known for a long time that dimensional changes can take place at lower irradiation temperatures by the accumulation of point defects.(8)

We have graphically displayed the fluence-temperature regimes studied by TEM (transmission electron microscopy) in figure IX-C-1. Note that approximately 1/2 of the studies have been performed below 450°C and the neutron fluence range covered above 450°C extends from 4×10^{19} n/cm^2 (E > 1MeV) to 8×10^{22} (E > 0.1MeV). The approximate dpa levels are given on the RHS of Figure IX-C-1. Hence it can be seen that very little data exist in the 700 - 1000°C temperature, 15 dpa regime which represents approximately one year exposure to the outer UWMAK-III TZM first wall.

Table IX-C-4 lists all the volume change information collected on neutron irradiated Mo or its alloys. In general the data below 300°C represents volume increases due to the accumulation of point defect and voids are only observed at temperatures above 300°C and fluences of $>10^{20}$ n/cm^2 (~0.05 dpa).

Unfortunately the studies have been conducted with many different types of Mo or Mo alloys, and in several reactors with sometimes questionable temperature measurement techniques. This makes any universal comparison on a temperature or fluence scale very difficult.

In an attempt to make some sense out of the data reported we have broken the data up into that eminating from thermal and fast reactors.

Table IX-C-3

Summary of Property Measurements

Made After Neutron Irradiation of Molybdenum

Irradiation Temperature Range	Number of studies[a]			
	TEM[b]	Resistivity	X-Ray and Stored Energy	Mechanical Property
0-100°K	5	30	-	4
100-273°K	-	-	-	-
0-50°C	22	13	15	13
50-200°C	24	14	3	26
200-450°C	14	1	1	8
450-750°C	42	1	-	12
700-1000°C	35	1	-	14
>1000°C	8	—	-	3
	153	60	19	80

a) Will not equal number in Table IX-C-2 because of duplication of properties measured.
b) Transmission Electron Microscopy

Figure IX-C-1

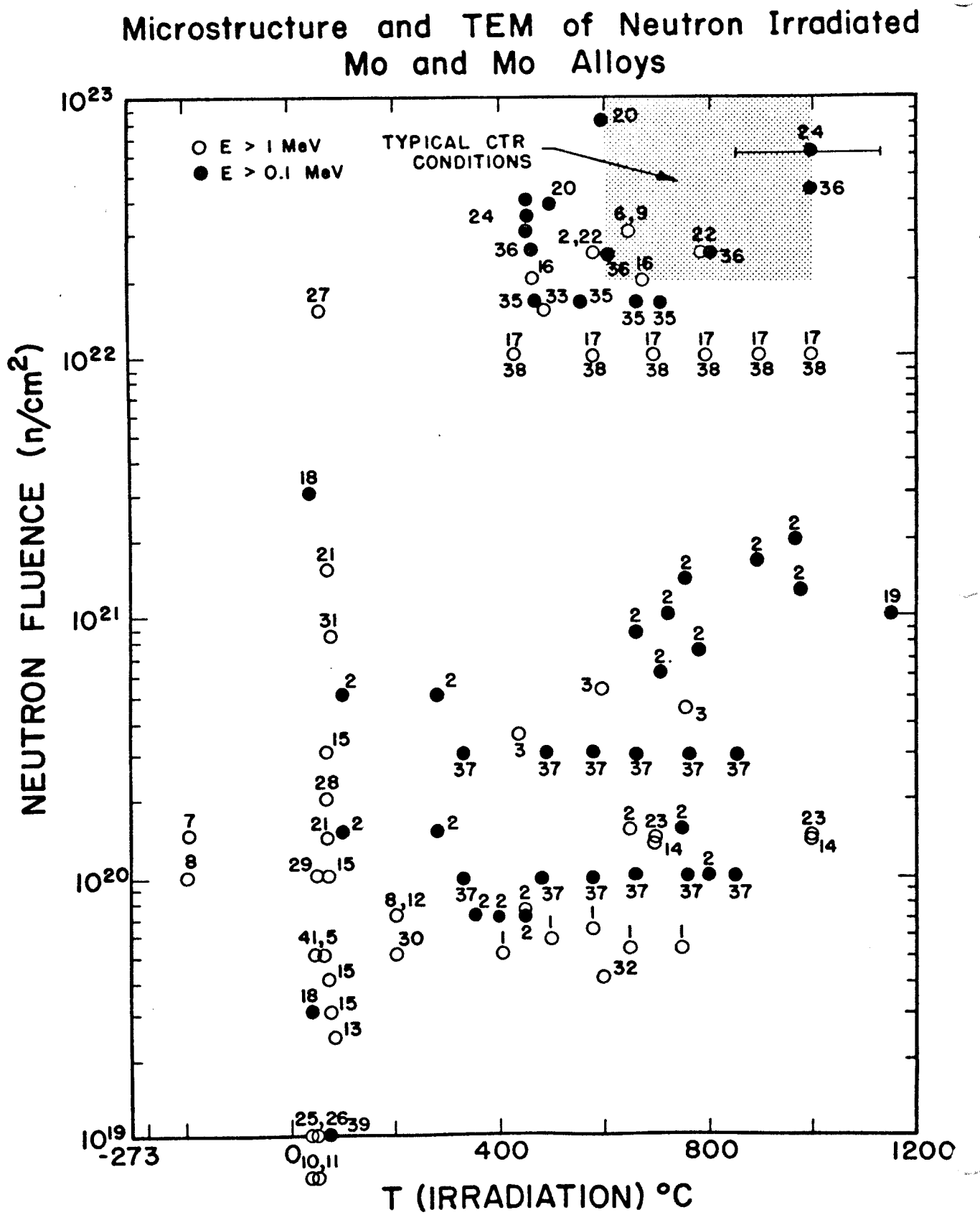
Microstructure and TEM of Neutron Irradiated Mo and Mo Alloys
O E > 1 MeV
● E > 0.1 MeV
TYPICAL CTR CONDITIONS
NEUTRON FLUENCE (n/cm²)
T (IRRADIATION) °C
10²³
10²²
10²¹
10²⁰
10¹⁹
-273
400
800
1200

Table IX-C-4

Volume Changes in Neutron Irradiated Molybdenum

Reactor	Temp. °C	Fluence x 10^{-21} n/cm^2 (E > 0.1 MeV)	ΔV/V %	Reference[a]
Hanford	40	0.03	0.08 [c]	8
Hanford	40	0.15	0.14 [c]	8
Hanford	40	0.3	0.15 [c]	8
NRX	50	0.07	0.08 [c]	9
ETR	100	0.15	0.07 [c]	10
ETR	100	0.5	0.15 [c]	10
ETR	280	0.15	0.06 [c]	10
ETR	280	0.5	0.11 [c]	10
Pluto	330	0.1 [b]	0.072	11
Pluto	330	0.1 [b]	0.036	11
Pluto	330	0.3 [b]	0.085	11
Pluto	330	0.3 [b]	0.046	11
Hanford	350	0.07	0.025 [c]	10
Hanford	400	0.07	0.012 [c]	10
EBR-II	430	55 [d]	1.6 [d]	12
HFR (Bel)	440	0.7	0.04	14
Hanford	450	0.07	0.015 [c]	10
EBR-II	450	8.0	0.9 [c]	10
Hanford	450	0.075	0.015	10
EBR-II	455	17	0.09	13
EBR-II	460	8	0.75	10
Pluto	475	0.1 [b]	0.16	11
Pluto	475	0.1 [b]	0.15	11
Pluto	475	0.3 [b]	0.18	11
Pluto	475	0.3 [b]	0.27	11
EBR-II	540	7.4	0.47	13
Pluto	575	0.1 [b]	0.17	11
Pluto	575	0.1 [b]	0.17	11
Pluto	575	0.3 [b]	0.12	11
Pluto	575	0.3 [b]	0.18	11
EBR-II	580	55 [d]	1.6	12
EBR-II	585	25	1.1	16
EBR-II	595	7.4	0.7	13
HFR (Bel)	600	0.52	0.07	14
Siloe	600	0.5	0.1	17
DFR	640	20	0.55	18
Hanford	650	0.15	0.028	10
Pluto	650	0.1 [b]	0.059	11
Pluto	650	0.1 [b]	0.056	11
Pluto	650	0.3 [b]	0.25	11
Pluto	650	0.3 [b]	0.25	11

Table IX-C-4 (continued)

Reactor	Temp. °C	Fluence x 10^{-21} n/cm^2 (E > 0.1 MeV)	ΔV/V %	Reference[a]
ETR	665	0.85	0.07	10
ETR	700	0.4	0.1	19
EBR-II	700	55 (d)	1.3	12
ETR	708	0.6	0.06	10
ETR	725	1.04	0.11	10
ETR	755	1.37	0.11	10
Pluto	750	0.1[b]	0.039	11
Pluto	750	0.1[b]	0.065	11
Pluto	750	0.3[b]	0.085	11
Pluto	750	0.3[b]	0.265	11
EBR-II	750	9	0.26	13
Hanford	750	0.15	0.045	10
HFR(Bel)	760	0.49	0.03	14
ETR	785	0.73	0.08	10
EBR-II	790	25.0	1.20	16
SILOE	800	0.5	0.2	17
EBR-II	800	55 (d)	0.85	12
Hanford	800	0.1[b]	0.045	10
Pluto	850	0.1[b]	0.028	11
Pluto	850	0.3[b]	0.11	11
Pluto	850	0.3[b]	0.302	11
ETR	900	1.61	0.09	10
SILOE	900	0.5	0.2-0.4	17
EBR-II	900	55 (d)	0.9 [d]	12
ETR	970	1.96	0.12	10
ETR	985	1.26	0.47	10
ETR	1000	0.4	0.19	19
EBR-II	1000	55 (d)	1.05	12
ETR	1050	0.9	0.17	20
ETR	1150	0.9	0.28	20
SILOE	1200	0.5	0.2	17
ETR	1230	1.68	0.032	10
ETR	~1300	1.98	<0.01	10
ETR	~1380	2.74	none	10

(a) Primary reference, results may be quoted in other papers.
(b) Fission spectra, E > 0.1 MeV is 70% of this value.
(c) Calculated from length change.
(d) Calculated from 10 x 10^{21} n/cm^2 (E > 1 MeV) in row 7.

In order to compare this data, we plot the swelling as a function of temperature and normalized to 2.5 x 10^{22}n/cm^2 (E > 0.1 MeV) with a 0.6 power law as suggested by Brimhall[90] (see Figure IX-C-2).* There is obviously far too much spread in the data to draw any major conclusions, but we might make some general observations about neutron irradiation of molybdenum.

(1) There should be little void induced swelling below 300°C (the lowest temperature at which void swelling has been observed is at 330°C[11]).

(2) There will probably be little swelling above 1300°C (very little swelling was observed after 2 x 10^{21}n/cm^2 at 1300°C and no swelling observed after 2.7 x 10^{21}n/cm^2 at 1380°C[10]).

(3) In the temperature region of interest (~600-1000°C), the swelling after ~13 dpa (2.5 x 10^{22}n/cm^2) might range from as low as 0.3% to as high as 5%.

There have been some self-consistent irradiation studies of pure molybdenum to determine the temperature variation of swelling. We have plotted the results of two such studies in Figure IX-C-3. The normalized swelling as a function of temperature does not show the "characteristic" bell shaped curve starting at 0.3 T_m and ending at 0.5 T_m. Instead, the low fluence (~10^{20}-10^{21}n/cm^2) data suggests a peak in the neighborhood of 0.3 T_m (600°C), a drop in the swelling up to 0.4 T_m and perhaps an increase after that. (Note that maximum temperature at which swelling is observed is ~1300°C, or 0.55 T_m).

The data for TZM, or a related alloy, Mo-0.5 Ti, is even more sparse than that for pure molybdenum. We have tried to summarize all the available alloy data in Table IX-C-5. Again there is no consistent trend from which to predict the behavior of Mo alloys with respect to swelling. However, a few qualitative remarks are in order.

(1) It appears that swelling in TZM does not increase rapidly with fluence at any temperature, in fact, very high fluence (3 to 8 x 10^{22}n/cm^2) irradiations show little if any swelling in that alloy.[15]

(2) The temperature dependence of swelling is rather flat from 475°C to 650°C for TZM[11] and from 430 to 1000°C for Mo-0.5Ti.[12]

(3) Swelling can occur at fluences as low as 10^{20}n cm^{-2} (0.05 dpa) and at temperatures as low as 330°C in TZM.

(4) Very complex precipitation behavior is observed in TZM and until it is understood, no confident predictions of the swelling in that alloy can be made.

---

* It is recognized that such a power law which seems to be valid for heavy ion irradiation may not be applicable to neutron irradiation but use of the n = 1 or higher laws makes the spread even worse.

Figure IX-C-2

Neutron Swelling in Molybdenum

Normalized to 2.5×10^{22} (E>0.1 MeV)

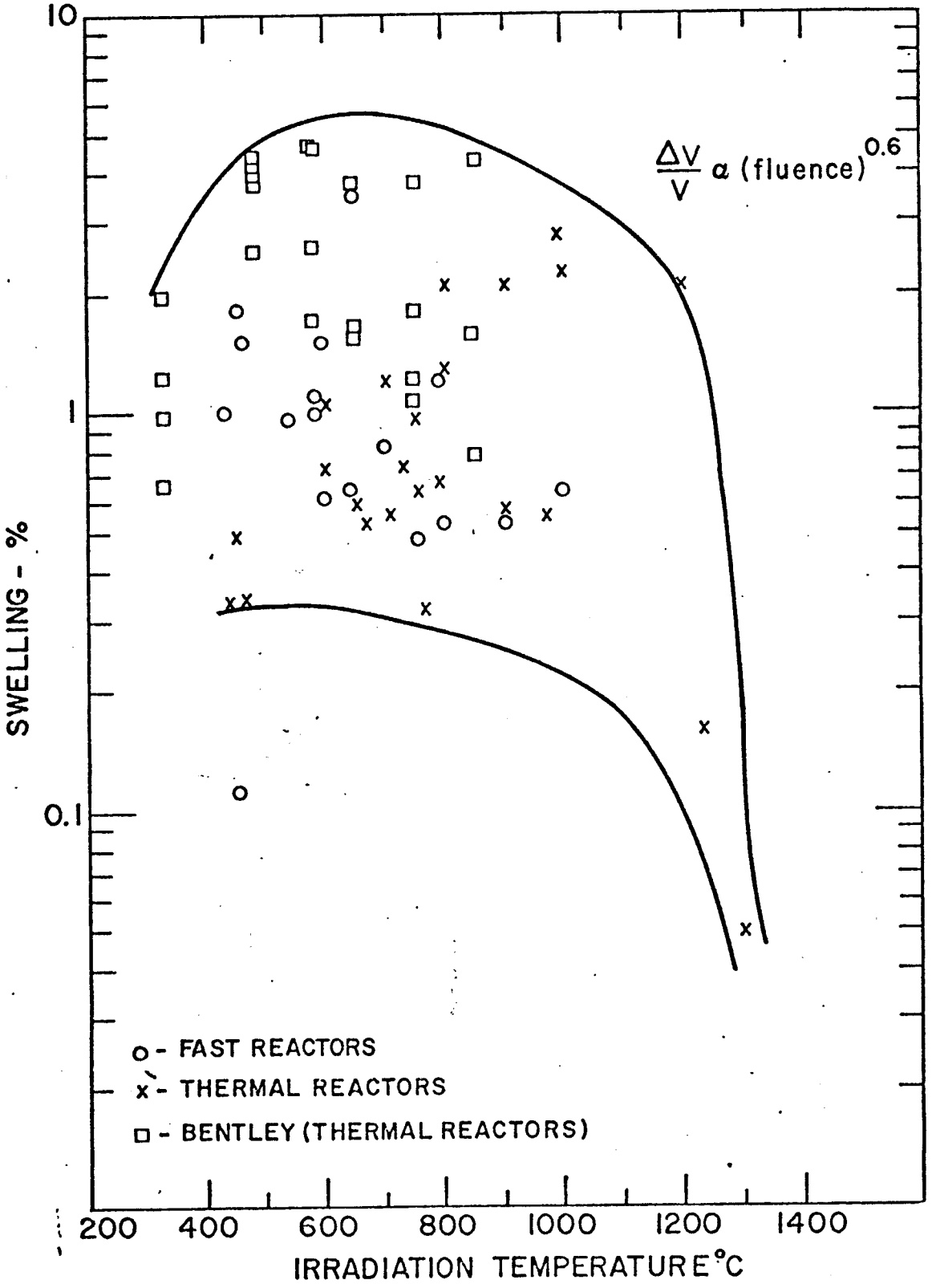

Figure IX - C - 3

TEMPERATURE DEPENDENCE OF SWELLING IN NEUTRON IRRADIATED MOLYBDENUM

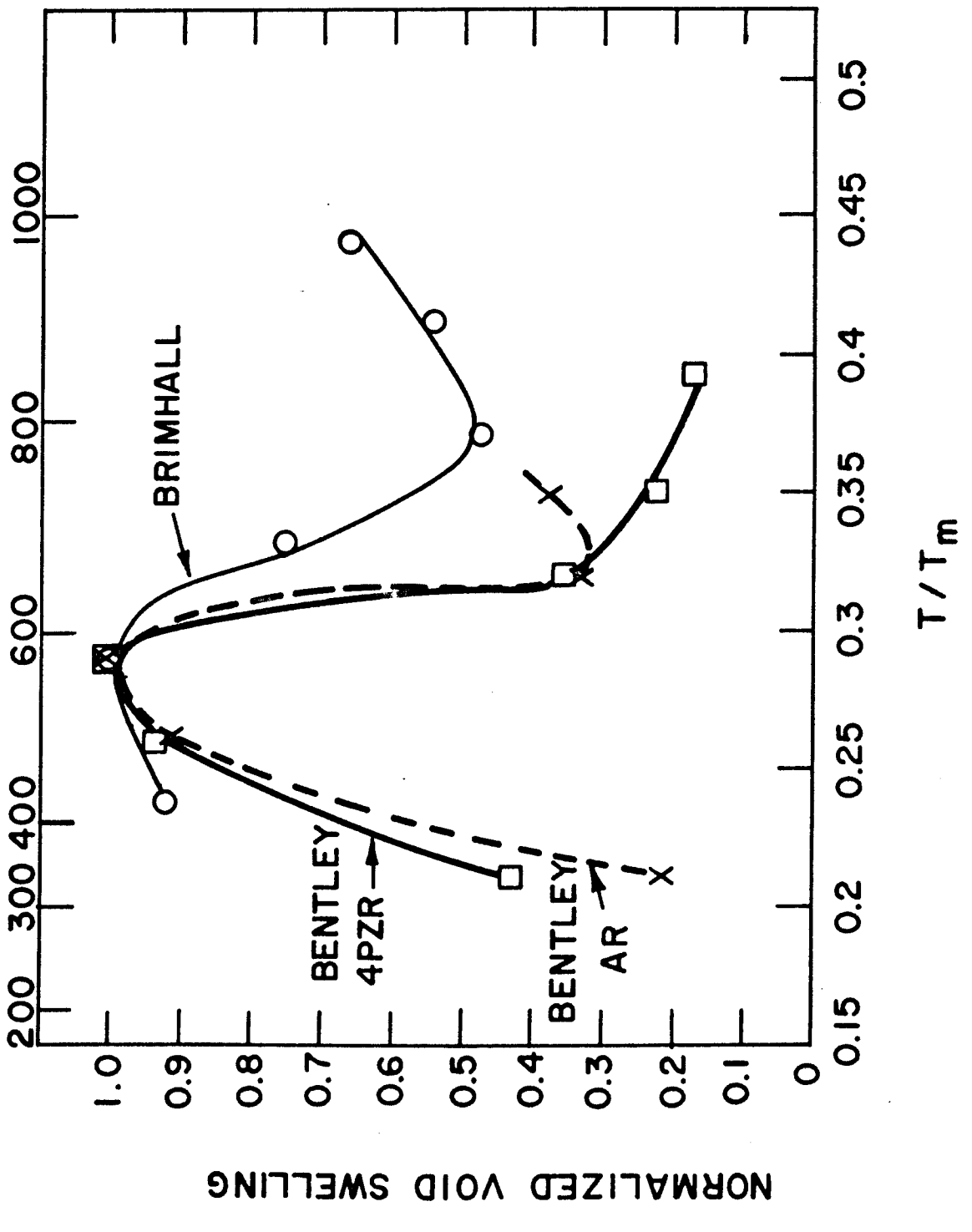

Table IX-C-5

Summary of Swelling Data on Neutron Irradiated Molybdenum Alloys

Reactor	Temp. °C	Fluence $n/cm^2 \times 10^{-21}$	Measured $\Delta V/V_o$%	Alloy	Reference
Pluto	330	0.3[a]	0.003	TZM	11
EBR-II	425	25	0	Mo-0.5Ti	16
EBR-II	430	10	0.26	Mo-0.5Ti	12
Pluto	475	0.1[a]	0.19	TZM	11
Pluto	475	0.3[a]	0.19	TZM	11
EBR-II	500	38	0	TZM	15
EBR-II	500	80	0.01	TZM	15
Pluto	575	0.1[a]	0.12	TZM	11
Pluto	575	0.3[a]	0.25	TZM	11
EBR-II	580	10	0.30	Mo-0.5Ti	12
EBR-II	585	25	1.1	Mo-0.5Ti	16
EBR-II	600	38	0.79	TZM	15
DFR	640	20	0.55	TZM	18
Pluto	650	0.3[a]	0.24	TZM	11
EBR-II	700	10	0.16	Mo-0.5Ti	12
EBR-II	790	25	1.2	Mo-0.5Ti	16
EBR-II	800	10	0.11	Mo-0.5Ti	12
EBR-II	900	10	0.14	Mo-0.5Ti	12
EBR-II	1000	10	0.15	Mo-0.5Ti	12

a. Fission Neutrons

There is another body of experimental results which may shed some light on the swelling in the Mo system, that is, light and heavy ion simulation studies. We have attempted to summarize the work report to date in Tables IX-C-6 thru IX-C-8. A recent interlaboratory program on Mo is included as well as the extensive irradiations of Stubbins.[21]

In addition to differences in material purity and experimental techniques, we face the problem of "temperature shifts" during the high damage rate studies. The effective temperature may be very crudely related to the actual sample temperature, the effective displacement rate, and the migration energy of the vacancies by

$$\frac{1}{T_{eff}} = \frac{1}{T_{ion}} + \frac{k}{Q_m^v} \ln \left(\frac{K_I}{K_e}\right)$$

where T_{ion} is the ion bombardment temperature

Q_m^v is the migration energy of the vacancies

K_I is the dpa rate of the ion bombardment

K_e is the dpa rate of the effective bombardment

We have quoted both the actual sample temperature and the effective temperature corresponding to a 5×10^{-7} dpa/sec damage rate which is close to that experienced in the first wall of UWMAK-III. A value of $Q_m = 1.5$ eV was used for these calculations. The reader should be cautioned that the effective temperatures depend on dislocation structure as well as other physical properties and the effective temperatures in Table IX-C-6 should only be considered as first order approximations.

Some selected results from two self-consistent studies[21,29] are plotted in Figure IX-C-4. The irradiation temperatures were in the 875-1000°C range and the "effective temperatures" range from 431 to 507°C. While there is considerable spread in the data and it is always risky to extrapolate ion bombardment data to neutron irradiation, we will attempt to draw some very general conclusions:

(1) The incubation period for void nucleation is low, even in Mo without helium impurities. The exact value is not known, but from Figure IX-C-4 and other studies, it could be ~0.1 dpa.

(2) The swelling is rather insensitive to temperature in the 900-1000°C region and it follows roughly a dpa 0.5 dependence. (Brimhall[33] projects a 0.6 power law.)

(3) The temperature threshold for void formation in pure Mo is 750°C or an effective temperature of ~350-400°C. This is consistent with the neutron results of Bentley.[11]

Table IX-C-6

Summary of Heavy Ion Simulation Studies on Molybdenum

Ion	Energy MeV	Irradiation Temperature °C	dpa/sec	Effective Temperature °C (a)	dpa	Swelling $\Delta V/V_o$ %	Reference
H	0.5	900	2×10^{-4}	520	3	1.2	22
N	2	790	7×10^{-3}	399	100	ND	23
N	2	870	7×10^{-3}	430	100	0.67	23
N	2	400	$\sim10^{-2}$	215	70	ND	24
↓	↓	500	↓	264	70	ND	↓
		600		311	70	Low	
		700		354	70	-	
		800		394	70	-	
		850		413	70	-	
		900		431	50	0.14	
		900		431	70	0.15	
		900		431	120	0.23	
		900		431	200	0.44	
↓	↓	900	↓	431	400	0.55	↓
Ni	5	650	8×10^{-3}	337	5	ND	25
	5	800	8×10^{-3}	400	5	0.34	
		900	8×10^{-3}	437	5	1.0	
↓	↓	1000	8×10^{-3}	473	5	0.48	↓
Ni	5	800	↓	426	20	0.65	2
		900		467	2	0.47	
		900		467	2	0.3	
		900		467	20	2.0	
		900		467	20	1.9	
↓	↓	1000	↓	506	21	0.47	↓
Cu	18	700	6×10^{-4}	424	-		27
	17	800	6×10^{-4}	474	2.2	0.075	
	19	900	6×10^{-4}	521	1.0	0.13	
	17	900	6×10^{-4}	521	2.1	0.27	
	19	1000	6×10^{-4}	566	1.3	0.63	
↓	18	900	6×10^{-4}	521	19	2.6	↓
Mo	0.45	700	-	-	100	ND	24
Mo	3.2	800	2.5×10^{-3}	431	2	0.2	13
	3.2	800	2.5×10^{-3}	431	20	1.6	
	3.2	900	2.5×10^{-3}	473	2	0.34	
↓	3.2	900	2.5×10^{-3}	473	20	2.1	↓
Ta	7.5	800	$\sim10^{-2}$	394	150	1.0	29
		940		445	170	2.5	
		1000		466	1	0.12	
					1	0.08	
					1.2	0.15	
					2.8	0.20	
					2.9	0.24	
					3	0.16	
					9	0.35	
					10	0.38	
					11	0.55	
↓	↓	↓	↓	↓	23	0.83	↓

Table IX-C-6 (continued)

Ion	Energy MeV	Irradiation Temperature °C	dpa/sec	Effective Temperature (a) °C	dpa	Swelling $\Delta V/V_o$%	Reference
					30	1.0	
					90	1.5	
					109	2.3	
					150	3.5	
					160	2.2	
Ta	7.5	900	10^{-2}	431	1.2	0.12	30
					1.2	0.14	
					2.6	0.2	
					3.0	0.17	
					9	0.35	
					10	0.4	
					30	1.0	
					40	0.8	
					100	1.5	
					120	1.5	
					150	3.2	
V	3.1	750	2.98×10^{13}	404	34.0	ND	21
		840	5.50×10^{13}	425	17.6	0.98	
		830	3.71×10^{13}	432	23.2	0.35	
		890	5.38×10^{13}	445	17.1	1.05	
		880	4.45×10^{13}	447	14.9	0.65	
		875	3.76×10^{13}	450	15.8	0.88	
		900	4.85×10^{13}	452	5.1	0.36	
		898	4.51×10^{13}	453	32.5	1.56	
		928	6.67×10^{13}	453	48.9	2.48	
		908	4.74×10^{13}	455	54.0	3.22	
		900	4.08×10^{13}	457	13.0	0.96	
		900	3.3×10^{13}	464	3.5	0.38	
		900	2.57×10^{13}	471	5.4	0.21	
		970	2.68×10^{13}	498	11.8	0.65	
		1107	3.43×10^{13}	503	15.1	0.98	
		990	2.57×10^{13}	507	5.9	0.38	
		1007	2.07×10^{13}	521	9.1	0.81	
		1108	5.06×10^{13}	525	10.2	1.43	
		1132	5.37×10^{13}	530	14.8	1.50	
		1120	2.62×10^{13}	554	10.2	1.21	
		1120	2.62×10^{13}	554	10.2	1.24	
		1120	2.02×10^{13}	564	2.1	0.57	
		1256	6.18×10^{13}	564	44.5	5.80	
		1256	5.75×10^{13}	567	41.0	8.10	
		1250	4.64×10^{13}	573	33.4	10.30	
		1295	4.17×10^{13}	592	35.0	8.10	
		1285	3.57×10^{13}	595	25.7	11.90	
		1287	2.08×10^{13}	620	15.0	10.00	
		1312	2.10×10^{13}	628	17.6	9.80	
		1507	4.15×10^{13}	653	34.9	12.80	

(a) Based on 5×10^{-7} dpa/sec, Qm = 1.5 eV, see text for comment on the interpretation of such temperatures.

ND = None Detected

Table IX-C-7

Summary of 3.1 MeV Vanadium Ion Bombardment of TZM [21]

Irr. Temp. (°C)	Dose Rate dpa/sec x 10^{-3}	Effective Temp. (°C)	Dose (dpa)	$(\Delta V/V_o)\%$
750	5.02	391	57.2	Void Visible
750	3.28	401	37.4	Visible
750	2.97	404	35.0	None Visible
800	3.18	424	36.3	1.10
850	5.28	430	16.9	0.25
850	3.90	439	24.4	0.57
850	3.81	439	12.2	0.24
850	3.03	446	9.7	0.15
880	5.79	439	66.0	0.35
897	3.98	457	57.3	0.84
900	7.05	441	16.0	0.51
900	6.77	442	7.1	0.38
900	5.38	449	19.2	0.47
911	3.38	467	24.3	0.39
926	2.81	479	40.4	0.91
927	2.86	479	20.6	0.87
990	7.51	471	17.3	0.10
998	7.58	473	17.4	0.32
1000	4.05	495	9.3	0.09
1072	6.57	503	18.3	0.41
1090	7.44	505	15.0	0.27
1090	4.42	523	4.6	0.02
1090	3.08	571	12.0	0.19
1227	4.79	565	34.5	3.20
1240	6.32	558	45.5	5.51
1293	2.67	611	19.2	2.68
1305	1.92	630	13.8	2.48
1420	3.74	638	31.4	2.58

Table IX-C-8

Summary of 3.1 MeV Vanadium Ion Bombardment of Mo-0.5%Ti[21]

Irr. Temp °C	Dose Rate dpa/sec x 10^{-3}	Effective Temp. °C	Dose (dpa)	$(\Delta V/V_0)$ %
		Small Grains		
880	3.09	458	9.9	0.43
880	2.84	460	9.1	0.52
889	1.40	487	10.1	0.67
900	4.31	455	13.7	0.58
900	4.28	455	9.0	0.77
900	3.90	458	4.1	0.31
900	3.74	460	15.7	0.77
900	3.74	460	15.7	0.89
927	4.73	463	34.4	0.86
990	3.53	496	8.1	1.49
998	3.95	495	17.4	1.86
1000	4.52	491	18.7	1.88
1033	5.14	498	22.6	2.16
1038	3.44	514	7.9	2.01
1090	3.75	529	3.9	0.78
1090	2.09	552	11.3	2.18
1102	5.55	519	15.3	2.03
1110	5.06	525	6.1	1.83
1113	6.75	516	18.1	2.23
1113	6.75	516	13.6	2.00
1120	3.57	542	13.9	2.12
1227	1.19	625	8.6	1.59
1293	5.51	579	39.7	7.67
1300	4.08	594	34.3	3.21
1312	3.20	609	26.9	4.41
		Large Grains		
750	1.10	431	12.6	None observed
750	0.68	445	7.7	" "
750	0.068	521	7.8	" "
800	0.077	546	8.8	Void visible
900	2.32	475	16.7	0.82
900	1.84	482	21.0	0.92
907	1.38	495	19.9	1.21
910	1.61	491	11.6	0.27
915	2.54	478	18.3	0.65
1247	3.75	581	27.0	4.88
1275	4.05	587	29.2	8.94
1300	2.94	609	24.7	8.65
1367	3.36	623	28.3	5.35
1430	4.00	633	33.6	4.41

Figure IX - C - 4
DAMAGE DEPENDENCE OF SWELLING IN HEAVY ION IRRADIATED Mo.

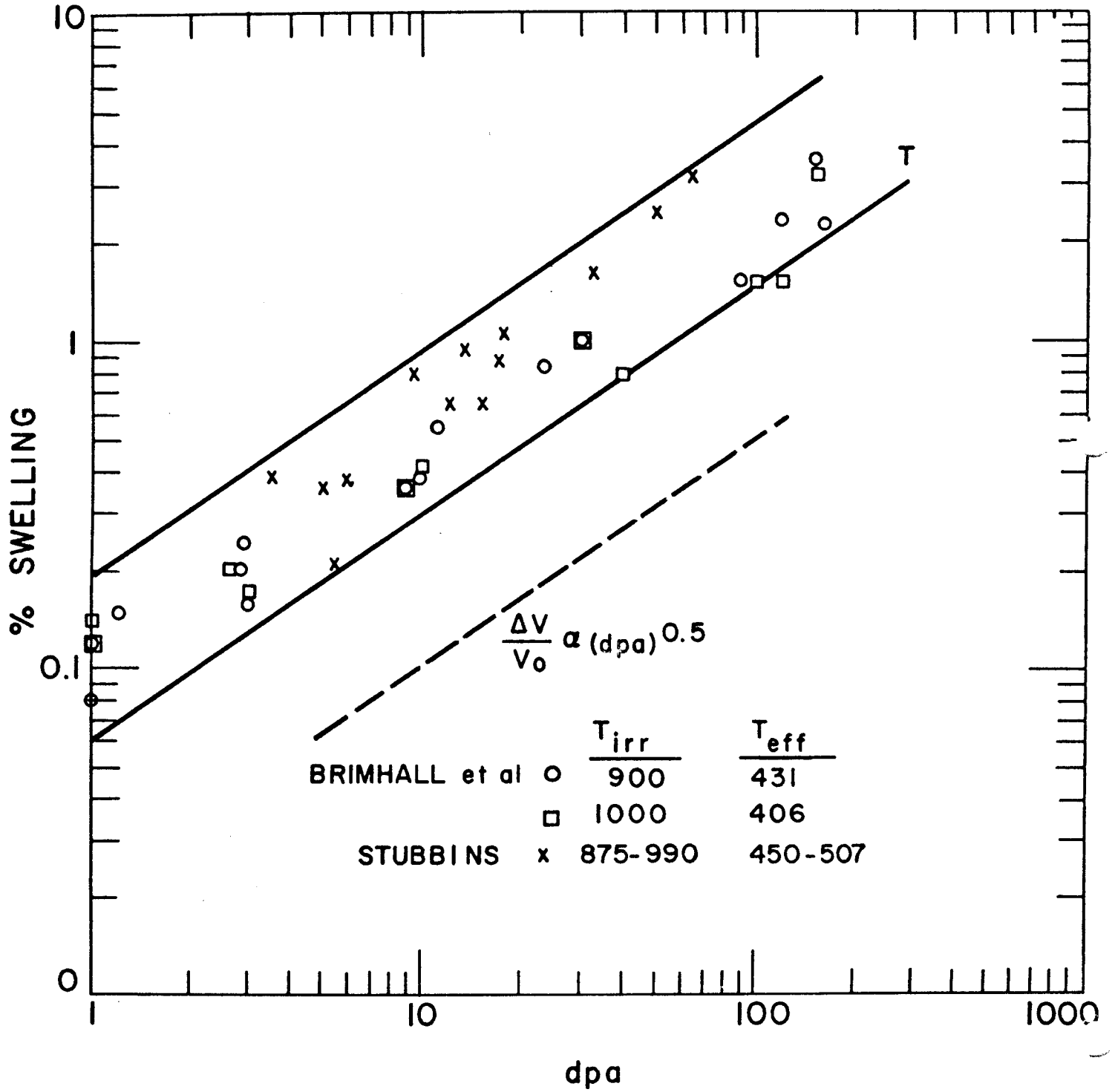

Brimhall[31] has also shown that the simultaneous injection of helium has very little effect on the swelling in Mo (in contrast to other metals). This is shown in Figure IX-C-5. The total helium injected in those studies was 10 to 100 appm (compared to over 100 appm/yr in UWMAK-III) but the general effect of helium in promoting swelling does not appear to be a dominating feature of the Mo system. The fact that voids form easily in the absence of helium should be particularly noted.

Finally, the Mo system, like that of Nb, Al, Ni and Ta[32] develops a superlattice structure after a sufficient damage at low temperatures and this may tend to limit the ultimate swelling of the metal. A summary of the void lattice parameter observed in various studies is given in Table IX-C-9. In the Nb and Ni systems, the onset of a superlattice signals a saturation in the swelling level, however, that has not been entirely the case for Mo and more work is needed to clarify that point. The effect of temperature on the void lattice constant is given in Figure IX-C-6 along with neutron data. The void lattice constant increases with increasing temperature but the value is much higher for neutron irradiation (this may be due to the rate effect). In any case, one may expect that at low effective temperatures, ordered void lattices will form in Mo, TZM, and Mo-0.5 Ti alloys after as little as one year of irradiation (~20 dpa).

The effect of temperature and damage level on swelling in Mo-0.5 Ti and TZM is displayed in Figure IX-C-7. At irradiation temperatures of ~900°C, the swelling increases to ~1% or less in ~20 dpa and is relatively constant after that. Higher temperature irradiation (1000 to 1100°C for Mo-0.05 Ti, and 1300°C for TZM) produces much more swelling which does not seem to saturate up to approximately 20 dpa for the Ti alloy or approximately 50 dpa for the TZM. The effect of irradiation temperature on the swelling in these alloys is shown in IX-C-7c. In all cases, the temperature threshold at 15 dpa is approximately 0.35 Tm and swelling continues until at least 0.55 T_m. The swelling in the Mo-0.5 Ti alloy exceeds that of pure Mo below 0.5 T_m but is lower above that temperature. The swelling in TZM is lower than in Mo at all temperatures.

IX-C-1-c-ii) Mechanical Property Effects

As pointed out earlier, the amount of work on the mechanical properties of Mo or Mo alloys is relatively small. Figure IX-C-8 summarizes the neutron fluence-irradiation temperature regimes that have been studied to date. There are four observations that can be made from that figure.

(1) More than half of the work has been related to irradiation temperatures <450°C.

(2) The maximum neutron fluence for creep and tensile experiments is ~7 x 10^{22}n/cm^2 (~35 dpa).

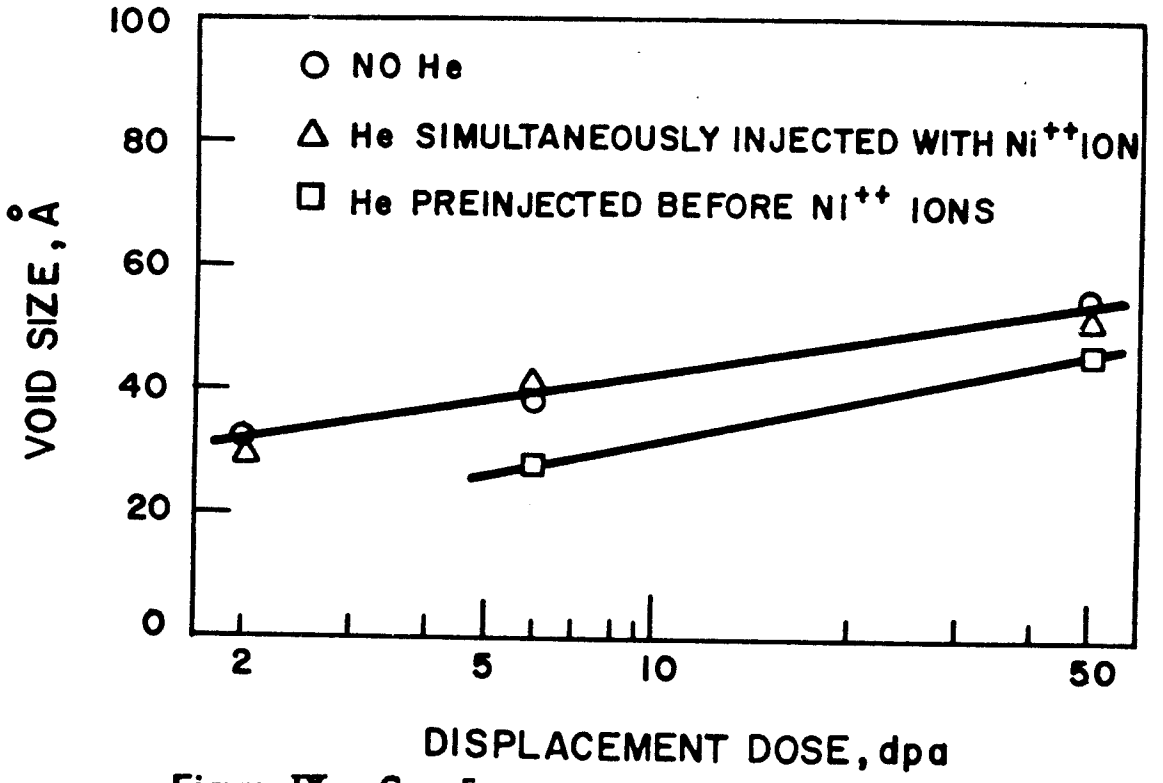

Figure IX - C - 5
DOSE DEPENDENCE OF VOID SIZE IN MOLYBDENUM BOMBARDED UNDER DIFFERENT CONDITIONS OF He AND Ni ION BOMBARDMENT. (33)

Table IX-C-9

Summary of Void Lattice Parameters for Mo & Mo Alloys

Ion	Irradiation Temp. °C	dpa	Void Dia. $2r_v$ Å	Void Lattice Parameter-a-A	$\frac{a}{r_v}$	Reference
			Molybdenum			
2 MeV N	870	~100	10	220	11	24
3.1 MeV V	898	33	82	480	11.7	21
5 MeV Ni	900	20	54	350	13	26
2.8 MeV Mo	900	20	80	350	8.8	13
18 MeV Cu	900	19	85	340	8	27
7.5 MeV Ta	900	130	60	230	7.7	32
3.1 MeV V	908	54	147	377	5.1	21
3.1 MeV V	928	49	102	410	8.0	21
7.5 MeV V	940	170	76	320	8.4	29
7.5 MeV Ta	1000	160	105	460	8.8	29
3.1 MeV V	1007	15	82	430	12.9	21
3.1 MeV V	1123	10	223	613	5.5	21
			TZM			
2 MeV N	870	300	~60	220	~7.3	24
3.1 MeV V	926	40	77	42.9	11.1	21
3.1 MeV V	927	21	68	40.7	12.0	21
			Mo-0.5 Ti			
3.1 MeV V	907	20	70	452	12.9	21
3.1 MeV V	917	18	67	424	12.7	21

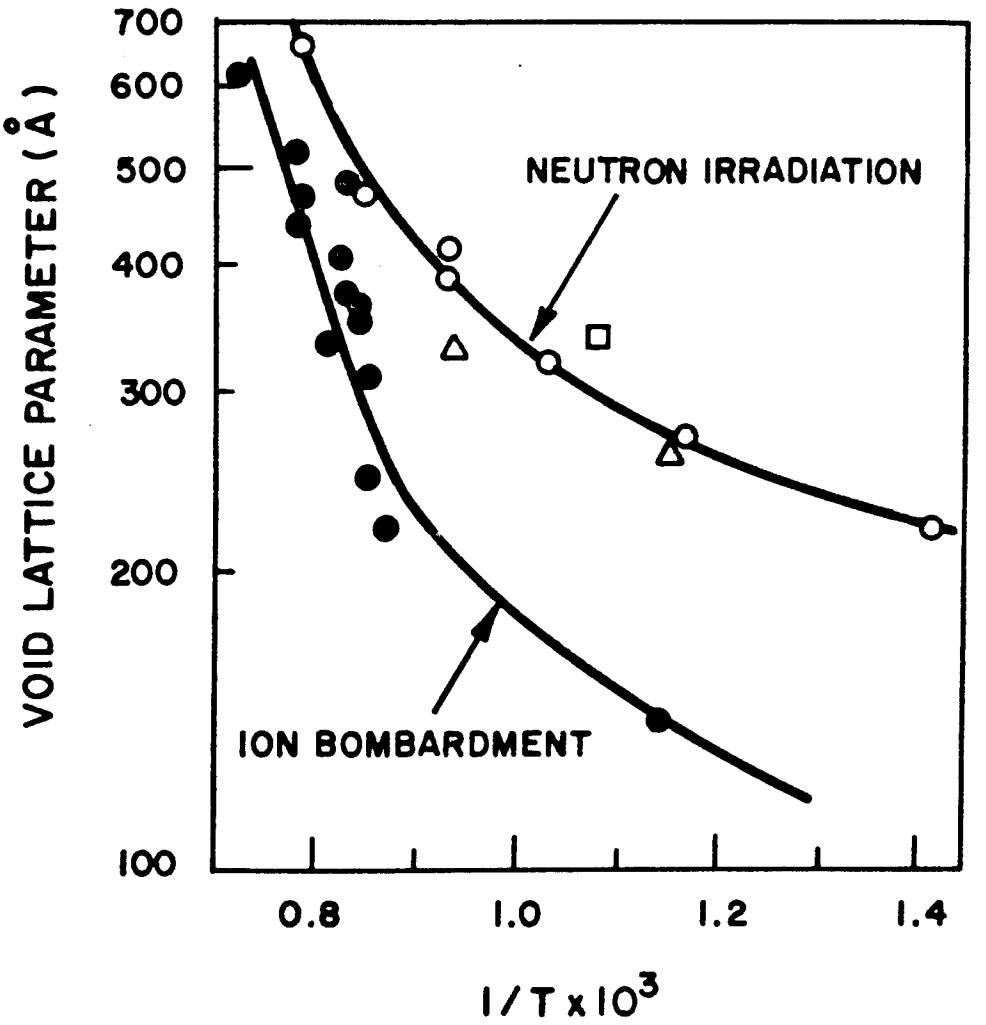

Figure IX - C - 6
TEMPERATURE DEPENDENCE OF VOID LATTICE PARAMETER IN MOLYBDENUM. (AFTER BRIMHALL)

Figure IX - C - 7a

SWELLING IN Mo - 0.5 Ti AFTER 3.1 MeV V ION BOMBARDMENT (21)

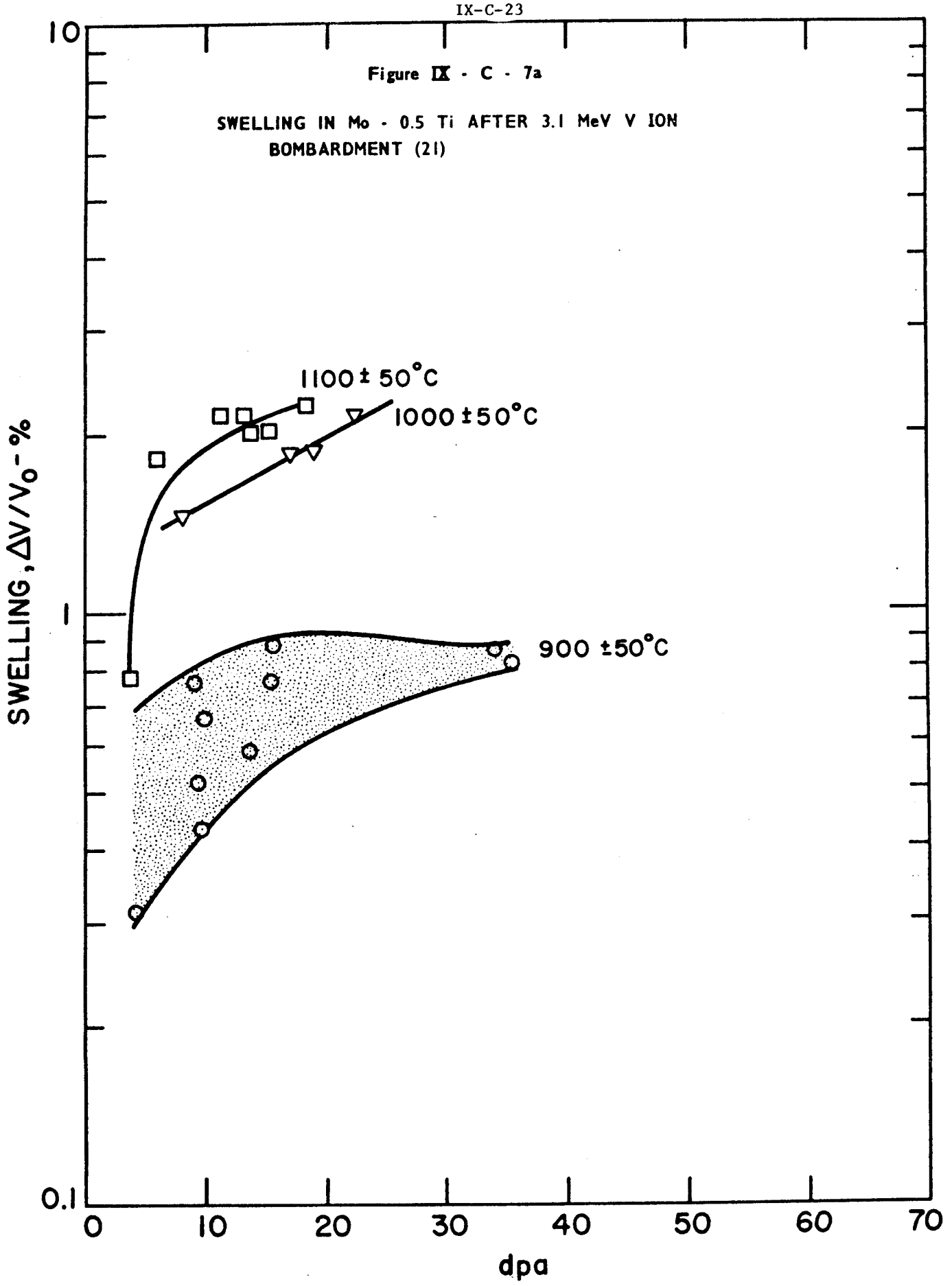

Figure IX - C - 7b

SWELLING IN TZM AFTER 3.1 MeV V ION BOMBARDMENT (21)

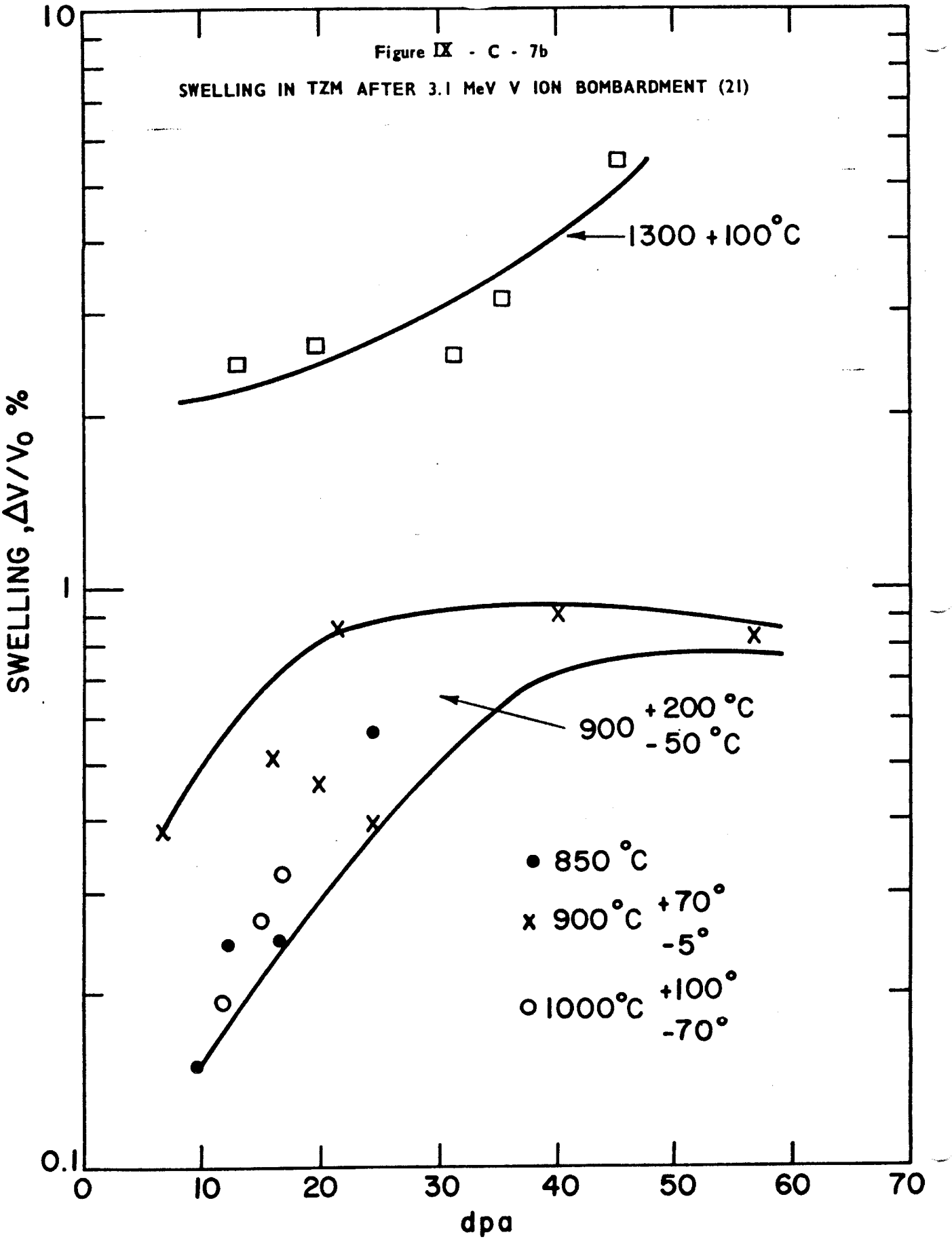

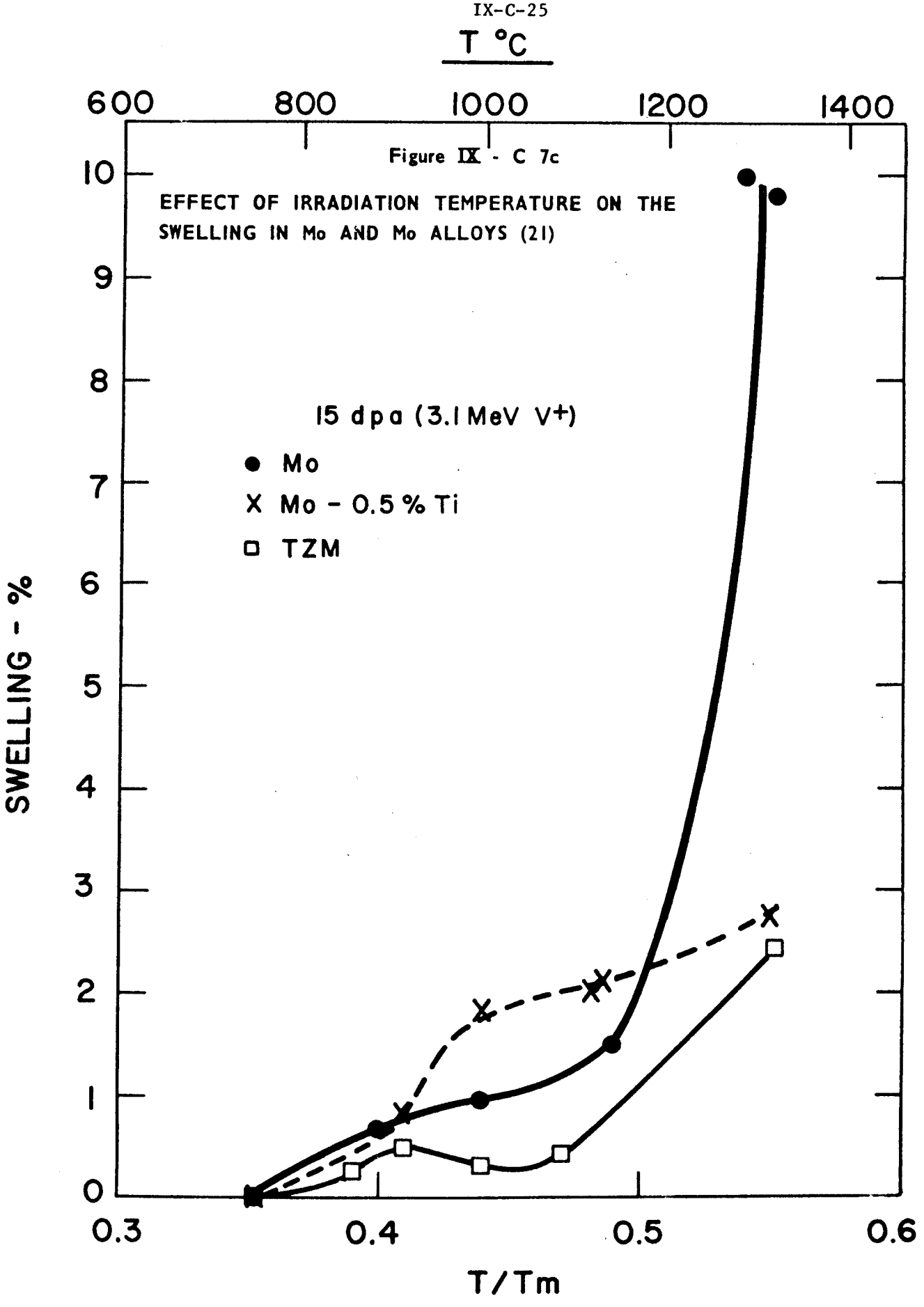
T °C
600
800
1000
1200
1400
Figure IX - C 7c
EFFECT OF IRRADIATION TEMPERATURE ON THE SWELLING IN Mo AND Mo ALLOYS (21)
15 dpa (3.1 MeV V+)
Mo
Mo - 0.5 % Ti
TZM
SWELLING - %
0
1
2
3
4
5
6
7
8
9
10
0.3
0.4
0.5
0.6
T/Tm

Figure IX-C-8

Mechanical Properties of Neutron Irradiated Mo and Mo Alloys

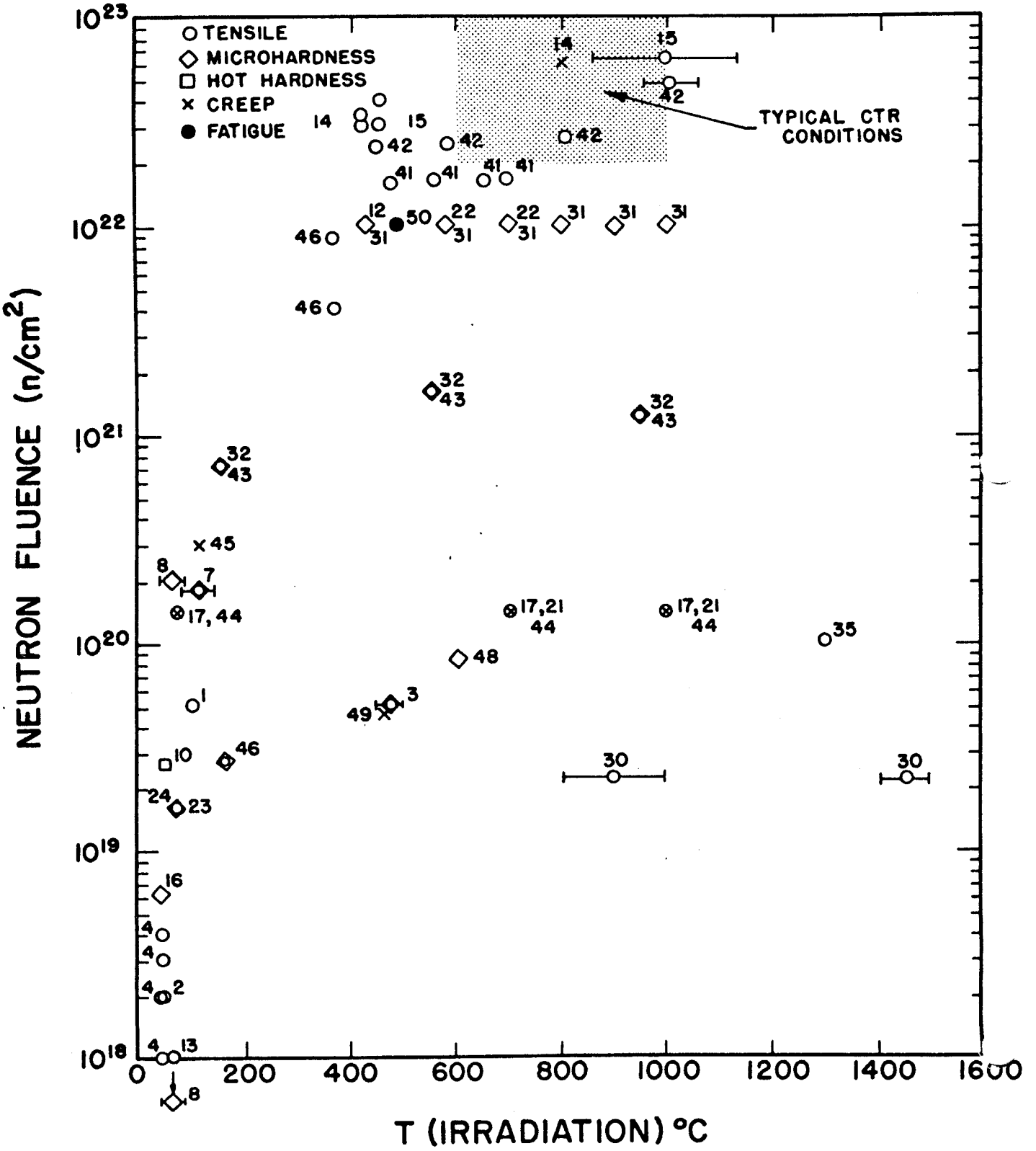

(3) All tests have been conducted outside the reactor; i.e., no insitu testing has taken place.

(4) About 1/2 of the data in the temperature range of interest comes from microhardness tests which can give an idea of changes in tensile strength but not ductility.

After considering all of the data, one finds that there are essentially seven papers of interest to the fusion reactor designer. We will quote just a few highlights below.

Tensile Behavior

The properties of importance in this area are the ultimate and yield strengths and the uniform and total elongations. The yield strength normally increases during irradiation and the ductility drops. For Mo, we also have the phenomena of the ductile to brittle transition tmperature (DBTT) to deal with (see Section IX-B-2). The major property that we will be concerned with in this analysis is the ductility as revealed by the shift in the DBTT.

The first thing to recognize about the very meager irradiation data available is that either samples have been irradiated at a temperature far too low to reveal any thing about high temperature (600-1000°C) fusion reactor performance, or the specimens have been irradiated at too low of a fluence.

There is only one[34] neutron irradiated sample in the 600-1000°C and 15 dpa range (typical of 1 year in UWMAK-III) and that specimen was tested at 550°C, a temperature far below the UWMAK-III first wall temperature.

Wiffen[34] has the highest fluence high temperature data on Mo and TZM while the Russians[35-38] also tested some materials in the appropriate temperature range. (See Table IX-C-10).

Wiffen[34] has classified the observed tensile behavior of molybdenum into three regions as follows:

(1) Conventional behavior observed in control specimens where the load vs elongation curve deviates from the modulus line at the proportional limit, the load increasing with elongation until a maximum is reached and then decreases as the elongation increases until the specimen fails.

(2) Brittle failure which occurs at the maximum load with less than 0.2% deviation from the modulus line.

(3) Unstable behavior where the maximum load occurs within 0.2% of the modulus line. Plastic instability is coincident with yielding but the specimen necks and shows appreciable elongation and reduction in area before failure at a load much below the maximum.

It was found that irradiation at 450°C increased the ultimate tensile strength by a factor of 2 to 3 for both Mo and Mo-0.5%, both of which showed nearly the same behavior. The ductile brittle transition temperature of specimens irradiated at 450°C was found to be as high as 550 to 650°C compared

Table IX-C-10

Summary of Tensile Properties of Mo Alloys After High Temperature Neutron Irradiation

Irradiation Temp. °C	Test Temp°C	Strain Rate(min^{-1})	Fluencex10^{22} n/cm^2 (a)	MPa		Ductility-%	
				0.2% Yield	Ultimate Strength	Uniform Elongation	Total Elongation
			Molybdenum[34]				
	-196	0.02		726	726	0	0
	- 80	0.02		817	817	0.1	0.1
	22	0.02		358	496	22.0	54.6
	200	0.02		143	352	39.0	56.1
	200	0.0002		118	299	38.0	47.0
	400	0.02		101	261	30.9	42.4
	550	0.02		72	230	31.7	41.8
	550	0.0002		65	221	28.1	37.1
	650	0.02		73	223	29.7	42.3
455	22	NA	4.0	NA	NA	NA	0.1
857 to 1136	22	0.02	6.1	857	857	0.1	0.2
455	200	0.0002	4.0	874	874	0	0
454	400	0.02	3.5	781	781	0.1	0.1
(c) 455 + anneal (b)	400	0.02	4.0	598	737	6.3	6.3
(c) 857 to 1136	550	0.02	6.1	563	697	5.7	10.5
454	550	0.02	3.5	696	696	0.2	0.2
454	550	0.0002	3.5	586	586	0.1	6.5
454	650	0.02	3.5	595	595	0.1	8.4
			Mo-0.5Ti[34]				
	-196	0.02		715	715	0	0
	- 80	0.02		690	768	3.8	3.8
	22	0.02		350	548	21.5	48.1
	400	0.02		99	306	34.0	50.1
	400	0.002		103	287	32.9	47.5
	400	0.0002		117	280	30.9	47.3
	650	0.02		96	277	29.3	39.6
445	400	0.02	3.0	813	813	0.1	0.1
445	400	0.002	3.0	707	707	0	0
445	400	0.0002	3.0	697	697	0.1	7.0
445	650	0.02	3.0	650	650	0.1	7.9
			TZM[35]				
-	200	NA	-	510	NA	NA	11
150	200	NA	0.07	723	NA	NA	8
-	500	NA	-	393	NA	NA	10
1500	500	NA	0.016	586	NA	NA	3
-	800	NA	-	215	NA	NA	11
950	800	NA	0.12	344	NA	NA	15

Table IX-C-10 (cont.)

Irradiation Temp. °C	Test Temp°C	Strain Rate(min^{-1})	Fluence x 10^{22} n/cm^2 (a) TZM(35)	MPa 0.2% Yield	MPa Ultimate Strength	Ductility-% Uniform Elongation	Ductility-% Total Elongation
(d)	RT	0.0035	-	620	NA	NA	16
150	RT		0.07	740	NA	NA	~0
(e)	RT		-	620	NA	NA	16
550	RT		0.16	1070	NA	NA	~0
(f)	RT		-	560	NA	NA	22
950	RT		0.12	590	NA	NA	15
(d)	100		-	470	NA	NA	18
150	100		0.07	760	NA	NA	~0
(e)	100		-	520	NA	NA	18
550	100		0.16	950	NA	NA	1
(f)	100		-	470	NA	NA	22
950	100		0.12	480	NA	NA	15
(d)	200		-	510	NA	NA	11
150	200		0.07	730	NA	NA	9
(e)	200		-	450	NA	NA	10
550	200		0.16	880	NA	NA	1
(f)	200		-	410	NA	NA	19
950	200		0.12	440	NA	NA	15
(d)	300		-	400	NA	NA	11
150	300		0.07	710	NA	NA	10
(e)	300		-	410	NA	NA	10
550	300		0.16	780	NA	NA	2
(f)	300		-	450	NA	NA	13
950	300		0.12	410	NA	NA	14
(d)	400		-	440	NA	NA	10
150	400		0.07	770	NA	NA	4
(e)	400		-	420	NA	NA	9
550	400		0.16	650	NA	NA	2
(f)	400		-	460	NA	NA	9
950	400		0.12	460	NA	NA	13
(d)	500		-	360	NA	NA	10
150	500		0.07	680	NA	NA	2
(e)	500		-	430	NA	NA	8
550	500		0.16	600	NA	NA	3
(f)	500		-	400	NA	NA	8
950	500		0.12	430	NA	NA	12
(d)	600		-	340	NA	NA	10
150	600		0.07	850	NA	NA	1
(e)	600		-	350	NA	NA	8
550	600		0.16	620	NA	NA	4
(f)	600		-	370	NA	NA	7
950	600		0.12	400	NA	NA	11
(d)	700		-	330	NA	NA	10
150	700		0.07	650	NA	NA	2
(e)	700		-	360	NA	NA	8
550	700		0.16	480	NA	NA	5
(f)	700		-	360	NA	NA	9
950	700		0.12	380	NA	NA	10

Table IX-C-10 (cont.)

Irradiation Temp. °C	Test Temp°C	Strain Rate(min^{-1})	Fluencex10^{22} n/cm^2 (a)	MPa 0.2% Yield	MPa Ultimate Strength	Ductility-% Uniform Elongation	Ductility-% Total Elongation
(d)	800	0.0035	-	280	NA	NA	10
150	800		0.07	550	NA	NA	5
(e)	800		-	360	NA	NA	6
550	800		0.16	460	NA	NA	6
(f)	800		-	320	NA	NA	11
950	800		0.2	350	NA	NA	15
			Mo-0.12 Zr-0.002 B-0.004C[35]				
(d)	RT		-	620	NA	NA	22
150	RT		0.07	670	NA	NA	~0
(e)	RT		-	590	NA	NA	18
550	RT		0.16	870	NA	NA	~0
(f)	RT		-	580	NA	NA	22
950	RT		0.12	660	NA	NA	23
(d)	100		-	550	NA	NA	15
150	100		0.07	770	NA	NA	10
(e)	100		-	540	NA	NA	15
550	100		0.16	960	NA	NA	~0
(f)	100		-	490	NA	NA	17
950	100		0.12	570	NA	NA	17
(d)	200		-	480	NA	NA	16
150	200		0.07	660	NA	NA	13
(e)	200		-	520	NA	NA	11
550	200		0.16	750	NA	NA	~0
(f)	200		-	540	NA	NA	11
950	200		0.12	560	NA	NA	15
(d)	300		-	460	NA	NA	11
150	300		0.07	830	NA	NA	10
(e)	300		-	520	NA	NA	10
550	300		0.16	910	NA	NA	1
(f)	300		-	480	NA	NA	10
950	300		0.12	540	NA	NA	12
(d)	400		-	460	NA	NA	10
150	400		0.07	660	NA	NA	10
(e)	400		-	490	NA	NA	8
550	400		0.16	730	NA	NA	3
(f)	400		-	450	NA	NA	9
950	400		0.12	510	NA	NA	13
(d)	500		-	740	NA	NA	11
150	500		0.07	800	NA	NA	7
(e)	500		-	500	NA	NA	9
550	500		0.16	670	NA	NA	4
(f)	500		-	430	NA	NA	9
950	500		0.12	500	NA	NA	13
(d)	600		-	420	NA	NA	10
150	600		0.07	620	NA	NA	10
(e)	600		-	480	NA	NA	7
550	600		0.16	600	NA	NA	5
(f)	600		-	410	NA	NA	11
950	600		0.12	480	NA	NA	12

Irradiation Temp°C	Test Temp°C	Strain Rate(min^{-1})	Fluencex10^{22} n/cm^2 (a)	MPa 0.2% Yield	MPa Ultimate Strength	Ductility-% Uniform Elongation	Ductility-% Total Elongation
(d)	700	0.0035	-	400	NA	NA	9
150	700	↓	0.07	600	NA	NA	7
(e)	700	↓	-	450	NA	NA	7
550	700	↓	0.16	600	NA	NA	5
(f)	700	↓	-	400	NA	NA	9
950	700	↓	0.12	460	NA	NA	11
(d)	800	↓	-	400	NA	NA	10
150	800	↓	0.07	600	NA	NA	5
(e)	800	↓	-	420	NA	NA	7
550	800	↓	0.16	550	NA	NA	5
(f)	800	↓	-	380	NA	NA	10
950	800	↓	0.12	440	NA	NA	11
			Mo(36)				
-	22	NA	-	703	NA	NA	7
450	22	NA	0.005	1015	NA	NA	1.7
-	22	NA	-	634	NA	NA	21
550	22	NA	0.003	820	NA	NA	2.6
			Mo(37)				
	200	0.1	-	NA	(No	NA	60
(c) 800-1000	200	0.1	0.0025	NA	Change)	NA	40
			Mo(38)	(Single Crystals)			
-	600	0.06	-	~34	~55	20	35
1600	600	0.06	>0.01	~34	~68	25	42
			TZM(39)				
-	500	0.02	0	138	NA	17	18
<150	500	↓	25 appm He	234	↓	12	12
-	600	↓	0	124	↓	10	16
<150	600	↓	25 appm He	207	↓	12	14
-	700	↓	0	131	↓	11	12
<150	700	↓	20 appm He	152	↓	13	14
-	800	↓	0	117	↓	12	13
<150	800	↓	20 appm He	128	↓	13	14

(a) E > 0.1 MeV
(b) 1 hr. at 1050°C
(c) Applicable to UWMAK-III temperature region

NA = Not Available or not reported

to the range of -80 to 20°C for control specimens. Whereas specimens irradiated at 450°C and tested below 550°C displayed brittle behavior those tested at 650°C displayed unstable behavior. The DBTT was observed at a slightly lower level for specimens tested at a lower strain rate of 0.0002 min^{-1} compared to the rates of 0.02 and 0.002 min^{-1} applied in the other measurements.

Two molybdenum specimens which had changed temperature during irradiation from 857 to 1136°C were tested at a strain rate of 0.02 min^{-1}. The sample tested at 22°C failed by brittle fracture while the other tested at 400°C showed conventional behavior. In fact, the latter specimen retained a uniform elongation of 5.7% after a ~30 dpa irradiation at 857 to 1136°C. A sample irradiated at 455°C and subsequently annealed at 1050°C for 1 hr also showed conventional behavior (6.3% uniform elongation at 400°C) which is an indication that the DBTT is lower than 400°C.

The results of Wiffen indicate that if Mo is irradiated at 450°C or below, the DBTT will increase to above that temperature and brittle behavior can be expected. However, his results also show that if Mo is irradiated to high damage levels at temperatures typical of CTR blankets, the DBTT will be below 550°C and one can expect rather ductile behavior at typical fusion blanket temperatures.

This conclusion is substantiated by the data of Kasakov et al.[35] who irradiated both TZM and a Mo-Zr-B-C alloy from 0.6-0.8 dpa at 550°C to 950°C. (See Table IX-C-10). Their work shows that irradiation of TZM at 550°C produces a strong, brittle material whose properties do not recover until ~800°C. On the other hand, irradiation of TZM (and the Mo-Zr-B-C alloy) at 950°C has essentially no effect on either the ductility or yield strength (see Figures IX-C-8b and 8C). Such behavior provides some hope that when Mo alloys are tested under typical CTR conditions, they will retain a reasonable amount of ductility, contrary to the conclusions that have been obtained from low temperature tests.

It is worthwhile to note that the helium content in Wiffen's samples is only 0.5 to 1 appm and one must remember that approximately 100 times that value will be present after one year of irradiation.

We can get some insight into the effect of helium on the mechanical properties of Mo alloys by examining work performed by Kramer et al.[39] They injected TZM with 20 appm of helium at 450°C and tested the samples at 700°C. The results are quoted in Table IX-C-10 and show that at 700°C the helium actually increased both the uniform and total elongations. This result coupled with the insensitivity of swelling in Mo to helium (see Figure IX-C-5) means that perhaps we can rely on the neutron data obtained from fission reactors.

EFFECT OF IRRADIATION AND TEST TEMPERATURE ON TOTAL ELONGATION OF TZM (35)

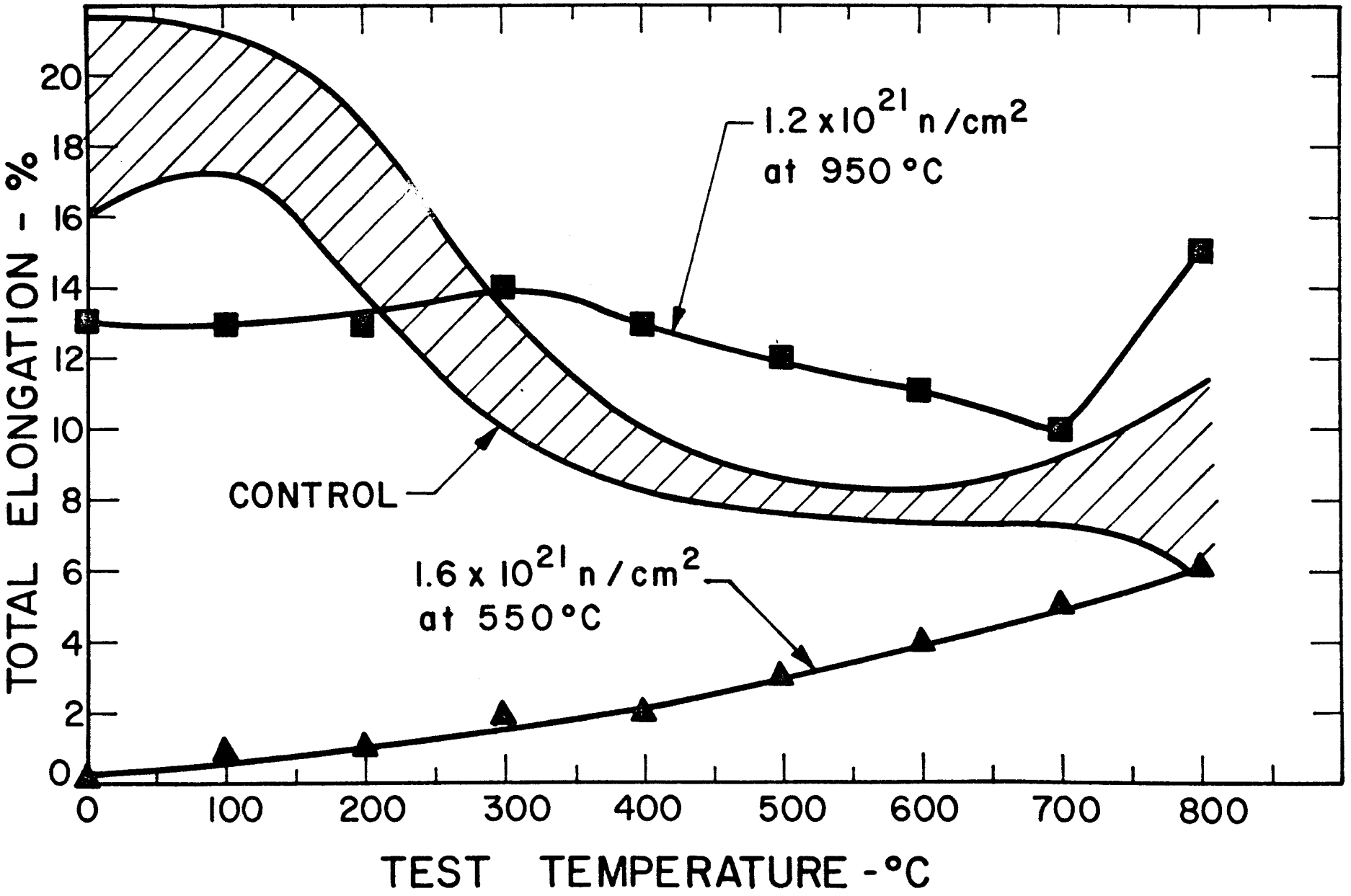

Figure IX-C-8b

EFFECT OF IRRADIATION AND TEST TEMPERATURE ON 0.2% YIELD STRENGTH OF TZM (35)

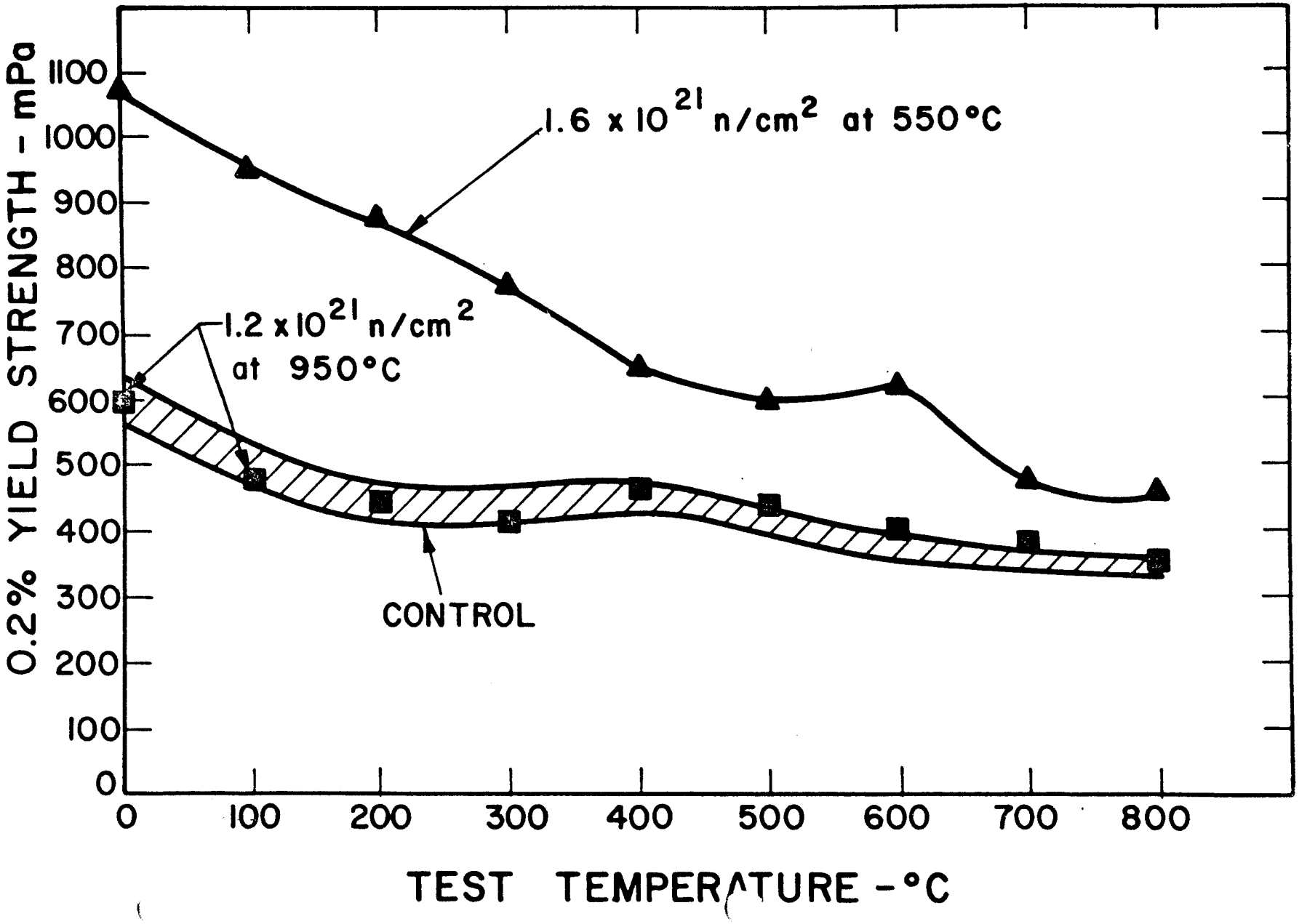

Figure IX-C-8c

Creep Behavior

Wiffen[34] tested two irradiated specimens in creep at 750°C and 1200°C after irradiation to a fluence of 6.1 x 10^{22} n/cm^2 (E > 0.1 MeV) at a temperature which increased from 860°C to 1140°C during irradiation. Compared to control specimens the creep life was lengthened considerably with only a small decrease in ductility. This is also important to a reactor designer but in-situ data would be more convincing.

Moteff and co-workers[40a] irradiated specimens at 70, 700, and 1000°C to a fast neutron fluence of 1.4 x 10^{20} n/cm^2 (E > 1 MeV), after which the specimens were creep-rupture tested at 750°C. They observed increased creep life, particularly for the higher irradiation temperatures, although not to the extent observed by Wiffen. The difference may be due to irradiation temperature or the higher neutron fluence in Wiffen's experiment.

In earlier experiments Moteff[40b] conducted creep-rupture tests on sheet specimens of irradiated TZM at 1310°C. Creep rates decreased approximately 20% with no apparent loss of ductility. It is believed that any irradiation-induced defects which would produce hardening were removed at the 1310°C test temperature. It must be remembered again that these samples contained very little helium.

Hardness Studies

The majority of work in this area has been conducted by Moteff and co-workers.[12, 40-42] They have established that with the proper empirical factors, one can accurately predict the yield strength of neutron irradiated Mo from hot hardness measurements. They have also been able to correlate microstructures with changes in hardness (yield strength) and have arrived at a reasonable qualitative understanding of the causes of irradiation induced hardening. Future work in this area may allow a quick, relatively easy measurement of the change in yield strength with damage.

Fatigue Behavior

There have been two pertinent studies of the effect of irradiation on the fatigue behavior of TZM.[43,44] The first study investigated the effects of preinjected helium on the fatigue life of TZM. The samples were injected with 10appm helium (1/10 year of UWMAK-III operation), and then tested at 900°C in a vacuum. The results showed that the effect of helium (over a control sample) was to increase the fatigue life and reduce the crack growth rate.

More recent work by Michel[44] showed that irradiation to 5 x 10^{22} n/cm^2 at 427°C also increased the fatigue life and reduced crack growth rates. Furthermore, samples which were subjected to an additional 10 appm He injection after the irradiation showed an even further increase in fatigue life. Quantitative results show that for 1 x 10^{22} n/cm^2 at 427°C (no helium injection) the fatigue life was increased by 60 to 100% in the strain per cycle range of 0.12 to 0.16%. Such strains are not hard to envision in a CTR during the time periods between burns. Further analysis of the NRL data is continuing but three things of importance should be emphasized.

1. The irradiation and testing temperature was lower than TZM would operate at in a typical CTR.

2. The tests were not done insitu.

3. The allowable strain for a fatigue life of 9000 cycles (close to two years of UWMAK-III operation) is >0.2% at 427°C.

This latter point is particularly significant in that it may mean we can design the first walls of UWMAK-III on the basis of unirradiated fatigue data and then expect to get an even better performance from the material during irradiation.

To summarize the situation with respect to irradiation effects on mechanical properties:

1. Irradiation of Mo to >5 dpa at <400°C causes an increase in the DBTT to 550 to 650°C but it also increases the fatigue life of TZM by a factor of ~2.

2. Irradiation at temperatures above 800°C appears to have very little effect on the DBTT and actually increases the post irradiation creep life.

3. Injection of helium in the 10-20 appm level and subsequent testing actually increases the fatigue life at 427°C and has little effect on the ductility above 700°C.

Therefore, we conclude, that the mechanical properties of Mo and TZM will not be severely degraded by fission neutron irradiation at 800-1000°C to fusion neutron damage levels of up to 5 dpa (25 appm He).

IX-C-1-d.) Surface effects

i.) Sputtering

There are two forms of sputtering to worry about in a fusion reactor; that due to ion charge exchange neutrals, and neutron sputtering. However, in UWMAK-III the molybdenum first wall is protected from plasma particle sputtering by a carbon curtain on the outside and the ISSEC on the inside. Nevertheless, we will briefly review the physical sputtering of Mo because of the use of a Mo collector plate in the divertor region.

Behrisch[47a] has recently summarized the light ion sputtering values for Mo and these are given in Figure IX-C-9a. The data comes from three groups, Wehner,[46] Finfgeld,[45], and Bay et al.[47b] A summary of the experimental values is given in Table IX-C-11. Behrisch has drawn the most likely curve through the data and estimated the sputtering curve for tritium. From Figure IX-C-9a, one might draw the following conclusions:

(1) There will be very little sputtering of Mo by D and T below 200 eV and by He below 100 eV.

Table IX-C-11

Sputtering Yields for Molybdenum

Energy (keV)	Average Yield (atoms/atom) H^{+} [45]	D^{+} [45]	He^{++} [46]
0.1			0.001
0.2			0.005
0.3			0.015
0.5			0.03 [47]
0.6			0.04
1.0	0.0017	0.0028	
2.0	0.0022	0.0035	
3.0	0.0022	0.0036	
4.0	0.0027	0.0046	
5.0	0.0024	0.0043	
6.0	0.0029	0.0051	
7.0	0.0034	0.0049	

(2) The maximum in the sputtering curve occurs at 3-4 keV for D & T and at approximately 5 keV for He.

(3) The maximum sputtering coefficients are; 0.008 for D+, 0.02 for T+ and 0.05 for helium.

A comparison of the sputtering yield for protons is given in Figure IX-C-9b and for 400 eV helium atoms in Figure IX-C-9c. These figures show that Mo is superior to lower Z elements or compounds as well as steel in the 6 keV or less range. Figure IX-C-9c shows that at least for 400 eV helium ions, the sputtering coefficient for Mo is at least a factor of 2 or less than for V and about the same as for Nb. There will of course be atoms sputtered from the surface of the TZM by the 14 MeV and back scattered neutrons in UWMAK-III. Unfortunately, there have been no 14 MeV neutron studies on Mo but as shown in Figure IX-C-10, the fission neutron sputtering coefficients for Mo are quite close to those of Nb which have been studied in great detail.(49-52) The current 14 MeV neutron sputtering values on Nb range from approximately 10^{-4} to 10^{-3} on the high side(49) to 10^{-5}-10^{-4} on the low side(50-52). Lacking any specific data and using Nb as a model for Mo, it appears to be reasonable to choose a value of 10^{-4} atom/14 meV neutron for this work. The conclusions of this study can be further updated as the exact values become better know.

IX-C-1d.) ii. Blistering

There have been at least five studies of blistering in Mo and a summary of the data obtained is given in Table IX-C-12.(53-57) Blisters can easily be formed in helium bombarded Mo at temperatures from 20°C to over 1000°C. The minimum fluence for blisters to form and exfoliate decreases with increasing temperatures ranging from ~10^{17}cm^{-2} at high temperatures to ~10^{18} at room temperature. The thickness of the blister corresponds almost exactly to the range values for the helium atom.

Similar results were obtained for deuteron bombardment, but the critical threshold for exfoliation is a factor of 2-4 higher, and the blister density is not so high.(54,55,57) It also appears that at high temperatures (>400°C) the re-emission rate of deuterium is so high that the threshold for blister formation is greater than 1 x 10^{18}ions/cm^2.(55) Finally, one study found that blisters could form at 900 to 1000°C, but that none were formed above 1040°C for 20 KeV ions.(57)

After having established that one can form blisters with He (and D^+ under certain circumstances), we are now faced with the question of how to relate this information to a reactor design. One <u>very</u> conservative approach is to simply measure the critical dose for exfoliation of the blisters, assume a material layer of thickness equal to the range of the projectile is removed, and then the process starts all over again. This can then be related into an "effective removal coefficient" analogous to the case for physical sputtering. The only complete data available is for 304SS and V (58,59) and we have also plotted data on Nb (60), Al (61) and Mo (62). The latter two data points were adjusted by the ratio of the range used (range for 500 keV helium ions). To project the maximum effect then one can simply multiply by the fluence. (See Figure IX-C-11).

FIGURE IX - C - 9a

SPUTTERING YIELDS FOR NORMAL INCIDENCE
OF DIFFERENT ION ON MOLYBDENIM (MOLTEN MATERIAL).

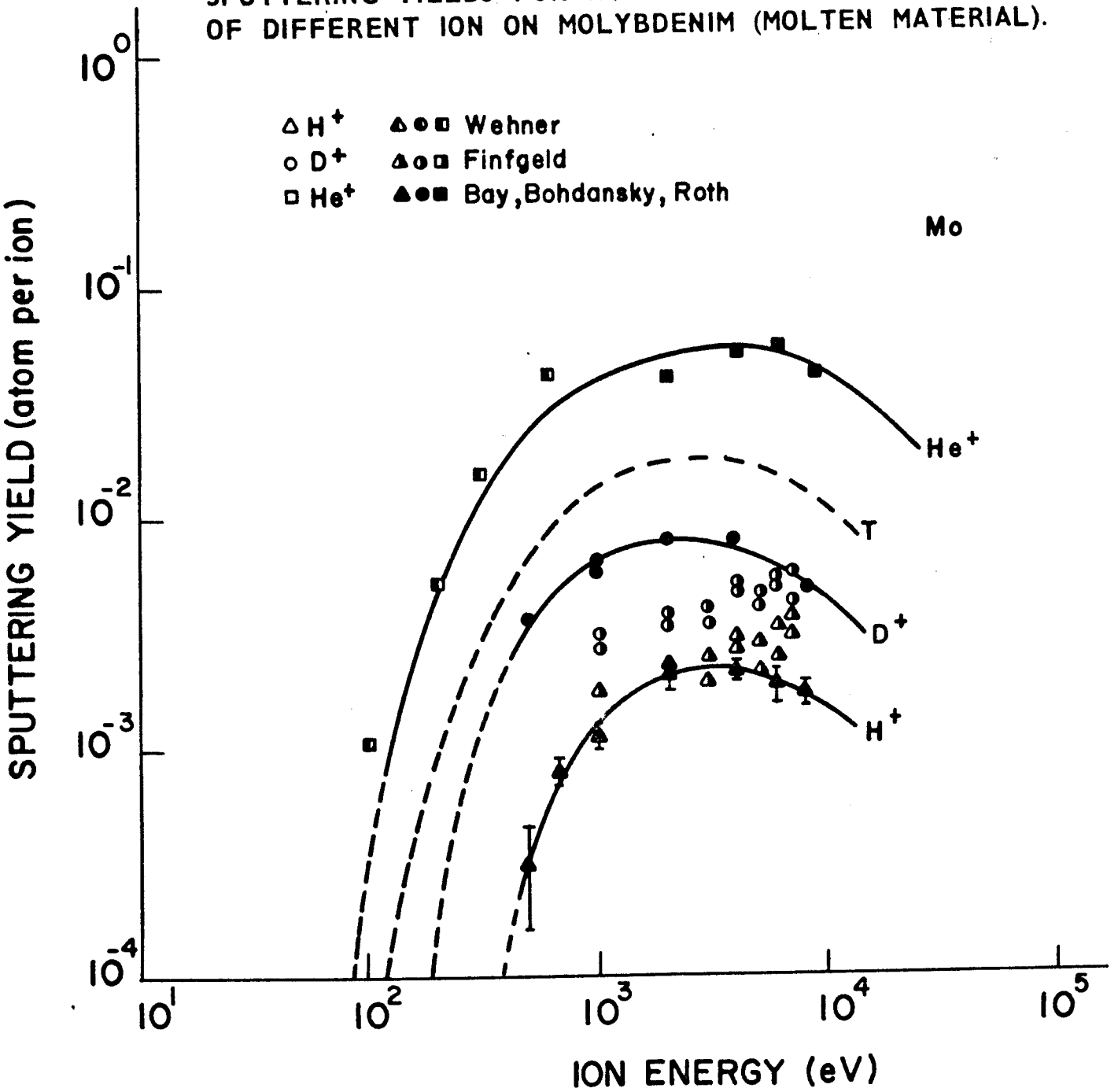

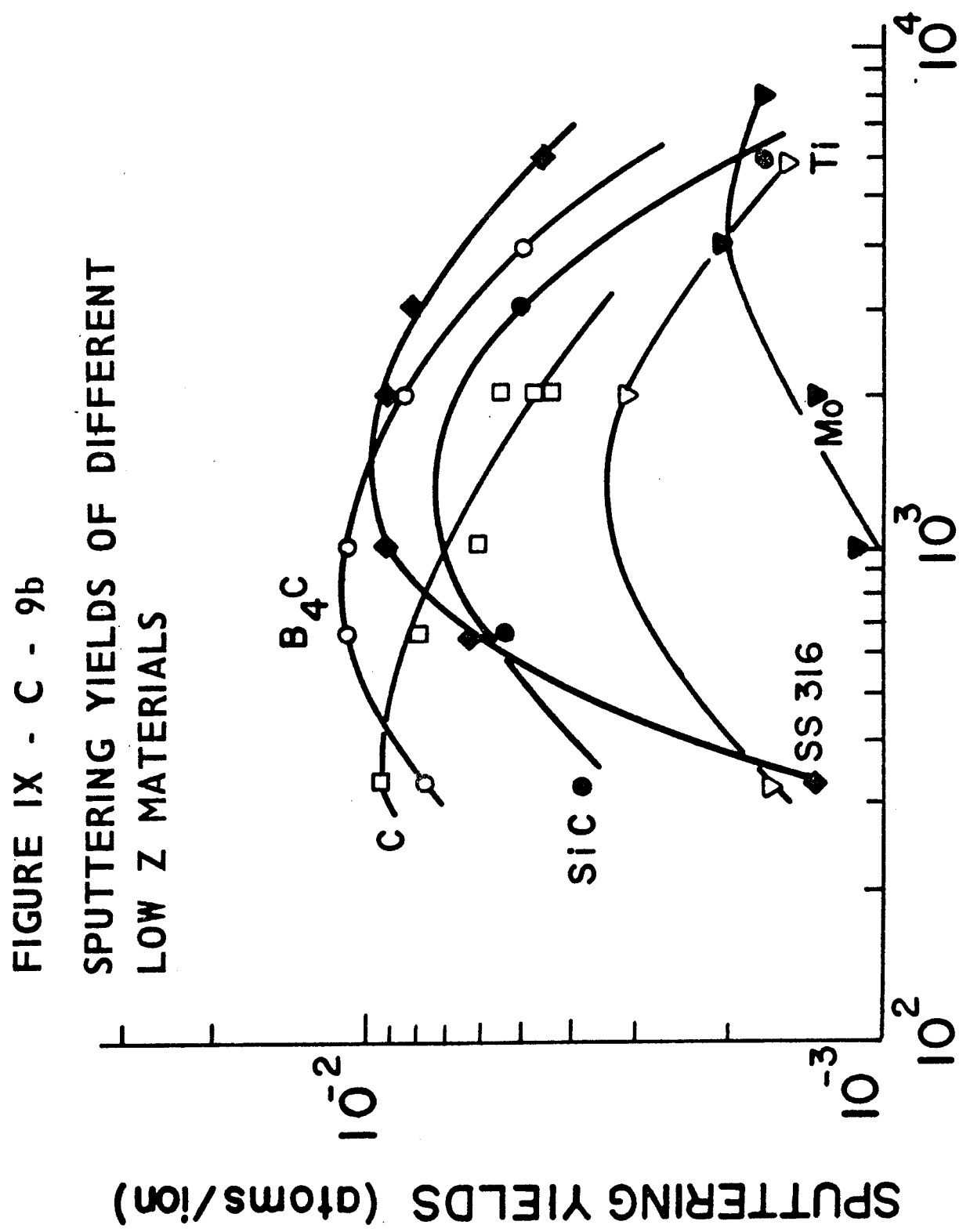

FIGURE IX - C - 9b
SPUTTERING YIELDS OF DIFFERENT
LOW Z MATERIALS

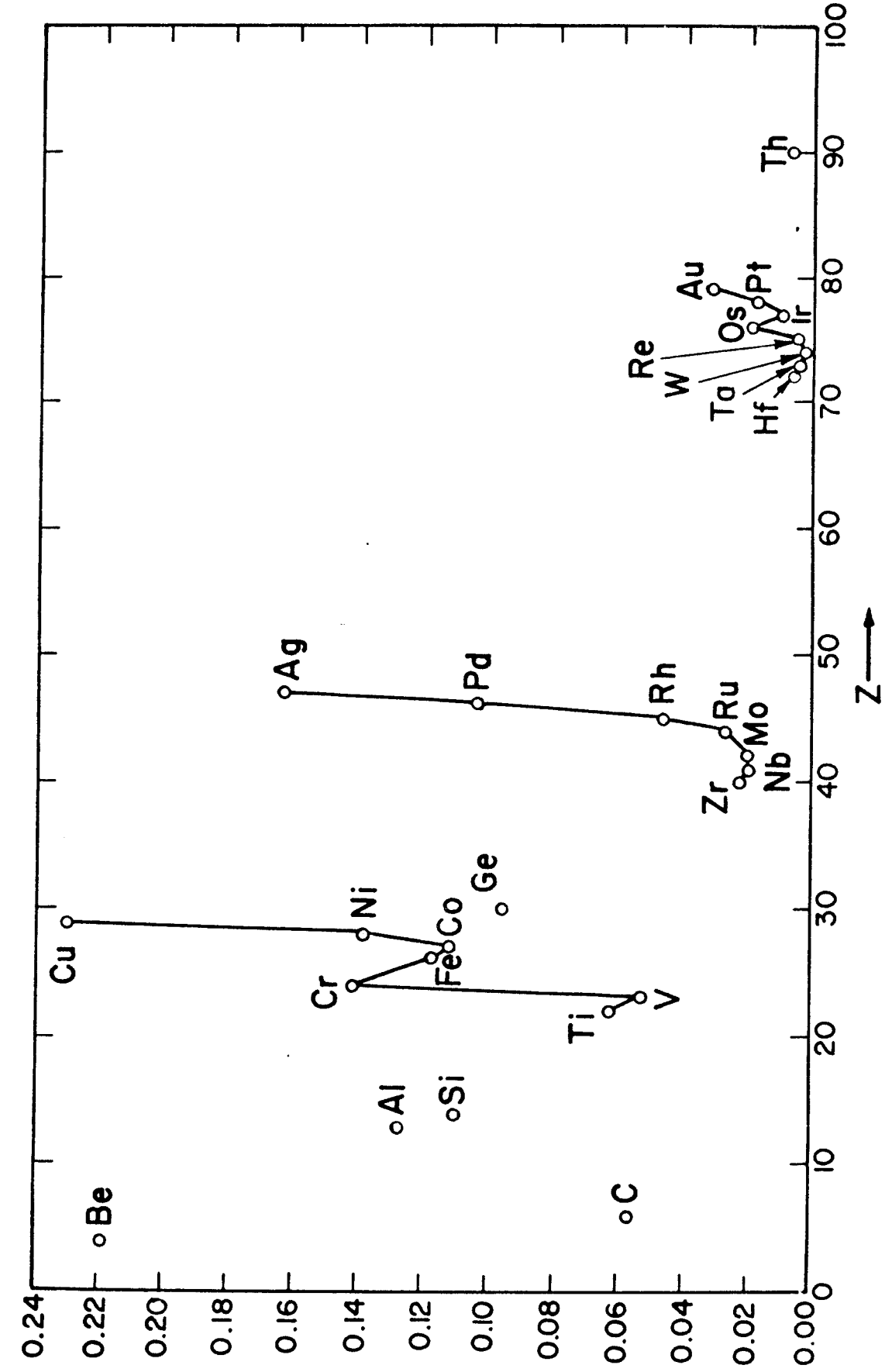

FIGURE IX-C-9c- SPUTTERING YIELDS AT 400 eV HELIUM ION ENERGY FOR 29 ELEMENTS VS. THE ELEMENT'S ATOMIC NUMBER (ROSENBERG AND WEHNER)

Figure IX - C - 10

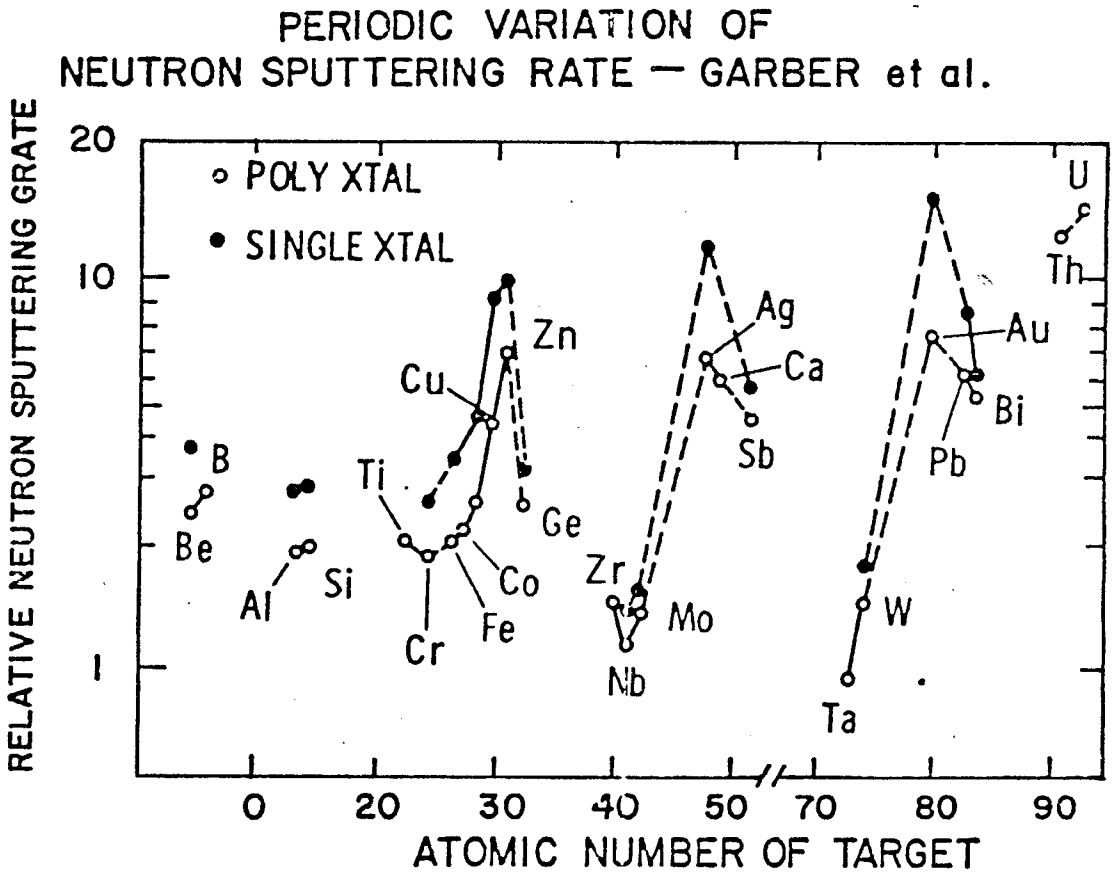

Figure. IX-C-11. Effect of Temperature on Effective Wall Erosion Coefficient For Blistering - 0.5 MeV Helium

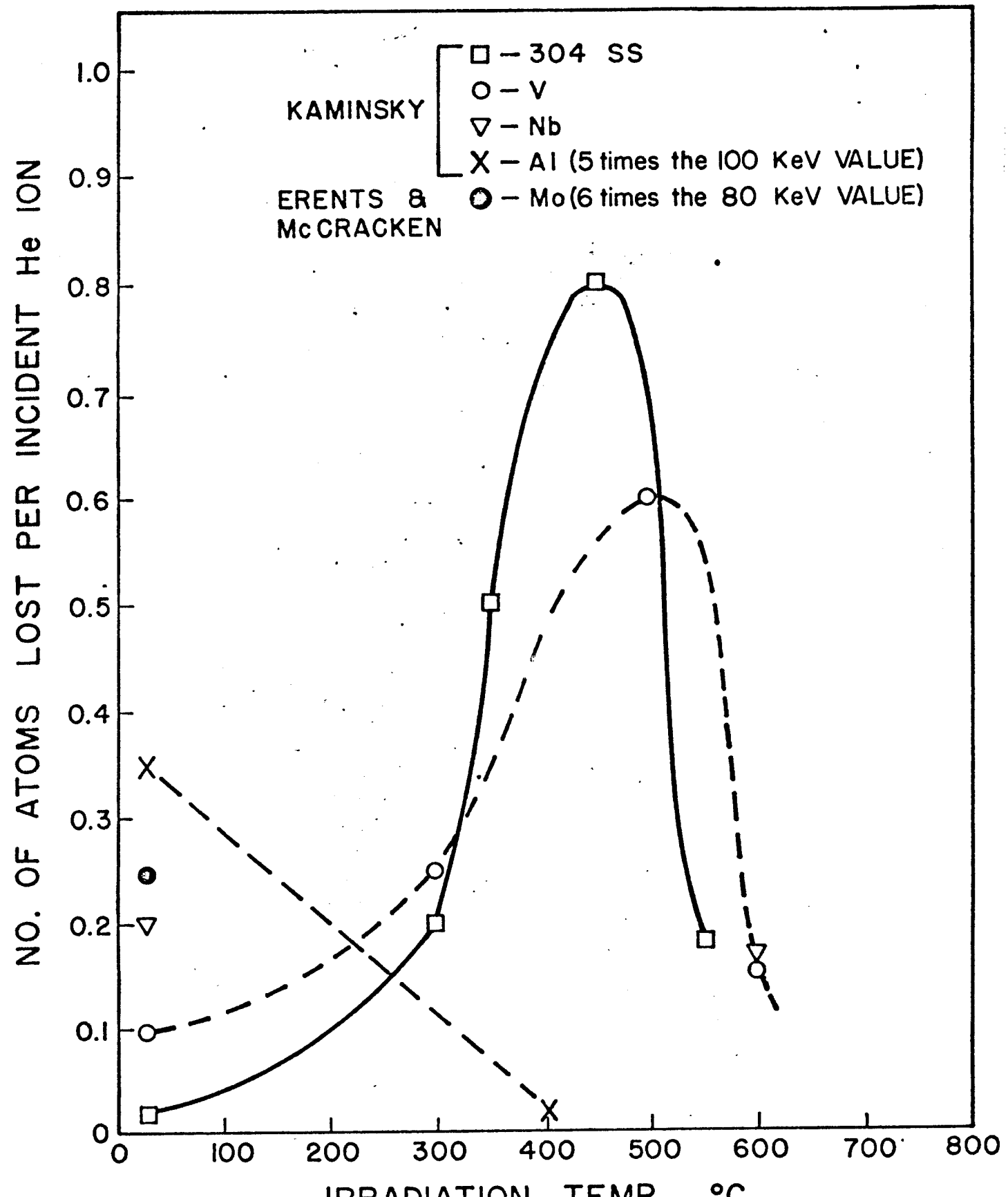

However, recent results by Roth et al [63] show that the above approach may not be valid, especially if the ions have a spread in energies, or if they strike the wall with varying angles of incidence. They would project that after the first few exfoliations; the surface becomes so porous that the bombarding particles diffuse out as fast as they are injected. If the later results can be substantiated to very high fluences ($>10^{20}$ cm^{-2}), then there is very little to worry about with respect to blistering, at least as it pertains to wall thinning.

We will use both boundary conditions in our later calculations and await further experimental verification.

IX-C-2.) Carbon

There are three places in UWMAK where carbon is used:

The curtain protecting the plasma and the outer first wall
The ISSEC protecting the inner first wall
The carbon reflector in the outer blanket

It is important to outline the potential problem areas for this material and it greatly contributed to the successful operation of UWMAK-III. There are four properties of graphite which we will consider here:

Compatability with vacuum environment
Interactions with neutrons (dimensional stability)
Physical and chemical sputtering
Effect of high helium gas contents

IX-C-2-a) Vacuum Properties

As the temperature of carbon is raised, single and multi-atom molecules of carbon are released which causes its vapor pressure to vary as shown in Figure IX-C-12.[64] A key value of vapor pressure is 10^{-5} torr because that is approximately equal to the anticipated background pressure around the UWMAK-III plasma. If the vapor pressure is higher than that value, serious contamination problems may arise. From Figure IX-C-12, we can see that such a consideration limits the maximum temperature of the carbon in the vacuum chamber to 2000°C.

Using the vaporization rates given in Table IX-C-12[64] we can see how much carbon is vaporized off of typical ISSECs or carbon curtains. The amount of carbon lost per square meter of surface area is listed in Table IX-C-13 along with the thinning rate. Again it can be seen that if the temperature exceeds 2000°C, both the rate of thinning (~1.2 cm/yr) and the amount of carbon vaporized (~9500 g/ m^2yr) are excessive.

Another problem to consider is the outgassing of graphite at high temperatures. It is difficult to quote a unique value for graphite because of the wide variation in the porosity and density of samples reported in the literature and the reader is referred to a recent compilation by Mantell.[65]

With general purpose extruded graphite, 300 torr-liters/g was evolved at temperatures up to 1400°C. Upon heating to 2000°C, an additional 75 torr-liters/g were evolved. The composition of all the gas released was 45% N_2, 45% CO, and 10% CO_2. At T < 1400°C, the predominant gas was N_2, at T > 1400°C the predominant gas was CO.

More recently, G. P. Lang and V. L. Holmes measured the gas content and sticking probabilities of WCA and Thornel 50S graphite fibers in simulated fusion reactor conditions.[66] WCA cloth is prepared by the pyrolysis and graphitization of rayon cloth. Thornel 50S (T-50S) is similar except that rayon yarn is stretched during pyrolysis resulting in higher crystal orientation.

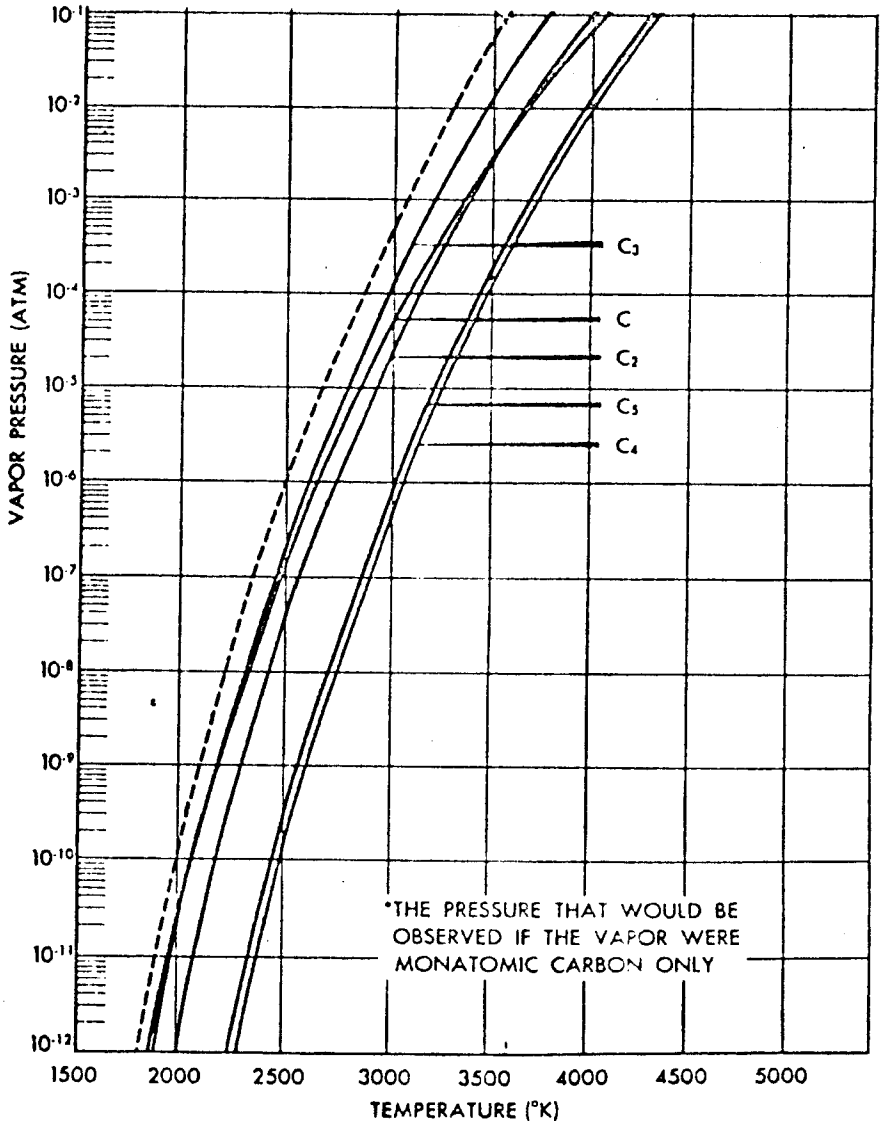

Figure-IX-C-12 Vapor Pressure of Graphite (Ref. 64)

Table IX-C-12

Summary of Blistering Studies on Mo

Ref.	Ion	Energy - kev	Temperature °C	Fluence - cm^{-2}	Observations
53	He	7, 20, 36, 50, 80	RT, 530, 830, 1330	~4×10^{18}	•Critical dose ~$1 - 7 \times 10^{17}$ cm^{-2}. •Blisters formed at all energies. •Diameters increase from 2000 at 7 heV to ~20,000 Å at 80 heV.
54	He	15	~RT	2.5×10^{18}	•Blister thickness ~3000 Å and diameter ~4.8 microns.
54	D^+	15	~RT	8×10^{18}	•Blister diameter was much smaller in annealed specimen.
54	H^+	150	~RT	$>5 \times 10^{18}$	•Found critical fluence decreases with flux.
[illegible]	D^+	5-35	RT→500	$<4 \times 10^{17}$	•Found that very little D^+ is trapped in the Mo at T_{irr} > 400°C.
56	He	300	400-1200°C	4×10^{18}	•400-600°C - mostly flaking and no blister. •800°C only blisters. •1200°C - holes, blisters.
57	D^+	20.5	750-1040	6×10^{18}	•Critical dose decreases with temperature. •Mo blisters at 750 and 1040°C. •Blisters only at grain boundaries at 850°C. •Maximum damage 900-1000°C.

Table IX-C-12 (Ref. 64)

Vapor Pressure of Graphite

Temperature		Partial Pressures of Species in Atmospheres					Equivalent Vapor Pressure (atm)*	Free Vaporization Rate (g/cm^2 sec)
°K	°C	C	C_2	C_3	C_4	C_5		
1200	927	1.01×10^{-23}					1.17×10^{-23}	5.19×10^{-23}
1300	1027	2.81×10^{-21}		2.38×10^{-27}			3.54×10^{-21}	1.51×10^{-20}
1400	1127	3.21×10^{-19}	1.015×10^{-21}	4.37×10^{-20}			4.54×10^{-19}	1.87×10^{-18}
1500	1227	1.95×10^{-17}	1.34×10^{-19}	3.96×10^{-18}			3.16×10^{-17}	1.26×10^{-16}
1600	1327	7.08×10^{-16}	8.55×10^{-18}	2.04×10^{-16}			1.34×10^{-15}	5.15×10^{-15}
1700	1427	1.68×10^{-14}	3.34×10^{-16}	6.55×10^{-15}	3.11×10^{-20}	4.47×10^{-20}	3.72×10^{-14}	1.39×10^{-13}
1800	1527	2.81×10^{-13}	8.65×10^{-15}	1.42×10^{-13}	1.62×10^{-18}	2.33×10^{-18}	7.25×10^{-13}	2.64×10^{-12}
1900	1627	3.47×10^{-12}	1.59×10^{-13}	2.45×10^{-12}	5.52×10^{-17}	8.00×10^{-17}	1.08×10^{-11}	3.81×10^{-11}
2000	1727	3.34×10^{-11}	2.21×10^{-12}	3.10×10^{-11}	1.03×10^{-15}	1.92×10^{-15}	1.31×10^{-10}	4.61×10^{-10}
2500	2227	1.79×10^{-7}	4.30×10^{-8}	2.62×10^{-7}	2.15×10^{-10}	3.17×10^{-10}	1.05×10^{-6}	3.23×10^{-6}
3000	2727	5.43×10^{-5}	3.03×10^{-5}	1.41×10^{-4}	6.05×10^{-7}	8.97×10^{-7}	5.38×10^{-4}	1.51×10^{-3}
3500	3227	3.18×10^{-3}	3.20×10^{-3}	1.38×10^{-2}	1.68×10^{-4}	2.49×10^{-4}	5.30×10^{-2}	0.138
4000	3727	6.67×10^{-2}	0.103	0.47	1.10×10^{-2}	1.64×10^{-2}	1.83	5.29
4500	4227	0.708	1.52	7.13	0.276	0.408	28.3	65.0
5000	4727	4.66	12.9	72.5	3.54	5.20	288	627
5500	5227	21.6	72.8	839	27.8	40.6	3000	6240
6000	5727	77.6	307	6390	152	220	21600	43000

*The equivalent pressure is that pressure which would be observed if the vapor were monatomic carbon.

Table IX-C-13

Rate of Carbon Loss and Thinning Rates in ISSECS and Carbon Curtains

T(°C)	Carbon Vaporized g/m^2-yr	Thinning Rate[(a)] cm/year
1127	5.9×10^{-7}	7.4×10^{-11}
1327	1.62×10^{-3}	2×10^{-7}
1527	0.832	1×10^{-4}
1727	145	1.8×10^{-2}
2000	9450	1.18
2227	1×10^{6}	125

(a) Assuming loss from two surfaces at equal temperatures and bulk density of 1.8 g/cm^3.

and in higher strength and modulus. Lang and Holmes measured the amount of gas released from the fibers as a function of fiber temperature up to 2000°C or higher. They then exposed the fibers to hydrogen or air at 10^{-3} torr pressure for 10 minutes or more at room temperature and also by approximately 800-850°C. The excess or nonabsorbed gas was removed by pumping the chamber down to a pressure of 10^{-6} torr. The absorbed gas was then removed by flash heating the fibers to 1000°C or higher and the total amount of gas evolved was measured. Their results are given in Figures IX-C-13 and IX-C-14. It is seen from the figures that relatively large amounts of gas are removed during the initial desorption, the total amount depending on temperature and length of time of pre-bake. After the first desorption, the amount of gas removed from the samples was very small. The conclusion here is that under proper initial degassing conditions, the carbon can be easily used under the demanding high vacuum conditions of tokamak fusion reactors.

Another problem to consider is the absorption of hydrogen or air onto carbon between maintenance operations. Table IX-C-14 shows the calculated sticking probabilities of hydrogen and air at tokamak operative conditions. Sticking probability is defined here as the number of molecules of hydrogen (air) absorbed divided by the total number of molecules of hydrogen (air) impinging on the sample during the exposure period. The results indicate that the sticking probability of molecular hydrogen or air on carbon is very low under conditions expected to be present in tokamaks and it should not present any serious problems.

Finally, one must be concerned with the injection of hydrogen isotopes into the carbon from the plasma.

Armstrong and Johnson[67] studied the deuterium ion implantation using 200 keV D+ ions in polycrystalline graphite over the temperature range of -175 to 175°C. They found high retention of deuterium in cold target but the amount of deuterium retained decreased with increasing temperature. For example, at 150°C the retention had fallen to half of what it was at -160°C.

Scherzer et al.[68] also studied the implementation and retention of deuterium in pyrolitic graphite using 30 keV D_2^+ and 20 keV D_3^+ beams. They found high retention, about 100% at room temperature and at doses below $10^{17} D^+/cm^2$. Above 2×10^{18} D/cm^2, the amount of trapped D atoms reached saturation and the saturation value decreased with increasing temperature and decreasing beam energy.

If we consider the fact that a carbon ISSEC might be running at high temperatures, over 1000°C, we can say that injection and retention of hydrogen isotopes in graphite will probably not present any significant problems to the vacuum system.

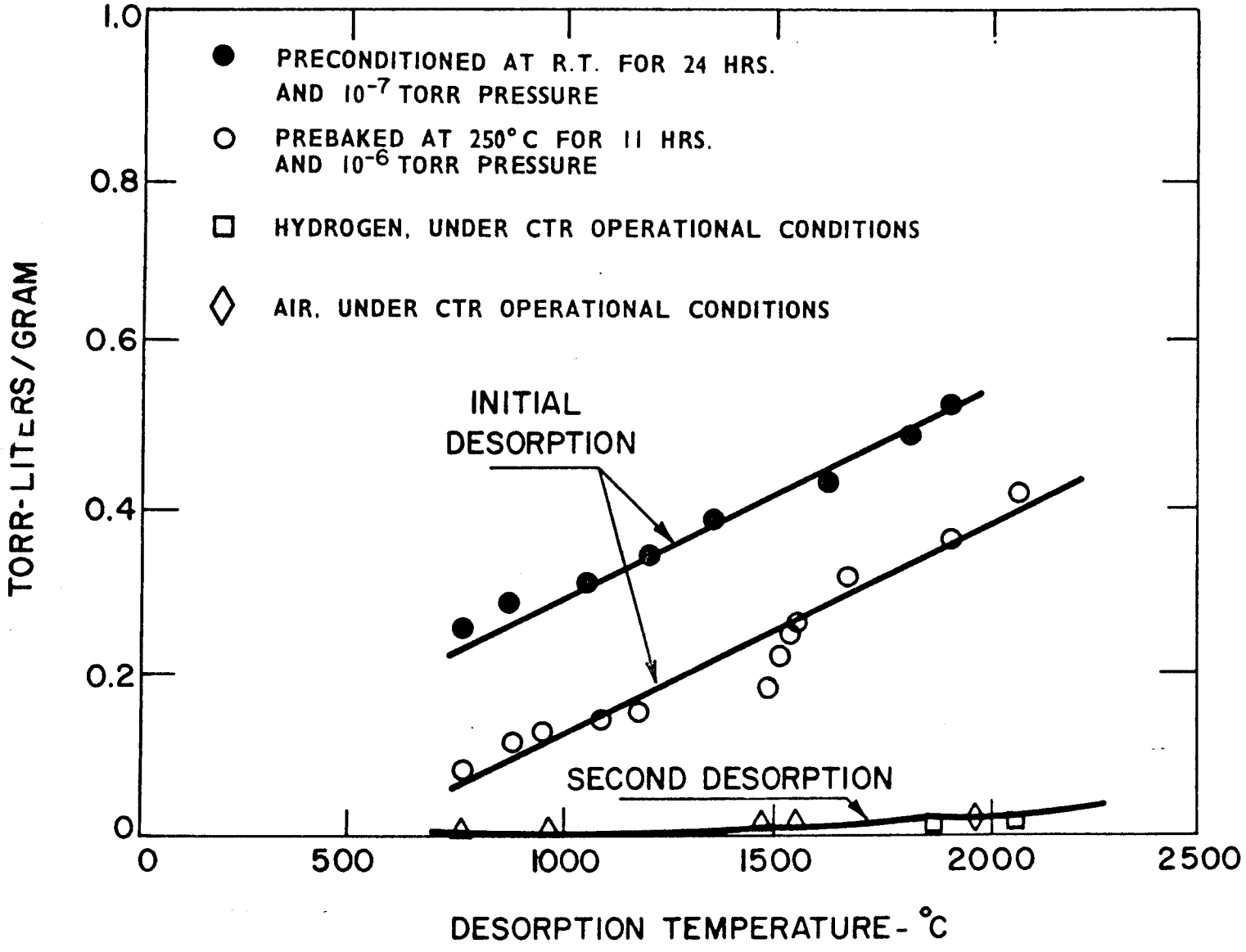

Figure IX-C-13. Gas Content-Thornel 50S Graphite Yarn[64]

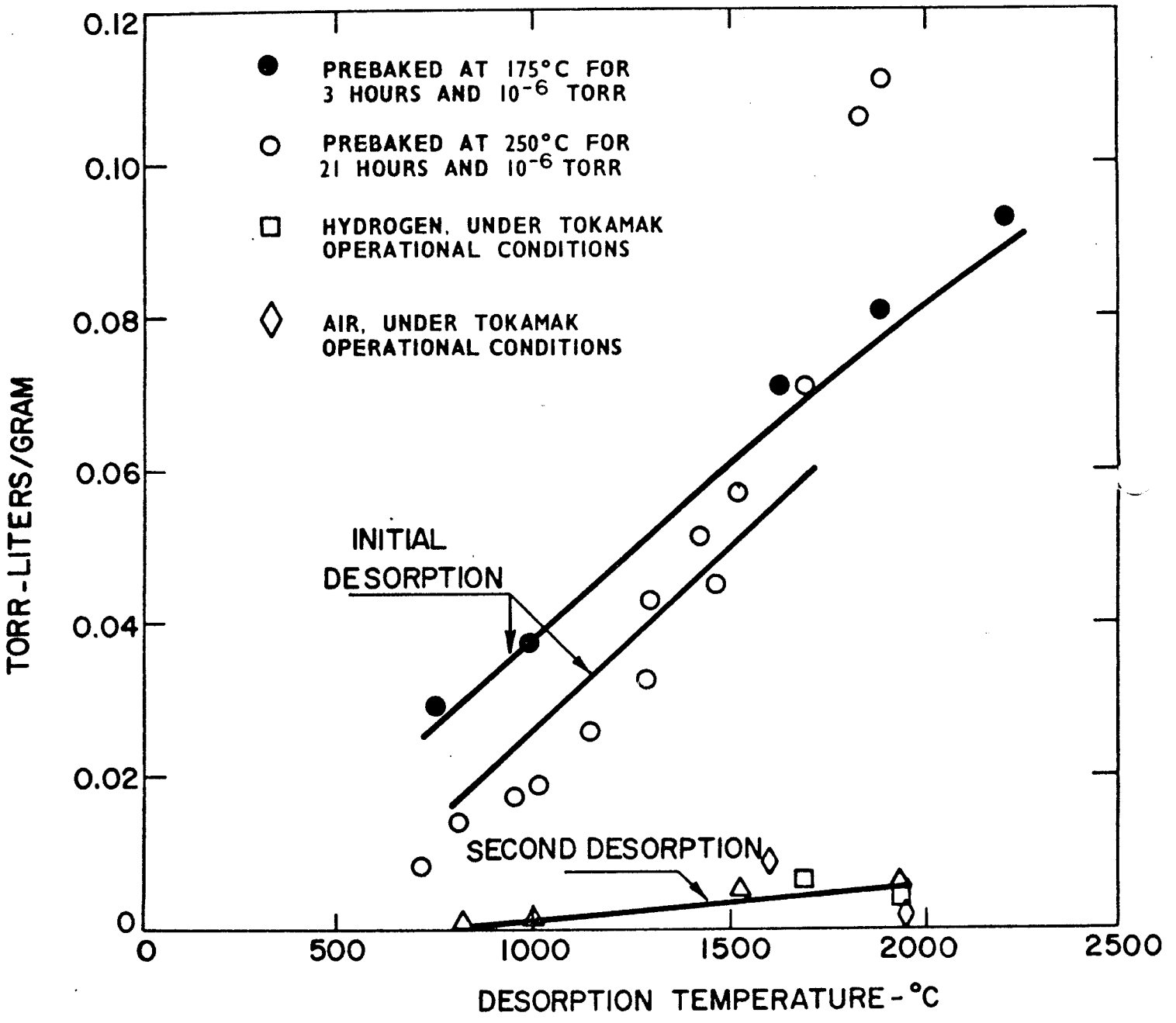

Figure IX-C-14. Gas Content- WCA Graphite Cloth[64]

Table IC-C-14 Sticking Probabilities of Air and Hydrogen on Graphite Materials (Ref. 66)

SPECIMEN TYPE AND NUMBER	EXPOSURE GAS	EXPOSURE CONDITIONS[1]			GAS REMOVAL CONDITION[2]		CALCULATED STICKING PROBABILITY
		EXPOSURE TEMP. (°C)	EXPOSURE PRESSURE (TORR)	TIME OF EXPOSURE (MIN)	FLASH HEATING TEMP (°C)	PRESSURE (TORR)	
WCA Cloth Specimen 1	Air	22	7.5×10^{-4}	11.5	1945	10^{-6}	4.3×10^{-9}
	Air	22	6.5×10^{-3}	10	1941	10^{-6}	5.9×10^{-10}
	Hydrogen	22	1.7×10^{-2}	12	1947	10^{-6}	1.3×10^{-10}
WCA Cloth Specimen 2	Hydrogen	816	3.2×10^{-3}	52	1683	10^{-6}	2.7×10^{-10}
	Air	804	1.3×10^{-3}	30	1579	10^{-6}	4.2×10^{-9}
Thornel 50S Specimen 1	Hydrogen	22	7.0×10^{-3}	10	1850	10^{-6}	3.3×10^{-9}
	Hydrogen	815	7.4×10^{-3}	10	1824	10^{-6}	1.1×10^{-8}
Thornel 50S Specimen 2	Hydrogen	841	3.0×10^{-3}	26	2031	10^{-6}	9.2×10^{-10}
	Air	859	1.6×10^{-3}	15	1960	10^{-6}	5.4×10^{-9}

1. These conditions are approximately those of a Tokamak Type fusion reactor during the recharge time of an operating cycle.

2. These conditions are approximately those of a Tokamak type fusion reactor during the thermonuclear burn part of a cy[illegible]

IX-C-2-b. Neutron Induced Damage in Carbon

IX-C-2-b-i. Damage Cross Sections

We have used the displacement cross sections as derived by Morgan[69] for this study and they are listed in Table IX-C-15. The helium production cross sections are also listed and one should note that the total helium production cross section is the sum of 3 times the (n,n')3 value plus the (n,α) cross section. There is no (n,p) cross section below 14 MeV.

IX-C-2-b-ii. Dimensional Instabilities

This area has been reviewed elsewhere[1,2,70-79] and will not be covered in detail here. Basically, the carbon or graphite goes through two stages during bombardment with neutrons. The first stage which is shrinkage by different amounts in the basal planes and the second stage of expansion. The expansion rate can approach very high values (Figure IX-C-15) and very quickly approaches a state of "run away" swelling. The fluence at which this reversal takes place is a function of temperature, but in general is in the region of 1-2 x 10^{22}n/cm^2 (5-10 dpa) at temperatures of 800°-1400°C. It has become conventional to quote the lifetime of a carbon component as the fluence required to bring the length change back to zero after the initial shrinkage phase.

There have been some recent results by VanDenBerg et al.[80] which suggest a behavior slightly different than that displayed in Figure IX-C-15. Their results are replotted on a relative basis in Figure IX-C-16. This data does not agree with most other data reported to date. Since the graphites used in the VanDenBerg irradiation were different from those in Figure IX-C-15. It is probably a good example of graphite that should not be used at high temperature. The data does not mean, as suggested by others, that all graphites will behave the same way and we will choose to use graphites typical of those in Figure IX-C-15 for our analysis.

IX-C-2-b-iii. Effect on the Thermal Conductivities

The effect of irradiation in the thermal conductivity of carbon and graphite materials has been summarized by Engle and Eatherly.[70] Figure IX-C-17 summarizes some of their findings. In general, it is found that the thermal conductivity is rapidly reduced in the first 10^{21} n/cm^2 (0.5 dpa) and then approaches a value which is approximately 10% of the unirradiated values at fluences greater than 20-30 x 10^{21}n/cm^2 (10-15 dpa). The above information is valid up to approximately 1300°C. However, Engle has found that at 1430°C and 5 x 10^{21}n/cm^2 the reduction of thermal conductivity is not as severe as for the lower temperatures and it is reasonable to expect that at T ~2000°C, the higher temperatures will promote more recombination and less degradation of the thermal properties. Unfortunately, one cannot arrive at that value from theory or experiment, so we will arbitrarily assume that the thermal conductivity at 1000-1500°C is constant at 0.1 cal/cm-s-°K.

Table IX-C-15
Summary of C Reaction Cross Sections Used in UWMAK-III Studies

Energy Group	Upper Energy-eV	dpa	Cross Section-barns (n,n')3α	(n,α)
1	1.4918 (+7)	1254	2.3883-01	1.4264-01
2	1.3499 (+7)	1378	1.8192-01	1.6358-01
3	1.2214 (+7)	1364	1.1372-01	1.8539-01
4	1.1052 (+7)	1015	5.8420-02	1.4000-01
5	1.0000 (+7)	1107	2.2693-02	1.2631-01
6	9.0484 (+6)	1038	4.9787-03	4.6423-02
7	8.1873 (+6)	1704	1.9270-04	5.2320-02
8	7.4082 (+6)	789	0	3.2750-03
9	6.7032 (+6)	967	0	5.7244-04
10	6.0653 (+6)	830	0	0
11	5.4881 (+6)	915		0
12	4.9659 (+6)	1047		0
13	4.4933 (+6)	1512		
14	4.0657 (+6)	1519		
15	3.6788 (+6)	1855		
16	3.3287 (+6)	1101		
17	3.0119 (+6)	1428		
18	2.7253 (+6)	845		
19	2.4660 (+6)	868		
20	1.8268 (+6)	916		
21	1.3534 (+6)	985		
22	1.0026 (+6)	1013		
23	7.4274 (+5)	997.1		
24	5.5023 (+5)	941.9		
25	4.0762 (+5)	863		
26	3.0197 (+5)	763		
27	2.2371 (+5)	647		
28	1.6573 (+5)	560		
29	1.2277 (+5)	547		
30	6.7379 (+4)	358		
31	3.1828 (+4)	194		
32	1.5034 (+4)	99.4		
33	7.1017 (+3)	49.5		
34	3.3546 (+3)	24.6		
35	1.5846 (+3)	12.0		
36	7.4852 (+2)	5.8		
37	3.5358 (+2)	2.8		
38	1.6702 (+2)	1.4		
39	7.8893 (+1)	0		
40	3.7267 (+1)	0		
41	1.7603 (+1)	0		
42	8.3153 (+0)	0		
43	3.9279 (+0)	0		
44	1.8554 (+0)	0		
45	8.7643 (-1)	0		
46	4.1399 (-1)	0		

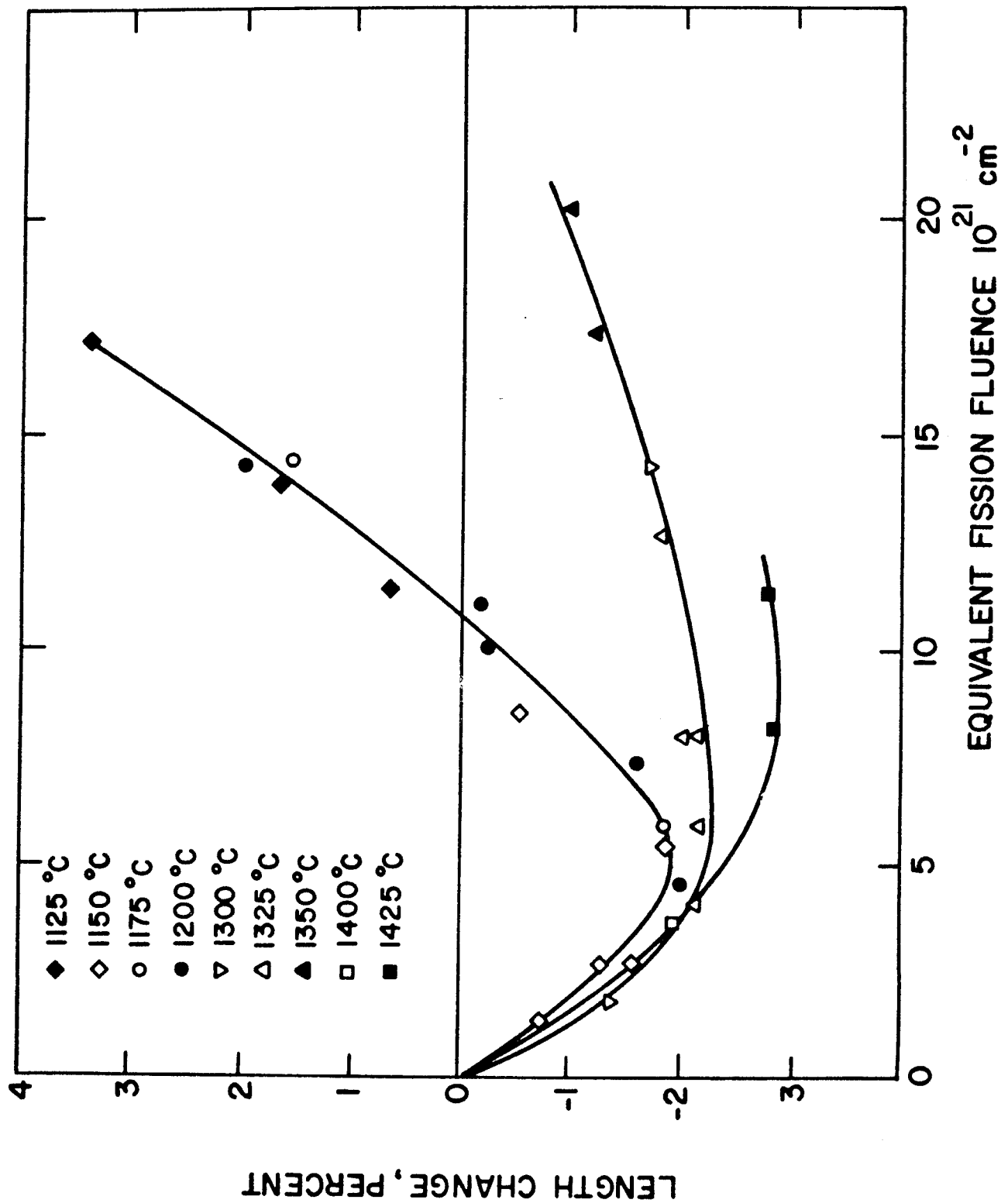

Figure IX-C-15

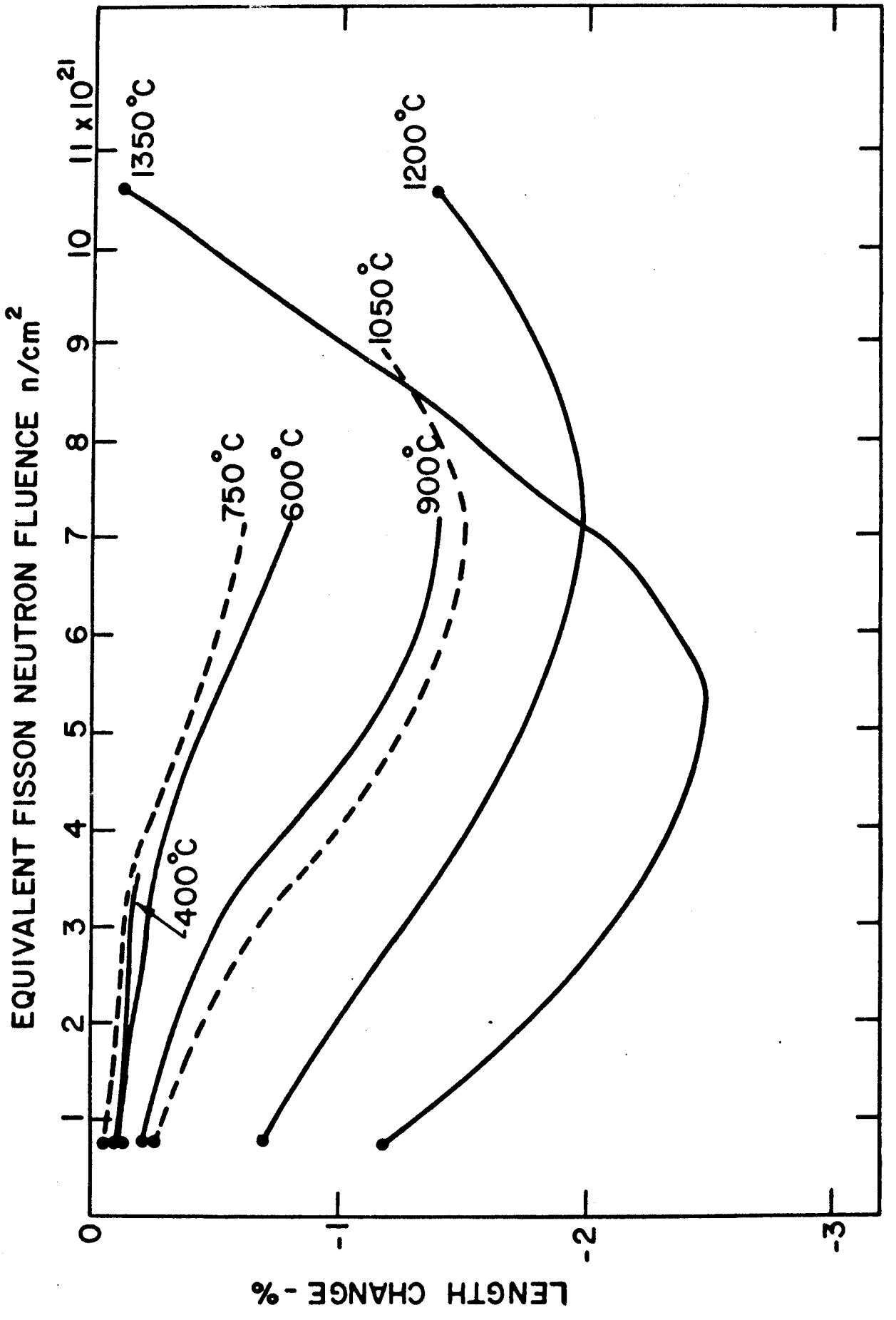

Figure IX-C-16

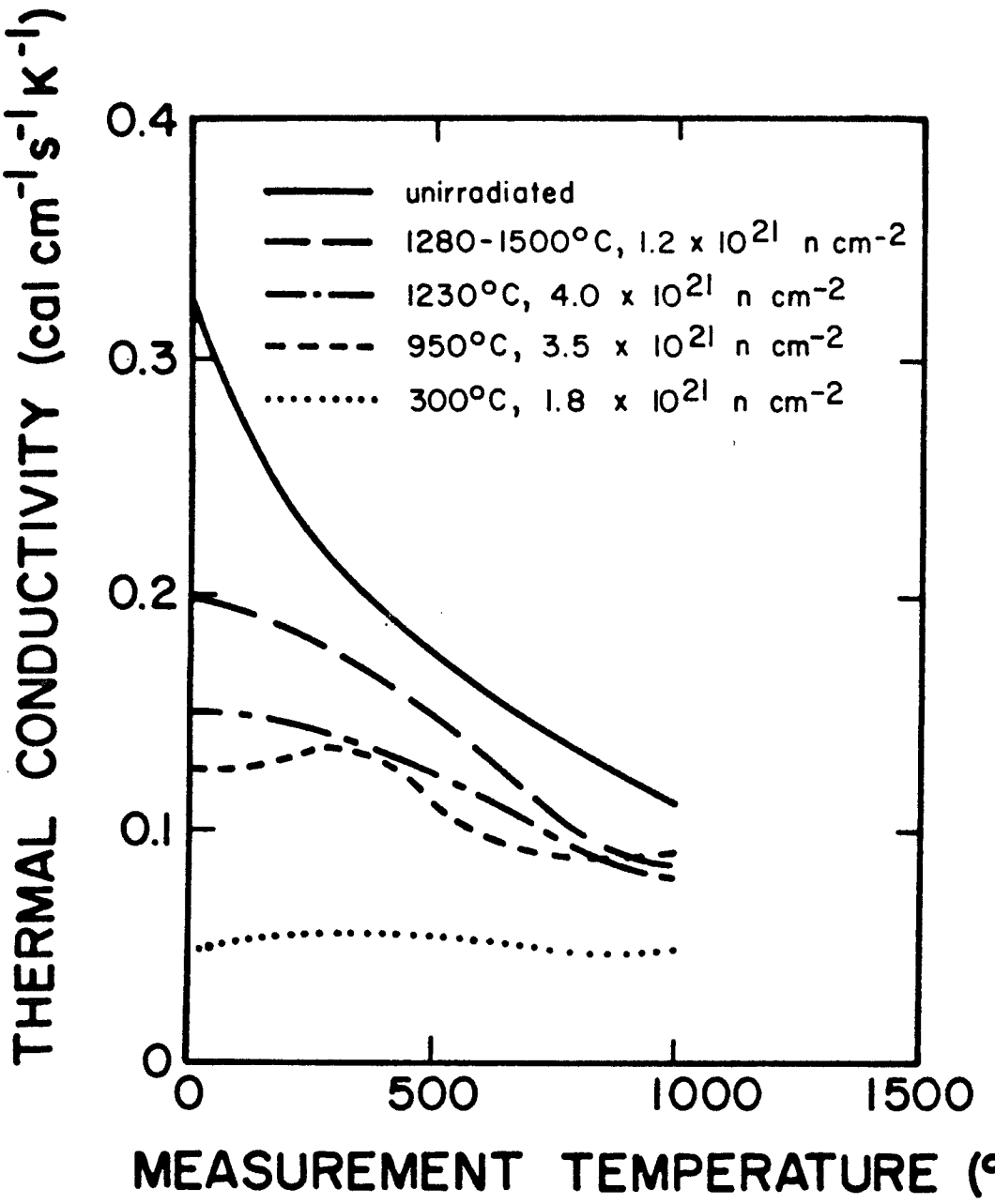

Figure IX-C-17. Thermal Conductivity Changes of Reactor Graphites Measured at the Irradiation Temperature.(70)

IX-C-2-c. Sputtering of Carbon

The side of the carbon ISSEC and carbon curtains facing the plasma in UWMAK-III will be subjected to high energy hydrogen and helium ions as well as 14 neutrons. All these particles will cause the carbon atoms to be sputtered from the surface. The sputtering will take place by two means: (1) physical sputtering when the incident ions collide with the carbon atoms and cause them to recoil into the plasma, (2) chemical sputtering where the incident ion reacts with carbon atoms to form a gaseous compound which later drifts into the plasma. Helium, neutron and impurity ion sputtering is mainly via the first means, while hydrogen and its isotopes can cause removal of carbon by both mechanisms. The sputtered atoms may undergo charge exchange, diffuse into the plasma and enhance the energy loss mechanisms, thus cooling the plasma. It is also possible that the impurity atoms could leak from the plasma at high energy to bombard the first wall, thus increasing the contamination to be removed by the divertor and/or vacuum pumps. The flux of sputtered atoms from the first wall can be calculated by

$$\phi = \sum_i S_i(E)\phi_i(E)$$

where
S_i (E) is the sputtering ration (atoms/particle) for the i'th particle with energy E on carbon.

ϕ_i(e) is the flux of i'th particles at energy E on the carbon surface. The difficulty is finding experimental values of S_i for D^+, T^+, He^{++} and neutrons at the appropriate energies characteristic of UWMAK-III. There have been a few very recent studies[81-85] utilizing hydrogen isotopes to measure the sputtering behavior of carbon and some results from these studies are summarized in Figures IX-C-18[81-85] and IX-C-19.[83] The basic difference between these studies is that the data in Figures IX-C-18 comes from 2-20 keV H,D and T ions on carbon which was heated to 1400°C while that in Figure IX-C-19 comes from carbon bombarded with very low energy (0.2 eV) hydrogen while the samples were heated to approximately 1900°C. Some general observations about Figures IX-C-18 and 19 are now in order:

(1) The sputtering coefficients rise from a value of 10^{-2} atom/atom at room temperature to a maximum of ~8 x 10^{-2} at 600°C. This peak has been found to be associated with methane formation.

(2) As the temperature is increased above 600°C, the sputtering values start to return to their low initial values. This is accompanied by a reduced methane formation.

(3) The sputtering coefficient from tritium is reduced as its energy is increased from 2 to 6 keV. However, 6 keV tritium is more effective in producing methane than is the same energy deuterium.

(4) The low energy hydrogen bombardment depicted in Figure IX-C-19 shows smaller absolute levels of methane formation than for higher energy hydrogen. Furthermore, the low energy sputtering is quite sensitive to crystal orientation.

Figure IX-C-I8

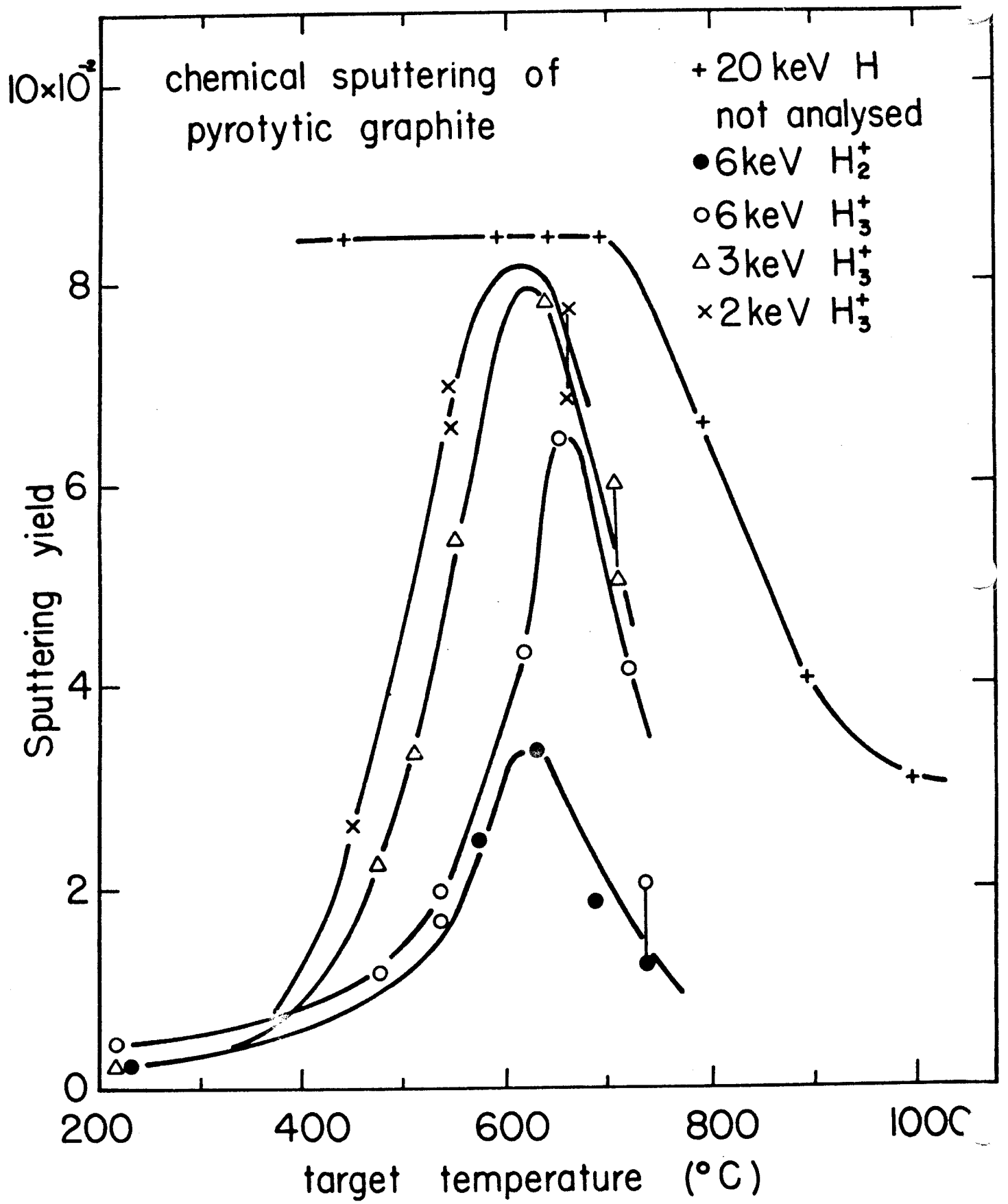

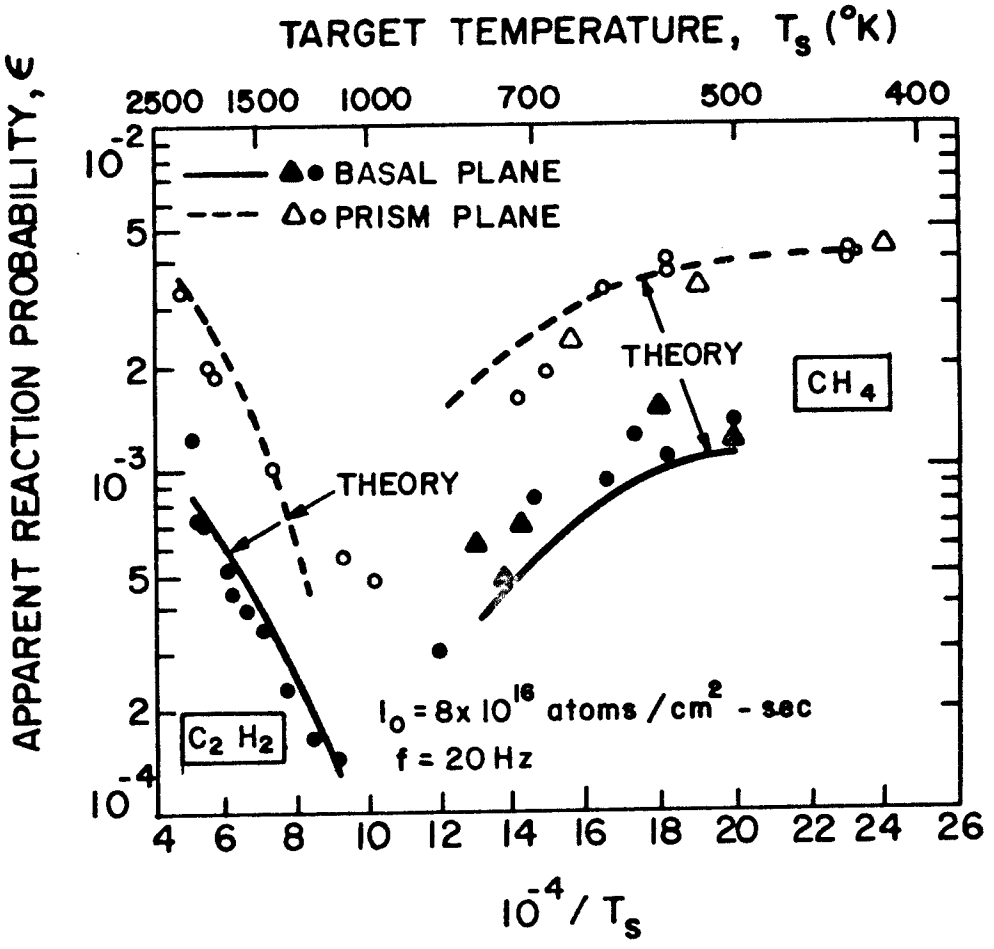

Figure IX-C-19

Effect of Temperature and Crystal Orientation on the Reaction Probability of Carbon (83)

(5) Above 1000°C, the formation of acetylene becomes important although the absolute values are still low ($<<10^{-2}$ atom/atom).

(6) There appears to be a region between 800 and 1200°C where little gasification occurs.

The peak in the sputtering yield vs. temperature curve around 600°C was also observed by other investigators.[82,87,88] G. J. Thomas et al.[89] also report high methane formation around 650°C when they bombarded pyrolitic graphite with 150-300 keV H+ but they also report the formation of propane and its derivatives in the 800-1200°C range which has not been found by others.

R. Ekern, S. K. Das and M. Kaminsky of Argonne National Laboratory[90] irradiated rayon based WCA graphite cloth at room temperature, 400°C and 800°C with deuterons and $^4He^+$ ions at 100 and 250 keV energy. They observed considerable flaking of individual fibers at room temperature irradiations but at 400°C and 800°C irradiation surface damage was greatly reduced. In fact, in high temperature irradiations with $^4He^+$ they did not observe any flaking or other surface damage.

S. K. Erents et al.[91] at Culham Laboratory in the United Kingdom also studied the methane formation during the interaction of energetic protons and deuterons with carbon. They found a behavior similar to that of the Garching group[81] with a maximum in methane production at about 575°C and a reduction in methane production and an increase in hydrogen release above 575°C. The maximum hydrogen release occured at 925°C.

Before going on further in this analysis, it is worthwhile to summarize the latest ideas about the mechanism of chemical sputtering in carbon. The theory of Balooch and Olander[83] is depicted schematically in Figure IX-C-20. It is well known that carbon is relatively inert to molecular hydrogen. This is due to the low probability of dissociative absorption of the H_2 molecule on a graphite surface. The reaction between carbon and hydrogen requires atomic hydrogen and the Balooch and Olander model (BO hereafter) assumed that the atomic hydrogen has a sticking probability of beta on a graphite surface. Thereafter, the absorbed hydrogen can take four possible paths.

(1) diffusion into the bulk of the sample (the Solution Branch)
(2) recombination with another absorbed hydrogen atom to form a gaseous methane molecule (Recombination Branch)
(3) formation of gaseous methane
(4) formation of gaseous acetylene

For the very low energy particles in the BO experiment (0.2 eV) the hydrogen undoubtedly resides on the surface and they have found values of $\eta = 0.02$ and 0.006 for the prism and basal planes respectively. They also found the solutioning branch to be relatively important for their work with methane formations inversely proportional to the fourth power of the solubility constant.

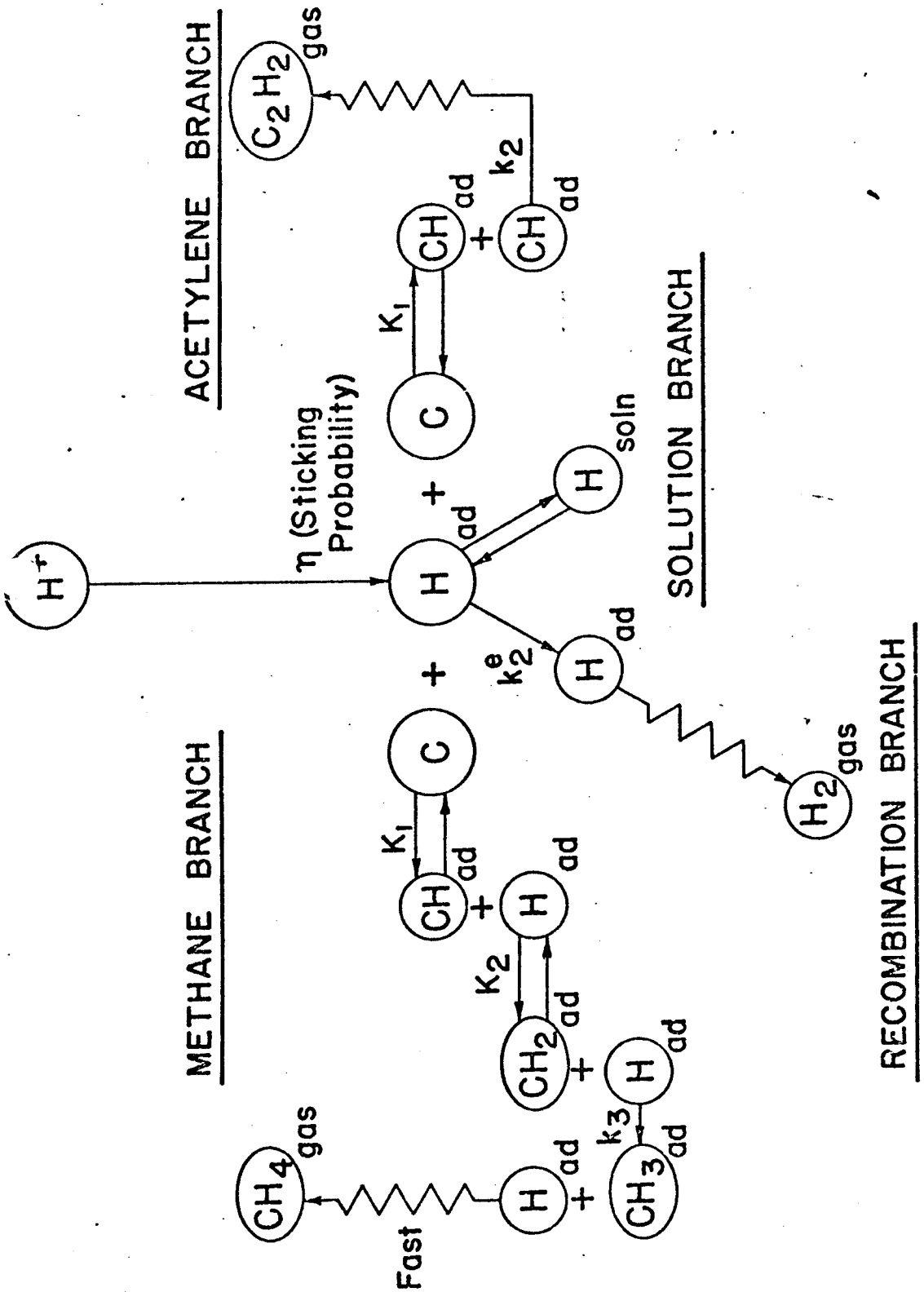

Figure IX-C-20 - Schematic of Chemical Sputtering of Carbon by Hydrogen (after Balooch and Olander(83))

The BO model explains the low temperature formation of methane by the sequence in Figure IX-C-20 which is assumed to be rate limited by K_3 (the formation of CH_3 from CH_2). However, as the temperature is increased above 600°C, the absorbed hydrogen becomes mobile and the probability of finding another hydrogen atom $k_2\eta^2$ is far greater than the product of $K_1K_2k_3\eta^3$ for forming CH_4 or $K_1k_2\eta^2$ for forming acetylene. This results in increased recombination, that is the evolution of molecular hydrogen and a reduced methane formation note.

As the temperature is further increased, the acetylene becomes more stable than the methane and the combination of two CH molecules to form C_2H_2 is greatly enhanced.

The BO model predicts that the reaction probability, ε, (a pseudo sputtering coefficient) for the gasification of carbon depends on the sticking coefficient, η, as follows:

$$\varepsilon_{CH_4} \alpha \eta$$

$$\varepsilon_{C_2H_2} \alpha \eta^{3/2}$$

One might then try to extrapolate the BO results to higher energies by noting that essentially all hydrogen above 1 keV will be trapped (η=1) below the surface and will have to diffuse back out. When the hydrogenic ion reaches the surface, it would then be free to form CH_4 or C_2H_2. Such a mechanism would predict sputtering coefficients associated with methane formation at 600°C on the basal planes to be ~0.05, very close to the values in Figure IX-C-18. A value of ~0.02 would be predicted for the same mechanism at 900°C, still within fair agreement with recent data. However, it should be noted that the reduction of CT_4 formation with increasing tritium energy does not agree with this result.

The 3/2 dependence for the acetylene formation, combined with the fact that 2 carbon atoms are removed per acetylene molecule, would predict an even higher sputtering value at high temperatures. Effective sputtering values would range from 0.4 at ~900°C to 3 at 2000°C. Such high values have not been measured to date, in fact, Guseva[85] has measured a yield of 0.03 at 1400°C for a 10 keV H^+ on WCA carbon cloth. Therefore, while the BO model may be successful in predicting the lower temperature methane formation, it would not seem to be applicable to the acetylene region. For the purpose of this work we will assume a linear dependence and this would predict effective sputtering coefficients of 0.03 at 900°C to 0.3 at 2000°C. This should give us the most pessimistic conditions.

Physical sputtering of graphite by helium ions is thought to be practically independent of temperature.[92] Two independent measurements give the sputtering ratio as 0.06 for 0.4 keV He ions[93] and 0.07 for 0.5 keV He ions.[94]

There is no experimental evidence reported so far as to blister formation in graphite with helium ion bombardment[82,89,90,95,96]. Samples of STC-10 graphite (composite of carbon felt and pyrolitic carbon) were irradiated in work described in reference 89 by 150-300 keV He^+ up to 2 x 10^{18} He/cm^2 dose of 400°C temperature and no blisters were observed to form. The re-emission of helium injected was a smooth function of dose reaching 100% at steady state. In 400 and 800°C irradiations of Ekern et al.,[90] with 100 and 250 keV He on graphite cloth, no flaking or blisters were observed either.

B. Feinberg et al.[82] bombarded WCA cloth samples with 1000 consecutive pulses of 600 eV He° atoms and He^+ ions (10^{20} He° atoms/cm^2 plus 5 x 10^{18} He ions/cm^2). They found ridges forming perpendicular to the fiber axis but they did not observe any blisters. The observed ridges were later found to be merely due to temperature cycling from pulsing.[86]

The sputtering yield results for carbon on carbon are even more scarce than hydrogen and helium bombardment results. One value quoted in the literature is 0.4 for 45 keV C on C.[97] Assuming that this value is correct, the self-sputtering yield of carbon under tokamak operating conditions (1-20 keV C on C) may be expected to be around 0.5-0.6.

The atomic sputtering ratio for neutrons on graphite is not known, and it is difficult to estimate it relative to other materials because the data is very scattered. A recent paper by O. K. Harling et al.[50] on the status of neutron sputtering of metals shows the neutron sputtering ratio of niobium to vary between 1.5 x 10^{-5} and 10^{-3}. The high sputtering yield results are from Kaminsky et al.[49] who have also reported to have observed micron size "chunks" being sputtered off the surface. In view of the lack of data we will assume a 14 meV neutron sputtering value of 10^{-4}. A summary of the available data on the sputtering of graphite is given in Table IX-C-16.

IX-C-2-d. Effect of High Helium Content in Carbon

Due to high $C^{12}(n,n')3He^4$ and $C^{12}(n,\alpha)Be^9$ reaction cross sections at high neutron energies the amount of helium generated in ISSEC will exceed 3000 appm per year per 1 MW/m^2 wall loading. It was originally thought that this much helium could coalesce to form large bubbles and cause considerable dimensional changes and tearing. Some recent experiments tend to show that helium generated may in fact diffuse out with almost 100% efficiency without any buildup inside. Thomas et al.[89] bombarded pyrolitic graphite with 300 keV He ions of temperatures 25, 800, 1200°C. The found that the re-emission rate of helium from carbon in basal plane orientation was very high (essentially 100%) of 1200°C temperature. Their results are shown in Figure IX-C-21. J. B. Holt et al.[101] at Livermore Laboratories measured the diffusion coefficient of helium in two types of graphite, as a function of temperature. In Figure IX-C-22, average distance (random migration) traveled by a helium atom in these two types of graphite is plotted as a function of temperature and time. The dots on the curves indicate the regions where the data was taken. We have extrapolated the data on both sides as shown in Figure IX-C-22. We see that average distance traveled by helium atoms in graphite is on the order of 1-10 microns per minute at 800°C. It is known[73] that the crystal size in graphite is about 4-5 microns.

Table IX-C-16

Summary of Data on Sputtering of Carbon

Particle	Energy-KeV	Target Temperature °C	S Atom/particle	Reference
H^+	10-20	600	0.082	84
		1000	0.03	84
	10	1400	0.03	85
D^+	6	400	0.006	81
		600	0.035	81
		800	0.006	81
T^+	2	400	0.012	81
		600	0.080	81
		700	0.068	81
	6	400	0.008	81
		650	0.064	81
		750	0.036	81
H°	~0.0002	300	~0.002	83
		800	~0.0004	83
		2000	~0.002	83
H° & H^+	0.580 & 0.875	150	0.03	82
		450	0.08	82
		750	0.02	82
He^+	0.4	-	0.06	93
He^+	0.5	-	0.07	94
C	45	-	~0.4	97
Ne	0.4	-	0.01	93
Ar	24	-	2.5	99
K	0.5	-	0.13	94
Kr	45	-	2.4	100
Xe	0.5	-	0.17	94
Cs	10	-	1.97	94
Hg	0.5	-	0.16	93
n	14,000	-	?	-

Figure IX-C-21

Re-Emission of Helium From Carbon (101)

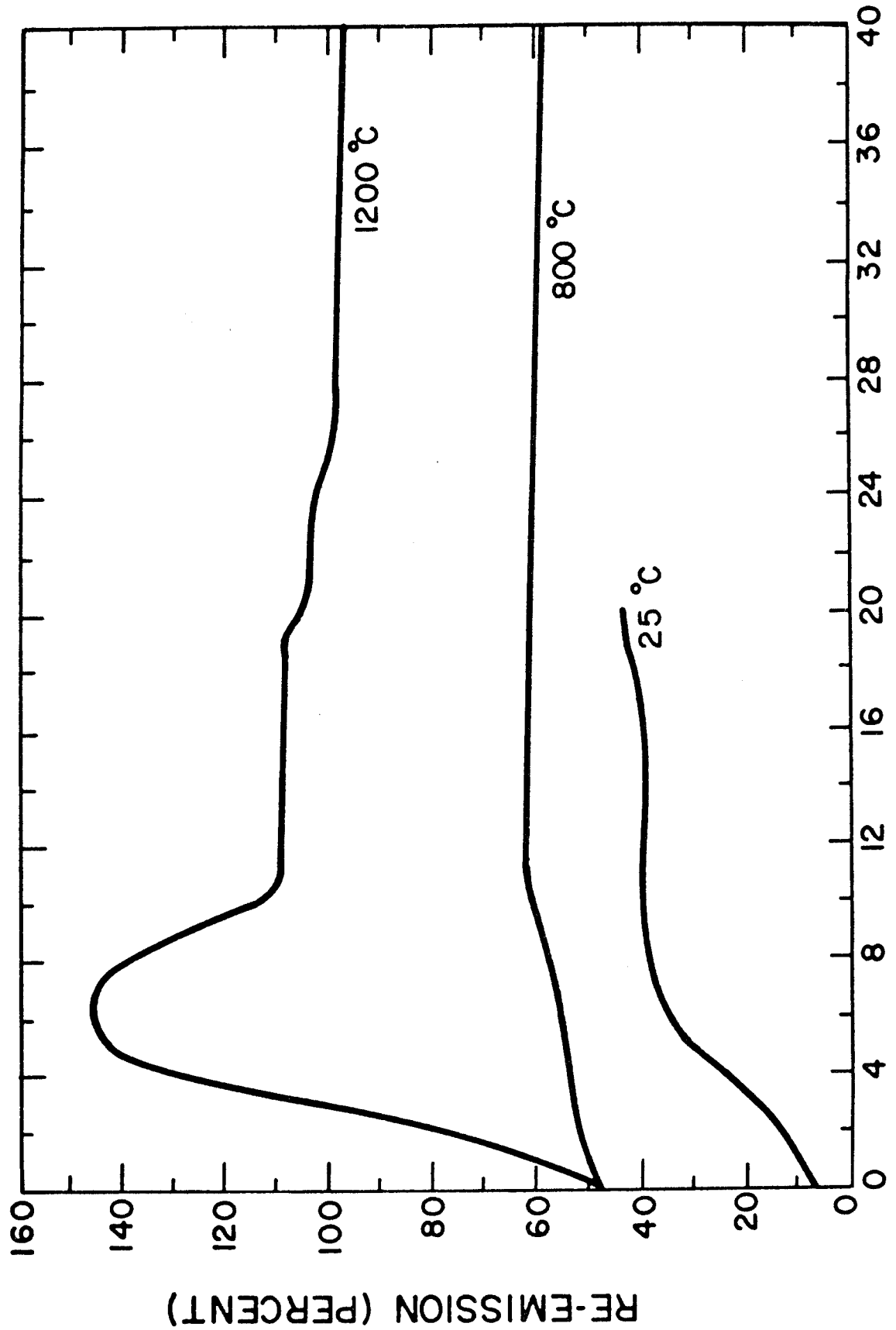

Figure IX-C-22 DIFFUSION OF HELIUM IN GRAPHITE

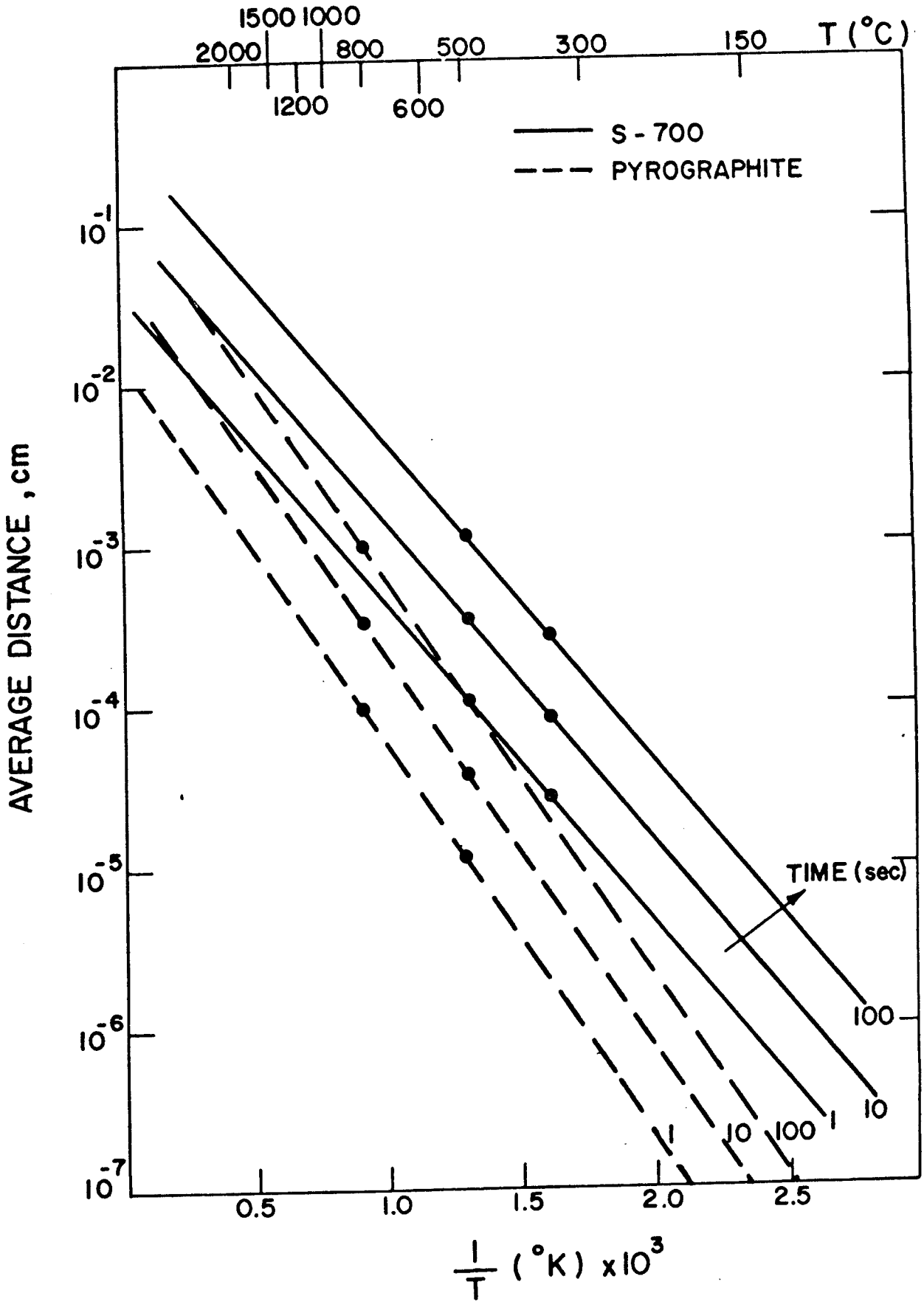

Some experiments performed by J. Scott at Oak Ridge[102] tend to show that once the helium atoms have diffused out of the crystallite into pores between crystallites, they may be assumed to be lost to the vacuum. This may especially be true if 3-dimensional woven graphite is used for ISSEC. Fibers in this can have diameters of about 6-10 microns.

IX-C-3. Radiation Effects in Boron Carbide

Boron carbide (B_4C) is found in two places in UWMAK-III, the shield for the inner blanket where it operates at a maximum temperature of 250°C and the outer cold shield where it operates at a maximum temperature of 200°C. The B_4C is mixed with an $Al_2O_3SiO_2$ binder that eases the fabrication costs. However, the use of this binder means that we cannot directly use the irradiation behaviors determined from hot pressed B_4C pellets. In order to obtain a feel for the potential problems, we will neglect this fact.

The density of the B_4C in the binder is assumed to 92% and the boron is assumed to be 100% enriched in B-10. This means that the B-10 concentration is 1.0×10^{23} atoms per cm^3.

The biggest problems for B_4C are the reduction in thermal conductivity with irradiation and the swelling induced by the helium gas generated by the $B^{10}(n,T)2He$ and $B^{10}(n,\alpha)Li^7$ reactions. It is important to determine how much of the helium will escape by the recoil and diffusion mechanism. A large amount of data has been analyzed by scientists at HEDL[103] and they have come up with the following empirical equation:

$$R(\text{Fractional Gas Release}) = A[1.32 - 0.032C + 5.9 \times 10^{-4}C^2]$$

where

$$A = 18.9 \exp\left(-\frac{8990}{T + 460}\right) + 0.37 \exp\left[(-0.18)\left(\frac{T - 1340}{100}\right)^2\right]$$

$T = °F$

$C = 10^{20}$ captures per cm^3 of B_4C.

At very low temperatures, the release is essentially zero and the swelling at 300°C is expected to be as shown in Figure IX-C-23. This figure shows that until the burnup reaches 10^{22} atoms per cm^3, the swelling should be minimal (i.e. < 5%).

The situation is quite different at 1250°C (which is 250°C above the maximum temperature for which the emperical equation is supposedly valid.) Figure IX-C-24 shows that for 25×10^{20} captures per cm^3, the fractional release varies from 50% at 760°C to 30% at 900°C and back up to 40 to 50% again at 1200°C. The amount of swelling (or diametral change) induced by the remaining gas can be described as follows.[103]

$$\% \frac{\Delta D}{D} = C\left(-0.211 + \frac{62.04}{T}\right)$$

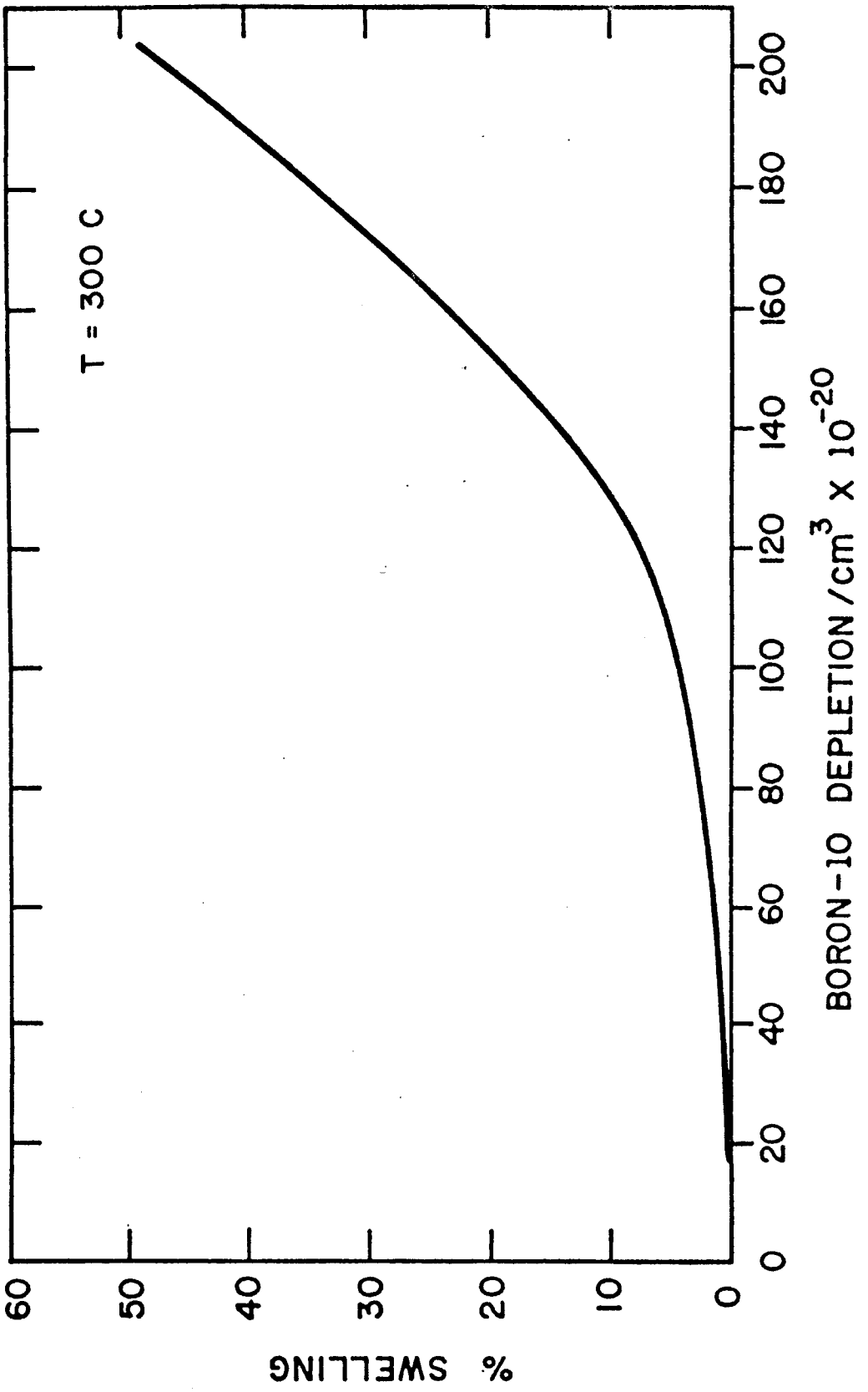

Figure IX-C-23

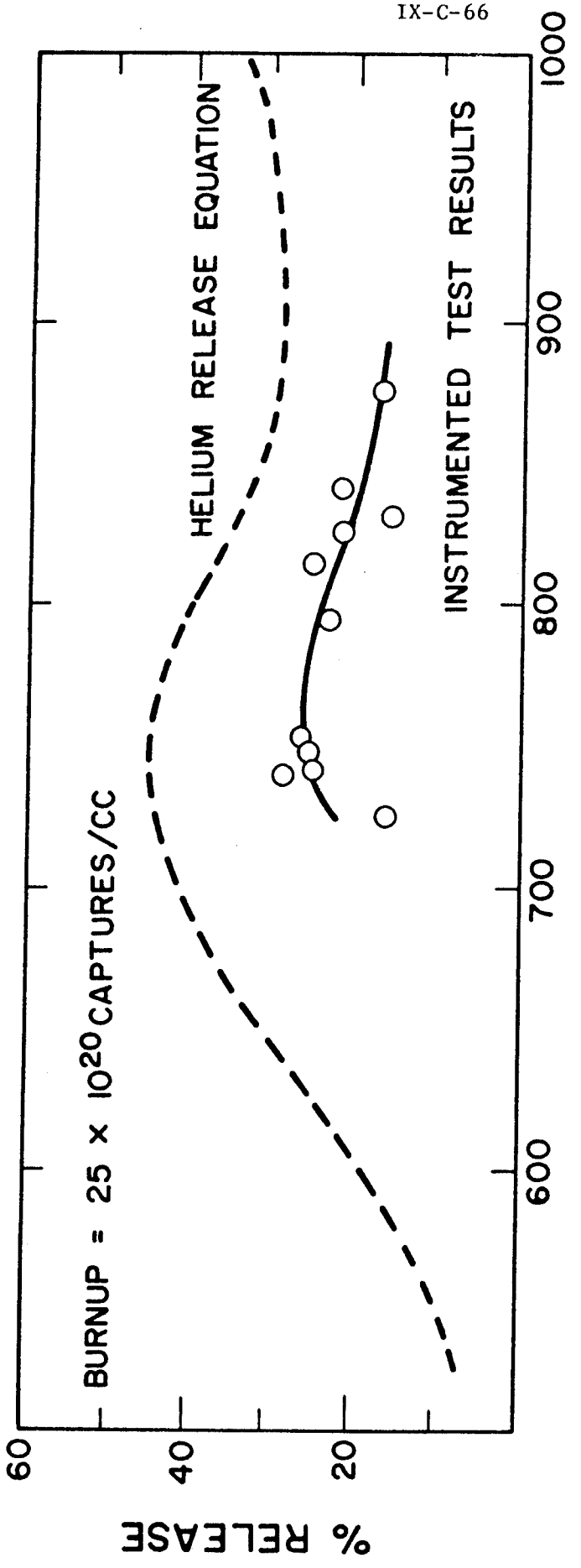

Figure IX-C-24 Helium Release in Instrumented EBR-II Test (103)

The form of this equation is displayed in Figure IX-C-25. If the equation is valid to 1250°C, then the diametral change would be 0.15% or a total swelling of only 0.5%. One should be careful about extrapolating the B_4C data to such high temperatures and if B_4C indeed is to be used in hot CTR blankets, a testing program should be initiated to duplicate the anticipated fusion reactor conditions.

The final point to be covered is the effect of irradiation on the thermal conductivity of B_4C. Irradiation at temperatures of 500-870°C have been shown to significantly reduce the thermal conductivity of B_4C as shown in Figure IX-C-26. This effect appears to be more pronounced at lower temperatures (Figure IX-C-27) and saturates at rather low burnups (5×10^{20} captures per cm^3).

IX-C-4. Lead

The lead in the outer shield and between the hot inner shield and the TF coil will also suffer radiation damage. The dpa rates for Pb have been recently calculated by Doran using the IAEA recommended model and Ed = 16 eV(104). There are no (n,α) reactions below 14 MeV so we need not worry about helium bubble formation.

The maximum displacement levels achieved in the Pb shield are $<10^{-4}$ dpa/yr. There is no known irradiation data of Pb to compare our work to at this time and due to the high temperature of operation for the lead (0.8 T/T_m) we do not expect any void swelling. Therefore, it appears that there should be relatively few dimensional stability problems with that material.

IX-C-5. Magnet Components

There are five materials to worry about in the superconducting magnet structure.

(a) Mylar insulation
(b) Epoxy electrical insulator
(c) Al stabilizer
(d) Ti Nb superconductor
(e) Aluminum alloy structure

We will address each material separately.

IX-C-5-a. Mylar Insulation

Previous analysis[1,2] of the radiation damage resistance of mylar has resulted in a threshold of observable damage to the mechanical properties of 30 M Rads. The mylar is expected to lose 25% of its tensile strength by 120 M Rads.

IX-C-5-b. Epoxy Electrical Insulator

This material is much more resistant to radiation damage than the mylar and its threshold for damage is estimated at 8000 M Rad. It will suffer a 25% reduction in insulating properties by 50,000 M Rads.[1,2]

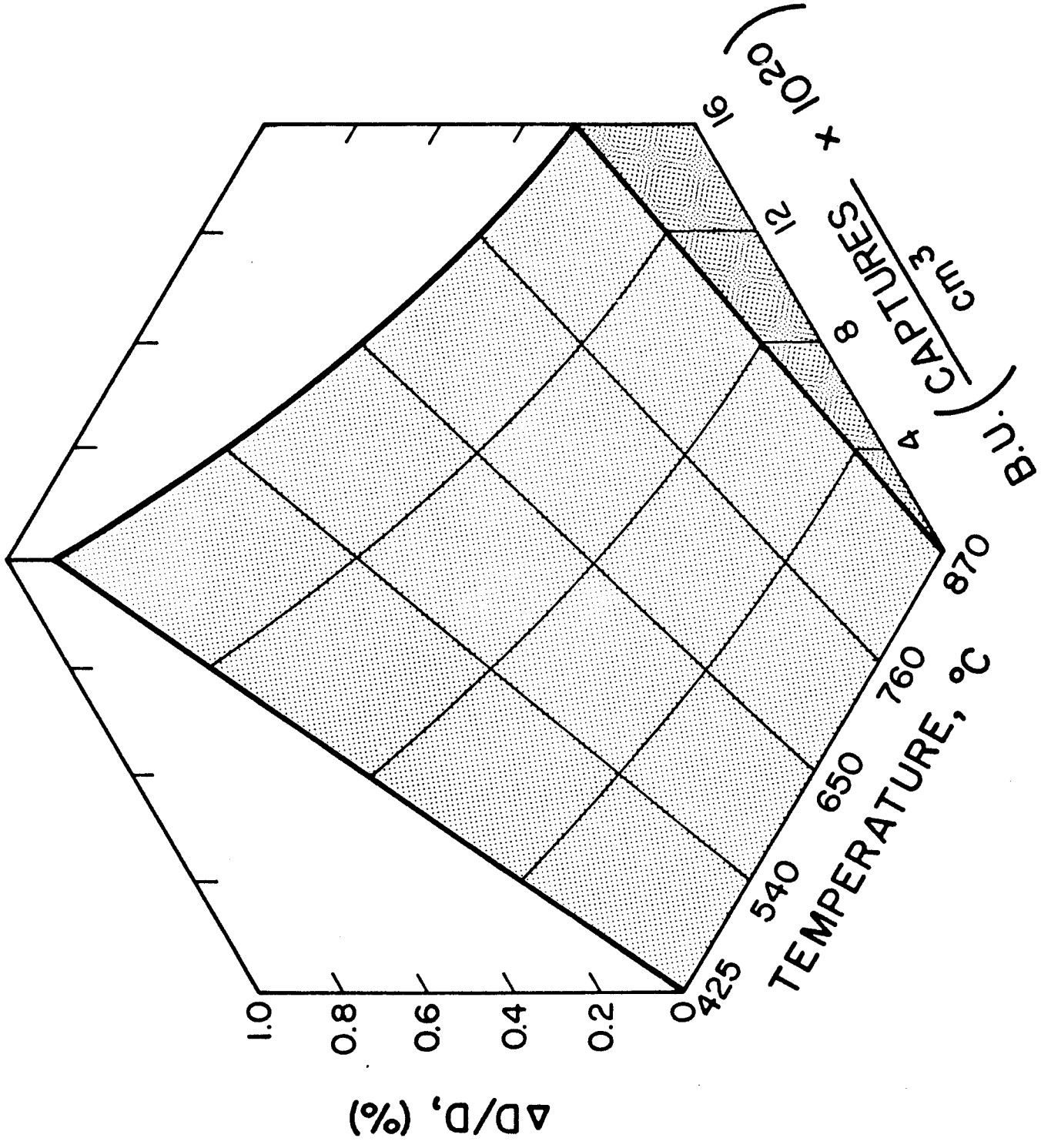

Figure IX-C-25 Diametral Swelling of Boron Carbide Pellets (103)

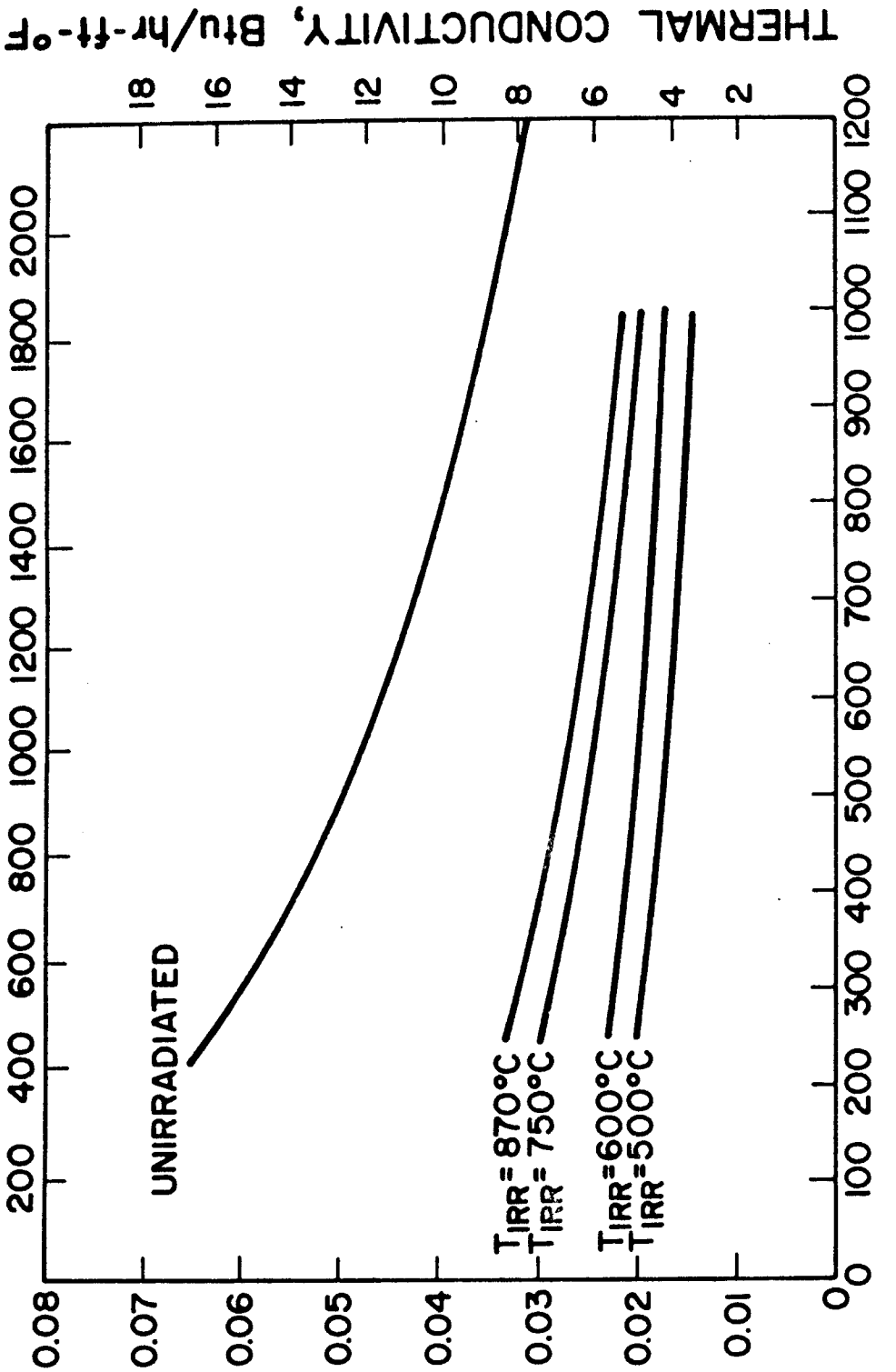

Figure IX-C-26 Thermal Conductivity of Unirradiated and Irradiated Boron Carbide (107)

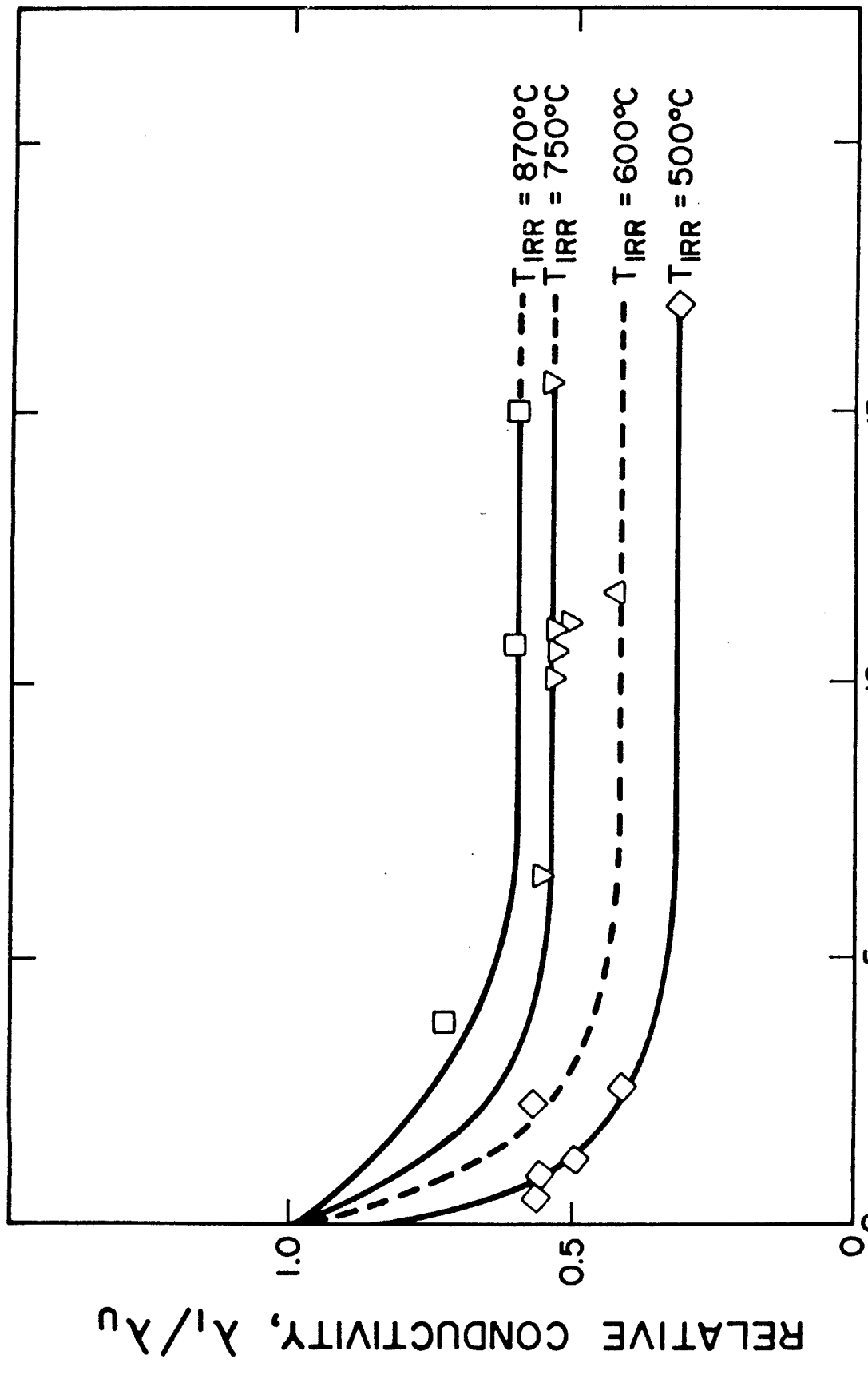

Figure IX-C-27 Exposure Dependence of Thermal Conductivity (103)

IX-C-5-c. Aluminum Stabilizer

The main problem here is the increase in resistivity due to the accumulation of defects at liquid helium temperatures. Blewett and Horak[105] have measured the resistivity increase with damage level and found that is saturates at 0.8 micro-ohm-cm at 10^{-3} dpa. This is shown in Figure IX-C-28. This is to be compared to the residual resistivity of 0.01 micro-ohm-cm. In other words, the resistivity could increase by a factor of 80 in 10^{-3} dpa. The level of damage to double the resistivity is slightly greater than 10^{-5} dpa.

The recovery of radiation damage in Al is also important because if one can periodically heat the magnet up to room temperature, essentially all of the damage can be removed. Figure IX-C-29 shows how the resistivity of Al recovers with isochronal annealing temperature. This data shows that essentially 100% of the irradiation induced damage could be annealed out. Hence, all one has to do now is to determine the allowable resistivity increase, calculate the time to accumulate that amount of displacement damage, and then warm the magnets up to room temperature at that time interval.

IX-C-5-d. TiNb Superconductor

It is generally accepted that the most sensitive property of the superconducting magnets is the critical current density. The effect of neutron irradiation at cryogenic temperature on the critical current of TiNb is shown in Figure IX-C-30. From that figure we can see that the damage must exceed 10^{-3} dpa before one gets a 10% reduction in the critical current density. We will use that as a criteria to determine the lifetime of the TiNb in the TF coils of UWMAK-III.

IX-C-5-e. Support Material

There have been only a few cryogenic radiation damage studies on Al alloys and these have been summarized by Kangilaski.[106] The irradiation exposure was at 77°K and to a fluence of $7.5 \times 10^{17} n/cm^2$ ($E > 1$ MeV). The results are summarized in Table IX-C-17. There was essentially no change in the yield on ultimate strength, nor the ductility of the sheet material. However, there was an increase in yield strength and a drop in ductility or forgings. Based on this limited data, we would recommend that the exposure on the structural material not exceed $5 \times 10^{18} n/cm^2$ ($E > 0.1$ MeV) or 5×10^{-3} dpa.

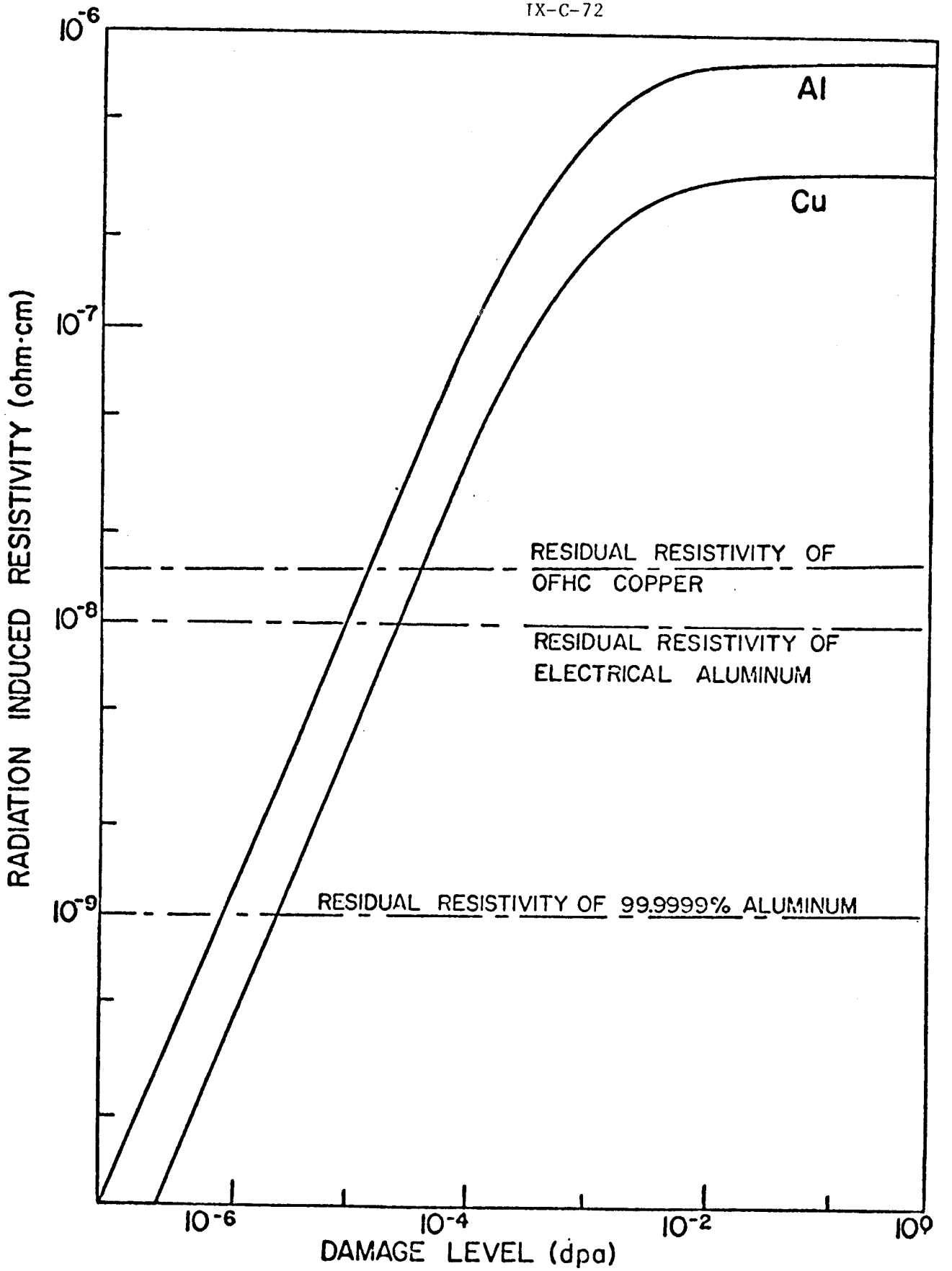

Figure IX-C-28 Radiation Induced Resistivity of Copper and Aluminum

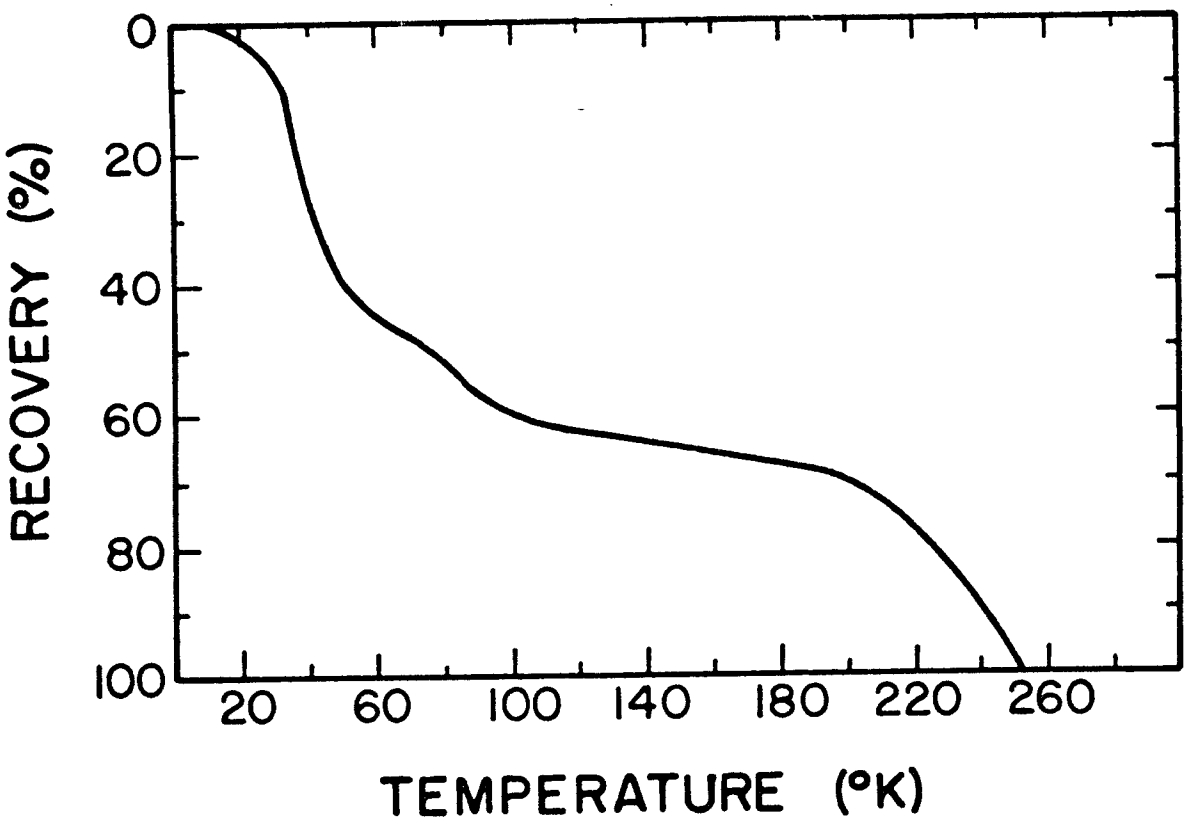

Figure IX-C-29. Recovery of Neutron Irradiated Aluminum. T. H. Blewitt, Defects and Radiation Damage in Metals, M. W. Thompson, Cambridge Press, 1969,P. 307. (Both Electrical Resistivity and Length Change Data Are Given.)

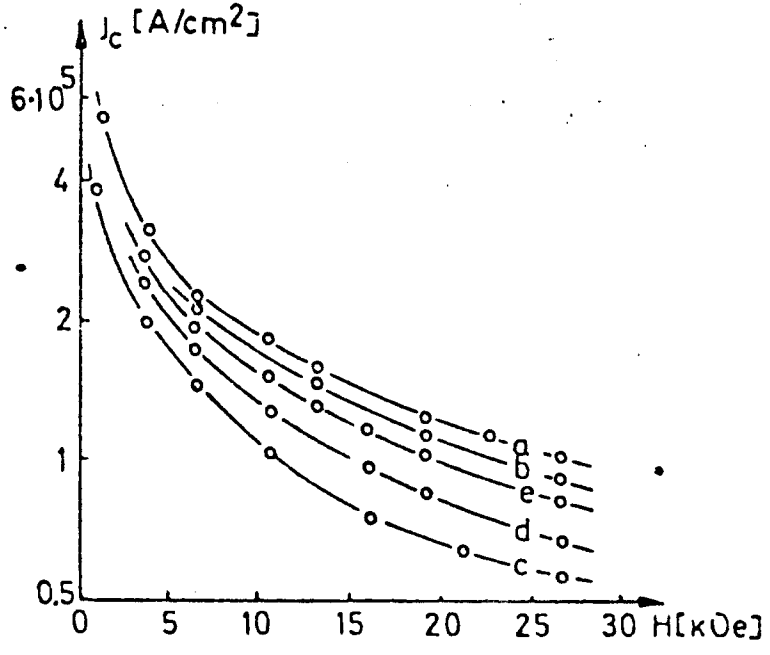

Critical current density j_c versus applied transverse magnetic field H for Nb-50wt%Ti at 5.3K. Curve a unirradiated, b irradiated with 3.2×10^{18} neutrons /cm² (E>0.1 MeV), c irradiated with 7.5×10^{18} n/cm², d annealed at 100 K, e annealed at 270 K (after Soell ref.2).

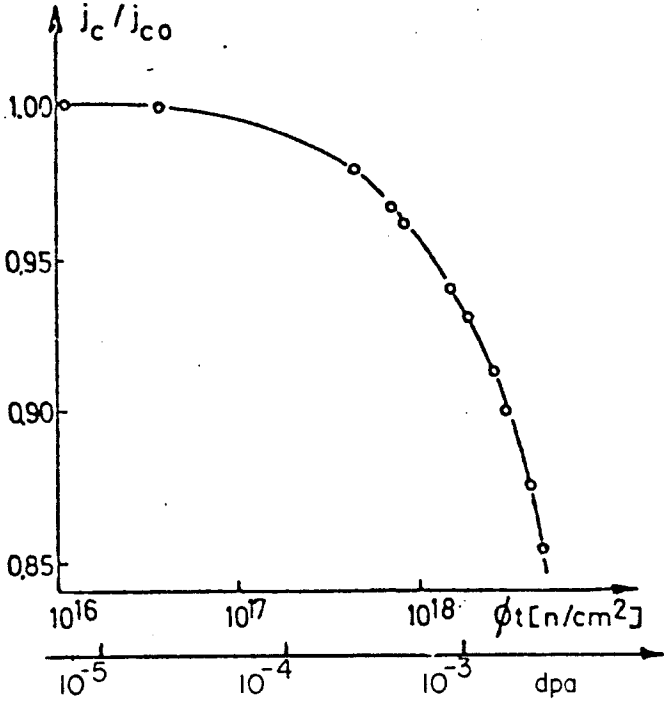

Relative Change of the critical current density j_c of a Nb-50wt% Ti sample at zero field (H=0) as a function of the neutron dose $\phi \cdot t$. j_{co} is the current density before the irradiation (after Soell ref. 2).

Figure IX-C-30 The effect of fast neutron irradiation at cryogenic temperature on the critical current of Nb-50 w/o Ti. The conversion to dpa was made using a typical thermal reactor spectrum.

Table IX-C-17

Summary of the Effect of Neutron Irradiation on the Mechanical Properties of 2219 Aluminum Alloy at Cryogenic Temperatures(107,108)(a)

Neutron Fluence x 10^{17}n/cm^2	T_{irrad} °C	T_{Test} °C	Yield Strength MPa		Ultimate Strength MPa		Total Elongation	
			Control	Irr	Control	Irr	Control	Irr
1	-257	-257	470	511	661	646	16.4	15.3
7.5	-196	-196	339	435	504	517	9.1	8.0
↓	↓	-196(b)	339	357	504	512	9.1	10.1
		27	290	286	412	403	7.0	6.8
		-196	370	545	499	556	7.6	2.3
		-196(b)	370	376	499	497	7.6	6.7
		27	325	325	428	423	7.4	6.6
		-196	357	540	516	555	14.3	5.6
		-196(b)	357	369	516	515	14.3	13.8
		27	314	323	426	426	10.9	11.4

References IX-C

1) B. Badger, M. A. Abdou, R. W. Boom, R. G. Brown, T. E. Cheng, R. W. Conn, J. M. Donhowe, L. A. El-Guebaly, G. A. Emmert, G. R. Hopkins, W. A. Houlberg, A. B. Johnson, J. H. Kamperschroer, D. Klein, G. L. Kulcinski, R. G. Lott, D. G. McAlees, C. W. Maynard, A. T. Mense, G. R. Neil, E. Normand, P. A. Sanger, W. E. Stewart, T. Sung, I. Sviatoslavsky, D. K. Sze, W. F. Vogelsang, L. J. Wittenberg, T. F. Yang, and W. D. Young, "A Wisconsin Toroidal Fusion Reactor Design," UWFDM 68, Nucl. Eng. Dept., University of Wisconsin, November 20, 1973.

2) B. Badger, R. W. Conn, G. L. Kulcinski, M. A. Abdou, R. Aronstein, H. I. Avci R. W. Boom, T. E. Cheng, J. Davis, J. M. Donhowe, G. A. Emmert, Y. Eyssa, N. M. Ghoniem, S. Ghose, W. Houlberg, J. Kesner, W. Lue, C. W. Maynard, A. Mense, N. Mohan, H. A. Peterson, T. Y. Sung, I. Sviatoslavsky, D. K. Sze, W. F. Vogelsang, R. Westerman, L. J. Wittenberg, T. F. Yang, J. Young, and W. C. Young, "A Conceptual Tokamak Power Reactor Design," UWFDM 112, Nucl. Eng. Dept., University of Wisconsin, October 1975.

3) G. L. Kulcinski, D. G. Doran, and M. A. Abdou, "Properties of Reactor Structural Alloys After Neutron or Particle Irradiation," ASTM-STP-570, Amer. Soc. Testing Materials, 1975 p. 329.

4) S. Pearlstein, J. Nucl. Energy, 27, 81, 1973.

5) P. G. Lucasson and R. M. Walker, Phys. Rev., 127, 485, 1962.

6) D. G. Doran, J. R. Beeler, M. D. Dudey, and M. J. Fluss, HEDL-TME-73-76, Hanford Engineering Development Laboratory, Richland, Washington, December 1973.

7) R. Schmunk and G. L. Kulcinski, to be published.

8) H. E. Kissinger, J. L. Brimhall, B. Mastel, and T. K. Bierlien, International Conference on Vacancies and Interstitials in Metals, ed. by J. Diehl, W. Schilling, and D. Schumacker (Kernforschungsavlage Julich, Germany) (1968), p. 681.

9) C. R. Piercy and R. H. Tuxworth, "The Effect of Fast Neutron Irradiation on the Density, X-Ray Lattice Parameter and the Line Breadth of Metals," CRRM-1010 (1961).

10) J. L. Brimhall, E. P. Simonen, and H. E. Kissinger, "Fluence and Temperature Dependence of Swelling in Irradiated Molybdenum," Journal of Nuclear Materials, 48, 339 (1973).

11) J. Bentley, "High Temperature Neutron Irradiation Damage in Molybdenum and TZM, Thesis, University of Birmingham, England, November 1974.

12) J. Moteff, D. J. Michael, and V. K. Sikka, "The Effect of Irradiation Temperature on the Hardening Behavior of the Refractory BCC Metals and Alloys," Nuclear Metallurgy, 18, 198 (1973).

13) F. A. Smidt, Jr., "Analysis of Microstructures of Molybdenum Neutron Irradiated in EBR-II," Naval Research Laboratory 1975 Annual Report, to be published.

14) J. D. Elen, "Voids Formed by Irradiation of Reactor Materials - Some Electron Microscope Observations on Voids in Vanadium, Niobium, and Molybdenum," British Nuclear Energy Society, European Conference, ed. by S. F. Pugh, M. H. Loretto, and D. I. R. Norris, pp. 51-62 (1971).

15) A. G. Pard and K. R. Garr, "Damage Structure in Neutron Irradiated TZM," in Radiation Effects and Tritium Technology for Fusion Reactors, eds. J. S. Watson and F. W. Wiffen, ConF-750989, Vol. I, 1976, p. 312.

16) F. W. Wiffen, "The Effect of Alloying and Purity on the Formation and Ordering of Voids in BCC Metals," Albany Conference on Radiation-Induced Voids in Metal, pp. 386-396, June 1971.

17) Y. Adda, "Report on the CEA Program of Investigations of Radiation-Induced Cavities in Metals: Presentation of Some Results," ibid pp. 31-83.

18) B. L. Eyre and A. F. Bartlett, AERE (Harwell-R-7027) (1972).

19) R. C. Rau, R. L. Ladd, and J. Moteff, "Voids in Tungsten and Molybdenum," J. Nucl. Matl., 33, 324 (1969).

20) G. L. Kulcinski, B. Mastel, and J. L. Brimhall, Radiation Effects, 2, 57 (1969).

21) J. F. Stubbins, Heavy Ion-Induced Radiation Damage and Void Formation in Molybdenum and its Alloys," PhD Thesis, University of Cincinnati, 1975.

22) D. W. Keefer, to be published.

23) B. L. Eyre and J. H. Evans, "British Nuclear Society European Conf. on Voids Formed by Irradiation by Reactor Materials," edited by S. F. Pugh, M. H. Loretto, and D. I. R. Norris, p.323 (1971).

24) J. H. Evans, Radiation Effects, 17, 69, 1973.

25) G. L. Kulcinski and J. L. Brimhall, Proc. of Mol. Conf. on Defects in Refractory Metals, ed. by R. DeBalist, J. Mihoul, and L. Stal, p. 291 (1972).

26) J. L. Brimhall, to be published in ASTM Radiation Effects Conf., St. Louis, May 1976.

27) E. R. Bradley and J. L. Brimhall, "Int. Conf. on Radiation Effects and Tritium Tech. for Fusion Reactor," ed. by J. S. Watson and F. W. Wiffen, ConF-750989, Vol. I, 1976, p. 337.

28) K. Y. Liou, to be published.

29) J. L. Brimhall and E. P. Simonen, J. Nucl. Mat., 52, 323 (1974).

30) J. L. Brimhall and E. P. Simonen, "Defects and Defect Clusters in BCC Metals and Their Alloys," Nuclear Metallurgy, 18, 321, 1973, ed. by R. J. Arsenault.

31) J. L. Brimhall, "The Physics of Irradiation Produced Voids," ed. R. S. Nelson, p. 197 (1974), AERE-R-7934.

32) G. L. Kulcinski and J. L. Brimhall, "Effects of Radiation on Substructure and Mechanical Properties of Metals and Alloys," ASTM-STP-529, Amer. Soc. Testing and Materials, 1973, p. 258.

33) J. L. Brimhall, "Int. Conf. on Radiation Effects and Tritium Tech. for Fusion Reactors," J. S. Watson and F. W. Wiffen, ConF-750989, Vol. I, 1976, p. 73.

34) F. W. Wiffen, "Defects and Defect Clusters in BCC Metals and Their Alloys," Nuclear Metallurgy, Vol. 18, ed. by R. J. Arsenault, p. 176, 1973.

35) V. A. Kasakov, A. N. Kolesnikov, V. A. Krassnoselov, Z. E. Ostrowsky, A. S. Pokrowsky, V. I. Prohopov, E. M. Loboda, A. V. Smirnoff, and V. K. Shamardin, to be published.

36) I. M. Voronin, V. D. Dmitriev, S. S. Ibragimov, and V. S. Lyashenko, Atomnaya Energiya, 6, 514, 1960.

37) V. A. Nikolaev, Yu. I. Patrikew, and S. K. Mikhailov, At. Energy (USSR), 25, 197, 1968.

38) S. K. Mikhailov, Yu. V. Solomko, S. I. Aleksandrov, and Yu. M. Golovchenko, Fiz. Metal. Metalloved., 23, No. 5, 957, 1967.

39) D. Kramer, K. R. Garr, A. G. Pard, and C. G. Rhodes, AI-AEC-13047, December 1972.

40a) F. D. Kingsburg and J. Moteff, Trans. Amer. Nuc. Soc., 12, 575, 1969.

40b) J. Moteff and F. D. Kingsburg, Trans. Amer. Nuc. Soc., 10, 428, 1967.

41) J. Moteff, R. C. Rau, and F. D. Kingsbury, "Radiation Damage in Reactor Materials," Vol. II, Int. Atomic Energy Agency, Vienna, p. 269, 1969.

42) J. Moteff, C. G. Schmidt, and F. W. Wiffen, "Radiation Effects and Tritium Technology for Fusion Reactors," ConF-750989, Vol. II, ed. J. S. Watson and F. W. Wiffen, p. 141, 1976.

43) D. J. Michel, C. Z. Serpan, H. H. Smith, and A. G. Pieper, Nucl. Tech., 22, 79, 1974.

44) D. J. Michel, to be published.

45) C. A. Finfgeld, "Proton Sputtering," ORO-3557-15, Roanoke College, Salem, Virginia.

46) D. Rosenburg and G. K. Wehner, J. Appl. Phys., 33, 1842, 1962, see also, G. K. Wehner, General Mills Report No. 2309, July 1962.

47a) R. Behrisch, To be published, 1976 Erice Summer School on Tokamak Reactors.

47b) H. Bay, J. Bohdansky and J. Roth, to be published.

48) D. Düchs, G. Haas, D. Pfirsch, and H. Vernickel, J. Nucl. Materials, 53, 102, 1974.

49) M. Kaminsky and S. K. Das, "14.1 MeV Neutron Sputtering of Polycrystalline and Monocrystalline Niobium with Different Surface Microstructures," to be published, J. Nucl. Mat. (see bibliography for earlier work by this group).

50) O. K. Harling, M. T. Thomas, R. L. Brodzinski, and L. A. Rancitelli, "Recent Neutron Sputtering Results and the Status of Neutron Sputtering," to be published, J. Nucl. Mat. (see bibliography in this reference for earlier work by this group).

51) R. Behrisch, "Neutron Sputtering," to be published, 6th Int. Conf. Atomic Collisions in Solids, Amsterdam, September 1975.

52) L. H. Jenkins, T. S. Noggle, R. E. Reed, and M. J. Saltmarsh, Appl. Phys. Letters, 26, 426, 1975.

53) S. K. Erents and G. M. McCracken, CLM-P-323, September 1972.

54) H. Verbeck and W. Eckstein, in "Applications of Ion Beams to Metals," ed. S. T. Picraux, E. P. Eernisse, and F. L. Vook, Plenum Publ. Corp., N.Y., p. 597, 1974.

55) G. M. McCracken and S. K. Erents, CLM-P-359, November 1973.

56) W. Bauer and G. J. Thomas, SLL-73-5266, June 1973.

57) R. W. Knoll, M. S. Thesis, University of Wisconsin, August 1974.

58) S. K. Das and M. Kaminsky, 5th Symp. on Engr. Prob. of Fusion Res., Princeton, November 1973.

59) S. K. Das and M. Kaminsky, "Defects and Defect Clusters in BCC Metals and Their Alloys," Nucl. Met., 18, 240, 1973.

60) M. Kaminsky and S. K. Das, Radiation Effects, 18, 245, 1973.

61) S. K. Das, M. Kaminsky, and T. Rossing, to be published, Int. Conf. on Ion Beam Surface Layer Analysis, Karlsrule, September 1975.

62) S. K. Erents and G. M. McCracken, CLM-P-323, September 1972.

63) J. Roth, R. Behrisch, and B. M. U. Scherzer, J. Nucl. Mat., 57, 365, 1975.

64) "The Industrial Graphite Engineering Handbook", Union Carbide Co., 1970.

65) C. L. Mantell, "Carbon and Graphite Handbook", Interscience, New York (1968).

66) G. P. Lang and V. L. Holmes, "Gas Content and Sticking Possibilities for Fibrous Forms of Graphite as Applied to Fusion Reactors", to be published in Nucl. Fusion.

67) T. R. Armstrong and P. B. Johnson, "Deuterium Implantation in Graphite", Dept. of Physics, Victoria University of Wellington, Wellington, New Zealand.

68) B. M. U. Scherzer, R. Behrisch, U. Litmark, J. Roth and M. K. Sinha, "Temperature Dependence of Trapping and Depth Profiles of 6 to 15 keV Deuterium in Carbon", 2nd International Conference on Surface Effects in Controlled Fusion Devices, San Francisco, California, Feb. 16-20, 1976.

69) W. C. Morgan, J. Nucl. Eng., 51, 209, 1974.

70) G. B. Engle and W. P. Eatherly, High Temperatures and High Pressures, 7, 319, 1969.

71) J. H. Cox and J. W. Helm, Carbon, 7, 319, 1969.

72) W. J. Gray and W. C. Morgan, BNWL-B-288 and BNWL-B-289, June 1973.

73) W. N. Reynolds et al. "Radiation Damage in Graphite at 1200°C", 2nd conference on Indust. Carbon and Graphite, Soc. Chem. Ind., April 1965.

74) B. T. Kelly et al., "Fast Neutron Induced Dimensional Changes in Graphites and Carbons", Ibid.

75) B. T. Kelly, "Dimensional Changes and Lattice Parameter Changes in Graphite Crystals Due to Interstitial Atoms and Vacancies", Ibid.

76) M. R. Everett et al., "Graphite Materials Data for High Temperature Nuclear Reactors", 3rd conf. on Ind. Carbon and Graphite, Soc. Chem. Ind., April 1970.

77) G. L. Tingey, W. C. Morgan and E. M. Woodroof, "Near-Isotropic Graphites for Helium Cooled Reactors - A Review", BNWL-B-478 (Feb. 1976).

78) J. W. Helm and J. M. Davidson, "Effect of Neutron Exposure on the Distortion of Reactor Graphite", Carbon 1, 435, (1964).

79) J. W. Helm, "Radiation Effects in Graphite at High Temperatures", Carbon 3, 493 (1966).

80) M. Van Den Berg, M. R. Iverett and A. Kingsbury, "12th Biennial Conf. on Carbon," Pittsburgh, Penn., 1975, p. 307.

81) H. Vernickel, EURATOM Association, Garching b. München, West Germany (private communication).

82) B. Feinberg and R. S. Post, "Graphite Surface Erosion and Blistering", Report UWFDM-141, Nuclear Engineering Department, University of Wisconsin, Madison, August, 1975.

83) M. Balooch and D. R. Olander, J. Chem. Phys. 63, No. 11, Dec. 1975.

84) I. P. Busharov, E. A. Gorbatov, V. M. Gusev, M. I. Geseva and Y. V. Martynenko, "Chemical Atomization of Graphite by H^+ Ions", The I. V. Kurchatov Order of Lenin Institute of Atomic Energy, Moscow, 1975.

85) M. I. Guseva, The I. V. Kurchatov Order of Lenin Institute of Atomic Energy (private communication).

86) B. Feinberg, Nuclear Engr. Dept., Univ. of Wisc., Madison, private communication.

87) S. Veprek and M. R. Hague, "On the Chemical Erosion of the First Wall in the Next Generation of Tokamak Devices for Controlled Fusion", Univ. of Zurich, Zurich, Switzerland.

88) B. J. Wood and A. Wise, J. Phys. Chem. 73, 1348 (1969).

89) G. J. Thomas, W. Bauer, P. L. Mattern and B. Granoff, "He and H implantation of Vitrious Silica and Graphite", report SAND75-8718, Sandia Lab., Albuquerque, NM. To be published in Proc. of Am. Chem. Soc. Mtg., Chicago Ill., August 21-22, 1975.

90) R. Ekern, S. K. Das and M. Kaminsky, "Temperature Dependence of Surface Damage in Graphite Cloth Irradiated with Deuterons and Helium Ions", presented at conference cited in ref. 68.

91) S. K. Erents, C. M. Braganza and G. M. McCracken, "Methane Formation During the Interaction of Energetic Protons and Deuterons with Carbon", in ref. 60.

92) J. Koth et al., "Physical and Chemical Sputtering of Graphite and SiC by Hydrogen and Helium in the Energy Range of 300 to 600 eV", in ref. 5.

93) N. Laegreid and G. K. Wehner, J. Applied Phys. 32, 365, (1961) and D. Rosenberg and G. K. Wehner, J. Appl. Phys. 33, 1842, (1962).

94) G. Carter and J. S. Colligen, Ion Bombardment of Solids (American Elseveier Publishing Co., New York: 1968), p. 323, p. 325.

95) R. Wright, R. Varma and D. M. Gruen, "Raman Scattering and SEM Studies of Graphite, CVD Pyrolitic and Vitreous Carbon, Etc.", in ref. 68.

96) L. H. Rovner and K. Y. Chen, "Surface Erosion of C and SiC by 0.5 - 3.5 MeV He^{+}", ref. 68. Also report GA-A13812, General Atomic Company, San Diego, California.

97) O. Almen and G. Bruce, Nucl. Inst. and Methods 11, 279, (1961).

98) R. W. Conn and J. Kesner, "Plasma Modeling and First Wall Interaction Phenomena in Tokamaks", to be published in J. Nucl. Mat. (1976).

99) G. Betz, R. Dobrozemsky, F. P. Viehsock and H. Wothe, page 90 in Phenomena in Ionized Gasses, a conference held in Bucharest, Romania, 1969.

100) O. Almen and G. Bruce, Trans. 8th Natl. Vac. Symp. Wash. 1, 245 (1961).

101) J. B. Holt et al. "Helium Generation and Diffusion in Graphite", Lawrence Livermore Laboratory, Livermore, California, April, 1976.

102) J. Scott, private communication.

103) "A Compilation of Boron Carbide Design Support Data for LMFBR Control Elements", HEDL-TME-75-19, 1975.

104) D. Doran, to be published.

105) J. A. Horak and T. H. Blewitt, Phys. Stat. Solidi, 9, 721, 1972

106) M. Kangilaski, "The Effects of Neutron Irradiation on Structural Materials", REIC Report #25, June, 1967.

107) C. A. Schwanbeck, Effect of Nuclear Radiation on Materials at Cryogenic Temperatures, Final Report, NASA-CR-54881 (N66-24695) January 1965.

108) J. J. Lombardo, C. E. Dixon, J. A. Begley, paper presented at 69th Annual Meeting of ASTM in Atlantic City, New Jersey, June 27, 1966.

IX-D. Specific Radiation Damage Effects in UWMAK-III

The object of this section is to calculate the damage conditions which will be characteristic of materials in UWMAK-III and to indicate where we think problems might arise. We will use the information given in section C of this chapter and the reader is urged to review that section if necessary.

IX-D-1. Neutron Flux and Energy Spectra

IX-D-1-a. Poloidal Variation

The neutron wall loading has been given in Appendix A-1 as calculated from a R-Z, shifted source, toroidal geometry model with the DOT code. Figure IX-D-1 shows how the wall loading varies with poloidal angle around the torus. The maximum wall loading is slightly over 3.4 MW/m^2 at the midplane on the outer blanket. The wall loading falls off as one moves toward the top (or bottom) of the reactor. The wall loading on the divertor shield, which is 100-120° on the poloidal scale, is ~1 MW/m^2. As one progresses past the inner divertor slot, the wall loading on the carbon ISSEC increases until it approaches 2.6 MW/m^2 at the midplane of the inner blanket.

It is important here to note that there is a difference between wall loading and neutron flux. The latter quantity is the most important in determining the response of the material to the radiation environment. The neutron flux as a function of poloidal angle is shown in Figure IX-D-2 for neutrons of E > 13.5 MeV, E > 0.1 MeV, and E > 0 MeV. Note that now the flux peaks around 50° above the midplane of the reactor. Table IX-D-1 gives the neutron spectra at selected positions in the first solid surfaces facing the plasma.

The flux of neutrons between 13.5 and 14.9 MeV varies from 1.6×10^{14} n $cm^{-2} s^{-1}$ at the outside midplane to a maximum of ~1.95×10^{14}n $cm^{-2}s^{-1}$ at 50° (a 22% increase). The flux of neutrons above 0.1 MeV and 0 MeV show less of a variation from the midplane, the increase amounting to 9 and 6% respectively as one examines the 0° and 50° positions. A similar variation is expected on the inside of the torus, but the data is not listed here.

The important feature of these observations is that the materials response (dpa, helium production, etc.) will also vary in the poloidal direction as we shall see later. A final listing on the ratio of 14.1 MeV neutron current, and the various fluxes is given below.

Neutron Energy - MeV	Ratio Flux/14.1 MeV n Current		
	0°	50°	180°
13.5-14.5	1.1	1.5	1.3
>0.1	4.5	5.6	4.7
>0	6.3	7.7	7.9

The important point from the data above is that one cannot simply scale materials response from the stated wall loading as has been done in the past from cylindrical calculations.

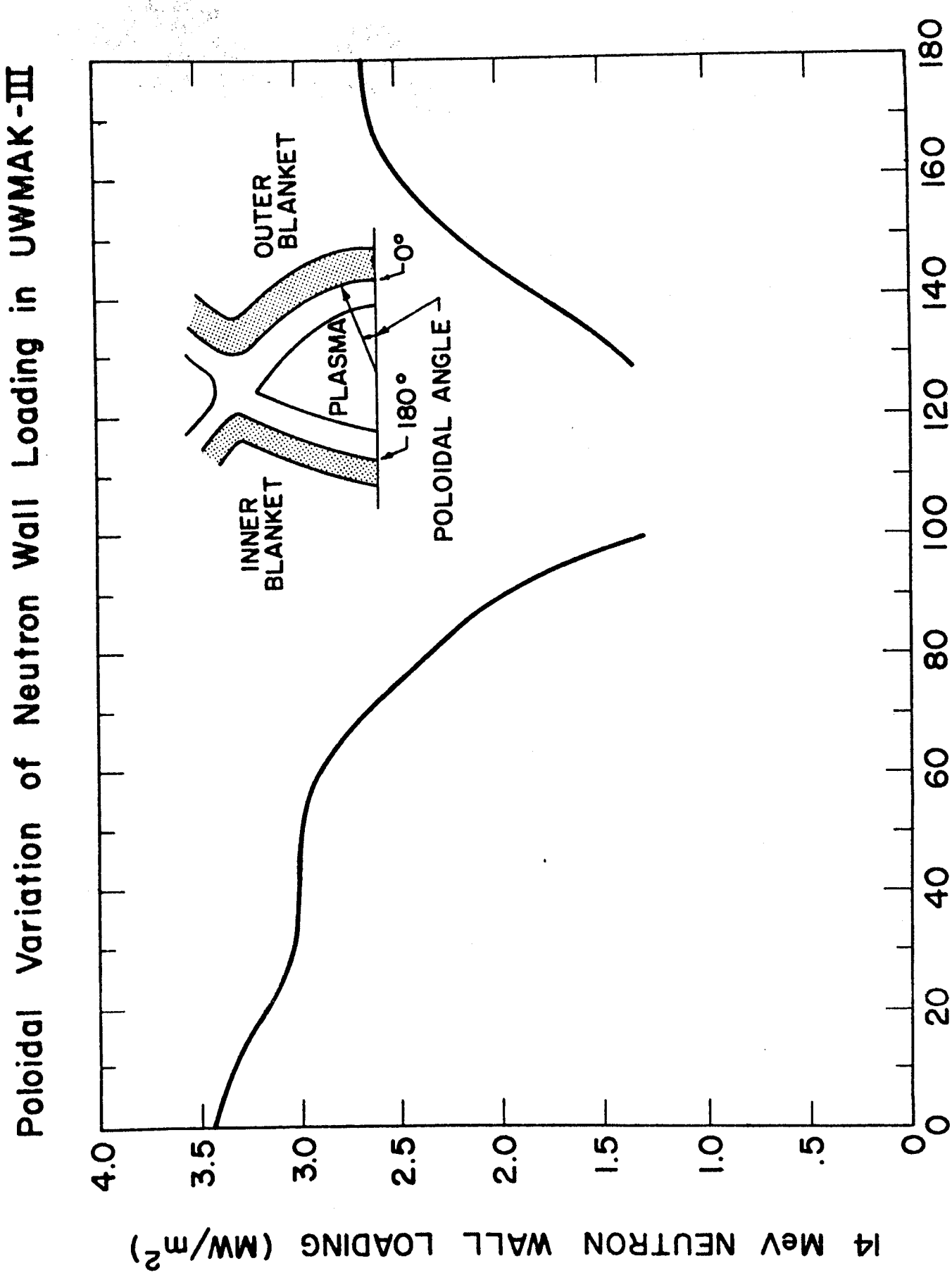
Poloidal Variation of Neutron Wall Loading in UWMAK-III
14 MeV NEUTRON WALL LOADING (MW/m²)
4.0
3.5
3.0
2.5
2.0
1.5
1.0
.5
0
0
20
40
60
80
100
120
140
160
180
POLOIDAL ANGLE (DEGREES)
OUTER BLANKET
INNER BLANKET
PLASMA
0°
180°
POLOIDAL ANGLE

FIGURE IX-D-1

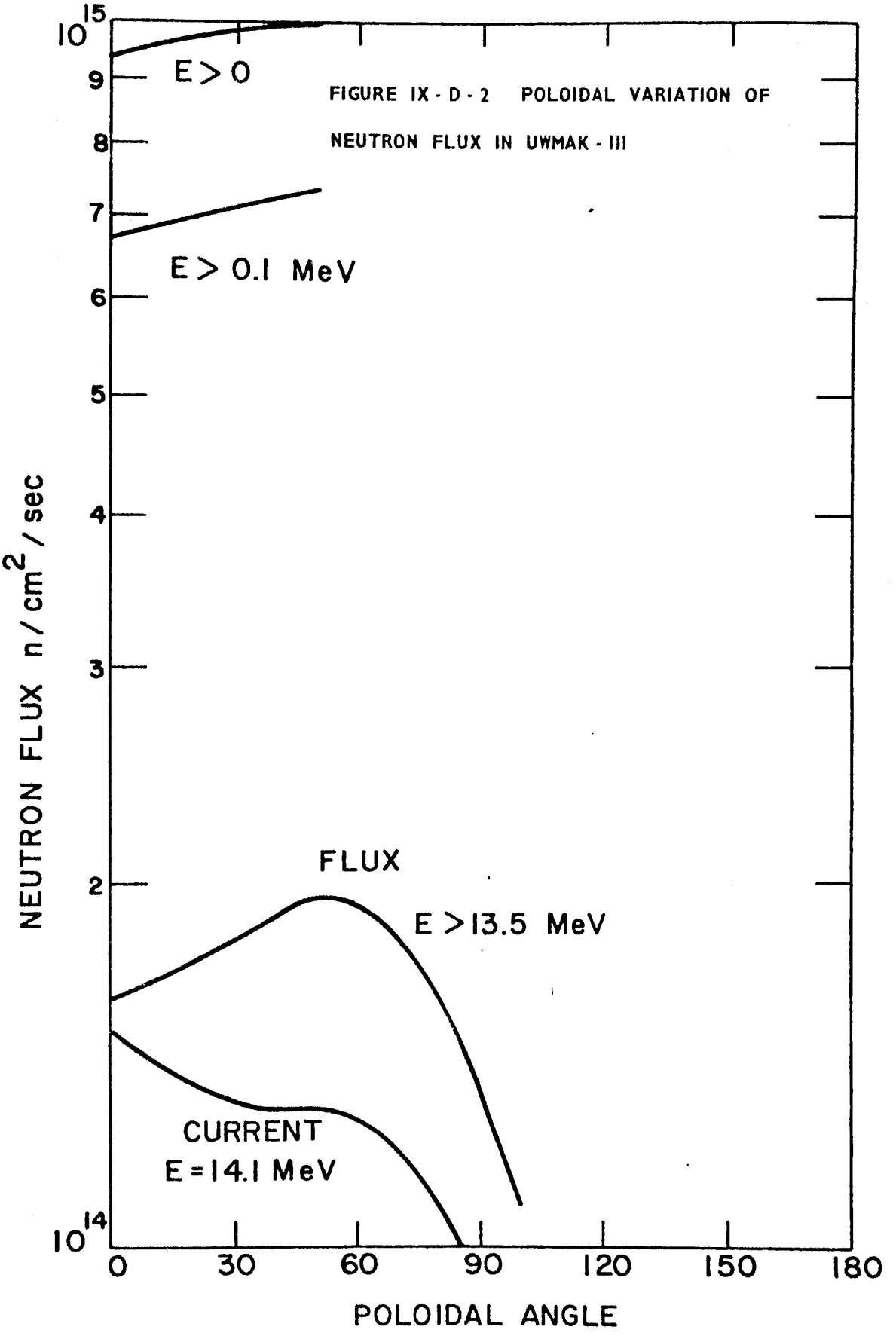

FIGURE IX - D - 2 POLOIDAL VARIATION OF NEUTRON FLUX IN UWMAK - III

Table IX-D-1

Neutron Spectra for Selected Positions in First Solid Surfaces of UWMAK-III

$n/cm^2/sec$

Gr. No.	Lower Energy—eV	θ = 0°	θ = 50°	θ = 180°
1	1.35+7	1.59+14	1.94+14	1.58+14
2	1.22+7	3.96+12	5.09+12	6.97+12
3	1.11+7	4.18+12	5.07+12	9.14+12
4	1.00+7	7.36+12	8.18+12	8.26+12
5	9.05+6	5.79+12	6.31+12	3.67+12
6	8.19+6	5.39+12	5.93+12	8.15+12
7	7.41+6	4.91+12	5.40+12	9.80+12
8	6.70+6	3.95+12	4.33+12	5.91+12
9	6.07+6	3.49+12	3.81+12	4.25+12
10	5.49+6	3.65+12	3.98+12	5.60+12
11	4.97+6	3.52+12	3.82+12	4.43+12
12	4.49+6	3.66+12	3.96+12	4.51+12
13	4.07+6	4.00+12	4.32+12	4.05+12
14	3.68+6	4.51+12	4.86+12	3.69+12
15	3.33+6	5.13+12	5.52+12	3.58+12
16	3.01+6	5.94+12	6.38+12	4.65+12
17	2.72+6	6.81+12	7.32+12	5.19+12
18	2.47+6	8.21+12	8.80+12	6.9+12
19	1.83+6	2.94+13	3.14+13	2.38+13
20	1.35+6	3.75+13	3.47+13	2.77+13
21	1.00+6	4.42+13	4.64+13	2.99+13
22	7.43+5	5.07+13	5.52+13	3.28+13
23	5.50+5	5.57+13	5.72+13	3.56+13
24	4.08+5	5.25+13	5.37+13	3.56+13
25	3.02+5	4.05+13	4.13+13	3.14+13
26	2.24+5	2.28+13	2.32+13	2.35+13
27	1.66+5	4.39+13	4.45+13	2.98+13
28	1.23+5	5.07+13	5.14+13	3.39+13
29	6.74+4	7.59+13	7.71+13	6.05+13
30	3.18+4	6.41+13	6.53+13	6.08+13
31	1.50+4	4.46+13	4.56+13	4.89+13

Gr. No.	Lower Energy- eV	$\theta = 0°$	$\theta = 50°$	$\theta = 180°$
32	7.10+3	3.09+13	3.18+13	3.94+13
33	3.35+3	2.08+13	2.15+13	3.15+13
34	1.58+3	1.33+13	1.40+13	2.51+13
35	7.49+2	8.65+12	9.11+12	2.01+13
36	3.54+2	3.20+12	3.47+12	1.47+13
37	1.67+2	4.38+12	4.70+12	1.32+13
38	7.89+1	1.52+12	1.66+12	1.05+13
39	3.73+1	3.19+11	3.77+11	7.45+12
40	1.76+1	1.23+12	1.36+12	6.63+12
41	8.31+0	9.78+11	1.08+12	5.82+12
42	3.93+0	9.55+11	1.04+12	5.08+12
43	1.86+0	8.14+11	8.83+11	4.47+12
44	8.76-1	6.86+11	7.45+11	3.91+12
45	4.14-1	5.79+11	6.32+11	3.45+12
46	2.20-2	3.56+12	3.98+11	2.43+13
$\sum_{i=1}^{28} \phi_i$	> 1+5	6.71+14	7.29+14	5.61+14
$\sum_{i=1}^{46} \phi_i$	> 2.2-2	9.39+14	1.01+15	9.46+14

IX-D-1-b. Variation Through Blanket and Shield

As one moves away from the first solid surfaces that intercept the neutrons from the UWMAK-III plasma, the neutron flux level drops and the spectrum softens.

The schematic of the UWMAK-III blanket and shield is given in Figure IX-D-3 and Figure IX-D-4 and IX-D-5 show how the neutron flux varies as a function of distance away from the first surfaces. Tables IX-D-2 and IX-D-3 summarize the neutron spectra at three convenient positions (θ = 0, 50°, 180°) and four depths into the blanket. The variations in the neutron flux and energy are too numerous to review here, but the reader can gain some appreciation of the complexities by examining Figures 4-8 and Table IX-D-2. Suffice it to say that all of these fluxes were used to calculate the response functions (i.e., dpa, gas production, transmutation rates, and heat generation). We will examine the response function in more detail later in this chapter.

The flux in the first energy group of the outer blanket drops off exponentially as exp-(nx) where $n = 6.97 \times 10^{-2}$ which implies an 'absorption' half thickness of 9.94 cm. As might be expected, the neutron flux above 0.1 MeV does not show an exponential decay and drops off slower than the first energy group because of the down scattered neutrons. This is even more evident for the total flux which, of course, includes a large number of thermal neutrons. As one approaches the shield containing B_4C, the total flux approaches that > 0.1 MeV because of the high thermal absorption of the B-10 isotope.

The attenuation of neutrons from the first wall to the magnet zone are summarized in Table IX-D-4. The attenuation of neutrons in the first energy group (> 13.5 MeV) is a factor of 2.3×10^{-9} for the inner shield. The damaging neutron flux (normally taken as > 0.1 MeV) is attenuated by a factor of 1.7×10^{-6} in the inner blanket. Finally, the total neutron flux to the magnet is attenuated by a factor 3×10^{-6} in the inner zone. We shall see the significance of these numbers when we calculate the response of functions in the next section.

IX-D-2. Displacement Rates in UWMAK-III

IX-D-2-a. Poloidal Variation

Using the fluxes of Section IX-D-1 and Mo displacement cross sections listed previously (Section IX-C), we have calculated the poloidal variations of displacement rates in UWMAK-III. These values are listed in Table IX-D-5 and displayed graphically in Figure IX-D-6. Note that the numbers are for a 100% Plant Factor.

The displacement rate in Mo (or TZM) of the outer blanket varies by almost a factor of 2 from the minimum by the divertor slots to the peak at 50°. This peak value is also 15% higher than the value at the midplane. Unfortunately, we can't obtain a complete picture of the poloidal variation in UWMAK-III for the displacement function in Mo because the Mo in the inner

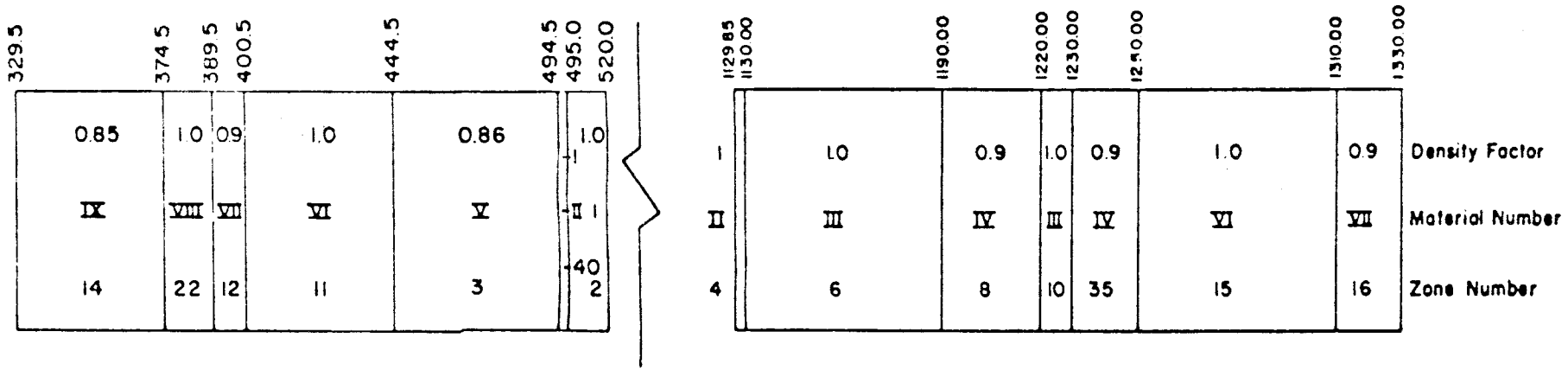

I 100% C

II 100% Mo

III 97% Li + 3% Mo

IV 99% C + 1% Mo

V 82% Mo + 18% $Al_2O_3 2SiO_2$

VI 50% S.S. + 32% B_4C + 8% $Al_2O_3 2SiO_2$

VII 90% Pb + 10% S.S.

VIII 32% S.S. 62% Cu

IX 100% Al

Figure IX-D-3 A schematic of UWMAK-III blanket and shield model for one dimensional calculation and R-Z neutron and photonic calculation at the midplane

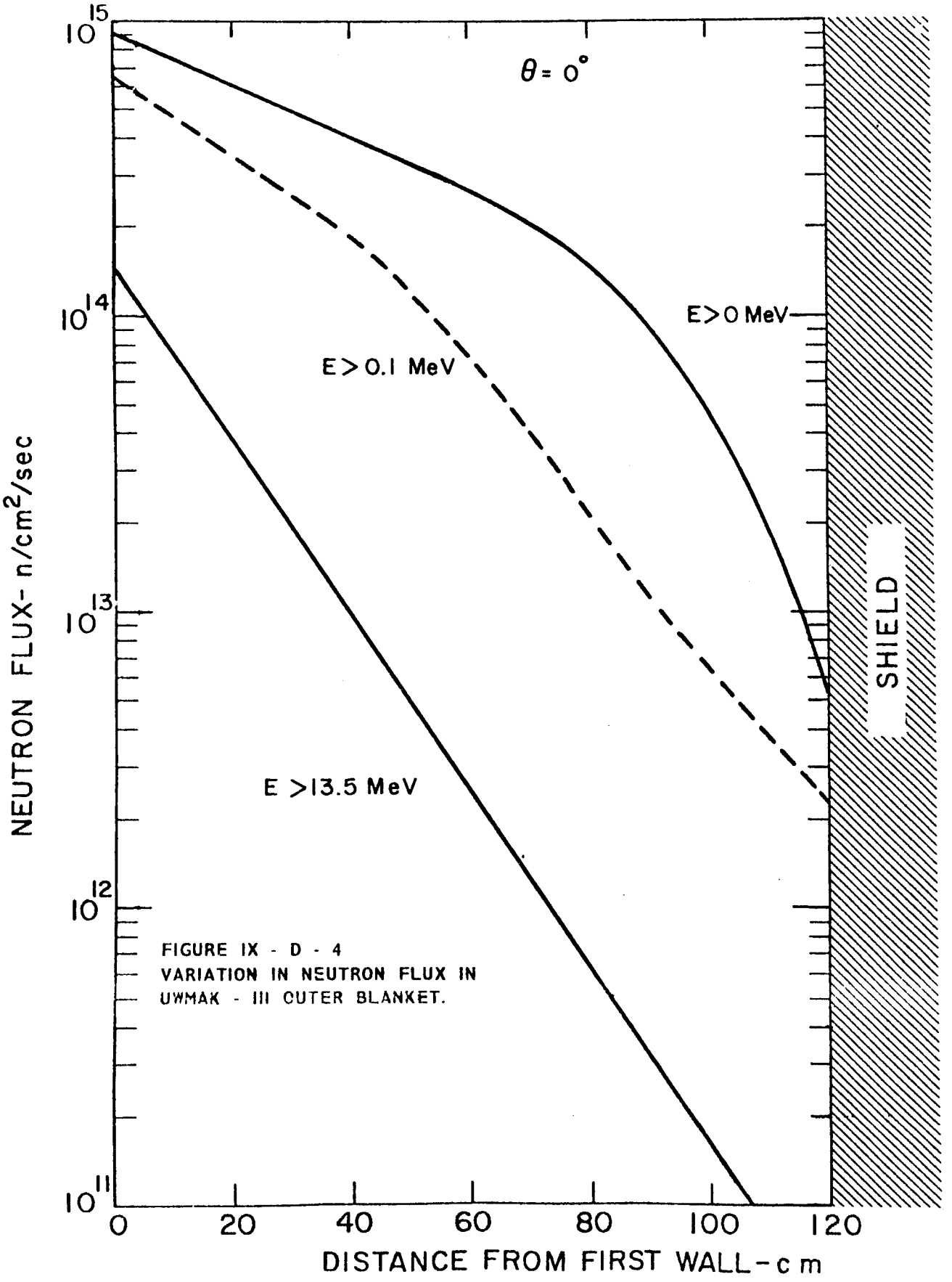

FIGURE IX - D - 4
VARIATION IN NEUTRON FLUX IN
UWMAK - III OUTER BLANKET.

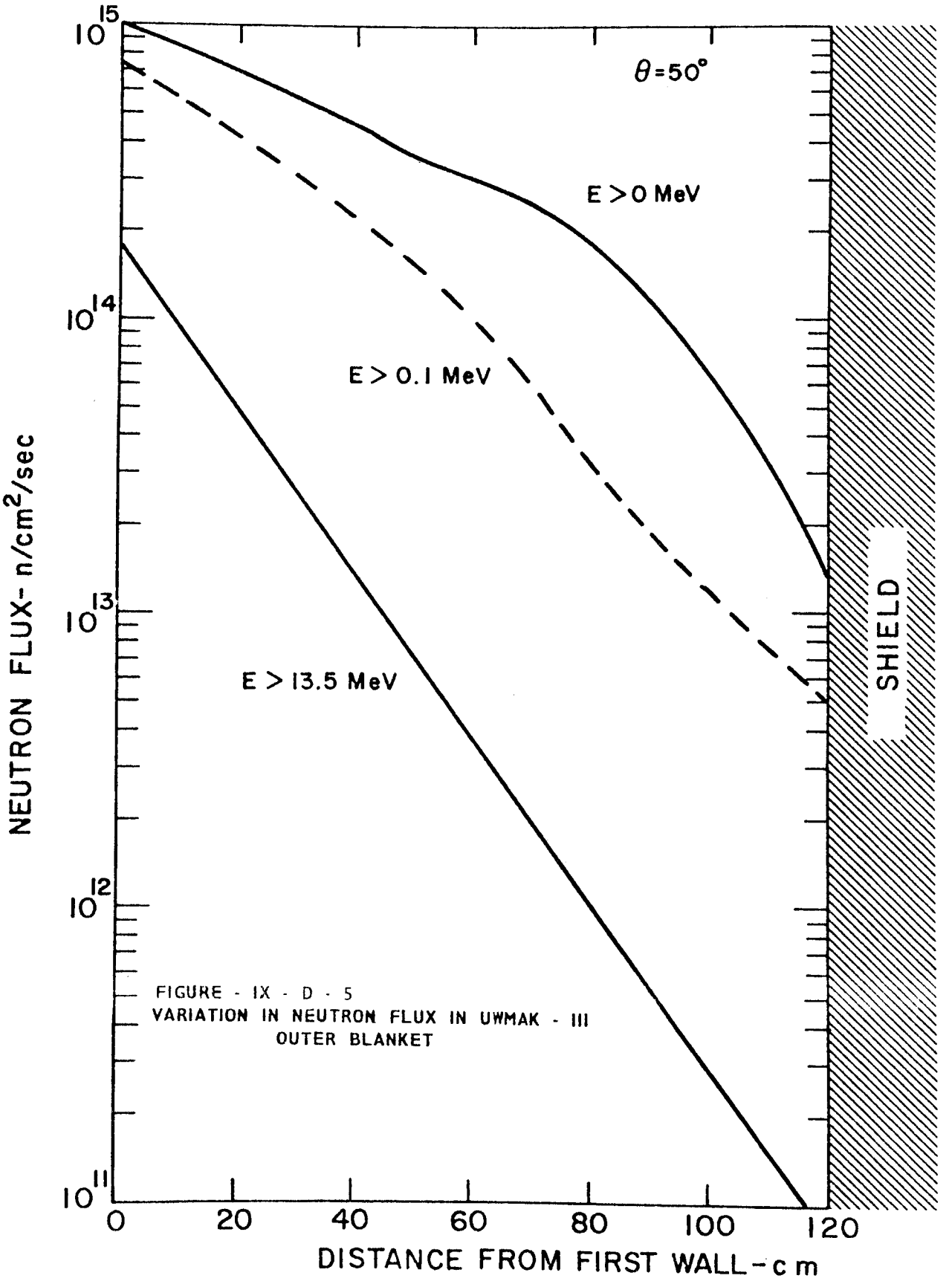

FIGURE - IX - D - 5
VARIATION IN NEUTRON FLUX IN UWMAK - III
OUTER BLANKET

Table IX-D-2

Summary of Neutron Spectra at Selected Positions in the UWMAK-III Outer Blanket and Shield

Group Number	θ = 0°				θ = 50°			
	R=1145*	R=1175	R=1205	R=1245	ΔX=0**	ΔX=32	ΔX=57	ΔX=99
1	5.11+13	7.53+12	8.88+11	3.97+10	6.88+13	8.59+12	1.81+12	1.11+11
2	1.69+13	5.41+12	8.38+11	4.68+10	1.97+13	5.88+12	1.59+12	1.21+11
3	7.53+12	3.18+12	6.21+11	4.03+10	8.87+12	3.48+12	1.13+12	9.9+10
4	8.08+12	2.65+12	5.27+11	3.89+10	9.86+12	2.92+12	9.20+11	8.87+10
5	6.16+12	2.20+12	3.12+11	2.19+10	7.46+12	2.42+12	5.98+11	5.82+10
6	5.09+12	1.87+12	3.93+11	3.02+10	6.18+12	2.06+12	6.53+11	6.59+10
7	4.69+12	1.71+12	3.19+11	2.10+10	5.66+12	1.88+12	5.79+11	5.38+10
8	4.09+12	1.53+12	6.22+11	5.87+10	4.89+12	1.68+12	8.55+11	9.62+10
9	3.65+12	1.37+12	4.28+11	4.02+10	4.36+12	1.50+12	6.26+11	7.26+10
10	3.52+12	1.32+12	5.24+11	4.97+10	4.21+12	1.44+12	7.30+11	8.43+10
11	3.26+12	1.22+12	4.91+11	5.04+10	3.90+12	1.34+12	6.63+11	8.12+10
12	2.98+12	1.11+12	5.18+11	5.31+10	3.58+12	1.21+12	6.76+11	8.22+10
13	3.03+12	1.13+12	4.49+11	4.67+10	3.64+12	1.24+12	6.01+11	7.46+10
14	3.28+12	1.24+12	3.53+11	3.62+10	3.94+12	1.35+12	5.15+11	6.52+10
15	3.61+12	1.37+12	2.55+11	2.63+10	4.33+12	1.50+12	4.27+11	5.44+10
16	3.97+12	1.51+12	3.76+11	3.78+10	4.75+12	1.65+12	5.79+11	7.15+10
17	4.39+12	1.67+12	3.58+11	3.48+10	5.25+12	1.82+12	5.95+11	7.26+10
18	4.93+12	1.87+12	5.15+11	5.01+10	5.88+12	2.04+12	8.04+11	9.77+10
19	1.75+13	6.66+12	1.86+12	1.87+11	2.08+13	7.25+12	2.85+12	3.54+11
20	2.10+13	7.90+12	2.11+12	2.17+11	2.47+13	8.58+12	3.28+12	4.12+11
21	2.34+13	8.67+12	2.11+12	2.21+11	2.73+13	9.40+12	3.41+12	4.27+11
22	3.09+13	1.18+13	2.05+12	2.18+11	3.55+13	1.28+13	3.87+12	4.68+11
23	3.81+13	1.56+13	2.02+12	2.16+11	4.32+13	1.67+13	4.57+12	5.13+11
24	3.79+13	1.63+13	2.09+12	2.08+11	4.24+13	1.74+13	4.99+12	5.26+11
25	2.65+13	1.14+13	2.34+12	2.23+11	2.98+13	1.21+13	4.67+12	4.76+11
26	7.62+12	3.37+12	2.60+12	2.37+11	8.68+12	3.54+12	3.88+12	3.52+11
27	3.82+13	1.73+13	2.14+12	2.01+11	4.21+13	1.82+13	4.63+12	4.67+11

* R is the radius from the reactor centerline in cm
**Δ is the distance from the first wall

Group Number	θ = 0°				θ = 50°			
	R=1145	R=1175	R=1205	R=1245	R=1145	R=1177	R=1202	R=124
28	4.89+13	2.56+13	1.97+12	1.91+11	5.29+13	2.68+13	6.12+12	5.65+
29	7.39+13	4.56+13	4.87+12	4.04+11	7.87+13	4.72+13	1.51+13	1.19+
30	6.23+13	4.41+13	8.34+12	5.44+11	6.56+13	4.53+13	2.00+13	1.54+
31	4.40+13	3.43+13	1.01+13	5.72+11	4.60+13	3.51+13	1.97+13	1.59+
32	3.05+13	2.58+13	1.11+13	5.92+11	3.19+13	2.63+13	1.86+13	1.66+
33	2.01+13	1.83+13	1.17+13	5.99+11	2.10+13	1.86+13	1.69+13	1.71+
34	1.20+13	1.18+13	1.17+13	5.96+11	1.26+13	1.19+13	1.49+13	1.70+
35	6.51+12	6.97+12	1.13+13	5.94+11	6.93+12	6.97+12	1.28+13	1.62+
36	2.38+12	3.12+12	1.02+13	5.71+11	2.59+12	3.04+12	1.03+13	1.34+
37	1.52+12	1.88+12	9.73+12	5.77+11	1.72+12	1.78+12	8.98+12	1.23+
38	3.74+11	6.65+11	8.54+12	5.50+11	4.80+11	5.88+11	7.28+12	9.05+
39	5.00+10	1.25+11	6.68+12	4.52+11	7.12+11	1.02+11	5.35+12	5.46+
40	5.75+10	9.24+10	5.95+12	3.87+11	9.55+10	6.93+10	4.53+12	4.06+
41	2.26+10	3.49+10	5.25+12	3.27+11	4.79+10	2.46+10	3.02+12	2.86+
42	9.46+09	1.25+10	4.65+12	2.72+11	2.58+10	8.52+09	3.25+12	1.98+
43	3.21+09	4.11+09	4.11+12	2.21+11	1.20+10	2.72+09	2.76+12	1.36+
44	9.91+08	1.29+09	3.62+12	1.76+11	5.23+09	8.22+08	2.34+12	9.36+
45	2.93+08	3.94+08	3.19+12	1.39+11	2.22+09	2.40+08	1.99+12	6.45+
46	1.07+08	1.64+08	2.18+13	4.71+11	2.18+09	7.56+07	1.04+13	1.45+
$\sum_{i=1}^{28} \phi_i$	4.30+14	1.65+14	3.01+13	2.84+12	5.03+14	1.77+14	5.67+13	6.01+
$\sum_{i=1}^{46} \phi_i$	7.32+14	3.57+14	1.82+14	1.09+13	7.74+14	3.74+14	2.36+14	2.23+

Table IX-D-3

Summary of Neutron Spectra at Midplane of UWMAK-III Inner Blanket and Shield (θ = 180°)

$n/cm^2/sec$

Gr. No.	R=507.5	R=490	R=450	R=439	R =406
1	4.55+13	7.21+12	1.03+10	1.84+09	6.19+06
2	1.14+13	2.56+12	4.11+09	8.41+08	5.47+06
3	7.52+12	1.06+12	1.67+09	3.78+08	3.37+06
4	4.93+12	6.73+11	1.13+09	2.68+08	2.38+06
5	2.08+12	3.92+11	8.16+08	2.04+08	1.93+06
6	6.53+12	1.04+12	1.04+09	2.34+08	1.98+06
7	7.92+12	1.07+12	1.16+09	2.67+08	2.05+06
8	6.21+12	1.40+12	1.49+09	3.29+08	2.50+06
9	4.20+12	9.62+11	1.52+09	3.46+08	2.52+06
10	5.76+12	1.09+12	1.44+09	3.38+08	2.62+06
11	4.37+12	9.91+11	1.50+09	3.51+08	2.69+06
12	4.53+12	1.06+12	1.78+09	4.00+08	2.82+06
13	3.85+12	1.01+12	2.01+09	4.52+08	3.51+06
14	3.08+12	8.97+11	2.05+09	4.58+08	3.40+06
15	2.55+12	8.30+11	2.16+09	4.82+08	3.85+06
16	3.67+12	1.10+12	2.76+09	6.12+08	4.87+06
17	3.89+12	1.18+12	3.32+09	7.15+08	5.48+06
18	5.53+12	1.65+12	4.44+09	8.78+08	6.38+06
19	1.92+13	5.89+12	1.48+10	3.38+09	3.33+07
20	2.11+13	8.02+12	2.45+10	4.92+09	4.83+07
21	2.09+13	1.01+13	4.34+10	8.00+09	7.50+07
22	2.01+13	1.36+13	1.00+11	1.57+10	1.35+08
23	1.94+13	1.61+13	1.97+11	3.06+10	2.55+08
24	1.91+13	1.41+13	1.80+11	2.63+10	2.14+08
25	1.90+13	1.70+13	2.85+11	4.80+10	3.68+08
26	1.91+13	1.77+13	3.76+11	5.76+10	4.32+08
27	1.78+13	1.75+13	4.92+11	7.07+10	4.87+08
28	1.72+13	1.82+13	6.87+11	1.00+11	6.11+08
29	3.63+13	3.31+13	1.89+12	3.05+11	1.08+09
30	4.77+13	3.07+13	2.04+12	3.61+11	1.03+09
31	4.79+13	2.79+13	2.19+12	3.47+11	7.38+08
32	4.68+13	1.94+13	1.31+12	3.12+11	7.52+08
33	4.46+13	1.36+13	5.89+11	1.91+11	8.28+08

* R is the radius from reactor centerline in cm

Gr. No.	R=5075	R=490	R=450	R=439	R=406
34	4.14+13	9.69+12	2.09+11	8.30+10	4.87+08
35	3.78+13	7.72+12	7.28+10	2.75+10	2.01+08
36	3.29+13	2.26+12	5.31+09	6.70+09	6.86+07
37	2.98+13	9.09+12	2.16+10	2.15+09	1.57+07
38	2.60+13	1.50+12	1.23+09	3.18+08	3.08+06
39	1.99+13	2.37+11	1.63+07	3.35+07	4.94+05
40	1.71+13	4.07+12	7.61+09	1.09+08	9.38+04
41	1.50+13	2.71+12	2.00+09	2.31+07	3.09+04
42	1.32+13	4.32+12	1.63+10	1.19+08	1.22+04
43	1.17+13	4.38+12	2.74+10	1.37+08	4.31+03
44	1.05+13	3.83+12	2.43+10	8.56+07	1.26+03
45	9.43+12	3.05+12	1.34+10	3.32+07	2.75+02
46	6.56+13	1.04+13	3.04+09	2.97+06	1.92+01
28 $\sum_{i=1} \phi_i$	3.27+14	1.64+14	2.44+12	3.75+11	2.72+09
46 $\sum_{i=1} \phi_i$	8.82+14	3.48+14	1.09+13	2.01+12	6.93+09

Table IX-D-4

Summary of Attenuation of Neutron Fluxes in UWMAK-III

$n/cm^2/sec$

Neutron Energy - MeV	First Wall	Blanket-Cold Shield Interface	Shield-TF Magnet Interface	Total Attenuation Factor From First Wall to TF Magnet
		$\theta = 0°$		
	R = 1129.85	R = 1250*	R = 1310	
> 13.5	1.59+14	3.97+10		
> 0.1	6.71+14	2.84+12	Not Available	
> 0	9.39+14	1.09+13		
		$\theta = 50°$		
	R = 1129.85	R = 1250	R = 1310	
> 13.5	1.94+14	1.11+11		
> 0.1	7.29+14	6.01+12	Not Available	
> 0	1.01+15	2.23+13		
		θ=180°		
	R = 507.5	R = 439	R = 374.5	
> 13.5	4.55+13	1.84+09	1.05+05	2.3-09
> 0.1	3.27+14	3.75+11	5.63+08	1.7-06
> 0	8.82+14	2.01+12	2.70+09	3-06

R = radius from centerline of reactor in cm

Table IX-D-5

Poloidal Variation in Mo and C Displacement Values (First Solid Surfac

dpa/yr at 100% PF

Poloidal Angle	Mo	C	Poloidal Angle	Mo[a]	C
0	16.4	23.5	180	3.7	22.3
4	16.4		176	3.7	
7	16.5		174	3.7	
10	16.5		171	3.7	
13	16.6		169	3.7	
16	16.7		166	3.7	
19	16.8		164	3.6	
21	17.0		161	3.6	
24	17.2		159	3.5	
27	17.4		157	3.4	
30	17.6		155	3.3	
33	17.8		152	3.2	
36	18.1		150	3.1	
39	18.4		149	3.0	
42	18.6		147	2.9	
44	18.7		145	2.9	
47	18.8		144	2.9	
50	18.9	25.6	142	2.8	
53	18.9		140	2.8	
56	18.7		138	2.8	
58	18.5		137	2.7	
61	18.2		135	2.7	
63	17.9		134	2.6	
65	17.5		132	2.5	
69	16.8		131	2.4	
71	16.3		130	2.3	
73	15.8		129	2.2	
75	15.3		128	2.1	
76	14.8		127	2.1	
79	14.0		125	2.0	
81	13.6		124	2.0	

dpa/yr at 100% PF

Poloidal Angle	Mo	C	Poloidal Angle	Mo[a]	C
84	12.9		122	2.2	
85	12.5				
88	12.0				
89	11.7				
91	11.3				
93	11.0				
94	10.8				
96	10.6				
97	10.6				
98	10.5				

a) Behind 25 cm of C ISSEC

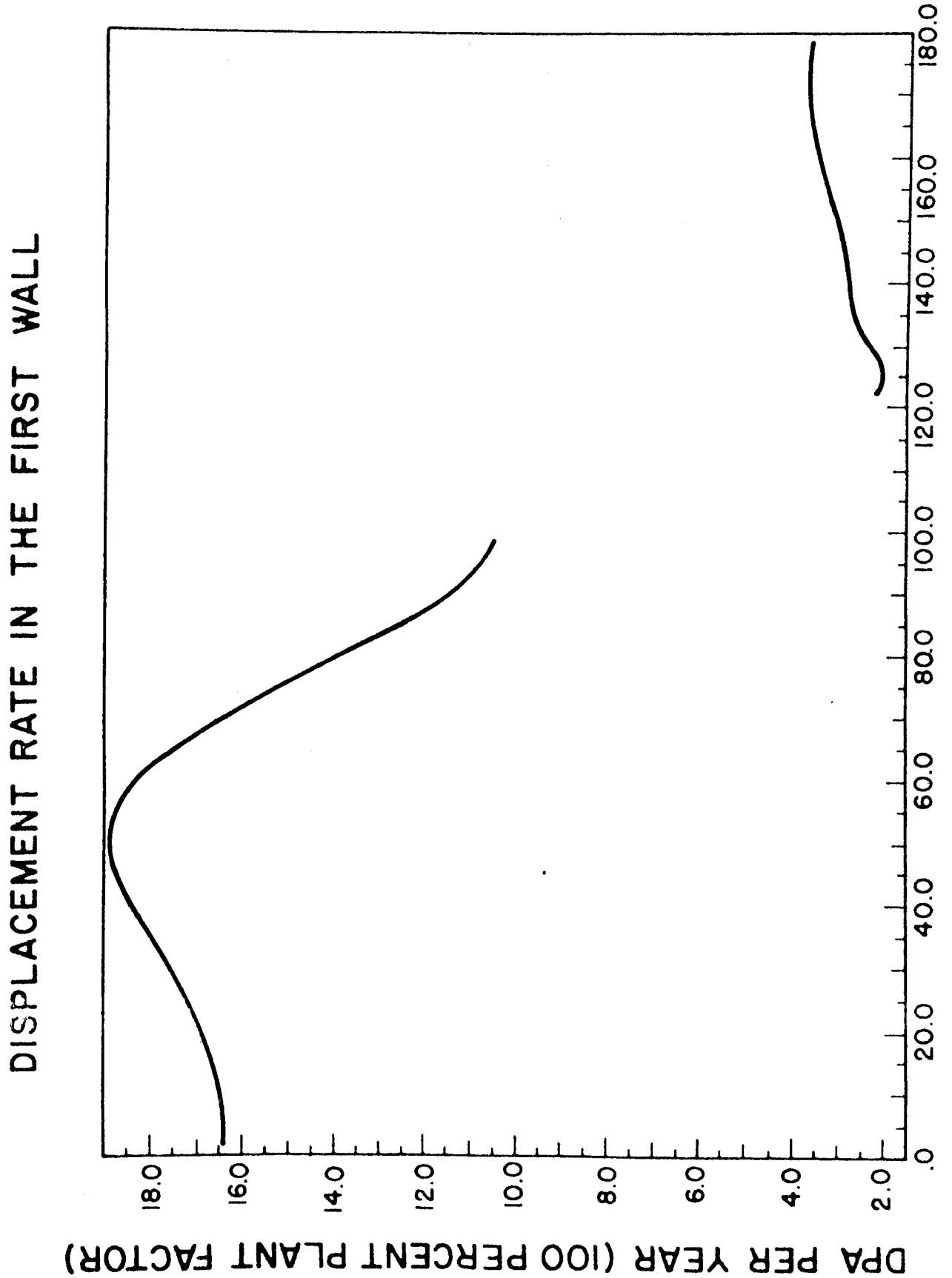
DISPLACEMENT RATE IN THE FIRST WALL
DPA PER YEAR (100 PERCENT PLANT FACTOR)
18.0
16.0
14.0
12.0
10.0
8.0
6.0
4.0
2.0
.0
20.0
40.0
60.0
80.0
100.0
120.0
140.0
160.0
180.0
POLOIDAL ANGLE (DEGREE)

FIGURE IX-D-6

blanket is behind a 25 cm carbon ISSEC. Nevertheless, one can see that the peak damage corresponds to 180° and the dpa values drop off as one progresses from 180° to 122°. The variation is still ~70% from the low to the high value.

It is also of interest to plot the total TZM first wall area above a given dpa rate. This is plotted in Figure IX-D-7. This curve shows that of the outer wall area, essentially all (or 1480 m^2) is above 9 dpa per year, 79% is above 10 dpa per year, 67% above 12 dpa per year, and 57% 14 dpa per year, 49% above 16 dpa per year, 22% above 18 dpa and approximately 15% above 18.5 dpa per year. Another important feature of UWMAK-III is that 19% of the TZM first wall area is protected by the ISSEC and essentially all of that receives less than 4 dpa per full year of operation.

An interesting perspective on the wall area versus dpa curves is that approximately 200 m^2 could receive greater than 18 dpa per year (100% PF) and an area twice the size of a football field will receive greater than 14 dpa/year. These facts point out how critical quality control and uniform cooling will be on a tokamak first wall because slight variations could cause premature failure.

The same general poloidal variation in dpa rate will also hold for the carbon curtain and graphite ISSEC although the absolute levels are different (see Figure IX-D-8). The maximum dpa rate in the ISSEC is ~22.3 dpa per year (100% PF) and this drops rapidly to ~11 dpa per year in the 120° region. The maximum dpa rate in the outer carbon curtain is ~26 per year.

IX-D-2-b. Variation of Dpa Rate Through Blanket and Shield of UWMAK-III

Tables IX-D-6-8 give the variation in dpa rate as one progresses from the first wall into the blanket, shield and magnet assemblies at 0°, 50° and 180° and some of the results are also displayed in Figure IX-D-9. The dpa rate in TZM is reduced by a factor of approximately 10 through the first 60 cm of the outer blanket and by a factor of ~320 at the start of the shield. The rate of reduction is the same at the 50° position. The first 25 cm of carbon at 180°C is quite successful in reducing the damage in TZM although it is difficult to tell quantitatively because the neutron flux at 180° is considerably different than at 0° and 50°. Nevertheless, the maximum dpa rate in the TZM of the inner blanket is only 3.7 dpa per year (100% PF) and the rate at which this is reduced in the inner blanket is even higher than in the outer blanket. This is possibly due to the angular flux differences and softer spectrum.

The dpa rate in the carbon ISSEC varies from a maximum of approximately 22 dpa per year at the front surface to approximately 5 dpa at the back surface. This variation is somewhat greater than for a similar distance in the metallic blankets. However, it is still too early to tell if such differences are due to the large number of neutrons entering at glancing angles or just a softened spectrum.

FIGURE IX - D - 7

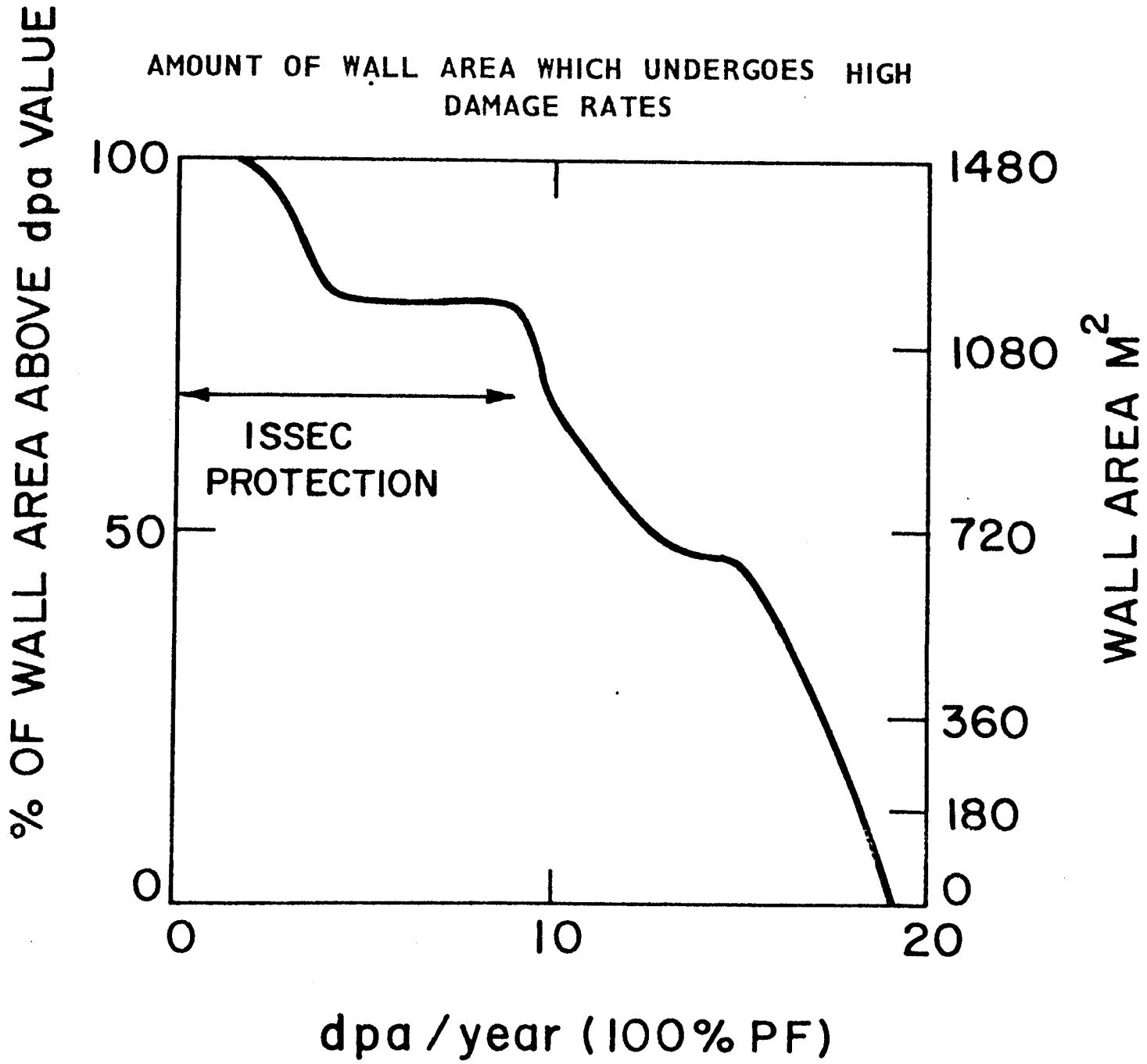
AMOUNT OF WALL AREA WHICH UNDERGOES HIGH DAMAGE RATES
% OF WALL AREA ABOVE dpa VALUE
100
50
0
ISSEC PROTECTION
0
10
20
dpa / year (100% PF)
1480
1080
720
360
180
0
WALL AREA M²

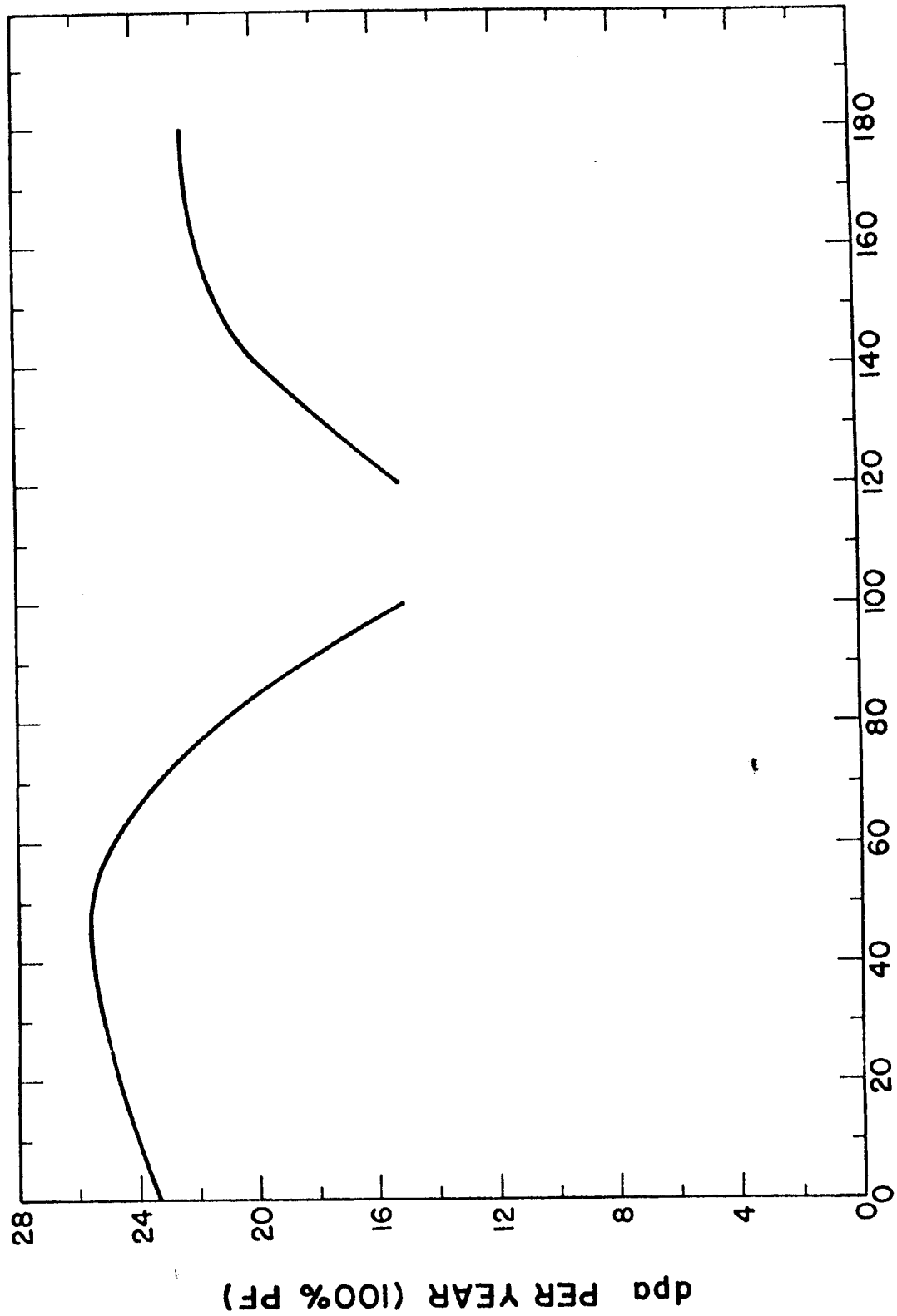

Figure IX - D - 8 Poloidal Variations in Carbon Displacement Rate

Table IX-D-6

Summary of Dpa Rates in Selected Positions - UWMAK-III - Outer Blanket

dpa/year[a]

Distance From First Wall - cm	C	Mo	SS
		$\theta = 0°$	
0	23.5	16.4	
5		13.1	
15		9.4	
25		6.5	
35		4.5	
45		3.0	
55		2.1	
65	2.8	1.3	
75	1.2	0.60	
85	0.57	0.30	
95		0.17	
105	0.21	0.10	
115	0.10	0.051	
125			0.031
135			8.8-03
145			2.4-03
155			6.3-04
165			1.6-04
175			4.5-05
185			1.9-05
195			8.1-06

(a) 100% PF

Table IX-D-7

dpa/year[a]

Distance From First Wall - cm	C	Mo	SS
	θ = 50°		
0	25.6	18.8	
15		11.5	
21.5		8.5	
40		4.5	
47		3.3	
53		2.4	
64		1.8	
72	2.4	1.1	
80	1.1	0.55	
88	0.72	0.36	
96		0.22	
105		0.16	
114	0.23	0.11	
122	0.13	0.060	
131			4.1-02
147			6.6-03
155			2.5-03
170			3.9-04
180			1.3-04
195			3.8-05

Table IX-D-8

dpa/year[(a)]

Distance From First Wall - cm	C	Mo	SS	Al
		θ = 180°		
0	22.3			
4	18.2			
12.5	12.1			
20.8	8.2			
30		3.6		
40		1.1		
50		0.28		
60		0.047		
70		5.9×10^{-3}		
81			7.0-03	
92			8.1-04	
103			1.6-04	
114			3.7-05	
125			1.8-05	
153				1.1-05
168				7.1-06
183				3.2-06

FIGURE IX - D - 9
VARIATION OF DPA RATE IN TZM FOR SELECTED POSITIONS IN UWMAK III BLANKET AND SHIELD

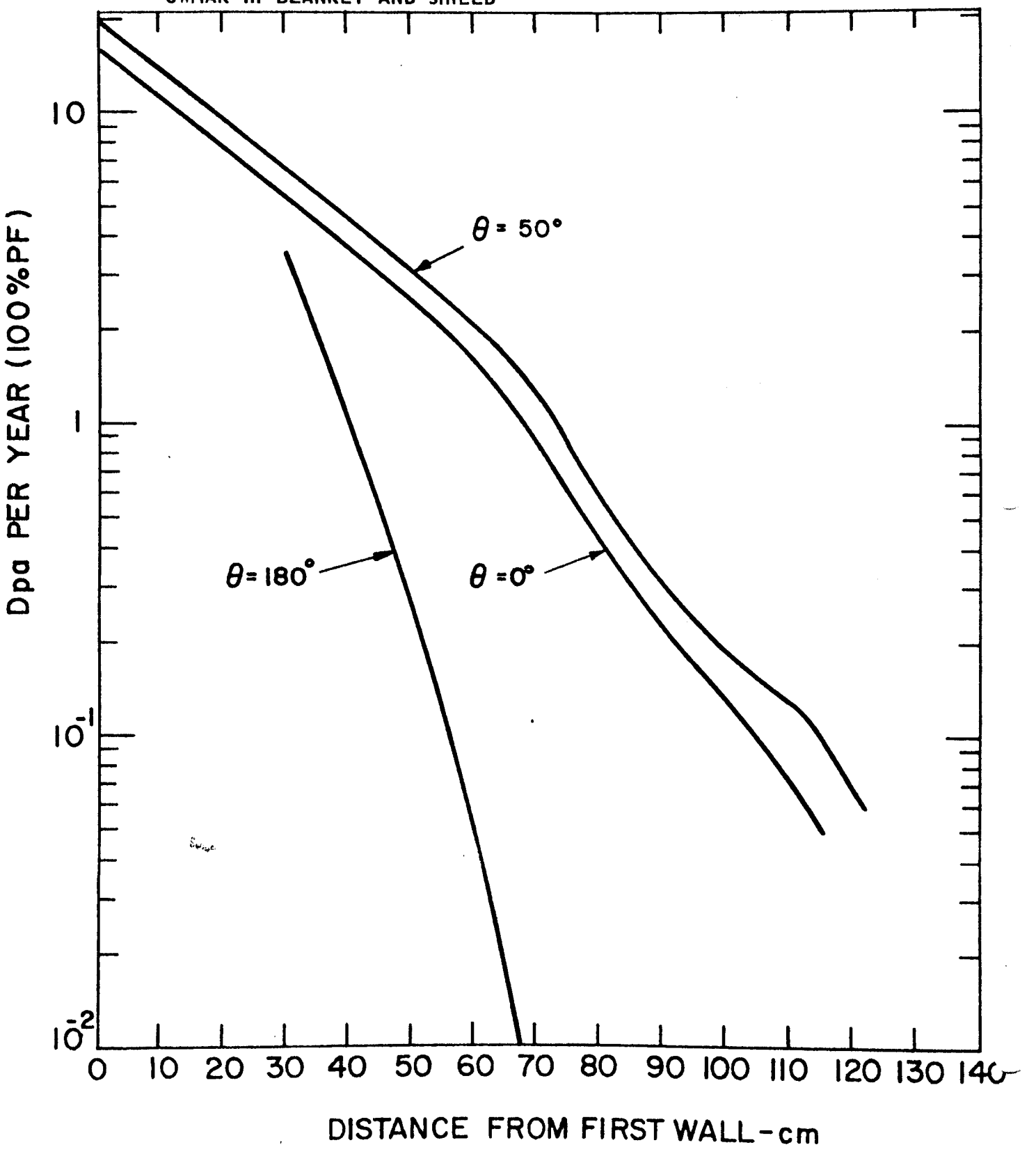

IX-D-3. Helium Production Rates

IX-D-3-a. Poloidal Variation

The production of helium is important in C, TZM, and the B_4C in UWMAK-III and just as for the displacement rates, there are considerably variations in the blankets. The poloidal variation in the helium production rates for TZM is given in Table IX-D-9 and displayed in Figure IX-D-10. Similar information is given for carbon in Table IX-D-9 and Figure IX-D-11.

The maximum helium production rate in TZM is 123 appm/year (100% PF) at 50° and the ISSEC lowers this value by a factor of 8 to approximately 13 appm He per year. On the other hand, the maximum helium production in the carbon is approximately 5700 appm/year at 100% plant factor in the curtain and over 4000 appm/year in the ISSEC. The poloidal variations are qualitatively the same as for the dpa values.

Table IX-D-9

Poloidal Variation in Helium Production Rates
For TZM and Carbon

	Maximum appm He $year^{-1}$ (100% PF)	
Poloidal Angle	TZM	C
0	101	4650
10	103	
20	105	
30	112	
40	118	
50	123	5680
60	119	
70	103	
80	81	
90	65	
	(Behind ISSEC)	(4.2 cm from front surface)
120	6.8	1425
130	7.7	2050
140	9.2	2800
150	10.2	3376
160	12.0	3530
170	12.7	3634
180	12.7	3698

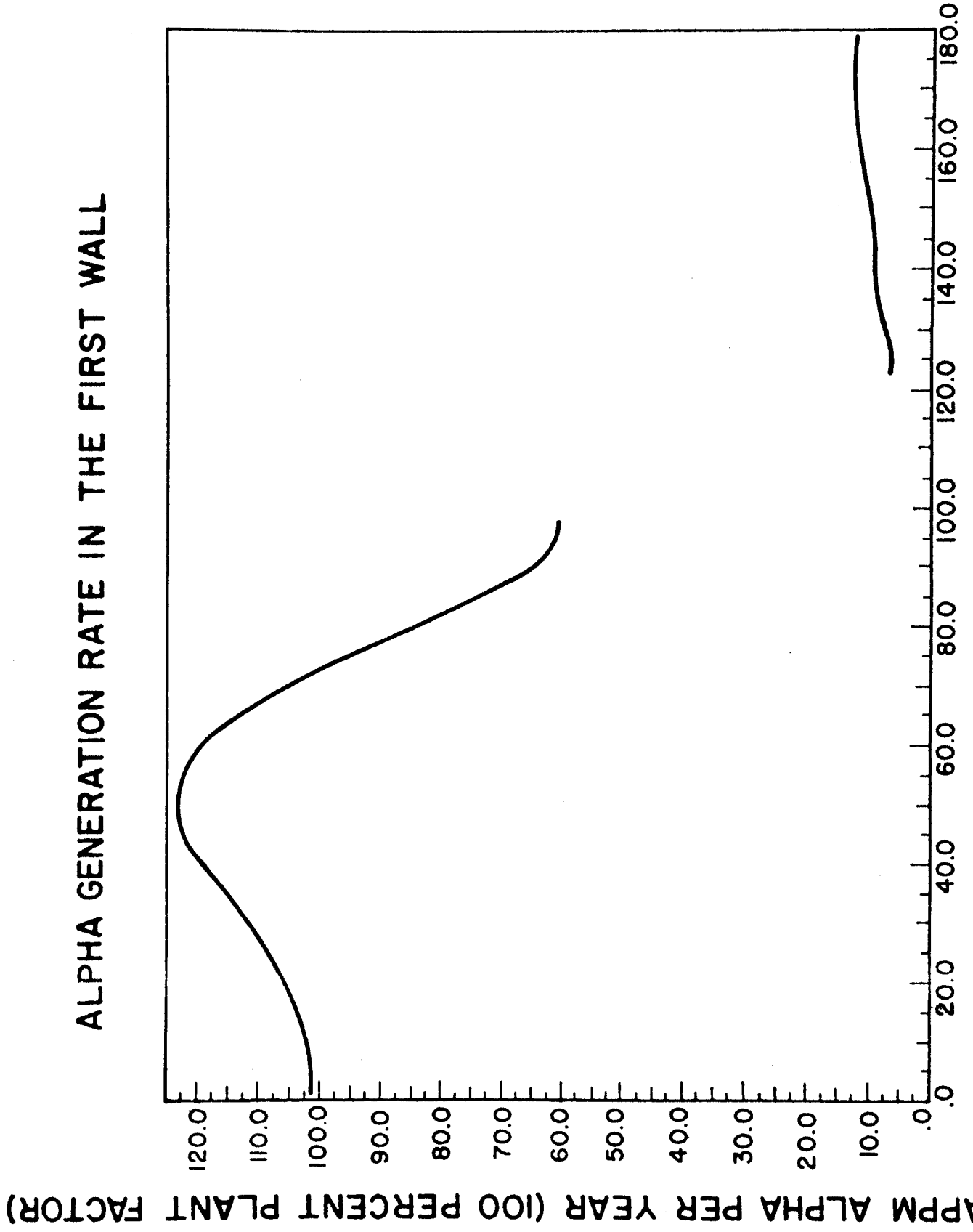

FIGURE IX-D-10.

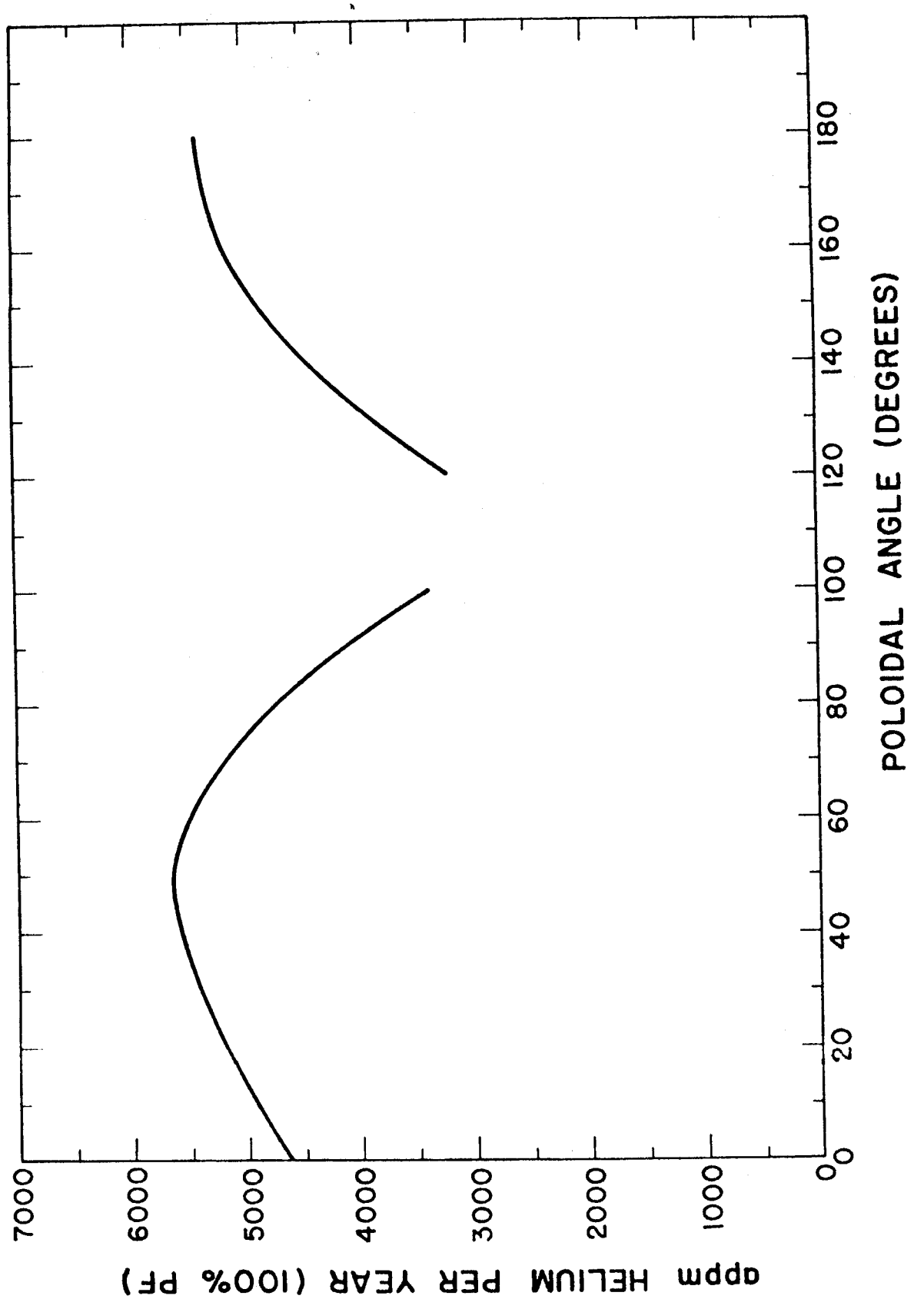
Figure IX - D - 11 Poloidal Variation in Helium Production - Carbon
appm HELIUM PER YEAR (100% PF)
7000
6000
5000
4000
3000
2000
1000
0
20
40
60
80
100
120
140
160
180
POLOIDAL ANGLE (DEGREES)

IX-D-3-b. Spatial Variation of Helium Production

The helium generation rates in materials of interest for UWMAK-III are listed in Table IX-D-10 and plotted in Figure IX-D-12. A few interesting points about this data are:

- The helium production rate is still 2 to 6 appm per year (100% PF). at a distance of approximately 60 cm from the first wall.
- The inner blanket and shield is much more effective in dropping the helium production rates, requiring only ~15 cm for an order of magnitude decrease vs approximately 35 cm for the outer blanket.

It is also seen from Table IX-D-11 that the helium production rates in the ISSEC vary by a factor of ~7 from the front to the back of the neutron spectral shifter. Finally, the maximum helium production rate in the stainless steel is 0.02 appm/year (or ~0.6 appm for 30 years at 100% PF).

Another way of characterizing the spatial damage is to calculate the ratio of the helium production rate to the displacement rate. This is given in Table IX-D-11 (Figure IX-D-13) for molybdenum. The ratio varies from ~6-6.5 at the first wall to ~2 at the back of the outer blanket. The ratio is significantly lower in the inner blanker where it varies from 0.3 to 0.6 which is still a factor of 3 to 6 higher than characteristic values for the High Flux Isotope Reactor (HFIR). The helium to displacement ratio for EBR-II is probably more pertinent because most of the high temperature neutron damage information has come from such a reactor. Comparing UWMAK-III to EBR-II we find that the appm He/dpa ratio is a factor of 30-100 higher in the outer blanket of UWMAK-III and a factor of 5-10 higher for the inner blanket.

IX-D-4. Charged Particle Fluxes to UWMAK-III Carbon Shields

In order to quote values for this reactor design we have to make the following assumptions:

- Total particle leakage rate $(D + T + \alpha) = 3.44 \times 10^{23} s^{-1}$.
- A fractional burnup of 6% gives 47% D, 47% T and 6% He in the plasma.
- The particles are subjected to a 99.9% efficient divertor, (Chapter III) operated in the unload mode (one way protection).
- Uniform leakage of particles to the wall surface (1480 m^2).
- Particle energy of thermalized D, T and He is 3 keV (Figure II-D-1).
- An average non-thermalized helium ion energy of 100 keV and 10% of total helium is not thermalized.

Table IX-D-10

Summary of Helium Generation Rates in Selected Position of UWMAK-III

appm per year (100% PF)

Distance from First Wall-cm	C	Mo	Steel
θ = 0°			
0	4650	101	
5		73	
15		46	
25		27	
35		16	
45		9.9	
55		6.0	
65		3.3	
75		1.5	
85		0.7	
95		0.3	
105		0.2	
115		0.09	
θ = 50°			
0	5680	123	
15		59	
21.5		39	
40		17	
47		11	
53		7.3	
64		4.9	
72		2.8	
80		1.4	
88		0.9	
96		0.5	
105		0.3	
114		0.2	
122		0.1	
θ = 180°			
0	5400		
4	3698		
12.5	1689		
20.8	778		
30		2.2	
40		0.4	
50		0.08	
60		0.02	
70		0.003	
81			0.02
92			0.004
103			6-04
114			1-04
125			2-05

Figure IX - D - 12 Helium Production Rates in TZM of UWMAK - III

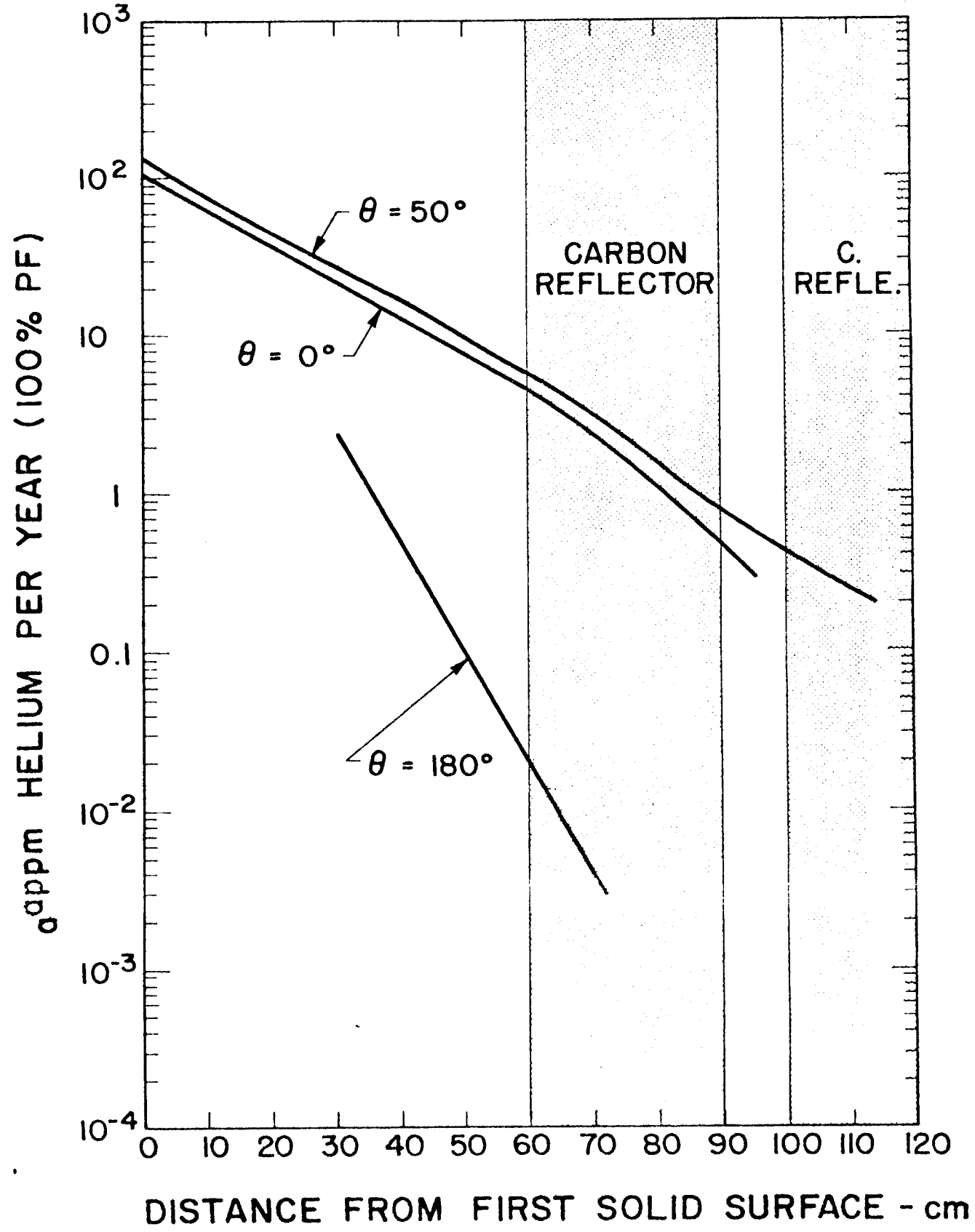

Table IX-D-11

Ratio of Helium Gas Production to Displacement Rates for TZM in UWMAK-III

appm Helium/dpa

Distance from Front Surface - cm	0°	50°	180°
0	6.2	6.5	
4			
5	5.6		
12.5			
15	4.9	5.1	
20.8			
21.5		4.6	
25	4.2		
30			0.61
35	3.6		
40		3.6	0.36
45	3.3		
47		3.3	
50			0.29
53		3.0	
55	2.9		
60			0.43
64		2.7	
65	2.5		
70			0.51
72		2.6	
75	2.4		
80		2.6	
81			
85	2.3		
88		2.5	
92			
95	1.8		
96		2.3	
103			
105	1.8	1.8	
114			
115			
122		1.7	
125	1.8		

Figure IX - D - 13 Characteristic Helium to Displacement Ratio For TZM in UWMAK III

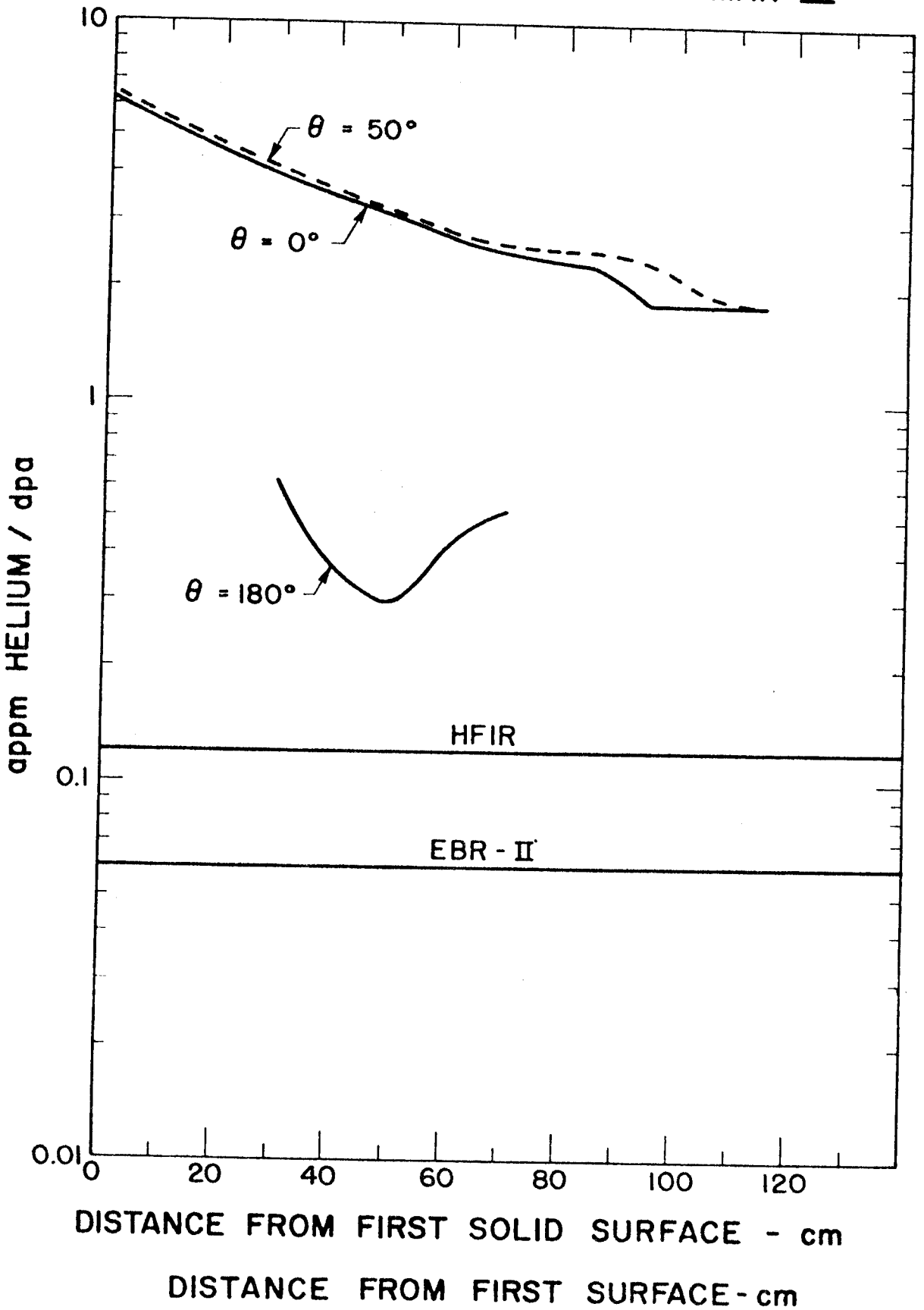

With the above assumptions, we calculate the charged particle fluxes listed in Table IX-D-12. The total charged particle flux is ~2.3 x 10^{13}cm^{-2}s^{-1} made up mostly of 3 keV D+ and T+. We have used the sputtering coefficients listed in Table IX-D-12 to calculate the reflux of carbon atoms to the wall. Such a calculation (including neutron sputtering) predicts a carbon atom flux of ~4 x 10^{8}cm^{-2}s^{-1}.

IX-D-5. Temperature Environment for UWMAK-III Materials

It is very difficult to do a complete analysis of the temperature through all parts of the blanket and shield for UWMAK-III and we must, of necessity, make some simple homogenizations. First of all, we will not calculate poloidal variations in the temperatures even though they are likely to exist. Secondly, we will not treat the situation between burns when the temperature is likely to drop, especially in the ISSEC. These variations should be examined in the future.

We have tried to represent, schematically, in Figure IX-D-14 the temperature profile of the C, TZM, 316 SS, B_4C, Pb, Cu, Al and NbTi at the midplane as a function of position from the center of the torus. The values are also listed in Table IX-D-13.

The temperature ranges over some 2400°C from a low of -269°C in the TF coils to ~ 2125°C in the carbon ISSEC. The 316 SS, B_4C, and Pb operate at a maximum temperature of 200°C and the TZM in the blanket operates from 675 to 1000°C. The Mo powder used in the inner shield is expected to operate at a maximum of 1250°C but it does not provide any structural integrity so mechanical properties are not important. Finally, the carbon in the outer blanket reflectors operates at 1050°C while the curtain is expected to reach 1400°C during operation. The carbon in the ISSEC is ~ 1800°C on the plasma side, it increases to over 2100° at ~ 10 cm from the front surface and drops to ~ 1500°C at the surface facing the TZM inner blanket.

IX-D-6 Summary of Damage Conditions in UWMAK-III

IX-D-6a TZM Environment

Figure IX-D-15 graphically outlines the displacement damage - temperature conditions to be experienced by the TZM structural material in one year at an eighty percent plant factor. The highest damage at 1000°C is ~ 3 dpa per year while ~ 15 dpa per year is accumulated at 950°C. Similarly, the highest damage at 675°C is ~ 3 dpa and ~ 15 dpa is experienced by material at 750°C. Some parts of the inner blanket will be subjected to damage rate at ~ 1000°C ranging from < 0.01 dpa/year (< 2 x 10^{19}n/cm2 of equivalent fission neutrons) to ~ 3 dpa per year (~ 8 x 10^{21}n cm^{-2} of fission neutrons).

A similar plot for the helium generation rate is given in IX-D-16. Here one sees that the maximum helium generation rate at 750 to 950°C is ~ 100 appm per year while it is ~ 30 appm per year at 1000°C. These production rates drop to ~ 0.1 appm per year at the back of the blanket where the temperature ranges from 650 to 1000°C. The carbon ISSEC keeps the helium production rates to ~ 2 appm per year in the inner blanket operating at 950 to 1000°C. Similar helium generation rates in the powdered Mo occur at 1200 - 1250°C.

Table IX-D-12

Summary of Charged Particles Striking the Carbon Shield for UWMAK-III

Particle	Mean Energy-keV	Flux-cm^{-2} s^{-1}	Physical Sputtering Coefficient on Carbon
D^+	3	1.1×10^{13}	0.01
T^+	3	1.1×10^{13}	0.01
He^{++}	3	1.3×10^{12}	0.1
He^{++}	100	1.3×10^{11}	0.05
$C^{(n+)}$	~3	4×10^{8}	0.6

Figure IX - D - 14 Temperature Variations in UWMAK III Materials (Reactor Midplane)

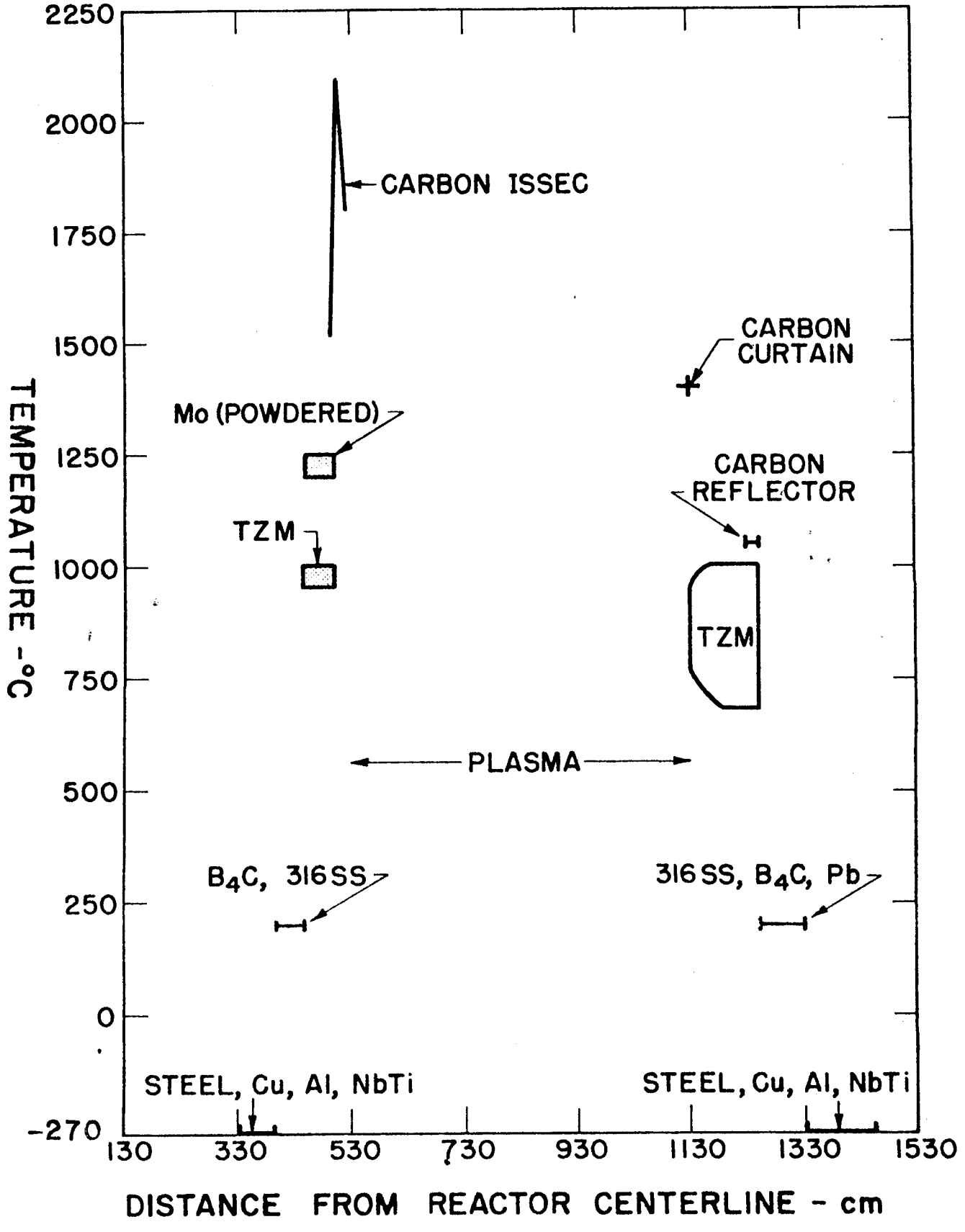

Figure IX - D - 15 Summary of Damage - Temperature Regime For TZM Structure in UWMAK III - One Year Operation

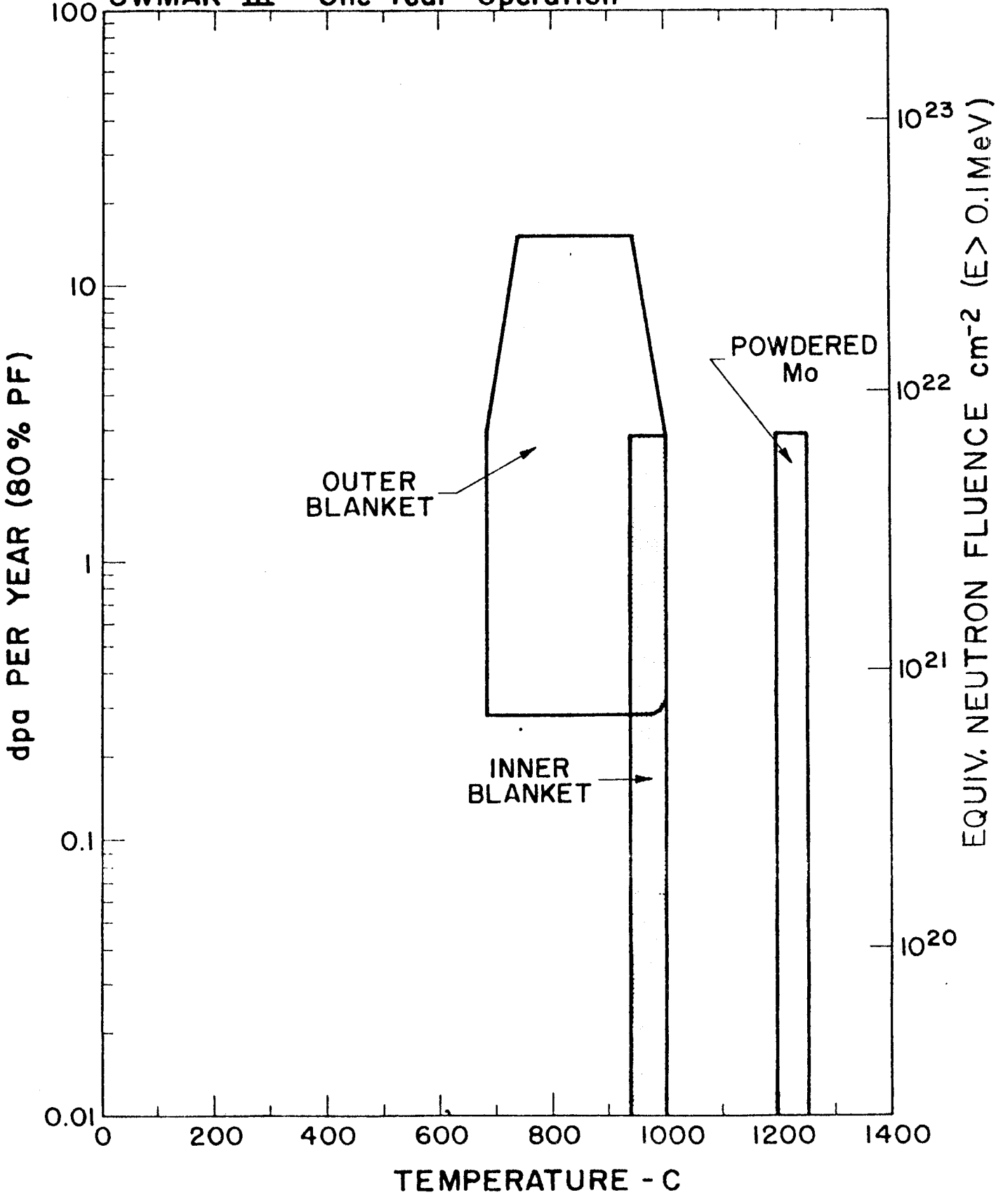

Table IX-D-13

Summary of Temperature Environment in UWMAK-III

Position-cm[a]	Approximate Temperature °C						
	C	TZM Structure	Mo Filler[b]	B_4C	316SS	Pb	Cu,Al,NbTi
329.5	–	–	–	–	–	–	-269
374.5	–	–	–	–	–	–	-269
389.5	–	–	–	–	–	–	-269
400.5	–	–	–	200	200	–	–
444.5	–	1000	1250	200	200	–	–
495	1530	1000	1250	–	–	–	–
507.5	2025	–	–	–	–	–	–
520	1800	–	–	–	–	–	–
1129.85	1400	770-950	–	–	–	–	–
1160	–	710-975	–	–	–	–	–
1190	–	650-1000	–	–	–	–	–
1220	–	650-1000	–	–	–	–	–
1230	1050	650-1000	–	–	–	–	–
1250	1050	650-1000	–	200	200	–	–
1310	–	–	–	200	200	200	–
1330	–	–	–	–	200	200	-269

(a) midplane - See Figure IX-D-3
(b) non-structural

Figure IX - D - 16 Summary of Helium Gas Production Rates vs Temperature in TZM - One Year of Operation

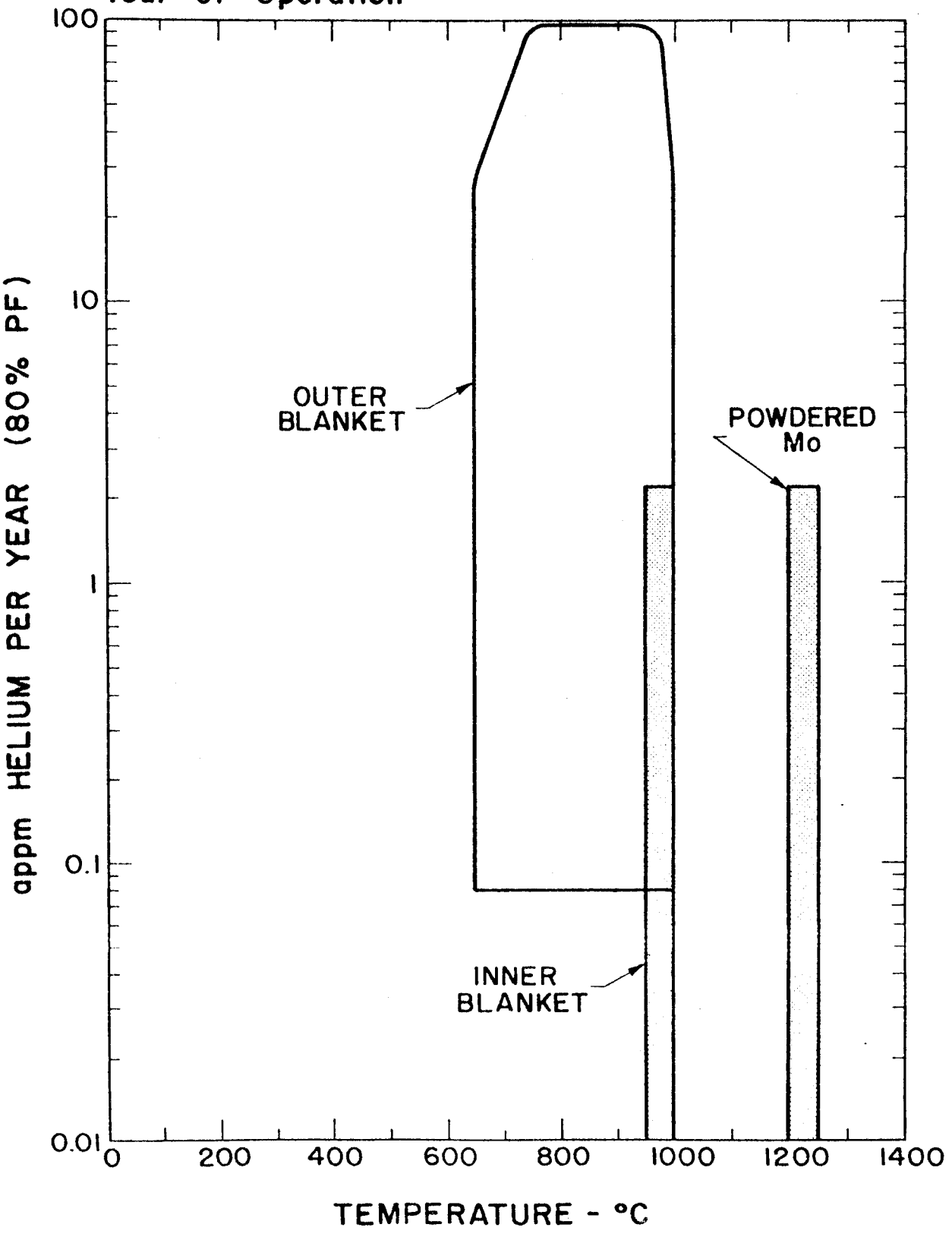

IX-D-6b Carbon Environment

Figure I-D-17 shows how the displacement damage varies with temperature in carbon. This displacement damage in the inner carbon reflector varies from 0.4 to over 2 dpa per year at 1000 to 1050°C. This is equivalent to 1 - 5 x 10^{21} fission neutron cm^{-2}. The damage rate in the outer reflector is a factor of 3 - 5 lower. The maximum damage rate in the curtain is ~ 18 dpa/year (80% PF) at ~ 1400°C which is equivlant to ~ 4 x 10^{22} fission neutrons cm^{-2} yr^{-1}. Finally, the carbon in the ISSEC suffers damage ranging from ~ 18 dpa per year at 1800°C to ~ 12 dpa per year at 2100°C and ~ 4 dpa at ~ 1500°C. The helium production rate is shown in figure IX-D-18 and the maximum production rate varies from ~ 4300 appm per year in curtain at 1400°C to ~ 3000 appm per year in the ISSEC at 1800°C. At 2100°C approximately 1000 appm Helium is generated per year while the minimum rate is as low as ~ 200 appm per year at the back of the ISSEC. The maximum helium generation rate in the curtain correspond to ~ 0.2% of the carbon atoms 'burned up' per year at 80% P.F.

IX-D-7 Anticipated Irradiation Effects in Carbon

IX-D-7a Surface Effects

Using the information in Tables IX-D-1 and IX-D-12 we calculate that the surface removal rate by physical sputtering alone is 1.5 x 10^{-3} mm/year (80% PF) from the carbon surface facing the plasma and 3 x 10^{-4} mm/year on the side of the curtain away from the plasma. This amount should be compared to ~ 2 x 10^{-5} mm per year due to thermal varporization of the curtain at 1400°C and ~ 4 x 10^{-4} mm per year on the back side of the ISSEC at 1500°C and ~ 0.6 mm per year on the front side of the ISSEC at 1800°C. A summary of the thinning rates is given in Table IX-D-14.

It is apparent from this table that the curtain thinning rate of 1.8 x 10^{-3} mm poses no significant problem to its dimensional stability even if it were required to last 30 years (less than 5% of the initial thickness would be sputtered away). The major contribution to the thinning rate is the physical sputtering by D^+, T^+ and He^{++} ions with evaporation contributing less than 2%. The total amount of carbon removed per year (assuming no redeposition) is ~ 8 kg/year. A much more serious problem comes from the ISSEC which will operate at ~ 1800°C on the plasma side and ~ 1500°C on the wall side. The vaporization rate on the plasma side is calculated to be ~ 0.6 mm/year amounting to ~ 840 kg of carbon removed per year. This is over 400 times the physical sputtering rate and reveals that even if the chemical sputtering ratio amounted to 0.1, Fig. IX-C-19, there would be little difference in the amount of free carbon in the chamber. The thinning in the ISSEC would amount to 1.9 cm after 30 years, or ~ 8% of the original thickness.

We have not been able to analyze the effect 850 kg of free carbon per year in the vacuum system. For example, fouling of cryopanels could be serious if the cryopumps are unable to handle the 2-3 kg of carbon per day.

The final conclusion here is that the thermal effects on the surface of the ISSEC far outweigh the radiation damage problems.

Figure IX - D - 17 Summary of Damage Temperature Regimes For One Year Operation in UWMAK - III - Carbon

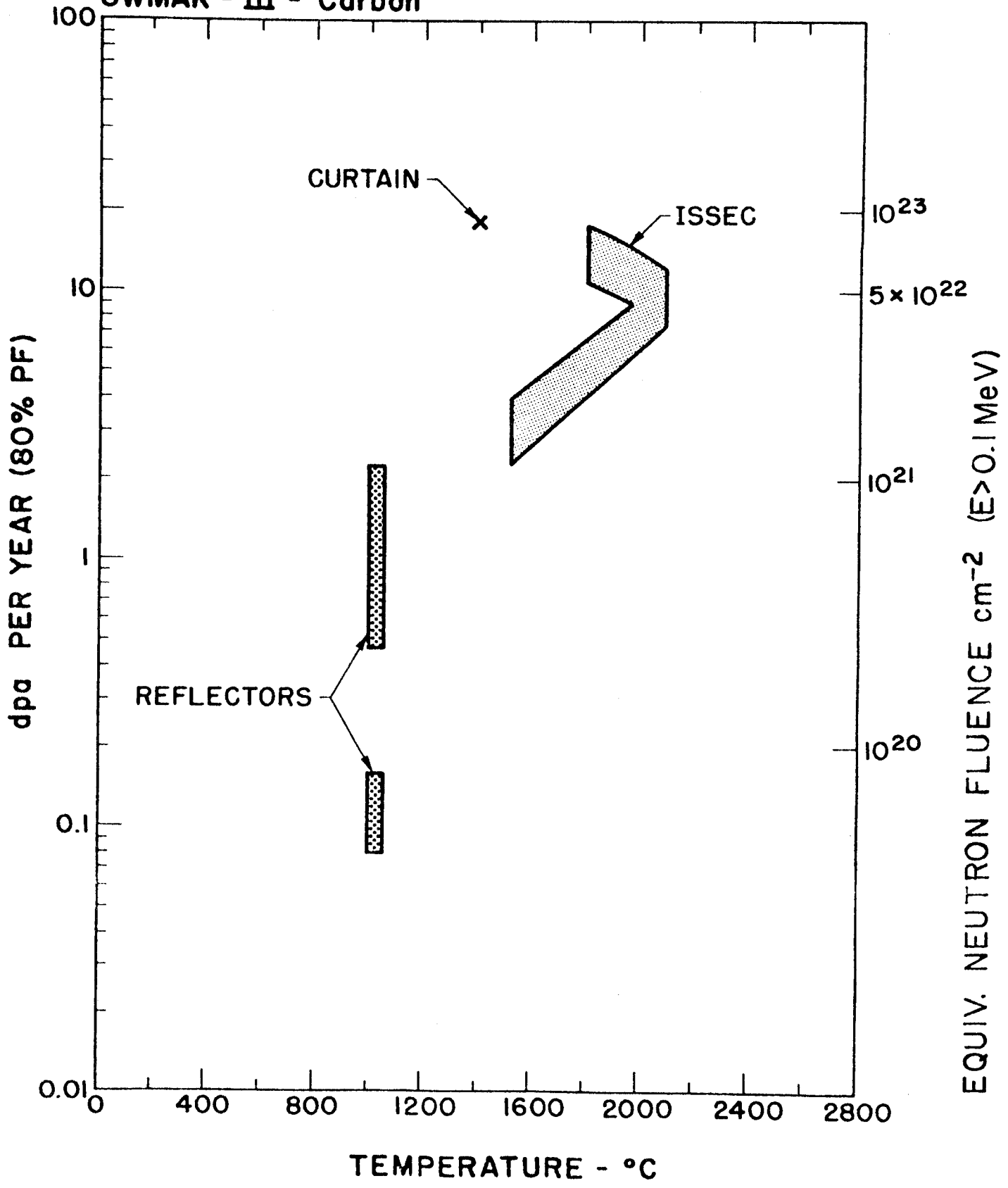

Figure IX - D - 18 Summary of Gas Production Rates vs Temperature in Carbon - One Year Operation

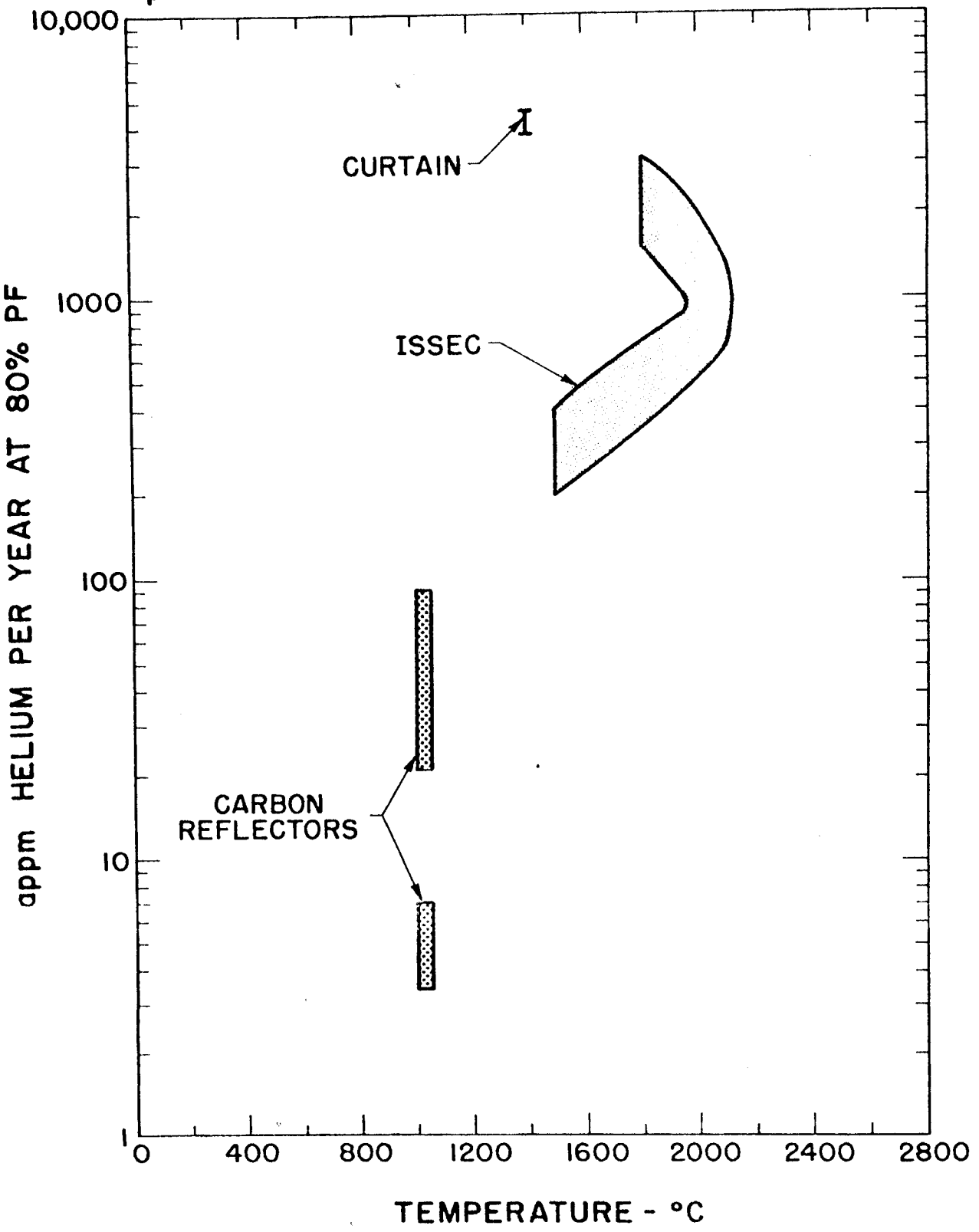

Table IX-D-14

Loss of Carbon From ISSEC and Curtain Surfaces in UWMAK-III

	Thinning Rate[a]		
	mm/year	g/m^2-year	total kg/year[c]
Curtain - Physical Sputtering			
Plasma Side	1.5×10^{-3}	6	6.9
Wall Side	3×10^{-4}	1.2	1.4
Vaporization[b]	1.6×10^{-5}	0.13	0.15
	1.8×10^{-3}	7.3	8.3
ISSEC - Physical Sputtering			
Plasma Side	1.5×10^{-3}	6	2.0
Wall Side	10^{-4}	0.4	0.13
Vaporization			
Plasma Side	0.64	2550	842
Wall Side	4×10^{-4}	1.6	0.5
	~ 0.64	~ 2560	845

a) 80% PF

b) equal loss both sides, equal temperature

c) 1150 m^2 curtain, 330 m^2 ISSEC

IX-D-7b Dimension Changes in Carbon Materials

IX-D-7b-i - Carbon Curtain

Consideration of Figures IX-C-15 and IX-C-16 would lead one to predict a pessimistic lifetime (defined as the fluence at which the dimensions return to the original value, $\Delta\ell = 0$) of 4 months or an optimistic value of ~ 1-1/2 years. Since the data in figure IX-C-16 at 1350°C refers to a specific type of carbon which would not be chosen for this type of an application, we would tend to discount the pessimistic values and assume a lifetime of 1-1/2 years for the curtain.

IX-D-7b-ii - ISSEC

Since there is no data on carbon irradiated above 1425°C it is difficult to estimate the lifetime of the ISSEC which operates at 1500 to 2100°C. It is our opinion that the lifetime will be extended as one increases the irradiation temperature and we would predict at least a 5 year lifetime for the back fibers of the ISSEC (~ 4 dpa/year at 1500°C) and would estimate at least a 3 year lifetime for the front fibers (~ 18 dpa/year at 1800°C).

IX-D-7b-iii - Reflector

Noting from figure IX-D-17 that the carbon in the reflector experiences a maximum displacement rate of 2 dpa per year at 950 - 1000°C, we would predict a minimum lifetime ~ 3 years for the first reflector in the outer blanket. The outer reflector should easily last 30 years at a maximum damage rate of 0.2 dpa yr^{-1}.

IX-D-7-c Changes in Thermal Conductivity of Carbon

The information in figure IX-C-17 can be used in conjunction with that in figure IX-D-17 to estimate a thermal conductivity of ~ 0.1 cal $^{-1}s^{-1}{}^{o}K^{-1}$ in the 1000-1500°C range. This represents a 20-30% reduction in the unirradiated value. There is no data on carbon irradiated above this temperature but the higher irradiation temperature should cause even less of a change in the thermal conductivity due to recombination of the point defects.

IX-D-8 - Anticipated Irradiation Effects in TZM

a. Dimensional Changes

As stated previously, there is very little data on which to make even a crude estimate of the void swelling in TZM irradiated under CTR conditions. However, we will use the information in Table IX-C-4, IX-C-5, IX-D-6, IX-D-12 and Figure IX-D-17 to obtain a rough idea of the possible maximum swelling in the TZM structure. A conversion factor of 3.2 dpa in Mo per 10^{22} n/cm^2 (E > 0.1 MeV) will be used. We will also use a 0.5 power law (see Section IX-C-1-c) and a linear extrapolation of the data. The reader should recognize that the swelling in TZM may be considerably different than in pure molybdenum due to the 0.5% Ti, 0.08% Zr, and 0.03% C alloying elements. The Mo-0.5% Ti alloy should be fairly representative. We are also unable to account for any effects of increased helium gas content due to lack of data.

We have listed in Table IX-D-15 possible yearly swelling values in the outer and inner blanket TZM structure at the conditions of maximum dpa levels. Important points to note are that the maximum swelling at 640 to 700°C may range from 0.2 to 0.4% per year depending on the scaling law used. At 800°C the Mo-0.5% Ti data suggests 0.3 to 0.6% per year with the pure Mo suggesting 0.8%. The swelling at 900°C may be 0.4 to 0.8% per year and that at 1000°C could range from 0.2 to 0.4%. Finally the maximum swelling in the first wall of the inner blanket could be in the 0.2 to 0.4% range.

The best judgment of the authors produces the following suggested values for UWMAK-III;

675°C - 3 dpa - 0.2% year^{-1}

800°C - 15 dpa - 0.6% year^{-1}

900°C - 15 dpa - 0.7% year^{-1}

1000°C - 3 dpa - 0.2% year^{-1}

Table IX-D-15

Estimate of Swelling in TZM From Existing Data

°C Temperature	Maximum[a] (dpa/year)	Predicted Swelling in TZM % Per Year					
		Linear Extrapolation[b]			0.5 Power Law[b]		
		TZM	Mo-0.5 Ti	Mo	TZM	Mo-0.5 Ti	Mo
			Outer Blanket				
640	3	0.2			0.4		
700	3						
800	15	-	0.6	0.8	-	0.3	0.8
900	15	-	0.7	0.8	-	0.4	0.8
1000	3	-	0.2	0.2	-	0.2	0.4
			Inner Blanket				
1000	3	-	0.2	0.2	-	0.2	0.4

(a) using an 80% P.F. in UWMAK-III
(b) 3.2 dpa = 10^{22} n cm^{-2} (E > 0.1 MeV)

IX-D-8-b - Embrittlement

There is even less data available here than there is for the case of swelling. However, it is clear from Section IX-C-1-c-ii that irradiation and testing at temperatures below 675°C is not applicable to this analysis. The only results which are applicable to UWMAK-III occur at rather low damage levels(35c)* (0.4 dpa) and one point at rather ill defined conditions at 20 dpa. A resynopsis of the pertinent data of Table IX-C-10 is given below.

It appears (excluding helium effects) that irradiation to 0.4 dpa of the two Mo alloys has very little effect on the usable ductility of the 700-800°C test range. Values of 10-15% are quite acceptable. The only high fluence displacement data point on pure Mo shows that this resistance to embrittlement may not be degraded at ~ 20 dpa (~ 16 months at the maximum damage level in UWMAK-III). Addition of 20 appm He (~ 3 months in UWMAK-III) to unirradiated TZM also seems to have little harmful effect on the ductility. Based on the above information we would conclude that it is reasonable to project a 3 year (~ 40 dpa) lifetime for the most heavily damage structural component from a ductility standpoint. This projection must obviously be viewed with considerable caution and checked against high fluence neutron damage now emerging from fast fission reactors.

* Reference 35 in Section IX-C

Damage Level dpa (a)	Irradiation Temperature °C	Test Temperature °C	0.2% Yield Strength-Mpa	Total Elongation-%
		Pure Mo		
20	857 to 1136	550	563	10.5
		TZM		
0.4	950	700	380	10
0.4	950	800	350	15
		Mo-0.12Zr-0.002B-0.004C		
0.4	950	700	460	11
0.4	950	800	440	11
		TZM		
(20 appm He)	< 150	> 00	152	14
(20 appm He)	< 150	800	128	14

a) 3.2 dpa = 10^{22} n cm^{-2} (E > 0.1 MeV)

IX-D-9 - Radiation Damage to Stainless Steel

The stainless steel in the shield for the outer blanket is subjected to rather low displacement rates (a maximum of 0.032 dpa per year) at ~ 200°C. Even if the shield must withstand a full 30 years of exposure, this would only amount to 0.96 dpa or ~ 2×10^{21} n cm^{-2} (E > 0.1 MeV). It is well known that steel can withstand that level of irradiation without significant property degradations.

The maximum damage levels in the steel of the magnets is ~ 1.4×10^{-5} dpa yr^{-1} or ~ 4×10^{-4} dpa [~ 9×10^{17} n cm^{-2} (E > 0.1 MeV)] in 30 years of exposure. Tests on steel irradiated to 7.5×10^{17} n cm^{-2} at 77°K show little effect on mechanical properties. (See Table IX-C-17).

IX-D-10 - Radiation Damage in B_4C

Boron carbide is used in the cold shields of both the inner and outer blankets. The maximum operating temperature is 200°C and the maximum helium production rate is ~ 5×10^{19} cm^{-3} per year and even after 30 years with no helium release, the swelling is << 1% (Figure IX-C-23); therefore, we do not anticipate a significant problem with the B_4C.

IX-D-11 - Radiation Damage to Lead

The lead in UWMAK-III is used in both the inner and outer blanket shields which are designed to keep the Pb temperature below 200°C (Pb melts at 327°C). The maximum displacement rate in the inner blanket is ~ 2×10^{-5} dpa per year or ~ 6×10^{-4} dpa after 30 years. This corresponds to ~ 2×10^{18} n cm^{-2} at 200°C. This is no known data on Pb in this regime but the fluence is probably too low for significant swelling to occur and the high homologous temperature (~ 80%) would also argue against any void formation. The gas production cross section is also very low for Pb so that bubble formation is probably not a significant problem.

IX-D-12 - Damage to Copper in the Vertical Field Coils

The closest copper coil to the first wall of UWMAK-III is at 130 cm from the inner ISSEC surface (see Figure IX-D-3). The copper is water cooled and expected to operate at T ~ 20-50°C. The maximum displacement rate is ~ 1×10^{-5} $year^{-1}$. This corresponds to ~ 2×10^{16} n cm^{-2} y^{-1} or 6×10^{17} n cm^{-2} after 30 years. Billington et al. (ORNL-380, 1949 and ORNL-1852, 1955) have shown that irradiation to 10^{18} n cm^{-2} at 20°C increases the resistivity by ~ 1.7 micro-ohm cm, a 0.2% increase over the room temperature value. Such an increase in I^2R loss is certainly acceptable in UWMAK-III.

IX-D-13 - Radiation Damage to Al Stabilizer

The maximum displacement rate in the Al stabilizer occurs in the TF coil at $\theta = 180°$. This is (Table IX-D-6) ~ 9×10^{-6} dpa y^{-1}. Such a damage rate increases the resistivity by ~ 100% per year (Figure IX-C-28). However, periodic annealing to 77°K can remove 50% of that damage and annealing to 260°K would remove essentially all of it (Figure IX-C-29). This technique coupled with a design which increases the stabilizer thickness by a factor of two in the first 5-10 cm of the TF coil should alleviate any safety problems.

IX-D-14 - Radiation Damage to NbTi Super Conductor

The maximum displacement rate to the NbTi superconductor is in the 10^{-5} dpa yr^{-1} range. Figure IX-C-30 and previous analysis in UWMAK-II reveals that such a level of damage, even if never allowed to anneal out, would not change the critical current or temperature by more than 5%.

Leakage of neutrons up divertor slots is another matter and careful analyses will have to be made to prevent such occurrences in UWMAK-III.

IX-D-15 - Radiation Damage to Organic Insulation

The most vulnerable point for the superinsulation is at $\theta = 180°$ and $R = 374.5$. Calculations show that the exposure level is 7 MRad yr^{-1} which, after 30 years is twice the 100 MRad level required for a 25% loss of ductility. Care will have to be taken for a design which does not require a great deal of flexibility during operation.

IX-D-16 - Summary of Major Radiation Effects in UWMAK-III

By now the reader must be painfully aware of the difficulty in making any firm predictions about the response of materials in UWMAK-III to all of the types of irradiation present. The following estimates of component lifetimes are made only so that other analyses such as outflow of radioactive material, resource requirements and cost estimates can be conducted. They must be viewed with a wide degree of latitude.

The best estimates of component lifetime are given in Table IX-D-16. The most critical items in UWMAK-III are the damage to the Al stabilizer, the growth in the carbon materials and the possible loss of ductility in the TZM. As previously stated the damage in the Al can be annealed out at $77^{o}K$ every few months during a maintenance and almost completely removed by warming up to room temperature every year or two.

The growth problems in the curtain may limit its lifetime to as short as 1.5 years, but since it does not support any loads, it is possible that this may be extended by a year without significant consequences. The situation in the reflector region is more critical in that it is presumably a solid of high density and if allowed to expand unrestrained, it could generate large stresses on the structural components.

The ductility limit on the first wall is probably on the pessimistic side and it is quite possible that the lifetime would be three years or more. However, since there is only one data point at 20 dpa (1-1/3 years of UWMAK-III operation) with no significant degradation of mechanical properties, it would be risky to extend the lifetime any further. Such a short lifetime does impact on the operation and maintenance cost of UWMAK-III and increases the down time for maintenance, but since we may have to change the carbon curtain and reflector on a 1-1/2 to 3 year time scale anyway, this requires that the whole blanket module be removed.

There is some question about the lifetime of the TZM in the inner blanket under the assumptions in Table IX-D-16. One would like to have a 30-year value and it is reasonable to project a 15-year lifetime on the basis that the 20 dpa sample in Table IX-C-10 showed 10.5% total elongation after irradiation. The authors are not certain whether one can retain reasonable ductility after a 60 dpa (~2 x 10^{23} n cm^{-2})* exposure at 1000°C. Further work is urgently required in this area.

In conclusion, we have decided to use a very conservative lifetime of 1-1/2 years for the outer blanket extending from $\pm 60^{0}$, to change the entire carbon curtain in the reactor at that time, and every other change out we will replace the rest of the outer blanket and the carbon ISSEC.

* Equivalent Fission Neutron Exposure, E > 0.1 MeV.

Table IX-D-16

Estimate of Component Lifetimes - UWMAK-III

Material	Design Criteria	Minimum Estimated Time to Reach Design Criteria-yr[a]
A) TZM	Swelling < 5%	
1) First Wall - Outer Blanket		7
2) First Wall - Inner Blanket		25
B) TZM		
1) First Wall - Outer Blanket	Total Elongation > 1%	> 1.5
2) First Wall - Inner Blanket		> 8
C) TZM First Wall - Outer Blanket	Wall Erosion < 10^{-2} cm	500
D) Carbon	Wall Erosion	
1) ISSEC	< 2.5 cm	40
2) Curtain	< 0.01 cm	55
E) Carbon	{Growth Break Away Regime ($\Delta\ell$=0)}	
1) ISSEC		> 3
2) Curtain		1.5
3) Reflector - Outer Blanket		> 3
E) Stainless Steel Inner Blanket	Uniform Elongation > 1%	> 30
F) Boron Carbon	$\Delta V/V_o$ < 5%	> 150
G) Copper Coil	$\Delta\rho/\rho$ < 1%	> 250
H) Al Stabilizer	$\Delta\rho/\rho$ < 100%	1
I) Super Conductor	$\Delta H_c/H_c$, $\Delta J_c/J_c$ and $\Delta T_c/T_c$ < 10%	> 50
H) Mylar	Exposure < 100 MRad.	15

a) 80% Plant Factor

X. Power Conversion System for UWMAK-III

The power conversion system for UWMAK-III has two distinct components, the power cycle associated with the heat deposited in the inner hot shield and the outer blanket, and the heat deposited in the divertor by particles diffusing from the plasma. The advanced power conversion system designed for the high temperature coolants of the inner hot shield and the outer blanket is based on a closed-cycle helium gas turbine system and yields a total power output of 1755 MW_e. The divertor power cycle is based on a conventional Rankine steam power cycle to utilize the 687 MW_t (average) in the divertor. The sodium coolant of the divertor plates leaves the reactor at 600°C and total power output is 295 MW_e. The gross electrical power output is 2050 MW_e and the net electrical output is 1985 MW. This gives a net plant efficiency of 41.9%.

In Section X-A through X-F, the power conversion system for the hot inner shield and the outer blanket is described. This work was carried out by Dr. S. Kuo of the United Technologies Research Center in collaboration with the University of Wisconsin. Section X-G describes the power cycle for the divertor system and was carried out jointly by Mr. D. Schluderberg of Babcock and Wilcox and the University of Wisconsin. Finally, Section X-H is a summary of the overall power system characteristics.

X-A. Introduction

Although the scientific feasibility of controlled thermonuclear fusion has yet to be demonstrated, recent achievements in fusion research indicate that the demonstration of scientific feasibility is indeed on the horizon. While the first commercial fusion power plant is not expected to be built before the turn of the century, the technological and engineering problems, that will have to be resolved before commercial implementation, require early investigation in order to avoid future technical and economic bottlenecks. Many not-yet-developed subordinate technologies will be required for this new energy system. Examples of such technologies are energy storage systems (Ref. 1) and advanced power conversion systems (Ref. 2, 3, and 4). Consequently, it is timely to investigate the technological and engineering problems other than those needed to produce, confine and sustain fusion plasma. One such class of problems is associated with efficient extraction and conversion of fusion energy for generating electric power.

Two contemporary and significant efforts in fusion technology and engineering now in progress involve conceptual design and system studies of Tokamak-type fusion power plants. These efforts are located at the University of Wisconsin on the UWMAK-I, -II, and -III reactors (Ref. 5 and 6), and at Princeton University on their fusion reactor designs (Ref. 7). These analytical studies serve the purpose of identifying the crucial technical problems and critical components or technologies which require development, examining the possible solutions and their limitations, suggesting alternative approaches to achieve the ultimate goals, and assessing the future prospects of fusion power plants relative to the existing and anticipated energy systems. The contribution of these design studies has been widely recognized, and their results often provide a guide for future research direction. However, most of the previous design studies were based on current or near-term technologies, and the role of power conversion systems have been deemphasized due in part to consideration only of well-developed steam power systems.

The conceptual UWMAK-III reactor represents an advanced-design second-generation fusion power reactor utilizing molybdenum structure materials to achieve high blanket coolant outlet temperatures suitable for integration with an advanced power conversion system to surpass the performance of earlier conceptual UWMAK-I and -II fusion reactor power plants. The advanced power conversion system envisioned is a closed-cycle helium gas turbine power system which would operate efficiently and economically at a turbine inlet temperature compatible with the estimated blanket capability and use dry cooling for waste heat rejection. The closed-cycle helium gas turbine offers the potential of high performance, low cost, and less environment effects, and would appear most suitable for integration (directly or indirectly) with advanced-design fusion reactors, such as UWMAK-III. In addition to the attractive thermal efficiency, the helium gas turbine will be smaller in size (about one-quarter) compared to the steam turbine of same output capacity, primarily because of a low overall expansion ratio (about 3:1 for the helium turbine compared to approximately 3000:1 for the steam turbine).

The study described in this report involved a two man-months effort on three tasks (see Table 1) performed over a seven-month period (see Fig. 1). The overall study procedure is shown in Fig. 2. In Task I, the power conversion system requirements and constraints were defined based on the general design philosophy established for the UWMAK-III fusion reactor. A baseline cycle configuration was selected using a compatibility matrix, and parametric analyses were conducted to estimate the performance and size characteristics for the baseline closed-cycle power system. In Task II, the critical integration parameters and crucial interface problems for the power conversion system were identified, and reference design conditions for the baseline cycle were selected based on consideration of trade-offs to alleviate interface problems among the critical integration parameters identified. Conceptual design studies for the major power conversion system components including turbomachinery, major heat exchangers, and piping systems were performed in Task III based on the reference design conditions and the integration scheme selected. Although the power system layout is not part of the present study, a preliminary conceptual power system layout diagram was prepared to indicate the relative location of the power conversion systems and the approximate power plant dimension. The overall system layout is discussed in Chapter XI.

TABLE I

UWMAK-III POWER CONVERSION STUDY PROGRAM

Tasks:

1 Cycle Alternatives & Parametric Analysis

2 Interface Problems & Tradeoff Studies

3 Preliminary Conceptual Design Studies

TABLE II

UWMAK-III POWER SYSTEM REQUIREMENTS AND CONSTRAINTS

1. Advanced Technology (Second Generation Fusion Powerplant)
2. High Performance (Surpass UWMAK I and II)
3. Dry Cooling Tower
4. Two-Zone Blankets
5. Acceptable Tritium Extraction and Containment
6. Around-the-Clock Operation with Thermal Storage
7. Compatibility with Helium/Lithium Temperature Rise in the Blankets and Heat Exchanger Loops
8. Moderate Maximum Helium Pressure (750 - 1000 psi), and Reasonable System Pressure Loss ($\sim$ 8%)
9. 3600-RPM Turbomachines/60 Hertz A-C Power
10. 1500 - 2000-Mwe Approximate Station Capacity
11. Acceptable Operational Characteristics

UWMAK–III FUSION POWER CONVERSION BY CLOSED–CYCLE GAS TURBINES

PROGRAM SCHEDULE

LEVEL OF EFFORTS: 2 MAN–MONTH

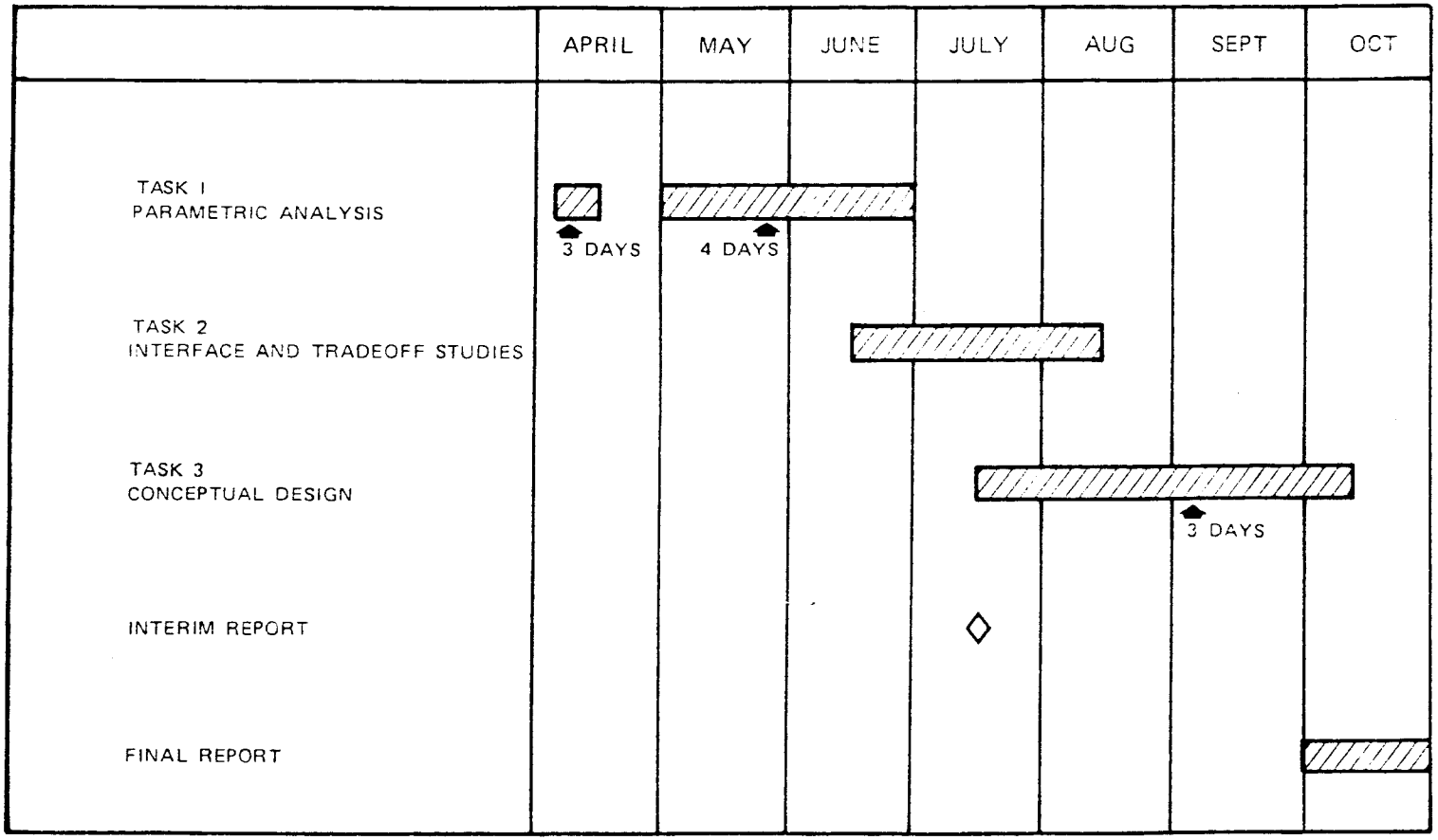

: SCHEDULED VISITS AND DURATION, AND CONFERENCES AT THE U. OF WISC

FIG. 1

R10–106–9

FIG. 2

UWMAK–III POWER SYSTEM STUDY PROCEDURE

CLOSED–CYCLE GAS TURBINES

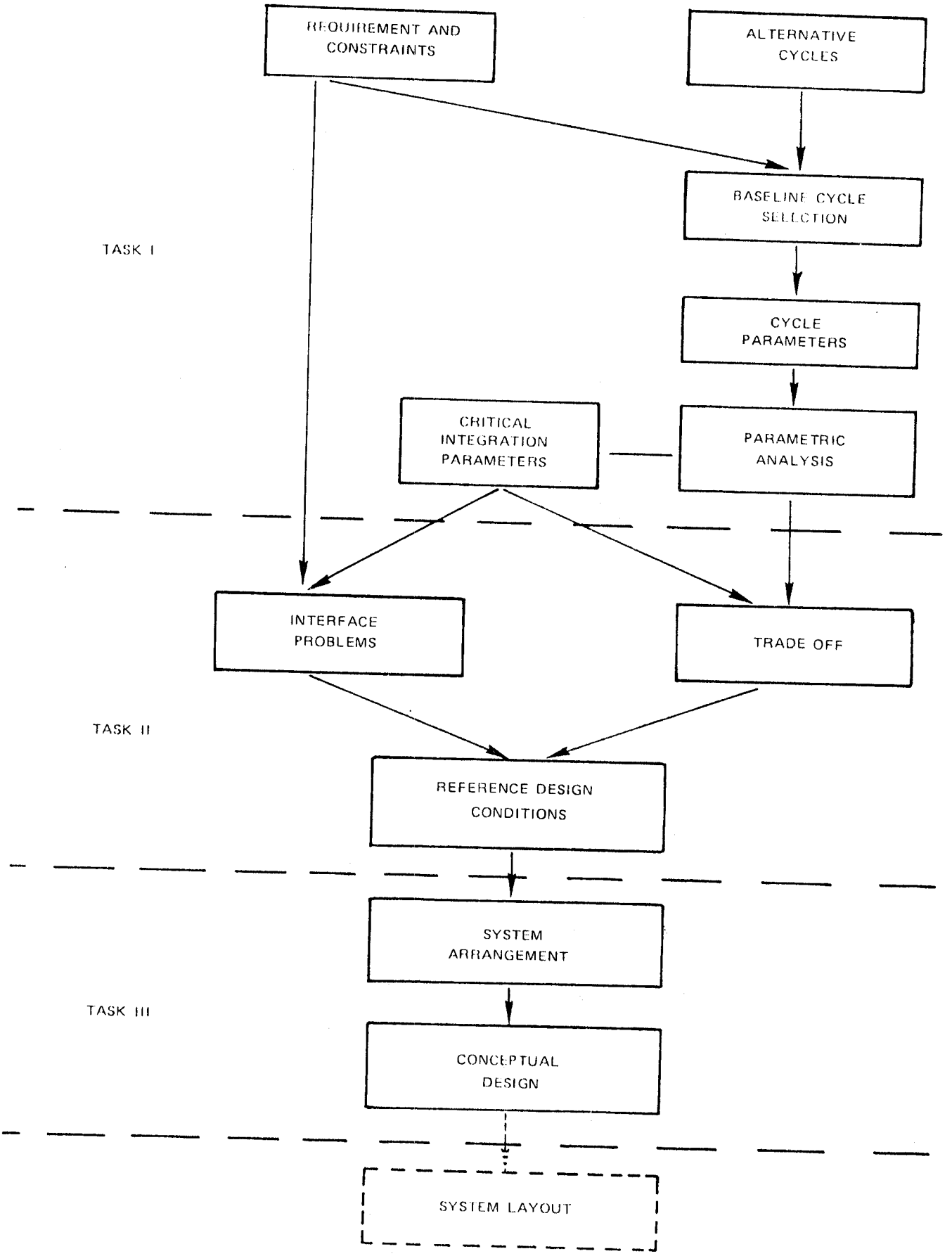

R10–106–2

X-B. POWER CONVERSION SYSTEM REQUIREMENTS AND CONSTRAINTS

The conceptual UWMAK-III reactor represents an advanced-design second-generation fusion power reactor utilizing molybdenum structural materials to achieve high blanket coolant outlet temperatures (as high as 980 C or 1796 F) suitable for integration with an advanced power conversion system, surpassing the performance of earlier conceptual UWMAK-I and -II fusion reactor power plants. The advanced power conversion system envisioned is a closed-cycle helium gas turbine power system which would operate efficiently and economically at a turbine inlet temperature compatible with the blanket capability, using dry cooling towers for waste heat rejection.

Based on the established design philosophy of the UWMAK-III fusion power reactor, the power conversion system requirements and constraints have been defined (as shown in Table II) and are discussed in the following sections.

Power Conversion System Alternatives

A practical power generation system, fossil or nuclear, often represents a compromise -- a compromise which is constrained by technological limitations and which results from a trade-off between the overall system performance and cost.

The energy available from the fusion reactor must be extracted and converted to produce electric power. A high overall conversion efficiency is desirable to assure small reactor size and low thermal discharge. However, higher systems performance generally require higher maximum cycle temperature and/or more complex designs which may lead, in turn, to larger component sizes or higher capital costs or both, indicating that appropriate trade-offs are necessary.

The choice of a particular heat engine for fusion power generation depends largely on such factors as the temperature capability of the blanket, the energy storage scheme used, the operating temperature and efficiency of the heat engine, the specified power rating and duty cycle, and most important of all the capital cost of the entire power generation system ($/kw).

For the UWMAK-III fusion power conversion system, both the Rankine steam power system or the closed-cycle Brayton power system could be utilized. Rankine cycle power systems are reasonably efficient, although they are limited to a maximum cycle temperature of about 1050°F and generally have the undesirable feature of low specific power (kw/lb), high operating pressure, and require a bulky condenser. Brayton power systems are more compact, reasonably efficient, more adaptable to dry cooling, and have many advantageous features suitable for fusion power conversion.

Performance Requirements

Since the first commercial fusion power plant probably won't be built before the turn of the century and since UWMAK-III is a conceptual second-generation fusion power plant, the advanced technologies considered in this study program are those judged to be available in the years 2010-2020. In this respect, it becomes apparent that the upper limit of the UWMAK-III power plant performance would be constrained by the blanket capability (i.e., temperature) rather than limitations imposed by helium gas turbine technologies. Current state-of-the-art helium gas turbine inlet temperature is between 1400 F and 1500 F, and by the year 2010 this temperature is expected to increase approximately two to three hundred degrees. To achieve this turbine inlet temperature range, lithium coolant outlet temperatures of at least 1800 F or higher, or helium coolant outlet temperatures of 1600 F or higher will be required. It appears that the limiting factor for higher power plant performance is most likely to come from the blanket outlet temperature imposed by material capability limitations attributable to the severe radiation and neutronic effects and/or liquid metal environment. For these reasons, a more conservative blanket outlet temperature of 1800 F lithium and 1600 F helium have been selected, leading to a baseline helium turbine inlet temperature of 1600 F.

The overall UWMAK-III plant efficiency is expected to surpass the efficiencies of earlier UWMAK-I (30 percent) and UWMAK-II (35 percent), and a goal of approximately 40 percent was selected. This would mean that a power cycle thermal efficiency of 43-44 percent will be required. Based on the previous United Technologies Corporation experience, a higher helium turbine inlet pressure level is generally preferable, but the inner blanket heat transfer design could be a limiting factor. A pressure level of 500-1000 psia and a system pressure loss of about 8 to 9 percent would appear appropriate.

Environmental Constraints

The major environmental constraints on the power conversion system will be the cooling water shortage; thermal discharge is a problem with any large fossil or nuclear power plant. Even now in many parts of the country, adequate supplies of cooling water for conventional power generating plants have been exhausted. With the electric power demand in the United States expected to grow continuously (if no longer doubling each decade), the thermal pollution problems attributable to power stations will become more serious every year, and it can be expected that by the time fusion power generation becomes practical, use of dry cooling for waste heat rejection will be imperative.

The closed-cycle helium gas turbine power system will be economically more adaptable to dry cooling because heat rejection takes place over a temperature range much higher than the condenser temperature in a Rankine steam power system.

Reactor Constraints

The two-zone (lithium/helium cooled) blanket design is certain to impose considerable constraints on the selection of power cycle configuration, the number of turbomachinery loops, the unit capacities (identical or different), the integration schemes for the turbomachines, and the thermal storage system. Breeding of tritium in the lithium coolant would require an intermediate heat exchanger for containing the tritium from diffusing into the power conversion loop, thus, resulting in a lower turbine inlet temperature which, in turn, reduces the power conversion efficiency. A helium gas turbine can be integrated directly with a helium-cooled blanket thus avoiding the above temperature loss, provided no tritium breeding is required in that blanket.

The UWMAK-III and any Tokamak fusion reactor have a unique operating cycle in which the "burning" of the fusion plasma has to be shut down periodically although only momentarily. While there is some flexibility in designing an operating cycle, a long-pulsed cycle with approximately 30 to 100 minutes burn time and 1 to 6 minutes downtime have been reported (Refs. 7 and 8). Since the power conversion system cannot tolerate even momentary cutoff from the heat source, means to store thermal energy for use during every reactor downtime will be required. Theoretically, the power conversion system should not detect the reactor downtime, but in reality the operation of the power conversion system can be complicated by provision of the thermal storage system.

There are also temperature and pressure compatibility problems between the reactor blanket and the power conversion system. In the case of a lithium-cooled blanket, fusion energy absorbed within the volume of lithium (plus a smaller fraction transferred from the first wall) is transferred to sodium (intermediate loop) which in turn heats the helium working fluid. Thus, the temperature rise of the lithium, sodium, and helium are constrained by the heat exchanger design which would require proper trade-off between performance vs size. In the case of a helium-cooled blanket, the pressure level and the temperature increase required by the power cycle have to match the blanket heat transfer, flow rate, and pressure level capabilities which may again require some design trade-off and/or compromise.

Based on the UWMAK-III fusion reactor design objectives, the total electric power output expected will be between 1500 and 2000 Mwe.

Utility Power Requirements

From the power utility viewpoint, a fusion power plant must be capable of delivering uninterrupted constant-output 60 Hertz ac power under normal operating conditions. This would require that the turbomachines must operate at 3600 rpm,

and that the operational characteristics of the power conversion systems must be adaptable to the existing power grids. Based on the power plant output level mentioned above, the two-zone blanket design, and the need to provide a reasonable system redundancy, turbomachinery unit capacity of approximately 500 to 600 Mwe would be required.

X-C. PARAMETRIC PERFORMANCE ANALYSES

Since closed-cycle gas turbines operate on the Brayton cycle, the four basic components required to operate such a cycle include the compressor, heater (blanket or subordinate heat exchanger), turbine expander, and the precooler. The thermal efficiency and specific work of a closed-cycle helium gas turbine depend upon many factors; for given maximum and minimum cycle temperatures, the thermal efficiency is dependent on the degree of cycle complexity provided in the system, such as intercooling, regeneration, and reheat. While the selection of power cycle configuration is largely dependent on the requirements or constraints (such as type of heat source and heat rejection scheme among others) imposed on the power conversion system, the levels of intercooling, regeneration, and reheat will have to be decided based on a trade-off between the system performance and cost. Therefore, appropriate parametric analyses were required for selecting the reference design system.

To achieve this objective, parametric performance analyses were conducted during the Task I study for selected power cycle configurations. The major steps taken in the Task I study are summarized in Table III, and each step is discussed further in the following sections.

Cycle Configuration Alternatives

Based on various combinations for intercooling (none, one, or two), regeneration (none or regenerative), and reheat (none or one), there results at least twelve different cycle configurations. For a closed-cycle gas turbine power system, the economic merit of using appropriate regeneration has been well established, and it should be given the first priority among the three feature components for improving the cycle thermal efficiency. While the technical and economic merit of these feature components require further parametric analyses, it must be mentioned that typically all intercoolers operate at the low temperature range (below 300 F), the regenerator operates at the intermediate temperature range (300-1000 F), and the reheater at the high temperature range (1000 F and above) of the power conversion cycle. Operating temperature range is the most important indicator for heat exchanger cost. For this reason, the reheater is seldom used in a closed-cycle gas turbine unless its economic merit is fully justified. A preliminary screening was made to select six more attractive ones out of the twelve possible cycle configurations mentioned earlier (see Fig. 3), based on the considerations stated heretofore, for further evaluation. A simple cycle with none of the feature components was included to provide a point of departure for all other cycle configurations.

Baseline Cycle Configuration

The selection of cycle configuration and the subsequent operating conditions for a given closed-cycle gas turbine (or any baseload power system) is often dictated by

TABLE III

TASK 1 OUTLINE

- Specify Power System Constraints
- Identify Cycle Configuration Alternatives
- Select Power Cycle Configuration
- Select Power System Parameters
- Specify Numerical Ranges and Computational Points for the Above Parameters
- Perform Parametric Analysis to Estimate Performance and Size Characteristics

CCGT CYCLE CONFIGURATION ALTERNATIVES

3(INTERCOOLING)X2 (REGEN.) X2 (REHEAT) = 12 CASES

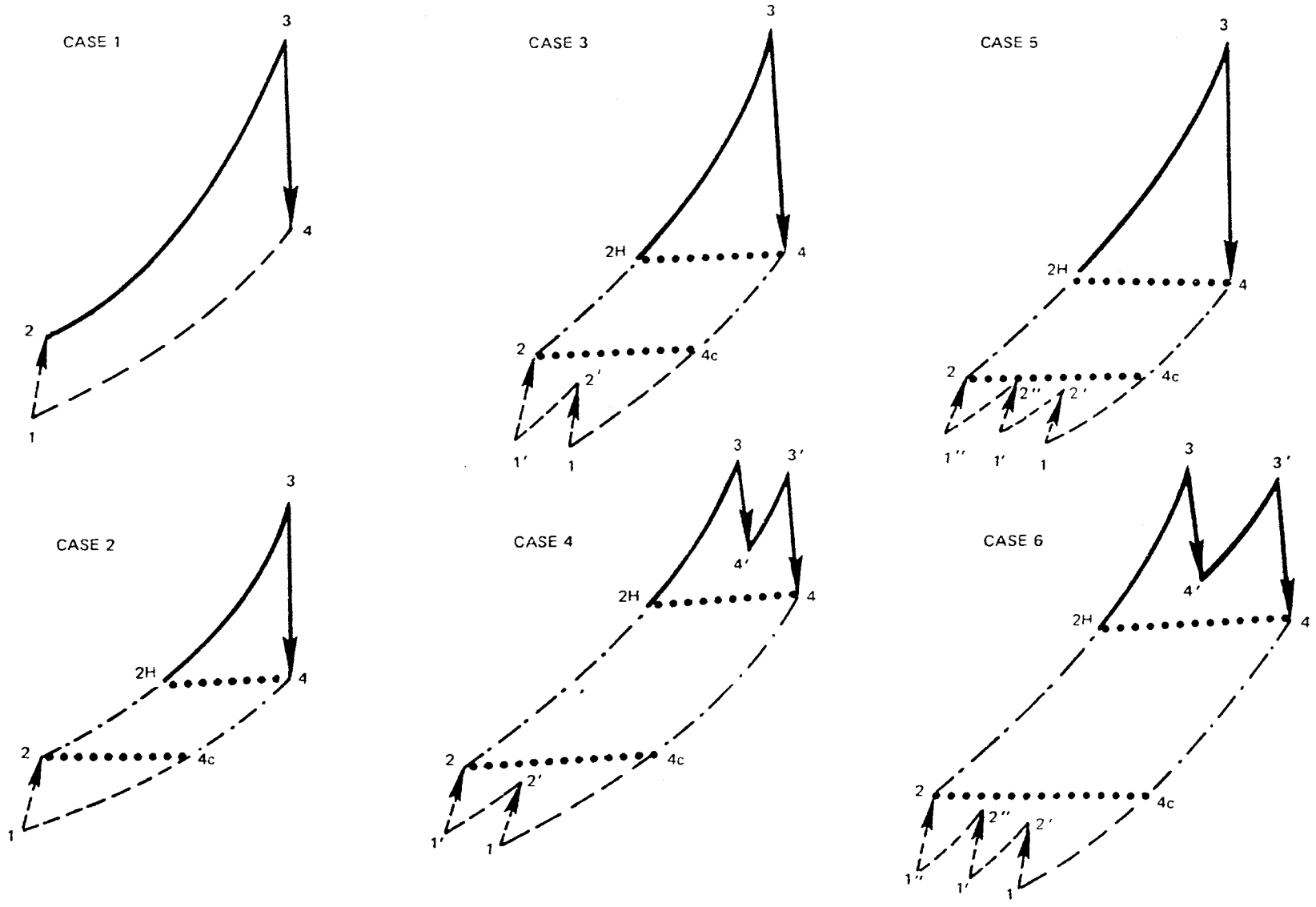

X-(;-3

FIG. 3

R07-30-5

the compatibility of the cycle with the requirements and constraints imposed on the power conversion system and a trade-off between the cycle performance (efficiency) and complexity (i.e., costs) for generating the lowest cost electric power. Past experience indicates that for a turbine inlet temperature of 1600 F, a simple closed-cycle gas turbine will have a cycle thermal efficiency of slightly above 30 percent which is too low to be competitive with the UWMAK-I and -II performances. Therefore, improvement of the cycle thermal efficiency by incorporating intercooling, or reheat with various degrees of regeneration would be imperative.

A baseline cycle configuration was selected using a "compatibility matrix", as shown in Fig. 4, to check the capability and/or compatibility for each of the six candidate cycle configurations to meet nine of the power conversion system requirements and constraints selected from Table II. The results were rated in terms of "good", "fair", and "poor". Past experience in analyzing closed-cycle gas turbine systems was utilized in making the judgments. The results indicate that the regenerated cycle with one intercooling stage would be most suitable for UWMAK-III power conversion. Therefore, a regenerated cycle with one intercooling was selected as the baseline cycle configuration for further parametric analysis. Intercooling is sometimes not desirable, from a cost point of view, when a cooling tower is used for heat rejection. However, the station thermal efficiency requirement for UWMAK-III would make single-stage intercooling imperative. Addition of single reheat to the baseline configuration by taking advantage of the two-zone blankets could be attractive, provided that the coolant outlet temperature and power level for the inner and outer blankets are similar, and that there is no tritium containment problem. Figure 5 shows a T-S diagram and a schematic flow diagram for the baseline cycle configuration selected.

Cycle Parameters and Ranges

Crucial parameters which could significantly affect the power conversion performance and/or equipment cost were identified, as shown in Table IV.

The turbine inlet temperature which is always constrained by the blanket coolant outlet temperature is the most significant parameter for the cycle thermal efficiency; 1500 F, 1600 F, 1800 F, and 2000 F were selected for parametric analyses based on the potential progress that can be expected for the blanket materials development. A high turbine inlet pressure is desirable for smaller power system equipment and a better heat transfer coefficient; 1000 psia was selected as the reference point but sensitivity analyses were made for 750, 1500, 2000, and 3000 psia. Eight overall pressure ratios, including 1.5, 1.74, 2.0, 2.45, 3.0, 3.86, 4.91, and 6.0 were selected as parametric points. The performance of the baseline cycle was analyzed for 0, 60, 70, 80, 90, and 100 percent regenerator effectiveness to see their impact on the cycle thermal efficiency; for the baseline configuration, an effectiveness of 88 percent was used in calculating parametric performance for other varying parameters.

CCGT CYCLE CONFIGURATION SELECTION MATRIX

(UWMAK–III)

REQ. OR CONSTRAINT \ CYCLE CONFIG.		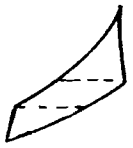	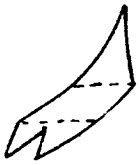	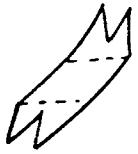	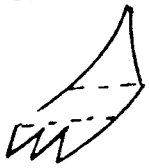	
1. ADV. TECH.	X	√	O	O	O	O
2. HIGH PERFOR.	X	√	O	O	O	O
3. DRY TOWER	O	O	√	√	X	X
4. 2x BLANKET	√	√	√	O	√	O
5. THERM. STORAGE	?	?	?	?	?	?
6. He ΔT	X	O	O	O	O	O
7. P_{max} & ΔP	√	O	O	X	√	X
8. 3600 rpm/60 Hz	O	O	O	√	√	√
9. 2000–Mwe	X	√	O	O	O	O

O GOOD √ FAIR X POOR

FIG. 4

FIG. 5

CYCLE DIAGRAM OF HELIUM GAS TURBINE SYSTEM

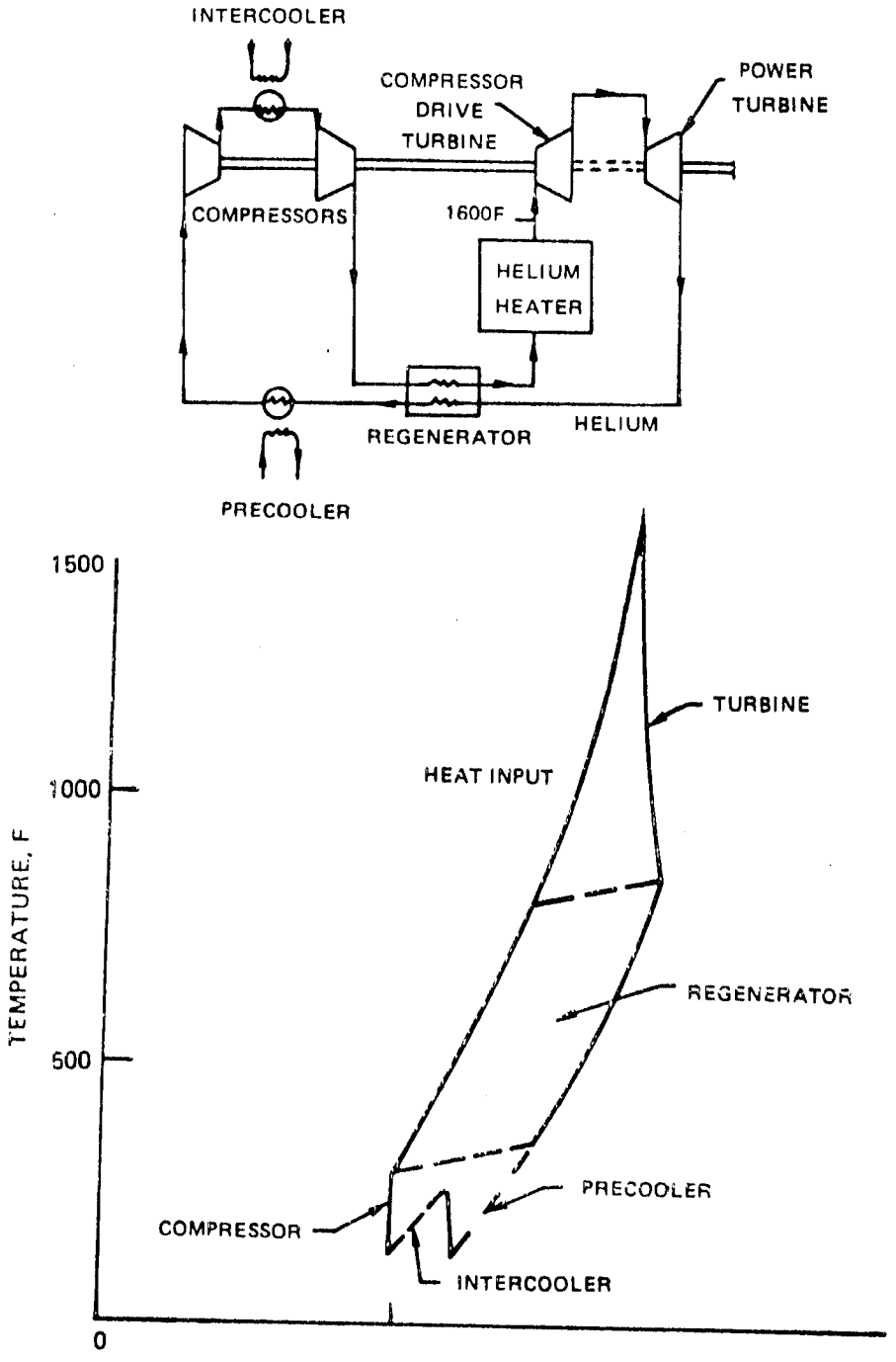

TABLE IV

UWMAK-III POWER CONVERSION CYCLE PARAMETERS

One Intercooling, No Reheat

- Turbine Inlet Temperature
- Turbine Inlet Pressure
- Overall Pressure Ratio
- Regenerator Effectiveness
- Compressor Inlet Temperature
- System Pressure Loss
- Turbine Efficiency
- Compressor Efficiency

Since dry cooling towers were specified for waste heat rejection, a compressor inlet temperature of 110 F was used as the reference point, but parametric data for 80, 100, 120, and 140 F were also calculated. The level of system pressure loss increases with the increase of cycle complexity, and 6, 8, 10, and 12 percent were selected as parametric points with 8 percent as the reference point. The cycle parameters considered and the parametric points picked are summarized in a parametric analysis decision three as shown in Fig. 6. An independent variation of all the parameters would result in over 15,000 design points which is beyond the scope of the current study. Therefore, some of the cycle parameters were varied only selectively to yield the number of design points within a manageable size.

Parametric Analyses

Extensive parametric performance analyses were carried out for the baseline and some off-baseline cycle configurations to (1) reassure the suitability of the baseline cycle configuration, and (2) generate sufficient data needed for subsequent trade-off studies. The results of these analyses for more than 100 parametric operating conditions are presented in Fig. 7 through 12, and a comparison of cycle thermal efficiency for the baseline configuration with alternative cycles is presented in Fig. 13.

Parametric Variation

The turbine inlet temperature is the single most important parameter which affects the thermal efficiency of the power conversion system; a higher turbine inlet temperature limited only by the material technology is desired for a higher power conversion efficiency. For this reason, the increase in turbine inlet temperature is generally regarded as indicative of the advancement in turbomachinery technology. The effect of turbine inlet temperature on the baseline cycle thermal efficiency is shown in Fig. 7; a maximum cycle thermal efficiency of nearly 44 percent at a turbine inlet temperature of 1600 F and total pressure ratio of about 2.8 would lead to a station efficiency of approximately 40 percent. For higher station efficiencies, above 40 percent, a turbine inlet temperature above 1600 F or lithium coolant outlet temperature above 1800 F would be required. Note that the cycle thermal efficiency increases approximately 1.8 point per 100 F increase in the turbine inlet temperature, and that the optimal pressure ratio for maximum efficiency increases with the increase in turbine inlet temperature. Figure 8 shows the thermal efficiency and specific work of a closed-cycle gas turbine for different turbine inlet temperatures and pressure ratios. While the cycle thermal efficiency reaches a maximum value at an optimal pressure ratio of about 2.8, the specific work continues to increase with the increase in pressure ratio, indicating that the selection of the design point could be a compromise between the thermal efficiency for system economy and the specific work for large unit capacity.

UWMAK–III POWER SYSTEM PARAMETRIC ANALYSIS DECISION TREE

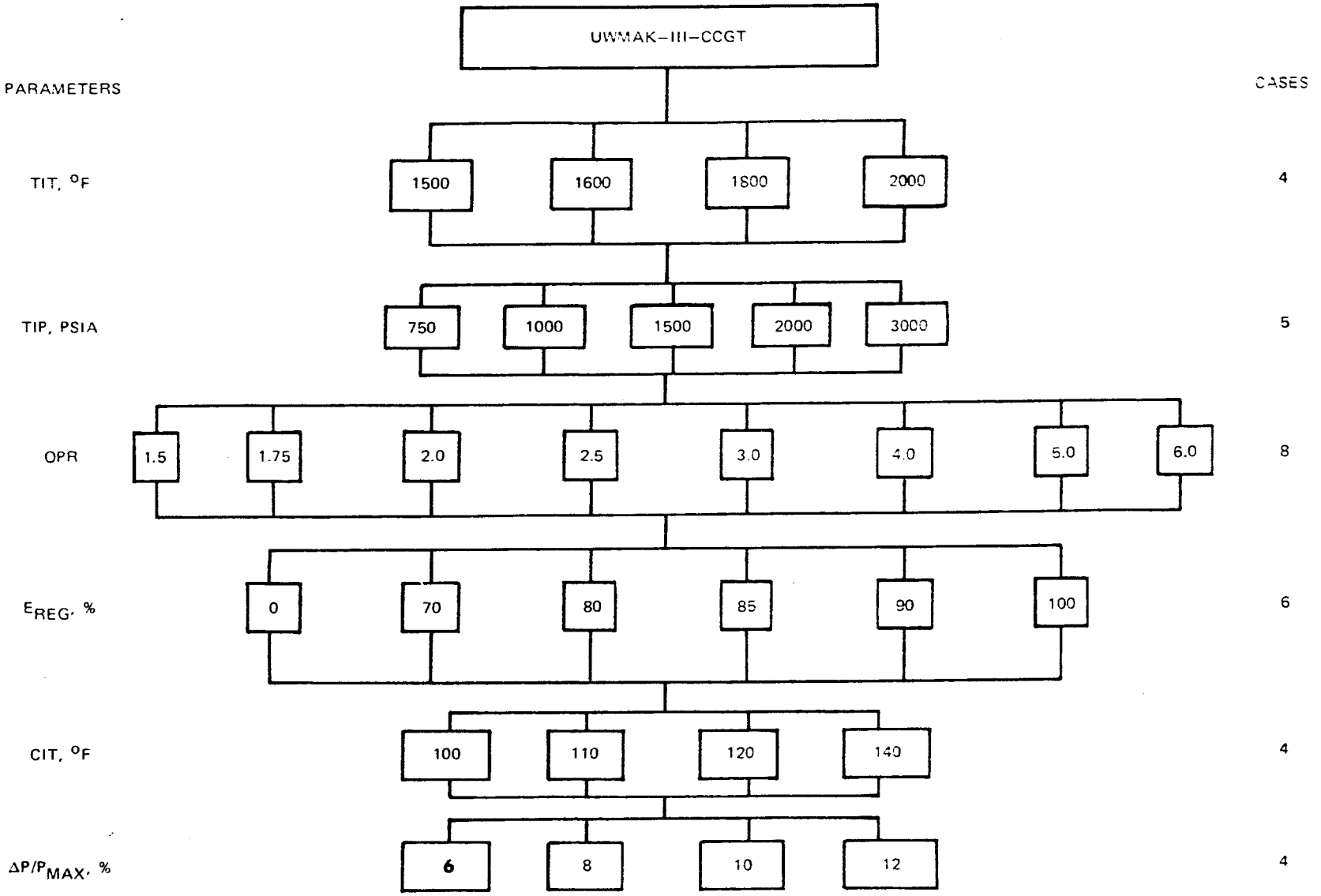

FIG. 6

FIG. 7

THE EFFECT OF TURBINE INLET TEMPERATURE ON THE PERFORMANCE OF A CLOSED–CYCLE HELIUM GAS TURBINE

REGENERATOR EFFECTIVENESS = 88%

COMPRESSOR INLET TEMPERATURE = 110°F

CYCLE PRESSURE DROP 8%

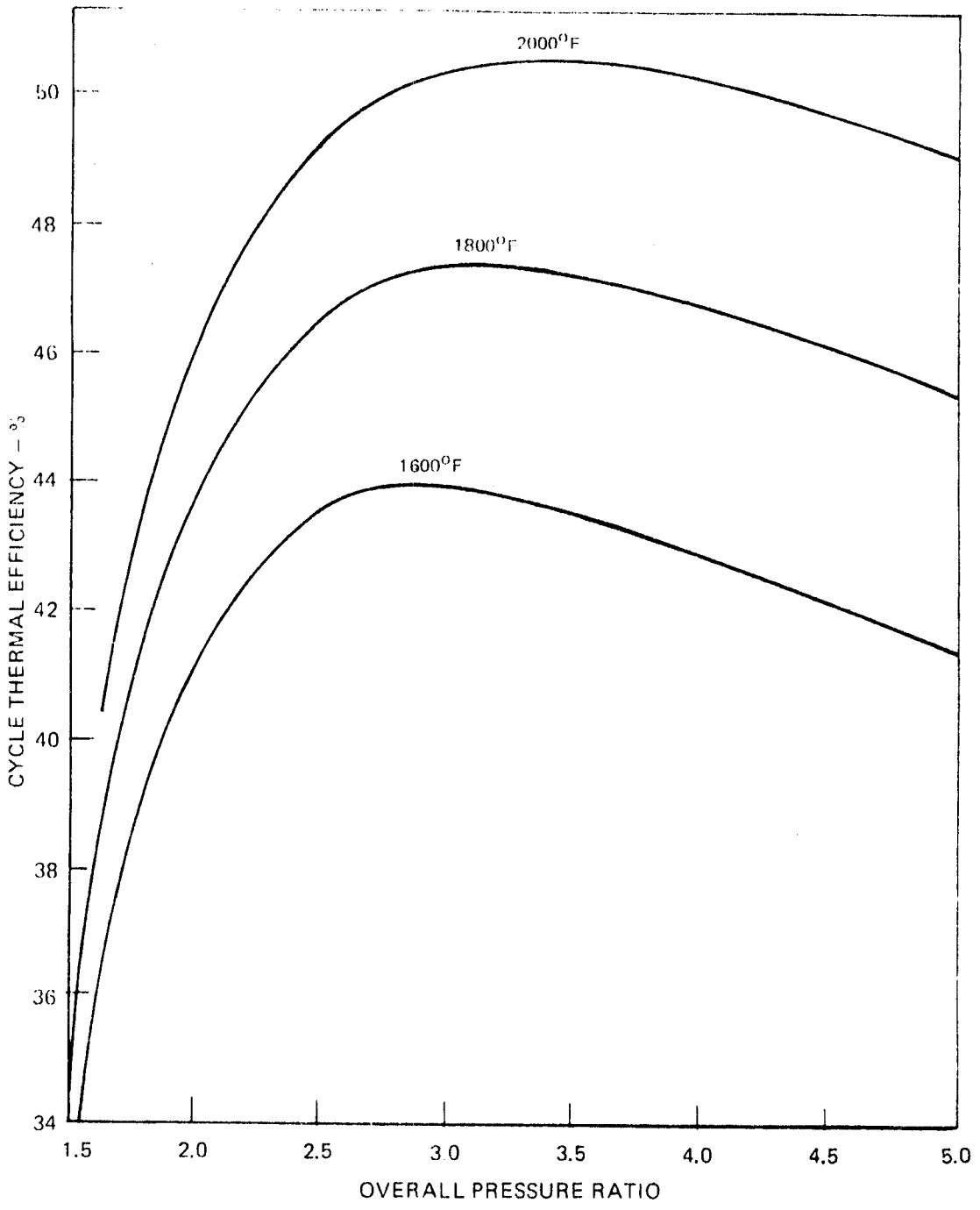

FIG. 8

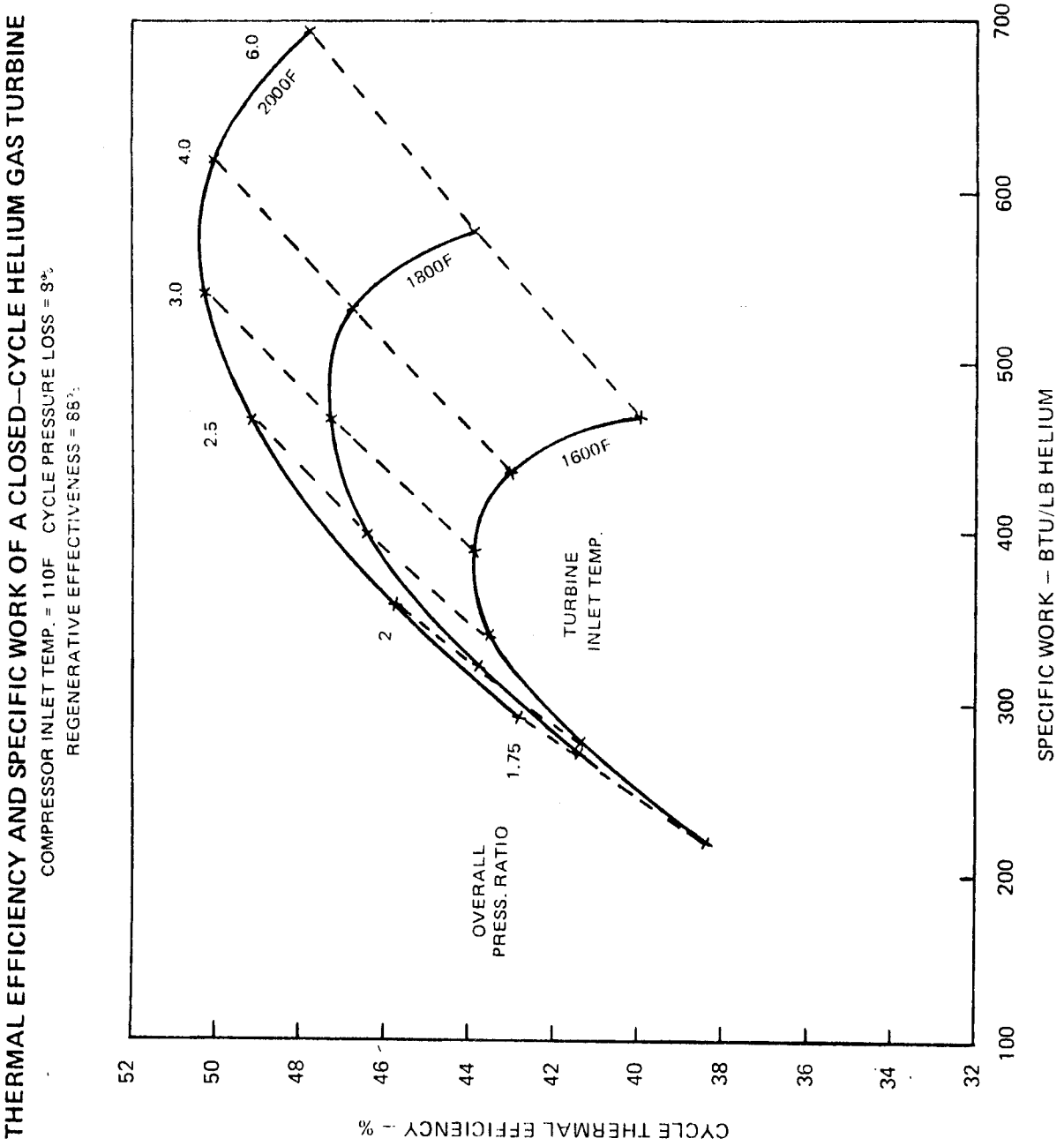
THERMAL EFFICIENCY AND SPECIFIC WORK OF A CLOSED–CYCLE HELIUM GAS TURBINE
COMPRESSOR INLET TEMP. = 110F CYCLE PRESSURE LOSS = 3%
REGENERATIVE EFFECTIVENESS = 88%
CYCLE THERMAL EFFICIENCY – %
SPECIFIC WORK – BTU/LB HELIUM
OVERALL PRESS. RATIO
TURBINE INLET TEMP.
2000F
1800F
1600F
6.0
4.0
3.0
2.5
2
1.75
52
50
48
46
44
42
40
38
36
34
32
100
200
300
400
500
600
700

Figure 9 shows the drastic improvement in cycle thermal efficiency attributable to regeneration. A trade-off between the cycle performance improvement and the regenerator cost increment would be necessary, however. Note that the optimal pressure ratio changes widely with the change in regenerator effectiveness. The compressor inlet temperature exerts a strong influence on the power system performance; a lower compressor inlet temperature is desirable for higher efficiency, but this temperature is always constrained by the waste heat rejection scheme available to the power plant. The cycle thermal efficiency drops for about 0.7 point per 10 F increase in the compressor inlet temperature (see Fig. 10). This is less severe than that for the steam power system which drops one point per 10 F.

Although the level of helium pressurization was found to have little effect on the cycle performance, its selection suitable for the blankets and/or the heat exchangers would depend on many factors including heat transfer coefficient, turbomachinery and other power plant equipment sizes, and creep strength and thermal fatigue of the materials used. The effect of total pressure loss on the cycle performance was found to be approximately 0.8 point decrease in thermal efficiency per 1 percent increase in pressure loss within the 6 to 12 percent range considered (see Fig. 11). A comparison of thermal discharge characteristics for the LWR and fossil steam plants with the closed-cycle helium gas turbine power system is given in Fig. 12. Note that the level of heat rejection from the UWMAK-III plant would be approximately 10 percent higher than that shown in the figure (based on cycle thermal efficiency).

Configuration Variation

A comparison of cycle thermal efficiency for the baseline cycle with the alternative cycles is depicted in Fig. 13. The simple and simple-intercooled cycles are apparently not acceptable because of excessively low thermal efficiency. The regeneration cycle (cycle #3) would be more adaptable to dry cooling, but its modest 40 percent cycle efficiency would lead to a station efficiency of about 35 percent, thus offers no improvement over UWMAK-II. The choice between adding intercooling or reheat to improve the regenerative cycle would appear rather clear; intercooling offers greater improvement without using expensive high-temperature heat exchangers. Combination of all three features (i.e., regeneration, intercooling, and reheat) would offer a rather attractive performance, but its technical feasibility would be constrained by the blanket capability among other factors. Therefore, it can be concluded here that the baseline configuration selected earlier by using compatibility matrix is technically sound. The selection of reference design condition would require considerations on interface and trade-off problems which are discussed in the following sections.

FIG. 9

THE EFFECT OF REGENERATOR EFFECTIVENESS ON THE PERFORMANCE OF A CLOSED-CYCLE HELIUM GAS TURBINE

TURBINE INLET TEMPERATURE = 1600°F

TURBINE INLET PRESSURE = 1000 PSIA

CYCLE PRESSURE DROP = 8%

COMPRESSOR INLET TEMPERATURE = 110°F

ONE INTERCOOLING

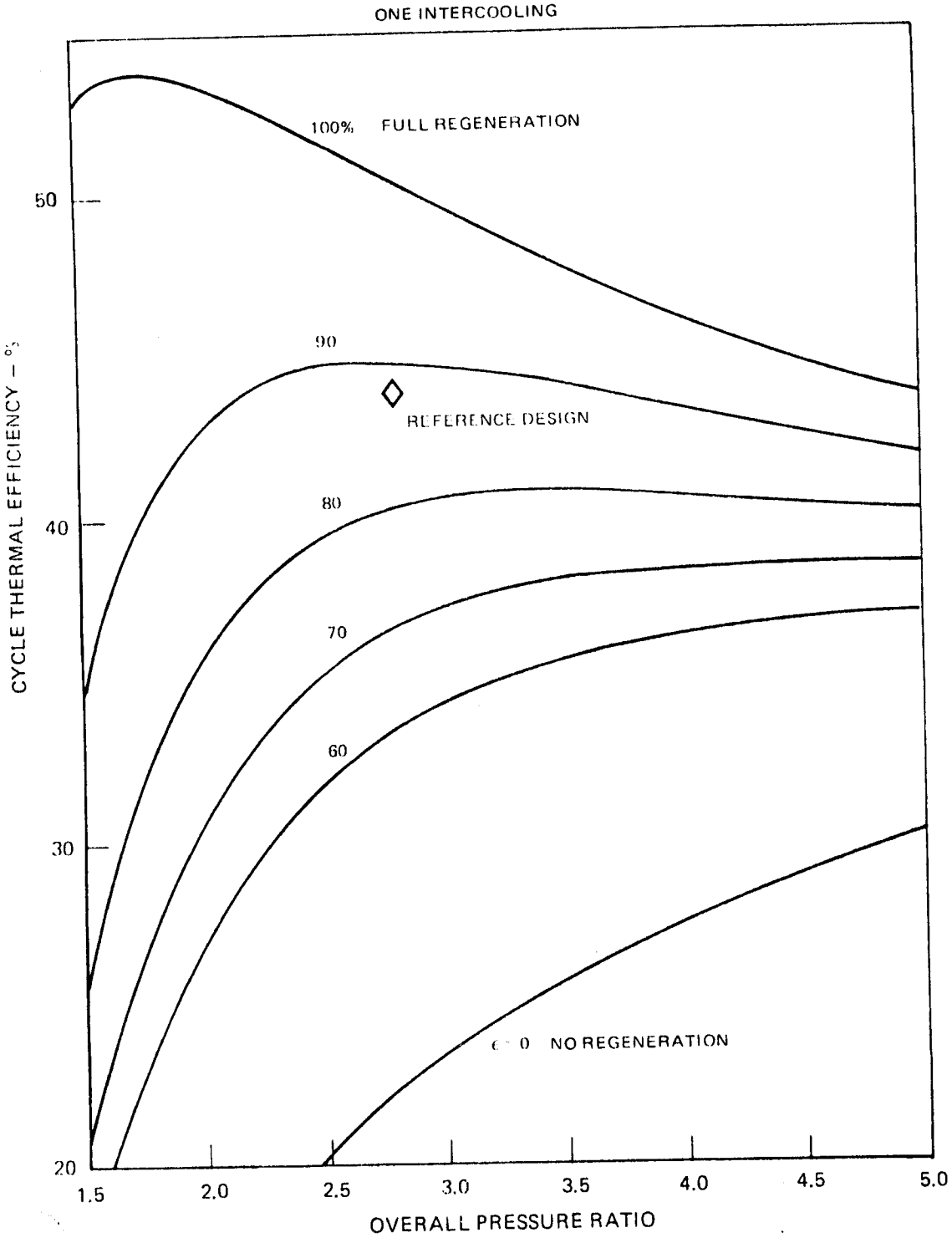

R07-30-3

FIG. 10

THE EFFECT OF COMPRESSOR INLET TEMPERATURE ON THE PERFORMANCE OF A CLOSED-CYCLE HELIUM GAS TURBINE

TURBINE INLET TEMPERATURE = 1600F
TURBINE INLET PRESSURE = 1000 PSIA
CYCLE PRESSURE LOSS = 8%
REGENERATOR EFFECTIVENESS = 88%
ONE INTERCOOLING

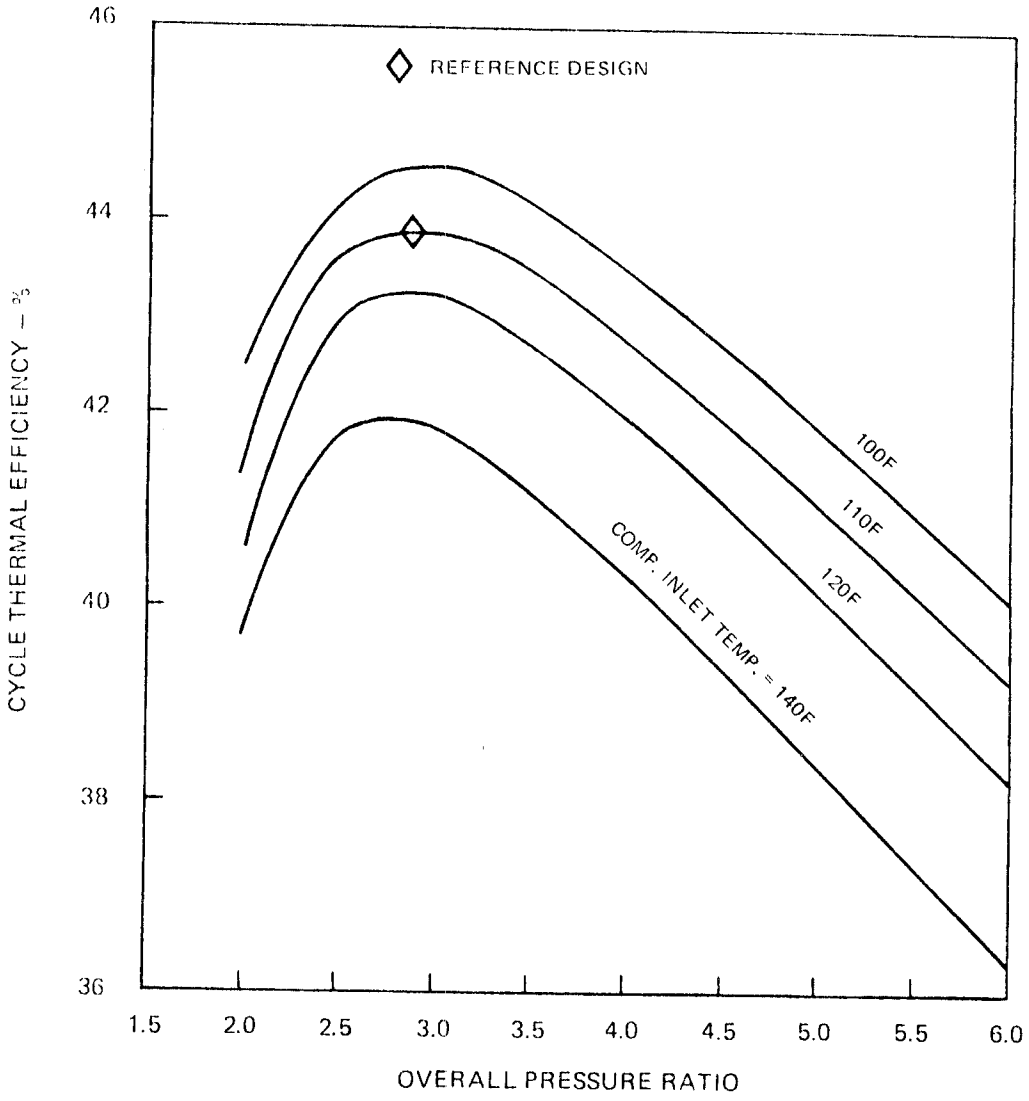

FIG. 11

THE EFFECT OF TOTAL PRESSURE LOSS ON THE PERFORMANCE OF A CLOSED–CYCLE HELIUM GAS TURBINE

TURBINE INLET TEMPERATURE = 1600F
REGENERATIVE EFFECTIVENESS = 88%
COMPRESSOR INLET TEMPERATURE = 110F
SINGLE INTERCOOLING

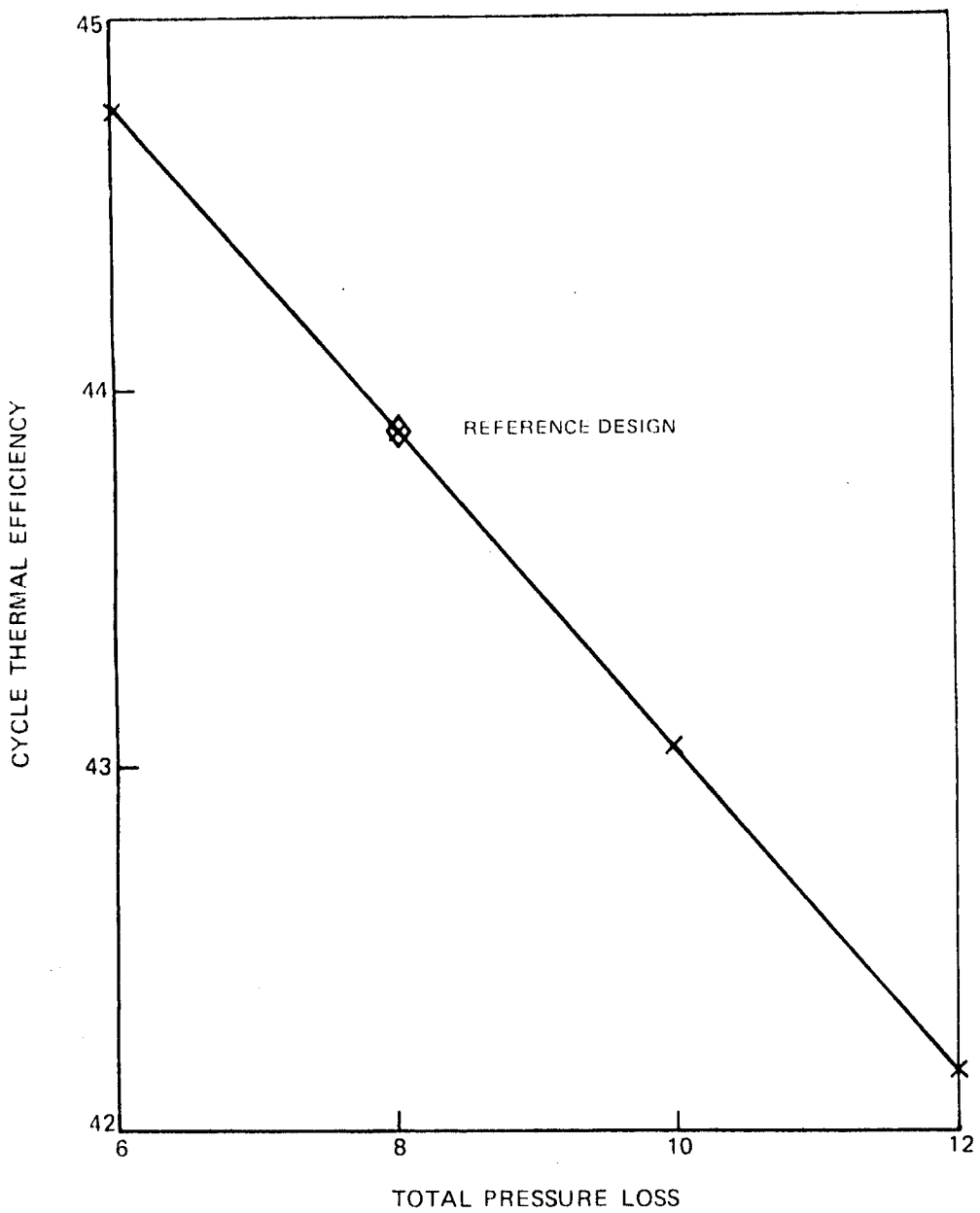

FIG. 12

COMPARISON OF THERMAL DISCHARGE CHARACTERISTICS FOR CLOSED-CYCLE HELIUM GAS TURBINE AND STEAM POWERPLANT

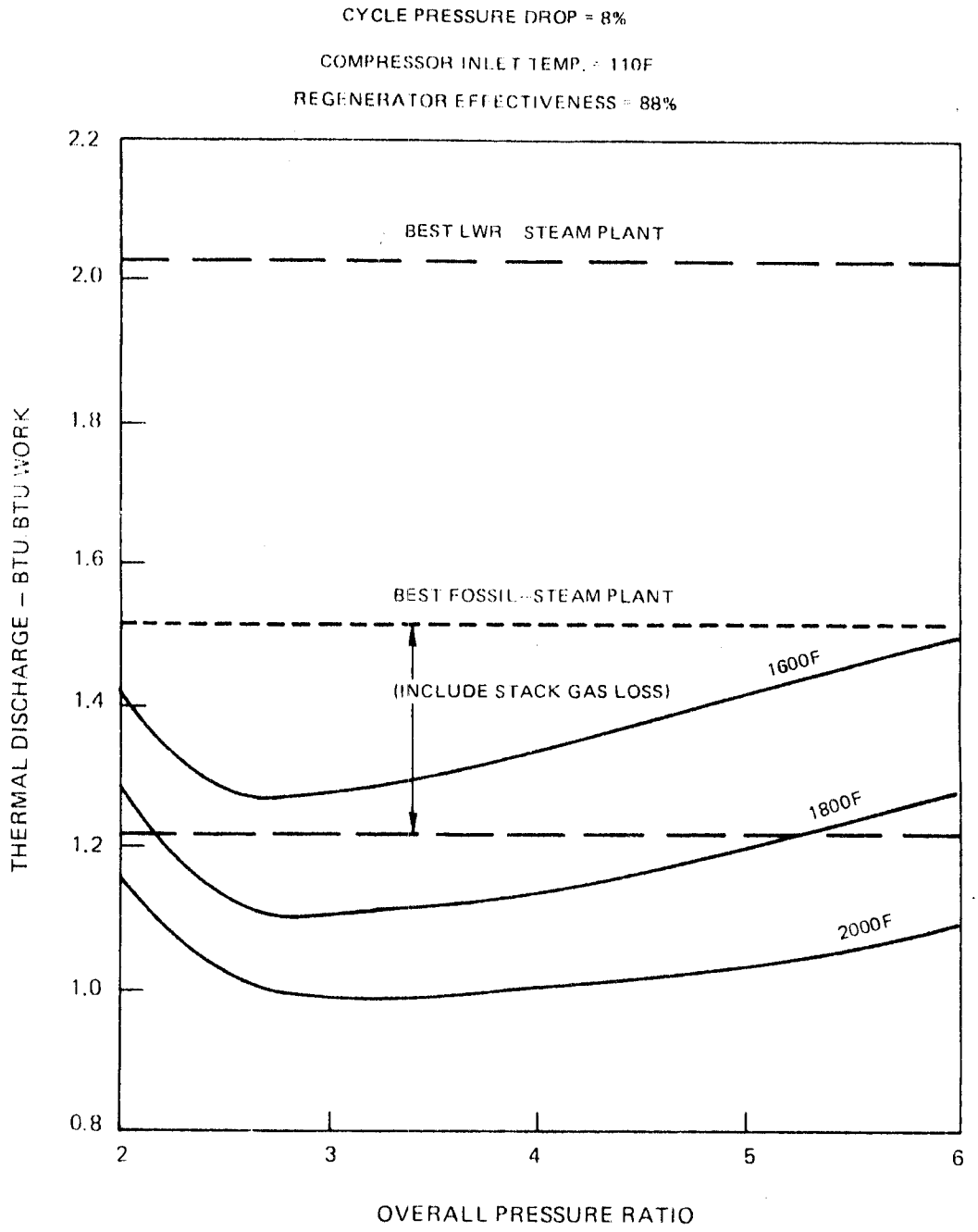

FIG. 13

CLOSED-CYCLE HELIUM GAS TURBINE PERFORMANCE
1600°F TURBINE INLET

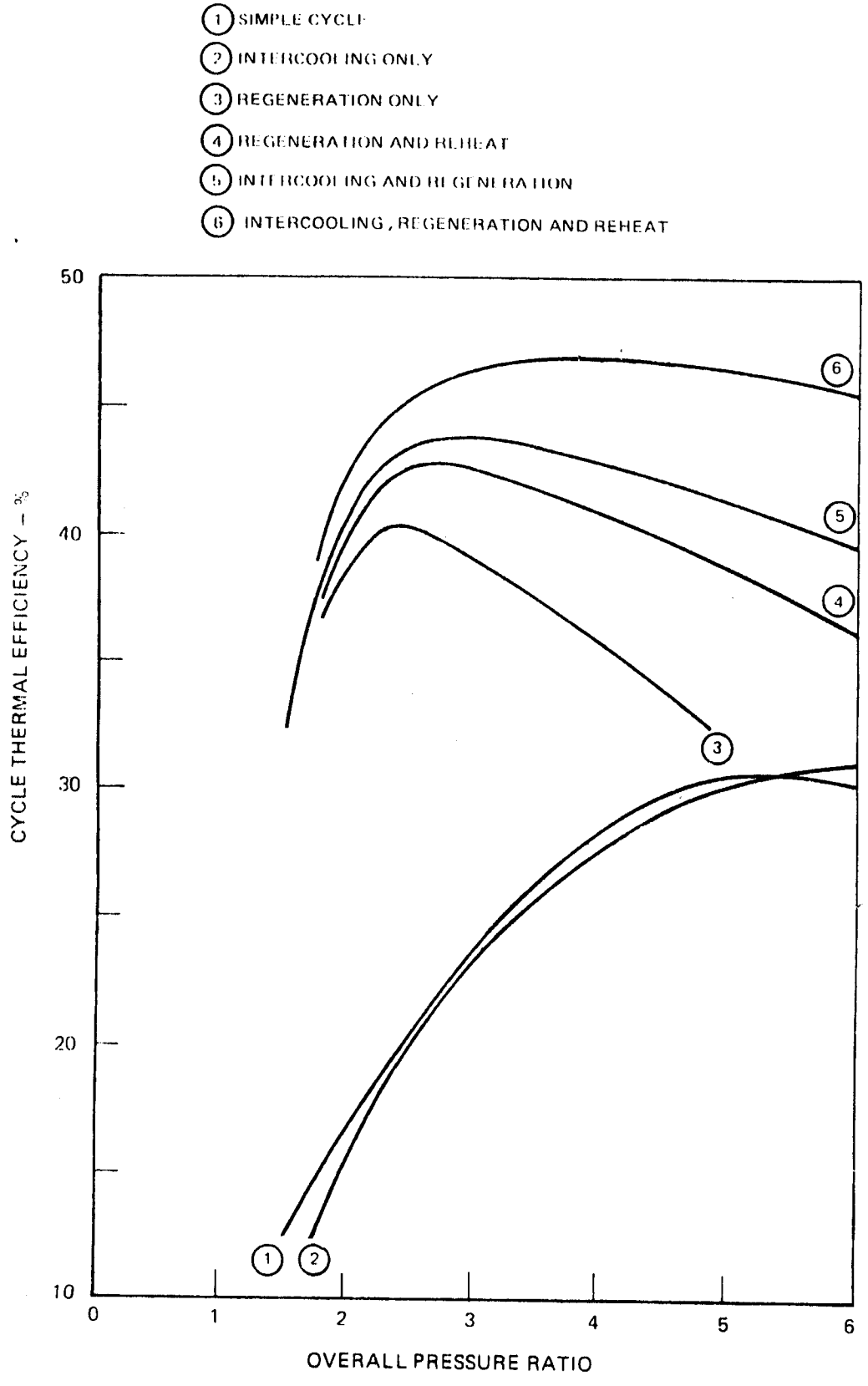

X-D. INTERFACE AND TRADE-OFF STUDIES

A Tokamak fusion power plant can be considered to consist of three major systems: a reactor, a thermal (or alternative) energy storage system, and a power conversion (heat engine-generator) system. The integration schemes for these systems capable of around-the-clock generation will be dependent on the reactor operating cycle and conditions, blanket configuration and capability range, tritium breeding and extraction methods, and the power conversion system characteristics. The types of fluid and their operating conditions in the blanket, heat exchanger loops, and the power conversion system are also important factors which influence the selection of integration schemes.

The crucial problems and critical parameters in integrating the power conversion system with the reactor blanket and the thermal storage system were identified by collating the power system requirements (see Table II) and the cycle parameters (see Table IV) and the results were used in selecting the reference design conditions for the baseline cycle configuration based on considerations given to alleviating the interface problems and trade-offs for the critical integration parameters identified. The major subtasks for this part of the study are summarized in Table V.

Crucial Interface Problems

The concept of two-zone blankets, inner and outer, with different tritium breeding requirements, type of coolant and exit temperatures, thermal power loading, and lifetimes (30 years for inner and 2 years for outer blankets) would certainly complicate the integration of the helium gas turbine power systems with the UWMAK-III fusion reactor. Some of the crucial interface problems for the power conversion systems are summarized in Table VI.

In principle, the inner and the outer blankets can be connected in series, in parallel, or separately with the helium gas turbine power systems. Figure 14 depicts some of the possible integration schemes. It is also possible to operate a reheat cycle with inner and the outer blankets each supplying heat to the low or high-pressure turbine. In any event, use of multiple helium turbines of identical design and power rating would be highly desirable. The final selection of the blanket configurations and capabilities and their integration with the power conversion systems have involved considerable iterations and modifications, and generally represents a compromise between the blanket and power system requirements without seriously penalizing the overall power plant performance.

The decision to have a helium-cooled inner blanket without tritium breeding and a lithium-cooled outer blanket with tritium breeding would mean that use of a primary heat exchanger to enable the containment and primary extraction of tritium within the lithium loop will be imperative (see Fig. 14 left and top diagram). If no intermediate loop is used, then the secondary loop of the primary heat exchanger and

TABLE V

TASK 2 OUTLINE

- Collate Power System Requirements and Cycle Parameters to Identify:
  1. Critical Integration Parameters
  2. Crucial Interface Problems

- Perform System Tradeoff Studies Based on the Critical Integration Parameters

- Analyze Crucial Interface Problems Pertinent to Power Conversion System Design and Operational Characteristics

- Select a Reference Design Conditions for the Baseline Power Conversion System

TABLE VI

CRUCIAL INTERFACE PROBLEMS

1. Integration Scheme (I/O Blanket - HX - CCGTs)
2. Temperature Compatibility
3. No. of CCGT/Unit Capacity
4. Tritium Inventory and Containment
5. Provision for Energy Storage
6. Material (Bimetal) Compatibility
7. Startup and Shutdown (Scheduled and Emergency)
8. Power Level Control
9. Scheduled Maintenance
10. Repairability
11. System Dynamics

FIG. 14

UWMAK–III POWER CONVERSION SYSTEM INTEGRATION SCHEMES

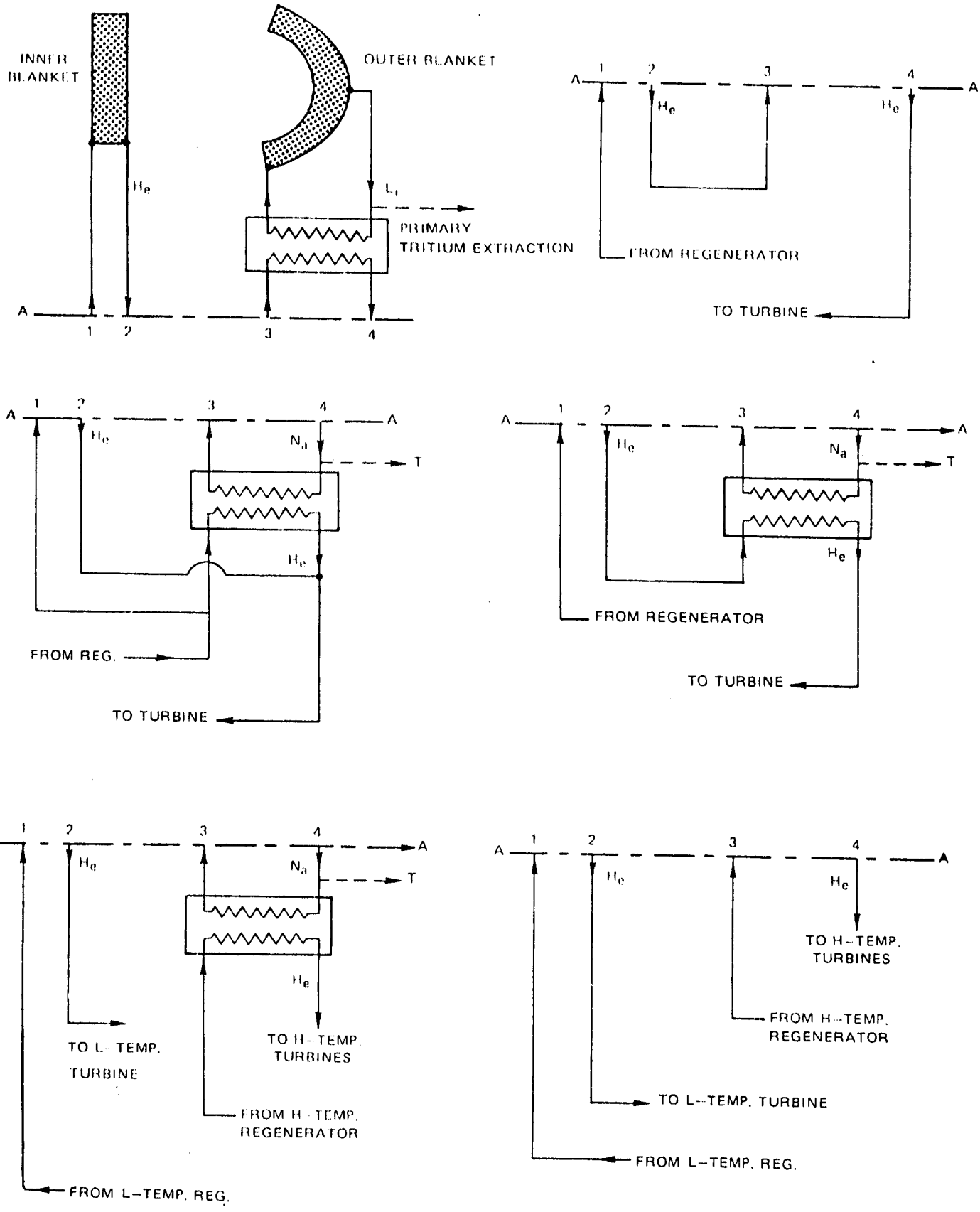

the inner blanket can be connected in series (Fig. 14 right and top), or in parallel (not shown) or separately (Fig. 14 right and bottom) with the helium gas turbine power systems. However, the need for secondary extraction and/or stringent containment of tritium and the need to store thermal energy using a liquid metal would require an intermediate sodium loop at a penalty of increased temperature drop between the lithium coolant and the helium turbine inlet. In this case again, the inner and the outer blankets can be connected in series (Fig. 14 right and middle), in parallel (Fig. 14 left and middle) or separately (Fig. 14 left and bottom) with the helium gas turbine power systems. Since the inner blanket is "clean" from tritium, the separate connection scheme would be generally preferable. In this case, the split between the inner and the outer blanket loading must be controlled such that the number of gas turbine loops and their unit capacity to be selected would be acceptable from the economic and operational points of view.

The temperature compatiblity problem would be more sensitive for the outer blanket power transport and conversion loops than the inner blanket loop. For the latter, it would be a direct-cycle power system, thus the blanket outlet temperature is the same with the turbine inlet temperature and the regenerator outlet temperature (high-pressure side) is identical with the inner blanket inlet temperature. Therefore, the selection of the inner blanket temperature (and thus the regenerator outlet) has to satisfy both the power cycle requirement and a reasonable helium flow rate compatible with heat transfer design based on the thermal power loading of the inner blanket. While these considerations must also be given in selecting the lithium and helium temperatures for the outer blanket power systems, additional interface considerations are required to select the temperature drops from lithium to sodium and from sodium to helium in such a way that the penalty on the power cycle performance (through decrease in turbine inlet temperature) will be minimized and that the primary and secondary heat exchanger sizes will be reasonably small. Figure 15 shows the relation of these heat transfer and working fluid temperatures.

It must be mentioned that since the heat exchangers and the thermal storage systems which link the blankets and the power conversion systems are not part of this study, only their potential impact and relevance to the power conversion system analysis and conceptual design have been considered.

The material compatibility is another serious interface problem for the UWMAK-III fusion reactor power plant. Since TZM has been selected as the structural material for the blankets, somewhere between the blankets and the power conversion system there exist bimetal junctions from TZM to conventional superalloys. The severe failure problems for the bimetal junction particularly in the liquid metal environment have been encountered in previous studies (Ref. 9). Again, since the material problems are not part of this study, no further discussion is given here.

FIG. 15

UWMAK–III FUSION POWER SYSTEM HEAT TRANSFER AND WORKING FLUIDS TEMPERATURE COMPATIBILITY

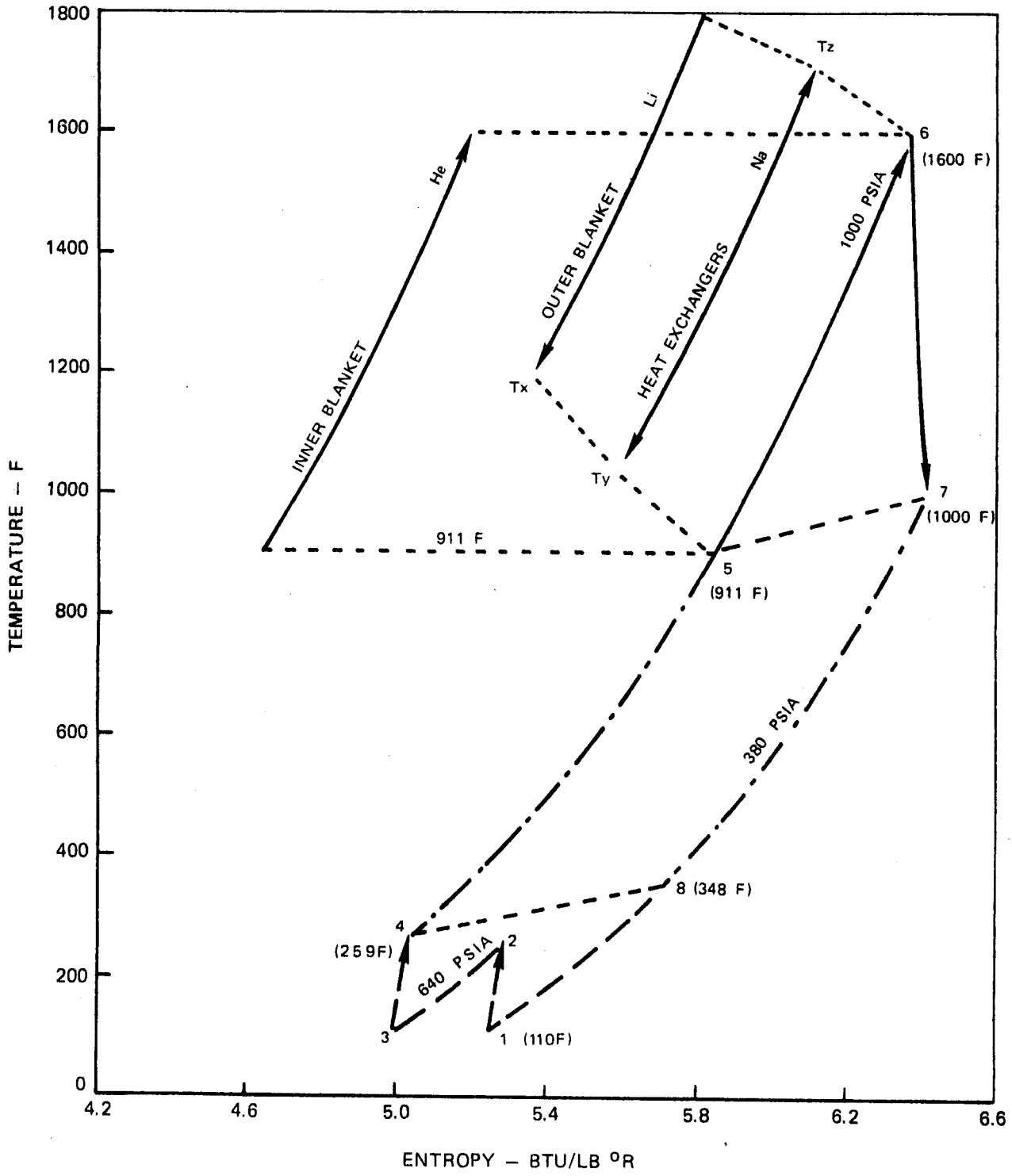

R10–106–1

Critical Integration Parameters

While each of the power cycle parameters, identified in Table IV, directly influence the performance of the helium gas turbine power system, selection for some of these parameters will be constrained because they either constitute the direct physical link between the power conversion systems and the reactor (with or without heat exchangers) or significantly influence the trade-offs required of the power conversion systems. The turbine inlet temperature and pressure, and the regenerator high-pressure-side outlet temperature, are the only three thermodynamic properties seen by the reactor blankets; thus they are important integration parameters. Although the helium flow (rate) also provides a direct link, it is not an integration parameter because its magnitude is determined by the above three integration parameters for a given power rating. The regenerator effectiveness and the overall cycle pressure ratio are indirect parameters. Table VII summarizes these critical integration parameters, the trade-offs required, and the physical constraints imposed in selecting their values.

Because the blanket outlet temperature is always higher or at least equal to the turbine inlet temperature and furthermore the blanket materials are exposed to extreme neutronic and other radiation environment, the limitation on the turbine inlet temperature would most likely to come from the blanket material capability rather than the turbomachinery technology. While the same constraints would also apply in selecting a higher turbine inlet pressure for higher heat transfer coefficient and smaller turbomachinery and heat exchanger sizes, use of excessively high helium pressure could require advanced seals technology for the gas turbines. Since the regenerator outlet temperature directly influences the blanket inlet temperature and thus the coolant flow rate, it could be constrained by the blanket heat transfer capability and limitation on one side, and the power cycle pressure ratio and regenerator effectiveness on the other. The regenerator effectiveness, in turn, depends on the performance vs cost trade-off and pressure loss limitations. The overall pressure ratio could be limited by the maximum tip speed of the turbomachinery. All these considerations indicate that the selection of the critical integration parameters will have to be based on consideration of not only the performance-cost trade-offs but also satisfaction of the many physical constraints inherent with the power plant components. Figure 16 shows that for a turbine inlet temperature of 1600 F, the possible regenerator exit temperature will be between 830 F to 1030 F based on an overall pressure ratio between 2.25 and 3.0 and a regenerator effectiveness of 80 to 90 percent. Figure 17 shows the major cycle point temperatures as a function of the overall pressure ratio.

Trade-off Considerations

The turbine inlet temperature which is the most important parameter for the power conversion efficiency is constrained by the blanket coolant outlet temperature and the total temperature drop across the heat exchangers used; for a given blanket coolant exit temperature, a higher turbine inlet temperature can be obtained by using

TABLE VII

CRITICAL INTEGRATION PARAMETERS

Direct	Trade-off	Constraints
TIT	η vs \$	Blanket Outlet Temp. Material Capability
TIP	Size vs \$	Seals, Material Strength Flow Path Heat Transfer
Regenerator Outlet Temp.	- - -	Blanket Inlet Temp. Flow Rate
Indirect		
Regenerator Effectiveness	η vs \$	$\Delta P/P$
Overall Press Ratio	η vs Sp. Power	Critical Tip Speed

FIG. 16

REGENERATOR OUTLET TEMPERATURE RANGE

TURBINE INLET TEMPERATURE = 1600F

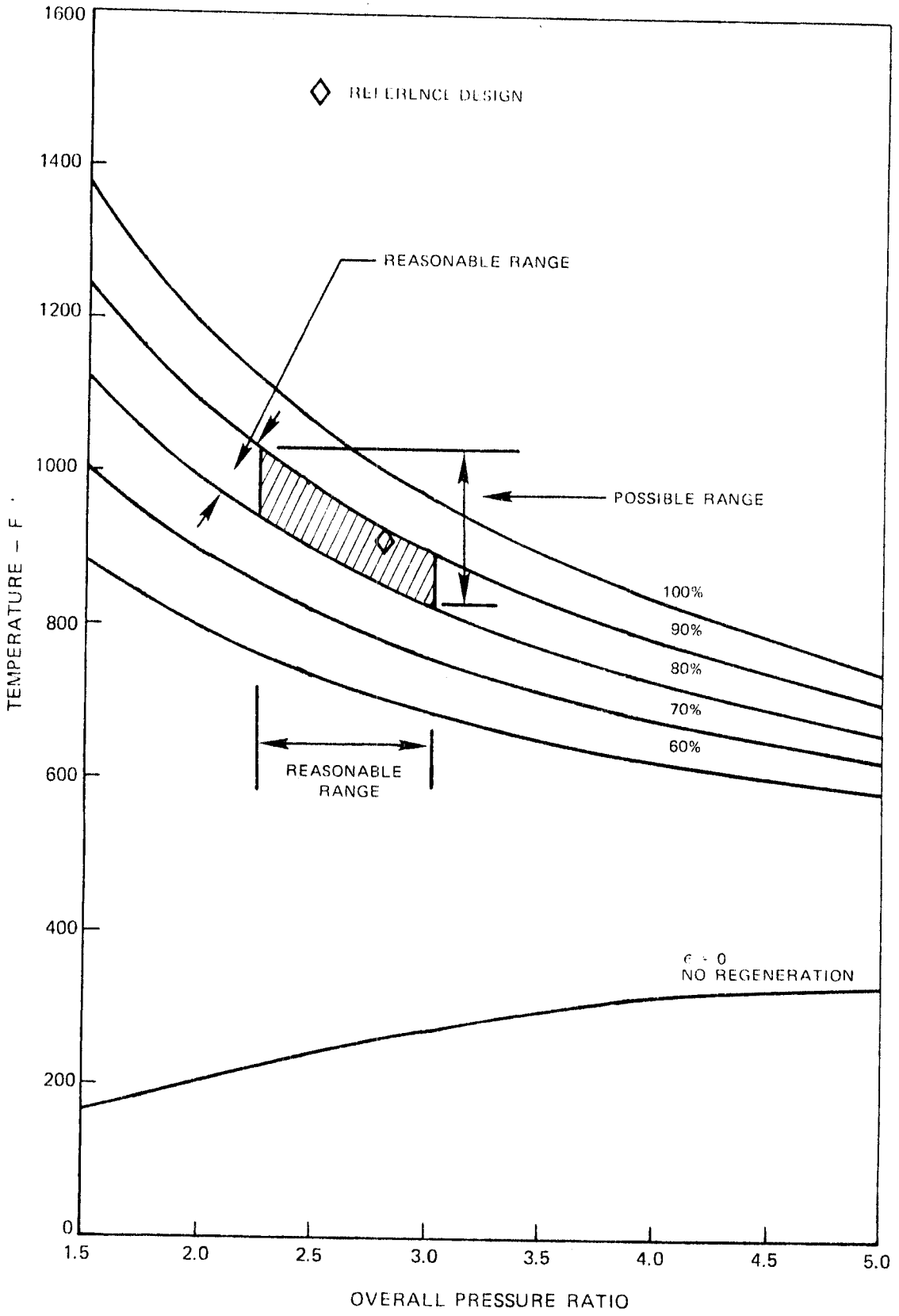

R10–106–4

FIG. 17

TEMPERATURE RANGES FOR THE CRUCIAL CYCLE POINTS

BASELINE CYCLE
REGENERATIVE EFFECTIVENESS = 88%

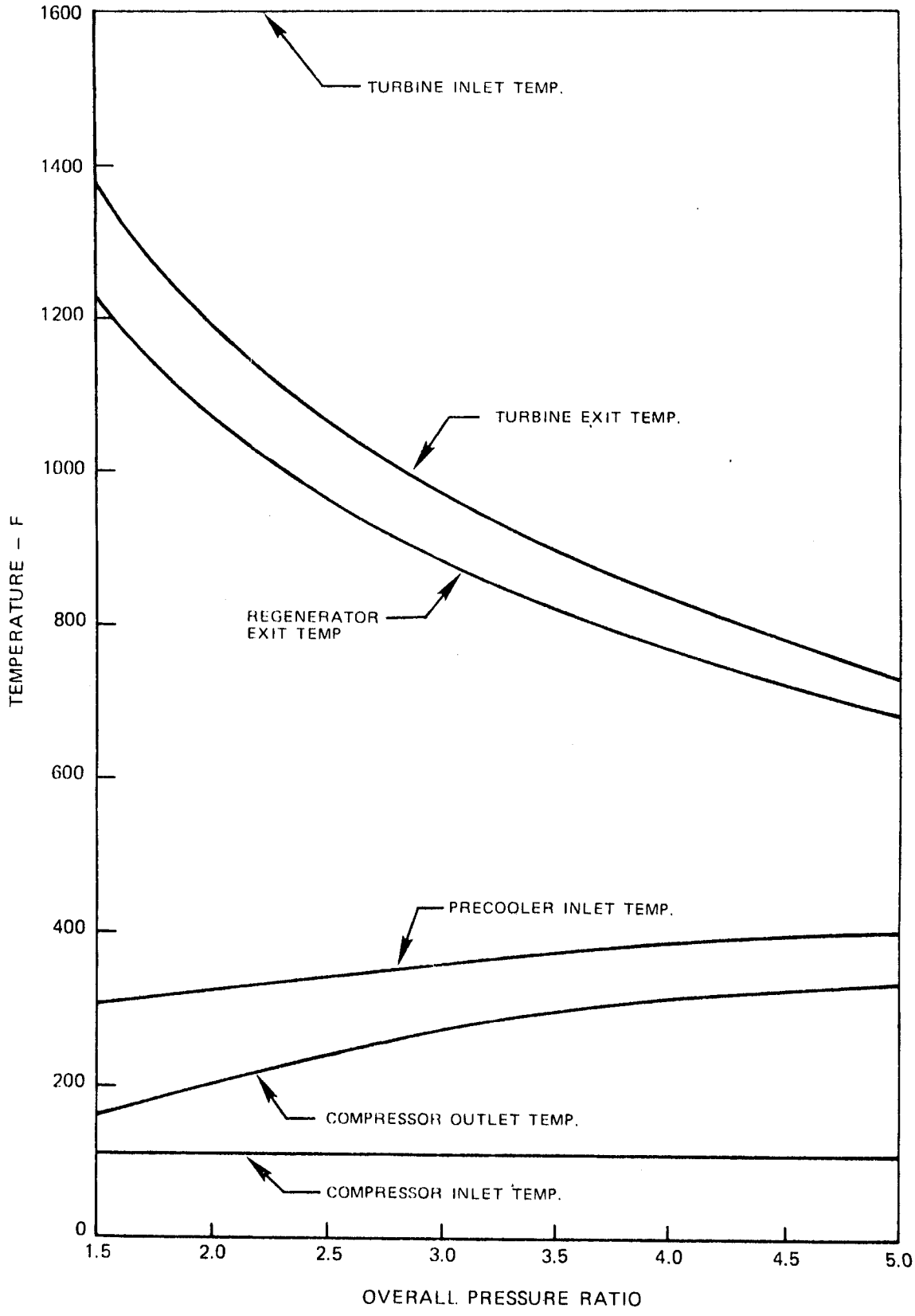

R10-106-8

higher heat exchanger effectiveness (thus larger size), indicating that a trade-off between system performance and heat exchanger cost will be required. This temperature drop is approximately in the 80-200 F range depending on whether an intermediate heat exchanger is used. Note that use of a lithium (blanket coolant) to helium (working fluid) heat exchanger still constitutes a "direct" cycle integration because of the volumetric heat generation within lithium in the blanket by neutron attenuation. However, if tritium breeding is not necessary, such as in the case of the inner blanket, direct integration is desirable not only for achieving the highest power conversion efficiency possible for a given blanket outlet temperature but also for simplicity of integration and possible lower power generation cost.

The thermal efficiency of a closed-cycle gas turbine depends upon many factors. For given maximum and minimum cycle temperatures, the thermal efficiency is dependent on the degree of complexity provided in the system, such as compressor intercooling, regeneration, and reheat. For example, based on a turbine inlet temperature of 1600 F and compressor inlet temperature of 110 F, the cycle thermal efficiencies range from approximately 30 percent for the simple cycle to nearly 47 percent for the most complex cycle with reasonable regeneration (see Fig. 13). These efficiencies are extremely attractive compared to the efficiencies of open-cycle gas turbines operating in the same temperature range. Figure 18 shows that while the cycle thermal efficiency increases almost linearly (reaching a maximum efficiency of about 50 percent at 100 percent regeneration), the regenerator size increases very rapidly with the increase in regenerator effectiveness (particularly for regenerator effectiveness levels above 90 percent), indicating that beyond certain (optimal) regenerator size the incremental regenerator cost is going to more than cancel the economic gain resulting from the thermal efficiency improvement. Past UTRC component and design studies for 100- to 500-Mwe closed-cycle gas turbine power systems indicate that the cycle employing one intercooler and a regenerator between 85 to 90 percent effectiveness without reheat offers the proper balance between capital and operating costs. It must be mentioned that determination of the optimal regenerator effectiveness requires not only the cost information for the regenerator but also the costs of all other power plant components as well as the fuel cost. Estimation of these cost data is not part of the current study, therefore past experience on closed-cycle power system performance and cost characteristics were utilized in selecting a reference-design regenerator of 88 percent effectiveness. Figure 19 shows that this regenerator effectiveness is desirable for the optimal overall pressure ratio of 2.8 for the power conversion system.

Reference Design Conditions

The reference design conditions for the baseline cycle configuration were selected based on the interface problems and preliminary trade-off considerations discussed heretofore. The temperature and pressure for the major cycle points are identified in the cycle flow diagram shown in Fig. 20. The turbine inlet temperature of 1600 F was selected essentially based on projected blanket capabilities with

FIG. 18

THE NEED FOR TRADEOFF BETWEEN THE CYCLE THERMAL EFFICIENCY AND REGENERATOR EFFECTIVENESS

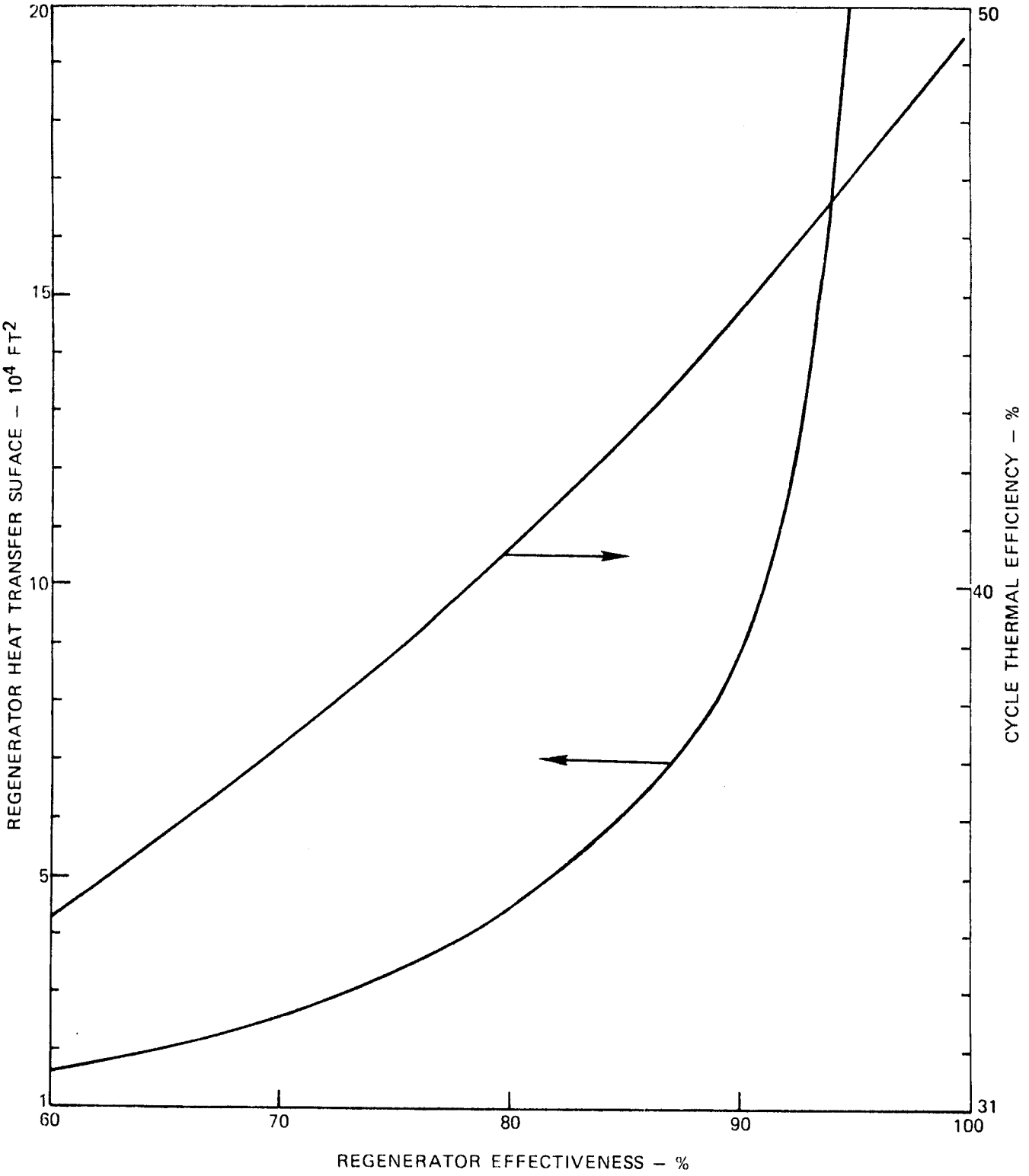

R10–106–5

FIG. 19

EFFECT OF REGENERATOR EFFECTIVENESS ON CYCLE THERMAL EFFICIENCY

TURBINE INLET TEMPERATURE = 1600F
ONE INTERCOOLING

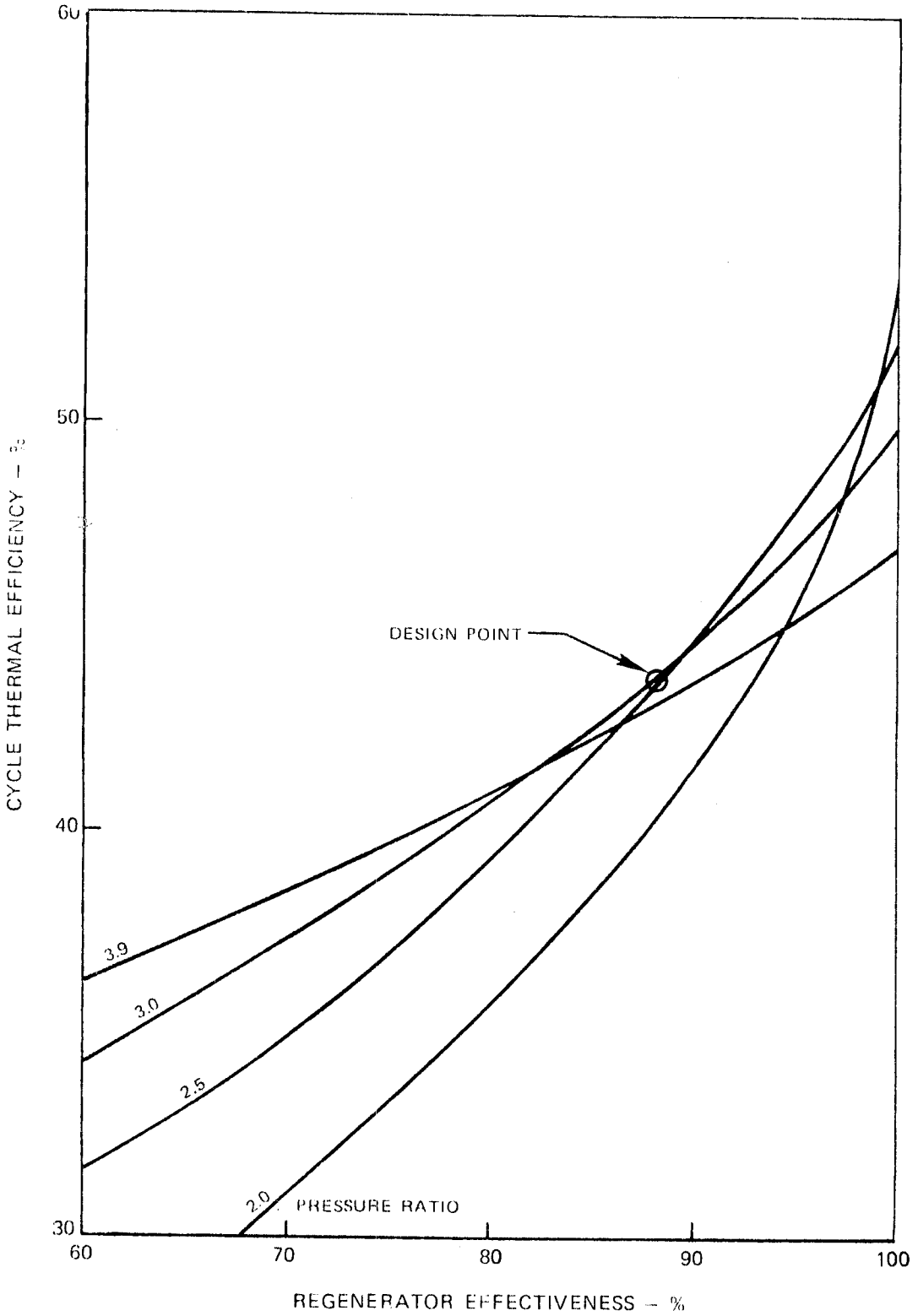

R10-106-10

consideration given to the heat exchanger temperature drops and the projected turbomachinery technology. As pointed out earlier, the limiting factor is the blanket outlet temperature, and thus the selection of turbine inlet temperature involved more system constraints than trade-offs. The compressor inlet temperature of 110 F was selected based on the dry cooling tower requirement and reasonable precooler and intercooler designs; despite the dry tower cooling, use of intercooling for more than three points gain in cycle efficiency is justifiable considering the potential saving in power generation cost over the lifetime of the fusion plant vs the capital cost of the intercooler.

The selection of the turbine inlet pressure is largely based on component sizes and heat transfer considerations. As will be mentioned later, use of 1000 psia inlet pressure was mandatory for a turbomachinery unit capacity in the 500- to 600-Mwe range. The overall pressure ratio of 2.8 (or 2.6 for turbine) was selected for a maximum cycle efficiency, and the intercooling pressure was selected so that the compressor work required will be a minimum. The regenerator effectiveness of 88 percent represents a compromise to accommodate the integration constraints yet generally provide a balance between the system performance and costs. Based on the operating conditions specified in Fig. 20, the cycle efficiency was estimated to be 43.9 percent, thus allowing an overall plant efficiency of approximately 40 percent.

REFERENCE–

DESIGN CLOSED–CYCLE HELIUM GAS TURBINE SYSTEM FOR UWMAK–III FUSION PLANT

THREE LOOPS NEEDED

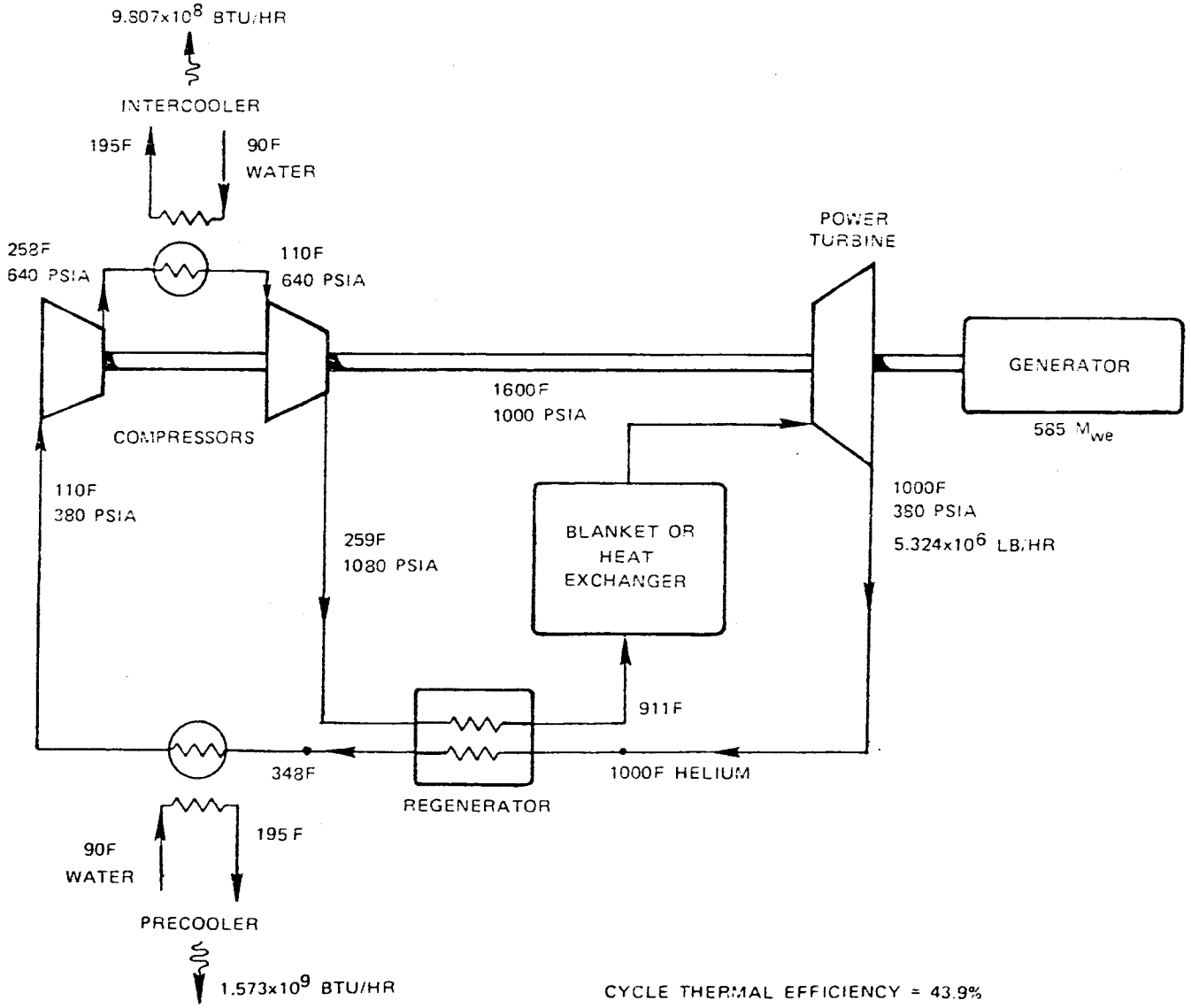

CYCLE THERMAL EFFICIENCY = 43.9%

X-D-15

FIG.20

R10–114–2

X-E. CONCEPTUAL DESIGN OF SYSTEM COMPONENTS

This part of the report summarizes the results of the Task 3 study (see Table VIII) for conceptual design of power conversion system components based on the reference design conditions and the integration scheme selected earlier. As indicated in Fig. 2, the power system layout is not part of this study, as such the possible arrangement of the power conversion components as integral part of the UWMAK-III fusion powerplant has not been investigated. However, a preliminary conceptual power systems layout diagram was prepared, based on a preliminary drawing obtained from Bechtel, to indicate the relative location of the power conversion systems with respect to the reactor plant, including approximate power plant dimensions.

System Arrangement

The UWMAK-III fusion power plant can be considered to consist of three systems: the reactor system, the heat exchange/thermal storage system, and the power conversion system. While the current study is concerned only with the power conversion system, the system arrangement to integrate the reference-design helium gas turbine systems (as depicted in Fig. 20) with the reactor blankets directly and through heat exchangers is briefly discussed here.

In designing the power system arrangement (not layout), the first question to be answered was the number of power conversion loops needed and the unit capacity for each loop. Every effort was made to utilize multiple units of a standardized power conversion system arrangement to benefit component capital cost reduction as well as easy operation, maintenance, and repair. However, attempts were also made to avoid use of too many units of small power output. A major disadvantage of the multiunit arrangement is the complex governing and valving systems needed to run individual turbomachinery. Therefore, the total number of branched turbomachinery units should be limited to 3 or 4, if possible. First glance at the thermal power rating of the UWMAK-III fusion reactor at 5000 Mwt would suggest that between 3 and 6 units of helium turbomachinery would seem appropriate. Further examination of the inner (helium) and outer (lithium) blankets temperature capabilities and possible thermal power split would narrow down the number of inner and outer blanket turbomachineries to 1+2, 1+3, 2+4, and 2+6, using a direct-cycle for the inner blankets. After more detailed examination on blanket and turbomachinery design characteristics, the 1+2 system arrangement using three identical 585-Mwe power conversion systems was selected, primarily based on the projected turbomachinery technology, and economic considerations.

TABLE VIII

TASK 3 OUTLINE

Select Power System Arrangements

Perform Conceptual Design to Estimate Physical Sizes for the Major Power System Components

Prepare Conceptual Power Systems Layout

The finalized system arrangement for the UWMAK-III fusion power plant is shown in Fig. 21. During each of the 30 minutes "burntime", the No. 1 and 2 power conversion systems will draw thermal energy from the outer blanket through the primary (lithium to sodium) and the secondary (sodium to helium) heat exchangers at a turbine inlet temperature of 1600F, while the No. 3 power conversion system will be integrated directly with the inner blanket thus also operating at the same 1600F turbine inlet temperature. During this burn time, the sodium thermal storage system will be "charged" to store sufficient thermal energy to operate all three power conversion systems during the subsequent 1.5 minute "downtime". During the downtime, thermal storage system will be "discharged" through the same sodium-helium heat exchanger to operate the No. 1 and 2 power loops and a separate sodium-helium heat exchanger to operate the No. 3 unit. Although extraction of tritium will take place primarily in the lithium loop, any stringent restriction on tritium level in the power conversion systems could require additional tritium extraction in the sodium intermediate loop. Operating temperatures and flow rates for key points in the inner and outer blanket heat transfer loops are also identified in Fig. 21.

Component Design

The results of design studies for the major power conversion system components, including the turbomachinery, the regenerator, the precooler and intercooler, and the piping systems which interconnect these components with the reactor are presented in the following sections. Past experience with turbomachinery and heat exchanger designs was utilized extensively in this part of the study.

Turbomachinery

One of the principal advantages for the closed-cycle helium gas turbine is its relatively small size; the helium turbomachinery is very compact compared to both open-cycle gas turbine and steam turbine, and its unit capacity can be many times larger than the open-cycle gas turbines which are currently limited to about 100-Mwe per unit. The principal reasons for this size advantage include the pressurization of the working fluid, the low (typically between 2:1 and 3:1) optimal pressure ratio, and the absence of tip Mach number constraints due to the very high (over 3000 fps) sonic velocity in the helium medium. The dilemma of excessively long last-stage turbine blades often encountered in steam turbines is less serious in the helium turbine designs. Therefore, there is every incentive to use the highest possible blade tip speed limited only by material strength capability, to minimize the number of stages required for the compressors and the turbine.

UWMAK–III FUSION PLANT FLOW DIAGRAM

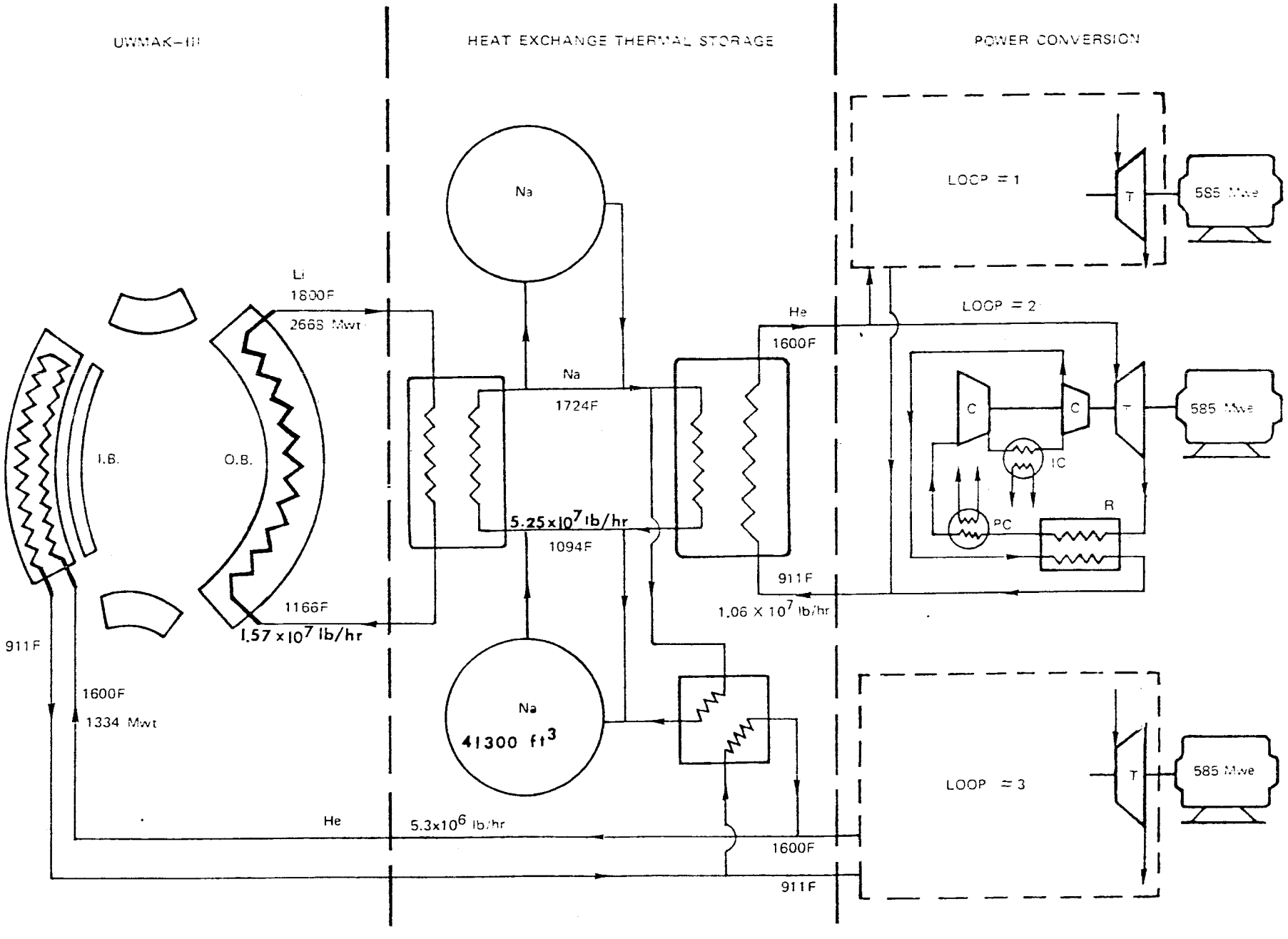

R10–114–4

FIG 21

For a given rotationary speed and operating temperature, the physical size of a turbomachinery is often limited by the maximum diameter of the last turbine stage where the maximum volume flow requires a maximum blade length, thus resulting in maximum stress levels (tensile and bending). In the compressor and turbine blade designs, it is desirable to use the highest possible speed with an optimum hub-to-tip ratio. Since the power turbine speed is fixed by the alternator (typically 3600 rpm), it may be necessary to split the shaft for small turbomachinery units to run the compressor and the high-pressure turbine at the optimum (higher) speed. Such is the case with the double-shaft turbomachinery configuration shown in Fig. 22. This turbomachinery configuration has the disadvantage of requiring bypass control to prevent power turbine overspeed in case of loss of external load, but has the advantage of using the starting motor to maintain the helium circulation in case the power turbine has to be shut down. For the larger turbomachinery units, however, the optimum speeds for the compressors become lower, and past experience indicates that for unit capacities of about 200-Mwe and larger, the single shaft configuration, as shown in Fig. 22, is preferable. In some cases, use of double-flow turbine may be necessary (particularly for low-pressure unit) to accommodate the large volume flow in a single shaft turbomachinery design. Single-shaft turbomachinery designs as large as 1200-Mwe rating (Ref. 10) have been reported and there seems to be no inherent mechanical limitation for such large turbomachinery.

Based on the foregoing discussions, the reference design 585-Mwe turbomachinery (3 needed) for the UWMAK-III fusion power plant was based on a single-shaft, single-flow configuration at 3600 rpm shaft speed. This single-shaft turbomachinery can be coupled directly to the alternator to avoid overspeed, and generally represents a fairly compact design without serious penalties in the performance of the compressors. Generally speaking, the turbomachinery can be designed for either maximum efficiency or maximum output (per unit weight or volume) or somewhere between. The current design is for maximum efficiency based on 50 percent reaction at the mean diameter and a flow coefficient of approximately 0.5. Based on the unit capacity and rpm specified, the current design using one intercooler is regarded as the best compromise satisfying the power plant requirements and constraints summarized in Table II.

The design data for the turbomachinery are summarized in Table IX, and Fig. 23 depicts the turbomachinery structure, including the arrangement of compressors and turbine, bearings and seals, and the overall dimensions. While conventional seals are regarded as sufficient for internal sealing, hermetic seals may be needed for the end seals. Because of the large flow area required at the turbine exit, an axial-flow flange design was adopted. The turbomachinery has the unique cost saving feature of employing the same constant hub diameter for the turbine and the compressors, all on the single shaft. The maximum diameter and blade length are

ALTERNATIVE HELIUM TURBOMACHINERY CONFIGURATIONS

ONE INTERCOOLING

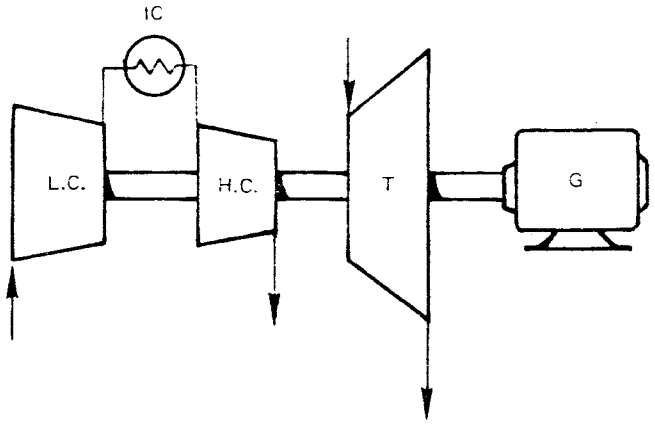

SINGLE SHAFT

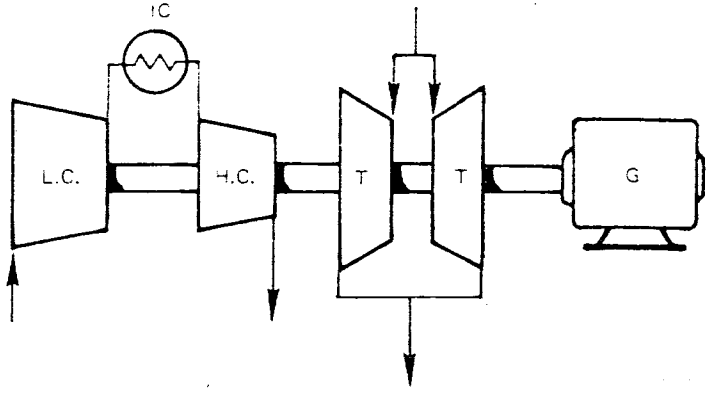

SINGLE SHAFT
(DOUBLE-FLOW TURBINE)

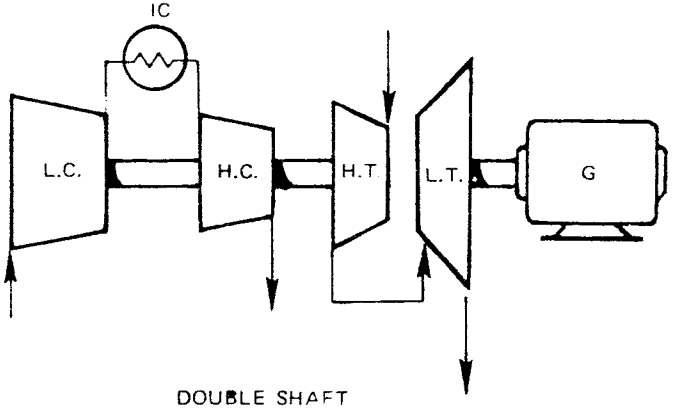

DOUBLE SHAFT

X-15-6

FIG. 2.2

R10-114-5

TABLE IX

CLOSED-CYCLE GAS TURBINE TURBOMACHINERY SUMMARY

Reference Design

585-Mwe Unit Output (3 units needed)

	Low Compressor	High Compressor	Turbine
Inlet Temperature - F	110	110	1600
Outlet Temperture - F	258	259	1000
Inlet Pressure - psia	380	640	1000
Outlet Pressure - psia	640	1080	380
Pressure Ratio	1.68	1.69	2.63
Efficiency (Adiabatic) - %	89	89	91
Number of Stages	10	10	9
Work per Stage - Btu/lb	18.6	18.9	75.1
Helium Flow - lb/sec	1472	1472	1472
Hub Diameter - in.	65	65	65
Inlet Tip Diameter - in.	79.7	73.9	79.8
Outlet Tip Diameter - in.	76.1	71.8	92.8
Wheel Speed, Hub - ft/sec	1021	1021	1021
Maximum Tip Speed	1251	1160	1458
Shaft Speed - rpm	3600	3600	3600

FIG. 23

R10-106-7

CLOSED-CYCLE HELIUM GAS TURBINES FOR UWMAK-III FUSION PLANT

585 MWe UNIT OUTPUT, 3 NEEDED

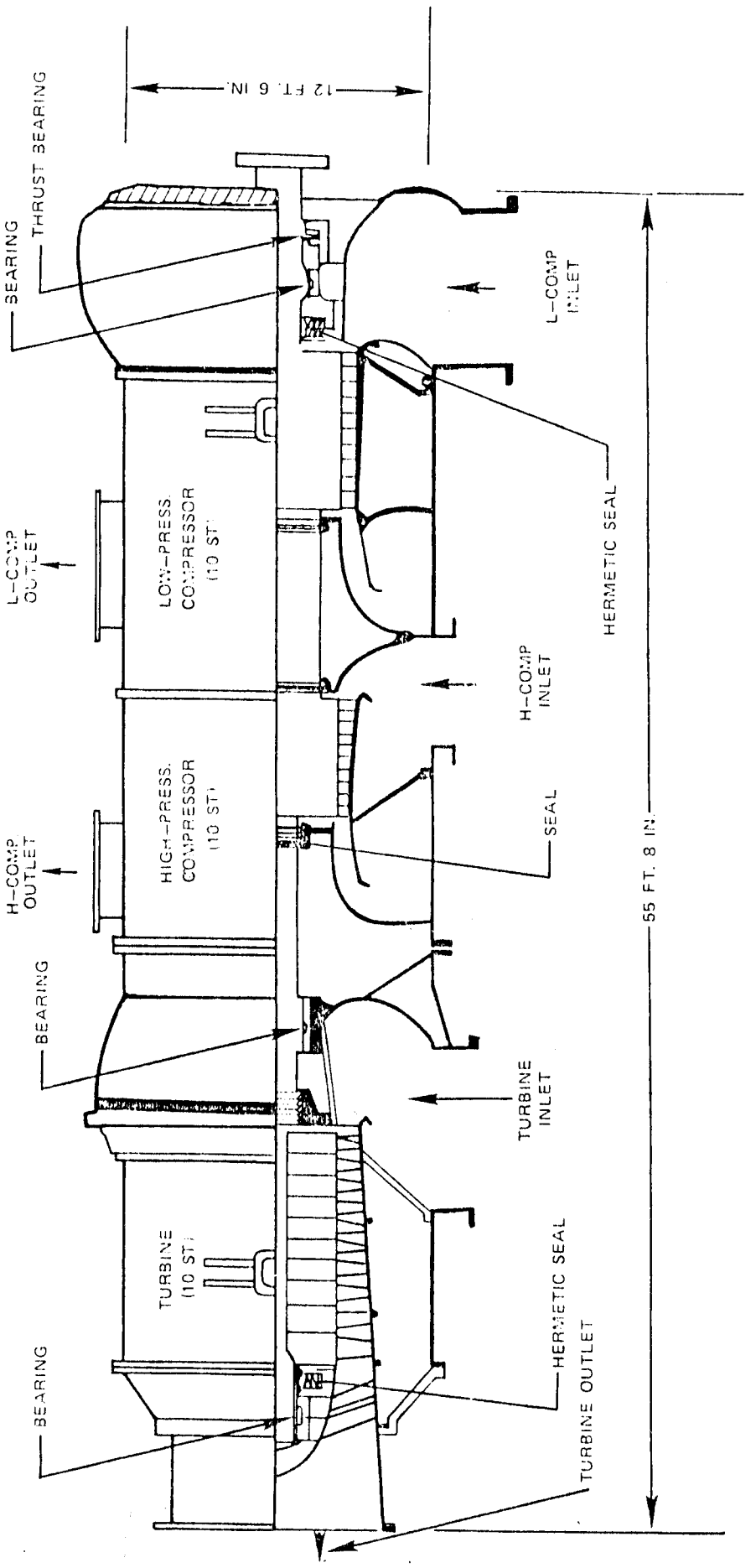

92.8 and 13.9 inches, respectively, and the stresses resulting from these configurations are regarded as well within the projected material capabilities.

The overall dimensions of the UWMAK-III helium turbomachinery is compared with the open-cycle FT4 and FT50 gas turbines and the 264-Mwe helium gas turbine designed for the high-temperature gas-cooled reactor, as shown in Fig. 24. It is seen that the 585-Mwe UWMAK-III helium turbomachinery is only slightly larger than the 88-Mwe FT50 open-cycle gas turbine.

Regenerator

The cost of a regenerator or any other heat exchanger increases with the increase in heat transfer surface area and operating temperature, and the complexity of fabrication. Use of reasonably high pressure helium is beneficial because of its excellent heat transfer coefficient (thus reduced heat transfer area) and high density (thus reduced flow area). For these reasons, the regenerator size for the closed-cycle helium gas turbine power system is more manageable than that for open-cycle air gas turbine systems. Some of the more crucial design parameters for a regenerator design include 1) effectiveness (thus size), 2) pressure loss, 3) flow pass configuration, 4) type of heat transfer surface (finned or unfinned), 5) material selection, and 6) fabricability.

Since the heat transfer coefficients are not too different between the high- and low-pressure sides, straight unfinned tubes were selected to provide the basic heat transfer surface to minimize hot- and cold-side pressure losses. Based on the operating conditions for the regenerator as defined in Fig. 20, preliminary design studies showed that a simple counter flow regenerator with a single tube-pass would offer a good compromise between performance and cost, particularly by utilizing standardized heat exchanger modules. The heat exchanger module which is somewhat similar to the fuel element concept used in the light water reactors will consist of 100 small heat transfer tubes arranged at one-inch pitch inside a 10-inch by 10 inch rectangular can, as shown in Fig. 25. The tube bundle merges to a single "connector" tube at both ends of the heat transfer element. The heat transfer elements are then stacked up inside the regenerator shell while the connector tubes are welded to the inlet and outlet headers, as shown in Fig. 26. The high-pressure "cold" helium will flow inside the tubes while the low-pressure "hot" helium will flow outside the tube bundles, through the heat exchanger cans, inside the regenerator shell. The physical dimensions for the heat exchanger element are also tabulated in Fig. 25. The inner tube diameter was selected to yield a hot/cold fluid flow area ratio of approximately 3 to achieve similar velocities for helium flows inside and outside the tube bundles. However, the helium flow velocities commensurate with the pressure drop allowed for a given heat transfer surface requirement would have to be governed by selection of an appropriate number of heat transfer elements (thus shell diameter) and length combination.

Fig. 24

OPEN-AND CLOSED-CYCLE TURBOMACHINERY SIZES

FT4

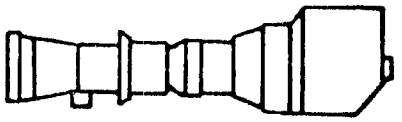

27 Mw

HTGR-CCGT

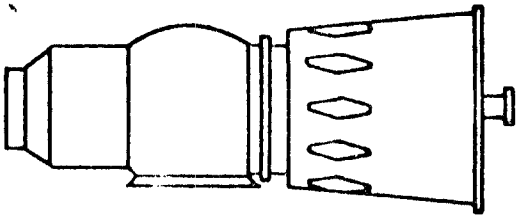

264 Mw

FT50

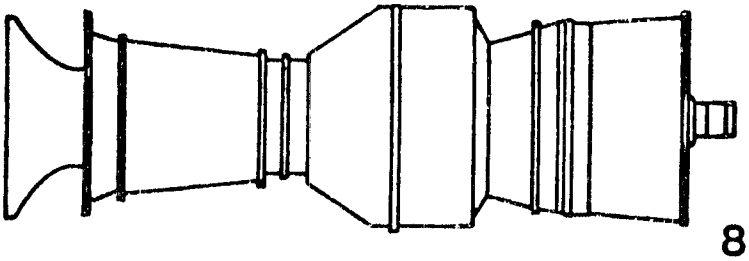

88 Mw

UWMAK-III

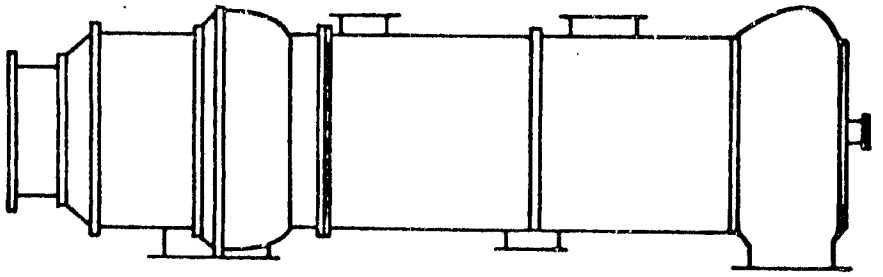

585 Mw

FIG. 25

HEAT EXCHANGER ELEMENTS FOR REGENERATOR, PRECOOLER AND INTERCOOLERS

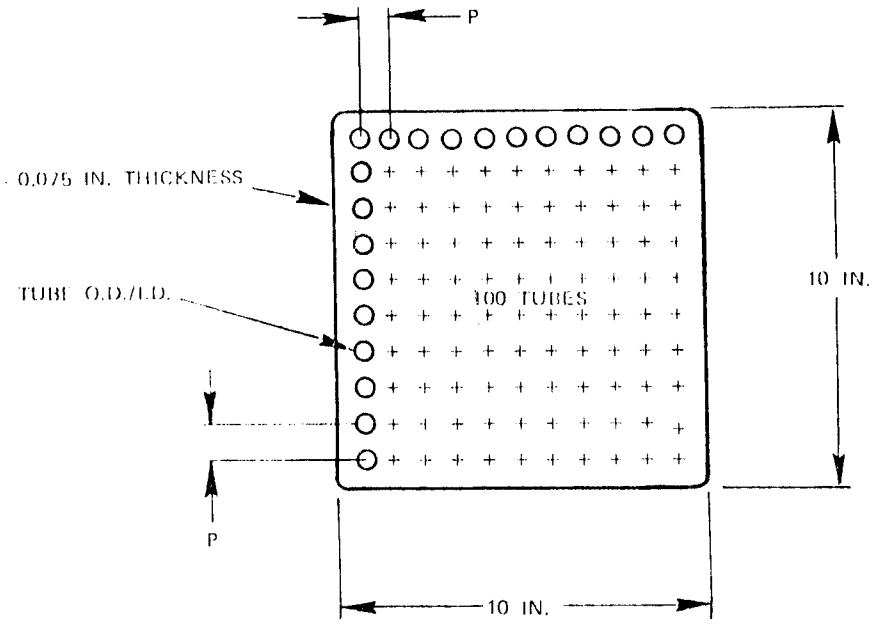

BASIC GEOMETRY

	REGENERATOR	PRECOOLER AND INTERCOOLER
TUBE O.D./I.D., IN.	0.625/0.545	0.5/0.37
TUBE THICKNESS, IN.	0.04	0.065
PITCH, P, IN.	1.0	1.0
NO. OF TUBES PER ELEMENT	100	100
TUBE CIRCULAR PERIPHERY, FT OUTER/INNER	0.1636/0.1427	0.1309/0.0969
TOTAL CIRCULAR PERIPHERY, FT OUTER/INNER	16.36/14.27	13.09/9.69
TOTAL FLOW AREA, FT^2	0.00162	0.0007467
TOTAL TUBE FLOW AREA, FT^2	0.162	0.07467
EXTERNAL FLOW AREA, FT^2	0.4814	0.5581
RATIO OF OUTER/INNER FLOW AREA	2.97	7.47

The reference-design regenerator has an inner shell diameter of 13 feet and an overall shell length of 75 feet; the effective tube length is 58 feet, as shown in Fig. 26. The details of the regenerator design data are summarized in Table X. The regenerator would require 150 heat exchanger elements which would result in reasonable pressure loss for the helium flow rate required. Since the maximum temperature in the regenerator is only 1000F at the hot gas inlet, one of the moderate-priced superalloys may be used. Because of the simple counter flow configuration, thermal gradient will be essentially in the longitudinal direction only, thus the thermal stress in the header and the tube bundle will not be excessively serious.

Precooler and Intercooler

The general design concept of the regenerator is also applicable to the precooler and intercooler, except that smaller tubes will have to be used to yeild an outer/inner (i.e., helium/water) flow area ratio of about 7.5; the tube diameter in this case will be 0.37 inch instead of 0.545 inch for the regenerator design. The heat exchanger element design data for the precooler as well as the intercooler are tabulated in Fig. 25. Cooling water inlet temperature of 90F and outlet temperature of 195F were used for both the precooler and the intercooler. In order to prevent local boiling of cooling water, pressurization would be necessary. However, the cooling water pressure must be maintained below the helium pressure so that in the event of tube leak, no moisture will leak into the helium loop. Table X also summarizes the design data for the precooler and the intercooler, and their shell diameters, effective tube lengths, and overall shell lengths are shown in Fig. 27 for comparison with the regenerator. Because of the relatively low operating temperature range (below 350F), a low-cost carbon steel or pipe steel can be used for the construction of precooler and intercooler.

Piping Systems

The piping system sizes for connecting the power conversion system components were estimated based on reasonable flow velocities for the flowing fluid at the existing temperature and pressure. The results are tabulated in Table XI. The layout of the power system components must be arranged to reduce the pipe length and minimize the pipe bend not only to reduce the piping cost but also to avoid excessive pressure loss in the piping systems. The largest pipe size required will be 8 feet 10 inches in diameter connecting the turbine exit with the regenerator while the smallest pipe will be 2 feet 6 inches in diameter for cooling water flow to the precooler and intercooler.

FIG. 26

UWMAK-III POWERPLANT REGENERATOR CONFIGURATION

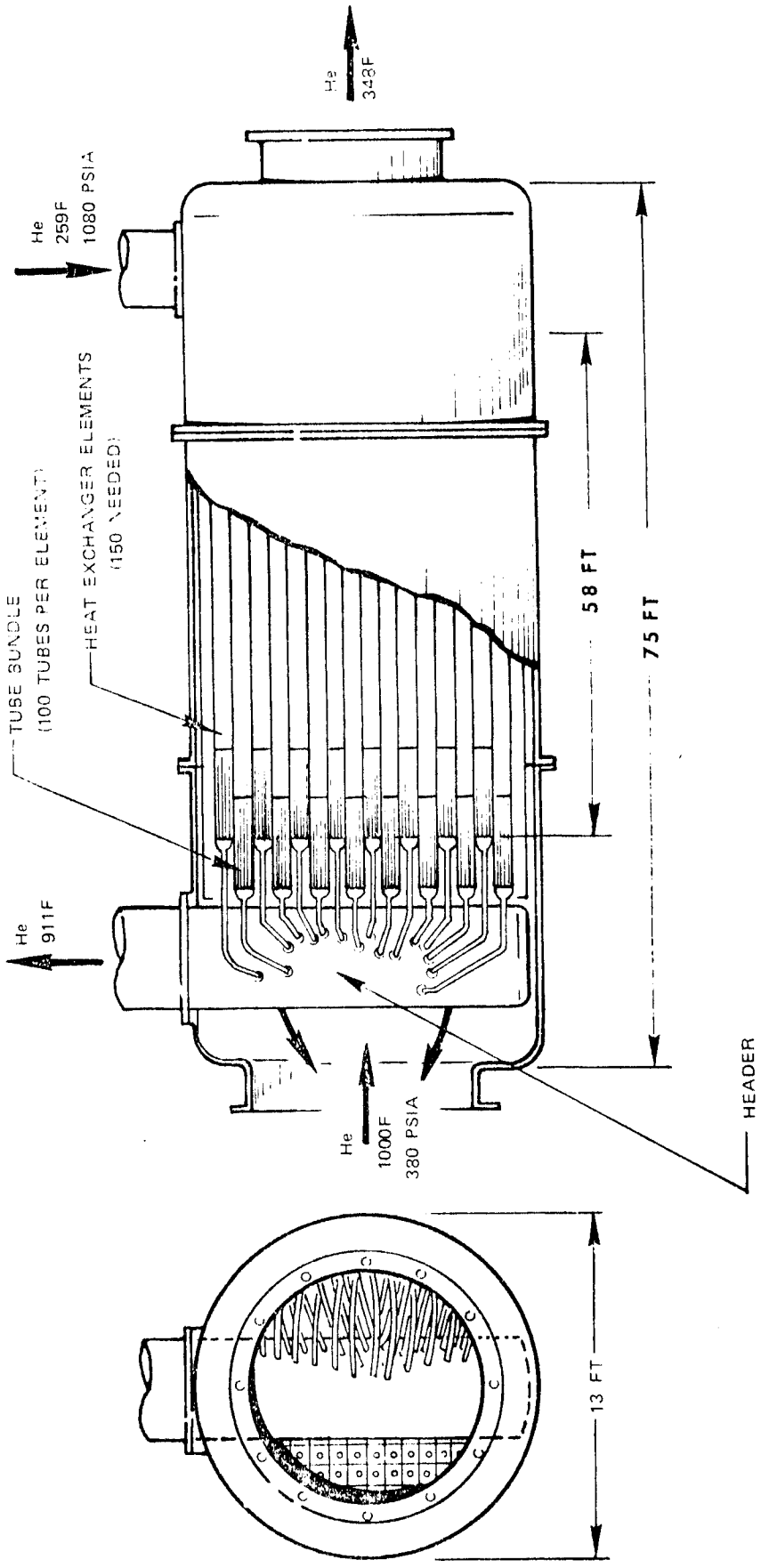

TABLE X

HEAT EXCHANGER DESIGN DATA SUMMARY

Reference Design

	Regenerator	Precooler	Intercooler
Heat Rate - Btu/hr	4.31×10^9	1.57×10^9	9.81×10^8
Flow Rate - lb/hr			
Hot Side (Helium)	5.324×10^6	5.324×10^6	5.324×10^6
Cold Side	5.324×10^6	1.5×10^7 water	9.34×10^6 water
Pressure Loss, $\Delta P/P$ - %			
Hot Side	2.8	1.3	1.1
Cold Side	1.0	---	---
Effectiveness - %	88	92	88
Overall Heat Transfer Coefficient - Btu/hr-ft^2-F	343	438	346
Heat Transfer Area - ft^2	1.41×10^5	6.95×10^4	5.97×10^4
Number of Heat Exchange Elements	150	150	150
Effective Tube Length - ft	58	36	31
Overall Shell Length - ft	75	48	42
Approximate Weight - ton	185	115	100

COMPARISON OF REGENERATOR, PRECOOLER AND INTERCOOLER SIZES

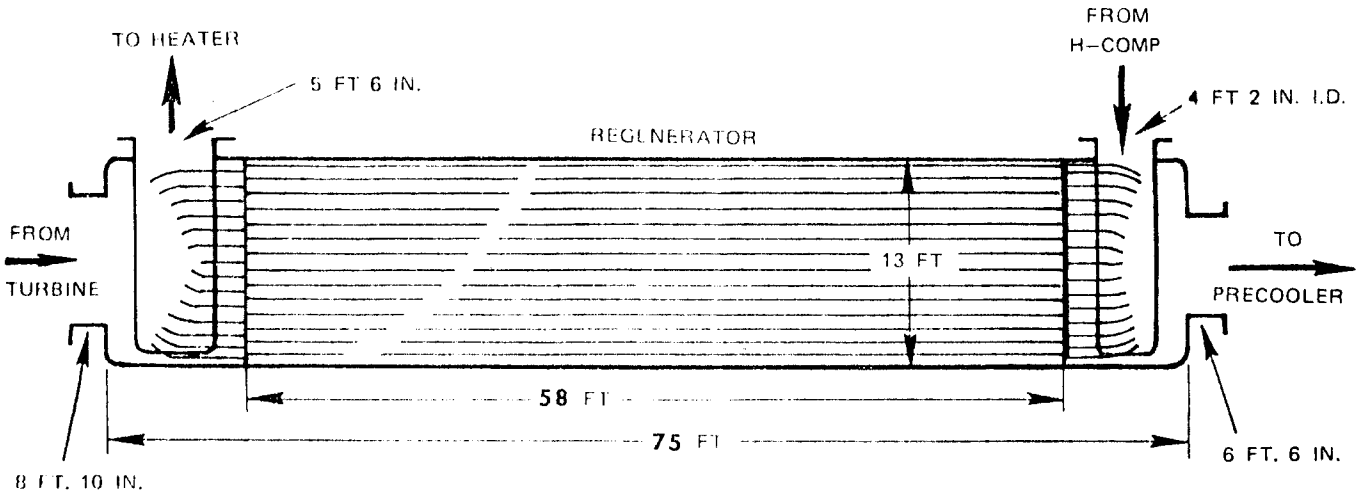

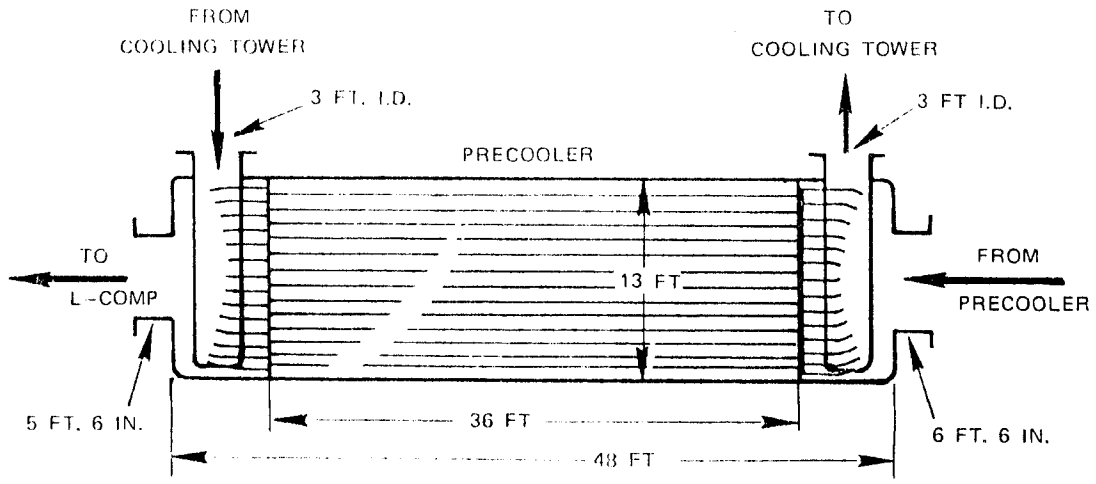

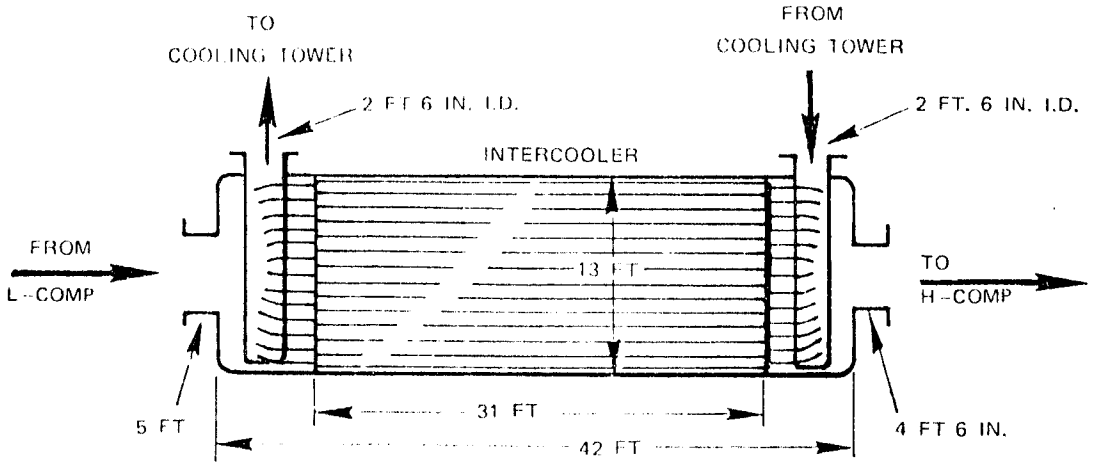

R10-114-1

TABLE XI

PIPING SYSTEM DESIGN DATA SUMMARY

Reference Design

From	To	Fluid	Temp., F	Press., psia	Diameter
Turbine exit	Regenerator	Helium	1000	380	8'10"
Regenerator	Precooler	Helium	348	380	6'6"
Precooler	Low Compressor	Helium	110	380	5'6"
Low Compressor	Intercooler	Helium	258	640	5'0"
Intercooler	High Compressor	Helium	110	640	4'6"
High Compressor	Regenerator	Helium	259	1080	4'2"
Regenerator	Blanket or Heat Exchanger	Helium	911	1000	5'6"
Blanket or Heat Exchanger	Turbine Inlet	Helium	1600	1000	6'6"
- -	Precooler Inlet	Water	90	15	3'0"
Precooler Outlet	- -	Water	195	15	3'0"
- -	Intercooler Inlet	Water	90	15	2'6"
Intercooler Outlet	---	Water	195	15	2'6"

Power Level Control

There are many control schemes possible, each offers different valving requirements and dynamic response of the power conversion system. The principal control scheme often suggested is through variation of helium pressure level by changing the helium inventory in the power conversion loop without changing the turbine inlet temperature. The unique feature of this control scheme is that the power conversion efficiency can be nearly constant over a very wide range of power output, and that all control devices can be located at the low temperature section of the power loop. The disadvantage of this scheme is its relatively long-time response and the need for surge tanks. The second control scheme is by variation of blanket outlet temperature through reactor control. This scheme is particularly useful when part-load requirement is imposed on the reactor rather than the power conversion system for extended periods of time. Again the dynamic response for this control scheme cannot be very rapid. Therefore, for rapid-response power control, use of bypass valves would appear mandatory; bypass of helium from compressor outlet to the turbine inlet or exit would appear most effective. Combination of these control schemes may be utilized for the conceptual-design turbomachinery depending on the response time requirements.

Crucial Technologies

The concept of closed-cycle gas turbine is well developed and related technologies are currently available for unit size up to about 50 Mw. Since the first commercial closed-cycle gas turbine (air as the working fluid) was built in Ravensburg, Germany, there have been more than a dozen units built in Germany, Russia, and Japan. These systems which use helium or air as the working fluid at turbine inlet temperatures not higher than about 1300F have been operating successfully with some of them in excess of 90,000 hours. However, there are many technical problems for the closed-cycle gas turbines particularly of larger unit sizes; seals and bearings designs are the two major problems in addition to fluid flow characteristics, flow path design, stresses, lubrication, dynamic behavior and power control and others.

Of the potential advances in turbomachinery, materials and fabrication techniques, heat transfer, etc., the most significant include (1) improved aerodynamics allowing compressor stage loadings for higher pressure ratios with a minimum number of stages; and (2) the development of advanced materials and cooling schemes for turbine inlet temperatures as high as 2000F. Advances in these areas will continue as will the development of light-weight composite materials for the cooler engine sections.

The closed-cycle gas turbine systems must be maintainable and easily accessible, thus necessitating the use of flanged connections in the system plumbing and turbomachinery. The design of unique flanges and seals to achieve essentially zero inert gas leakage will be a significant technical challenge due to the high pressure and high temperature environment in the closed-cycle system. Under high pressure and high temperature conditions, flanges can deflect and seals can become partially unseated. Low deflection flanges and flexible seal designs will be needed.

Output shaft seals with a long life requirement will present a challenge. This life requirement probably will rule out the use of a simple rubbing seal and would require an advanced noncontacting seal. The use of materials in a high pressure, high temperature helium environment may require extensive material testing to establish their design properties. During previous testing of the Astroloy material under NASA Contract NAS8-26191 in hydrogen and helium environments, it was noted that notched strength of the materials was lower in helium than in hydrogen of elevated temperatures (1600F). Additional testing was conducted which verified this occurrence. Metallographic examination of failed specimens did not define reasons for their property reversal. While the significance of this result is not understood, the test results did illustrate that a helium environment can influence material response, particularly at elevated temperatures. Materials such as molybdenum and columbium (niobium) alloys, as well as ceramics, are especially suited for use in nonoxidizing inert gas working fluids and offer the prospect major strength increases at elevated temperatures.

X-F. CONCLUDING REMARKS

The closed-cycle gas turbine power system is not a new concept. Several dozen closed-cycle systems have been operating in Europe and Asia for more than twenty years (Ref. 11). However, the introduction of the High-Temperature Gas-Cooled Reactor (HTGR) by the General Atomic Company has given impetus to potential applications of the closed-cycle helium gas turbine system operating at temperatures well above those of closed-cycle systems currently being used. As part of the effort on the HTGR/closed-cycle helium turbine system, United Technologies, through the Research Center and its Power Systems Division has made detailed investigations of helium gas turbine alternative configurations and reference design power plants. The following paragraphs briefly discuss the potential advantages for the closed-cycle gas turbine power conversion system.

In addition to the attractive performance potential of the closed-cycle gas turbine, it has a number of substantial advantages when considered for utility power applications. A key advantage is the high density of the working fluid at the turbine exit which is a result of the pressurization of the working fluid and the very modest expansion ratio required for the system. Closed-cycle gas turbines using helium as the working fluid have the potential advantages of being smaller in size and costing less when compared with the steam turbines and conventional gas turbines. More specifically, a helium gas turbine (with 1600F/1000 psia turbine inlet condition) would deliver approximately eight to ten times the output power of a conventional gas turbine of the same size, and its size would be approximately 1/4 to 1/6 that of a steam turbine of the same output. It must be mentioned that these advantages in size for the helium gas turbine will apparently become less significant with the decrease in unit output and turbine inlet pressure. The closed-cycle gas turbine system requires considerably less auxiliary equipment than the Rankine cycle system and because of the ability to vary the pressure level of the working fluid, efficient operation is possible over a wider range of load conditions than with conventional steam and organic power. The capability to maintain high partload efficiency has been indicated in tests of the Brayton power system. A substantial advantage of the closed-cycle system is the fact that the heat rejection process from such a system does not occur at essentially a constant temperature (inside the condenser) of the Rankine system but over a range of temperatures (inside the precooler). This provides a greater temperature difference for heat rejection and, therefore, where dry cooling towers are used, an important cost savings to the overall power conversion and reactor system.

Although the largest helium gas turbine in operation or being built is only 50 Mw, unit sizes in the range of 50 to 600 Mw would be regarded as technically and economically feasible for the period 1985-1990, and unit capacities exceeding 1000 Mw could become available after the turn of the century. It is estimated

that the cost of helium turbomachinery only would be approximately $50/Kw based on current 1975 dollars. This turbomachinery cost could lead to considerable savings for the helium gas turbine power system compared with the conventional gas turbine and steam turbine power conversion systems. These advantages are summarized in Table XII.

TABLE XII

ADVANTAGE OF CLOSED-CYCLE HELIUM GAS TURBINE
POWER SYSTEMS COMPARED WITH LWR STEAM POWER SYSTEMS

Working Fluid: Helium
Nuclear Reactors: UWMAK-III

Significantly Higher Station Thermal Efficiencies
(40% compared to 28-33%)

Elimination or Significant Reduction of Thermal Pollution

Extremely Compact and Large Output Turbomachines
(Over 1000 Mw per unit output possible)

Moderate Maximum Cycle Pressure and Temperature

Simplicity of Arrangement and Reduction in Size for Powerplant Components

Potentially Low Capital Costs

Substantially Lower Fuel Costs

Improved Nuclear Safety

Potentially Low Power Generating Costs

X-G. Divertor Power Cycle

A conventional Rankine steam power cycle was selected to utilize 686.84 MWt (time averaged) contained in sodium leaving the reactor at 600°C and returning at 400°C. Steam conditions are 2400 psig at 1000°F with 1000°F reheat. Net MW output is estimated at 295.

Brief descriptions of the steam generator, reheater and turbine generator designs are given below.

X-G-1. Steam Generator

The steam generator incorporates double-walled design to reduce materials compatibility problems and enhance safety and reliability. In fact, the actual design is identical to that furnished for UWMAK-I, except for the materials contacting sodium and steam.

Higher operating temperatures required use of molybdenum for sodium platens, pigtails, transfer pipes and headers. Similarly, SA-213 Stainless Steel (type 316 is specified for steam generator tubes, module heaters, upper pigtails and outlet steam header. Croloy 2 1.4 (as before) is used for lower pigtails and inlet steam header.

Principal design parameters are shown in Table XIII. Total heating surface (3088 M^2) exceeds the estimated required value by 27.5%. This is a typical design margin. The high thermal conductivity of molybdenum (70 BTU/hr ft °F, or 121.13 W/m °K) is ideally suited to heat conduction purposes utilized in the tube configuration of this steam generator design.

X-G-2. Reheater

This heat exchange apparatus heats steam from the high pressure turbine exhaust to 537.8°C (1000°F) after which it flows to the intermediate pressure turbine for further expansion.

The general arrangement of this component, shown in Figure 28, is an adaptation of that used for the steam generator. It utilizes the same heat transfer configuration with other design features typical of that required for reheater service. Principal design parameters are listed in Table XIV.

As in the steam generator, this double-walled heat transfer configuration avoids compromise in materials selection and permits use of molybdenum in contact with steam temperatures approaching this value. Single-wall designs would not appear praticable for this application. Nominal steam tube wall thickness is .0305" (.25" O.D.).

X-G-3. Turbine-Generator

This equipment is typical of that utilized in fossil-fired steam power plants. The design selected is a 3600 RPM tandem compound two flow design with

TABLE XIII

PRINCIPAL DESIGN PARAMETERS OF UWMAK-III STEAM GENERATOR

Sodium Flow Rate to Boiler kg/hr	8.279×10^6
Na Temperature Drop in Boiler ^oC	200
Na Inlet/Outlet Temperature, ^oC	600/400
Heat Load, kW	686,840
Steam Flow, kg/hr	891,670
Steam Pressure at Boiler Outlet Header, psia	2450
kg/cm^2	1.41×10^2
Steam Temperature at Boiler Outlet Header, ^oC	537.7
Steam Generator Tube Heating Surface per Boiler, m^2	3088
Dry Weight of Steam Generator, kg/unit	157,212
H_2O Inventory at Full Power, KG/unit	2970
Na Inventory at Operating Temperature, Kg/unit	21780
Total Weight/Unit, kg	181962
Sodium Inlet and Outlet Pipe, OD/ID, cm	107/102
Steam Outlet Pipe Size, OD cm	30.5
Feed Water Pipe Size, cm	20.3 sch 40
Sodium Inlet Pipe Location, cm above Vessel $\underline{\text{¢}}$	93.7
Sodium Outlet Pipe Location, cm below Vessel $\underline{\text{¢}}$	101.9
Steam Pipe Location, cm above Vessel $\underline{\text{¢}}$	200.3
Feed Pipe Location, cm below Vessel $\underline{\text{¢}}$	208.3
Na Pressure Drop Through Unit - psi	13.26
Na Pressure Drop Through kg/m^2	9.31×10^3
Feedwater Temperature at 100% Power, ^oC	243.4

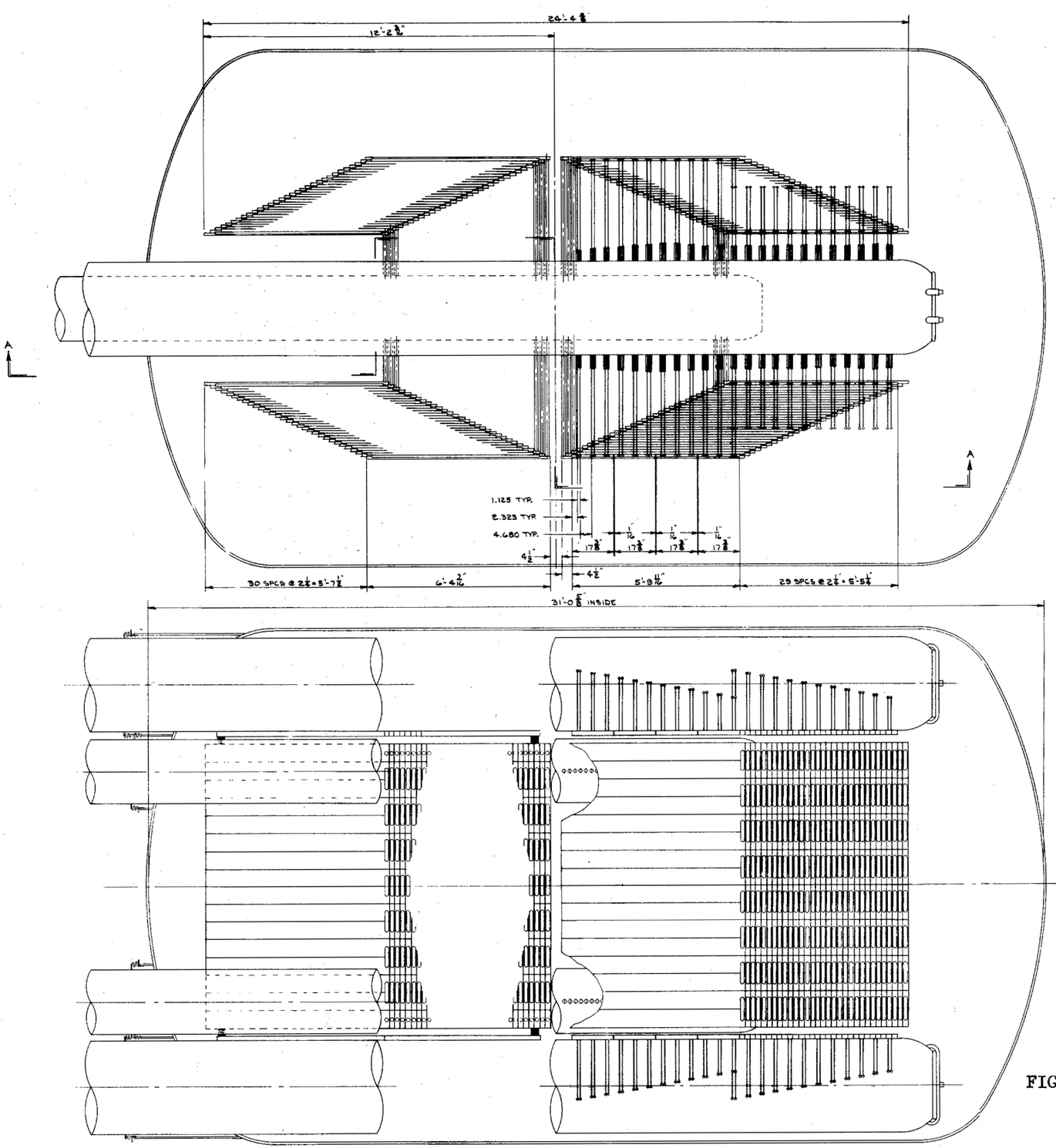

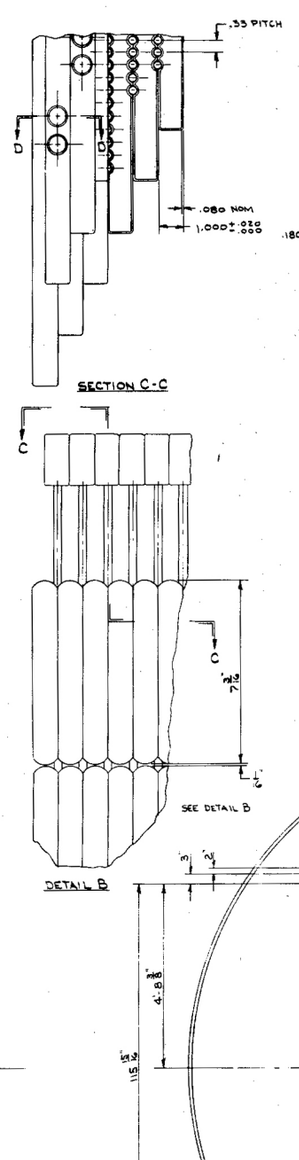

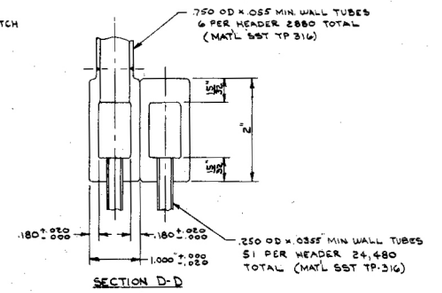

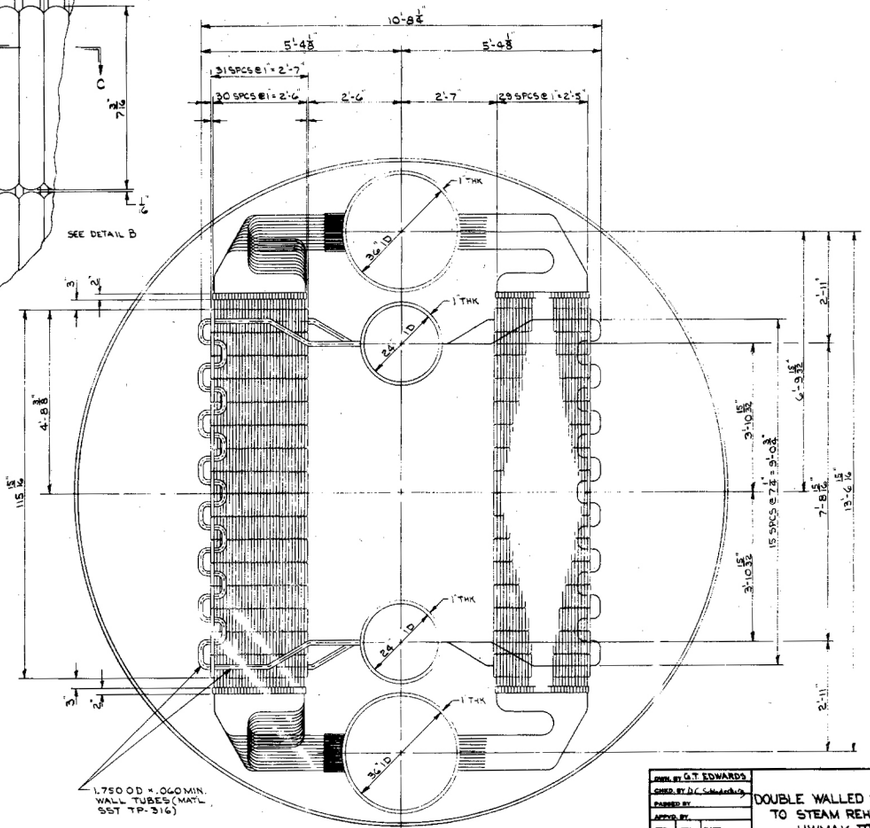

FIGURE 28

DWN. BY G.T. EDWARDS	DOUBLE WALLED SODIUM TO STEAM REHEATER UWMAK III	THE BABCOCK & WILCOX CO. NUCLEAR ENERGY GROUP
CHKD BY D.C. Schaefer		
PASSED BY		
APPVD BY		
STD. / SPL. / DATE		
DO NOT SCALE - USE DIMENSIONS	SCALE	EDO-111175 F

TABLE XIV

PRINCIPAL DESIGN PARAMETERS OF UWMAK-III STEAM REHEATER
AS DESCRIBED IN FIGURE I

Sodium Flow Rate, kg/hr	1.538×10^6
Na Temperature Drop in Reheater, ^oC	200
Na Inlet/Outlet Temperature, ^oC	600/400
Heat Load, kW	107,695
Steam Flow, kg/hr	778,356
Steam Pressure at Inlet Header, kg/cm^2	36.158
Steam Pressure at Outlet Header, kg/cm^2	34.430
Steam Temperature at Inlet Header, ^oC	323.7
Steam Temperature at Outlet Header ^oC	537.8
Heating Surface, approx. m^2	1389.3
Dry Weight, approx. kg	113816
Na Inventory, approx. kg	12732
Total Weight, approx. kg	126,547
Na Pressure Drop Through Unit, kg/m^2	2.672
Reheater Steam Tube OD and Nominal Wall, approx. cm	.635/.0900
Reheater Steam Tube Material	Type 316, ASME SA213
Sodium Platens, Piping, and Headers	Molybdenum

TURBINE HEAT BALANCE DIAGRAM

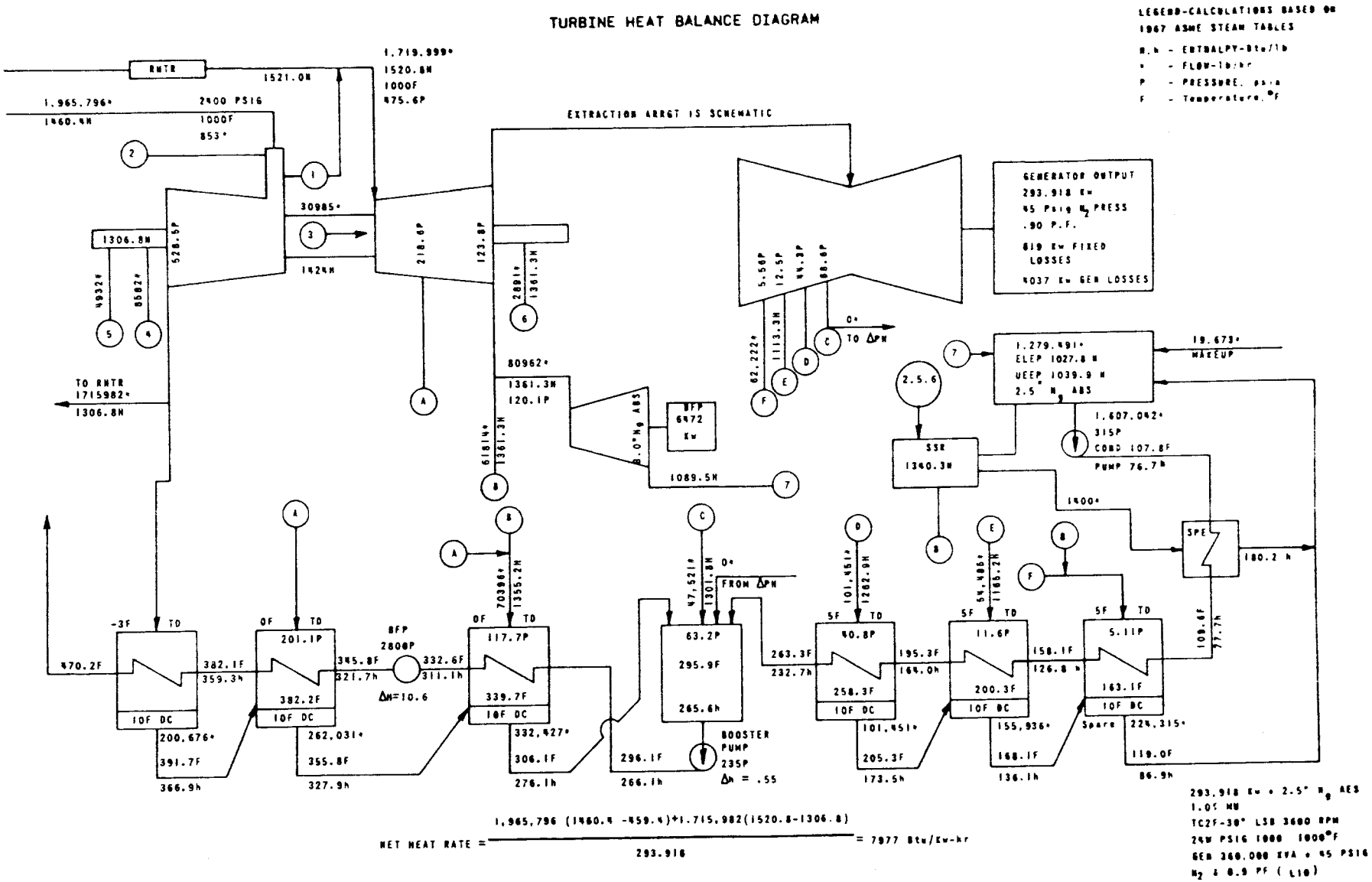

$$\text{NET HEAT RATE} = \frac{1{,}965{,}796\,(1460.4 - 459.4) + 1{,}715{,}982\,(1520.8 - 1306.8)}{293{,}918} = 7977 \text{ Btu/Kw-hr}$$

FIGURE 29

30" last stage blading. The flows, heat rate, pressures, temperatures, etc., shown on Figure 29, were obtained by linear interpolation of similar data supplied by the turbine manufacturer at power levels of 712.8 MWt and 614.7 MWt. This practice is considered acceptable for the purpose intended.

X-H. Summary of Power Cycle for UWMAK-III

A summary of the power cycle parameters for UWMAK-III are listed on Tables XV and XVI. The continuous electrical output from the outer blanket is 1170 MW while for the hot inner shield, it is 585 MW. The power cycle for these two elements is a closed cycle helium gas turbine system. The divertor cycle operates at lower temperatures and is thus based on a Rankine steam cycle involving a sodium to steam system. The steam pressure is 2400 psi and the power output is 295 MW. Thus, for 4735 MW_t continuous output, the gross electrical output is 2050 MW, the net electrical output is 1985 MW, and the net plant efficiency is 41.9%.

TABLE XV

POWER CYCLE PARAMETERS FOR UWMAK - III

OUTER BLANKET

THERMAL POWER	2668MW
POWER CYCLE	Li - Na - He
Li - Na IHX AREA	5750 m^2
Na TEMPERATURES	590 - 940 °C
Na - He IHX AREA	12300 m^2
He TEMPERATURE	488 - 870 °C
POWER OUTPUT	1170MW

INNER BLANKET

THERMAL POWER	1334MW
POWER CYCLE	He - DIRECT
HELIUM TEMPERATURES	488 - 870 °C
HELIUM PRESSURE	1000 psi
Na - He HX - THERMAL STORAGE	6150 m^2
POWER OUTPUT	585MW

TABLE XVI

POWER CYCLE PARAMETERS FOR UWMAK-III

DIVERTOR CYCLE

THERMAL POWER	686MW
POWER CYCLE	Na-Steam
Na TEMPERATURES	400-600°C
STEAM GENERATOR AREA	6176m^2
STEAM TEMPERATURE	538°C
STEAM PRESSURE	2400psi
POWER OUTPUT	295MW

PLANT POWER SYSTEM

THERMAL POWER (CONTINUOUS)	4735MW
GROSS ELECTRICAL POWER	2050MW
NET ELECTRICAL POWER	1985MW
NET PLANT EFFICIENCY	41.9%

References for Chapter X

1. Kuo, S. C.: Energy Storage Systems for UWMAK-III and other Tokamak-Type Fusion Reactors. UTRC Suggested Program P75-233-1 submitted to EPRI, June 30, 1975.

2. Forster, S.: The Closed Helium Turbine Cycle with a Fusion Reactor as Energy Source. ASME Paper 72-WA/Ener-10, November 1972.

3. Kuo, S. C.: Closed Cycle Helium Gas Turbine Power Systems for UWMAK Fusion Reactor Powerplant. A Colloquim presented at the University of Wisconsin, Madison, Wisconsin, November 1972.

4. Meader, M. D. and F. R. Biancardi: Evaluation of a Fusion-Powered Closed-Cycle Gas Turbine Power Generating System. Contract Report No. 322776S for Brookhaven National Laboratory, June 1974.

5. Kulcinski, G. L. and R. W. Conn: The Conceptual Design of a Tokamak Fusion Power Reactor, UWMAK-I.

6. Conn, R. W., et al: Major Design Features of the Conceptual D-T Tokamak Power Reactor, UWMAK-II, Proceedings of the 5th IAEA Conference on Plasma Physics and Controlled Nuclear Fusion Research, Tokyo, Japan, November 1974.

7. Mills, R. G.: A Fusion Power Plant. MATT-1050, Princeton University, August 1974.

8. Personal communication with Prof. R. Conn, The University of Wisconsin, October 1975.

9. Kuo, S. C.: ANP Material Technology. Unpublished UTRC report, May 1972; Also in: Analysis of Nuclear Propulsion and Power Conversion Systems for Large Subsonic Aircraft. AFPAL-TR-72-47 (Confidential), August 1972.

10. Enders, W.: Large Helium Turbines for Nuclear Power Plants. ASME Paper 70-GT-99, May 1970.

11. Bammert, K. and E. Bohm: Nuclear Power Plants with High Temperature Reactor and Helium Turbine. ASME Paper 69-GT-43, March 1969.

XI. Plant Design

XI-A. Introduction

With the ever increasing successes in fusion development programs world-wide and with the hope of building commercial fusion power plants, the requirements of integrated plant design have begun to receive serious attention. The importance of the balance-of-plant should not be underestimated. For fission plants, the balance-of-plant amounts to over 80% of the total capital cost. For fusion plants, this share may decrease somewhat. However, the fact remains that the design of the balance-of-plant and construction planning will have significant impacts upon the economic viability of fusion power plants. The conceptual design and the corresponding cost estimate play a major role in identifying the high-cost areas of the balance-of-plant and form the basis for development of design approaches with greater cost-effectiveness.

There exists very little prior work to provide guidance for the design of many of the facilities for fusion plants. Many of the requirements are not defined in detail and some of them probably have not yet been identified. Only approximate allowances can be made to accommodate these unknowns and uncertainties. Until further design and analysis is done, these uncertainties will remain and must be recognized in performing and evaluating this design study.

Within this framework, the conceptual plant design study for the UWMAK III fusion plant was undertaken to accomplish the following objectives:

- Develop a conceptual system design for:
  - The Plant Heat Rejection System
  - The Blanket Solid Radwaste Handling System (Solid radioactive waste generated from blanket replacement)
  - The Plant Electrical System
- Develop a conceptual plant arrangement
- Perform conceptual design of the major buildings and structures

In conjunction with the above objectives, the present study was also intended to identify areas in which there are

significant technical or cost uncertainties and to provide a basis for an order-of-magnitude cost estimate. (Refer to Chapter XIII for cost estimate.)

The designs presented in this study are conceptual, without benefit of optimization and consideration of a broad spectrum of alternatives. In addition, they have been subject only to first order analyses. However, the designs selected are believed to be technically feasible and reasonably economic. Further, they provide a reasonable basis for evaluating the balance-of-plant design and engineering problems of the UWMAK III type of fusion power plant.

The experience of Bechtel Corporation in fission plant design has provided much of the basis for the present study. Areas unique to the UWMAK III fusion plant have been emphasized while aspects which are similar to a fission plant have been extrapolated from fission plant design practices.

The arrangement of equipment and plant is based on the concept of identifying system functions and functional interrelationships and assigning these into modules. This forms the framework for definition of major buildings and functional requirements. For the UWMAK-III design these are:

- A Containment Building containing the reactor and other components of the nuclear island.
- A Hot Cell for handling irradiated blanket segments.
- A Reactor Auxiliary Building containing safety-related equipment and other equipment closely associated with the nuclear island.
- A Heat Exchanger Building containing the reactor heat exchange and transport equipment. (It also contains the thermal storage equipment).
- A Turbine Building containing the energy conversion equipment.
- A Control Building containing the central plant control equipment.
- A Diesel Generator Building containing the diesel generators.
- A Radwaste Building containing the equipment for processing radioactive wastes.

- A Helium Storage Building containing the equipment for storing high pressure helium.

- An Inductive Energy Storage Building containing equipment associated with magnet energy supply system.

The site characteristics were specified by the University of Wisconsin. The plant design was based on a hypothetical site having site characteristics (soil, seismic and meteorological) similar to those of Madison, Wisconsin.

The following paragraphs provide a synopsis of the salient features of the balance-of-plant design covered under the present study.

The Plant Heat Rejection System provides the heat sink for the power cycles, various components of the nuclear island and other plant equipment and rejects this heat to the atmosphere. Guidelines for the heat rejection system design were established by the University of Wisconsin and are based on the concept of "zero water use". Consistent with this concept, dry cooling towers were selected for rejecting the plant heat to the atmosphere.

The replacement of the blanket segments from the outer blanket generates large volumes of solid radioactive wastes. A preliminary concept was developed for the removal, processing, storing and off-site disposal of these wastes. The guideline used to establish the concept was to reduce the specific activity of the blanket to a sufficiently low level (200 Ci/cc) so that the shielding requirement during off-site transportation is reduced to a minimum.

Consideration was given to the Plant Electrical System to identify the major equipment associated with the main generation system and the system leading to the ultra high voltage (700KV) switchyard. The study also defines the major plant load centers and identifies the essential (Class 1E) loads related to plant safety.

Conceptual design studies were performed for the plant buildings and structures, and for the plant, equipment and piping arrangement. The building design effort was confined to the major structures, viz., the Containment Building, Hot Cell, Radwaste Building, Reactor Auxiliary Building, Heat Exchanger Building, and the Turbine Building. Only superficial

consideration could be given to the plant, equipment and piping arrangement.

Although not described in the report, a large number of auxiliary systems will be needed in the plant. The list of these systems will have to be developed and will include the following:

- Cover gas system
- Containment/Hot Cell inerting gas sytems
- Containment/Hot cell cooling systems
- Component preheating and pipe heating systems
- Inert gas receiving and processing systems
- Extraction, condensate, condensate makeup, feedwater heating, auxiliary steam systems
- Fuel handing system
- Sodium and lithium handling systems
- Sodium and lithium fire protection systems

XI-B. Plant Heat Rejection System

The plant heat rejection system has the following basic functions:

- Remove heat from the energy conversion cycle
- Remove heat from the reactor shield coolant
- Remove heat from the miscellaneous plant components and systems such as lube oil cooling, generator cooling, Containment/Hot Cell cooling, etc.
- Maintain the temperature of equipment and materials within the prescribed limit
- Reject the removed heat to the atmosphere

The energy conversion cycles and the reactor shield coolant represent the major sources of waste heat and their heat rejection system design is emphasized. The basic precept for the heat rejection system design, established by the University of Wisconsin, was that of "zero water use". This precept appears reasonable in the light of the increasingly stringent environmental requirements, particularly in regions where water is scarce. Consistent with this, dry cooling towers are used for rejecting the plant heat to the atmosphere.

The requirements and constraints for the heat rejection system are governed primarily by the reactor and the turbine system designs. The parameters reflecting these requirements and constraints, provided partly by the University of Wisconsin and partly by United Technology, are summarized in Table XI-1.

The use of dry cooling tower also imposes some constraints on the performance of the energy conversion cycles. (Note that UWMAK III uses three closed loop gas turbines and one steam turbine. Refer to Chapter X for a description of the power cycle.) The minimum temperature obtained in the cycles with a dry tower is considerably higher than that obtained by a wet tower - the reason being that the dry tower approaches the dry bulb temperature while the wet tower approaches the wet bulb temperature. This has a significant deleterious effect on the cycle efficiency. However, this sacrifice can probably be justified in locations where availability of water is scarce.

A schematic drawing showing the heat rejection system is presented in Figure XI-1. The cooling towers and the associated systems and equipment selected are based on the present state-of-the-art as dramatic improvements are not foreseen in the performance of dry cooling tower systems. The design is based on a dry bulb temperature of 24°C (75°F).

The system uses two closed cooling water loops - one loop - referred to as the main loop - serves the energy conversion cycles and the component cooling, and the other - referred to as the waste heat loop - serves the reactor shield cooling system. The rationale for providing a separate cooling loop for shield coolant is twofold. First, it allows independent operation of the shield cooling system. The independent operation is needed for afterheat removal when the reactor is shutdown, during which time the main loop need not remain operative. Secondly, it can be made more reliable by providing redundancy so that the failure of one wasteheat loop does not require shutdown of the entire plant.

XI-B-1. Energy Conversion Cycle Heat Rejection

The cooling water loop for the energy conversion cycles removes heat from the three closed loop gas turbine cycles and also from the steam turbine cycle, and removes this heat to the atmosphere by main cooling towers. Cooling water is circulated through a precooler and an intercooler in each gas turbine cycle and through the condenser of the steam turbine cycle as shown in Figure XI-1. This cooling water loop uses three one-third capacity circulating water pumps each rated at 273,000 LPM, 46M TDH (73,000 GPM, 150 FT TDH).

This arrangement offers high operational reliability since any two pumps together are capable of carrying the full cooling load at the pump runout condition in the event of failure of the third pump.

XI-B-2. Shield Cooling System Heat Rejection

The waste heat from the shield cooling cycle is rejected to the atmosphere by the waste heat cooling tower. As this cooling loop is needed to maintain afterheat removal even after the reactor is shutdown, a high degree of reliability is required. This is accomplished by providing 100 percent redundancy in the pumping and the cooling equipment.

The cooling water is circulated through the shield cooling helium heat exchanger and the waste heat dry tower as shown in Figure XI-1. Two full-capacity waste heat cooling water pumps each rated at 15,000 LPM, 46M TDH (4,000 GPM, 150 FT TDH) and two full-capacity cooling cells each capable of rejecting the total waste heat (50 MWt) are provided. Normal operation of the plant requires only one cooling cell along with one cooling water pump - leaving one cell and one pump as standby.

XI-B-3. Dry Cooling Towers

Heat rejected from the various equipment is released to the atmosphere by circulation of the cooling water through the mechanical draft dry cooling towers. To accomodate the heat rejection rate of approximately 9 billion btu per hour, cooling towers are provided as depicted in Figure XI-2. Drawing XI-M-1, Plot Plan, shows the location of these towers relative to the other buildings and structures of the plant. The design of these cooling towers was established using Madison, Wisconsin weather data and the basis of their design is shown in Table XI-2.

The circulating water from the heat exchangers and the condenser flows through the multi-pass cooling coils where it is cooled by drawing air up through the cells. The cells are arranged on the plant site at right angles to the prevailing wind direction for maximum efficiency (i.e., for minimum interference between cell exhaust air which is discharged upward from each cell). For plant arrangement convenience, a north-south prevalent wind direction was assumed. However, the true direction will have to be determined for proper arrangement of the cells.

Table XI-1

Heat Rejection System

Design Requirements

UWMAK-III

Parameters		Temp. °C (°F)	Total Heat Rejected GJ/Sec (Btu/Hr)
Gas Turbine Cycle:			
Precooler -			1.383
Cooling Water,	In	32.2 (90)	(4.72 x 10^9)
	Out	90.6 (195)	
Intercooler -			0.861
Cooling Water,	In	32.2 (90)	(2.94 x 10^9)
	Out	90.6 (195)	
Divertor Turbine Cycle:			
Condenser -			0.445
Cooling Water,	In	32.2 (90)	(1.52 x 10^9)
	Out	57.2 (135)	
Shield Cooling HX			0.047
Cooling Water,	In	32.2 (90)	(0.16 x 10^9)
	Out	90.6 (195)	

Table XI-2

Cooling Tower Design Basis

Design Dry Bulb Temperature	24°C (75°F)
Design Approach	8.3°C (15°F)
Design Cooling Range	30°C (86°F)

	Energy Conversion System	Shield Cooling System
Flow Rate (per cell)	17000 lpm (4500gpm)	15000 lpm (4000gpm)
Number of cells	48	2
Cell Size (LxWxH)	30Mx24Mx28M (100'x80'x93')	30Mx24Mx20M (100'x80'x65')
Overall Tower Size (LxWxH)	381Mx108Mx28M (1250'x354'x93')	30Mx54Mx20M (100'x177'x65')
Fan Power (per cell)	500 HP	500 HP

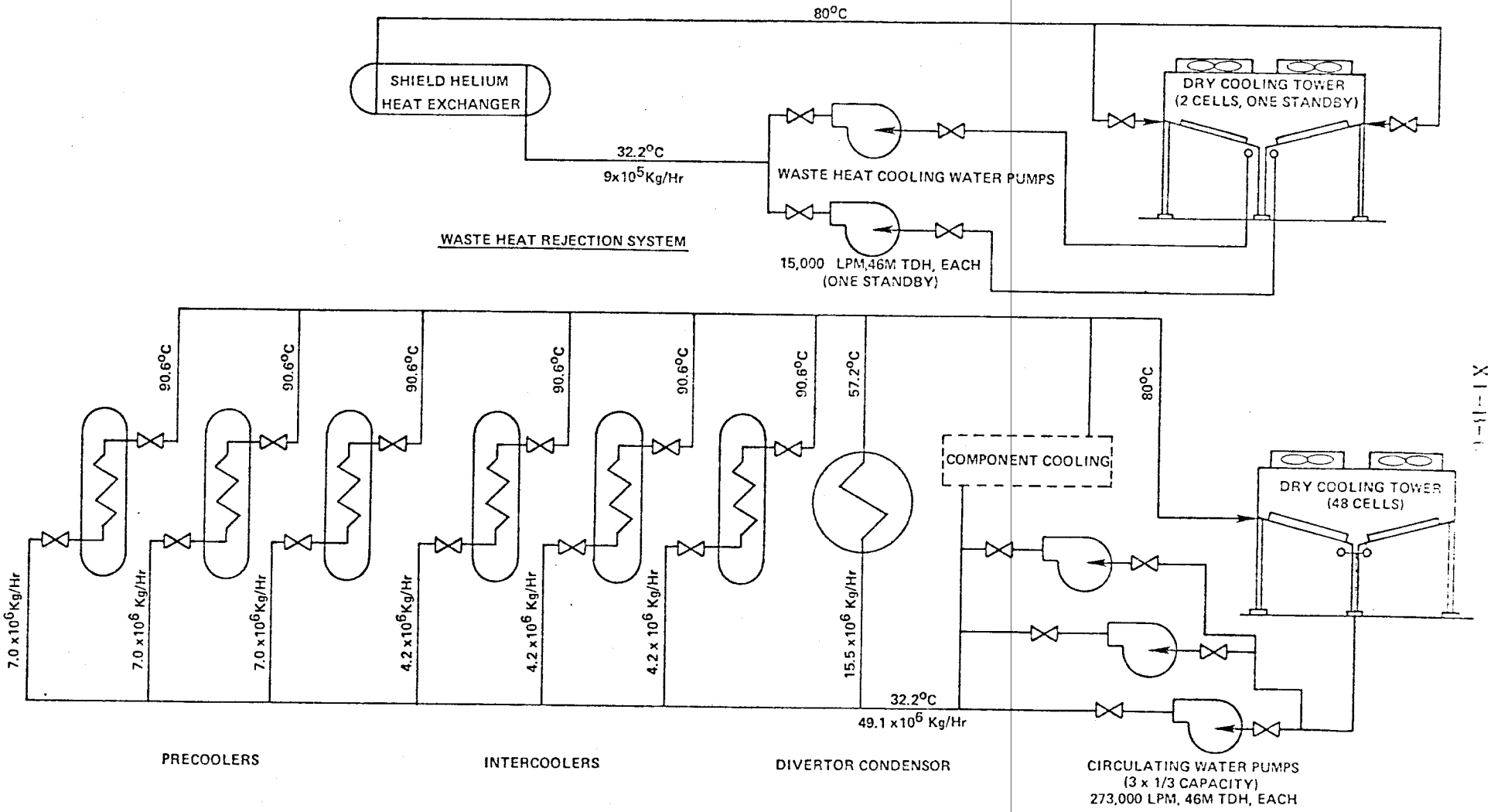

FIGURE XI-1

UWMAK III PLANT HEAT REJECTION SYSTEM

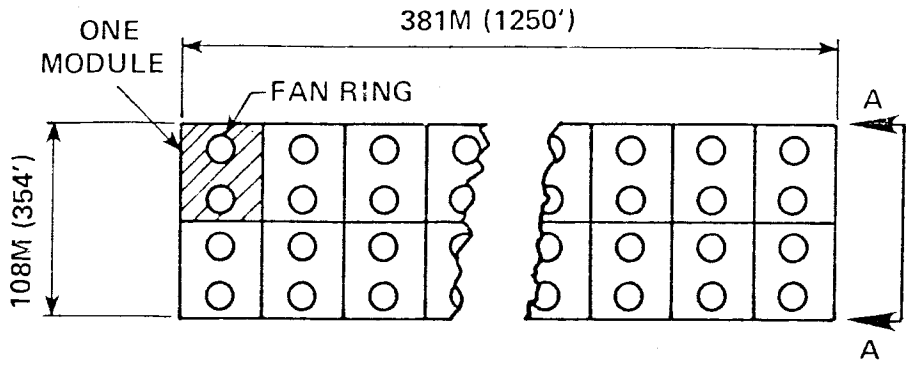

PLAN

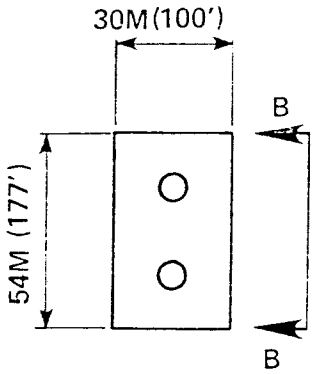

PLAN

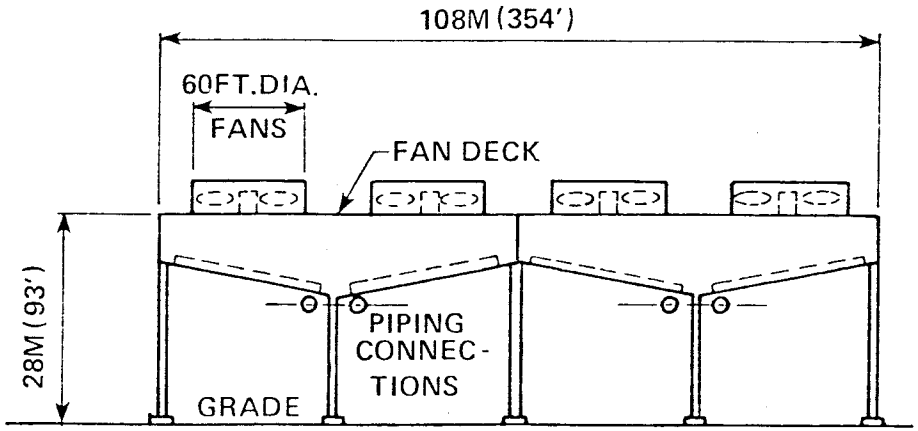

VIEW A-A (ENLARGEMENT)

MAIN COOLING TOWER (48 CELLS)

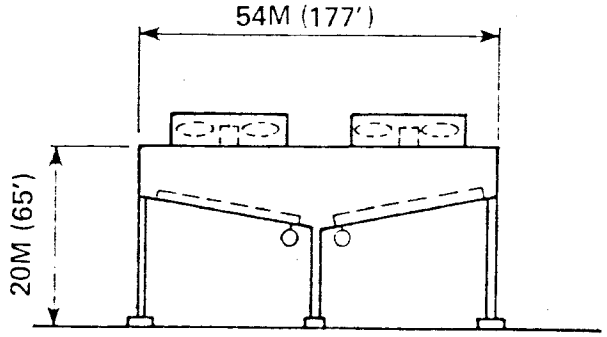

VIEW B-B (ENLARGEMENT)

WASTE HEAT COOLING TOWER (2 CELLS)

FIGURE XI-2
UWMAK III COOLING TOWER ARRANGEMENT

XI-C. Solid Radwaste Handling System

This section describes the concept for disposal of solid radioactive wastes generated from the periodic replacement of blanket. (Refer to Chapter V for a description of the blanket replacement plan.) The blanket is subjected to high energy neutron bombardment, and radiation from the extremely high-temperature plasma which cause severe material damage. Therefore, periodic replacement of the blanket is necessary. Initially the blanket was expected to last one year. In this study, half of the blanket is assumed to be replaced every six months. In the final radiation damage study, the estimated first-wall life turned out to be between 1.5 and 3 years depending on the location of the blanket segment.

The following information was used as the basis for developing blanket disposal concept.

- Total weight of blanket; disposed of annually: metallic - 164 tonnes (0.36×10^6 lb), non-metallic - 472 tonnes (1.04×10^6 lb)
- Total volume of blanket; disposed annually: metallic - $32 M^3$ ($1130 ft^3$) (includes 50% void space), non-metallic - $250 M^3$ ($8828 ft^3$) (includes 50% void space)
- Weight of the largest piece of blanket: 42.6 tonnes (9.37×10^4 lb)
- Total volume of the largest piece of blanket: $64 M^3$ ($2260 ft^3$).
- There are four regions of the blanket as follows:

Region		Thickness (cm)	Material
I	- first wall	0.15	100% TZM
II	- breeding zone #1	60	97% Li, 3% TZM
III	- reflector	30	99% C, 1% TZM
IV	- breeding zone #2	4	97% Li, 3% TZM

The metallic components of the used blanket are highly radioactive, and on-site storage for a period of time is desirable to reduce shielding requirements during transportation. Figure XI-3 shows the total blanket activity as a function of time after reactor shutdown. The specific activity of the blanket decays from more than 1 Ci/cc at the time of shutdown to about 200 Ci/cc at 1000 days. Beyond 1000 days, the activity does not decrease much further as the main contribution to the remaining activity is from Mo-93 (half-life 3×10^3 years), Nb-93 M

(half-life 12 years), and Tc-99 (half-life 2×10^5 years). Therefore, storage has been provided for a three-year decay of the used blanket.

The blanket process block diagram is shown in Figure XI-4. It is described briefly in the following paragraphs.

The decay heat from the blanket at the time of the reactor shutdown is about 9 MWt; it is therefore necessary to circulate coolant to remove the decay heat. Figure XI-5 shows the generation of decay heat after reactor shutdown as a function of time. The decay heat is reduced by a factor of about 40 in seven days at which time gas cooling can take over. The lithium is drained from the cooling system. The modules are then transferred to the storage area for further decay.

The metallic components of the blanket will be held in the storage area for 3 years before processing for disposal. However, the frame attached to the blanket can be re-used and it will be separated from the blanket during the first six months in storage so that the frame can be welded to a new blanket module. The separation is by laser cutting of the welded joint. The welded joint attaching the frame to a new blanket is made by a remote-operated welding machine. Both operations take place in the hot work shop under a helium atmosphere. (Helium atmosphere is used in the Hot Cell to provide a common environment as in the Containment Building.) These operations are carried out in the Hot Cell building. Drawing XI-M-1, Plot Plan, shows the relative location of the Hot Cell with respect to the other buildings.

At the end of three years, the used blanket is transferred to the hot work shop where the large pieces will be cut into small pieces (1M x 2M) using a laser. The small pieces are then passed through a vacuum lock to the decontamination area which has an air atmosphere.

The first step in the processing of the blanket is decontamination which includes covering the blanket with moist nitrogen so that any lithium remaining in the blanket is converted into lithium hydroxide. The lithium hydroxide is then removed by water spray. The blanket pieces then go through a crushing machine where they are crushed into tiny pieces a few inches in diameter. The final pieces will be solidified with cement and stored in $2.83 M^3$ ($100 ft^3$) containers. These are placed in the container storage area until shipment to an approved disposal site.

Non-metallic portions of the blanket, on the other hand, do not require long term storage prior to disposal. Therefore, once they are separated from the metallic blanket components, they may be immediately processed for off-site disposal (Figure XI-4).

XI-C-1. Hot Cell Arrangement

The Hot Cell arrangement is shown in Figure XI-6. The lower level is the used blanket storage area. This reduces the shielding requirement since the lower level is partially underground. The storage area is of sufficient volume to hold one full complement of new blanket and those portions of spent blanket awaiting shipments. Helium gas is circulated through the area to remove decay heat. The decay heat removal and HVAC systems are located in the auxiliary system area. The blanket storage area is maintained under helium atmosphere to prevent lithium fire.

The upper level of the building is divided into two areas; one with a helium atmosphere and one with air. The hot work shop and the area used to transfer the blanket from containment to the storage area have inert (helium) atmospheres. The solidification system, control room, container storage area, new blanket (not yet welded to the frame) storage area, and service shop which is used to do the maintenance or repair work for the equipment in the hot work shop have air atmospheres.

An overhead crane is provided in each area. Truck and railway share the same entrance area which is located at the lower level.

XI-C-2. Container and Shipping

The annual metallic blanket waste volume is $32M^3$ ($1130\ ft^3$) and weighs 164 tonnes (0.36×10^6 lb). Solidification is accomplished by mixing one part of blanket fragments with four parts of cement. The waste will be shipped in $2.83M^3$ ($100\ ft^3$) containers with 6.35 cm (2 1/2 inch) lead shielding. There will be 57 containers required annually. It may be more economical to use larger containers but shielding requirements and activity contents of the waste may limit the container size; however, no optimization was done in this study.

The transportation of containers to an approved off-site disposal area can be either by truck or railway. Based on the present load allowance for a truck, 19 tonnes (42,000 lb.), only one container can be shipped per truck. It is, therefore, more suitable to use railroad transportation as 8-10 containers could be shipped per rail car.

Requirements for containing and shipping the non-metallic portions of the blanket have not been addressed in this study. However, they do not appear to pose any shielding problems because of their low activity. Therefore, they can readily be shipped off-site shortly after removal from the reactor.

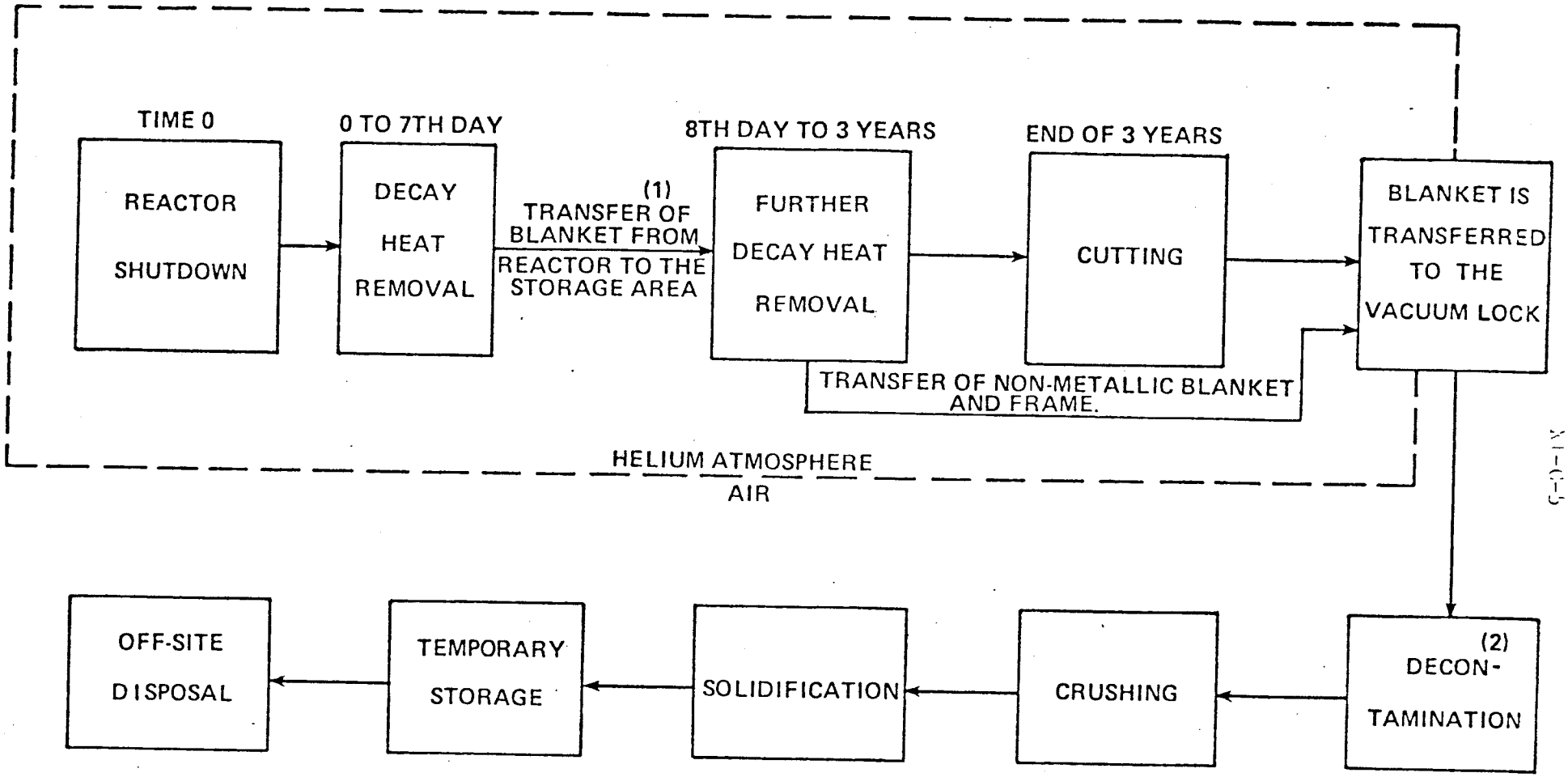

NOTE: (1) TRANSFER OF THE LARGEST BLANKET PIECE TAKES ABOUT 8 HOURS
(2) ANY LITHIUM LEFT IN THE BLANKET IS CONVERTED INTO LiOH AND THEN REMOVED

FIGURE XI-4
BLANKET PROCESS BLOCK DIAGRAM

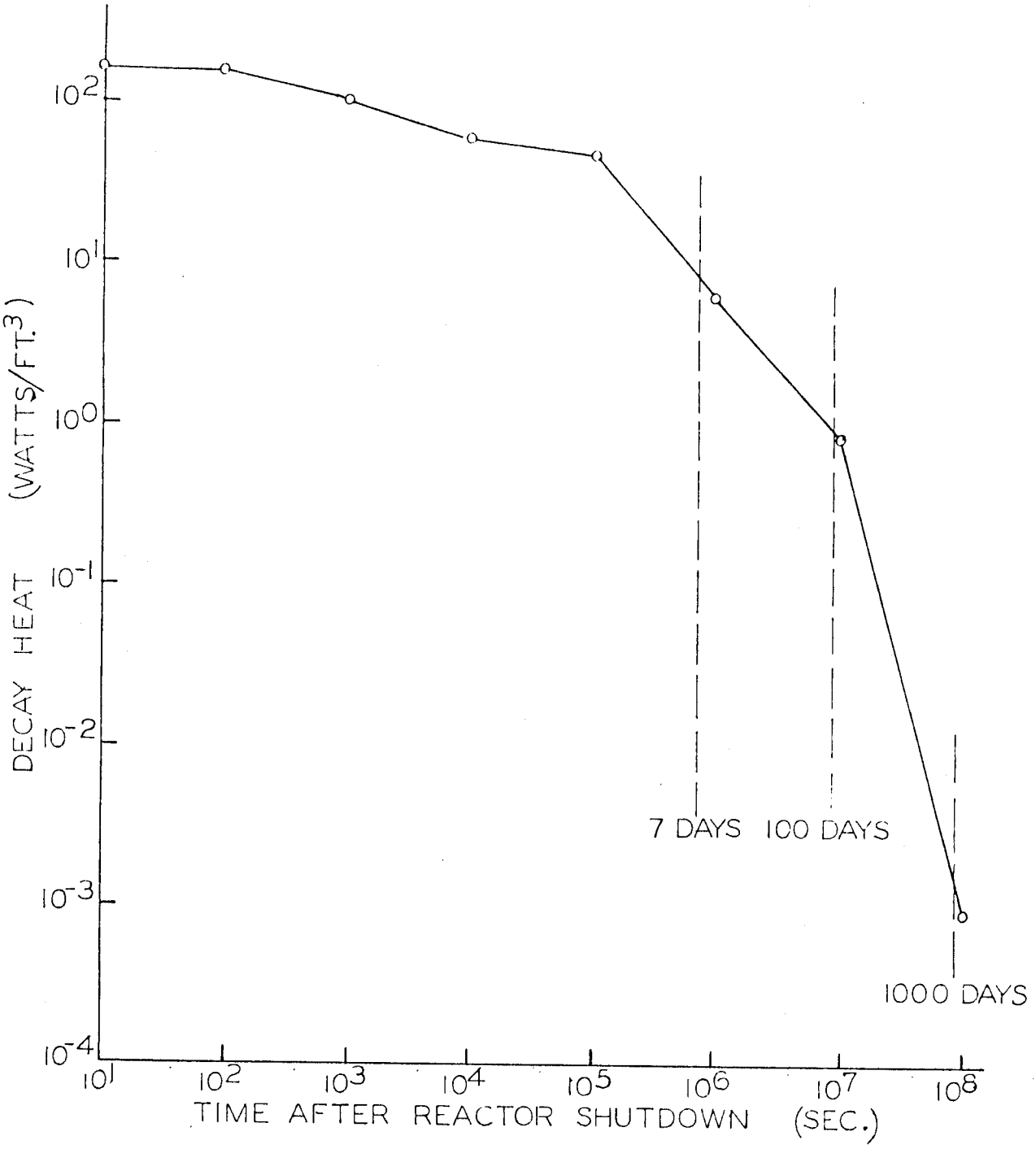

FIGURE XI-5

BLANKET DECAY HEAT
VS
TIME AFTER REACTOR SHUTDOWN

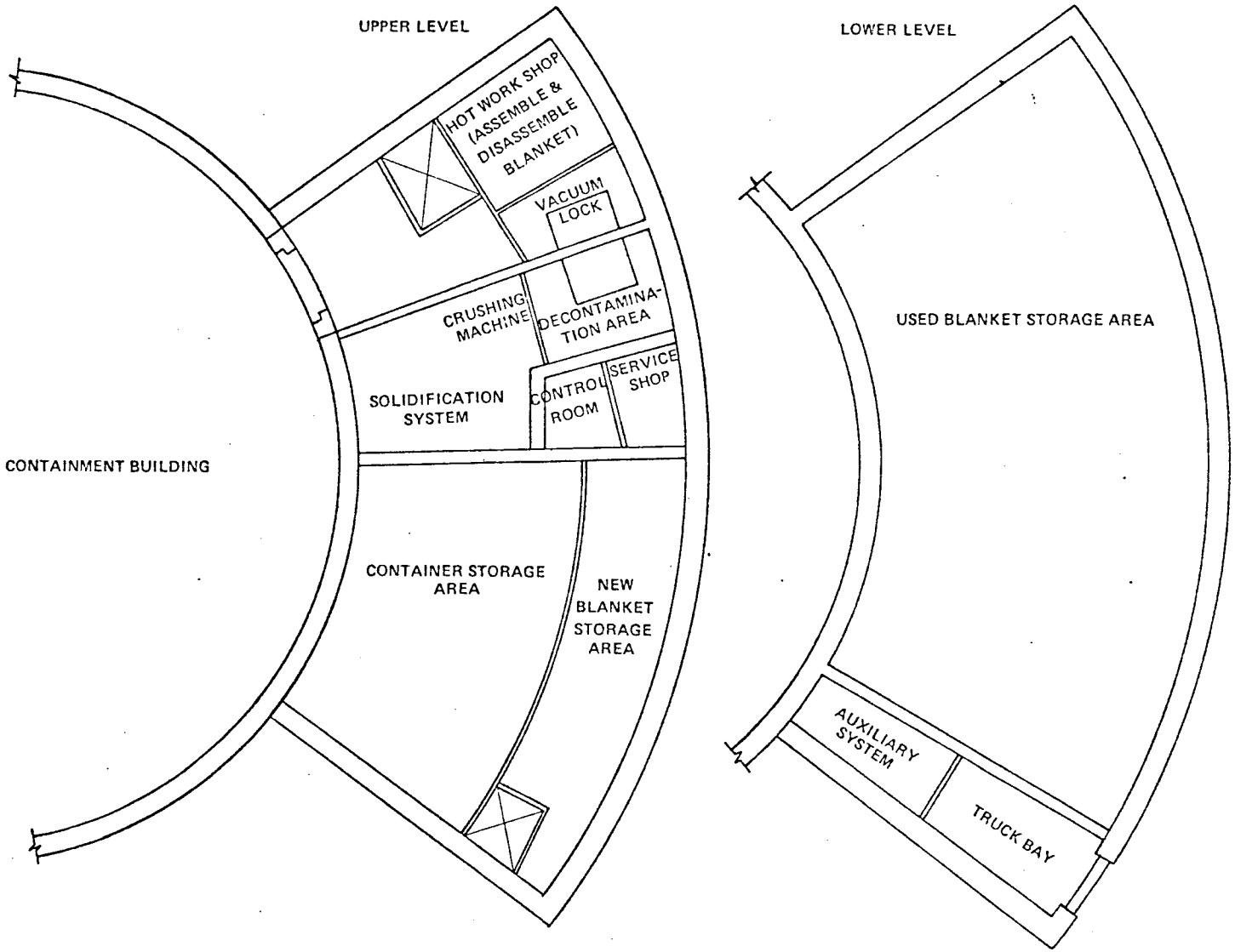

FIGURE XI-6
HOT CELL ARRANGEMENT

XI-D. Plant Electrical System

The function of the Electrical Power System is to provide power for the plant equipment, generate electric power and transmit net electric power to the off-site power system.

The principal design features are summarized below.

Safety:

- An on-site power supply system is provided to meet plant emergency power requirements.
- The on-site power supply system has full redundancy. Each consists of an alternating-current power system, a direct current power system and a control and instrumentation power system.
- The on-site power supply system is connected to two off-site power sources.

Power Generation:

- In order to ensure high reliability of power supply, each main bus of the auxiliary distribution system is transferable between two redundant connections to the switchyard power sources.
- Each redundant component of the plant distribution system is provided with an isolating means for testing and maintenance of the equipment without interfering with plant operation.
- Each turbine-generator is provided with a separate overcurrent protection system and an isolating device. Each also has a means to synchronize the output with the switchyard sources.
- An electrical fault in a generatcr or any component of one power path from the switchyard to the switchgear does not require a forced shutdown of the plant. In the case of the converter equipment associated with the reactor magnets, the above feature applies only up to the incoming breakers of the converter system.
- The design is based on simplicity and economics without jeopardizing the requirement for high reliability. ANSI standards is used wherever possible.

- The voltage regulation and frequency at the distribution buses is such that equipment can operate within the limits prescribed by the National Electrical Manufacturer's Association (NEMA).

The conceptual design for the plant electrical system is described in the following paragraphs. A single-line diagram of the system is shown on Drawing XI-E-1.

The power generation system consists of four turbine-generators - three rated at 650 MVA and one 330 MVA. Power is generated at 26 kV, 3 phase and 60 hertz frequency. Each unit is connected to a circuit breaker and a disconnect switch through an isolated phase bus duct. An isolated phase bus duct also connects two generators at the load side of the disconnect switch and ties these generators to a common step-up transformer which is connected to the switchyard. Each of the two step-up (main) transformers is made up of three single phase units and one spare. Each single phase unit has a low voltage of 26 kV and a high voltage of 404 kV. When connected in a delta-wye configuration, the three units develop 700 kV high voltage which matches the voltage at the switchyard.

Each combination of two generators and main transformer is associated with a power supply group (Supply Groups 1 and 2). Each supply group has three auxiliary transformers connected to the isolated phase bus through a current limiting reactor. This current limiting reactor enables the use of standard circuit breakers for the primary protection of each auxiliary transformer. The auxiliary transformers of one supply group are used during normal plant operation and those of the other group serve as 100% redundant stand-by units.

The two transformers of the converter system are not redundant to each other. One supplies power for the inductive storage unit and the other supplies power to the transformer and diverter coils of the reactor magnet system. The arrangement is such that this load combination is connectible to either Supply Group 1 or Supply Group 2 isolated phase bus through a current limiting reactor. Automatic power supply transfer capability is provided.

There are six 4160-volt main switchgear buses, each being accessible to an auxiliary transformer. Some degree of redundancy is provided in the load equipment and for the sake of discussion, they may be grouped into Load Groups 1 and 2. Three switchgear buses are associated with each load group. Each

switchgear bus has an automatic power supply transfer so that load groups will not experience a power outage unless both supply groups are out of service.

Two of the switchgear buses, one in each load group, are Class 1E category and each has a standby diesel generator connectible to the bus. However, the Class 1E loads constitute only a portion of the total bus load and amount to 1333 kVA. These Class 1E loads are supplied at 480 volts through a Class 1E load-center unit substation. Some of the remaining loads, although not Class 1E, are very important and must be energized during a loss of off-site power. These loads include the waste heat cooling tower fan, lithium pumps, and sodium pump pony motors. The lithium pumps are of the electro-magnetic (E-M) type and are powered by a motor-generator set or a variable voltage converter. Approximately 10% of the E-M pump load is required during loss of off-site power. All other non-Class 1E loads are automatically shut down in an emergency.

There are both ac and dc Class 1E loads. The Class 1E ac loads consist of essential lighting, essential heating and motor loads, and control and instrumentation. The dc Class 1E loads are supplied by a dc system which is not shown in the single line diagram Dwg. XI-E-1. These loads are emergency lighting, Class 1E switchgear control annunciation, diesel generator field flashing and Class 1E dc motors. A non-Class 1E dc system is also provided for non-Class 1E switchgear control, the invertor for the uninterruptible ac power supplies and non-Class 1E dc motors and control equipment.

During cold start-up the generators are initially open and power is supplied to the plant auxiliaries through the main transformer and the auxiliary transformers of a power supply group. The transformers of the other supply group are also energized but are not connected to the switchgear buses.

With supply power available, the inductive storage unit stores magnetic energy through the dc flowing in its coils. During the reactor charging period power is supplied to the transformer and divertor coils partly (MW) from the storage unit through a dc/ac/dc converter system and partly from (MW) from the off-site sources.

As soon as sufficient thermal power from the reactor is available the turbine-generators are brought up to rated speed, frequency and voltage. One generator is synchronized with the off-site supplies at a time. After synchronization, the

generator breaker is closed and the generator is controlled to supply the loads and transmit power to the switchyard.

In case an electrical fault occurs in a generator unit, its associated breaker is tripped by corresponding protective relays. A fault in the isolated phase bus, a current limiting reactor or in the main transformer trips the generator breakers of that supply group as well as a switchyard breaker connected to the main transformer. Simultaneously an automatic transfer is made at each switchgear from the faulted supply group to the standby supply group. Maintenance work may then be made to clear the fault without tripping the reactor.

A fault in an auxiliary transformer trips its primary breaker and causes a supply transfer at the associated switchgears. A fault in a switchgear isolates itself and its loads are put out of service. Whether or not the reactor trips depends on the degree of redundancy in the mechanical systems served by the motor loads.

Since there is no redundancy in the magnet converter system an electrical fault in the system may result in a forced reactor shutdown. However, utmost care is taken in the choice of the components and in the design in order to minimize faults.

In the extreme case of simultaneous loss of power from both supply groups, the reactor trips. The standby diesel generators automatically start up and in about 10 seconds power is available at the Class 1E buses to supply the standby and emergency loads as well as important non-Class 1E loads.

During the 10-second interval when no ac power is available, the dc battery systems provide emergency lighting in critical areas and continue to provide control and instrumentation power for essential equipment.

The standby and emergency loads are supplied by the diesel generators for as long as it takes to shutdown the various reactor and reactor coolant systems. Certain turbine auxiliaries must also be supplied from the diesel generators, such as turbine turning gear and lub-oil pumps. The diesel generators require manual shut down.

XI-E. Plant Arrangement

XI-E-1. General

A principal aim of this portion of the study is to develop a conceptual plant arrangement that will meet the requirements for operation and maintenance. Space is provided for necessary equipment and functions; allowance is made for unidentified equipment and for "design growth".

The general plant arrangement and the internal arrangement of the buildings are patterned, wherever possible, after the concepts developed by Bechtel for fission reactor plants. The greatest effort was devoted to those areas unique to UWMAK-III, such as the Containment Building, the Heat Exchanger Building, the Turbine Building, and the Hct Cell. Other buildings such as the Control Building, the Radwaste Building, etc., are similar to those in other nuclear plants, and their arrangements can be adopted readily to this plant.

The general plant arrangement is shown in Drawing XI-M-1. The major features of the arrangement include the following:

- The Containment Building is centrally located relative to the other buildings.

- The Heat Exchanger Building, Radwaste Building, Reactor Axuiliary Building, Hot Cell, and the Maintenance Building are arranged around the Containment Building. This arrangement seems to have an advantage in handling blanket sections and radioactive wastes, and in arranging the reactor primary coolant piping between the Containment Building and the Heat Exchanger Building. This arrangement renders the plant layout very compact with maximum utilization of space around the containment by locating the reactor support systems and facilities close to the nuclear island. This is also expected to offer some economic advantage for piping, cabling and structural considerations.

- The peninsular arrangement of the Turbine Building orients the axes of the turbine-generators such that any missiles generated by the machines will not strike the Containment Building.

- Access corridors run the length of the Turbine Building and interconnect with the Control Building and the

This drawing and the design it covers are the property of BECHTEL. They are merely loaned and on the borrower's express agreement that they will not be reproduced, copied, loaned, exhibited, nor used except in the limited way and private use permitted by any written consent given by the lender to the borrower.

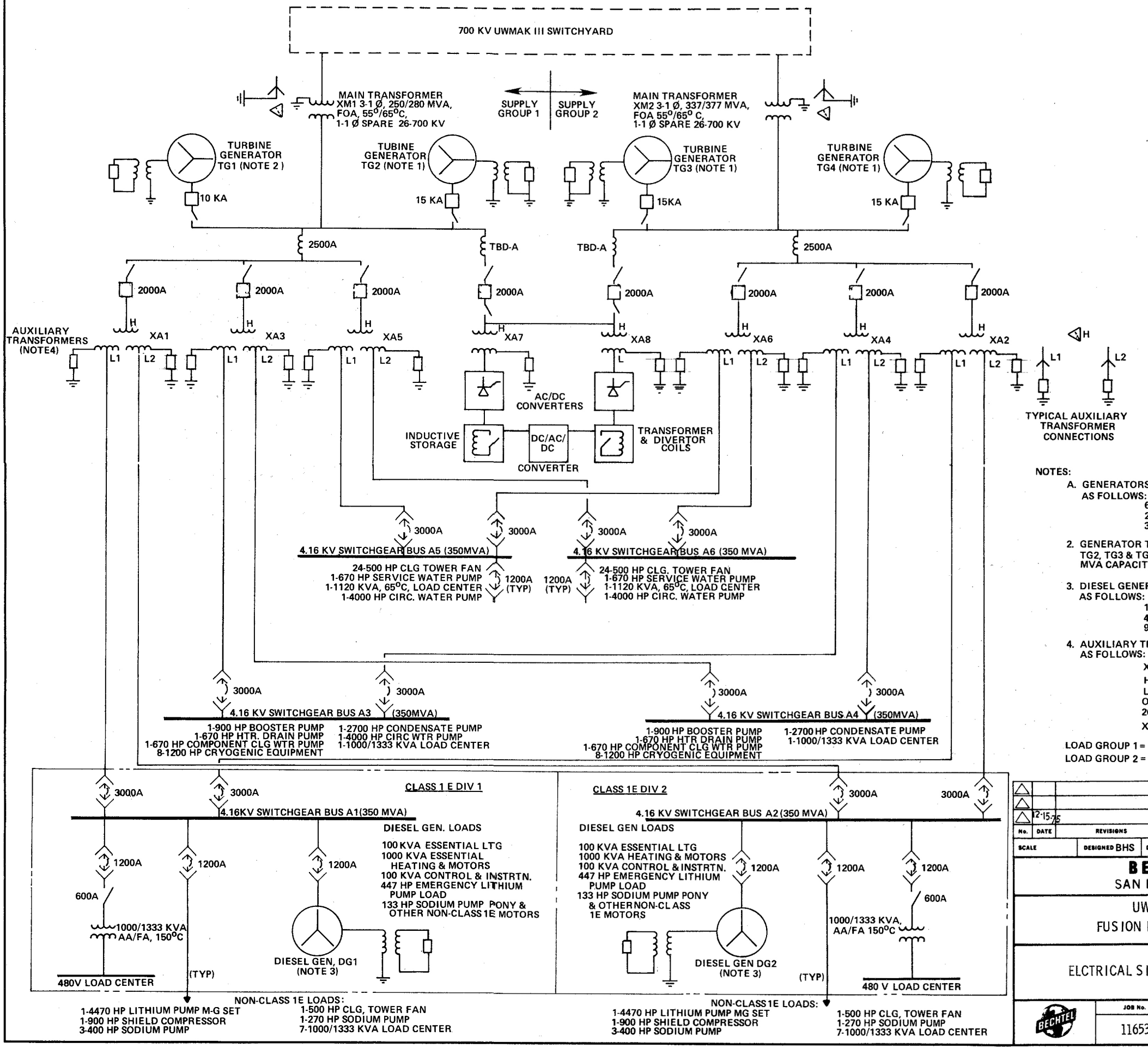

NOTES:

A. GENERATORS TG 2,TG3 & TG4 ARE RATED AS FOLLOWS:
   650 MVA 0.9 pf
   26 KV, 3 Ø, 60 HZ
   3600 RPM

2. GENERATOR TG1 HAS THE SAME RATINGS AS TG2, TG3 & TG4 WITH THE EXCEPTION THAT THE MVA CAPACITY IS 330.

3. DIESEL GENERATORS DG1 & DG2 ARE RATED AS FOLLOWS:
   1500 KW,0.8 pf
   4160 R GNDY/2400 V, 3 Ø 60HZ,
   900 RPM

4. AUXILIARY TRANSFORMERS ARE RATED AS FOLLOWS:
   XA1 TO XA6
   H=21/28/35 MVA
   L1=L2= 10.5/14/17.5 MVA
   OA/FOA/FOA AT 65°C
   26-4.16 R GNDY/2.4 KV, 3-PHASE.
   XA7 & XA8 - TBD

LOAD GROUP 1 = LOADS ON BUS A1,A3,A5
LOAD GROUP 2 = LOADS ON BUS A2,A4,A6

No.	DATE	REVISIONS	BY	CHDK	DESIGN SUPV	ENGR	PROJ ENGR	APPR
	12-15-75							

SCALE | DESIGNED BHS | DRAWN WADDELL | CHIEF ENGR

BECHTEL
SAN FRANCISCO

UWMAK-III
FUSION POWER PLANT

ELCTRICAL SINGLE LINE DIAGRAM

JOB No.	DRAWING No.	REV.
11653	X1-E-1	

17 x 22 "C" SIZE

Reactor Auxiliary Building to provide accessibility to all equipment.

A brief description of these features and of the various buildings is given in the following sections.

XI-E-2. Containment Building

XI-E-2-a. Function

The Containment Building houses the entire nuclear island and the blanket handling facilities. The building is designed to:

- Provide a protective barrier against leakage of radioactive material from the nuclear island to the environment under all postulated accident conditions.
- Contain internal pressure in the event the reactor helium coolant depressurizes into the containment and/or liquid helium from cryogenic systems is discharged into the containment.
- Protect the reactor against missiles and detrimental environmental conditions.

In addition, the Containment Building must accomodate fuel injection equipment, plasma heating equipment, and primary coolant piping, and provide sufficient space for equipment handling and other maintenance operations.

XI-E-2-b. Equipment Arrangement

Arrangement of major equipment, piping and supporting structures within the Containment Building is shown on arrangement drawings XI-M-2 and XI-M-3.

The major equipment items located within the building in addition to the reactor are:

- Primary helium, lithium and sodium piping
- Fuel injection and plasma heating equipment
- Heating and ventilation equipment
- Machines for handling the blanket sections.

This drawing and the design it covers are the property of BECHTEL. They are merely loaned and on the borrower's express agreement that they will not be reproduced, copied, loaned, exhibited, nor used except in the limited way and private use permitted by any written consent given by the loaner to the borrower.

SCALING RULES

SIZE E

SWITCHYARD
(700 KV)

WASTE HEAT
COOLING TOWER
(2 CELLS)

PUMP HOUSE

WAREHOUSE AND SHOPS

PLANT NORTH

HOT CELL

REACTOR AUXILIARY BUILDING

REACTOR CONTAINMENT BUILDING

MAINTENANCE BUILDING

RADWASTE BUILDING

HEAT EXCHANGER BUILDING

DIESEL GENERATOR

HELIUM STORAGE

CONTROL BUILDING

ADMIN. OFFICE

AUXILIARY BOILER

AUX. TRANS.

TURBINE-GENERATOR BUILDING

MAIN TRANSFORMERS

PARKING AND SECURITY

ENTRANCE ROAD

AUX. TRANS.

MAIN TRANS.

INDUCTIVE ENERGY STORAGE BUILDING

INVERTER BUILDING

MAIN COOLING TOWER
(48 CELLS)

PUMP HOUSE

0 25 50 75 100
METERS
GRAPHIC SCALE

No.	DATE	REVISIONS	BY	CHKD	ENGR GROUP APPR	ENGR APPR	PROJ ENGR	APPR
△	12-15-75							

SCALE GRAPHIC | DESIGNED GREEN | DRAWN LNG | ENGR GROUP

BECHTEL
SAN FRANCISCO

UWMAK III
FUSION POWER PLANT

PLOT PLAN

JOB No.	DRAWING No.	REV.
11653	XI-M-1	

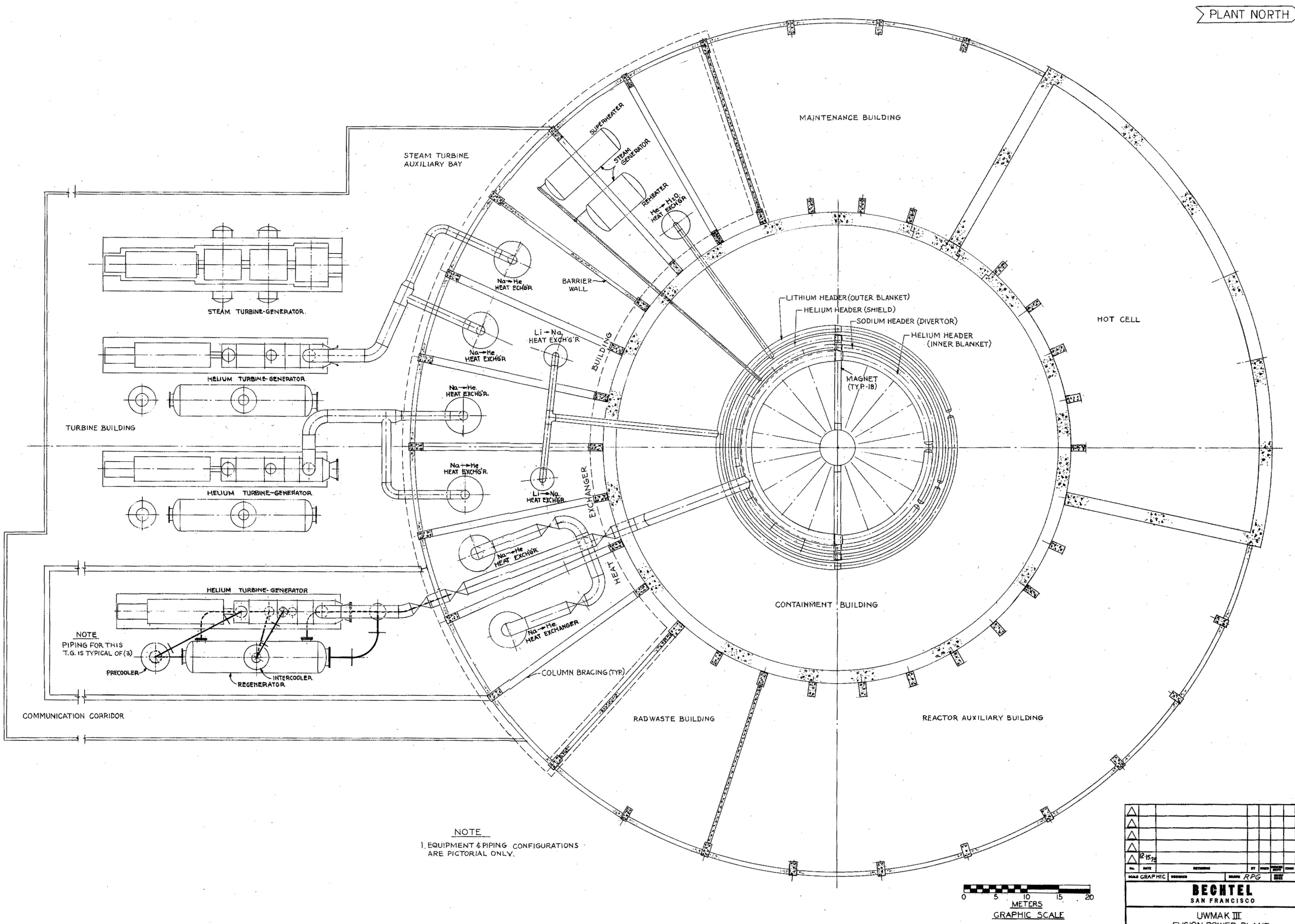

NOTE
1. EQUIPMENT & PIPING CONFIGURATIONS ARE PICTORIAL ONLY.

No.	DATE	REVISIONS	BY	CHKD	DESIGN SUPV	ENGR	PROJ ENGR	APPR
△	12-15-75							

SCALE GRAPHIC | DESIGNED | DRAWN RPG | SHEET ENGR

BECHTEL
SAN FRANCISCO

UWMAK III
FUSION POWER PLANT

CONTAINMENT, HEAT EXCHANGER, & TURBINE BUILDINGS
PLAN

JOB No.	DRAWING No.	REV.
11653	XI-M-2	

This drawing and the design it covers are the property of BECHTEL. They are merely loaned and on the borrower's express agreement that they will not be reproduced, copied, loaned, exhibited, nor used except in the limited way and private use permitted by any written consent given by the lender to the borrower.

This drawing and the design it covers are the property of BECHTEL. They are merely loaned and on the borrower's express agreement that they will not be reproduced, copied, loaned, exhibited, nor used except in the limited way and private use permitted by any written consent given by the lender to the borrower.

CROSS SECTION VIEW OF UWMAK III TOKAMAK POWER PLANT

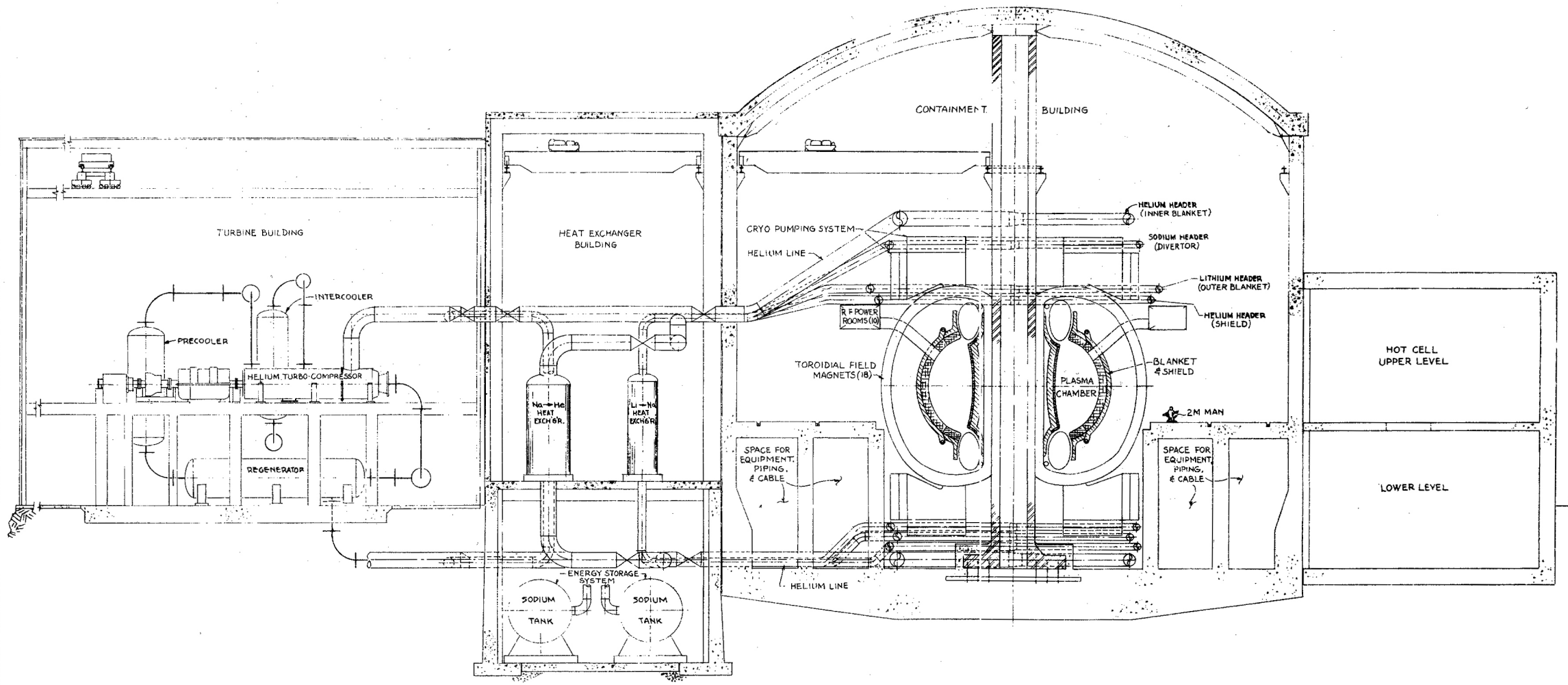

NOTES

1. FOR PURPOSE OF PRESENTATION ALL CONNECTING PIPING IS SHOWN IN THE PLANE OF THIS DRAWING.
2. EQUIPMENT & PIPING CONFIGURATIONS ARE PICTORIAL ONLY.

0 5 10 15 20
METERS
GRAPHIC SCALE

△			
△			
△			
△			
△	12-15-75		
SCALE GRAPHIC	DESIGNED	DRAWN RPG	

BECHTEL
SAN FRANCISCO

UMWAK III
FUSION POWER PLANT

CONTAINMENT, HEAT EXCHANGER, & TURBINE BUILDINGS
TYPICAL CROSS SECTION

JOB No.	DRAWING No.	REV.
11653	X1-M-3	

The arrangement effort for this building was directed toward the primary coolant piping and the nuclear island. The primary coolant removes heat from the inner blankets, outer blankets, divertor plates and shield sections. Helium, lithium, sodium, and helium are the respective coolants. (Refer to Chapter X for energy conversion system description.) Expansion joints are assumed in the piping systems to accomodate differential expansion. However, these are not shown in the drawings.

The reactor is made up of 18 segmented modules of inner and outer blankets, divertor plates and shield sections arranged around the reactor core (refer to Chapter V for reactor description), and a separate coolant supply is needed for each individual segment. To conveniently supply coolant to these segments, four cold leg ring headers - one (helium) for the inner blanket, one (lithium) for the outer blanket, one (sodium) for the divertor plate, and one (helium) for the shield section are arranged below the reactor. To collect the hot coolant from the segments, four similar hot leg ring headers are located above the reactor. To conserve material, each of the cold and hot leg ring headers is made up of two different sized sections.

Hot coolant from the respective ring headers are transported to the Heat Exchanger Building through several coolant lines. A helium line (hot leg) conveys the thermal energy from the inner blanket hot leg ring header directly to a gas turbine-generator (located in the Turbine Building) for conversion to electrical energy. The cold helium leaving the gas turbine is piped back to the cold leg ring header through another helium line (cold leg). Both these lines traverse the entire width of the Heat Exchanger Building to connect the gas turbine and the reactor.

Two lithium lines (hot legs) transport hot lithium from the outer blanket hot leg ring header to two lithium-to-sodium heat exchangers located in the Heat Exchanger Building. Two cold lithium lines (cold legs) carry the lithium from the heat exchangers back to the cold leg ring header.

Hot sodium from the divertor hot leg ring header is transported by a sodium line (hot leg) to the steam generator (superheater and reheater modules) located in the Heat Exchanger Building. The cold sodium flows to the cold leg ring header through a cold sodium line (cold leg). A similar arrangement is used for the shield coolant (helium) flow path. A helium line (hot leg) conveys the hot helium from the hot leg ring header to the helium-to-water heat exchanger and another helium line (cold leg) conveys the cold helium back to the cold leg ring header.

XI-E-2-c. Equipment Handling

Space is provided within the Containment Building to carry out a number of reactor maintenance and equipment handling operations. The removal of blanket sections is expected to be a major operation and a special machine capable of reaching and handling all the outer blanket sections is needed. A conceptual sketch of this special blanket handling machine is shown in Drawing XI-M-4. Two such machines are used (to reduce the reactor downtime) - one for removing the irradiated sections and the other for installing the rebuilt sections.

The blanket handling machine shown in the drawing should not be considered to represent a true design. The design of such a machine is beyond the scope of this study. Inclusion of such a machine in the plant arrangement drawing is intended only to conceptualize a scheme for removal and replacement of irradiated blanket segments.

The handling machines travel on a circular track installed on the Containment Building floor. The circular track runs in an annular region between the reactor and the Containment Building wall. Radial tracks between the toroidal magnets enable the machines to travel into the reactor and reach the blanket sections. The irradiated (or spent) sections are removed and transferred to the Hot Cell through an equipment hatch. The new sections are also brought from the Hot Cell and installed in the reactor by the same machines.

An overhead annular travelling crane is provided in the Containment Building. This crane is required during reactor installation and also will be used after the plant is operational for maintenance work.

XI-E-2-d. Penetraticns

A large number of pipes and electrical and instrumentation cables must pass through the containment wall. Most of the penetrations are through the wall of the Containment Building into the Reactor Auxiliary Building. Separate penetration zones are needed to separate mechanical (piping) penetrations from electrical penetrations. The helium, lithium and sodium piping penetrations are located in the wall of the Containment Building adjacent to the Heat Exchanger Building. Most electrical penetrations are on the wall adjacent to the Reactor Auxiliary Building.

This drawing and the design it covers are the property of BECHTEL. They are merely loaned and on the borrower's express agreement that they will not be reproduced, copied, loaned, exhibited, nor used except in the limited way and private use permitted by any written consent given by the lender to the borrower.

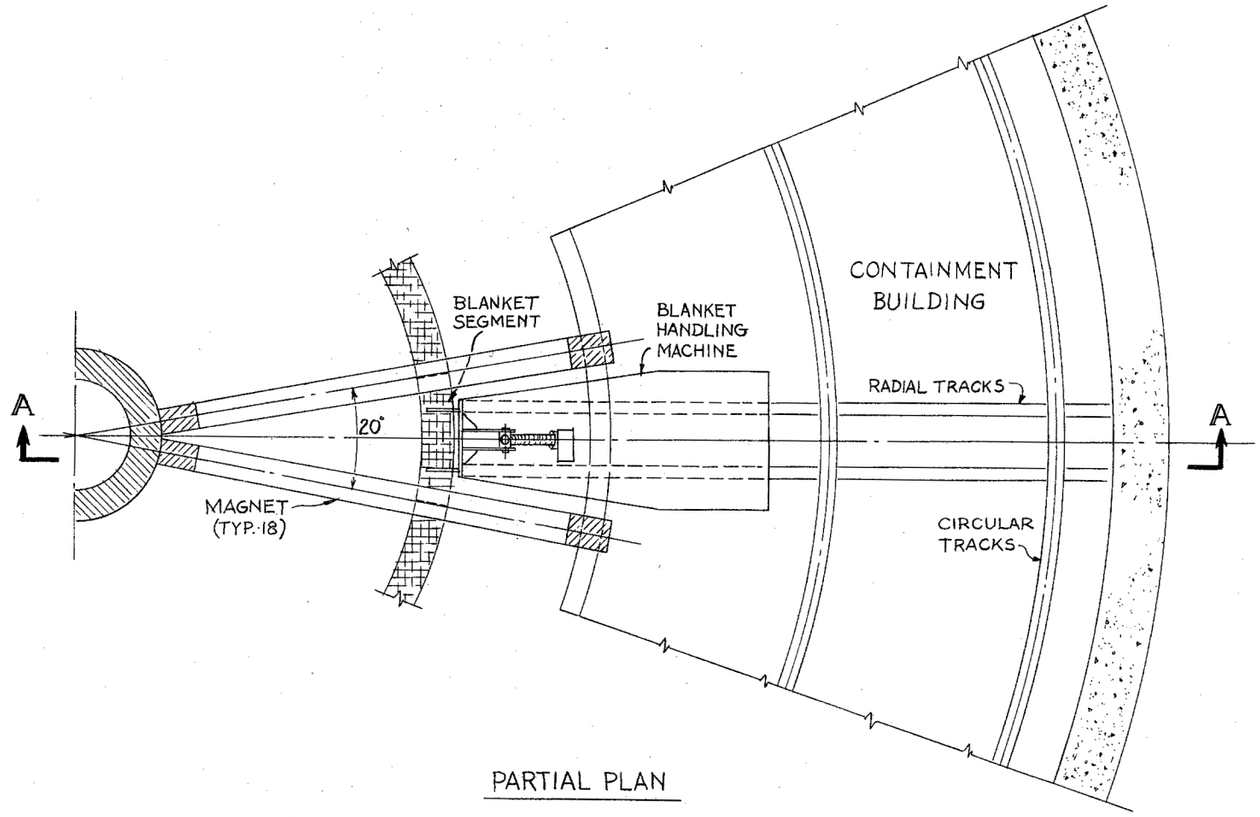

PARTIAL PLAN

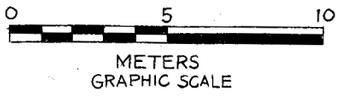

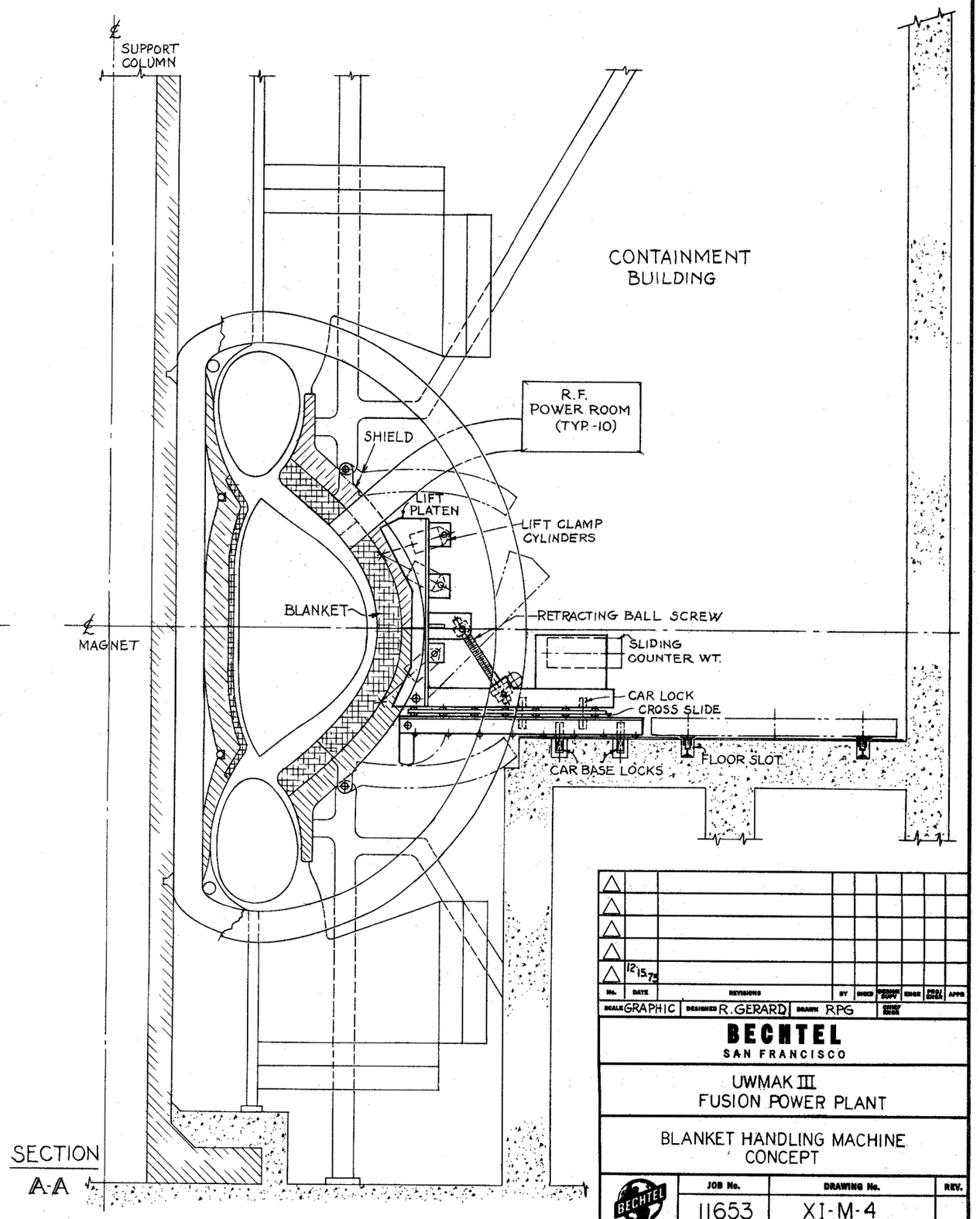

SECTION A-A

No.	DATE	REVISIONS	BY	CHKD	ENGR	PROJ ENGR	APPR
1	12/15/75						

SCALE GRAPHIC | DESIGNED R. GERARD | DRAWN RPG

BECHTEL
SAN FRANCISCO

UWMAK III
FUSION POWER PLANT

BLANKET HANDLING MACHINE CONCEPT

JOB No.	DRAWING No.	REV.
11653	XI-M-4	

22 X 34 "D" SIZE

Personnel access to the Containment Building is through a personnel airlock located in the Auxiliary Building. A large equipment hatch between the Containment Building and the Auxiliary Building is used for transfer of fuel handling, plasma heating and other large equipment. The Containment Building is inaccessible during reactor operation. An inert (helium) atmosphere is maintained within the containment to prevent a lithium or sodium fire in case of a piping leak.

XI-E-3. Hot Cell

The Hot Cell is located adjacent to the Containment Building. The functions of the building are to:

- Receive the irradiated blanket sections
- Separate the blanket section from the supporting frame
- Store blanket sections for a radioactive decay period
- Decontaminate, crush, solidify and package radioactive material
- Provide temporary storage of packaged wastes before off-site disposal

A description of the functional arrangement of the Hot Cell is given in Section XI-B and is shown in Figure XI-6.

The equipment needed in the Hot Cell is not yet identified. Additional studies are needed to determine the equipment requirements.

XI-E-4. Reactor Auxiliary Building

The Reactor Auxiliary Building is wrapped around the north-east side of the Containment Building and contains the equipment that must be located close to the reactor. The location of the building relative to the Containment Building is shown in Drawing XI-M-2. This building contains the majority of the cryogenic equipment, equipment for tritium extraction from helium and lithium, lithium and helium clean-up systems equipment, blanket tritium recovery equipment, etc.

A separate floor is provided for the containment clean-up system equipment and for the fans, blowers, chillers, filters, and associated equipment required for the heating, ventilating

and air conditioning (HVAC) systems of the Reactor Auxiliary Building.

The requirements for the equipment to be located in this building have not been established. As a result, only approximate areas for various equipment are allowed.

XI-E-5. Heat Exchanger Building

The building contains the following heat exchangers, thermal energy storage components and the associated equipment:

- Lithium-to-sodium heat exchangers (IHX) for the outer blanket cooling system.
- Sodium-to-helium heat exchangers (SHX) for the both inner and outer blanket cooling systems.
- Helium-to-water heat exchanger (IHX) for the shield cooling system.
- Steam generator (superheater and reheater modules) for the divertor cooling system.
- Hot and cold sodium storage tanks for thermal energy storage system.

Drawings XI-M-2 and XI-M-3 show the arrangement of this building. The Heat Exchanger Building is wrapped around the southern portion of the Containment Building. In addition to the equipment mentioned above, this building is required to accommodate the complex primary, intermediate and secondary piping system. The analysis, design and arrangement of this piping is beyond the scope of the present study, and, as a result, the locations and configuration of the major piping and equipment are only approximate.

Since it houses reactor primary coolant piping, the building is shielded to provide containment and a protective barrier against leakage of radioactive material from the primary system under accident conditions (lithium, sodium or helium pipe break) and protection from tornados and missiles. A separate enclosure is provided for the divertor steam generating equipment to prevent any accidental contact of water with lithium and sodium of the blanket cooling systems. An inert atmosphere is maintained within the building.

The hot and cold sodium storage tanks for thermal energy storage are located on a floor below the heat exchanger floor (see Drawing XI-M-3). (The thermal storage system is described in Chapter X.)

Only superficial consideration has been given to the design of this building; detailed analysis and study is needed to develop the design further.

XI-E-6. Turbine Building

The Turbine Building houses the turbine-generators and the associated energy conversion equipment. The power cycle (see Chapter X) for the UWMAX-III uses four turbine-generator units - two closed-cycle helium turbine-generators serving the outer blankets, one closed-cycle helium turbine-generator serving the inner blanket, and one steam turbine-generator serving the divertor.

The unit serving the inner blanket receives helium directly from the reactor. This unit is located in a separately shielded bay of the Turbine Building to provide containment and a protective barrier against leakage of radioactive material in case of any accidental release of tritium-bearing helium. The turbine-generator units handling non-radioactive fluids are located in the non-shielded areas of the Turbine Building.

A typical arrangement of the regenerative cycle components of the helium turbines is shown in Drawings XI-M-2 and XI-M-3. These components include regenerator, precooler, intercooler and the associated connecting piping. Equipment and piping arrangement for the steam turbine regenerative cycle is not shown here, since these are more conventional and can readily be adopted from fission plant designs.

An overhead travelling crane is provided in each of the shielded and non-shielded sections of the building for equipment handling and to permit disassembly of the turbine-generators for maintenance. Equipment hatches allow access to the various equipment and components with the overhead crane. A truck access and loading bay is provided. Communication corridors run the length of the building at various levels. These corridors provide access to the equipment for operation and maintenance and serve as major accessways to convey the control cable trays to the central control room and piping to other areas of the plant. Access to the control room from the upper communication corridor is possible.

XI-E-7. Control Building

The design of the Control Building is adopted from the generic fission plant. The building contains a central control room, cable spreading rooms, switchgear, auxiliary panels, and M-G sets. It also houses the heating, ventilating and air-conditioning equipment for the entire building. The building will be provided with an area from where all access to potentially radioactive areas of the plant is controlled. Facilities for monitoring levels of radioactivity, and showers and change facilities for controlling radioactive contaimination are provided in this building. The following facilities are also located in the Control Building.

- Radiation Chemistry Lab
- Clean Chemistry Lab
- Counting Room
- Contaminated Clothing Laundry
- Health Physics Office
- First Aid Facilities

The Control Building is located 100 M away from the center of the Containment Building to minimize the effect of the magentic field on the control instruments. The building structure serves as the magnetic barrier.

XI-E-8. Maintenance Building

This building is located on the west side of the Containment Building, and adjacent to the Heat Exchanger Building and the Hot Cell. Maintenance of the radioactive components is assumed to be carried out in this building eliminating the necessity for transporting any radioactive component outside the shielded areas. The blanket handling machines and other equipment - located within the Containment Building which require maintenance can be readily transferred to this building. Only an approximate area is indicated in the Drawing XI-M-2 and further study is needed to develop a design of this building.

XI-E-9. Other Buildings and Facilities

Other Buildings and facilities shown in the general plot plan drawing, XI-M-1, are described briefly in the following paragraphs:

XI-E-9-a. Radwaste Building

All equipment and facilities for processing solid, liquid and gaseous radioactive wastes are located in this building. The primary sources of these radioactive wastes are the tritium handling systems and coolant (lithium, helium and sodium) purification systems. These wastes are transferred to the Radwaste Building from the Heat Exchanger Building and the Auxiliary Building for processing and disposal. Thus, the Radwaste Building is conveniently located adjacent to both these buildings.

XI-E-9-b. Cooling Towers

Location and arrangement of the cooling towers for plant heat rejection is shown on the plot plan drawing. The main cooling tower is located along the southern boundary of the plot and is oriented at right angles to the prevailing wind direction to minimize inteference between the thermal plumes which are dischanged upward from each cell. There is a total of 48 cells in the main tower and it occupies a land area of approximately 41,000 M^2 (10 acres).

The waste heat cooling tower - rejecting heat from the shield - is located north of the Containment Building. This tower consists of two cells (one standby) and is oriented at right angles to the prevailing wind direction. Space needed for this tower is approximately 1700 M^2 (18000 ft^2).

XI-E-9-c. Inductive Energy Storage Building

This building houses the superconducting solenoid magnets to store electrical energy for charging and discharging of divertor and transformer coils during the reactor burn cycle. The building is located more than 100 M away from the center of the Containment Building to minimize the effect of interactions of the magnetic fields generated by the inductive field coils and the toroidal field coils.

XI-E-9-d. Helium Storage Building

This building contains the cylinders used for storage of purified helium when the blanket and shield cooling systems are depressurized. The cylinders are stacked in racks within this building. The building is designed to withstand the consequences of any potential cylinder failure. The helium purification equipment, transfer compressors and associated equipment are located in the Auxiliary Building.

XI-E-9-e. Administration Building

This is a two-story office building located adjacent to the Control Building at the front (east) side of the plant. It contains offices, other administrative facilities, a lunchroom, and a locker room.

XI-E-9-f. Warehouse and Shop Building

A permanent warehouse and shop building is part of the plant supporting facilities. Depending on the services available in the vicinity of the plant site, it might contain, for example, an electrical shop, an instrument shop, a dismantling room, a tool room, and welding area. Because of the special nature of many of the components of the plant (e.g., magnets, cryogenerators, vacuum pumps), some of the shops are likely to be more elaborate than those in fission plants.

XI-E-9-g. Diesel-Generator Building

This building houses the emergency diesel generators and their associated diesel oil storage tank, day tanks, and the exhaust silencers. In the event of an off-site power failure, they will automatically start and be ready to assume load in about 10 seconds. The generators are self-cooled and are equipped with static excitation systems. The building design provides for protection of the diesel-generator equipment from tornados and missiles.

XI-F. Building Design

Conceptual civil/structural design was performed for major structures of the plant to determine their technical feasibility and to provide information required for the conceptual cost estimate. The major effort was directed to the design of the Containment Building, Heat Exchanger Building and Turbine Building.

The buildings of the plant are classified as Category I and non-Category I depending upon the required protection against damage due to environmental conditions as per NRC Regulatory Guide 1.29. The Category I buildings are required to withstand the effects of earthquakes, flocds and tornadoes so that the occurrence of any of these natural disasters will not impair the safety of the structures as well as that of the plant. Moreover, it is required that these structures be able to withstand the impact of any wind-generated and plant-generated missiles. The non-Category I buildings are designed such that their failure will not cause a loss of safety function of any Category I system.

The following list classifies the buildings into the above two categories:

Containment Building	-	Category I
Hot Cell	-	Category I
Turbine Building	-	Part Category I Part non-Category I
Diesel Generator Building	-	Category I
Reactor Auxiliary Building	-	Category I
Main Cooling Tower	-	non-Category I
Waste Heat Cooling Tower	-	Category I
Administration Building	-	non-Category I
Heat Exchanger Building	-	Category I
Radwaste Building	-	Category I
Maintenance Building	-	Category I
Control Building	-	Category I
Support Buildings	-	non-Category I

Standard structural theory and methods of design were used. The following manuals and codes of practice were used for designing the structures:

- American Concrete Institute (ACI)
  - ACI 318-71 "Building Code Requirements for Reinforced Concrete"
- American Institute of Steel Construction (AISC)
  - "Specifications for the Design, Fabrication, and Erection of Structural Steel for Buildings" 7th Edition 1970
- Uniform Building Code (UBC), 1973 Edition
- Nuclear Regulatory Commission (NRC)
  - Regulatory Guides 1.60, 1.61 and 1.76
- American Society of Mechanical Engineers (ASME)
  - "ASME Boiler and Pressure Vessel Code", Section III, Division 2 Code for Concrete Reactor Vessels and Containments, 1975 Edition

The plant is assumed to be located in the State of Wisconsin. The loading and soil conditicns used in the design are as follows:

Loading

- Dead Loads. Consist of the weights of the concrete walls, dome, base mat, permanent equipment and machinery. Weights used for dead load calculations were: concrete 2323 Kg/M^3 (145lb/ft^3), reinforcing steel and plates, 7834 Kg/M^3 (489lb/ft^3).
- Live Loads. Consist of all loads except dead, accident, seismic, flood and wind loads. Snow loading of 185 Kg/M^2 (40psf) was adopted (UBC).
- Wind and Tornado Loads. The State of Wisconsin is located in an area designated as Zone 1 in the NRC/AEC Regulatory Guide 1.76 titled "Design Basis Tornado for Nuclear Power Plants". In Zone 1 tornados with maximum wind speed of 580 Km/hr (360 mph) along with a pressure drop of 0.21 Kg/cm^2 (3 psi) in 1.5 seconds could occur.

- Seismic Load. The NRC/AEC's Seismic and Geology Siting Criteria requires that, for the purpose of analysis and design, two design earthquakes be specified for each site, viz., Safe Shutdown Earthquake (SSE) and the Operating Basis Earthquake (OBE). In the State of Wisconsin, only low-intensity earthquakes are expected to occur. Hence, the assumed design response spectra, adopted from NRC/AEC Regulatory Guide 1.60, have maximum horizontal ground accelerations of 0.2g and 0.1g for SSE and OBE, respectively.

Soil Condition

The soil in the area is composed of dense silty-sand. The allowable soil bearing pressure, based on information supplied by the University of Wisconsin, is 48.8 tonnes/M^2 (5 ton (U.S.)/ft^2).

XI-F-1. Plant Structure

As previously mentioned, the major effort was devoted to the conceptual design of the Containment Building, the Heat Exchanger Building, and the Turbine Building. Less detailed considerations were given to the Hot Cell and the Reactor Auxiliary Building.

These buildings are significantly larger than those of a fission plant, and, consequently may involve departures from fission plant engineering practices as well as having a greater influence on costs. The other buildings such as the Diesel Generator Building, the Control Building, the Administration Building and Support Buildings of this plant are similar in size and function to those of a fission power plant and therefore, their costs can be estimated based on experience from fission plants. Hence, only those structures which are expected to influence the cost estimate significantly are described.

XI-F-1-a. Containment Building

The Containment Building is a reinforced concrete structure consisting of a circular mat foundation, a cylindrical wall and a spherical dome. The cross-sectional view of this building is shown in Drawing XI-M-3.

The spherical dome has an inside radius of 48.8M (160 ft) and a rise of 14M (46 ft) above the spring line (interface with cylinder wall). The thickness of the dome is 2M (6.56 ft) based on shielding requirements determined by the University of

Wisconsin. The central angle subtended by this dome is 90°. The ratio of thickness to radius for the dome is 1/25 and it was designed on the basis of non-shallow thin shell theory. A reinforced concrete edge (ring) beam 4M (13.12 ft) deep by 3M (9.84 ft) wide is provided to take horizontal thrust from the dome.

The cylindrical building is 70M (230 ft) in diameter and has a height of 57.5M (190 ft) above base mat. Wall thickness at the top is 2M (6.56 ft). At the junction with the base mat, the wall is 3.50M (11.50 ft) thick and uniformly tapers to 2M (6.56 ft) over a distance of 10M (32.81 ft). This increased thickness of wall at the base is necessary to carry the large bending moment which would result from an accidental pressurization of the Containment Building (1.06 Kg/cm^2 (15 psig) internal pressure based on information supplied by the University of Wisconsin). There are penetrations in the containment walls to permit transfer of radioactive materials into the adjacent Hot Cell and the Maintenance Building and for piping and cables leading to the Heat Exchanger Building and the Auxiliary Building.

The Building foundation is a reinforced concrete mat 6.50M (21.33 ft) thick at center tapering to 3.50M (11.48 ft) at the junction with the cylindrical wall. Two concentric ducts above the base mat carry piping, electrical cable and instrumentation leads. Equipment will be located in these areas as well. The top slab of these rectangular ducts forms the operating floor of the Containment Building.

Nine three-hinged arches are provided below the dome; at the crown these arches are connected to a compression ring to avoid congestion. These arches are box-girders fabricated from 3 steel plates. During construction, the containment liner plate is laid on the top of the arches and concrete shielding is poured over the liner. Thus, the arches support wet concrete during construction; using the containment liner as part of the formwork minimizes the forming required for the concrete.

For leak tightness, and to minimize hazards from Li fires, 6.5mm (1/4 in.) thick stainless steel plate stiffened with structural sections is used to line the Containment Building.

An overhead annular crane is provided in this building. The crane is supported on brackets attached to the containment wall and the central column.

The cylinder wall and the dome are constructed of 352 kg/cm² (5000 psi) concrete and are reinforced with reinforcing bars. The base mat is constructed of 457 kg/cm² (6500 psi) concrete, reinforced with several layers of reinforcing bars. It is sized to accommodate all loads without exceeding the allowable bearing pressure on soil.

Only a preliminary evaluation could be made of the actions of lateral forces (tornado and seismic) on the structure. This indicated that the structure would be able to withstand their actions without loss of stability and safety.

The central steel column supports the weight of the reactor assembly. In order to prevent excessive sway of the reactor due to actions of seismic forces, the column is extended up to the underside of the dome and is connected to the arch compression ring. This arrangement limits the sway of the reactor assembly to within an acceptable range. Also, the preliminary calculations show that the column will be able to sustain the actions of seismic forces without exceeding the allowable stress in steel.

XI-F-1-b. The Heat Exchanger Building

The Heat Exchanger Building, shown on Drawing XI-M-2 and XI-M-3, is located to the south of the Containment Building and occupies a sector with a 125 degree included angle. The superstructure of this building houses the heat exchangers and steam generators while the substructure houses the hot and cold sodium storage tanks and the associated equipment for the thermal energy storage system.

The building is 30M (100 ft) wide and 68.5M (225 ft) high and occupies an approximate area of 3400M² (37000 ft²). The superstructure of this building is protected against missile impact. The roof is a 457mm (1.50 ft) thick reinforced concrete slab supported on 2.134M (7 ft) deep by 1.219M (4 ft) wide by 30M (100 ft) long prestressed girders spaced radially at 10 degrees apart. The ends of the girders are supported on 1.219M (4 ft) by 2.19M (7.2 ft) columns. The columns by the side of the Containment Building are braced in the longitudinal direction against lateral buckling. The exterior columns are supported by the 610mm (2 ft) thick missile proof wall. The reinforced concrete floor slab is 1.00M (3.28 ft) thick and is supported on a series of 2.134M (7 ft) deep by 1.219M (4 ft) wide prestressed concrete beams spaced radially and supported by the substructure retaining walls.

The superstructure wall and columns extend below the floor slab and form the substructure wall and columns. The columns are supported on individual spread footings resting on sound soil. The lateral earth pressure is supported by substructure walls spanning between the columns. The walls taper from a thickness of 1.52M (5 ft) at the base to 1.25M (4.10 ft) at the top. The base slab is 1.0M (3.28 ft) thick and rests on a layer of compacted gravel or crushed stone.

For leak tightness, and to minimize hazards from Li fires, 6.5 mm (1/4 in.) thick steel plate stiffened with structural sections is used to line the Heat Exchanger Building.

For handling the heat exchangers, piping, etc., an overhead annular travelling crane is provided in this building. The crane is supported by crane runway girders which, in turn, are supported on brackets attached to columns.

XI-F-1-c. Turbine Building

The Turbine Building, shown on Drawings XI-M-2 and XI-M-3 is located to the south of the Heat Exchanger Building. A portion of this building is a Category I structure and the remaining portion is non-Category I. There are four turbines in this building. The turbine, which handles radioactive helium from the reactor, is housed in the Category I area of the building and the other three turbines are located in the non-Category I section.

The Category I section is a reinforced concrete framed building 95M (312 ft) long by 20M (66 ft) wide by 45M (148 ft) high. The frames are spaced at 8.25M (27.10 ft) apart. The roof slab is 457mm (1.5 ft) thick and walls are 610mm (2 ft) thick. The columns are 1.219M (4 ft) square in cross-section and are monolithic (rigidly connected) with beams having cross-section 1.219M (4 ft) square.

The non-Category I section is a single story steel frame building, 60M (197 ft) wide by 45M (148 ft) high and is 95M (312 ft) long. The roof is constructed of built-up roofing (rigid insulation on a steel deck) all supported by a system of trusses and purlines. The columns and trusses are spaced at 8.25M (27.10 ft) on centers. The two exterior side walls are of insulated metal siding.

An overhead travelling crane is provided in each of the sections of this building. The capacity of these cranes is

suitable for lifting the heaviest part of turbine-generator units. The crane girder is a built-up tee section spanning between the columns. The steel columns are also of built-up sections and crane girders rest directly on them. The reinforced concrete columns have brackets which support the crane girders. The cranes have access to the laydown area. The foundations for columns are individual spread footing resting on sound soil.

The turbine generator pedestals are massive reinforced concrete structures designed to support the turbine generators with no objectionable settlement. Each pedestal consists of a 2.134M (7 ft) thick base mat, a 2.0M (6.56 ft) thick top slab and 12 columns ranging in cross-section from 1M (3.3 ft) square to 1.52M (5 ft) square.

XI-G. General Comments

The present design allows an initial assessment of the problems associated with the plant design for tokamak-type reactor plants in general and the UWMAK-III reactor plant in particular. The design and analyses are relatively superficial and conceptual in nature. Many of the systems and associated equipment are not defined in detail and some of them probably have not yet been identified. Allowances have been made to accommodate these unknowns and uncertainties; but until further design and analysis is done, many uncertainties remain. On the basis of the present study, the following comments are in order:

- The plant layout including equipment and piping arrangement is conceptual. Further study is needed to detail and improve the arrangements. The primary piping arrangement is a critical aspect of the plant layout and can have a large impact on building costs. The layout is based on the use of expansion joints in the primary piping. This will require development and testing to gain ASME Code acceptance. No consideration has been given to the arrangement of the reactor internal piping or its interface with the external primary piping systems.

- The design and layout of high temperature piping is critical. No stress analysis has been performed to substantiate the piping arrangement. The stress analysis will likely rely heavily on inelastic analysis and other sophisticated techniques leading to high design costs. Special design configurations such as concentric and externally-cooled pipe might be required.

- The operating temperatures of the blanket heat transfer systems are beyond the present state -of-the-art and there is no experience in designing and operating large systems at these temperatures. The following are some factors that must be considered in developing the system design:

  - Section III of the ASME Boiler and Pressure Vessel Code and other applicable codes will likely require modification to provide a basis to determine the strucutral adequacy of piping and components.

  - Basis data is needed on the behavior of materials and structures at the anticipated operating conditions. These should include long-term behavior and properties, interaction with coolant and other system materials, corrosion, compatibility, mass transfer, creep racketing, and creep-fatigue evaluation.

- Piping supports and expansion joints will require development and testing.

- Reactor Maintenance problems, especially in regard to blanket removal and replacement, constitute another area where only preliminary consideration could be given. A conceptual blanket handling scheme has been proposed, but studies are needed to evaluate the feasibility of the concept and develop procedures and conceptual equipment designs. It is likely that major R&D programs will be necessary to develop and improve blanket handling equipment and procedures. The problem of radioactive contamination of the plant and equipment has not been looked at and must be given a serious consideration.

- Analysis of the effects of magnetic fields (generated by toroidal field coils) on plant equipment and components is necessary. It may be necessary to consider relocation of some of the buildings and equipment. To avoid interference with the magnetic field, non-magnetic materials are needed for the piping and the containment liner.

- The equipment requirements for the Hot Cell have not been defined. Concepts for handling the blanket sections, disassembling, processing and reassembling the new sections must be developed. The building sizes and arrangements shown are preliminary and may change considerably after detail engineering is undertaken.

- Details have to be worked out to determine an acceptable method of ultimate disposal of solid radioactive wastes. Several alternatives are possible such as: on-site storage versus buried vaults, air-cooled versus forced convection systems.

- An annular arrangement of the reactor support buildings surrounding the Containment Building is proposed. This arrangement seems to offer some advantage. It makes the plant layout very compact with maximum utilization of space around the Containment Building by locating all the reactor support facilities near the nuclear island. Some cost saving will also result because the containment wall is made common to the support buildings. This arrangement results in the Containment Building being completely surrounded which can make scheduling of the construction of the various buildings difficult because of the need for construction access.

- To accommodate the four turbine-generator units along with their associated regenerative cycle components, a large Turbine Building is needed. The unit handling the

tritium-bearing helium imposes a further constraint on the building design.

- Piping arrangement in the Heat Exchanger Building represents probably the most complex piping system in the plant. The design of the complex intermediate sodium piping arrangement for the thermal storage system could not be addressed in this study. A detailed study is needed for this cost intensive area of the plant design. The thermal storage system may be a fruitful area for study of new concepts.

- The structures in this plant are significantly larger than those in fission power plants. All the structures are very massive because of shielding and other safety requirements. The conceptual design, as described, is considered to be a feasible design consistent with current technology and industry practice. However, some aspects of the design/analysis of the structures have to be investigated further before a method for their design can be established, and they are identified as follows:

  - In the Containment Building, special vehicles, possibly running on tracks, have to be built for removing blankets, which will subject the floor slab to moving dynamic loads. A thorough analysis of the floor slab, subjected to moving loads, is needed.

  - The dome has been analyzed on the assumption that its thickness is uniform throughcut. The domes are usually thickened near the edges. This necessitates a finite element analysis to study the propagation of edge disturbances into the dome.

  - The phenomenon of instability of the dome and the cylinder has been studied on the basis of classical linear theory. However, it is also known that, due to imperfections and boundary conditions different from those used in linear theory, the buckling load of shells can be significantly lower than those given by the classical theory. An estimate of this lower buckling load should be obtained by non-linear analysis in conjunction with realistic boundary conditions. At springline level, the arches will exert considerable thrust producing radial expansion of the cylinder. It is, therefore, necessary to evaluate the interactions between the arches, the dome and the cylinder.

  - The long, narrow penetrations on the cylinder wall leading to the adjacent buildings requires thorough investigation. A "closed-form" solution (which could

be used for designing the penetration) for this problem does not exist in literature. It is, therefore, necessary to investigate the effect of this opening in a pressurized shell by using finite element methods.

XII. Availability of Metals for UWMAK-III

XII-A. General Statement

UWMAK-III requirements for metals are in general much reduced below those of UWMAK-I[1] and UWMAK-II[2], and the problems of metal procurement are correspondingly less severe. A few of the metals, however, may present serious problems. The following appraisal is in terms of metals required for construction of reactors for generation 10^6 MWe. Detailed estimates of United States and world reserves have already been given in the reports on UWMAK-I[1] and UWMAK-II.[2] The proposed requirements for UWMAK-III are given in Table XII-1 and XII-2. United States reserves and resources, together with U.S. 1974 production are summarized in Table XII-3.

XII-B. Specific Considerations for Individual Elements

XII-B-1. Aluminum

The United States has very limited bauxite reserves and imports over 90 percent of its bauxite supply. An adequate domestic supply of aluminum ore would require development of resources of high-alumina clays, anorthosite, alunite, and dawsonite, singly or in combination. The resources of aluminum in such materials are very large. The necessary technology is available for extraction from clays, anorthosite, and alunite, but energy costs and dollar costs would be above those of extraction of aluminum from buaxite. Mining of these three materials would be open cast, but no unusual environmental problems would be involved. Dawsonite production would be involved with oil shale production and would share the environmental and other problems facing the oil shale effort.

XII-B-2. Boron

United States reserves of boron are very large relative to prospective demand for conventional purposes and relative to the requirements for UWMAK-III. The production of about 500,000 tons over the period 2000 to 2020 should be achieved without difficulty.

XII-B-3. Chromium

If the chromite resources in the Stillwater Complex, Montana, are not used for other purposes, the UWMAK-III requirement could be met from that source, at prices probably not very much higher than present prices. Otherwise, the requirement might be met from domestic sources only by paying high prices for domestic chromite concentrates, probably 3X present prices or higher.

XII-B-4. Niobium

The requirement for niobium is approximately equal to the amount of niobium in ore blocked out by exploration of the Powderhorn Complex, Colorado, the only sizeable domestic resource. This is not a comfortable situation. Stockpiling of niobium in advance of use appears to be the only answer to the problem of procurement, unless new deposits can be discovered in the United States.

XII-B-5. Iron

The requirement of 60 million tons, spread out over a period of 20 years, it small relative to United States reserves of iron ore and steel producing capacity. The necessary amounts should be readily available.

XII-B-6. Lead

The UWMAK-III requirement should be met without difficulty from domestic deposits.

XII-B-7. Lithium

J. D. Vine (Amer. Nuclear Soc., Trans., vol. 22, 1975, pp. 55-56) has recently revised the U. S. Geological Survey estimate of lithium reserves and resources. He states that the identified resources of lithium in the United States likely to reach the marketplace by the year 2000 are scarcely adequate to meet the anticipated growth of the industry for conventional use and are grossly inadequate for the anticipated requirement for new energy-related uses. A search for new deposits is needed. The brines of western saline basins and certain types of clay deposits appear to offer much promise. Further exploration of pegmatite in the Kings Mountain district should discover substantial new reserves.

XII-B-8. Copper

The copper requirement for UWMAK-III is small relative to the estimated reserves of 85,000,000 tons. However, these reserves will be about half depleted by the end of the century at present rates of production. Even now, domestic production is not quite equal to domestic consumption. The use of copper in fusion reactors will have to compete with conventional uses for available domestic supply, and it is not certain that present rates of domestic copper production can be maintained to the end of the century. Much will depend on success in discovering new deposits of copper during the next 25 years.

If it becomes necessary to draw on foreign sources of copper, the outlook for such supplies is fairly favorable. At least seven countries should be producing large amounts of copper during the first quarter of the 21st century - Peru, Mexico, Chile, Panama, Zambia, Zaire, and Papua-New Guinea. Copper from the deep sea nodules should also have entered the market by that time.

XII-B-9. Manganese

World reserves of manganese are enormous, but the United States has no manganese reserves. At 3X present prices, the UWMAK-III requirement could probably be met from off-grade resources in Maine, Arizona and Minnesota. The nodules of the deep sea basins are another potential source. Presumably the present dispute over jurisdiction of deep-sea mining will have been resolved.

XII-B-10. Molybdenum

Molybdenum could be the most serious problem of procurement presented by the UWMAK-III design. United States reserves of molybdenum are estimated by the U.S. Geological Survey at 3,000,000 tons and by the U. S. Bureau of Mines at

4,000,000 tons. The Survey estimates identified marginal resources at 17,500,000 tons. These figures suggest that at prices somewhat higher than present prices, the UWMAK-III requirement could be met, but information on possible rates of production of molybdenum beyond the end of the century is not available. The current rate of production is only about 55,000 mt. per year.

XII-B-11. Nickel

Current reserves of nickel in the United States are too small to meet the UWMAK-III requirement and will be virtually exhausted by the end of the century. However, nickel deposits in the Duluth Complex, Minnesota, should be in production by the end of the century and should be able to supply the necessary amounts. Nickel won from the manganese nodules of the deep sea floors could be an alternative source.

XII-B-12. Other Metals

The other metals on the list should be available in more than necessary amounts.

Table XII-1

Materials Requirements - UWMAK-III Nuclear Island (Metric Tonnes)

Elements	Blanket: Initial Structure (a)	Blanket: Partial First Wall Replacement 19 Times-30 Yrs. (b)	Blanket: Balance First Wall Replacement 9 Times-30 Yrs. (c)	Balance of Plasma Chamber and Vacuum Plenum	Shield: Inner and Outer Shield	Shield: ISSEC Replacement 9 Times-30 Yrs. (d)	Magnets: T.F. Coils, Dewars and Cent. Struc.	Magnets: VF & OH Coils and Dewars	Shield, Blanket and Coil Support Structure	Vacuum Pumps	Total 30 Yrs.	Tonnes/MWe Based on 1985 MWe
Al					167.73		4623.56			20	4811.3	2.42
B					942.26						942.3	0.47
C	1039	9080.5	5049.35		494.33	2098.8					17,762.0	8.95
Cr				50	1128.63		23.8	71.4	300	35.2	1609.0	0.81
Nb							50	33			83.0	0.04
Cu							382.34	889		14.3	1285.6	0.65
He							18	13			31.0	0.02
Fe				165	3724.49		78.54	236	900	116.6	5310.2	2.68
Pb					3611.06						3611.1	1.82
Li	395										395	0.20
Ti	1.97	17.22	5.46	0.55	0.48		30.23	17			72.9	0.04
Mn				5	112.86		16.93	7.14	30	3.52	175.5	0.09
Mo	335.6	3107.95	987.56	99.33	1049.34						5599.8	2.82
V							6.35				6.4	0.003
Ni				30	677.18		14.28	43	180	21.12	965.6	0.49
Zr	0.43	3.76	0.93	0.12	0.10		10.58				15.9	0.01
TOTAL	1792	12,209.4	6043.3	350	11,908.5	2098.8	5254.6	1309.5	1500	210.3	42,676.6	21.50
COMPONENT WEIGHTS (MT)												
$Al_6Si_2O_{13}$					441.4						441.4	0.22
304 SS				250	5643.17		119	357	1500	176	8045.2	4.05
TZM	358	3128.92	944.22	100	86.67						4667.8	2.35
Mo					963.25						963.3	0.49
Al alloy 2219							4233			20	4253	2.14
Hi Purity Al							716.5				716.5	0.36
B_4C											1203.4	0.61
Carb. St. 1020					1203.4					14.3	998.3	0.50
Cu											126	0.06
NbTi							95	889				
							76	50				

(a) 18 Modules Plus 3 Spares
(b) 18 Partial Modules Replaced Every 1 1/2 Years Plus 3 Spares on Hand
(c) 18 Balance of Modules Replaced Every 3 Years Plus 3 Spares on Hand
(d) ISSEC Graphite Replaced Every 3 Years Plus 3 Spares on Hand

Table XII-2

Materials Requirements - UWMAK-III Balance of Plant (Metric Tonnes)

Element	Heat Exchangers: Li-Na[a]	Heat Exchangers: Na-He[b]	Heat Exchangers: Na-Steam[c]	Piping Li,Na He & Steam	Tritium Extraction System[d]	Thermal Flywheel Na Tanks	Li & Na Dump Tanks[e]	Li & Na Pumps	Containment Building Liner	Buildings	Energy Storage Unit	Turbine Machinery[f]	Generator and Exciters[g]	Regenerator Precooler Intercooler He-Steam	Miscell.	Total	Tonnes / MWe Based on 1955 MWe
Al												2.96				2.96	.001
Cr		79	60		0.4			120	222		81	30.72	50	32		675.1	0.34
Mo					9.26						7.5					16.75	.008
Ge		19		1.0							362		295			657	0.33
Fe		261	197	33,796	1.3			396	733	78,486	15				37.5(h)	72.5	0.037
Mn		8	6	204				12	22	474	269	230.9	1980	319.3		116,670	58.78
Mo	99.4	423		993	1.0	49.7	178.8	745			8	1.32		4.5		739.8	0.37
Ni		47	36		0.24			72	133		49	7.42	20			2517.3	1.27
Na		400	500	180		900						68.56		19.2		425	0.21
Ti	0.50		2.3	5.5		0.27	1.0	4.1			4	3.56				1980	1.00
V					0.02											21.2	0.01
Zr	0.40		0.5	1.2		0.06	0.22	1.0								0.02	
Pd					0.50											3.08	.001
Li	20			50												0.50	
B																70	.035
Concrete										304,000m^3		13.9				13.9	.007
TOTAL	120	1237	801.8	35,230.7	12.72	950	180	1350	1110	78,960	795.5	359.3	2345	370.5	37.5	123,865	62.4
304SS		395	298		2.0			600						160		2565	1.29
316SS											400					400	0.20
Carb. St. 1020				34,000						78,960				215		113,175	57
INCM	100	426		1,000	1.0	50	180	750								2507	1.26
Cu											382					362	0.18
METI											11.5					11.5	0.006
Concrete										304,000m^3							

(a) 2 heat exchangers
(b) 6 " "
(c) 2 " "
(d) Material needed for 30 yrs of operation
(e) Li dump tanks and divertor Na dump tanks. Thermal flywheel tanks are used as dump tanks for the intermediate Na loop.
(f) Turbine is made of blades-UDIMET-700, Casing-INCONEL 718, disc- A-286, Compressors (2) are made of blades-PWA-IN-4017, casing and valves-ASTM A-487 2 1.4 Cr, 1 Mo, and disc-D6AC
(g) Silicon Steel 495 MT, Carbon steel 500, Copper 50, Cr.Mo.V. Stainless Steel 163, insulation 25.
(h) Liquid He in storage

Table XII-3

United States Production, Reserves and Resources of Metals Required for UWMAK-III

($m.t. \times 10^6$)

Metal	Requirement for 10^6 MWe	United States		
		Production-1974[1]	Reserves[2]	Resources[3]
Al	2.42	.40	~2.0	Very large
B	.47	.18	10.1	Very large
Cr	1.08	0	-	1.53
Nb	.06	0	.006	.07
Cu	.98	~1.59	85.0	100.0
Fe	60.28	50.0[2]	2,000.0[5]	10,000.0
Pb	1.82	.68	59.0	Large
Li	0.24	~.002	1.5	1.7
Mn	0.46	0	-	10.0
Mo	4.08	.06		
Ni	.67	.015	.20	16.0
Na	1.0	.200[6]	Unlimited	
Ti	.05	.29	34.0	29.0
Y	$<10^{-5}$	.00004	Probably large	
Zr	0.01	.07	10.0	No data
Pd	<0.001	0	0	Large[7]
Co	0.003	1,000	Included in resources	800,000

(1) Primary metal only.

(2) Metal in ores minable under current economic conditions.

(3) Metal in material judged available at prices up to 3X present prices.

(4) Fe content of domestically mined ores.

(5) Fe content of ore minable under current economic conditions.

(6) Metal only. Approximately 1 percent of total production of sodium minerals.

(7) Assumes development of newly discovered deposits in the Stillwater Complex, Montana

Data from U.S.G.S. (Prof. Paper 820, 1973), U. S. Bureau of Mines (Commodity Data Summaries, 1975), and J. D. Vine (Lithium, ANS Trans., Vol. 22, 1975).

XIII. Economic Analysis

XIII-A. Introduction

The role of an economic study for an early conceptual design such as UWMAK-III is to provide us with an indication of where the major cost areas might be in tokamak reactors. This helps guide future tokamak reactor studies and indicates areas where increased research and design effort can pay the greatest dividends. On the other hand, many parts of the UWMAK-III system, by the nature and scope of the study, remain undefined and this means that an accurate determination of absolute costs is extremely difficult. This is particularly true if one tries to compare fusion with power systems like fission reactors where the designs are known in much greater detail. Therefore, we place greater emphasis on the relative costs of key items in UWMAK-III than on any absolute figures.

It is also important to recognize that the economic analysis for UWMAK-III is specific to this system. That is, many of the items that have a strong impact on the results are governed by certain design choices peculiar to UWMAK-III. Different design choices can have very different effects on cost so that a generalization regarding the costs of tokamak reactors is not possible at this time. (As a specific example, one will note in the following sections that the estimated cost of high temperature refractory metal piping was a substantial cost driver. These costs would be sharply reduced if stainless steel had been chosen as the structural material.)

Turning to the estimating procedure itself, it is normal estimating practice, when engineering is well defined, to derive the cost estimate by building up the cost item by item. In a less well defined study, where perhaps only 60 percent of the equipment is identified, this method can still be used, but a large portion of the cost must be based on allowances and factors. However, in a pre-conceptual estimate, such as the UWMAK-III study, where less definition is available, a different approach is necessary. The plant must be viewed as a series of systems which should be similar in content (but not necessarily in function) to systems in existing analogous plants, and the costs obtained by inductive reasoning using the costs of the analogous known systems. The estimate is thus derived by macro, rather than micro, approach. There is still considerable margin for variation in the unknown systems, but the potential variation is diminished by using this composite systems approach.

Existing nuclear power plants are the most comparable source of pertinent data, and the cost estimate and schedule for UWMAK-III rely heavily on data from recent Bechtel Corporation power plant experience. The basis for the estimate is discussed in Section XIII-B and the resultant capital cost for the entire plant is summarized in Section XIII-C. The engineering and construction schedule is given in Section XIII-D, and the estimated cost of power is discussed in Section XIII-E.

An important part of this chapter is the work reported in Sections XIII-F and XIII-G. In Section XIII-F, we attempt to place the estimate of plant economics for UWMAK-III in perspective by providing some comparison with estimates

of electric power costs for other methods of generating electricity. In these sections, we have asked how the costs developed for UWMAK-III compare with cost estimates developed by the same group for other, non-fuel limited approaches to electric power generation. (It is important to maintain consistency by using the estimates of a particular group since we find estimates by various groups, including costs developed with Federal Government guidelines, to vary widely.) Other approaches to electricity generation include fission breeder reactors, solar power, fuel cells, and coal fired MHD plants. Also included for reference are estimates for light water reactors, coal fired steam plants and gas turbines. These systems, particularly LWR's and gas turbines, are not truly comparable because the fuel supply will no longer be available at the time advanced technologies like breeder reactors and fusion are ready to play a substantial role.

Also included in Section XIII-G is an analysis of the key design decisions and cost items that most affect the economics of UWMAK-III. This includes a discussion of design choices made at the beginning of the study which turned out, after the fact, to have more strongly affected the estimated costs than had been anticipated. From these considerations, we draw conclusions regarding directions for future work.

XIII-B. Basis of Estimate

The facility under discussion in the study is taken to be a first generation model designed in a time when the major equipment functions have been successfully demonstrated. At that time industry will have developed the capability to produce the equipment, a capability which does not necessarily exist today. Development and first-of-a-kind costs are therefore not considered.

In general, the costs of the reactor plant equipment were provided by the University of Wisconsin and the Balance of Plant costs were determined by Bechtel. The costs are in fourth quarter, 1975, dollars with no allowance for escalation. The format of the estimate conforms generally with NUS 531* modified where necessary to accommodate the special aspects of fusion power plants.

The basis of the estimate is the plot plan, plan and elevation of the power block buildings (the main structures housing the reactor and power generation facilities), and a single-line electrical diagram. All of these were used as guides and, with the exception of building volumes and some quantities of concrete and lengths of main heat transfer piping, no quantity takeoffs were made. Fuller understanding of the engineering scope and extent and type of systems was provided in informal discussions with the engineering team.

The capital cost estimate is composed of field costs, engineering costs, a contingency allowance, owner's costs and interest during construction. The largest category, field costs, comprises the direct costs of permanent plant equipment and the indirect costs of temporary construction materials, supervision, etc, that are to be distributed across the entire facility.

XIII-B-1. Reactor Plant

The costs of the reactor plant and equipment were developed by the University of Wisconsin and transmitted to Bechtel in support of this cost estimate. Generally, the university priced components on a dollars-per-kilogram basis or extrapolated them from UWMAK I costs. However, in the following instances these costs were derived from other sources or by other relationships.

- Magnets: The costs were developed by the University of Wisconsin.
- Tritium cleanup: The costs are based on information provided by Gulf General Atomics as well as extrapolations from the costs of systems at Mound Laboratory.
- Turbo-Generators: Equipment prices (on a dollars-per-kilowatt basis) were provided by United Technologies Research Center.
- RF Heating: The University of Wisconsin assumed dollars-per-watt cost.
- Primary Loop Piping: The cost per lineal foot for 3-meter diameter

* Guide for Economic Evaluations of Nuclear Plant Design, USAEC Report NUS-531, NUS Corporation, January 1969.

refractory lined pressure pipe was developed by Bechtel, and was based on discussions with vendors for the material costs, and on other high temperature pipe studies for the determination of costs of fittings, supports and installation. The costs of the other primary and secondary loop piping were derived by the University of Wisconsin from this figure.

As is discussed under XIII-D-3, reactor assembly will require a special building. The cost of this building and any special equipment in it has not been included in the estimate.

XIII-B-2. Balance of Plant

Recent fission plant experience has seen the ratio of the total construction cost to the cost of the Nuclear Steam Supply System and the Turbo Generator increase from 2.5:1 to 5:1. The reason for this is that while the latter costs have remained relatively stable, both the extent and cost of the balance of plant have increased dramatically. Key factors that have contributed are more stringent safety requirements; the necessicity for cooling towers instead of river or ocean cooling; less favorable sites and the requirement that class III structure be able to withstand tornadoes and aircraft crashes. A particular result of this trend is that the volumes of the main buildings have increased: e.g. Turbine Building volumes have nearly doubled for essentially the same thermal output over the last five years or so.

In Bechtel's experience, there is a remarkably consistent relationship between the volumes of the main power block buildings and the total cost of bulk materials such as electrical wire and cable, instrumentation, piping, concrete and structural steel. Thus the volumes generated for UWMAK III provide the basis for the costs of the bulk material items, a substantial part of plant costs. The relationships of the volumes of UWMAK III to the reference Light Water Reactor are shown in the Appendix of Estimate Factors in section XIII-G. It should be noted that the UWMAK III buildings have been compared with functionally identical LWR buildings where possible. In the case of the Heat Exchanger Building, however, a comparison has been drawn with the Reactor Auxiliaries Building, since it is considered to provide the most accurate basis.

This volume/bulk material relationship discussed above has been applied to the UWMAK III volumes to derive these costs which fall into four categories: civil & structural, piping, electrical, and instrumentation.

In joint discussions beteween the design and cost engineers, the relative weighting of each of the categories was developed for each of the major building elements of the UWMAK III facility: containment, turbine, hot cell and radwaste, reactor auxiliaries, heat exchanger, diesel generator and control. These weighting factors established the cost density of the fusion facility relative to the reference LWR and provided the bulk material costs for the estimate. They are shown in the Appendix of Estimate Factors in section XIII-G.

The following discussion sets down some of the major considerations used in the assessment of the bulk materials factors.

XIII-B-2-a. Civil/Structural

For costing purposes, only conventional materials have been considered. However, since the containment is considerably larger than any existing LWR containments, and because unusual structural problems are anticipated in the supporting of the magnets, headers, cryogenic pumps etc, the containment will cost more than an LWR on a unit volume basis.

The turbine building differs from current LWR turbine buildings in that one bay will have to be designed to prevent the release of radioactive gases in the event of a helium pipe rupture, and this considerably increases the cost. The remaining bays are typical for the conventional steam turbine and somewhat less than the typical cost for the gas turbine arrangements.

The heat exchanger building will also have to be designed to contain radioactive gases and to minimize the hazard from liquid metal fires. As such, it will include a liner, cells, massive foundations and high density concrete, considerably increasing the unit costs.

XIII-B-2-b. Piping

Primary loop piping is excluded in the bulk material comparison as it has been separately identified, estimated and added to the total costs.

The turbine building piping is less complex than an LWR because most of the working fluid is a recirculating gas. Only one machine is steam driven and thus the total condensate return system is much smaller.

The hot cell is essentially for dry handling compared with LWR radwaste, necessitating less pipe, but more equipment.

The heat exchanger building is packed with costly and very extensive sodium, lithium and helium systems and thus has a higher cost per unit volume than an LWR.

XIII-B-2-c. Electrical Bulk Materials

Considerable deviation from LWR experience in electrical bulk equipment (cable, conduit and trays) is expected as the equipment in the containment is assumed to be nearly twice as complex. In the turbine building there is less complexity in the fluid return system (gas instead of condensate) but there are more machines (four instead of one) resulting in a moderate unit increase.

The UWMAK III radwaste building (excepting the used blanket storage area) incorporates more complex equipment, and the heat exchanger building, by virtue of the density and complexity of the sodium systems, is estimated to be more complex than the LWR Reactor Auxiliaries Building.

XIII-B-2-d. Instrumentation

Instrumentation for the reactor is estimated to be ten times as complex as that for an LWR there being, in fact, little of comparable scope. However

the containment volume is almost three times that of an LWR, giving an overall unit cost of more than three times.

The turbine building has more machines than the LWR reference, and hence more instrumentation. The heat exchanger building has heat tracing and many secondary motors, and the hot cell includes the back-up systems for the various remotely controlled equipment.

The control room is assumed to contain about twice the instrumentation of an LWR, handling, as it does, the magnet and cryogenic systems.

XIII-C. Estimate of Capital Cost

The capital cost estimate is composed of direct field costs, indirect field costs, engineering costs, a contingency allowance, owner's costs and interest during construction. The largest category, field costs, comprises the direct costs of permanent plant equipment and the indirect costs of temporary construction materials, supervision, etc, that are to be distributed across the entire facility.

Table XIII-C-1 shows the summary total plant costs and it will be noted that these are in a somewhat different format from that described in section XIII-B. This is discussed under the direct field cost section following.

XIII-C-1. Direct Field Costs

Direct field costs are the costs for permanent plant equipment, materials, labor and subcontract items, and form the bulk of the field costs. These are derived from two basic sources: the bulk materials, and equipment. In general both are available from current and historic sources in a system and category format. Thus the estimate shown on Table XIII-C-1 was first prepared in the system and category format and then translated into the required format for presentation; in this case NUS 531. The discussion of the bulk materials in section XIII-B and the equipment following are in terms of the system and category derivation. A direct cost percentage comparison between fission and fusion plants is shown in the Appendix of Estimate Factors in section XIII-G.

XIII-C-1-a. Equipment

The major items of reactor equipment have been estimated by University of Wisconsin and these have been included without comment. Items that lie in the Balance of Plant category, e.g. cooling towers, have been estimated using current price guidelines from major manufacturers and current pricing data from within Bechtel. The costs of other equipment have been established as a function of the appropriate building, as discussed in section XIII-B-2.

The bulk of the mechanical equipment peculiar to UWMAK III has been priced by the University of Wisconsin. Peripheral equipment such as pumps, condensers, and heating, ventilating and air conditioning equipment has been estimated by eliminating from an LWR mechanical account all those items related to a fission reactor and scaling up the remainder of the costs to the increased capacity.

The cooling tower was treated separately. Its duty corresponds to that of an equivalent 800MWe LWR plant, except that the circulating flow is half and the temperature much higher. Its price is estimated to be 40 percent higher than that of an equivalent wet cooling tower.

Remote handling equipment was also treated separately and an allowance included, although little is known beyond the general function and certainly no equipment of the sort exists today.

Table XIII-C-1

CAPITAL COST SUMMARY

UWMAK III - 1985 MWe

Acct.	Item	Cost $ Millions	
	Direct Field Costs		
20	Land and Land Rights	1	
21	Structures & Site Facilities	568	
22	Reactor Plant Equipment	812	
23	Turbine Plant Equipment	561	
24	Electric Plant Equipment	280	
25	Miscellaneous Plant Equipment	60	
26	Special Materials	8	
	TOTAL DIRECT COST	2,290	
	Indirect Field Costs		
91	Construction Facilities and Services	530	
	TOTAL FIELD COST	2,820	
92	Engineering Services	450	
		3,270	
	Contingency	980	
	TOTAL ESTIMATED CONSTRUCTION COST	4,250	
93	Other Owner Costs	340	
94	Interest During Construction	1,100	
	TOTAL ESTIMATED CAPITAL COST: 4th Quarter 1975 Dollars	5,690	
	TOTAL CONSTRUCTION COST	2,140	$/KWe

There is a close correlation between the station load of a power plant and the cost of the electrical equipment. On a net basis UWMAK III is more efficient than an LWR facility, but its equipment is more sophisticated. In sum, on a per-megawatt basis UWMAK III's electrical equipment is assessed to be 90 percent of that in an LWR plant, excluding the unique equipment for a fusion plant, and was estimated on this basis. To this base figure was added the estimated cost of the unique systems, the energy storage and inverter facilities and a low-voltage, cryogenic transmission system from the energy storage facility to the containment building.

XIII-C-1-b. Labor

The wage rate included is based on a craft mix and wage agreements as experienced in the Pacific Northwest, which is a representative area for the U.S.

Plant siting has a considerable effect on labor availability and consequent productivity. For this study, labor productivity is again based on the Pacific Northwest experience and is generally regarded as good.

XIII-C-1-c. Subcontracts

It is normal for a part of the work to be subcontracted, examples being earth work, cooling towers, insulation, and building finishings. In this respect a fusion plant is regarded as being normal and thus standard power plant relationships have been used.

XIII-C-2. Indirect Costs

Previous UWMAK studies have used the WASH 1230 report as a guide to determining indirect costs. However they are probably understated in WASH 1230, (20% of direct labor costs compared with 90% to 110% in Bechtel's experience). However, the different bases of the cost scope make comparisons difficult. For UWMAK III, an approach consistent with Bechtel scope has been used.

The main categories of indirect costs and their approximate percentages for a typical fission facility are:

• Temporary construction facilities	15%
• Miscellaneous construction services (cleanup, maintenance of tools and equipment, material handling, guards, welder tests, etc)	18%
• Construction equipment, tools, supplies and utilities	19%
• Field office costs (supervision, engineering, administration warehousing, field purchasing, medical and overhead)	42%
• Other (insurance, taxes and miscellaneous)	6%
	100%

In the UWMAK III estimate, indirect costs are calculated at 100% of direct labor costs. The labor cost is not separately identified but is generally in the range of 20 to 25 percent of the total direct cost, and an average of 23% is assessed on the basis of a high bulk materials component, these being labor intensive. The resulting indirect costs are therefore 23% of total direct costs.

XIII-C-3. Engineering Services

The cost of services provided include engineering costs, home office costs and fee. Engineering includes both preliminary and final designs , specifications, etc. Home office costs, which comprise estimating and scheduling services, procurement, start-up, quality assurance and project management, lie in the 50 to 60 percent range of engineering cost. Fee is normally a function of the total project cost and there are commonly accepted guidelines on appropriate schedules.

The sum of these three categories falls into historically consistent percentages in the range of 12%-22%, depending on the complexity of the project. For Light W ter Reactor plants 12-15% is normal. For this study a figure of 16 percent of total field costs has been used as it is considered that many of the problems lie in equipment and material specifications and in construction procedures, increasing the relative cost of engineering services.

XIII-C-4. Contingency

Contingency is the sum of money added to an estimate to provide for items not specified in the engineering detail but which are known from experience to be a necessary part of a facility. Implicitly, it will be used, and it is not a drawdown fund to compensate for overruns or changes and additions to the project scope. Commonly used ranges for large complex facilities are from 15% of total construction costs for well defined projects to 30% or more for highly conceptual studies. As UWMAK III is a first generation plant, there will be many problems unique to the facility and thus the contingency allowance has been set at 30%.

It is important to recognize that contingency provides for the unknown in the design only to the extent that the engineering is understood, and experience shows that it is quite difficult to assess the degree to which future processes are understood in the hardware sense. If the arrangement of the plant components contains major uncertainties, or the materials selected prove to be deficient, or the duty more severe than anticipated, or if additional major subsystems are required, then the scope of the engineering is inadequate and this is not covered by contingency.

XIII-C-5. Other Owner Costs

These include the owner's general office and accounting costs, startup and operator training, spare part and inventory costs, and environmental impact studies. These costs lie in a range of 4%-12%, and a figure of 8% has been selected as typical. This is based on the assumption that major equipment and start-up problems have been resolved and that environmental data acquisition and reports present no unusual concern.

XIII-C-6 Interest During Construction

The center of gravity of cash flow is taken at the two thirds completion point of construction, estimated from the schedule to be three years from the plant fuel load date.

Interest during construction is calculated at 8% of the total construction cost for three years.

XIII-C-7. Escalation

No provision is made for future escalation and estimates are based on fourth quarter, 1975, dollars.

XIII-C-8. Capital Cost Account Detail

The capital cost estimate is further defined in Table XIII-C-2. This shows each of the major accounts from Table XIII-C-1 broken into one, two and occassionally three further levels of detail. The breakdown is to a considerable extent subjective in that neither design scope nor cost estimating exists in the detail necessary to make the cost sub-division. Thus the numbers are indicators of cost relationships rather than estimates of expected costs and they should be regarded in this respect and so used.

Table XIII-C-2

CAPITAL COST ACCOUNT DETAIL

Account Number	Account Title	Costs in Thousands Dollars Bechtel	U W
20	Land and Land Rights		1,000
201	Land and Privilege Acquisition)	1,000	
202	Relocation of Buildings, Utilities, Etc.)		
21	Structures & Site Facilities		568,000
211	Site Improvements and Facilities		7,000
.1	General yard improvements	2,000	
.3	Highway access)		
.4	Railway access)	5,000	
212	Reactor Building Incl. Radwaste & Fuel Handling Areas		195,000
.1	Basic building structures	178,000	
.2	Building service	17,000	
213	Turbine Building Incl. Control Room Heater Bay, Diesel Generator Area		133,000
.1	Basic building structures	122,000	
.2	Building service	11,000	
215	Reactor Auxiliaries Building Including Switchgear Bay and Heat Exchange Building		195,000
.1	Basic building structures	178,000	
.2	Building service	17,000	
216	Hot Cell		21,000
.1	Basic building structures	19,000	
.2	Building service	2,000	
218	Miscellaneous Buildings		17,000
A	Service building)	1,200	
D	Inductive coil storage building)		
.2	Building services	100	
E	Helium storage building	640	
.2	Building services	60	
F	Miscellaneous structures & building work)	15,000	
I	Inner wall assembly building)		

Table XIII-C-2 (Cont'd)

Account Number	Account Title	Costs in Thousands Dollars			
		Bechtel		UW	
22	Reactor Plant Equipment		300,450		511,735
221	Reactor Equipment				286,480
.1	Magnet and central support structure			99,140	
.2	Shield			114,020	
.3	Blanket & carbon curtain			30,220	
.4	R F heating			20,000	
.5	Blanket and shield support			21,000	
.6	Secondary vacuum walls between TF coils			1,500	
.7	Divertor collector plates			600	
222	Main Heat Transfer & Transport System		265,450		109,658
.1	Primary helium coolant system (inner blanket)				
.11	Piping & insulation	107,200			
.12	Tritium extraction (incl. coolant purification)			4,000	
.2	Divertor system				
.21	Pumping			5,220	
.22	Piping	23,400			
.23	Steam generator	12,400			
.24	Tanks			1,600	
.25	Divertor collector plates			600	
.26	Sodium purification system			308	
.27	Tritium extraction (from cryo pumps)			500	
.3	Intermediate Sodium Loop System				
.31	Pumps & motor drives			8,280	
.32	Piping & insulation	55,300			
.33	Heat exchangers (steam generator & clean-up regenerative)	2,750		42,500	
.34	Clean-up system (sodium purification)			7,600	
.36	Sodium dump, hot storage & make-up tanks			6,700	
.37	Tritium extraction (including tanks)			1,200	
.4	Primary lithium coolant system (outer blanket)				
.41	Pumps & motor drives			5,920	
.42	Piping & insulation	61,000			
.43	Heat exchangers			8,450	
.44	Tanks	3,400		4,900	
.45	Tritium extraction			6,000	
.46	Clean-up			5,880	

Table XIII-C-2 (Cont'd)

Account Number	Account Title	Costs in Thousands Dollars Bechtel		UW
223	Auxiliary Cooling Systems			32,092
.1	Shield cooling (He)			
.11	Pumping		372	
.12	Piping		212	
.13	Heat exchangers		492	
.14	Purification		36	
.15	Tritium extraction		30	
.2	Magnet cooling system			
.21	Cryogenic system		25,000	
.22	Piping		3,750	
.23	Tanks		2,200	
.24	Transport system			
224	Radioactive Waste Treatment & Disposal			10,000
225	Nuclear Fuel Handling & Storage Systems (Fuel Injection)			10,550
.1	Liquefaction		950	
.2	Pellet fabrication		1,700	
.3	Pellet injection		7,400	
.4	Storage equipment		500	
226	Other Reactor Plant Equipment			62,955
.1	Inert gas system			
.2	Special heating systems			
.3	Coolant receiving, storage & make-up systems		4,000	
.4	Fluid leak detection			
.5	Auxiliary cooling systems			
.6	Tritium removal from reactor building		525	
.7	Secondary vacuum systems		800	
.8	Primary vacuum system		57,250	
.9	Magnet vacuum system		380	
227	Instrumentation and Control	35,000		
.1	Reactor & process I&C equipment			
.2	Automatic monitoring & computation equipment	35,000		
.3	Radiation monitoring systems			
.4	Isolated indicating & recording gauges, etc.			
.5	Control & instrumentation piping, tubing, & wiring			

Table XIII-C-2 (Cont'd)

Account Number	Account Title	Cost in Thousands Dollars Bechtel		UW	
23	Turbine Plant Equipment		398,000		163,000
231	Turbine-Generators		123,000		133,000
.1	Turbine-generators & accessories (for Blanket System)				
.11	Three 585 MW, 3600 RPM tandem compound turbo-compressors with two stage compression				
.12	Three 650 MVA generators @. 90P. F. and . 50 SCR	4,000		114,000	
.13	All other standard & non standard accessories				
.14	Piping, valves & hangers including insulation	90,000			
.2	Turbine-generator & accessories (for Divertor System)				
.21	One 294 MW, 3600 RPM tandem compound, four flow steam turbine with 38" last stage blades	1,000		19,000	
.22	One 330 MVA generator@0. 90P. F. and . 50 SCR				
.23	All other standard & non standard accessories				
.24	Piping, valves, hangers including insulation	28,000			
232	Heat Rejection Systems		41,000		
.2	Circulating water systems	1,000			
.3	Cooling towers	40,000			
233	Condensing Systems (for Divertor Steam Cycle)		16,000		
.1	Condensers				
.2	Condensate system	16,000			
.3	Gas removal system				
.4	Turbine by-pass system				
234	Feed Heating System (for Divertor Steam Cycle)		35,000		4,200
.2	Pumps			4,200	
.3	Piping & tanks	35,000			

Table XIII-C-2 (cont'd)

Account Number	Account Title	Costs in Thousands Dollars Bechtel	UW
235	Other Turbine Plant Equipment	158,000	25,800
.1	Main steam (or other vapor) piping)		
.2	Turbine auxiliaries)		
.3	Auxiliaries cooling system)		25,800
.4	Make-up treatment system)		
.5	Chemical treatment & condensate)		
.6	Central lubrication service system)		
.7	Closed cycle helium system)		
.71	Piping and insulation	35,000	
.72	Heat exchangers (regenerator, precooler, intercooler)	123,000	
236	Instrumentation & Control	25,000	
24	Electric Plant Equipment	224,000	56,000
241	Switchgear	35,000	
.1	Generator circuits)	35,000	
.2	Station service)		
242	Station Service Equipment	45,000	
.1	Station service)		
.2	Low voltage unit substations & lighting transformers)	9,000	
.3	Auxiliary power sources (incl. four 500 kW diesels))		
.4	Main power transformers	16,000	
.5	Cryogenic system	20,000	
243	Switchboards (Incl. Heat Tracing)	4,000	
244	Protective Equipment	1,000	
245	Electric Structures & Wiring Containers	15,000	
246	Power and Control Wiring	50,000	
.1	Generator circuits wiring)		
.2	Station service power wiring)	50,000	
.3	Control wiring)		
247	Divertor Coil Power Supply System $40/kWe Bridges & Rectifiers		36,500
248	Inductive Energy Storage		19,500

Table XIII-C-2 (Cont'd)

Account Number	Account Title	Costs in Thousands Dollars Bechtel	UW
249	Electric Installation		74,000
.1	Contractor furnished material-conduits, lighting fixtures, etc.	74,000	
.2	Construction & erection labor		
25	Miscellaneous Plant Equipment		60,000
251	Transportaion & Lifting Equipment		53,000
.1	Cranes, hoists, monorails & conveyors		
.11	Two 250 ton/25 capacity turbine room cranes	600	
.12	Reactor hall crane	550	
.13	Miscellaneous hoists cranes, jobs & trolleys for equipment maintenance	600	
.14	One 150 ton/10 ton inductive coil storage building crane	300	
.15	Blanket storage cell trolleys	900	
.16	Blanket replacement equipment	50,000	
.2-.6	Railway & roadway equipment, watercraft, aircraft & vehicle maintenance equipment	50	
252	Air and Water Service Systems		6,130
.1	Air systems	560	
.2	Water systems	3,390	
.3	Auxiliary heating boilers	2,180	
253	Communications Equipment		270
254	Furnishings & Fixtures		600
26	Special Materials		8,280
261	Reactor Coolant		5,200
262	Intermediate Coolant (Sodium)		720
263	Turbine Cycle Working Fluids		720
264	Liquid Helium		1,640

XIII-D. Engineering & Construction Schedule

Fig. XIII-D-1 shows a possible construction schedule for UWMAK III alongside that of a typical Light Water Reactor. It is envisaged that to design and construct UWMAK III will take 11 years, two years more than the LWR. Due to the lack of any detailed information on major equipment lead times, it is not possible at the present level of design for UWMAK III to define the critical path for construction activities; however, the critical activities in a fission plant construction generally involve supply and delivery of the Nuclear Steam Supply System (NSSS). The manufacture of the analogous reactor plant equipment is likewise assumed to be the governing activity with UWMAK III.

There are two major differences between the plants that contribute to the longer overall schedule for UWMAK. First, the design of the fusion reactor is much more complex than a fission reactor, requiring a greater lead time. Second, the reactor is much larger and this has a major impact on the containment design and construction.

The reactor in a fission plant is small in relation to the containment and it can be installed while the containment is under construction and after many of the subsystems such as heat exchangers, pumps and piping are in place. On the other hand, the magnet assembly is much larger relative to the UWMAK III containment. As a result, very few of the subsystems can be installed until the magnet support assembly is in place. The magnet assembly is also considerably more complex than a fission reactor; and it will take considerably longer to build.

XIII-D-1. Licensing

Fission plants are experiencing increasingly more stringent licensing requirements and have also to contend with delays arising from socio-political pressures. However, it is assumed that many of the major issues will have been resolved when commercial fusion plants are built and that the licensing period will be no greater than that currently forecast for fission plants.

XIII-D-2. Containment Construction

The general procedure in fission plant construction is to construct a base slab and then erect the steel containment liner for the shell. Placement of reinforcing steel and concrete can begin when the liner construction is sufficiently advanced to avoid problems of overlapping work areas. Three months is a normal interval. A large construction opening is left in the wall to permit the reactor to be installed. The dome is constructed, again by installing the liner plate first, which acts as the lower formwork for the first layer of concrete.

The UWMAK containment can be constructed in the same way. It is, however, nearly double the size of an LWR containment and is likely to take two and a half years to construct. To build the dome before the central column is in place is not seen to be a major problem; temporary stays may be used or a more pronounced curvature for the dome can be adopted.

ENGINEERING & CONSTRUCTION SCHEDULE

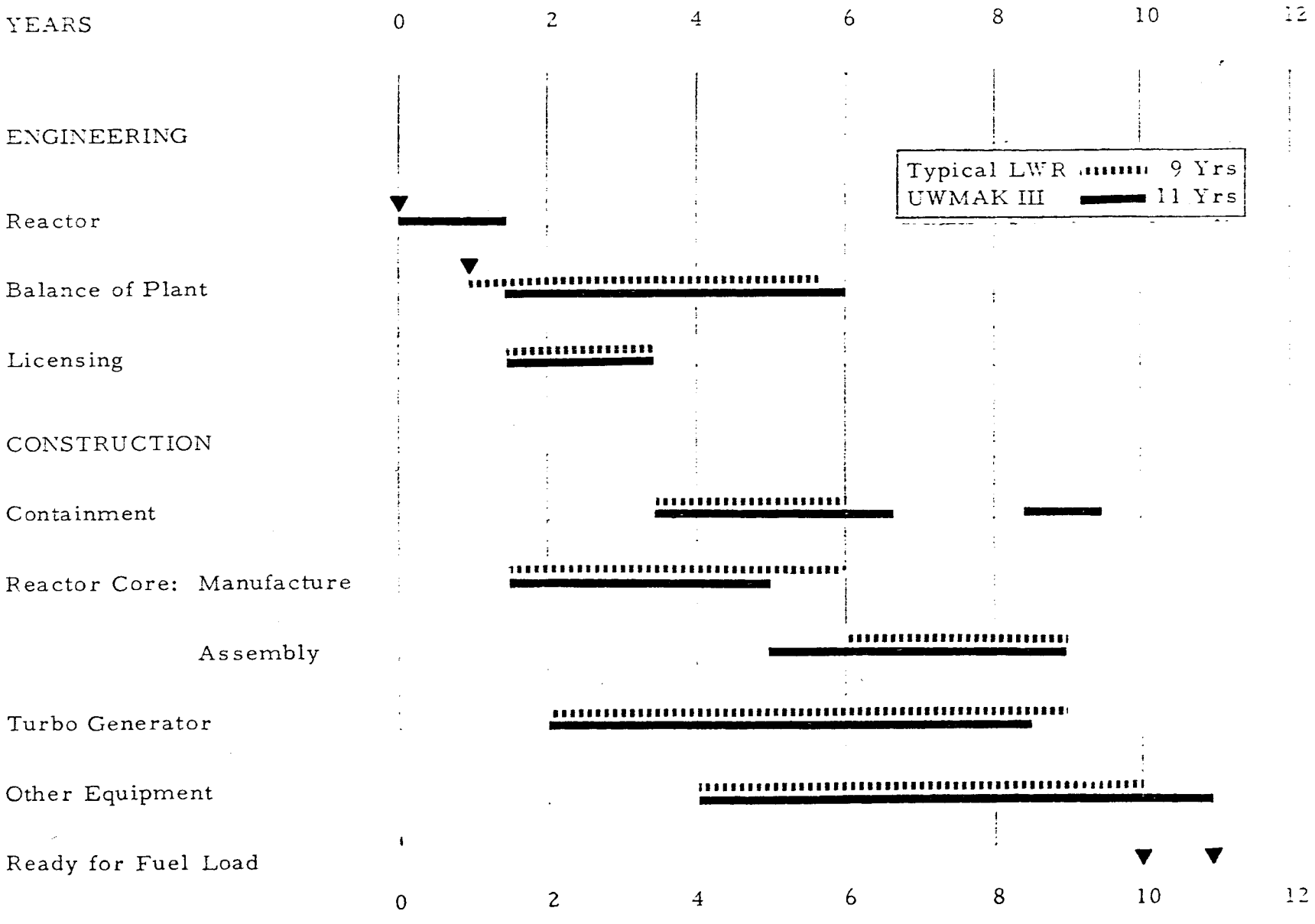

Fig. XIII-D-1

XIII-D-3. Reactor Plant

The reactor plant presents two unusual problems. The first is that the components are too big to be shipped, and the second is that the magnet assembly is too vulnerable to be installed before other heavy overhead equipment (including the roof and coolant headers) are in place.

The solution may be to assemble the components at a special site facility. When completed, the whole assembly would be moved through a large opening in the containment into position. If the assembly of the reactor components had to await completion of the dome, not only would the critical torus construction be delayed, but eventual assembly within the containment would take place under much more confined and generally less ideal conditions than in a separate, special area. There remains the closure of the access opening although this does not appear to be a critical item.

The construction of this special assembly building is not considered to be part of the contract scope and has therefore been excluded.

XIII-D-4. Turbo-Generators

The time required to manufacture the turbo-generators for UWMAK is assumed to be the same as for existing plants. However, since the machines are smaller (an average 500 MWe) than currently preferred nuclear generators (1100 MWe-1300 MWe) it is quite likely that they could be built in less time. Installing four machines simultaneously though, presents problems. Considerable space is required for laydown area, and the logistical problems in assembly may extend the installation period. However, it is not a critical activity, and delay will not extend the overall schedule.

XIII-D-5. Other Equipment

The other equipment would not appear to pose special problems of schedule apart from the delay occasioned by the reactor plant. This results in approximately a one-year extension of the schedule.

XIII-D-6. Testing and Start-up

Although UWMAK will be considerably more complex than a fission plant, testing and start-up times are shown as being similar. With substantial capital tied up in the facility, unusual and expensive approaches will be required to achieve this goal.

XIII-E. Cost of Electric Power

The estimated cost of energy at the busbar for UWMAK III is discussed in detail below, and summarized on Table XIII-E-1. In general, the UWMAK I and II approach has been adopted, escalated as appropriate. The unit costs are based on 1985 MWe net output and a plant factor of 0.80.

XIII-E-1. Operation and Maintenance Cost

The operation and maintenance costs are composed of the following:

XIII-E-1-a. Salaries

A normal operating staff of 112 was estimated for UWMAK II, and considered to be an appropriate number for UWMAK III. It is based on an assumed average cost of $14,500 per annum including fringe benefits.

XIII-E-1-b. Miscellaneous Supplies and Equipment

These are the materials and equipment used in the routine day-to-day operation of the power plant. UWMAK II was based on fission power plant experience. UWMAK III uses UWMAK II with appropriate escalation.

XIII-E-1-c. Outside Support Services

These include the routine speciality services and the personnel borrowed from other plants, where the installation and staffing of facilities would be more expensive than use of outside help. UWMAK II was based on fission power plant experience and UWMAK III uses this cost with appropriate escalation.

XIII-E-1-d. Miscellaneous and Administrative Costs

These sundry costs are those that do not fit into the other cost categories used here and the charges for administrative activities such as purchasing. These costs are assumed to be 15 percent of the cost for salaries, supplies and equipment, and outside support.

XIII-E-1-e. Blanket Rebuilding Cost

Twice a year, the plant will be shut down to replace a portion of the outer blanket. This requires a special crew trained to remotely dismantle the reactor, move the irradiated segments to the hot cell, and replace them with new segments. The entire operation must be directed remotely from a control room located in the hot cell. The operation is expected to be a round-the-clock effort for three weeks, requiring 25 men per shift. The material cost for replacing the segments is assumed to be the same as for the original manufacture of the fabricated TZM, reflector graphite, carbon curtain and coolant manifolds and tubes.

Table XIII-E-1

UWMAK III ELECTRICITY COST

Item	Annual Cost in $ Thousands	Unit Cost (Mills/kWh)
A. OPERATION & MAINTENANCE	20,715	1.49
a. Salaries	1,624	
b. Miscellaneous Supplies	1,200	
c. Outside Services	450	
d. Administrative (15% of above)	491	
e. Blanket Rebuilding	16,800	
f. Coolant Makeup	150	
B. FUEL	149	.01
C. RETURN ON CAPITAL	852,000	61.25
TOTAL ESTIMATED ELECTRICITY COST: 4th Quarter 1975	872,864	62.75

The labor to rebuild the segments, also by remote handling, is assumed to be a continuous operation, and the cost of equipment is included.

XIII-E-1-f. Coolant Makeup:

For safety reasons the loss of lithium and sodium must be kept to negligible proportions. Leakage of helium however is considered inevitable, and a 5 percent inventory loss each year is allowed.

XIII-E-2. Fuel Costs

UWMAK III operates on a mixture of 50% deuterium and 50% tritium. The initial tritium inventory will be a substantial capital cost which has not been taken into account; however, after start of routine operation a surplus of tritium will exist for which no credit has been allowed, so it has been assumed that tritium is available at zero cost. Deuterium is burned and lost in the operation of the plant, and an allowance for recycling is made.

The cost of fabricating fuel pellets, which occurs on site, is included in the Operations and Maintenance costs.

XIII-E-3. Annual Return on Capital

The annual return on capital depends on many factors, particularly the financial structure of the utility, and longterm interest rates. Consistent with recent experience and UWMAK II, a 15 percent fixed charge rate is used.

XIII-F. Perspective

XIII-F-1. Cost of Electricity Comparison

Figure XIII-F-1 shows the estimated cost of power for UWMAK III in approximate relation to other base load plants. The systems have been arranged into three groups according to the time period that they will probably be required to reach commercial operation. The figure has been developed using Bechtel experience and published reports adjusted where necessary to be comparable to UWMAK III. Thus all costs are in present day dollars and include interest during construction, but exclude future escalation costs. The cost of power for each facility is divided into capital cost, fuel cost and operating and maintenance cost. The ranges of cost include the various types of facilities and differing site conditions. Coal was priced at $23 per ton and oil at $12 per barrel.

Escalation was not considered in the calculation because it would distort the basis of comparison, since its inclusion would entail some arbitrary assessment of when each type of plant is likely to be in commercial operation. However, excluding escalation introduces another bias resulting from neglecting the effect of escalating fuel prices.

For fission plants scheduled for operation in 1982 the cost of fuel might be from 6 to 12 mills/kWh on a 15 year levelized cost basis, depending on whether fuel costs escalate at 5% or nearer 10%. For coal-fired plants the cost could be from 22 to 42 mills/kWh on the same basis. The higher figure represents approximately 29 percent of total generating costs for fission plants, and about 56% for coal-fired plants, compared with roughly 21 percent and 36 percent respectively, for units starting up in 1978-79, but based on 1976 dollars. Further extrapolation would be difficult, but it is possible that fuel costs may continue to escalate faster than capital costs, gradually increasing the incentive for high capital cost/low fuel cost plants such as UWMAK III.

Peak shaving and standby power systems are excluded from the comparison since criteria other than pure economic consideration govern their selection: reliability, simplicity or low capital costs are frequently the dominant factors. Hydro power is also excluded since the potential for a significant capacity increase in the continental U.S. is limited .

Comments and sources of information on the various systems are included in section XIII-F-3.

XIII-F-2. Comparison With Updated Previous Studies

Comparisons of UWMAK I and II with UWMAK III are inevitable, but since the basis for the earlier estimates was WASH 1230*, which results in substantially lower estimates of costs than the Bechtel basis, direct cost comparisons inherently lack validity. However, some perspective is possible when the costs are brought up to a common calender price basis of fourth quarter, 1975 dollars. Thus UWMAK I was escalated from mid 1974 at 22% based on Bechtel escalation figures and the Handy Whitman Index, and UWMAK II

* WASH 1230 (Vol. 1) "Pressurized Water Reactor Plant, 1000 MWe Central Station Power Plants - Investment Cost Study," United Engineers and Constructors, June, 1971.

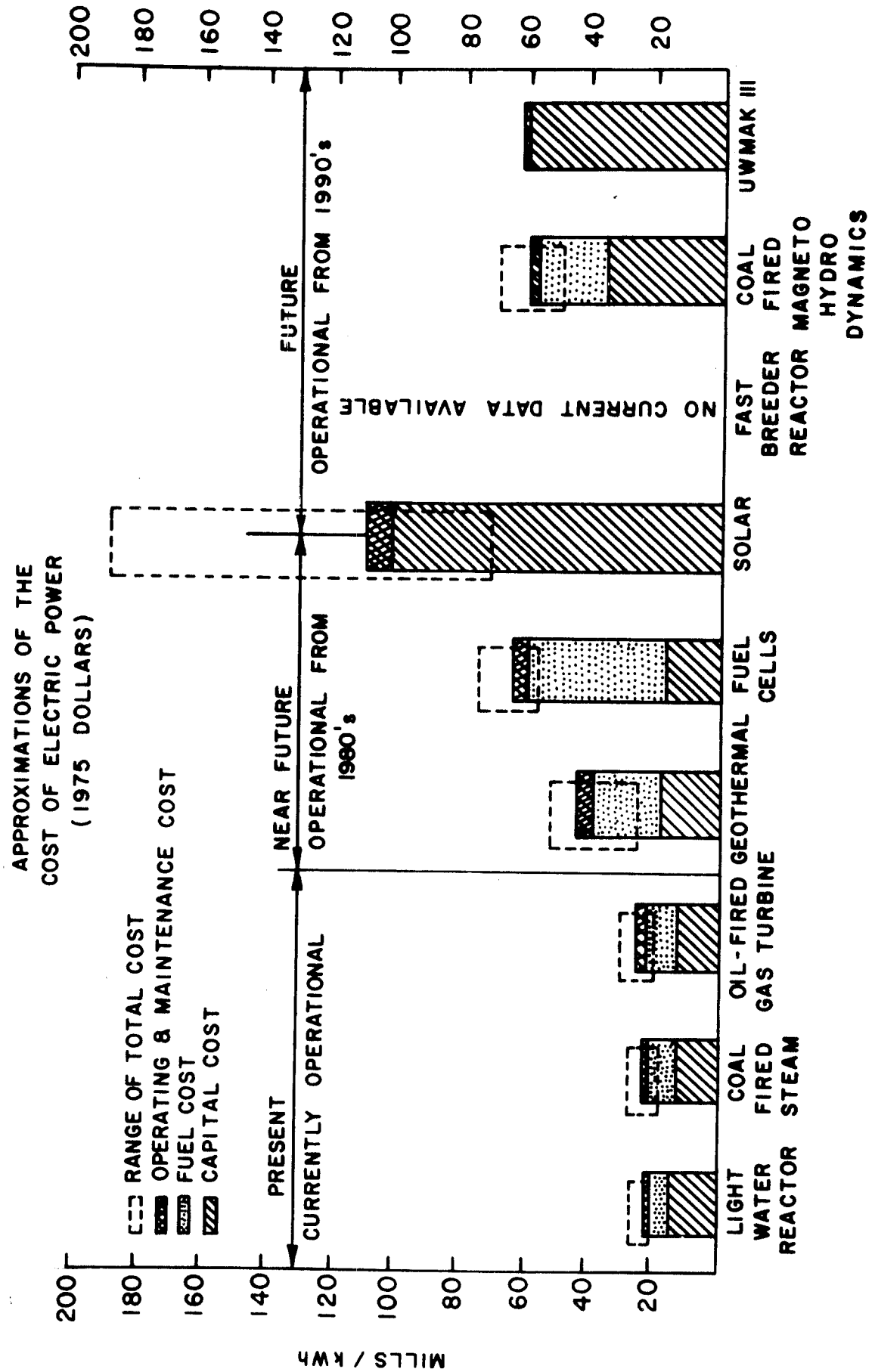

Figure XIII-F-1

was escalated from 1st quarter 1975 at 10% using the same basis. Similarly, indirect costs, engineering services, contingency, etc. were revised to use the same basis as UWMAK III, resulting in the figures shown in Table XIII-F-1.

XIII-F-3. Comments And Sources

Light Water Reactor:
Source: Bechtel

Gas Turbine:
Source: GE NASA Study/Bechtel

In the lower range are combined cycle gas turbine/steam plants, and in the higher range are closed cycle regenerative plants.

Geothermal:
Source: Bechtel, PG&E

The lowest figures reflect Pacific Gas & Electric experience with their Geysers plants. However, the conditions are unique (relative cleanliness and high temperature with superheat). The high capital cost is a reflection of the relatively large steam turbine and cooling towers required for a low grade heat cycle. High temperature brine plants require more extensive equipment.

Coal Fired Steam:
Source: Bechtel

Fuel Cells:
Source: GE NASA Study/Bechtel

The fuel source for fuel cells is likely to be coal derived. Both high and low temperature fuel cells fall within the same approximate range with the former having the higher capital cost and lower fuel costs.

Magnetohydrodynamics:
Source: GE NASA Study/Bechtel

Includes open cycle, closed cycle inert gas and closed cycle liquid metal MHD plants. The open cycle is the least expensive, the liquid metal the most expensive and the inert gas in the middle range.

Solar:
Source: Bechtel Studies and in-house information

The types of plants considered range from small solar ponds to large ocean thermal gradient powered plants. Also included at about the mid range are solar plants using heliostats focusing on a central tower furnace which powers a steam plant. To be comparable with other base load plants, the central tower system includes a heat storage system to accommodate night generation of power.

Table XIII-F-1

COMPARISON WITH UPDATED PREVIOUS UWMAK STUDIES

	$ Millions		
	UWMAK I 1474 MWe	UWMAK II 1709MWe	UWMAK III 1985 MWe
TOTAL DIRECT COST	1,040	1,200	2,290*
ESCALATION TO 4th QUARTER 1975	230	120	-
	1,270	1,320	2,290
INDIRECT FIELD COSTS			
91 Construction Facilities and Services	290	300	530
TOTAL FIELD COST	1,560	1,620	2,820
92 Engineering Services	250	260	450
	1,810	1,880	3,270
Contingency	540	560	980
TOTAL ESTIMATED CONSTRUCTION COST	2,350	2,440	4,250
93 Other Owner Costs	190	200	340
Interest During Construction	610	630	1,100
TOTAL ESTIMATED CAPITAL COST 4th Quarter 1975 Dollars	3,150	3,270	5,690
TOTAL CONSTRUCTION COST $/kWe	1,595	1,425	2,140

* Scope & basis different from UWMAK I & II

A major physical problem with land-based solar plants is the space required. A system designed to run on solar power for eight hours during the day and have sufficient thermal storage to carry a reduced night load would require 3 1/2 to 4 square miles for 100 MWe. Further, unless summer loads are considerably higher than winter loads, the peak seasonal demand and generating capacity will be out of phase.

Ocean thermal gradient plants have neither of these problems. However, their overall efficiency is very low (in the order of 2% to 3%), and the environmental effects of transposing 4000 MWt of energy between the top and bottom of the ocean to generate 100 MWe have yet to be analyzed.

XIII-G. Discussion

XIII-G-1. Discussion of the Perspective

The perspective provided by Fig. XIII-F-1 is that the electricity costs as developed for UWMAK-III appear to be comparable with estimates developed by Bechtel for several other advanced energy systems such as fuel cells and coal fired MHD plants. All costs are less than estimates for central station solar power. The dashed boxes on Fig. XIII-F-1 indicate a range of possible total costs but such a range has not been developed for UWMAK-III. This should be done by changing several of the key design choices, such as the choice of the primary structural material, and assessing the impact.

Fuel cells, with a low capital cost but a high fuel cost, appear to be the type of system ideally suited for peaking plants. Fusion and coal fired MHD are considered as based loaded plants because the capital costs make up a greater part of the electricity costs. The capital cost associated with the coal fired MHD system (approximately 40 mills/kWh) is higher than for coal fired steam because of the high temperature materials and cryogenic magnets associated with the MHD power cycle. The fuel costs add about a third to the electricity cost for both coal fired steam and coal fired MHD. In contrast, the fusion power costs are primarily related to capital costs while the fuel costs are only 1-2 mills/kWh. This is important if fuel costs escalate faster than capital costs. Past patterns of price behavior are a poor guide in predicting the future but, from an economics standpoint, if the scarcity of fuel is perceived to be greater than the scarcity of capital (not an unlikely event since fossil sources are finite, whereas capital sources are not) the cost of fuel will indeed rise faster than capital costs.

The solar estimates, which range from 70 to 200 mills/kWh, exceed those of all other systems. Further, solar power plants may not be feasible as based loaded systems except in the southwestern part of the U.S. because of the high load requirements during winter. Providing the energy storage capacity necessary for a base loaded plant in other parts of the country would roughly double the costs indicated on Fig. XIII-F-1. (This does not detract from the positive role to be played by solar energy for space heating on homes and other buildings.)

The other potential base-loaded system not yet discussed is the Liquid Metal Fast Breeder Reactor (LMFBR). The LMFBR is the most highly developed of the non-fuel-limited power plants of the future, but consistent costs for this system were not available. Because it is found that costs vary widely depending upon the estimator, we did not feel it was appropriate to place a value not developed by Bechtel onto the Fig. XIII-F-1. The only cost we will note is the relatively hard cost estimate for the Clinch River Breeder Reactor (CRBR) project.

The total estimated construction cost for CRBR is $891 million in 1974 dollars. (See ERDA Congressional Testimony, 1976). We have used 4th quarter, 1975 dollars in this report and, as discussed in section XIII-F-2, mid-1974 prices are to be escalated by 22% based on Bechtel escalation figures and the Handy Whitman Index. This would bring the CRBR estimated construction cost to $1.087 million

in the 4th quarter, 1975 dollars or $3105/kWe. Adding owner costs and interest during construction on the basis applied earlier gives a total estimated capital cost for CRBR of $1.455 billion, or $4157/kWe. The contribution to the cost of electricity from return on capital based on a 15% fixed charge rate is 89 mills/kWh. These costs do not include development costs, fuel costs, operating costs, or escalation beyond 1975. The plant is scheduled to operate in 1982.

The above costs are not strictly comparable because the CRBR is a demonstration plant and it is difficult to consistently estimate the cost of commercial plants from CRBR costs. This point has been made in a recent article by Levenson, Murphy and Zaleski. (See Nuclear News 19, 54 (1976).) However, Levenson, et al. do point out that demonstration plants such as Shippingport for light water reactors proved to be about twice as expensive as commercially built light water reactors like Dresden and Yankee. They also point out that "the cost of Shippingport, after normalization to 1974 conditions, is the same as the estimated cost of CRBR with a 15 percent contingency." If one infers that fast breeder reactors will experience a similar cost reduction on commercialzation, then a commercial LMFBR will cost about $2000/kWe and will have electricity costs in the range of 45-55 mills/kWh, (1975 dollars). This result is in basic agreement with current reports by the French for the costs of Superphenix, a 1200 MWe LMFBR which will follow the French demonstration LMFBR, Phenix. The electricity costs for Superphenix are projected to be approximately double the costs of light water reactors. Lower costs than these will mean the commercial LMFBR's will have to be less than half the costs of demonstration fast breeder reactors. The costs for CRBR are summarized in Table XIII-G-1.

XIII-G-2. Analysis of UWMAK-III Costs

The costs developed in section XIII-C have been analyzed to understand which items were key to determining the costs. The unanticipated result is that the cost of high temperature refractory metal piping is critical while the costs of the toroidal field magnet system is relatively less important. This last result is crucial because it is opposite from the accepted folklore that the magnet costs are the primary factor in determining fusion plant costs.

The piping costs were high because it is necessary to protect refractory metals from the atmosphere to avoid oxide formation and hydrogen embrittlement. Importantly, this is a general characteristic of refractory metals and is not specific to the use of molybdenum based alloys. The cost estimate developed for such pipe in the primary system is approximately $35,000/ft, and the range of piping costs are given in the appendix, section XIII-H. As such, about a quarter of the nuclear island costs and about a third of the closed cycle helium gas turbine plant equipment costs were for pipe. It will be of great interest to redesign UWMAK-III (a relatively small unit physically with R = 8m) using a lower technology structural material such as 316 stainless steel. Clearly, the absolute costs will be reduced significantly and it is important to determine just how much.

Table XIII-G-1

Estimated Capital Costs for 350 MW_e CRBR

(4th Quarter, 1975 Dollars)

(In Millions of Dollars)

Total Estimated Construction Costs ($891 million*(1974 dollars) + 22% escalation to 1975)	$1,087
Other Owner Costs	87
Interest During Construction	261
Total Estimated Capital Costs	$1,435
Total Construction Costs ($/kWe)	$3,105/kWe
Total Capital Costs ($/$kW_e$)	$4,100/kWe

Estimated Electricity Costs for CRBR

	(mills/kWh)
A. Operation and Maintenance	1
B. Fuel	--
C. Return on Capital	89
Total Estimated Electricity Cost	90 mills/kWh

* 1976 ERDA Congressional Testimony

An important auxiliary result is the breakdown by major category of the total costs. The direct costs are 40% of the total costs. Since all indirect costs are computed as a percentage of direct costs, every saving of $1 in direct costs means a savings of $2.5 in total costs. Therefore, a substantial reduction in piping costs (part of direct costs) will have a multiple effect on total estimated costs.

The direct costs in UWMAK-III were divided as follows: 25% for buildings, 35% for the reactor plant equipment (nuclear island), 25% for the turbine plant, 12% for electric plant equipment, and 3% for remaining miscellanous items. Therefore, the nuclear island is 35% of the direct costs while the balance of plant is 65%. The toroidal field magnets were estimated to be 10% of the reactor plant equipment costs or just 3.5% of the total direct costs. This is much lower than anticipated and leads us to conclude that we can afford to pay for higher magnetic field.

This result has some very important implications. In particular, it has an implication for the size of tokamak reactors. There are two reasons one would make a tokamak large. The first is to improve the confinement time of the plasma and the second is to keep the neutron wall loading to a prescribed but low value. A wall loading constraint at some level (high or low) is applicable to all magnetic approaches to fusion and is not specific to tokamaks. On the other hand, increasing the size to improve confinement time is more peculiar to closed line devices like tokamaks than it is to an open ended system like a mirror machine. However, almost all theories, as well as experience, indicates the confinement time improves with magnetic field. Therefore, within a given wall loading constraint, tokamaks can be made as small as possible by increasing the magnetic field. The cost penalty on the coils will not be overwhelming whereas keeping the size small will lower the costs of buildings, piping, blanket systems and so on.

Turning to the role of the structures in this design, the building costs were about a quarter of the direct costs and the reactor building was approximately a third of the total building costs. Future designs of the reactor building should therefore aim for a highly optimized design. A constraint is the apparent need for access to a tokamak from both the side and the top. This leads to a tall, large diameter building for UWMAK-III. However, further examination may allow for improvements.

The choice of power conversion cycle also merits further careful study. The cost of a closed cycle helium plant appears to be in the same range as a steam cycle (about $140/kWe for the turbogenerator island.) In this case, the determining factor in the choice of the cycle would be the power conversion efficiency and since capital costs are relatively high, the choice of an efficient power cycle is very important. There are indications from other studies that advanced steam cycles can produce comparable efficiencies at lower costs compared to closed cycle helium gas systems. (See "Study of Advanced Energy Conversion Techniques for Utility Application Using Coal or Coal Derived Fuels" Oral Briefing on Results of Task II, General Electric Co., February 10, 1976.)

Lastly, a comment about the intermediate loop. We have felt that the use of liquid lithium as the primary coolant would necessitate the use of an intermediate loop to isolate the primary coolant from the turbine cycle. This entails an added heat exchanger, an extra building, and added pipe length. The intermediate sodium loop in UWMAK-III is about 15% of the nuclear island costs. The development of a blanket design and cooling systems that can eliminate the need for the intermediate loop and thus lead to a potential savings in total direct costs. An example of such a blanket system is the use of Li_2O particles in a moving bed system similar to those used in the chemical industry. (For a reference, see D. K. Sze, et al., Trans. Am. Nucl. Soc. 22, 21, 1975). Combined with the lower costs associated with a material like stainless steel, such a system will be less expensive than the UWMAK-III design employing TZM and thus should be investigated.

In summary, the economic analysis of UWMAK-III has shown that costs can be determined by certain key design decisions made early in a reactor study. For this system, the choice of a refractory metal alloy caused piping costs to be a main cost driver. It has been found that magnet costs are not dominant and that it will make good sense to increase magnetic fields to achieve the required plasma confinement time. One can then design the reactor in a minimum size consistent with other design constraints. It is also found that the need for an intermediate loop results in increased costs. Yet this loop is required only for certain choices of coolant and breeder materials and may be eliminated with alternative blanket designs. Thus, there are many avenues open for reducing the cost of tokamak systems below those of UWMAK-III. Finally, a cost comparison shows UWMAK-III costs to be in the same range as those projected for other advanced energy systems. As noted earlier, directly comparable LMFBR costs were not available for inclusion here but estimates based on the analyses of others indicate that these costs will also be in approximately the same range.

XII-H. Appendix of Estimate Factors

COMPARISON OF VOLUMES

POWER BLOCK BUILDINGS

LWR BUILDINGS		UWMAK III BUILDINGS		
			Actual Volume Factor	Normalized Volume Factor (See Note)
Containment	1.0	Containment	4.1	2.6
Turbine	1.0	Turbine	2.2	1.4
Radwaste	1.0	Hot Cell & Radwaste	1.4	.9
Reactor Auxiliaries	1.0	Reactor Auxiliaries	1.4	.9
Reactor Auxiliaries	1.0	Heat Exchanger	4.0	2.5
Diesel Generator	1.0	Diesel Generator	1.0	.6
Control	1.0	Control	1.8	1.1
Total Volume	1.0	Total Volume	3.0	1.9

Note: The capacity of the UWMAK III facility is approximately 1.6 times the output capacity of the reference LWR facility. The normalized volume factor given above is defined as:

$$\frac{\text{(Actual Volume Factor)}}{1.6}$$

and is provided to give a comparison of volumes per unit of electrical output.

COMPARISON OF BULK MATERIAL RATES

(DOLLARS PER UNIT VOLUME)

POWER BLOCK BUILDINGS

LWR BUILDINGS		UWMAK III BUILDINGS				
			Civil	Piping	Elec.	Instru.
Containment	1.0	Containment	1.3	1.0	1.9	3.6
Turbine	1.0	Turbine	1.9	0.8	1.4	2.0
Radwaste	1.0	Hot Cell & Radwaste	1.0	0.6	1.3	3.0
Reactor Auxiliaries	1.0	Reactor Auxiliaries	1.0	1.0	1.1	1.0
Reactor Auxilaires	1.0	Heat Exchanger	2.5	2.1	1.3	1.3
Diesel Generator	1.0	Diesel Generator	1.0	1.0	1.0	1.0
Control	1.0	Control	1.0	1.0	1.0	2.1

Note: The factors are independent of size and are unit volume costs. As an example, under Electrical of the Heat Exchanger building, the 1.3 factor indicates that the electrical bulk materials (conduit, cable tray, and wire & cable) will be 30 percent more dense for UWMAK III than for a fission plant auxiliary building, therefore on a dollars-per-cubic-foot of building basis will cost 30% more.

UWMAK III

PIPING COST BREAKDOWN

ACCT.	PIPING DESCRIPTION	$ 1000				
		PRIMARY			OTHER	TOTAL
		L.F.	$/L.F.	TOTAL		
222.11	Inner Blanket	1,300	35.5	46,200	48,000	106,200
	Valves			12,000		
222.22	Diverter	1,300	18.0	23,400	-	23,400
222.32	Intermediate Na Loop	1,100	23.0	25,300	30,000	55,300
222.42	Outer Blanket	1,000	23.0	23,000	38,000	61,000
231.14	Gas Turbine	300	20.0	6,000	84,000	90,000
231.24	Steam Turbine	-	-		28,000	28,000
234.3	Feed Heating	-	-		35,000	35,000
235.71	Other Turbo Generator Equipment	-	-		35,000	35,000
				$135,900	$298,000	$433,900

XIV. General Conclusions

There are many conclusions and implications for further work that have come out of the UWMAK-III study. To be consistent with the structure of this report, the major conclusions and implications for further work are summarized here by subject category beginning with the plasma analysis and following through to the study of materials resources. Only the more general conclusions are listed here while detailed advances in analysis or technique and more specific results are described in the individual sections.

XIV-1. Plasma Considerations

XIV-1-a. MHD Analysis of Noncircular Plasmas

The detailed MHD study indicates it is possible to design moderately noncircular plasmas with both the poloidal beta value and the height to width ratio about two using discrete external coils and no conducting shell. Further, the plasma can be designed to be bounded by a separatrix which allows for operation of a double neutral point poloidal divertor. Control of the vacuum vertical field for overall stability of the plasma loop is a sensitive matter and can limit the achievable plasma height to width ratio. The UWMAK-III plasma shape with flux surfaces having a "D" or triangular shape is most satisfactory from a stability viewpoint and is conveniently compatible with the natural "D" shape assumed by constant tension toroidal field magnets. The plasma design allows for a relatively high value of β (about 9%) which ultimately allows us to achieve the high power output in this relatively small (R = 8.1 m) machine.

XIV-1-b. Heating of Reactor Grade Tokamak Plasmas

The examination of the potential of RF heating has included an initial examination of the fast magnetosonic, lower hybrid, and low frequency Alfven modes. We have decided at this point that the fast wave is best due to its direct heating by linear processes of the ions, the potential for accessibility and heating of the plasma core, and the demonstrated experimental viability on tokamak plasmas. A small to moderate development program is required to produce generators which can supply the needed 40-200 MW @ 60 MHz supplementary heating power for a large tokamak reactor. The launching structure should be fanned in the poloidal sense on the outside wall in order to provide low poloidal m values for the mode and to allow the capability of low $k_{\parallel}$ excitation.

Further work on a more detailed design of a suitable waveguide or loop launching structure for optimum heating of the plasma core is required. Also, a more advanced treatment of the heating processes and their effect on plasma transport is needed. Materials considerations for RF heating do not seem to be a serious problem other than the viability of ceramic-filled waveguides. This latter approach would allow a reduction in the size of the waveguide but guides without cerami appear quite feasible. Ceramics might also find use as coaxial insulators so that the effect of neutron and plasma particle bombardment on their dielectric properties should be examined further.

The potential of direct ion heating within the plasma by means of the fast magnetosonic mode could prove very beneficial if the electron energy confinement time in larger tokamaks becomes anomalously small. Clearly, the availability of high power sources and the existence of known heating mechanisms for this wave mode calls for further work on such RF supplementary heating of tokamak plasmas.

XIV-1-c. Spatial Plasma Profile Effects on Fractional Burnup and Tritium Inventory

Space dependent plasma simulation calculations indicate that the spatial profiles of density and temperature in a reacting plasma can be much sharper than is normally assumed (e.g. parabolic) if microinstabilities, such as trapped particle modes, govern the transport. The result is a rapid diffusion of particles out of the plasma even though the confinement time near the center of the device is adequately long. As such, the particle confinement time, τ_p, can be much less than the energy confinement time, τ_E. The result is that the fractional burnup is much lower than previously predicted from global, space independent analyses. The consequence is a large tritium inventory (~50 kg) associated with the refueling system. If born out, this would effectively negate efforts to reduce tritium inventory through the use of solid breeding materials in the blanket.

XIV-1-d. Impurity Control and Divertors

An axisymmetric poloidal divertor design in which the particles are collected in a system outside the toroidal field magnets appears feasible and can allow a relatively high thermal efficiency to be associated with the divertor heat removal system. Particles are spread out spatially to reduce the surface heating rate on the solid TZM plates used to pick up the energy of the particles. The pumping of all particles is then accomplished with cryopumps protected by a set of baffles staggered at 300°K, 77°K, and 20°K.

Placing the divertor particle and heat collection system outside the TF coils also allows one to design for high flow conductance to the pumps with low flow conductance for gas back to the plasma chamber. Such a design also opens the possibility for using direct conversion on the plasma in the divertor. This option deserves considerable additional work, as does the basic idea of the proposed divertor system.

XIV-2. Toroidal Field Magnet Design

TiNb superconducting magnets that are fully cryogenically stable and achieve between 8 and 9T maximum fields are satisfactory for this noncircular tokamak concept. Further, the use of pure aluminum as the conductor stabilizer has great promise and should be pursued. Experiments at the University of Wisconsin show that reinforced aluminum (such as in a conductor) does not exhibit a large resistivity increase when subjected to cyclic loading in which the material is stressed beyond its yield point. The use of aluminum will save weight and cost by comparison with copper because between 2 and 5 times less material is required.

In addition, the use of a high strength aluminum alloy as the structural material for the magnets has equal promise for saving weight and cost compared to the use of an austenitic stainless steel. Used in conjunction with Al as the conductor stabilizer, one has substantially fewer themal stress problems on cool down or warm up because there are no differences in thermal conductivity, as there are between Cu and stainless steel. Finally, the high thermal conductivity of aluminum should allow magnet cool down to be accomplished more quickly than with a magnet using stainless steel structure.

The ohmic heating and equilibrium field coils are based on a design due to Cornish which provides for more cooling surface than in previous designs and for a fairly inexpensive construction technique in which all three coil elements - conductor, insulator and structure - are wound simultaneously. This concept should be pursued further.

XIV-3. Vacuum Systems for Tokamaks

Most large tokamak devices have vacuum systems which call for the use of cryopumps in some form. The analysis here indicates that the use of molecular sieves in cryopumps gives the simplest, the safest, and the most easily maintained system available.

A pumping speed of 10 liters/sec/cm^2 for D and T is routinely obtained at the present time. This capacity could probably be increased to 15 liters/sec/cm^2 by a combination of better design and less efficient baffles, at the expense of a higher rate of cryogen use. It appears that such a system can be designed to operate without the aid of any auxiliary particle collection plates.

XIV-4. Blanket and Shield Design

The blanket and shield design developed for UWMAK-III is highly attractive and should be developed further. The partial ISSEC concept based on neutron spectrum shaping to protect the structure on the inner portion of the torus from radiation damage works well. Toroidal transport calculations using R as the primary variable indicates 25 cm of graphite protecting the inner first structural wall reduces the radiation damage (dpa rate) by a factor of 9 compared to an unprotected structure. The helium production rate is reduced even more.

It is possible to breed tritium using liquid lithium as the coolant in the outer blanket only. This greatly simplifies the use of a liquid metal coolant since it is used where space is plentiful and the toroidal field is low. As such the pressure in the system can be kept low (~80 psi). The inner blanket is therefore actually a hot shield. It is used to breed energy and can be cooled with helium. Further analysis should and will be done using R-Z toroidal neutron transport calculations. This will also allow one to determine the maximum graphite thickness that can be used in the role of a partial ISSEC since this thickness is governed by heat transfer considerations.

The problem of isolating the inlet and outlet cooling channels in the outer blanket design can be accomplished by using an effectively stagnant lithium layer between the inlet and outlet zones of the basic blanket module. Also, the inner blanket can be designed with a helium coolant such that the outlet conditions match those associated with the outer blanket power cycle. As such, the same turbomachinery can be used.

However, the pulsed nature of tokamak operation makes it necessary to provide some form of thermal energy storage such that the system can generate electricity continuously. An intermediate sodium loop between the primary lithium and the helium can be used for this purpose. This sodium provides enough energy storage that intermediate heat exchangers for the helium coming from the inner blanket is not necessary. However, further study is clearly desirable on thermal storage and the problem of continuously operating turbines in a pulsed reactor.

A feasible modular blanket design has been developed in which a skeletal frame is used to hold blanket sections within a module. This feature allows removal of a single section of blanket or the entire module depending on need. Opening the shield at the midplane by means of hinged sections appears to be a reasonable way of providing access to the outer blanket. The general question of blanket handling and removal is one which will become increasingly important and continues to deserve attention.

XIV-5. Tritium and Induced Radioactivity

XIV-5-a. Tritium

The tritium inventory is very high in UWMAK-III, perhaps intolerably so, primarily because of the low value of particle confinement time. As noted in the conclusions regarding the plasma physics analysis, this is caused by the rapid transport of plasma near the edge. We thus have a long energy confinement time but a short particle confinement time. If this is confirmed experimentally in large plasmas, then a lower tritium inventory will be difficult to achieve. Several design changes can, however, be made. These include recycling the cryo-pumps more frequently and redesigning the purification system to purify only a fraction of the stream each time through the reactor.

In addition, several items have only been examined in a cursory way and deserve greater study. These items include fuel storage, the design of the pellet fueling system itself, and the design of valves that can operate at high temperatures (~900°C) and not leak tritium. In addition, further attention should be given to the problems of coolant purification for the lithium, sodium, and helium.

The high temperature in the blanket system means the tritium concentrations there must be kept low (to 1-2 appm) in order to avoid excessive diffusion of tritium through the piping and heat exchangers. There is no really straight forward way to do this at the present time and experimental verification of acceptable techniques is highly desirable.

We have examined in detail the use of a niobium window to remove the tritium from the liquid lithium. In principle, one can keep the tritium concentration low by providing a large enough window. Our analysis indicates the use of a Nb window will probably work but it has its problems. In the first place, it is necessary to getter the tritium on the downstream side and the best method is to use oxygen. However, the use of oxygen in the downstream carrier gas means the Nb must be coated. Palladium can protect the Nb but it has a special problem in that Pd attacks the Nb. To prevent this, a coating of yttrium between the Nb and Pd appears to be a feasible overall solution. In order to have more confidence in this high temperature system, it is necessary to have more experimental data on the interaction of oxygen with Pd (particularly, diffusion of O through Pd and the formation of Pd oxides). Another concern is the transport of carbon to the Nb from the TZM causing embrittlement of the window. This could be a potential safety problem with this system.

Another problem requiring further study is the removal of helium from the liquid lithium coolant prior to the excessive formation of bubbles. Helium is produced at a rate equal to the tritium production rate and can thus build up to substantial levels if not removed.

The shield contains boron carbide and some tritium will therefore be produced. It will be tied up in the shield and thus contribute to the overall system inventory. We estimate the buildup rate at about 0.2 gm/day so that for a 30 year life, the tritium will build in the shield to a level of about 2 kg at the

end of life. This is not particularly large compared to the total system inventory but it is not negligible.

Finally, more experimental data is needed on tritium permeation through materials at low tritium partial pressures.

XIV-b. Radioactivity and Afterheat

The induced radioactivity and afterheat using TZM in UWMAK-III is generally quite similar in magnitude to values calculated in our previous studies on stainless steel. There are however some significant differences. The buildup of radioactivity in the reactor following startup of operation tends to reach an asymptotic level in less than a month that is the order of 1 Ci/W_{th}. The initial value of afterheat following a shutdown is only 0.4% of the thermal operating power.

The decay of the radioactivity and afterheat following shutdown is quite different in TZM from what we have previously found for stainless steel systems. In particular, both the radioactivity and the afterheat decrease by a factor of about 200 just one month after shutdown. Two years after shutdown, the radioactivity has been reduced by four orders of magnitude and the afterheat by five orders of magnitude. This is a much more rapid decay than one would find with stainless steel. Beyond two years, the decay is dominated by long lived isotopes and there is little further reduction. Thus, TZM appears not to present any new problems following shutdown. It is clearly superior to stainless steel with respect to radioactivity levels at intermediate times and is somewhat worse, though not intolerable, at long times.

XIV-6. Materials and Radiation Damage

XIV-6-a. Structural Material

The molybdenum based alloy, TZM, is the most attractive refractory metal alloy for use at high temperatures (~1000°C). The reasons are that, by comparison with Nb, V, or their alloys, it has the highest strength-to-weight ratio and heat capacity, the lowest values of electrical resistivity, vapor pressure, coefficient of expansion and thermal induced stress, the highest yield strength at the maximum operating temperature, and the best 10,000 hour creep strength at temperature. Neutronically, it has the highest (n,2n) cross section, the lowest (n,p) cross section, and the lowest high energy absorption cross section. In terms of chemical compatibility, Mo can be used with either liquid lithium or He coolant (as contrasted to Nb or V alloys) and it has the lowest solubility and the lowest contamination rate from impurities (C,O,N) in liquid lithium. As for tritium considerations, TZM has the lowest in situ generation of helium from tritium decay. It also has the lowest permeability to tritium and therefore the lowest leakage rate via diffusion through the structure.

Importantly, Mo or TZM has the lowest cost per unit weight and the long term availability of Mo is good since the United States has larger reserves of Mo when compared to any other refractory metal.

The irradiation damage effects in TZM appear to be quite manageable. Swelling in the outer blanket appears to be less than 1% per year and it may be as low as 0.2% per year in the inner blanket. If the TZM is irradiated at high temperatures (700-1000°C), it appears that it can retain reasonable ductility up to ~20 dpa (about 1.5 years of UWMAK-III operation). No evidence for loss of creep strength or fatigue life has yet been found in high temperature irradiated and tested Mo alloys. They also seem to be relatively unsensitive to helium embrittlement. We feel that a 25 dpa and 150 appm He content limit in the 750-950°C region is a reasonable lifetime and it may in fact be too conservative.

The primary difficulty with the use of TZM by comparison with Nb or V alloys is in joining components particularly in the field. It has been demonstrated that under strict quality assurance, welds can be made in Mo and TZM which can undergo a 180° bend without breaking. It has also been found that diffusion bonding can result in a structure that is strong and which does not promote significant grain growth. The potential advantages of TZM clearly justify the need for further work on joining techniques such as brazing, and the development of special brazing materials.

XIV-6-b. Neutron Reflector and ISSEC Spectrum Shaper

Graphite is used in the form of carbon cloth as a thin low Z liner on the outer blanket and as bulk graphite, 25 cm thick, to protect the inner blanket and shield from radiation damage. The anticipated life of both the thin carbon liner (or carbon curtain) and the thicker ISSEC zone is anticipated to be of the same order as that for the outer first wall structure, i.e., 30 dpa, or ~1.5 years when the average wall loading is about 2.5 MW/m^2.

Erosion rates of the ISSEC and curtain appear to be limited by vaporization rather than physical or chemical sputtering. It is also expected on the basis of experiments that helium produced in the graphite will diffuse out. Further experiments are required to determine the high temperature damage limit for the use of graphite as a reflector inside the first structural wall. It is anticipated that the curtain should be changed every 1.5 years of UWMAK-III operation and the ISSEC every 3 years.

XIV-6-c. Shield and Magnets

Materials used in the shield are not anticipated to be any special problem and the structural role of aluminum in the magnets will not be affected. It appears that radiation damage to the magnet insulator material, mylar, is a serious effect and that, with the shields in UWMAK-III, the mylar lifetime is ~15 years. The resistivity increase in the aluminum stabilizer from radiation effects is such that it will double its resistance every year unless periodic annealing is performed. However, heating up to RT every year should remove essentially all the damage.

XIV-7. Power Cycle Analysis

The conceptual UWMAK-III fusion power cycle utilizing closed-cycle helium gas turbines would offer an attractive station efficiency (above 40 percent) without requiring cooling water supply for waste heat rejection. Direct integration of a closed-cycle gas turbine with a helium-cooled fusion blanket offers the highest promise in terms of power conversion efficiency and cost saving. However, integration with a lithium-cooled blanket with tritium breeding will require a primary or even intermediate heat exchanger, thus resulting in a temperature loss for the turbine inlet.

The cycle configuration most suitable for UWMAK-III power conversion would require single intercooling with regeneration (88 %) operating at 1600°F (870°C) and 1000 psia (6.9 MPa) helium turbine inlet conditions. The use of an intercooler for three points gain in thermal efficiency is preferred instead of increasing the turbine inlet temperature by 150 F (to 1750 F or 954°C) without intercooling in or to achieve a cycle thermal efficiency of approximately 44 percent or a station efficiency of about 42 percent. Potential improvement in UWMAK-III power plant efficiency by using higher turbine inlet temperatures would be constrained by the temperature capabilities of the blanket material rather than the turbomachinery.

The power conversion system parameters interfacing with the fusion reactor include the turbine inlet temperature and pressure, and the regenerator outlet temperature. These parameters will require some design trade-offs and/or compromise with the blanket heat transfer, flow rate, and pressure level capabilities. Selection of the regenerator effectiveness has a crucial influence on the trade-off between the system performance and cost, as well as on the interface compatibility between the reactor blanket and the power conversion system. A thermal power split one-to-two between the inner and outer blankets, respectively, would permit utilization of three identical power conversion loops of 585-MWe each, representing a well-balanced power system integration arrangement. While this is somewhat subject to blanket design, it may not always be possible to match on a 2 to 1 basis and, for a design like UWMAK-III, a 3 to 1 split of energy between the outer and inner blanket is readily achieved. Although a single-shaft turbomachine designed for 585-MWe output would result with the three-loop power system arrangement, unit capacities as large as 1000-MWe would appear technically possible; at least two power loops will be needed for UWMAK-III.

Preliminary heat exchanger design studies indicate that use of standardized heat exchanger modules containing unfinned tube bundles with simple counter-flow arrangement could result in compact regenerator, precooler, and intercooler designs offering reasonable pressure loss characteristics.

The material compatibility at the bimetal junctions involving transition from the blanket material (TZM) to power system materials, particularly in the presence of a liquid metal, can potentially limit the temperature capability of the blanket as well as the turbine inlet. Another important problem is the need for thermal energy storage to allow continuous power output despite the

inherent cyclic nature of Tokamak operation. Failure to develop a viable energy storage system could hamper the implementation of UWMAK-III or any Tokamak-type fusion power plant.

The principal advantages of closed-cycle helium gas turbines for fusion power generation include: (1) attractive thermal efficiency at moderate temperature, (2) compact turbomachinery with large unit capacity, (3) simple components design, (4) adaptable to dry cooling tower, (5) working fluid inert to radioactivity, and (6) potentially low capital costs. It is anticipated that increasing application of closed-cycle gas turbines for fossil, fission, and solar power generation will be realized and that the technological progress resulting from these developments will be directly applicable to fusion power systems.

The power cycle associated with the heat of particles diffusing from the plasma into the divertor can be as much as 15% of the plant thermal power and it is important to collect this energy at high efficiency. The use of TZM plates cooled with a liquid metal at high temperature is attractive for this purpose. In addition, as mentioned earlier, the placement of the collector system outside the TF coils also opens the possibility to use direct conversion on the diffusing particles. This requires further investigation.

XIV-8. Balance of Plant Analysis

The present design allows an initial assessment of the problems associated with the plant design for tokamak-type reactor plants in general and the UWMAK-III reactor plant in particular. The design and analyses are relatively superficial and conceptual in nature. Many of the systems and associated equipment are not defined in detail and some of them probably have not yet been identified. Allowances have been made to accommodate these unknowns and uncertainties; but until further design and analysis is done, many uncertainties remain. On the basis of the present study, the following comments are in order.

The plant layout including equipment and piping arrangement is preliminary. Further study is needed to detail and improve the arrangements. The primary piping arrangement is a critical aspect of the plant layout and can have a large impact on building costs. No consideration has been given to the arrangement of the reactor internal piping or its interface with the external primary piping systems.

Use of large size piping size piping for transporting high temperature coolant is of some concern. No stress analysis has been performed to substantiate the piping arrangement.

Reactor Maintenance problems, especially in regard to blanket removal and replacement, constitute another area where only preliminary consideration could be given. A conceptual blanket handling scheme has been proposed, but studies are needed to evaluate the feasibility of the concept and develop procedures and conceptual equipment designs. It is likely that major R&D programs will be necessary to develop and improve blanket handling equipment and procedures. The problem of radioactive contamination of the plant and equipment has not been looked at and must be given a serious consideration.

Analysis of the effects of magnetic fields on plant equipment and components is necessary. As a result, it may be necessary to consider relocation of some of the buildings and equipment. To avoid interference with the magnetic field, non-magnetic materials are needed for the piping and the containment liner.

The equipment requirements for the Hot Cell have not been defined. Concepts for handling the blanket sections, disassembling, processing and reassembling the new sections must be developed. The building sizes and arrangements shown are preliminary and may change considerably after detail engineering is undertaken.

Details have to be worked out to determine an acceptable method of ultimate disposal of solid radioactive wastes. Several alternatives are possible such as: on-site storage versus buried vaults, air-cooled versus forced convection systems.

An annular arrangement of the reactor support buildings surrounding the Containment Building is proposed. This arrangement seems to offer some advantage. It makes the plant layout very compact with maximum utilization of space around the Containment Building by locating all the reactor support facilities near the nuclear island. Some cost saving will also result because the containment wall is made common to the support buildings. This arrangement results in the Containment Building being completely surrounded. This can make scheduling of the construction of the various buildings difficult because of the need for construction access.

To accommodate the four turbine-generator units along with their associated regenerative cycle components, a large Turbine Building is needed. The unit handling the tritium-bearing helium imposes a further constraint on the building design.

Piping arrangement in the Heat Exchanger Building represents probably the most complex piping system in the plant. The design of the complex intermediate sodium piping arrangement for the thermal storage system could not be addressed in this study. A very detailed study is needed for this cost intensive area of the plant design. The thermal storage system may be a fruitful area for study of new concepts.

The structures in this plant are significantly larger than those in fission power plants. All the structures are very massive because of shielding and other safety requirements. The conceptual design, as described, is considered to be a feasible design consistent with current technology and industry practive. However, some aspects of the design/analysis of the structures have to be investigated further before a method for their design can be established, and they are identified as follows:

In the Containment Building, special vehicles, possibly running on tracks, have to be built for removing blankets, which will subject the floor slab to moving dynamic loads. A thorough analysis of the floor slab, subjected to moving loads, is needed.

The dome has been analyzed on the assumption that its thickness is uniform throughout. The domes are usually thickened near the edges. This necessitates a finite element analysis to study the propagation of edge disturbances into the dome.

The phenomenon of instability of the dome and the cylinder has been studied on the basis of classical linear theory. However, it is also known that, due to imperfections and boundary conditions different from those used in linear theory, the buckling load of shells can be significantly lower than those given by the classical theory. An estimated of this lower buckling load should be obtained by non-linear analysis in conjunction with realistic boundary conditions. At springline level, the arches will exert considerable thrust producing radial expansion of the cylinder. It is, therefore, necessary to evaluate the interactions between the arches, the dome and the cylinder.

XIV-9 Materials Resources

The reduced overall size of UWMAK-III compared to earlier reactor designs of similar thermal power rating has greatly reduced the problems of metal procurement. However, several materials are used for different, and more significant, purposes in UWMAK-III-namely, aluminum and molybdenum-and we summarize the conclusion regarding reserves and resources for these materials and for lithium. Conclusions for other materials have been summarized in great detail in our previous reports, UWMAK-I, Vol. II, (UWFDM-68) and UWMAK-II (UWFDM-112). Recall that the resource analysis is based on a 10^6 MWe economy of UWMAK-III type reactors so that procurement of materials for five to ten systems presents much less serious problems.

The United States has very limited bauxite reserves and imports over 90 percent of its bauxite supply. An adequate domestic supply of aluminum ore would require development of resources of high-alumina clays, anorthosite, alunite, and dawsonite, singly or in combination. The resources of aluminum in such materials are very large. The necessary technology is available for extraction from clays, anorthosite, and alunite, but energy costs and dollar costs would be above those of extraction of aluminum from bauxite. Mining of these three materials would be open cast, but no unusual environmental problems would be involved. Dawsonite production would be involved with oil shale production and would share the environmental and other problems facing the oil shale effort.

Molybdenum could be a most serious problem because of procurement difficulties rather than United resources. United States reserves of molybdenum are estimated by the U.S. Geological Survey at 3×10^6 tons and by the U.S. Bureau of Mines at 4×10^6 tons. The survey estimates identified marginal resources at 17.5×10^6 tons. These figures suggest that at prices somewhat higher than present prices, the UWMAK-III, 10^6MWe, requirements could be met but information on possible rates of production of molybdenum beyond the end of the century is not available. The current rate of production is only about 55,000 metric tonnes per year. Finally, the U. S. Geological Survey states that the identified resources of lithium in the United States likely to reach the marketplace by the year 2000 are scarcely adequate to meet the anticipated growth of the industry for conventional use and are grossly inadequate for the anticipated requirement for new energy-related uses. A search for new deposits is needed. The brines of western saline basins and certain types of clay deposits appear to offer the most promise.

XIV-10. Economics

The perspective provided by Fig. XIII-F-1 is that the electricity costs as developed for UWMAK-III are somewhat high but appear to be comparable with estimates developed for several other advanced energy systems such as fuel cells, coal fired MHD plants, and fast breeder reactors. All costs are less than estimates for central station solar power.

The detailed costs have been analyzed to understand which items were keys to determining the costs. The unanticipated result is that the cost of high temperature refractory metal piping is critical while the cost of the toroidal field magnet system is relatively less important. This last result is crucial because it is opposite from the accepted folklore that the magnet costs are the primary factor in determining fusion plant costs.

The piping costs were high because it is necessary to protect refractory metals from the atmosphere to avoid oxide formation and hydrogen embrittlement. Importantly, this is a general characteristic of refractory metals and is not specific to the use of molybdenum based alloys. The cost estimate developed for such pipe in the primary system is approximately $35,000/ft. As such, about a quarter of the nuclear island costs and about a third of the closed cycle helium gas turbine plant equipment costs were for pipe. It will be of great interest to redesign UWMAK-III (a relatively small unit physically with R = 8m) using a lower technology structural material such as 316 stainless steel. Clearly, the absolute costs will be reduced significantly and it is important to determine just how much.

An important auxiliary result is the breakdown by major category of the total costs. The direct costs are 40% of the total costs. Since all indirect costs are computed as a percentage of direct costs, every saving of $1 in direct costs means a savings of $2.50 in total costs. Therefore, a substantial reduction in piping costs (part of direct costs) will have a multiple effect on total estimated costs.

The direct costs in UWMAK-III were divided as follows: 25% for buildings, 35% for the reactor plant equipment (nuclear island), 25% for the turbine plant, 12% for the electric plant equipment, and 3% for remaining miscellaneous items. Therefore, the nuclear island is 35% of the direct costs while the balance of the plant is 65%. The toroidal field magnets were estimated to be 10% of the reactor plant equipment costs or just 3.5% of the total direct costs. This is much lower than anticipated and leads us to conclude that we can afford to pay for higher magnetic field.

This result has some very important implications. In particular, it has an implication for the size of tokamak reactors. There are two reasons one would make a tokamak large. The first is to improve the confinement time of the plasma and the second is to keep the neutron wall loading to a prescribed but low value. A wall loading constraint at some level (high or low) is applicable to all magnetic approaches to fusion and is not specific to tokamaks. On the other hand, increasing the size to improve confinement time is more peculiar to closed line devices like tokamaks than it is to an open ended system like a mirror machine. However, almost all theories, as well as

experience, indicated the confinement time improves with magnetic field. Therefore, within a given wall loading constraint, tokamaks can be made as small as possible by increasing the magnetic field. The cost penalty on the coils will not be overwhelming whereas keeping the size small will lower the costs of buildings, piping, blanket systems and so on.

Turning to the role of the structures in this design, the building costs were about a quarter of the direct costs and the reactor building was approximately a third of the total building costs. Future designs of the reactor building should therefore aim for a highly optimized design. A constraint is the apparent need for access to a tokamak from both the side and the top. This leads to a tall, large diameter building for UWMAK-III. However, further examination may allow for improvements.

The choice of power conversion cycle also merits further careful study. The cost of a closed cycle helium plant appears to be in the same range as a steam cycle (about $140/kWe for the turbogenerator island). In this case, the determining factor in the choice of the cycle would be the power conversion efficiency and since capital costs are relatively high, the choice of an efficient power cycle is very important. There are indications from other studies that advanced steam cycles can produce comparable efficiencies at lower costs compared to closed cycle helium gas systems. (See "Study of Advanced Energy Conversion Techniques for Utility Application Using Coal or Coal Derived Fuels", Oral Briefing on Results of Task II, General Electric Co., Feb. 10, 1976.)

The use of liquid lithium as the primary coolant and the burn cycle employed for UWMAK-III necessitates the use of an intermediate loop to isolate the primary coolant from the turbine cycle. This entails an added heat exchanger, and added pipe length. The intermediate sodium loop in UWMAK-III is about 15% of the nuclear island costs. A blanket design and cooling system that can eliminate the need for the intermediate loop can thus lead to a potential savings in total direct costs. An example of such a blanket system is the use of Li_2O particles in a moving bed similar to those used in the chemical industry. Combined with the lower costs associated with a material like stainless steel, such a system will be less expensive than the UWMAK-III design employing TZM and thus should be investigated.

In sum, the economic analysis of UWMAK-III has shown that costs can be determined by certain key design decisions made early in a reactor study. For this system, the choice of a refractory metal alloy caused piping costs to be a main cost driver. It has been found that magnet costs are not dominant and that it will make good sense to increase magnetic fields to achieve the required plasma confinement time. One can then design the reactor in a minimum size consistent with other design constraints. It is also found that the need for an intermediate loop results in increased costs. Yet this loop is required only for certain choices of coolant and breeder materials and may be eliminated with alternative blanket designs. Thus, there are many avenues open for reducing the cost of tokamak systems below those of UWMAK-III.

APPENDIX

Final Analysis of UWMAK-III

After the design of UWMAK-III had been frozen and the performance evaluated, there was still a concern over the use of a neutronic calculational model that did not explicitly treat toroidal geometry effects. For this reason, a calculation using R-Z geometry to represent the toroidal configuration was undertaken. There are some other minor geometry and composition changes also included in these new calculations. The results of the R-Z calculation and its consequence for breeding, heating, and radiation damage are given here.

The R-Z coordinate system used to describe the geometry is shown in Fig. A-1. It is clear that any multigroup, two dimensional R-Z transport code can be used to account for toroidal geometry. The multigroup two dimensional transport codes which exist now are DOT(1), TWOTRAN(2), and TRIPLET (3). The TRIPLET code solves only planar geometry (x-y,r-θ), and so cannot be used to account for toroidal effects.

The calculation reported here was completed using the DOT program and employed a 46 neutron, 21 gamma group cross section data set. The data set is based on the DLC(37) library generated from ENDF/B-IV. The calculation was done in S_6 (60 directions) with a P_3 approximation on the scattering cross section.

The neutron source distribution has been represented as a function of R and Z as

$$S(R,Z) = S(R,0)\ [1 - Z/Zi)^2]^3,$$

$$S(R,0) = S(0,0)[1 - ((R - 900)/180)^2]^3, \quad 1080 > R > 900,$$

$$S(R,0) = S(0,0)[1 - ((900 - R)/360)^2]^3, \quad 540 > R > 900,$$

where the above equations represent a source peaked at R = 900 cm (i.e., shifted 90 cm toward the outside blanket from the plasma center at R = 810 cm) but symmetric about the midplane. Zi is the vertical boundary of the source distribution as shown in Fig. A-2.

The geometry model used in this calculation is shown in Fig. A-3, where the source distribution, divertor slots, and the different coil positions are based on the plasma physics analysis. A schematic of the geometry at the midplane is shown in Fig. A-4. The material zone thicknesses are kept almost constant in the poloidal direction.

Table A-1 shows the tritium production rates per D-T neutron in each zone. The total breeding ratio is 1.25. The breeding ratio from the R-Z calculation is thus greater than the breeding ratio from the x-y calculation by about 16%. In fact this increase in the breeding ratio is not completely due to the correction from the toroidal effect. Careful comparison with the tritium production rates per zone from Table V-5 shows that the toroidal effect increases the breeding by about 9%. The remaining 7% increase is due to a change in the composition of the shielding and to a change in the thickness of the last zone of the outer blanket. The last zone of the outer blanket (zone no. 10 of Fig. A-4) has been increased in thickness from 4 cm to 10 cm, as required by mechanical consideration of the lithium headers.

Also, the first zone of the outer shield has been changed from B_4C and stainless steel to carbon. This change has the effect of reflecting more low energy neutrons to increase the ^6Li $(n,\alpha)T$ reaction rate.

In chapter V, we did report one dimensional toroidal geometry calculations using R as the coordinate. These one dimensional calculations show a higher value for the breeding ratio (by about 15%) compared to the R-Z calculation. This can be seen by comparing the tritium production rate from Table V-3 for zone 16 with that from Table A-1 for zone 6.

Summary results of the heat deposition per zone are given in Tables A-2, A-3, and A-4. The R-Z calculational result is that 17.57 MeV per D-T neutron is deposited in the blanket and shield. It can be noted from Table A-4 that the heat deposition in the outer blanket is 4 times that in the inner (including the ISSEC). This distribution for the heat deposition is approximately the same distribution that results from a one dimensional, R-calculation.

The variation of the wall loading, heat deposition, displacements per atom, alpha particle production rate, and hydrogen and tritium production rates as one moves around the plasma in the poloidal direction are given in Figs. A-5 to A-22 for various zones in the blanket. Fig. A-5 shows the variation of the wall loading in the first wall in the poloidal direction. As a result of the shifted neutron source and the shape of the wall around the plasma, the wall loading has a maximum at the outer wall of 4.5 MW/m^2 at 100% plant factor.

The heat deposition in the first wall of the outer blanket and the first wall behind the ISSEC is given in Fig. A-6. Here the heat deposition shows a behavior similar to the first wall loading, but the maximum to minimum value is not as extreme. In the interpretation of these results, we should keep in mind the behavior of the Kerma factors as a function of energy and the effect of the ISSEC on the neutron spectrum. The displacements per atom (dpa) are 3.7 and 16.4 dpa/year in the inner and outer wall at the midplane, respectively, as shown in Fig. A-7. This shows that the effect of the ISSEC protection is to reduce the dpa rate by a factor of 4 to 5 and to reduce helium and hydrogen production rates by factors of 8 and 12, respectively. (See Figs. A-8 and A-9.)

The heat deposition rate in the graphite ISSEC is given in Fig. A-10 as a function of the poloidal angle and at a depth of 4 cm in the ISSEC. The heat deposition rate has a maximum of 9.6 W/cm^3 at the midplane. The displacements per atom and the helium production at the same depth in the ISSEC are shown in Figs. A-11 and A-12.

The tritium production rates at three different depths in the outer blanket and in the lithium zone behind the reflector are shown in Fig. A-14. The heat deposition rates in the outer blanket and the reflector are shown in Figs. A-15 and A-16. It is clear that the heat deposition behaves in a manner quite similar to that of the wall loading. The heat deposition rates in the cold shield are shown in Figs. A-17 and A-18, where the heat deposition is a function of position relative to the neutron source.

The effects of the divertor slots on the toroidal field magnets are shown in Figs. A-19 to A-22. These results can be explained by examining the flux distributions shown in Figs. A-22 and A-25. The effects of neutron streaming up the divertor slots is clear. Based on these results, an additional shield of about 20 cm thickness must be used in front of the slots to protect the toroidal field magnets.

References

1. F. R. Mynatt, et al., "The DOT-III Two Dimensional Discrete Ordinates Transport Code", Oak Ridge National Laboratory Report ORNL-TM-4280 (Sept. 1973).
2. K. D. Lathrop, F. W. Brinkley, "TWOTRAN-II: An Interfaced, Exportable Version of the Two Tran Code for Two - Dimensional Transport", Los Alamos Scientific Laboratory Report, LA-4848-MS (July 1973).
3. Wm. H. Reed, et al., "TRIPLET: A Two Dimensional, Multigroup Triangular Mesh, Planar Geometry Explicit Transport Code, Los Alamos Scientific Laboratory Report LA-5428-MS (Oct. 1973).

Table 1

Tritium Production Rates* by Zone

From R-Z Toroidal Calculation

Zone	$^{6}Li(n,\alpha)T$	$^{7}Li(n,n'\alpha)T$	Total/Zone
6	0.6675	0.4021	1.0696
10	0.0770	0.0334	0.1104
7	0.0683	0.0032	0.0715
Total	0.8128	0.4387	1.2515

*Reactions per D-T neutron

Table 2

Neutron and Gamma Heating Rates* by

Zone From R-Z Toroidal Calculation

in UWMAK-III Blanket

Zone	Neutron Heating	Gamma Heating	Total Heating/Zone
2	1.3481	0.6775	2.0256
3	0.0697	1.5886	1.6583
4	0.0841	1.0409	1.1250
5	0.0117	0.1781	0.1898
6	8.0960	1.7348	9.8308
10	0.3711	0.0809	0.4520
7	0.7874	0.1815	0.9689
8	0.3136	0.4979	0.8115
9	0.0300	0.0384	0.0684
36	0.0166	0.0424	0.0590
	11.1283	6.0610	17.1893

*All the heating rates are in MeV per D-T neutron

Table 3

Total Heating Rates by Zone

From R-Z Toroidal Calculation

in UWMAK-III Shielding

Zone	Total Heating/Zone
11	0.006786
15	0.190242
17	0.59860
35	0.122627
12	0.000011
16	0.000020
Total	0.380266

*All the heating rates are in MeV per D-T neutron

Table 4

Power Distribution for UWMAK-III

Zone	Percent	Power* (MW)
ISSEC	9.6	480
INNER blanket (hot shield)	7.9	395
Outer blanket	57.9	2895
Divertor	6.1	305
Divertor plates (α particles)	16.7	835
Inner shield (cold shield)	0.9	45
Outer shield	0.6	15
Divertor shield	0.3	30

* Total thermal output 5000 MW during the burn.

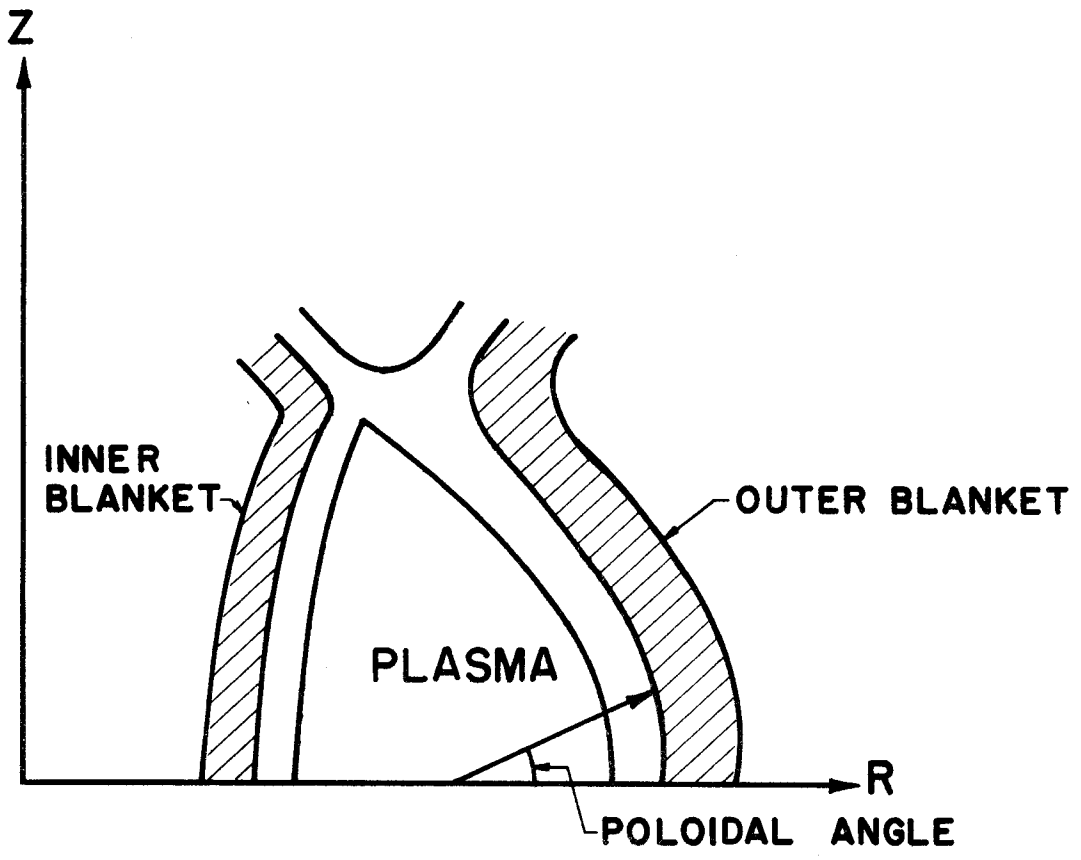

Figure 1 R-Z COORDINATE SYSTEM USED IN UWMAK-III CALCULATIONS

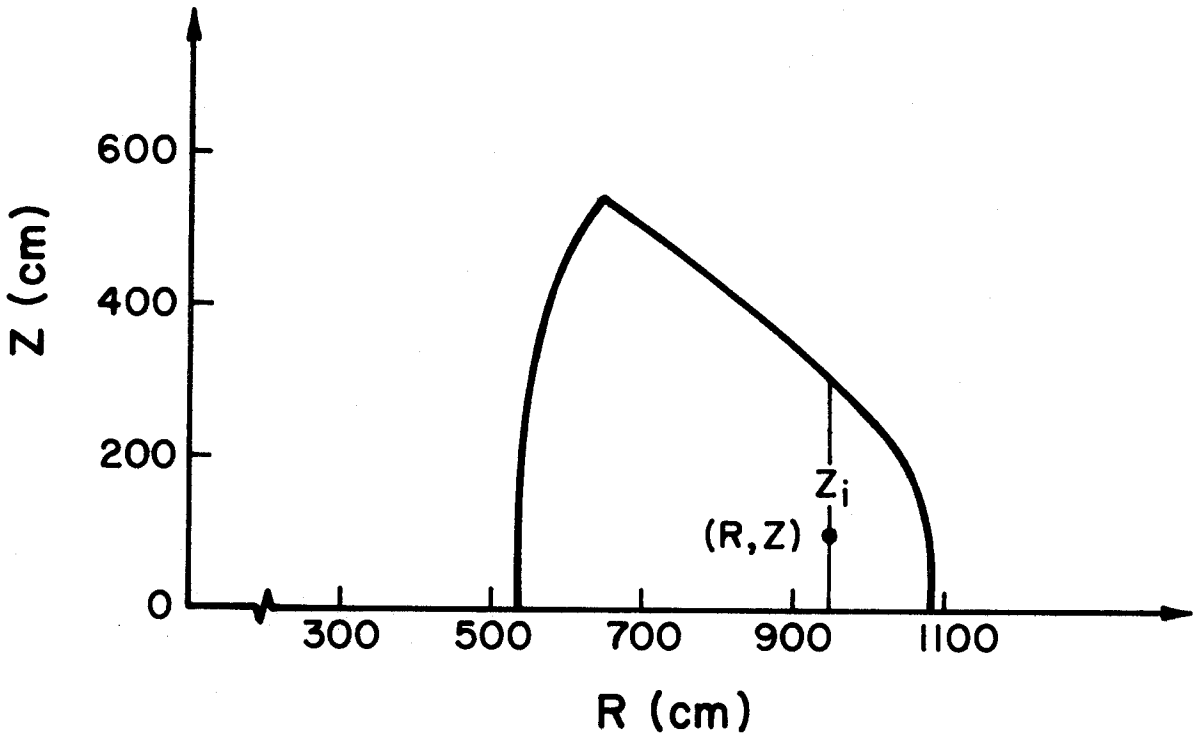

Figure 2 Neutron Source Boundary

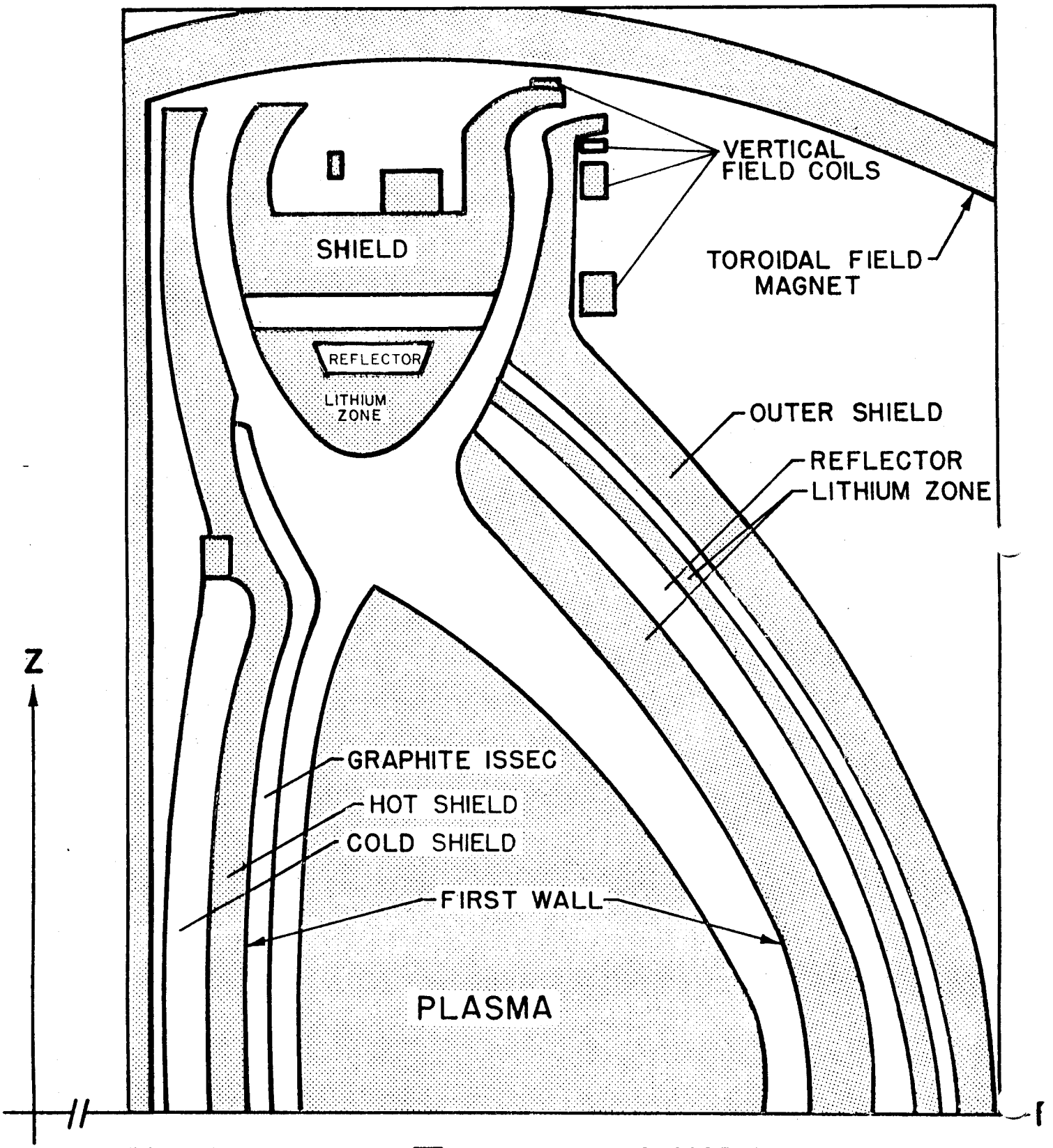

Fig. 3 UWMAK - III GEOMETRIC MODEL USED FOR THE NEUTRONICS CALCULATION

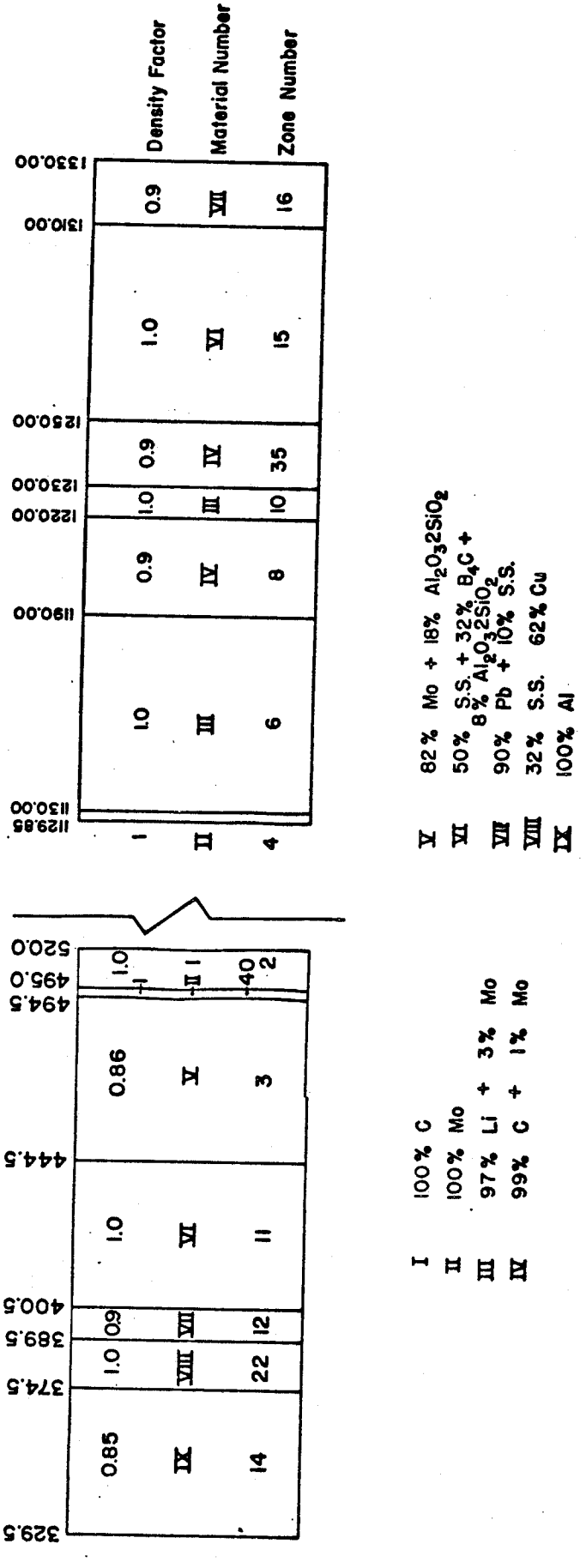

Figure 4 A Schematic of UWMAK - III Blanket and Shield For RZ Toroidal Calculation at the Midplane

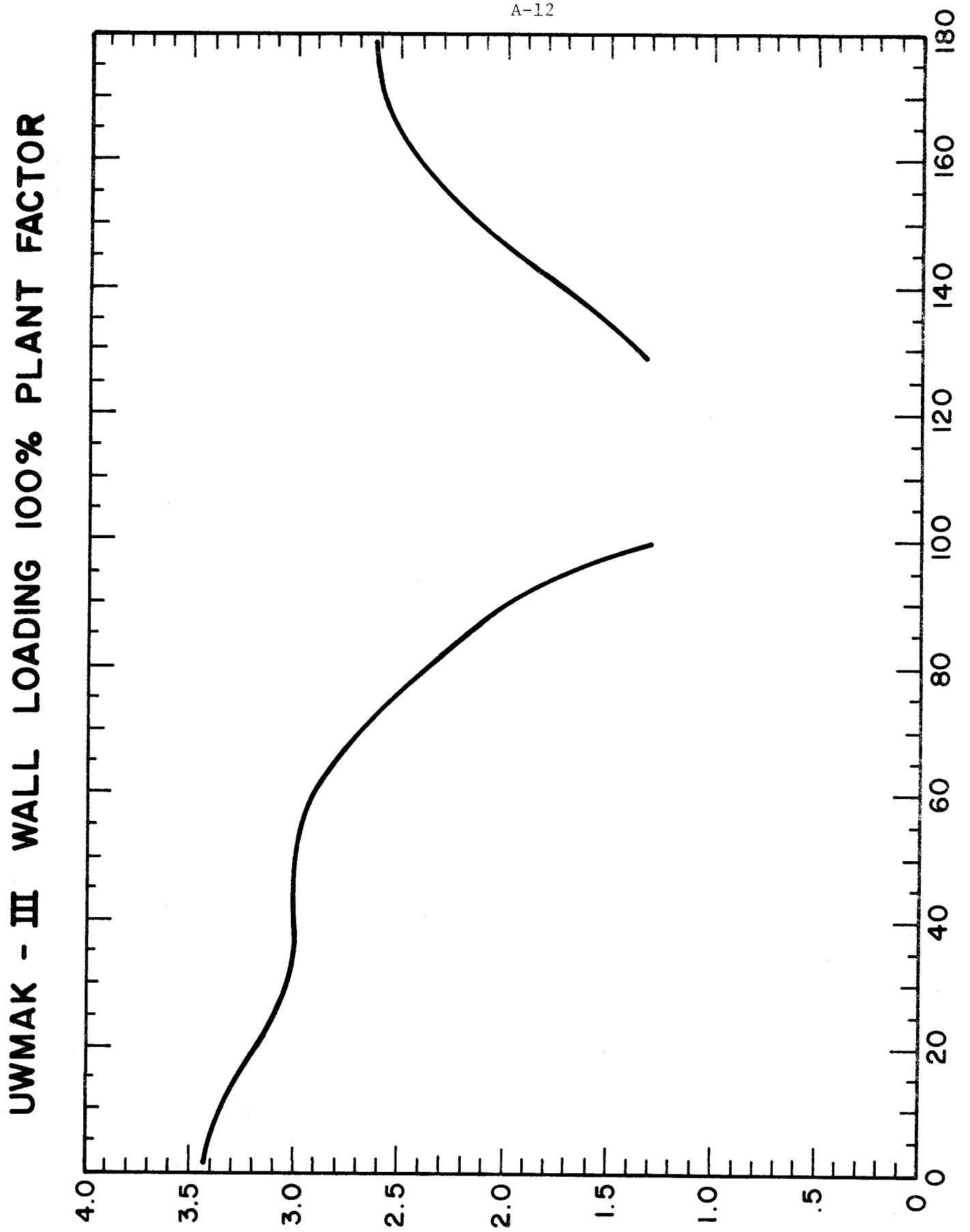
UWMAK - III WALL LOADING 100% PLANT FACTOR
NEUTRON WALL LOADING (MW/M2)
4.0
3.5
3.0
2.5
2.0
1.5
1.0
.5
0
0
20
40
60
80
100
120
140
160
180
POLOIDAL ANGLE (DEGREE)

Figure 5

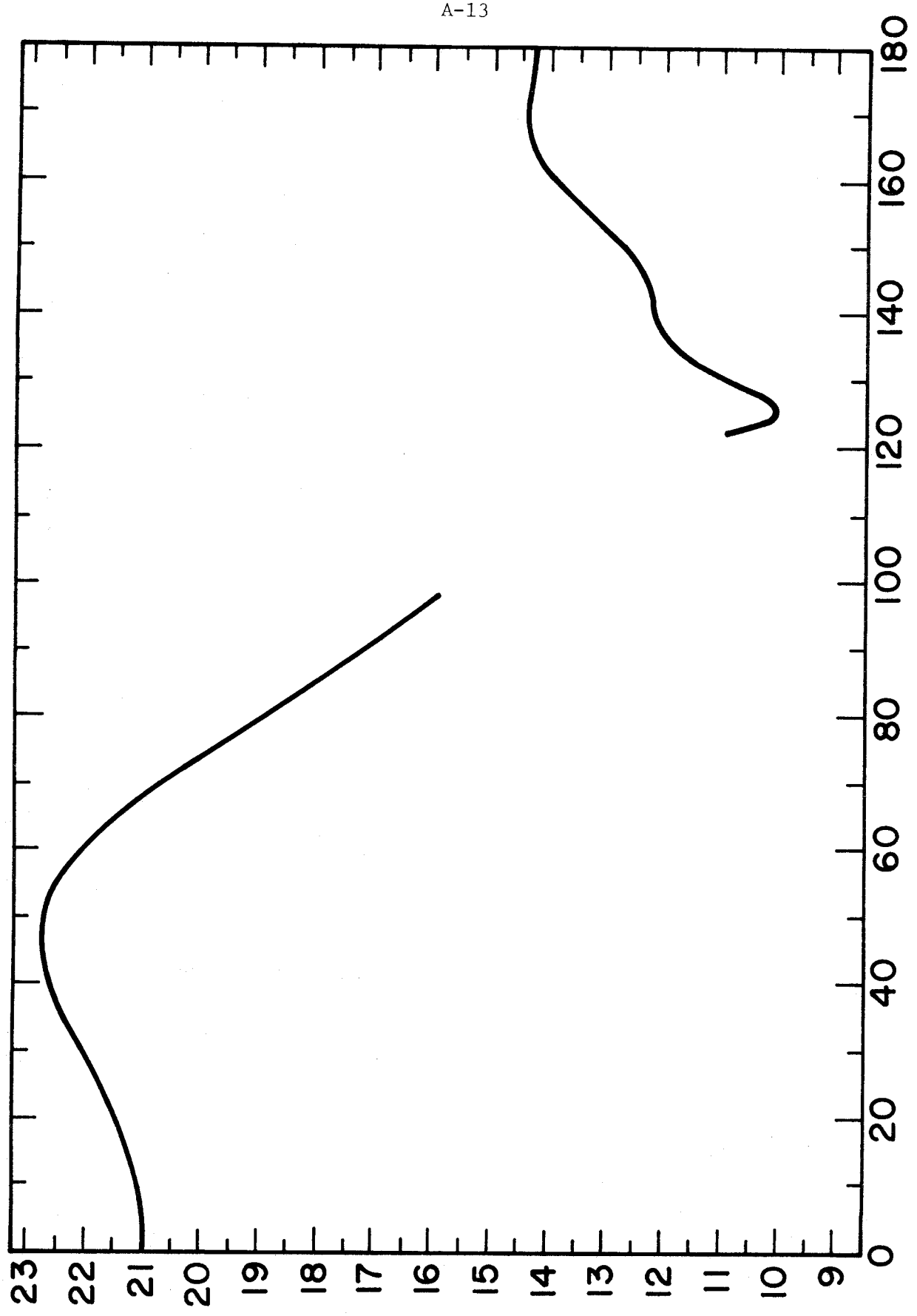
HEAT DEPOSITION RATE IN THE FIRST WALL
HEAT DEPOSITION RATE (W/CM³)
POLOIDAL ANGLE (DEGREE)
23
22
21
20
19
18
17
16
15
14
13
12
11
10
9
0
20
40
60
80
100
120
140
160
180

Figure 6

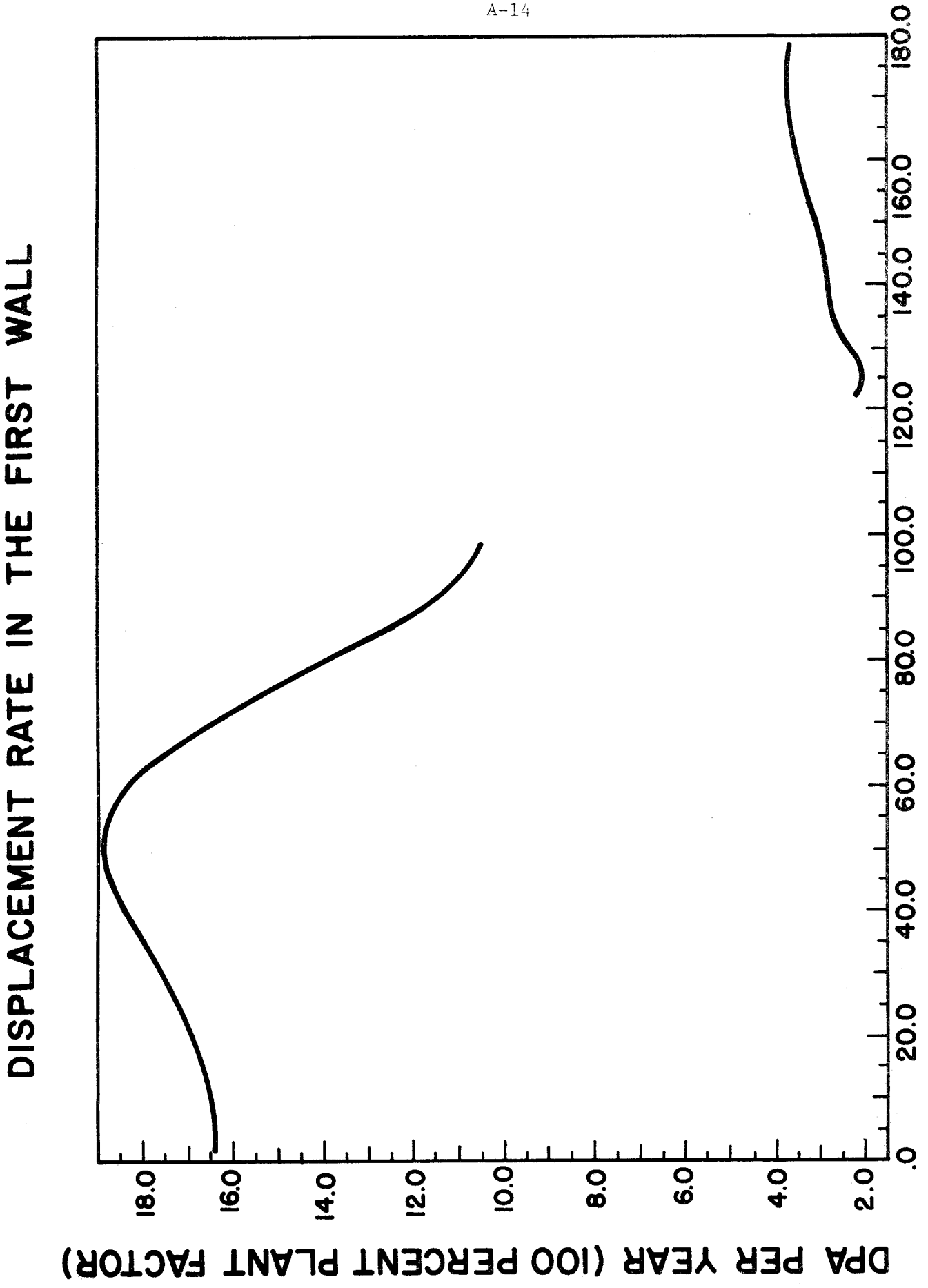
DISPLACEMENT RATE IN THE FIRST WALL
DPA PER YEAR (100 PERCENT PLANT FACTOR)
18.0
16.0
14.0
12.0
10.0
8.0
6.0
4.0
2.0
.0
20.0
40.0
60.0
80.0
100.0
120.0
140.0
160.0
180.0
POLOIDAL ANGLE (DEGREE)

Figure 7

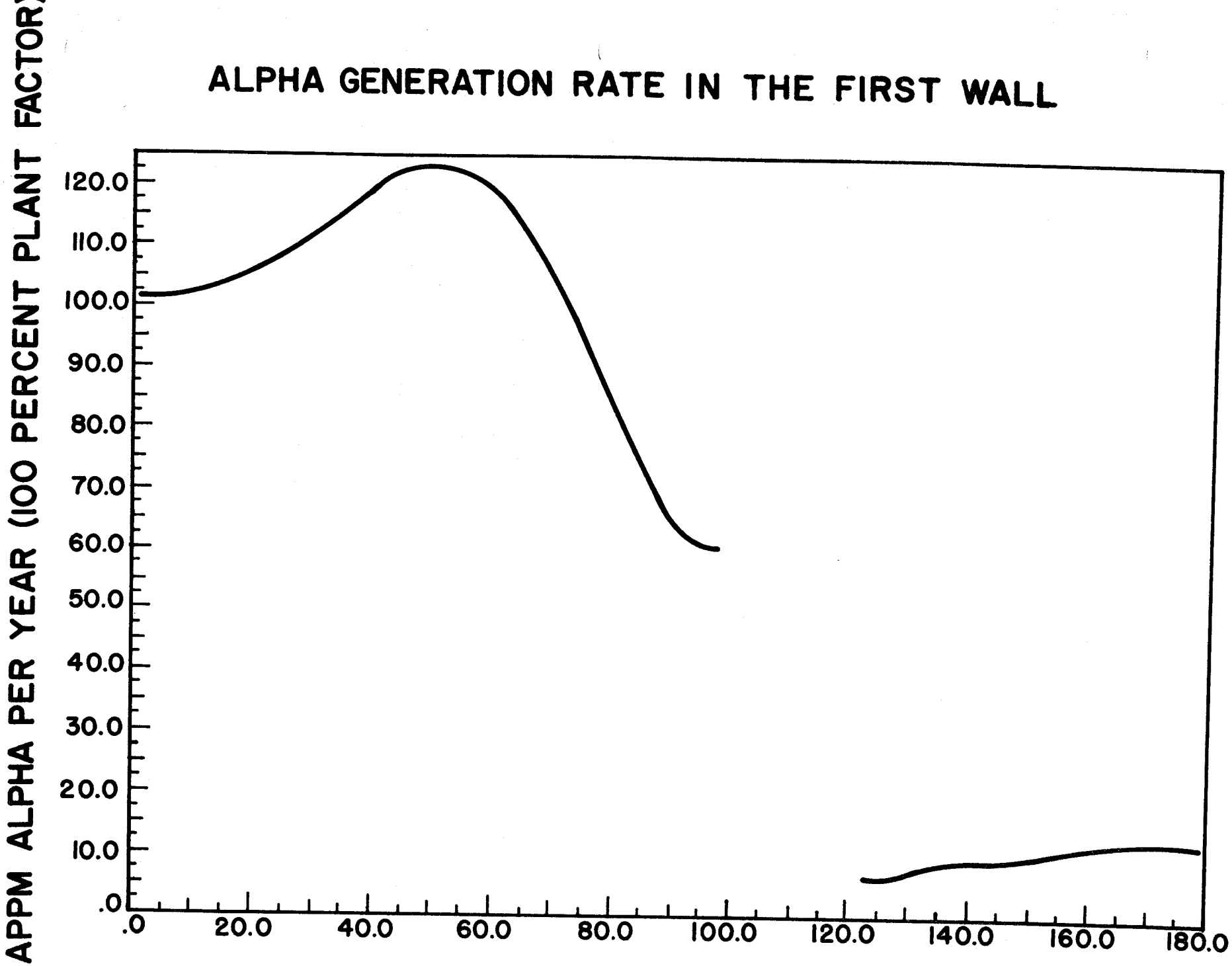
ALPHA GENERATION RATE IN THE FIRST WALL
APPM ALPHA PER YEAR (100 PERCENT PLANT FACTOR)
120.0
110.0
100.0
90.0
80.0
70.0
60.0
50.0
40.0
30.0
20.0
10.0
.0
.0
20.0
40.0
60.0
80.0
100.0
120.0
140.0
160.0
180.0
POLOIDAL ANGLE (DEGREE)

Figure 8

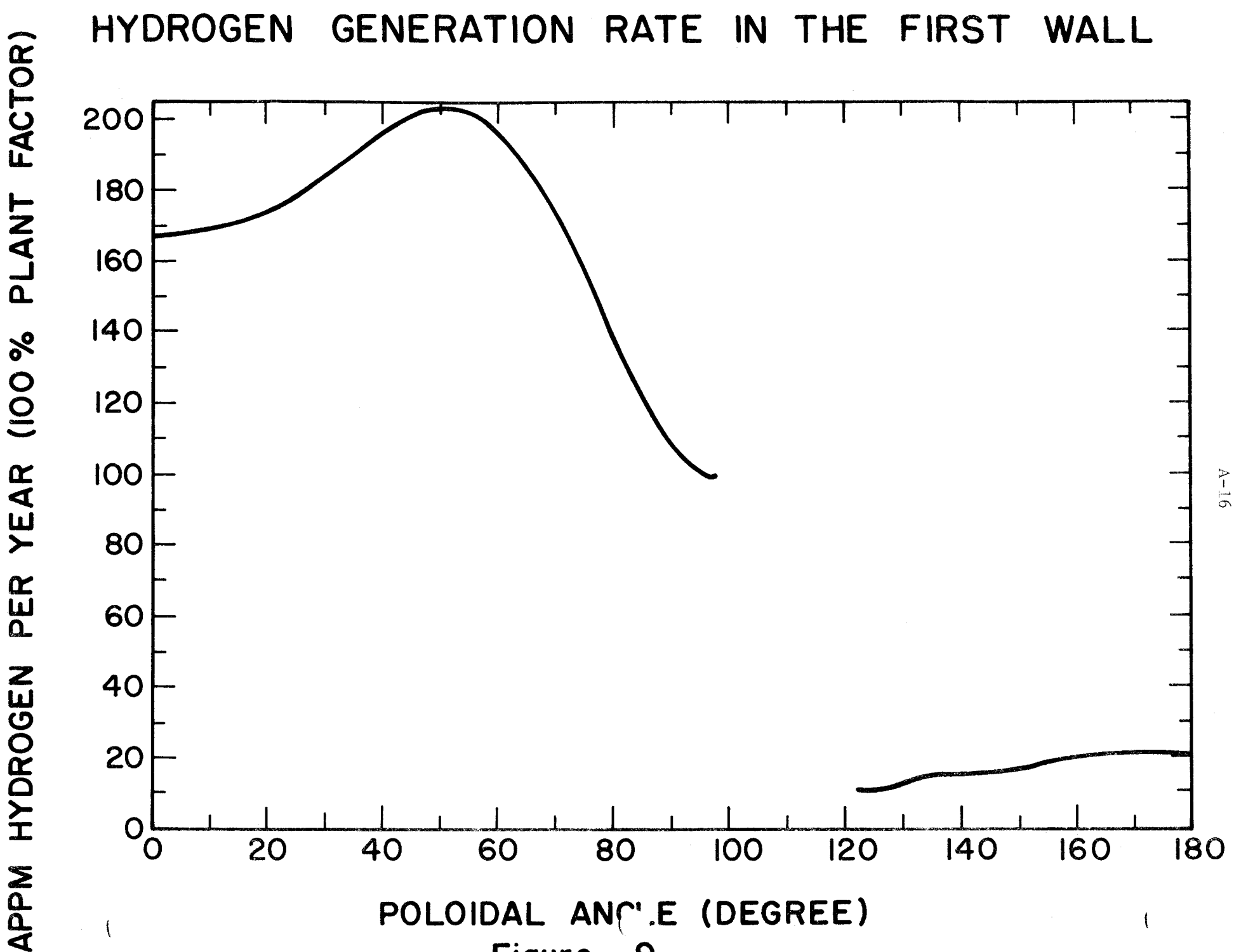
HYDROGEN GENERATION RATE IN THE FIRST WALL
APPM HYDROGEN PER YEAR (100% PLANT FACTOR)
0
20
40
60
80
100
120
140
160
180
200
0
20
40
60
80
100
120
140
160
180
POLOIDAL ANGLE (DEGREE)

Figure 9

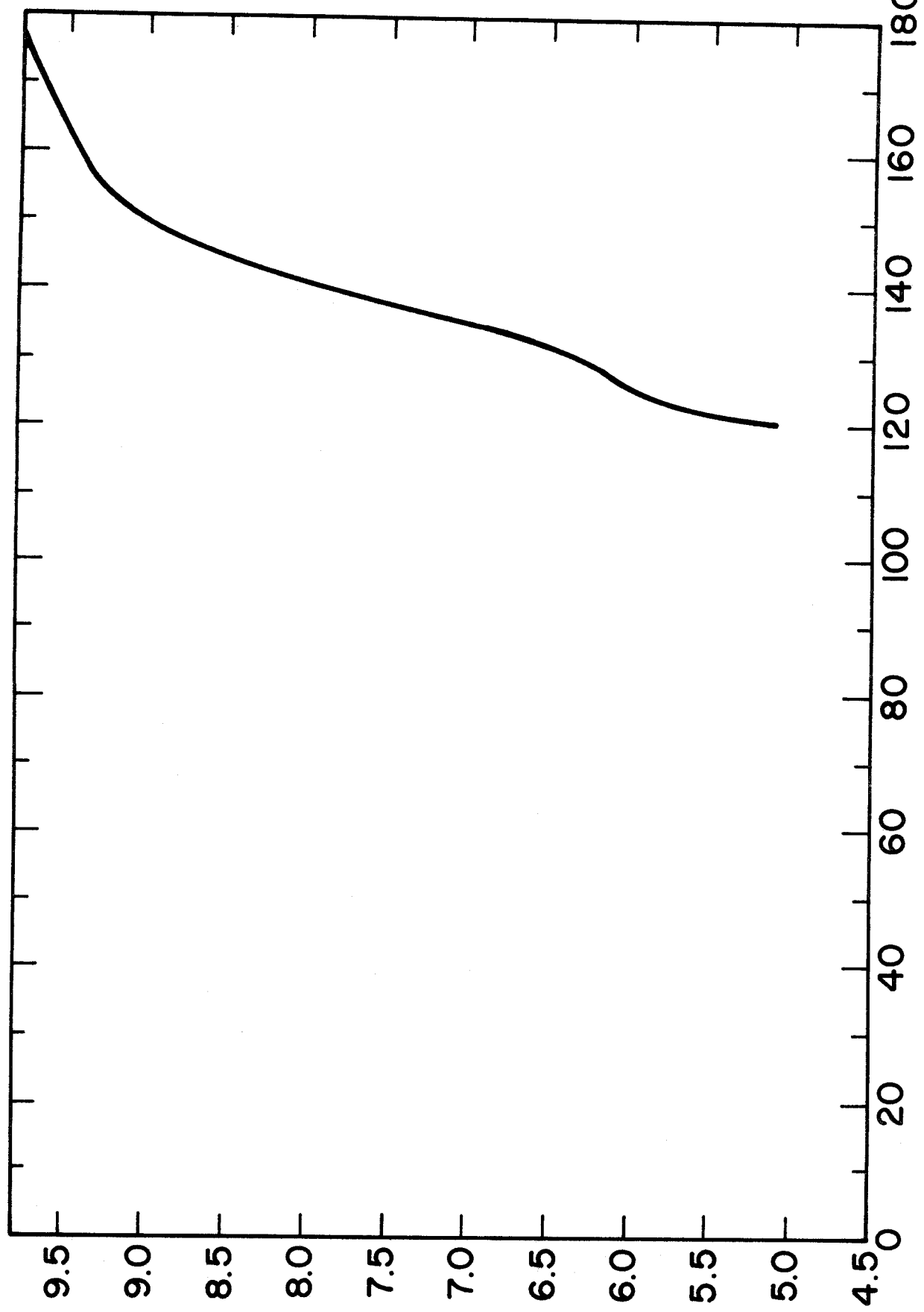
HEAT DEPOSITION RATE IN ISSEC
HEAT DEPOSITION RATE (W/CM³)
9.5
9.0
8.5
8.0
7.5
7.0
6.5
6.0
5.5
5.0
4.5
0
20
40
60
80
100
120
140
160
180
POLOIDAL ANGLE (DEGREE)

Figure 10

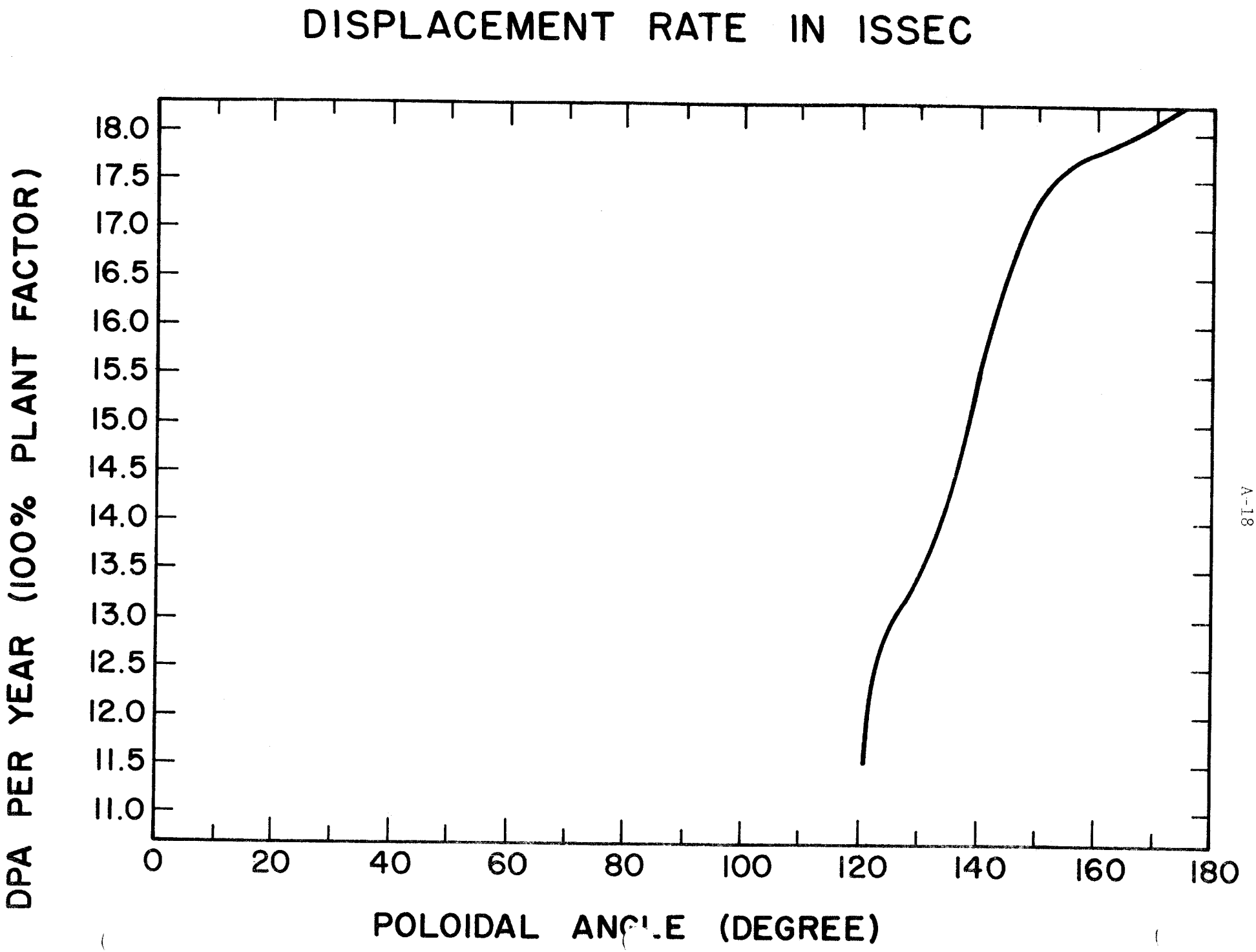
DISPLACEMENT RATE IN ISSEC
DPA PER YEAR (100% PLANT FACTOR)
18.0
17.5
17.0
16.5
16.0
15.5
15.0
14.5
14.0
13.5
13.0
12.5
12.0
11.5
11.0
0
20
40
60
80
100
120
140
160
180
POLOIDAL ANGLE (DEGREE)

Figure 11

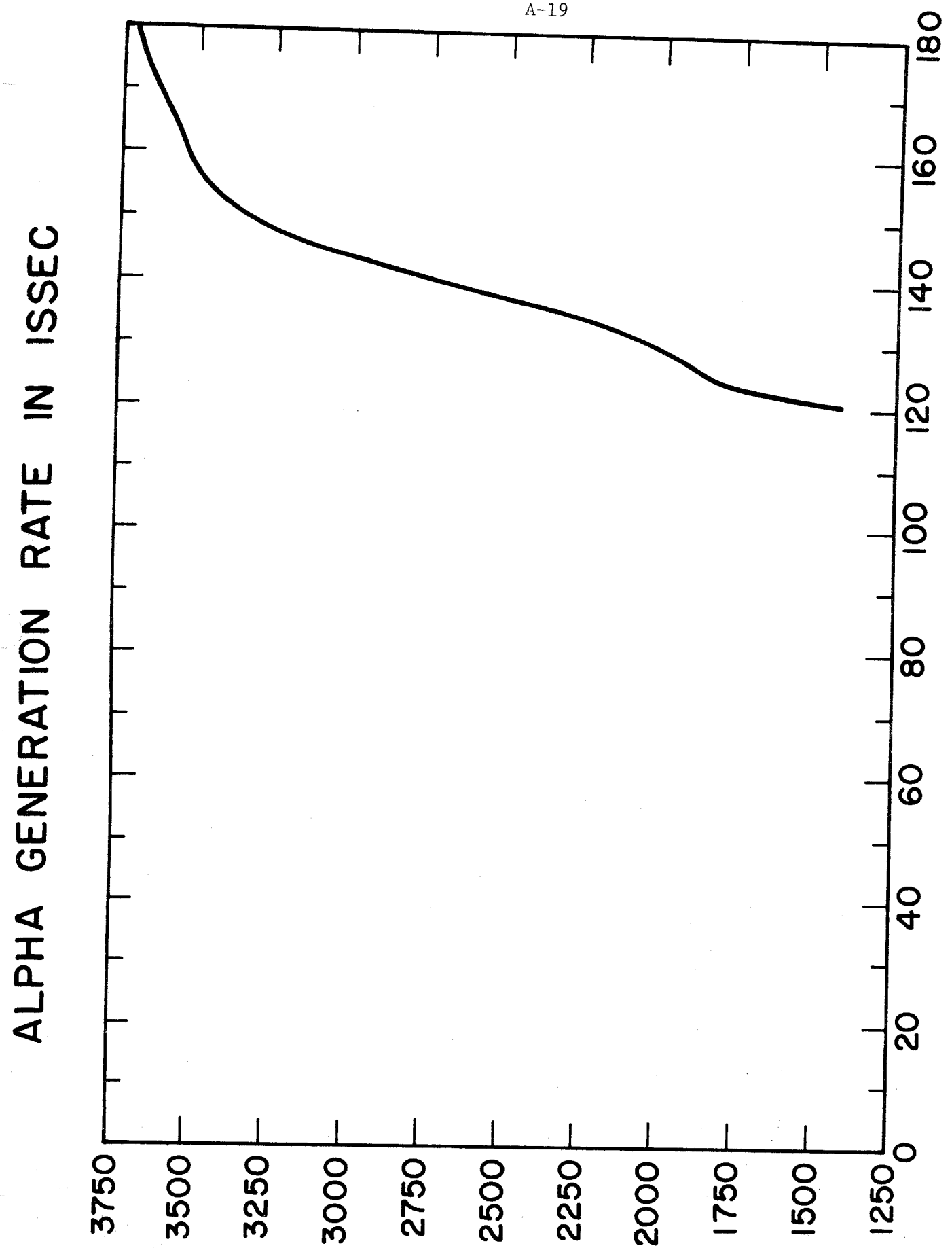
ALPHA GENERATION RATE IN ISSEC
APPM ALPHA PER YEAR (100% PLANT FACTOR)
3750
3500
3250
3000
2750
2500
2250
2000
1750
1500
1250
0
20
40
60
80
100
120
140
160
180
POLOIDAL ANGLE (DEGREE)

Figure 12

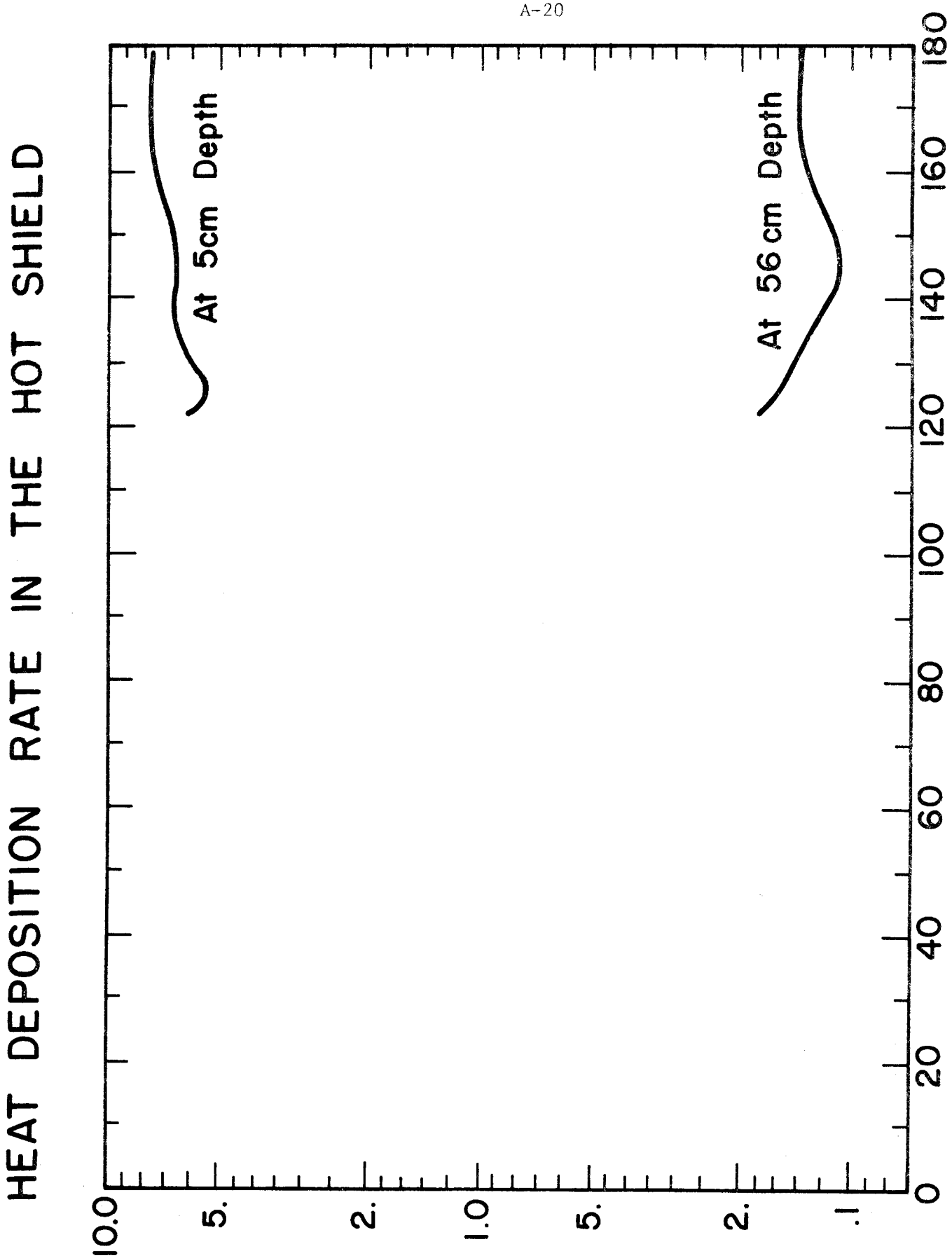
HEAT DEPOSITION RATE IN THE HOT SHIELD
At 5cm Depth
At 56 cm Depth
HEAT DEPOSITION RATE (W/CM³)
10.0
5.
2.
1.0
5.
2.
.1
0
20
40
60
80
100
120
140
160
180
POLOIDAL ANGLE (DEGREE)

Figure 13

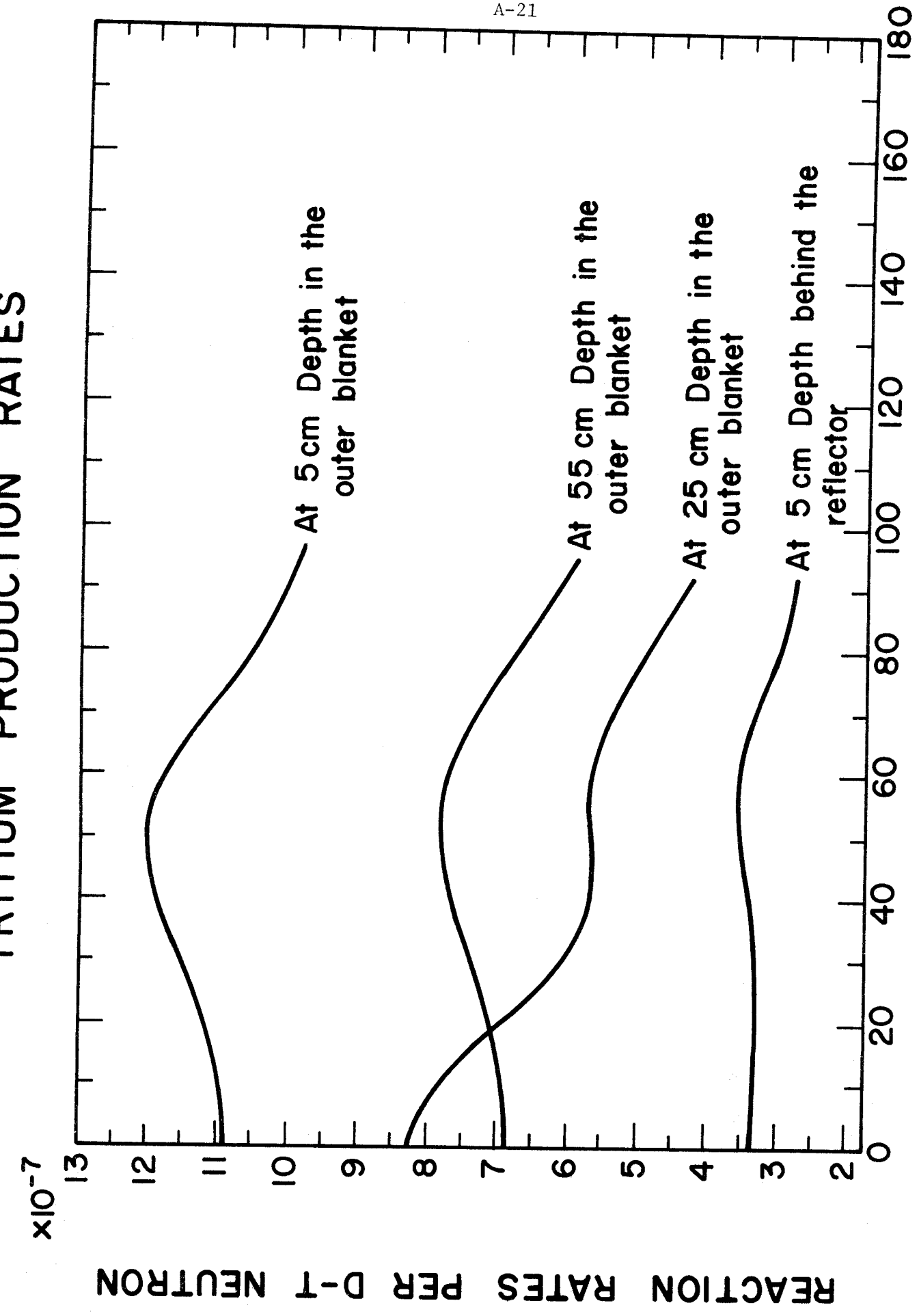
TRITIUM PRODUCTION RATES
REACTION RATES PER D-T NEUTRON
x10⁻⁷
13
12
11
10
9
8
7
6
5
4
3
2
0
20
40
60
80
100
120
140
160
180
POLOIDAL ANGLE (DEGREE)
At 5cm Depth in the outer blanket
At 55 cm Depth in the outer blanket
At 25 cm Depth in the outer blanket
At 5 cm Depth behind the reflector

Figure 14

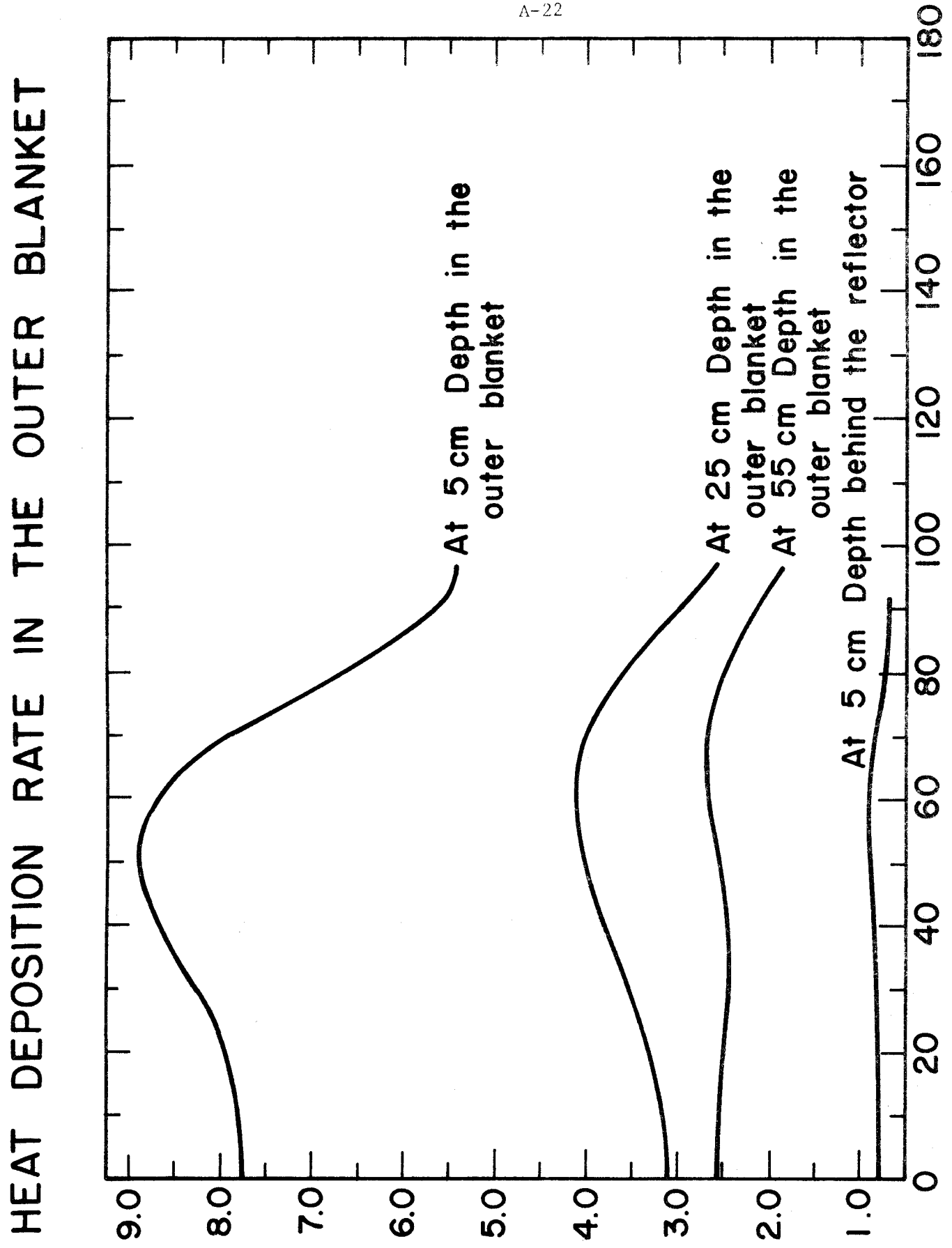
HEAT DEPOSITION RATE IN THE OUTER BLANKET
HEAT DEPOSITION RATE (W/CM³)
9.0
8.0
7.0
6.0
5.0
4.0
3.0
2.0
1.0
0
20
40
60
80
100
120
140
160
180
POLOIDAL ANGLE (DEGREE)
At 5 cm Depth in the outer blanket
At 25 cm Depth in the outer blanket
At 55 cm Depth in the outer blanket
At 5 cm Depth behind the reflector

Figure 15

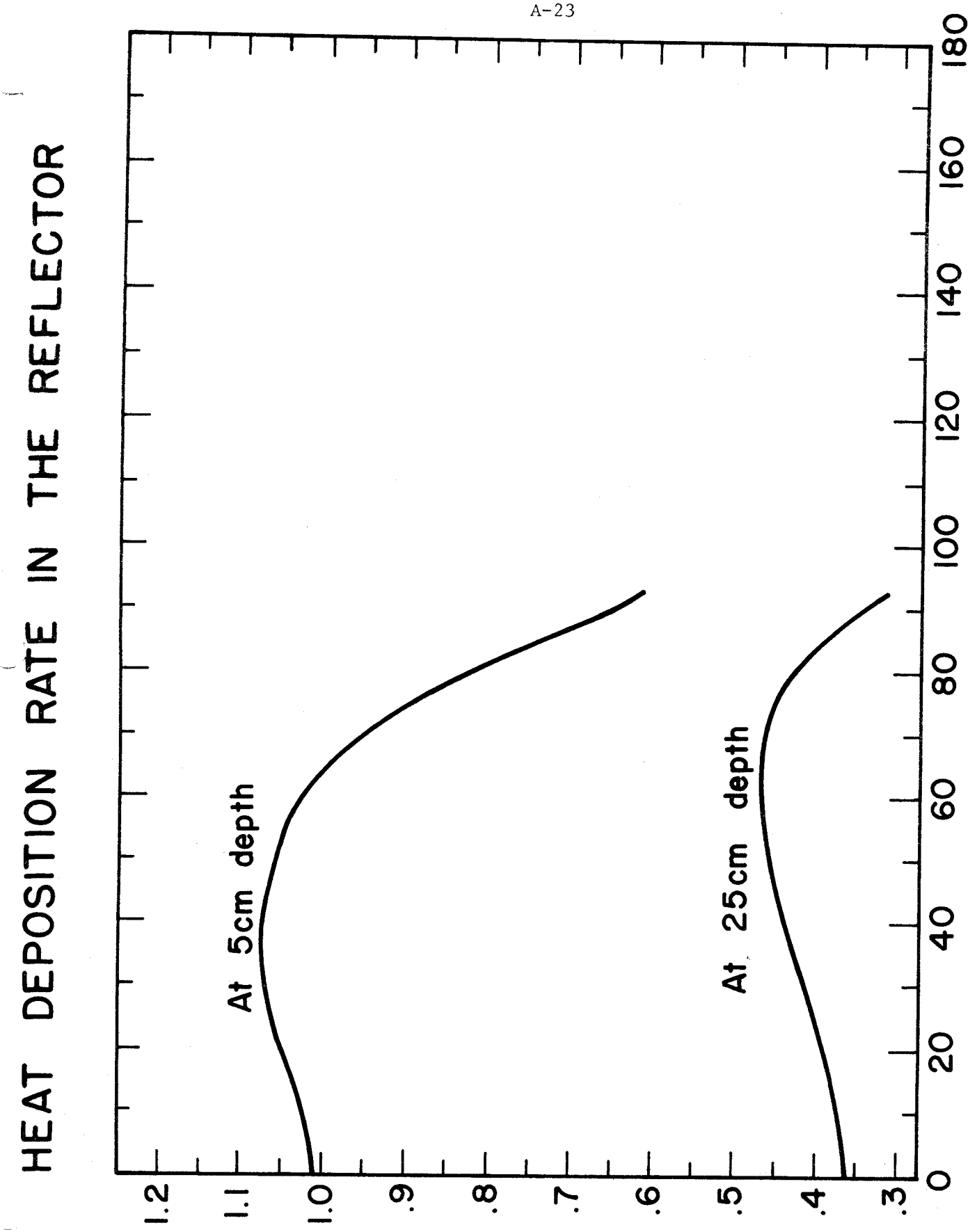
HEAT DEPOSITION RATE IN THE REFLECTOR
HEAT DEPOSITION RATE (W/CM³)
1.2
1.1
1.0
.9
.8
.7
.6
.5
.4
.3
0
20
40
60
80
100
120
140
160
180
POLOIDAL ANGLE (DEGREE)
At 5cm depth
At 25cm depth

Figure 16

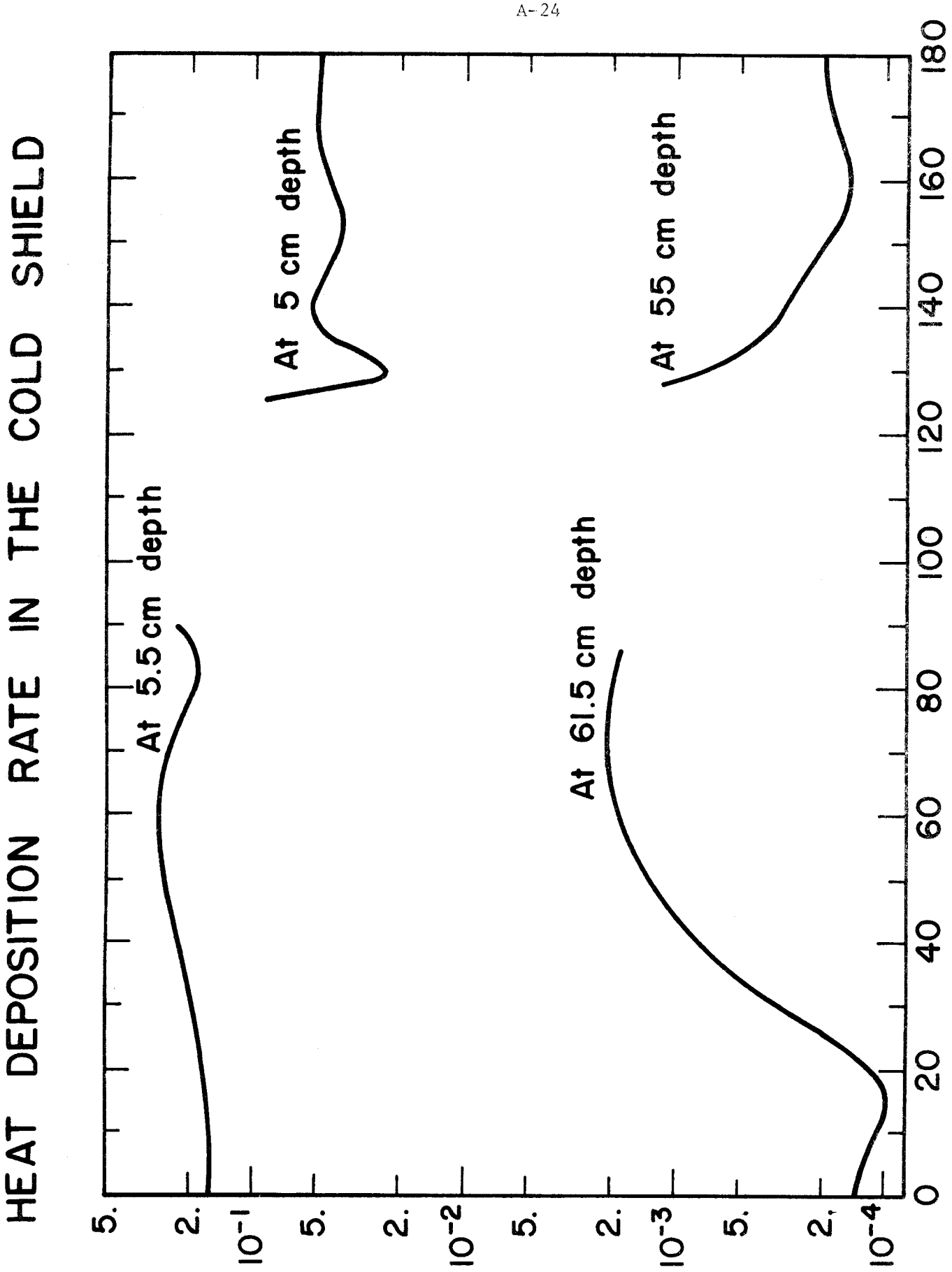
HEAT DEPOSITION RATE IN THE COLD SHIELD
At 5.5 cm depth
At 5 cm depth
At 61.5 cm depth
At 55 cm depth
HEAT DEPOSITION RATE (W/CM³)
POLOIDAL ANGLE (DEGREE)
5.
2.
10⁻¹
5.
2.
10⁻²
5.
2.
10⁻³
5.
2.
10⁻⁴
0
20
40
60
80
100
120
140
160
180

Figure 17

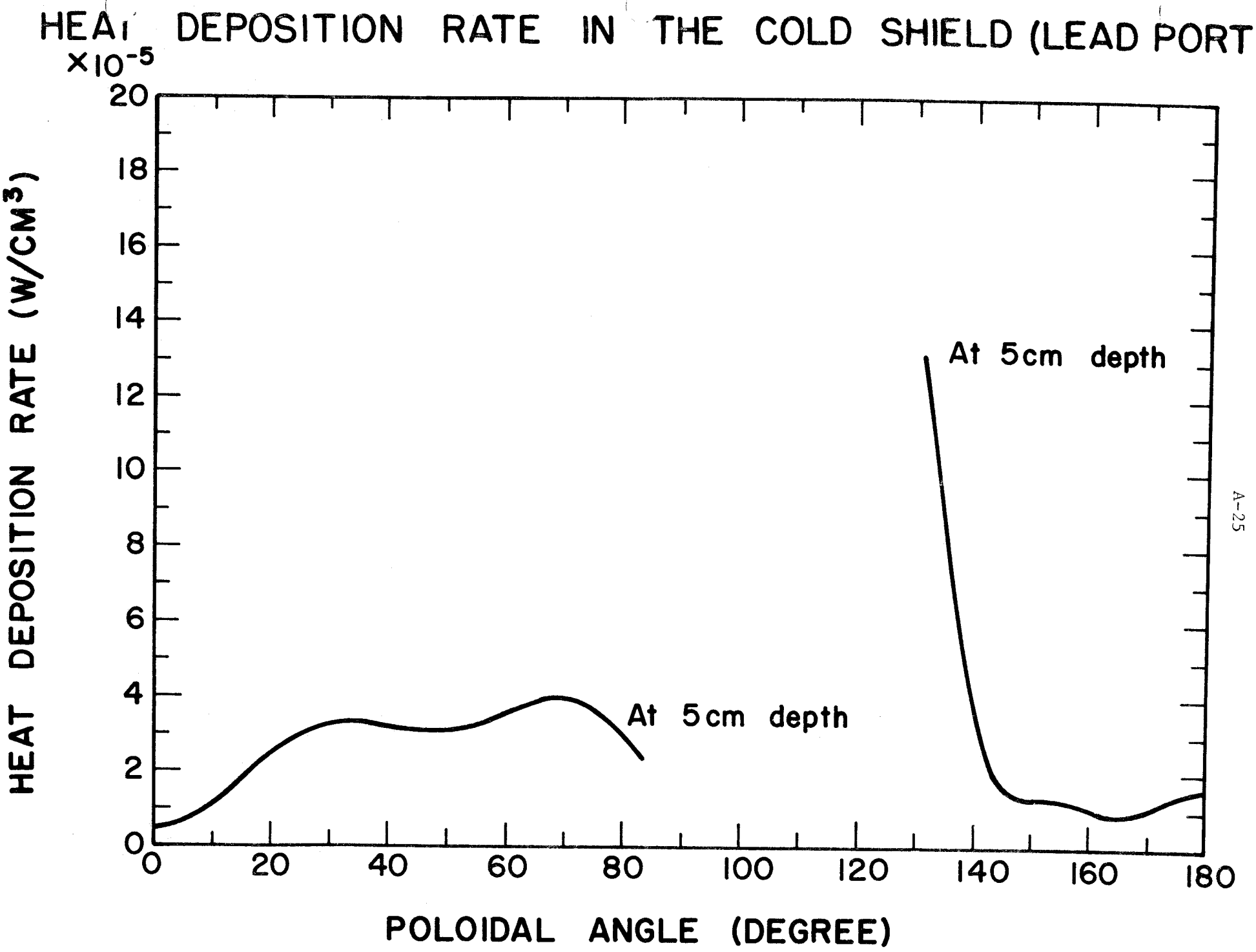
HEAT DEPOSITION RATE IN THE COLD SHIELD (LEAD PORTION
HEAT DEPOSITION RATE (W/CM³)
×10⁻⁵
20
18
16
14
12
10
8
6
4
2
0
0
20
40
60
80
100
120
140
160
180
At 5cm depth
At 5cm depth
POLOIDAL ANGLE (DEGREE)

Figure 18

HEAT DEPOSITION RATE IN THE TOROIDAL FIELD MAGNET

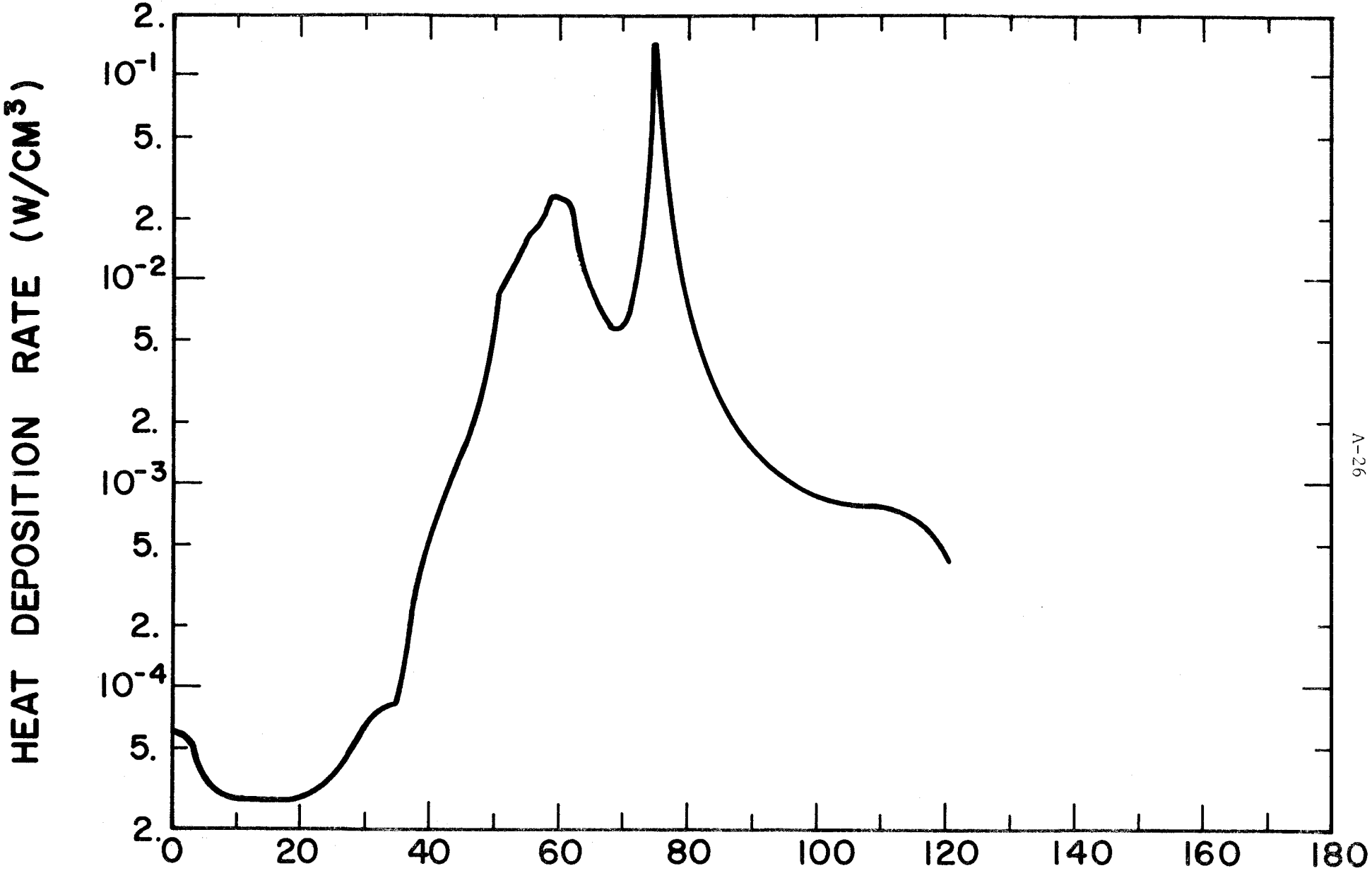

A-26

Figure 19

DISPLACEMENT RATE IN THE TOROIDAL FIELD MAGNET

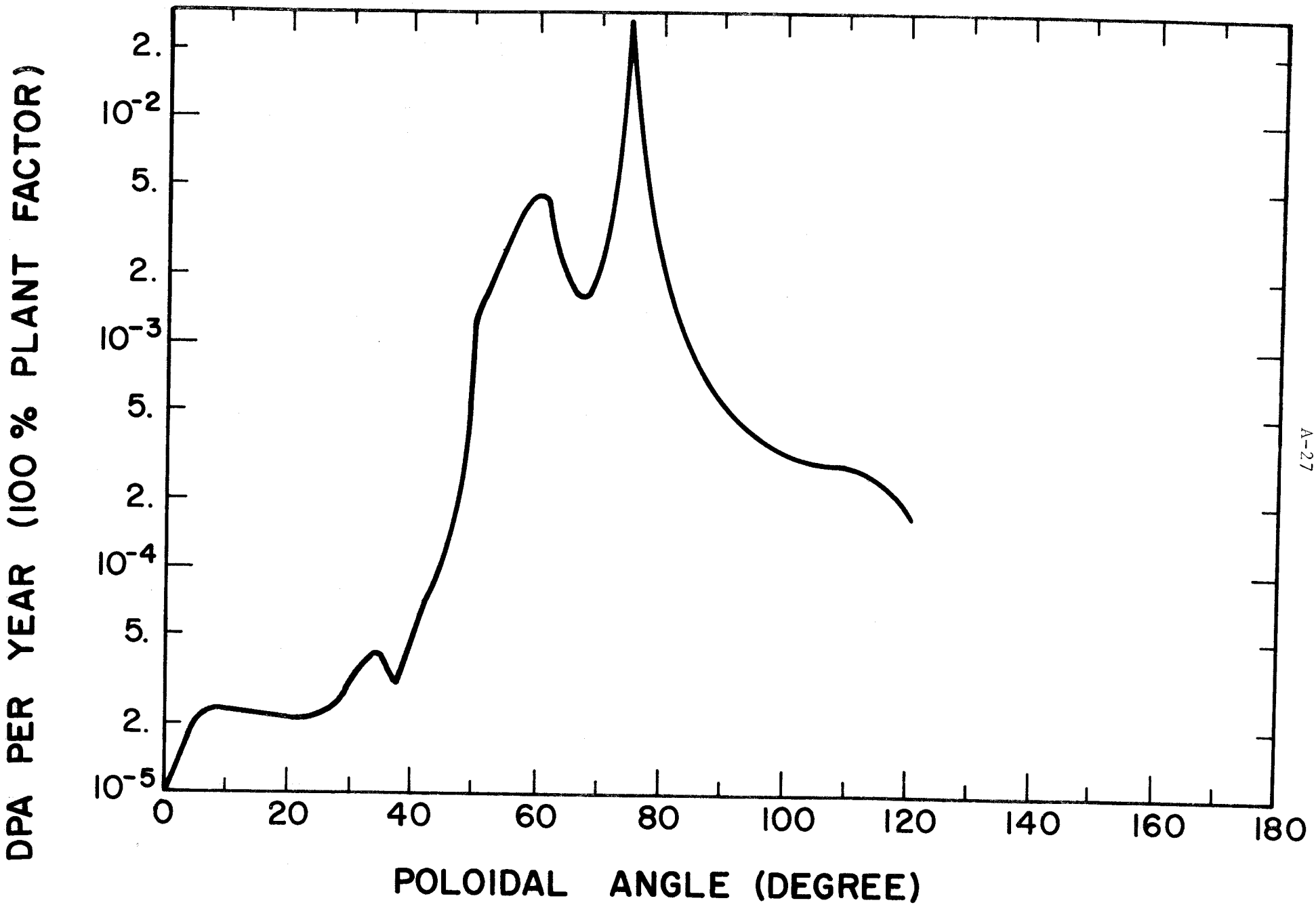

Figure 20

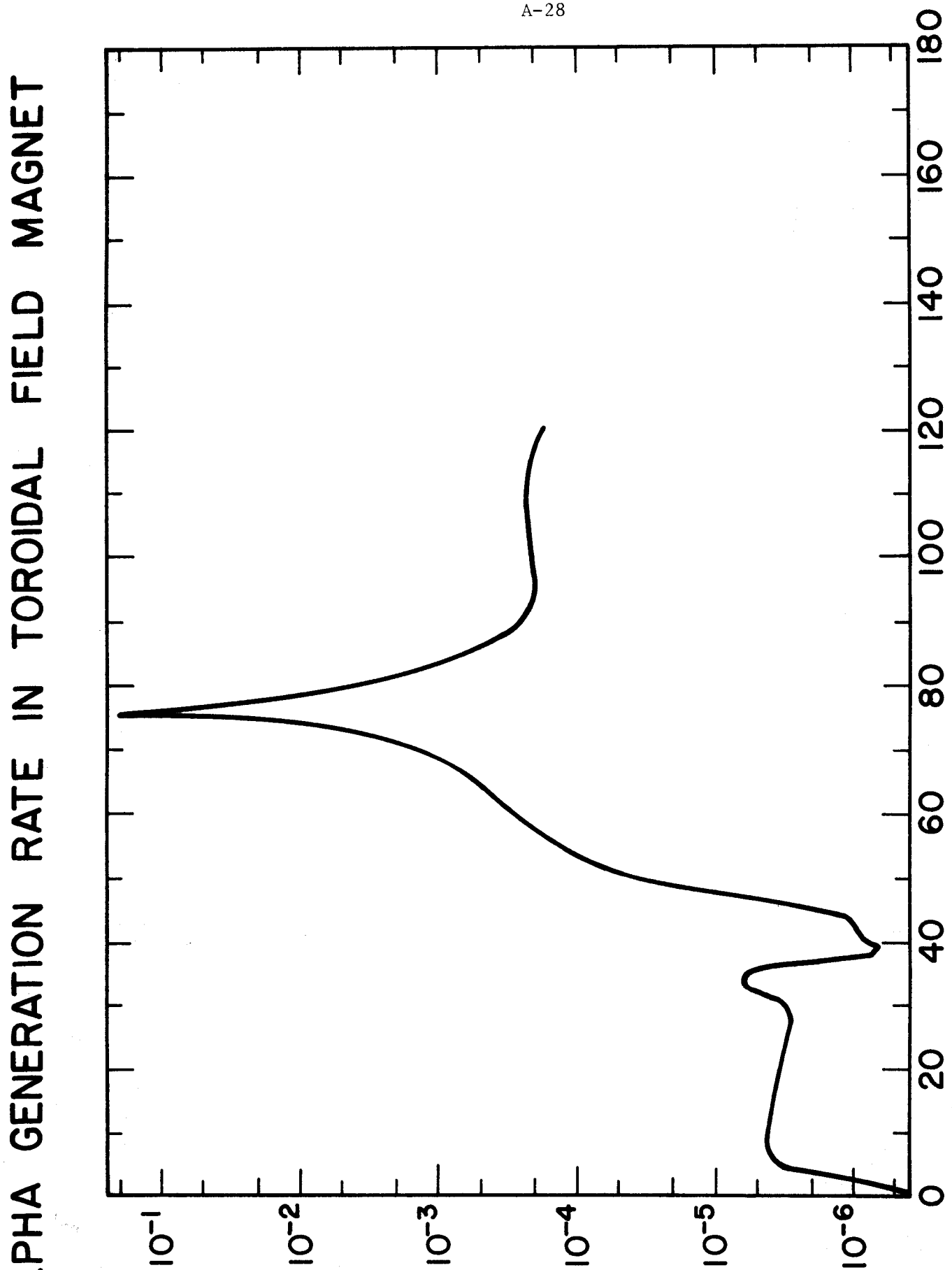
ALPHA GENERATION RATE IN TOROIDAL FIELD MAGNET
APPM ALPHA PER YEAR (100% PLANT FACTOR)
10^{-1}
10^{-2}
10^{-3}
10^{-4}
10^{-5}
10^{-6}
0
20
40
60
80
100
120
140
160
180
POLOIDAL ANGLE (DEGREE)

Figure 21

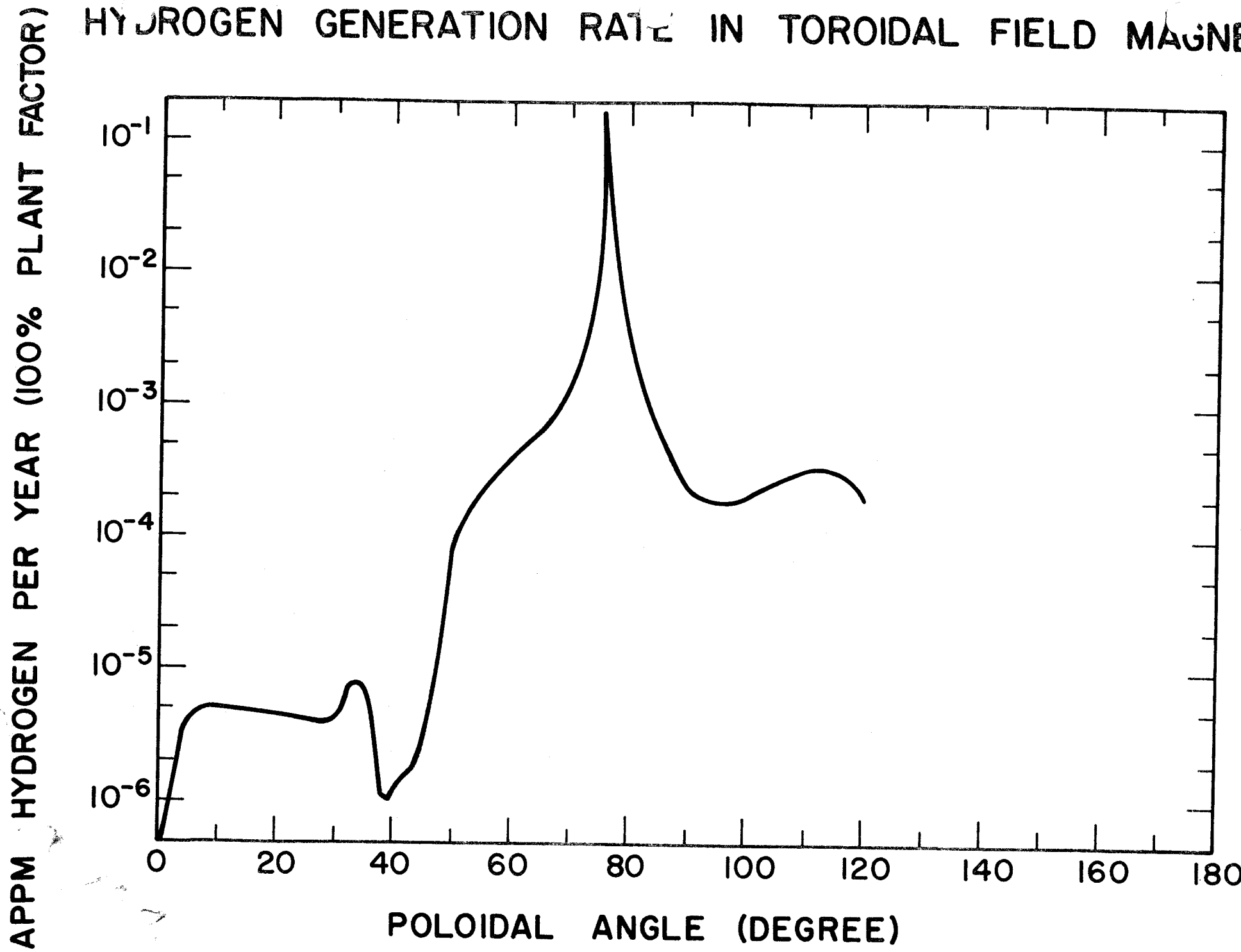
HYDROGEN GENERATION RATE IN TOROIDAL FIELD MAGNET
APPM HYDROGEN PER YEAR (100% PLANT FACTOR)
10^{-1}
10^{-2}
10^{-3}
10^{-4}
10^{-5}
10^{-6}
0
20
40
60
80
100
120
140
160
180
POLOIDAL ANGLE (DEGREE)

Figure 22

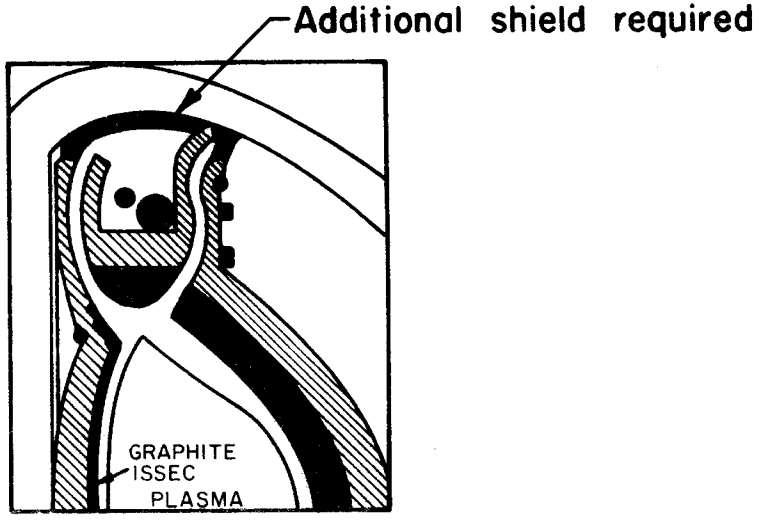

Fig. 23 Modification of the shielding for toroidal field magnet.

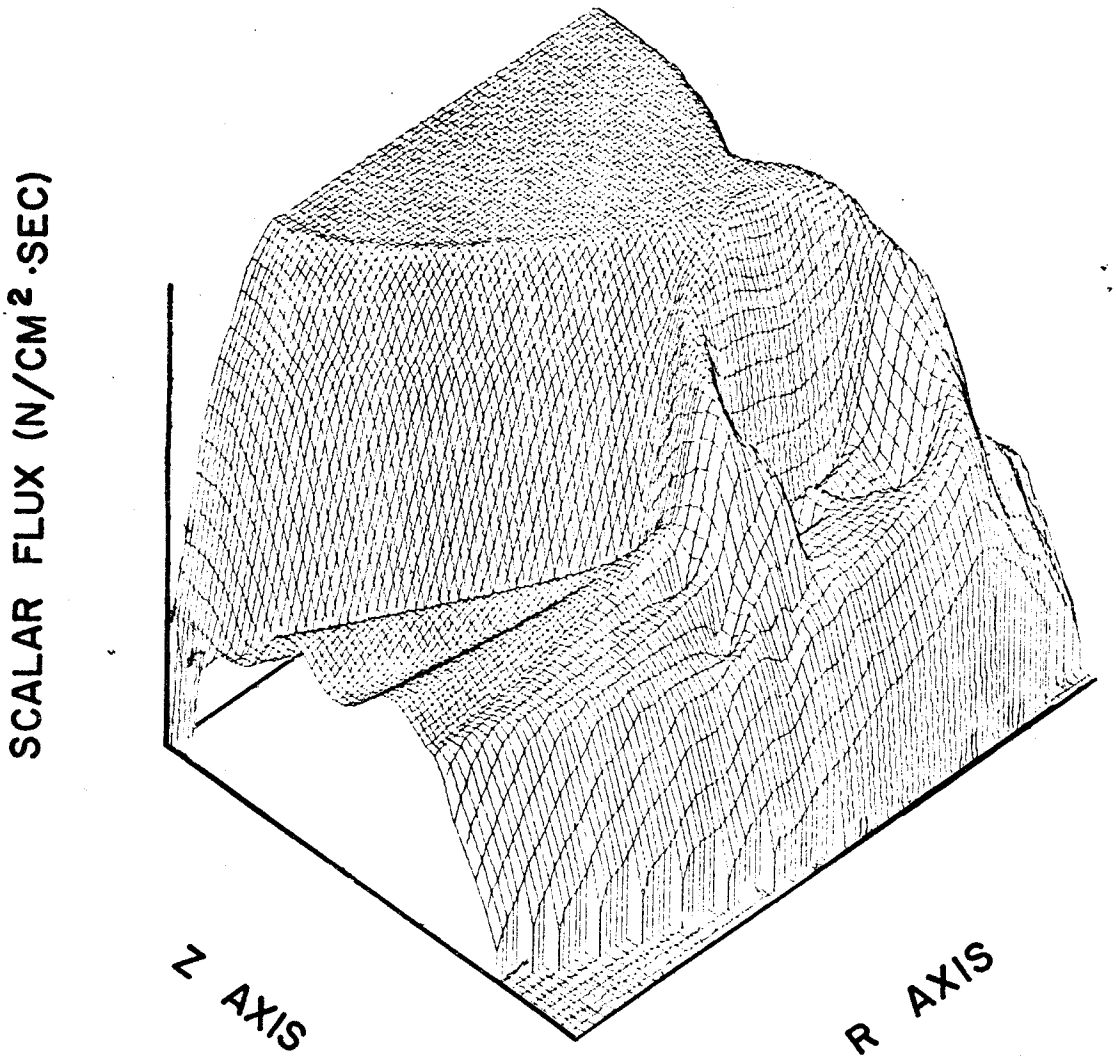

NEUTRON FLUX GROUP NO. 1

Figure 24

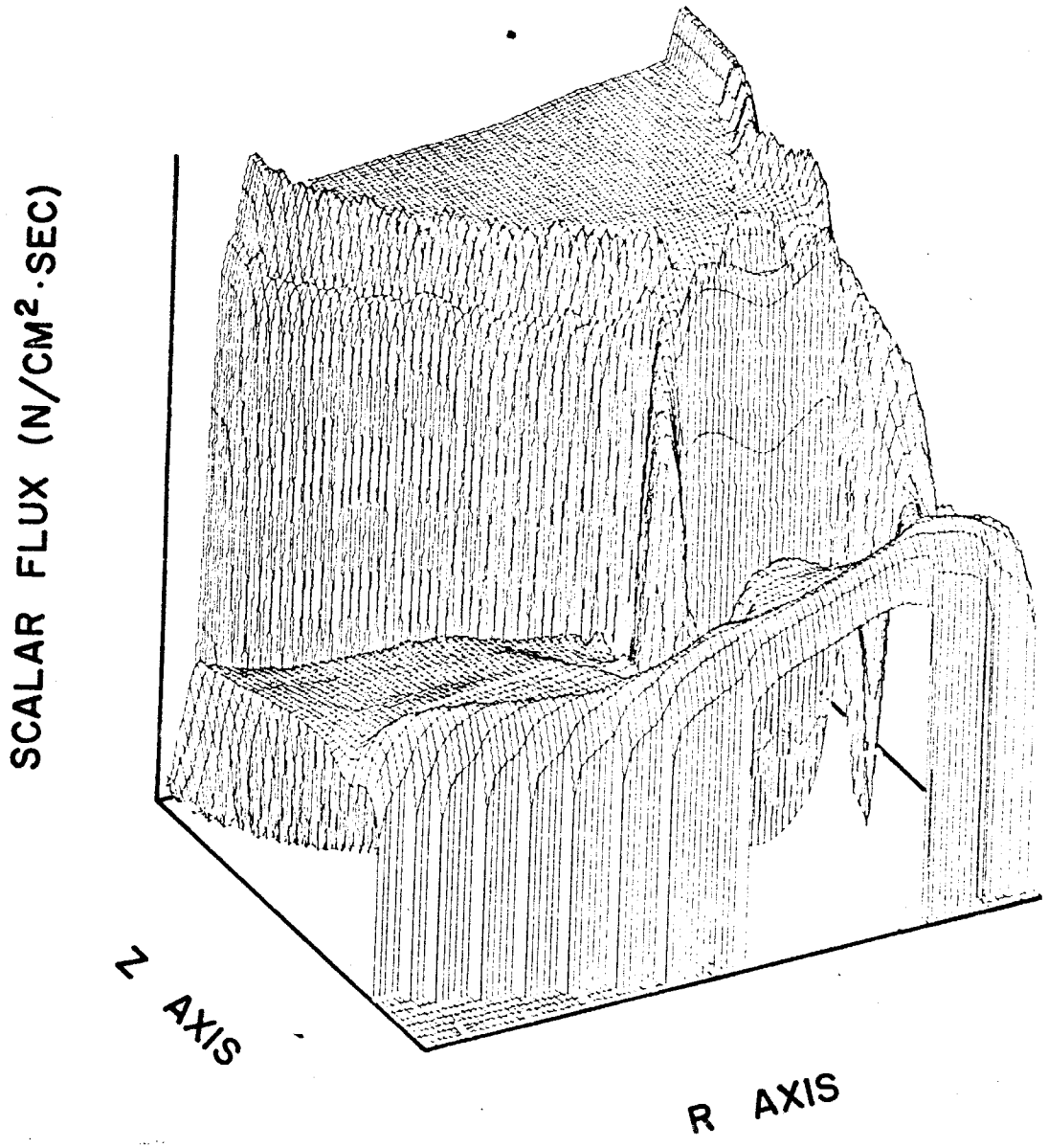

NEUTRON FLUX GROUP NO. 40

Figure 25